Springer Geology

Mingguo Zhai
Yue Zhao
Taiping Zhao *Editors*

Main Tectonic Events and Metallogeny of the North China Craton

Springer

Springer Geology

More information about this series at http://www.springer.com/series/10172

Mingguo Zhai · Yue Zhao
Taiping Zhao
Editors

Main Tectonic Events and Metallogeny of the North China Craton

Springer

Editors
Mingguo Zhai
Institute of Geology and Geophysics
Chinese Academy of Sciences
Beijing
China

Taiping Zhao
Guangzhou Institute of Geochemistry
Chinese Academy of Sciences
Guangzhou
China

Yue Zhao
Institute of Geomechanics
Chinese Academy of Geological Sciences
Beijing
China

ISSN 2197-9545 ISSN 2197-9553 (electronic)
Springer Geology
ISBN 978-981-10-1063-7 ISBN 978-981-10-1064-4 (eBook)
DOI 10.1007/978-981-10-1064-4

Library of Congress Control Number: 2016940320

Printed on acid-free paper

This Springer imprint is published by Springer Nature
The registered company is Springer Science+Business Media Singapore Pte Ltd.

Contents

About the Editors

Mingguo Zhai is Research Professor at the Institute of Geology and Geophysics, Chinese Academy of Sciences; Professor at Northwest University (China); Guest Professor at the University of Chinese Academy of Sciences and Jilin University, and Visiting Chair Professor at Sun Yat-Sen University. He received his B.Sc. (1976) from Northwest University (China), and his M.Sc. (1982) and Ph.D. (1989) from the Chinese Academy of Sciences. He was elected member of the Chinese Academy of Sciences (Academician) in 2009. His professional fields cover Precambrian geology, metamorphic geology, and petrology. His research focus is on early crustal evolution, continental geodynamics and metallogeny.

Yue Zhao is Research Professor and Vice-Director of the Institute of Geomechanics, Chinese Academy of Geological Sciences, Beijing. He earned Bachelor's degree in Geology from Changchun College of Geology in 1982 and MS degree in Structural Geology and Tectonics from the Chinese Academy of Geological Sciences in 1986. His research interests include structural and tectonic evolution of East Asian and the East Antarctica. He first proposed that the Jurassic deformations in northern North China Craton is related to geotectonics transition from Paleoasian system and Paleotethyan system to Paleopacific active continental margin of eastern Asia. He is also the first one explained the meaning of the Pan-African events in Prydz Bay, East Antarctica, and its inference on East Gondwana tectonics.

Taiping Zhao is Research Professor at the Guangzhou Institute of Geochemistry, Chinese Academy of Sciences. His research interests include magmatism and related ore-forming processes. He has been focused on the study of the igneous rocks and related ore deposits in North China Craton and East Qinling–Dabie orogenic belt in the last two decades. His current researches mainly include two aspects, major Precambrian geological events and related ore-forming processes on the southern margin of the North China craton, and the petrogenesis and tectonic settings of the Mesozoic granitoids and metallogeny of the associated Mo–Au–Ag–Pb–Zn ore deposits on the southern margin of the North China Craton.

1 Corresponding Main Metallogenic Epochs to Key Geological Events in the North China Craton: An Example for Secular Changes in the Evolving Earth

Mingguo Zhai and Xiyan Zhu

Abstract

Precambrian period is an oldest and longest eon from 545 Ma to about 4500 Ma, taking over ~90 % of the Earth's history. The 80–90 % continental crust in the Earth generated in Precambrian and records complicated geotectonic processes. The most important geological events in Precambrian tectonic evolution include Neoarchean enormous crustal growth, tectonic regime inversion from pre-plate tectonics to plate tectonics, and Great Oxidention Event (GOE) in Paleoproterozoic. The North China Craton (NCC) is one of oldest cratons in the world and records almost all the important geological events occurred in other cratons of the Earth. The NCC also demonstrates some special characteristics, such as multi-stage cratonization, Paleoproterozoic rift–subduction–collision event, Earth's paleo-climate and paleo-environment change, and Late Paleoproterozoic–Neoproterozoic multi-stage rifting event. These important geological events controlled mineralization with tectonic evolution and formed various and abundant ore deposits in the NCC. Here, we summarize geological events and metallogenic systems of the NCC and conclude that from Early Precambrian through Late Precambrian to Paleozoic and Mesozoic, the NCC records a transition from primitive- to modern-style plate tectonics. The NCC went through five major tectonic cycles: (1) the Neoarchean crustal growth and stabilization, (2) Paleoproterozoic rifting–subduction–accretion–collision with imprints of the Great Oxidation Event (GOE), (3) Late Paleoproterozoic–Neoproterozoic multi-stage rifting, (4) Paleozoic orogenesis at the margins of the craton; and (5) Mesozoic extensional tectonics associated with lithosphere thinning and decratonization. Coinciding with these major geological events, five major metallogenic systems are identified as follows: (1) Archean BIF system, (2) Paleoproterozoic Cu–Pb–Zn and Mg-B systems, (3) Mesoproterozoic REE–Fe–Pb–Zn system, (4) Paleozoic orogenic Cu-Mo system, and (5) Mesozoic intracontinental Au and Ag–Pb–Zn and Mo systems. The ore deposit types in each of these metallogenic systems show distinct characteristics and tectonic affinities. The NCC provides one of the best examples to address secular changes in geological history and metallogenic epochs in the evolving Earth. This regular pattern is suitable to other continent blocks in the world, which reveals coevolution and irreversible character of Earth system on material, structure, and environment.

Keywords

Geological events • Metallogenic epochs • North China Craton • Evolving earth

M. Zhai (✉)
Institute of Geology and Geophysics, Chinese Academy of Sciences, Beijing, China
e-mail: mgzhai@mail.igcas.ac.cn

M. Zhai · X. Zhu
State Key Laboratory of Geodynamics, Northwest University, Xian, Shaanxi, China

M. Zhai et al. (eds.), *Main Tectonic Events and Metallogeny of the North China Craton*, Springer Geology, DOI 10.1007/978-981-10-1064-4_1

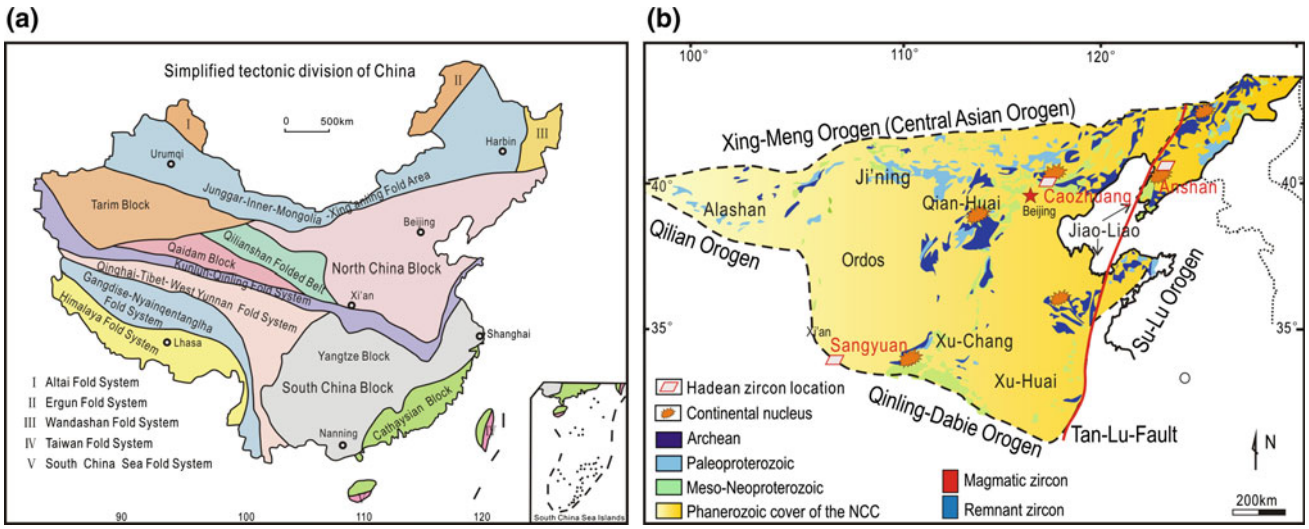

Fig. 1.1 **a** Chinese map of regional geological units (modified from Ren 1989); **b** sketch map showing early Precambrian rocks in the NCC

1.1 Introduction

The present continents went through long and complicated evolving histories, although they all are consisted of two fundamental litho-tectonic units, i.e., Precambrian craton and Phanerozoic orogenic belt. It is generally acknowledged that the Precambrian Era, from ca. 4.56–0.545 Ga covers almost 90 % of this planet's history and 60–80 % of the volume of crustal rocks were generated in the Archean (Brown 1979; Dewey and Windley 1981; Mclennan and Taylor 1983; Goodwin 1991). The Archean super-craton was probably similar in scale to the Phanerozoic Supercontinent Pangea (Rogers and Santosh 2003), but our knowledge of this segment of the early Earth history remains elusive. Surface processes and mantle dynamics as we observe today were probably different in the past and several questions have been raised including why the oldest rock is felsic orthogneiss, what the mechanisms of the growth and destruction of continental crust are, and when modern-style plate tectonics started operating on our globe. Precambrian terranes offer important clues to answer some of these problems.

Recently, author and others (Zhai and Santosh 2011, 2013; Zhai 2014; Zhai et al. 2015) summarized three key geological events in Earth's evolving history as follows:

1. Archean big-scale crustal growth and stabilization, indicating lithosphere formation and crust–mantle coupling.
2. Important tectonic mechanism transition from pre- through primitive- to modern-style plate tectonics.
3. Earth's geological environment changes from oxygen poor to oxygen enrichment.

Metallogeny, as specific material evolution record, shows clear characteristics of epoch-explosion and nonrepeatability corresponding to continental evolution.

The Chinese Continent consists of several cratons and surrounding orogenic belts (folded belts). Figure 1.1a is a Chinese regional tectonic map (after Huang et al. 1980; Ren 1989; Zhai 2013). The North China Block consists of the Precambrian metamorphic basement, Late Paleoproterozoic–Paleozoic sedimentary cover, and Mesozoic intrusives. It is traditionally termed as the North China Craton or Sino-Korea Craton. The North China Craton (NCC) covers over 300,000 km^2 (Fig. 1.1b). Although a relatively small craton among the major Archean cratons on the globe, the NCC has attracted considerable attention in terms of its complex evolutionary history during the Precambrian and Phanerozoic, with the preservation of some of the oldest rock records ranging up to ~3.8 Ga, and also because of its abundant mineral resources (Cheng 1994; Zhai 2010; Fig. 1.1b).

The crustal growth and stabilization of the NCC relate to three major geological events in the Precambrian.

1. A major phase of continental growth at ca. 2.7 Ga, and the amalgamation of micro-blocks and cratonization at ca. 2.5 Ga: The major period of continental growth during 2.9–2.7 Ga in the NCC correlates with the global growth of the Earth's crust recognized from other regions. The enormous volume of tonalite–trondhjemite–granodiorite (TTG) rocks and associated komatiite-bearing magmatic suites developed during this period possibly suggest the manifestation of plume tectonics. The cratonization of the NCC at the end of Neoarchean at ca. 2.5 Ga (Archean–Proterozoic boundary) through the amalgamation of micro-blocks was accompanied by granulite facies metamorphism and voluminous intrusion of crustally derived granitic melts leading to the construction of the basic tectonic framework of the NCC.
2. Paleoproterozoic rifting and subduction–accretion–collision tectonics during ca. 1.95–1.82 Ga (The Hutuo

Movement): The next major imprint in the NCC is the Paleoproterozoic orogenic events during 2.35–1.97 Ga which involved rifting followed by subduction–accretion–collision processes. The Paleoproterozoic volcanic-sedimentary rocks record GOE on stable isotopic elements and trace elements. Extreme crustal metamorphism and formation of high-pressure (HP) and ultra-high-temperature (UHT) regions during 1950–1830 Ma accompanied the subduction–collision process and suturing of continental blocks within the Paleoproterozoic supercontinent Columbia. With the emplacement of extensive mafic dyke swarms associated with continental rifting, and the intrusion of anorogenic magmatic suites, the evolution of the NCC into a stable continental platform was finally accomplished.

3. Meso-Neoproterozoic multi-rifting events with vast and thick sedimentary sequences deposited on the early metamorphic basement: After when the NCC evolved into a stable platform or para-platform tectonic setting in Earth's middle age period extending longer than ~1.0 Ga, vast and thick Late Proterozoic–Neoproterozoic sedimentary sequences were extensively deposited on the early metamorphic basement. Four stages of magmatic activity are recognized during the Late Paleoproterozoic–Neoproterozoic, which suggest that the NCC was situated in a within-plate setting for an extended time from ~1.8 to ~0.7 Ga or even younger, and the magmatic events were associated with multi-stage rifting activities. Zhai et al. (2015) suggest that the Earth's middle age represents a particular tectonic evolution period, during which the Earth had a stable lithosphere with underlying secular warm mantle that resulted in multi-magmatism and rifting from Late Paleoproterozoic to Neoproterozoic.

Another two geological events took place in the NCC are Paleozoic (Triassic) orogenesis at the margins of the craton; and Mesozoic (Cretaceous) extensional tectonics associated with lithosphere thinning and decratonization.

Coinciding with these major geological events, five major metallogenic systems are identified as follows: Archean BIF system, Paleoproterozoic Cu–Pb–Zn and Mg-B systems, Mesoproterozoic REE–Fe–Pb–Zn system, Paleozoic orogenic Cu-Mo system, and Mesozoic intracontinental Au and Ag–Pb–Zn and Mo systems. The ore deposit types in each of these metallogenic systems show distinct characteristics and tectonic affinities. Metallogeny diversified with time, from the dominant BIFs in the Archean to polymetallic deposits in the Proterozoic and Phanerozoic. Figure 1.2 is a sketch map showing distribution of ore deposits in the NCC.

More than five major metallogenic systems in the NCC is closely related to some of the major geological tectonic events on the globe, and shows a regular pattern and systematic change with time from Early Precambrian to Mesozoic on the type of metal, nature of mineral deposit, spatial distribution, mechanisms of formation, and metallogenic system. Therefore, the NCC provides a key area to address the relationship between geological process and ore-mineralization. As an excellent case, the metallogenesis in the NCC provides to address the link between metallogenic processes and secular changes in the Earth System, including mantle dynamics and crust–mantle interaction on a global perspective.

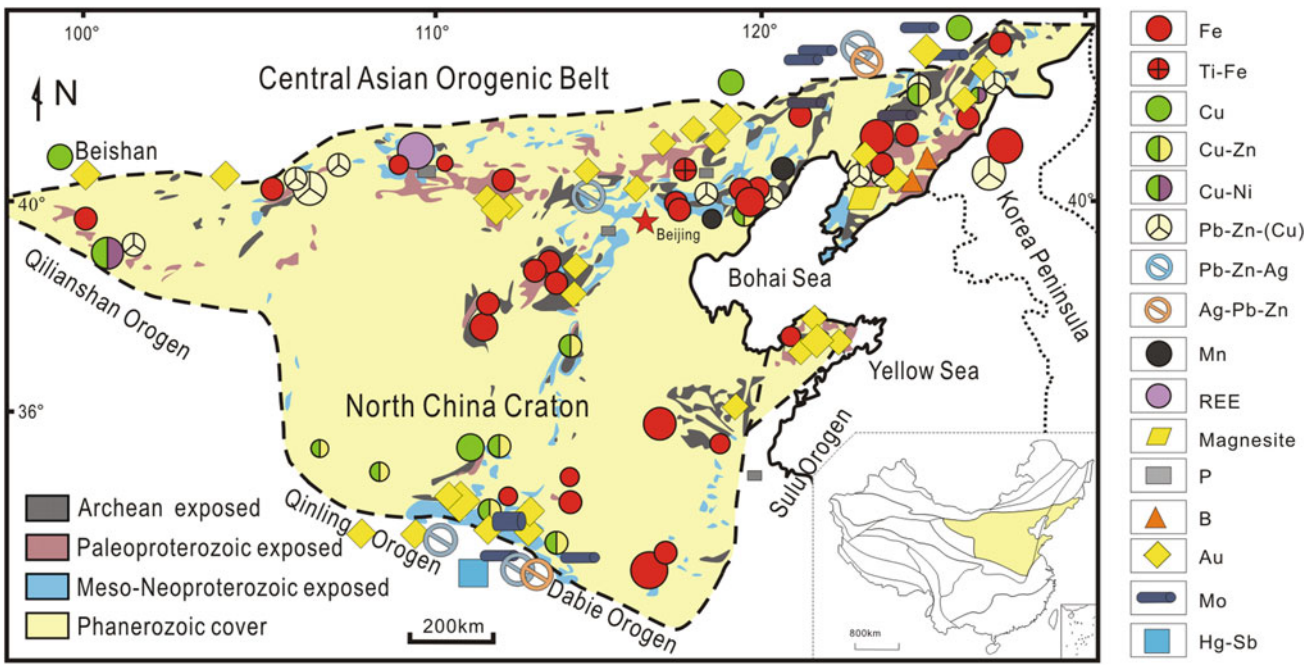

Fig. 1.2 Sketch map showing distribution of ore deposits in the NCC

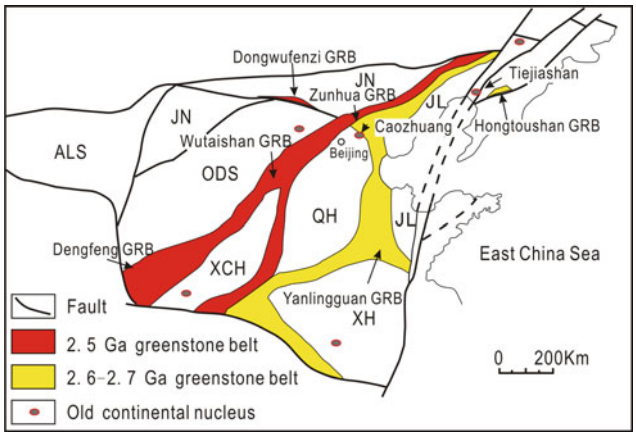

Fig. 1.3 Distribution of Archean greenstone belts and micro-clocks in the NCC

1.2 Precambrian Multi-stage Crustal Growth and BIF Metallogenic System

1.2.1 Precambrian Multi-stage Crustal Growth

The NCC has a history with multi-stage crustal growth, and finally established cratonization at the end of Neoahcean (~2.51–2.45 Ga).

Our studies propose that the NCC can be divided into six micro-blocks with ≳3.0–3.8 Ga old continental nuclei that are surrounded by Neoarchean greenstone belts (GRBs). The micro-blocks are also termed high-grade regions (HGRs) and are mainly composed of orthogneisses with minor gabbros and BIF-bearing supracrustal beds or lenses, all of which underwent strong deformation and metamorphism of granulite to high-grade amphibolite facies. The micro-blocks are, in turn, from east to west, the Jiaoliao (JL), Qianhuai (QH), Ordos (ODS), Ji'ning (JN) and Alashan (ALS) blocks, and the Xuchang (XCH) blocks in the south (Fig. 1.3). Recent studies led to a consensus that the basement of the NCC was composed of different blocks/terranes that were finally amalgamated to form a coherent craton at the end of Neoarchean.

Six > 3.3 Ga old continental nuclei have been proposed (in Fig. 1.3, Zhai and Liu 2003). Recently, more Archean rocks have been acquired from drilling cores and small outcrops in the Ordos that is covered by Phanerozoic sedimentary rocks (e.g., Wang 2013). ~4.1 Ga Hadean zircon grain was reported from the Ordovician ignimbrite, which is in a low-grade greenschist facies terrigeneous clastic-volcanic association in Sangyuan, the North Qinling Orogenic Belt (Wang et al. 2007, see Fig. 1.1b), and it is believed that are trapped zircons from basement rocks in the southern margin of the NCC. The Cameca IMS 1280 analysis gave a U–Pb age of 4027 ± 12 Ma. The ε_{Hf} (t) and two-stage model age (T^2_{DM}) for the core are −4.6 and 4449 Ma, respectively, and for the rim they are −7.1 and 4357 Ma, respectively (Diwu et al. 2013). Combining the oxygen isotopic and REE data, these zircons were believed to come from 4449 Ma orthogneiss with perhaps the intermediate generation of TTGs and experience water–rock interaction in ca. 4027 Ma, similar to zircons reported from Jack Hill.

Zircon U–Pb isotopic ages of ≧3.8 Ga have been reported near Anshan, northeast China and near Caozhuang, eastern Hebei in the NCC, indicating the presence of old continental crust at least from two localities (see Fig. 1.1b). The Tiejiashan complex in Anshan area is composed of trondhjemitic-quartz diorite gneisses and granitic gneiss with subordinate meta-sedimentary rocks. The trondhjemitic and granitic gneisses show two zircon populations with ages 3805 ± 5 Ma and 3300 Ma (Liu et al. 1992; Wan et al. 2001). The Caozhuang complex in Eastern Hebei is composed of a suite of volcano-sedimentary rocks metamorphosed to upper amphibolite to granulite facies. Tonalitic magmas (ca. 3.3 Ga; U–Pb zircon age) intruded into the Caozhuang supracrustal rocks (Zhao et al. 1993). Detrital zircons from the fuchsite quartzite show two prominent U–Pb age peaks of 3794 ± 15 Ma and 3733 ± 17 Ma, and single-stage Hf modal ages between 3965 and 3633 Ma with a mean age of 3799 Ma (Wu et al. 2005). ~3.3 Ga zircon ages in TTG gneisses and metamorphosed supracrustal rocks from the Anshan and Caozhang areas have been reported and interpreted as a reworking of ancient crust and magmatic event (Zhai 2014).

Zircon U–Pb data show that TTG gneisses in the HGRs have two prominent age peaks at ca. 2.9–2.7 Ga and 2.6–2.5 Ga which may correspond to the earliest events of major crustal growth in the NCC. Hafnium isotopic model ages range from ca. 3.8 to 2.5 Ga and mostly are in the range of 3.0–2.6 Ga with a peak at 2.82 Ga. Recent studies reveal a much larger volume of TTG gneisses in the NCC than that previously considered, with a dominant ca. 2.7 Ga magmatic zircon ages. Most of the ca. 2.7 Ga TTG gneisses underwent metamorphism in 2.6–2.5 Ga as indicated by ubiquitous metamorphic rims around the cores of magmatic zircon in these rocks. Abundant ca. 2.6–2.5 Ga orthogneisses have Hf-in-zircon and Nd whole-rock model ages mostly around 2.9–2.7 Ga and some around 2.6–2.5 Ga, indicating the timing of protolith formation or extraction of the protolith magma from the mantle (Fig. 1.4a). Therefore, it is suggested that the 2.6–2.5 Ga TTGs probably represent a coherent event of continental accretion and major reworking (crustal melting).

Figure 1.4b is a diagram of Archean–Paleoproterozoic zircon formation age versus zircon $^{176}Hf/^{177}Hf$ ratios from the

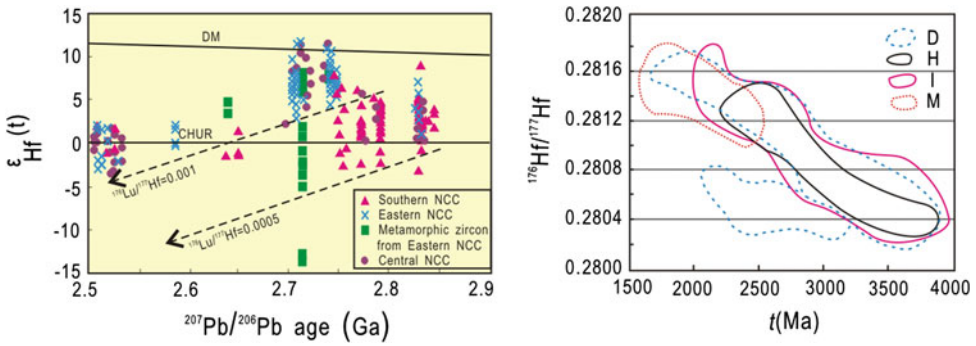

Fig. 1.4 **a** ε_{Hf} versus $^{207}Pb/^{206}Pb$ age plot of TTGs in the NCC (modified from Zhai and Santosh 2011); **b** Zircon formation age versus zircon $^{176}Hf/^{177}Hf$ ration diagrams. d-detrital zircons, h-inherited zircons, I-magmatic zircons, M-metamorphic zircons (modified from Geng et al. 2012 with new data see text references)

NCC. Four kinds of zircon have been classified, which are detrital zircons (D), inherited zircons (core, H), magmatic zircons (I), and metamorphic zircons (rim, M). The fields of I and H zircons in Fig. 1.4b demonstrate a regular change trend of increasing $^{176}Hf/^{177}Hf$ ratios along with decreasing ages from <4000 to ~1600 Ma (Geng et al. 2012), indicating more material from continental source. Paleoproterozoic magmatic zircons were mainly selected from ~2.35 to 2.0 Ga granites. Metamorphic zircons yield ~2.5–1.8 Ga age peak, and their high $^{176}Hf/^{177}Hf$ ratios are attributed to affection of metamorphic fluid. Detrital zircons were mainly collected from Proterozoic sedimentary rocks. They fall into two fields, one of which is similar to H and M zircons, another of which has low $^{176}Hf/^{177}Hf$ ratio, probably were affected in supergene process.

As a distinct characteristic, nearly all GRBs in the NCC underwent amphibolite facies metamorphism. Zircon U–Pb ages of metamorphosed GRB mafic rocks mainly show two peak ranges at ~2.6–2.5 and 2.8–2.7 Ga. The mafic rocks are commonly believed to be derived from metabasalts, and possibly that the ages represent the time of metamorphism. The tectonic settings of the GRBs are still a problem. Their geochemical characteristics are, respectively, similar to back-arc basins, rifts, island arcs or suggest imprints of mantle plumes. BIFs occur in all GRBs but also in the HGRs. This metallogenic specificity is quite different from all Phanerozoic geotectonic settings.

The ~2.5 Ga metamorphic-magmatic event is stronger than in most other cratons in the world. How to understand the geological significance of the 2.5 Ga event? The following points are emphasized: (1) nearly all old rocks >2.5 Ga underwent metamorphism at ~2.52–2.5 Ga; (2) Archean basement rocks in the NCC experienced strong partial melting and migmatization; (3) granitoid rocks derived from partial melting include potassium granites, TTG granites and monzonites. These granitoids rocks intruded both the Archean greenstone belts and micro-blocks; (4) ~2.5 Ga mafic dikes (amphibolites), granitic dikes (veins) and syenitic-ultramafic dykes are also developed. Therefore, we suggest an assembly model that all micro-blocks in the NCC were welded together by late Archean greenstone belts at the end of the late Neoarchean. We also propose that the various micro-blocks were surrounded by small ocean basins, and the old continental crust and the oceanic crust were hotter than today. Subduction and collision were on much smaller scales as compared to the Phanerozoic plate tectonic regime, although the tectonic style and mechanisms were more or less similar. The formation of crustal melt granites is one of the processes of cratonization, inducing generation of stable upper and lower crustal layers. This process also generated an upper crust of more felsic composition and a lower crust of more mafic composition, due to molten residual materials and some underplated gabbros.

1.2.2 Archean BIF Metallogenic System

BIFs occur extensively throughout the Archean units in the NCC, and four major iron metallogenic provinces have been identified: Anshan in NE China, Eastern Hebei and Wutai in northern NCC, and Xuchang–Huoqiu in southern NCC. The BIFs have been metamorphosed to granulite facies and display strong deformational features. The BIFs occur not only in the greenstone belts, but also in HGRs within the all micro-blocks, mostly in association with mafic metavolcanics suggesting the imbrication of oceanic crust and pelagic sediments onto the continent during early accretionary growth of the NCC. The Archean high-grade domains in the NCC consist of upper amphibolite to granulite facies TTG gneisses, amphibolites, metagabbros and minor supracrustal rocks. Lenses and boudins of the BIFs of different sizes occur as enclaves within the orthogneisses with or without associated meta-supracrustal rocks. The host orthogneisses and associated supracrustal rocks yield ~3.3–2.55 Ga zircon U–Pb ages, suggesting that BIFs formed

Table 1.1 Correlation table of Archean and Early Proterozoic BIF-bearing supracrustal rocks in North China Craton

District	Archean					Early Proterozoic	
	Early	Middle		Upper			
	HR1	HR2	GB2	HR3	GB3	Lower part P1	Upper part P2
E.Hebei	Caozhuang (>3.0)	Qianxi (2.8-3.0)			Qinglonghe (2.5) Dantazi (2.5)		
Anshan(NE China)		Baishanzhen Gr. (2.5) Longgang	Lower Qingyuan (2.8)	Anshan (2.7-2.5) Sandaogou (2.5)	Qingyuan (2.5)		
Wutaishan-Taihangshan (Shanxi Prov.)		Fuping (>2.6) Sushui		Jiehekou	Wutai (2.5)		
Yinshan (Inner Mougoulia-North Shanxi Prov.)		Jining (>2.8)				Erdaowa	
Taishan (Shandong Prov.)				Taishan Jiaodong	Yanlingguan (2.7-2.5)	Yuanjiacun	
Southern Margin (Henan Prov. And Anhui Prov.)				Taihua (2.7-2.5)	Huoqiu Dengfeng (2.5)	Upper Huoqiu	

HR= high grade region; GB= greenstone belt; P= Proterozoic; Arabic numerals= isotope age (Ga)

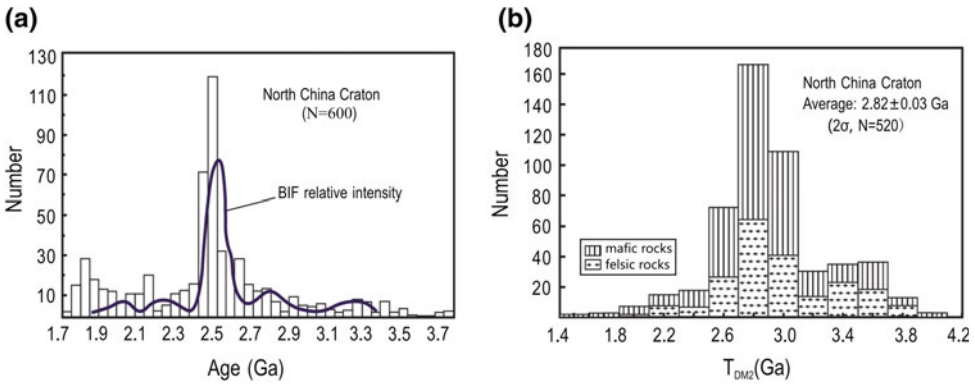

Fig. 1.5 Relationship between BIFs and volcanic activities (**a**) and TTGs (**b**)

during Meso to Neoarchean. Table 1.1 shows the correlation of Archean and Early Proterozoic BIF-bearing supracrustal rocks in the NCC.

Although BIFs were developed accompanied by continental growth epochs in early Precambrian era since ~3.3 Ga in the NCC, Late Neoarchean (2.65–2.5 Ga) is a peak iron ore-forming period according to new chronological data (Zhang et al. 2012a). It is difficult to determine age of BIFs. The zircons U–Pb zircon ages from interlayered amphibolites are usually to restrict BIF's ages. Protolith rocks of amphibolites are suggested to be metamorphosed volcanic rocks and formed at same time as BIF's precipitation. Zhang et al. (2012a) suggested that core ages and rim ages of zircons are, respectively, forming ages and metamorphic ages. Figure 1.5a, b show ages of volcanic activities and TTG gneisses in the NCC. The peak times are 2.5–2.65 Ga for volcanic rocks (amphibolites) and 2.82 Ga for TTGs, respectively. Therefore, Zhang et al. (2012a) conclude that peak time of BIFs is synchronized with amphibolites and youger than TTGs. In fact, the protoliths of amphibolites interlayered with BIFs are basalts. Volcanic magmatic zircons are rarely found in basalts. Thus, most zircons from amphibolites are metamorphic zircons rather than magmatic zircons. Figure 1.4a shows that ~2.5 Ga zircons from TTGs are classified into two groups on basis of $\varepsilon_{Hf}(t)$ range from −4 to +3, indicating a part of ~2.5 Ga TTGs are reworked older TTGs. We have reasons to suggest that a part of amphibolites, at least, are reworked metabasites. A lot of BIFs should form earlier than ~2.5 Ga (Fig. 1.5a), and it is possible that is synchronous as TTGs (Fig. 1.5b).

Recently, Zheng et al. (2015) report that the Xingshan BIF ore deposit, which is located in the Caozhuang area, eastern Hebei, is hosted in amphibolites (Fig. 1.6). Zircons from amphibolite yield U–Pb ages (LA-ICP-MS) are 2859 ± 22 Ma and 2491 ± 13 Ma. These two ages are probably metamorphic ages, although Zheng et al. (2015) suggest that 2859 ± 22 Ma zircon perhaps magmatic zircons and metamorphic zircons on the basis of CL images.

The oxygen isotopic compositions of the BIFs in the NCC have been reported by Wei (1985) and Zhai (1993).

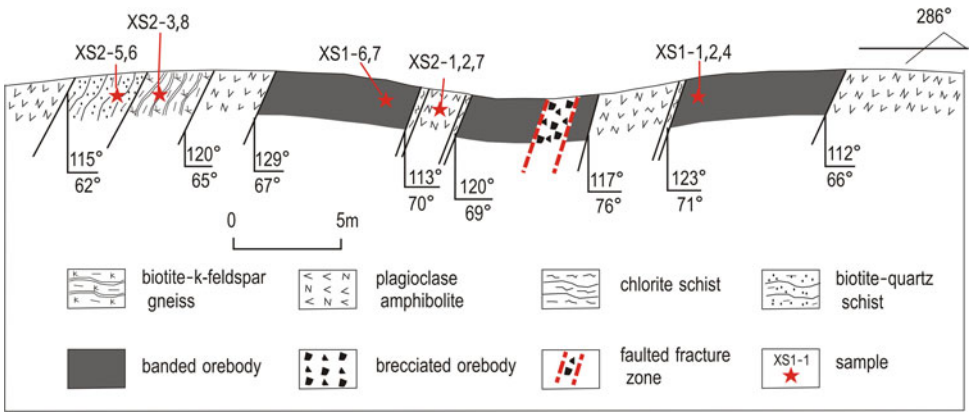

Fig. 1.6 Geological profile of Daxingshan orebody at the depth of −75 m in Xingshan BIF ore deposit (after Zheng et al. 2015)

The $\delta^{18}O$ values of magnetite from the BIF range from −5.04 to +6.16 ‰, and that of hematite shows a range of −3.79 to +1.44 ‰. The samples from drillings do not show any obvious change from depth to surface. The $\delta^{18}O$ values of quartz in BIF in surface range from +5.22 to +16.13 ‰, with most of the values concentrated between +8 to and +11 ‰. The $\Delta\delta^{18}O$ values of BIF in drill holes range from +7.97 to +16.22 ‰, and most values are around +13 to +14 ‰. The temperatures calculated by oxygen isotopic thermometer are 400–500 °C. The $\delta^{18}O$ values of quartz in the BIF are 16.7–22 ‰ estimated by extrapolation, similar to the $\delta^{18}O$ value of quartz in BIF from Isua, West Greenland and the $\delta^{18}O$ value of SiO_2 in the Archean ocean (Perry and Ahmad 1987). Therefore, Zhai (1993) proposed that the BIFs in the NCC formed in a weakly oxidized shallow sea environment with PH value of 6–8 and Eh value of 0–0.3, with the depth of precipitation estimated as about 244–549 m, at a distance from the shoreline of about 37 km (Goodwin 1973; Zhai 1993). From regional geology, lithologic association geochemical features of the associated metavolcanics and orthogneisses, Zhai and Windley (1990) suggested that the high-grade type of BIF formed in arcs, which were intruded by voluminous tonalities and granodiorites, which were later converted by deformation and high-grade metamorphism into orthogneisses. The greenstone type of BIF formed in a geological environment similar to rifts or back-arc basins and arcs. However, the above suggestion is controversial by comparison with Phanerozoic geotectonic setting, where no any BIF-bearing is of rift or back-arc basin and arc affinities.

1.2.3 Great Oxidation Event and Mg-Boron-Graphite System

Some of the 2.35–1.97 Ga rift-margin and passive continental margin deposits, volcanic rocks, and BIF-bearing rock formations in old cratons seem to belong to an important geological event in the early Earth's history, termed the GOE or Lomagundi and Jatulian Event (Zahnle et al. 2006; Konhauser et al. 2009; Sato 2009; Tang et al. 2011). The GOE is the appearance and continuous increase of oxygen in atmosphere in ~2.35–2.1 Ga closely following a global glacial epoch (Fig. 1.7). The model for GOE generation and evolution can be summarized as two types up to the end of twenties century (Zhao 2010): the first one is so-called C-W-K-O model which postulates an atmosphere prior to 2.2 Ga with $p(O_2)$ level between 10 and 13 and 0.1 % of present atmospheric level (PAL), and a dramatic rise of $p(O_2)$ to >15 % PAL between 2.2 and 2.0 Ga; the second one is D-K-O model which postulates an essentially constant atmospheric $p(O_2)$ level (probably within ±50 % of PAL) since ~4.0 Ga. Another oxygen increasing event took place in Neoproterozoic after Neoproterozoic snow ball event (see Fig. 1.7), and gave rise to Cambrian life exploration. The worldwide 2.33–2.06 Ga unique positive $\delta^{13}C_{carb}$ excursion has been correlated with the GOE (Anbar et al. 2007; Konhauser et al. 2009; Zhao 2010). The GOE event marks a sudden change in Earth's environment from oxygen-poor to oxygen-rich (e.g., Young 2012).

In the NCC, Paleoproterozoic volcano-sedimentary rocks are extensively distributed. Chen et al. (1991) paid attention to thick sedimentary strata of graphite-bearing paragneiss and magnesite developed in the northeastern, northern and southern NCC, and indicated that Paleoproterozoic geological environment was probably experienced an enormous transformation. The further studies demonstrate that the NCC records the GOE during 2.35–2.0 Ma coincident with similar global events. It is represented by the deposition of vast and thick magnesite-marble-graphite rocks which were later metamorphosed to felsic gneisses. The abundant carbonates and evaporates in northeastern (NE) China show clear positive $\delta^{13}C_{carb}$ excursion, with geological and geochemical characteristics similar to those proposed for the global GOE event (Chen et al. 2000; Tang et al. 2009, 2011). However, Proterozoic sedimentary BIFs (Superior type) are not developed in the NCC, which occur probably in several locations with small-scale in Shanxi and Henan provinces only. Zhai and Santosh (2013) proposed that there were

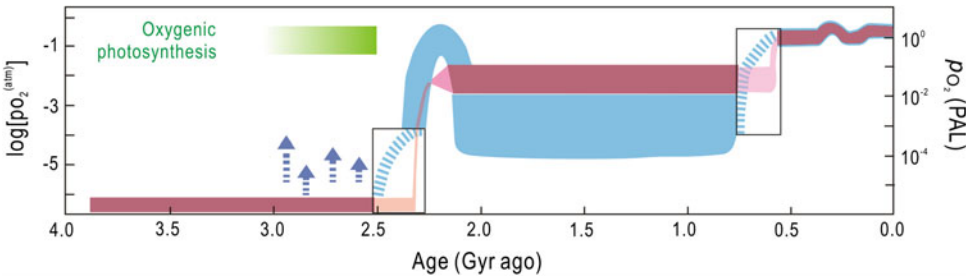

Fig. 1.7 Atmospheric oxygen level change with age (modified after Chen Y.J., oral speak, 2015)

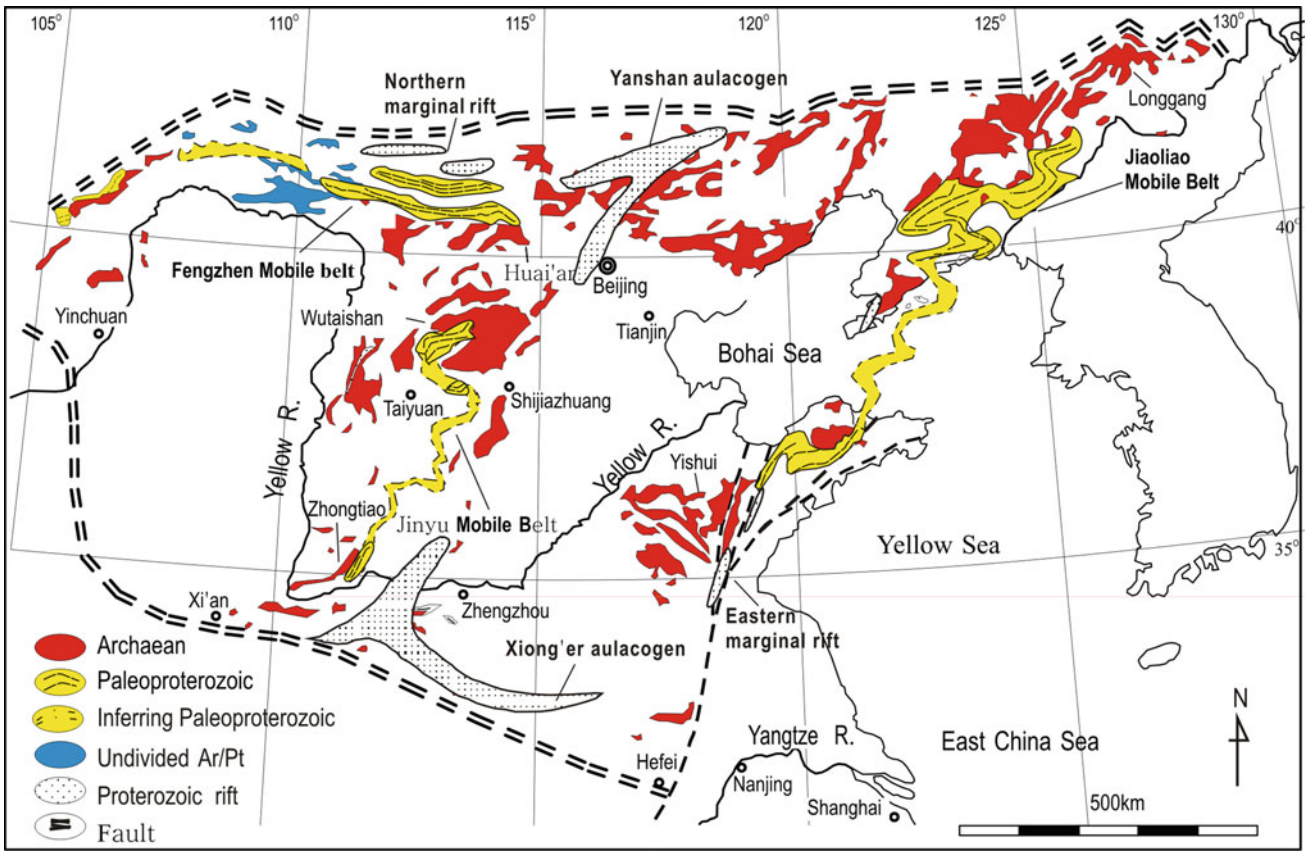

Fig. 1.8 Paleoproterozoic mobile belts and Meso-Neoproterozoic rifts in the NCC (after Zhai and Santosh 2011)

several remnant ocean basins that formed in Late Neoarchean and rift basins with shallow water depth formed in Paleoproterozoic during 2350–1970 Ma in the NCC, where evaporates and carbonates were deposited, in the absence of BIF. This is in contrast to some of the other regions of the world such as Superior of Canada, where a huge volume of BIFs was deposited (Zhao 2010).

The magnesite-bearing sedimentary sequences in the lower Liaohe Group occur only in the Jiaoliao mobile belt (Fig. 1.8), whereas the graphite-bearing sedimentary sequences occur widely in the northeastern, northwestern, central and southern NCC. The Liaohe Group includes the lower Langzishan, Lieryu, Gaojiayu, Dashiqiao and Ganxian Units (Formations), with a total thickness of 2959 m. The detrital zircon U–Pb ages range from 2242 to 2025 Ma, whereas the zircons from felsic fine- grained gneiss (meta-rhyolite) and granite vein in the Dashiqiao Formation show ages between 2179 and 2173 Ma (Li et al. 2012). These rocks underwent greenschist-amphibolite facies metamorphism. The Dashiqiao Formation hosts the giant Dashiqiao magnesite deposit, with a thick (1144 m) orebody. Boron-ore hosted in the fine-grained felsic gneiss occur in the Lieryu Formation, and sedimentary Pb–Zn ore deposits are also developed in the Gaojiayu Formation.

Tang et al. (2009, 2011, 2012) recently evaluated the impact of the GOE in the NCC based on investigations of the Dashiqiao giant magnesite deposits. The dolomitic-marble samples with 0.91 ± 0.03 of CaO/MgO (mol) ratios

show higher $\delta^{13}C_{PDB}$ values of 0.6–1.4 ‰ (av. 1.2 ± 0.3 ‰) than those of normal marine carbonates over the globe. However, they display lower $\delta^{18}O_{SMOW}$ of 16.4–19.5 ‰ (av. 18.2 ± 1.1‰) as compared to their contemporaneous counterparts, suggesting that the primary carbonates in the Dashiqiao Formation possess positive $\delta^{13}C$ anomaly (possibly 4.2 ‰) reflecting the impact of the GOE. The $\delta^{13}C$ and $\delta^{18}O$ have been depleted inpost-sedimentation diagenesis and/or regional metamorphism. The >550 m thick magnesite layer in the studied section has CaO/MgO ratios of 0.01–0.23 (av. 0.12 ± 0.1, n = 6). These rocks show $\delta^{13}C$ and $\delta^{18}O$ values of 0.1–0.6 ‰ and 9.2–12.7 ‰, with average values of 0.4 ± 0.2 ‰ and 10.9 ± 1.4 ‰, respectively. These values are lower than those of the underlying dolomites (Fig. 1.9). The depletions of ^{13}C and ^{18}O in magnesites relative to dolomitic marbles reflect hydrothermal alteration related to regional metamorphism leading to rock recrystallization and mass exchange. This inference is supported by the hanging-wall dolomitic marble and the veinlet-filled magnesite from ore layer. The former contains mega-crystals of cylindrical talc with $\delta^{13}C$ of −2.6 ‰ and $\delta^{18}O$ of 14.1 ‰, indicating that a local fluid-rock interaction between (argillic) dolomite and (siliceous) hydrothermal fluids poor in ^{13}C and ^{18}O resulted in the formation of talc and further depletion both in $\delta^{13}C$ and in $\delta^{18}O$. The veinlet-filled magnesite shows $\delta^{13}C$ and $\delta^{18}O$ values of −2.7‰ and 16.2 ‰. Their $\delta^{13}C$ values are lower and $\delta^{18}O$ values are higher as compared to those of massive magnesite in the adjacent strata. These features support the interpretation that the massive magnesite interacted with low-$\delta^{13}C$ fluids which were possibly sourced from low temperature meteoric during the post-ore stage. Thus, the formation of the Dashiqiao magnesite deposits involved primary sedimentation, diagenesis, regional metamorphism, hydrothermal replacement, and local post-ore fluid-rock interaction.

As an important and typical metallogenic type related to LOE, Superior-type BIFs are associated with clastic-carbonate rocks. They are larger and their deposition occurred in relatively shallow marine conditions under transgressing seas, perhaps on the continental shelves of passive tectonic marginsor in intracraton basins (González et al. 2009). Significant aspects of earth history, such as the atmospheric evolution of early earth, the geochemistry of the Ancient Ocean and records of early organisms, can be better understood via these BIFs. Recent studies suggested that several BIF deposits in the NCC are probably belonged to the Superior-type BIFs, although their research are preliminary and their deposit scales are much smaller than Archean BIFs in the NCC.

The Yuanjiacun BIF, located in the Lüliang area of Shanxi Province, is found in the sedimentary rock succession of the Paleoproterozoic Yuanjiacun Formation (2.3–2.1 Ga) of the Lüliang Group. Primary microbands are laterally continuous and defined by an alternation of iron-rich and quartz-rich microlaminae. These microbands display weak deformation even though they have undergone greenschist-to low-amphibolite facies metamorphism. Subhedral-anhedral magnetite grains intergrown with quartz constitute the predominant mineral assemblages of the Yuanjiacun BIF; other minerals are rarely present. Geochemical analyses of the Yuanjiacun BIF samples show low abundances of Al_2O_3 and TiO_2 (<0.5 %) and of trace elements such as Th, Hf, Zr, and Sc (<1.5 ppm) and lack of co-variance between Al_2O_3 and TiO_2, revealing that the Yuanjiacun BIF samples are very pure chemical sediments with negligible contamination from crustal detritus. REE+Y patterns are typical of ambient seawater, including positive La and Y anomalies and HREE

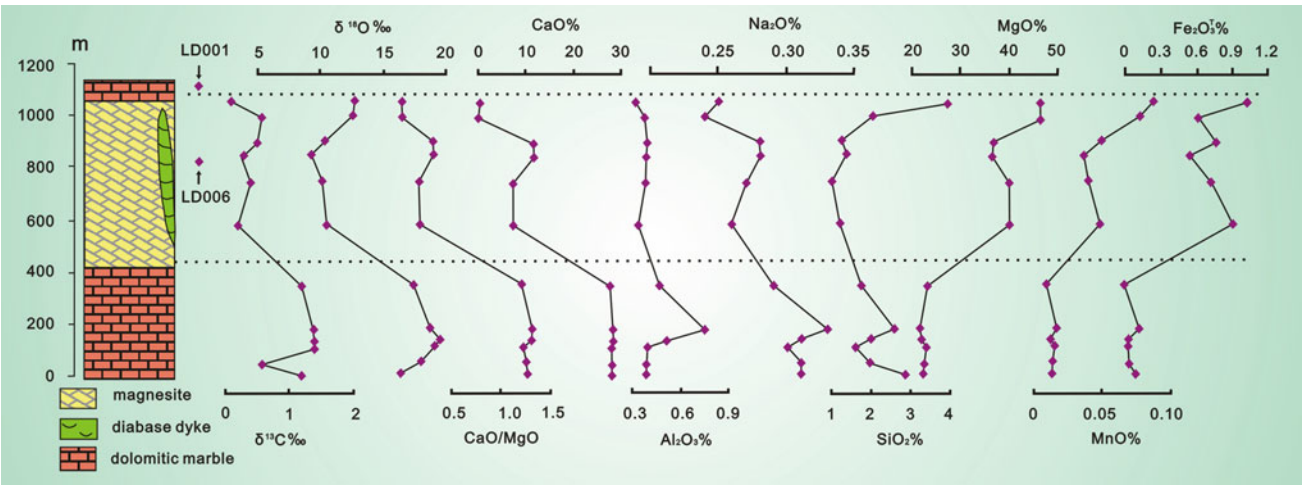

Fig. 1.9 Stratigraphic column and chemical variations of the Dashiqiao magnesite deposit

enrichment relative to LREE in PAAS-normalized REE diagrams. These REE + Y patterns are imprinted by high-*T* (>250 °C) hydrothermal fluid, characterized by consistently positive Eu anomalies. The observed small-scale variation of Eu anomalies may indicate short-term variability of $(Eu/Eu^*)_{SN}$ ratios of seawater, most likely resulting from temporal variation of the activity of high-*T* fluids rather than post-depositional metamorphism. The overall geochemical features of the Yuanjiacun BIF are very similar to those of the Superior-type BIFs. Therefore, Wang et al. (2014) suggested that the Yuanjiacun BIF appears to have formed near the redoxcline and lower level reduced marine water under the specific redox conditions of the ancient ocean may be related to the GOE.

1.2.4 Paleoproterozoic Rifting–Subduction–Collision

The NCC behaved as a stable continent block during ~2500–2350 Ma (Condie 2001, 2004), subsequent to which continental rifting was initiated during ~2350–2000 Ma, similar to other cratons in the world (Condie and Kröner 2008). Some of the 2.35–1.97 Ga rift-margin and passive continental margin deposits, volcanic rocks and BIF-bearing rock formations in other cratons seem to be comparable with those in the NCC, which are formed in relative oxygen enrichment environment like the GOE as mentioned above. The Paleoproterozoic rifts widened into ocean basins, and following which subduction was initiated. The subduction–accretion–collision process built three major collisional sutures (mobile belts) during Late Paleoproterozoic, which are traditionally termed the Hutuo Movement (or Lüliang Movement). These linear fold belts show imprints of intense deformation and the high-grade metamorphic orogens in these belts show P-T conditions corresponding to HP and high ultra-high-temperature. They are distinct from the Archean granite-greenstone belts, and display characteristics similar to Phanerozoic orogenic belts including the preservation of volcanic-sedimentary strata, deformation style and degree of metamorphism. The representative rock sequences are the Liaohe Group and the Fengzishan Group in the Jiaoliao belt, the Lüliang Group, the Hutuo Group and Zhongtiao Group in the Jinyu belt, and the Fengzhen Group and the Erdaowa Group in the Fengzhen belt. The rock sequences in these mobile belts are typically divided into two formations. The lower formation is composed of basic-acid volcanic and sedimentary rocks metamorphosed to low-grade amphibolite-greenschist facies. The volcanic rocks display bimodal features and geochemical characteristics suggestive of within-plate or island-arc type affinity. The upper formation is layered detrital–argillite–carbonate sedimentary rocks. The sedimentary rocks include argillaceous schists, siltstones and marbles, with the common presence of graphite, and have been metamorphosed to granulite facies under temperatures of 800–850 °C (HT). These rocks are popularly known as the khondalite sequence. In the Fengzheng belt, the khondalite sequence of rocks has witnessed extreme thermal metamorphism under ultra-high-temperature (UHT) conditions (Santosh et al. 2012; Guo et al. 2012). The Mg- and Al-rich varieties of these rocks carry diagnostic UHT indicator minerals including sapphirine-bearing assemblages, which yield metamorphic temperatures of 900–1000 °C. The Paleoproterozoic collisional belts indicate that the NCC experienced a major rift–subduction–collision process during ~2300–1970 Ma. The western part, central part, northern part and eastern part witnessed continental assembly through oceanic plate subduction and collision along major sutures (mobile belts), causing the tilting of basements adjacent to the margins of continental massifs. Some lower-middle crust rocks were metamorphosed to high-pressure (HP) granulite facies and high-temperature to ultra-high-temperature (HT–UHT) granulites facies (Santosh et al. 2007, 2012). Zhao et al. (2005) suggested subduction–collision models along the Trans-North China Orogen, Kusky et al. (2007a, b) suggsted the subduction–collision occurred along the Northern Hebei-Inner Mongolia orogenic belt. A double-sided subduction has also been suggested (Santosh 2010). Zhai and Santosh (2011) proposed a Paleoproterozoic tectonic model (Fig. 1.10) and emphasized that subduction depth in the Paleoproterozoic mobile belts in the NCC are limited, corresponding with pressures of greenschist facies low-amphibolite facies for volcanic-sedimentary rocks of the Hutuo Group, Lüliang Group, Zhongtiao Group, Erdaowa Group and the lower Liaohe Group. The Paleoproterozoic mobile belts demonstrate Phanerozoic orogenic characteristics on some aspects, differed from the Archaean greenstone-granite belts. It is suggested that the NCC experienced a rifting–subduction–collision orogenic process after ~2.5 Ga cratonization, providing an example of primeval plate tectonic in Paleoproterozoic. Although the subduction and collision are much smaller in the scale than Phanerozoic plate tectonic regime, the tectonic mechanism possibly is similar. The boundary faults of the subduction rock units in mobile belts could be in depth scale of the crust rather than lithosphere. The pulling-apart stage in the NCC probably occurred at 2300–2000 Ma, including formation of rift and extension of ancient remnant ocean basin. The tectonic compressional stage from subduction to collision operated at 2010–1950 Ma. According to Zhai and Santosh (2011), the high-grade metamorphism of HP or HT-UHT granulite facies represent overprinting in an extensional tectonic setting with mantle upwelling that closely followed the ~1.97 Ga collisional event. The HP and HT-UHT metamorphism displaying extreme thermal conditions developed along the collisional sutures at ca. 1.95–1.82 Ga suggesting thermal

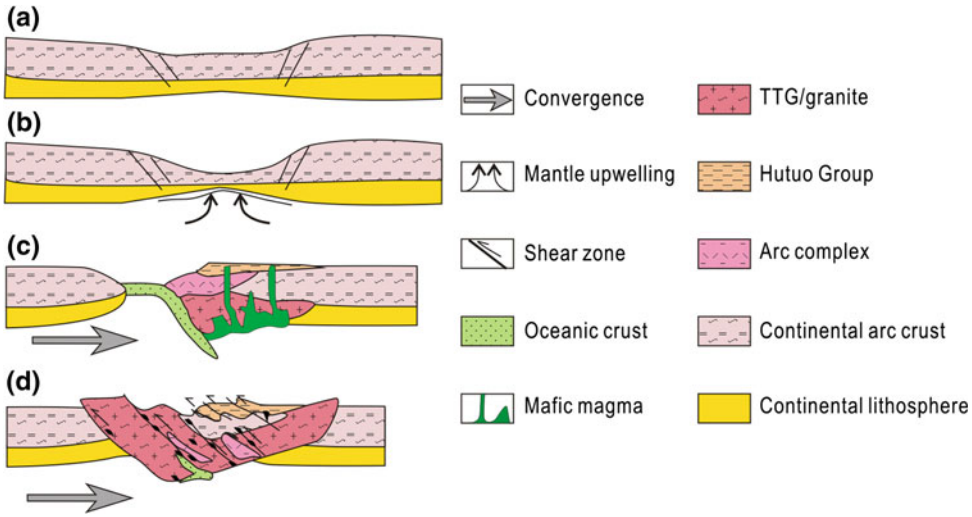

Fig. 1.10 Tectonic model of the Jinyu Paleoproterozoic mobile belt. **a** Rifting and Jinyu basin formation. **b** Mantle upwelling. **c** Active margin. **d** Collision

input from the sub-lithospheric mantle, probably related to slab-break off and asthenospheric injection (Santosh et al. 2012). During 1.82–1.65 Ga, rift-related anorogenic magmatism and mafic dyke emplacement took place, possibly representing associated with the global disruption of the Columbia supercontinent, subsequent to when the NCC entered into a platform regime.

The Paleoproterozoic orogenic-like metallogenic systems mainly include Cu, Cu–Mo, Cu–Co and Cu–Pb–Zn deposits. These ore deposits formed in rift and subduction environments and have characteristics of orogenic metallogeny (Sun and Hu 1993; Geng et al. 2000; Chen et al. 2009). The Tongkuangyu and Luojiahe Cu deposits are located in the Zhongtiaoshan area in Shanxi Province, and the host rocks of Cu-orebody are the Zhongtiao Group in the Jinyu belt. The Zhongtiao Group can be divided into the Jiangxian Formation in the lower part and the Zhongtiao Formation in the upper part, unconformably covered by ~1.78 Ga Xiyanghe Group and the Danshishan Group. The Jiangxian Formation mainly consists of bimodal volcanic rocks and a sedimentary sequence at the bottom. The new SIMS U–Pb zircon ages for amphibolites from the Jiangxian and Zhongtiao groups are, respectively, 2160–2190 Ma and 2059–2086 Ma (Liu et al. 2015a). These rocks underwent amphibolite facies and greenschist facies metamorphism at ~1.9 and 1.85 Ga, respectively, with peak temperature-pressure conditions of ~600 °C-10 Kb, and retrograde P-T conditions of 680 °C-7 Kb and late stage conditions of 550 °C-3 kb (Sun and Hu 1993).

The Zhongtiao Mountain region is endowed with some of the largest Cu deposits in northern China, among which the Tongkuangyu Cu deposit contains 70 % of the total reserves of copper. The orebodies in this deposit are confined to metamorphosed volcanic tuff and monzogranitic porphyry which are enclosed within metasediments. Metamorphism and deformation resulted in intense modification of the deposit, leading to debates surrounding its genesis. Sedimentary Cu deposit commonly occurs in the lower part of the Jiangxian Formation, and volcanic porphyry sulfide Cu-Mo deposits are associated with the high-K bimodal volcanic rocks of the middle-upper Jiangxian Formation. The main orebodies are of sub-volcanic porphyry type, with hydrothermal type orebodies also occurring in altered tuffs. Sulfide minerals are mainly chalcopyrite, pyrite and pyrrhotite. $\delta^{34}S$ values of sulfide minerals from Cu-Mo ore range from +1.12 to +6.8, with an average of +3.87. The single zircon U–Pb age of Cu-bearing porphyry is 2195–2187 Ma. The Cu–Co ore deposits are related to gabbroic-ultramafic intrusive bodies. Geochronological and geochemical study shows that the intrusive bodies and volcanic rocks have same magma source. New study (Liu et al. 2015b) shows prominent lithological control, and the orebodies are confined within the metamorphosed tuff and porphyry. Precise zircon U–Pb dating by SIMS method reveals that the porphyry was emplaced at 2180–2190 Ma, which is close to the formation timing of the surrounding mafic volcanic rocks (~2220 Ma), volcanic tuff, and sedimentary sequences. The data suggest that the porphyry was emplaced as a sill rather than as a stock or dyke. The Re–Os dating on pure molybdenites confirms that the Tongkuangyu copper mineralization occurred at ~2120 Ma. Combining geologic features including the geometry of the orebodies, occurrence of the porphyry sill and mineralization zonation, they propose that the porphyry copper model is not viable for this deposit. In consideration with the available models, Liu et al. (2015a) propose that the Tongkuangyu deposit formed through a process similar to that of sediment-hosted stratiform copper deposits. The difference of 70 million years between mineralization and magmatic activity in the region as revealed by the molybdenite Re–Os and zircon

U–Pb geochronology also exclude any genetic link between the magmatic rocks and the copper mineralization. The tectonic setting of the Zhongtiao Mountain was probably under extensional environment (continental rifting or back-arc rifting) at ~2120 Ma, thus supporting a genetic model similar to a sediment-hosted stratiform copper system. However, genetic issues regarding this model continue, since typical SSC deposits are commonly hosted in sedimentary rocks, whereas most of the ores at Tongkuangyu are hosted in the tuff and monzogranitic porphyry. Therefore, they exclude a porphyry copper model for the deposit and favor sediment-hosted stratiform explanation for this deposit. Geological process and ore deposits similar to the Zhongtiaoshan also occurred in the lower Liaohe Group in the Jiaoliao belt (Zhang 1984; Li et al. 1998; Shen et al. 2006).

1.2.5 Mesoproterozoic (Earth's Middle Age) Rift System

After the Hutuo Movement, the NCC was a stable platform or para-platform during Late Paleoproterozoic–Neoproterozoic, on which vast and thick sedimentary sequences were deposited and are well preserved in the NCC. The major sedimentary basins are the Xiong'er aulacogen system in the southern central NCC (Fig. 1.8), the Yan-Liao aulacogen system in the northern-central NCC, the Northern marginal rift system in the northwestern NCC, and the Eastern marginal rift system in the eastern NCC and the Korean Peninsula. Although some researchers suggested that all these rifts were linked up each other in the history (Zhao et al. 1993), they occur separately on the surface in present. The individual rift systems have some differences with different starting and ending sedimentary times and different sedimentary thicknesses. However, they show characteristics of multi-stage rifting and long-term development (Fig. 1.11).

The Yan-Liao aulacogen system is located in the Yanshan, Chengde and western Liaoning. The Yanshan area is a typical area, where the Late Paleo- and Mesoproterozoic sedimentary sequences are made the type section of the Stratigraphic Lexicon of China (Cheng et al. 2009). The four stratigraphic units from bottom to up in the Yanshan Area are, respectively, the Changcheng System, Jixian System, Await Name System, and Qingbaikou System (Gao et al. 2009). The bottom boundary age of the Changcheng System is traditionally approved to be 1.8 Ga. The boundary ages between the Jixian System, Await Name System and the Qingbaikou System are, respectively, 1.6, 1.4, and 1.0 Ga. The upper boundary age of the Qingbaikou system is not ensured. Neoproterozoic sequences are rarely developed in the Yanshan Area, which are developed in NE China and the southern margin or eastern margin-Korean Peninsula. The

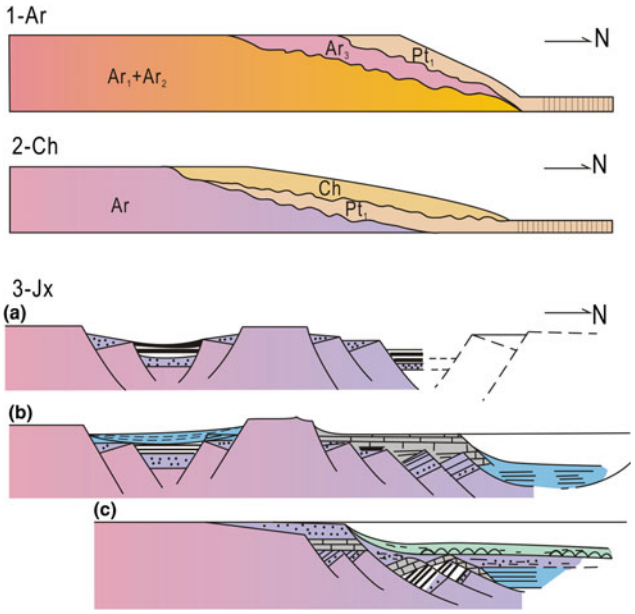

Fig. 1.11 Schematic diagram for multi-stage rifting in Yanshan area in the northern-central NCC

Neoproterozoic strata include the Qingbaikou System (1000–780 Ma, $Pt_{3\text{-}1}$), the Nanhua System (780–635 Ma, $Pt_{3\text{-}2}$), and the Sinian System (635–542 Ma, $Pt_{3\text{-}3}$). Some researchers argued that bottom boundary age of the Changcheng System is probably younger than ~1.7 Ga even 1.65 Ga, because of no precious chronological data or fossil. However, the field investigation and discussion in a workshop in 2014 do not reach an agreeable opinion.

Our study reported the magmatic zircon ages are ~1.78 Ma from volcanic rocks of the Xiong'er Formation (Zhao et al. 2004), revealing that the succession of Late Paleoproterozoic strata from the section of the Xiong'er aulacogen is possibly more complete, in other words, the Xiong'er aulocogen started to operate earlier than the Yan-Liao aulacogen. Here, we suggest that the Xionger Formation is the lowermost layer of Changcheng System (Zhao et al. 2015; Zhai et al. 2015), therefore the boundary time between Paleoproterozoic and Mesoproterozoic in the NCC is 1.6 Ga, i.e., the Changcheng System belongs to the Paleoproterozoic strata and the Jixian System belongs to Mesoproterozoic strata (Zhai et al. 2015).

Detrital zircon U–Pb ages from sedimentary rocks in motioned above four rifts show two major peaks of the detrital zircons are ~2.5 and ~1.85 Ga, which are consistent with the ages of metamorphic basement rocks (Hu et al. 2012). Another three weak peaks are ~2.7, ~1.6 and ~1.2 Ga. The ~2.7 Ga old rocks mainly occur in eastern, southern and northeastern parts in the NCC, ~1.6 Ga igneous rocks mainly occur in the Changcheng Formation and also in the Xiong'er Formation. ~1.2 Ga magmatic rocks are rarely outcropped in the NCC. Two granitite

samples yield ~1.2 Ga magmatic zircon U–Pb ages that collected from the northwest Korea near the Dandong city of China (Zhao et al. 2006) and from northern Liaoning (unpublished data). Figure 1.5 also shows that the detrital zircons from the Northern marginal rifts and Yan-Liao aulacogen are mainly concentrated at ~2.5 and ~1.85 Ga, and not on ~1.6 and ~1.2 Ga. In the eastern rifts, the age peaks of ~1.6 and ~1.2 Ga imply that sedimentary sources changed. The characteristic of zircon is also consistent with the distribution of the sedimentary strata on the surface, i.e., the Neoproterozoic sequences, specially the Nanhua System (up to 635 Ma) and Sinian System (up to 542 Ma), mainly occur in the eastern NCC and NE NCC.

Four stages of magmatic activity are recognized during the Late Paleoproterozoic–Neoproterozoic: (1) the ~1800–1780 Ma Xiong'er igneous province (XIP), (2) ~1720–1620 Ma anorogenic magmatic association, (3) ~1350–1320 Ma diabase sill swarm, and (4) a ~900 Ma mafic dyke swarm.

The emplacement of mafic dyke swarms widely intruded the basement rocks of the NCC. The mafic dyke swarms yield an age range of 1800–1760 Ma (with a peak at 1780 Ma), volcanic rocks from the lower part of the Xiong'er aulacogen yield age of ca. 1780–1760 Ma (Peng et al. 2005). The isotopic characteristics of Paleoproterozoic metabasites (with 1900–1760 Ma ages from gabbroic bodies and doleritic dykes) show that their source composition obviously transformed from an enriched to depleted mantle with time, with ε_{Nd} values ranging from +5 to −2 at ca. 2.5 Ga and −2 to −10 at ca. 1.9–1.7 Ga (Zhai et al. 2001). The geometry of the dykes and the rift-arms are well correlated. Peng et al. (2008) suggested that the dykes could be the feeders of the Xiong'er volcanic edifice, and dykes and volcanic rocks constitute a large igneous province possibly related to plume tectonics.

A large-scale anorogenic magmatic event affected the NCC during ~1.76–1.65 Ga, such as the Damiao anorthosite-gabbro complex in northern Hebei, the Miyun rapakivi granitic bodies in Beijing, A-type granites and alkali granites in southern NCC, and bimodal volcanic rocks in the Yan-Liao aulacogen. The Damiao anorthosite complex includes anorthosite, norite, mangerite, and gabbro with Fe–Ti–P ore deposits. The zircon U–Pb ages of norite and mangerite are 1742–1693 Ma (Zhao and Zhou 2009). The $\varepsilon_{Nd}(t)$ values of the whole rocks range from −4.0 to −5.4, and $\varepsilon_{Hf}(t)$ values of zircons from −4.7 to −7.5. The Miyun rapakivi granite has zircon U–Pb ages of 1735–1681 Ma (Yang et al. 2005; Gao et al. 2008). The average $\varepsilon_{Hf}(t)$ value from zircons is about −5, and their two-stages $T_{DM2}Hf$ range from 2.8 Ga to 2.6 Ga, indicating rapakivi granite magma is derived from partial melting of Neoarchean crust. The Dahongyu Formation and Tuanshanzi Formation with bimodal volcanic rocks mainly outcrop in Eastern Hebei and the Beijing–Tianjin areas. Its thickness is up to 700 m. Volcanic rocks of the upper Tuanshanzi Formation and upper Dahongyu Formation have, respectively, zircon ages of 1625, 1683, 1637 and 1641 Ma (Gao et al. 2011; Zhang et al. 2013). Geochemically, the volcanic rocks show enrichment in LILE and LREE and depletion in HFSE with weak negative abnormal of Nb and Ta, and $\varepsilon_{Nd}(t)$ values range from −0.66 to +0.63. The ~1.72–1.62 Ga igneous rocks in the NCC commonly constitute a series of anorogenic association (Zhai et al. 2001).

Large volumes of diabase sills occur within the Late Paleoproterozoic to Mesoproterozoic sedimentary rocks in the northern part of the NCC. They mainly intrude the Await Name System (the Xiamaling Formation), and also the Jixian and Changcheng systems. Li et al. (2009), Gao et al. (2011), Zhang et al. (2012b) reported accurate zircon and baddeleyite SHRIMP, LA-ICP-MS and SIMS U–Pb analyses on representative samples of the diabase sills. The results show emplacement ages ranging from 1325 ± 5 Ma to 1316 ± 37 Ma, suggesting voluminous magmatism leading to the formation of the diabase sill swarms (the Yanliao mafic sill swarms) in the Mid-Mesoproterozoic. The Xiamaling Formation consists of dark to black shales, sandstones, siltstones, and marl layers. Diabase sills are very common within the Xiamaling Formation throughout the northern NCC. Geochemically, the Mid-Mesoproterozoic diabase sills in the northern NCC were likely generated by partial melting of the depleted asthenosphere mantle coupled with minor crustal assimilation in a continental rifting environment.

The Neoproterozoic igneous rocks comprise the ~925 Ma mafic dyke swarm, ~900 Ma mafic sills, and ~890–830 Ma bimodal volcanic rocks. The mafic dykes are distributed in the central and southern parts of the NCC. They are typically un-metamorphosed and some of them are unconformably covered by Cambrian strata. It is worth pointing out that we have opportunity to survey geology in the North Korea and discovered the Sariwon sills that are distributed in the Pyongnam basin at the center of the Korean Peninsula, eastern part of the NCC or the Sino-Korea Craton (Peng et al. 2011). These sills possibly originated from a depleted mantle source (e.g., asthenosphere), rather than from the ancient lithospheric mantle of the NCC, and have experienced significant assimilation of lithospheric materials. Except the discovery of ~925–900 Ma mafic swarm, another discovery is bimodal volcanic rocks in Langshan-Zhaertai rift in the Northern marginal rift system (Peng et al. 2014; Fig. 1.12). Basaltic and dacitic rocks are layered with crystalline limestone, shale and sandstone, associated with SEDEX-Type Pb–Zn deposits.

The four anorogenic magmatic events suggest that the NCC was situated in a within-plate setting for an extended time from ~1.8 to ~0.7 Ga or even younger, and the

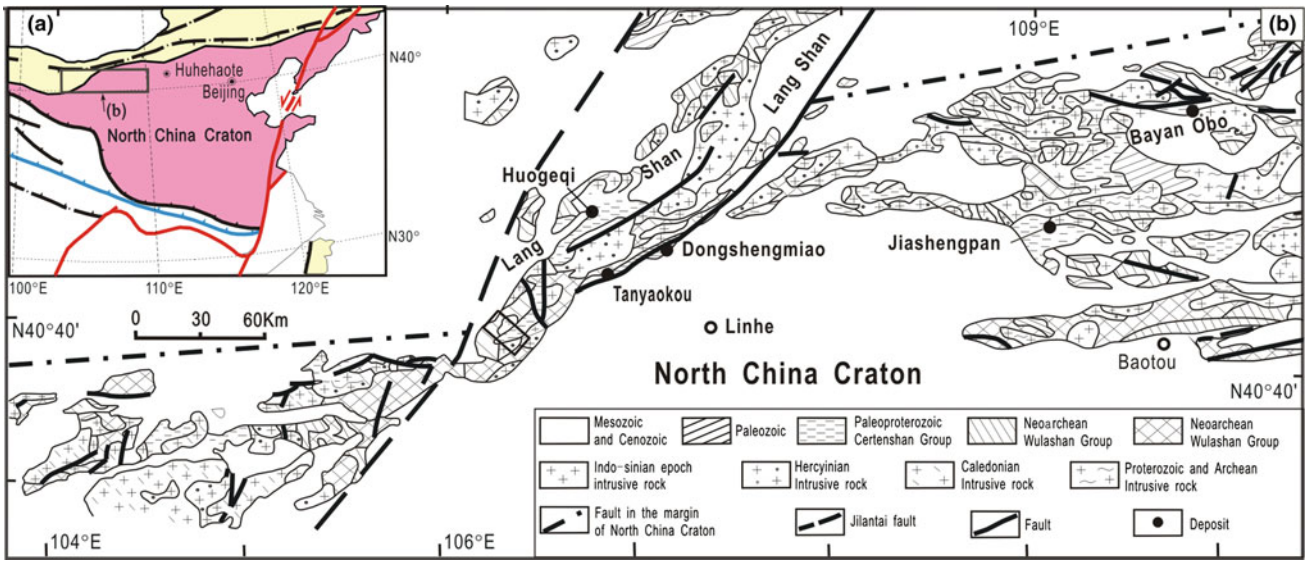

Fig. 1.12 **a** Lanshan-Zaertai area in the NCC and **b** Sketch geology map

magmatic events were associated with multi-stage rifting activities. We document that the NCC landed in a long-term extensional tectonic setting during Late Paleoproterozoic–Neoproterozoic era. Combining geological characteristics of adjacent blocks to the NCC, it is possible that the Proterozoic NCC was located at the remote edge of the Nuna supercontinent if such a supercontinent existed. However, any evidence of the Grenville or other orogenic event is not found in the NCC (Zhang et al. 2012b). Or, there is another case, i.e., the period from Late Paleoproterozoic to Neoproterozoic represents a particular tectonic evolving period, in which the Earth had a stable lithosphere with an underlying secular warm mantle. During that time, the lithosphere mantle was warm enough to result in widespread melting of the lower crust, and also result in rifting (Zhai et al. 2015). This period of Late Paleoproterozoic–Neoproterozoic era is called Earth's middle age (Cawood and Hawkesworth 2014).

The major ore deposits related to Late Paleoproterozoic–Neoproterozoic multiple-rifting events are sedimentary hematite as occurring as discontinuous layers and lenses in the Chuanlinggou Group. Another iron ore deposit is the titanic magnetite related to anorogenic gabbro-leucogabbro association in the Damiao and Miyun in Yanshan aulacogen. The REE deposit, associated with Nb-bearing iron ores in Bayan Obo constitute another important ore deposit formed during this time. The middle Bayan Obo Group includes a series of clastic rock–sandstone–argillaceous slate–shale and black shale–dolomite. Several layers of dolomites have been distinguished. The REE mineralization is believed to be closely related with the carbonatite dykes (Fan et al. 2001; Yang et al. 2011a). Three types of carbonatite dykes are dolomite, calcite and coexisting dolomite–calcite. Intrusion of calcite carbonatite dykes were later than the dolomite dykes, which indicates that carbonatite magma had special evolution trend from dolomite through coexisting dolomite–calcite to calcite type dykes. Moreover, the content of LREE in carbonatite dykes gradually increases with the proportion of calcite minerals from dolomite via coexisting calcite type dykes. Geochemical data also show that long-term crystallization—differentiation was the main mechanism of concentrating the REE, especially LREE, and their accumulation in the residual magma. Carbonatites are known to contain high concentrations of REE. The contact relations show that the intrusion of calcite carbonatite dykes post-date the dolomite dykes during the process of evolution of the carbonatite magma. The geochemical data show that the content of Sr and light (L) REE in these dykes gradually increases from dolomite [$(La/Yb)_N$ values range from 1.6 to 3.8], through calcite-dolomite [$(La/Yb)_N$ ranging from 51 to 57], to calcite type [$(La/Yb)_N$ ranging from 85 to 4617]. This evolutionary trend suggests the crystal fractionation of the carbonatite magma, which might have played a critical role for the giant REE accumulation in the Bayan Obo region (Yang et al. 2011a, b). The $\varepsilon_{Nd}(t)$ values of the carbonatitic dykes show a tight cluster between −0.47 and +0.65, whereas the initial Sr isotope values show a broad range from 0.703167 to 0.708871. The massive ore-hosting dolomite marbles show comparable element content and Nd isotope composition, and a Sm–Nd isochron age similar to that of the carbonatite dykes, implying a close relationship during their magmatic origin. This interpretation is also supported by the intrusive contact between the ore-hosting dolomite marble and Mesoproterozoic Bayan Obo Group, as well as the presence of wall-rock xenoliths in the dolomite marble. Recent studies reported precise U–Pb ages and Sm–Nd isochron and model ages (Fan et al. 2001, 2006;

Yang et al. 2011a, b), suggesting that the carbonatites were formed from mantle magmas at ~1320–1230 Ma. We correlate the carbonatites in Bayan Obo with the diabase sills in the Xiamaling Group in Yanshan area. The REE metallogenesis was possibly controlled by late Mesoproterozoic rifting and associated mantle upwelling. The Nb–Fe formation, black shale and dolomite rocks in the middle Bayan Obo Group are also to be considered as the REE sources. Zhang et al. (2013) also suggested that the Mesoproterozoic rifting was related to break-up of the Columbia supercontinent.

Mesoproterozoic rifts in northern and southern NCC are potential cites of Pb–Zn–Cu–Fe ore deposits, such as the Dongshengmiao in Langshan in the Northern Marginal Rifts in northwestern NCC and the Luanchuan, Henan Province in southern NCC. The major ore deposits are SEDEX-type Pb–Zn deposits, hosted in a sandstone fine-grained sandstone-calcic fine-grained sandstone sequence. This type of submarine exhalative-sedimentary lead–zinc–copper–iron sulfide deposits is considered to be related to extensional process in the NCC (Peng et al. 2010).

1.2.6 Paleozoic Orogeny in Northern and Southern Margins of the NCC and Orogenic Metallogenic System

A suggestion is proposed that the NCC was in a relative geological environment during Late Neoproterozoic to Middle Permian, although there were a Paleo-Mongolia Ocean and a Paleo-Qinling Ocean neighboring the NCC (Cheng et al. 2009; Wan et al. 2011a). The major Paleozoic orogenies along the northern and southern boundary zones of the NCC are represented by the CAOB formed through the closure of the Paleo-Asian (Mongolia) Ocean leading to the collision of the Siberia Craton and the NCC, and the QOB constructed through the subduction of the Paleo-Qinling Ocean and collision between the Yangtze Craton and the NCC. These two orogenic belts preserve the imprints of different tectonic processes and resultant ore deposits, most of which show features typical of orogenic mineralization (Cheng et al. 2009).

1.2.6.1 The QOB Metallogenesis

It is suggested that the South China Block (SCB) and the NCC were separated by the Paleo-Qinling Ocean, which was a part of the Paleo-Tyths Ocean. Figure 1.13 shows geological processes between the SCB and the NCC throughout opening and closure of the Paleo-Qinling Ocean (After YJ Chen, oral report, 2012). The QOB was formed by the amalgamation of the North and South China blocks, but the timing of the assembly is controversial, which obviously stems from different approaches to the reconstruction of the collisional history (Hsü et al. 1987; Zhang 1988; Xu et al. 1988; Okay and Sengör 1993). Meng and Zhang (1999, 2000) proposed the geologic framework of the QOB through the interplay of three blocks, the North China block (including the North Qinling), the South Qinling, and the SCB, separated by the Shangdan and Mianlüe sutures. The Shangdan suture resulted from Middle Paleozoic collision of the North China block and the South Qinling. The Mianlüe

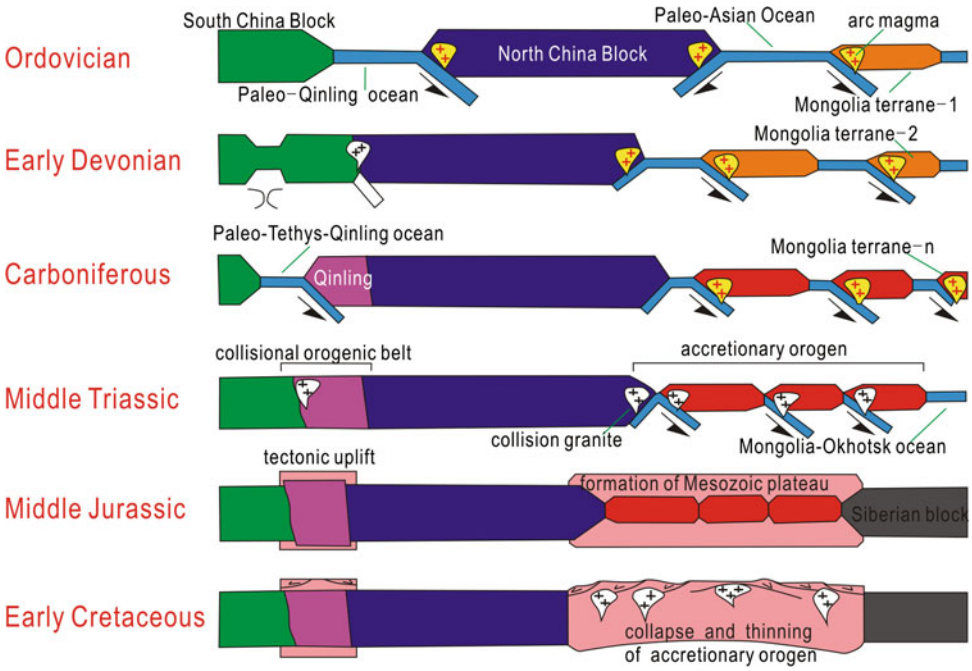

Fig. 1.13 Tectonic Schematic diagram for Paleozoic orogenic belts along margins of the NCC

suture resulted from Late Triassic collision of the South Qinling and the SCB. The present upper crust of the Qinling is dominantly characterized by thrust-fold systems. The North Qinling displays thick-skinned deformation with the involvement of the crystalline basement, whereas the South Qinling is characterized by thin-skinned thrusts and folds detached above the Lower Sinian. Two types of Precambrian basement, crystalline and transitional, are defined according to lithology and metamorphic grade and their difference in ages. Stratigraphic and sedimentary architecture is characterized by a distinct zonation. The QOB experienced a prolonged continental divergence and convergence between the blocks. During the period from Late Neoproterozoic to Early Paleozoic, the South Qinling was the northern margin of the SCB, and the North Qinling was the southern margin of the North China block, separated by a Proto-Tethyan Qinling Ocean. The North Qinling evolved into an active margin when the Proto-Tethyan Qinling Ocean subducted northward during Ordovician. Collision of the South and North Qinling took place in Middle Paleozoic along the Shangdan suture. Synchronous with the collision, rifting occurred at the southern rim of the South Qinling and was followed by the opening of the Paleo-Tethyan Qinling Ocean during the Late Paleozoic, resulting in the splitting of the SCB from the South Qinling. Collision of the South Qinling and the SCB occurred in the Late Triassic along the Mianlüe suture. Recently, Dong et al. (2013) suggested a two-stage subduction–collision orogenic model. Their model proposed that Paleo-Shangdan Ocean was closed in Upper Devonian along the Shangdan suture zone and the Paleo-Mianlüe Ocean was closed in Triassic (228–215 Ma) along the Mianlüe suture zone, formed a united NCC–SCB continent welded by the North Qingling Terrain (NQT) and South Qinling Terrain (SQT). The Late Triassic collisional orogeny caused extensive fold-and-thrust deformation and granitoid intrusions throughout Qinling, and led to the final amalgamation of the North and South China blocks. Subsequently, the QOB experienced another compressional-fold event followed by an extensional structure, and resultant uplifting of the Qinling Mountains. This event has been suggested to be related to subduction of the West Pacific Plate (such as Mao et al. 2002; Cheng et al. 2009). However, Zhu et al. (2008) and Zhang (2012, oral report) emphasize that this event has very different characteristics from the general subduction–collision process associated with plate tectonic regime, and therefore considered it to be intracontinental orogeny.

Corresponding to the complex orogenic processes summarized above, three major tectonic evolution stages have been identified (Zhu et al. 2008): (1) the first stage is the formation of the orogenic basements in Precambrian; (2) the second stage is the main orogenic stage in Late Proterozoic–Middle Triassic, which is characterized by subduction–collision, including the formation of both Shangdan and the Mianlüe suture zones; and (3) the last phase is the Mesozoic-Cenozoic intercontinental tectonic evolutionary stage. Significant metallic deposits were formed during the last two stages. We address the ore deposits in the Qinling Mountains as the QOB orogenic metallogenic system (Fig. 1.14), although the Mesozoic-Cenozoic mineralization is debatable.

1.2.6.2 The CAOB Metallogenesis

The CAOB is a well-established accretionary orogenic belt (Fig. 1.12). The boundary between the CAOB and NCC in the eastern part of North China is marked by the Xilamulun-Bayan Obo fault. The orogenic history of the eastern CAOB can be tracked down to Late Neoproterozoic. Pan-African granites occur discontinuously along the Inner Mongolia and Heilongjiang Province in NE China. Zhang and Zhai (2010), Zhang et al. (2008, 2009b, 2010) studied the magmatic rocks in the eastern CAOB and northern margin of the NCC, and suggested that the northern boundary of the NCC experienced various types of crustal accretion associated with the CAOB orogenic processes. The three accreting stages identified are: (1) lateral accretion of the early oceanic and continental arcs; (2) lateral accretion of continental arc and reworking; and (3) late continental margin vertical accretion and reworking. Possible tectonic model for the eastern CAOB is shown in Fig. 1.12 (modified from Xiao et al. 2003; Jian et al. 2008; Zhang and Zhai 2010).

Recently, Xiao et al. (2015) suggested that the Central Asian Orogenic Belt records the accretion and convergence of three collage systems that were finally rotated into two major oroclines between the NCC and Siberian Block. The Mongolia collage system was a long, N-S-oriented composite ribbon that was rotated to its current orientation when the Mongol-Okhotsk orocline was formed. The components of the Kazakhstan collage system were welded together into a long, single composite arc that was bent to form the Kazakhstan orocline. The cratons of Tarim and North China were united and sutured by the Beishan orogen, which terminated with formation of the Solonker suture in northern China. All components of the three collage systems were generated by the Neoproterozoic and were amalgamated in the Permian-Triassic. The Central Asian Orogenic Belt evolved by multiple convergence and accretion of many orogenic components during multiple phases of amalgamation, followed by two phases of orocline rotation.

Permian bimodal volcanic rocks are extensively distributed in central-eastern Inner Mongolia and NE China. Cu-Mo porphyry deposits occur in various arc complexes in different geological periods. The Duobaoshan Cu deposits formed in Early Paleozoic, and their host rocks are granodiorite with zircon U–Pb ages of 482 Ma and intermediate-felsic volcanics with zircon U–Pb ages of 508–489 Ma. The Bainaimiao Cu–Mo porphyry deposit occur in porphyry

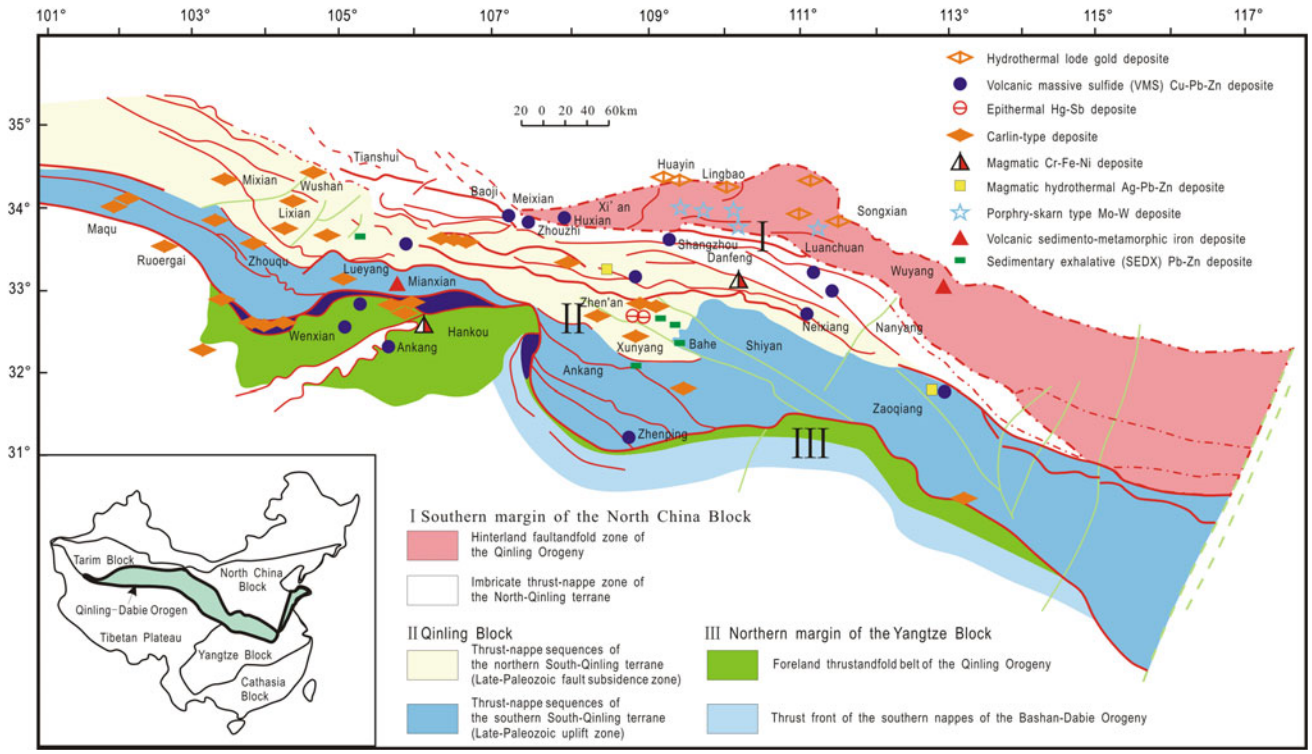

Fig. 1.14 Distribution of ore deposits in the QOB (after Zhu et al. 2008)

granodiorites, from which zircons yield 430–445 Ma U–Pb ages (Miao et al. 2007; Cheng et al. 2009). The Tonghugou Mo-(Cu) deposits formed in Late Permian (Wan et al. 2009; Zhang et al. 2009b), and the Rb–Sr age for chalcopyrite in orebody is 256 ± 7 Ma.

1.2.7 Mesozoic Lithospheric Thinning Under the Eastern NCC and Metallogenic System

The extensive Mesozoic magmatic activity, lithospheric thinning and craton destruction in the NCC with associated metallogeny is one of the most important thrust areas where global attention is focused (Fan and Hooper 1991; Fan and Menzies 1992; Menzies et al. 1993; Xu 2001a; Zhang et al. 2012c). This peak of this event occurred during Cretaceous. Various models have been suggested for the lithospheric thinning and craton destruction in the eastern and central NCC (for example: Xu 2001b; Zheng et al. 2002, 2003; Wu et al. 2003; Zhu et al. 2012). The time span of Mesozoic tectonic inversion in the eastern NCC is from 150–140 Ma to 110–100 Ma, with a peak stage at 120–110 Ma (Zhai et al. 2004a). The basin-range framework of the NCC, in general, changed from EW-trending to NE–NNE-trending, and the dominant compressive tectonic regime linked with the Paleozoic marginal orogeny switched to an extensional tectonic regime in early Cretaceous (Zhai et al. 2004b). However, the Mesozoic tectonic inversion process was complex, showing multi-stage inversion of compression and extension. Variations both in time-space and along the margins versus cratonic interior have been identified. In the south (east) of the craton, a compressive structural event occurred mainly in 230–210 Ma, and the peak stage of extensional tectonic inversion was in 130–110 Ma. In the north, two compressive events occurred in 230–210 and 180(170)–160(150) Ma, respectively, and the peak stage of extensional tectonic inversion was also in 130–110 Ma. The evolution of Mesozoic basins shows diversity. In the Yanshan area, the pre-Late Jurassic basins belong to compressive-flexure associated with NEE-trending thrust zones. The Late Jurassic NEN-trending rift basins coexist with uplift zones. The post-Late Jurassic basins trending NE-NEN are coeval with the active uplift zones and are controlled by NEE-trending thrust zones. The south and north Dabieshan units have different uplift histories. Petrological, geochemical and geophysical studies bearing on the deep structure beneath the NCC have clearly identified a drastically thinned lithosphere beneath the eastern NCC, and large-scale replacement of the lower crust with upwelling mantle material during Mesozoic, with a peak at 130–110 Ma (Fan and Menzies 1992; Menzies et al. 1993; Cai et al. 2012). The Mesozoic tectonic regime inversion shows no characteristics of orogenic belt. Zhai et al. (2007) suggested that the lower crust was thinned together with

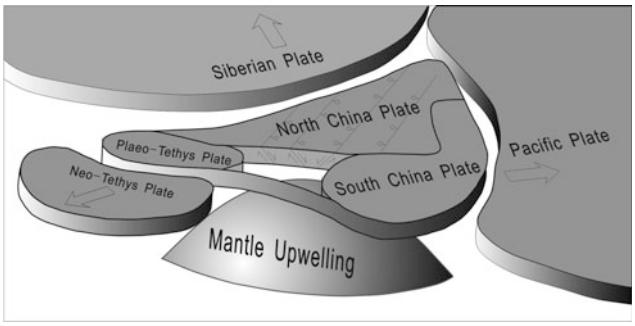

Fig. 1.15 Tectonic model for Lithospheric thinning of the eastern NCC (after Zhai et al. 2004a, b)

lithosphere mantle in the eastern NCC. Formation of the present lower crust through underplating and its replacement with the old one are closely related to lithosphere mantle thinning (Fig. 1.15). The lower crust thinning/replacement and the lithosphere mantle thinning are both controlled by the same dynamic mechanism and displaying a cause and effect mechanism.

As the type area of large-scale metallogenesis and hosting the largest clusters of mineral deposits in China, the Jiaodong (East Shandong) Peninsula occupies only less than 0.2 % of China's whole area, but yields more than a quarter of the gold production of the whole country. Three sub-cluster districts for gold deposits are the Linglong, Yantai and Kunyushan from west to east. Our studies (Zhai and Liu 2003; Zhai et al. 2004b) identified the eastern boundary of the Jiaodong gold deposit cluster, separating these from the gold-poor area and the Sulu region, respectively. The host rocks of the gold lodes are early Precambrian basement rocks which have undergone high-grade metamorphism, and the Mesozoic intrusive granitoids. The ore-forming ages mostly range within a short period of 10 Ma from 125 Ma to 115 Ma (Fan et al. 2003; Zhai et al. 2004b; Guo et al. 2013). Geochemical data also suggest that metallogenic sources are the Precambrian basement of Jiaodong complex in the NCC and its underlying mantle. The Sr–Nb–Pb and S–O–H isotopic data of the ore lodes show crust-mantle mixing characteristics, corresponding to multiple sources from the metamorphic country rocks and the intermediate-basic dykes. Gold deposits not only occur along the margins of the basement, but also within the basement. All the gold deposits in this region have broadly similar characteristics with regard to the metal source, ore-forming process, ore deposit type, metallogenic epoch and the wall rocks of ore lodes. This metallogenesis is termed as the "Mesozoic metallogenic explosion," because of the huge volume of the metallogenic province and the metallic resources generated, sustained energy system and the short metallogenic epoch. Recent studies have established that the metallogeny in eastern and central NCC are closely related to the lithospheric thinning and decratonization process with a strong mantle–crust replacement in the Mesozoic era, reaching a peak at 130–110 Ma (e.g., Zhai et al. 2004a; Li et al. 2013). The Mesozoic tectonic inversion bears no characteristics of orogeny, and is clearly related to intracratonic extensional regime, crust-mantle interaction and regional asthenospheric upwelling. Thus, the Jiaodong-type metallogenesis represent Mesozoic tectonic inversion, and a magma-fluid-mineralization system that was derived from upwelling mantle and mantle–crust replacement.

The eastern NCC, from the Luxi fault at the center, and probably even more west to Helanshan in the northwestern and West Qinling Mountains in the south-western NCC, carries the largest association of gold deposits. Hundreds of gold deposits of different scales, commonly in groups or belts, constitute ten gold-clusters (Fig. 1.16I–X). In contrast, there are no industrial grade gold deposits in the neighboring areas of the UHP Sulu region and the northern margin of the Yangtze craton. The host rocks of the gold deposits are mainly Precambrian high-grade metamorphic rocks and granites (anatectic melts derived from the Precambrian basement rocks). Traditionally the gold deposits were considered to be of the Archean greenstone type. However, recent geochronology of granitoid bodies and veins related to gold mineralization and gold-bearing minerals in ore lodes reveals that the main metallogenic episode was 110–130 Ma not only in Jiaodong, but also in all other nine clusters (Zhai et al. 2004b). Geochemical data, Sr–Nb–Pb and S–O–H isotopes also show characteristics similar to those of the Jiaodong gold deposits. Clear signatures of lateral variations in the strength of the lithosphere and the role of extensional tectonics in extensively modifying the lithospheric architecture have been documented (Zhang et al. 2012a). In a recent study, Guo et al. (2013) synthesized the available geophysical and geochemical information from the eastern part of the NCC. The Moho depth on both sides of the Tan-Lu fault is identified to be broadly similar with only a minor variation. The LAB (lithosphere–asthenosphere boundary) in the Jiaodong region to the east of the Tan-Lu fault is shallower than that in the Luxi area to the west. Thus, the Tan-Lu fault is identified as a major corridor for asthenosphere upwelling. The mantle beneath the Luxi area is mainly of EMI type, whereas the mantle in the eastern part, close to the Tan-Lu fault shows mixed EMI and EMII features. On the other hand, the mantle beneath the Jiaodong area is mainly of EMII type that suggests the existence of more ancient lithospheric mantle beneath the Luxi area, in comparison to the extensively modified lithospheric mantle and asthenosphere beneath the Jiaodong area. The differences in the character and intensity of gold mineralization between the Western and Eastern Shandong regions is interpreted as a reflection of the contrasting tectonic histories. A seismic velocity image of the NCC (from Song Xiao-Dong, quoted in Zhai and Satosh 2013) shows a low

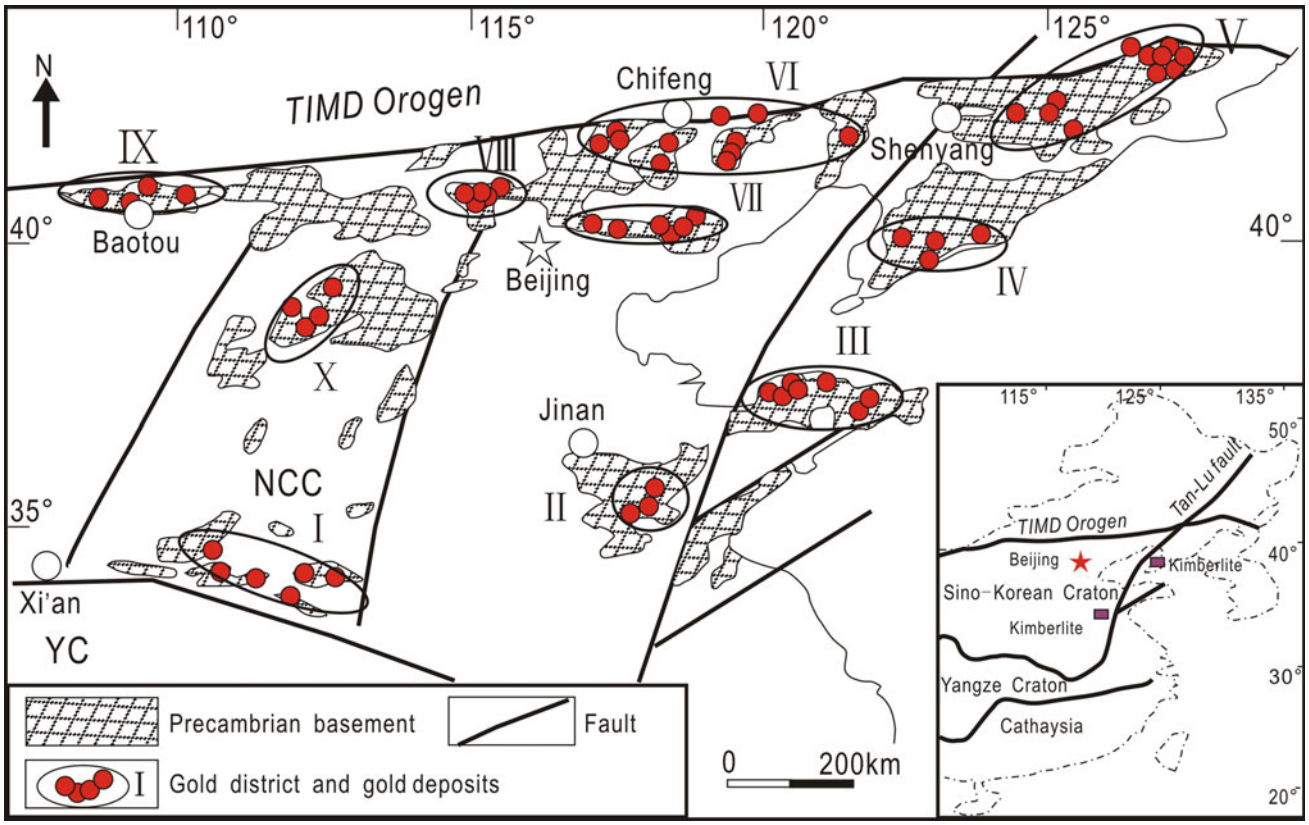

Fig. 1.16 Distribution of Mesozoic gold deposits in the NCC

velocity area in the NCC, including all eastern NCC and a part of central NCC, north of the Xilamulun fault and south of the northern boundary of the Dabieshan orogenic belt. This area coincides with the region of gold distribution, and is also the area affected by craton destruction. This furthers the notion that the gold-metallogenesis is controlled by the crust–mantle interaction with lithospheric thinning. Orogenic gold deposits are an important type of gold mineralization (Goldfarb et al. 2011) and the gold deposits Jiaodong have been considered by some workers as orogenic gold (e.g., Hua and Mao 1999; Shen et al. 2000; Mao et al. 2002). Clearly, the Mesozoic gold ore deposits in the Jiaodong and elsewhere in the NCC are distinctly different from the orogenic-type gold deposits. Two key factors controlled the Mesozoic gold mineralization in the NCC. One is reworking and partial melting of Precambrian basement of the NCC, especially pre-greenstone belt-type gold formation, a process that provided most of metallogenic materials. The second is the upwelling mantle, which provided the heat and fluid source as well as a part of the gold enrichment. These two conditions were achieved as a result of the Mesozoic tectonic inversion and lithospheric thinning under the eastern NCC. In summary, based on the characteristic features and tectonic setting of the gold deposits in the eastern NCC, a new gold metallogenic type—the Jiaodong-type gold deposit has been proposed by Zhai et al. (2004b).

The Paleozoic CAOB has been superimposed by Mesozoic extensional tectonic process, and was suggested to be related to Mesozoic Mogol-Okhotsk Ocean closure. Meng (2003) suggested that the North China-Mongolia tract (NCMT) consists of eastern and southern central Mongolia and northern China. It is a composite terrane bounded on the north by the Mesozoic Mongol-Okhotsk suture zone. The Mogol-Okhotsk Ocean, which existed since latest Paleozoic separating the NCMT from Siberia, finally closed in Middle-Late Jurassic. Following Middle-early Late Jurassic crustal contraction, the NCMT experienced intense extensional deformation and magmatism in Late Jurassic- Early Cretaceous. Some researchers (such as Davis et al. 2002; Zhang et al. 2010a) prefer the effect of subduction from the Paleo-Pacific Plate to be more important to Mesozoic extensional deformation in eastern CAOB (the Xing'an--Mongolian orogenic belt). Figure 1.12b shows the tectonic evolution of the Xing'an-Mongolian orogenic belt in Jurassic- Early Cretaceous. In Early–Late Jurassic, the NCC and the Siberian Plate constituted a united continental block involving the Xing'an-Mongolian orogenic belt that consists of a series of accretionary complexes and the relatively small

Ergune block. The Xing'an-Mongolian orogenic belt was impacted by subduction of the Paleo-Pacific Plate, generating the 180–150 Ma Cu-Mo mineralization, and the 140–120 Ma Mo and Ag–Pb–Zb mineralizations.

More than 70 Mo ore deposits have been discovered in northern margin of the NCC and NE China, and most of these were formed in Mesozoic with three peak-mineralization pulses at 240–210 Ma, 180–150 Ma and 140–120 Ma. Recent studies show that porphyry Cu deposits are closely related to subducted oceanic crust whereas the porphyry Mo deposits show close relationship with melting of continental crust (Zeng et al. 2009; Zhang et al. 2010).

1.3 Discussion and Conclusion

1.3.1 Corresponding Main Metallogenic Epochs to Key Geological Events in the NCC

The NCC experienced complex geological evolution since the early Precambrian onwards, and carries important records of the secular changes in tectonics and metallogeny. Here, we synthesize the salient geological and tectonic features of the evolution and destruction of the NCC (Fig. 1.17) vis-à-vis the major metallogenic events and formation of potential ore deposits (Fig. 1.18b).

We identify a close relationship among the major geological events in the NCC with that elsewhere on the globe. We trace the records of a regular change in the pattern of metallogeny, mineral deposit character, spatial distribution, and genetic mechanisms which match well with the timings and styles of the major tectonic events in this craton.

Figure 1.17 shows change trends of geological history and crust growth in the NCC (red line) and other cratonsin the world (black line). For continental crust growth, the NCC experienced multi-stage growth process with a ~2.9–2.7 Ga peak (Wan et al. 2011a, b). By contrast, ~2.5 Ga crustal growth in the NCC is obviously stronger than those in other cratones. Zhai (2014) has been interpreted that ~2.5 Ga crust growth event represents cratonization of the NCC throughout assembly of micro-blocks and reworking of old metamorphic basement. Another crustal reworking took place in ~1.9–1.8 Ga, which was caused by the Paleoproterozoic Hutuo Movement.

For key geological events, the NCC and other cratones in the world have relative uniformity, except that ~1.9–1.8 Ga orogenic event is strong and missing record of Neoproterozoic snow ball event. The Mesozoic destruction (or lithosphereic thinning) of the NCC is a noticeable tectonic event. In summary, the NCC went through five major tectonic cycles: (1) the Neoarchean crustal growth and stabilization, (2) Paleoproterozoic rifting–subduction–accretion–collision with imprints of the Great Oxygen Event (GOE), (3) Late Paleoproterozoic–Neoproterozoic multi-stage rifting, (4) Paleozoic orogenesis at the margins of the craton; and (5) Mesozoic extensional tectonics associated with lithosphere thinning and destruction.

Coinciding with these major geological events, five major metallogenic systems are identified as follows: Archean BIF system, Paleoproterozoic Cu–Pb–Zn system and Mg–B system, Mesoproterozoic REE–Fe–Pb–Zn system, Paleozoic orogenic Cu-Mo system, and Mesozoic intracontinental Au and Ag–Pb–Zn and Mo systems. The ore deposit types in each of these metallogenic systems show distinct characteristics and tectonic affinities.

The five metallogenic systems are strictly controlled by Earth's geological environment and tectonic regime, showing irreversibility with Earth's evolution from ancient to present. Archean BIF system is closely related to oxygen-poor

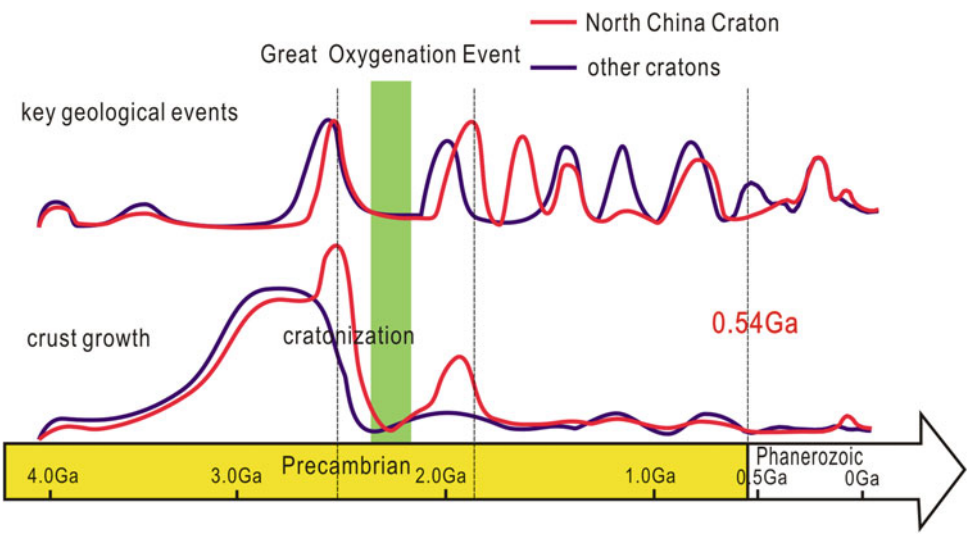

Fig. 1.17 Comparison on geological events and crust growth between the NCC and other cratons in the world

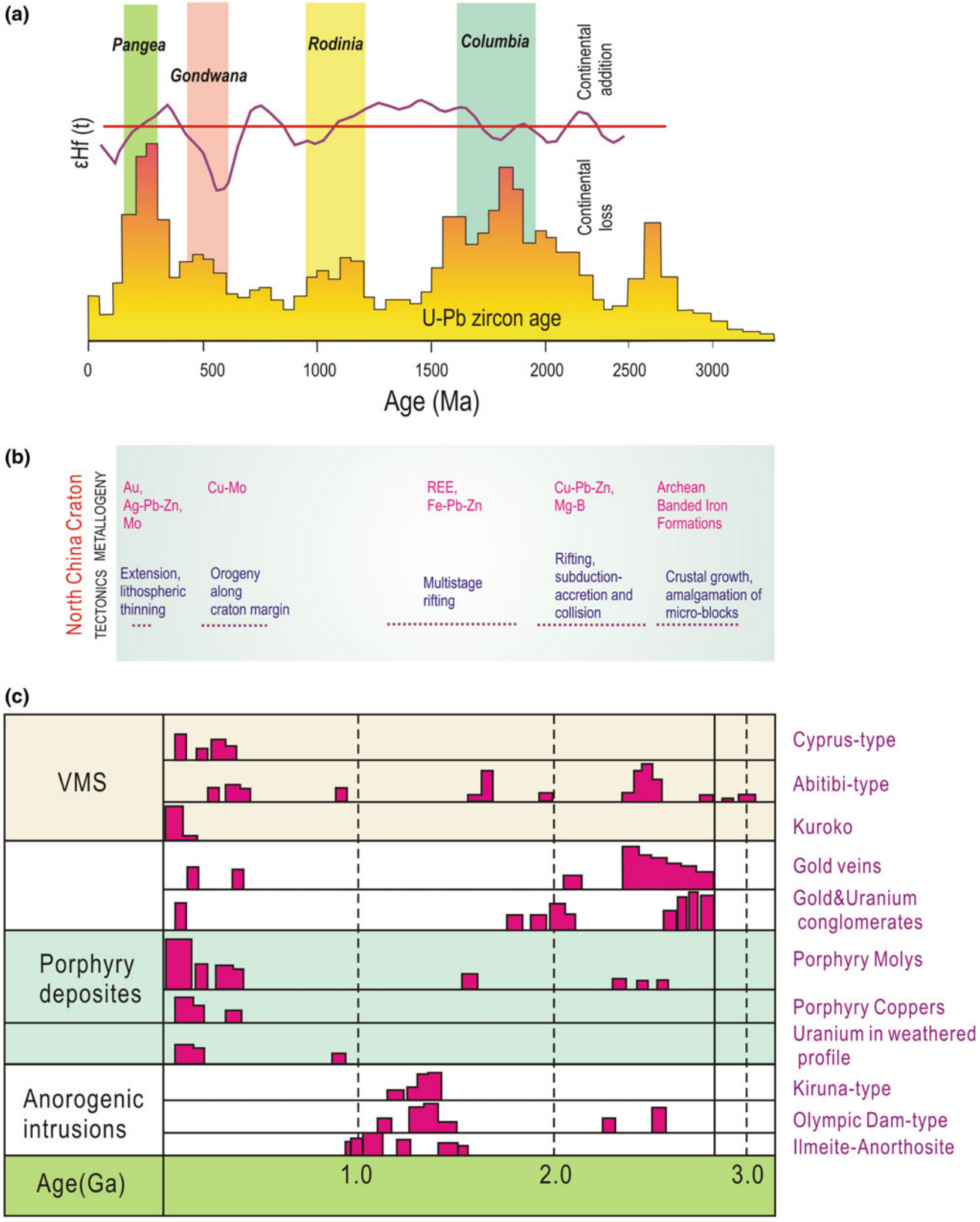

Fig. 1.18 **a** Compilation of global zircon Hf data plotted as U–Pb zircon age versus ε_{Hf} (initial); **b** correlation between major geological/tectonic events and the dominant metallogenic epochs in the NCC; **c** secular variation in global metallogenic types (Zhai and Santosh 2013)

environment and differentiation of chemical elements in crustal generation and growth. Mg-B system is closely related to very thick maritime-lagoonal facies deposition in oxygen-rich environment. Cu–Pb–Zn system is attributed to limited crust-mantle interaction in rifting–subduction–collision processes in Paleoproterozoic mobile belt. Pb–Zn mineralization is generally considered that water plays important role and Proterozoic multi-rifting may provide these conditions. Ore genesis of REE–Nb–Fe system is controversial. We consider that Mesoproterozoic mantle upwelling and igneous carbonatite dykes are needful conditions. Up to Paleozoic, orogenic porphyry Cu–Mo deposits become most important metallogenic type, which are obviously closely related to ocean-continent interaction under plate tectonic regime. Cratonic destruction has caught large-scale re-melting of lower crust and transformation of lithosphere mantle, leading large-scale gold mineralization.

Figure 1.18a shows compilation of global zircon Hf data plotted as U–Pb zircon age versus εHf (initial), and histogram of zircon U–Pb ages (data from Roberts 2012; Kerrich et al. 2005). Positive and negative excursions of the ε_{Hf} (t) curve represent increased continental addition and continental loss, respectively. Overlap between U–Pb maxima, supercontinent formation and negative ε_{Hf} excursions indicate a link between the supercontinent cycle and changes in continental crust growth rate. Thus, supercontinent amalgamation is characterized by a decreased growth rate, along with a possible increase in preservation of crust during these periods. Production of new crust occurs during supercontinent break-up through rift-related juvenile magmatic input. All above-mentioned may well explain secular variation of metallogenic types in the NCC (Fig. 1.18b). Figure 1.18c shows secular variation in global metallogenic types. VMS-type deposits mainly developed in early Precambrian, magma intrusion-type deposits mainly developed in Proterozoic, but porphyry deposits prefer form in Phanerozoic. This metallogenic regular pattern has specific time-bound character (Zhai and Santosh 2013).

1.3.2 Conclusion

1. From Early Precambrian to Late Precambrian to Paleozoic and Mesozoic, the tectonic evolution of the NCC went through from a primitive- to modern-style plate tectonics with evidence for rifting, subduction, accretion and collision at different times.
2. The global Great Oxidation Event left its imprints in the metallogenic systems in the NCC formed during ~2350–2000 Ma.
3. The five major events in NCC include: Neoarchean crustal growth and stabilization, Paleoproterozoic rifting–subduction–collision, Late Paleoproterozoic–Neoproterozoic multi-stage rifting, Paleozoic orogeny on the craton margins, and Mesozoic extensional tectonics and lithosphere thinning leading to voluminous magmatism and decratonization.
4. Accompanying the major tectonic events, five metallogenic systems were generated including the Archean BIF system, Paleoproterozoic Cu–Pb–Zn system and Mg-boron-graphite system, Mesoproterozoic REE–Fe–Pb–Zn system, Paleozoic orogenic Cu-Mo system, and Mesozoic intracontinental Au and Ag–Pb–Zn and Mo system.
5. Metallogeny diversified with time, from the dominant BIFs in the Archean to polymetallic deposits in the Proterozoic and Phanerozoic.
6. The NCC provides an excellent case to address the link between metallogenic processes and secular changes in the Earth System, including mantle dynamics and crust–mantle interaction on a global perspective.

References

Anbar, A. D., Duan, Y., Lyons, T. W., Arnold, G. L., Kendall, B., Creaser, R. A., et al. (2007). A whiff of oxygen before the great oxidation event? *Science, 317*, 1903–1906.

Brown, G. C. (1979). The changing pattern of batholith emplacement during earth history. In M. P. Atherton & J. Tarney (Eds.), *Origin of granite batholiths* (pp. 106–115). Natwich: Siva.

Cai, Y.-C., Fan, H.-R., Santosh, M., Liu, X., Hu, F.-F., Yang, K.-F., et al. (2012). Evolution of the lithospheric mantle beneath the southeastern North China Craton: Constraints from mafic dikes in the Jiaobei terrain. *Gondwana Research* doi:org/10.1016/j.gr. 13 Nov 2012.

Cawood, P. A., & Hawkesworth, C. J. (2014). Earth's middle age. *Geology, 42*(6), 503–506.

Chen, Y.-J., Ji, H.-Z., Zhou, X.-P., & Fu, S.-G. (1991). The challenge to the traditional geological theorise from revelation of the catastrophe at 2300 Ma: New knowledge on several important geological subjects. *Advance in Earth Science, 6*(2), 63–68. (In Chinese with English abstract).

Chen, Y.-J., Liu, C. Q., Chen, H. Y., Zhang, Z. J., & Li, C. (2000). Carbon isotope geochemistry of graphite deposits and ore-bearing khondalite series in North China: implications for several geoscientific problems. *Acta Petrologica Sinica, 16*, 233–244. (in Chinese with English abstract).

Chen, Y.-J., Zhai, M.-G., & Jiang, S.-Y. (2009). Significant achievement and open issues in study of orogenesis and metallogenesis surrounding the North China Continent. *Acta Petrologica Sinica, 25*, 2695–2726. (in Chinese with English abstract).

Cheng, Y.-Q. (1994). Regional Geology of China, Geological Publishing House, Beijing, pp. 1–517 (in Chinese).

Cheng, Y.-Q., Wang, Z.-J., & Huang, Z.-G. (Eds.). (2009). *Stratifical lexicon of China* (pp. 39–47). Beijing: Geological Publishing House.

Condie, K. C. (2001). *Earth plumes and their record in earth history* (p. 305). Cambridge: Cambrodge University Press.

Condie, K. C. 2004. Precambrian superplume event. In: Eriksson, P. G., Altermann, W., Nelson, D. R., Mueller, W. U., Catuneanu, O. (Eds.), The Precambrian Earth Tempos and Events. Development in Precambrian Geology, 12, Elsevier, Amsterdan, pp. 163–172.

Condie, K. C., & Kröner, A. (2008). When did plate tectonics begin? Evidence from the geologic record. *Geological Society of America, 440*, 281–294.

Davis, G. A., Darby, B. J., Zheng, Y. D., & Spell, T. L. (2002). Geometric and temporal evolution of an extensional detachment fault, Hohoht metamorphic core complex, Inner Mongolia, China. *Geology, 30*, 1003–1006.

Dewey, J. F., & Windley, B. F. (1981). Growth and differentiation of the continental crust. *Philosophical Transactions of the Royal Society of London, A301*, 189–206.

Diwu, C.-R., Sun, Y., Wilde, S. A., Wang, H.-L., Dong, Z.-C., Zhang, H., & Wang, Q. (2013). New evidence for ~4.45 Ga terrestrial crust from zircon xenocrysts in Ordovician ignimbrite in the North Qinling Orogenic Belt, China. *Gondwana Research, 23*, 1484–1490.

Dong, Y.-P., Liu, X.-M., Neubauer, F., Zhang, G.-W., Tao, N., Zhang, Y.-G., et al. (2013). Timing of Paleozoic amalgamation between the North China and South China Blocks: Evidence from detrital zircon U–Pb ages. *Tectonophysics, 586*, 173–191.

Fan, Q.-C., & Hooper, P. R. (1991). The Cenozoic basaltic rocks of Eastern China: Petrology and chemical composition. *Journal of Petrology, 32*, 765–810.

Fan, H.-R., Hu, F.-F., Yang, K.-F., & Wang, K.-Y. (2006). Intrusive age of No.1 carbonatite dyke from Bayan Obo REE-Nb-Fe deposit, Inner Mongolia: with answers to comment of Dr. Le Bas. *Acta Petrologica Sinica, 22*, 519–520. (in Chinese with English abstract).

Fan, W.-M., & Menzies, M. A. (1992). Destruction of aged lower lithosphere and asthenosphere mantle beneath eastern China. *Geotectonica et Metallogenia, 16*, 171–179. (in Chinese).

Liu X., Fan, H.-R., Santosh, M., Yang, K.-F., Qiu, Z.-J., HU, F.-F., et al. (2015b). Geological and geochronological constraints onthe genesis of the giant Tongkuangyu Cu deposit (Palaeoproterozoic), North China Craton. *International Geology Review* doi:10.1080/00206814.2015.1056759

Fan, H.-R., Xie, Y.-H., Wang, K.-Y., & Yang, X.-M. (2001). Carbonatitic fluids and REE mineralization. *Earth Science Frontiers, 8*, 289–295. (in Chinese with English abstract).

Liu X., Fan, H.-R., Yang, K.-F., HU, F.-F., Guo, S.-L., Zhao, F.-C., et al. (2015a). Formation ages of the Jiangxian and Zhongtiao groups in the Zhongtiao Mountain region, North China Craton: Insights from SIMS U–Pb dating on zircons of intercalated plagioclase amphibolites. *Acta Petrologica Sinica 31*(6), 1564–1572 (in Chinese with English abstract).

Fan, H.-R., Zhai, M.-G., Xie, Y.-H., & Yang, J.-H. (2003). Ore–forming fluids associated with granite–hosted gold mineralization at the Sanshandao deposit, Jiaodong gold province, China. *Mineralium Deposita, 38*(6), 739–750.

Gao, L.-Z., Liu, P.-J., Yin, C.-Y., Zhang, C.-H., Ding, X.-Z., Liu, Y.-X., & Song, B. (2011). Detrital Zircon Dating of Meso-and Neoproterozoic Rocks in North China and Its Implications. *Acta Geologica Sinica (English Edition), 85*(2), 271–282.

Gao, W., Zhang, C.-H., Gao, L.-Z., Shi, X.-Y., Liu, Y.-M., & Song, B. (2008). SHRIMP zircon U–Pb ages of Miyun rapakivi granite and their tectonic implication. *Geological Bulletin, 27*(6), 793–798. (in Chinese with English abstract).

Gao, L.-Z., Zhang, C.-H., Liu, P.-J., Ding, X.-Z., Wang, Z.-Q., & Zhang, Y.-J. (2009). Recognition of Meso-and Neoproterozoic stratigraphic framework in North and South China. *Acta Geosientica Sinica, 30*(4), 433–446. (in Chinese with English abstract).

Geng, Y.-S., Du, L.-L., & Ren, L.-D. (2012). Growth and reworking of the early Precambrian continental crust in the North China Craton: constraints from zircon Hf isotopes. *Gondwana Research, 21*, 517–529.

Geng, Y.-S., Wan, Y.-S., Shen, Q.-H., Li, H.-M., & Zhang, R.-X. (2000). Chronological framework of the Early Precambrian important events in the Lüliang area, Shanxi, Province. *Acta Geologica Sinica, 74*, 216–223. (in Chinese with English abstract).

Goldfarb, R. J., Grovers, D. I., & Gardill, S. (2011). Orogenic gold and geological time: A synthesis. *Ore Geology Reviews, 18*, 1–75.

González, P. D., Sato, A. M., Llambías, E. J., & Petronilho, L. A. (2009). Petrology and geochemistry of the banded iron formation in the Eastern Sierras Pampeanas of San Luis (Argentina): Implications for the evolution of the Nogolí Metamorphic Complex. *Journal of South American Earth Sciences, 28*, 89–112.

Goodwin, A. M. (1973). Archean iron-formation and tectonic basins of the Canadian Shield. *Economic Geology, 68*, 915–933.

Goodwin, A. (1991). *Precambrian geology*. London: Academic Press.

Guo, J.-H., Peng, P., Chen, Y., Jiao, S.-J., & Windley, B.-F. (2012). UHT sapphirine granulite metamorphism at 1.93–1.92 Ga caused by gabbronorite intrusions: Implications for tectonic evolution of the northern margin of the North China Craton. *Precambrian Research, 222–223*, 124–142.

Guo, P., Santosh, M., & Li, S. R. (2013). Geodynamics of gold metallogeny in the Shandong Province, NE China: An integrated geological, geophysical and geochemical perspective. *Gondwana Research, 24*, 1172–1202.

Hsü, K. J., Wang, Q., Li, J., Zhou, D., & Sun, S. (1987). Tectonic evolution of Qinling Mountains, China. *Eclogae Geologicae Helvetiae, 80*, 735–752.

Hu, B., Zhai, M.-G., Li, T. S., Li, Z., Peng, P., Guo, J.-H., & Kusky, T. M. (2012). Mesoproterozoic magmatic events in the eastern North China Craton and their tectonic implications: Geochronological evidence from detrital zircons in the Shandong Peninsula and North Korea. *Gondwana Research, 22*, 828–842.

Hua, R.-M., & Mao, J.-W. (1999). A preliminary discussion on the Mesozoic metallogenic explosion in east China: Mineral deposits 18: 301–308 (In Chinese).

Huang, J.-Q., Ren, J.-S., Jiang, C. F., Zhang, Z.-H., & Qin, D.-Y. (1980). *Geotectonics and evolution in China*. Beijing: Scientific Press. (In Chinese).

Jian, P., Liu, D.-Y., Kroner, A., Windley, B. F., Shi, Y.-R., Zhang, F.-Q., et al. (2008). Time scale of an Early to Mid-Paleozoic orogenic cycle of long-lived Central Asian Orogenic belt, Inner Mongolia of China: Implications for continental growth. *Lithos, 101*, 233–259.

Kerrich, R., Goldfarb, R. J., & Richards, J. P. (2005). Metallogenic provinces in an evolving geodynamic framework. *Economic Geology, 100*, 1097–1136.

Konhauser, K. O., Pecoits, E., Lalonde, S. V., Papineau, D., Nisbet, E. G., Barley, M. E., et al. (2009). Oceanic nickel depletion and a methanogen famine before the Great Oxidation Event. *Nature, 458*, 750–753.

Kusky, T. M., Li, J.-H., & Santosh, M. (2007a). The Paleoproterozoic North Hebei Orogen: North China Craton's collisional suture with Columbia supercontinent. *Gondwana Research, 12*, 4–28.

Kusky, T.M., Windley, B.F., & Zhai, M.-G. (2007b). Tectonic evolution of the North China Block: from orogen to craton to orogen. In: M. G. Zhai, B. F. Windley, T.M. Kusky, Q.R. Meng (Eds.), Mesozoic sub-Continental Lithospheric Thinning Under Eastern Asia. Geological Society Special Publication, London, 280, pp:1–34.

Li, S.-Z., Liu, Y.-J., Yang, Z.-S., & Ma, R. (1998). Relations between deformation and metamorphic recrystallization in metapelite of Liaohe Group. *Acta Petrologica Sinica, 14*, 351–365. (in Chinese with English abstract).

Li, H.-K., Lu, S.-N., Li, H.-M., Sun, L.-X., Xiang, Z.-Q., Geng, J.-Z., et al. 2009). Dating of zircon and baddeleyite for basic sills in the Xiamaling Group: constrain to division of Mesozoic strata in the North China Craton. *Geological Bulletin, 28*(10), 1396–1404. (in Chinese with English abstract).

Li, S.-R., Santosh, M., Zhang, H.-F., Shen, J.-F., Dong, G.-C., Wang, J.-Z., et al. (2013). Inhomogeneous lithospheric thinning in the central North China Craton: Zircon U–Pb and S–He–Ar isotopic record from magmatism and metallogeny in the Taihang Mountains. *Gondwana Research, 23*, 141–160.

Li, S.-Z., Zhao, G.-C., Santosh, M., Liu, X., Dai, L.-M., Suo, Y.-H., et al. (2012). Paleoproterozoic structural evolution of the southern segment of the Jiao-Liao-Ji Belt, North China Craton. *Precambrian Research, 200–203*, 59–73.

Liu, D.-Y., Nutman, A. P. W., Compston, W., Wu, J.-S., & Shen, Q.-H. (1992). Remnants of ≥3800 Ma crust in the Chinese part of the Sino-Korean Craton. *Geology, 20*, 339–342.

Mao, J.-W., Qiu, Y.-M., Goldfarb, R. J., Zhang, Z.-C., Garwin, S., & Ren, F.-S. (2002). Geology. *Distribution, and classification of gold deposits in the western Qinling belt, central China: Mineralium Deposita, 37*, 355–372.

Mclennan, S. M., & Taylor, S. R. (1983). Continental freeboard sedimentation rates and growth of continental crust. *Nature, 306*, 169–172.

Meng, Q.-R. (2003). What drove late Mesozoic extension on the northern China-Mogolia tract? *Tectonophysics, 369*, 155–174.

Meng, Q.-R., & Zhang, G.-W. (1999). Timing of collision of the North and South China Blocks: controversy and reconciliation. *Geology, 27*, 123–126.

Meng, Q.-R., & Zhang, G.-W. (2000). Geologic framework and tectonic evolution of the Qinling. *Tectonophysics, 323*, 183–196.

Menzies, M. A., Fan, W. M., & Zhang, M. (1993). Palaeozoic and Cenozoic lithoprobes and the loss of >120 km of Archean lithosphere, Sino-Korean craton, China. *Geological Society of London, Special Publication, 76*, 71–81.

Miao, L.-C., Zhang, F.-Q., Fan, W.-M., & Liu, D.-Y. (2007). Phanerozoic evolution of the Inner Mongolia-Daxinganling orogenic belt in the North China: Constraints from geochronology of ophiolites and associated formations. In: Zhai, M.G., Windley, B.F., Kusky, T.M., Meng, Q.R. (Eds.), Mesozoic sub-continental Lithospheric Thinning under East Asia (Vol. 280, pp. 223–237). Geological Society London, Special Publications.

Okay, A. I., & Sengör, A. M. C. (1993). Tectonics of an ultrahigh-pressure metamorphic terrane: The Dabie Shan/Tongbai Shan orogen, China. *Tectonics, 12*, 1320–1334.

Perry, E.C. Jr., & Ahmad, S. N. (1987). Oxygen isotope determinations of quartz and magnetite from Krivoy Rog. Presented at VIIth National Isotope Symposium (pp. 23–27). Moscow.

Peng, P., Zhai, M.-G., Ernst, R. E., Guo, J.-H., Liu, F., & Hu, B. (2008). A 1.78 Ga large igneous province in the North China craton: The Xiong'er volcanic province and North China dyke swarm. *Lithos, 101*, 260–280.

Peng, P., Zhai, M.-G., Li, Q.-L., Wu, F.-Y., Hou, Q.-L., Li, Z., et al. (2011). Neoproterozoic (~900 Ma) Sariwon sills in North Korea: Geochronology, geochemistry and implications for the evolution of the south-eastern margin of the North China Craton. *Gondwana Research, 20*, 243–354.

Peng, R.-M., Zhai, Y.-S., Wang, J.-P., & Liu, Q. (2010). Discovery of Neoproterozoic acid volcanic rock in the south-western section of Langshan, Inner Mongolia. *Chinese Science Bulletin, 55*(26), 2611–2620. (in Chinese with English abstract).

Peng, R.-M., Zhai, Y.-S., Wang, J.-P., & Liu, Q. (2014). The discovery of the Neoproterozoic rift-related mafic volcanism in the northern margin of North China Craton: Implications for Rodinia reconstruction and mineral exploration. International Conference on Continental Dynamics, 2014, Xi'an, China.

Peng, P., Zhai, M.-G., Zhang, H.-F., & Guo, J.-H. (2005). Geochronological constraints on Paleoproterozoic evolution of the North China craton: SHRIMP zircon ages of different types of mafic dikes. *International Geological Review, 47*, 492–508.

Ren, J.-S. (1989). New knowledge of geotectonic evolution of eastern China and adjacent regions. *Chinese Regional Geology, 4*, 3–14. (in Chinese with English abstract).

Roberts, N. M. W. (2012). Increased loss of continental crust during supercontinent amalgamation. *Gondwana Research, 4*, 994–1000.

Rogers, J. J. W., & Santosh, M. (2003). Supercontinents in Earth history. *Gondwana Research, 6*, 357–368.

Santosh, M. (2010). Assembling North China Craton within the Columbia supercontinent: The role of double-sided subduction. *Precambrian Research, 178*, 149–167.

Santosh, M., Liu, S.-J., Tsunogae, T., & Li, J.-H. (2012). Paleoproterozoic ultrahigh-temperature granulites in the North China Craton: Implications for tectonic models on extreme crustal metamorphism. *Precambrian Research*. doi:10.1016/j.precamres.2011.05.003

Santosh, M., Wilde, S. A., & Li, J.-H. (2007). Timing of Paleoproterozoic ultrahigh-temperature metamorphism in the North China Craton: Evidence from SHRIMP U–Pb zircon geochronology. *Precambrian Research, 159*, 178–196.

Sato, M. A. (2009). Less nickel for more oxygen. *Nature, 458*, 714–715.

Shen, B.-F., Zhai, A.-M., Chen, W.-M., Yang, C.-L., Hu, X.-D., Cao, X.-L., & Gong, X.-H. (2006). *The precambrian mineralization of China* (pp. 40–314). Beijing: Geological Publishing House.

Shen, Y.-C., Zhang, L.-C., & Liu, T.-B. (2000). Interlayer slide fault and its ore-controlling process. *Geology and Prospecting, 37*, 11–14. (in Chinese).

Sun, D.Z., & Hu, W.X. (1993). Precambrian Chronological-Tectonic Framework and Crustal Texture in Zhongtiao Mountains. Geological Publishing House, Beijing, pp. 1–180. (in Chinese).

Tang, H.-S., Chen, Y.-J., Santosh, M., Zhong, H., & Yang, T. (2012). REE geochemistry of carbonates from the Guanmenshan Formation, Liaohe Group, NE Sino-Korean Craton: Implications for seawater compositional change during the Great Oxidation Event. *Precambrian Research* .doi:10.1016/j.precamres.2012.02.005

Tang, H.-S., Chen, Y.-J., Wu, G., & Lai, Y. (2011). Paleoproterozoic positive δ^{13} C_{carb} excursion in northeastern Sino-Korean craton: Evidence of the Lomagundi Event. *Gondwana Research, 19*, 471–481.

Tang, H. S., Wu, G., & Lai, Y. (2009). The C–O isotope geochemistry and genesis of the Dashiqiao magnesite deposit, Liaoning Province, NE China. *Acta Petrologica Sinica, 25*, 455–467. (in Chinese with English Abstract).

Wan, B., Henger, E., Zhang, L.-C., Rocholl, A., Wu, H.-Y., & Chen, F.-K. (2009). Rb-Sr geochronology of chalcopyrite from Chenhugou porpgyry Mo-Cu deposit (Northeast China) and geochemical constraints on the origin of hosting granites. *Economical Geology, 104*, 351–362.

Wan, Y.-S., Liu, D. Y., Wang, W., Song, T.-R., Kröner, A., Dong, C.-Y., et al. (2011a). Provenance of Meso-to Neoproterozoic cover sediments at the Ming Tombs, Beijing, North China Craton: An integrated study of U–Pb dating and Hf isotopic measurement of detrital zircons and whole-rock geochemistry. *Gondwana Research, 20*, 219–242.

Wan, Y.-S., Liu, D.-Y., Wang, S.-J., Yang, E.-X., Wang, W., Dong, C.-Y., et al. (2011b). ~2.7 Ga juvenile crust formation in the North China Craton (Taishan-Xintai area, western Shandong Province): Further evidence of an understated event from U–Pb dating and Hf isotopic composition of zircon. *Precambrian Research, 186*, 169–180.

Wan, Y.-S., Song, B., Liu, D.-Y., Li, H.-M., Yang, C., Zhang, Q.-D., et al. (2001). Geochronology and geochemistry of 3.8–2.5 Ga Archaean rock belt in Dongshan scenic park. *Anshan area. Acta Geologica Sinica, 75*, 363–370. (in Chinese with English abstract).

Wang, W. (2013). Phase equilibria modeling and zircon U–Pb geochronology of the Erdos basement rocks for the tectonic

evolution of the North China Craton (Oral speak). In: International Meeting of Precambrian and Deep Exploration of the Continental Lithosphere, Beijing, China, 6–9 Oct.

Wang, H.-L., Chen, L., Sun, Y., Liu, X.-M., Xu, X.-Y., Chen, J.-L., et al. (2007). ~4.1 Ga xenocrystal zircon from Ordovician volcanic rocks in western part of North Qinling Orogenic belt. *Chinese Science Bulletin, 52*, 3002–3010.

Wang, C.-L., Zhang, L.-C., Lan, C.-Y., & Dai, Y.-P. (2014). Rare earth element and yttrium compositions of thePaleoproterozoic Yuanjiacun BIF in the Lüliang area andtheir implications for the Great Oxidation Event (GOE). *Science China Earth Sciences, 57*(10), 2469–2485.

Wei, J.-Y. (1985). Oxygen isotopic composition of iron ore from Gongchangling, Anshan. In: Paper Compilation of Geological Study. Peking University Press, Beijing.

Wu, F.-Y., Ge, W.-C., & Guo, C.-L. (2003). Discussion of lithospheric thinning in East China. *Earth Science Fouties, 10*, 51–60 (in Chines with English abstract).

Wu, F. Y., Yang, J. H., Liu, X. M., Li, T. S., Xie, L. W., & Yang, Y. H. (2005). Hf isotopes of the 3.8 Ga zircons in eastern Hebei Province, China: implications for early crustal evolution of the North China Craton. *Chinese Science Bulletin, 50*, 2473–2480.

Xiao, W.-J., Windley, B. F., Hao, J., & Zhai, M.-G. (2003). Accretion leading to collision and the Permian Solonker suture. Inner Mongolia, China: Termination of the central Asian orogenic belt. *Tectonics, 22*, 1069–1076.

Xiao, W.-J., Wiondley, B., Sun, S., Li, J.-L., Huang, B.-C., Han, C.-M., et al. (2015). A Tale of Amalgamation of Three Permo-Triassic Collage Systems in Central Asia: Oroclines, Sutures, and Terminal Accretion. *Annual Review of Earth and Planetary Sciences, 43*, 477–507.

Xu, P.-F. (2001a). 3-D velocity structures of lithological layer in the Diabie-Sulu orogenic belt and eastern North China block: Beijing, China, Institute of Geology and Geophysics, Chinese Academy of Sciences, unpubl. Report. pp. 36–49 (in Chinese).

Xu, Y.-G. (2001b). Thermo-tectonic destruction of the Archean lithospheric keel beneath the Sino-Korea craton in China: evidence, timing and mechanism. Physics and Chemistry of the Earth, Part A: Solid Earth and Geodesy 26, 741–757.

Xu, Z.-Q., Lu, Y.-L., Tang, Y.-Q., & Zhang, Z.-T. (1988). Formation of composite mountain chains of the East Qinling-Deformation, evolution, and plate dynamics (p. 193). Beijing: China Environmental Science Press (in Chinese with English abstract).

Yang, K.-F., Fan, H.-R., Santosh, M., Hu, F.-F., & Wang, K.-Y. (2011a). Mesoproterozoic carbonatitic magmatism in the Bayan Obo deposit, Inner Mongolia, North China: Constraints for the mechanism of super accumulation of rare earth elements. *Ore Geology Reviews, 40*, 122–131.

Yang, K.-F., Fan, H.-R., Santosh, M., Hu, F.-F., & Wang, K.-Y. (2011b). Mesoproterozoic mafic and carbonatitic dykes from the northern margin of the North China Craton: Implications for the final breakup of Columbia supercontinent. *Tectonophysics, 498*, 1–10.

Yang, J.-H., Wu, F.-Y., Liu, X.-M., & Xie, L.-W. (2005). Zircon U–Pb age and Hf-isotope composition and geological significance. *Acta Petrologica Sinica, 21*(6), 1633–1644.

Young, G.-M., (2012). Precambrian supercontinents, glaciations, atmospheric oxygenation, metazoan evolution and an impact that may have changed the second half of Earth history. Geoscience Frontiers. doi:org/10.1016/j.gsf.2012.07.003

Zahnle, K. J., Claire, M. W., & Catling, D. C. (2006). The loss of mass-independent fractionation of sulfur due to a Paleoproterozoic collapse of atmosphere methane. *Geobiology, 4*, 271–283.

Zeng, Q.-D., Liu, J.-M., Chen, W.-J., Qin, F., Zhang, R.-B., Yu, W.-B., et al. (2009). Mineralizing types, geological characteristics and geodynamics background of molybdenum deposits in Xilamulu molybdenum polymetal metallogenic belt on northern North China Craton. *Acta Petrologica Sinica, 25*(5), 1225–1238. (in Chinese with English abstract).

Zhai, M.-G. (1993). Archean Anshan BIFs and gneisses. In Zhao, Z.P., et al. (Eds.), Precambrian Crustal Evolution of the Sino-Korean Paraplatform (pp. 389–390). Beijing: Science Press (in Chinese).

Zhai, M.-G. (2010). Tectonic evolution and metallogenesis of North China Craton. *Mineral Deposit, 39*(1), 24–36. (in Chinese with English abstract).

Zhai, M.-G. (2013). The main old lands in China and assembly of Chinese unified continent. *Science China, Earth Sciences, 56*(11), 1829–1852.

Zhai, M.-G. (2014). Multi-stage crustal growth and cratonization of the North China Craton. *Geoscience Frotiers, 5*, 457–469.

Zhai, M.-G., Bian, A. G., & Zhao, T. P. (2001). Amalgamation of the supercontinental of the North China craton and its break up during late–middle Proterozoic. *Science in China (D), 43*, 219–232.

Zhai, M. G., Fan, H. R., Yang, J. H., & Miao, L. C. (2004a). Large-scale cluster in east Shandong: Anorogenic metallogenisis. *Earth Science Frontiers, 11*, 85–98.

Zhai, M.-G., Fan, Q.-C., Zhang, H.-F., & Sui, J.-L. (2007). Lower crustal processes leading to Mesozoic lithospheric thinning beneath Eastern North China: Underplating, replacement and delamination. *Lithos, 96*, 36–54.

Zhai, M.-G., Hu, B., Zhao, T.-P., Peng, P., & Meng, Q.-R. (2015). Late Paleoproterozoic–Neoproterozoic multi-rifting events in the North China Craton and their geological significance: a study advance and review. *Tectonophysics*. doi:10.1016/j.tecto.2015.01.019

Zhai, M.-G., & Liu, W.-J. (2003). Paleoproterozoic tectonic history of the North China craton: a review. *Precambrian Research, 122*, 183–199.

Zhai, M.-G., Liu, J.-M., Zhang, H.-F., Liu, W., & Zhu, R.-X. (2004b). Time-range of Mesozoic tectonic regim inversion in eastern north China block. *Science in China (D), 34*(2), 151–159.

Zhai, M.-G., & Santosh, M. (2011). The early Precambrian odyssey of North China Craton: A synoptic overview. *Gondwana Research, 20*(1), 6–25.

Zhai, M.-G., & Santosh, M. (2013). Metallogeny of the North China Craton: Link with secular changes in the evolving Earth. *Gondwana Research, 24*, 275–297.

Zhai, M.-G., & Windley, B. F. (1990). The Archean and Early Proterozoic iron formation of North China: Their characteristics, geotectonic relations, chemistry and implications for crustal growth. *Precambrian Research, 48*, 267–286.

Zhang, Q.-S. (1984). *Geology and Metallogeny of the Early Precambrian in China* (pp. 171–192). Changchun: Jilin People Press.

Zhang, G.-W. (Ed.) (1988). Formation and evolution of the Qinling orogen: Xi'an, pp. 192, Northwest University Press, (in Chinese, with English abstract).

Zhang, S.-H., Li, Z.-X., Evans, D. A. D., Wu, H.-C., Li, H.-Y., Dong, J. et al. (2012a). Pre-Rodinia supercontinent Nuna shaping up: A global synthesis with new paleomagnetic results from North China. *Earth and Planetary Science Letters, 353–354*, 145–155.

Zhang, H.-F., Sun, M., Zhou, X.-H., Fan, W.-M., Zhai, M.-G., & Ying, J.-F. (2002). Mesozoic Lithosphere destruction beneath the North China Craton: evidence from major, trace element, and Sr–Nd–Pb isotope studies of Fangcheng basalt. *Contribution to Mineralogy and Petrology, 144*, 241–253.

Zhang, Z., Wu, J., Deng, Y., Teng, J., Zhang, X., Chen, Y., Panza, G. et al. (2012b). Lateral variation of the strength of lithosphere across

eastern North China Craton: New constraints on lithospheric destruction. *Gondwana Research, 22*, 1047–1059.

Zhang, X.-H., Wilde, S. A., Zhang, H.-F., Tang, Y.-J., Zhai, M.-G. et al. (2009a). Geochemistry of hornblende gabbros from Sonizuoqi, Inner Mongolia, North China: Implication for magmatism during the final stage of super-subduction zone ophiolite formation. *International Geology Review, 51*, 345–373.

Zhang, L.-C., Wu, H.-Y., Xiang, P., Zhang, X.-J., Chen, Z. C., Wan, B. et al. (2010a). Ore-forming processes and mineralization of complex tectonic system during the Mesozoic: A case from Xilamulun Cu-Mo metallogenic belt. *Acta Petrologica Sinica, 26*(5), 1351–1362. (in Chinese with English abstract).

Zhang, X.-H., & Zhai, M.-G. (2010). Magmatism and its metallogenetic effects during the Paleozoic continental construction in the North China: An overview. *Acta Petrologica Sinica, 26*(5), 1329–1341. (in Chinese with English abstract).

Zhang, L.-C., Zhai, M.-G., Zhang, X.-J., Xiang, P., Dai, Y.-P., Wang, C.-L., & Pirajno, F. (2012c). Formation age and tectonic setting of the Shirengou Neoarchean banded iron deposit in eastern Hebei Province: Constraints from geochemistry and SIMS zircon U–Pb dating. *Precambrian Research, 222–223*, 325–338.

Zhang, X.-H., Zhang, H.-F., Jiang, N., Zhai, M.-G., & Zhang, Y.-B. (2010b). Early Devonian alkaline intrusive complex from the northern North China Craton: A petrologic monitor of post-collisional tectonics. *Journal of the Geological Society (London), 167*, 717–730.

Zhang, X.-H., Zhang, H.-F., Tang, Y.-J., Wilde, S. A., & Hu, Z.-C. (2008). Geochemical of Permian bimodel volcanic rocks from Central Inner Mongolia, North China: implication for tectonic setting and Phanerozoic continental growth in Central Asia Orogenic Belt. *Chemical Geology, 249*, 261–281.

Zhang, S.-H., Zhao, Y., Hu, J.-M., & Wu, F. (2013). New constrains on ages of the Chuanglinggou and Tuanshanzi formations of the Changcheng System in the Yan-Liao area in the northern China Craton. *Acta Petrologica Sinica, 29*(07), 2481–2490. (in Chinese with English abstract).

Zhang, S.-H., Zhao, Y., Yang, Z.-Y., He, Z.-F., & Wu, H. (2009b). The 1.35 Ga diabase sills from the northern North China Craton: Implications for breakup of the Columbia (Nuna) supercontinent. *Earth and Planetary Science Letters, 288*, 588–600.

Zhao, Z.-F., et al. (1993). Precambrian crustal evolution of the Sino-Korean Paraplatform, pp. 389–390. Beijing: Science Press, (in Chinese).

Zhao, Z.-H. (2010). Banded Iron Formation and related great oxidation event. *Earth Science Fronties, 17*(2), 1–12. (in Chinese with English abstract).

Zhao, G.-C., Cao, L., Wilde, S. A., Sun, M., Choe, W. J., & Li, S.-Z. (2006). Implications based on the first SHRIMP U-Pb zircon dating on Precambrian granitoid rocks in North Korea. *Earth and Planetary Science Letters, 251*, 365–379.

Zhao, T.-P., Deng, X.-Q., Hu, G.-H., Zhou, Y.-Y., Peng, P., & Zhai, M.-G. (2015). The Paleoproterozoic-Mesoproterozoic boundary of the North China Craton and the related geological issues: A review. *Acta Petrologica Sinica, 31*(6), 1495–1508.

Zhao, G.-C., Sun, M., Wilde, S. A., & Li, S.-Z. (2005). Late Archean to Paleoproterozoic evolution of the North China Craton: key issues revisited. *Precambrian Research, 136*, 177–202.

Zhao, T.-P., Zhai, M.-G., Xia, B., Li, H., Zhang, Y.-X., & Wan, Y.-S. (2004). SHRIP zircon chronology of the Xiong'er volcanic rocks and constrain to starting time of the cover of the North China Craton. *Chinese Scientific Bulletin, 9*(23), 2495–2502.

Zhao, T.-P., & Zhou, M. (2009). Geochemical constraints on the tectonic setting of Paleoproterozoic A-type granites in the southern margin of the North China Craton. *Journal of Asian Earth Sciences, 36*, 183–195.

Zheng, J.-P., Su, M., Lu, F.-X., & Person, N.-J. (2003). Mesozoic lower crustal xenoliths and their significance in lithospheric evolution beneath the Sino-Korea. *Tectonophysics, 361*, 37–60.

Zheng, M.-T., Zhang, L.-C., Wang, C.-L., Zhu, M.-T., Li, Z.-Q., & Wang, T.-T. (2015). Formation age and origin of the BIF-type iron deposit in eastern Hebei Province. *Acta Petrologica Sinica, 31*(6), 1636–1652. (in Chinese with English abstract).

Zhu, R.-X., Xu, Y.-G., Zhu, G., & Zhang, H.-F. (2012). Destruction of the North China Craton. *Science China, 55*(10), 1565–1587.

Zhu, L.-M., Zhang, G.-W., Li, B., & Guo, B. (2008). Main geological events, genetic types of metallic deposits and their geodynamical setting in the Qinling Orogenic Belt. *Bulletin of Mineralogy, Petrology and Geochemistry, 27*(4), 384–390. (in Chinese with English abstract).

Part I
Archean Crustal Growth and Metallogeny

Archean Continental Crust in the Southern North China Craton

2

Chunrong Diwu, Chengli Zhang, and Yong Sun

Abstract

The Archean-Paleoproterozoic metamorphic basement is well exposed in the southern North China Craton (NCC), and can be divided into three distinct tectonic complexes, naming, the Sushui, Dengfeng and Taihua complexes. Their equivalents probably extend into the Huoqiu and Bengbu areas of Anhui Province in the southeastern margin of the NCC, and the Longshan area of Gansu Province in the southwestern margin. In the last decade, a large number of the Mesoarchean–Neoarchean (ca. 2.85–2.50 Ga) rocks have been widely recognized in those complexes, which provides important insights into the formation and evolution of NCC during this period. Based on the available isotopic data, the Archean continental crust of the southern NCC can be divided into the 2.85–2.70 Ga and ca. 2.50 Ga rock associations. Most of zircons in the 2.85–2.70 Ga rocks that consist predominantly of TTG gneisses have variable but positive $\varepsilon_{Hf}(t)$ values, and their magmatic zircon domains that are characterized by oscillatory zoning in CL images present mantle-like O isotopes, reflecting a somewhat geochemically heterogeneous but depleted mantle Hf isotope reservoir dominates the source of these rocks. The whole-rock Nd isotopic data show similar geochemical characteristics, confirming juvenile sources for their provenance. Although majority of Chinese Precambrian geologists suggested that the ca. 2.50 Ga tectonothermal events were mainly involved in crustal reworking or partial melting of the early Neoarchean mafic crust formed at 2.85–2.70 Ga, we emphasize that ca. 2.50 Ga is another major period of continental crust growth in the southern NCC as well as the whole NCC based on the following lines of evidence: (1) a variable proportion of metabasaltic rocks with ca. 2.50 Ga zircon U–Pb ages exposed in both the high-grade gneissic complexes and the low-grade granite-greenstone terrenes. (2) the metabasaltic rocks present mixed MORB- and/or arc-like geochemical affinities, suggesting that they were derived from mantle source with minor continental crust contamination. (3) most of the ca. 2.50 Ga magmatic zircons from TTG gneisses, amphibolites and related rocks have positive $\varepsilon_{Hf}(t)$ values that are similar to those of the contemporaneous depleted mantle, and their Hf model ages of 2.85–2.49 Ga are close to corresponding U–Pb ages, suggesting that these rocks originated from the juvenile crust at ca. 2.50 Ga. (4) the whole-rock Nd isotopic data of the ca. 2.50 Ga rocks show similar geochemical characteristics, confirming juvenile sources for their provenance. In summary, we suggeste that the southern NCC underwent two marked episodes of continental crust growth at 2.85–2.70 Ga and ca. 2.50 Ga during the Archean, and all the complexes in the southern NCC were welded together to form a coherent ancient terrane at the end of the Neoarchean, we named it the "Southern Archean Block (SAB)". The SAB show an east–west trending belt from Gansu across Shaanxi and

C. Diwu (✉) · C. Zhang · Y. Sun
State Key Laboratory of Continental Dynamics, Department of Geology, Northwest University, Xi'an, China
e-mail: diwuchunrong@nwu.edu.cn

M. Zhai et al. (eds.), *Main Tectonic Events and Metallogeny of the North China Craton*,
Springer Geology, DOI 10.1007/978-981-10-1064-4_2

Henan into Anhui Province, stretching over 1000 km long, it may has experienced a long geological history which can be traced back to the Hadean. The ca. 2.50 Ga K-rich granitoid rocks were recognized from the southern NCC, which are commonly considered as the proxy of the final stabilization of the block lithosphere.

Keywords
Precambrian • Archean • North China Craton • Continental crust growth • Zircon

2.1 Introduction

Compared with the oceanic crust, the continental crust is stable, thick, and ancient. Although it constitutes only 0.6 % mass of the silicate earth and 40 % of the surface area of the Earth (Rudnick and Gao 2014), it is the archive of the geological history of the Earth. The Archean era (4.5–2.5 billion years) covers more than half of the entire history of the Earth. Models based on the U–Pb, Hf and O isotopic compositions of detrital zircons suggested that at least 60–70 % of the present volume of continental crust had been generated at the end of the Neoarchean, and there was a marked decrease in the rate of crustal growth at ca. 3.0 Ga in global scale (Belousova et al. 2010; Cawood et al. 2013; Hawkesworth et al. 2013). However, a large volume of Archean continental crust have been destroyed by weathering/erosion, crustal reworking or recycled back into the mantle, it was documented that less than 5 % of the current volume at that time was preserved today (Cawood et al. 2013), most of old remnants Archean crust are within craton now presently character by thick lithospheric mantle roots (Bowring and Housh 1995).

The database of global zircon ages from both granitoids and detrital sediments show two major age peaks or peak clusters at 2.70 and 1.90 Ga during the early Precambrian period (Condie et al. 2009a; Condie and Aster 2010), only the 2.70 Ga cluster is prominent and unique, it registers a global event on the continents, thus some researchers suggested that the first supercontinent named Kenorland was as far back as 2700–2650 Ma with a corresponding age cluster of 2.7 Ga (Bleeker 2003). However, the North China Craton (NCC) is one of the oldest cratons in the world preserving continental rocks up to 3.80 Ga old (Liu et al. 1992, 2008; Wan et al. 2005, 2012; Wu et al. 2008). It presents a younger U–Pb age peaks at ca. 2.50 Ga in the period of the Archean, and a large volume of Tonalitic–trondhjemitic–granodioritic (TTG) gneisses, mantle-derived granites and minor supracrustal rocks were formed during this time (Zhai et al. 2003; Zhai and Santosh 2011, 2013), thus some researchers emphasized that the ca. 2.50 Ga tectonothermal event represents a major period of continental crust growth in the NCC (Diwu et al. 2011; Liu et al. 2009b), which is one of the characteristics of the NCC, and markedly different from most other cratons worldwide. Recently, 2.85–2.70 Ga rocks were also recognized in several regions in the NCC (Wan et al. 2014), such as Wuchuan, Hengshan, Fuping, Zanhuang, Shandong, Zhongtiao, Lushan, Xiaoqinling, and Huoqiu. The whole-rock Sm–Nd isotopic data and zircon Hf isotopic compositions indicate that the major continental crust growth event in the NCC occur at 2.85–2.70 Ga, similar to many other cratons in the world, whereas the 2.50 Ga tectonothermal event was mainly involved in crustal reworking or partial melting of the early Neoarchean mafic crust formed at 2.85–2.70 Ga (Wu et al. 2005; Geng et al. 2012; Zhao 2014). The Archean basement rocks are well exposed in the southern NCC, therefore, it is an excellent area for understanding the formation and evolution of NCC at this period. In this contribution, we review the spatial and temporal distribution of the Archean rocks, and present an integrated available whole-rock Nd and Hf-in-zircon isotopic data with a principal aim to provide a comprehensive scenario for the Archean continental crust growth and evolution of the southern NCC.

2.2 Major Archean Lithotectonic Units

The early Precambrian (>1.80 Ga) rocks in the southern NCC show an east–west trending belt from the Gansu across Shaanxi and Henan into Anhui Province, stretching over 1000 km long, which are mainly occurred as high-grade gneissic complexes or low-grade granite-greenstone terranes in Zhongtiaoshan, Dengfeng, Lushan, and Xiaoqinling areas (Fig. 2.1), they were named Sushui, Dengfeng, and Taihua complexes, respectively. Moreover, their equivalents probably extend into the Longshan area of Gansu Province in the most southwestern margin and the Huoqiu area of Anhui Province in the most southeastern margin of the NCC.

2.2.1 Sushui Complex

The Sushui Complex chiefly occurred along the northwestern area of the Zhongtiaoshan, Shanxi Province, it presents a

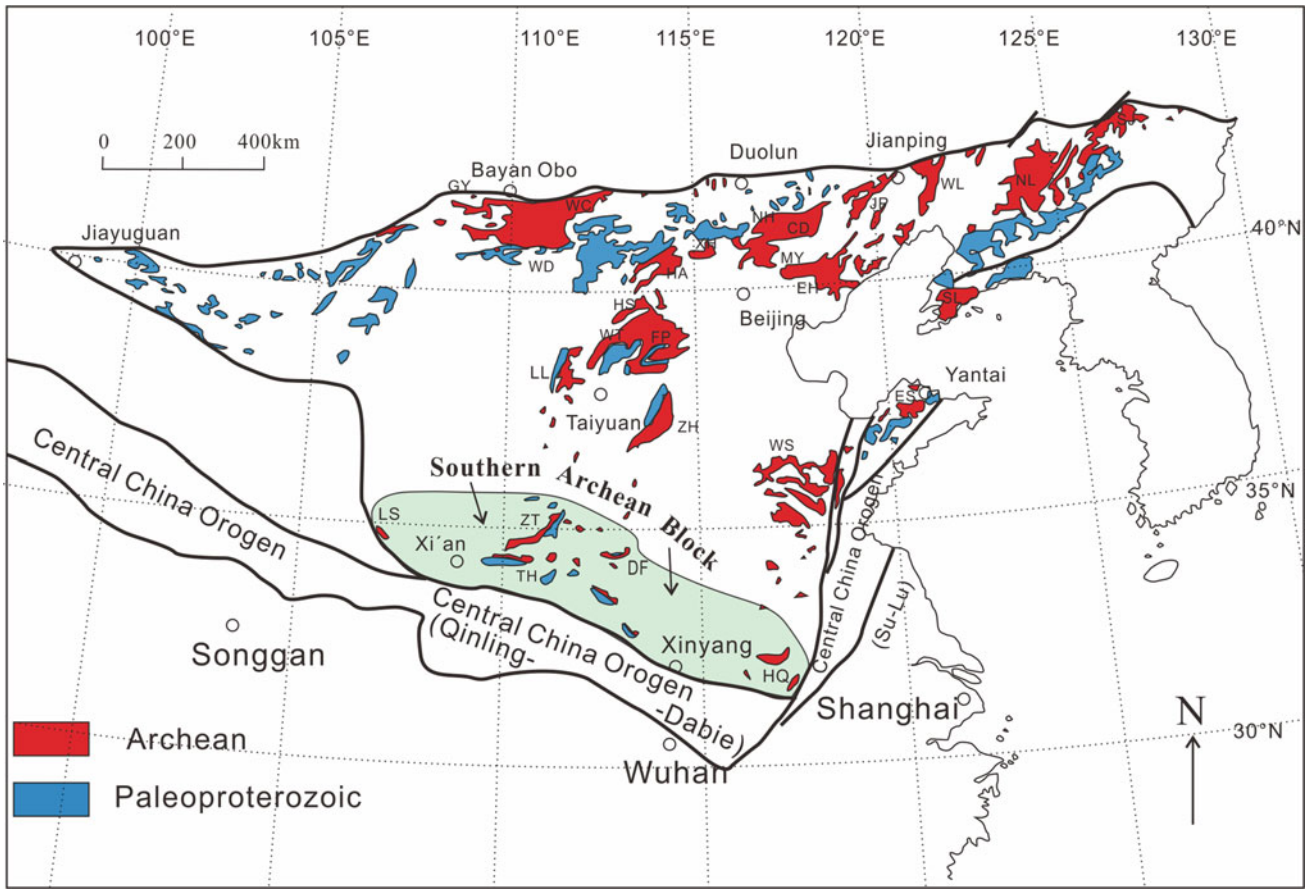

Fig. 2.1 Simplified geological map showing the distribution of metamorphic complexes in the NCC (revised after Zhao et al. 2005). Abbreviations for metamorphic complexes: *CD* Chengde; *D* Dengfeng; *EH* Eastern Hebei; *ES* Eastern Shandong; *FP* Fuping; *GY* Guyang; *HA* Huai'an; *HL* Helanshan; *HQ* Huoqiu; *HS* Hengshan; *JN* Jining; *LG* Langrim; *LL* Lüliang; *LS* Longshan; *MY* Miyun; *NH* Northern Hebei; *NL* Northern Liaoning; *QL* Qianlishan; *SJ* Southern Jilin; *SL* Southern Liaoning; *TH* Taihua; WD Wulashan-Daqingshan; *WL* Western Liaoning; *WS* Western Shandong; *WT* Wutai; *XH* Xuanhua; *ZH* Zanhuang; *ZT* Zhongtiao

northeast–southwest trending zone, extending 200 km long. The complex also scarcely exposed in Yumenkou area of the northern Hancheng, Shaanxi Province.

The Sushui Complex in the Zhongtiaoshan is unconformably overlain by Paleoproterozoic Jiangxian, Zhongtiao, and Danshanshi groups and Mesoproterozoic Xiyanghe and Ruyang groups (Sun et al. 1990; Sun and Hu 1993; Bai et al. 1997) (Fig. 2.2). It consists principally of the Neoarchean granitoid plutons and supracrustal rocks. The former can be subdivided into the Neoarchean (ca. 2.75–2.50 Ga) Xiyao, Zhaizi, and Beiyu TTG gneisses, Neoarchean (Ca. 2.60 Ga) Henglingguan and Haizhou monzogranitic gneisses, and Paleoproterozoic (ca. 2.30 Ga) Yanzhuang potassic granitoid rocks. The latter make up of Lengkou and Chaijiayao supracrustal rocks.

The Xiyao gneisses are mainly exposed in Xiaxian and Haizhou areas in the southwestern part of the Zhongtiaoshan. They are composed predominantly of medium-grained TTG gneisses with minor dioritic gneisses, enclosing amphibolite gneisses, most of which have been strongly deformed with fine banded structures and the migmatized zones, suggesting evidence of in situ melting and advanced anatexis. The Xiyao gneisses were previously considered to have been formed at Mesoarchean. However, recent U–Pb zircon ages reveal that they were mainly emplaced at late Neoarchean (ca. 2.50 Ga) (Tian et al. 2006; Guo et al. 2008; Zhang 2015); it is noteworthy that sparse ca. 2.70 Ga trondhjemitic and dioritic gneisses were also recognized from the Xiyao gneisses (Zhu et al. 2013), confirming the existence of ca. 2.70 Ga crustal components in the Zhongtiaoshan.

The Neoarchean (ca. 2.50 Ga) Zhaizi gneisses are distributed in the areas of Lengkou-Yanzhuang and Caojiagou-Xipingchun with an outcrop area of 35 km^2 in the Northwestern part of the Zhongtiaoshan. Whereas the Neoarchean Beiyu gneisses are composed of orthogneisses with trondhjemitic composition and have coarse-grained texture and massive to gneissic structure, which only

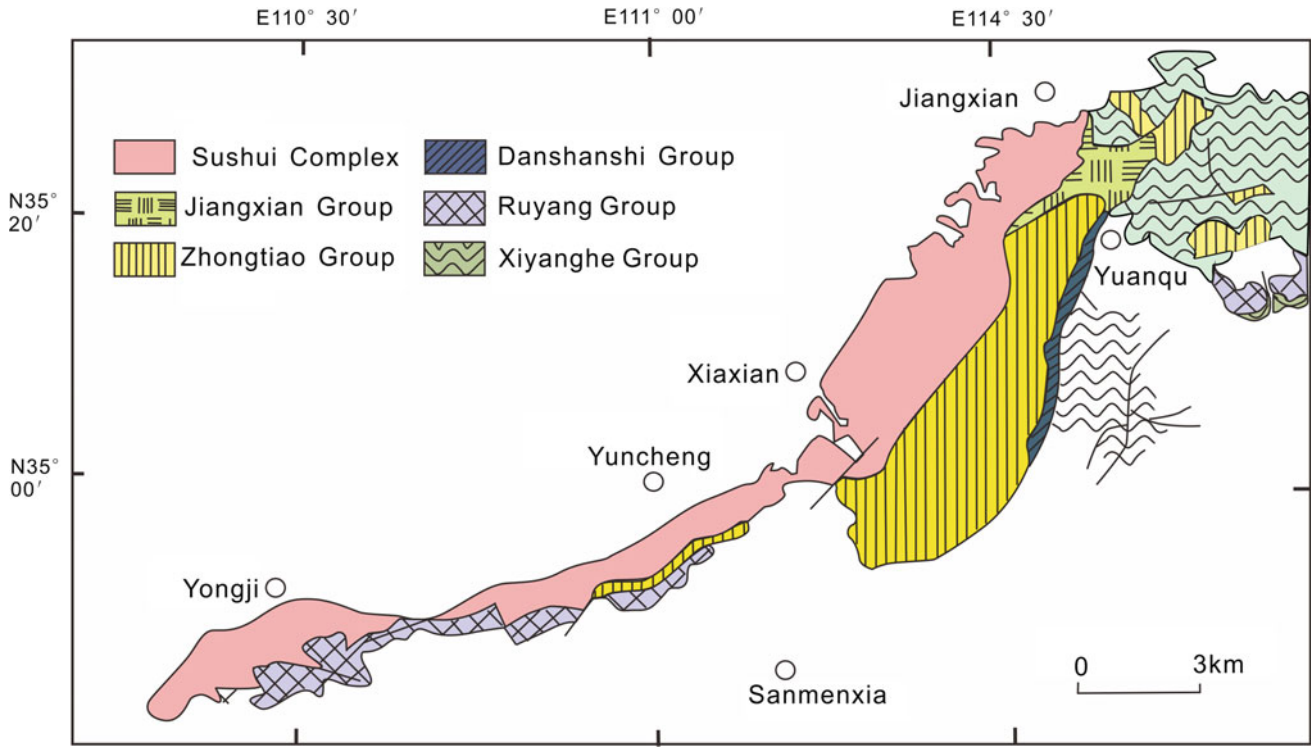

Fig. 2.2 Geological map of the Zhongtiaoshan area (Bai et al. 1997)

exposed at the core of the Hujiayu anticline in the Beiyu area of middle segment of the Zhongtiaoshan covering an area of 2.5 km^2.

The Lengkou supracrustal rocks are unconformably overlain by Quaternary in the northwest and tectonically contacted with Zhaizi gneisses in the southeast. They outcrop predominantly in the Lengkou-Zuantianling area with an area of approximately 6 km^2, and consist of various mica schists and amphibolites with metamorphic grade from greenschist to lower amphibolite faces and composition from mafic to felsic (Sun et al. 1990). Whereas the Chaijiayao supracrustal rocks, which mainly occurred in the Chaijiayao area of the southern Zhongtiaoshan are composed chiefly of metasediments, including large quantities of metapelite and quartzite, and variable amounts of carbonate and conglomerate (Sun et al. 1990). Zircons in an amphibolite sample of the Lengkou area yielded an upper intercept age of 2561 ± 22 Ma using a LA-ICPMS technique, suggesting that the supracrustal rocks of the Zhongtiao Mountains were formed in the Neoarchean (Zhang 2015).

2.2.2 Dengfeng Complex

The Dengfeng Complex, named by Ma Xing-Yuan (1957), is geographically exposed in the Junzhao and Linru areas in the central Henan Province (Fig. 2.3). It is comprised of two distinct lithologic units of the Neoarchean granitoid plutons and supracrustal rocks with essential features of Neoarchean granite–greenstone terrene worldwide (Zhang et al. 1985; Guo 1987, 1988, 1989; Guo and Zhou 1990). The complex also has been identified in drillhole samples from the Xuchang region of Hennan province.

The supracrustal assemblage in the Junzhao and Linru areas was previously named "Dengfeng Group" and "Angou Group", respectively (Zhang et al. 1985; Guo 1987, 1988, 1989; Guo and Zhou 1990). The Dengfeng Group is a metamorphosed volcano-sedimentary succession, from bottom to top, which has been subdivided into the Guojiayao, Jinjiamen and Laoyanggou formations (Fig. 2.4). The lowermost Guojiayao Formation is chiefly of mafic volcanic rocks with minor felsic volcanics and sedimentary rocks, whereas the overlying Jinjiamen and Laoyanggou formations are composed dominantly of metamorphosed argillo-arenaceous, argillic and siliceous ferruginous rocks with minor mafic volcanic rocks, most of which have been metamorphosed to the medium-pressure almandine-amphibolite facies (Zhang et al. 1982, 1985; Diwu et al. 2011). The Angou group is underlain by the upper part of the Dengfeng supracrustal rocks, and overlain by Paleoproterozoic quartzite of the Songshan Group (Fig. 2.5). Compared with the Dengfeng Group, it has similar rock assemblages, and it also can be subdivided into two parts of Zhaigou and Shitigou formations. The lower Zhaigou Formation comprises bimodal volcanic, volcaniclastic sediments,

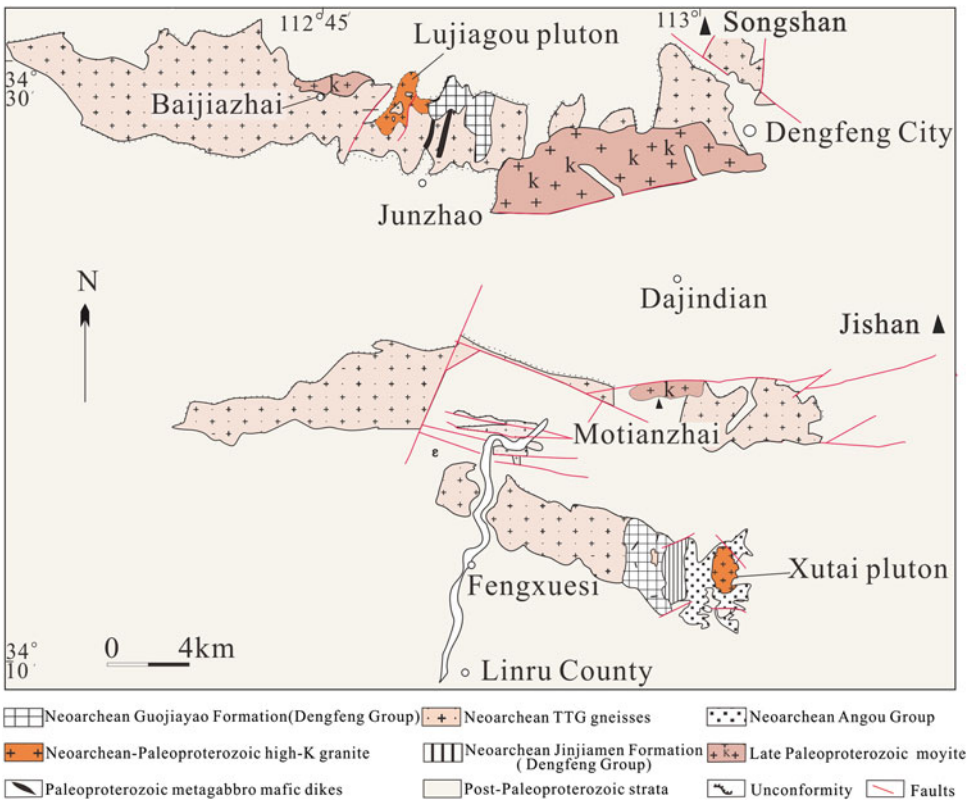

Fig. 2.3 Simplified geological map of the Junzhao-Linru area

and minor sedimentary rocks; while the upper Shitigou Formation consists mainly of littoral-shallow marine terrigenous clastic rocks interbedded associated with minor bimodal volcanic and volcaniclastic rocks. The Angou Group has undergone lower metamorphosed to greenschist facies and less deformed, locally preserving igneous textures, such as amygdaloidal, pillow, and blastoporphyritic primary structures (Zhang et al. 1982; Guo 1987). Previously, based on differences of lithological, structural, metamorphic, and geochronological features, some researchers suggested that the Angou Group is underlain by the Dengfeng Group (Fig. 2.5), thus its formation age is probably younger than that of the Dengfeng Group, and can be limited to the Paleoproterozoic (Zhang et al. 1982; Guo 1987). However, according to the recent SHRIMP zircon U–Pb ages, the Angou Group also formed in the late Neoarchean, which is nearly coeval with the Dengfeng Group (Yang et al. 2009).

The Neoarchean granitoid plutons, which are mainly composed of TTG gneisses, metadiorites, and potassic granites, outcropped in the Junzhao area of the western Dengfeng city (Fig. 2.4), and frequently occurred at the cores of domes or antiforms. They have undergone amphibolite facies metamorphism with strongly polyphase deformation and foliation. The sharp and discordant contacts with surrounding rocks identified in some places suggest that the granitic plutons have been forcefully intruded (Zhang et al. 1982, 1985; Diwu et al. 2011). The metadiorites, named as "Shipaihe metadiorite mass" (Wang et al. 1987, 2004), are located in the central part of the complex in the Junzhao area, and occur as intrusions in the Dengfeng supracrustal assemblage. They are often found to be intruded by ptygmatic felsic veins or dykes in the field. The potassic granites are exposed in the Lujiagou area of the west of the Songshan and Xutai area to the east of the Jishan. The Liujiagou potassic granites crop out with an area of $\sim$3.2 km^2. They intrude into the Neoarchean TTG gneisses and in the lower part of the Dengfeng supracrustal rocks, and are overlain by the Paleoproterozoic Songshan Group in the east and Mesoproterozoic Wufoshan Group in the north. The Xutai potassic granites are about $\sim$4 km^2 in the outcrop, which intrude into the Anguo Group (Fig. 2.5).

2.2.3 Taihua Complex

The Taihua Complex is discontinuously exposed along the southern NCC, extending from Gansu across Shaanxi and Henan to Anhui Province over a distance of 1000 km (Fig. 2.6). In the southeastern margin of the NCC, the equivalents of the Taihua Complex in the Huoqiu and Bangbu areas of Anhui Province have traditionally been named the Huoqiu Group and the Wuhe Group, respectively. Although Huoqiu Group is completely covered by Phaneroic strata and Quaternary sediments, some Archean-Paleoproterozoic rocks

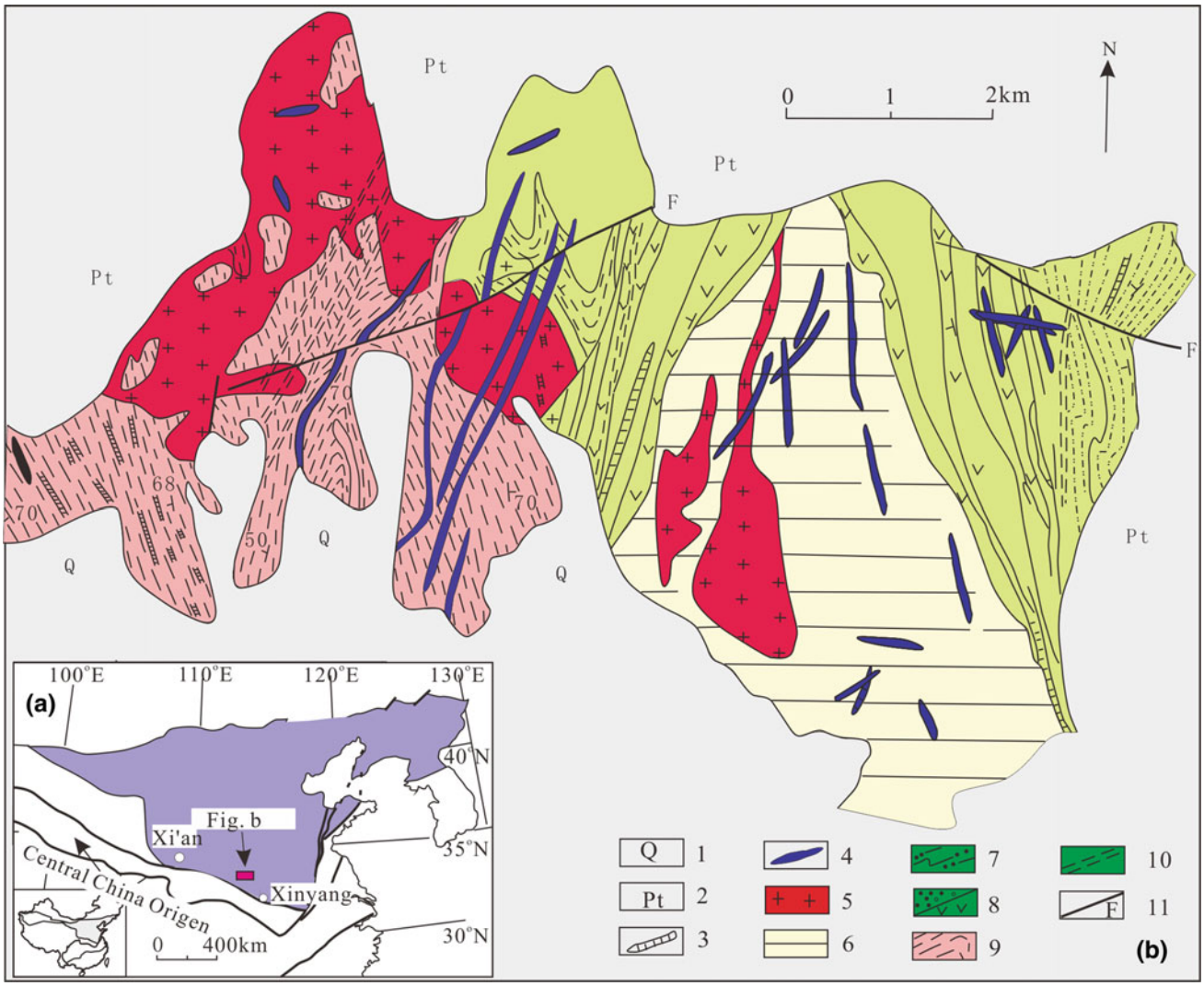

Fig. 2.4 Sketch geological map of the Dengfeng Complex in the Junzhao area (revised after Zhang et al. 1985). *1* Quaternary; *2* early and middle Proterozoic with basal unconformity; *3* felsic dike; *4* mafic dike; *5* granite; *6* metadiorite; *7* metsedimentary; *8* metsedimentary and metavolcanics (amphibolites); *9* TTG gneisses; *10* shear zone; *11* fault

in the Huoqiu area have also been recognized by drilling and zircon U–Pb dating studies (Wan et al. 2010; Wang et al. 2014). Meanwhile, in the most southwestern margin of the NCC, some researchers proposed that the Longshan Complex in the Longshan area of Gansu Province is the equivalents of the Taihua Complex, and some ca. 2.50 Ga tonalitic gneisses have been reported in there (Fig. 2.1) (He et al. 2005).

The Taihua Complex is chiefly located in the Lushan and Xiaoqinling areas. Although it is not a simple lithostratigraphic succession in terms of international stratigraphic nomenclature, it has been traditionally termed as the "Taihua Group", and was subdivided into lower and upper sequences, named the "Upper Taihua Group" and the "Lower Taihua Group", respectively. The most complete and best-exposed succession of the complex was found in the Lushan County, Henan Province (Fig. 2.7), and shows features as other typical high-grade metamorphic terranes throughout the world (Sun 1983; Zhang et al. 1985).

In the Lushan area, the Taihua Complex is in fault contact with or unconformably overlain by the Paleoproterozoic Xiong'er Group in the southwest and by the Neoproterozoic Ruyang Group or Cambrian sedimentary rocks in the northeast (Fig. 2.7). Based on the differences of lithological, structural, metamorphic, and geochronological data, we subdivide the Taihua Complex into high-grade gneissic complexes and supracrustal rocks, respectively, which are roughly separated from each other by Dangze River (Sun et al. 1994; Diwu et al. 2010a, 2014). The former located on the north side of the river is composed predominantly of TTG gneisses with minor supracrustal rocks and associated granitic plutons, whereas the latter located on the south side of the river is consisted mainly of high-grade sillimanite-garnet gneisses,

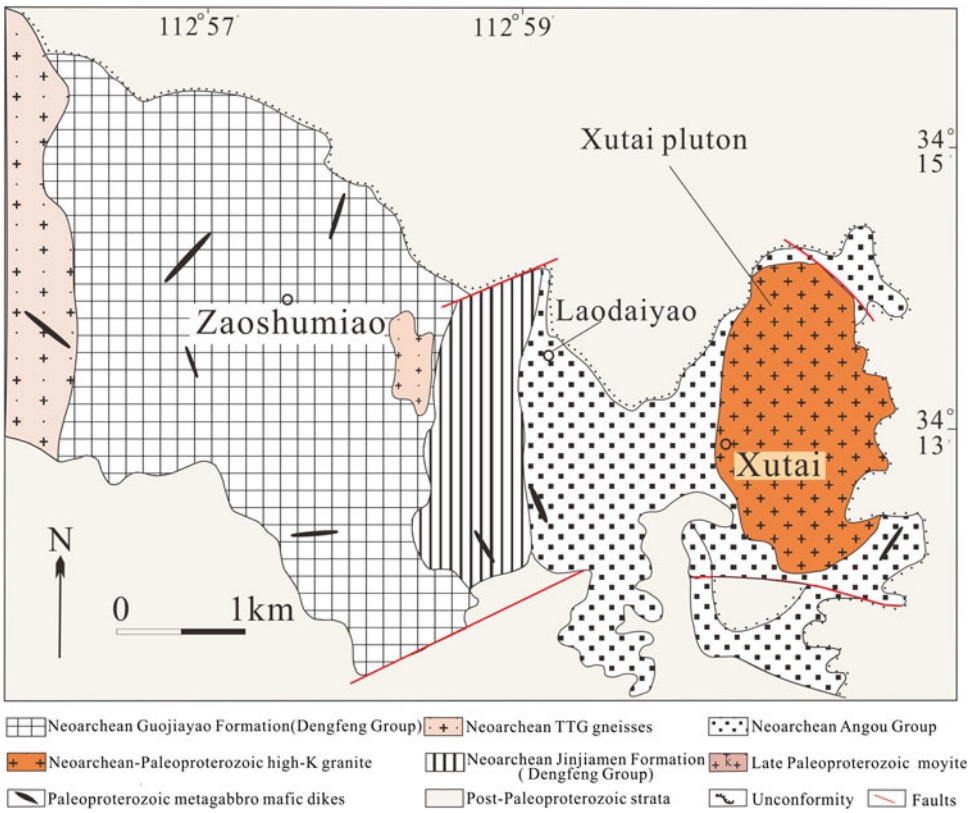

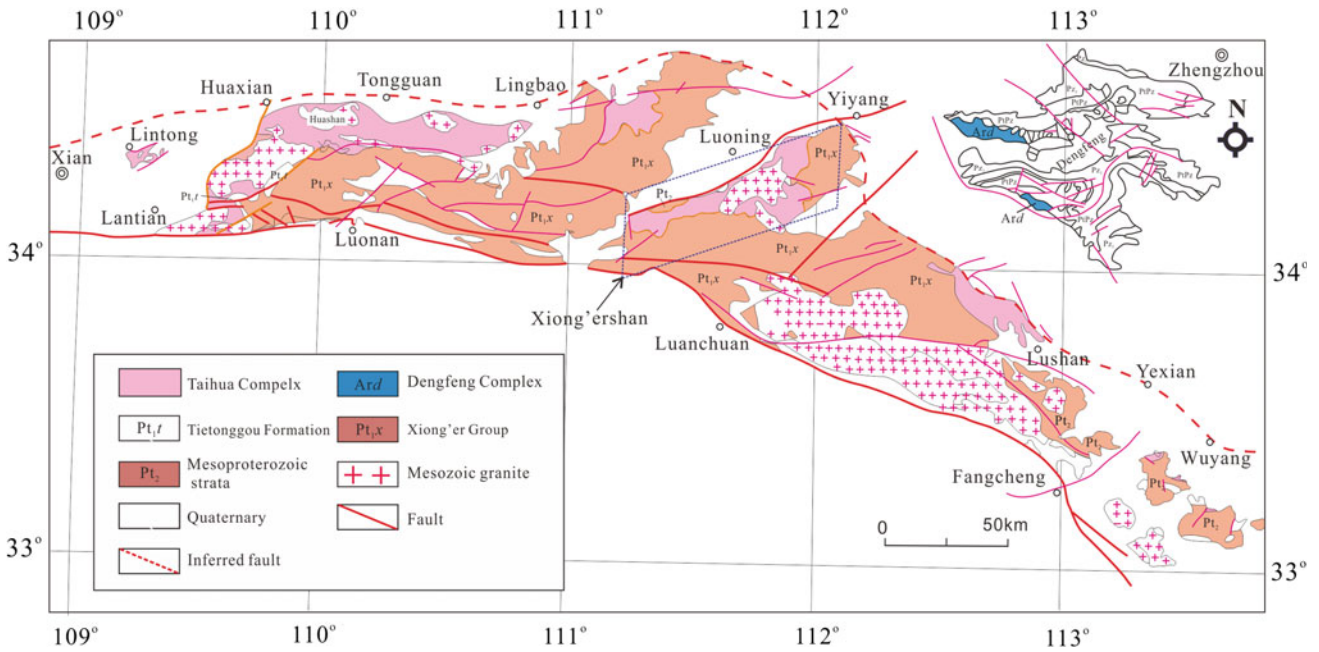

Fig. 2.5 Sketch geological map of the Dengfeng Complex in the Linru area

Fig. 2.6 Geological distribution of the Taihua Complex along the southern NCC (revised after Diwu et al. 2014)

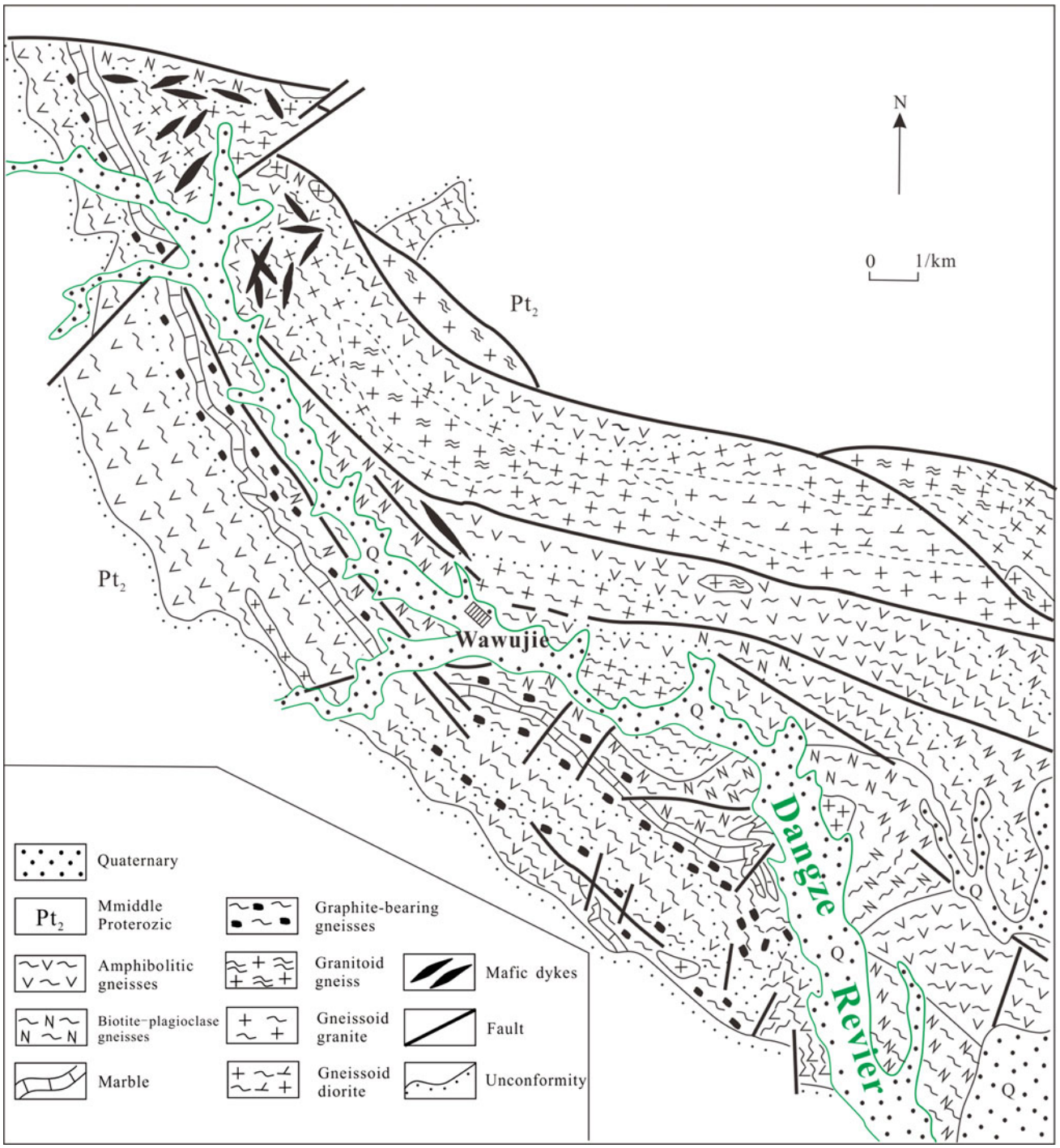

Fig. 2.7 Simplified geological map of the Taihua Complex in the Lushan area, Henan Province (revised after Sun et al. 1994)

graphite-bearing gneisses, quartzite, banded iron formations, and marble, with minor mafic granulites, amphibolites, and syn- or post-tectonic granitoid rocks (Sun 1983, 1994; Zhang et al. 1985). The structural style has revealed a remarkable difference in the two lithological units. The gneissic series are characterized by the development of gneiss domes and tight to isoclinal folds. However, the supracrustal rocks are characterized by layers, and is relatively undeveloped with respect to the above minor structures (Zhang et al. 1982, 1985). Sun (1982, 1983) previously discovered pyroxene granulites, garnet-plagioclase pyroxenites and sillimanite-garnet gneisses from the supracrustal rocks. The P-T calculations indicate that they have experienced a high amphibolite or granulite-facies metamorphism with a

relatively high pressure conditions (680–720 °C and 8.0–10.0 kbar). In addition, the geochronological data indicate that the high-grade gneissic complexes were formed at Neoarchean (Sun et al. 1994; Liu et al. 2009a; Diwu et al 2010a; Huang et al. 2010), whereas the formation of the supracrustal rocks can be limited to Palaeoproterozoic (Wan et al. 2006; Diwu et al. 2010a).

Traditionally, the boundary region between the Shaanxi and Henan provinces has been referred to be Xiaoqinling area, where the Taihua Complex is unconformably or tectonically overlain by the widespread Paleoproterozoic Xiong'er Group or locally covered by the Paleoproterozoic Tietonggou Formation (Diwu et al. 2013a). The Taihua Complex in the Xiaoqinling extends from Lintong in the west and across Lantian-Tongguan-Lingbao to the Xiong'ershan in the east, which was previously regarded as a succession of Upper Taihua Group in the Lushan area. However, according to detailed field-based structural, metamorphic, geochemical, and geochronological investigations, they are more complex than previous studies: (1) very rareness of late Mesoarchean basement rocks with the ages of 2827–2802 Ma and abundant of late Neoarchean basement rocks have been recognized most recently (our unpublished data), suggesting that the whole southern NCC has experienced a long geological history can be traced back to Mesoarchean; (2) the database of global zircon ages from both granitoids and detrital sediments show an exceptionally strong minimum between 2450 and 2200 Ma, and this unusual period of time was referred to as a crustal age gap (Condie et al. 2009b), whereas tremendous 2.45–2.20 Ga TTG gneisses and minor dioritic gneisses with peak age of ca. 2.30 Ga were reported in the Xiaoqinling area (Diwu et al. 2014), which makes the southern NCC different from other blocks in the NCC as well as other cratons worldwide, and serve as an excellent key area to investigate the generation and evolution of continental crust during the span of the global crustal age gap. (3) Large Mesozoic and Cenozoic granites intrude into the Taihua Complex in this area, resulting in intensive deformation and dismembered or overprinted original geological relationships of the rocks from the Taihua Complex.

2.3 Distribution and Composition

2.3.1 Hadean-Paleoarchean Crustal Components

The two ca. 4.10 Ga and one ca. 3.90 Ga xenocrystic zircons from the Ordovician Caotangou Group volcanics have been discovered in the North Qinling Orogenic Belt of the central China (Fig. 2.8) (Wang et al. 2007; Diwu et al. 2010b, 2013b), which is the first report of Hadean crustal material in Phanerozoic igneous rocks, the zircon xenocrysts were incorporated either from the source region or during magma ascent. Moreover, those ancient zircon grains provide important evidence regarding the nature of the basement of the NCC, from which this portion of the orogenic belt is considered to be derived (Zhang et al. 2001; Dong et al. 2011), suggesting that the oldest crustal rocks within the NCC formed as ca. 4.10 Ga (Zhai and Santosh 2011). The $\varepsilon_{Hf}(t)$ values of the North Qinling zircons range from to −4.6 to chondritic, with Hf model ages ranging from 4076 to 4449 Ma, indicate the survival of source rocks as old as ca. 4.45 Ga within the basement of the NCC.

Detrital zircons from both the Paleoproterozoic Songshan quartzites in the Dengfeng area and early Precambrian felsic gneiss in the Jiaozuo area yielded a well-defined upper intercept age of ca. 3.40 Ga (Diwu et al. 2008; Wan et al. 2009b), a few of those ca. 3.40 Ga zircons have low negative $\varepsilon_{Hf}(t)$ values (−4.6 to −3.4) and plot on the average crustal evolution trend of 3.80 Ga, indicating that these zircons may have come from an ancient crust as old as 3.80 Ga (Diwu et al. 2008). Moreover, >3.20 Ga detrital zircons with $^{207}Pb/^{206}Pb$ ages up to ca. 3.60 Ga have also been found from the Paleoproterozoic quartzites of the Tietonggou Formation, they exhibit negative $\varepsilon_{Hf}(t)$ values with the corresponding two-stage Hf continental model ages of 4.40–4.00 Ga (Diwu et al. 2013a). Taken together, it can be inferred that the crustal remnants older than 3.40 Ga might be widely distributed in the southern NCC.

2.3.2 Mesoarchean (2.85–2.80 Ga) Rocks

The Mesoarchean (2.85–2.80 Ga) rocks in the southern NCC have been found only in the Taihua Complex. Since the late 1980s and early 1999s, Kröner et al. (1988) and Sun et al. (1994) reported $^{207}Pb/^{206}Pb$ zircon evaporation ages of 2841 ± 6 Ma, 2806 ± 7, and 2807 ± 4 Ma for TTG gneisses in the Lushan area. These ages were interpreted as the emplacement time of its igneous precursor. Recently, Liu et al. (2009a) used SHRIMP technique to determine U–Pb ages of the high-grade gneissic complexes of the Taihua Complex, they found that the magmatic zircons from tonalite and amphibolite were essentially coeval with a small spread of ages from 2829 ± 18 to 2832 ± 11 Ma in the tonalites and from 2838 ± 35 to 2845 ± 23 Ma in amphibolites, which are identical within error. It is noteworthy that very rareness of the late Mesoarchean basement rocks were also discerned from the Xiaoqinling area, e.g., biotite-plagioclase gneiss (TTG) samples collected from the Xiaofuyu area yielded an upper intercept age of 2827–2802 Ma, which are interpreted as their protolithic ages (our unpublished data).

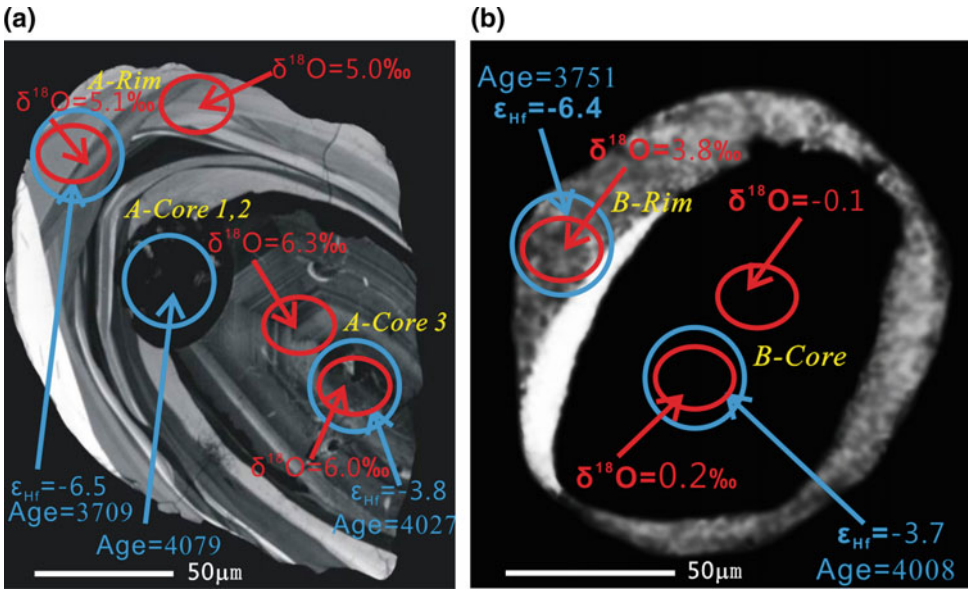

Fig. 2.8 The ca. 4.1–3.9 Ga xenocrystic zircons from Ordovician volcanics of the Caotangou Group (after Diwu et al. 2013b). The *red circles* and numbers show the $\delta^{18}O$ results, the *blue circles* show the location of the U–Pb analytical sites with age in Ma, and they also show the εHf(t) values, where available

2.3.2.1 Neoarchean (2.80–2.50 Ga) Rocks

Neoarchean crustal formation and evolution of the southern NCC were mainly involved in two major episodic geological events, namely, an early Neoarchean event (2.80–2.70 Ga) and a late Neoarchean event (2.60–2.50 Ga). Although eight of ca. 2.60 Ga zircon grains from a trondhjemitic gneiss of the Dengfeng Complex defined an upper intercept age of 2624 ± 47 Ma (MSWD = 2.3), which is interpreted as the crystallization age of the granitic gneiss protolith (Zhou et al. 2009), we note that there is significant lead loss in some 2.60 Ga zircons; moreover, 2.28–1.90 Ga zircons also contained in the sample, thus whether or not ca. 2.60 Ga crust was preserved in the Dengfeng area is open to question and requires further study. The same to ca. 2.60 Ga granitoid rocks that reported in the Xiezhou and Xiaxian area of the southern–middle region of the Zhongtiaoshan. (Zhang et al. 2012).

The early Neoarchean rocks are widely exposed in the high-grade gneissic complexes of the Taihua Complex in the Lushan area. Zircon dating revealed that abundant of TTG gneisses and amphibolites have been formed during the period of 2794–2752 Ma, and a large number of ca. 2.90 Ga and ca. 3.10 Ga xenocrystic zircons were found in those early Neoarchean rocks (Diwu et al. 2010a; Huang et al. 2010), suggesting that ancient crustal materials as old as 3.10–2.90 Ga probably preexisted in the Lushan area. Moreover, two metamorphic stages in the Neoarchean were recognized in the area: the earlier stage occurred between 2792 and 2772 Ma, and the later occurred at 2671–2638 Ma (Liu et al. 2009a). This can be interpreted as the preexisting inherited zircons were metamorphosed during the close spatial-temporal association magmatic crystallization (Diwu et al. 2010a). Recently, two trondhjemitic and one dioritic gneiss samples were collected from the Changping area of the southern Sushui Complex, and yielded SIMS and LA-ICPMS zircon U–Pb ages of 2722–2702 Ma and ca. 2704 Ma, respectively, indicating that the early Neoarchean rocks were also preserved sparsely in the Zhongtiaoshan (Zhu et al. 2013).

Hundreds of geochronological data, especially in situ zircon U–Pb ages obtained from Precambrian metasedimentary rocks or modern sediment (rive sands) in the NCC indicate that the most important and major tectonothermal events occur at ca. 2.50 Ga (Diwu et al. 2012b; Wan et al. 2011b, 2015). Similar to other high-grade gneissic complexes or low-grade granite–greenstone terranes, the major tectonothermal events in the southern NCC also extensively occurred at ca. 2.50 Ga. A large number of 2.60–2.50 Ga orthogneisses, composed dominantly of TTGs with minor metadioritic gneisses and potassic granites, are extensively distributed in the southern NCC. These 2.60–2.50 Ga rocks which usually contain contemporary layers or lenses amphibolites are widely exposed as high- to medium-grade gneissic complexes in the Jiangxian–Xiaxian–Haizhou areas of the Sushui Complex (Tian et al. 2006; Guo et al. 2008; Zhang et al. 2012), southern Junzhao area of the Dengfeng Complex (Wan et al. 2009a; Zhou et al. 2009, 2011; Diwu et al. 2011) and Xiaoqinling area of the Taihua Complex (our unpublished data). Meanwhile, most of the 2.60–2.50 Ga supracrustal rocks also mainly occurred in the Lengkou and Chaijiayao supracrustal rocks of the Sushui Complex (Sun et al. 1990; Sun and Hu 1993; Zhang 2015), and the Dengfeng as well as the Angou supracrustal rocks of the Dengfeng Complex (Guo 1987; Guo and Zhou 1990; Wan et al. 2009a; Diwu et al. 2011), in which bimodal volcanic assemblages, clastic metasedimentary rocks, BIF and minor limestone were formed during the period.

2.4 Discussion and Synthesis

2.4.1 Coherent Southern Archean Block

With the rapid development of microanalysis in the last decade, including secondary ion mass spectrometry (e.g., SHRIMP, CAMECA) and laser ablation inductively coupled plasma mass spectrometry (including quadrupole and multiple collector), large amounts of high-quality in situ zircon U-Pb isotopic data were obtained from basement rocks in the southern NCC. The spatial and temporal distribution of Archean rocks and xenocrystic or detrital zircons in them suggest that the southern NCC must be a coherent Archean terrane (Fig. 2.1), herein referred to as the Southern Archean Block (SAB) based on the following lines of evidence:

1. The Mesoarchean–Neoarchean (ca. 2.85–2.50 Ga) rocks in southern NCC show an east–west trending belt from the Gansu across Shaanxi and Henan into Anhui Province, stretching over 1000 km long. They are widely developed in the Sushui (Zhang 2015), Dengfeng (Wan et al. 2009a; Diwu 2011) and Taihua complexes (Liu et al. 2009a; Diwu et al. 2014). Moreover, their equivalents probably extend into the Longshan area of Gansu Province in the southwestern margin and the Huoqiu and Bangbu areas of Anhui Province in the most southeastern margin. For example, the ca. 2.50 Ga tonalitic gneisses have been cofirmed in the Longshan Complex (He et al. 2005); a few Archean rocks have also been recognized from the Huoqiu Complex by drilling and zircon U–Pb dating studies in the Huoqiu area (Wan et al. 2010; Wang et al. 2014).
2. Although 2.45–2.20 Ga TTG gneisses associated with coeval dioritic gneisses occurred intensively in the Xiaoqinling area (Diwu et al. 2014), minor ca. 2.10 Ga TTG gneisses, K-feldspar granitic gneisses and granites have also been recognized (Huang et al. 2012). The 2.45–2.20 Ga TTGs and related rocks have two-stage Hf model ages of 2.85–2.70 Ga, which are similar to the crystallization ages of the high-grade gneissic complexes in the Lushan area, indicating that although limited Mesoarchean–Neoarchean rocks are recognized (unpublished data), continental crustal materials as old as 2.85–2.70 Ga probably preexisted in the Xiaoqinling area and constituted sources of those magmatic rocks (Diwu et al. 2014). The recent recognition of 2827–2802 Ma biotite-plagioclase (TTG) gneiss samples further confirm the existence of Mesoarchean–Neoarchean crust in the Xiaoqinling area (unpublished data).
3. It is noteworthy that some 2.85–2.70 Ga rocks in the Lushan Taihua Complex contain a large number of ca. 2.90 Ga and ca. 3.10 Ga xenocrystic zircons (Diwu et al. 2010a; Huang et al. 2010), and some grains show obvious negative $\varepsilon_{Hf}(t)$ values (upto -5.8), and their corresponding Hf model ages (3074–3277 Ma) are significantly older than their crystallization ages (2791–2751 Ma) (Diwu et al. 2010a), suggesting that ancient crustal materials as old as 3.10–2.90 Ga probably preexisted in the Lushan area, and these zircons may be derived from recycled ancient crust with a relatively long crustal residence (Diwu et al. 2010a). Moreover, the ca. 4.10–3.90 Ga xenocrystic zircons from Ordovician volcanics of the Caotangou Group have been discovered in the North Qinling Orogenic Belt (Diwu et al. 2010b, 2013b; Wang et al. 2007), from which this portion of the orogenic belt is considered to be derived of the basement of the southern NCC (Dong et al. 2011; Zhang et al. 2001), indicating that some of Hadean-Eoarchean crustal components were still survival in the basement of the southern NCC during the early Paleozoic, and the SAB may was experienced a long geological history which can be traced back to the Hadean.

2.4.2 Two Marked Episodes of Crustal Growth (2.85–2.70 and Ca. 2.50 Ga)

As we all known, zircon is one of the robust accessory phases in sedimentary, igneous, and metamorphic rocks, which can provide the most valuable information. Individual zircons can be analyzed for U–Pb isotopes to identify a specific sequence of major magmatic events, and their Lu–Hf and O isotopic compositions can provide information on whether the zircon crystallized from juvenile or reworked crustal material. Thus, the combined U–Pb and Lu–Hf isotopic studies have long played a key role in crustal evolution studies (Scherer et al. 2007; Hawkesworth et al. 2010, 2013; Diwu et al. 2012a; Cawood et al. 2013; Kröner et al. 2013; Kemp and Hawkesworth 2014).

The modeling combined zircon U–Pb and Lu–Hf isotopic studies suggest that about 60 % of the present crustal volume of the NCC was generated during the period between the Mesoarchean and late Neoarchean (3.00–2.50 Ga) (Fig. 2.9) (Diwu et al. 2012a, b). Subsequently, the continental crust kept a stable rate of growth and completely formed at the end of the Neoproterozoic (ca. 541 Ma) (Fig. 2.9), which indicates that the present continental crust of the NCC was mainly growth during Precambrian, and the juvenile additions to the continental crust are almost negligible during Phanerozoic (Diwu et al. 2012a).

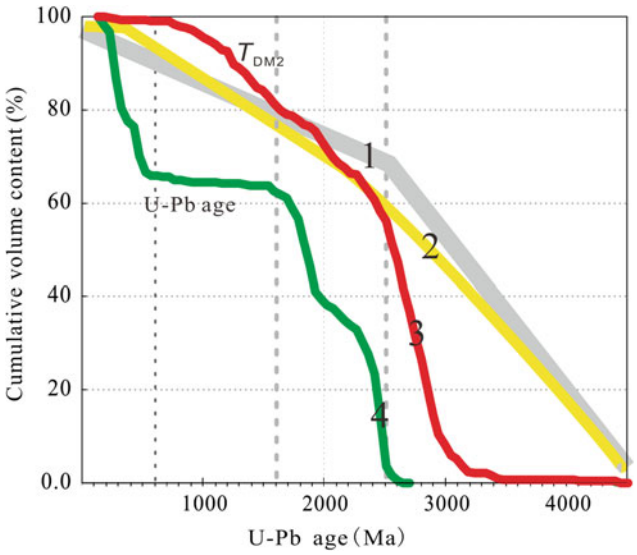

Fig. 2.9 The global lithospheric architecture mapping curve (line 1, after Belousova et al. 2010), global integrated crustal growth curve (line 2, after Belousova et al. 2010), and continental crust growth curves of the NCC that based on two-stage Hf model ages (line 3) and U–Pb ages (line 4) (after Diwu et al. 2012b)

There is no doubt that the most important and intensive tectonothermal events could occured at ca. 2.50 Ga in the NCC during the Archean (Wan et al. 2011b, 2015; Diwu et al. 2012b; Geng et al. 2012). A large volume of TTG gneisses, mantle-derived granites and minor supracrustal rocks were formed during this time, and nearly all the Archean rocks have underwent a strong metamorphism from amphibolite facies to granulite facies, therefore some researchers suggested that the NCC formed through amalgamation of various microblocks by arc-continent collision at the end of the Neoarchean (Zhai et al. 2003; Zhai and Santosh 2011, 2013). However, as discussed above, it still remains controversial about timing of the crust growth in the NCC during the Archean, with one school of researches emphasized that the major crustal growth event in the NCC occur at 2.85–2.70 Ga, similar to many other cratons in the world, whereas the ca. 2.50 Ga tectonothermal event was mainly involved in crustal reworking or partial melting of the early Neoarchean mafic crust formed at 2.85–2.70 Ga (Wu et al. 2005; Geng et al. 2012; Zhao 2014); whereas another group of researchers favored that the age of ca. 2.50 Ga represents a major growth period of continental crust in the NCC (Liu et al. 2009b; Diwu et al. 2011).

The key to solve this debate first is how to define the "juvenile crust" or "crustal growth". The continental crustal growth is the emplacement of new magma directly derived from the mantle and increase in the overall volume of the continental crust through time, whereas the juvenile crust is defined as magmas generated directly from the depleted mantle, or by remelting of material recently extracted from depleted mantle (Belousova et al. 2010; Hawkesworth et al. 2010; Kemp and Hawkesworth 2014). In practice, juvenile crust is likely to have been generated from the mantle in more than one stage, for example, it can be generated from crystallization and remelting of basalt, and radiogenic isotope ratios of the crust have not evolved significantly away from that of its contemporary mantle source (Hawkesworth et al. 2010; Kemp and Hawkesworth 2014).

If a zircon has positive $\varepsilon_{Hf}(t)$ value close to that of the contemporaneous depleted mantle, which can indicate juvenile magmas directly via mantle-derived mafic melts or by remelting of young mantle-derived mafic lower crust, thus zircon U–Pb crystallization age is close roughly to the timing when the Hf isotopic composition of a crustal rock has been isolated from its depleted mantle. Although zircons have considerably variable positive $\varepsilon_{Hf}(t)$ values, which may reflect either insufficient mixing in melting processes or heterogeneity source, the source magma was still dominated by a Hf isotope budget of the depleted mantle (Zheng et al. 2007a, b). The zircon crystallization age can also be utilized to estimates the timing when a new crustal addition in specific regions. Whereas, if a zircon has negative $\varepsilon_{Hf}(t)$ value, which is indicative of rock formation due to the reworking of old continental crust, the timing of Hf crust formation age can be constrained by its model Hf age, and the model age far exceed than its corresponding U–Pb age. However, so far as we known, there are great uncertainties with Hf model ages, for example: (1) the choice of the mantle reservoir from which the new crust was extracted; (2) Lu/Hf ratios and the composition of initial continental crust (Diwu et al. 2012a; Hawkesworth et al. 2010; Kemp and Hawkesworth 2014).

Rocks with ages of 2.85–2.70 Ga are mainly found locally in the gneiss series of the Taihua Complex in Lushan area (Liu et al. 2009a; Diwu et al. 2010a; Huang et al. 2010), majority of the 2.85–2.70 Ga zircons in those rocks have variable but positive $\varepsilon_{Hf}(t)$ values (Fig. 2.10a), and magmatic zircon domains which characterized by oscillatory zoning in CL images present mantle-like O isotopes ($\delta^{18}O$ = 5.1–5.9 ‰) (Liu et al. 2009a), the isotopic characters reflect a somewhat geochemically heterogeneous but depleted mantle Hf isotope reservoir that dominates the source of these rocks. The whole-rock Nd isotopic data show similar characteristics, confirming juvenile sources for their provenance (Fig. 2.10b) (Diwu et al. 2014). Whereas, a few 2.85–2.70 Ga zircon grains show negative $\varepsilon_{Hf}(t)$ values, and their corresponding Hf model ages (3277–3074 Ma) are significantly older than their crystallization ages, which suggests that these were derived from recycled Paleoarchean to Mesoarchean crust with a relatively long residence (0.30–0.40 Ga) time in the local crust (Diwu et al. 2010a). In addition, the majority of ca. 2.70 Ga zircons from the Sushui Complex have high $\varepsilon_{Hf}(t)$ values close to contemporaneous depleted mantle values, and their Hf model ages (2.85–2.70 Ga) are close to the

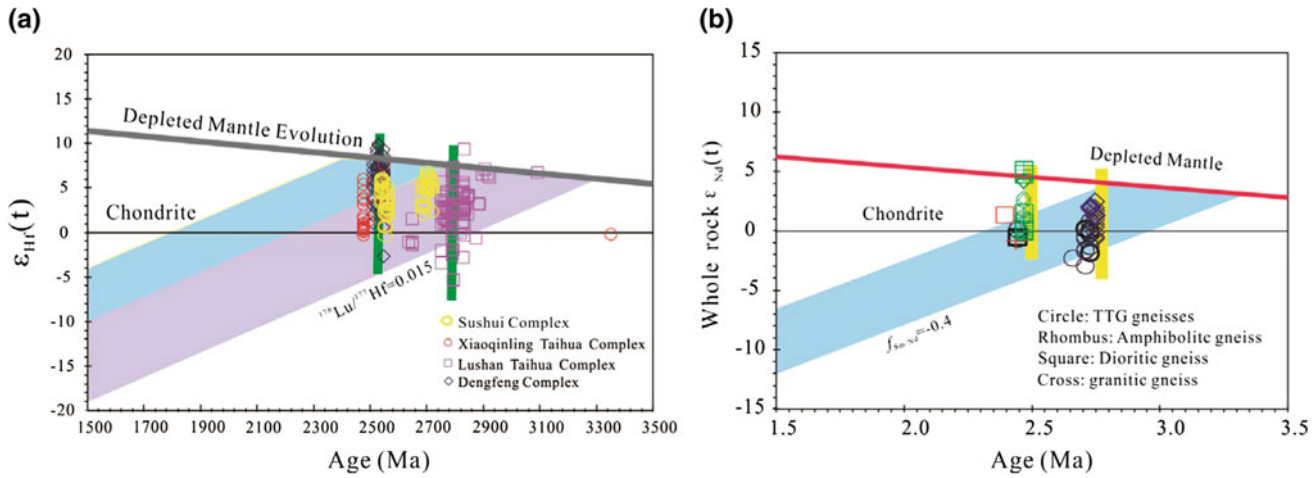

Fig. 2.10 **a** Diagrams of εHf(t) versus $^{207}Pb/^{206}Pb$ age and **b** $\varepsilon_{Nd}(t)$ versus age for samples from the Sushui, Dengfeng and Taihua complexes in the southern NCC. The major age clusters (ca. 2.8 Ga and ca. 2.5 Ga) are shown by the green and yellow lines in Fig. 2.10a and b, respectively. Data from (Liu et al. 2009a; Diwu et al. 2010a, 2011; Huang et al. 2012, 2013; Yu et al. 2013; Zhu et al. 2013; Zhang 2015)

rock-forming ages (Zhu et al. 2013). Hence it can be concluded that the 2.85–2.70 Ga episode with a most prominent peak at ca. 2.80 Ga was a major period of magmatic activity and crustal growth in the southern NCC.

As we discussed above, the Chinese Precambrian geologists commonly agreed that the major continental growth in the NCC occurred at ca. 2.85–2.70 Ga (Wan et al. 2011a, 2014; Zhai and Santosh 2011; Geng et al. 2012; Zhao 2014), and the crustal growth event is suggested to be related to a mantle plume event; whereas the ca. 2.50 Ga tectonothermal event was regarded as mainly involved in crustal reworking or partial melting of the early Neoarchean mafic crust formed at 2.85–2.70 Ga (Wu et al. 2005; Geng et al. 2012; Zhao 2014). Herein, we still suggest that ca. 2.50 Ga is another major period of crustal growth in the NCC as well as in the southern region based on the following lines of evidence:

1. a variable proportion of metabasaltic rocks with ca. 2.50 Ga zircon U–Pb ages exposed in the high-grade gneissic complexes as well as the low-grade granite-greenstone terrenes. Take the Dengfeng Group for example, it is composed of metamorphosed volcano-sedimentary rocks, the ratio of volcanics to sediments being ~5:1, approximately 58 % of the volcanics are mafic (Zhang et al. 1982; Guo 1987).
2. those metabasaltic rocks in the Dengfeng Group have mixed MORB- and/or arc-like geochemical affinities which are often seen in the back-arc basins, suggesting that they were derived from mantle source with minor continental crust contamination (Diwu et al. 2011).
3. most of the magmatic zircons from TTG gneisses, amphibolites and related rocks in southern the NCC have positive $\varepsilon_{Hf}(t)$ values which similar to those of the contemporaneous depleted mantle at ca. 2.50 Ga (Fig. 2.10 a) (Diwu et al. 2011, 2014), and their Hf model ages of 2.85–2.49 Ga are close to the U–Pb ages of zircons, suggesting that these rocks originated from the juvenile crust at ca. 2.5 Ga.
4. the whole-rock Nd isotopic data of the ca. 2.60–2.50 Ga rocks show similar characteristics (Fig. 2.10b) (Diwu et al. 2014, and references therein), confirming juvenile sources for their provenance.
5. the ca. 2.5 Ga K-rich granite-granodiorite-monzogranite suites (e.g. the Xutai and Lujiagou plutons) were also recognized from the southern NCC (Zhou et al. 2011), which are commonly considered as the proxy of the ending of orogenic processes and final stabilization of the cratons or blocks lithosphere (Laurent et al. 2014).

2.5 Conclusions

1. The Archean rocks are widely recognized in the southern NCC, which show an east-west trending belt from Gansu across Shaanxi and Henan into Anhui Province, stretching over 1000 km long.
2. All the complexes in the southern NCC were aggregated together to form a coherent ancient terrane at end of the Neoarchean, we named it the “Southern Archean Block”.
3. The southern NCC as well as the whole NCC has undergone two marked episodes of continental crust growth at 2.85–2.70 Ga and ca. 2.50 Ga during the Archean. It may have experienced a long geological history that can be traced back to the Hadean.

Acknowledgments Diwu thank Prof. Yusheng Wan and Taiping Zhao for their helpful and constructive comments. This study was supported financially by the National Basic Research Program of China (973 Program; grant No. 2012CB416606), the National Natural Science Foundation of China (NSFC; grant No. 41421002, 41272004), and MOST Special Funds from the State Key Laboratory of Continental Dynamics.

References

Bai, J., Yu, Z., Yan, Y., & Dai, F. (1997). *Precambrian geology of Zhongtiaoshan* (pp. 1–143). Tianjin: Tianjin Science and Technology Press.

Belousova, E. A., Kostitsyn, Y. A., Griffin, W. L., Begg, G. C., O'Reilly, S. Y., & Pearson, N. J. (2010). The growth of the continental crust: Constraints from zircon Hf-isotope data. *Lithos, 119*, 457–466.

Bleeker, W. (2003). The late Archean record: a puzzle in ca. 35 pieces. *Lithos, 71*, 99–134.

Bowring, S., & Housh, T. (1995). The earth's early evolution. *Science, 269*, 1535–1540.

Cawood, P. A., Hawkesworth, C. J., & Dhuime, B. (2013). The continental record and the generation of continental crust. *Geological Society of America Bulletin, 125*, 14–32.

Condie, K. C., Belousova, E., Griffin, W. L., & Sircombe, K. N. (2009a). Granitoid events in space and time: Constraints from igneous and detrital zircon age spectra. *Gondwana Research, 15*, 228–242.

Condie, K. C., O'Neill, C., & Aster, R. C. (2009b). Evidence and implications for a widespread magmatic shutdown for 250 My on earth. *Earth and Planetary Science Letters, 282*, 294–298.

Condie, K. C., & Aster, R. C. (2010). Episodic zircon age spectra of orogenic granitoids: The supercontinent connection and continental growth. *Precambrian Research, 180*, 227–236.

Diwu, C.-R., Sun, Y., Lin, C.-L., Wang, H.-L. (2010a). LA-(MC)-ICPMS U-Pb zircon geochronology and Lu-Hf isotope compositions of the Taihua complex on the southern margin of the North China Craton. *Chinese Science Bulletin, 55*, 2557–2571.

Diwu, C.-R., Sun, Y., Dong, Z.-C., Wang, H.-L., Chen, D.-L., Chen, L., et al. (2010b). In situ U–Pb geochronology of Hadean zircon xenocryst (4.1 similar to 3.9 Ga) from the western of the Northern Qinling Orogenic Belt. *Acta Petrologica Sinica, 26*, 1171–1174.

Diwu, C.-R., Sun, Y., Gao, J.-F., & Fan, L.-G. (2013a). Early Precambrian tectonothermal events of the North China Craton: Constraints from in situ detrital zircon U–Pb, Hf and O isotopic compositions in Tietonggou Formation. *Chinese Science Bulletin, 58*, 3760–3770.

Diwu, C.-R., Sun, Y., Guo, A.-L., Wang, H.-L., & Liu, X.-M. (2011). Crustal growth in the North China Craton at ~2.5 Ga: Evidence from in situ zircon U–Pb ages, Hf isotopes and whole-rock geochemistry of the Dengfeng complex. *Gondwana Research, 20*, 149–170.

Diwu, C.-R., Sun, Y., & Wang, Q. (2012a). The crustal growth and evolution of North China Craton: Revealed by Hf isotopes in detrital zircons from modern rivers. *Acta Petrologica Sinica, 28*, 3520–3530.

Diwu, C., Sun, Y., Zhang, H., Wang, Q., Guo, A.-L., & Fan, L.-G. (2012b). Episodic tectonothermal events of the western North China Craton and North Qinling Orogenic Belt in Central China: Constraints from detrital zircon U–Pb ages. *Journal of Asian Earth Sciences, 47*, 107–122.

Diwu, C.-R., Sun, Y., Yuan, H.-L., Wang, H.-L., Zhong, X.-P., & Liu, X.-M. (2008). U-Pb ages and Hf isotopes for detrital zircons from quartzite in the Paleoproterozoic Songshan Group on the southwestern margin of the North China Craton. *Chinese Science Bulletin, 53*, 2828–2839.

Diwu, C.-R., Sun, Y., Wilde, S. A., Wang, H.-L., Dong, Z.-C., Zhang, H., & Wang, Q. (2013b). New evidence for ~4.45 Ga terrestrial crust from zircon xenocrysts in Ordovician ignimbrite in the North Qinling Orogenic Belt. *China. Gondwana Research, 23*, 1484–1490.

Diwu, C., Sun, Y., Zhao, Y., & Lai, S.-C. (2014). Early Paleoproterozoic (2.45–2.20 Ga) magmatic activity during the period of global magmatic shutdown: Implications for the crustal evolution of the southern North China Craton. Precambrian Research 255. *Part, 2*, 627–640.

Dong, Y.-P., Zhang, G.-W., Neubauer, F., Liu, X.-M., Genser, J., & Hauzenberger, C. (2011). Tectonic evolution of the Qinling orogen, China: Review and synthesis. *Journal of Asian Earth Sciences, 41*, 213–237.

Geng, Y.-S., Du, L.-L., & Ren, L.-D. (2012). Growth and reworking of the early Precambrian continental crust in the North China Craton: Constraints from zircon Hf isotopes. *Gondwana Research, 21*, 517–529.

Guo, A.-L. (1987). The Angou group greenstone belt of early Proterozoic and its tectonic environment in the Jishan of central Henan, China. *Journal of Northwest University, 24*, 18–28.

Guo, A.-L. (1988). Relationships between the TTG gneisses and the greenstone belt in the Archean Dengfeng granite-greenstone terrane, Central Henan and their implications for crustal evolution. *Geology Review, 34*, 123–131.

Guo, A.-L. (1989). Archean grey gneisses on the southern margin of the north China Craton and their genesis. *Acta Petrologica Sinica, 9*, 18–28.

Guo, L.-S., Liu, S.-W., Liu, Y.-L., Tian, W., Yu, S.-Q., Li, Q.-G., & Lü, Y.-J. (2008). Zircon Hf isotopic features of TTG gneisses and formation environment of Precambrian Sushui complex in Zhongtiao mountains. *Acta Petrologica Sinica, 24*, 139–148.

Guo, A.-L., & Zhou, D.-W. (1990). Dengfeng archean granite-greenstone terrane in Central Henan province. *Henan Geology, 8*, 31–37.

Hawkesworth, C., Cawood, P., & Dhuime, B. (2013). Continental growth and the crustal record. *Tectonophysics, 609*, 651–660.

Hawkesworth, C. J., Dhuime, B., Pietranik, A. B., Cawood, P. A., Kemp, A. I. S., & Storey, C. D. (2010). The generation and evolution of the continental crust. *Journal of the Geological Society, 167*, 229–248.

He, Y.-H., Sun, Y., Chen, L., Li, H.-P., Yuan, H.-L., & Liu, X.-M. (2005). Zircon U–Pb chronology of Longshan complex by LA-ICP-MS and its geological significance. *Acta Petrologica Sinica, 21*, 125–134.

Huang, X.-L., Niu, Y.-L., Xu, Y.-G., Yang, Q.-J., & Zhong, J.-W. (2010). Geochemistry of TTG and TTG-like gneisses from Lushan-Taihua complex in the southern North China Craton: Implications for late Archean crustal accretion. *Precambrian Research, 182*, 43–56.

Huang, X.-L., Wilde, S. A., Yang, Q.-J., & Zhong, J.-W. (2012). Geochronology and petrogenesis of gray gneisses from the Taihua Complex at Xiong'er in the southern segment of the Trans-North China Orogen: Implications for tectonic transformation in the Early Paleoproterozoic. *Lithos, 134–135*, 236–252.

Huang, X.-L., Wilde, S. A., & Zhong, J.-W. (2013). Episodic crustal growth in the southern segment of the Trans-North China Orogen across the Archean-Proterozoic boundary. *Precambrian Research, 233*, 337–357.

Kemp, A. I. S., & Hawkesworth, C. J. (2014). 4.11 - Growth and Differentiation of the Continental Crust from Isotope Studies of Accessory Minerals. In H. D. H. K. Turekian (Ed.), *Treatise on geochemistry (second edition)* (pp. 379–421). Oxford: Elsevier.

Kröner, A., Compston, W., Guo-wei, Z., An-lin, G., & Todt, W. (1988). Age and tectonic setting of Late Archean greenstone-gneiss terrain in Henan Province, China, as revealed by single-grain zircon dating. *Geology, 16*, 211–215.

Kröner, A., Kovach, V., Belousova, E., Hegner, E., Armstrong, R., Dolgopolova, A., Seltmann, R., Alexeiev, D.V., Hoffmann, J.E., Wong, J., Sun, M., Cai, K., Wang, T., Tong, Y., Wilde, S.A., Degtyarev, K.E., Rytsk, E. (2013). Reassessment of continental growth during the accretionary history of the Central Asian Orogenic Belt. Gondwana Research.

Laurent, O., Martin, H., Moyen, J. F., & Doucelance, R. (2014). The diversity and evolution of late-Archean granitoids: Evidence for the onset of "modern-style" plate tectonics between 3.0 and 2.5 Ga. *Lithos, 205*, 208–235.

Liu, D. Y., Nutman, A. P., Compston, W., Wu, J. S., & Shen, Q. H. (1992). Remnants of $\geq$ 3800 Ma crust in the Chinese part of the Sino-Korean craton. *Geology, 20*, 339–342.

Liu, D.-Y., Wilde, S. A., Wan, Y.-S., Wu, J.-S., Zhou, H.-Y., Dong, C.-Y., & Yin, X.-Y. (2008). New U-Pb and Hf isotopic data confirm Anshan as the oldest preserved segment of the North China Craton. *American Journal of Science, 308*, 200–231.

Liu, D.-Y., Wilde, S. A., Wan, Y.-S., Wang, S.-Y., Valley, J. W., Kita, N., et al. (2009a). Combined U-Pb, hafnium and oxygen isotope analysis of zircons from meta-igneous rocks in the southern North China Craton reveal multiple events in the Late Mesoarchean-Early Neoarchean. *Chemical Geology, 261*, 140–154.

Liu, F., Guo, J.-H., Lu, X.-P., & Diwu, C.-R. (2009b). Crustal growth at similar to 2.5 Ga in the North China Craton: evidence from whole-rock Nd and zircon Hf isotopes in the Huai'an gneiss terrane. *Chinese Science Bulletin, 54*, 4704–4713.

Ma, X.-Y. (1957). On the Pre-cambrian stratigraphy of the Sungshan area, Honan, and the problems of its correlation. *Acta Geologica Sinica*, *37*(1), 11–32.

Rudnick, R. L., & Gao, S. (2014). 4.1. composition of the continental crust. In H. D. H. K. Turekian (Ed.), *Treatise on geochemistry (second edition)* (pp. 1–51). Oxford: Elsevier.

Scherer, E. E., Whitehouse, M. J., & Münker, C. (2007). Zircon as a monitor of crustal growth. *Elements, 3*, 19–24.

Sun, Y. (1982). Polymetamorphism of the Taihua Group at the Lushan, Henan. *Journal of Northwest University,*, 44–65 (Special Issue for Precambrian Geology).

Sun, Y. (1983). Rocks in the granulite facie of the Taihua Group at Lushan, Henan. *Journal of Northwest University, 1*, 92–98.

Sun, D.-Z., & Hu, W. (1993). *The Geochronological Framework and Crustal Structures of Precambrian Basement in the Zhongtiaoshan Area* (pp. 108–117). Beijing: Geological Publishing House.

Sun, Y., Yu, Z.-P., & Alfred, K. (1994). Geochemistry and single zircon geochronology of Archaean TTG gneisses in the Taihua high-grade terrain, Lushan area, central China. *Journal of Southeast Asian Earth Sciences, 10*, 227–233.

Sun, D.-Z., Hu, W.-X., Tang, M., Zhao, F.-Q., & Condie, K. C. (1990). Geochemistry and mineralization of Proterozoic Mobile Belts Origin of Late Archean and Early Proterozoic rocks and associated mineral deposits from the Zhongtiao Mountains, east-central China. *Precambrian Research, 47*, 287–306.

Tian, W., Liu, S.-W., Liu, C.-H., Yu, S.-Q., Li, Q.-G., & Wang, Y.-R. (2006). Zircon SHRIMP geochronology and geochemistry of TTG rocks in Sushui Complex from Zhongtiao Mountains with its geological implications. *Progress in Natural Science: Materials International, 16*, 492–500.

Wan, Y.-S., Liu, D.-Y., Song, B., Wu, J.-S., Yang, C.-H., & Zhang, Z.-Q. (2005). Geochemical and Nd isotopic compositions of 3.8 Ga meta-quartz dioritic and trondhjemitic rocks from the Anshan area and their geological significance. *Journal of Asian Earth Sciences, 24*, 563–575.

Wan, Y.-S., Liu, D.-Y., Wang, S.-Y., Zhao, Y., Dong, C.-Y., Zhou, H.-Y., et al. (2009a). Early Precambrian crustal evolution in the Dengfeng area, Henan province (eastern China): constraints from geochemistry and SHRIMP U-Pb zircon dating. *Acta Geologica Sinica, 7*, 982–999.

Wan, Y.-S., Dong, C.-Y., Wang, W., Xie, H.-Q., & Liu, D.-Y. (2010). Archean Basement and a Paleoproterozoic Collision Orogen in the Huoqiu Area at the Southeastern Margin of North China Craton: Evidence from sensitive high resolution ion micro-probe U-Pb Zircon Geochronology. *Acta Geologica Sinica-English Edition, 84*, 91–104.

Wan, Y.-S., Liu, D.-Y., Dong, C.-Y., Nutman, A., Wang, W., & Xie, H.-Q. (2009b). The oldest rocks and zircons in China. *Acta Petrologica Sinica, 25*, 1793–1807.

Wan, Y.-S., Liu, D.-Y., Dong, C.-Y., Xie, H.-Q., Kröner, A., Ma, M.-Z., Liu, S.-J., Xie, S.-W., Ren, P. (2015). Formation and evolution of archean continental crust of the North China Craton. In M. Zhai (Ed.), *Precambrian Geology of China* (pp. 59–136). Berlin, Heidelberg: Springer.

Wan, Y.-S., Liu, D.-Y., Nutman, A., Zhou, H.-Y., Dong, C.-Y., Yin, X.-Y., & Ma, M.-Z. (2012). Multiple 3.8–3.1 Ga tectono-magmatic events in a newly discovered area of ancient rocks (the Shengousi Complex), Anshan, North China Craton. *Journal of Asian Earth Sciences, 54–55*, 18–30.

Wan, Y.-S., Liu, D.-Y., Wang, W., Song, T.-R., Kroener, A., Dong, C.-X., et al. (2011b). Provenance of Meso-to Neoproterozoic cover sediments at the Ming Tombs, Beijing, North China Craton: An integrated study of U-Pb dating and Hf isotopic measurement of detrital zircons and whole-rock geochemistry. *Gondwana Research, 20*, 219–242.

Wan, Y.-S., Liu, D.-Y., Wang, S.-J., Yang, E.-X., Wang, W., Dong, C.-Y., et al. (2011a). $\sim$2.7 Ga juvenile crust formation in the North China Craton (Taishan-Xintai area, western Shandong Province): Further evidence of an understated event from U–Pb dating and Hf isotopic composition of zircon. *Precambrian Research, 186*, 169–180.

Wan, Y.-S., Song, B., Liu, D.-Y., Wilde, S.-A., Wu, J.-S., Shi, Y.-R., Yin, X.-Y., Zhou, H.-Y. (2006). SHRIMP U–Pb zircon geochronology of palaeoproterozoic metasedimentary rocks in the North China Craton: Evidence for a major late palaeoproterozoic tectonothermal event. *Precambrian Research*, *149*, 249–271.

Wan, Y.-S., Xie, S.-W., Yang, C.-H., Kröner, A., Ma, M.-Z., Dong, C.-H., et al. (2014). Early Neoarchean ($\sim$ 2.7 Ga) tectono-thermal events in the North China Craton: A synthesis. *Precambrian Research, 247*, 45–63.

Wang, H.-L., Chen, L., Sun, Y., & Diwu, C.-R. (2007). Similar to 4.1 Ga xenocrystal zircon from Ordovician volcanic rocks in western part of North Qinling Orogenic Belt. *Chinese Science Bulletin, 52*, 3002–3010.

Wang, Q.-Y., Zheng, J.-P., Pan, Y., Dong, Y.-M., Liao, F.-X., Zhang, Y., et al. (2014). Archean crustal evolution in the southeastern North China Craton: New data from the Huoqiu Complex. *Precambrian Research, 255*, 294–315.

Wang, Z.-J., Shen, Q.-H., & Jin, S.-W. (1987). Petrology, geochemistry and U-Pb isotopic dating of Shipaihe "metadiorite mass" in Dengfeng country, Henan province, China. *Bulletin of the Chinese Academy of Geological Scince, 16*, 215–225.

Wang, Z.-J., Shen, Q.-H., & Wan, Y.-S. (2004). SHRIMP U-Pb zircon geochronology of the Shipaihe "metadiorite mass" from Dengfeng country, Henan province. *Acta Geoscience Sinica, 25*(3), 295–298.

Wu, F.-Y., Zhang, Y.-B., Yang, J.-H., Xie, L.-W., & Yang, Y.-H. (2008). Zircon U–Pb and Hf isotopic constraints on the Early Archean crustal evolution in Anshan of the North China Craton. *Precambrian Research, 167*, 339–362.

Wu, F.-Y., Zhao, G.-C., Wilde, S. A., & Sun, D.-Y. (2005). Nd isotopic constraints on crustal formation in the North China Craton. *Journal of Asian Earth Sciences, 24*, 523–545.

Yang, C.-H., Du, L.-L., Ren, L.-D., Wan, Y.-S., Song, H.-X., Yuan, Z.-L., & Wang, S.-Y. (2009). SHRIMP U-Pb ages and stratigraphic correlation of the Angou Group on the southern margin of the North China Craton. *Acta Petrologica Sinica, 25*, 1853–1862.

Yu, X.-Q., Liu, J.-L., Li, C.-L., Chen, S.-Q., & Dai, Y.-P. (2013). Zircon U Pb dating and Hf isotope analysis on the Taihua Complex: Constraints on the formation and evolution of the Trans-North China Orogen. *Precambrian Research, 230*, 31–44.

Zhai, M.-G., Guo, J.-H., Li, Y.-G., Liu, W.-J., Peng, P., & Shi, X. (2003). Two linear granite belts in the central-western North China Craton and their implication for Late Neoarchaean-Palaeoproterozoic continental evolution. *Precambrian Research, 127*, 267–283.

Zhai, M.-G. (2011). Cratonization and the Ancient North China Continent: A summary and review. *Science China-Earth Sciences, 54*, 1110–1120.

Zhai, M.-G., & Santosh, M. (2011). The early Precambrian odyssey of the North China Craton: A synoptic overview. *Gondwana Research, 20*, 6–25.

Zhai, M., & Santosh, M. (2013). Metallogeny of the North China Craton: Link with secular changes in the evolving Earth. *Gondwana Research, 24*, 275–297.

Zhang, R.-Y. (2015). *The composition and evolution of the Sushui complex in the Zhongtiao Mountains, the south of North China Craton* (pp. 1–160) (Ph.D. Thesis of Northwest University).

Zhang, G.-W., Bai, Y.-B., Sun, Y., Guo, A.-L., Zhou, D.-W., & Li, T.-H. (1985). Composition and evolution of the archaean crust in central Henan, China. *Precambrian Research, 27*, 7–35.

Zhang, R.-Y., Zhang, C.-L., Diwu, C.-R., & Sun, Y. (2012). Zircon U–Pb geochronology, geochemistry and its geological implications for the Precambrian granitoids in Zhongtiao Mountain, Shanxi Province. *Acta Petrologica Sinica, 28*, 3559–3573.

Zhang, G.-W., Zhang, B., Yuan, X., & Xiao, Q. (2001). *The Qinling Orogenic Belt and continental dynamics* (pp. 1–855). Beijing: Science Press.

Zhang, G.-W., Zhou, D.-W., Zhang, T.-A., Bai, Y.-B. (1982). Correlation of tectonic sequence of Dengfeng Group with Taihua group in cental part of Henan. Journal of Northwest University (Special Issue for Precambrian Geology), 1–10.

Zhao, G.-C. (2014). Chapter 2-Archean geology of the Eastern block. In G. Zhao (Ed.), *Precambrian evolution of the North China Craton* (pp. 15–69). Boston: Elsevier.

Zhao, G.-C., Sun, M., Wilde, S.-A.., Li, S.-Z. (2005). Late Archean to Paleoproterozoic evolution of the North China Craton: key issues revisited. Precambrian Research, 136, 177–202.

Zheng, Y.-F., Chen, R.-X., Zhang, S.-B., Tang, J., Zhao, Z.-F., & Wu, Y.-B. (2007b). Zircon Lu-Hf isotope study of ultrahigh-pressure eclogite and granitic gneiss in the Dabie orogen. *Acta Petrologica Sinica, 23*, 317–330.

Zheng, Y.-F., Zhang, S.-B., Zhao, Z.-F., Wu, Y.-B., Li, X.-H., Li, Z.-X., & Wu, F.-Y. (2007a). Contrasting zircon Hf and O isotopes in the two episodes of Neoproterozoic granitoids in South China: Implications for growth and reworking of continental crust. *Lithos, 96*, 127–150.

Zhou, Y.-Y., Zhao, T.-P., Xue, L.-W., Wang, S.-Y., & Gao, J.-F. (2009). Petrological, geochemical and chronological constraints for the origin and geological significance of Neoarchean TTG gneiss in the Songshan area, North China Craton. *Acta Petrologica Sinica, 25*, 331–347.

Zhou, Y.-Y., Zhao, T.-P., Wang, Christina Yan, & Hu, G.-H. (2011). Geochronology and geochemistry of 2.5 to 2.4 Ga granitic plutons from the southern margin of the North China Craton: Implications for a tectonic transition from arc to post-collisional setting. *Gondwana Research, 20*, 171–183.

Zhu, X.-Y., Zhai, M.-G., Chen, F.-K., Lyu, B., Wang, W., Peng, P., & Hu, B. (2013). $\sim$2.7-Ga crustal growth in the North China Craton: Evidence from zircon U-Pb ages and Hf isotopes of the Sushui complex in the Zhongtiao terrane. *Journal of Geology, 121*, 239–254.

Structural Architecture and Spatial-Temporal Distribution of the Archean Domains in the Eastern North China Craton

3

Peng Peng

Abstract

Globally, the Archean domains are composed of tonalite–trondhjemite–granodiorite (TTG) gneisses, diorites and granites, and supracrustal successions (commonly greenstone belts), which metamorphosed to greenschist facies, but less commonly up to granulite facies. However, the Archean domains in the Eastern North China craton were mostly metamorphosed to high-grades. For example, the majority of the Anshan-Qingyuan region was built at 2570–2500 Ma with a few 3800–3000 Ma rocks, and it suffered high-amphibolite to granulite facies metamorphism with anticlockwise *P-T*-paths at ~2480 Ma. The majority of the Huai'an-Zunhua region formed at 2560–2500 Ma with a few ~3300 Ma rocks, and it also experienced high-amphibolite to granulite facies metamorphism with anticlockwise *P-T*-path at ~2480 Ma, but its west part (the Huai'an-Chengde area) was overprinted by a ~1950–1800 Ma metamorphism up to high-pressure granulite facies with clockwise *P-T*-paths. The Archean rocks of the Anshan-Qingyuan and Huai'an-Zunhua regions were strongly deformed, and the supracrustal rocks occur as relic bodies with varied scales up to kilometers intruded by the TTG gneisses-dominated plutons. They show quite different architecture from the typical dome-and-keel structure, which likely formed under significant vertical tectonism. Based on the spatial-temporal distribution of different rock series and the spatial distribution of varied metamorphic grades of the Neoarchean in different regions of the Eastern North China craton, we propose that the craton can be divided into four blocks, i.e., the Lushan-Jiaobei, Zhongtiao-Taishan, Liaonan-Qingyuan, and Wutai-Zunhua blocks. This spatial-temporal distribution of the Neoarchean blocks approves a horizontal growth of crust, which is also supported by the chemistry of the igneous rocks; however, the presence of mafic rocks from primitive mantle and the anatexis in high-grade regions may indicate the coexisting of vertical growth of the crust. These Archean high-grade regions may be the exhumed lower crust of arc-like terrains produced by the Archean-style subduction, i.e., a mantle-wedge-weak 'hot' flat subduction with significant mantle upwelling under the arc crust, resulting in their amalgamation at ~2480 Ma.

Keywords

The Eastern North China Craton • Archean • Greenstone belt • Structural architecture • *P-T*-paths • Spatial-temporal distribution • Tectonics

P. Peng (✉)
State Key Laboratory of Lithospheric Evolution, Institute of Geology and Geophysics, Chinese Academy of Sciences, Beijing, 100029, China
e-mail: pengpengwj@mail.iggcas.ac.cn

M. Zhai et al. (eds.), *Main Tectonic Events and Metallogeny of the North China Craton*, Springer Geology, DOI 10.1007/978-981-10-1064-4_3

3.1 Introduction

The Archean domains are commonly composed of greenstone belts which are deformed and metamorphosed volcano-sedimentary successions, and TTG gneisses-granites which intruded the former (Windley 1995; Anhaeusser 2014). The Archean domains have been metamorphosed almost without exception to a greater or lesser extent following successive stages of deformation, and many of them have been affected by greenschist facies metamorphism, but some of them with grades up to granulite facies, e.g., those in Southwest Greenland (Rollinson 2002; Windley and Garde 2009; Anhaeusser 2014). To discuss the differences/relationships between the granite-greenstone terrains being metamorphosed into high-grades and the traditionally defined high-grade terrains (or the granulite-gneiss terrains) (e.g., Windley 1995), is out the scope of this paper.

The high-grade domains may have been metamorphosed during Proterozoic orogenic processes (e.g., the Kapuskasing zone: Percival and West 1994), but some of them are metamorphosed in the Archean following extensive TTG-dominated magmatism (e.g., Windley and Garde 2009; Szilas et al. 2011). Sizova et al. (2015) suggest that different from the granite-greenstone terrains with dome-and-keel geometry, which formed over delaminating–upwelling mantle subjected mostly to vertical tectonics, the strongly deformed high-grade domains represents reworked (accreted) crusts that were subjected to both strong horizontal shortening and vertical tectonics and are related to subduction. The spatial-temporal distribution of the Archean domains and the subdivision of blocks/terrains in a craton can give evidence for the growth history of the crust, as well as geological processes of its cratonization. In addition to the structural architecture and spatial-temporal distribution of the Archean regions, their composition and rock series are important in understanding the Archean geodynamics of Earth. It should be noticed that the geothermal gradient was high and the crust was possibly thick in the Archean, and these would have affected the dehydration/melting and metamorphism processes (e.g., Shirey and Hanson 1984; Martin 1987, 1999; Drummond and Defant 1990; Kelemen 1995; Rapp et al. 1999, 2003; Foley et al. 2002; Smithies et al. 2003; Martin et al. 2005).

In this paper, the structural architecture, chemistry of different rock series, and spatial-temporal distribution of the Archean domains in the Eastern North China craton (simplified as the ENCC) will be analyzed to understand its cratonization.

3.2 Lithological Relations and Structural Architecture: Examples from the Anshan-Qingyuan and Huai'an-Zunhua Regions (North China)

Separated by the Cenozoic faults, numbers of Neoarchean domains are preserved in the North China block (Fig. 3.1), which may comprise two cratons, the Western and Eastern North China cratons (ENCC) following asubdivision of Peng et al. (2014). Many of them have been metamorphosed to relatively high-grade (high-amphibolite to granulite facies), except a few, for example, the Taishan (Luxi) and Zhongtiao regions (greenschist to low amphibolite facies, Wan et al. 2015a). In the ENCC, most regions were affected by a Neoarchean regional anticlockwise metamorphism up to granulite facies (Fig. 3.2; Cui et al. 1991; Li 1993; Sun et al. 1993; Ge et al. 1994; Wang and Cui 1994; Chen et al. 1994; Zhao et al. 1998; Zhao 2009; Wu et al. 2013); but the western and eastern margins of the craton have been overprinted by a Paleoproterozoic high-grade metamorphism (Fig. 3.2; Peng et al. 2014). Thus, the high-grade regions in the ENCC can be classified into two kinds types, one metamorphosed at ~2480 Ma (e.g., the Anshan-Qingyuan region; Wan et al. 2005a, b; Bai et al. 2014, 2015; Peng et al. 2015), and the other at both ~2480 and ~1950–1800 Ma (e.g., the western part of the Huai'an-Zunhua region; Liu et al. 2012; Peng et al. 2012).

The Anshan-Qingyuan region is located in eastern Liaoning and southern Jilin Provinces, covering an area of about 500 km × 120 km (Fig. 3.3). About 70–80 % of the exposed rocks are granitoids in composition, and the trondhjemite gneiss in the Anshan area give the oldest crystallization age of ~3800 Ma (Bai et al. 2014, 2015; Wu et al. 2008; Wan et al. 2012a; Wang et al. 2015a, b, c). The supracrustal rocks are known as the Anshan, Chentaigou, Benxi and Qingyuan Complexes/Groups, within which there are large iron ore deposits (Zhai et al. 1985; Wan 1993; Wan et al. 2005a, 2012a, b; Dai et al. 2014; Wang et al. 2014; Zhu et al. 2015a). They have undergone metamorphism up to granulite facies at ~2470–2480 Ma (Wan et al. 2005a; Bai et al. 2014; Peng et al. 2015) and comprise of serpentinite, (pyroxene) amphibolite, granitic gneisses, banded iron formation, sillimanite- and/or kyanite-bearing gneisses, muscovite-biotite-quartz schist, and marble (Zhai et al. 1985; Wan et al. 2005a). The Qingyuan Complex is the host to the Hongtoushan volcanic-associated massive sulphide–Cu deposit (Zhai et al. 1985; Gu et al. 2007; Zhang et al. 2014a, b;

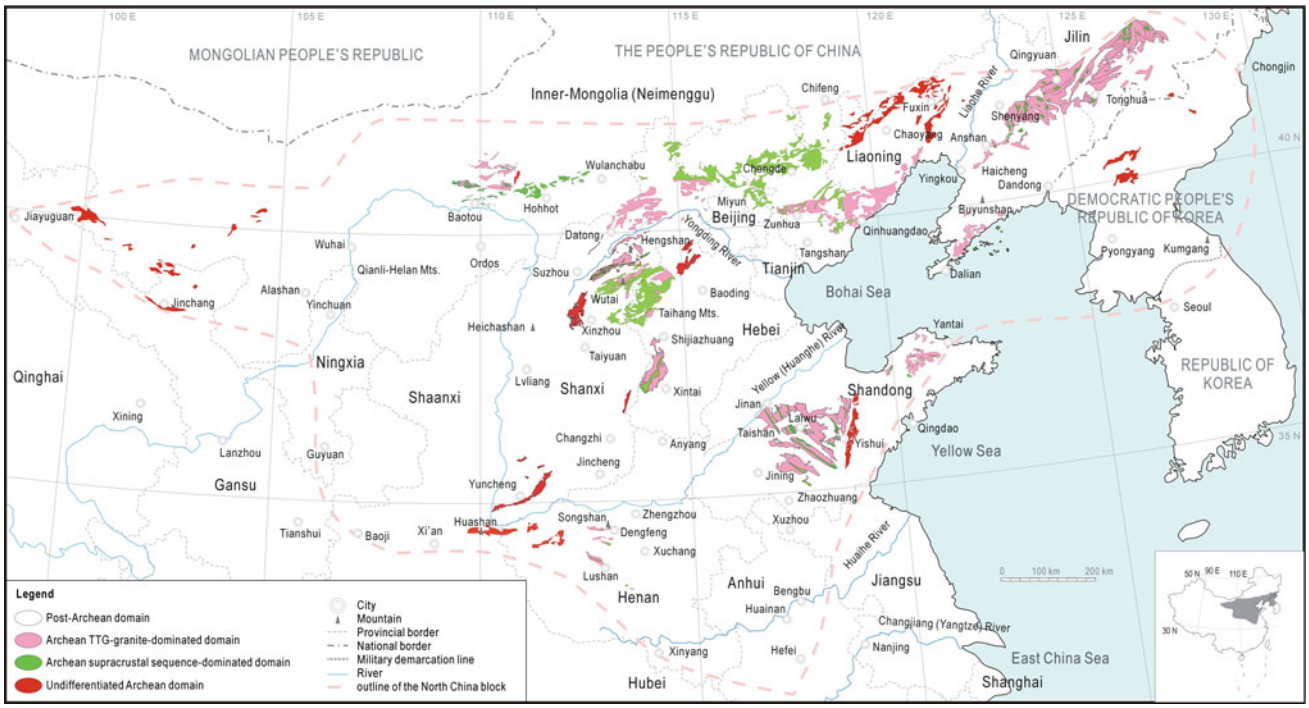

Fig. 3.1 Geological map showing the Archean domains in the North China block

Zhu et al. 2015b). It has been well-documented that the supracrustal rocks were deposited/erupted mainly at ~2570–2510 Ma; whereas the batholith rocks were emplaced during 2570–2490 Ma (Li and Shen 2000; Wan et al. 2005a; Miao et al. 2005; Lu 2009; Liu et al. 2011b; Bai et al. 2014; Peng et al. 2015; Fig. 3.3a), with a few in the Anshan area at ~3800–3000 Ma (Liu et al. 1992, 2008; Wu et al. 2008; Wan et al. 2012a; Wang et al. 2015a, b, c).

The Huai'an-Zunhua region is located in northern Hebei Province and northern Beijing City, covering an area of about 600 km × 250 km (Fig. 3.4). 60–70 % of the exposed rocks are TTG-dominated gneisses and granites in composition, and the oldest rock was reported from near Caozhuang, Qian'an (tonalite, ~3300 Ma; Nutman et al. 2011). The supracrustal rocks are classified as a series of Complexes/Groups (e.g., Hongqiyingzi, Dantazi, Zhuzhangzi, Miyun, Sihetang, Zunhua, Qianxi, Lulong, Qinglong, etc.), which compose of meta-volcanosediments with varied ages but mainly at ~2560–2500 Ma: e.g., Liu et al. 2011a, b, 2012, 2013; Wan et al. 2011; Zhang et al. 2011; Lv et al. 2012; Peng et al. 2012; Guo et al. 2013, 2015a, b; Nutman et al. 2011; Shi et al. 2012). These sequences were metamorphosed up to granulite facies at 2500–2460 Ma, with grades varying from medium-pressure granulite facies in Miyun-Zunhua area to low amphibolite facies in Qinglong-Lulong area (Fig. 3.1; Nutman et al. 2011; Liu et al. 2012, 2013; Shi et al. 2012); and in addition, the western part (Huai'an-Chengde, Fig. 3.1) was overprinted by 1950–1800 Ma metamorphism up to high-pressure granulite facies (Zhai et al. 1992, 1996; Guo et al. 2001, 2005, 2015a, b; Zhao et al. 1998, 2001). The supracrustal rocks compose of mainly (pyroxene) amphibolite, granulite, felsic gneisses, banded iron formation, quartzite, and marble, with a few sillimanite- and/or kyanite-bearing gneisses (Liu et al. 2012; Lv et al. 2012; Peng et al. 2012; Guo et al. 2013, 2015a, b; Nutman et al. 2011; Shi et al. 2012; Liu et al. 2013).

Figure 3.5 shows some representative cross sections in the two regions; whereas Fig. 3.6 shows some typical outcrops. Though all the sequences have been metamorphosed to amphibolite to granulite facies, the sedimentation layers can be partly differentiated (Fig. 3.5). The oldest rocks in the two regions include the ~3800–3000 Ma TTGs near Anshan city (Fig. 3.6a) and the ~3300 Ma tonalite near Qian'an County (Caozhuang village), which occur as relic bodies in the TTGs (Liu et al. 2008; Nutman et al. 2011; Wang et al. 2015a, b, c). Other old rocks are serpentinite (Fig. 3.6b) and pyroxene hornblendite (Fig. 3.6c), which also occur as deformed bodies in the TTG gneisses. The meta-norite/gabbro bodies are also common in the two regions (Fig. 3.6d–g), though they generally show in situ melts/veins: Fig. 3.6d, e show some in situ to quasi-in situ melts/veins; whereas Fig. 3.6f shows exotic veins. Figure 3.6g shows relic blocks of pyroxenite/hornblendite. Figure 3.6h, on the other hand, shows some deformed/metamorphosed gabbroic dykes, which possibly intruded the TTG gneisses during the middle-late

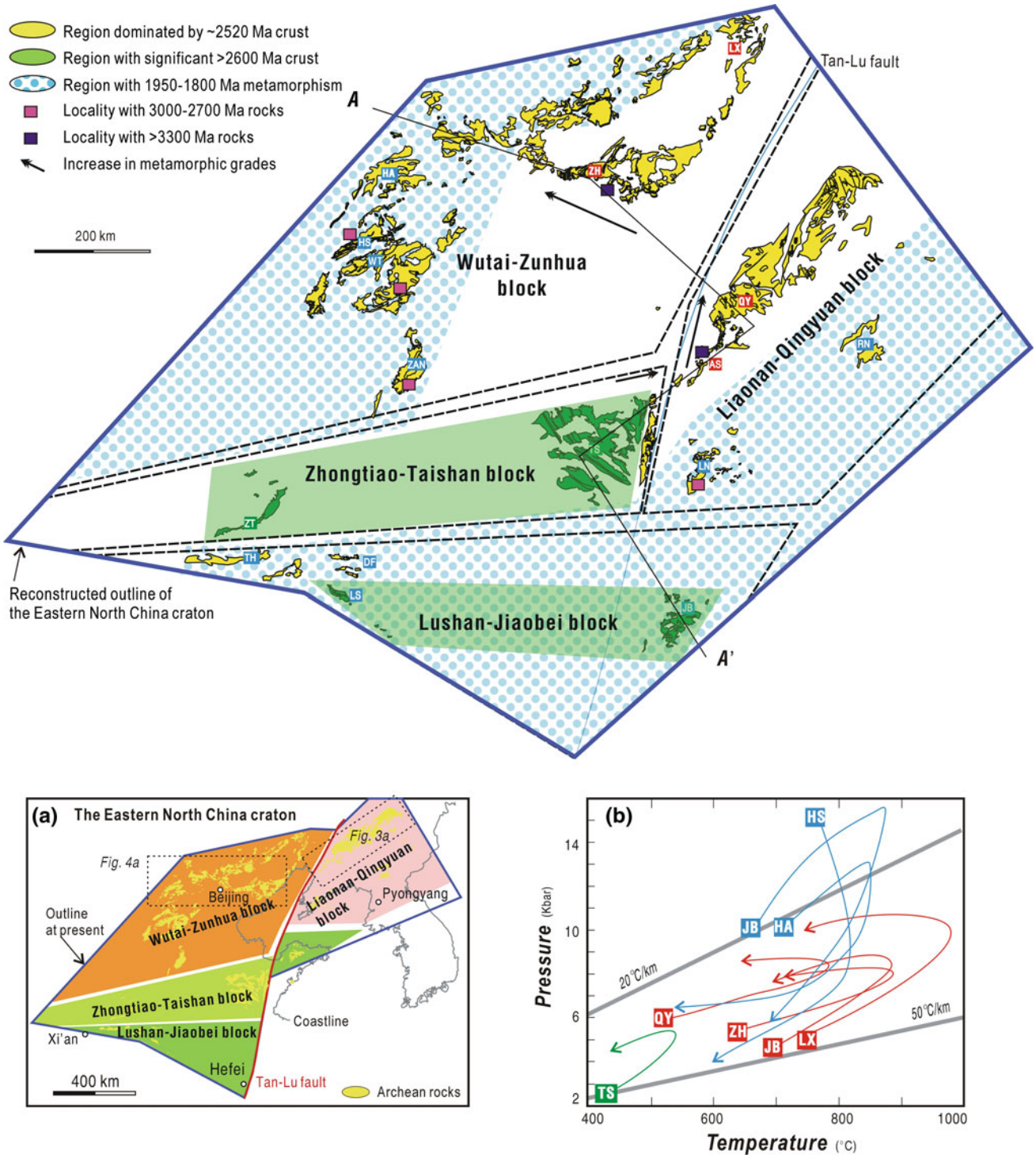

Fig. 3.2 The Archean domains in the Eastern North China craton with Phanerozoic deformation partly reconstructed and the Paleoproterozoic metamorphism affected areas after Peng et al. (2014) shown (the outline of the craton is reconstructed back to Precambrian assuming that there was a ~550 km strike-slip movement along the Tan-Lu fault during the Phanerozoic). The regions with reported >2700 Ma rocks are also indicated (after Wan et al. 2015a). *Inset A*: outline of the craton at present day. *Inset B*: The *P-T*-paths of some representative areas (compiled from Peng et al. 2014, 2015). *QY* Qingyuan; *AS* Anshan; *LX* Liaoxi; *LN* Liaonan; *ZH* Zunhua; *JB* Jiaobei; *HA* Huai'an; *WT* Wutai; *ZAN* Zanhuang; *TS* Taishan; *ZT* Zhongtiao; *DF* Dengfeng; *HS* Hengshan; *RN* Rangnim. AA′ section is presented in Fig. 3.10

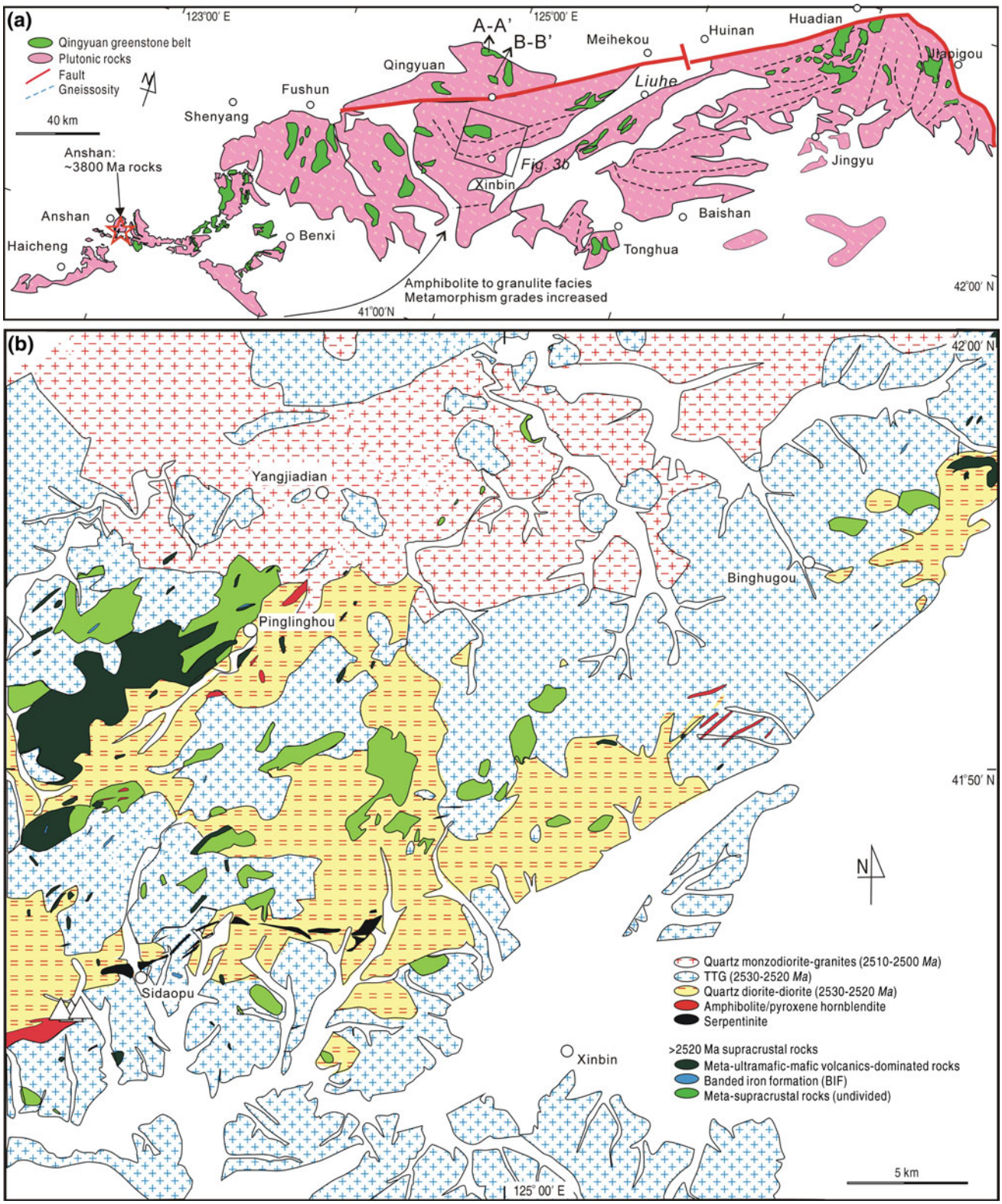

Fig. 3.3 **a** Simplified geological map of the Anshan-Qingyuan region. **b** Detailed map in the Xinbin area showing the relationship among different lithological units (revised after Peng et al. 2015)

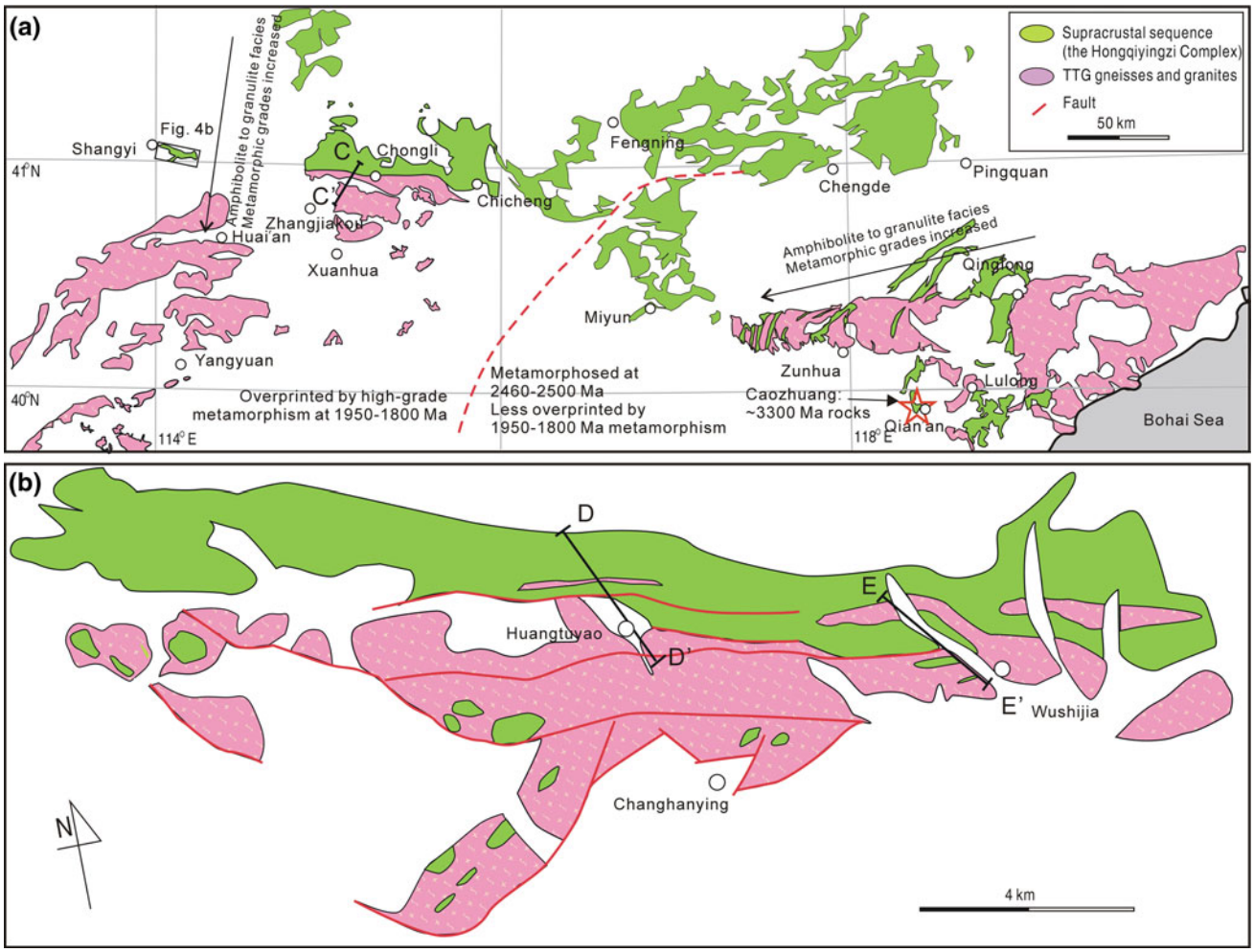

Fig. 3.4 **a** Simplified geological map for the Huai'an-Zunhua region. **b** Detailed map showing the distribution of granites and supracrustal rocks in the Huangtuyao area near Shangyi County (revised after Peng et al. 2012)

Paleoproterozoic (see also Peng et al. 2012). Figure 3.6i–k show some relic stratigraphic units: though being strongly deformed and metamorphosed, two sequences can be differentiated, i.e., a clastic rocks-dominated sequence including marble layers (Fig. 3.6k), metapelite, metasandstone (Fig. 3.6m) and quartzite (Fig. 3.6n), and a volcanics-dominated sequence with meta-mafic/felsic lavas and sedimentary interlayers (Fig. 3.6l). There are layers of banded iron formation (BIF; Fig. 3.6m, o–p) in both sequences (Fig. 3.7): the BIFs in the volcanics contain mafic minerals such as amphiboles and/or pyroxenes (Fig. 3.6o); while those in the clastic rocks rarely have mafic minerals (Fig. 3.6m). Locally, the metapelites show (ultra-)high-temperature granulite facies, e.g., they contain garnet, sillimanite, spinel and eulite (Fig. 3.6q). In the volcanic layers in Qingyuan area (Hongtoushan village), there is a sulphide–Cu ore deposit (Fig. 3.6r).

In the Anshan-Qingyuan region, the supracrustal rocks appear as relic units/pieces up to kilometers in scales, intruded by the TTG gneisses-granitoids (Figs. 3.3, 3.5 and 3.6g). However, the supracrustal rocks and the plutonic rocks of the Huai'an-Zunhua region are more or less tectonically separated: the supracrustal rocks show better relic stratigraphy (i.e., their original components in the Neoarchean) than those of the Anshan-Qingyuan region, though being penetrated by late foliations (Figs. 3.5 and 3.6k). A cross section from lowermost crust to middle crust can be differentiated in the western part (Huai'an-Chengde area) of the Huai'an-Zunhua region (Figs. 3.4 and 3.5; Peng et al. 2012); whereas, the supracrustal rocks in the eastern part occur as deformed narrow zones in the TTG gneisses (Fig. 3.4). In general, the architecture of the Anshan-Qingyuan and Huai'an-Zunhua regions is characterized by strong deformation with supracrustal sequences as deformed relic bodies; and these are distinct from the dome-and-keel structure, which is common in the low-grade granite-greenstone terrains (e.g., Condie 1984; Windley 1995; Harris et al. 2012).

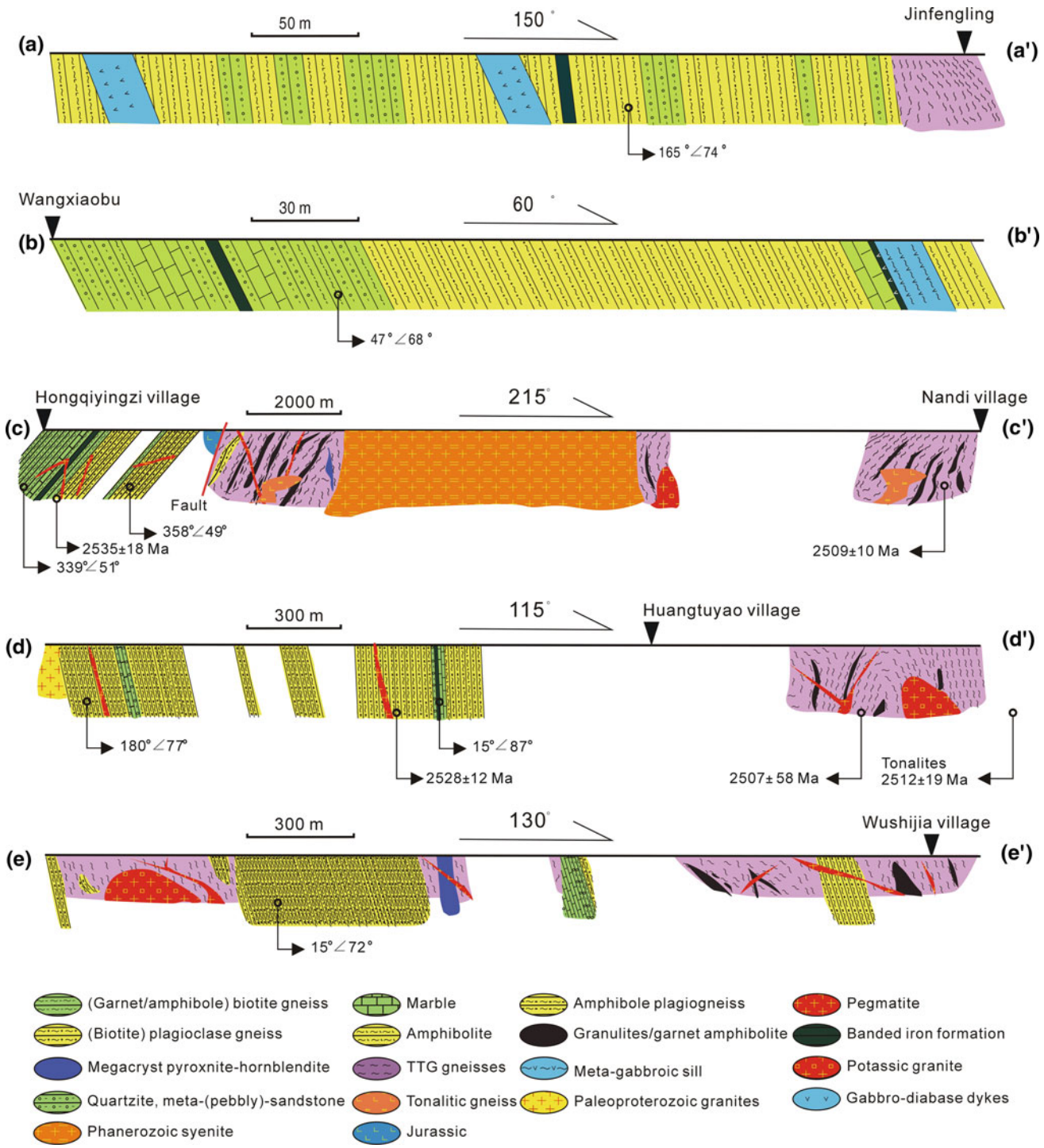

Fig. 3.5 Representative cross sections of the Archean domains in the Huai'an-Zunhua and Anshan-Qingyuan regions. See locations of **aa′** and **bb′** sections in Fig. 3.3, and **cc′**, **dd′** and **ee′** sections in Fig. 3.4. Sections **c**–**e** are after Peng et al. (2012)

Figure 3.7 is a hypothesis stratigraphy of the supracrustal rocks in the two regions based on the occurrences of the supracrustal rocks (Fig. 3.5). It comprises two units, one with ultramafic to mafic to felsic volcanics, with minor banded iron formation and clastic rocks; whereas the other unit is dominated by sandstone, pelite and carbonates. Though carbonates rarely occurred in the Archean greenstone belts, there are some as old as >3000 Ma in a global prospective, which indicate epicontinental sea environments (Allwood et al. 2006; van Kranendonk 2006; Lowe and

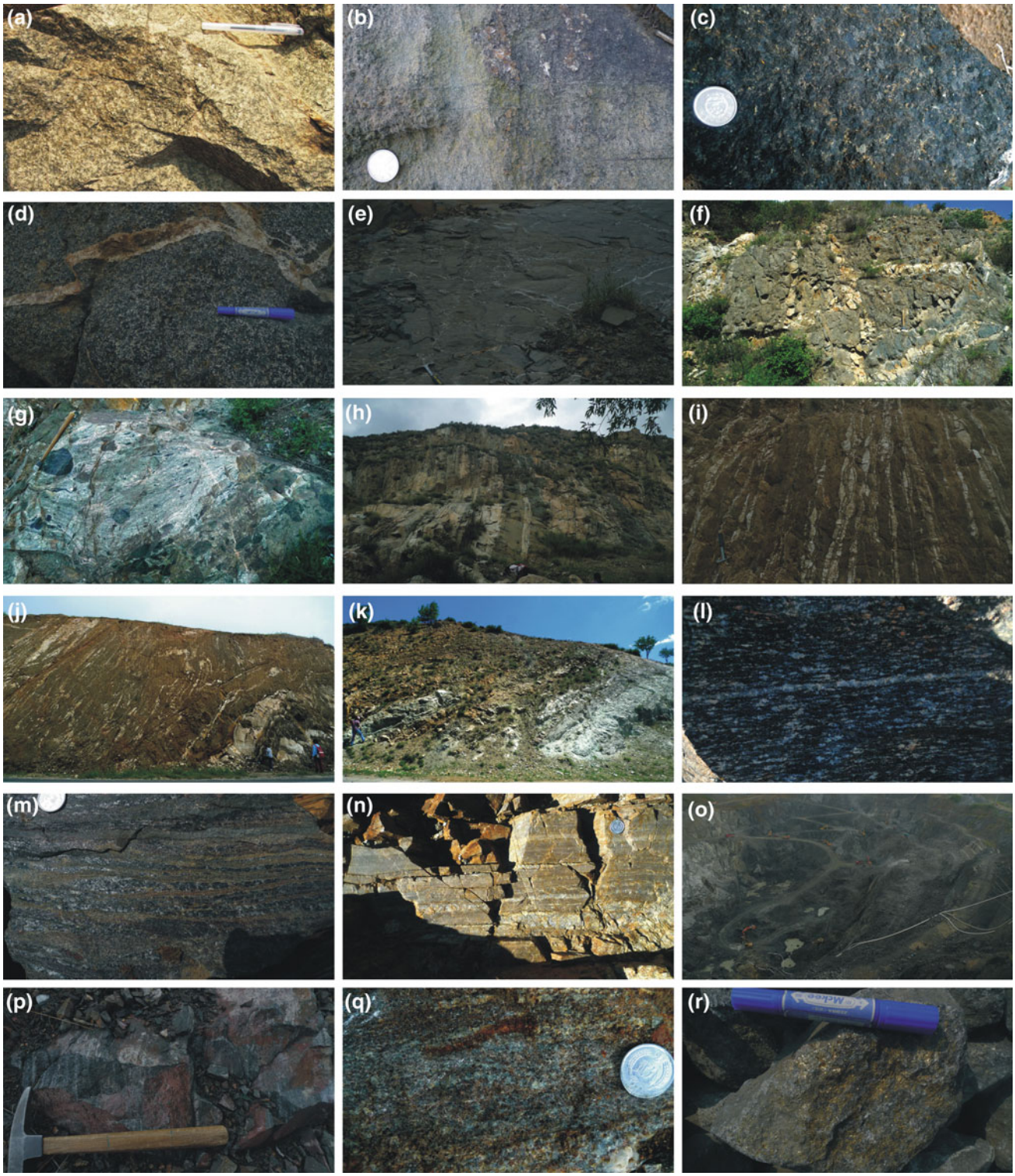

Fig. 3.6 Representative photos from the Huai'an-Zunhua and Anshan-Qingyuan Archean domains. **a** TTG gneisses (locality: Anshan); **b** Serpentinite (Xinbin); **c** pyroxene hornblendite (Shangyi); **d** Meta-gabbro leucogranitic veins (Qingyuan); **e** Meta-gabbro with vein-net (Qingyuan); **f** Meta-gabbro with leucogranitic vein-net (Shangyi); **g** TTG gneisses with meta-gabbroic bodies (Shangyi); **h** sheet-like meta-gabbro layers in the TTG gneisses (Chongli); **i** strongly deformed amphibolite (meta-basalt) with leucogranitic veins (Lulong); **j** strongly deformed amphibolite (meta-basalt) with leucogranitic veins (Lulong); **k** Strongly deformed meta-volcano-sedimentary sequence (the whitish parts are marbles, Chongli); **l** Gneissic amphibolite (meta-basalt, Chongli); **m** Quartzite interlayer with meta-sandstone (Shangyi); **n** quartzite (Shangyi); **o** Iron deposit pit (Qingyuan); **p** banded iron formation (Qingyuan); **q** garnet-bearing quartzite (Qian'an); **r** Massive sulphide ore (Qingyuan). See localities in Fig. 3.1

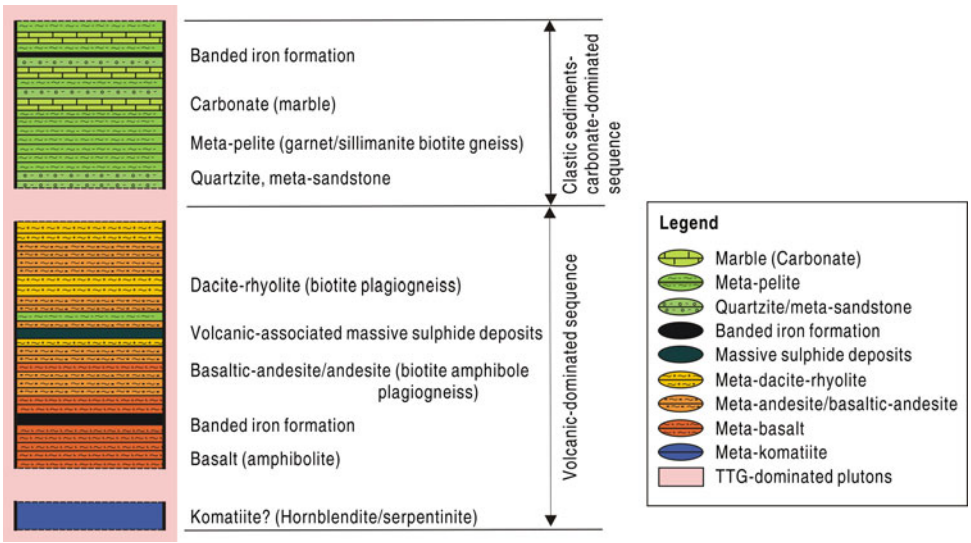

Fig. 3.7 A hypothesis stratigraphy of the volcano-sedimentary sequences in the Anshan-Qingyuan and Huai'an-Zunhua regions

Byerly 2007; Riding et al. 2014; Fralick and Riding 2015). The carbonates are common in the study area (Fig. 3.6k) and were metamorphosed to marbles, which may deposit in open basins/platform.

3.3 Geochemical Features and Petrogenesis of Different Igneous Series in the Anshan-Qingyuan and Huai'an-Zunhua Regions

It has been noticed that even in the Eoarchean, there are some similarities in petrochemistry of volcanic sequences between those in modern arcs and the Archean greenstone belts (supracrustal sequences) (e.g., Turner et al. 2014). However, Condie and Benn (2006) suggest that arc- and non-arc-affinitive rocks coexist in the Archean greenstone belts. For example, there is about 35 % rocks in the Neoarchean greenstone belts with non-modern arc-signature, and this ratio is >80 % in the Eoarchean. There are extensive 2570–2490 Ma magmatic events in the Archean domains of the ENCC, e.g., Li and Shen 2000; Wan et al. 2005a, 2011, 2012c, 2014; Miao et al. 2005; Yang et al. 2008; Zhao 2009; Lu 2009; Liu et al. 2011a, b, 2012, 2013a, b, c; Zhang et al. 2011, 2012; Nutman et al. 2011; Zhou et al. 2011; Lv et al. 2012; Peng et al. 2012, 2015; Wang and Liu 2012; Meng et al. 2013; Wang et al. 2013a, b, c; Guo et al. 2013, 2015a, b; Shi et al. 2012; Bai et al. 2014). Similarly, the majority of the igneous rocks in the Anshan-Qingyuan and Huai'an-Zunhua regions formed within 100 Ma (~2550 Ma). To evaluate the types of the rock series, the ~2550 Ma igneous rocks in these regions are classified and compared, irrespective of their intrusive or extrusive/eruption phases.

Figure 3.8 shows the trace element patterns of some selected rocks (the intermediate rocks are omitted), which present four groups, a ultrabasic/ultramafic group (SiO_2 < 45 wt%), two basic groups (groups 1 and 2: 45 wt % < SiO_2 < 54 wt%), and a granitic (acidic) group (SiO_2 > 65 wt%). The ultrabasic/ultramafic group and the group 1 basic rocks show relatively flat rare earth element (REE) patterns, and they have little depletion in high field-strength elements (HFSE) or enrichment in large ion lithophile elements (LILE) (except Ce for ultrabasic/ultramafic rocks, see Peng et al. 2015; Fig. 3.8a–d). The group 2 comprises basic rocks and it shows enriched light REE with some negative Eu-anomalies, and clear depletion in HFSE and enrichment in LILE (Fig. 3.8c, d). The granitic group shows enriched REEs and more depleted heavy REE, and it has more distinct depletion in HFSE and enrichment in LILE than the group 2 basic rocks (Fig. 3.8a–d). It has positive to non-Eu-anomalies (Fig. 3.8a, b).

The features of the mafic rocks are one key to the petrogenesis of the igneous rocks in the high-grade domains. As the basic rocks have high MgO-concentrations (mostly >5 wt%) and depleted Nd and Hf isotopes (the Anshan-Qingyuan and Huai'an-Zunhua region: e.g., Liu et al. 2012; Bai et al. 2014, 2015; Guo et al. 2013, 2015a, b; other regions of the ENCC: e.g., Diwu et al. 2011, 2012; Wan et al. 2015a), they could be originated from the mantle. The group 1 basic rocks have flat REE and trace element patterns, and this may indicate a relatively primitive mantle source. This group 1 (basic rocks) is a representative component of mafic crust generated from primitive mantle in the Archean with basically no crustal contamination; they can also be a representative protolith for felsic rocks. However, the group 2 basic rocks have distinct light REE and LILE enrichment but HFSE depletion (Fig. 3.8c, d), which are modern arc features (e.g., Defant and

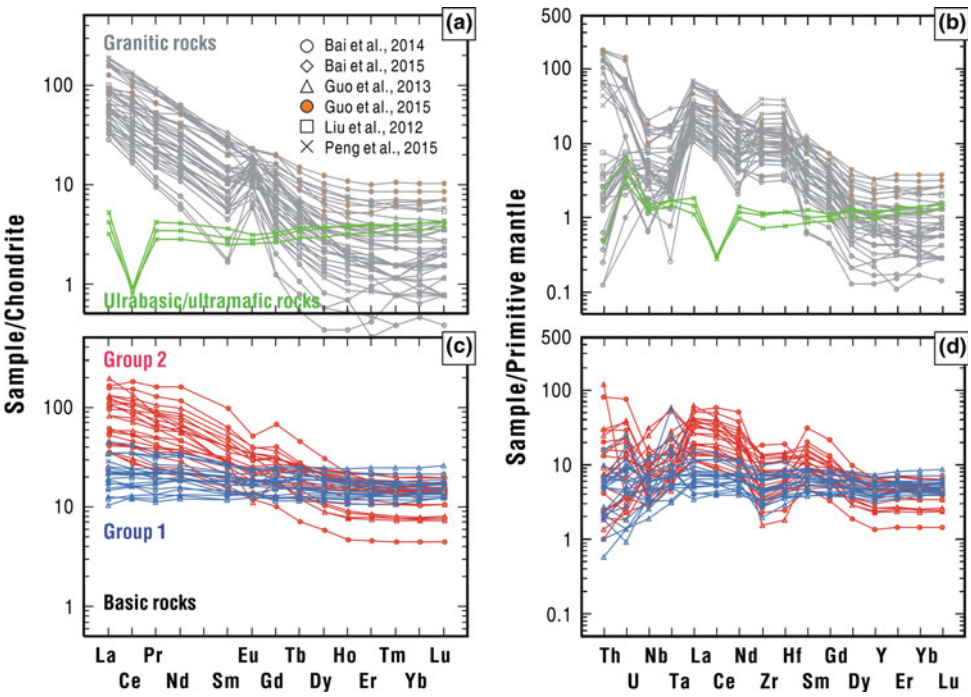

Fig. 3.8 Chondrite-normalized rare earth element patterns (**a**, **c**) and primitive mantle-normalized trace element diagrams (**b**, **d**) for ~2500 Ma granitic and basic igneous rocks in the Anshan-Qingyuan and Huai'an-Zunhua regions. Normalized to values of Sun and McDonough (1989). Data sources: Liu et al. (2012), Bai et al. (2014, 2015), Guo et al. (2013, 2015a, b) and Peng et al. (2015)

Drummond 1990). It is possible that their primitive magma was contaminated by the crustal melts or their mantle regions have been metasomatized by crustal materials. In a diagram deduced by Moyen and van Hunen (2012), the groups 1 and 2 fill into non-arc- and arc-like fields respectively (Fig. 3.9a). The ultrabasic rocks show relatively low trace element concentrations with negative Ce-anomalies (Fig. 3.8a, b), which might be related with alteration or weathering (c.f., Neal and Taylor 1989), and they could be either originally komatiites, or accumulates or relic phases from mafic magma.

The felsic rocks, including the TTG gneisses, are another key to the petrogenesis of the high-grade terrains. Though the felsic rocks are varied in occurrences and series and some of them may contain melts from mantle (e.g., Liu et al. 2004; 2015a, b; Bai et al. 2015), these rocks need extensive slab melting or melting of thickened crust, (Shirey and Hanson 1984; Martin 1987, 1999; Drummond and Defant 1990; Kelemen 1995; Rapp et al. 1999, 2003; Foley et al. 2002; Smithies et al. 2003; Martin et al. 2005; Xiong 2006; Xiong et al. 2006; Moyen 2009; Zhang and Zhai 2012). Figure 3.9b, c show plots for intermediate to granitic (acidic) rocks (SiO_2 > 54 wt%): there are two trends, one has constant Yb_N (normalized to chondrite, the same as below) with large variations in La/Yb_N; while the other has constant La/Yb_N but variant Yb_N. The two trends were interpreted to be similar to the modern adakites and arc calc-alkalines, respectively (Fig. 3.9b; e.g., Drummond and Defant 1990). It has been widely discussed that the TTGs may be analogue of modern adakites (Shirey and Hanson 1984; Martin 1999; Drummond and Defant 1990; Kelemen 1995; Rapp et al. 1999, 2003; Foley et al. 2002; Smithies et al. 2003; Martin et al. 2005; Xiong 2006; Xiong et al. 2006; Moyen 2009) and were produced during the melting of mafic rocks eclogite, granulite or amphibolite (e.g., Foley et al. 2002). However, there are two strings of ideas for the genesis of the TTG gneisses, (1) melting of subducted slab (e.g., Drummond and Defant 1990; Martin 1999; Smithies et al. 2003; Xiong 2006; Windley and Garde 2009; Szilas et al. 2011, 2013), or (2) melting of thickened lower crust or underplated basalt from a paleo-plume or mantle overturn (e.g., Davies 1995; Smithies 2000; Condie 2005; Bédard 2006; van Kranendonk et al. 2007). Figure 3.9c is a plot for granitic (acidic) rocks (SiO_2 > 62 wt%), it shows that these rocks are likely similar to the TTGs produced under high- to medium-pressure, and thus similar to those in subduction system (cf. Moyen and van Hunen 2012; Moyen 2011). Nevertheless, in Fig. 3.9d, the increase of Sr/Y ratios in the granitic rocks may be resulted from deeper melting (Defant and Drummond 1990; Moyan 2009); while the increase of Zr/Sm may be resulted from fractionation of Zr from Sm by amphiboles (Foley et al. 2002; Foley 2008). Thus, it is possible that some granites were originated from the anatexis of the amphibolites and/or granulites.

Based on the arc features of both mafic and felsic igneous rocks (Figs. 3.8 and 3.9) and the fact the geodynamic conditions are different in the Archean, an Archean-style subduction need to be introduced: (1) It is somewhat similar to modern 'hot'-subduction (well-documented from the northern Cascade arc: Abbott et al. 1994; Mullen and McCallum 2014) as the geothermal gradient was high in the Archean

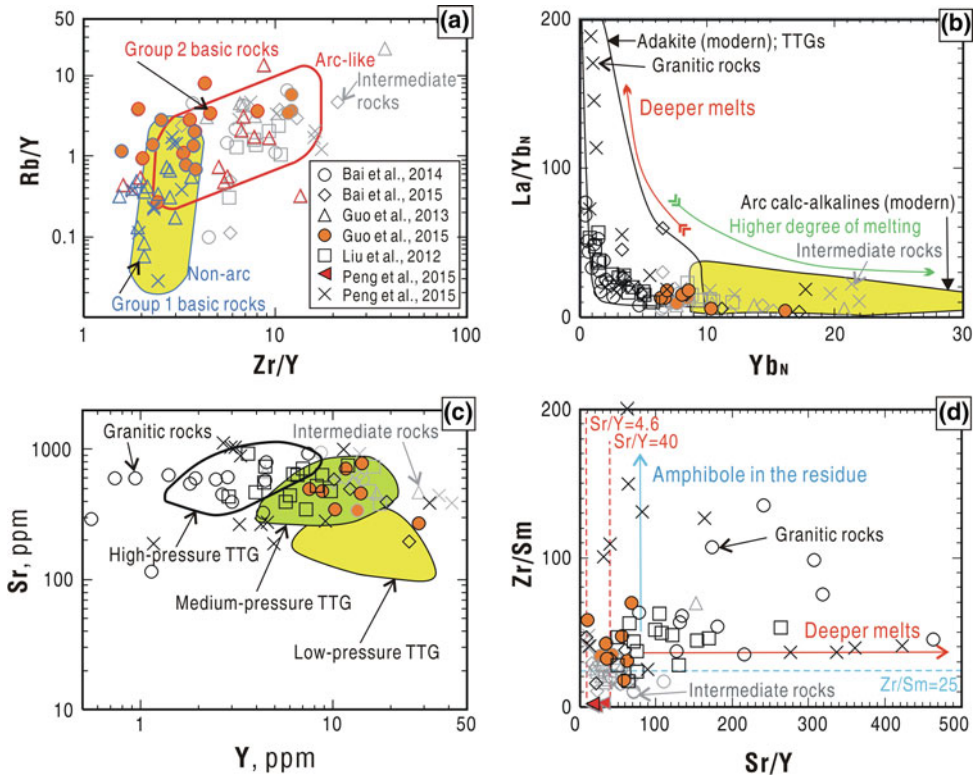

Fig. 3.9 **a** Rb/Y versus Zr/Y plot for basic rocks ($SiO_2 \leq 54$ wt%) and intermediate rocks (54 wt% < $SiO_2 \leq 62$ wt%). The fields are from Moyen and van Hunen (2012) based on chemistry of the 2750–2680 Ma Western Abitibi greenstone belts and TTGs. **b–d** Plots for granitic ($SiO_2 \geq 62$ wt%) and intermediate (62 wt% > $SiO_2 \geq 54$ wt %) rocks: **b** La/Yb_N versus Yb_N plot (fields of 'adakite' and 'arc calc-alkalines' are after Drummond and Defant 1990). Normalized to values of Sun and McDonough (1989). **c** Sr versus Y plot (The fields are from Moyen (2011) based on a compilation of TTGs). **d** Zr/Sm versus Sr/Y plot (Sr/Y = 40 is a threshold for adakites from Defant and Drummond (1990) and Moyen (2009); and Sr/Y = 4.6 and Zr/Sm = 25 are ratios of primitive mantle after Sun and McDonough (1989)). Data sources: Liu et al. (2012), Bai et al. (2014, 2015), Guo et al. (2013, 2015a, b) and Peng et al. (2015)

(e.g., Drummond and Defant 1990; Kelemen 1995; Foley et al. 2002; Smithies et al. 2003; Martin et al. 2005); (2) it could be a 'flat'-subduction as the crust was thick and buoyant in the Archean (Smithies et al. 2003; Laurent et al. 2014); (3) it may have slab melting in the subducting slab rather than dehydration first as at the present (Shirey and Hanson 1984; Martin 1987, 1999; Drummond and Defant 1990; Kelemen 1995; Rapp et al. 1999, 2003; Foley et al. 2002; Smithies et al. 2003) and there could be hydrate minerals preserved even to eclogite facies in the subducting slab; (4) there may be limited dehydration and flux melting in mantle depth, and thus no or only weak modern style mantle wedge in function (Peng et al. 2015); and (5) there could be also synchronous vertical tectonism occurring along with the horizontal tectonism (subduction) (e.g., Lin 2005; Lin and Beakhouse 2013), which can be indicated from the widespread anatexis features inside the high-grade domains (Fig. 3.6c–g), as well as the non-arc features of igneous rocks (Figs. 3.8 and 3.9). Consequently, this Archean-style subduction could be a mantle-wedge-weak 'hot' flat subduction with significant mantle upwelling under the arc region.

3.4 Tectonic Environments of the Two Types of *P-T*-Paths in the Archean Domains

There are two types of metamorphism in the Archean domains of the ENCC: one has anticlockwise *P-T*-paths with the peak metamorphism at medium-pressure/high-temperature granulite facies (P: 5–9 kbar; T: 500–1000 °C: geothermal gradient <20 °C/km) at 2500–2460 Ma; whereas the other one show clockwise *P-T*-paths with the peak metamorphism at high-pressure/high-temperature granulite facies (P: 10–15 kbar; T: 800–900 °C: geothermal gradient >20 °C/km) at ~1950–1800 Ma (Fig. 3.2 inset B). It has been well established that the late Paleoproterozoic metamorphism with clockwise *P-T*-paths in the marginal areas of the ENCC was caused by a subduction–collision process (e.g., Zhao et al. 2001, 2005; Kusky and Li 2003; Liu et al. 2005, 2006; Guo et al. 2005, 2015a, b; Trap et al. 2009; Zhai and Santosh 2011, 2013; Zhai et al. 2011; Peng et al. 2014; Zhao 2014). Actually, such a kind of high-grade metamorphism is rarely recorded at the Archean, for example, the Gridino Complex from Russia

could be the oldest eclogite known so far (~2700–2600 Ma: Li et al. 2015a, b), but its metamorphism age is controversial.

The 2500–2460 Ma high-grade metamorphism with anticlockwise *P-T*-paths (Fig. 3.2, e.g., Cui et al. 1991; Ge et al. 1994; Sun et al. 1993; Wang and Cui 1994; Zhao et al. 1998; Zhao 2009; Wu et al. 2013) seems to have been across the craton except for the low-grade areas along the Zhongtiao-Luxi (Taishan) zone and the uncertain areas with strong late Paleoproterozoic overprinting. Thus this event is likely distributed in a large area rather than a belt zone as those Late Precambrian to Phanerozoic orogens (cf., the Grenville Orogen), and thus their tectonic environments are controversial: some authors suggest that these rocks were built in continent marginal arcs and their high-grade metamorphism was resulted from arc-related magmatism and collision, and the widespread distribution of the metamorphism area was caused by the amalgamation of some small terrains (e.g., Wu et al. 1998; Kusky and Li 2003; Wan et al. 2005a, b, 2012b, c, 2014, 2015a, b; Nutman et al. 2011; Kusky 2011; Wang and Liu 2012; Wang et al. 2011, 2013a, b, c, 2015a, b; Shi et al. 2012; Liu et al. 2012, 2015a, b; Wang et al. 2013a; Guo et al. 2013; Li et al. 2015a, b); however, some others favor a plume or mantle upwelling model according to the anticlockwise *P-T*-paths as well as their widespread spatial distribution (Zhai et al. 1985; Zhao et al. 2001; Ge et al. 2003; Zhai and Peng 2007; Yang et al. 2008; Geng et al. 2012; Wu et al. 2012, 2013). For the Anshan-Qingyuan region, Zhai et al. (1985) propose that the supracrustal rocks were erupted in a paleo-continental rift. Wu et al. (2013) suggest that the Archean domain was formed by a paleo-mantle plume based on the lithology and the anticlockwise *P-T*-path, which involves isobaric cooling. However, some other authors (Li et al. 1999; Li and Shen 2000; Wan et al. 2005a, b; Peng et al. 2015) suggest that they evolved in a continental arc environment followed by arc-arc/continent collision processes. For the Huai'an-Zunhua region, many authors have proposed an arc-accretion environment (e.g., Nutman et al. 2011; Liu et al. 2012; Zhang et al. 2012; Bai et al. 2014).

Based on case study and theoretical analysis in other regions, anticlockwise *P-T*-paths are thought to be related to intrusion and underplating magma which occur in plume regimes (Bohlen 1987), granite emplacement (Sandiford et al. 1991), incipient rift environments (Sandiford and Powell 1986), inception of subduction (Wakabayashi 2004; Hacker 1991; Aoya et al. 2002; Gerya et al. 2002), or in arc regions (Wells 1980; Bohlen 1987) especially at deep crustal levels during the cessation of arc magmatism (Pickett and Saleeby 1993; Lucassen and Franz 1996; Wakabayashi 2004). Consequently, many authors have reconstructed arc-related subduction in the Archean granite-greenstone terrains (e.g., Parman et al. 2001; Polat et al. 2002, 2011; Wyman et al. 2002; Polat and Hofmann 2003; Sandeman et al. 2004; Hollings and Kerrich 2006; Garde 2007; Jenner et al. 2009; Windley and Garde 2009; O'Neil et al. 2011). For example, Szilas et al. (2011, 2013) specify that the greenstone belts from Greenland with grades varied from greenschist to granulite facies were remnants of the arc-related middle Archean crust, and the TTGs intruded the greenstone belts were generated by slab melting; Arai et al. (2015) suggest that the Isua greenstone belt (Greenland) with large metamorphic variations represents an accretionary complex, which was a Pacific-type orogenic belt.

Sizova et al. (2015) suggest that the granite-greenstone crusts with dome-and-keel geometry were formed over delaminating-upwelling mantle which is mostly subjected to vertical tectonics processes; whereas the strongly deformed granite–greenstone crusts represents reworked (accreted) crusts related to subduction subjected to both strong horizontal shortening and vertical tectonics processes based on geodynamic modeling. The high-grade granite-greenstone regions in the ENCC show strong deformation and indistinctive dome-and-keel geometry, and accordingly, they more likely represent reworked crusts related to subduction. This is consistent with the observation that the >2600 Ma rocks recycled in the ~2520 Ma sequences played a more important role than juvenile adding (Wan et al. 2015a, b). We suggest that the anticlockwise *P-T*-paths of the high-grade domains could record the underplating of the arc magmatism and the subsequent cooling and cessation of arc magmatism at the time of arc amalgamation, as proposed by some authors in other studies (Pickett and Saleeby 1993; Lucassen and Franz 1996; Wakabayashi 2004). As the clockwise *P-T*-paths and high-pressure rocks were rarely reported in the Neoarchean (e.g., Li et al. 2015a, b), this may indicate that there were rare rocks being subducted into the deep crust or the mantle at the Archean, or even if there were such processes, the high-pressure rocks can be rarely exposed. Probably, it is the high geothermal gradient, as well as the high-degrees of melting in the downgoing slabs (subducting slabs, or vertically sinking crust) that resisted the ultrahigh-pressure rocks to be exhumed but delaminated. On the other hand, the widespread distribution of high-grades metamorphism may represent amalgamation of micro-continents.

3.5 Spatial-Temporal Distribution of the Archean Domains in the ENCC

It has long been discussed on the tectonic subdivision of the North China block (e.g., Bai et al. 1993; Wu et al. 1998; Deng et al. 1999; Li et al. 2000; Zhao et al. 2005; Zhai and Peng 2007). For example, recently, Wang et al. (2015a, b), Liu et al. (2015a, b) and Li et al. (2015a, 2015b) propose that there was an arc system along the western margin of the

>2700 Ma continent of the ENCC. On the other hand, Wan et al. (2015a) illustrate the distribution of >2600 Ma rocks in the North China block, and they further propose that this block can be subdivided into three ancient terrains based on the distribution of the >2600 Ma rocks, i.e., the Eastern, Southern, and Central Ancient Terranes.

The spatial-temporal distribution of the Archean domains in the ENCC can help understanding the tectonic subdivision of the craton. Figure 3.2 shows the Archean domains in this craton, within which the outline of the craton is reconstructed back to Precambrian assuming that there was a ~550 km strike-slip movement along the Tan-Lu fault during the Phanerozoic (e.g., Xu and Zhu 1995; Uchimura et al. 1996; Leech et al. 2013; Huang et al. 2015; Zhang et al. 2015). It shows three key features:

Firstly, most of the Archean domains of the ENCC are dominated by 2500–2600 Ma TTG gneisses and supracrustal rocks, and there are two special regions: one zone with some 3000–2700 Ma TTG gneisses and supracrustal rocks, including the Jiaobei region (Liu et al. 2013a, b, c) and the Lushan region (Liu et al. 2009); and the other zone with significant ~2700 Ma TTG gneisses and supracrustal rocks including the Taishan (Luxi) region (Wang et al. 2013b; Wan et al. 2015b) and the Zhongtiao region (Zhu et al. 2013) (Fig. 3.2). In addition, there are minor ~3300–3800 Ma relic granitoids, including the Anshan trondhjemite (Liu et al. 1992, 2008; Wu et al. 2008; Wang et al. 2015a, b, c) and the Caozhuang tonalites (Nutman et al. 2011). It should be noticed that there are still minor ~2700 Ma relic rocks/xenoliths in other ~2500 Ma rocks-dominated regions (Wan et al. 2015a and references therein). As the Lushan and Jiaobei regions show some similarities in age populations for the Archean rocks, they might belong to a same block in the Neoarchean (the Lushan-Jiaobei block). This is possibly also the case for the Zhongtiao and Taishan regions, which might comprise another block (the Zhongtiao-Taishan block).

Secondly, most Archean domains have suffered high-grade (high-amphibolite to granulite facies) metamorphism except several regions, e.g., the Luxi and Zhongtiao regions; however, it needs to be noticed that the margins of the craton were metamorphosed up to high-pressure granulite facies during the late Paleoproterozoic (1950–1800 Ma, Fig. 3.2; Peng et al. 2014). Except these marginal areas, the other areas show different metamorphic grades in the Neoarchean (Fig. 3.2). In the Taishan region, the metamorphic grades vary from low amphibolite facies in Jinan area (west) to granulite facies in Yishui area (east, Figs. 3.1 and 3.2: Wu et al. 2012); In the Anshan-Qingyuan region, the grades vary from amphibolite facies in Anshan area (southwest) to granulite facies in Qingyuan region (northeast, Figs. 3.1 and 3.2; Zhao 2009; Wu et al. 2013); and in the Zunhua region (East Hebei Province), the metamorphic grades vary from low amphibolite facies in Qinglong area (east) to granulite facies in Zunhua-Qianxi area (west, Figs. 3.1 and 3.2: Zhao et al. 1998; Lv et al. 2012). Based on the spatial distribution of the Taishan, Anshan-Qingyuan and Huai'an-Zunhua regions in Fig. 3.2 and the spatial variation of metamorphic grades among these regions, we propose that these three regions might belong to different blocks in the Archean. In addition to the Lushan-Jiaobei and Zhongtiao-Taishan blocks subdivided by different age population of rocks, there were possibly two other blocks, namely, the Liaonan-Qingyuan block and the Wutai-Zunhua block (Fig. 3.2). However, it should be noticed that the boundary of the different Archean terrains/blocks is defined by Mesozoic-Cenozoic faults and basins (Fig. 3.2), and their uplifting is correlated with two major events: the uplifting of the late Paleoproterozoic regions defined by the 1950–1800 Ma metamorphism (Zhao et al. 2001, 2005 2014; Kusky and Li 2003; Zhai and Santosh 2011, 2013; Guo et al. 2005; Liu et al. 2005, 2006; Peng et al. 2014); and/or the uplift of the present mountain ranges during the extension and the thinning of the lithospheric mantle of North China during the Mesozoic-Cenzoic (Li et al. 2012; Liu et al. 2013a, b, c, 2015a, b; Meng et al. 2014; Zhang et al. 2014a, b; Xu and Li 2015). Thus, the basins, e.g., the Huabei Basin among the Archean terrains may cover in boundariesbetween ancient blocks.

Thirdly, as the low-grade regions of the Zhongtiao and Taishan regions have more significant >2600 Ma rocks, it is possible that the Archean domains in the ENCC with relatively high-grades may also have more >2600 Ma rocks in the middle crustal levels, before the erosion and losing of these parts of crust.

3.6 Discussion: Neoarchean Tectonic Framework of the ENCC

Based on the spatial-temporal distribution of the high-grade domains in the ENCC (Fig. 3.2), we propose that this craton may be composed by 4 blocks, i.e., the Lushan-Jiaobei block, the Zhongtiao-Taishan block, the Liaonan-Qingyuan block, and the Wutai-Zunhua block, though their boundary is arbitrarily defined by different rock associations and/or spatial variation in metamorphic grades. Based on the published data and the spatial-temporal distribution of these regions, as in Fig. 3.2, we can further deduce the following, (1) the ~2550 Ma rocks dominated most Archean domains; (2) the domains with significant >2600 Ma rocks might be protolith of some ~2500 Ma rocks (Diwu et al. 2011, 2012; Jiang et al. 2010; Liu et al. 2012; Wan et al. 2015a); (3) except the areas that were overprinted by the Late Paleoproterozoic metamorphism, the >2600 Ma nuclei were metamorphosed at low grade (middle crustal level) while some of the ~2550 Ma rocks-dominated regions were

metamorphosed at high-grades (lower crustal level); and thus it is possible that the middle crust of the Archean regions had more distinct >2600 Ma rocks than the lower crust which was dominated by ~2550 Ma rocks. Considering that some ~2550 Ma crust are supracrustal sequences and thus the upper crusts were likely dominated by ~2550 Ma rocks. This 'sandwich' texture (Fig. 3.10a) of the Neoarchean crust is similar to those predicted by numerical modeling (e.g., Johnson et al. 2014; Sizova et al. 2015) and hypothetic models (Kamber 2015), and it approves significant vertical crustal growth in the Neoarchean domains.

The chemical features of the basic rocks indicate that these rocks have both arc- and non-arc-associated features (Figs. 3.8 and 3.9a); while the chemistry and field occurrence of felsic rocks suggest that their melts were possibly from both subduction slab and the preexisting crust itself (Figs. 3.6c–g, 3.8 and 3.9b–d). The *P-T*-paths of the related rocks (Fig. 3.2 inset) can be explained by a subduction process, e.g., the underplating and the subsequent cooling and cessation of arc magmatism at the time of amalgamation (cf., Pickett and Saleeby 1993; Lucassen and Franz 1996; Wakabayashi 2004). It has been well established that the high-grade domains of the ENCC are deep remnants of ~2500 Ma arcs (e.g., Kusky and Li 2003; Wan et al. 2005a, b, 2012a, b, 2014; Nutman et al. 2011; Kusky 2011; Wang and Liu 2012; Wang et al. 2011, 2013a, b, c, 2015a, b; Shi et al. 2012; Liu et al. 2012, 2015a, b; Guo et al. 2013; Peng et al. 2015; Li et al. 2015a, b).

Consequently, we propose a multi-block amalgamation scenario to interpret the forming of the ENCC and the outcropping of the basements (Fig. 3.10). We consider that the geodynamic conditions were different at the Neoarchean (e.g., Drummond and Defant 1990; Kelemen 1995; Foley et al. 2002; Smithies et al. 2003; Martin et al. 2005), and thus it was more likely the Archean-style subduction, i.e., a mantle-wedge-weak 'hot' flat subduction with significant mantle upwelling under the arc region (e.g., Peng et al. 2015). There would be crustal flow (cf., Chardon et al. 2009) and dropping of eclogitized crust (cf., Thienen et al. 2004), and the subducted slab could be even the Archean domains rather than oceanic crust (Fig. 3.10a). The 'sandwich' structure of the crust in Fig. 3.10a is consistent with those reported by Johnson et al. (2014), Sizova et al. (2015) and Kamber (2015). As revealed from numerical model calculation, the subduction in the Archean would be intermittent because of the weak slab with frequent slab break-off events (Fig. 3.10a; Moyen and van Hunen 2012; van Hunen and van den Berg 2008), and this would have shortened the lifespan of subduction cycles, and prevent the backtrack of

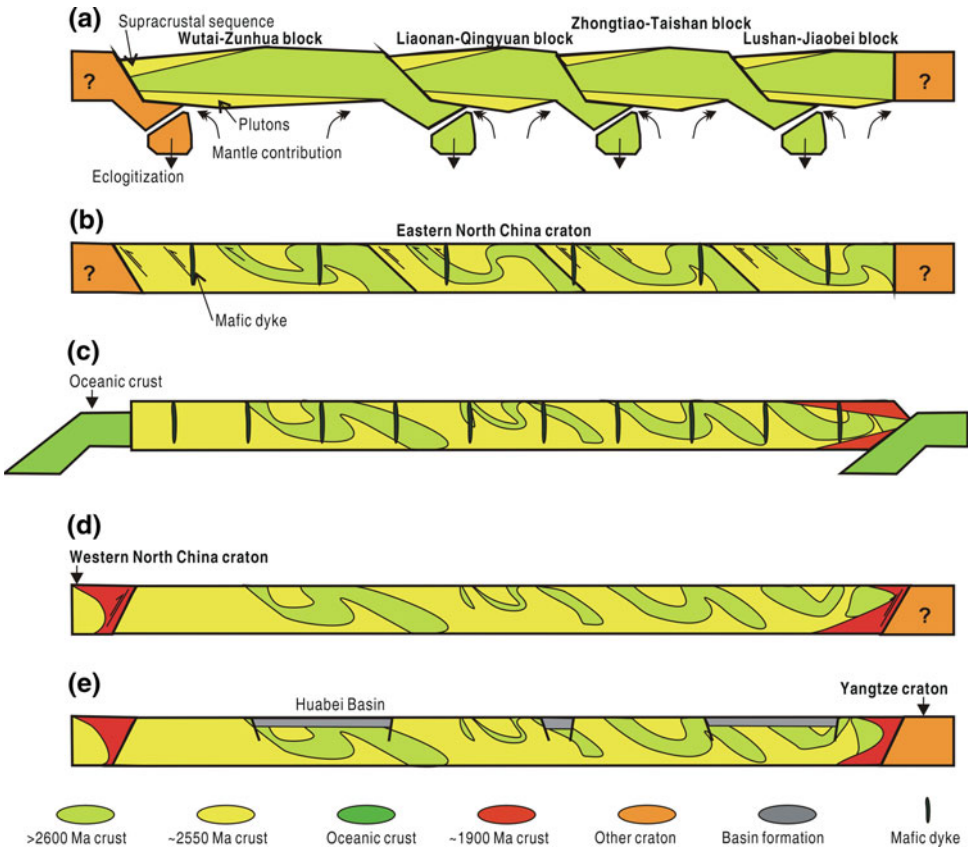

Fig. 3.10 Conceptual cartoons show the amalgamation of the Archean blocks to form the Eastern North China craton. See AA′ section from Fig. 3.2. **a** ~2550 Ma: Building of ~2570–2500 Ma crust under the Archean-style subduction: a mantle-wedge-weak 'hot' flat subduction with significant mantle upwelling under the arc regions; **b** ~2480 Ma: Amalgamation of different blocks; **c** ~1950 Ma: Building of arc sequences along the eastern margin (after Peng et al. 2014); **d** ~1800 Ma: Amalgamated with the Western North China craton; **e** present: Present outcrops of different Archean domains

materials being subducted into the mantle, and this, combined with the high thermal gradient, has negated the forming and exhumation of ultrahigh-pressure metamorphism with the clockwise *P-T*-path. The distribution of the undeformed ~2500 Ma mafic dyke swarms (e.g., Li et al. 2010; Deng et al. 2014; Peng 2015; Fig. 3.10b) and potassium granitic veins (e.g., Wan et al. 2011) in several regions of the craton indicate the unification of different blocks at the end of the Neoarchean (2500–2480 Ma). The uplifting of the Neoarchean domains were mostly affected by two later events: the collision and subsequent exhumation of the late Paleoproterozoic regions recorded by the 1950–1800 Ma high-grade metamorphism (Fig. 3.10c, d; Zhao et al. 2001, 2005, 2015; Kusky and Li 2003; Trap et al. 2009; Zhai and Santosh 2011, 2013; Guo et al. 2005; Liu et al. 2005, 2006; Peng et al. 2014) and the uplift of the present mountain ranges during the extension and the thinning of the lithospheric mantle of North China during the Mesozoic-Cenozoic (Fig. 3.10e; Menzies et al. 1993, 2007; Griffin et al. 1998; Xu 2001; Wu et al. 2006; Zhu et al. 2012; Li et al. 2012; Liu et al. 2013a, b, c, 2015a, c; Meng et al. 2014; Zhang et al. 2014a, b; Xu and Li 2015).

Acknowledgement This work is financially supported by the National Basic Research Program of China (973 project, 2012CB416601), the National Natural Science Foundation of China (41322018), and the National High-Level Talents Special Support Plan. We appreciate kind help and valuable suggestions from the colleagues of the 973 project. Thank Dr Lianchang Zhang and Shuwen Liu for their constructive comments and suggestions.

References

Abbott, D. H., Drury, R., & Smith, W. H. F. (1994). A flat to steep transition in subduction style. *Geology, 22*, 937–940.

Allwood, A. C., Walter, M. R., Kamber, B. S., Marshal, C. P., & Burch, I. W. (2006). Stromatolite reef from the Early Archean era of Australia. *Nature, 441*, 714–718.

Anhaeusser, C. R. (2014). Archean greenstone belts and associated rocks-a review. *Journal of African Earth Sciences, 100*, 684–732.

Aoya, M., Uehara, S., & Wallis, S. (2002). Thermal consequences of a subduction boundary jump: A numerical model for generating subduction-related clockwise pressure—temperature paths. *Tectonics 21*, 4-1–4-17.

Arai, T., Omori, S., Komiya, T., & Maruyama, (2015). Intermediate P/T-type regional metamorphism of the Isua Supracrustal Belt, southern west Greenland: The oldest Pacific-type orogenic belt? *Tectonophysics, 662*, 22–39.

Bai, J., Huang, X.-G., Dai, F.-Y., & Wu, C.-H. (1993). *The Precambrian crustal evolution in China* (pp. 1–204). Beijing: Geological Publishing House.

Bai, X., Liu, S.-W., Guo, R.-R., & Wang, W. (2015). Zircon U-Pb-Hf isotopes and geochemistry of two contrasting Neoarchean charnockitic rock series in Eastern Hebei, North China Craton: Implications for petrogenesis and tectonic setting. *Precambrian Research, 267*, 72–93.

Bai, X., Liu, S.-W., Yan, M., Zhang, L.-F., Wang, W., Guo, R.-R., & Guo, B.-R. (2014). Geological event series of Early Precambrian metamorphic complex in South Fushun area, Liaoning Province. *Acta Petrologica Sinica, 30*, 2905–2924.

Bédard, J. H. (2006). A catalytic delamination-driven model for coupled genesis of Archean crust and sub-continental lithospheric mantle. *Geochimica et Cosmochimica Acta, 70*, 1188–1214.

Bohlen, S. R. (1987). Pressure—temperature—time paths and a tectonic model for the evolution of granulites. *Journal of Geology, 95*, 617–632.

Chardon, D., Gapais, D., & Cagnard, F. (2009). Flow of ultra-hot orogens: A review from the Precambrian, clues for the Phanerozoic. *Tectonophysics, 477*, 105–118.

Chen, N.-S., Wang, R.-J., Shan, W.-Y., & Zhong, Z.-Q. (1994). Isobaric cooling PeT-t path of the western section of the Miyun Complex and its tectonic implications. *Scientia Geologica Sinica, 29*, 354–364 (in Chinese).

Condie, K. C. (1984). *Archaean crustal evolution. Developments in Precambrian Geology* (Vol. 3). Amsterdam: Elsevier.

Condie, K. C. (2005). TTGs and adakites: Are they both slab melts? *Lithos, 80*, 33–44.

Condie, K. C., Benn, K. (2006). Archean geodynamics: Similar to or different from modern geodynamics? In *Archean geodynamics and environments*. *Geophysical monograph series* (Vol. 164, pp. 47–59).

Cui, W.-Y., Wang, C.-Q., & Wang, S.-G. (1991). Geochemistry and metamorphic *P-T*-t path of the Jianping Complex in the western Liaoning Province. *Acta Petrologica Sinica, 7*, 13–26 (in Chinese).

Dai, Y.-P., Zhang, L.-C., Zhu, M.-T., Wang, C.-L., Liu, L., & Xiang, P. (2014). The composition and genesis of the Mesoarchean Dagushan banded iron formation (BIF) in the Anshan area of the North China Craton. *Ore Geology Reviews, 63*, 353–373.

Davies, G. F. (1995). Punctuated tectonic evolution of the Earth. *Earth and Planetary Science Letters, 136*, 363–379.

Defant, M. J., & Drummond, M. S. (1990). Derivation of some modern arc magmas by melting of young subduction lithosphere. *Nature, 347*, 662–665.

Deng, H., Kusky, T. M., Polat, A., Wang, J. P., Wang, L., Fu, J.-M., et al. (2014). Geochronology, mantle source composition and geodynamic constraints on the origin of Late Archean mafic dikes in the Zanhuang Complex, Central Orogenic Belt, North China Craton. *Lithos, 205*, 359–378.

Deng, J., Wu, Z., Zhao, G., & Zhao, H. (1999). Precambrian granitoids, continental crustal evolution and craton formation of the North China platform. *Acta Petrologica Sinica, 15*, 190–198.

Diwu, C.-R., Sun, Y., Guo, A.-L., Wang, H.-L., & Liu, X.-M. (2011). Crustal growth in the North China Craton at ~2.5 Ga: Evidence from in situ zircon U-Pb ages, Hf isotopes and whole-rock geochemistry of the Dengfeng complex. *Gondwana Research, 20*, 149–170.

Diwu, C.-R., Sun, Y., Zhang, H., Wang, Q., Guo, A.-L., & Fan, L.-G. (2012). Episodic tectonothermal events of the western North China Craton and North Qinling Orogenic Belt in central China: Constraints from detrital zircon U-Pb ages. *Journal of Asian Earth Sciences, 47*, 107–122.

Drummond, M. S., & Defant, M. J. (1990). A model for trondhjemite-tonalite-dacite genesis and crustal growth via slab melting: Archean to modern comparisons. *Journal of Geophysical Research, B, Solid Earth and Planets, 95*, 21503–21521.

Foley, S. (2008). A trace element perspective on Archean crust formation and on the presence or absence of Archean subduction. In K. C. Condie & V. Pease (Eds.), *When did plate tectonics begin on planet earth*? *Geological society of America*, *Special Paper* (Vol. 440, pp. 31–50).

Foley, S., Tiepolo, M., & Vannucci, R. (2002). Growth of early continental crust controlled by melting of amphibolite in subduction zones. *Nature, 417*, 837–840.

Fralick, P., & Riding, R. (2015). Steep Rock Lake: Sedimentology and geochemistry of an Archean carbonate platform. *Earth-Science Reviews, 151*, 132–175.

Garde, A. A. (2007). A mid-Archean island arc complex in the eastern Akia terrane, Godthåbsfjord, southern West Greenland. *Journal of the Geological Society, London, 164*, 565–579.

Ge, W.-C., Sun, D.-Y., Wu, F.-Y., & Lin, Q. (1994). *P-T-t* path and tectonic evolution of Archean rocks in southern Jilin Province. *Acta Mineralogica et Petrologica, 13*, 23–32 (in Chinese).

Ge, W.-C., Zhao, G.-C., Sun, D.-Y., Wu, F.-Y., & Lin, Q. (2003). Metamorphic *P-T-path* of the Southern Jilin Complex: Implications for the tectonic evolution of the Eastern Block of the North China Craton. *International Geology Review, 45*, 1029–1043.

Geng, Y.-S., Du, D.-L., & Ren, L.-D. (2012). Growth and reworking of the early Precambrian continental crust in the North China Craton: Constraints from zircon Hf isotopes. *Gondwana Research, 21*, 517–529.

Gerya, T. V., Stöckhert, B., & Perchuk, A. L. (2002). Exhumation of high-pressure etamorphic rocks in a subduction channel-a numerical simulation. *Tectonics 21*, 6-1–6-19.

Griffin, W. L., Zhang, A., O'Reilly, S. Y., & Ryan, C. G. (1998). Phanerozoic evolution of the lithosphere beneath the Sino-Korean Craton. In M. F. J. Flower, S. L. Chung, C. H. Lo & T. Y. Lee (Eds.), *Mantle dynamics and plate interaction in East Asia geodynamics series* (Vol. 27, pp. 107–126).

Gu, L.-X., Zheng, Y.-C., Tang, X.-Q., Zaw, K., Della-Pasque, F., Wu, C.-Z., et al. (2007). Copper, gold and silver enrichment in ore mylonites within massive sulphide orebodies at Hongtoushan VHMS deposit, N.E. China. *Ore Geology Review, 30*, 1–29.

Guo, R.-R., Liu, S.-W., Santosh, M., Li, Q.-G., Bai, X., & Wang, W. (2013). Geochemistry, zircon U-Pb geochronology and Lu-Hf isotopes of metavolcanics from eastern Hebei reveal Neoarchean subduction tectonics in the North China Craton. *Gondwana Research, 24*, 664–686.

Guo, R.-R., Liu, S.-W., Wyman, D., Bai, X., Wang, W., Yan, M., & Li, Q.-G. (2015a). Neoarchean subduction: A case study of arc volcanic rocks in Qinglong-Zhuzhangzi area of the Eastern Hebei Province, North China Craton. *Precambrian Research, 264*, 36–62.

Guo, J.-H., Sun, M., Chen, F.-K., & Zhai, M.-G. (2005). Sm-Nd and SHRIMP U-Pb zircon geochronology of high-pressure granulites in the Sanggan area, North China Craton: Timing of Paleoproterozoic continental collision. *Journal of Asian Earth Sciences, 24*, 629–642.

Guo, J.-H., Zhai, M.-G., Peng, P., Jiao, S.-J., Zhao, L., & Wang, H.-Z. (2015b). Paleoproterozoic Granulites in the North China Craton and Their Geological Implications. In M. G. Zhai (Ed.), *Precambiran Geology of China* (pp. 137–170). Berlin: Springer.

Guo, J.-H., Zhai, M.-G., & Xu, R.-H. (2001). Timing of the granulite facies metamorphism in the Sanggan area, North China Craton: Zircon U-Pb geochronology. *Science in China (D), 44*, 1010–1018.

Hacker, B. R. (1991). The role of deformation in the formation of metamorphic gradients: Ridge subduction beneath the Oman ophiolite. *Tectonics, 10*, 455–474.

Harris, L. B., Godin, L., & Yakymchuk, C. (2012). Regional shortening followed by channel flow induced collapse: A new mechanism for "dome and keel" geometries in Neoarchean granite-greenstone terrains. *Precambrian Research, 212–213*, 139–154.

Hollings, P., & Kerrich, R. (2006). Light rare earth element depleted to enriched basaltic flows from 2.8 to 2.7 Ga greenstone belts of the Uchi Subprovince, Ontario Canada. *Chemical Geology, 227*, 133–153.

Huang, L., Liu, C.-Y., & Kusky, T. M. (2015). Cenozoic evolution of the Tan–Lu Fault Zone (East China)—Constraints from seismic data. *Gondwana Research, 28*, 1079–1097.

Jenner, F. E., Bennett, V. C., Nutman, A. P., Friend, C. R. L., Norman, M. D., & Yaxley, G. (2009). Evidence for subduction at 3.8 Ga: Geochemistry of arc-like metabasalts from the southern edge of the Isua Supracrustal Belt. *Chemical Geology, 261*, 83–98.

Jiang, N., Guo, J.-H., Zhai, M.-G., & Zhang, S.-Q. (2010). ~2.7 Ga continental crust growth in the North China Craton. *Precambrian Research, 179*, 27–49.

Johnson, T. E., Brown, M., Kaus, B. J. P., & VanTongeren, J. A. (2014). Delamination and recycling of Archean crust caused by gravitational instabilities. *Nature Geoscience, 7*, 47–52.

Kamber, B. S. (2015). The evolving nature of terrestrial crust from the Hadean through the Archean into the Proterozoic. *Precambrian Research, 258*, 48–82.

Kelemen, P. B. (1995). Genesis of high Mg andesites and the continental crust. *Contributions to Mineralogy and Petrology, 120*, 1–19.

Kusky, T. M. (2011). Geophysical and geological tests of tectonic models of the North China Craton. *Gondwana Research, 20*, 26–35.

Kusky, T. M., & Li, J.-H. (2003). Paleoproterozoic tectonic evolution of the North China Craton. *Journal of Asian Earth Sciences, 22*, 383–397.

Laurent, O., Martin, H., Moyen, J. F., & Doucelance, R. (2014). The diversity and evolution of late-Archean granitoids: Evidence from the onset of 'modern-style' plate tectonics between 3.0 and 2.5 Ga. *Lithos, 205*, 208–235.

Leech, M. L., & Webb, L. E. (2013). Is the HP–UHP Hong'an–Dabie–Sulu orogen a piercing point for offset on the Tan–Lu fault? *Journal of Asian Earth Sciences 63*, 112–129.

Li, Z.-L. (1993). Metamorphic *P-T-t* path of Archean rocks in eastern Shandong Province and its implications. *Shandong Geology, 9*, 31–41 (in Chinese).

Li, S.-Z., Li, X.-Y., Dai, L.-M., Liu, X., Zhang, Z., Zhao, S.-J., et al. (2015a). Precambrian geodynamics (VI): Formation of North China Craton. *Earth Science Frontier, 22*(6), 77–96.

Li, J.-H., Qian, X.-L., Huang, X.-N., & Liu, S.-W. (2000). Tectonic framework of North China block and its cratonization in the early Precambrian. *Acta Petrologica Sinica, 16*, 1–10.

Li, J.-J., & Shen, B.-F. (2000). Geochronology of Precambrian continental crust in Liaoning Province and Jilin Province. *Progress in Precambrian Research, 23*, 249–255 (in Chinese).

Li, J.-J., Shen, B.-F., Li, S.-B., & Mao, D.-B. (1999). Archean greenstone belts in northern Liaoning province and southern Jilin province. *Journal of Geology and Mineral Resources of North China, 14*, 27–34.

Li, T.-S., Zhai, M.-G., Peng, P., Chen, L., & Guo, J.-H. (2010). Ca. 2.5 billion year old coeval ultramafic–mafic and syenitic dykes in Eastern Hebei: Implications for cratonization of the North China Craton. *Precambrian Research, 180*, 143–155.

Li, X.-L., Zhang, L.-F., Wei, C.-J., & Slabunov, A. I. (2015b). Metamorphic PT-path and zircon U-Pb dating of Archean eclogite association in Gridino complex, Belomorian province, Russia. *Precambrian Research, 268*, 74–96.

Li, S.-Z., Zhao, G.-C., Dai, L.-M., Liu, X., Zhou, L.-H., Santosh, M., et al. (2012). Mesozoic basins in eastern China and their bearing on the deconstruction of the North China Craton. *Journal of Asian Earth Sciences, 47*, 64–79.

Lin, S.-F. (2005). Synchronous vertical and horizontal tectonism in the Neoarchean: Kinematic evidence from a synclinal keel in the northwestern Superior craton, Canada. *Precambrian Research, 139*, 181–194.

Lin, S.-F., & Beakhouse, G. P. (2013). Synchronous vertical and horizontal tectonism at late stages of Archean cratonization and genesis of Hemlo gold deposit, Superior craton, Ontario Canada. *41*, 359–362.

Liu, F., Guo, J.-H., Peng, P., & Qian, Q. (2012). Zircon U-Pb ages and geochemistry of the Huai'an TTG gneisses terrane: Petrogenesis and implications for ~2.5 Ga crustal growth in the North China Craton. *Precambrian Research, 212–213*, 225–244.

Liu, Y.-Q., Kuang, H.-W., Peng, N., Xuu, H., Zhang, P., Wang, N.-S., et al. (2015a). Mesozoic basins and associated Paleogeographic evolution in North China. *Journal of Paleogeography, 4*, 189–202.

Liu, J.-H., Liu, F.-L., Ding, Z.-J., Liu, C.-H., Yang, H., Liu, P.-H., et al. (2013a). The growth, reworking and metamorphism of early Precambrian crust in the Jiaobei terrane, the North China Craton: Constraints from U-Th–Pb and Lu–Hf isotopic systematics, and REE concentrations of zircon from Archean granitoid gneisses. *Precambrian Research, 224*, 287–303.

Liu, S.-W., Lü, Y.-J., Wang, W., Yang, P.-T., Bai, X., & Feng, Y.-G. (2011a). Petrogenesis of the Neoarchean granitoid gneisses in northern Hebei Province. *Acta Petrologica Sinica, 27*, 909–921 (in Chinese).

Liu, D.-Y., Nutman, A. P., Compston, W., Wu, J.-S., & Shen, Q.-H. (1992). Remnants of 3800 *Ma* crust in the Chinese part of the Sino-Korean Craton. *Geology, 20*, 339–342.

Liu, S.-W., Pan, Y.-M., Xie, Q.-L., Zhang, J., & Li, Q.-G. (2004). Archean geodynamics in the Central Zone, North China Craton: Constraints from geochemistry of two contrasting series of granitoids in the Fuping and Wutaishan complexes. *Precambrian Research, 130*, 229–249.

Liu, S.-W., Pan, Y.-M., Xie, Q.-L., Zhang, J., Li, Q.-G., & Yang, B. (2005). Geochemistry of the Paleoproterozoic Nanying granitic gneisses in the Fuping Complex: Implications for the tectonic evolution of the Central Zone, North China Craton. *Journal of Asian Earth Sciences, 24*, 643–658.

Liu, S.-W., Santosh, M., Wang, W., Bai, X., & Yang, P.-T. (2011b). Zircon U-Pb chronology of the Jianping Complex: Implications for the Precambrian crustal evolution history of the northern margin of North China Craton. *Gondwana Research, 20*, 48–63.

Liu, S.-F., Su, S., & Zhang, G.-W. (2013b). Early Mesozoic basin development in North China: Indications of cratonic deformation. *Journal of Asian Earth Sciences, 62*, 221–236.

Liu, S.-J., Wan, Y.-S., Sun, H.-Y., Nutman, A. P., Xie, H.-Q., Dong, C.-Y., et al. (2013c). Paleo- to Eoarchean crustal evolution in eastern Hebei, North China Craton: New evidence from SHRIMP U-Pb dating and in-situ Hf isotopic study of detrital zircons from paragneisses. *Journal of Asian Earth Sciences, 78*, 4–17.

Liu, S.-W., Wang, W., Bai, X., Guo, R.-R., Guo, B.-R., Hu, F.-Y., et al. (2015b). Precambrian geodynamics (VI): Formation and evolution of early continental crust. *Earth Science Frontier, 22*(6), 97–108.

Liu, D.-Y., Wilde, S. A., Wan, Y.-S., Wang, S.-Y., Valley, J.-W., Kita, N., et al. (2009). Combined U-Pb, hafnium and oxygen isotope analysis of zircons from meta-igneous rocks in the southern North China Craton reveal multiple events in the Late Mesoarchean-Early Neoarchean. *Chemical Geology, 261*, 140–154.

Liu, D.-Y., Wilde, S., Wan, Y.-S., Wu, J.-S., Zhou, H.-Y., Dong, C.-Y., et al. (2008). New U-Pb and Hf isotopic data confirm Anshan as the oldest preserved segment of the North China Craton. *American Journal of Science, 308*, 200–231.

Liu, S.-W., Zhao, G.-C., Wilde, S. A., Shu, G.-M., Sun, M., Li, Q.-G., et al. (2006). Th–U–Pb monazite geochronology of the Lvliang and Wutai Complexes: Constraints on the tectonothermal evolution of the Trans-North China Orogen. *Precambrian Research, 148*, 205–225.

Lowe, D. R., & Byerly, G. R. (2007). An overview of the geology of the Barberton greenstone belt and vicinity: Implications for early crustal development. *Developments in Precambrian Geology 15*, 481–526.

Lu, X.-P. (2009). Geochronology of the granites and Archean crustal growth and evolution in south Jilin area, North China Craton. Postdoctoral report, Institute of Geology and Geophysics (83 p). Beijing: Chinese Academy of Sciences (in Chinese).

Lucassen, F., & Franz, G. (1996). Magmatic arc metamorphism: Petrology and temperature history of metabasic rocks in the coastal Cordillera of northern Chile. *Journal of Metamorphic Geology, 14*, 249–265.

Lv, B., Zhai, M., Li, T., & Peng, P. (2012). Zircon U-Pb ages and geochemistry of the Qinglong volcano-sedimentary rock series in Eastern Hebei Implication for ~2500 Ma intra-continental rifting in the North China Craton. *Precambrian Research, 208–211*, 145–160.

Martin, H. (1987). Petrogenesis of Archean trondhjemites, tonalites and granodiorites from eastern Finland: Major and trace element geochemistry. *Journal of Petrology, 28*, 921–953.

Martin, H. (1999). Adakitic magmas: Modern analogues of Archean granitoids. *Lithos, 46*, 411–429.

Martin, H., Smithies, R. H., Rapp, R., Moyen, J. F., & Champion, D. (2005). An overview of adakite, tonalite-trondhjemite-granodiorite (TTG), and sanukitoid: Relationships and some implications for crustal evolution. *Lithos, 79*, 1–24.

Meng, E., Liu, F.-L., Liu, J.-H., Liu, P. H., Cui, Y., Liu, C. H., et al. (2013). Zircon U-Pb and Lu–Hf isotopic constraints on Archean crustal evolution in the Liaonan Complex of northeast China. *Lithos, 177*, 164–183.

Meng, Q.-R., Wei, H.-H., Wu, G.-L., & Duan, L. (2014). Early Mesozoic tectonic settings of the northern North China Craton. *Tectonophysics, 611*, 155–166.

Menzies, A., Fan, W.-M., & Zhang, M. (1993). Paleozoic and Cenozoic lithoprobes and the loss of >120 km of Archean lithosphere, Sino-Korean craton, China. In Prichard, H. M., et al. (Ed.), *Magmatic processes and plate tectonics geological society (London) special publications* (Vol. 76, pp. 71–81).

Menzies, M., Xu, Y. G., Zhang, H. F., & Fan, W. M. (2007). Integration of geology, geophysics, and geochemistry: A key to understanding the North China Craton. *Lithos, 96*, 1–21.

Miao, L.-C., Qiu, Y.-M., Fan, W.-M., Zhang, F.-Q., & Zhai, M.-G. (2005). Geology, geochronology and tectonic setting of the Jiapigou gold deposits, outhern Jilin province, China. *Ore Geology Reviews, 26*, 137–165.

Moyen, J.-F. (2009). High Sr/Y and La/Yb ratios: The meaning of the 'adakitic signature'. *Lithos, 112*, 556–574.

Moyen, J.-F. (2011). The composite Archaean grey gneisses: Petrological significance, and evidence for a non-unique tectonic setting for Archaean crustal growth. *Lithos, 123*, 21–36.

Moyen, J.-F., & van Hunen, J. (2012). Short-term episodicity of Archean plate tectonics. *Geology, 40*, 451–454.

Mullen, E. K., & McCallum, I. S. (2014). Origin of basalts in a hot subduction setting: Petrological and geochemical insights from Mt. Baker, northern Cascade arc. *Journal of Petrlogy, 55*, 241–281.

Neal, C. R., & Taylor, L. A. (1989). A negative Ce anomaly in a peridotite xenolith: Evidence for crustal recycling into the mantle or mantle metasomatism. *Geochim. et Cosmochim. Acta, 53*, 1035–1040.

Nutman, A. P., Wan, Y. S., Du, L. L., Friend, C. R. L., Dong, C. Y., Xie, H. Q., et al. (2011). Multistage late Neoarchean crustal evolution of the North China Craton, eastern Hebei. *Precambrian Research, 189*, 43–65.

O'Neil, J., Francis, D., & Carlson, R. W. (2011). Implications of the Nuvvuagittuq greenstone belt for the formation of Earth's early crust. *Journal of Petrology, 52*, 985–1009.

Parman, S. W., Grove, T. L., & Dann, J. C. (2001). The production of Barberton komatiites in an Archean subduction zone. *Geophysical Research Letters, 28*, 2513–2516.

Peng, P. (2015). Precambrian mafic dyke swarms in the North China Craton and their geological implications. *Science China: Earth Sciences, 58*, 649–675.

Peng, P., Li, Y., Liu, F., & Wang, F. (2012). Geological relation of Late Archean lithologic units in Northwest Hebei, North China Craton: Implication for building of early continental crust. *Acta Petrologica Sinica, 28*, 3531–3544 (in Chinese with English abstract).

Peng, P., Wang, C., Wang, X., & Yang, S. (2015). Qingyuan high-grade granite–greenstone terrain in the Eastern North China Craton: Root of a Late Archean arc. *Tectonophsics, 662*, 7–21.

Peng, P., Wang, X., Windley, B. F., Guo, J., Zhai, M., & Li, Y. (2014). Spatial distribution of ~1950–1800 Ma metamorphic events in the North China Craton: Implications for tectonic subdivision of the craton. *Lithos, 202–203*, 250–266.

Percival, J. A., & West, G. F. (1994). The Kapuskasing uplift: A geological and geophysical synthesis. *Canadian Journal of Earth Sciences, 31*, 1256–1286.

Pickett, D. A., & Saleeby, J. B. (1993). Thermobarometric constraints on the depth of exposure and conditions of plutonism and metamorphism at deep levels of the Sierra Nevada batholith, Tehachapi Mountains, California. *Journal of Geophysical Research, 98*, 609–629.

Polat, A., Appel, P. W. U., & Fryer, B. J. (2011). An overview of the geochemistry of Eoarchean to Mesoarchean ultramafic to mafic volcanic rocks, SW Greenland: Implication for mantle depletion and petrogenetic processes at subduction zones in the early Earth. *Gondwana Research, 20*, 255–283.

Polat, A., & Hofmann, A. W. (2003). Alteration and geochemical patterns in the 3.7–3.8 Ga Isua greenstone belt, West Greenland. *Precambrian Research*, *126*, 197–218.

Polat, A., Hofmann, A. W., & Rosing, M. T. (2002). Boninite-like volcanic rocks in the 3.7–3.8 Ga Isua greenstone belt, West Greenland: Geochemical evidence for intra-oceanic subduction zone processes in the early Earth. *Chemical Geology, 184*, 231–254.

Rapp, R. P., Shimizu, N., & Norman, M. D. (2003). Growth of early continental crust by partial melting of eclogite. *Nature, 425*, 605–609.

Rapp, R. P., Shimizu, N., Norman, M. D., & Applegate, G. S. (1999). Reaction between slab-derived melts and peridotite in the mantle wedge: Experimental constraints at 3.8 GPa. *Chemical Geology, 160*, 335–356.

Riding, R., Fralick, P., & Liang, L. (2014). Identification of an Archean marine oxygen oasis. *Precambrian Research 251*, 232–237.

Rollinson, H. R. (2002). The metamorphic history of the Isua greenstone belt, West Greenland. In C. M. R. Fowler, C. J. Ebinger, C. J. Hawkesworth (eds.), *The early earth: Physical, chemical and biological development. Geological society* (Vol. 199, pp. 329–350). London: Special Publications.

Sandeman, H. A., Hanmer, S., Davis, W. J., Ryan, J. J., & Peterson, T. D. (2004). Neoarchean volcanic rocks, Central Hearne supracrustal belt, Western Churchill Province Canada: Geochemical and isotopic evidence supporting intra-oceanic, suprasubduction zone extension. *Precambrian Research, 134*, 113–141.

Sandiford, M., Martin, N., Zhou, S.-H., & Fraser, G. (1991). Mechanical consequences of granite emplacement during high-T, low-P metamorphism and the origin of "anticlockwise" *PT* paths. *Earth and Palnetary Science Letters, 107*, 164–172.

Sandiford, M., & Powell, R. (1986). Deep crustal metamorphism during continental extension: Ancient and modern examples. *Earth and Planetary Science Letters, 79*, 151–158.

Shi, Y.-R., Wilde, S.-A., Zhao, X.-T., Ma, Y.-S., Du, L.-L., & Liu, D.-Y. (2012). Late Neoarchean magmatic and subsequent metamorphic events in the northern North China Craton: SHRIMP zircon dating and Hf isotopes of Archean rocks from Yunmengshan Geopark, Miyun, Beijing. *Gondwana Research, 21*, 785–800.

Shirey, S. B., & Hanson, G. N. (1984). Mantle-derived Archean monzodiorites and trachyandesites. *Nature, 310*, 222–224.

Sizova, E., Gerya, T., Stüwe, K., & Brown, M. (2015). Generation of felsic crust in the Archean: A geodynamic modeling perspective. *Precambrian Research, 271*, 198–224.

Smithies, R. H. (2000). The Archean tonalite-trondhjemite-granodiorite (TTG) series is not an analogue of Cenozoic adakite. *Earth and Planetary Science Letters, 182*, 115–125.

Smithies, R. H., Champion, D. C., & Cassidy, K. F. (2003). Formation of Earth's early Archean continental crust. *Precambrian Research, 127*, 89–101.

Sun, D.-Y., Liu, Z.-H., & Zheng, C.-Q. (1993). *Metamorphism and tectonic evolution of early Precambrian Rocks in the Fushun Area, Northern Liaoning Province* (pp. 99–120). Beijing: Seismological Press (in Chinese).

Sun, S.-S., & McDonough, W. F. (1989). Chemical and isotopic systematics of oceanic basalts implications for mantle composition and process. In A. D. Saunders & M. J. Nony (Eds.), *Magmatism in the Ocean Basins*. *Geological society of London, special publication* (Vol. 42, pp. 313–354).

Szilas, K., van Hinsberg, V. J., Kisters, A. F. M., Hoffman, J. E., Windley, B. F., Kokfelt, T. F., et al. (2013). Remnants of arc-related Mesoarchean oceanic crust in the Tartoq Group of SW Greenland. *Gondwana Research, 23*, 436–451.

Szilas, K., Van Hinsberg, V. J., Kisters, A. F. M., Kokfelt, T. F., Scherstén, A., & Windley, B. F. (2011). Remnants of Mesoarchean oceanic crust in the Tartoq Group, South-West Greenland. *Geological Survey of Denmark and Greenland Bulletin, 23*, 57–60.

Thienen, P., Berg, A. P., & Vlaar, N. J. (2004). Production and recycling of oceanic crust in the early Earth. *Tectonophysics, 386*, 41–65.

Trap, P., Faure, M., Lin, W., Monié, P., Meffre, S., & Melleton, J. (2009). The Zanhuang Massif, the second and eastern suture zone of the Paleoproterozoic Trans-North China Orogen. *Precambrian Research, 172*, 80–98.

Turner, S., Rushmer, T., Reagan, M., & Moyen, J.-F. (2014). Heading down early on? Start of subduction on Earth. *Geology, 42*, 139–142.

Uchimura, H., Kono, M., Tsunakawa, H., Kimura, G., Wei, Q., Hao, T., & Liu, H. (1996). Paleomagnetism of late Mesozoic rocks from northeastern China: The role of the Tan-Lu fault in the North China Block. *Tectonophysics, 262*, 301–319.

van Hunen, J., & van den Berg, A. (2008). Plate tectonics on the early Earth: Limitations imposed by strength and buoyancy of subducted lithosphere. *Lithos, 103*, 217–235.

van Kranendonk, M. J. (2006). Volcanic degassing, hydrothermal circulation and the flourishing of early life on Earth: A review of the evidence from c. 3490–3240 Ma rocks of the Pilbara Supergroup, Pilbara Craton, Western Australia. *Earth Science Review, 74*, 197–240.

van Kranendonk, M. J., Smithies, R. H., Hickman, A. H., & Champion, D. C. (2007). Review: Secular tectonic evolution of Archean continental crust: Interplay between horizontal and vertical process in the formation of the Pilbara Craton, Australia. *Terra Nova, 19*, 1–38.

Wakabayashi, J. (2004). Tectonic mechanisms associated with *P-T*-paths of regional metamorphism: Alternatives to single-cycle thrusting and heating. *Tectonophysics, 392*, 193–218.

Wan, Y.-S. (1993). *Formation and Evolution of the Iron-bearing Rock Series of Gongchangling Area, Liaoning Province* (pp. 1–108). Beijing: Beijing Science and Technology Press Ltd.

Wan, Y.-S., Dong, C.-Y., Liu, D.-Y., Kroner, A., Yang, C.-H., Wang, W., et al. (2011). Zircon ages and geochemistry of Late Neoarchean

syenogranites in the North China Craton: A review. *Precambrian Research, 222–223*, 265–289.

Wan, Y.-S., Dong, C.-Y., Wang, S.-J., Kröner, A., Xie, H.-Q., Ma, M.-Z., Zhou, H.-Y., et al. (2015b). Middle Neoarchean magmatism in western Shandong, North China Craton: SHRIMP zircon dating and LA-ICP-MS Hf isotope analysis. *Precambrian Research 255*, 865–884.

Wan, Y.-S., Dong, C.-Y., Xie, H.-Q., Wang, S.-J., Song, M.-C., Xu, Z.-Y., et al. (2012a). Formation ages of early Precambrian BIFs in North China Craton: SHRIMP zircon U-Pb dating. *Acta Geologica Sinica, 86*, 1447–1478 (in Chinese with English abstract).

Wan, Y.-S., Liu, D.-Y., Dong, C.-Y., Xie, H.-Q., Kröner, A., Ma, M.-Z., et al. (2015a). Formation and Evolution of Archean Conitnental Crust of the North China Craton. In M.-G. Zhai (Ed.). *Precambrian geology of China* (pp. 59–136). Berlin: Springer.

Wan, Y.-S., Liu, D.-Y., Nutman, A., Zhou, H.-Y., Dong, C.-Y., Yin, X.-Y., & Ma, M.-Z. (2012b). Multiple 3.8-3.1 Ga tectono-magmatic events in a newly discovered area of ancient rocks (the Shengousi Complex), Anshan, North China Craton. *Journal of Asian Earth Sciences, 54–55*, 18–30.

Wan, Y.-S., Song, B., Yang, C., & Liu, D.-Y. (2005a). Zircon SHRIMP U-Pb geochronology of Archean rocks from the Fushun-Qingyuan Area, Liaoning Province and its geological significance. *Acta Geological Sinica, 79*, 78–87 (in Chinese).

Wan, Y.-S., Song, B., Yang, C., & Liu, D.-Y. (2005b). Geochemical Characteristics of Archean Basement in the Fushun-Qingyuan Area, Northern Liaoning Province and its geological significance. *Geological Review, 51*, 128–137 (in Chinese).

Wan, Y.-S., Wang, S.-J., Liu, D.-Y., Wang, W., Kroner, A., Dong, C.-Y., et al. (2012c). Redefinition of depositional ages of Neoarchean supracrustal rocks in western Shandong Province, China: SHRIMP U-Pb zircon dating. *Gondwana Research, 21*, 768–784.

Wan, Y.-S., Xie, S.-W., Yang, C.-H., Kroner, A., Ma, M. Z., Dong, C. Y., et al. (2014). Early Neoarchean (~2.7 Ga) tectono-thermal events in the North China Craton: A synthesis. *Precambrian Research, 247*, 45–63.

Wang, C.-Q., & Cui, W.-Y. (1994). Granulites from the Dengchang-Houshan area, northern Hebei Province: Geochemistry and metamorphism. In X. L. Qian & R. M. Wang (Eds.), *Geological evolution of the granulite terrain in the Northern Part of the North China Craton* (pp. 166–175). Beijing: Seismological Press (in Chinese).

Wang, J.-P., Kusky, T., Polat, A., Wang, L., Deng, H., & Wang, S.-J. (2013a). A late Archean tectonic mélange in the Central Orogenic Belt, North China Craton. *Tectonophysics, 608*, 929–946.

Wang, Y.-F., Li, X.-H., Jin, W., & Zhang, J.-H. (2015a). Eoarchean ultra-depleted mantle domains inferred from ca. 3.81 Ga Anshan trondhjemitic gneisses, North China Craton. *Precambrian Research, 263*, 88–107.

Wang, A.-D., & Liu, Y.-C. (2012). Neoarchean (2.5–2.8 Ga) crustal growth of the North China Craton revealed by zircon Hf isotope: A synthesis. *Geoscience Frontiers, 3*, 147–173.

Wang, W., Liu, S.-W., Bai, X., & Guo, R.-R. (2015b). Precambrian geodynamics (VI): Late Archean crustal growth models recorded in the North China Craton. *Earth Science Frontier, 22*(6), 109–124.

Wang, W., Liu, S.-W., Bai, X., Yang, P.-T., Li, Q.-G., & Zhang, L.-F. (2011). Geochemistry and zircon U-Pb–Hf isotopic systematics of the Neoarchean Yixian-Fuxin greenstone belt, northern margin of the North China Craton: Implications for petrogenesis and tectonic setting. *Gondwana Research, 20*, 64–81.

Wang, W., Liu, S.-W., Santosh, M., Bai, X., Li, Q.-G., Yang, P.-T., & Guo, R.-R. (2013b). Zircon U-Pb-Hf isotopes and whole-rock geochemistry of granitoid gneisses in the Jianping gneissic terrane, Western Liaoning Province: Constraints on the Neoarchean crustal evolution of the North China Craton. *Precambrian Research, 224*, 184–221.

Wang, W., Liu, S.-W., Santosh, M., Wang, G.-H., Bai, X., & Guo, R.-R. (2015c). Neoarchean intra-oceanic arc system in the Western Liaoning Province: Implications for Early Precambrian crustal evolution in the Eastern Block of the North China Craton. *Earth-Science Reviews, 150*, 329–364.

Wang, E.-D., Xia, J.-M., Fu, J.-F., Jia, S.-S., & Men, Y.-K. (2014). Formation mechanism of Gongchangling high-grade magnetite deposit hosted in Archean BIF, Anshan-Benxi area, Northeastern China. *Ore Geology Reviews, 57*, 308–321.

Wang, W., Yang, E.-X., Zhai, M.-G., Wang, S.-J., Santosh, M., Du, L.-L., et al. (2013c). Geochemistry of ~ 2.7 Ga basalts from Taishan area: Constraints on the evolution of early Neoarchean granite-greenstone belt in western Shandong Province. *China. Precambrian Research, 224*, 94–109.

Wells, P. R. A. (1980). Thermal models for magmatic accretion and subsequent metamorphism of continental crust. *Earth Planet Science Letter, 46*, 253–265.

Windley, B. F. (1995). *The evolving continents* (544 p). New York: Wiley.

Windley, B. F., & Garde, A. A. (2009). Arc-generated blocks with crustal sections in the North Atlantic craton of West Greenland: Crustal growth in the Archean with modern analogues. *Earth-Science Reviews, 93*, 1–30.

Wu, J.-S., Geng, Y.-S., Shen, Q.-H., Wan, Y.-S., & Liu, D.-Y., Song, B. (1998). *Archean geological characteristics and tectonic evolution of the China-Korea Paleocontinent* (p. 217). Beijing, China: Geological Publishing House (in Chinese).

Wu, F.-Y., Walker, R. J., Yang, Y.-H., Yuan, H.-L., & Yang, J.-H. (2006). The chemical–temporal evolution of lithospheric mantle underlying the North China Craton. *Geochimica et Cosmochimica Acta, 70*, 5013–5034.

Wu, F.-Y., Zhang, Y.-B., Yang, J.-H., Xie, L.-W., & Yang, Y.-H. (2008). Zircon U-Pb and Hf isotopic constraints on the Early Archean crustal evolution in Anshan of the North China Craton. *Precambrian Research, 167*, 339–362.

Wu, K.-K., Zhao, G.-C., Sun, M., Yin, C.-Q., He, Y.-H., & Tam, P.-Y. (2013). Metamorphism of the northern Liaoning Complex: Implications for the tectonic evolution of Neoarchean basement of the Eastern Block, North China Craton. *Geoscience Frontier, 4*, 305–320.

Wu, M.-L., Zhao, G.-C., Sun, M., Yin, C.-Q., Li, S.-Z., & Tam, P.-Y. (2012). Petrology and *P-T*-path of the Yishui mafic granulites: Implications for tectonothermal evolution of the Western Shandong Complex in the Eastern Block of the North China Craton. *Precambrian Research, 222–223*, 312–324.

Wyman, D., Kerrich, R., & Polat, A. (2002). Assembly of Archean cratonic mantle lithosphere and crust: Plume-arc interaction in the Abitibi-Wawa subduction–accretion complex. *Precambrian Research, 115*, 37–62.

Xiong, X.-L. (2006). Trace element evidence for the growth of early continental crust by melting of rutile-bearing hydrous eclogite. *Geology, 34*, 945–948.

Xiong, X.-L., Xia, B., Xu, J.-F., Niu, H.-C., & Xiao, W.-S. (2006). Na depletion in modern adakites via melt/rock reaction within the sub-arc mantle. *Chemical Geology, 229*, 273–292.

Xu, J.-Q., & Li, Z. (2015). Middle-Late Mesozoic sedimentary provenances of the Luxi and Jiaolai areas: Implications for tectonic evolution of the North China Block. *Journal of Asian Earth Sciences, 111*, 284–301.

Xu, J.-W., & Zhu, G. (1995). Discussion on tectonic models for the Tan-Lu fault zone, Eastern China. *Journal of Geology and Mineral Resources of North China, 10*, 121–133 (in Chinese).

Xu Y. G. (2001). Thermo-tectonic destruction of the Archaean lithospheric keel beneath eastern China: evidence, timing and mechanism. *Physics and Chemistry of the Earth (A), 26*, 747–757

Xu Y.G. (2001). Thermo-tectonic destruction of the Archaean lithospheric keel beneath eastern China: evidence, timing and mechanism. *Physics and Chemistry of the Earth (A)*, 26: 747-757.Yang, J.-H., Wu, F.-Y., Wilde, S. A., & Zhao, G.-C. (2008). Petrogenesis and geodynamics of Neoarchean magmatism in eastern Hebei, eastern North China Craton: Geochronological, geochemical and Nd–Hf isotopic evidence. *Precambrian Research, 167*, 125–149.

Zhai, M.-G., Guo, J.-H., Li, Y.-G., Li, J.-H., Yan, Y.-H., & Zhang, W.-H. (1996). Retrograded eclogites in the Archean North China Craton and their geological implication. *Chinese Science Bulletin, 41*, 315–321.

Zhai, M.-G., Guo, J.-H., Yan, Y.-H., & Li, Y.-G. (1992). The discovery of high-pressure basic granulite in the Archean North China Craton and preliminary study. *Science in China (series B), 12*, 1300–1325 (in Chinese).

Zhai, M.-G., & Peng, P. (2007). Paleoproterozoic events in the North China Craton. *Acta Petrologica Sinica, 23*, 2665–2682 (in Chinese with English abstract).

Zhai, M.-G., & Santosh, M. (2011). The early Precambrian odyssey of North China Craton: A synoptic overview. *Gondwana Research, 20*, 6–25.

Zhai, M.-G., & Santosh, M. (2013). Metallogeny of the North China Craton: Link with secular changes in the evolving Earth. *Gondwana Research, 24*, 275–297.

Zhai, M.-G., Santosh, M., & Zhang, L.-C. (2011). Precambrian geology and tectonic evolution of the North China Craton. *Gondwana Research, 20*, 1–5.

Zhai, M.-G., Yang, R.-Y., Lu, W.-J., & Zhou, J.-E. (1985). Geochemistry and evolution of the Qingyuan Archean granite-greenstone terrain, NE China. *Precambrian Research, 27*, 37–62.

Zhang, J.-D., Hao, T.-Y., Dong, S.-W., Chen, X.-H., Cui, J.-J., Yang, X.-Y., et al. (2015). The structural and tectonic relationships of the major fault systems of the Tan-Lu fault zone, with a focus on the segments within the North China region. *Journal of Asian Earth Sciences 110*, 85–100.

Zhang, Y.-J., Sun, F.-Y., Li, B.-L., Huo, L., & Ma, F. (2014a). Ore textures and remobilization mechanisms of the Hongtoushan copper–zinc deposit, Liaoning, China. *Ore Geology Review, 57*, 78–86.

Zhang, Q., & Zhai, M.-G. (2012). What is the Archean TTG? Acta Petrologica Sinica 28: 3446–3456 (in Chinese).

Zhang, H.-F., Zhai, M.-G., Santosh, M., Diwu, C.-R., & Li, S.-R. (2011). Geochronology and petrognesis of Late Archean potassic meta-granites from Huia'an Complex: Implications for the evolution of the North China Craton. *Gondwana Research, 20*, 82–105.

Zhang, L.-C., Zhang, X.-J., Zhai, M.-G., & Pirajno, F. (2012). Formation age and genesis of the Shirengou Neoarchean banded iron deposit in eastern Hebei Province: Constraints from SIMS zircon U-Pb dating and O-Hf isotopes. *Precambrian Research, 222–223*, 325–338.

Zhang, S.-H., Zhao, Y., Davis, G. A., Ye, H., & Wu, F. (2014b). Temporal and spatial variations of Mesozoic magmatism and deformation in the North China Craton: Implications for lithospheric thinning and decratonization. *Earth-Science Reviews, 131*, 49–87.

Zhao, G.-C. (2009). Metamorphic evolution of major tectonic units in the basement of the North China Craton: Key issues and discussion. *Acta Petrologica Sinica, 25*, 1772–1792 (in Chinese).

Zhao, G.-C. (2014). *Precambrian evolution of the North China Craton* (p. 194). Oxford: Elsevier.

Zhao, G.-C., Sun, M., Wilde, S. A., & Li, S.-Z. (2005). Late Archean to Paleoproterozoic evolution of the North China Craton: Key issues revisited. *Precambrian Research, 136*, 177–202.

Zhao, G.-C., Wilde, S. A., Cawood, P. A., & Lu, L.-Z. (1998). Thermal evolution of Archean basement rocks from the eastern part of the North China Craton and its bearing on tectonic setting. *International Geology Review, 40*, 706–721.

Zhao, G.-C., Wilde, S. A., Cawood, P. A., Sun, M., & Lu, L.-Z. (2001). Archean blocks and their boundaries in the North China Craton: Lithological, geochemical, structural and *P-T*-path constraints. *Precambrian Research, 107*, 45–73.

Zhou, Y.-Y., Zhao, T.-P., Wang, C.-Y., & Hu, G.-H. (2011). Geochronology and geochemistry of 2.5 to 2.4 Ga granitic plutons from the southern margin of the North China Craton: Implications for a tectonic transition from arc to post-collisional setting. *Gondwana Research, 20*, 171–183.

Zhu, M.-T., Dai, Y.-P., Zhang, L.-C., Wang, C.-L., & Liu, L. (2015a). Geochronology and geochemistry of the Nanfen iron deposit in the Anshan-Benxi area, North China Craton: Implications for ~2.55 Ga crustal growth and the genesis of high-grade iron ores. *Precambrian Research, 260*, 23–38.

Zhu, R.-X., Yang, J.-H., & Wu, F.-Y. (2012). Timing of destruction of the North China Craton. *Lithos, 149*, 51–60.

Zhu, X.-Y., Zhai, M.-G., Chen, F.-K., Lv, B., Wang, W., Peng, P., & Hu, B. (2013). ~2.7 Ga crustal growth in the North China Craton: Evidence from zircon U-Pb ages and Hf isotopes of the Sushui Complex in the Zhongtiao terrane. *Journal of Geology, 121*, 239–254.

Zhu, M.-T., Zhang, L.-C., Dai, Y.-P., & Wang, C.-L. (2015b). In situ zircon U-Pb dating and O isotopes of the Late Archean Hongtoushan VMS Cu–Zn deposit in the North China Craton: Implication for the ore genesis. *Ore Geology Reviews, 67*, 354–367.

Formation Ages and Environments of Early Precambrian Banded Iron Formation in the North China Craton

4

Yu-Yheng Wan, Dun-Yi Liu, Hang-Qiang Xie, Alfred Kröner, Peng Ren, Shou-Jie Liu, Shi-Wen Xie, Chun-Yan Dong, and Ming-Zhu Ma

Abstract

The North China Craton (NCC) has had a long geological history back to ca. 3.8 Ga ago, but the most important tectonothermal event occurred at the end of the Neoarchean, the most important period of BIF formation. There are three ancient terranes (>2.6 Ga) in the NCC. Most BIFs are distributed along the western margin of the Eastern Ancient Terrane, accounting for about 89 % of the total identified BIF iron ore resources in the NCC. They are considered to have formed on a continental basement in terms of rock association of the BIF-bearing supracrustal sequences which were intruded by slightly younger crustally derived granites. Most BIFs in the NCC show positive Y anomalies, implying that Fe in the BIFs had an affinity to seawater; however, positive Eu anomalies in the BIFs may suggest that high-temperature fluids also played a role in their formation. It seems that the BIFs were deposited on a continental margin, or more likely a back-arc basin environment, and a stable environment was one of the key factors for the formation of large-scale BIFs. In this paper, we provide new BIF metallogenic prospects for the NCC, namely in the northeast of Anben, between Anben and eastern Hebei, and between eastern Hebei and western Shandong.

Keywords

BIF • North China Craton • Eastern Ancient Terrane • Archean • Geochemistry

4.1 Introduction

The North China Craton (NCC) has a triangular shape with a total area of ca. 300,000 km^2. Its major Precambrian structures are cut off by surrounding younger orogenic belts, suggesting that the NCC is a fragment of a once larger craton. The craton is characterized by rocks that were subjected to strong late Neoarchean tectonothermal events but is similar to many other cratons in containing pre-late Neoarchean continental crust, as indicated by the widespread occurrence of 2.75–2.6 Ga and older rocks and zircons (Kröner et al. 2005a, b; Liu et al. 2011a, b, c; Shen et al. 2005; Wan et al. 2014a, b, 2015; Wilde et al. 2004, 2005; Zhai and Santosh 2011; Zhao 2014; Zhao and Zhai 2013). BIF-related iron deposits are the most important type of iron deposit in China, accounting for approximately 64 % of all identified mineral resources (Li et al. 2014). These are mainly Archean in age and predominantly occur in the NCC. In this paper, we first outline the spatial and temporal distribution and general compositional features of BIFs in the NCC and then focus on late Neoarchean BIFs in the Eastern Ancient Tarrane, the best understood of three ancient tarranes (>2.6 Ga) recently identified in the NCC. Finally, we discuss several important issues relating to the conditions of formation and depositional environment of the BIFs.

Y.-Y. Wan (✉) · D.-Y. Liu · H.-Q. Xie · P. Ren · S.-J. Liu
S.-W. Xie · C.-Y. Dong · M.-Z. Ma
Beijing SHRIMP Center, Institute of Geology,
Chinese Academy of Geological Sciences,
26 Baiwanzhuang Road, Beijing, 100037, China
e-mail: wanyusheng@bjshrimp.cn

A. Kröner
Department of Geosciences, University of Mainz, 55099 Mainz, Germany

M. Zhai et al. (eds.), *Main Tectonic Events and Metallogeny of the North China Craton*,
Springer Geology, DOI 10.1007/978-981-10-1064-4_4

4.2 Spatial and Temporal Distribution of Banded Iron Formations

Based on the spatial distribution of ancient rocks and zircons, Wan et al. (2015) defined three ancient terranes in the NCC, namely the Eastern, Southern, and Central Ancient Terrane (Fig. 4.1). Because the NCC is cut off on its margins by young orogenic belts, its original area must have been larger than present and at least the Southern Ancient Terrane is a remainder of a larger terrane. It is evident that most BIFs occur in the ancient terranes with some being distributed in adjacent areas (Fig. 4.1). According to recent statistics (H.-M. Li, personal communication), the total iron resources from BIFs in the NCC are ~46 billions tons. Those in Anben (Anshan-Benxi), eastern Hebei, and western Shandong are ~25, ~9, and ~7 billions tons, respectively, accounting for about 89 % of the total identified BIF iron ore resources in the NCC. Therefore, it is also evident that most BIFs occur in the Eastern Ancient Terrane.

BIFs are important components of Precambrian supracrustal sequences. The most important method to determine their formation ages is zircon U-Pb dating of spatially and temporarily associated metavolcano-sedimentary rocks. The oldest Fe-bearing chert in the NCC occurs in the 3.3 Ga Chentaigou supracrustal sequences in Anshan, southwest of Anben but contains low total iron contents (commonly <10 %) and is only found on a small scale. Therefore, it cannot be called BIF in terms of the strict definition by James (1954) that total iron of BIF should be higher than 15 %. A few BIFs occur as inclusions in the 3.0–2.9 Ga Tiejiashan granite in Anben, but the relationship between them is unknown (tectonic or intrusive?). The Dagushan BIFs in Anben and the Xingshan BIFs in eastern Hebei were considered to be Mesoarchean and Paleoarchean in formation age, respectively (Dai et al. 2014; Han et al. 2014a), but more work is required to confirm this conclusion (see below). Early Neoarchean (~2.7 Ga) BIFs have so far not been reported from the NCC. A exception is the Changyi BIF in Shandong which was considered to form during the early Neoarchean (Wang et al. 2015), but samely, more work is required to confirm the conclusion.

Although BIFs in the NCC show large variations in formation age from the Paleoarchean to the Paleoproterozoic, they are predominantly concentrated in the late Neoarchean with some in the Paleoproterozoic (Wan et al. 2012a; Zhang et al. 2012b). Paleoproterozoic BIFs include those in

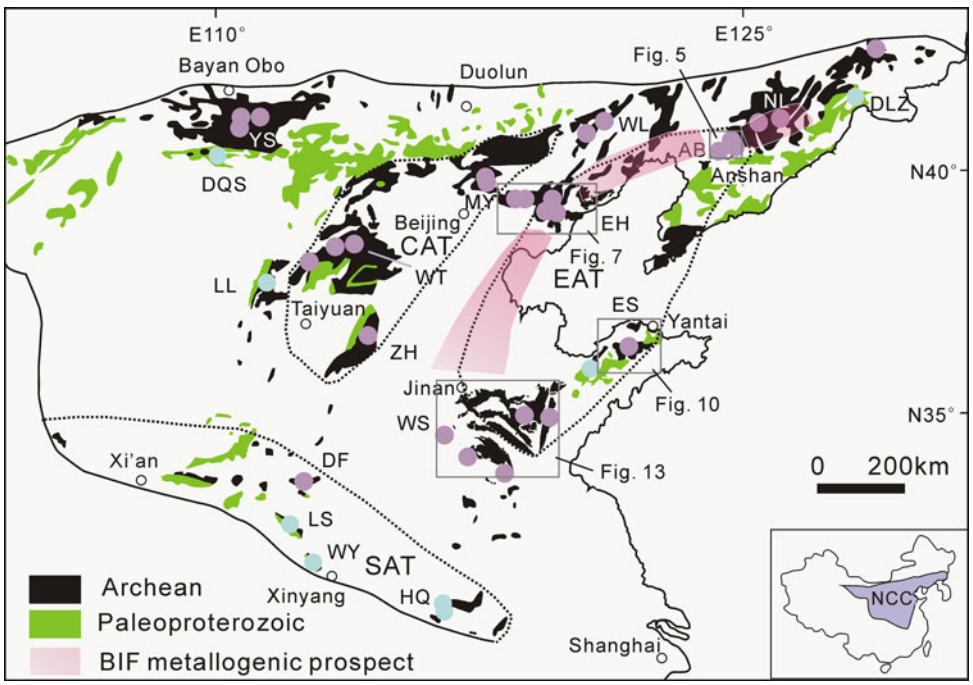

Fig. 4.1 Geological sketch map of the North China Craton showing distribution of three ancient (>2.6 Ga) terranes (Wan et al. 2015) and BIFs (Li et al. 2014). *Purple* and *blue circles* represent late Neoarchean and Paleoproterozoic iron deposits, respectively. Also shown are the BIF metallogenic prospects revealed based on this study. *EAT* Eastern Ancient Terrane; *SAT* Southern Ancient Terrane; *CAT* Central Ancient Terrane. Also shown are the locations of Figs. 4.5, 4.7, 4.10 and 4.13. *AB* Anben; *DF* Dengfeng; *DLZ* Dalizi; *DQS* Daqingshan; *EH* eastern Hebei; *ES* eastern Shandong; *HQ* Huoqiu; *LL* Lüliang; *LS* Lushan; *MY* Miyun; *NL* northern Liaoning; *WL* weastern Liaoning; *WS* western Shandong; *WT* Wutai; *WY* Wuyang; *YS* Yinshan; *ZH* Zanhuang

Yuanjiacun in Shanxi, Dalizi in Jilin, Changyi in Shandong, Huoqiu in Anhui, Wuyang in Henan, and Daqingshan in Inner Mongolia (Fig. 4.1). Many of them are associated with metasedimentary rocks, with some containing volcanic rocks, thus belonging to the Superior-type or being transformation between Algoma- and Superior-type BIFs. The exact formation ages are unknown for some of these BIFs because of the lack of suitable minerals for dating. However, it seems likely that most formed during the early Paleoproterozoic period (2.5–2.14 Ga) in terms of zircon dating of volcanic rocks, metasedimentary rocks, and intrusive rocks cutting the supracrustal sequences. The late Neoarchean BIFs occur in many areas of the NCC but mainly in the Eastern Ancient Terrane, as indicated above.

Figure 4.2 shows the age distribution of magmatic and metamorphic zircons from late Neoarchean supracrustal sequences. This compilation excludes magmatic zircon ages from metabasalt samples because of the scarcity of magmatic zircon in basaltic magma (alkline basalt may contain magmatic zircon). Therefore, most "magmatic" zircons are xenocrysts. However, metamorphic zircon ages of metabasalt samples are included in the compilation. The magmatic and metamorphic zircons vary in age from 2.59 to 2.50 Ga (mainly ≤2.56 Ga, $n = 48$) and 2.55–2.37 Ga (mainly ≤2.52 Ga, $n = 26$), respectively. It seems likely that some young magmatic and metamorphic zircon ages in some areas, such as eastern Hebei and eastern Shandong, are due to strong late Paleoproterozoic tectonothermal events. The late Neoarchean supracrustal sequences commonly formed earlier than, or contemporaneously with intrusive rocks of the TTG association (tonalite-trondhjemite-granodiorite)-rocks.

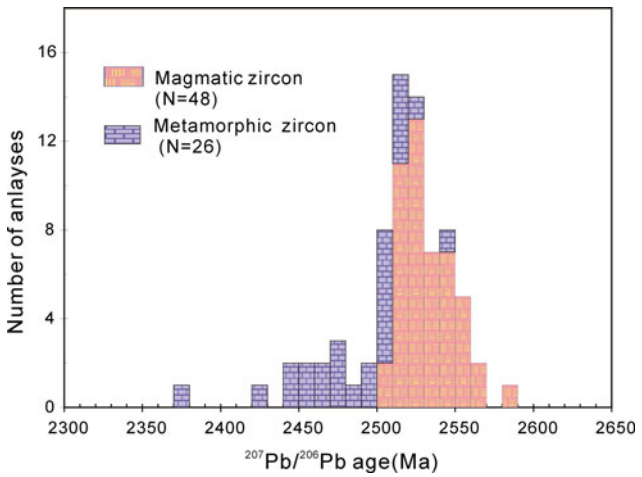

Fig. 4.2 Histogram of $^{207}Pb/^{206}Pb$ zircon ages for late Neoarchean supracrustal sequences in the North China Craton. Data are from Cui et al. (2014a, b), Dai et al. (2013), Dong et al. (2012), Guo et al. (2013), Jian et al. (2012), Liu et al. (2012, 2011b, c), Lü et al. (2012), Ma et al. (2012), Nutman et al. (2011), Peng et al. (2012), Shi et al. (2012), Sun et al. (2010), Wan et al. (2012a, 2012b), Wang et al. (2010, 2011, 2012, 2013), Wilde et al. (2004), Wu et al. (2013, 2014), Yang et al. 2008, 2009), Zhang et al. (2011, 2012a) and YS Wan (unpublished data)

4.3 Geochemical Features of Banded Iron Formation

Based on a large amount of geochemical data for the BIFs in the NCC (Cui et al. 2014b; Dai et al. 2012, 2013, 2014; Ding et al. 2009; Han et al. 2014a, b; Huang et al. 2013; Lan et al. 2012, 2013, 2014; Li et al. 2008, 2010c; Liu 2012; Liu and Yang 2013; Liu et al. 2012, 2014a, b; Ma et al. 2014; Peng et al. 2013b; Shen et al. 2009, 2011; Sun et al. 2014; Wang et al. 2014a, c, d, e; Xiang et al. 2012; Yang et al. 2013, 2014; Yao et al. 2014; Zhang et al. 2011; J Chen, personal communication), these rocks are mainly composed of SiO_2 and TFe_2O_3 with other major elements commonly being very low. They are also characterized by very low REE and other trace element contents, including high field strength elements (Nb, Ta), large ion lithosphere elements (Rb, Sr, Ba), and compatible elements (Cr, Ni).

An oxidation–reduction environment and depositional sources are important factors to form BIF deposits, which may be revealed by the composition of BIFs. Under oxidizing conditions, Ce^{3+} in seawater is oxidized to Ce^{4+}, and Ce is partly scavenged by suspended material, including Fe oxyhydroxides (Nozaki et al. 1999; Sholkovitz et al. 1994). This leads to a negative Ce anomaly in seawater in PAAS (Post-Archean Average Australian Shale)-normalized REE patterns (McLennan 1989). Under reducing conditions, Ce is not fractioned from the other REEs, so there is no Ce anomaly. Therefore, the Ce anomaly in seawater and associated sediments can be used to define the redox conditions. However, a superficial negative Ce anomaly may be related to a positive La anomaly. Bau and Dulski (1996) suggested to use a Ce/Ce*-Pr/Pr* diagram ($Ce/Ce^* = 2(Ce)_{PAAS}/((La)_{PAAS} + (Pr)_{PAAS})$, $Pr/Pr^* = 2(Pr)_{PAAS}/((Ce)_{PAAS} + (Nd)_{PAAS})$) to identify a real Ce anomaly. As shown in Fig. 4.3a and b, only a few analyses of late Neoarchean and early Paleoproterozoic BIFs in the NCC display real negative Ce anomalies. Using the calculation suggested by Bolhar et al. (2004) in which $La/La^* = (La)_{PAAS}/(3*(Pr)_{PAAS} - 2*(Nd)_{PAAS})$, $Ce/Ce^* = (Ce)_{PAAS}/(2*(Pr)_{PAAS} - (Nd)_{PAAS})$, only ~10 % of all analyses yield Ce/Ce* ratios <0.95, with ~90 % of the analyses having La/La* ratios >1. Therefore, most late Neoarchean and early Paleoproterozoic BIFs of the NCC do not show real negative Ce anomalies but positive La anomalies. This indicates that the ocean remained in anoxic or suboxic conditions until the middle Paleoproterozoic although some oxygen was needed to cause voluminous Fe deposition in the late Neoarchean and early Paleoproterozoic. Considering the positive La anomaly of seawater, the

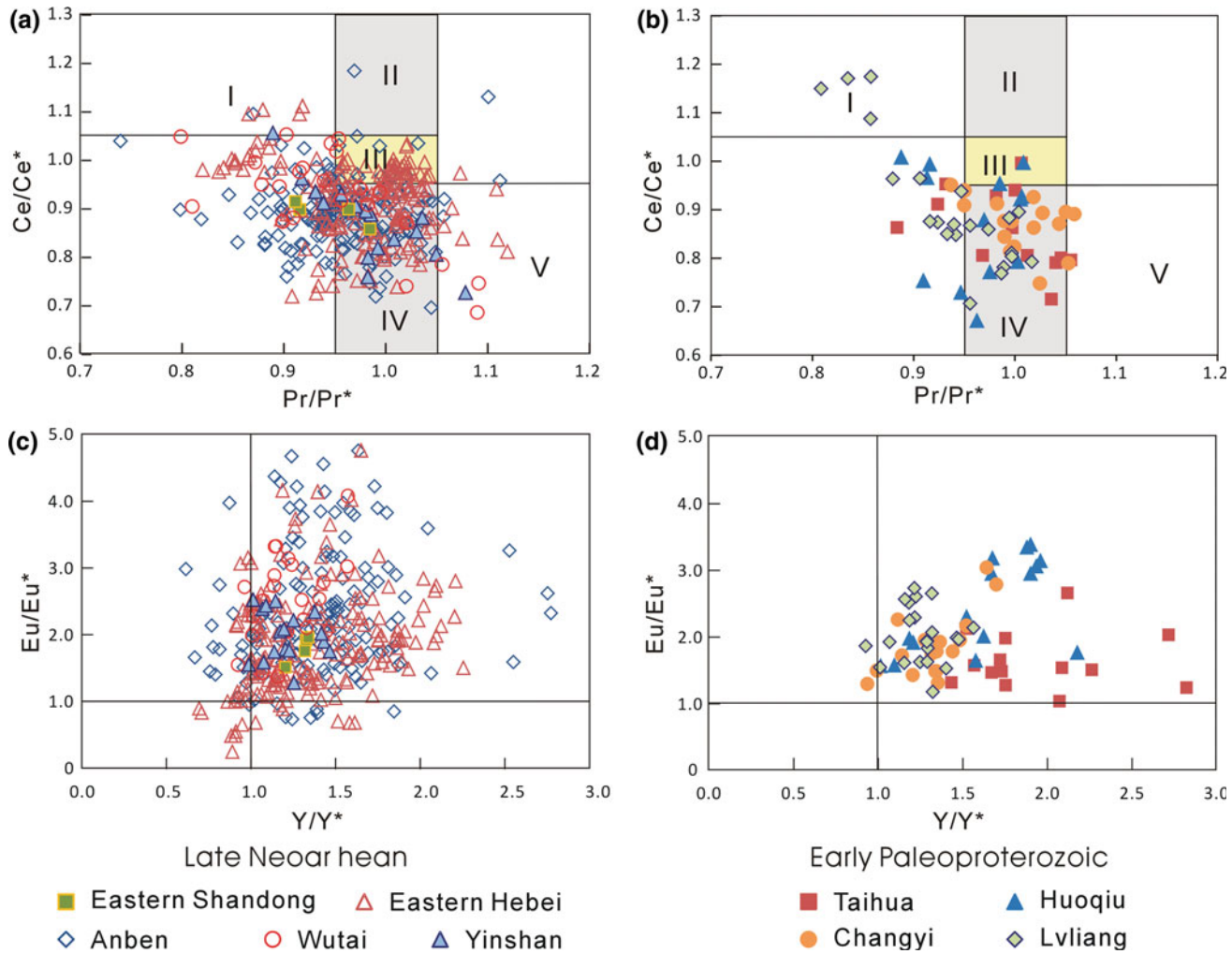

Fig. 4.3 Geochemical diagrams for early Precambrian BIFs of the North China Craton. **a** Pr/Pr*-Ce/Ce* diagram of late Neoarchean BIFs; **b** Pr/Pr*-Ce/Ce* diagram of early Paleoproterozoic BIFs; **c** Y/Y*-Eu/Eu* diagram of late Neoarchean BIFs; **d** Y/Y*-Eu/Eu* diagram of early Paleoproterozoic BIFs. Normalizing values are PAAS (Post-Archean Average Australian Shale) (McLennan, 1989). In figures **a** and **b**, *I* Positive Ce anomaly; *II* Negative La anomaly; *III* No anomaly; *IV* Positive La anomaly; *V* Negative Ce anomaly. See text for data sources

widespread positive La anomalies in BIFs suggest that seawater may have played an important role in BIF formation.

Besides a positive La anomaly, a positive Y anomaly can also be used to determine whether seawater played a role in the formation of BIFs. It is difficult to fractionate Y from the REE element Ho during magmatic and metamorphic events because both are similar in ionic radius and valence. However, the residence time for Y in seawater is about twice that of Ho, resulting in an obvious positive Y anomaly compared to adjacent REEs (Ho and Dy) with Y/Y* > 1 (Nozaki et al. 1997). Most BIF samples in the NCC show positive Y anomalies (Fig. 4 3c, d), implying that Fe in the BIFs had an affinity to seawater. However, most samples also show positive Eu anomalies (Eu/Eu* > 1) (Fig. 4 3c, d) that were probably not caused by seawater but by high-temperature hydrothermal fluids. Therefore, the positive Eu anomalies in BIFs may suggest that high-temperature fluids also played a role in the formation of BIFs.

The Fe isotopic composition of BIFs is another potential tool for tracing the redox environment. Almost all Fe will be precipitated from seawater under oxidizing conditions. This kept the isotopic equilibrium with seawater which had δ^{56}Fe of ~0 or slightly negative (Johnson et al. 2008). Under suboxic conditions, on the other hand, partial precipitation of Fe would lead to Fe isotopic fractionation, resulting in enriched heavy Fe isotopes in BIFs (Balci et al. 2006). Fe isotopes have been analyzed in Neoarchean BIF samples from Anben and early Paleoproterozoic BIF samples from Lüliang (Hou et al. 2014; Li et al. 2008, 2012; Liu 2011). As shown in Fig. 4.4, the BIF samples in both areas show

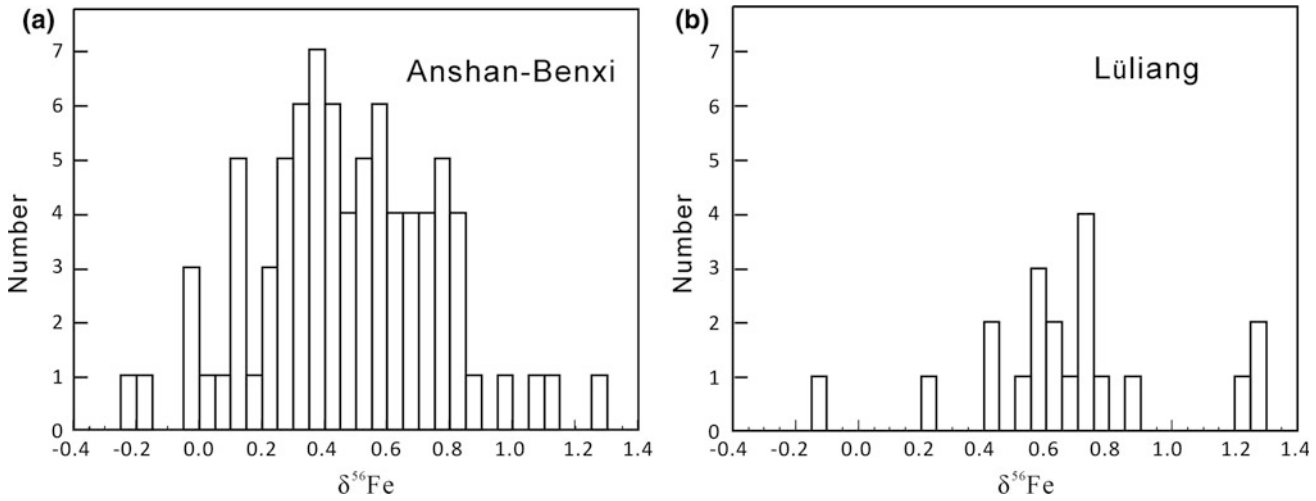

Fig. 4.4 Fe isotope composition of early Precambrian BIFs in the North China Craton. Data are from Hou et al. (2014), Li et al. (2008, 2012) and Liu (2011). **a** Late Neoarchean BIFs in Anben; **b** early Paleoproterozoic BIFs in Lüliang

similar features with positive δ^{56}Fe values. Heavy Fe isotope precipitation would keep more light Fe isotopes in the seawater, so we speculate that seawater was oxygen-deficient during the late Neoarchean and early Paleoproterozoic when BIFs were deposited, consistent with the trace element data. Although no obvious negative δ^{56}Fe values have been obtained from the NCC BIFs, such values were identified in some BIFs worldwide such as the Transvaal and Hamersley basins (Czaja et al. 2010; Steinhoefel et al. 2010; Tsikos et al. 2010).

4.4 Banded Iron Formations in the Eastern Ancient Terrane

Late Neoarchean BIFs are well developed in the Eastern Ancient Terrane. However, compared with Anben, eastern Hebei and western Shandong, eastern Shandong only contains a few BIFs. In this section, we outline the BIFs and related rocks in these areas.

4.4.1 Anben Area

Anben has a long geological history up to 3.8 Ga (Liu et al. 2008; Song et al. 1996; Wan et al. 2005, 2012c; Wu et al. 2008) (Fig. 4.5). In the Anshan area, southwestern part of Anben, three complexes with ages of 3.8–3.1 Ga have been identified, namely the Baijiafen, Donshan, and Shengousi complexes, along with more widespread 3.3–2.9 Ga rocks of different origins and ages, including the 3.35 Ga Chentaigou supracrustal sequences, 3.3–3.1 Ga Chentaigou granite, 3.14 Ga Lishan trondhjemite, 3.0 Ga Dong'anshan granite, and 3.0–2.9 Ga Tiejiashan K-rich granite. Recent studies indicate that the Tiejiashan K-rich granite extends eastwards to Gongchangling with a total area of >200 km^2. More importantly, the element and Nd-O-Hf isotope compositions of the widespread 2.5 Ga Qidashan syenogranite suggest that it formed through recycling of mature, old continental crust, including metasedimentary sources, and that there is more than one area where Paleo- to Eoarchean magmatism occurred in Anben, consistent with abundant 3.8–3.6 Ga xenocrystic zircons in the syenogranite in Waitoushan-Jiguanshan (Wan et al. 2015).

The Anshan "Group" (we use the word group with quotation marks to indicate that it constitutes a tectono-stratigraphic term) occurs in a "sea" of the Qidashan syenogranite. It only has a total exposed area of less than 10 %. However, BIFs occur in every area where there are supracrustal sequences of the Anshan "Group," and the abundant BIFs makes Anben the most important area of iron ore deposits in China. In some areas, such as Gongchangling, there are BIF-related Fe-rich iron ores, which are considered to be of sedimentary origin, or more likely, be at least partly related to hydrothermal alteration. Besides BIFs, the Anshan "Group" is mainly composed of amphibolites, fine-grained gneisses (leptynites), quartzites, phyllites, and schists of volcano-sedimentary origin (Zhai et al. 1990; Wan 1993). These rocks underwent greenschist- to amphibolite-facies metamorphism. The late Neoarchean supracrustal sequences show spatial variations in rock association, metamorphism, deformation, and BIF features. Being different from the supracrustal sequences in Waitoushan-Benxi, those in Anshan are dominated by metasedimentary rocks and show weak metamorphism and deformation, with a few iron-rich layers of BIFs but single iron-rich layers being thick.

In Gongchangling, there are fuchsite quartzite (Fig. 4.6a) containing 3.6 Ga detrital zircons and garnet-mica schist

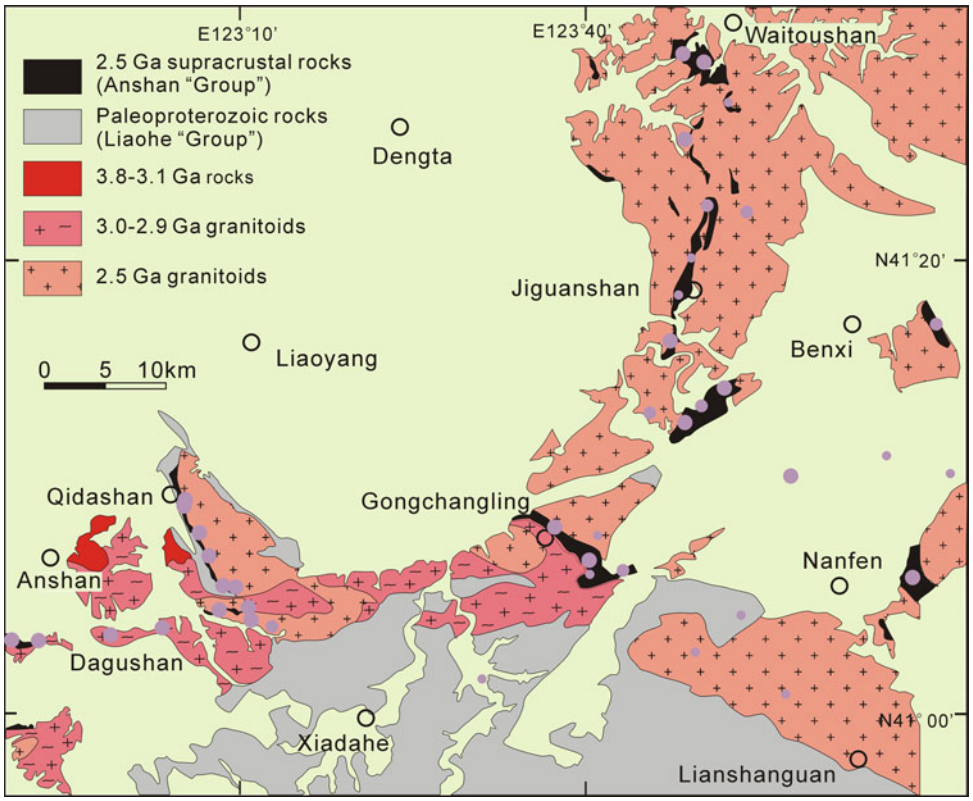

Fig. 4.5 Geological map of the Anben area, modified after Wan et al. (2015). Locations of BIF iron deposits are from Xiong et al. (2013). See Fig. 4.1 for location of this figure in the NCC. Large, medium, and small circles represent large, medium, and small-scale iron ore deposits, respectively

(Fig. 4.6b). The latter shows a transitional relationship with fine-grained biotite gneiss (Fig. 4.7). In early studies, the Anshan "Group" was considered to be early Neoarchean in age on the basis of a whole-rock Sm–Nd isochron age (Qiao et al. 1990) and SHRIMP U-Pb zircon dating (Wan 1993). However, new SHRIMP U-Pb zircon dating, combined with cathodoluminescence (CL) images, on fine-grained biotite gneiss interlayered with BIF in Gongchangling (Fig. 4.6c, d) indicated that the ~2.7 Ga zircons are xenocrystal and 2.53 Ga zircons are volcanic in origin. The Anshan "Group" is cut by 2.5 Ga syenogranite (Fig. 4.6e, f) that defines a younger age limit for supracrustal deposition. Mainly based on zircon dating, Dai et al. (2014) concluded that the BIF-bearing Dagushan supracrustal sequences were formed at ca. 3.1 Ga. However, these BIFs are similar in many aspects to other BIF-bearing supracrustal sequences in the same area. More work is therefore requried to confirm the formation age of the Dagushan supracrustal sequences.

4.4.2 Eastern Hebei

Eastern Hebei is another area where Archean rocks and BIF-related iron ore deposits widely occur (Bai et al. 2014; Geng et al. 2006; Guo et al. 2013; Li et al. 2010b; Nutman et al. 2011; Wu et al. 2005) (Fig. 4.8). In the Huangbaiyu area, abundant 3.88–3.4 Ga detrital zircons have been discovered in several types of metasedimentary rocks of the Caozhuang Complex, including fuchsite quartzite, garnet-mica schist (Fig. 4.9a) and para-amphibolite; 3.4 Ga gneissic quartz diorite and 3.3–3.0 Ga gneissic tonalites have also been identitified (Nutman et al. 2011; Liu et al. 2013b, unpublished data). In Shuangshanzi, 3.6–2.9 Ga detrital zircons were discovered in fine-grained biotite gneiss of the ~2.5 Ga Dantazi "Group" (Y.-S. Wan, unpublished data). Therefore, eastern Hebei is another terrane with Paleo- to Eoarchean crust in the NCC. However, the Caozhuang Complex in the Huangbaiyu area is not Paleoarchean (~3.5 Ga) in age, as thought before, but is limited between 3.4 and 2.5 Ga (Liu et al. 2013b; Nutman et al. 2014). In Xingshan, ~1.5 km northwest of Huangbaiyu, Fe-rich ore cutting BIF (Fig. 4.9b) indicates that at least some of the Fe-rich ore is hytrothermal rather than sedimentary in origin. Based on the interpretation of zircons as magmatic, Han et al. (2014a) concluded that the supracrustal sequences in the Xingshan area, that also belong to the Caozhuang Complex, were deposited at 3.39 Ga. However, the dated rock contains abundant garnet and 3.76–3.43 Ga zircons, and it is therefore possible that the 3.39 Ga zircon is detrital in origin. We recently dated a fine-grained biotite gneiss (J1313) cut by 2.5 Ga red granite at Huangbaiyu (Fig. 4 9c, d). This rock is mainly composed of biotite, plagioclase, and quartz, and its protolith is considered to be dacite. The zircons show core-rim textures in CL images (Fig. 4.10a), and

Fig. 4.6 Field photographs of late Neoarchean rocks in the Anben area. **a** Fuchsite quartzite of the Anshan "Group", Gongchangling; **b** two-mica quartz schist of the Anshan "Group," Gongchangling; **c** fine-grained biotite gneiss interlayered with BIF, Anshan "Group," Gongchangling (Wan et al. 2012a); **d** fine-grained biotite gneiss of the Anshan "Group," Gongchangling (Wan et al. 2012a); **e** 2.5 Ga syenogranite (Qidashan granite) intruding BIF-bearing supracrustal sequences of the Anshan "Group," Qidashan; **f** 2.5 Ga syenogranite (Qidashan granite) intruding BIF-bearing supracrustal sequences of the Anshan "Group," Jiguanshan

the cores have an age of ~2.52 Ga (Fig. 4.10b), considered to represent the time of volcanism. Therefore, we suggest that at least some of the supracrustal sequences of the Caozhuang complex were deposited during the late Neoarchean. In fact, recent studies indicate that almost all BIFs in eastern Hebei were deposited in the late Neorchean (Han et al. 2014a; Wan et al. 2012a, b, c; Zhang et al. 2012a), including those in the Qianxi "Group" which was once considered to be Mesoarchean in age (Wu et al. 1998).

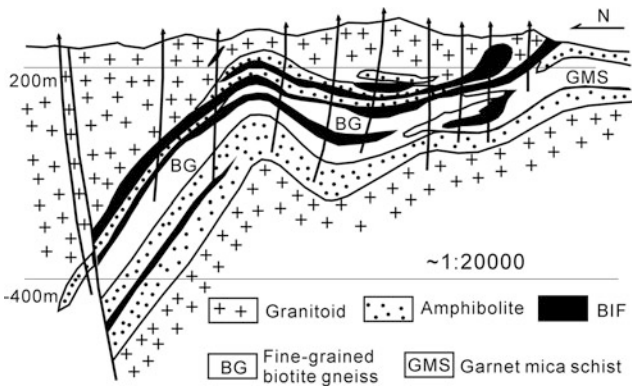

Fig. 4.7 Exploration section in the Lingdong Mine of the Gongchangling area (Wan 1993)

Recent studies indicate that 2.55–2.53 Ga tonalites and quartz diorites are more predominant in the west, and 2.53–2.51 Ga granites are more predominant in the east (Nutman et al. 2011). Late Neoarchean supracrustal sequences commonly occur as enclaves of variable sizes in granitoids and have different names in different areas (Fig. 4.8). The Zunhua and Qianxi "groups" in the west are mainly composed of biotite plagioclase gneiss, hornblende plagioclase gneiss, two-pyroxene granulite, amphibolite, meta-ultramafic rocks and BIF, all in granulite-facies, and commonly retrogressed to amphibolite-facies. The Luanxian "Group" in the east is composed of fine-grained biotite gneiss, amphibolite, and BIF and shows anatexis to variable degrees. The Dantazi "Group"

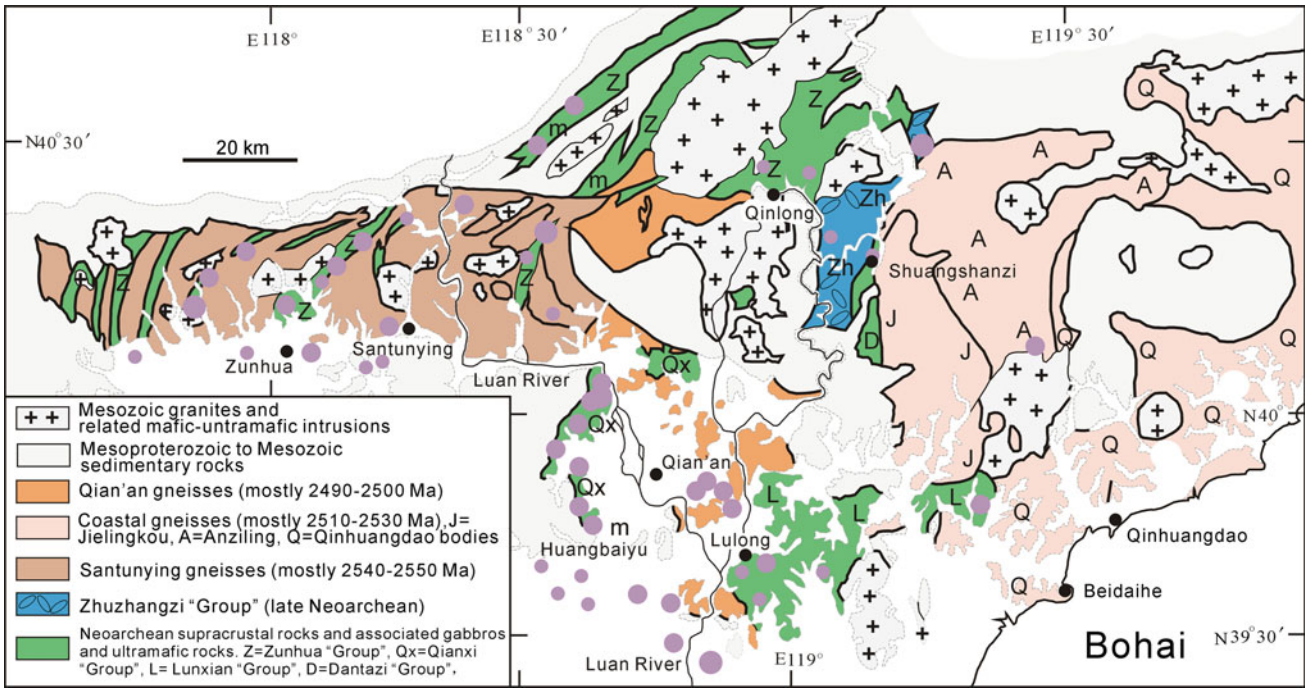

Fig. 4.8 Geological map of eastern Hebei. Modified after Nutman et al. (2011). Locations of BIF iron ore deposits from Zhang et al. (2014). *Large*, *medium*, and *small circles* represent large, medium, and small-scale iron ore deposits, respectively. See Fig. 4.1 for location of this figure in the NCC

is dominated by fine-grained two-mica gneiss, garnet-mica schist, two-mica quartz schist, mafic and felsic metavolcanic rocks, and BIF. It is covered unconformably by the Zhuzhangzi "Group," which contains fine-grained two-mica gneiss, fine-grained biotite gneiss, mica schist, quartz schist, biotite hornblende schist, and BIF, besides conglomerate at the base. Both of these experienced lower amphibolite-facies metamorphism, but the granitoids of the Anziling complex farther east show strong anatexis and deformation. All ~2.5 Ga supracrustal sequences contain BIFs.

It is uncertain where the western boundary of the Eastern Ancient Terrane in eastern Hebei is situated. The 2.5 Ga BIF-bearing supracrustal sequences were cut by crustally derived granites in the Huangbaiyu-Yangyashan and more eastern areas (Fig. 4.9e), and ca. 2.5 Ga metasedimentary rocks have been identified in the Santunying area (Fig. 4.9f). Therefore, the western boundary should be to the west of Santunying. In eastern Hebei, late Neoarchean BIFs mainly occur in the Eastern Ancient Terrane but some also occur in adjacent areas to the west.

4.4.3 Eastern Shandong

In eastern Shandong, 2.9, 2.7, and 2.5 Ga rocks (mainly tonalites) occur widely (Liu et al. 2013a; Wang et al. 2014b; Wu et al. 2014; Xie et al. 2013, 2014), but their spatial distribution is uncertain (Fig. 4.11). Abundant 3.45–3.0 Ga detrital and xenocrystic zircons have also been discovered, suggesting the existence of more ancient rocks in the region. However, Mesoarchean (~2.9 Ga) and late Neoarchean (~2.5 Ga) supracrustal sequences are much less abundant than thought before, most of the rocks originally assigned to the Mesoarchean Tangjiazhuang "Group" and late Neoarchean Jiaodong "Group" are metamorphosed and deformed TTGs. Mesoarchean (~2.9 Ga) supracrustal sequences were only identified in the Qixia area (Jahn et al. 2008). In the northeast of Nanshu, BIF-bearing supracrustal sequences have also been identified (Fig. 4.12a), containing garnet-biotite gneiss, biotite gneiss (Fig. 4.12b), marble, and BIF (Fig. 4.12c), and are cut by granite veins (Fig. 4.12d).

The biotite gneiss (JD1453) is mainly composed of plagioclase, quartz, and biotite. The zircons are stubby or rounded in shape with complex textures in CL images (Fig. 4.13a). Detrital cores show oscillatory or banded zoning with variable recrystallization and have $^{207}Pb/^{206}Pb$ ages of 2.91–2.59 Ga (Fig. 4.13b). The ~2.7 Ga zircons show clear zoning and are considered to have crystallized close to the formation age of the sources from which the detrital zircons were derived. Metamorphic zircons record ages of 2.48–2.35 Ga (4 analyses) and 1.96–1.82 Ga (3 analyses), suggesting that the rock underwent two tectonothermal events. We speculate that the early event occurred at ca. 2.5 Ga and the high U metamorphic zircons becoming younger in apparent age is due to

Fig. 4.9 Field photographs of late Neoarchean rocks in eastern Hebei. **a** Grt-Bt gneiss (J1112) of the Caozhuang Complex at Huangbaiyu containing abundant 3.8–3.4 Ga detrital and 2.5 Ga metamorphic zircons; **b** iron-rich ore enclave in low-grade BIF of the Caozhuang Complex, Xingshan; **c**, **d** fine-grained biotite gneiss (J1313) of the Caozhuang Complex, Huangbaiyu; **e** ca. 2.5 Ga granite intruding ca. 2.5 Ga BIF-bearing supracrustal sequences (Qianxi "Group," Yangyashan; **f** ca. 2.5 Ga garnet-biotite gneiss showing anatexis, Santunying

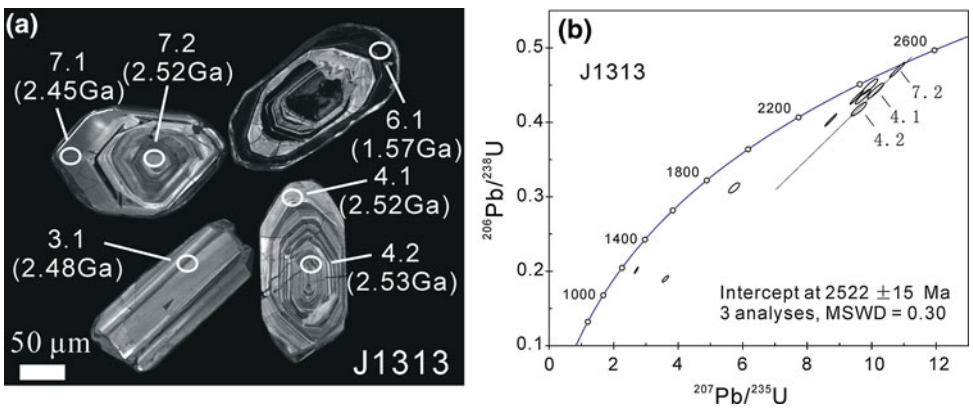

Fig. 4.10 Cathodoluminescence images and concordia diagram of SHRIMP U-Pb data for zircons from fine-grained biotite gneiss (J1313) in Huangbaiyu, eastern Hebei

partial resetting of the U-Th–Pb isotopic system during the late Paleoproterozoic event. Considering that the age of ~2.5 Ga has been obtained for supracrustal sequences in eastern Shandong (Wan et al. 2012a), we suggest that the BIF-bearing supracrustal sequences are late Neoarchean in age. However, compared with Anben, eastern Hebei and western Shandong, eastern Shandong is rare in late Neoarchean supracrustal sequences (including BIFs).

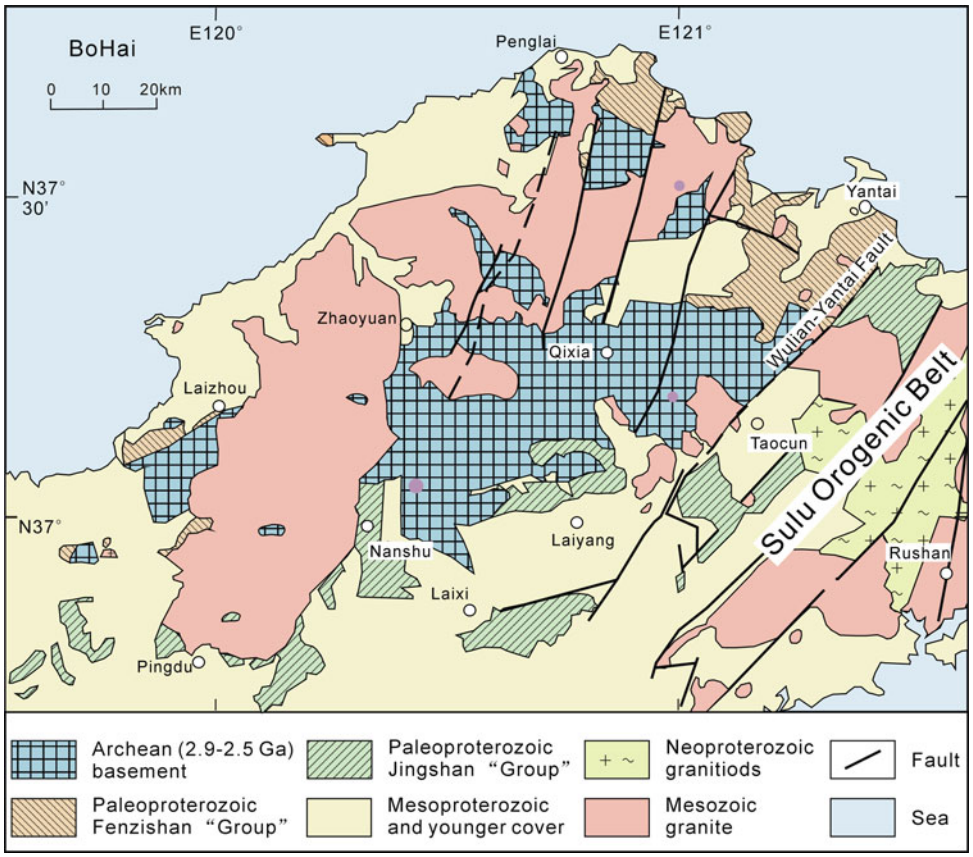

Fig. 4.11 Geological map of eastern Shandong showing location of BIF iron ore deposits. Modified after Wan et al. (2015). *Small circles* represent small-scale iron ore deposits. See Fig. 4.1 for location of the figure in the NCC

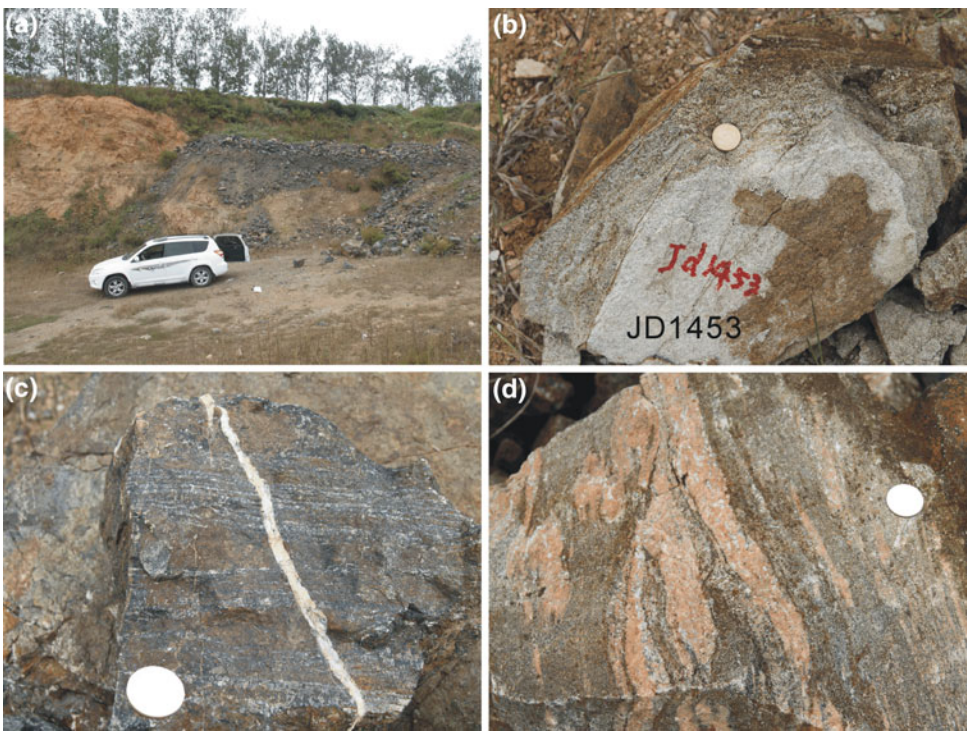

Fig. 4.12 Field photographs of late Neoarchean rocks northeast of Nanshu, eastern Shandong. **a** Open pit of iron ore mine; **b** biotite gneiss (JD1453); **c** BIF, cut by a quartz vein; **d** red granite veins cutting biotite gneiss

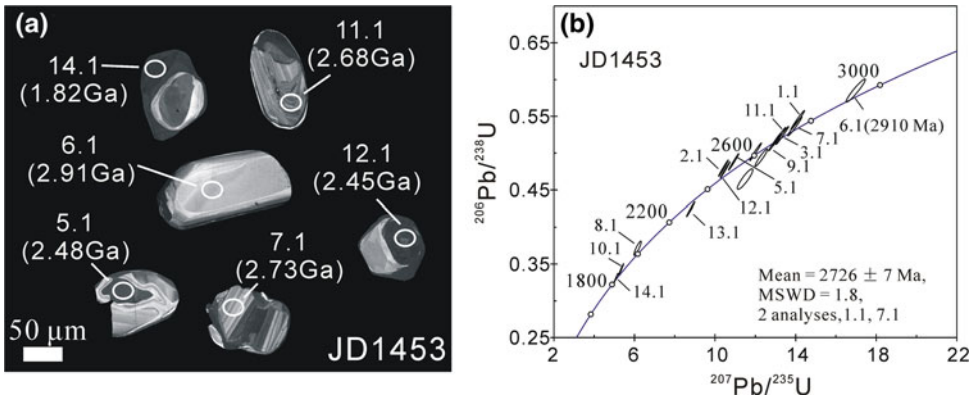

Fig. 4.13 Cathodoluminescence images and concordia diagram of SHRIMP U-Pb data for zircons from biotite gneiss (JD1453) northeast of Nanshu, eastern Shandong

4.4.4 Western Shandong

The Neoarchean basement in western Shandong, with a total area of >10,000 km^2, extends roughly in a northwest-southeast direction and is truncated by the huge Tanlu Fault Zone in the east. It is mainly composed of 2.75–2.5 Ga supracrustal sequences and intrusive rocks (Cao 1996; Du et al. 2003, 2005; Jiang et al. 2010; Lu et al. 2008; Peng et al. 2013a; Polat et al. 2006; Wan et al. 2010, 2011, 2012b, 2014b; Wang et al. 2010, 2011). Based on abundant zircon ages, Wan et al. (2010, 2011) divided the Archean basement into three belts (Fig. 4.14). Belt A is a late Neoarchean belt of crustally derived granitoids in the northeast that predominantly consists of 2.53–2.49 Ga monzogranite and syenogranite, with different migmatite types as a result of anatexis of early supracrustal sequences and granitoid rocks; Belt B is an early Neoarchean belt in the center that is mainly composed of 2.75–2.60 Ga TTGs and supracrustal sequences; Belt C is a late Neoarchean belt of juvenile rocks in the southwest that is dominated by granodiorite, gabbro, quartz diorite, and tonalite, with minor monzogranite and syenogranite and other types of rocks.

Western Shandong is the only area where early Neoarchean supracrustal sequences have so far been identified in the NCC. The early Neoarchean Yanglingguang-Liuhang succession occurs in Belt B and is mainly composed of amphibolite and metamorphosed ultramafic rocks. Some meta-ultramafic rocks contain fine spinifex textures, and some amphibolites have abundant pillow structures. The late Neoarchean Shancaoyu-Jining succession occurs in all three belts and mainly consists of metaconglomerate, fine-grained biotite gneiss, fine-grained two-mica gneiss, mica schist and BIF. The metaconglomerates are interlayered with fine-grained biotite gneiss (Fig. 4.15a), and some fine-grained biotite gneisses show sedimentary structures (Fig. 4.15b). A felsic metavolcanic sample (TS09104, Fig. 4.15c) has magmatic zircons of 2.52 Ga with abundant xenocrysts of 2.7–2.6 Ga (Wan et al. 2012b). It is notable that only the late Neoarchean supracrustal sequences contain BIFs. These BIF-bearing supracrustal sequences are cut by crustally derived granite (Fig. 4.15d). The BIFs occur in different belts but are concentrated in Belt C and are covered by Paleozoic or younger sedimentary rocks (Fig. 4.14). Belt C is mainly composed of juvenile rocks, but also contains crustally derived granites, and the BIF-bearing supracrustal sequences contain detrital and xenocrystic zircons (Wan et al. 2012b). We propose that the BIF-bearing supracrustal sequences in Belt C are separated from the Eastern Ancient Terrane. Late Neoarchean BIFs also occur in the Tanlu Fault Zone, where the rocks underwent high grade metamorphism (commonly granulite-facies) compared with the Neoarchean rocks above.

4.5 Discussion

4.5.1 Common Features of BIFs in the Eastern Ancient Terrane

Similar to BIFs in other areas of the NCC, most BIFs in the Eastern Ancient Terrane are late Neoarchean (2.55–2.52 Ga) in age, although more work is required to confirm the formation ages of some BIFs in Anben and eastern Hebei.

The BIFs mainly occur on the western margin of the Eastern Ancient Terrane and adjacent areas. It seems that the dimensions of the BIFs are related to the maturity of the local basement. In Anben, which has a long geological history up to 3.8 Ga, the BIFs are best developed; in western Shandong, where the continental crust was mainly formed during the early Neoarchean, the BIFs are relatively small in scale. BIFs are rare in eastern Shandong. It is uncertain whether this is due to erosion of the ~2.5 Ga supracrustal sequences, which also occur only locally.

The late Neoarchean BIF-bearing supracrustal sequences are composed of mafic to felsic metavolcanic rocks, as well as volcano-sedimentary and sedimentary rocks, with most

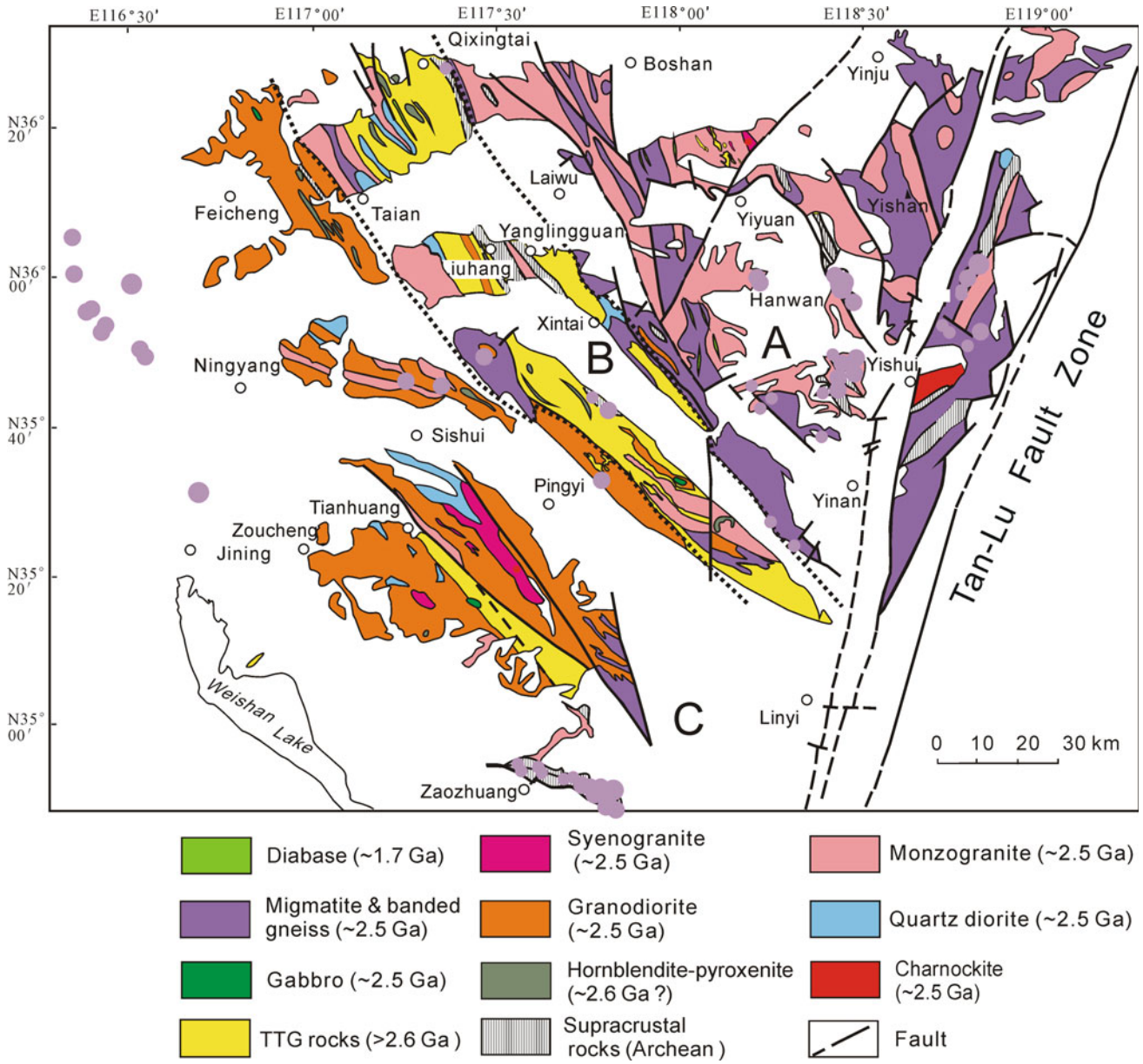

Fig. 4.14 Geological map of western Shandong, modified after Wan et al. (2011). *Belt A*: Late Neoarchean crustally derived granite belt; *Belt B*: Early Neoarchean belt; *Belt C*: Late Neoarchean belt of juvenile rocks. Location of BIF iron ore deposits are from Li et al. (2010a). *Large*, *medium*, and *small circles* represent large, medium, and small-scale iron ore deposits, respectively. See Fig. 4.1 for location of the figure in the NCC

of the BIFs belonging to the Algoma-type. However, the Luanxian "Group" in eastern Hebei and the Shancaoyu-Jining succession in western Shandong are mainly composed of metasedimentary rocks with some volcanic rocks, thus the BIFs belong to the Superior-type or show transformation features from Algoma to Superior-type BIFs. In some areas, such as Anben, the late Neoarchean supracrustal sequences show spatial variations in rock association and BIF features, with transformation between Algoma- and Superior-types. The metavolcano-sedimentary and metasedimentary rocks in all areas contain detrital and xenocrystic zircons. Same as those in other areas, banded structures are well developed in the BIFs in the Eastern Ancient Terrane, at least some of the straight bands are of sedimentary origin. This suggests that the BIF precipitated below storm wave base, but existence of Al_2O_3 and other minor elements in the BIFs indicates that the deposition location is not far away a continent. The latter is consistent with the associated sedimentary rocks showing sedimentary structures and containing old detrital zircons.

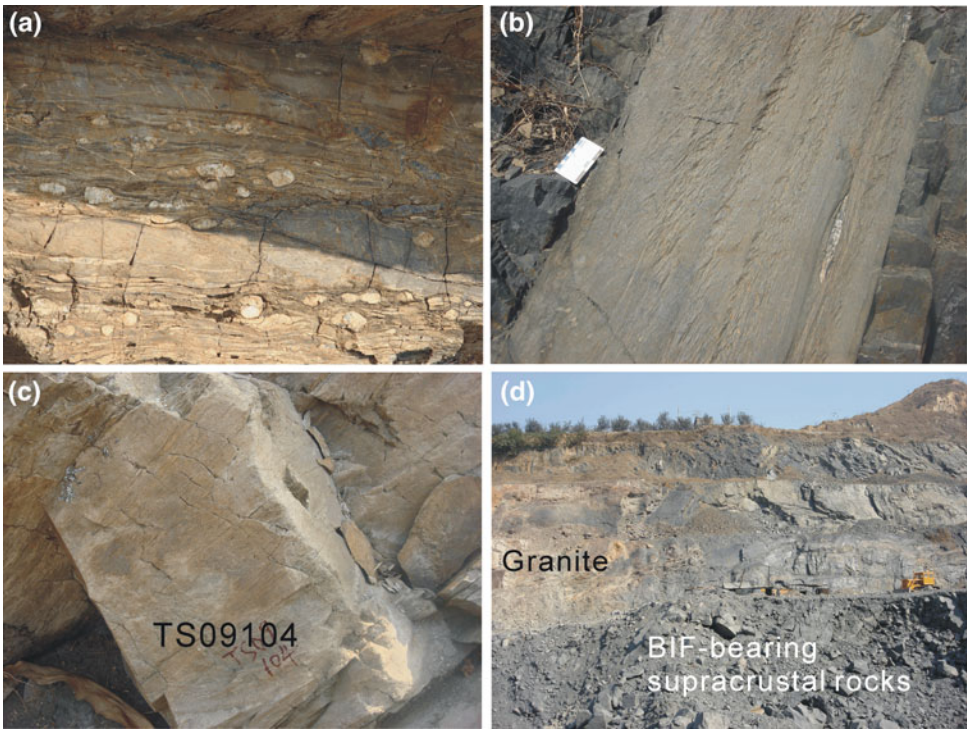

Fig. 4.15 Field photographs of late Neoarchean rocks in western Shandong. **a** Conglomerate interlayered with metasediments, Shancaoyu-Jining succession, showing strong deformation, Liuhang; **b** metasedimentary rock showing bedding with fine-grained sandstone interlayered with pelitic siltstone, Shancaoyu-Jining succession, Qixingtai (Wan et al. 2012b); **c** felsic metavolcano-sedimentary rock (TS09104) within conglomerates, Shancaoyu-Jining succession, northwest of Liuhang (Wan et al. 2012b); **d** 2.5 Ga red granite intruding BIF-bearing supracrustal sequences of the Shancaoyu-Jining succession, Hanwan

In every area where the late Neoarchean BIF-bearing supracrustal sequences occur, contemporary intrusive rocks are also well developed. Based on isotopic dating, juvenile TTG rocks were formed at the same time as, or more commonly slightly later than, the supracrustal sequences, whereas the crustally derived granites almost always formed later than the supracrustal sequences, as indicated by cross-cutting relationships.

The supracrustal sequences show variations in metamorphism, ranging from greenschist-facies to granulite-facies. The rocks in eastern Hebei and eastern Shandong commonly underwent stronger metamorphism, with at least some recording late Neoarchean and late Paleoproterozoic tectonothermal events. Large variations in metamorphism can occur even in small areas.

The BIFs are generally low in iron grade, with most being around 30 %. There are some BIF-related iron-rich deposits, such as those in Gongchangling of Anben, and Xingshan of Eastern Hebei. However, these were mostly formed as a result of the hydrothermal alteration of BIFs.

4.5.2 Sources of BIFs Revealed by Their Compositions

The geochemical composition of BIFs indicates that seawater and high-temperature fluids played critical roles in BIF formation, and the question arises which one was more important. Because BIFs commonly have more positive Eu anomalies than La and Y anomalies, many authors suggested that Fe mainly originated from hydrothermal fluids (Nozaki et al. 1997). However, high temperature hydrothermal fluids show strong positive Eu anomalies and weak positive La and Y anomalies compared with seawater, and their trace element concentration is two orders of magnitude higher than that of seawater (Bolhar et al. 2005). This would lead to an obvious increase of light REE in BIFs, even when only minor hydrothermal fluids are involved. Considering possible La and Ce anomalies and low Pr concentrations, we used the normalized ratio $(Nd/Yb)_{PAAS}$ to represent light and heavy REE fractionation of BIFs. Most BIFs in the NCC have $(Yb)_{PAAS} < 1$ and $(Nd/Yb)_{PAAS} < 1$ (Fig. 4 16a, b), which is inconsistent with the hydrothermal fluid model. Positive La and Y anomalies are features of both BIFs and seawater, so we propose that it was seawater rather than hydrothermal fluids that concentrated Fe in the BIFs. The Fe content should have been much higher than today in seawater when the BIFs formed. No significant chemical difference occurs between late Neoarchean and early Paleoproterozoic BIFs. However, some late Neoarchean BIF samples show more pronounced positive Eu anomalies, probably suggesting that more hydrothermal fluid was involved in their formation.

It is possible that there was abundant Fe^{2+} in the ancient oceans as a result of hydrothermal fluid activity or derived from weathering of iron-bearing material. The seawater would also have been rich in Si, as indicated by SiO_2 layers in BIFs, commonly with negative $\delta^{30}Si$ values (Hou et al. 2014).

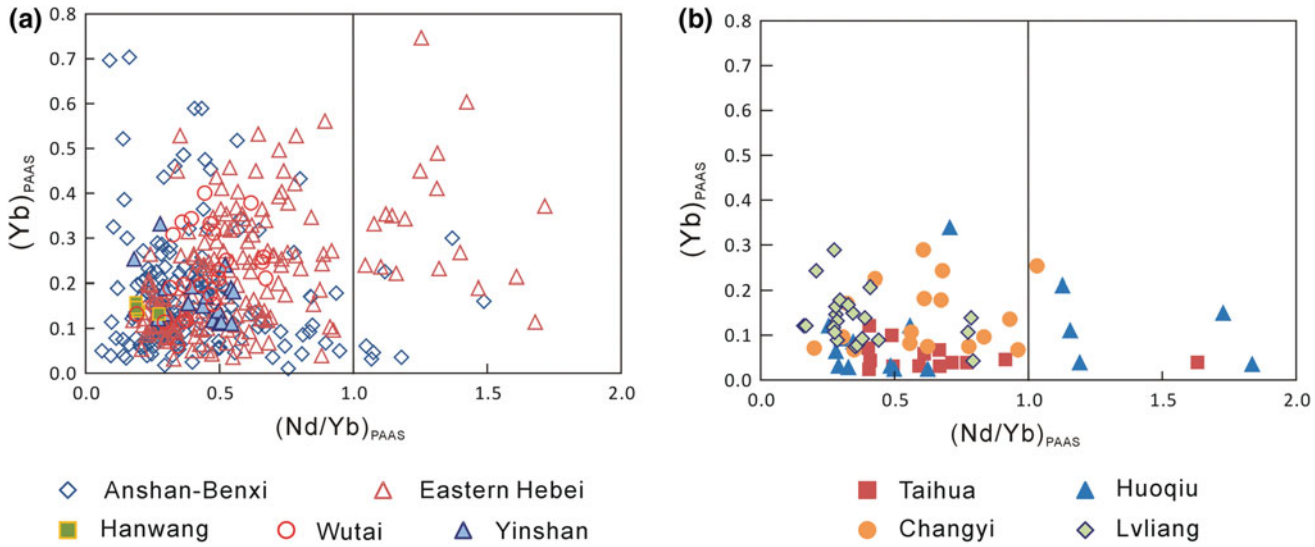

Fig. 4.16 $(Nd/Yb)_n$-Yb_n diagrams of BIFs in the North China Craton. See text for data sources. **a** Late Neoarchean; **b** early Paleoproterozoic

Oxidizing conditions were necessary for the deposition of Fe^{2+}. The generally suboxic and oxidizing conditions for BIF deposition suggest a quickly changing depositional environment during the formation of BIFs. There are at least two explanations: (1) Short-term variations of conditions in a shallow water environment, e.g., seasonal variation of Fe^{2+} dissolution or biological activity; (2) upwelling of reducing seawater from ocean bottom into a slightly oxidizing shallow water environment. We prefer the second explanation because of widespread positive Eu anomalies in BIFs due to hydrothermal fluid additions. Frequent periodic events such as hydrothermal fluid activity triggered upwelling of bottom water into relatively oxidizing shallow water environments to deposit BIFs; the upwelling is also considered to be the reason for BIFs showing Si–Fe-rich interbedded layers. Another possibility to cause upwelling of bottom sea water currents are circulating within the oceans. This explanation is supported by a study of the Ge and Si relationship in BIFs. Hamade et al. (2003) indicated that the sources of iron- to silica-rich layers in BIFs are different in terms of their different Ge/Si ratios; they used the model by Morris (1993) to explain the difference in which upwelling of bottom seawater caused an alternation of iron- and silica-rich layers. Ge was only analyzed in a few BIF samples from the NCC (Shen et al. 2009, 2011; Liu 2012, Liu and Yang 2013; Dai et al. 2013; Yang et al. 2014), and the limited data show a negative correlation between the Ge/Si ratio and SiO_2 content, similar to what was found by Hamade et al. (2003).

The exchange between reducing bottom water and oxidizing shallow water was probably of great significance for BIF deposition. Relatively oxidizing conditions in shallow water suggest that the oxygen-producing mechanism had worked at least during the late Neoarchean. Fe deposition consumes oxygen and restrains the rapid increase in aerial oxygen. We speculate that aerial oxygen could increase rapidly only after precipitation of most Fe from where seawater could easily exchange with shallow water. This is identical to the fact that most BIFs in the NCC formed prior to the ~2.3 Ga Great Oxidation Event (GOE) (Bekker et al. 2004). However, we cannot rule out the existence of reducing water reservoirs after the GOE, as indicated by the formation of 1.9–1.8 Ga BIFs in the Superior Province of Canada (Addison et al. 2005; Fralick et al. 2002). Other factors may have affected the Fe isotopes in BIFs such as biologic action and photosynthesis, but more work is required to test these processes.

4.5.3 Environment of Formation of BIFs in the Eastern Ancient Terrane

The BIF depositional environment in the NCC is uncertain. Wan et al. (2011, 2012b) proposed an arc model for BIF-bearing supracrustal sequences in western Shandong, based on evidence that: (1) magmatic rocks of different ages and compositions occur in different zones and spatially show an asymmetrical distribution; (2) the older rocks (2560–2525 Ma) commonly underwent stronger deformation and metamorphism than the younger rocks (2525–2480 Ma); (3) magmatic rocks of different composition are depleted in Nb and Ta and thus display a subduction-related chemical signature, and (4) the intrusive and volcanic activities broadly occurred during a same period, therefore, the intrusive rocks were uplifted very quickly to the surface to

become the source region for the late Neoarchean sedimentary basin. The BIFs are mainly distributed along the western margin of the Eastern Ancient Terrane, consistent with a continental margin, or more probably a back-arc basin environment. In any case, most BIFs must have formed on a continental basement for the reasons that (1) the BIFs are associated with sedimentary rocks containing ancient detrital zircons; (2) the BIF-bearing supracrustal sequences are cut by slightly younger crustally derived granites. Therefore, although the late Neoarchean BIF-bearing supracrustal sequences contain abundant MORB-type basalts in some areas, a thick and wide ocean crust was never developed in the deposition basins.

The BIFs in the Eastern Ancient Terrane were much better developed compared with those in other terranes of the NCC. This is considered to be due to the Eastern Ancient Terrane having been more mature and stable at the time of BIF deposition. The relationship between basement maturity and the scale of BIF deposition is also revealed in the Eastern Ancient Terrane itself, as mentioned above. It seems that a stable depositional environment was required for the formation of large-scale BIF deposits. The NCC was unstable compared with other cratons worldwide. This may be an important reason why the NCC contains less BIFs than other cratons. In the Pilbara Craton, Western Australia, where the late Neoarchean to early Paleoproterozoic extensive Hamersley BIFs were deposited on a basement which had been stable long before deposition of the BIFs (Van Kranendonk et al. 2012). The same is the case for the Transvaal BIFs in Southern Africa (Eriksson et al. 2006).

Based on above discussion, we speculate that BIF metallogenic prospecting should be undertaken along the western margin of the Eastern Ancient Terrane, especially in the northeast of Anben, between Anben and eastern Hebei, and between eastern Hebei and western Shandong, besides Anben, eastern Hebei and western Shandong (Fig. 4.1). It is important to establish the boundary of the western margin of the Eastern Ancient Terrane, not only for understanding the Archean evolution of the NCC but also for providing targets for BIF prospecting.

4.6 Conclusions

1. The BIFs in the Eastern Ancient Terrane are mostly late Neoarchean (2.55–2.52 Ga) in ages, similar to those in other areas of the NCC, but the formation ages of some BIFs in Anben and eastern Hebei are uncertain.
2. The BIFs mainly occur along the western margin of the Eastern Ancient Terrane, such as Anben, eastern Hebei and western Shandong, thus accounting for 89 % of the total identified BIF resources in the NCC.
3. The geochemical composition of BIFs indicates that seawater and high-temperature fluids played important roles in BIF formation; the exchange between reducing bottom water and oxidizing shallow water was probably of great significance for BIF deposition.
4. The BIFs are considered to have been deposited on a continental margin, or more probably a back-arc basin environment. It would appear that a stable tectonic environment is a key factor for the formation of large-scale BIFs.

Acknowledgments We thank Jinghui Guo, Yuansheng Geng, Jianhua Hou, Shoufa Lin, Shuwen Liu, Allen Nutman, Dominic Papineau, Qihan Shen, Zhiyong Song, Zhengshuang Ten, Jingxiang Tian, Huichu Wang, Laiming Wang, Shijin Wang, Simon A. Wilde, Meiling Wu, Chonghui Yang, Xiaoyong Yang, Mingguo Zhai, Lianchang Zhang, Guangli Zheng and Guochun Zhao for discussions and assistance during this research. We also thank Academician Minggou Zhai for originating this book. This study was financially supported by the Major State Basic Research Program of the People's Republic of China (2012CB416600, 2015FY310100), the National Natural Science Foundation of China (41172127, 41472168, 41472169) and the Key Program of the Ministry of Land and Resources of China (12120114021301, 1212010811033, 12120115070301).

References

Addison, W. D., Brumpton, G. R., Vallini, D. A., McNaughton, N. J., Davis, D. W., Kissin, S. A., et al. (2005). Discovery of distal ejecta from the 1850 Ma Sudbury impact event. *Geology, 33*, 193–196.

Bai, X., Liu, S.-W., Guo, R.-R., Zhang, L.-F., & Wang, W. (2014). Zircon U-Pb-Hf isotopes and geochemistry of Neoarchean dioritic-trondhjemitic gneisses, Eastern Hebei, North China Craton: Constraints on petrogenesis and tectonic implications. *Precambrian Research, 251*, 1–20.

Balci, N., Bullen, T. D., Witte-Lien, K., Shanks, W. C., Motelica, M., & Mandernack, K. W. (2006). Iron isotope fractionation during microbially stimulated Fe(II) oxidation and Fe(III) precipitation. *Geochimica et Cosmochimica Acta, 70*, 622–639.

Bau, M., & Dulski, P. (1996). Distribution of yttrium and rare-earth elements in the Penge and Kuruman iron-formations, Transvaal Supergroup, South Africa. *Precambrian Research, 79*, 37–55.

Bekker, A., Holland, H. D., Wang, P.-L., Rumble, I. D., Stein, H. J., Hannah, J. L., et al. (2004). Dating the rise of atmospheric oxygen. *Nature, 427*, 117–120.

Bolhar, R., Kamber, B. S., Moorbath, S., Fedo, C. M., & Whitehouse, M. J. (2004). Characterisation of early Archaean chemical sediments by trace element signatures. *Earth and Planetary Science Letters, 222*, 43–60.

Bolhar, R., Van Kranendonk, M. J., & Kamber, B. S. (2005). A trace element study of siderite-jasper banded iron formation in the 3.45 Ga Warrawoona Group, Pilbara Craton—Formation from hydrothermal fluids and shallow seawater. *Precambrian Research, 137*, 93–114.

Cao, G.-Q., et al. (1996). *Early Precambrian geology of western Shandong* (pp. 1–193). Beijing: Geological Publishing House (in Chinese with English abstract).

Cui, P.-L., Sun, J.-H., Sha, D.-M., Wang, X.-J., Zhang, P., Gu, A.-L., et al. (2014a). Oldest zircon xenocryst (4.17 Ga) from the North China Craton. *International Geology Review, 55*, 1902–1908.

Cui, M.-L., Zhang, L.-C., Wu, H.-Y., Xu, Y.-X., & Li, W.-J. (2014b). Timing and tectonic setting of the Sijiaying banded iron deposit in the eastern Hebei province, North China Craton: Constraints from geochemistry and SIMS zircon U-Pb dating. *Journal of Asian Earth Sciences, 94*, 240–251.

Czaja, A. D., Johnson, C. M., Beard, B. L., Eigenbrode, J. L., Freeman, K. H., & Yamaguchi, K. E. (2010). Iron and carbon isotope evidence for ecosystem and environmental diversity in the ~2.7 to 2.5 Ga Hamersley Province, Western Australia. *Earth and Planetary Science Letters, 292*, 170–180.

Dai, Y.-P., Zhang, L.-C., Wang, C.-L., Liu, L., Cui, M.-L., Zhu, M.-T., et al. (2012). Genetic type, formation age and tectonic setting of the Waitoushan banded iron formation, Benxi, Liaoning Province. *Acta Petrologica Sinica, 28*, 3574–3594. (in Chinese with English abstract).

Dai, Y.-P., Zhang, L.-C., Zhu, M.-T., Wang, C.-L., & Liu, L. (2013). Chentaigou BIF-type iron deposit, Anshan area associated with Archean crustal growth: Constraints from zircon U-Pb dating and Hf isotope. *Acta Petrologica Sinica, 29*, 2537–2550. (in Chinese with English abstract).

Dai, Y.-P., Zhang, L.-C., Zhu, M.-T., Wang, C.-L., Liu, L., & Xiang, P. (2014). The composition and genesis of the Mesoarchean Dagushan banded iron formation (BIF) in the Anshan area of the North China Craton. *Ore Geology Reviews, 63*, 353–373.

Ding, W.-J., Chen, Z.-L., Chen, B.-L., Dong, F.-X., & Cui, L.-L. (2009). Geochemical characters of band iron formation from Xingshan Iron Deposit in Qian'an area, Hebei province: Implication for their origin. *Journal of Geomechanics, 15*, 363–373. (in Chinese with English abstract).

Dong, X.-J., Xu, Z.-Y., Liu, Z.-H., & Sha, Q. (2012). Zircon U-Pb geochronology of Archean high-grade metamorphic rocks from Xi Ulanbulang area, central Inner Mongolia. *Science in China Series D-Earth Science, 55*, 204–212.

Du, L.-L., Zhuang, Y.-X., Yang, C.-H., Wan, Y.-S., & Wang, X.-S. (2005). SHRIMP U-Pb zircon chronology of fine-grained amphibolite in the Mengjiatun area, western Shandong. *Acta Geoscientica Sinica, 26*, 429–434. (in Chinese with English abstract).

Du, L.-L., Zhuang, Y.-X., Yang, C.-H., Wan, Y.-S., Wang, X.-S., Wang, S.-J., et al. (2003). Characters of zircons in the Mengjiatun Formation in Xintai of Shandong and their chronological significance. *Acta Geologica Sinica, 77*, 359–366. (in Chinese with English abstract).

Eriksson, P. G., Altermann, W., & Hartzer, F. J. (2006). The Transvaal Supergroup and its Precursors. In M. R. Johnson, C. R. Anhaeusser, & R. J. Thomas (Eds.), *The Geology of South Africa* (pp. 237–260). Johannesburg: Geological Society of South Africa.

Fralick, P., Davis, D. W., & Kissin, S. A. (2002). The age of the Gunflint Formation, Ontario, Canada: Single zircon U-Pb age determinations from reworked volcanic ash. *Canadian Journal of Earth Sciences, 39*, 1085–1091.

Geng, Y.-S., Liu, F.-L., & Yang, C.-H. (2006). Magmatic event at the end of the Archean in eastern Hebei Province and its geological implication. *Acta Geologica Sinica, 80*, 819–833.

Guo, R.-R., Liu, S.-W., Santosh, M., Li, Q.-G., Bai, X., & Wang, W. (2013). Geochemistry, zircon U-Pb geochronology and Lu-Hf isotopes of metavolcanics from eastern Hebei reveal Neoarchean subduction tectonics in the North China Craton. *Gondwana Research, 24*, 664–686.

Hamade, T., Konhauser, K. O., Raiswell, R., Goldsmith, S., & Morris, R. C. (2003). Using Ge/Si ratios to decouple iron and silica fluxes in Precambrian banded iron formations. *Geology, 31*, 35–38.

Han, C.-M., Xiao, W.-J., Su, B.-X., Chen, Z.-L., Zhang, X.-H., Ao, S.-J., et al. (2014a). Neoarchean Algoma-type banded iron formations from Eastern Hebei, North China Craton: SHRIMP U-Pb age, origin and tectonic setting. *Precambrian Research, 251*, 212–231.

Han, C.-M., Xiao, W.-J., Su, B.-X., Sakyi, P. A., Chen, Z.-L., Zhang, X.-H., et al. (2014b). Formation age and genesis of the Gongchangling Neoarchean banded iron deposit in eastern Liaoning Province: Constraints from geochemistry and SHRIMP zircon U-Pb dating. *Precambrian Research, 254*, 306–322.

Hou, K.-J., Li, Y.-H., Gao, J.-F., Liu, F., & Qin, Y. (2014). Geochemistry and Si-O-Fe isotope constraints on the origin of banded iron formations of the Yuanjiacun Formation, Lvliang Group, Shanxi, China. *Ore Geology Reviews, 57*, 288–298.

Huang, H., Zhang, L.-C., Liu, X.-F., Li, H.-Z., & Liu, L. (2013). Geological and geochemical characteristics of the Lee Laozhuang iron mine in Huoqiu iron deposit: Implications for sedimentary environment. *Acta Petrologica Sinica, 29*, 2593–2605. (in Chinese with English abstract).

Jahn, B.-M., Liu, D.-Y., Wan, Y.-S., Song, B., & Wu, J.-S. (2008). Archean crustal evolution of the Jiaodong peninsula, China, as revealed by zircon SHRIMP geochronology, elemental and Nd-isotope geochemistry. *American Journal of Science, 308*, 232–269.

James, H. L. (1954). Sedimentary facies iron formation. *Economic Geology, 49*, 235–293.

Jian, P., Kröner, A., Windley, B. F., Zhang, Q., Zhang, W., & Zhang, L.-Q. (2012). Episodic mantle melting-crustal reworking in the late Neoarchean of the northwestern North China Craton: Zircon ages of magmatic and metamorphic rocks from the Yinshan Block. *Precambrian Reseach, 222–223*, 230–254.

Jiang, N., Guo, J.-H., Zhai, M.-G., & Zhang, S.-Q. (2010). ~2.7 Ga crust growth in the North China craton. *Precambrian Research, 179*, 37–49.

Johnson, C. M., Beard, B. L., & Roden, E. E. (2008). The iron isotope fingerprints of redox and biogeochemical cycling in modern and ancient earth. *Annual Review of Earth and Planetary Sciences, 36*, 457–493.

Kröner, A., Wilde, S. A., Li, J. -H., Wang, K. -Y. (2005b). Age and evolution of a late Archean to Paleoproterozoic upper to lower crustal section in the Wutaishan/Hengshan/Fuping terrain of northern China. *Journal of Asian Earth Sciences*, *24*, 577–595.

Kröner, A., Wilde, S. A., O'Brien, P. J., Li, J. -H., Passchier, C. W., Walte, N. P., et al. (2005a). Field relationships, geochemistry, zircon ages and evolution of a late Archaean to Palaeoproterozoic lower crustal section in the Hengshan terrain of northern China. *Acta Geologica Sinica*, *79*, 605–629.

Lan, T.-G., Fan, H.-R., Hu, F.-F., Yang, K.-F., Cai, Y.-C., & Liu, Y.-S. (2014). Reprint of "Depositional environment and tectonic implications of the Paleoproterozoic BIF in Changyi area, eastern North China Craton: Evidence from geochronology and geochemistry of the metamorphic wallrocks". *Ore Geology Reviews, 63*, 444–464.

Lan, T.-G., Fan, H.-R., Hu, F.-F., Yang, K.-F., Zheng, X.-L., & Zhang, H.-D. (2012). Geological and geochemical characteristics of Paleoproterozoic Changyi banded iron formation deposit, Jiaodong Peninsula of eastern China. *Acta Petrologica Sinica, 28*, 3595–3611. (in Chinese with English abstract).

Lan, C.-Y., Zhang, L.-C., Zhao, T.-P., Wang, C.-L., Li, H.-Z., & Zhou, Y. Y. (2013). Mineral and geochemical characteristics of the Tieshanmiao-type BIF-iron deposit in Wuyang region of Henan Province and its implications for ore-forming processes. *Acta Petrologica Sinica, 29*, 2567–2582. (in Chinese with English abstract).

Li, Q. -P., Ren, X. -Z., Zhang, Y. -X. (2010). *Regional metallogenic map and explanation of iron deposits in Shandong Province* (pp 1–41).

Li, T.-S., Zhai, M.-G., Peng, P., Chen, L., & Guo, J.-H. (2010b). Ca. 2.5 billion year old coeval ultramafic-mafic and syenitic dykes in Eastern Hebei: Implicaitons for cratonization of the North China Craton. *Precambrian Research, 180*, 143–155.

Li, H.-M., Zhang, Z.-J., Li, L.-X., Zhang, Z.-C., Chen, J., & Yao, T. (2014). Types and general characteristics of the BIF-related iron deposits in China. *Ore Geology Reviews, 57*, 264–287.

Li, Z.-H., Zhu, X.-K., & Tang, S.-H. (2008). Characters of Fe isotopes and rare earth elements of banded iron formations from Anshan-Benxi area: Implications for Fe source. *Acta Petrologica et Mineralogica, 27*, 285–290. (in Chinese with English abstract).

Li, Z.-H., Zhu, X.-K., & Tang, S.-H. (2012). Fe isotope compositions of banded iron formation from Anshan-Benxi area: Constraints on the formation mechanism and Archean ocean environment. *Acta Petrologica Sinica, 28*, 3545–3558. (in Chinese with English abstract).

Li, Z.-H., Zhu, X.-K., Tang, S.-H., & Liu, H. (2010c). Characteristics of rare earth elements and geological significations of BIF from Jidong, Wutai and Lüliang Area. *Geoscience, 24*, 840–846. (in Chinese with English abstract).

Liu, S. -Q. (2011). *Discuss on the genesis of magnetite-rich ore in Gongchangling, Liaoning Province: Evidence from the iron stable isotope* (pp. 1–79). China University of Geosciences (Beijing), Ms. Thesis (in Chinese with English abstract).

Liu, D. -W. (2012). *The research of the geochemical characteristics of mineralization surrounding rocks in Gongchangling iorn ore, Liaoning Province, China* (pp. 1–79). Beijing: China University of Geosciences, Ms. Thesis (in Chinese with English abstract).

Liu, Q.-Q., Li, Y.-F., Luo, Z.-Z., Xie, K.-J., & Huang, Z.-L. (2014a). Geochemical characteristics of Jingshansi iron deposit in Wuyang, Henan Province, and their geological significance. *Mineral Deposits, 33*, 697–712. (in Chinese with English abstract).

Liu, J.-H., Liu, F.-L., Ding, Z.-J., Liu, C.-H., Yang, H., Liu, P.-H., et al. (2013a). The growth, reworking and metamorphism of early Precambrian crust in the Jiaobei terrane, the North China Craton: constraints from U-Th-Pb and Lu-Hf isotopics ystematics, and REE concentrations of zircon from Archean granitoid gneisses. *Precambrian Research, 224*, 287–303.

Liu, J.-H., Liu, F.-L., Liu, P.-H., Wang, F., & Ding, Z.-J. (2011a). Polyphase magmatic and metamorphic events from early Precambrian metamorphic basement in Jiaobei area: evidence from the Zircon U-Pb dating of TTG and granitic gneisses. *Acta Petrologica Sinica, 27*, 943–960. (in Chinese with English abstract).

Liu, S.-W., Lü, Y.-J., Wang, W., Yang, P.-T., Bai, X., & Feng, Y.-G. (2011b). Petrogenesis of the Neoarchean granitoid gneisses in northern Hebei Province. *Acta Petrologica Sinica, 27*, 909–921. (in Chinese with English abstract).

Liu, S.-W., Santosh, M., Wang, W., Bai, X., & Yang, P.-T. (2011c). Zircon U-Pb chronology of the Jianping Complex: Implications for the Precambrian crustal evolution history of the northern margin of North China Craton. *Gondwana Research, 20*, 48–63.

Liu, S.-J., Wan, Y.-S., Sun, H.-Y., Nutman, A., Xie, H.-Q., Dong, C.-Y., et al. (2013b). Paleo- to Eoarchean crustal materials in eastern Hebei, North China Craton: New evidence from SHRIMP U-Pb dating and in-situ Hf isotopic studies in detrital zircons of supracrustal rocks. *Journal of Asian Earth Sciences, 78*, 4–17.

Liu, D.-Y., Wilde, S. A., Wan, Y.-S., Wu, J.-S., Zhou, H.-Y., Dong, C.-Y., & Yin, X.-Y. (2008). New U-Pb and Hf isotopic data confirm Anshan as the oldest preserved segment of the North China Craton. *Amirecan Journal of Science, 308*, 200–231.

Liu, L., & Yang, X.-Y. (2013). Geochemical characteristics of the Huoqiu BIF ore deposit in Anhui Province and their metallogenic significance: Taking the Bantaizi and Zhouyoufang deposits as examples. *Acta Petrologica Sinica, 29*, 2551–2566. (in Chinese with English abstract).

Liu, L., Zhang, L.-C., & Dai, Y.-P. (2014b). Formation age and genesis of the banded iron formations from the Guyang Greenstone Belt, Western North China Craton. *Ore Geology Reviews, 63*, 388–404.

Liu, L., Zhang, L.-C., Dai, Y.-P., Wang, C.-L., & Li, Z.-Q. (2012). Formation age, geochemical signatures and geological significance of the Sanheming BIF-type iron deposit in the Guyang greenstone belt, Inner Mongolia. *Acta Petrologica Sinica, 28*, 3623–3637. (in Chinese with English abstract).

Lu, S. -N., Chen, Z. -H., Xiang, Z. -Q. (2008). *The World Geopark of Taishan: Geochronological Framework of Ancient Intrusives* (pp. 1–90). Geological Publishing House, Beijng (in Chinese).

Lü, B., Zhai, M.-G., Li, T.-S., & Peng, P. (2012). Ziron U-Pb ages and geochemistry of the Qinglong volcano-sedimentary rock series in Eastern Hebei: Implication for ~2500 Ma intra-continental rifting in the North China Craton. *Precambrian Research, 208–211*, 145–160.

Ma, X.-D., Fan, H.-R., Santosh, M., & Guo, J.-H. (2014). Chronology and geochemistry of Neoarchean BIF-type iron deposits in the Yinshan Block, North China Craton: Implications for oceanic ridge subduction. *Ore Geology Reviews, 63*, 405–417.

Ma, M.-Z., Wan, Y.-S., Santosh, M., Xu, Z.-Y., Xie, H.-Q., Dong, C.-Y., et al. (2012). Decoding multiple tectonothermal events in zircons from single rock samples: SHRIMP zircon U-Pb data from the late Neoarchean rocks of Daqingshan, North China Craton. *Gondwana Research, 22*, 810–827.

McLennan, S. M. (1989). Rare earth elements in sedimentary rocks: influence of provenance and sedimentary processes. In B. R. Lipin, G. A. McKay (Eds.), *Geochemistry and mineralogy of rare earth elements. Reviews in Mineralogy and Geochemistry* (vol. 21, pp. 169–200).

Morris, R. C. (1993). Genetic modeling for banded iron formation of the Hamersley Group, Pilbara Craton, Western Australia. *Precambrian Research, 60*, 243–286.

Nozaki, Y., Alibo, D. S., Amakawa, H., Gamo, T., & Hasumoto, H. (1999). Dissolved rare earth elements and hydrography in the Sulu Sea. *Geochimica et Cosmochimica Acta, 63*, 2171–2181.

Nozaki, Y., Zhang, J., & Amakawa, H. (1997). The fractionation between Y and Ho in the marine environment. *Earth and Planetary Science Letters, 148*, 329–340.

Nutman, A. P., Maciejowski, R., & Wan, Y.-S. (2014). Protoliths of enigmatic Archaean gneisses established from zircon inclusion studies: Case study of the Caozhuang quartzite, E. Hebei. *China. Geoscience Frontiers, 5*, 445–455.

Nutman, A. P., Wan, Y.-S., Du, L.-L., Friend, C. R. L., Dong, C.-Y., Xie, H.-Q., et al. (2011). Multistage late Neoarchaean crustal evolution of the North China Craton, eastern Hebei. *Precambrian Research, 189*, 43–65.

Peng, P., Li, Y., Liu, F., & Wang, F. (2012). Geological relation of late Archean lithologic units in northwest Hebei, North China Craton: Implication for building of early continental crust. *Acta Petrologica Sinica, 28*, 3531–3544. (in Chinese with English abstract).

Peng, T.-P., Wilde, S. A., Fan, W.-M., & Peng, B.-X. (2013a). Late Neoarchean potassic high Ba-Sr granites in the Taishan granite-greenstone terrane: Petrogenesis and implications for continental crustal evolution. *Chemical Geology, 344*, 23–41.

Peng, M.-S., Zhang, P., Yang, H.-Z., Wang, X.-J., & Qiao, S.-Y. (2013b). Geochemical Characteristics and Geological Significance of Iron Deposit in Nanfen, Liaoning. *Science and Technology Report, 31*, 33–37. (in Chinese with English abstract).

Polat, A., Li, J., Fryer, B., Kusky, T., Gagnon, J., & Zhang, S. (2006). Geochemical characteristics of the Neoarchean (2800–2700 Ma) Taishan greenstone belt, North China Craton: Evidence for plume-craton interaction. *Chemical Geology, 230*, 60–87.

Qiao, G.-S., Zhai, M.-G., & Yan, Y.-H. (1990). Geochronological study of Archean rocks in Anshan, Liaoning Province. *Scientia Geological Sinica, 2*, 158–165. (in Chinese with English abstract).

Shen, Q.-H., Geng, Y.-S., Song, B., & Wan, Y.-S. (2005). New information from the surface outcrops and deep crust of Archean rocks of the North China and Yangtze Blocks, and Qinling-Dabie Orogenic Belt. *Acta Geologica Sinica, 79*, 616–627. (in Chinese with English abstract).

Shen, Q.-H., Song, H.-X., Yang, C.-H., & Wan, Y.-S. (2011). Petrochemical characteristics and geological significations of banded iron formations in the Wutai Mountain of Shanxi and Qian'an of eastern Hebei. *Acta Petrologica et Mineralogica, 30*, 161–171. (in Chinese with English abstract).

Shen, Q.-H., Song, H.-X., & Zhao, Z.-R. (2009). Characteristics of Rare Earth Elements and Trace Elements in Hanwang Neo-Archaean Banded Iron Formations, Shandong Province. *Acta Geoscientica Sinica, 30*, 693–699. (in Chinese with English abstract).

Shi, Y.-R., Wilde, S. A., Zhao, X.-T., Ma, Y.-S., Du, L.-L., & Liu, D.-Y. (2012). Late Neoarchean magmatic and subsequent metamorphic events in the northern North China Craton: SHRIMP zircon dating and Hf isotopes of Archean rocks from Yunmengshan Geopark, Miyun, Beijing. *Gondwana Research, 21*, 785–800.

Sholkovitz, E. R., Landing, W. M., & Lewis, B. L. (1994). Ocean particle chemistry: The fractionation of rare earth elements between suspended particles and seawater. *Geochimica et Cosmochimica Acta, 58*, 1567–1579.

Song, B., Nutman, A. P., Liu, D.-Y., & Wu, J.-S. (1996). 3800 to 2500 Ma crustal evolution in the Anshan area of Liaoning Province, northeastern China. *Precambrian Research, 78*, 79–94.

Steinhoefel, G., von Blanckenburg, F., Horn, I., Konhauser, K. O., Beukes, N. J., & Gutzmer, J. (2010). Deciphering formation processes of banded iron formations from the Transvaal and the Hamersley successions by combined Si and Fe isotope analysis using UV femtosecond laser ablation. *Geochimica et Cosmochimica Acta, 74*, 2677–2696.

Sun, H.-Y., Dong, C.-Y., Xie, H.-Q., Wang, W., Ma, M.-Z., Liu, D.-Y., et al. (2010). The formation age of the Neoarchean Zhuzhangzi and Dantazi Groups in the Qinglong area, eastern Hebei Province: Evidence from SHRIMP U-Pb zircon dating. *Geological Review, 56*, 888–898. (in Chinese with English abstract).

Sun, X.-H., Zhu, X.-Q., Tang, H.-S., Zhang, Q., & Luo, T.-Y. (2014). Reprint of "The Gongchangling BIFs from the Anshan-Benxi area, NE China: Petrological-geochemical characteristics and genesis of high-grade iron ores". *Ore Geology Reviews, 63*, 374–387.

Tsikos, H., Matthews, A., Erel, Y., & Moore, J. M. (2010). Iron isotopes constrain biogeochemical redox cycling of iron and manganese in a Palaeoproterozoic stratified basin. *Earth and Planetary Science Letters, 298*, 125–134.

Van Kranendonk, M. J., Altermann, W., Beard, B. L., Hoffman, P. F., Johnson, C. M., Kasting, J. F., et al. (2012). A Chronostratigraphic division of The Precambrian: A Chronostratigraphic division of the Precambrian: possibilities and challenges. In: F. M. Gradstein, J. G. Ogg, M. Schmitz, G. Ogg (Eds.), *The geologic time scale* (pp. 299–392). Elsevier.

Wan, Y.-S. (1993). *The formation and evolution of the iron-bearing rock series of the Gongchangling area, Liaoning Province* (pp. 1–108). Beijing: Beijing Science and Technology Publishing House (in Chinese with English abstract).

Wan, Y.-S., Dong, C.-Y., Wang, S.-J., Kröner, A., Xie, H.-Q., Ma, M.-Z., et al. (2014a). Middle Neoarchean magmatism in western Shandong, North China Craton: SHRIMP zircon dating and LA-ICP-MS Hf isotope analysis. *Precambrian Research, 256*, 865–884.

Wan, Y.-S., Dong, C.-Y., Xie, H.-Q., Wang, S.-J., Song, M.-C., Xu, Z.-Y., et al. (2012a). Formation ages of early Precambrian BIFs in North China Craton: SHRIMP zircon U-Pb dating. *Acta Geologica Sinica, 86*, 1447–1478. (in Chinese with English abstract).

Wan, Y. -S., Liu, D. -Y., Dong, C. -Y., Xie, H. -Q., Kröner, A., Ma, M. -Z., et al. (2015). Formation and evolution of Archean continental crust of the North China Craton. In: M. G. Zhai (Ed.), *Precambrian geology of China* (pp. 59–136). Springer.

Wan, Y.-S., Liu, D.-Y., Nutman, A., Zhou, H.-Y., Dong, C.-Y., Yin, X.-Y., & Ma, M.-Z. (2012b). Multiple 3.8–3.1 Ga tectono-magmatic events in a newly discovered area of ancient rocks (the Shengousi Complex), Anshan, North China Craton. *Journal of Asian Earth Sciences, 54–55*, 18–30.

Wan, Y.-S., Liu, D.-Y., Song, B., Wu, J.-S., Yang, C.-H., Zhang, Z.-Q., & Geng, Y.-S. (2005). Geochemical and Nd isotopic compositions of 3.8 Ga meta-quartz dioritic and trondhjemitic rocks from the Anshan area and their geological significance. *Journal of Asian Earth Science, 24*, 563–575.

Wan, Y.-S., Liu, D.-Y., Wang, S.-J., Dong, C.-Y., Yang, E.-X., Wang, W., et al. (2010). Juvenile magmatism and crustalrecycling at the end of the Neoarchean in Western Shandong Province, NorthChina Craton: evidence from SHRIMP zircon dating. *American Journal of Science, 310*, 1503–1552.

Wan, Y.-S., Liu, D.-Y., Wang, S.-J., Yang, E.-X., Wang, W., Dong, C.-Y., et al. (2011). ~2.7 Ga juvenile crust formation in the North China Craton (Taishan-Xintai area, western Shandong Province): further evidence ofan understated event from U-Pb dating and Hf isotopic composition of zircon. *Precambrian Research, 186*, 69–180.

Wan, Y.-S., Wang, S.-J., Liu, D.-Y., Wang, W., Kröner, A., Dong, C.-Y., et al. (2012c). Redefinition of depositional ages of Neoarchean supracrustal rocks in western Shandong Province, China: SHRIMP U-Pb zircon dating. *Gondwana Research, 21*, 768–784.

Wan, Y.-S., Xie, S.-W., Yang, C.-H., Kröner, A., Ma, M.-Z., Dong, C.-Y., et al. (2014b). Early Neoarchean (~2.7 Ga) tectono-thermal events in the North China Craton: A synthesis. *Precambrian Research, 247*, 45–63.

Wang, H. C., Kang, J. L., Ren, Y. W., Chu, H., Lu, S. N., & Xiao, Z. B. (2015). Identification of ~ 2. 7 Ga BIF in North China Craton: Evidence from geochronology of iron-bearing formation in Laizhou-Changyi area. *Jiaobei terrane. Acta Petrologica Sinica, 31*, 2991–3011.

Wang, W., Liu, S.-W., Bai, X., Yang, P.-T., Li, Q.-G., & Zhang, L.-F. (2011). Geochemistry and zircon U-Pb-Hf isotopic systematics of the Neoarchean Yixian-Fuxin greenstone belt, northern margin of the North China Craton: Implications for petrogenesis and tectonic setting. *Gondwana Research, 20*, 64–81.

Wang, A.-D., Liu, Y.-C., Gu, X.-F., Hou, Z.-H., & Song, B. (2012). Late-Neoarchean magmatism and metamorphism at the southeastern margin of the North China Craton and their tectonic implications. *Precambrian Research, 220–221*, 65–79.

Wang, W., Liu, S.-W., Santosh, M., Bai, X., Li, Q.-G., Yang, P.-T., & Guo, R.-R. (2013). Zircon U-Pb-Hf isotopes and whole-rock geochemistry of granitoid gneisses in the Jianping gneissic terrane, Western Liaoning Province: Constraints on the Neoarchean crustal evolution of the North China Craton. *Precambrian Research, 224*, 184–221.

Wang, W., Wang, S.-J., Liu, D.-Y., Li, P.-Y., Dong, C.-Y., Xie, H.-Q., et al. (2010). Formation age of the Neoarchaean Jining Group (banded iron formation) in the western Shandong Province: constraints from SHRIMP zircon U-Pb dating. *Acta Petrologica Sinica, 26*, 1171–1174. (in Chinese with English abstract).

Wang, E.-D., Xia, J.-M., Fu, J.-F., Jia, S.-S., & Men, Y.-K. (2014a). Formation mechanism of Gongchangling high-grade magnetite deposit hosted in Archean BIF, Anshan-Benxi area, Northeastern China. *Ore Geology Reviews, 57*, 308–321.

Wang, W., Zhai, M.-G., Li, T.-S., Santosh, M., Zhao, L., & Wang, H.-Z. (2014b). Archean-Paleoproterozoic crustal evolution in the eastern North China Craton: zircon U-Th-Pb and Lu-Hf evidence from the Jiaobei terrane. *Precambrian Research, 241*, 146–160.

Wang, C.-L., Zhang, L.-C., Lan, C.-Y., & Dai, Y.-P. (2014c). Petrology and geochemistry of the Wangjiazhuang banded iron formation and associated supracrustal rocks from the Wutai greenstone belt in the North China Craton: Implications for their origin and tectonic setting. *Precambrian Research, 255*, 603–626.

Wang, C.-L., Zhang, L.-C., Lan, C.-Y., & Dai, Y.-P. (2014d). Rare earth element and yttrium compositions of the Paleoproterozoic Yuanjiacun BIF in the Lüliang area and their implications for the Great Oxidation Event(GOE). *Science China (Earth Sciences), 57*, 2469–2485.

Wang, Q.-Y., Zheng, J.-P., Pan, Y.-M., Dong, Y.-J., Liao, F.-X., Zhang, Y., et al. (2014e). Archean crustal evolution in the southeastern North China Craton: New data from the Huoqiu Complex. *Precambrian Research, 255*, 294–315.

Wilde, S. A., Cawood, P. A., Wang, K.-Y., & Nemchin, A. A. (2005). Granitoid evolution in the Late Archean Wutai Complex, North China Craton. *Journal of Asian Earth Science, 24*, 597–613.

Wilde, S. A., Cawood, P. A., Wang, K.-Y., Nemchin, A. A., & Zhao, G.-C. (2004). Determining Precambrian crustal evolution in China: a case-study from Wutaishan, Shanxi Province, demonstrating the application of precise SHRIMP U-Pb geochronology. *Journal of the London Geological Society, 226*, 5–25.

Wu, J. -S., Geng, Y. -S., Shen, Q. -H., Wan, Y. -S., Liu, D. -Y., & Song, B. (1998). *Archaean geology characteristics and tectonic evolution of China-Korea Paleo-continent* (pp. 1–212). Beijing: Geological Publishing House (in Chinese).

Wu, F.-Y., Yang, J.-H., Liu, X.-M., Li, T.-S., Xie, L.-W., & Yang, Y.-H. (2005). Hf isotopes of the 3.8 Ga zircons in eastern Hebei Province, China: Implications for early crustal evolution of the North China Craton. *Chinese Science Bulletin, 50*, 2473–2480.

Wu, F.-Y., Zhang, Y.-B., Yang, J.-H., Xie, L.-W., & Yang, Y.-H. (2008). Zircon U-Pb and Hf isotopic constraints on the Early Archean crustal evolution in Anshan of the North China Craton. *Precambrian Research, 167*, 339–362.

Wu, M.-L., Zhao, G.-C., Sun, M., Li, S.-Z., Bao, Z.-A., Yuk, T. P., et al. (2014). Zircon U-Pb geochronology and Hf isotopes of major lithologies from the Jiaodong Terrane: implications for the crustal evolution of the Eastern Block of the North China Craton. *Lithos, 190–191*, 71–84.

Wu, M.-L., Zhao, G.-C., Sun, M., Li, S.-Z., He, Y.-H., & Bao, Z.-A. (2013). Zircon U-Pb geochronology and Hf isotopes of major lithologies from the Yishui Terrane: Implications for the crustal evolution of the Eastern Block, North China Craton. *Lithos, 170–171*, 164–178.

Xiang, P., Cui, M.-L., Wu, H.-Y., Zhang, X.-J., & Zhang, L.-C. (2012). Geological characteristics, ages of host rocks and its geological significance of the Zhoutaizi iron deposit in Luanping, Hebei Province. *Acta Petrologica Sinica, 28*, 3655–3669. (in Chinese with English abstract).

Xie, H.-Q., Wan, Y.-S., Wang, S.-J., Liu, D.-Y., Xie, S.-W., Liu, S.-J., et al. (2013). Geology and zircon dating of trondhjemitic gneiss and amphibolite in the Tangezhuang area, eastern Shandong. *Acta Petrologica Sinica, 29*, 619–629. (in Chinese with English abstract).

Xie, S.-W., Xie, H.-Q., Wang, S.-J., Kröner, A., Liu, S.-J., Zhou, H.-Y., et al. (2014). Ca. 2.9 Ga granitoid magmatism in eastern Shandong, North China Craton: Zircon dating, Hf-in-zircon isotopic analysis and whole-rock geochemistry. *Precambrian Research, 255*, 538–562.

Xiong, S.-Q., Fan, Z.-G., Huang, X.-Q., Zhou, D.-Q., Zhang, H.-R., Yang, X., et al. (2013). *Aeromagnetic Altas of integrated exploration areas in china* (pp. 1–307). Beijing: Geological Publishing House.

Yang, C.-H., Du, L.-L., Ren, L.-D., Wan, Y.-S., Song, H.-X., Yuan, Z.-L., & Wang, S.-Y. (2009). SHRIMP U-Pb ages and stratigraphic comparison of Angou group, on the southern margin of North China Craton. *Acta Petrologica Sinica, 25*, 1853–1862. (in Chinese with English abstract).

Yang, X.-Q., Li, H.-M., Xue, C.-J., Li, L.-X., Liu, M.-J., & Chen, J. (2013). Geochemical characteristics of two iron ores from the Waitoushan Iron deposit, Liaoning Province: Constraints on ore-forming mechanism. *Acta Geologica Sinica, 87*, 1580–1592. (in Chinese with English abstract).

Yang, X., Liu, L., Lee, I., Wang, B., Du, Z., Wang, Q., et al. (2014). A review on the Huoqiu banded iron formation (BIF), southeast margin of the North China Craton: Genesis of iron deposits and implications for exploration. *Ore Geology Reviews, 63*, 418–443.

Yang, J.-H., Wu, F.-Y., Wilde, S. A., & Zhao, G.-C. (2008). Petrogenesis and geodynamics of Late Archean magmatism in eastern Hebei, eastern North China Craton: Geochronological, geochemical and Nd-Hf isotopic evidence. *Precambrian Research, 167*, 125–149.

Yao, T., Li, H.-M., Yang, X.-Q., Li, L.-X., Chen, J., Zhang, J.-Y., & Liu, M.-J. (2014). Geochemical characteristics of Banded Iron Formations in Liaoning-eastern Hebei area:II. Characteristics of rare earth elements. *Acta Petrologica Sinica, 30*, 1239–1252. (in Chinese with English abstract).

Zhai, M.-G., & Santosh, M. (2011). The early Precambrian odyssey of the North China Craton: a synoptic overview. *Gondwana Research, 20*, 6–25.

Zhai, M.-G., Windey, B. F., & Sills, J. D. (1990). Archaean Gneisses, Amphibolites and Banded Iron-Formations from the Anshan Area of Liaoning Province, NE China: Their Geochemistry, Metamorphism and Petrogenesis. *Precambrian Research, 46*, 195–216.

Zhang, Z.-C., Hou, T., Santosh, M., Li, H.-M., Li, J.-W., Zhang, Z.-H., et al. (2014). Spatio-temporal distribution and tectonic settings of the major iron deposits in China: An overview. *Ore Geology Reviews, 57*, 247–263.

Zhang, L.-C., Zhai, M.-G., Wan, Y.-S., Guo, J.-H., Dai, Y.-P., Wang, C.-L., & Liu, L. (2012a). Study of the Precambrian BIF-iron deposits in the North China Craton: Progreese and problems. *Acta Petrologica Sinica, 28*, 3431–3445. (in Chinese with English abstract).

Zhang, L.-C., Zhai, M.-G., Zhang, X.-J., Xiang, P., Dai, Y.-P., Wang, C.-L., & Franco, P. (2012b). Formation age and tectonic setting of the Shirengou Neoarchean Banded iron deposit in eastern Hebei Province: Constrains from geochemistry and SIMS zircon U-Pb dating. *Precambrian Research, 222–223*, 325–388.

Zhang, X.-J., Zhang, L.-C., Xiang, P., Wan, B., & Pirajno, F. (2011). Zircon U-Pb age, Hf isotopes and geochemistry of Shuichang Algoma-type banded iron-formation, North China Craton: Constraints on the ore-forming age and tectonic setting. *Gondwana Research, 20*, 137–148.

Zhao, G. -C. (2014). *Precambrian evolution of the North China Craton* (pp. 1–194). Elsevier.

Zhao, G.-C., & Zhai, M.-G. (2013). Lithotectonic elements of Precambrian basement in the North China Craton: Review and tectonic implications. *Gondwana Research, 23*, 1207–1240.

Neoarchean Banded Iron Formations in the North China Craton: Geology, Geochemistry, and Its Implications

5

Lianchang Zhang, Changle Wang, Mingtian Zhu, Hua Huang, and Zidong Peng

Abstract

The distribution of Banded iron formations (BIFs) in the North China Craton (NCC) has some obvious characteristics. Large-scale BIFs and BIF-type iron deposits occur mainly in greenstone belts area such as Anshan-Benxi, eastern Hebei, Wutai, Guyang, western Shandong and Huoqiu; formation ages of BIFs in NCC show a wide range spanning from Mesoarchean to early Paleoproterozoic, with a peak in the late Neoarchean (2.6–2.5 Ga); BIFs can be divided into two types, Algoma-type and Superior Lake-type, most BIFs occurring in Neoarchean greenstone belts in NCC belong to the former, whereas only the Paleoproterozoic Yuanjiacun BIF in the Lüliang area has typical characteristics similar to Superior-type BIFs. The Neoarchean BIFs are mainly distributed in paleo-intracratonic basins and/or their margins. The BIFs can be developed in either marine volcanic-sedimentary environment or submarine exhalation sedimentary environment, either shallow marine clastic sedimentary environment or marine clastic-carbonate transition environment. All the BIFs in NCC experienced relatively high-grade metamorphism and strong deformation, forming most sedimentary metamorphic iron deposits with magnetite as a major economic mineral. Large amounts of geochemistry results of the Neoarchean BIFs in NCC show that the BIFs are composed predominantly of SiO_2 + $Fe_2O_3^T$, and the contents of Al_2O_3, TiO_2, K_2O, Na_2O, MnO, and P_2O_5 are very low, suggesting that BIFs belong to typical chemical sedimentary rocks. The Post-Archean Australian Shale-normalized REY patterns of the BIFs display an enrichment in heavy rare earth elements with positive La, Eu, and Y anomalies, indicating that the primary chemical precipitate is a result of solutions that represent mixtures of seawater and high-temperature hydrothermal fluids. The ε_{Nd}(2.55 Ga) values (3.0–4.5) in Anshan-Benxi BIFs are close to those of the coeval depleted mantle, implying that the iron was most likely derived from the hydrothermal leaching of oceanic mafic crusts; the ε_{Nd}(2.55 Ga) values (2.89 to −2.58) in the Wutai and E. Hebei BIFs suggest that the iron sources are mixing oceanic crusts and continental crusts. At the same time, the BIFs lack negative Ce anomalies with consistently positive δ^{56}Fe values (0.12–1.87 ‰), which suggest that they formed in a low-oxygen or anoxia environment. A possible tectonic setting where the NCC BIFs and associated supra crustal rocks form is a back-arc basin or island arc related to a subducted ocean slab.

Keywords

Banded iron formation (BIF) • Neoarchean • North China Craton • Material sources • Tectonic setting • Depositional model

L. Zhang (✉) · C. Wang · M. Zhu · H. Huang · Z. Peng
Key Laboratory of Mineral Resources, Institute of Geology and Geophysics, Chinese Academy of Sciences, Beijing, 100029, China
e-mail: lczhang@mail.igcas.ac.cn

M. Zhai et al. (eds.), *Main Tectonic Events and Metallogeny of the North China Craton*, Springer Geology, DOI 10.1007/978-981-10-1064-4_5

5.1 Introduction

Banded iron formations (BIFs) are marine chemical sediments containing at least 15 % iron and characterized by alternating Fe- and Si-rich layers (James 1954). Two types of BIFs have been distinguished: volcano-sedimentary Algoma-type which occurs commonly in greenstone belts, and continent-derived Superior type which forms in stable sedimentary basins and cratonic margins (Gross 1980). In general, the former is commonly of Archean age and the latter is of Paleoproterozoic age with considerably more Fe (Gross 1980, 1983). Formed throughout much of the Precambrian (3.8–0.5 Ga), the overall volume of BIFs reached a maximum at ~2.5 Ga (Klein and Beukes 1992; Klein 2005). BIFs precipitated directly from ambient seawater and consequently retained chemical signatures of the seawater, and thus they have been extensively studied as reliable proxies for the compositional evolution of paleo-seawater (Bau and Dulski 1996; Bolhar et al. 2004) and as an indicator for the chemical and biological evolution of early Earth (Ohmoto et al. 2006).

The BIF-hosted iron ore deposit is one of the world's most important iron resource types, with the quantity of both exploitation and resource reserve ranking first in the world (>80 %). Proven BIF iron ore reserves account for over 60 % of the total iron in China. Some large BIF-type iron and high-grade iron orebodies have recently been discovered in the North China Craton (NCC) (Li et al. 2012, 2014; Dai et al. 2014), such as Gongchangling in Anshan, Jining in W. Shandong, Dataigou in Benxi of Liaoning, Macheng and Xingshan in E. Hebei.

There are two important periods for the BIF relevant research in China. One is during 1980s–1990s, when BIF-hosted high-grade iron ores were prospected and BIF have also been extensively studied. It is shown that the BIF iron deposits in China have the following characteristics: (1) BIFs are formed mainly on paleocontinental margins or in greenstone belts of the NCC (Zhai et al. 1990; Zhai and Windley 1990); (2) they commonly occur in Neoarchean supracrustal rock successions, with minor BIFs found in the early Proterozoic rocks; (3) these supracrustal rocks associated with BIFs often consist mainly of metavolcanic rocks and minor metasedimentary rocks (Algoma-type iron deposit) (Zhai and Windley 1990); (4) the orebodies display multiple-period and intense deformational features and steep occurrences. The other period, since 2010, along with development of isotopic geochemistry, new geochronology methods were used to relevant geological fields. For example, scientists successfully obtained zircon U–Pb ages through SHIRIMP or LA-ICPMS methods, and distinguished the origin of zircons (i.e., magmatic, metamorphic). The zircon U–Pb ages play an important part in constraining the time of significant geological events, including crust growth and Great Oxidation Event (GOE), which likely coincided with deposition of BIFs (Zhang et al. 2012a, b; Dai et al. 2012, 2014; Wang et al. 2015a). In addition, Fe, Hf, and Nd isotope features can provide constraints on material sources and deposition environment of BIFs.

Given their economic importance, BIFs have been extensively studied, but many aspects of their origin remain enigmatic because modern analogues are unknown. In this paper, we summarized recent achievements of geochronology, geology, and geochemistry characteristics of the BIFs in NCC in order to decipher the genetic mechanism of BIFs.

5.2 Geology of the Neoarchean BIFs in NCC

5.2.1 Geologic Features and Distributions of BIFs

The NCC is bounded by the Central Asian Orogenic Belt to the North, the Qinling-Dabie Orogenic Belt to the South and by the Su–Lu Orogenic Belt to the East (Fig. 5.1). Beneath a vast Phanerozoic cover, the NCC is comprised dominantly of ca. 3.8–2.5 Ga migmatite, tonalite-trondhjemite-granodiorite gneisses (TTG), amphibolite, mica schist, sillimanitic gneiss, and BIFs. The Archean rocks are overlain by the Palaeoproterozoic Liaohe Group and Mesoproterozoic Changcheng Group (Ouyang et al. 1995). The NCC is divided into the eastern and western block, separated by the intervening Central Orogenic Belt (COB) (Zhao et al. 2001). The collision time of the two blocks along COB is controversial: either at ca. 1850 Ma (Wilde et al. 2004; Guo et al. 2005; Zhao et al. 2005), or at ca. 2500 Ma (Kusky and Li 2003; Zhai and Liu 2003). The western Block is a stable continent with a thick platform sedimentary cover. In contrast, the eastern block consists of a variety of ca. 3800–2500 Ma gneissic rocks, greenstone belts, and BIFs (Zhai and Liu 2003; Geng et al. 2006).

BIFs occur extensively throughout the Neoarchean units of the NCC, and five major iron metallogenic provinces have been identified: Anshan-Benxi in Northeastern NCC, Miyun-Eastern Hebei in the eastern NCC, Wuyang-Huoqiu in the southern NCC, Guyang in western NCC, and Wutai-Lüliang in the central NCC (Fig. 5.1). The hosted rocks, lithology, metamorphic facies, BIF scale, mineral assemblages, and representative BIFs are listed in Table 5.1.

In the Anshan-Benxi (or Anben) area, where the metamorphic degree is relatively low, BIF-bearing greenstone rocks are distributed as belts in granitic complexes.

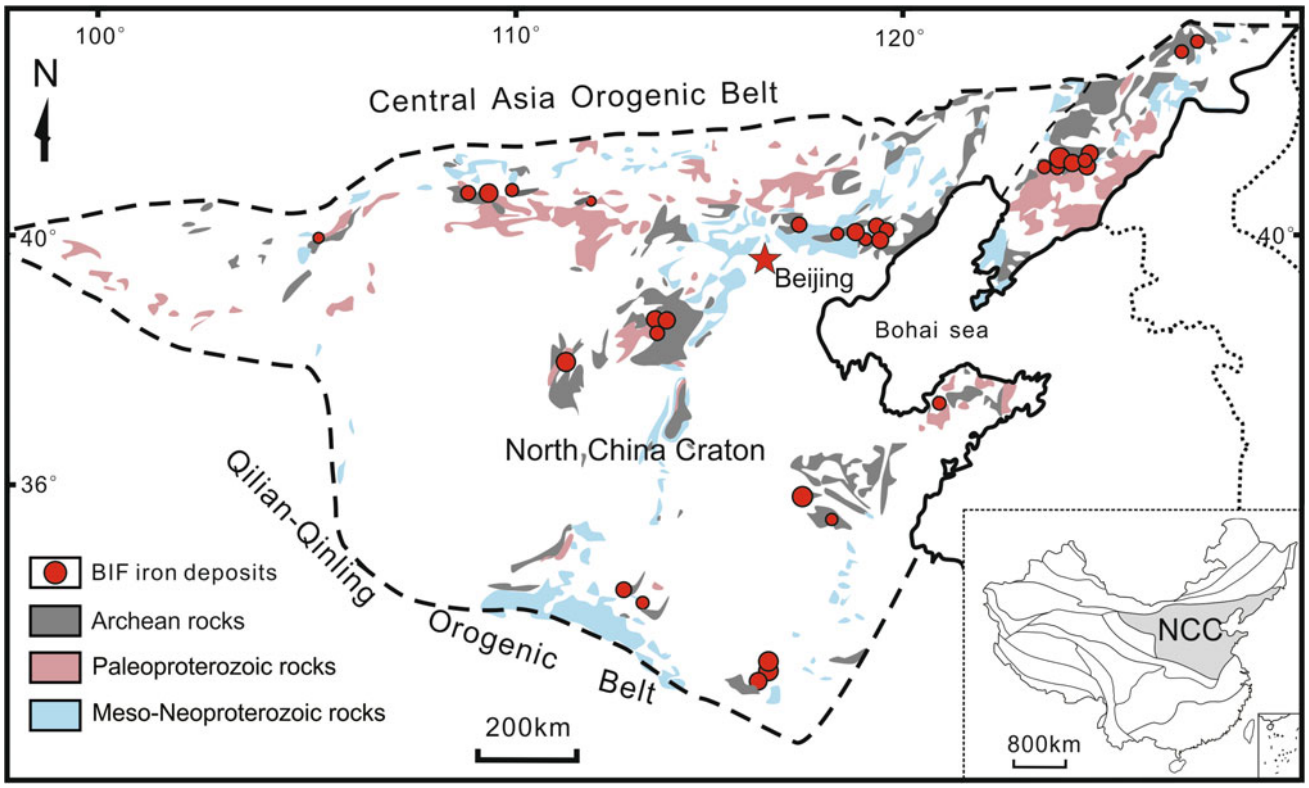

Fig. 5.1 Distribution sketch of major BIF iron deposits in the NCC

The greenstone rocks is mainly composed of amphibolites, leptynites, quartzites, phyllites, and schists of volcano-sedimentary origin (Zhai et al. 1990). It underwent greenschist to amphibolite facies metamorphism. The footwall surrounding rocks of BIF consist of amphibolite and amphibole-plagioclase gneiss, while its hanging wall rocks comprising of amphibole-plagioclase gneiss, biotite-plagioclase, and garnet-chlorite schist. The protoliths of these rock series are mostly felsic volcanic-sedimentary rocks, clay clastic rocks, and mafic volcanics. They have undergone epidote-amphibolite- (i.e., East Anshan and West Anshan BIFs) or amphibolite facies metamorphism in some localities (i.e., Waitoushan and Nanfen BIFs) (Zhou 1994).

The main BIFs in E. Hebei have undergone either amphibolites or granulite-facies metamorphism. For example, the Shuichang and Xingshan BIF deposit has undergone granulite-facies metamorphism. The BIF-hosting Archean Qianxi Group in the Shuichang and Xingshan area consists predominantly of hypersthene granulite, biotite-plagioclase gneiss, pyroxene–plagioclase gneiss, plagioclase amphibolite gneiss, biotite migmatitic gneiss, hypersthene migmatitic gneiss, pyrigarnite and magnetite quartzite. The main minerals of the granulite are hypersthene, plagioclase, biotite, and quartz, while the principal minerals of these gneisses are plagioclase, quartz, biotite, hornblend, hypersthene, and garnet. The Shirengou iron deposit is hosted in metamorphic rocks of the Neoarchean Malanzhuang Formation in the Qianxi Group. The metamorphic rocks consist of hornblende plagiogneiss, plagioclase amphibolites, granitic migmatite and magnetite quartzite. But, the Luanxian Group of Hosting Sijiaying BIF is composed of fine-grained schist, leptynites, amphibolite and BIF, and shows greenschist-amphibolite metamorphism.

The Wutai BIF-bearing greenstone belt is located in the central section of the NCC. The supracrustal sequences here are developed above a granitic gneiss basement with magmatic zircon U–Pb ages of 2.53–2.57 Ga (Wilde et al. 2004; Wang et al. 2014b). The supracrustal rocks can be subdivided into three formations as follows: the amphibolite facies Jingangku Formation, the greenschist-facies Wutai Formation, and subgreenschist-facies turbidites. This sequence thus defines a typical accreted oceanic plate stratigraphy on a paleo-convergent margin, as recognized in other Precambrian terranes. The BIFs are interlayered with amphibolites and greenschists that represent metamorphosed basaltic rocks. All these metavolcanics show island arc geochemical affinities and thus represent arc accretion during continent growth in the late Neoarchean.

The Huoqiu iron deposit is located on the southern margin of the NCC. The Huoqiu area is a large-scale BIF iron ore field, the orebodies occur in a Neoarchean iron formation with middle-high grade metamorphism. After decades of

Table 5.1 Geological features of the BIFs (iron deposits) in the NCC

	Anshan	Benxi	Zunhua	Qianxi	Luanxian	Wutai	Guyang	Luxi	Huoqiu
Host Group	Anshan G.	Anshan G.	Zunhua G.	Qianxi G.	Luanxian G.	Wutai G.	Sertanshan G.	Luxi G.	Huoqiu G.
Host rocks	Chlorite-quartz schist, sericite-quartz schist	Plagioclase, amphibolite, actinolite schist, biotite-amphibole gneiss, leptynite	Biotit-amphibole-plagioclase gneiss, biotite-plagioclase gneiss	Biotite-plagioclase gneiss, pyroxene-plagioclase gneiss, amphibole-plagioclase gneiss	Biotite leptynite, two-mica leptynite, two-mica quartz schist	Plagioclase amphibolite, sericite schist, chlorite-amphibole schist	Plagioclase amphibolite, tremolite schist, garnet-biotite schist	Greenschist, phyllite	Amphibole-plagioclase gneiss. Leptynite, plagioclase amphibolite, marble
Metamorphic facies	Greenschist facies	Greenschist-amphibolite	Amphibolite	Amphibolite-granulite	Greenschist-amphibolite	Greenschist-amphibolite	Amphibolite	Greenschist	Amphibolite
Monolayer thickness (m)	20–300	20–200	10–100	10–100	20–200	10–130	10–100	20–300	20–200
Length (km)	0.2–14.5	0.2–10	0.1–3	0.1–3	0.2–10	0.1–4.3	0.1–1	0.2–5	0.2–10
Layer count	Thick monolayer	Thick monolayer and multilayer	Multilayer	Multilayer	Monolayer and multilayer	Multilayer	Multilayer	Thick monolayer	Multilayer
Economic grade (%)	28–35	28–35	25–35	25–35	25–35	26–33	25–32		25–35
Scale	Super large	Large	Medium	Large-medium	Super large-large	Medium-small	Medium-small	Super large	Large-medium
Mineral facies	Mainly oxide facies, minor silicate facies	Mainly oxide facies, minor silicate facies	Mainly oxide facies, minor silicate facies	Oxide facies	Oxide facies	Oxide and silicate facies	Oxide and silicate facies	Oxide facies	Oxide and carbonate facies
Mineral component	Magnetite, martite, siderite, quartz, tremolite, chlorite, ankerite, stilpnomelane	Magnetite, martite, siderite, quartz, actinolite, tremolite, ankerite	Magnetite, quartz, hornblende, biotite	Magnetite, quartz, amphibole, biotite, hypersthene, diopside	Magnetite, martite, quartz, siderite, actinolite, tremolite, chlorite	Magnetite Mg-soderite, quartz, chlorite, Mg-grunerite, stilpnomelane	Magnetite, quartz, tremolite, actinolite, biotite	Magnetite, quartz, amphibole, chlorite, biotite, carbonate	Magnetite, hematite, quartz, hornblende, grunerite, actinolite, siderite, Fe-magnesite, dolomite
Example of BIF (iron deposits)	Qidashan, E. Anshan, W. Anshan, Dagushan, Yanqianshan	Dataigou, Waitoushan, Nanfen, Beitai	Shirengou, Malanzhuang	Shuichang, Malanzhuang, Xingshan	Sijiaying, Macheng, Dajiazhuang	Wangjiazhuang, Dayangping, Ekou	Sanheming, Guyiming, Dongwufenzi	Jining	Zhangzhuang, Zhouji, Zhouyoufang, Lilaozhuang, Lilou

prospecting, more than ten large iron deposits have been proven and explored, namely, Zhouji, Zhangzhuang, Lilaozhuang, Zhouyoufang, Fanqiao, Wuji, and Lilou iron deposits (Wan et al. 2011a, b; Yang et al. 2014a, b). The Huoqiu Group comprises mainly of magnetite quartzite, amphibole schist, biotite-quartz schist, granulite, biotite-plagioclase gneiss, and plagioclase amphibolite. The ore types in the Huoqiu BIF are mainly quartz + magnetite (or hematite), silicate + magnetite, and carbonate + magnetite.

BIFs in the Guyang greenstone belt are situated in the western NCC. Three large iron deposits, namely, the Gongyiming, Dongwufenzhi, and Sanheming were distributed in the greenstone belt. The iron ore bodies are lens-shaped or interlayered with plagioclase amphibolites in the greenstone sequence. The Sanheming iron deposit has been described by Liu et al. (2014). Magnetite quartzite is the main ore type, with interlayered amphibolites of 2562 ± 14 Ma. The magnetite quartzite is characterized by granular crystalloblastic or granular columnar crystalloblastic texture and banded or laminated structure, and consists predominantly of magnetite and quartz with minor grunerite. The protoliths of the amphibolites are sub-alkaline and high-Fe tholeiite.

5.2.1.1 Mineral Composition and Evolution of BIFs

BIFs are defined by their unusual mineralogy, which includes mostly silica and a wide range of Fe-rich and Al-poor minerals (Table 5.1). The mineralogy of BIFs from the best preserved sequences is remarkably uniform, consisting mainly of quartz, magnetite, hematite, Fe-rich silicate minerals (stilpnomelane, minnesotaite, and riebeckite), carbonate minerals (siderite, ankerite, calcite, and dolomite), and less sulfides (pyrite and pyrrhotite).

Most of BIF is well banded oxide facies iron formation composed of alternating quartz-rich and magnetite-rich layers (Fig. 5.2a–e). Some BIFs of wrinkling deformation were seen in Nanfen of Anben area and in Sijiaying of E. Hebei (Fig. 5.2f, g). Some activated quartz vein in BIFs was also seen in W. Anshan (Fig. 5.2h).

Main characteristics of compositional minerals in BIFs are shown as follows: (Figs. 5.2 and 5.3):

Magnetite occurs as subhedral grains in BIFs. It is particularly abundant in Fe-rich layers with various grain sizes typically between 0.06 and 0.55 mm (Fig. 5.3a). A small amount of magnetite grains are found in Si-rich layers. Some quartz crystals contain magnetite inclusions. Magnetite is commonly replaced by hematite (termed martite, Fig. 5.3b). Magnetite often formed mostly during late diagenesis and metamorphism.

Quartz (or chert) is the most common mineral in BIF (50–65 %). It occurs as microbands, alternating with millimeter-thick microbands of Fe-rich silicate and carbonate minerals. Some quartz and amphibole often occur in Fe-rich layers (Fig. 5.2c–e). The quartz grains are subhedral with 0.06–0.3 mm in size. Some quartz show undulatory extinction and stretched occurrence.

Hematite (or martite) has either primary or replacement origin. Magnetite commonly is replaced by martite or hematite in NCC BIFs (Fig. 5.3b). Whether primary hematite exists needs further study. In the Anshan area, near the surface, some BIFs are oxidized and show a high Fe^{3+}/Fe^{2+} ratio. Oxidation processes are weakened away from the surface, suggesting that it is a recent phenomenon.

Siderite is the most common carbonate mineral in BIFs, typically occurring as minute, single, rhomb-shaped crystals. Small siderite nodules are common in some layers, where they display evidence of differential compaction, thus indicating that the nodules probably formed before deep burial. The texturally earliest siderite is present as minute (<20 mm) spheroids (Fig. 5.3c). This siderite appears to have replaced or overgrown an earlier phase, which occurs in the core of some crystals, indicating a diagenetic origin for the siderite.

Grunerite tends to be noticeably smaller in size, varying from 0.05 to 0.2 mm, occurring as subhedral to enhedral grains (Fig. 5.3d, e). Grunerite often makes up microbands that alternate with quartz microbands. Grunerite is commonly found in rocks derived from regional metamorphism of Ca-poor and Fe- and Mg-rich protoliths, such as Guyang and Huoqiu iron formations.

Stilpnomelane is the most common iron silicate within the BIF (Fig. 5.3e). This mineral ranges in length from 0.05 to 0.2 mm and forms thin, continuous laminations or very fine-grained sheaves and needles in iron-poor microbands. It is closely associated with quartz, magnetite, and ankerite.

Ankerite and ferroan dolomite occur in many quartz layers typically as coarse, euhedral rhombs that overgrow and contain inclusions of quartz, hematite, magnetite, and Fe-silicate minerals, indicating that these carbonates were among the last minerals to form (Fig. 5.3f).

Actinolite is often completely or partially replaced by chlorite and/or mica (Fig. 5.3g).

Grunerite or cummingtonite occurs locally. In the Waitoushan BIF, it is intergrown with actinolite, but in the Yanqianshan BIF, it occurs as small needles intergrown with quartz.

Trace minerals include pyrite, apatite, monazite, xenotime, zircon, ilmenite, and K-feldspar.

Representative mineral assemblages in BIF are quartz-magnetite-tremolite, quartz-megnetite-grunerite, and magnetite-actinolite-carbonate ± stilpnomelane.

The main minerals now present in BIFs (e.g., quartz, hematite, magnetite, carbonates, and ferrous silicates) in NCC are actually of secondary origin. A diagram showing relative mineral stabilities in BIF, ranging from low to high metamorphic grade is given in Fig. 5.4.

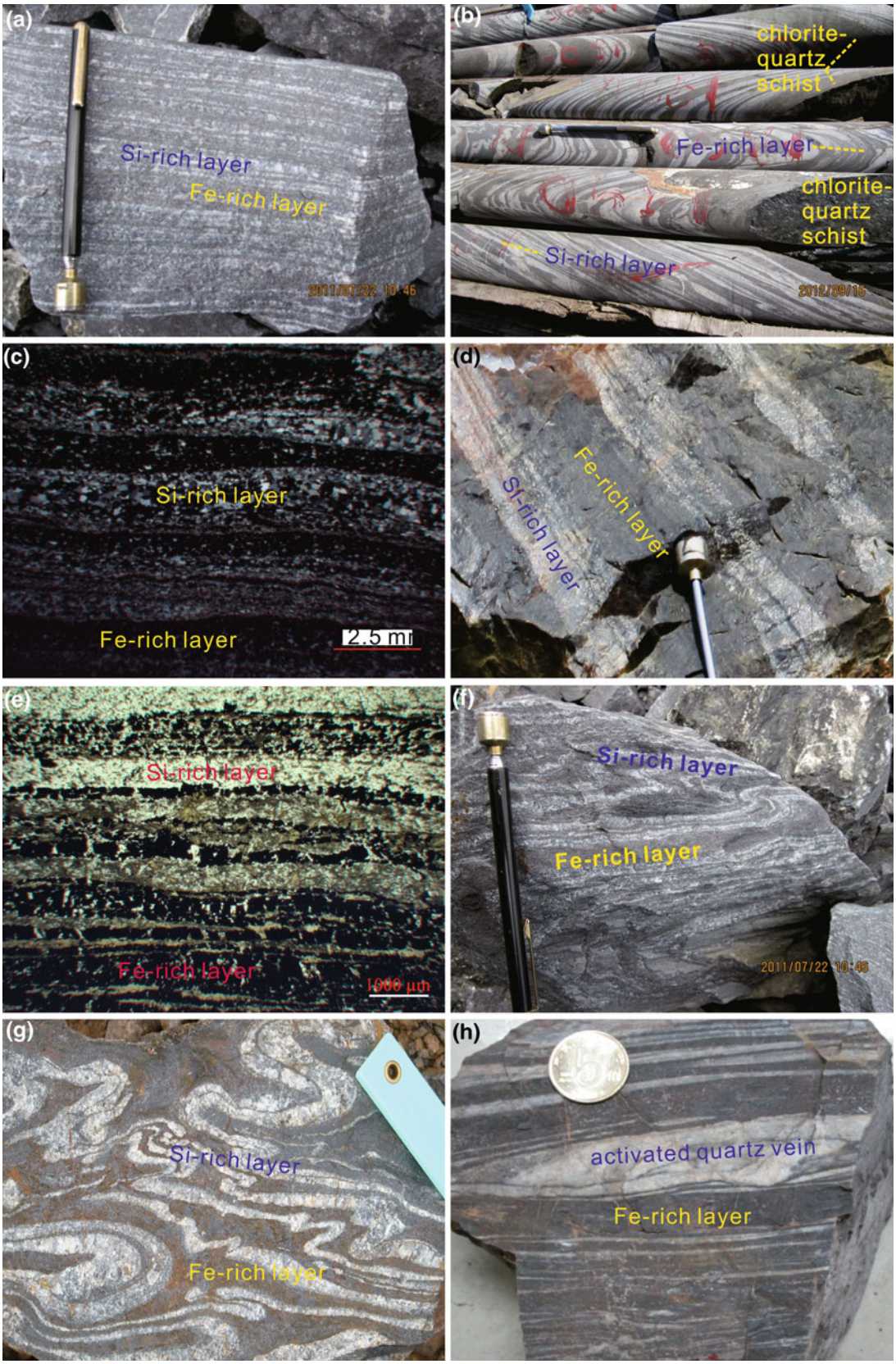

Fig. 5.2 Photomicrographs and field photos showing representative textures of BIFs from the NCC. **a** Alternating Fe-rich and Si-rich microlayers from Waitoushan BIF of Anben area; **b** alternating Fe-rich and Si-rich microbands with chlorite-quartz schist interbed from Chentaigou BIF of Anben area. **c** quartz-rich microbands with scattered crystals of dusty magnetite and magnetite-rich microbands with scattered quartz from Nanfen BIF of Anben area; **d** thick alternating Fe-rich and Si-rich microbands from Sanheming BIF of Guyang area; **e** alternating Fe-rich and Si-rich microbands from Sanheming BIF of Guyang area; **f** wrinkling deformationfrom Nanfen BIF of Anben area; **g** wrinkling deformation from Sijiaying BIF of E. Hebei; **h** activated quartz vein from W. Anshan BIF of Anben area

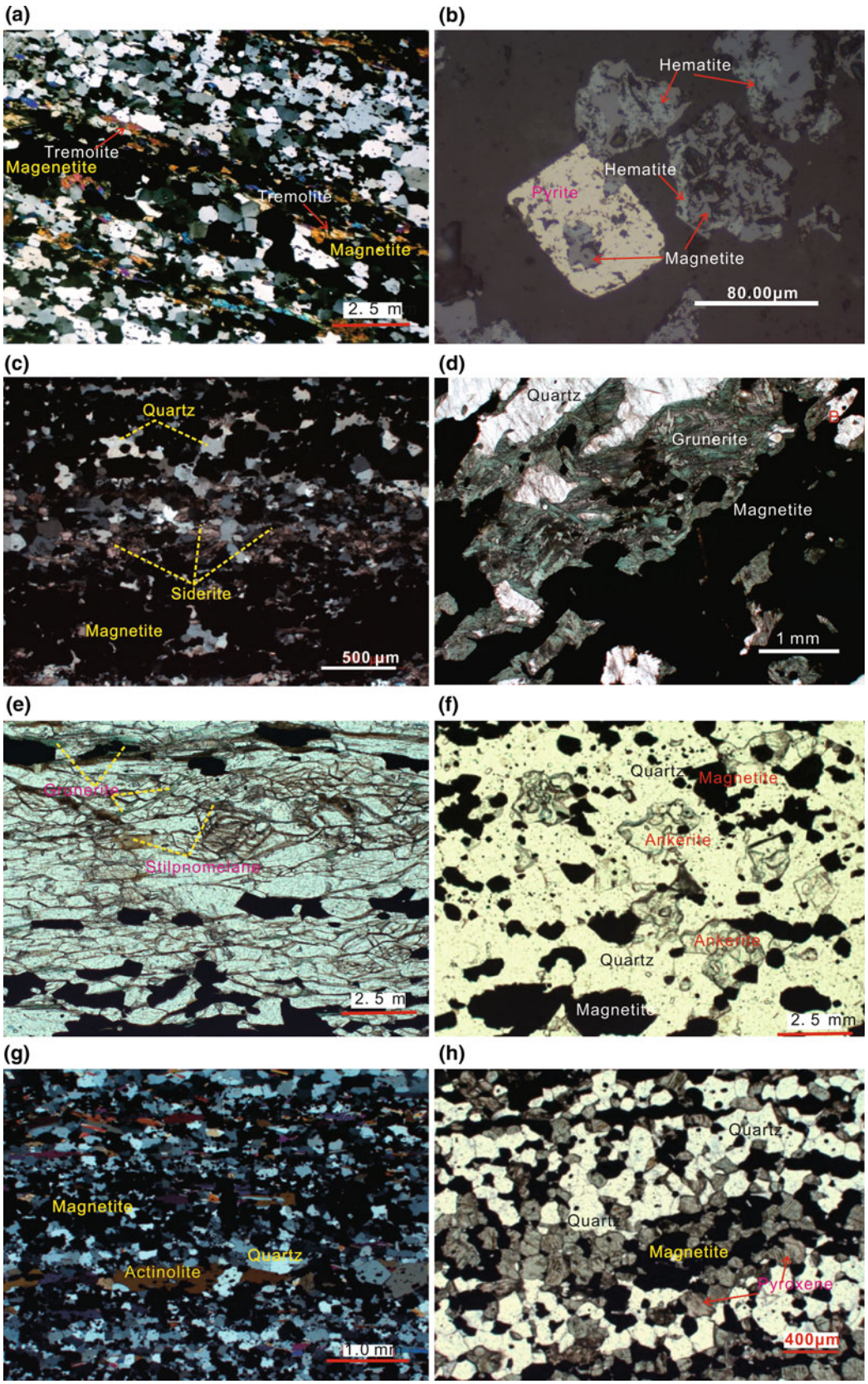

Fig. 5.3 Photomicrographs showing composition of BIFs from the NCC. **a** Quartz-magnetite-tremolite assemblages in E. Anshan BIF; **b** pyrite granules containing magnetite inclusions and the edge of magnetite granules are replaced by hematite in Dagushan BIF; **c** quartz-magnetite-siderite assemblages in Dagushan BIF; **d** quartz-magnetite-grunerite assemblages in Gongyiming BIF; **e** remnant stilpnomelane granules locally in quartz-rich microbands in Dataigou BIF; **f** quartz-magnetite-Ankerite assemblages in Dataigou BIF; **g** quartz-magnetite-actinolite assemblages in Nanfen BIF; **h** quartz-megnetite-pyroxene assemblages in Gongyiming BIF

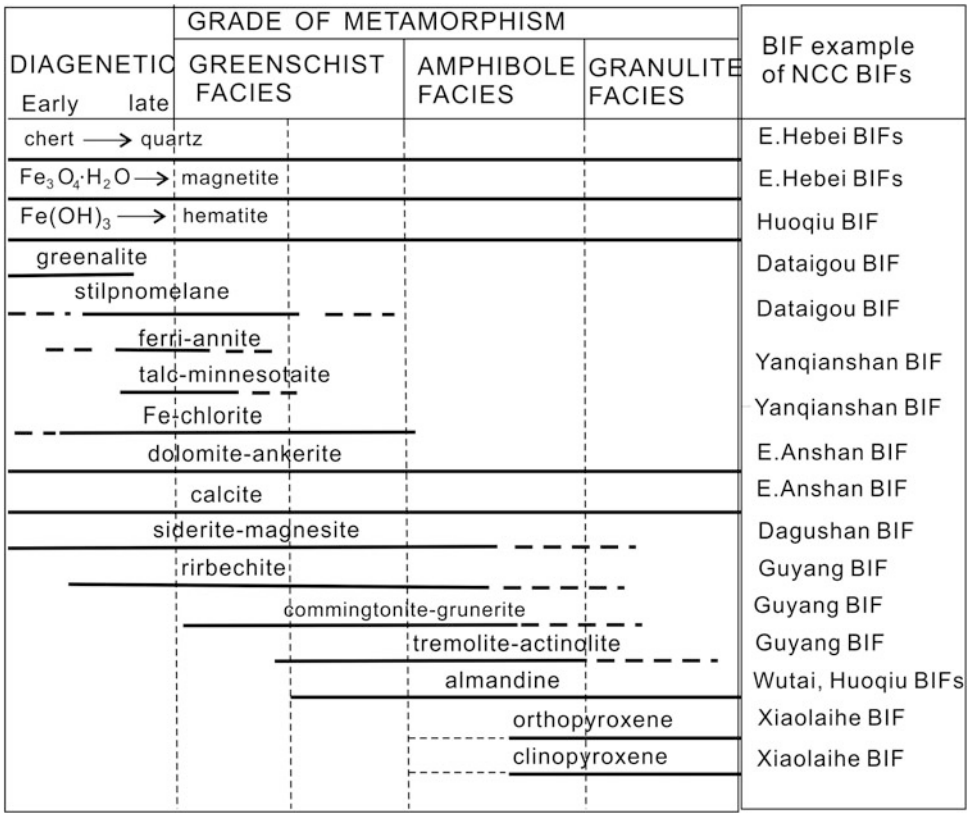

Fig. 5.4 Relative stabilities of minerals in NCC metamorphosed iron formations as a function of metamorphic zones (modified from Klein 2005)

The BIFs in NCC underwent metamorphism of greenschist to lower amphibolite facies (i.e., E. Anshan, W. Anshan, Yanqianshan BIFs), amphibolite facies (i.e., Qidashan, Waitoushan, Nanfen, Shirengou, Sijiaying BIFs) and granulite facies (i.e., Xiaolaihe, Fig. 5.3h, Shuichang, Xingshan BIFs). Sometimes, some BIFs display shear metamorphic deformation and migmatization features, in which high-grade ores formed in local sections.

5.3 Ages and Geochemistry of the Neoarchean BIFs in NCC

5.3.1 Ages of BIF

Precise and accurate constraints at the timing of volcanic and metamorphic events are critical for the deposition of iron formation and subsequent metamorphism. Zircon is an ideal mineral to date the timing of high-grade metamorphism because it can recrystallize or grow a new as single grains or overgrowth rims around preexisting zircon cores during metamorphism (Vavra et al. 1999; Harley et al. 2007). Metamorphic zircons are commonly internally homogeneous, with very low Th/U ratios and high $\delta^{18}O$ values, which are distinct from magmatic zircons that are generally characterized by magmatic oscillatory zoning, variable luminescence and relatively high Th/U ratios and low $\delta^{18}O$ values (Hoskin and Schaltegger 2003; Harley et al. 2007; Rubatto and Hermann 2007).

Zhang et al. (2012a, b) provided data of SIMS zircon U–Pb and oxygen isotopes for the Shirengou BIF iron deposit. The zircon U–Pb age and oxygen isotope results show: (i) igneous zircons from two samples of plagioclase amphibolite and hornblende plagiogneiss have U–Pb ages of 2541 ± 21 and 2553 ± 31 Ma, respectively, suggesting a Neoarchean age for the volcanic protolith. Because the Shirengou BIF is an Algoma-type deposit, the U–Pb age (2541–2553 Ma) for zircons from intercalated volcanic rocks can constrain the depositional age of the BIF. (ii) Metamorphic overgrowth zircons from amphibolite and gneiss show two U–Pb ages of 2510 ± 21 and 2512 ± 13 Ma, respectively, corresponding to the Neoarchean matemorphism. (iii) The igneous zircons have $\delta^{18}O$ values of 5.9–7.6 ‰, whereas, the zircons with $\delta^{18}O$ values of 6.8–9.9 ‰, suggest that exotic high $\delta^{18}O$ fluids were involved during metamorphism.

Based on photomicrographs of zircon CL images, U–Pb ages and $\delta^{18}O$ values, Zhang et al. (2012a, b) grouped zircons into three types (Fig. 5.5). Type 1 exhibits a clear oscillatory zoning in core with a weak rim (Fig. 5.5a, d). The oscillatory zoning, high luminescence, and high Th/U ratios (>0.4) are typical of magma origin. The $^{207}Pb/^{206}Pb$ ages of

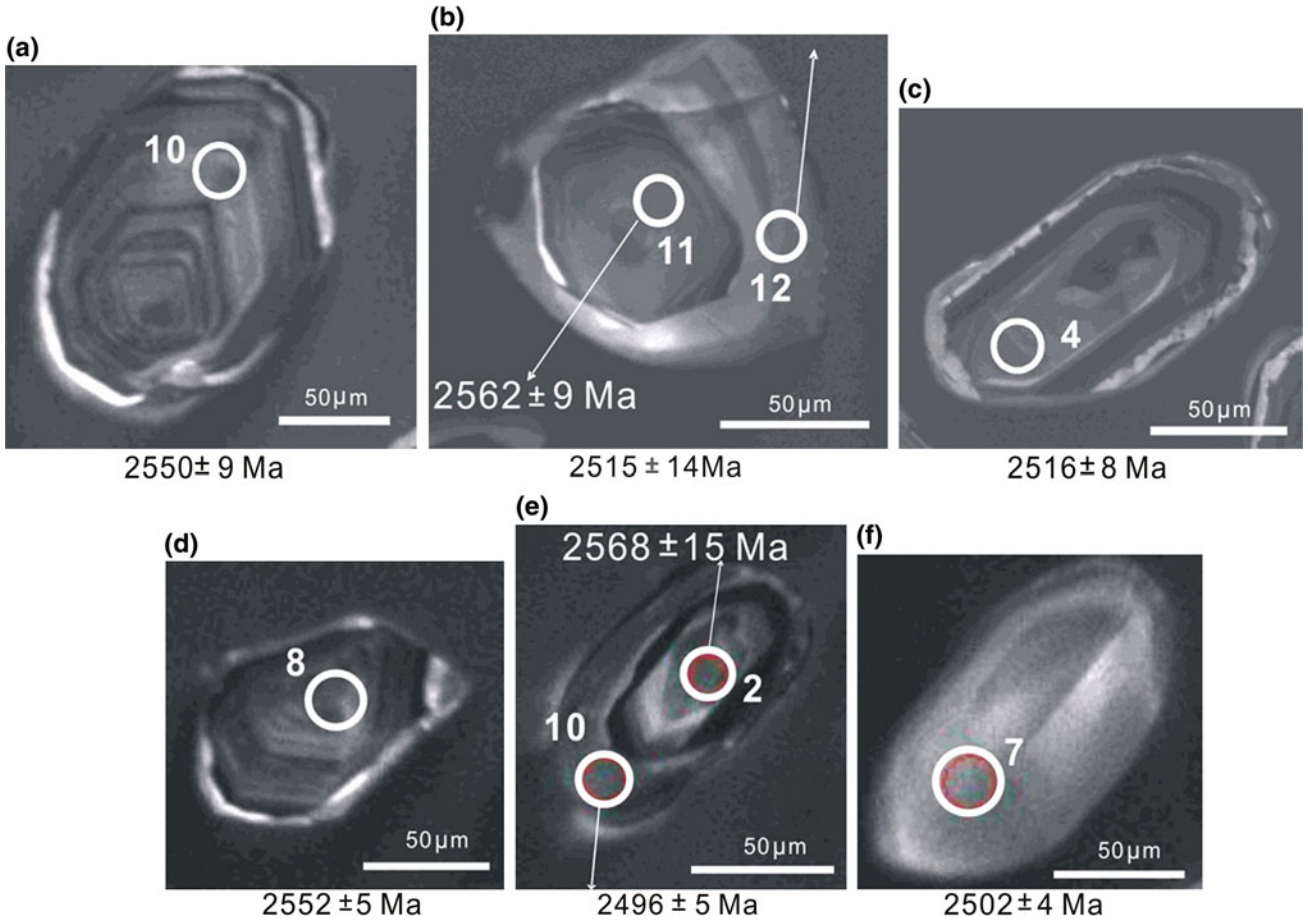

Fig. 5.5 CL images of magmatic zircon cores and metamorphic rims form core-rim texture, in the Shirengou ore area of the NCC. **a**, **b** and **c** are CL images of zircons from sample SRG-1, respectively; **d**, **e**, and **f** are CL images of zircons from sample SRG-2, respectively (Zhang et al. 2012a, b)

Type 1 zircons range from 2550 to 2552 Ma. Type 2 exhibits a clear core and rim, and both the core and rim show sector zoning and are highly luminescent in CL images (Fig. 5.5b, e), also with Th/U ratios lower than 0.2 for rim and higher than 0.4 for core, suggesting a metamorphic and magmatic origin, respectively. The cores yield $^{207}Pb/^{206}Pb$ ages of 2568–2562 Ma and the rims give $^{207}Pb/^{206}Pb$ ages of 2515–2496 Ma. Type 3 are light brown and nearly spherical (Fig. 5.5c, f). The weak sector zoning, high luminescence and low Th/U ratios (<0.2) are typical of metamorphic origin. The $^{207}Pb/^{206}Pb$ ages of Type 3 zircons range from 2516 to 2502 Ma.

In recent years, large amounts of zircon U–Pb ages of metavolcanic rocks associated with the Algoma-type BIFs in NCC have been obtained in order to constrain the formation age of the BIFs (Table 5.2), i.e., 2547 Ma of Shuichang BIF (Zhang et al. 2011), 2520–2600 Ma of Sijiaying BIF (Cui et al. 2014), 2552 Ma of Nanfen (Zhu et al. 2015a, b), 2533 Ma of Waitoushan BIF (Dai et al. 2012), 2528 Ma of Gongchangling BIF (Wan et al. 2012a, b), 2551 Ma of Chentaigou BIF (Dai et al. 2013), 2522 Ma of Jining BIF (Wan et al. 2012a, b), 2562 Ma of Sanheming BIF in the Guyang area (Liu et al. 2014), and 2543 Ma of Wutai BIF (Wang et al. 2014a). The metamorphic or hydrothermal events have been recognized in some BIFs in the NCC, such as the Gongchangling iron deposit, Li et al. (2014) have recognized a ~1840 Ma hydrothermal event based on the SHRIMP zircon U–Pb age of the garnet-rich altered rocks. Moreover, a ~2.50 Ga metamorphic event has been widely identified in some BIFs, e.g., the Nanfen, Shuichang and Xiaolaihe BIFs. Actually, in the NCC, most BIFs formed in the late Neoarchean with a peak at 2.52–2.48 Ga. Table 5.2 show formational and metamorphic ages of major Archean BIF-hosting rocks in the NCC. It shows that formation ages of BIFs in NCC cover a wide range from Mesoarchean to early Paleoproterozoic, among which the late Neoarchean (2.6–2.50 Ga) is the peak period (Fig. 5.6).

Table 5.2 Ages of major Neoarchean BIF-hosting rocks in the NCC

Area	BIF	Dated sample	Method	Formation age (Ma)	Metamorphic ages (Ma)	Reference
Anshan-Benxin, Liaoning Province	Dagushan	Chlorite-quartz schist	SIMS	3110 ± 32		Dai et al. (2014)
	Chentaigou	Chlorite-quartz schist	LA-ICP-MS	2551 ± 10	2469 ± 23	Dai et al. (2013)
	Nanfen	Chlorite-amphibole schist	LA-ICP-MS	2554 ± 14	2484 ± 12	Zhu et al. (2015a, b)
	Nanfen	Magnetite quartzite	LA-ICP-MS		2480 ± 63	Zhu et al. (2015a, b)
	Waitoushan	Plagioclase amphibolite	SIMS	2533 ± 11		Dai et al. (2012)
	Qidashan	Biotite leptynite	Dilute method	2533 ± 53		Wang and Zhang (1995)
	Qidashan	Biotite-chlorite-quartz schist	SHRIMP	2530 ± 6		Yang (2013)
	Qidashan	Amphibole leptynite	SHRIMP	2528 ± 10		Wan et al. (2012a, b)
	E.Anshan	Biotite-chlorite-quartz schist	SHRIMP	2544 ± 8		Yang et al. (2013)
	Gongchangling	Amphibole leptynite	SHRIMP	2528 ± 10		Wan et al. (2012a, b)
	Gongchangling	Garnet altered rock	SHRIMP		1861 ± 25	Liu (2013)
Qingyuan	Xiaolaihe	Amphibole leptynite	SHRIMP		2515 ± 6	Wan et al. (2005)
	Hongtoushan	Amphibolite gneiss	SIMS	2571 ± 10		Zhu et al. (2015a, b)
Luxi	Jining	Metavolcanics	SHRIMP	2522 ± 7		Wan et al. (2012a, b)
	Hanwang	Biotite leptynite	SHRIMP	2520		Wan et al. (2012a, b)
	Changyi	Biotite plagioclase leptynite	SHRIMP	2726	1839	Wang et al. (2015d)
E. Hebei	Xingshan	Plagioclase amphibolite	SIMS	2800/2500	2500	Zheng et al. (2015)
	Wangsiyu	Biotite plagioclase gneiss	LA-ICP-MS	2516 ± 9		Qu et al. (2013)
	Shirengou	Amphibole-plagioclase gneiss	SIMS	2541 ± 21	2512 ± 13	Zhang et al. (2012a, b)
		plagioclase amphibolite	SIMS	2553 ± 31	2510 ± 21	
	Shuichang	Plagioclase amphibole gneiss	SIMS	2547 ± 7	2513 ± 4	Zhang et al. (2011)
	Sijiaying	Biotite leptynite	SHRIMP	2534 ± 8		Nutman et al. (2011)
		Biotite leptynite	SIMS	2537 ± 13		Cui et al. (2014)
		Biotite plagioclase gneiss	SIMS	2543 ± 14		Cui et al. (2014)
	Zhoutaizi	Plagioclase amphibolite	SIMS	2512 ± 21		Xiang et al. (2012)
	Zhuzhangzi	Metavolcanics	SHRIMP	2516 ± 8		Wan et al. (2012a, b)
Guyang, Inner Mongolia	Sanheming	Plagioclase amphibolite	SIMS	2562 ± 14		Liu et al. (2014)
	Gongyiming	Plagioclase amphibolite	SIMS	2569 ± 78		Liu et al. (2014)
Wutai, Shanxi Province	Wangjiazhuang	Plagioclase amphibolite	SIMS	2543 ± 4		Wang et al. (2014a)
	Wutai	Plagioclase amphibolite	SHRIMP	2528 ± 6		Wilde et al. (2004)

5.3.2 Major Elements

In this paper, we report average contents of major elements for the NCC BIFs including BIFs in the Anshan-Benxi, E. Hebei, Wutai, Huoqiu, and Guyang areas. The results show that the BIFs are mostly composed of SiO_2 + $Fe_2O_3^T$ (the average content of 91–93 %). The average concentrations of MgO and CaO are 1.95 and 1.95 %, respectively. The contents of Al_2O_3, TiO_2, K_2O, Na_2O, MnO, and P_2O_5 are very low, indicating that BIFs are typical chemical sedimentary rocks, the protolith of BIFs are colloid composed of silicious, iron and small amounts of carbonate mud; Both Al_2O_3 and TiO_2 simultaneously increase in the studied BIFs, suggesting that these chemical sediments incorporate minor

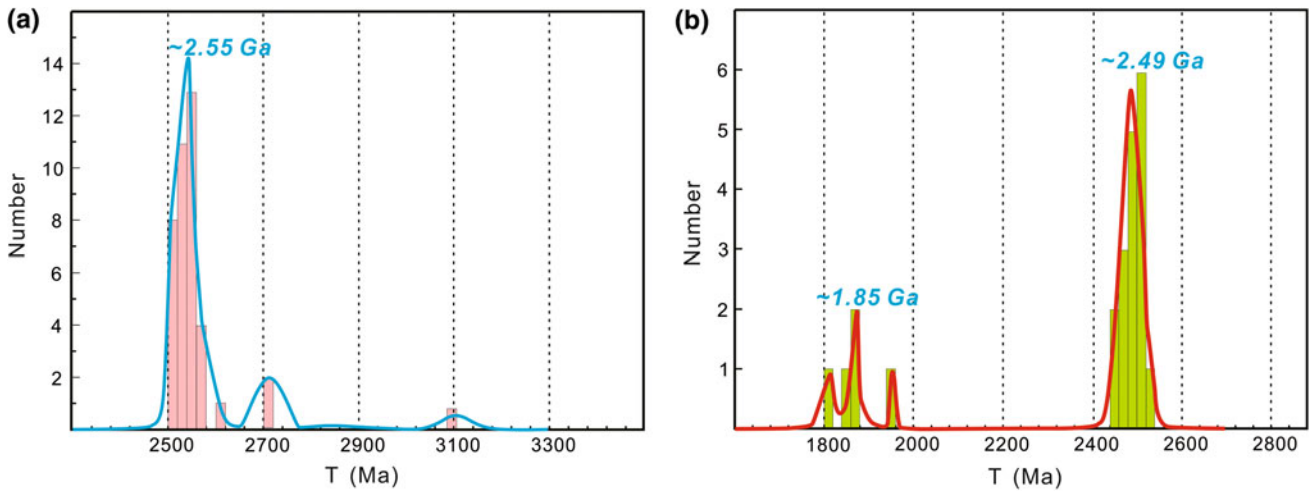

Fig. 5.6 The statistical charts of U–Pb ages of magmatic (**a**) and metamorphic (**b**) zircons from BIF-associated rocks in the NCC

Table 5.3 Average contents of major elements (wt%) in NCC BIFs

Area (BIF)	SiO_2	$Fe_2O_3^T$	FeO	Al_2O_3	CaO	MgO	K_2O	Na_2O	MnO	TiO_2	P_2O_5
An-ben	50.83	42.33	14.97	0.85	1.98	1.85	0.08	0.09	0.09	0.05	0.11
E.Hebei	48.84	42.11	14.90	1.82	2.12	2.76	0.34	0.16	0.11	0.12	0.22
Wutai	50.13	42.68	18.10	1.09	2.82	1.72	0.06	0.05	0.13	0.03	0.04
Guyang	56.81	40.12	15.80	0.42	1.21	1.32	0.96	0.05	0.06	0.02	0.14
Huoqiu	45.30	48.12		1.81	1.62	2.11	0.20	0.09	0.07	0.10	0.05
Algoma	48.90	38.2	13.30	3.7	1.89	2.0	0.62	0.43			0.23
Superior	47.10	39.1	10.90	1.5	2.24	1.93	0.1	0.13			0.08

Notes Guyang from Liu et al. (2014), Wutai from Wang et al. (2014), Huoqiu from Huang (2014), Anben and E. Hebei from Yao et al. (2014), Algoma and Superior from Gross and Mcleod (1980)

detrital components. In E. Hebei BIFs, this correlation is more obvious, and major element concentrations are higher than that of BIFs in the Anshan-Benxi area except for $SiO_2 + Fe_2O_3^T$, suggesting that E. Hebei BIFs have more detrital material input. The average major oxide contents of BIFs under different grade metamorphism conditions, from greenschist to granulite facies, are very similar, these suggest that metamorphic reaction is essentially isochemical. The Na_2O/K_2O values of BIFs in Anshan-Benxi area and E. Hebei, Wutai, Guyang and Huoqiu area are different. Combined with their geological characteristics, these likely indicate that material sources of Anshan-benxi BIFs are different from that of other BIFs in NCC (Table 5.3).

5.3.3 Trace Elements

Rare earth element (REE) pattern is generally regarded as a valid method to understand relevant formation conditions of BIFs (Bau and Dulski 1996; Alexander et al. 2008). There are two main objectives in REE study of BIFs: (1) tracing Fe sources; and (2) using the redox-dependent properties of REE to decipher oxidation mechanisms for iron deposition. Although the REE data for the NCC BIFs are also quite variable, all the REE data for the Anshan-Benxi, Eastern Hebei, and Wutai BIFs normalized to the Post-Archean Australian Shale (PAAS) values (McLennan 1989), are characterized by mild to strong HREE enrichment relative to LREE and distinctly positive Eu anomalies ($Eu/Eu^* = 1.37–6.68$) (Fig. 5.7).

Compared to the E. Hebei BIFs, the Anshan-Benxi BIFs have more hydrothermal contribution. Although the Ce/Ce* ratios are lower (0.77–1.09), the lack of true negative Ce anomalies in all samples indicates that Anshan-Benxi BIFs were formed in an anoxic ocean. Moreover, a large range of REE contents, Eu and Y anomalies, and Y/Ho ratios suggests a significant detrital input into the Anshan-Benxi BIFs during deposition. The variation range of positive Eu and Y anomalies in the E. Hebei BIFs is not greater than that of the Anshan-Benxi BIFs. In addition, Y/Ho values of the Anben

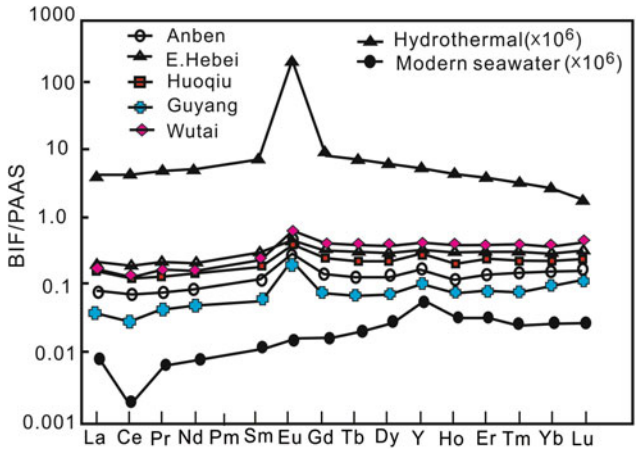

Fig. 5.7 Post-Archean Australian shale (PAAS)-normalized REY distributions of average BIFs from the NCC, average high-temperature (>350 °C) hydrothermal fluids ($\times 10^6$), average Modern seawater ($\times 10^6$) [seawater and high-temperature hydrothermal after Robert and Ali (2007); Anben and E. Hebei BIFs after Yao et al. (2014); Guyang BIFs after Liu et al. (2014); Huoqiu BIFs after Huang (2014); Wutai BIFs after Wang et al. (2014a)]

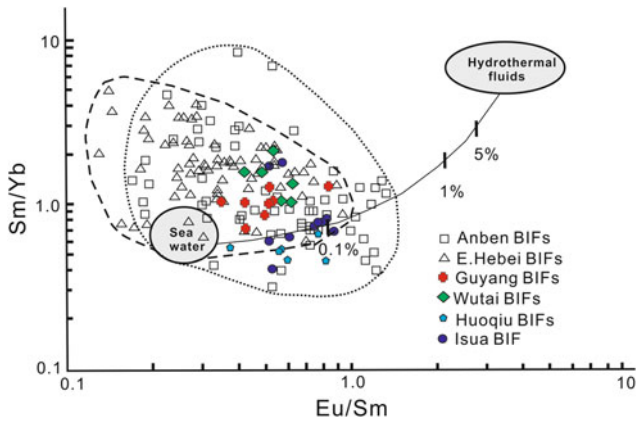

Fig. 5.8 The two-component conservative mixing lines of Sm/Yb versus Eu/Sm rations [modified from Alexander et al. (2008), Mloszewska et al. (2012)]. Isua BIFs after Bolhar et al. (2004); high-temperature (>350 °C) hydrothermal fluids after Bau and Dulski (1999); Pacific seawater after Alibo and Nozaki (1999); E. Hebei and Anben BIFs after Yao et al. (2014), Dai et al. 2014); Guyang BIFs after Liu et al. (2014); Huoqiu BIFs after Huang (2014); Wutai BIFs after Wang et al. (2014a)

BIFs vary from 20 to 80. BIF Sm/Yb–Eu/Sm mixing discrimination diagram display a mixing genesis of high-T hydrothermal fluids and seawater (Fig. 5.8).

All the BIF samples from different deposits have very low contents of sulfur (from 0.04 to 0.5 %, generally <0.2) and CO_2 (except for some carbonate-bearing samples). The Cu, Pb, Zn, Mn, Ni, P, Ti, V, and Cr contents are also very low or absent in magnetite.

5.3.4 Fe and Nd Isotopes

A number of recent iron isotope studies of BIFs have been conducted in order to track the biogeochemical cycling and redox conditions in early Earth. Importantly, iron isotope work has bolstered evidence for a rain of ferric oxyhydroxides during BIF deposition, for early diagenetic microbial iron cycling, and for a hydrothermal iron source for BIFs (e.g., Anbar and Rouxel 2007; Heimann et al. 2010; Planavsky et al. 2012). Iron isotopes are typically reported as δ^{56}Fe values with a range of 5 ‰ in nature. In general, the largest iron isotope fractionations occur during redox reactions. For instance, during Fe(III) reduction and Fe(II) oxidation, there is ~1.5‰ fractionation. Bekker et al. (2013) collected 490 δ^{56}Fe values of BIFs (Fig. 5.9). It include 83 data points for the ~1.88 Ga GIF from the Animikie basin, North America, 138 data points for the ~2.5 Ga Brockman Iron Formation, Western Australia, 58 data points for the ~2.5 Ga Transvaal Supergroup BIF, South Africa, 27 data points for the ~2.7 Ga Shurugwi and Belingwe greenstone belts BIF, Zimbabwe, 137 data points for the Eoarchean Isua, Akilia, and Innersuartuut BIF and metamorphic rocks, 12 data points for the Neoproterozoic Rapitan IF, 52 data points for IF and Mn formations from the Paleoproterozoic Hotazel Formation, Transvaal Supergroup, South Africa, and 45 data points for other Paleoproterozoic and Archean IFs.

Based on Bekker et al. (2013), we collected δ^{56}Fe values of NCC BIFs (Fig. 5.9). The δ^{56}Fe values of the Anben and Guyang BIFs are 0.43–1.88 ‰ and 0.2–1.0 ‰, respectively, indicating that all Neoarchean BIFs have consistently positive δ^{56}Fe values. These suggest that ancient ocean is under anoxia and reduced condition during BIF deposition.

It is worth noting that the δ^{56}Fe values of Paleoproterozoic Yuanjiacun BIF is similar to those of Neoarchean BIFs in NCC, which suggest that Yuanjiacun BIF was also formed in anoxia environment below chemocline, although the Proterozoic ocean was redox-stratified, from oxic shallow waters to deeper anoxic waters.

Whether or not components of the BIFs were derived from continental sources, or had its origin in hydrothermal alteration of the oceanic crust has been a long-standing debate. Neodymium (Nd) isotopes have been used to successfully trace the continental versus hydrothermal input to the BIFs (Beukes and Gutzmer 2008). Wang et al. (2015d) collected Neodymium isotopic signatures of the Archean and Paleoproterozoic BIFs older than 1.8 Ga (Fig. 5.10). It is shown that the BIFs older than 1.84 Ga have $\varepsilon_{Nd}(t)$ values between −5 and +5, with much of the data describing the Archean BIFs. Many BIFs, with ages of 2.3–3.7 Ga, have predominantly positive $\varepsilon_{Nd}(t)$ values, suggesting that hydrothermal alteration of oceanic crust dominates the Nd

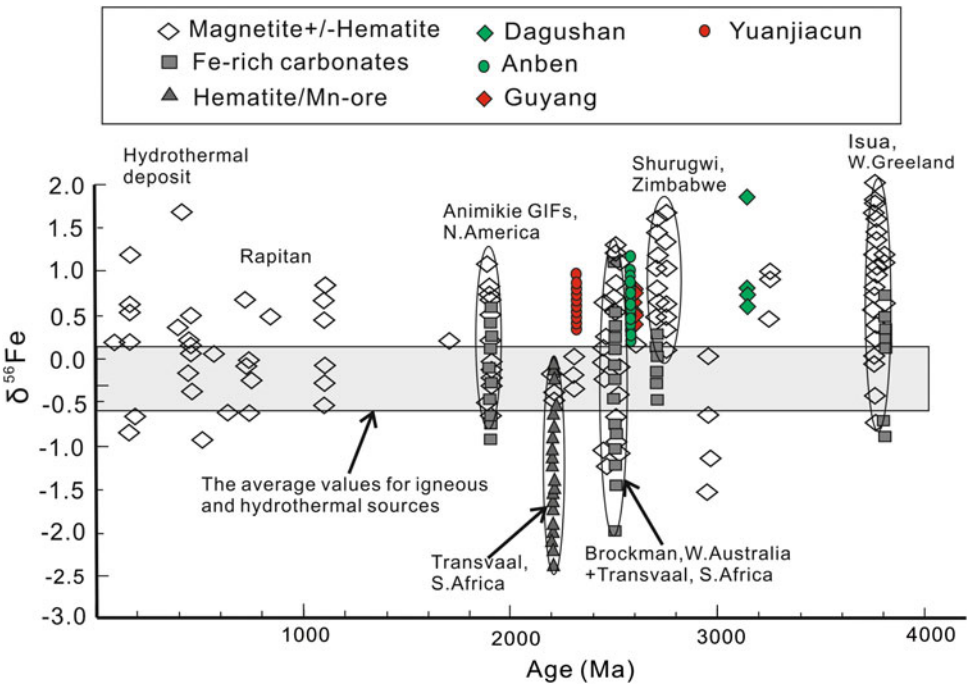

Fig. 5.9 Secular variations in δ^{56}Fe values for Precambrian iron formations (after Bekker et al. 2013). Detailed δ^{56}Fe and age data of the NCC BIFs and relevant references are presented in Li et al. (2008) and Dai (2014). *Gray horizontal bar* represents the average δ^{56}Fe values for igneous rocks and hydrothermal sources. For comparison, iron isotope values of jaspers and iron formations from Phanerozoic hydrothermal deposits are shown

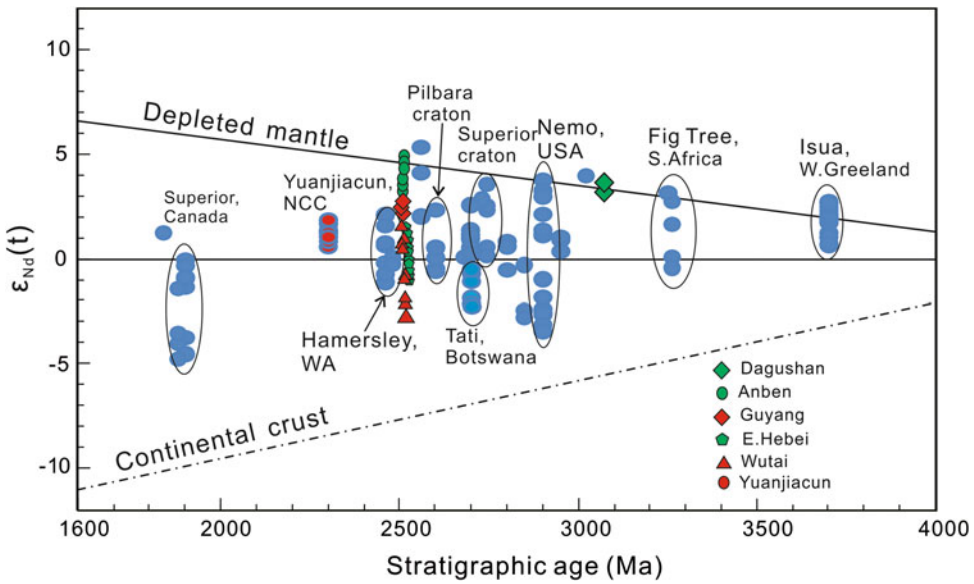

Fig. 5.10 Neodymium isotopic signatures of the Archean and Paleoproterozoic BIFs older than 1.8 Ga (data are screened to distinguish reliable samples which represent the best archives of coeval Precambrian seawater ^{143}Nd/^{144}Nd. Detailed $\varepsilon_{Nd}(t)$ and age data and relevant references are presented in Appendix Table from Wang et al. 2015c)

flux to ancient seawater. The positive, mantle-like $\varepsilon_{Nd}(t)$ values of the BIFs also contrast obviously with the negative, continental-like $\varepsilon_{Nd}(t)$ values of Phanerozoic and modern seawater. Their Nd budget is dominated by weathering of continental silicates and derived riverine inputs into the oceans (Piepgras and Wasserburg 1982).

Here we present neodymium (Nd) isotopic data for the ~3.1 Ga Dagushan BIF and ~2.55 Ga Anshan, E. Hebei and Guangyang BIFs in the NCC (Fig. 5.10). It is shown that the ε_{Nd}(3.1 Ga) values (3.3–4.0) in the Dagushan BIFs and ε_{Nd}(2.55 Ga) values (3.0–4.5) in Anshan-Benxi BIFs are close to those of the coeval depleted mantle, implying that the iron were most likely derived from the leaching of oceanic crust; the ε_{Nd}(2.55 Ga) values (2.89 to −2.58) in the Wutai and E. Hebei BIFs suggest that iron is sourced from mixing oceanic and continental crusts.

5.4 Implications of the NCC BIFs

5.4.1 Tectonic Setting

The metallogeny in Precambrian was closely related to the evolution of the cratons (Zhai 2010). The majority of BIFs in NCC were deposited in arc-related basins at ca. 2.55 Ga (Zhang et al. 2012a, b). As Zhai (2010), Zhai and Santosh (2011) proposed, the Archean basement of the NCC can be divided into seven micro-blocks, which are considered to be amalgamated through arc-arc, arc-continent, and continent-continent collisions during the Late Neoarchean. Although the tectonic style and mechanisms were similar to Phanerozoic plate tectonic regime, the scale was much smaller (Zhai and Santosh 2011). It is noteworthy that the volcanic and hydrothermal activities during the amalgamation process generated abundant Fe and Si in the seawater, which resulted in the BIF deposition in arc-related basins during the quiescence. The tonalite in NCC was emplaced at ~2.56 Ga (Liu et al. 2014). However, previous studies also recognized widespread ~2.5 Ga TTG in the NCC, suggesting that the amalgamations of micro-blocks occurring at the end of the Late Neoarchean were accompanied by extensive intrusions of TTG, which were derived from partial melting of mafic crusts.

Trace element characteristics of the rocks associated with the NCC BIFs, including amphibolites and leptynites, are all consistent with the geochemical signature of subduction zone. Especially the geochemistry of amphibolite samples displays a striking similarity with the normal mid-ocean ridge basalt (N-MORB) and back-arc basin basalt (BABB) (Zhang et al. 2012a, b; Liu et al. 2014; Wang et al. 2014a). Collectively, these features are more likely to reflect an interaction between depleted mantle-derive (MORB-like) and subduction zone-derived melts or fluids. On the Th/Yb versus Nb/Yb and Zr versus Ti discrimination plots (Pearce et al. 1982), amphibolite samples plot are close to or in the field of N-MORB and volcanic-arc basalt, also indicating their geochemical affinity with both MORB- and arc-like components. Thus, a back-arc basin setting is the most possible tectonic setting for the NCC BIFs (Zhang et al. 2012a, b; Dai et al. 2012; Wang et al. 2014a).

Nearly all of Archean BIF-bearing greenstone belt terranes worldwide are formed in a convergent margin supra-subduction zone. Moreover, plume-arc interactions are also responsible for formations of some greenstone belts such as the Abitibi and Pickle Lake greenstone belts. In China, typical greenstone belts, for example, the Wutai, Guyang and Qingyuan greenstone belts, have similar ages (~2.55 Ga) and inferred geodynamic settings (arc/back-arc basins) with that of most BIFs in the NCC (Zhang et al. 2012a, b).

In Anshan-Benxi area, geochemical analyses show that the Dagushan and Chentaigou wall rocks have the characteristics of arc volcanics, while the Nanfen and Waitoushan rocks are similar to the back-arc basin basalts (Dai et al. 2014). So, the BIFs in the Anshan-Benxi area were deposited in the volcanic-arc setting. Moreover, the BIFs in the NCC show a planar distribution, suggesting that there were probably many oceans and volcanic arcs in the Neoarchean. Hf isotopic analyses also indicate that the zircons in the rocks have peaks of T_{DM2} at ~3.40 and ~2.85 Ga, while the $\varepsilon_{Hf}(t)$ values of some ~3.10 and ~2.55 Ga zircons are equal to those of the coeval depleted mantle. Nd isotopic analyses show that the $\varepsilon_{Nd}(t)$ values of wall rocks are close to the depleted mantle. Combining with the previous studies, we propose that: (1) enormous Fe and anoxic environment during the BIF deposition processes were probably associated with igneous activities; and (2) the Archean crustal growth of the NCC are most likely episodic which mainly occurred during 2.8–2.7 Ga, and the ~2.55 Ga magmatism resulted from the reworking of ~2.85 Ga ancient crust with a few signatures of continental crustal growth.

5.4.2 Formation Conditions and Sources

All the Neoarchean BIFs consist predominantly of alternating iron-rich and silica-rich layers and were generally deposited in relatively deep-water environments with the absence of indications for wave or storm effects. The alternating magnetite-rich and quartz-rich bands in the NCC BIFs reflect stable basin conditions, and their precipitation may occur below storm-wave base, about 200 m, which is the average depth of modern storm-wave base (Klein 2005). Large amounts of geochemical studies on BIFs in the NCC indicate that these BIFs lack apparent Ce anomaly and have positive iron isotope values, which suggest that these iron deposits formed in low-oxygen or anoxic environments. The positive Eu anomaly may infer that these BIFs have the same features with high-temperature fluids. A possible mechanism may be that some elements such as iron and silica were leached from newly formed mafic-ultramafic oceanic crust by the convective circulation of seawater, then they precipitated in the ocean floor due to changes of physico-chemical conditions. The periodicity and magnitude of hydrothermal fluids may lead to the varved microbands of BIFs.

Zhai (1993) proposed that the BIFs in the NCC formed in a weakly oxidized shallow sea environment with a pH value of 6–8 and an Eh value of 0–0.3, and with the depth of precipitation estimated as about 244–549 m at a distance away from the shoreline of about 37 km (Goodwin 1973; Zhai 1993). In terms of regional geology, lithologic association and geochemical features of the associated metavol-

canics and orthogneisses, Zhai and Windley (1990) proposed that the high-grade metamorphosed BIFs formed initially in an arc-related environment, which were intruded by voluminous tonalities and granodiorites. These granitoids were later converted into orthogneisses by subsequent deformation and high-grade metamorphism. The greenstone-type BIFs were likely formed in a geological environment, most likely in rifts or back-arc basins and arcs.

It is generally accepted that the accumulation of large masses of iron requires three conditions: (1) a stable reservoir; (2) a large supply of Fe; (3) low sulfur and oxygen fugacity (Bekker et al. 2010; Li et al. 2010). Algoma-type BIFs are often restricted in the Archean greenstone belt, and associated with volcanics, also spanning a wide range of petrologies from ultramafic to felsic. The BIFs in the NCC are interlayered with meta-basalts (amphibolites and greenschists), which represent distinct volcanic successions, from mafic to felsic and clastic rocks. These BIFs represent relatively slow sedimentation over substantial time periods, during which there was no volcanism. Thus, a genetic relationship between the greenstone belt and the BIFs can be inferred. Based on geochemistry of the NCC BIFs, there are three contrasting REE sources: continental weathering, seawater, and high-T hydrothermal fluids. Iron was introduced to the seawater through high-T water–rock exchange (Isley and Abbott 1999) or anoxic weathering processes (Rye and Holland 2000) over a certain period of time, ultimately resulting in the formation of a ferrous ocean. Along with appearance of the ~2.55 Ga greenstone belts, vigorous hydrothermal activity associated with enhanced submarine volcanism, especially mafic volcanic eruption, would leach silica and iron out of underlying basalt and komatiites in the ocean floor, and mixed with ferrous seawater subsequently. It is worth noting that underlying ultramafic-mafic volcanics, as parts of oceanic crust, are not volcanics in the greenstone belts. In other words, volcanics in the NCC greenstone belts cannot be regarded as an essential source of the BIFs or with little contribution to the BIFs.

The NCC greenstone belts have been inferred forming in a convergent margin supra subduction zone, back-arc basins can be stable sites for the deposition of the BIFs. Recently, the most sensible Fe(II) oxidizing mechanism of the Archean BIFs could have been metabolic Fe oxidation under very low levels of free oxygen based on a theoretical model (Konhauser et al. 2002), REY compositions of the BIFs (Planavsky et al. 2010), and mineral ecophysiological data (Li et al. 2011). Episodic Fe delivery to the oceans from hydrothermal fluids during peaks in submarine volcanic activity and stable basinal conditions could, therefore, have had dramatic impacts on ocean productivity and ecosystem structure, resulting in the formation of the NCC BIFs.

The concentrations of Al_2O_3 and TiO_2 can measure the degree of detrital contribution. Dai et al. (2014b) considered that Nanfen quartz-magnetite BIFs are chemically pure with very low concentrations of Al_2O_3 and TiO_2 (Al_2O_3 + TiO_2 = 0.13–0.77 wt%) and low contents of HFSEs, and there is no correlation between Eu/Eu* ratios and Al_2O_3 contents, suggesting a negligible effect of clastic contamination on Eu anomalies. These geochemical signatures suggest that little crustal materials contributed to the Nanfen BIF during precipitation. The PAAS-normalized REY pattern of the Nanfen BIF display a LREE depletion with positive La and Y anomalies and super chondritic Y/Ho ratios, similar to those of modern seawater (Alibo and Nozaki 1999). Distinctly positive Eu anomalies also exhibited, which is a typical feature of submarine high-T hydrothermal fluids (Bau and Dulski 1999). The SiO_2–Al_2O_3 and (Co + Ni + Cu)—REY diagrams indicates that the Nanfen BIF has a genetic link with submarine hydrothermal activity (Dai et al. 2014b). It is generally assumed that Fe and REEs are not fractionated during transport from exhalative centers (Bekker et al. 2010). Alexander et al. (2008) introduced the Sm/Yb–Eu/Sm diagram to measure the proportion of modern seawater and high-T hydrothermal fluids (Fig. 5.8), which indicates that extremely small amounts of submarine high-T hydrothermal fluids (~0.1 %) are enough to yield prominent positive Eu anomalies in the Nanfen BIF. According to these geochemical features the Nanfen BIFs are considered to be the products of chemical sedimentation from paleo-seawater with significant input of volcanic hydrothermal fluids. Bau and Dulski (1996) suggested the Ce/Ce*–Pr/Pr* diagram to identify true Ce anomalies because positive La anomalies can create 'false' negative Ce anomalies. In this paper, Ce/Ce* was calculated as $Ce/Ce^* = Ce_{PAAS}/(2Pr_{PAAS} - Nd_{PAAS})$ (Bolhar et al. 2004). Based on the results of Dai (2014), it is evident that the Nanfen BIF shows no significantly negative Ce anomalies, suggesting a low atmosphere-hydrosphere redox state during the deposition of the Nanfen BIF.

5.4.3 Deposition Model

A general sketch of a possible depositional model for the NCC BIFs is shown in Fig. 5.11. We propose that the NCC Neoarchean BIFs were deposited in a back-arc or island arc setting related to subduction of an ocean slab.

The Archean anoxia ocean dissolved a mass of Fe^{2+}. Currently, the viewpoints about the iron and silicon sources in ancient ocean are the weathering of basic crust and the basic volcanic-hydrothermal activity. More and more geochemical evidence, such as Eu anomaly, REE anomaly and Nd, and Fe isotopic characteristics tend to support that the main material of BIFs was from the seafloor hydrothermal fluids.

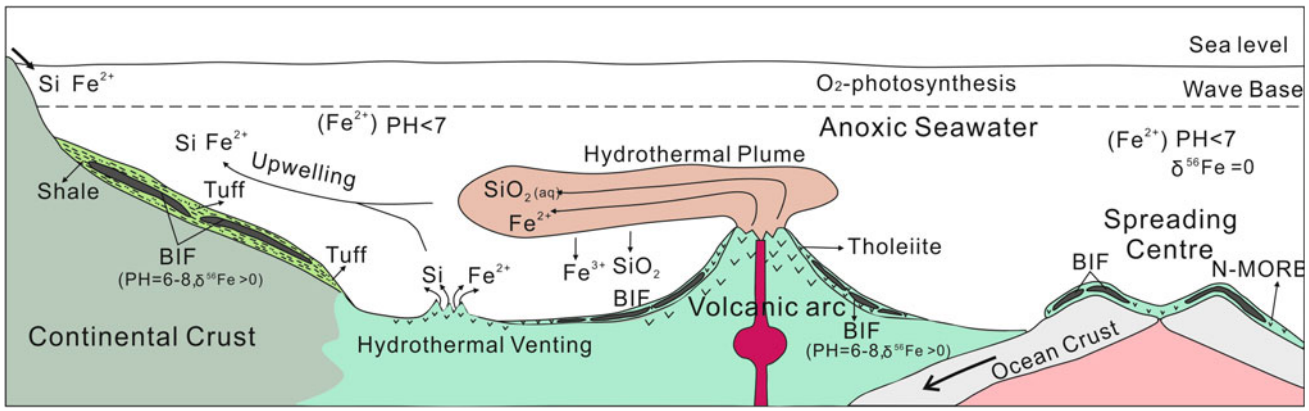

Fig. 5.11 Formation model of late Neoarchean banded iron formations for the NCC

Y/Ho ratio is an important indicator to differentiate the marine sedimentation from the nonmarine sedimentation, research indicates that modern seawater have Y/Ho ratios of 44–74, crust rocks and terrigenous detrital sediments have Y/Ho ratios of 26–28, while the mid-ocean ridge high-T hydrothermal fluids have Y/Ho ratios of 28–30 and high positive Eu anomaly. The late Archean Anshan Algoma-type BIFs in the NCC have Y/Ho ratios of 20–80 (average of 38), showing that the forming materials were supplied from high-T hydrothermal fluids and seawater. Moreover, BIFs with positive Eu, La, Y anomalies, as well as, Sm/Yb–Eu/Sm mixing discrimination diagram display a mixing genesis of high-T hydrothermal fluids and seawater. Positive iron isotopic values and positive correlation between iron isotopic composition and Eu anomaly also support that high-T hydrothermal fluids play an important part in origin for BIFs in NCC.

During the juvenile formation period of the NCC, when significant crustal growth occurred due to the subduction of oceanic plates in the Neoarchean, extensive submarine volcanic and hydrothermal activities close to the arc area supplied large amounts of Fe(II) and other reduced gases like CH_4 into acidic seawater (pH < 7). Mixing of two typical waters resulted in changes of physico-chemical conditions, and then the ferrous iron was oxidized and precipitated as ferric oxyhydroxides. But near to the continental side, precipitation of iron occurred due to upwelling of reducing, slightly acidic, and Fe(II)-rich bottom water into a redoxcline. For instance, the BIF in the Anshan area formed in a back-arc basin close to the continent, and the associated rocks consist predominantly of clastic sedimentary rocks (shale) with less volcanic rocks (Tuff), whereas the BIF in the Benxi area was deposited likely in a back-arc basin near to the arc side or island arc, and the associated rocks are composed of basic volcanics (tholeiite). In some localities (i.e., Waitoushan), these volcanic rocks have geochemical affinities with mid-oceanic ridge basalts (N-MORB), and are suggested to form near the mid-oceanic ridges (Fig. 5.11).

5.5 Summary

On the basis of the presented geological, geochronological, geochemical, and isotopic data of the BIF-type iron deposits in the NCC, the following conclusions are supported:

1. Large-scale BIFs occur mainly in some greenstone belts. Formation ages of BIFs in NCC span a wide range varying from Mesoarchean to early Paleoproterozoic, among which late Neoarchean is the peak period (2.6–2.50 Ga). All the BIFs in NCC have undergone relatively high-grade metamorphism and strong deformation.
2. Genetic types of BIFs can be divided into two types, Algoma and Superior Lake. BIFs in the Neoarchean greenstone belts in NCC belong to the former. Moreover, nearly all of the Neoarchean BIFs are formed in a back-arc or arc setting related to subduction of an ocean slab. The BIFs can form in either marine volcanic-sedimentary environment or submarine exhalation sedimentary environment.
3. Geochemistry results of the Neoarchean BIFs in NCC indicate that the BIFs have similar geochemical features. The BIFs are composed mostly of $SiO_2 + Fe_2O_3^T$, the contents of Al_2O_3, TiO_2, K_2O, Na_2O, MnO, and P_2O_5 are very low, suggesting that BIFs are typical chemical sedimentary rocks. An enrichment in heavy REE relative to LREE with positive La, Eu, and Y anomalies in PAAS-normalized REE diagrams, indicates their precipitation from marine seawater imprinted by high-T hydrothermal fluids; The ε_{Nd}(2.55 Ga) values (3.0–4.5) in Anshan-Benxi BIFs are close to those of the coeval depleted mantle, implying that the iron was most likely

derived from the leaching of oceanic crust; the ε_{Nd}(2.55 Ga) values (2.89 to −2.58) in the Wutai and E. Hebei BIFs imply that the iron was sourced from mixing compositions of oceanic and continental crusts. The BIFs lack negative Ce anomalies, coupled with consistently positive δ^{56}Fe (0.12–1.87 ‰) values, suggesting that iron deposits are formed in low-oxygen or anoxia environments.

Acknowledgments This study was financially supported by the Major State Basic Research Programme of the People's Republic of China (No. 2012CB416601), the National Natural Science Foundation of China (No. 41572076), and the Knowledge Innovation Programme of the Chinese Academy of Sciences (No. KZCX2-YW-Q04-07). We appreciate much help from prof. Mingguo Zhai, Dr. Yanpei Dai, Mengtian Zheng, and Zhiquan Li.

References

Alexander, B. W., Bau, M., Andersson, P., & Dulski, P. (2008). Continentally-derived solutes in shallow Archean seawater: rare earth element and Nd isotope evidence in iron formation from the 2.9 Ga Pongola Supergroup, South Africa. *Geochimica et Cosmochimica Acta, 72*, 378–394.

Alibo, D. S., & Nozaki, Y. (1999). Rare earth elements in seawater: Particle association, shale-normalization, and Ce oxidation. *Geochimica et Cosmochimica Acta, 63*, 363–372.

Anbar, A. D., & Rouxel, O. (2007). Metal stable isotopes in paleoceanography. *Annual Review of Earth and Planetary Sciences, 35*, 717–746.

Bau, M., & Dulski, P. (1996). Distribution of yttrium and rare-earth elements in the Penge and Kuruman iron formations, Transvaal Supergroup, South Africa. *Precambrian Research, 79*, 37–55.

Bau, M., & Dulski, P. (1999). Comparing yttrium and rare earths in hydrothermal fluids from the Mid-Atlantic Ridge: Implications for Y and REE behaviour during near-vent mixing and for the Y/Ho ratio of Proterozoic seawater. *Chemical Geology, 155*, 77–90.

Bekker, A., Planavsky, N. J., Krapež, B., Rasmussen, B., Hofmann A., Slack, J. F., et al. (2013). Iron formation: Their origins and implications for ancient seawater chemistry. In F. T. Mackenzie (Eds.), *Sediments, diagenesis, and sedimentary rocks: Treatise on geochemistry* (2nd ed., Paper 7, pp. 561–628). Amsterdam: Elsevier.

Bekker, A., Slack, J. F., Planavsky, N., Krapez, B., Hofmann, A., Konhauser, K. O., et al. (2010). Iron formation: The sedimentary product of a complex interplay among mantle, tectonic, oceanic and biospheric processes. *Economic Geology, 105*, 467–508.

Beukes, N. J., & Gutzmer, J. (2008). Origin and paleoenvironmental significance of major iron formations at the Archean-Paleoproterozoic boundary. *Reviews in Economic Geology, 15*, 5–47.

Bolhar, R., Kamber, B. S., Moorbath, S., Fedo, C. M., & Whitehouse, M. J. (2004). Characterisation of early Archaean chemical sediments by trace element signatures. *Earth and Planetary Science Letters, 222*, 43–60.

Cui, M.-L., Zhang, L.-C., Wu, H.-Y., Xu, Y.-X., & Li, W.-J. (2014). Timing and tectonic setting of the Sijiaying banded iron deposit in the eastern Hebei province, North China Craton: Constraints from geochemistry and SIMS zircon U-Pb dating. *Journal of Asian Earth Sciences, 94*, 240–251.

Dai, Y.-P., Zhang, L.-C., Wang, C.-L., Liu, L., Cui, M.-L., Zhu, M.-T., et al. (2012). Genetic type, formation age and tectonic setting of the Waitoushan banded iron formation, Benxi, Liaoning Province. *Acta Petrologica Sinica, 28*, 3574–3594. (in Chinese with English abstract).

Dai, Y.-P., Zhang, L.-C., Zhu, M.-T., Wang, C.-L., &Liu, L. (2013). Chengtaigou BIF-type iron deposit, Anshan area associated with Archean crustal growth: constraints from zircon U-Pb dating and Hf isotopes. *Acta Petrologica Sinica, 29*, 2537–2550 (in Chinese with English abstract).

Dai, Y.-P., Zhang, L.-C., Zhu, M.-T., Wang, C.-L., Liu, L., & Xiang, P. (2014). The composition and genesis of the Mesoarchean Dagushan banded iron formation (BIF) in the Anshan area of the North China Craton. *Ore Geology Review, 63*, 353–373.

Geng, Y.-S., Liu, F.-L., & Yang, C.-H. (2006). Magmatic event at the end of the Archean in eastern Hebei Province and its geological implication. *Acta Geologica Sinica, 80*, 819–833.

Goodwin, A. M. (1973). Archean iron-formation and tectonic basins of the Canadian Shield. *Economic Geology, 68*, 915–933.

Gross, G. A. (1980). A classification of iron formations based on depositional environments. *Canadian Mineralogist, 18*, 215–222.

Gross, G. A. (1983). Tectonic systems and the deposition of iron-formation. *Precambrian Research, 20*(2–4), 171–187.

Gross, G. A., & McLeod, C. R. (1980). A preliminary assessment of the chemical composition of iron formations in Canada. *Canadian Mineralogist, 16*(2), 223–229.

Guo, J.-H., Sun, M., Chen, F.-K., & Zhai, M.-G. (2005). Sm-Nd and SHRIMP U-Pb zircon geochronology of high pressure granulites in the Sanggan area, North China Craton: Timing of Paleoproterozoic continental collision. *Journal of Asian Earth Sciences, 24*, 629–642.

Harley, S. L., Kelly, N. M., & Móller, A. (2007). Zircon behaviour and the thermal histories of mountain chains. *Elements, 3*, 25–30.

Heimann, A., Johnson, C. M., Beard, B. L., Valley, J. W., Roden, E. E., Spicuzza, M. J., & Beukes, N. J. (2010). Fe, C, and O isotope compositions of banded iron formation carbonates demonstrate a major role for dissimilatory iron reduction in ~2.5 Ga marine environments. *Earth and Planetary Science Letters, 294*, 8–18.

Hoskin, P. W. O., & Schaltegger, U. (2003). The composition of zircon and igneous and metamorphic petrogenesis. *Reviews in Mineralogy Geochemistry, 53*, 27–62.

Huang, H. (2014). *The mineralization age, forming environment and genesis of Huoqiu BIF iron deposit in southern margin of the North China Craton* (pp. 1–117) (Ph.D. Thesis. Chengdu: University of Chengdu Science and Engineering) (in Chinese with English abstract).

Isley, A. E., & Abbott, D. H. (1999). Plume-related mafic volcanism and the deposition of banded iron formation. *Journal of Geophysical Research: Solid Earth, 104*, 15461–15477 (1978–2012).

James, H. L. (1954). Sedimentary facies of iron-formation. *Economic Geology, 49*(3), 235–293.

Klein, C. (2005). Some Precambrian banded iron-formations (BIFs) from around the world: Their age, geologic setting, mineralogy, metamorphism, geochemistry, and origin. *American Mineralogist, 90*, 1473–1499.

Klein, C., & Beukes, N. J. (1992). *Time distribution, stratigraphy, sedimentologic setting, and geochemistry of Precambrian iron-formations* (pp. 139–146). Cambridge: Cambridge University Press.

Konhauser, K. O., Hamade, T., Morris, R. C., Ferris, F. G., Southam, G., Raiswell, R., & Canfield, D. (2002). Could bacteria have formed the Precambrian banded iron formations? *Geology, 30*, 1079–1082.

Kusky, T. M., & Li, J. H. (2003). Paleoproterozoic tectonic evolution of the North China Craton. *Journal of Asian Earth Sciences, 22*, 383–397.

Li, H. M., Chen, Y. C., Li, L. X., & Wang, D. H. (2012). *Metallogenic regularity of iron deposits in China* (pp. 1–246). Beijing: Geological Publishing House (in Chinese).

Li, Y.-H., Hon, K.-J., Wan, D.-F., Zhang, Z.-J., & Yue, G.-L. (2010). Formation mechanism of Precambrian Banded Iron Formation and atmosphere and ocean during early stage of the Earth. *Acta Petrologica Sinica, 4*(9), 1359–1373. (in Chinese with English abstract).

Li, Y.-L., Konhauser, K. O., & Cole, D. R. (2011). Mineral ecophysiological data provide growing evidence for microbial activity in banded-iron formations. *Geology, 39*, 707–710.

Li, H.-M., Zhang, Z.-J., Li, L.-X., Zhang, Z.-C., Chen, J., & Yao, T. (2014). Types and general characteristics of the BIF-related iron deposits in China. *Ore Geology Reviews, 57*, 264–287.

Li, Z.-H., Zhu, X.-K., & Tang, S.-H. (2008). Characters of Fe isotopes and rare earth elements of banded iron formations from Anshan-Benxi area: Implications for Fe source. *Acta Petrologica et Mineralogica, 27*(4), 285–290. (in Chinese with English abstact).

Liu, M. J. (2013). *Hydrothermal reworking processes and its significance for meta-sedimentary iron deposit of Gongchangling in Liaoning Province* (pp. 1–113) (Master Thesis. Beijing: China University of Geosciences) (in Chinese).

Liu, L., Zhang, L.-C., & Dai, Y.-P. (2014). Formation age and genesis of the banded iron formations from the Guyang Greenstone Belt, Western North China Craton. *Ore Geology Reviews, 63*, 388–404.

McLennan, S.-M. (1989). Rare earth elements in sedimentary rocks: Influence of provenance and sedimentary processes. In B. R. Lipin & G. A. McKay (Eds.), *Geochemistry and mineralogy of rare earth elements* (Vol. 21, pp. 169–200) (Reviews in Mineralogy and Geochemistry).

Mloszewska, A. M., Pecoits, E., Cates, N. L., Mojzsis, S. J., O'Neil, J., Robbins, L. J., & Konhauser, K. O. (2012). The composition of Earth's oldest iron formations: The Nuvvuagittuq Supracrustal Belt (Québec, Canada). *Earth and Planetary Science Letters, 317*, 331–342.

Nutman, A. P., Wan, Y.-S., Du, L.-L., Friend, C. R. L., Dong, C.-Y., Xie, H.-Q., et al. (2011). Multistage late Neoarchaean crustal evolution of the North China Craton, Eastern Hebei. *Precambrian Research, 189*, 43–65.

Ohmoto, H., Watanabe, Y., Yamaguchi, K. E., Naraoka, H., Haruna, M., Kakegawa, T., et al. (2006). Chemical and biological evolution of early Earth: Constraints from banded iron formations. *Geological society of America Memoirs, 198*, 291–331.

Ouyang, Z.-Y., Zhang, F.-Q., Lin, W.-Z., & Wang, S.-J. (1995). Tectonic framework of the North China craton and evolving model. *Chinese Science Bulletin, 40*, 734–736.

Pearce, J. A., Harris, N. B. W., & Tindle, A. G. (1982). Trace element discrimination diagrams for the tectonic interpretation of granitic rocks. *The Journal of Geology, 25*, 956–983.

Piepgras, D. J., & Wasserburg, G. J. (1982). Isotopic composition of neodymium in waters from the Drake Passage. *Science, 217*, 207–214.

Planavsky, N., Bekker, A., Rouxel, O. J., Kamber, B., Hofmann, A., Knudsen, A., & Lyons, T. W. (2010). Rare earth element and yttrium compositions of Archean and Paleoproterozoic Fe formations revisited: New perspectives on the significance and mechanisms of deposition. *Geochimica et Cosmochimica Acta, 74*, 6387–6405.

Planavsky, N., Rouxel, O. J., Bekker, A., Hofmann, A., Little, C. T. S., & Lyon, T. W. (2012). Iron isotope composition of some Archean and Proterozoic iron formations. *Geochimica et Cosmochimica Acta, 80*, 158–169.

Qu, J.-F., Li, J.-Y., & Liu, J.-F. (2013). Formation age and its significance of Wangsiyu BIF type iron deposit in Eastern Hebei. *Geology Bulletin, 32*(2–3), 260–266.

Robert, F., & Ali, P. (2007). Source heterogeneity for the major components of 3.7 Ga Banded Iron Formations (Isua Greenstone Belt, Western Greenland): Tracing the nature of interacting water masses in BIF formation. *Earth and Planetary Science Letters, 253* (1), 266–281.

Rubatto, D., & Hermann, J. (2007). Zircon behaviour in deeply subducted rocks. *Elements, 3*, 31–35.

Rye, R., & Holland, H. D. (2000). Geology and geochemistry of paleosols developed on the Hekpoort basalt, Pretoria Group, South Africa. *American Journal of Science, 300*, 85–141.

Vavra, G., Schmidt, R., & Gebauer, D. (1999). Internal morphology, habit and U-Th-Pb microanalysis of amphibolite-to-granulite facies zircons: Geochronology of the Ivrea Zone (Southern Alps). *Contributions to Mineralogy and Petrology, 134*, 380–404.

Wan, Y.-S., Song, B., Yang, D., & Liu, D.-Y. (2005). Zircon SHRIMP U–Pb geochronology of Archean rocks from the Fushun–Qingyuan Area, Liaoning Province and its geological significance. *Acta Geologica Sinica, 79*, 78–87 (in Chinese with English abstract).

Wan, Y.-S., Dong, C.-Y., Liu, D.-Y., Kröner A., Yang, C.-H., Wang, W. et al. (2012a). Zircon ages and geochemistry of late Neoarchean syenogranites in the North China Craton: A review. *Precambrian Research, 222–223*, 265–289.

Wan, Y.-S., Dong, C.-Y., Xie, H.-Q., Wang, S.-J., Song, M.-C., Xu, Z.-Y. et al. (2012b). Formation ages of early Precambrian BIFs in North China Craton: SHRIMP zircon U-Pb dating. *Acta Geologica Sinica, 86*, 1447–1478 (in Chinese with English abstract).

Wan, Y.-S., Liu, D., Wang, W., Song, T., Kröner A., Dong, C., et al. (2011b). Provenance of Meso to Neoproterozoic cover sediments at the Ming Tombs, Beijing, North China Craton: An integrated study of U-Pb dating and Hf isotopic measurement of detrital zircons and whole-rock geochemistry. *Gondwana Research, 20*(1), 219–242.

Wan, Y.-S., Liu, D., Wang, S., Yang, E., Wang, W., Dong, C., et al. (2011a). ~2.7 Ga juvenile crust formation in the North China Craton (Taishan-Xintai area, western Shandong Province): Further evidence of an understated event from U-Pb dating and Hf isotopic composition of zircon. *Precambrian Research, 186*(1–4), 169–180.

Wang, H.-C., Kang, J.-L., Ren, Y.-W., Chu, H., Lu, S.-N., & Xiao, Z.-B. (2015d). Identification of ~2.7 Ga BIF in North China Craton: Evidence from geochronology of iron formation in Laizhou-Changyi area, JIaobei terrane. *Acta Petrologica Sinica, 31*(10), 2991–3011 (in Chinese with English abstract).

Wang, C.-L., Konhauser, K.O., & Zhang, L.-C. (2015a). Depositional environment of the Paleoproterozoic Yuanjiacun Banded Iron Formation in Shanxi Province, China. *Economic Geology, 110*, 1515–1539.

Wang, C.-L., Konhauser, K. O., Zhang, L.-C., & Li, W.-J. (2015c). Decoupled sources of the ~2.3 Ga Yuanjiacun banded iron formation: Implications for the Nd cycle in Earth's early oceans, Precambrian Research (in press).

Wang, S.-L., & Zhang, R.-H. (1995). Single zircon age and its significance of biotite leptynite in Qidashan iron deposit. *Mineralium Geology, 14*(3), 216–219. (in Chinese with English abstract).

Wang, C.-L., Zhang, L.-C., Dai, Y.-P., & Lan, C.-Y. (2015b). Geochronological and geochemical constraints on the origin of clastic meta-sedimentary rocks associated with the Yuanjiacun BIF from the Lüliang Complex, North China. *Lithos, 212–215*, 231–246.

Wang, C.-L., Zhang, L.-C., Dai, Y.-P., & Li, W.-J. (2014b). Source characteristics of the ~2.5 Ga Wangjiazhuang Banded Iron Formation from the Wutai greenstone belt in the North China Craton: Evidence from neodymium isotopes. *Journal of Asian Earth Sciences, 93*, 353–373.

Wang, C.-L., Zhang, L.-C., Lan, C.-Y., & Dai, Y.-P. (2014a). Rare earth element and yttrium compositions of the Paleoproterozoic Yuanjiacun BIF in the Lüliang area and their implications for the Great Oxidation Event (GOE). *Science China Earth Sciences, 57*, 2469–2485.

Wilde, S. A., Cawood, P. A., Wang, K.-Y., Nemchin, A., & Zhao, G.-C. (2004). Determining Precambrian crustal evolution in China: A case-study from Wutaishan, Shanxi Province, demonstrating the application of precise SHRIMPU-Pb geochronology. In J. Malpas, C. J. N. Fletcher, J. R. Ali, & J. C. Aichison (Eds.), *Aspects of the tectonic evolution of China* (Vol. 226, pp. 5–26). Geological Society of London, Special Publication.

Xiang, P., Cui, M.-L., Wu, H.-Y., Zhang, X.-J., & Zhang, L.-C. (2012). Geological characteristics, ages of host rocks and its geological significance of the Zhoutaizi iron deposit in Luanping, Hebei Province. *Acta Petrologica Sinica, 28*, 3655–3669. (in Chinese with English abstract).

Yang, X. Q. (2013). *Ore-forming processes of iron deposits in Anshan-Benxi metamorphic rock area* (pp. 1–136) (Master Thesis. China University of Geoscience).

Yang, X.-Q., Li, H.-M., Li, L.-X., Yao, T., Chen, J., & Liu, M.-J. (2014a). Geochemical characteristics of banded iron formations in Liaoning-Eastern Hebei area: I. Characteristics of major elements. *Acta Petrologica Sinica, 30*(5), 1218–1238 (in Chinese with English abstract).

Yang, X.-Y., Liu, L., Lee, I., Wang, B., Du, Z., Wang, Q. (2014b). A review on the Huoqiu banded iron formation (BIF), southeast margin of the North China Craton: Genesis of iron deposits and implications for exploration. *Ore Geology Reviews, 63*, 418–443.

Yao, T., Li, H.-M., Yang, X.-Q., Li, L.-X., Chen, J., Zhang, J.-Y., et al. (2014). Geochemical characteristics of banded iron formations in Liaoning-Eastern Hebei area: II. Characteristics of rare earth elements. *Acta Petrologica Sinica, 30*(5), 1239–1252. (in Chinese with English abstract).

Zhai, M.-G. (1993). Archean Anshan BIFs and gneisses. In Z.-P. Zhao (Eds.), *Precambrian crustal evolution of the Sino-Korean Para-platform*, (pp. 389–390). Science Press (in Chinese).

Zhai, M.-G. (2010). Evolvement and ore-forming processes of North China Craton. *Mineralium Geology, 39*(1), 24–36.

Zhai, M.-G., & Liu, W.-J. (2003). Paleoproterozoic tectonic history of the North China Craton: A review. *Precambrian Research, 122*, 183–199.

Zhai, M.-G., & Santosh, M. (2011). The early Precambrian odyssey of the North China Craton: A synoptic overview. *Gondwana Research, 20*, 6–25.

Zhai, M.-G., & Windley, B. F. (1990). The Archaean and early Proterozoic banded iron formations of North China: Their characteristics geotectonic relations, chemistry and implications for crustal growth. *Precambrian Research, 48*, 267–286.

Zhai, M.-G., Windley, B. F., & Sills, J. D. (1990). Archaean gneisses amphibolites, banded iron-formation from Anshan area of Liaoning, NE China: Their geochemistry, metamorphism and petrogenesis. *Precambrian Research, 46*, 195–216.

Zhang, L.-C., Zhai, M.-G., Wan, Y.-S., Guo, J.-H., Dai, Y.-P., Wang, C.-L., et al. (2012a). Study of the Precambrian BIF-iron deposits in the North China Craton: Progresses and questions. *Acta Petrologica Sinica, 28*, 3431–3445 (in Chinese with English abstract).

Zhang, L.-C., Zhai, M.-G., Zhang, X.-J., Xiang, P., Dai, Y.-P., Wang, C.-L., et al. (2012b). Formation age and tectonic setting of the Shirengou Neoarchean banded iron deposit in eastern Hebei Province: Constraints from geochemistry and SIMS zircon U–Pb dating. *Precambrian Research, 222*, 325–338.

Zhang, X.-J., Zhang, L.-C., Xiang, P., Wan, B., & Pirajno, F. (2011). Zircon U–Pb age, Hf isotopes and geochemistry of Shuichang Algoma-type banded iron-formation, North China Craton: Constraints on the ore-forming age and tectonic setting. *Gondwana Research, 20*, 137–148.

Zhao, G.-C., Sun, M., Wilde, S. A., & Li, S.-Z. (2005). Late Archean to Paleoproterozoic evolution of the North China craton: Key issues revisited. *Precambrian Research, 136*, 177–202.

Zhao, G.-C., Wilde, S. A., Cawood, P. A., & Sun, M. (2001). Archean blocks and their boundaries in the North China Craton: Lithological geochemical, structural and P–T path constraints and tectonic evolution. *Precambrian Research, 107*, 45–73.

Zheng, M.-T., Zhang, L.-C., Wang, C.-L., Zhu, M.-T., Li, Z.-Q., & Wang, Y.-T. (2015). Formation age and origin of the Xingshan BIF type iron deposit in eastern Hebei Province. *Acta Petrologica Sinica, 31*(6), 1636–1652. (in Chinese with English abstract).

Zhou, S. T. (1994). *Geology of the BIF in Anshan-Benxi* (pp. 1–277). Beijing: Area Geological Publishing House (in Chinese).

Zhu, M.-T., Dai, Y.-P., Zhang, L.-C., Wang, C.-L., & Liu, L. (2015a). Geochronology and geochemistry of the Nanfen iron deposit in the Anshan-Benxi area, North China Craton: Implications for ~2.55 Ga crustal growth and the genesis of high-grade iron ores. *Precambrian Research, 260*, 23–38.

Zhu, M.-T., Zhang, L.-C., Dai, Y.-P., & Wang, C.-L. (2015b). In situ zircon U-Pb dating and O isotopes of the Neoarchean Hongtoushan VMS Cu-Zn deposit in the North China Craton: Implication for the ore genesis. *Ore Geology Reviews, 67*, 354–367.

Archean Continental Crustal Accretion and Banded Iron Formations, Southeastern North China Craton

6

Xiaoyong Yang and Lei Liu

Abstract

The Huoqiu Complex (HQC) in the southeastern margin of the North China Craton (NCC) is dominated by Neoarchean TTG gneisses, amphibolites and voluminous metasediments. Geochemical characteristics of TTG gneisses such as high Sr/Y and $(La/Yb)_N$ with steep REE patterns and trace element modeling suggest that they are generated by partial melting of hydrous meta-basalts (amphibolites) at the base of a thickened mafic continental crust, leaving a rutile-bearing eclogite residue. LA-MC-ICPMS U–Pb age data from magmatic zircon grains show protolith emplacement ages of 2.76–2.71 Ga. Hf isotopic compositions of zircon grains from the amphibolite and TTG gneiss show $\varepsilon_{Hf}(t)$ values of 2.4–15.5 and −3.0 to 1.5, respectively. The t_{DM2}(Hf) model ages of the TTG gneisses range from 2.87 to 3.14 Ga, and are identical to the t_{DM1}(Hf) ages of amphibolites (2.84–3.16 Ga) within analytical uncertainty, refining that the TTG gneisses formed by partial melting of amphibolite, and attest to large-scale remelting of the Mesoarchean continental rocks during early Neoarchean. The NCC represents one of only a few cratonic nuclei with a geological history extending back to the Eoarchean. However, extensive ca. 2.5 Ga crustal reworking has destroyed a considerable portion of the pre-existing crustal record, hindering the investigation of tectonothermal evolution prior to 2.5 Ga. The HQC represents rare material that survived the ca. 2.5 Ga tectonothermal events relatively intact, thus preserving valuable information on prior crustal growth. In situ detrital zircon U–Pb dating and Hf isotope analyses were conducted on three schists from three drilling holes cutting cross the basement of the HQC in order to decipher the nature (such as episodic vs. continuous, juvenile vs. reworked) and tectonic setting of continental crust formation and preservation, and to place the results into a broader geodynamic context. In combination with published data, the concordant age spectra of all detrital zircons (n = 204) yield $^{207}Pb/^{206}Pb$ ages of 2343–3997 Ma that cluster into two principal age populations with peaks at 3015 and 2755 Ma. The ca. 3.01 and 2.75 Ga zircons with positive $\varepsilon_{Hf}(t)$ values plot close to the depleted mantle evolutional line and their U–Pb ages are similar to or only slightly younger than the t_{DM1} model ages, hence indicating at least two predominant episodes of juvenile continental crustal accretions (3.01 and 2.75 Ga). The older episode finds only a minor correspondence in other cratons, suggesting little juvenile crustal growth occurred globally at a time of subdued mantle-derived magmatism. By contrast, the younger episode is coincident with a global rise in superplume activity in the Neoarchean. According to the geochemical and geochronological data, the 3.01 Ga juvenile

X. Yang (✉) · L. Liu
CAS Key Laboratory of Crust-Mantle Materials and Environments, School of Earth and Space Sciences, University of Science and Technology of China, Hefei, 230026, China
e-mail: xyyang555@163.com

L. Liu
e-mail: liu01@ustc.edu.cn

M. Zhai et al. (eds.), *Main Tectonic Events and Metallogeny of the North China Craton*,
Springer Geology, DOI 10.1007/978-981-10-1064-4_6

crust was likely generated in an island-arc subduction system, whereas the 2.75 Ga crustal rocks were probably formed during magmatic underplating and subsequent partial melting of lower crustal mafic rocks. Consequently, they record a tectonic transition from a compressive to an extensional setting on the southeastern margin of the NCC between 3.01 and 2.75 Ga. This sequence of the events heralds a shift, from a mixture of net crustal growth and crustal reworking during multiple short-lived magmatic pulses, to fragmentation and dispersal of the early continental nucleus within 250 Ma. The Huoqiu iron deposits with a typical banded iron formation (BIF) are hosted by Precambrian high-grade metamorphic rocks, mostly occurring as metasedimentary rocks. From three BIF samples 88 detrital zircons have been collected, they display clear oscillatory zoning, high Th/U ratio, and low to variable luminescence, indicating magmatic origin. There are two peaks of 2753 Ma and 2970 Ma in concordant $^{207}Pb/^{206}Pb$ ages distribution plot, which is well consistent with the protolith ages of regional wall rocks (e.g., TTG gneiss and amphibolite) in this region. These appearances in association with the relatively good linear correlations between Al_2O_3 and TiO_2 for BIF and their wall rocks, suggest that at least minor terrigenous clastic sediments contributed to BIF deposition, which thus constrained the upper limited age of BIF deposition at 2.75 Ga. In addition, no detrital zircons record recently reported 2.71 Ga magmatic event in this region and neighboring blocks, probably constrained the lower limited age of BIF deposition at 2.71 Ga. The flysch rhythmic structure occurrence in BIF-bearing strata, abundant carbonate minerals such as primary breunnerite association with magnetite, and no volcanic record present within BIF ore body or adjacent rocks inferred that the Huoqiu BIF deposited in continental marginal sea or back-arc basin environment with little contributions from submarine volcanic hydrothermal fluids, thus belonged to Superior-type. They show similar REE patterns to seawater, however, the positive Eu anomalies and reduced Y/Ho ratios relative to seawater indicates a possible mixture of hydrothermal fluids. Thus, their material sources were dominated by seawater, with minor contributions from the volcanic hydrothermal fluids and terrigenous sediments.

Keywords
Zircon • Geochemistry • Crustal evolution • Southeast NCC • BIF

6.1 Introduction

6.1.1 The Importance of Archean Continental Crustal Accretion

The Earth's crust is mainly composed of two types, continental crust and oceanic crust. The continental crust (abbreviate to CC) has the most important significance in human life. It constitutes 40 % of the surface area of the Earth, and yet occupies almost 70 % of the total volume of the Earth' crust (Hawkesworth et al. 2010). The CC is the record of the history of the Earth, of the processes and events that have controlled our planet's evolution, thus it is very important to explore its generation and evolution (Hawkesworth et al. 2013). The CC, as considered here, following Rudnick and Gao (2003), is taken to extend vertically from the Earth's surface to the Mohorovicic discontinuity that is interpreted as marker of the crust–mantle boundary. Although the longstanding question how the processes involved in the generation of the continental crust changed through time is always in debate (Fig. 6.1), a consensus is reached that most continental crust are formed prior to 2.5 Ga. Which means the Archean CC is the most important component in the present CC, even some geologists argued that at least 60–70 % CC had been generated by 3 Ga (e.g., Hawkesworth et al. 2013). One of the most key issues involved in CC growth is that its growth was a continuous (e.g., Hawkesworth et al. 2013; Cawood et al. 2013) or an episodic process (e.g., Arndt and Davaille 2013; Condie and Aster 2010; Condie et al. 2011). Another critical unresolved question is the basically petrogenesis of the major rock suite such as the tonalite–trondhjemite–granodiorite (TTG) suite, which is composed mainly component of the Archean CC (Condie 2000, 2005; Martin 1999; Martin et al. 2005).

The episodic nature of the continental crust formation was recognized many years ago (e.g., Gastil 1960; Stein and Hofmann 1994). Abundant Phanerozoic records offer clear evidence for crustal growth through multiple accretion

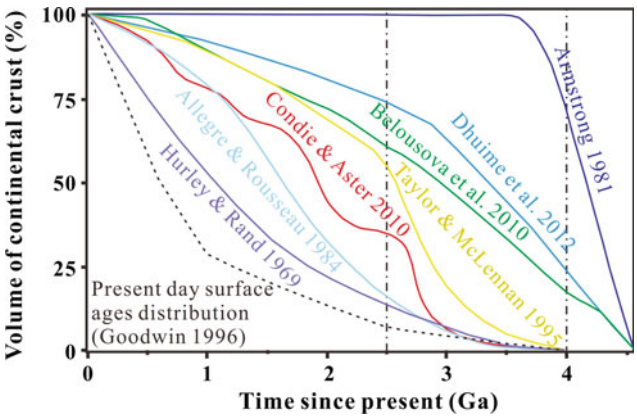

Fig. 6.1 A summary of crustal growth models of Hurley and Rand (1969), Armstrong (1981), Allègre and Rousseau (1984), Taylor and McLennan (1985), Belousova et al. (2010), Condie and Aster (2010) and Dhuime et al. (2012) compared to the age distribution of presently preserved crust from Goodwin (1996) (modified after Hawkesworth et al. 2013)

events induced by slab subduction and continent collision (e.g., Xiao and Santosh 2014; Zhang et al. 2014), and similar processes have been recognized in the Precambrian rock archive (Condie 2000; Hawkesworth and Kemp 2006). Recently, the importance of enhanced preservation of newly formed continental crust during episodic supercontinent assembly, rather than pulsed generation of juvenile crust, has been highlighted (Condie and Kröner 2013; Hawkesworth et al. 2013; Kamber 2015). Nevertheless, in terms of systematic variations in hafnium and oxygen isotopes in zircons of different ages, Dhuime et al. (2012) revealed the proportions of reworked crust and of juvenile crust through time, and then they proposed that growth of CC appears to have been a continuous process, albeit at variable rates. Recently, age and radiogenic isotopic data on rocks and minerals have triggered a variety of models on the rate of growth of the CC, furthermore, most models believe that the CC has increased in volume through time (Fig. 6.1). Abundant studies argue that crustal growth has been continuous, with early models proposing steady or increasing rates of accretion, and subsequent studies emphasizing an earlier period of more rapid crustal growth, particularly in the late Archean or early Proterozoic, followed by decreasing rates of growth to the present day (Cawood et al. 2013; Hawkesworth et al. 2013 and references therein). A systematic and considerable decrease in the rate of crustal growth after 3 Ga may be as a consequence of the onset of subduction-driven plate tectonics, where volume of juvenile crust were recycled into mantle (Dhuime et al. 2012; Hawkesworth et al. 2013; Cawood et al. 2013).

The TTG suite represents the most voluminous rock type in the preserved Archean CC on the globe (Condie 2000, 2005; Martin 1999; Martin et al. 2005). These rocks have therefore been widely employed to understand the origin and early chemical evolution of continents (Condie 2000, 2005), despite we have no enough insights on their petrogenesis as a result of most ancient rocks suffered multiple intense deformations and high-grade metamorphisms which can easily erase their primitive fingerprints. Archean TTG are silica-rich (SiO_2 > 64 wt%, but commonly ca. 70 wt% or greater) with high Al, Si, Na contents (3.0–7.0 wt%) as well as high ratios of Na_2O/K_2O > 2 (Moyen and Martin 2012). They are poor in ferromagnesian elements with an average Mg# of 0.43 and average Ni and Cr contents of 18 and 40 ppm, respectively (Moyen and Martin 2012). They are also characterized by steep negative rare-earth element (REE) patterns and low heavy rare-earth element (HREE) contents (e.g., high La/Yb) (Martin 1999; Martin et al. 2005). Furthermore, typical TTG exhibit enrichment in incompatible elements but are depleted in Ti–Nb–Ta (Martin 1999; Martin et al. 2005). These features have been interpreted to suggest that the TTG were derived from the partial melting of hydrated basaltic crust at amphibolite or eclogite facies depth, leaving a garnet-bearing amphibolite or rutile-bearing eclogite residue (Fig. 6.2; Barth et al. 2002; Foley et al. 2002, 2003; Rapp et al. 1991, 2003; Xiong et al. 2005; Xiong 2006). However, it has been noted that major and trace element features alone are not conclusive evidence to distinguish the melting of garnet-bearing amphibolite from that of rutile-bearing eclogite (Martin 1999; Foley et al.

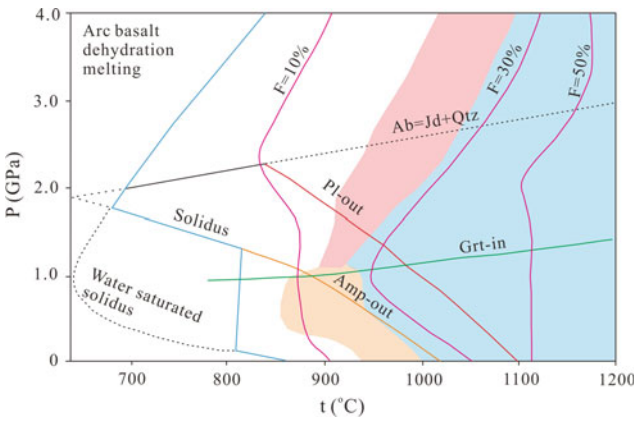

Fig. 6.2 Generalized mineral stability diagrams for arc basalt as sources used in the modeling TTG melt compositions (modified after Moyen and Stevens 2006 and Moyen and Martin 2012). The theoretical water saturated solidus is displayed (*black dotted line*) and distinguished from the actual solidus (*blue solid line*). The reactive line of Ab = Jd + Qtz is also shown. The *purple lines* correspond to approximate iso-melt lines of 10, 30, and 50 %, implying the corresponding melting degree (partial melting fraction, *F*) from *left* to *right* in diagram (Jiao et al. 2013). The colored fields are modeled melt compositions for corresponding rocks. *Light blue* field in the *right side* denotes tonalite, *light pink* field in the *upper side* represents Trondhejmite and *light brown* field under the diagram records the granodiorite compositions. Mineral abbreviations are after Kretz (1983)

2002; Rapp et al. 2003; Xiong 2006; Foley 2008; Hoffmann et al. 2011). Therefore, models on amphibolite and eclogite residue have long been debated (Foley et al. 2002, 2003; Rapp et al. 2003).

Many experiments modeling TTG generation commonly choose three different starting materials such as Komatiitic basalt, tholeiitic basalt, and arc basalt (Moyen and Stevens 2006; Moyen and Martin 2012). Except for starting materials, the water availability, melting depth (pressure), temperature, partial melting fraction (*F*) and residual minerals exert dominated control on TTG melt compositions. For example, in the case of arc basalt as starting materials, TTG melt compositions are changed in the P–T diagram (e.g., Fig. 6.2). Combination with diagram of tholeiitic basalt as source material (Fig. 8c in Moyen and Martin 2012), three main aspects have been emphasized: the role of the source (enriched source give more granitic/granodioritic compositions), the role of temperature (high *F* values, warm melt are more tonalitic), and the role of the pressure (high pressures are more trondhjemitic). Although amphibole/plagioclase ratios vary from 0.18 to >4 in the source rocks, most experiments were designed amphibolites as the starting materials, with the exception of Skjerlie and Douce (2002), which set an eclogitic composition. A compilation of the published data on experimental melting of amphibolites suggests a mineralogical model for amphibolite melting, which can be used for modeling the major and trace element compositions for produced TTG melt. Most geologists believe that TTG are generated over a large range of depths, from at least 1.0 to 2.5 GPa, which reflected in TTG trace element features (e.g., Na/Ta, La/Yb, Eu/Eu*, Sr/Y and HREE contents) (Moyen and Stevens 2006 and references therein).

6.1.2 The Significance of BIF

Banded iron formations are economically important sedimentary rocks in the world that mostly formed in the Precambrian marine sedimentary successions (Bekker et al. 2010; Klein 2005; Thurston et al. 2012). More than 95 % of the iron ore resources of the world occurred in iron formations. The largest BIF sequences are preserved in the Hamersley Range, Australia (e.g., Trendall and Blockley 1970) and the Transvaal Supergroup, South Africa (e.g., Beukes 1983), deposited during periods of relative tectonic stability. Following the Klein (2005), BIF is define as a chemical sediment, typically thin or thick bedded, containing an anomalously high content of iron, commonly but not necessarily containing layers of chert. In these rocks, iron-bearing minerals such as magnetite, hematite, pyrite, pyrrhotite, and siderite are common (Gross 1980; Klein 2005). The bedding features are the primary bedding of the associated unit, at least two main types of BIF have been recognized based on depositional setting: Algoma-type (hereafter A-type), generally associated with mafic volcanic rocks erupted on the seafloor; and Superior-type (hereafter S-type), represented by the shallower-water BIF found in the Superior province of North America (Gross 1980). The third type is Rapitan-type BIF with rarely reported, which is exclusively Neoproterozoic in age and are characterized by a glacially influenced depositional environment, mostly restricted to Phanerozoic mobile belts (Gross 1980, 1983, 1993; Klein and Beukes 1992; Ilyin 2009; Bekker et al. 2010).

Most BIF formed in large greenstone belts, which have been variably deformed, metamorphosed, and dismembered (Klein 2005). Researches on BIF have yielded important constraints on the history of greenstone belt development, the evolution of continental crust, sediment formation, palaeo-ocean environment, and palaeo-atmospheric conditions (Thurston et al. 2012). Although the exact conditions resulting BIF precipitation are not well known, it is widely accepted that secular changes in the style of their precipitation are linked to the environmental and geochemical evolution of Earth (Bekker et al. 2010; Zhai and Santosh 2013).

In particular, accompanying by the quickly development and improvement of precision and accuracy in iron isotope analysis by state-of-the-art facility (MC-ICPMS), the redox balance of the Archean atmosphere–ocean system and the emergence of early life on Earth has been explored through iron isotope studies on Precambrian BIF samples. For example, the average oxidation state of Archean through mid-Proterozoic BIF is $Fe^{2.4+}$, significantly greater than that of igneous rocks (Klein and Beukes 1992), and many studies have proposed that iron formations reflect oxidation of ferrous Fe-rich hydrothermal waters in a stratified ocean basin as they interacted with relatively oxygen-enriched layers in the upper water column (Johnson et al. 2003). Although biological process can cause the iron isotope fractionation by microbial dissimilatory iron reduction (DIR) in precursor BIF sediment before lithification (Johnson et al. 2003, 2008, 2013; Heimann et al. 2010; Li et al. 2015; Yoshiya et al. 2015), there are always no available unraveling evidence that the precipitation of Fe-rich phases was the result of direct microbial interaction (essentially lack organic C and reports of well-documented microfossils that interplayed with BIF lithologies) (Klein 2005). Therefore, iron isotope studies of BIF are inconclusive as to any possible biological processes account for their precipitation (Klein 2005). In this case, some studies have considered the negative $\delta^{56}Fe$ values of BIF (actually BIF samples have the greatest $\delta^{56}Fe$ value variation ranges in the measured nature samples, −2.5 to 1.5 ‰ relative to IRM014) as reflect partial oxidation of hydrothermal Fe(II) (Bekker et al. 2010; Planavsky et al. 2012; Rouxel et al. 2005),

whereas others have interpreted the negative $\delta^{56}Fe$ in BIF reflect microbial DIR in BIF precursor (Johnson et al. 2008, 2013; Heimann et al. 2010).

As mentioned above, it is very important to using new methods and new means to investigate the BIF samples because of they are documented essential fingerprints and evidence of the earliest life on Earth and the environmental and geochemical evolution of early Earth. On the other hand, on the basis of the new methods, the currently key controversial on BIF source and pathways in the Precambrian oceans has been well constrained by updated means. For example, combined Fe and Nd isotope signatures in BIF samples, Li et al. (2015) proposed high $\delta^{56}Fe$ and $\varepsilon_{Nd}(t)$ values in some BIF samples record a hydrothermal component, whereas correlated decrease in $\delta^{56}Fe$ and $\varepsilon_{Nd}(t)$ values reflect contributions from a continental component, then thus suggested a new dual-source model for BIF genesis in contrast to currently prevailing model of hydrothermal fluid as dominated source for BIF precipitation. Meanwhile, the continental Fe source is best explained by Fe mobilization on the continental margin through microbial DIR, and confirms a microbially driven Fe shuttle for the largest BIF (Hamersley Basin, Western Australia).

6.1.3 A Unique Occurrence from Southeastern NCC

The Huoqiu Complex (HQC), located at the southeastern margin of the North China Craton (NCC), is characterized by zircon ages of mainly >2.6 Ga (Wan et al. 2010; Wang et al. 2014; Liu et al. 2015; Liu and Yang 2015; Yang et al. 2012, 2014), and this distinguishes it significantly from most other Neoarchean complexes in the NCC with mostly having ca. 2.5 Ga zircons. Petrological, geochemical, and geochronological evidence indicate that this complex survived from the extensive reworking events at ca. 2.5 Ga (Wang et al. 2014; Liu et al. 2015). Thus, these intact well-preserved rocks provide an excellent window to study the early NCC evolution of the Meso- to Neoarchean continental crust. Mesoarchean rocks such as 3.0–2.9 Ga amphibolites and metasedimentary rocks have also been reported from this region (Wan et al. 2010; Liu et al. 2015). However, in fact, the other later geological events, e.g., uplift and erosion, have strongly overprinted these relic ancient rocks, thus pristine evidence for the tectonic regimes during their formation resides chiefly in the detrital zircon record, see below for detailed discussion.

The Huoqiu iron deposit with a typical BIF, hosted by Precambrian high-grade metamorphic rocks, most are metasedimentary rocks. 88 detrital zircons have been collected from three BIF samples, and they are displayed clear oscillatory zoning, high Th/U ratio and low to variable luminescence, indicating magmatic origin (Liu and Yang 2015). There are two peaks of 2753 and 2970 Ma in concordant $^{207}Pb/^{206}Pb$ ages distribution plot, which is well consistent with the protolith ages of wall rocks (e.g., TTG gneiss and amphibolite) in this region. These appearances in association with the relatively good linear correlations between Al_2O_3 and TiO_2 for BIF and their wall rocks, suggest that at least some terrigenous clastic sediments contributed to BIF formation, which thus constrained the upper limited age of BIF deposition at 2.75 Ga (Liu and Yang 2013, 2015). In addition, no detrital zircons record recently reported 2.71 Ga magmatic event in this region and neighboring blocks, probably constrained the lower limited age of BIF formation at 2.71 Ga. By contrast, most other BIFs in the NCC are formed at later Neoarchean (2.5–2.6 Ga, Zhang et al. 2011a, b, 2012a, b and references therein).

The flysch rhythmic structure occurrence in BIF-bearing strata, abundant carbonate minerals such as primary breunnerite association with magnetite, and no volcanic records present within BIF ore body or adjacent rocks suggested that the volcanisms have no or little (if have) direct influences (e.g., volcanic ash and clast contributions) on Huoqiu BIF deposits, thus implied they deposited in continental marginal sea or back-arc basin environment, belonged to Superior-type. This is very different from most BIFs occurring in later Neoarchean greenstone belts in the NCC, which belong to the Algoma-type, such as Anshan-Benxi and eastern Hebei, they are formed in island-arc setting (Zhang et al. 2011a, b, 2012a, b).

6.2 Geological Setting and BIF Deposits

6.2.1 The Precambrian Basement

The Precambrian basement in the Huai River region in Anhui Province are part of the Henan-Anhui subdivision of the metamorphic tectonic units in the NCC, made up of the Neoarchean Huoqiu Complex and Wuhe Group followed by the Paleoproterozoic Fengyang Group (No. 313 Geol. Team 1986; No. 313 Geol. Team 1991). Both the Neoarchean complexes were unconformably overlain by the Paleoproterozoic Fengyang Group. They are formed the two tectonic units of Jianghuai platform uplift and Huai River depression (Yang et al. 2012, 2014).

The Jianghuai platform uplift is located at Huoqiu, Shouxian and Yingshang Counties at the northwest Anhui, eastward link to the Tan-Lu Fault (TLF) zone, and Wuyang-Lushang in Henan province in the west. The uplift basement is mainly composed of the HQC, which consists of a series of volcanic-sedimentary rocks with suffering intensive migmatization and metamorphism. The regional

metamorphism called Bengbu Tectonic movement exerts sodic migmatization with medium pressure facies on the HQC. Therefore, rocks of the HQC have experienced middle-to-upper amphibolite-facies metamorphism and migmatization. The metasedimentary rocks consist predominately of Al-rich schist and gneiss, BIF, dolomitic marble (Wang et al. 2014). Based on the protolith restoration and chemical composition, the granitoids can be divided into orthogneiss, paragneiss and high-K granite (Liu et al. 2015). Most rocks previously classified as migmatites are potassic granites in composition, which underwent intensive metamorphism, remelting and deformation. The regional structural direction occurs nearly from east to west at the early stage followed by from north to south, then the latter stage overprints the early stage, which reworked the tectonic pattern and generated an isoclinal fold.

The Huai River depression distributed from Wuhe–Jiashan–Fenyang–Bengbu–Huaiyuan–Lixin cities of Anhui Province, westward extending to Xuchang–Dengfeng in Henan province. This block are separated by the Liufu Fault and Lixin Fault, can further divided into two sub-blocks as follow: the Bengbu uplift and the Huainan depression.

6.2.2 Geological Structure

The basement rocks of the HQC are completely covered by Proterozoic strata and Quaternary sediments, thus they have been found only in a limited region extending along the north–south direction from Nanzhaoji to Wuji towns (Fig. 6.3). The basement extends for over 60 km from south to north, with a total area of more than 1500 km^2. The length of BIF ore field is of ca. 40 km length with 2–8 km width, which is composed of 10 deposits, proven reserve is 2000 million tons, and expected reserves more than 3000 million tons. The Fe-bearing minerals are dominantly magnetite and hematite (and/or specularite).

Due to poor exposures, the geological framework of this region is inferred through available information from lithological association and drill core data. According to the rock association from drill core, the HQC can be divided into three formations (Fig. 6.3 b, c) in ascending order: Huayuan, Wuji and Zhouji formations (Fm). The boundaries lines between the three Formations are in conformable contact. The lower units comprise the Huayuan Formation and the Wuji Formation which are conformably overlain by the upper Zhouji Formation (Fig. 6.3c). The Huayuan Formation (Fm) is mainly composed of migmatized biotite-hornblende-plagioclase gneiss, plagioclase amphibolite and a small amount of biotite-plagioclase leptynite, these rock series are experienced strong or weak migmatization, then formed augen-like migmatite. According to rock associations, the Wuji Fm can be divided into two sections with total thickness of 950–1100 m, where the lower section is dominated by banded migmatite, migmatized biotite-plagioclase leptynite and hornblende-biotite-plagioclase gneiss, spatially sandwiched between plagioclase amphibolite with 420–590 m thickness. The upper part consists of biotite-plagioclase leptynite, schistose garnet-plagioclase-biotite rocks, magnetite quartzite and spatially associated with dolomite marble and plagioclase amphibolite (180–210 m in thickness). The Zhouji Fm is also divided into two sections with total thickness of 450–655 m in terms of rock associations, where the lower section is mainly composed of migmatized garnet-biotite-plagioclase leptynite, migmatite, biotite-plagioclase gneiss and spatially interbedded with plagioclase amphibolite of 80 m in thickness and thinner layer amphibole magnetite (20 m). The upper section is represented by dolomite marble, magnetite quartzite and spatially associated with quartz schist (Fig. 6.3c; Wan et al. 2010; Yang et al. 2012, 2014). In addition, considering all stratigraphic sequences together, they show large-scale rhythmic depositions, especially in the Zhouji Fm, equally as terrigenous clastic rocks-argillaceous shale-carbonate sandwiched between BIFs (Fig. 6.3c; Qi and Yao 1982). Their protolith is considered to be formed by a basic volcanic-sedimentary cycle (No. 337 Geol. Team 1986). Regionally, the HQC, Wuhe Group (east Anhui) and Taihua-Dengfeng Groups (Henan) are regarded as same period (Fig. 6.4), despite they have fair different metamorphism.

The P–T conditions of regional metamorphism are constrained at 650–750 °C and 5.5 ± 0.5 kbar, based on the mineral assemblage of garnet, sillimanite, kyanite, staurolite, biotite, muscovite, feldspar and quartz in the metasedimentary rocks (Qi 1987). In addition, the presence of olivine in the marble also constrains the metamorphic temperature to be >600 °C (No. 313 Geol. Team 1991).

Previous studies based on whole rock Rb–Sr and conventional zircon U–Pb dating suggest that the magmatic units in the HQC formed at ~2.7 Ga and were subjected to metamorphism during 2.3–2.2 and 1.8–1.4 Ga, respectively (Ying et al. 1984). Recent studies applied more precise dating techniques including laser ablation-inductively coupled plasma mass spectrometry (LA-ICPMS) and sensitive high resolution ion micro-probe (SHRIMP) in zircon grains from the BIF and surrounding wall rocks such as the gneiss and amphibolite from Wuji Fm. (Wan et al. 2010; Yang et al. 2012). Zircon U–Pb dating from plagioclase amphibolites yielded an age of 2.8 Ga, which is interpreted as the protolith age. Both these lithologies record a common and prominent tectonothermal event at 1.84 Ga (Wan et al. 2010; Yang et al. 2012), which is also widely developed elsewhere in the NCC, and was the possible cause for extensive melting and migmatization in the HQC.

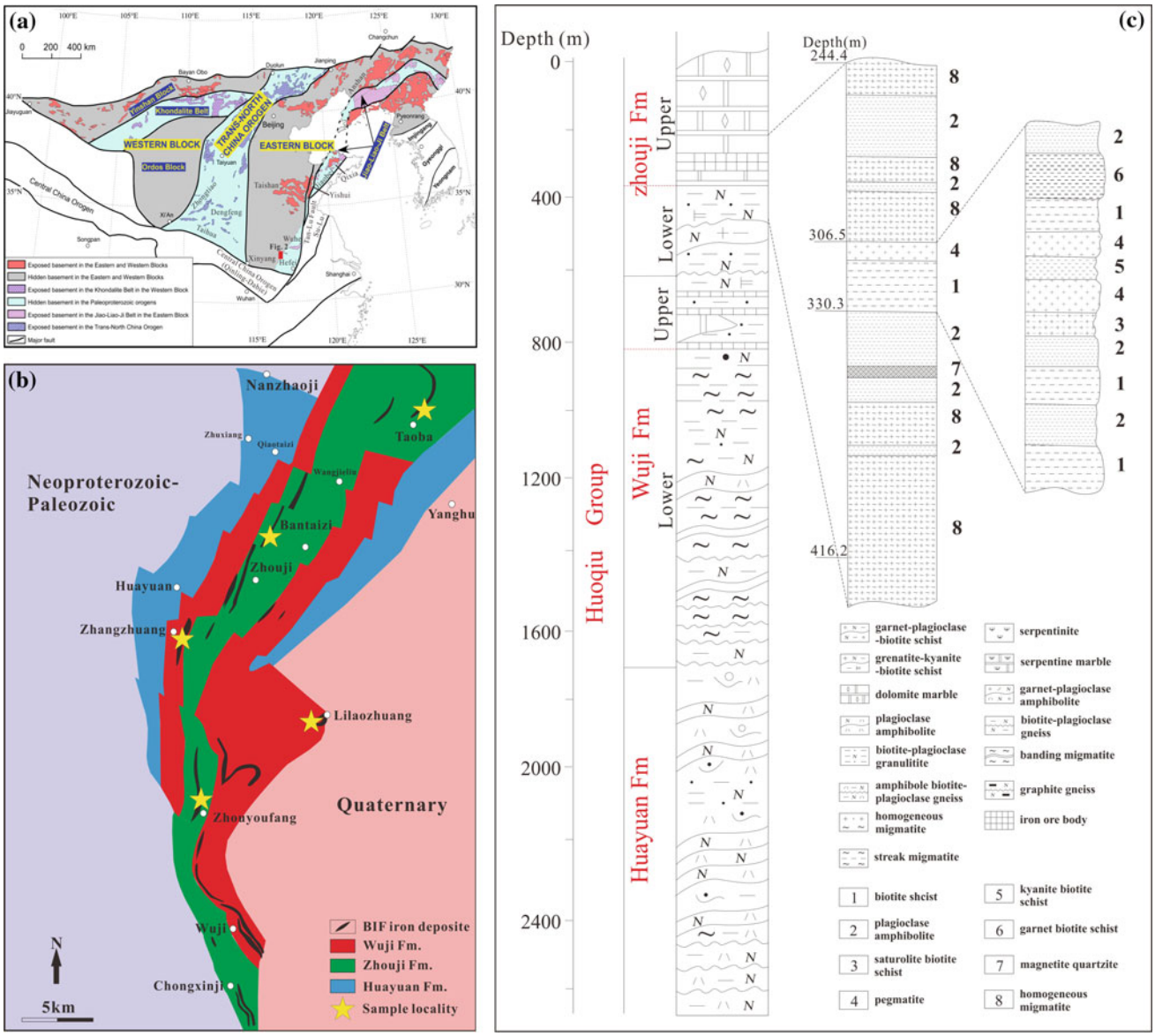

Fig. 6.3 **a** Tectonic subdivision of the North China Craton (modified from Zhao et al. 2005). Three major Paleoproterozoic belts have been identified in the NCC, e.g., the 1.95 Ga Jiao–Liao–Ji Belt (JLJB) that welded two Archean continental nuclei to form the Eastern Block, the 1.92 Ga Inner Mongolia Suture Zone (IMSZ) (incorporating the Khondalite Belt) that joined the Ordos Block and the Yinshan Block to yield the Western Block, and the 1.85 Ga Trans-North China Orogen (TNCO) that amalgamated the Western Block to the Eastern Block to form the NCC. **b** Geological sketch map of the Huoqiu complex (revised after the No. 337 Geol. Team 1986; No. 313 Geol. Team 1991). See text for detailed rock distribution in Wuji Fm, Zhouji Fm and Huayuan Fm. As all samples are from drill cores, here only show the horizontal position. **c** General stratigraphic column of the HQC (*left*), and the column recorded a flysch structure in the Zhouji Fm (*middle* and *right*)

6.2.3 Features of BIF Mineralization

In terms of mineral assemblages, the iron ores can be subdivided into four types: (1) quartz + magnetite; (2) quartz + specularite; (3) magnetite + quartz + silicate (hornblende, iron amphibole-magnesium iron amphibole, actinolite, tremolite, and diopside); (4) quartz + specular hematite iron ore + silicate (hornblende, actinolite tremolite, and diopside).

According to the characteristics of iron oxide, the iron ores can be subdivided into hematite and magnetite phase. Magnetite is the major mineral hosting iron ores, but it was transformed to martite by oxidation. In this case, hematite is used to develop along the rim of the magnetite grains and octahedron crack due to replacement, forming replacement grid or frame structure. Magnetite grains are 0.05–0.25 mm in size, mainly appeared as subhedral granular form, with a small amount of euhedral granular

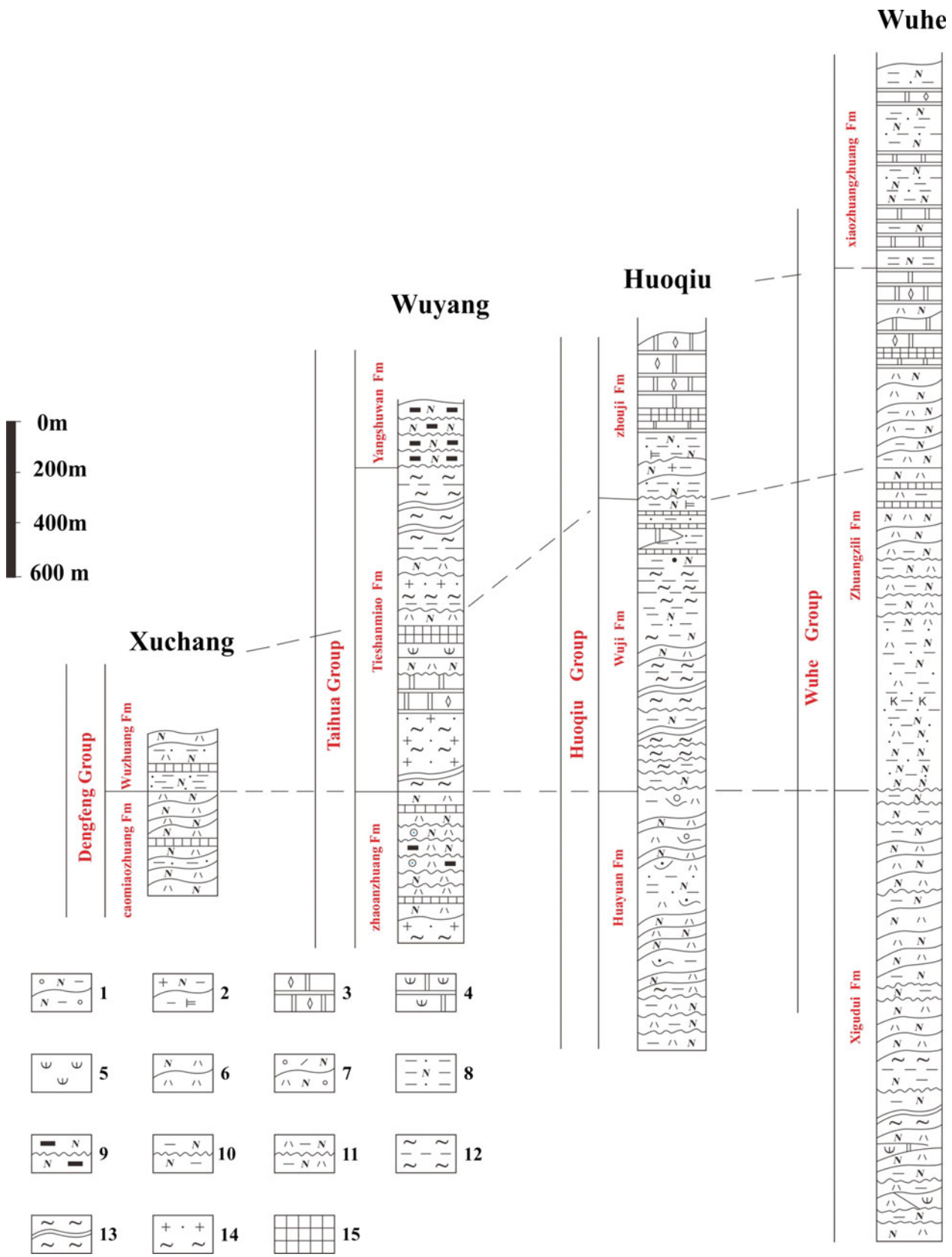

Fig. 6.4 Comparative strata cross sections of the HQC and its adjacent regions (according to BGMRA 1987, 1997; BGMRH 1989). *1* Garnet-plagioclase-biotite schist; *2* grenatite-kyanite-biotite schist; *3* dolomite marble; *4* serpentine marble; *5* serpentinite; *6* plagioclase amphibolite; *7* garnet-plagioclase amphibolite; *8* biotite-plagioclase granulitite; *9* graphite gneiss; *10* biotite-plagioclase gneiss; *11* amphibole biotite-plagioclase gneiss; *12* streak migmatite; *13* banding migmatite; *14* homogeneous migmatite; *15* iron ore body

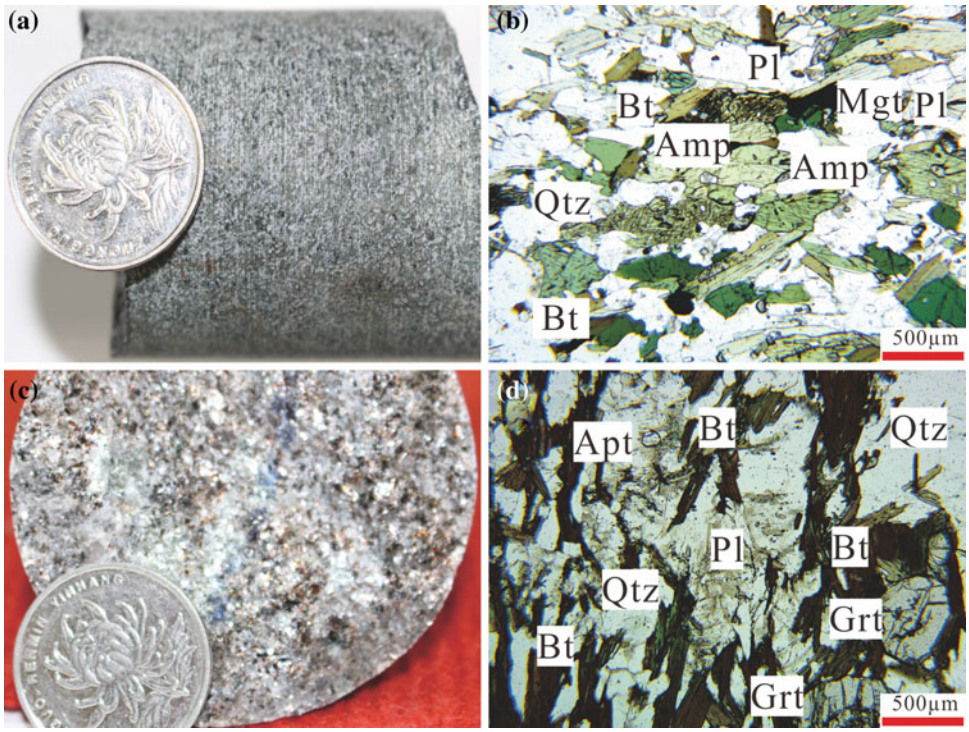

Fig. 6.5 Photomicrographs of BIF and associated rocks from the Huoqiu iron deposit (modified from Liu and Yang 2015). **a** Drill core photograph of amphibolite, showing black, massive and gneissic structure; and **b** photomicrograph in plane polarized light of amphibolite, showing hornblende (*Hbl* 40 %), plagioclase (*Pl* 45 %), biotite (*Bt* 10 %) and minor quartz (*Qtz*), this sample is from the Zhangzhuang deposit; **c** field photograph of garnet gneiss, showing gneissic structure; **d** photomicrograph in plane polarized light of garnet gneiss, showing *Pl* (30–60 %), *Qtz* (10–20 %), *Bt* (10–25 %) and minor garnet (*Grt*) and apatite (*Ap*), this sample is from the Bantaizi deposit. Mineral abbreviations are after Kretz (1983)

(0.05–0.25 mm). Ore textures are mainly shown as blastic shapes with a small amount of contained, crushed, colloidal and microscopic reticulated veins with striped or banded and fine stripe forms of structure, a small amount of massive structure, crushing structure, and wrinkles, sometimes occurred as residual cross-bedding grain structure.

6.3 Multiple Continental Accretion and Reworking

6.3.1 Evidence from Amphibolite and TTG Gneiss

The HQC is predominated by Neoarchean dark amphibolites, gray TTG gneisses, pink K-rich granite and voluminous metasediments. Here we reported samples all are from drill core range from Neoarchean to Paleoproterozoic. The amphibolite samples occur as massive and schistose structures, dark green to gray color and display prismatic or blastic texture. They are dominantly composed of 30–60 % hornblende, 10–40 % plagioclase and 5–10 % quartz, occasionally biotite and garnet are also observed (Fig. 6.5a, b), and are hence referred to plagioclase amphibolite. The accessory minerals include apatite, zircon and titanite. The TTG gneisses show typically blocky structure with gneissic textures. They are commonly composed of plagioclase (30–60 %), quartz (10–20 %) and biotite (10–25 %) and minor garnet (Fig. 6.5c, d). The major end-member component of garnet is almandine, occurring as porphyroblasts in the silicate matrix.

Twenty-eight amphibolite samples collected from Taoba, Zhangzhuang and Bantaizi deposits were analyzed for major and trace elements and the results are listed in Table 6.1. These amphibolites have variable SiO_2 contents varying from 46.26 to 55.70 wt% with an average of 49.66 wt%. They also have medium to high components of alkalis (0.49–4.74 wt% K_2O; 0.50–3.28 wt% Na_2O), and relatively high Al_2O_3 contents (12.04–17.86 wt%). The TFe_2O_3 (total iron oxides as Fe_2O_3) contents fall between 8.96 and 23.40 wt%. The TiO_2 contents are relatively low with range of 0.48–3.00 wt%, whereas the CaO contents are relatively high, ranging from 1.74 to 9.64 wt% with an average of 8.26 wt%. Most samples have low contents of MgO (3.86–7.85 wt% with an average of 5.63 wt%). The

Table 6.1 Chemical compositions of whole rocks for amphibolites in the HQC

Sample	ZK242-46-2	ZK242-43	ZK242-44	ZK242-45-1	ZK242-48	ZK242-49	ZK242-50	ZK242-51	ZK242-53	ZK242-54	ZZZK49-1-1	ZZZK49-1-2	ZZZK49-1-3
Location	Taoba	Taoba	Taoba	Taoba	Taoba	Taoba	Taoba	Taoba	Taoba	Taoba	Zhangzhuang	Zhangzhuang	Zhangzhuang
Al_2O_3	13.28	13.28	12.83	13.47	12.4	14.63	12.9	13.1	12.86	12.84	15.4	15.23	15.31
BaO	0.04	0.07	0.08	0.07	0.03	0.04	0.03	0.03	0.03	0.03	0.01	0.02	0.02
CaO	8.61	8.24	7.49	8.53	8.99	9.37	9.21	9.33	9.23	9.02	9.62	9.64	9.53
Cr_2O_3	0.03	0.03	0.02	0.03	0.03	0.05	0.03	0.03	0.03	0.03	0.02	0.02	0.02
Fe_2O_3T	16.29	15.28	15.1	15.71	18.15	13.02	15.98	15.58	15.82	16.06	12.36	12.55	12.43
K_2O	1.65	2.01	1.89	1.75	1.62	1.63	1.16	1.09	0.81	1.19	0.51	0.49	0.74
MgO	5.17	4.65	3.86	4.97	6.09	7.84	5.26	5.56	5.35	5.38	7.75	7.85	7.8
MnO	0.23	0.21	0.19	0.21	0.27	0.21	0.23	0.22	0.23	0.23	0.14	0.13	0.15
Na_2O	2.12	2.02	2.17	2.31	1.53	1.93	2.13	2.31	2.38	2.07	3.11	3.01	2.94
P_2O_5	0.145	0.499	0.511	0.45	0.196	0.07	0.207	0.189	0.195	0.206	0.11	0.109	0.104
SiO_2	49.8	50.43	51.78	48.8	47.11	48.35	49.58	49.55	49.4	49.08	49.39	49.23	49.12
SrO	0.02	0.03	0.04	0.04	0.02	0.03	0.03	0.03	0.03	0.03	0.03	0.03	0.03
TiO_2	1.44	2.39	2.37	2.19	1.78	0.89	1.99	1.88	1.95	1.98	0.76	0.76	0.75
LOI	0.83	0.7	0.61	0.77	0.96	1.44	1	0.86	0.69	1.14	0.59	0.69	0.72
Total	99.65	99.82	98.95	99.29	99.18	99.49	99.72	99.76	98.99	99.29	99.81	99.77	99.66
Ag	0.24	0.21	0.2	0.2	0.29	0.24	0.22	0.16	0.16	0.21	0.11	0.11	0.11
Al	6.91	6.76	6.69	7.07	6.37	7.22	6.77	6.95	6.97	7.04	7.07	6.94	6.13
As	<0.2	<0.2	<0.2	0.4	0.2	0.6	0.4	<0.2	<0.2	0.6	<0.2	<0.2	<0.2
Ba	270	510	730	560	140	240	180	210	210	250	50	70	100
Be	1.11	1.21	1.16	1.1	2.28	0.67	0.89	0.81	0.79	0.88	2.76	1.21	1.09
Bi	0.38	0.15	0.24	0.25	0.61	0.28	0.07	0.05	0.04	0.07	0.27	0.24	0.25
Ca	6.01	5.75	5.31	6.04	6.12	6.4	6.47	6.55	6.75	6.64	6.5	6.47	6.19
Cd	0.25	0.24	0.19	0.21	0.3	0.22	0.17	0.21	0.16	0.19	0.15	0.16	0.15
Ce	21.5	97.5	110.5	84.3	23.7	10.65	47.2	42.1	38.8	42	16.95	16.6	15.65
Co	46.2	42.6	38.1	41.7	44.3	48.3	51.1	48.7	47.6	50	57.8	58.8	58.7
Cr	57	41	35	60	35	168	57	69	66	67	68	66	62
Cs	1.71	3.35	3.23	2.96	3.14	3.71	0.54	0.97	0.34	1.06	0.23	0.24	0.23
Cu	112	32.7	35.2	41.8	89.9	112.5	89.5	20	82.8	109.5	<0.2	0.7	<0.2
Dy	5.94	6.83	7.15	6.48	7.9	3.56	7.78	7.07	7.16	7.6	2.78	2.74	2.59
Er	3.86	3.84	4.02	3.65	5.19	2.39	4.72	4.26	4.38	4.68	1.82	1.78	1.7
Eu	1.33	2.45	2.57	2.34	1.82	0.83	1.96	1.77	1.86	1.96	0.95	0.92	0.86
Fe	10.75	9.92	10.1	10.7	11.75	8.51	10.65	10.45	10.9	11.25	7.95	7.98	7.73
Ga	20	22	21.9	20.7	22.1	16.95	20.2	19.2	18.6	19.95	20.3	18.2	17.4

(continued)

Table 6.1 (continued)

Sample	ZK242-46-2	ZK242-43	ZK242-44	ZK242-45-1	ZK242-48	ZK242-49	ZK242-50	ZK242-51	ZK242-53	ZK242-54	ZZZK49-1-1	ZZZK49-1-2	ZZZK49-1-3
Location	Taoba	Taoba	Taoba	Taoba	Taoba	Taoba	Taoba	Taoba	Taoba	Taoba	Zhangzhuang	Zhangzhuang	Zhangzhuang
Gd	4.92	7.16	7.81	6.88	6.42	2.86	7.16	6.47	6.71	7.25	2.62	2.46	2.37
Ge	0.23	0.3	0.31	0.29	0.36	0.19	0.27	0.24	0.18	0.19	0.15	0.17	0.2
Hf	0.8	0.9	0.9	0.9	1	0.6	1	1	1	1	0.6	0.6	0.6
Ho	1.31	1.39	1.45	1.32	1.75	0.8	1.65	1.51	1.47	1.56	0.62	0.6	0.58
In	0.131	0.111	0.114	0.107	0.203	0.086	0.129	0.122	0.113	0.118	0.063	0.07	0.061
La	8.1	45	51	38.8	8	4.2	19.9	17.9	16.6	18	8	7.9	7.3
Li	31.5	46.9	43.8	39.9	37	44.5	19.9	24.8	15.5	28.6	15.2	16.4	19.8
Lu	0.51	0.46	0.5	0.45	0.7	0.34	0.59	0.53	0.57	0.59	0.28	0.28	0.27
Mg	3	2.63	2.25	2.92	3.51	4.51	3.1	3.29	3.27	3.31	4.15	4.23	3.8
Mn	1660	1460	1410	1560	1880	1460	1650	1600	1700	1730	990	947	1070
Mo	0.83	1.41	1.13	2.18	1.08	0.48	0.73	1.32	0.81	0.96	0.11	0.48	0.69
Na	1.55	1.46	1.59	1.7	1.11	1.39	1.57	1.72	1.82	1.61	2.32	2.24	2.15
Nb	5.3	10.9	10.5	9.3	10.9	2.8	9	8.1	8.3	8.9	2.4	2.6	2.3
Nd	15.3	49.9	54.3	43.4	19.2	7.8	28.9	25.9	24.9	26.7	9	8.8	8.3
Ni	47.8	34.3	26.7	41.6	35.3	124	52.6	54.7	51.3	53.7	83	83.8	82.7
Pb	5.8	11.6	12.2	8.2	6.9	7.1	3.7	6.7	4.2	7.4	12.4	11.4	11.1
Pr	3.23	12.55	14	10.85	3.85	1.64	6.61	5.87	5.33	5.75	2.17	2.12	1.98
Rb	40.7	78.3	63.2	49.4	62.2	66.2	34.9	30.3	19.6	42.1	6.1	7.1	10.5
Re	0.002	0.003	0.003	0.003	0.002	0.002	0.003	0.003	0.003	0.003	<0.002	<0.002	<0.002
S	0.18	0.2	0.17	0.13	0.19	0.12	0.17	0.03	0.14	0.18	<0.01	<0.01	<0.01
Sb	0.08	0.08	0.08	0.12	0.1	0.06	0.07	0.06	0.05	0.06	0.07	0.06	0.06
Sc	40.8	31.6	31.5	30.1	55.1	41.2	41.5	39.3	38.8	40.7	46	43.3	41.2
Se	2	3	3	2	3	1	3	2	2	2	2	2	2
Sm	4.9	10.3	11.05	9.21	6.44	2.6	7.99	7.08	6.43	6.83	2.15	2.14	2.03
Sn	2.1	1.8	1.6	1.7	6.6	1.3	1.9	1.7	1.8	1.9	3.2	2.4	3.1
Sr	109.5	195.5	250	233	55	119.5	124.5	156	191	160.5	250	232	240
Ta	0.34	0.69	0.72	0.63	0.94	0.18	0.61	0.55	0.59	0.61	0.15	0.14	0.13
Tb	0.9	1.13	1.2	1.08	1.19	0.53	1.24	1.12	1.14	1.23	0.43	0.41	0.39
Te	<0.05	<0.05	<0.05	<0.05	<0.05	<0.05	<0.05	<0.05	<0.05	<0.05	<0.05	<0.05	<0.05
Th	0.3	3.5	4.6	3.1	0.4	0.4	2.1	1.9	2	2.1	0.7	0.6	0.6
Tl	0.22	0.44	0.34	0.26	0.36	0.41	0.18	0.16	0.11	0.23	0.06	0.06	0.1
Tm	0.51	0.48	0.51	0.47	0.7	0.33	0.61	0.55	0.59	0.62	0.28	0.26	0.26
U	0.4	0.8	0.8	0.6	2.3	1.1	0.4	0.4	0.4	0.4	0.1	0.1	0.1

(continued)

Table 6.1 (continued)

Sample	ZK242-46-2	ZK242-43	ZK242-44	ZK242-45-1	ZK242-48	ZK242-49	ZK242-50	ZK242-51	ZK242-53	ZK242-54	ZZZK49-1-1	ZZZK49-1-2	ZZZK49-1-3
Location	Taoba	Taoba	Taoba	Taoba	Taoba	Taoba	Taoba	Taoba	Taoba	Taoba	Zhangzhuang	Zhangzhuang	Zhangzhuang
V	354	269	291	261	405	267	338	332	353	357	207	208	203
W	0.4	0.7	0.6	0.8	0.6	0.3	0.3	0.3	0.3	0.4	0.1	0.1	0.2
Y	30.5	32.6	33.6	29.6	40.9	19.6	38	34.6	36.2	38.3	17.3	17.1	15.9
Yb	3.3	3.03	3.21	2.85	4.52	2.17	3.8	3.49	3.75	3.93	1.76	1.77	1.68
Zn	136	137	139	145	152	100	129	133	133	135	101	106	98
Zr	13.3	11.3	12.9	12.7	14.7	10.1	12.5	13.2	14.1	15.1	11.6	11.5	10.3
Eu*	0.27	0.29	0.28	0.29	0.28	0.3	0.26	0.26	0.28	0.28	11.47	12.49	9.82
Mg#	42.5	41.5	37.3	42.4	43.9	58.4	43.4	45.4	44.1	43.8	39	38.2	32.1
Ce*	4.2	4.1	4.14	4.11	4.27	4.06	4.12	4.11	4.12	4.13	6	5.45	4.07
Sr*	5.95	2.65	3.03	3.65	2.56	13	3.27	4.59	6	4.67	0	0	0
REET	75.61	242.02	269.27	212.08	91.38	40.7	140.11	125.62	119.69	128.7	49.81	48.78	45.96
A/CNK	0.63	0.65	0.67	0.64	0.6	0.67	0.6	0.6	0.6	0.61	0	0	0
Nb/Y	0.174	0.334	0.313	0.314	0.267	0.143	0.237	0.234	0.229	0.232	0.139	0.152	0.145
Nb/Ta	15.6	15.8	14.6	14.8	11.6	15.6	14.8	14.7	14.1	14.6	16	18.6	17.7
Ta/Yb	0.1	0.23	0.22	0.22	0.21	0.08	0.16	0.16	0.16	0.16	0.09	0.08	0.08
K_2O/Yb	0.5	0.66	0.59	0.61	0.36	0.75	0.31	0.31	0.22	0.3	0.29	0.28	0.44
K_2O/Na_2O	0.8	1	0.9	0.8	1.1	0.8	0.5	0.5	0.3	0.6	0.2	0.2	0.3
FeOT	14.7	13.7	13.6	14.1	16.3	11.7	14.4	14	14.2	14.5	11.1	11.3	11.2
FeO	12.5	11.7	11.5	12	13.9	9.96	12.2	11.9	12.1	12.3	9.45	9.6	9.51
La/Lu	15.9	97.8	102	86.2	11.4	12.4	33.7	33.8	29.1	30.5	28.6	28.2	27
$(La/Yb)_N$	1.67	10.11	10.81	9.27	1.2	1.32	3.56	3.49	3.01	3.12	3.09	3.04	2.96
$(Th/U)_N$	0.19	1.12	1.47	1.32	0.04	0.09	1.34	1.21	1.28	1.34	1.79	1.53	1.53

Sample	ZZZK28-1-2	ZZZK28-1-3	BTZK509-4-2	BTZK3-1	BTZK3-2	BTZK3-3	BTZK3-4	BTZK3-5	BTZK3-6	BTZK3-7	BT209-6	BT816-1	BT816-2	BT3-1	BT3-2
Location	Zhangzhuang	Zhangzhuang	Bantaizi	Bantaizi	Bantaizi	Bantaizi	Bantaizi	Bantaizi	Bantaizi	Bantaizi	Bantaizi	Bantaizi	Bantaizi	Bantaizi	Bantaizi
Al_2O_3	12.47	13.47	13.99	12.04	16.38	17.86	12.86	12.05	13.38	13.18	12.3	12.39	15.38	12.32	12.33
BaO	0.04	0.1	0.13	0.02	0.09	0.08	0.02	0.02	0.03	0.02	0.01	0.03	0.03	0.01	0.01
CaO	7.85	9.26	8.55	8.95	1.74	2.43	8.98	9.1	8.6	8.91	9.1	4.29	8.87	9	8.81
Cr_2O_3	0.02	0.03	0.04	0.03	0.04	0.04	0.03	0.03	0.03	0.03	0.01	0.02	0.02	<0.01	<0.01
Fe_2O_3T	16.59	14.16	10.94	20.27	12.02	10.42	20.52	20.12	15.99	15.72	20.04	23.4	8.96	19.87	19.41
K_2O	2.01	3.92	1.87	0.83	4.74	3.8	0.7	0.92	1.32	0.72	0.94	1.19	1.44	0.78	0.8
MgO	6.05	7.05	6.07	4.77	6.02	4.21	4.94	4.7	6.09	5.79	4.86	4.24	5.96	4.84	4.65
MnO	0.22	0.2	0.24	0.28	0.09	0.15	0.26	0.28	0.23	0.25	0.27	0.13	0.15	0.26	0.26
Na_2O	1.34	1.5	2.59	0.76	2.14	3.28	0.93	0.77	1	1.42	0.8	0.5	2.64	0.75	0.74

(continued)

Table 6.1 (continued)

Sample	ZZZK28-1-2	ZZZK28-1-3	BTZK509-4-2	BTZK3-1	BTZK3-2	BTZK3-3	BTZK3-4	BTZK3-5	BTZK3-6	BTZK3-7	BT209-6	BT816-1	BT816-2	BT3-1	BT3-2
Location	Zhangzhuang	Zhangzhuang	Bantaizi	Bantaizi	Bantaizi	Bantaizi	Bantaizi	Bantaizi	Bantaizi	Bantaizi	Bantaizi	Bantaizi	Bantaizi	Bantaizi	Bantaizi
P_2O_5	0.24	0.136	0.368	0.295	0.123	0.052	0.312	0.308	0.228	0.244	0.296	0.037	0.093	0.285	0.301
SiO_2	47.5	47.87	51.54	47.93	54.13	55.70	46.26	47.91	49.43	51.27	47.96	50.47	53.58	48.48	48.7
SrO	0.02	0.04	0.05	0.02	0.03	0.05	0.02	0.02	0.02	0.03	0.01	0.01	0.03	0.01	0.01
TiO_2	2.04	1.25	1.1	2.95	1.04	0.6	3	2.88	1.85	1.77	2.98	0.48	0.64	2.9	2.8
LOI	3.37	1.01	1.59	0.21	1.36	1.04	0.1	0.3	1.52	0.58	0.34	2.77	1.71	0.3	0.38
Total	99.76	99.99	99.07	99.35	99.96	99.7	98.93	99.4	99.73	99.93	99.91	99.95	99.51	99.81	99.21
Ag	0.1	0.22	0.21	0.27	0.12	0.14	0.27	0.27	0.3	0.27	0.08	0.12	0.09	0.13	0.1
Al	6.69	7.18	7.5	6.64	8.3	8.97	6.96	6.64	7.28	7.16	6.27	6.26	7.63	6.38	6.34
As	<0.2	<0.2	1.3	0.4	<0.2	<0.2	0.6	0.4	0.3	0.3	<0.2	<0.2	<0.2	<0.2	<0.2
Ba	330	920	730	80	870	730	80	100	180	90	80	320	290	70	70
Be	1.08	1.7	2.71	1.09	2.03	1.83	1.27	1.04	0.97	0.81	0.77	1.24	1.2	0.94	0.89
Bi	0.14	0.89	2.98	0.61	0.19	0.16	0.47	0.58	0.39	0.41	0.51	1.18	0.77	0.6	0.6
Ca	5.4	6.45	6.09	6.55	1.33	1.83	6.47	6.66	6.33	6.37	6.02	2.97	6.06	6.08	5.96
Cd	0.13	0.22	0.21	0.24	0.04	0.09	0.26	0.25	0.25	0.21	0.19	0.11	0.13	0.18	0.26
Ce	33.9	26.2	92.4	50.8	30.5	37.5	54.1	52.1	40.7	37	45.1	19.2	18.2	43.7	44.5
Co	55.2	57.3	34.8	56	44.5	25	53.5	55.9	49.4	47.6	53.1	24.3	40.8	56.3	53.9
Cr	60	87	102	39	116	145	38	36	86	81	33	136	144	34	34
Cs	2.89	0.94	2.29	0.51	22.8	15.75	0.37	0.54	3.27	0.75	0.46	4.01	2.12	0.42	0.47
Cu	110.5	155.5	70.8	95.9	2	1.3	52.6	69.2	84.1	72.5	88.3	74.3	37.3	87.8	70.1
Dy	7.61	4.7	4.27	10.2	2.45	2.59	10.45	10.5	7.61	6.98	10.35	2.48	2.7	10.1	10.1
Er	4.45	3	2.38	6.22	1.43	1.52	6.12	6.39	4.75	4.45	6	1.43	1.58	5.93	5.94
Eu	2.17	1.29	2	2.64	0.89	1.08	2.75	2.71	1.92	1.81	2.63	1.27	0.77	2.57	2.64
Fe	11.25	9.6	7.44	14.1	8.33	7.18	14	14.05	11.1	10.8	12.75	15.5	6.06	12.85	12.5
Ga	24.3	21.9	22.5	22.2	20.6	20.7	23.3	22.3	20.3	19	24.2	29.3	18.9	24.4	24.1
Gd	7.67	4.43	5.25	9.43	2.78	2.77	9.84	9.8	6.91	6.39	9.49	2.38	2.49	9.26	9.43
Ge	0.33	0.27	0.2	0.3	0.17	0.14	0.28	0.28	0.19	0.15	0.37	0.36	0.19	0.4	0.39
Hf	0.9	0.7	0.6	0.8	0.5	0.6	0.8	0.8	0.8	0.8	0.8	0.5	0.5	0.8	0.8
Ho	1.58	1.02	0.83	2.08	0.48	0.51	2.09	2.16	1.57	1.46	2.2	0.52	0.56	2.11	2.09
In	0.161	0.093	0.082	0.161	0.059	0.046	0.166	0.167	0.124	0.118	0.131	0.286	0.047	0.127	0.134
La	14	11.9	39.5	20.5	13.5	17.2	21.7	21.2	17.9	16.1	17.3	9.4	8.4	16.7	17.1
Li	49.9	15.4	54.8	18.2	125	95.5	23.5	18.8	41.9	24.3	13	159.5	53.6	16.5	17.3
Lu	0.62	0.47	0.33	0.78	0.21	0.22	0.73	0.81	0.63	0.6	0.69	0.16	0.19	0.68	0.67
Mg	3.58	4.19	3.67	2.92	3.61	2.46	2.97	2.89	3.76	3.53	2.67	2.37	3.33	2.72	2.6

(continued)

Table 6.1 (continued)

Sample	ZZZK28-1-2	ZZZK28-1-3	BTZK509-4-2	BTZK3-1	BTZK3-2	BTZK3-3	BTZK3-4	BTZK3-5	BTZK3-6	BTZK3-7	BT209-6	BT816-1	BT816-2	BT3-1	BT3-2
Location	Zhangzhuang	Zhangzhuang	Bantaizi	Bantaizi	Bantaizi	Bantaizi	Bantaizi	Bantaizi	Bantaizi	Bantaizi	Bantaizi	Bantaizi	Bantaizi	Bantaizi	Bantaizi
Mn	1620	1450	1760	2120	657	1120	1920	2090	1740	1860	1850	910	1070	1800	1800
Mo	0.51	0.59	0.7	0.93	1.9	2.26	1.06	0.73	0.97	0.99	0.6	0.32	0.66	0.58	0.6
Na	1.03	1.14	1.97	0.6	1.62	2.52	0.71	0.6	0.77	1.08	0.6	0.37	1.93	0.58	0.57
Nb	10.4	5.7	9.7	12.9	6.3	5.6	13.6	13.1	8.4	7.8	13.4	8.4	3.3	12.9	13.3
Nd	22.9	14.6	43.8	36.3	16.2	17.3	37.8	36.8	25.4	23.4	28.2	8.1	8.6	27.2	27.9
Ni	54.9	80.1	90.1	42.6	104	82.9	41.4	43.2	55.4	51.1	41.5	59.4	71.4	45.6	44.9
Pb	6	26.5	16.1	3.3	20.6	28.5	4.3	3.7	11.5	13.9	3.7	5.7	14.5	3.6	3.6
Pr	4.95	3.36	11.4	7.39	3.87	4.49	7.75	7.56	5.52	5.02	6.32	2.14	2.16	6.03	6.25
Rb	102.5	121	97.6	33	156.5	132	25.6	37.2	45.5	14.1	39.4	60.4	68.4	31.8	32.4
Re	0.002	0.005	0.002	0.004	0.003	0.002	0.003	0.004	0.003	0.002	0.005	<0.002	<0.002	0.004	0.004
S	0.08	0.39	0.16	0.24	<0.01	<0.01	0.14	0.22	0.08	0.06	0.26	0.71	0.07	0.23	0.2
Sb	<0.05	0.07	0.16	<0.05	<0.05	<0.05	<0.05	<0.05	0.1	0.09	0.08	0.09	0.1	0.06	0.06
Sc	48.3	49.9	31.1	44.5	25.3	16.4	44.9	44.3	44.5	42.2	43.1	12.5	33.2	45.8	44.2
Se	4	3	1	4	1	<1	4	4	2	2	5	2	2	5	5
Sm	6.42	3.73	7.12	9.75	3.27	3.17	10.15	10	6.37	5.94	8.75	2.12	2.37	8.38	8.54
Sn	2.9	1.4	6.2	2.5	2.4	1.7	2.9	2.6	2.2	1.7	2.1	5.6	1	2.1	2.1
Sr	151.5	341	334	57.9	198.5	298	54.8	50.3	105	145	62.2	48	257	57.1	52.9
Ta	0.68	0.37	1.04	0.9	0.41	0.46	0.95	0.92	0.59	0.53	0.87	0.87	0.22	0.86	0.87
Tb	1.21	0.72	0.76	1.62	0.42	0.45	1.69	1.68	1.2	1.1	1.65	0.41	0.42	1.58	1.6
Te	<0.05	0.08	<0.05	0.05	<0.05	<0.05	<0.05	0.05	<0.05	<0.05	0.05	0.11	<0.05	0.05	0.06
Th	1.2	1.2	2.5	1.5	2.5	4.8	1.6	1.5	2	1.9	1.8	2.9	2.1	1.7	1.7
Tl	0.54	0.66	0.57	0.2	0.92	0.68	0.15	0.23	0.27	0.1	0.23	0.39	0.56	0.17	0.17
Tm	0.63	0.45	0.32	0.83	0.2	0.21	0.79	0.86	0.64	0.61	0.9	0.21	0.23	0.84	0.85
U	0.3	0.2	1.7	0.3	0.7	1.3	0.3	0.3	0.3	0.3	0.4	3.4	0.6	0.4	0.4
V	324	311	204	435	180	119	426	439	352	338	408	111	169	428	398
W	0.8	0.6	0.6	1.4	1	0.5	0.6	0.7	1.1	0.5	0.7	0.7	0.4	0.6	0.6
Y	43.7	28.8	21.4	49.6	11	13	49.9	50.6	38	36.9	55	15.5	14.8	53.5	53.7
Yb	3.99	2.89	2.08	5.27	1.29	1.35	4.92	5.38	4.14	3.87	5.35	1.23	1.43	5.2	5.12
Zn	137	140	178	182	129	99	185	180	157	137	169	104	86	175	167
Zr	13.5	12.6	16	11.2	16.3	21.7	12.4	12.6	13.3	15.4	11.9	11.3	8.2	11.3	11.2
Eu*	11.5	15.61	0.33	0.28	0.3	0.36	0.28	0.27	0.29	0.29	0.29	0.57	0.32	0.29	0.29
Mg#	20.3	10.6	56.4	35.4	53.9	48.5	35.9	35.2	47	46.2	36.1	29.7	60.8	36.2	35.8
Ce*	0.77	1.33	4.35	4.13	4.22	4.27	4.17	4.12	4.09	4.12	4.31	4.28	4.27	4.35	4.3

(continued)

Table 6.1 (continued)

Sample	ZZZK28-1-2	ZZZK28-1-3	BTZK509-4-2	BTZK3-1	BTZK3-2	BTZK3-3	BTZK3-4	BTZK3-5	BTZK3-6	BTZK3-7	BT209-6	BT816-1	BT816-2	BT3-1	BT3-2
Location	Zhangzhuang	Zhangzhuang	Bantaizi	Bantaizi	Bantaizi	Bantaizi	Bantaizi	Bantaizi	Bantaizi	Bantaizi	Bantaizi	Bantaizi	Bantaizi	Bantaizi	Bantaizi
Sr*	0.01	0.01	4.9	1.33	8.5	10.9	1.19	1.13	3.18	4.8	1.7	3.52	19.18	1.61	1.46
REET	112.1	78.76	212.44	163.81	77.49	90.36	170.88	167.95	125.26	114.73	144.93	51.05	50.1	140.28	142.73
A/CNK	0.01	0.01	0.64	0.65	1.39	1.28	0.69	0.64	0.72	0.68	0.65	1.25	0.7	0.67	0.68
Nb/Y	0.238	0.198	0.453	0.26	0.573	0.431	0.273	0.259	0.221	0.211	0.244	0.542	0.223	0.241	0.248
Nb/Ta	15.3	15.4	9.3	14.3	15.4	12.2	14.3	14.2	14.2	14.7	15.4	9.7	15	15	15.3
Ta/Yb	0.17	0.13	0.5	0.17	0.32	0.34	0.19	0.17	0.14	0.14	0.16	0.71	0.15	0.17	0.17
K_2O/Yb	0.5	1.36	0.9	0.16	3.67	2.81	0.14	0.17	0.32	0.19	0.18	0.97	1.01	0.15	0.16
K_2O/Na_2O	1.5	2.6	0.7	1.1	2.2	1.2	0.8	1.2	1.3	0.5	1.2	2.4	0.5	1	1.1
FeOT	14.9	12.7	9.84	18.2	10.8	9.38	18.5	18.1	14.4	14.1	18	21.1	8.06	17.9	17.5
FeO	12.7	10.8	8.37	15.5	9.19	7.97	15.7	15.4	12.2	12	15.3	17.9	6.85	15.2	14.8
La/Lu	22.6	25.3	119.7	26.3	64.3	78.2	29.7	26.2	28.4	26.8	25.1	58.8	44.2	24.6	25.5
$(La/Yb)_N$	2.39	2.8	12.92	2.65	7.12	8.67	3	2.68	2.94	2.83	2.2	5.2	4	2.19	2.27
$(Th/U)_N$	1.02	1.53	0.38	1.28	0.91	0.94	1.36	1.28	1.7	1.62	1.15	0.22	0.89	1.09	1.09

Data from Liu et al. (2015), Liu and Yang (2015)

remaining other major elements contents are less than 1 wt %. With respect to trace elements, they display enrichments in REE (REE_{Total}: 40.7–269.3 ppm), in particular for LREE (light rare earth elements) (e.g. La/Lu ratios from 11.4 to 119.7). They also have high LILE (large ion lithophile elements) contents (such as Rb: 6.1–156.5 ppm; Ba: 50–920 ppm). Moreover, their Th and U contents are lower relative to Rb and Ba (0.3–4.8 ppm with an average of 1.9 ppm for Th; 0.1–3.4 ppm with an average of 0.7 ppm for U), and the $(Th/U)_N$ (N denotes normalization to primitive mantle) ratios vary widely from 0.04 to 1.79. However, they are markedly depleted in HFSE (high field strength elements) in spider diagrams (Fig. 6.6a, c, e). The REE patterns range from flat to significantly LREE enriched with $(La/Yb)_N$ of 1.2–12.9 (Fig. 6.6b, d, f). Together, Nd and Ce show a marked positive anomaly. Therefore, in general, the amphibolite samples display the geochemical affinity to island-arc basalts.

The analytical results of sixteen TTG gneisses for major and trace compositions are listed in Table 6.2. They have SiO_2 contents ranging from 59.3 to 73.6 wt% and high Al_2O_3 contents (13.4–21.0 wt%, Ave. = 15.3 wt%). They display relatively low MgO (0.5–3.6 wt%, Ave. = 1.4 wt%; Mg# = 24–63, Ave. = 46), Ni (1.3–115 ppm, Ave. = 12.8 ppm) and Cr (3–175 ppm, Ave. = 23.6 ppm) contents. The Fe_2O_3T contents vary from 1.8 to 8.7 wt% with an average of 3.6 wt%. They also show medium K_2O contents (1.0–3.0 wt%, Ave. = 1.9 wt%) and high Na_2O contents (3.2–7.1 wt%, Ave. = 4.8 wt%) with a high Na_2O/K_2O ratios >1.4 (Ave. = 2.8). Three samples are metaluminous (A/CNK = 0.96–0.98) and the remains are peraluminous (A/CNK = 1.02–1.57). The rocks are characterized by high Sr/Y (12–92) and La/Yb_N (3–155, N denotes chondrite-normalized), while the HREE are depleted. On chondrite-normalized REE patterns (Fig. 6.7a, c, e), all TTG show strongly fractionated REE patterns (La/Lu_N = 3–111, Gd/Yb_N = 1.5–8.5) with slight negative to visible positive Eu anomalies (Eu* = 0.62–1.47) and weak positive Ce anomalies (Ce* = 1.01–1.11). On N-MORB-normalized spider diagrams (Fig. 6.7b, d, f), the rocks show the following characteristics: (1) LILE enrichments such as Rb, Ba, Th and U relative to LREE; (2) considerable positive Pb anomalies (Pb* = 5.8–68.8); and (3) strong depletions in HFSE (e.g., Nb, Ta, Ti, Zr and Hf).

Zircons from two amphibolites and two TTG gneiss samples are analyzed for U–Pb dating by LA-MC-ICPMS, and their results are listed in Table 6.3. Corresponding concordia diagrams of these zircons U–Pb data are shown in Fig. 6.8. The zircon grains from amphibolite sample ZK122-1 are gray to dark gray and are mostly subhedral, with lengths of 150–250 μm, and length to width ratios of 1:1–2:1 (Fig. 6.8a). Their U contents vary from 92 to 427 ppm and Th from 34 to 274 ppm with Th/U ratios of 0.27–1.00

(Table 6.3), indicating magmatic origin. Thirteen available spots define an upper-intercept age of 2966 ± 33 Ma (MSWD = 6.3) (Fig. 6.8a). On the other hand, another amphibolite ZX84-3 give a discordia upper-intercept age of 3012 ± 21 Ma (MSWD = 5.4) (Fig. 6.8b), which agrees with the ages of ZK122-1 within error.

The zircons from TTG gneisses are mainly subhedral equant, stubby or prismatic with rounded terminations, and in size from 80 to 150 μm (Fig. 6.8c, d). Most of the zircons are gray in CL images with distinct to indistinct oscillatory zoning (Fig. 6.8c, d). Based on the ages obtained, in combination with the crystal shapes and internal structures, the zircon population in the gneisses can be dived into three types. Type 1 zircons are prismatic or stubby grains with oscillatory-zoned cores surrounded by structureless overgrowth rims, which appear dark in CL images. The oscillatory-zoned cores yield $^{207}Pb/^{206}Pb$ spot ages in the range of 2900–2929 Ma (Liu et al. 2015). Type 2 zircons are stubby or prismatic grains with subhedral equant and rounded terminations in shape (Fig. 6.8c, d). Their overgrowth rims exhibit irregular or discontinuous features, and occasionally individual zircons retain complete rims. Their oscillatory-zoned cores yield $^{207}Pb/^{206}Pb$ upper-intercept ages of 2765 ± 11 Ma and 2752 ± 24 Ma, for samples ZK3-511 and ZX34-40, respectively. These ages broadly coincide with those previously reported from the Huoqiu granitoid gneiss (Wan et al. 2010; Yang et al. 2012, 2014; Wang et al. 2014). Type 3 zircons are present only in sample ZX34-40, where they are prismatic grains with length to width ratios of ca. 2:1–3:1. Some zircons exhibit a clear core-rim structure. The cores show low luminescence and the rims display high luminescence in CL images (Fig. 6.8 d), suggesting that the cores are magmatic and the rims were formed by metamorphism. Seven analyses on the magmatic cores yield upper-intercept ages of 2444 ± 29 Ma on a concordia diagram, with one spot showing $^{207}Pb/^{206}Pb$ age

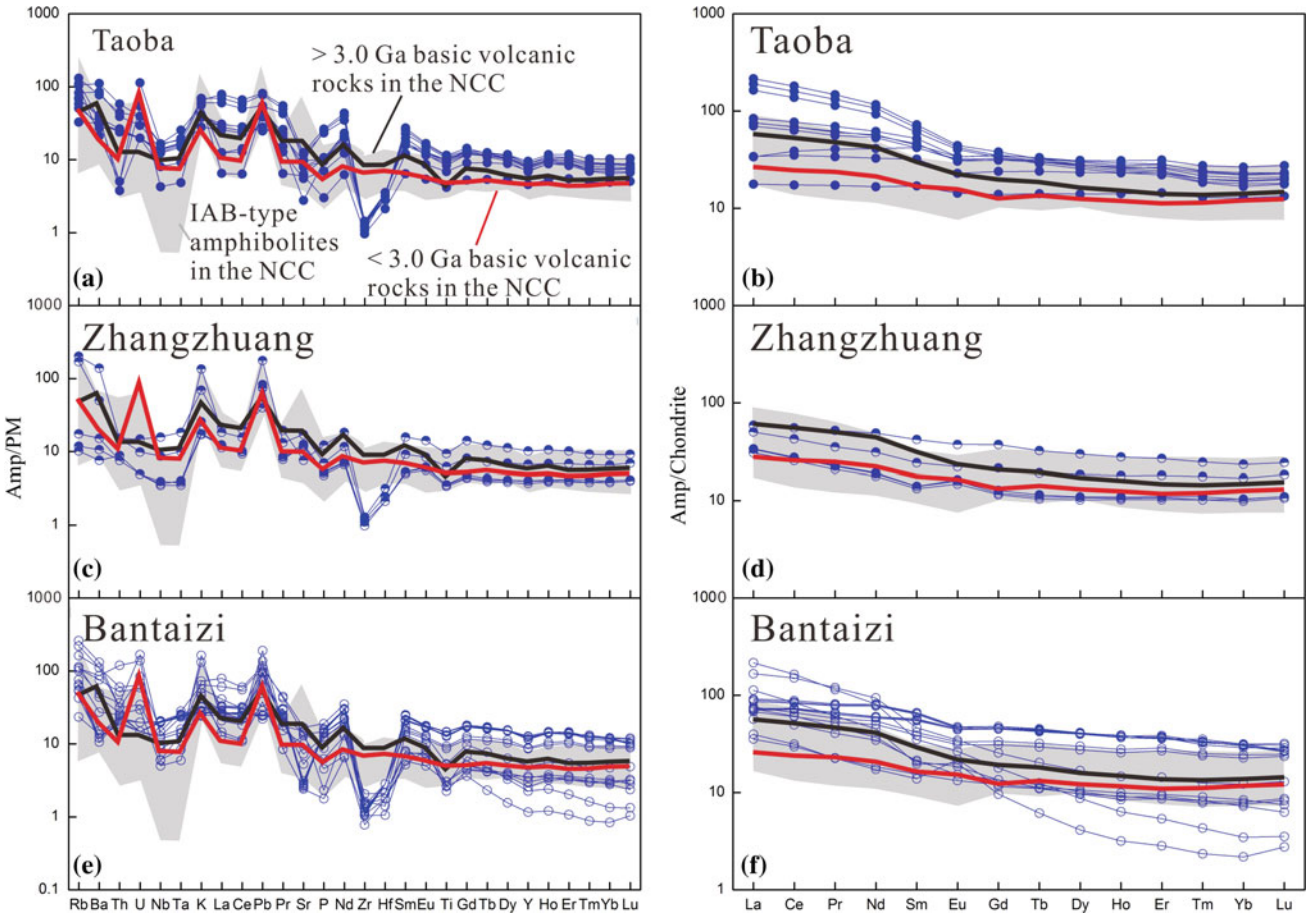

Fig. 6.6 Primitive mantle (PM) normalized spider diagram and chondrite-normalized REE pattern of amphibolites in the Huoqiu iron deposit. *Black line* and *red line* represent basic volcanic rocks of >3.0 Ga and <3.0 Ga in the NCC, respectively. The *shaded gray* field is the range of IAB-type amphibolites in the NCC (Wang et al. 2004). Primitive mantle and chondrite values are from McDonough and Sun (1995) and Sun and McDonough (1989), respectively. Taoba, Zhangzhuang and Bantaizi are exactly deposits distributed in HQC (detailed see in Fig. 6.3b in this chapter)

Table 6.2 Major (wt%) and trace (ppm) element compositions for TTG gneisses in the HQC

Sample	ZK242-45-2	ZK242-47	ZK242-55	ZZZK62-2-1	ZZZK62-2-2	ZZZK62-2-3	ZZZK62-3-1	ZZZK62-3-2	BTZK509-4-1	BT209-5	BT209-8	BT209-9	BT816-3	ZK242-46-1	ZZZK62-3-3	BT403-1
Rock	Ta	Td	Td	Td	Td	Td	Td	Td	Td	Td	Td	Td	Td	Gd	Gd	Gd
Location	TB	TB	TB	ZZ	ZZ	ZZ	ZZ	ZZ	BTZ	BTZ	BTZ	BTZ	BTZ	TB	ZZ	BTZ
Al_2O_3	16.1	15.0	14.1	15.3	15.8	14.4	15.0	21.0	13.9	14.6	13.4	13.4	14.8	16.1	14.7	17.8
BaO	0.1	0.1	0.0	0.1	0.1	0.0	0.0	0.1	0.1	0.1	0.1	0.0	0.1	0.1	0.1	0.1
CaO	4.2	2.9	2.3	1.6	1.7	1.7	1.8	2.5	2.9	1.8	2.2	1.8	1.9	4.7	2.5	2.0
Cr_2O_3	0.01	0.01	0.01	0.01	0.01	<0.01	0.01	0.01	0.02	0.01	0.01	0.02	<0.01	0.02	0.01	0.03
Fe_2O_3T	4.2	2.4	2.2	2.9	3.7	1.8	2.7	3.1	2.0	2.5	2.3	3.5	4.9	8.7	2.3	7.6
K_2O	1.3	1.8	1.0	2.2	2.2	1.1	1.5	3.0	2.0	2.2	1.6	1.4	1.5	2.3	2.6	2.3
MgO	1.1	0.6	0.5	1.6	1.8	0.8	1.0	1.1	0.9	0.7	1.6	2.5	0.7	2.7	1.0	3.6
MnO	0.1	0.0	0.0	0.0	0.0	0.0	0.0	0.0	0.0	0.0	0.1	0.0	0.1	0.2	0.0	0.1
Na_2O	4.5	4.6	5.1	5.3	5.4	5.7	5.3	7.1	4.3	4.9	4.0	4.1	4.9	3.6	3.9	3.2
P_2O_5	0.4	0.1	0.0	0.1	0.1	0.1	0.1	0.1	0.2	0.1	0.1	0.1	0.1	0.2	0.1	0.1
SiO_2	66.2	71.4	73.6	70.1	67.4	73.5	71.2	60.1	71.6	71.1	72.9	71.5	70.3	59.3	71.2	61.0
SrO	0.1	0.0	0.0	0.0	0.0	0.0	0.0	0.0	0.1	0.0	0.0	0.0	0.0	0.0	0.0	0.0
TiO_2	0.5	0.3	0.2	0.3	0.4	0.2	0.4	0.4	0.1	0.3	0.2	0.3	0.1	1.0	0.3	0.8
LOI	0.5	0.3	0.4	0.6	0.6	0.7	1.2	1.1	0.6	0.8	0.8	0.9	0.6	0.7	1.1	1.6
Total	99.2	99.5	99.4	100.2	99.4	99.9	100.3	99.4	98.5	99.3	99.1	99.6	99.9	99.5	99.8	100.1
Ba	560	430	250	700	590	350	360	800	430	720	510	350	510	590	610	450
Be	1.15	1.3	1.19	1.82	1.77	2.61	1.48	2.46	5.86	1.55	2.85	1.3	1.63	1.51	1.84	5.29
Bi	0.3	0.13	0.05	0.3	0.25	1.09	0.02	0.03	0.28	0.06	0.13	0.14	0.11	0.12	0.12	0.50
Ce	31.1	26.2	24.9	69.3	64.7	72.6	81.5	111.5	15.25	57.8	55.1	34.6	34.5	23.3	54.9	69.8
Co	8.5	4.2	2.9	4.7	6.1	3.4	3.8	5	4.9	3.9	3.4	9.8	3.8	20.9	3.3	30.4
Cr	20	14	11	5	8	3	3	3	31	10	14	29	15	32	5	175
Cs	2.24	0.8	0.77	5.66	6.97	2.31	1.44	3.31	2.78	1.41	5.32	4.79	1.45	3.45	4.34	14.15
Cu	12.4	6.5	10.8	0.3	11.5	13.8	<0.2	<0.2	1.8	0.9	0.5	29	17.5	4.6	<0.2	39.3
Dy	2.23	0.58	0.75	0.62	0.83	0.67	0.85	1.74	1.16	0.64	0.79	1.02	0.96	2.86	0.72	3.55
Er	1.08	0.28	0.31	0.22	0.29	0.23	0.3	0.63	0.61	0.23	0.33	0.4	0.55	1.79	0.24	1.88
Eu	0.88	0.56	0.51	0.68	0.72	0.68	0.65	0.97	0.42	0.65	0.82	0.82	0.51	0.97	0.59	1.25
Fe	2.77	1.55	1.52	1.91	2.41	1.1	1.75	1.91	1.38	1.77	1.6	2.41	3.33	5.62	1.5	4.98
Ga	21	20.9	18.7	21.9	23.9	17.85	21	29.1	20	22.2	17.55	16.6	19.75	23.3	20.9	22.1
Gd	2.99	0.95	1.16	1.36	1.65	1.52	2.16	3.59	1.43	1.67	1.69	1.91	1.23	2.97	1.58	3.53
Hf	0.4	0.6	0.5	1	0.9	1	1.4	1.3	1	1.1	0.6	0.4	0.7	0.9	0.7	0.4
Ho	0.42	0.11	0.12	0.1	0.13	0.11	0.13	0.28	0.21	0.1	0.13	0.16	0.19	0.61	0.11	0.70
In	0.027	0.018	0.018	0.016	0.02	0.01	0.025	0.02	0.012	0.023	0.017	0.021	0.024	0.064	0.022	0.043
La	12.1	12.8	13.5	40.9	37.3	41.3	43.7	59.1	7.2	32.4	31.4	17.3	17.1	8.3	28.6	33.8
Li	28.9	22.6	24.7	45.1	50	23.8	33	36.2	36.5	33.2	47.5	57	37.2	51.1	40.5	91.9
Lu	0.11	0.04	0.03	0.04	0.05	0.04	0.05	0.08	0.09	0.05	0.05	0.05	0.08	0.27	0.05	0.24
Mo	0.81	0.57	0.71	0.2	0.08	0.19	0.1	0.09	0.91	0.6	0.95	1.1	0.79	0.85	0.05	2.10
Nb	3.5	3	2.7	5.5	7	3.2	5.5	6.5	4.7	5.1	3.8	2.5	3.4	11.7	4.6	7.0

(continued)

Table 6.2 (continued)

Sample	ZK242-45-2	ZK242-47	ZK242-55	ZZZK62-2-1	ZZZK62-2-2	ZZZK62-2-3	ZZZK62-3-1	ZZZK62-3-2	BTZK509-4-1	BT209-5	BT209-8	BT209-9	BT816-3	ZK242-46-1	ZZZK62-3-3	BT403-1
Rock	Ta	Td	Td	Td	Td	Td	Td	Td	Td	Td	Td	Td	Td	Gd	Gd	Gd
Location	TB	TB	TB	ZZ	ZZ	ZZ	ZZ	ZZ	BTZ	BTZ	BTZ	BTZ	BTZ	TB	ZZ	BTZ
Nd	15.1	9	8.9	22.3	21.9	24.6	28.2	40.1	6.5	19.6	18.4	15.2	11.5	14.3	18.7	26.0
Ni	10.1	4.3	1.9	1.9	2.8	1.4	1.5	1.8	16.3	2.7	2.3	15.8	4.9	20.7	1.3	115.0
Pb	12.6	13.1	25	18.2	17.4	17.1	14.5	28.5	33.7	19.6	11.3	10.2	19.8	9.7	18	35.1
Pr	3.9	2.78	2.54	6.96	6.63	7.54	8.57	12.05	1.73	5.85	5.51	4.02	3.57	3.32	5.69	7.58
Rb	35	47.3	39.5	73.6	82.2	35.5	61.4	104	80.9	76.1	83.8	55.1	58.6	63.7	114.5	162.5
Sc	5.3	2.4	2.1	3.5	4.8	2.1	3.8	4.9	4.8	4.2	2.5	5.3	3.1	14.8	3.4	23.5
Sm	3.38	1.42	1.38	2.96	3.13	3.33	4.25	6.42	1.41	2.77	2.53	2.52	2.01	3.53	2.84	4.43
Sn	1	1.6	1.3	1.9	2.3	1.7	2.1	2.1	1.9	2.2	2.9	1	2.5	2.5	3.1	2.0
Sr	357	229	183.5	170.5	170.5	169	200	291	375	238	144.5	265	253	245	227	211
Ta	0.16	0.17	0.16	0.34	0.43	0.24	0.39	0.56	1.51	0.44	0.28	0.21	0.39	1.21	0.45	0.50
Tb	0.42	0.12	0.16	0.14	0.16	0.14	0.2	0.38	0.22	0.17	0.19	0.23	0.17	0.48	0.16	0.58
Th	0.8	2.8	2.5	15	13.1	19.4	22.4	40.5	3.3	18.7	15.2	6	9.3	1.5	15.6	8.0
Tl	0.25	0.25	0.24	0.38	0.43	0.19	0.31	0.53	0.51	0.39	0.5	0.26	0.27	0.44	0.7	0.97
Tm	0.13	0.04	0.03	0.03	0.03	0.03	0.03	0.07	0.08	0.03	0.04	0.05	0.08	0.25	0.04	0.28
U	0.5	0.5	0.3	1.2	1.4	1.9	1.7	3.6	7.3	2.4	2	2.5	7.1	0.8	1.4	0.8
V	48	21	12	25	33	13	25	25	25	23	17	49	18	146	23	142
W	0.2	0.1	0.1	0.5	0.5	0.3	0.3	0.3	0.2	0.3	0.2	0.2	0.6	0.4	0.5	2.7
Y	9.6	2.8	3.3	2.7	3.4	2.8	3.4	7.4	6.2	2.6	3.7	4.3	6.1	14.4	3	17.8
Yb	0.73	0.24	0.19	0.18	0.2	0.19	0.21	0.43	0.54	0.19	0.24	0.29	0.60	1.66	0.23	1.79
Zn	59	48	43	19	25	11	36	36	28	32	20	42	19	111	34	125
Zr	13.2	22	22.6	41.4	36.4	34.2	55.3	49.3	25.6	45.3	24.6	13.4	20.9	22.6	27.6	12.30
Eu*	0.85	1.47	1.23	1.04	0.97	0.92	0.66	0.62	0.90	0.92	1.21	1.14	0.99	0.92	0.85	0.97
Mg#	38	37	32	56	53	51	45	44	50	39	62	63	24	42	50	52
Ce*	1.11	1.08	1.04	1.01	1.01	1.01	1.03	1.02	1.06	1.03	1.03	1.02	1.08	1.09	1.06	1.07
Pb*	12.0	16.1	33.0	8.7	8.8	7.7	5.8	8.2	68.8	11.2	6.8	9.1	18.7	11.6	10.7	16.0
REET	75	55	54	146	138	153	171	237	37	122	117	79	73	65	114	155
A/CNK	0.98	1.02	1.03	1.09	1.09	1.06	1.10	1.08	0.97	1.06	1.09	1.16	1.13	0.96	1.06	1.57
Sr/Y	37.2	81.8	55.6	63.1	50.1	60.4	58.8	39.3	60.5	91.5	39.1	61.6	41.5	17.0	75.7	11.9
K_2O/Na_2O	0.3	0.4	0.2	0.4	0.4	0.2	0.3	0.4	0.5	0.5	0.4	0.3	0.3	0.6	0.7	0.7
Gd/Yb_N	3.4	3.3	5.1	6.3	6.8	6.6	8.5	6.9	2.2	7.3	5.8	5.4	1.7	1.5	5.7	1.6
Nb/La	0.29	0.23	0.20	0.13	0.19	0.08	0.13	0.11	0.65	0.16	0.12	0.14	0.20	1.41	0.16	0.21
$Na_2O + K_2O$	5.8	6.4	6.2	7.6	7.6	6.8	6.8	10.0	6.2	7.1	5.6	5.6	6.4	5.9	6.5	5.5
T_{Zr} (°C)	594	634	639	679	668	668	703	676	641	686	649	613	638	616	653	617
La/Yb_N	11.3	36.3	48.4	154.6	126.9	147.9	141.6	93.5	9.1	116.1	89.0	40.6	19.4	3.4	84.6	12.9

Data from Liu et al. (2015), Liu and Yang (2015)

Notes *Ta* tonalite, *Td* trondhjemite, *Gd* granodiorite; *TB* Taoba, *ZZ* Zhangzhuang, *BTZ* Bantaizi. Calculation of zircon saturation temperatures referred to Watson and Harrison (1983). Letter *T* as postfix denotes total contents. Letter N in footnote means normalize to chondrite, and the value referred to Sun and McDonough (1989)

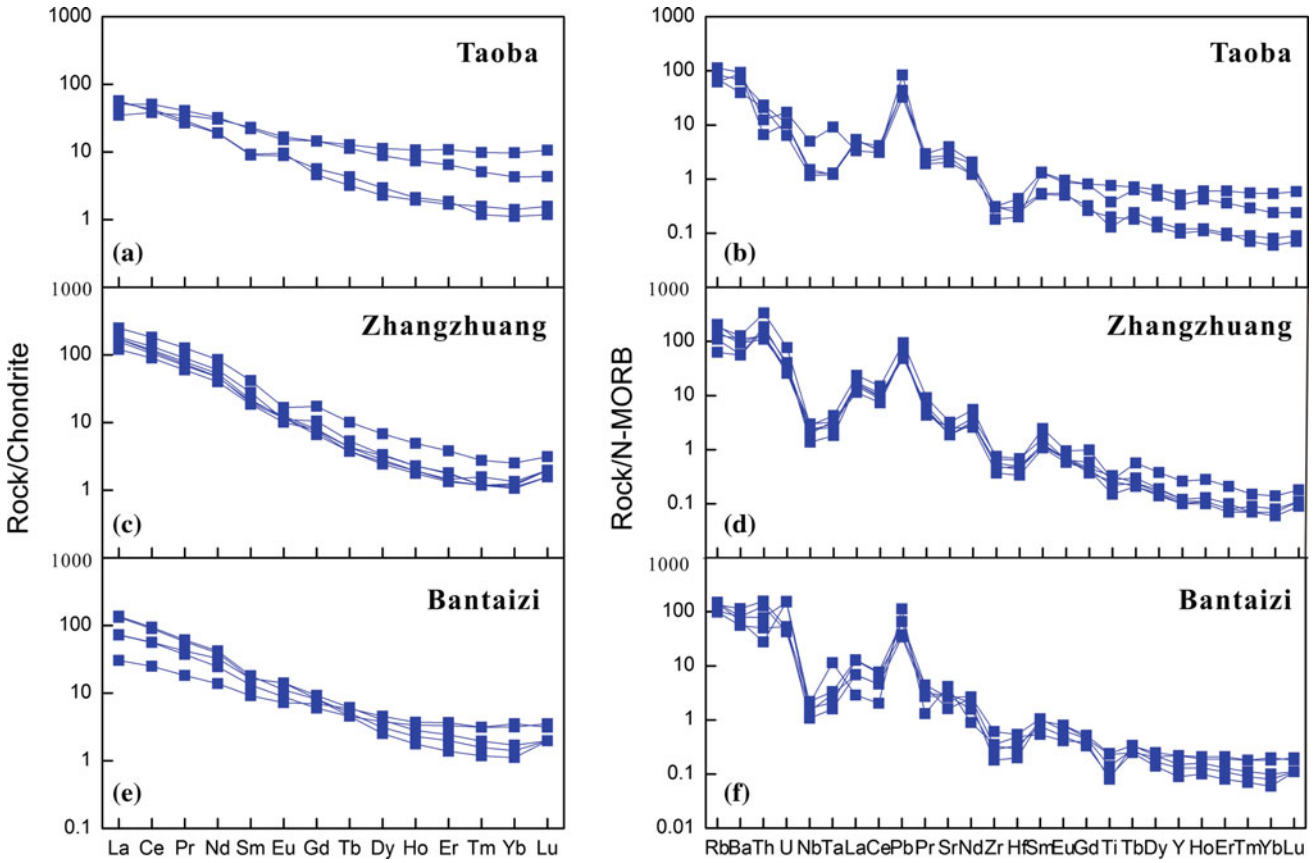

Fig. 6.7 Chondrite-normalized REE patterns and N-MORB-normalized spidergrams for the TTG gneisses in the HQC. **a**, **b** Taoba deposit; **c**, **d** Zhangzhuang deposit and **e**, **f** Bantaizi deposit. Normalization values of chondrite and N-MORB are referred to Sun and McDonough (1989)

of 2442 ± 10 Ma, and falling on the concordia line. The relatively large uncertainties in sample ZX34-40 was possibly caused by ~2.5 Ga metamorphic event, which disturbed the U–Pb system, metamorphic reworking recrystallization in the presence of fluids (e.g., Xia et al. 2009, 2010). Th/U ratios in the second type (Ave. = 0.4–0.5) are higher than those of the third type (Th/U = 0.3). In combination with CL images, we interpret the ages from the zircon cores to represent the magmatic crystallization ages of the protolith of the gneiss. The older age group (2.90–2.92 Ga) confirms the existence of a Mesoarchean crust in the Huoqiu area, similar to the report from the Yishui terrane of the NCC (Wu et al. 2013). The younger ages (2444 ± 29 Ma) are close to that of the voluminous granitic sheets intruding into the neighboring blocks in the NCC (ca. 2.5 Ga, Geng et al. 2012; Zhai and Santosh 2013). These ages are also consistent with the zircon ages reported from granodiorite (2440 ± 26 Ma) (Zhao et al. 2008) and biotite-monzogranites (2437 ± 10 Ma) from the Huai'an complex in the NCC (Zhang et al. 2011a, b). The dominant ages in the range of 2711–2765 Ma from the zircon population in our rocks indicate that peak crustal growth (both juvenile and partly recycled, see discussion below) occurred at 2.71–2.76 Ga. Previous studies in the NCC also identified a major period of juvenile crustal accretion in the NCC at this time, as inferred from Nd and zircon Hf isotopic data (Zhao and Zhai 2013), in spite of the fact the 2.5–2.6 Ga rocks make up ~80 % of the Precambrian basement of the NCC (Zhao and Zhai 2013; Zhai and Santosh 2013).

In situ Hf isotopic data of zircons from the amphibolite (sample ZX84-3) and TTG gneiss (ZK3-511 and ZX34-40) are summarized in Table 6.4 and shown in Fig. 6.9. From Chongxinji rocks 24 analyses on magmatic zircons are done (ZX84-3, this sample is the same as reported in Yang et al. (2012), whereas with relatively large uncertainties in ages, e.g., 2946 ± 41 Ma) show slightly variable $^{176}Hf/^{177}Hf$ ratios (0.280972–0.281393) with $\varepsilon_{Hf}(t)$ (t = 3012 ± 21 Ma) values ranging from 2.4 to 15.5 and t_{DM2} ranging from 2.45 to 3.25 Ga. The t_{DM1} vary from 2.66 to 3.16 Ga, which is similar to t_{DM2}. Nineteen analyses were made on the magmatic zircons from Chongxinji TTG gneiss (ZX34-40), among which 12 analyses yielded an upper-intercept age of 2752 ± 24 Ma, whereas six analyses yielded an upper-intercept age of 2444 ± 29 Ma (Fig. 6.8d). The zircons show high $^{176}Hf/^{177}Hf$ ratios (0.281156–0.281299) as compared to those from the amphibolite with $\varepsilon_{Hf}(t)$ values

Table 6.3 LA-MC-ICPMS data for zircons from the amphibolites and TTG gneisses in the HQC

Analysis	Concentrations (ppm)				Isotopic ratios						Isotopic ages (Ma)					
	Pb	Th	U	Th/U	$^{206}Pb/^{238}U$	1σ	$^{207}Pb/^{235}U$	1σ	$^{207}Pb/^{206}Pb$	1σ	$^{206}Pb/^{238}U$	1σ	$^{207}Pb/^{235}U$	1σ	$^{207}Pb/^{206}Pb$	1σ
ZK122-1 Amp.																
1	104	274	273	1.00	0.2523	0.0046	7.6542	0.1183	0.2200	0.0026	1450	27	2191	34	2981	19
2	173	188	427	0.44	0.3190	0.0034	9.0933	0.1210	0.2068	0.0019	1785	19	2347	31	2880	15
3	138	123	244	0.50	0.4549	0.0048	12.7441	0.1645	0.2032	0.0016	2417	25	2661	34	2852	13
4	102	89	160	0.56	0.5097	0.0084	13.9692	0.1950	0.1988	0.0015	2655	44	2748	38	2816	13
5	159	236	365	0.65	0.3429	0.0057	9.4104	0.1404	0.1991	0.0015	1900	32	2379	35	2819	12
6	150	116	416	0.28	0.2903	0.0032	8.0056	0.1231	0.2000	0.0024	1643	18	2232	34	2826	20
7	127	111	166	0.67	0.5691	0.0051	17.2082	0.2234	0.2193	0.0018	2904	26	2947	38	2976	13
8	93	100	115	0.87	0.5886	0.0066	17.5892	0.2296	0.2167	0.0018	2984	33	2968	39	2956	13
9	90	72	152	0.48	0.4891	0.0060	13.3363	0.1739	0.1978	0.0018	2567	32	2704	35	2808	15
10	118	118	173	0.68	0.5562	0.0052	16.2969	0.2103	0.2125	0.0016	2851	26	2894	37	2925	12
11	124	87	181	0.48	0.5274	0.0042	16.2965	0.2164	0.2241	0.0017	2731	22	2894	38	3010	12
12	80	62	123	0.51	0.5388	0.0067	14.2907	0.1928	0.1924	0.0013	2778	35	2769	37	2762	11
13	61	46	92	0.50	0.5451	0.0053	14.6110	0.1859	0.1944	0.0013	2805	28	2790	36	2780	11
14	150	236	240	0.98	0.4538	0.0054	12.9556	0.1824	0.2070	0.0019	2412	29	2676	38	2882	15
15	86	46	120	0.38	0.5839	0.0056	18.0935	0.2294	0.2247	0.0019	2965	28	2995	38	3015	13
16	77	124	158	0.78	0.3815	0.0031	10.0168	0.1268	0.1905	0.0016	2083	17	2436	31	2746	14
17	122	186	338	0.55	0.2945	0.0027	7.4337	0.0942	0.1831	0.0016	1664	15	2165	27	2681	14
18	114	77	194	0.40	0.4849	0.0066	14.0546	0.1907	0.2102	0.0016	2549	35	2753	37	2907	13
19	133	219	231	0.95	0.3918	0.0068	12.2494	0.1699	0.2268	0.0028	2131	37	2624	36	3029	20
20	137	50	135	0.37	0.7812	0.0062	37.1241	0.4701	0.3446	0.0024	3722	30	3697	47	3683	11
21	101	75	166	0.45	0.4996	0.0039	13.8776	0.1744	0.2015	0.0016	2612	20	2741	34	2838	13
22	130	83	241	0.34	0.4357	0.0107	14.6381	0.2505	0.2436	0.0019	2332	57	2792	48	3144	12
23	108	105	150	0.70	0.5636	0.0050	16.2229	0.2088	0.2088	0.0018	2881	26	2890	37	2896	14
24	124	112	203	0.55	0.4829	0.0043	14.1041	0.1817	0.2119	0.0020	2540	23	2757	36	2920	15
25	100	54	155	0.35	0.5550	0.0073	16.3226	0.2284	0.2133	0.0020	2846	37	2896	41	2931	15
26	117	152	274	0.56	0.3532	0.0031	9.1722	0.1190	0.1884	0.0016	1950	17	2355	31	2728	14
27	60	50	94	0.53	0.5247	0.0053	14.3682	0.1868	0.1986	0.0017	2719	27	2774	36	2815	14
28	108	209	283	0.74	0.3038	0.0025	8.0613	0.1009	0.1925	0.0016	1710	14	2238	28	2763	14
29	76	156	175	0.89	0.3435	0.0036	8.9720	0.1184	0.1894	0.0015	1903	20	2335	31	2737	13
30	100	119	144	0.82	0.5278	0.0042	15.3421	0.1941	0.2108	0.0017	2732	22	2837	36	2912	13

(continued)

Table 6.3 (continued)

Analysis	Concentrations (ppm)				Isotopic ratios						Isotopic ages (Ma)					
	Pb	Th	U	Th/U	$^{206}Pb/^{238}U$	1σ	$^{207}Pb/^{235}U$	1σ	$^{207}Pb/^{206}Pb$	1σ	$^{206}Pb/^{238}U$	1σ	$^{207}Pb/^{235}U$	1σ	$^{207}Pb/^{206}Pb$	1σ
31	83	58	117	0.50	0.5644	0.0053	17.5760	0.2484	0.2258	0.0023	2885	27	2967	42	3023	16
32	70	34	123	0.27	0.4970	0.0117	14.8355	0.2594	0.2165	0.0020	2601	61	2805	49	2955	15
ZX84-3 Amp.																
1	79	63	179	0.35	0.3691	0.0028	11.4055	0.1508	0.2241	0.0020	2025	15	2557	34	3011	14
2	91	128	213	0.60	0.3603	0.0027	9.0528	0.1124	0.1823	0.0015	1983	15	2343	29	2673	14
3	92	67	196	0.34	0.4118	0.0031	10.5383	0.1278	0.1856	0.0015	2223	17	2483	30	2704	13
4	54	29	84	0.35	0.5507	0.0045	16.5318	0.1999	0.2177	0.0017	2828	23	2908	35	2964	13
5	114	37	194	0.19	0.5081	0.0034	15.6620	0.1702	0.2235	0.0018	2649	18	2856	31	3006	13
6	436	143	342	0.42	0.5309	0.0183	38.6078	1.7838	0.5274	0.0078	2745	95	3736	173	4320	22
7	193	99	262	0.38	0.4393	0.0033	19.1667	0.3086	0.3164	0.0036	2347	18	3050	49	3553	18
8	64	27	155	0.17	0.3330	0.0024	10.5324	0.1164	0.2294	0.0018	1853	13	2483	27	3048	13
9	91	37	136	0.27	0.5747	0.0040	17.9049	0.1915	0.2260	0.0018	2927	20	2985	32	3024	13
10	94	37	227	0.16	0.3622	0.0028	9.7044	0.1050	0.1943	0.0015	1993	15	2407	26	2779	13
11	109	71	166	0.43	0.4292	0.0046	17.0354	0.2393	0.2879	0.0024	2302	25	2937	41	3406	13
12	72	50	93	0.54	0.6052	0.0039	19.1624	0.1979	0.2296	0.0018	3051	20	3050	31	3050	12
13	72	32	101	0.31	0.5995	0.0040	18.7900	0.1953	0.2273	0.0017	3028	20	3031	31	3033	12
14	91	42	154	0.27	0.5092	0.0037	15.2864	0.1639	0.2177	0.0017	2653	19	2833	30	2964	13
15	71	73	137	0.54	0.4145	0.0028	11.2333	0.1220	0.1966	0.0015	2235	15	2543	28	2798	13
16	56	29	80	0.36	0.5964	0.0039	18.2753	0.1913	0.2223	0.0017	3015	20	3004	31	2997	13
17	748	114	328	0.35	0.9199	0.0182	73.0200	1.8145	0.5757	0.0054	4205	83	4371	109	4448	14
18	194	211	290	0.73	0.3220	0.0039	18.7957	0.3610	0.4233	0.0041	1800	22	3031	58	3994	14
19	116	12	195	0.06	0.4862	0.0032	19.2531	0.2680	0.2872	0.0035	2554	17	3055	43	3402	19
20	51	21	80	0.26	0.5582	0.0042	16.5801	0.1815	0.2154	0.0016	2859	21	2911	32	2947	12
21	89	52	177	0.30	0.4164	0.0037	12.8337	0.1769	0.2236	0.0018	2244	20	2668	37	3006	13
22	87	103	165	0.62	0.4325	0.0031	11.0722	0.1195	0.1857	0.0014	2317	17	2529	27	2704	13
23	90	102	138	0.74	0.5201	0.0036	13.9606	0.1470	0.1947	0.0015	2700	19	2747	29	2782	13
24	86	53	120	0.44	0.5966	0.0042	18.4426	0.1982	0.2242	0.0017	3016	21	3013	32	3011	12
25	68	92	156	0.59	0.3587	0.0030	9.0855	0.1111	0.1837	0.0015	1976	16	2347	29	2686	13
26	91	117	184	0.64	0.4083	0.0042	10.3971	0.1414	0.1847	0.0014	2207	23	2471	34	2696	13
27	73	80	134	0.60	0.4385	0.0048	11.8691	0.2085	0.1963	0.0019	2344	26	2594	46	2796	15
28	58	25	96	0.26	0.5301	0.0035	16.5822	0.1753	0.2269	0.0018	2742	18	2911	31	3030	12

(continued)

Table 6.3 (continued)

Analysis	Concentrations (ppm)				Isotopic ratios						Isotopic ages (Ma)					
	Pb	Th	U	Th/U	$^{206}Pb/^{238}U$	1σ	$^{207}Pb/^{235}U$	1σ	$^{207}Pb/^{206}Pb$	1σ	$^{206}Pb/^{238}U$	1σ	$^{207}Pb/^{235}U$	1σ	$^{207}Pb/^{206}Pb$	1σ
29	126	32	166	0.19	0.4932	0.0038	22.0027	0.3939	0.3236	0.0043	2584	20	3184	57	3587	20
30	84	183	233	0.79	0.2546	0.0019	7.7111	0.1082	0.2197	0.0022	1462	11	2198	31	2978	16
31	59	34	83	0.41	0.6007	0.0042	18.8962	0.2118	0.2281	0.0019	3033	21	3037	34	3039	13
32	82	129	225	0.57	0.3013	0.0041	7.7629	0.1524	0.1869	0.0018	1698	23	2204	43	2715	15
ZK3-511 TTG																
1	24	19	36	0.52	0.5458	0.0034	14.9209	0.1127	0.1983	0.0013	2808	18	2810	21	2812	11
2	34	31	51	0.59	0.5481	0.0035	14.5941	0.0965	0.1931	0.0011	2817	18	2789	18	2769	10
3	102	78	161	0.49	0.5436	0.0034	14.4731	0.0944	0.1931	0.0011	2798	18	2781	18	2769	9
4	70	53	105	0.51	0.4969	0.0041	15.9834	0.3289	0.2333	0.0034	2600	21	2876	59	3075	23
5	92	94	147	0.64	0.5211	0.0040	13.8078	0.1110	0.1922	0.0011	2704	21	2737	22	2761	9
6	150	119	198	0.60	0.5611	0.0070	18.4131	0.5757	0.2380	0.0039	2871	36	3012	94	3107	26
7	111	155	203	0.77	0.4500	0.0046	11.9583	0.1282	0.1927	0.0011	2395	25	2601	28	2766	9
8	96	110	180	0.61	0.4488	0.0029	11.8234	0.0810	0.1911	0.0011	2390	15	2591	18	2751	10
9	114	149	216	0.69	0.4287	0.0044	11.5389	0.1180	0.1952	0.0012	2300	23	2568	26	2787	10
10	87	84	165	0.51	0.4464	0.0036	11.8415	0.1027	0.1924	0.0011	2379	19	2592	22	2763	9
11	66	63	105	0.60	0.5231	0.0033	14.0876	0.0925	0.1953	0.0011	2712	17	2756	18	2788	9
12	106	104	240	0.43	0.3646	0.0026	10.1601	0.0762	0.2021	0.0012	2004	14	2449	18	2843	10
13	105	147	260	0.57	0.3482	0.0027	8.5179	0.0696	0.1774	0.0010	1926	15	2288	19	2629	9
14	100	88	157	0.56	0.5392	0.0048	14.5920	0.1694	0.1963	0.0012	2780	25	2789	32	2795	10
15	37	31	60	0.52	0.5201	0.0038	13.6891	0.1100	0.1909	0.0011	2700	20	2728	22	2750	9
16	80	104	166	0.62	0.3867	0.0054	10.6207	0.1261	0.1992	0.0017	2108	29	2491	30	2819	14
17	87	120	177	0.67	0.4085	0.0031	10.4913	0.0900	0.1863	0.0012	2208	17	2479	21	2710	10
18	45	35	72	0.48	0.5265	0.0033	13.9759	0.0936	0.1925	0.0011	2727	17	2748	18	2764	10
19	88	11	187	0.06	0.4488	0.0056	11.5416	0.1631	0.1865	0.0011	2390	30	2568	36	2712	10
20	69	61	113	0.54	0.5215	0.0035	13.6799	0.0968	0.1903	0.0011	2706	18	2728	19	2744	9
21	88	80	151	0.53	0.5003	0.0046	13.0201	0.1287	0.1887	0.0011	2615	24	2681	27	2731	9
22	73	49	106	0.46	0.5868	0.0036	15.5609	0.1011	0.1923	0.0011	2977	18	2850	19	2762	9
23	59	49	123	0.40	0.4027	0.0043	10.7388	0.1258	0.1934	0.0013	2181	23	2501	29	2771	11
24	72	42	133	0.32	0.4594	0.0034	12.1652	0.1014	0.1921	0.0012	2437	18	2617	22	2760	10
25	18	6	31	0.19	0.5045	0.0032	13.9332	0.1104	0.2003	0.0014	2633	17	2745	22	2829	12
26	48	37	88	0.42	0.4422	0.0032	12.6529	0.0937	0.2075	0.0014	2361	17	2654	20	2886	11

(continued)

Table 6.3 (continued)

Analysis	Concentrations (ppm)				Isotopic ratios						Isotopic ages (Ma)					
	Pb	Th	U	Th/U	$^{206}Pb/^{238}U$	1σ	$^{207}Pb/^{235}U$	1σ	$^{207}Pb/^{206}Pb$	1σ	$^{206}Pb/^{238}U$	1σ	$^{207}Pb/^{235}U$	1σ	$^{207}Pb/^{206}Pb$	1σ
27	52	29	85	0.35	0.4992	0.0038	13.9184	0.2289	0.2022	0.0020	2610	20	2744	45	2844	16
28	31	13	49	0.26	0.5311	0.0034	14.0491	0.0938	0.1918	0.0011	2746	18	2753	18	2758	10
29	67	28	93	0.30	0.5525	0.0035	18.3417	0.1543	0.2408	0.0016	2836	18	3008	25	3125	11
30	91	81	176	0.46	0.4276	0.0033	11.8192	0.1029	0.2005	0.0012	2295	18	2590	23	2830	9
31	70	47	124	0.38	0.4836	0.0035	12.9658	0.0960	0.1944	0.0011	2543	18	2677	20	2780	9
32	51	38	80	0.48	0.5466	0.0037	14.5744	0.1028	0.1934	0.0011	2811	19	2788	20	2771	9
ZX34-40 TTG																
1	191	221	631	0.35	0.2531	0.0023	6.3682	0.0616	0.1825	0.0011	1455	13	2028	20	2675	10
2	107	62	448	0.14	0.2143	0.0013	4.9530	0.0326	0.1676	0.0010	1252	7	1811	12	2534	10
3	111	73	208	0.35	0.4696	0.0028	12.2652	0.0780	0.1894	0.0011	2482	15	2625	17	2737	9
4	243	122	667	0.18	0.3488	0.0022	7.7240	0.0531	0.1606	0.0009	1929	12	2199	15	2462	9
5	78	121	441	0.27	0.1636	0.0014	3.3973	0.0336	0.1506	0.0009	977	8	1504	15	2353	10
6	200	174	638	0.27	0.2855	0.0017	6.5129	0.0412	0.1654	0.0009	1619	10	2048	13	2512	9
7	89	176	427	0.41	0.1856	0.0015	3.8560	0.0326	0.1507	0.0009	1097	9	1605	14	2354	10
8	84	116	384	0.30	0.2012	0.0016	4.5898	0.0406	0.1655	0.0010	1182	9	1747	15	2512	10
9	123	170	527	0.32	0.2138	0.0014	4.4707	0.0335	0.1516	0.0009	1249	8	1726	13	2364	10
10	318	175	762	0.23	0.3966	0.0024	8.5297	0.0565	0.1560	0.0009	2153	13	2289	15	2413	10
11	90	150	707	0.21	0.1211	0.0008	2.0046	0.0161	0.1200	0.0007	737	5	1117	9	1957	11
12	135	94	912	0.10	0.1429	0.0009	2.6585	0.0176	0.1349	0.0008	861	6	1317	9	2163	10
13	256	75	543	0.14	0.4540	0.0032	9.9336	0.0865	0.1587	0.0010	2413	17	2429	21	2442	10
14	96	231	685	0.34	0.1320	0.0011	2.2752	0.0232	0.1250	0.0007	799	7	1205	12	2029	11
15	298	125	839	0.15	0.2503	0.0018	8.9291	0.0747	0.2588	0.0016	1440	10	2331	19	3239	10
16	504	163	991	0.16	0.4793	0.0038	11.3070	0.0979	0.1711	0.0010	2524	20	2549	22	2568	10
17	114	157	879	0.18	0.1225	0.0016	2.2635	0.0340	0.1340	0.0008	745	10	1201	18	2152	11
18	137	169	847	0.20	0.1487	0.0010	2.8391	0.0208	0.1385	0.0008	893	6	1366	10	2209	10
19	180	29	473	0.06	0.3655	0.0023	8.9800	0.0596	0.1782	0.0010	2008	12	2336	15	2636	9
20	184	187	1225	0.15	0.1414	0.0011	2.8634	0.0234	0.1469	0.0009	852	6	1372	11	2310	10

Data from Liu et al. (2015), Liu and Yang (2015)

For decline the uncertainties of zircon $\varepsilon_{Hf}(t)$ values in sample ZX84-3, we analyzed the zircons from the same sample as Yang et al. (2012) reported (2946 ± 41 Ma, 1σ, MSWD = 1.04) by LA-MC-ICPMS at the laboratory of the Tianjin Institute of Geology and Mineral Resource, Chinese Academy of Geological sciences, the analytical method and step are identical with those in this study

ranging from −3.0 to 1.5 and t_{DM2} ranging from 2.87 to 3.14 Ga. Most of the analyzed zircons are located along the Hf isotopic evolutionary line (Fig. 6.9), indicating that they have close links to petrogenesis. Previous studies have also reported Neoarchean gneisses with positive zircon $\varepsilon_{Hf}(t)$ values from the Eastern Block of the NCC such as in the gneisses from Yishui terrane (Wu et al. 2013), and Baijiafen (Wu et al. 2008). The consistence between t_{DM2} in TTG gneiss and t_{DM1} in amphibolite implies a genetic link between these rocks.

Two amphibolites with ca. 3.0 Ga from the HQC further confirm the existence of a Mesoarchean crust in the southeastern margin of the NCC. Mesoarchean crust has been identified from the Yishui terrane of Luxi in the Eastern Block (Wu et al. 2013). The first report of 2.9–3.0 Ga amphibolite and TTG gneiss was from Liu et al. (2015). Yet they have not given the further petrogenesis and tectonic constraints, such are they Mesoarchean bimodal volcanic rocks producing in extending continental rift setting? In spite of these, the most abundant igneous zircons from TTG gneisses are of 2.75 Ga, We therefore focus on their petrogenesis below.

Archean TTG are characterized by strongly fractionated REE patterns, HFSE depletions, LREE and LILE enrichments, and elevated La/Yb and Sr/Y. The TTG gneisses in the HQC have typical Archean TTG signatures (Fig. 6.7). In addition, they show low Ni and Cr contents (Ni = 1.3–20.7 ppm, Cr = 3–32 ppm with sample BT403-1 as outlier). These features have been taken to reflect the absence of any significant interaction of TTG magmas with peridotite in the mantle wedge (Rapp et al. 1999; Smithies 2000; Condie 2005; Martin et al. 2005). Furthermore, most samples are

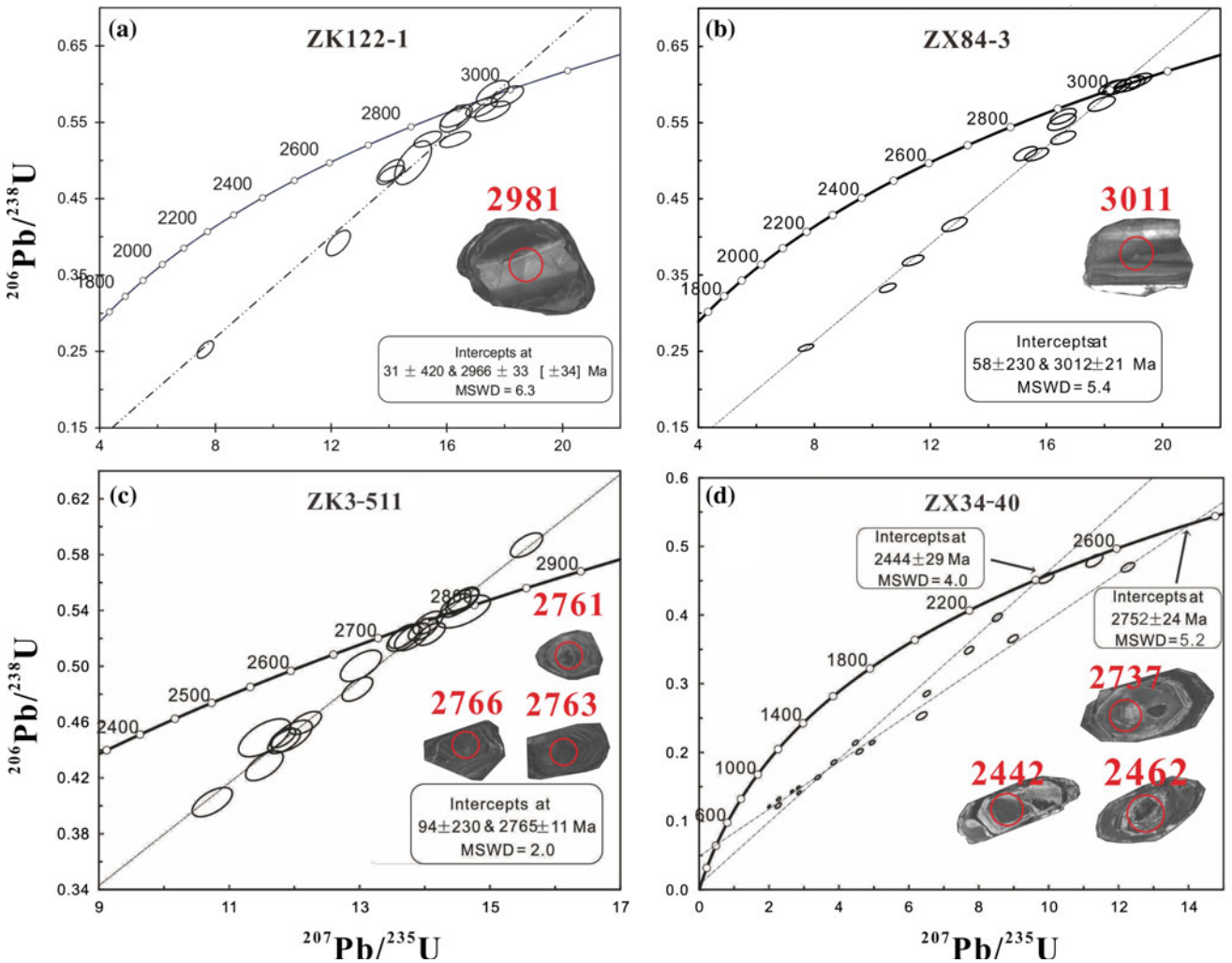

Fig. 6.8 Concordia diagrams of zircon U–Pb data from amphibolites and TTG gneisses in the HQC. **a** Amphibolite ZK122-1 from Zhangzhuang deposit; **b** amphibolite ZX84-3 from Chongxinji deposit; **c** leucocratic gneiss ZK3-511 from Bantaizi area; **d** TTG gneiss ZX34-40 from Chongxinji area. *Insert* show their reprehensive zircon CL images. *Red* number close to the *red circle* (denotes the ablated location and size, 35 μm) are also shown

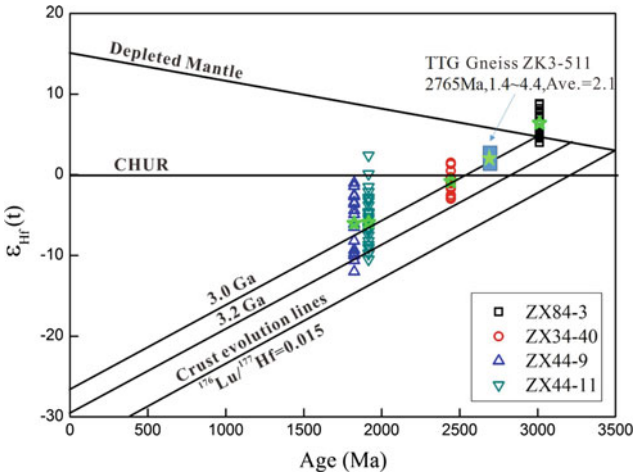

Fig. 6.9 U–Pb age versus $\varepsilon_{Hf}(t)$ for amphibolite, TTG gneiss and granites in the Huoqiu region (except for sample ZK3-511, data for other samples are from Liu et al. (2015), and they are listed in Table 6.4 together). Lu–Hf evolution line for depleted mantle is constrained by a present-day $^{176}Hf/^{177}Hf$ ratio of 0.28325 (Nowell et al. 1998) and $^{176}Lu/^{177}Hf$ ratio of 0.0384 (Griffin et al. 2000). Crust evolution line with $^{176}Lu/^{177}Hf$ = 0.015 corresponds to the average continental crust

located outside the range of experimental melts produced by subducted oceanic slab melting at 1–4 GPa (Fig. 4b in Liu et al. 2015). These features allow us to suggest that the initial TTG magmas in the HQC formed by partial melting of hydrous basaltic material (represented by amphibolite) at the base of the thickened lower crust.

Several lines of evidence support this possibility, including the close spatiotemporal association between amphibolite and TTG gneiss, their zircon Hf isotopes and geochemical features. The formation ages of the amphibolite were determined at 3012 ± 21 and 2966 ± 33 Ma; whereas the TTG gneiss sample yield a formation age of 2752 Ma. Thus, the amphibolites are older than TTG gneisses by ca. 200 Ma. Meanwhile, the TTG gneiss sample has t_{DM2} of 2.87–3.14 Ga, overlapping with the formation age of the amphibolite, and importantly, consistent with the t_{DM1} of the amphibolite (2.84–3.16 Ga, with spots No. 16 and 18 as outliers, Table 6.4). In addition, most zircons from these rocks are located on the 3.0 Ga evolutional line of zircon $\varepsilon_{Hf}(t)$ (Fig. 6.9).

We use trace element modeling to test whether the TTG magmas (gneisses) were formed by partial melting of a hydrous basaltic source (amphibolites). Modeling of batch melting was done using an amphibolite sample (ZZZK49-1-2, compositions see in Table 6.1), with low K content from the Zhangzhuang area as the source rock, and a typical TTG as the partial melt (TTG gneisses from Zhangzhuang). Two models were chosen: (1) partial melting of hydrous basalts (amphibolite), generating TTG melts in equilibrium with a garnet amphibolite residue containing 20 % garnet and 80 % amphibole; and (2) partial melting of hydrous basalts (amphibolites), producing TTG melts in equilibrium with a rutile-bearing eclogite residue composed of 49 % clinopyroxene, 50 % garnet and 1 % rutile (Drummond and Defant 1990; Rapp and Watson 1995). The results for partial melting with an amphibolite residue show that the Zhangzhuang TTG gneisses cannot be modeled successfully with a garnet amphibolite residue by 1–20 % melting, whereas a rutile-bearing eclogite residue is in equilibrium with a partial melt similar in composition to the Zhangzhuang TTG gneisses (Fig. 6.10). Furthermore, most samples fall on the line of melting of quartz eclogite, although they deviate from the line of melting of garnet amphibolite (Rapp and Watson 1995; Fig. 5b in Liu et al. 2015). This suggests that eclogite faces melting was the main mechanism to produce TTG magmas in the HQC.

In summary, the gneisses are similar to Archean TTG in composition and show close spatial relationship with amphibolites. Geochemical characteristics such as high Sr/Y and $(La/Yb)_N$ with steep REE patterns and trace element modeling suggest that there TTG gneisses were generated by partial melting of amphibolites at the base of a thickened crust, leaving a rutile-bearing eclogite residue. A similar model has also been suggested for the Mesoarchean to Neoarchean orthogneisses (2.95–2.79 Ga) in the Fiskenæsset region, southern West Greenland (Polat 2012; Huang et al. 2013a). LA-MC-ICPMS U–Pb age data from magmatic zircon grains show protolith emplacement ages of 2.76–2.71 Ga. Hf isotopic compositions of zircon grains from the amphibolite and gneiss show $\varepsilon_{Hf}(t)$ values of 2.4–15.5 and −3.0 to 1.5, respectively. The t_{DM2}(Hf) model ages of the gneisses range from 2.87 to 3.14 Ga, and are identical to the t_{DM1}(Hf) ages of amphibolites (2.84–3.16 Ga) within analytical uncertainty, suggesting that the gneisses formed by partial melting of amphibolite, and attest to large-scale remelting of the Mesoarchean continental rocks during Neoarchean.

6.3.2 Evidence from Detrital Zircon

The NCC represents one of only a few cratonic nuclei with a geological history extending back to the Eoarchean. However, extensive ca. 2.5 Ga crustal reworking has destroyed a considerable portion of the pre-existing crustal record, hindering the investigation of tectonothermal evolution prior to 2.5 Ga. The HQC represents rare material that survived the ca. 2.5 Ga tectonothermal events relatively intact, thus preserving valuable information on prior crustal growth. In situ detrital zircon U–Pb dating and Hf isotope analyses were conducted on three schists from three drilling holes cutting cross the basement of the HQC in order to decipher the nature (such as episodic vs. continuous, juvenile vs.

Table 6.4 Lu–Hf isotope analysis results of zircons from the amphibolite and TTG gneisses in the HQC

Sample/No.	Age (Ma)	$^{176}Lu/^{177}Hf$	$^{176}Yb/^{177}Hf$	$^{176}Hf/^{177}Hf$	2σ	$^{176}Hf/^{177}Hfi$	$\varepsilon Hf\ (0)$	$\varepsilon Hf\ (t)$	2σ	$t_{DM}T_{DM1}$	T_{DM2}	fLu/Hf
ZX84-3 (amphibolite)												
1	3012	0.00084	0.026572	0.281059	0.000012	0.281012	−60.6	5.6	0.42	3040	3056	−0.97
2	3012	0.000534	0.017854	0.281107	0.000013	0.281077	−58.9	7.9	0.45	2951	2914	−0.98
3	3012	0.001389	0.043186	0.281147	0.000012	0.281069	−57.5	7.6	0.44	2963	2935	−0.96
4	3012	0.000662	0.021284	0.281071	0.000015	0.281034	−60.2	6.4	0.52	3010	3009	−0.98
5	3012	0.001	0.031001	0.28111	0.000013	0.281053	−58.8	7.1	0.45	2984	2967	−0.97
6	3012	0.001084	0.035305	0.281028	0.000011	0.280967	−61.7	4	0.39	3101	3154	−0.97
7	3012	0.000675	0.022336	0.281028	0.000015	0.28099	−61.7	4.8	0.52	3068	3103	−0.98
8	3012	0.000683	0.020225	0.281039	0.00001	0.281	−61.3	5.2	0.36	3054	3080	−0.98
9	3012	0.000536	0.017365	0.281115	0.000011	0.281085	−58.6	8.2	0.4	2941	2897	−0.98
10	3012	0.000758	0.02397	0.281041	0.00001	0.280999	−61.2	5.1	0.34	3057	3085	−0.98
11	3012	0.001818	0.057423	0.281204	0.000013	0.281101	−55.4	8.7	0.46	2918	2865	−0.95
12	3012	0.000912	0.030101	0.281083	0.000007	0.281031	−59.7	6.3	0.26	3014	3015	−0.97
13	3012	0.000757	0.024929	0.281061	0.000011	0.281018	−60.5	5.8	0.4	3030	3042	−0.98
14	3012	0.000672	0.020532	0.281073	0.000013	0.281035	−60.1	6.4	0.46	3008	3006	−0.98
15	3012	0.00062	0.020169	0.281137	0.000013	0.281102	−57.8	8.8	0.45	2918	2861	−0.98
16	3012	0.001813	0.063014	0.281393	0.000015	0.28129	−48.8	15.5	0.55	2655	2454	−0.95
17	3012	0.00057	0.019075	0.281101	0.000014	0.281069	−59.1	7.6	0.49	2962	2931	−0.98
18	3012	0.001045	0.032072	0.281313	0.00001	0.281254	−51.6	14.2	0.36	2710	2530	−0.97
19	3012	0.001001	0.029892	0.281182	0.00001	0.281125	−56.2	9.6	0.36	2886	2811	−0.97
20	3012	0.000904	0.029084	0.281034	0.000012	0.280983	−61.5	4.5	0.43	3079	3120	−0.97
21	3012	0.000335	0.011161	0.281057	0.000011	0.281038	−60.7	6.5	0.4	3004	2998	−0.99
22	3012	0.000635	0.019276	0.281195	0.000008	0.281159	−55.8	10.9	0.29	2841	2735	−0.98
23	3012	0.000866	0.02859	0.280972	0.000011	0.280923	−63.6	2.4	0.4	3159	3248	−0.97
24	3012	0.000865	0.027731	0.281034	0.00001	0.280986	−61.4	4.7	0.37	3075	3113	−0.97
ZK3-511 (TTG gneiss)												
1	2765	0.000806	0.030334	0.281065	0.000038	0.28102	−60.4	−0.6	1.34	3029	3211	−0.98
2	2765	0.001354	0.049943	0.281004	0.000035	0.28093	−62.5	−5.1	1.26	3156	3440	−0.96
3	2765	0.001973	0.087898	0.281076	0.000047	0.28098	−60.0	−5.2	1.67	3108	3392	−0.94
4	2765	0.003203	0.143762	0.281140	0.000044	0.28097	−57.7	−2.3	1.55	3121	3319	−0.90
5	2765	0.000700	0.022503	0.281048	0.000040	0.28101	−61.0	4.8	1.41	3044	3081	−0.98
6	2765	0.001204	0.046119	0.281063	0.000042	0.28100	−60.4	−0.6	1.50	3063	3239	−0.96
7	2765	0.000816	0.028974	0.281048	0.000041	0.28101	−61.0	−1.4	1.47	3053	3255	−0.98
8	2765	0.002344	0.085318	0.281038	0.000043	0.28090	−61.3	0.4	1.54	3193	3325	−0.93
9	2765	0.001740	0.063917	0.280971	0.000036	0.28087	−63.7	−1.9	1.29	3234	3424	−0.95

(continued)

Table 6.4 (continued)

Sample/No.	Age (Ma)	$^{176}Lu/^{177}Hf$	$^{176}Yb/^{177}Hf$	$^{176}Hf/^{177}Hf$	2σ	$^{176}Hf/^{177}Hfi$	εHf (0)	εHf (*t*)	2σ	$t_{DM}T_{DM1}$	T_{DM2}	fLu/Hf
10	2765	0.000493	0.015974	0.281192	0.000038	0.28117	−55.9	5.9	1.36	2834	2863	−0.99
ZX34-40 (TTG gneiss)												
1	2444	0.000594	0.025460	0.281204	0.000013	0.281172	−55.5	−1.7	0.45	2827	3062	−0.98
2	2444	0.000714	0.029646	0.281227	0.000010	0.281189	−54.6	−1.1	0.35	2804	3023	−0.98
3	2444	0.000697	0.024748	0.281173	0.000007	0.281136	−56.6	−3.0	0.26	2876	3140	−0.98
4	2444	0.000668	0.028070	0.281270	0.000010	0.281235	−53.1	0.5	0.37	2742	2925	−0.98
5	2444	0.000772	0.033826	0.281189	0.000010	0.281149	−56.0	−2.5	0.36	2859	3111	−0.98
6	2444	0.000475	0.019925	0.281204	0.000011	0.281179	−55.5	−1.5	0.40	2818	3050	−0.99
7	2444	0.000222	0.010334	0.281156	0.000013	0.281144	−57.2	−2.8	0.46	2863	3128	−0.99
8	2444	0.000805	0.035438	0.281299	0.000011	0.281257	−52.1	1.3	0.39	2713	2876	−0.98
9	2444	0.000449	0.018192	0.281287	0.000012	0.281263	−52.5	1.5	0.42	2704	2866	−0.99
10	2444	0.000589	0.024830	0.281289	0.000013	0.281258	−52.4	1.3	0.47	2711	2876	−0.98
11	2444	0.000792	0.031679	0.281252	0.000011	0.281210	−53.8	−0.3	0.40	2775	2977	−0.98
12	2444	0.000555	0.022369	0.281222	0.000011	0.281192	−54.8	−1.0	0.38	2800	3019	−0.98

Except for sample ZX3-511, all other data from Liu et al. (2015), Liu and Yang (2015)

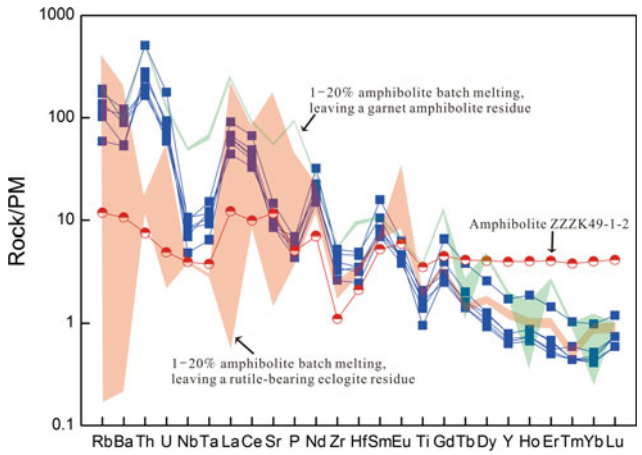

Fig. 6.10 Results of 1–20 % batch partial melting of a hydrous basaltic protolith (Zhangzhuang amphibolite ZZZK49-1-2, compositional data in Table 6.1) compared to the Zhangzhuang TTG gneisses. The partition coefficients employed were mainly compiled from Barth et al. (2002) (garnet and clinopyroxene), and Xiong (2006) (amphibole and rutile). Normalizing values of primitive mantle is from Sun and McDonough (1989)

reworked) and tectonic setting of continental crust formation and preservation, and to place the results into a broader geodynamic context.

Twenty-four zircons from sample BT3.406 are analyzed, the age concordance is better than 90 % (unpublished data). Their Pb and U contents show moderate variation, from 29 to 61 ppm and from 47 to 88 ppm, respectively. The Th/U ratios are moderately high, varying from 0.15 to 0.59, with one exception (analysis spot 19). The $^{207}Pb/^{206}Pb$ ages vary from 2690 to 3058 Ma with an average of 2973 Ma. Most grains yielded the Mesoarchean ages of 2.95–3.01 Ga. Of 32, 26 analyzed zircon data from sample ZZ221.8 are available (unpublished data). Their U, Pb contents and Th/U ratios are similar to those of sample BT3.406, e.g., variations of 34–264 ppm for U, 22–156 ppm for Pb and 0.22–0.66 for Th/U ratios. The relatively high Th/U combined with their CL images indicate they are of magmatic origin. The ages of 2870–2900 Ma are the main age pool in the age distribution diagram. From sample LY105.461, totally 32 zircons were analyzed, for which data of 25 zircons are available (unpublished data). The oldest zircon has the age of 3997 ± 8 Ma, its Th/U ratio is 0.44, with moderately high U and Pb contents. The age concordance reaches at 98 %, thus this oldest zircon may records the Eoarchean crustal evolution. The zircons from this sample have the highest U and Pb contents of 33–391 and 18–226 ppm, respectively. The Th/U ratios are also the highest among three samples, ranging from 0.22 to 1.09 with an average of 0.52. In combination the available detrital zircon data from this region (Wan et al. 2010; Wang et al. 2014; Liu and Yang 2015), and precluding some data that show less than 90 %

concordance, the summarized age spectrum of detrital zircons from a variety of metasedimentary rocks (n = 204) is shown in Fig. 6.11. Two principal populations are apparent: a Mesoarchean and a Neoarchean one. In the diagram, the major modes are registered at 2755 and at 3015 Ma. Minor modes are visible, one with two sub-peaks with the range of 2965–2985 Ma, and one recording the age of 2875 Ma. Thus, the data clearly define at least two major episodic magmatic events during Mesoarchean and Neoarchean.

In situ Lu–Hf isotope analyses were carried out on four samples, that is, two samples for which U–Pb dates were obtained, and two BIF samples from the same region, which have detrital zircon U–Pb ages reported in Liu and Yang (2015). The Hf isotope results are shown in Figs. 6.14 and 6.15. Initial $^{176}Hf/^{177}Hf$ ratios, $\varepsilon_{Hf}(t)$ values and two-stage depleted mantle model ages (t_{DM2}) were calculated based on the formation age of individual detrital zircon. The $\varepsilon_{Hf}(t)$ values show a large variation range from −5.2 to 6.2, and the corresponding t_{DM2} ages range from 2.82 to 3.56 Ga. In particular, most $\varepsilon_{Hf}(t)$ values are positive, indicating that their source rocks are derived from juvenile crust and/or depleted mantle. The main age mode of 3.17 Ga indicates that the major source of these detrital zircons is derived from the Mesoarchean crustal materials. In addition to the four samples investigate in our study, two paragneiss samples (ZK26-1, ZK26-3) from the HQC are reported by Wang et al. (2014), they are incorporated into the Fig. 6.12 for comparison with nearby Archean terranes in the NCC. This shows that, in contrast to them, the HQC is characterized by two age groups (Neoarchean and Mesoarchean),

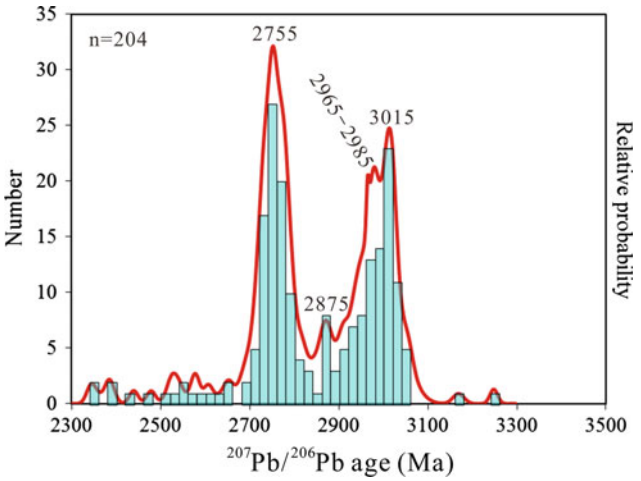

Fig. 6.11 All detrital zircon U–Pb age (Ma) spectra from the HQC. In addition to data from this study, the data from three BIF samples (ZYF1, ZYF9, and ZZZK221.1) (Liu and Yang 2015) and two paragneiss samples (ZK26-1 and ZK26-3) (Wang et al. 2014) have been incorporated into the diagram. The age populations give four major age modes at 3015, 2985–2965, 2875 and 2755 Ma

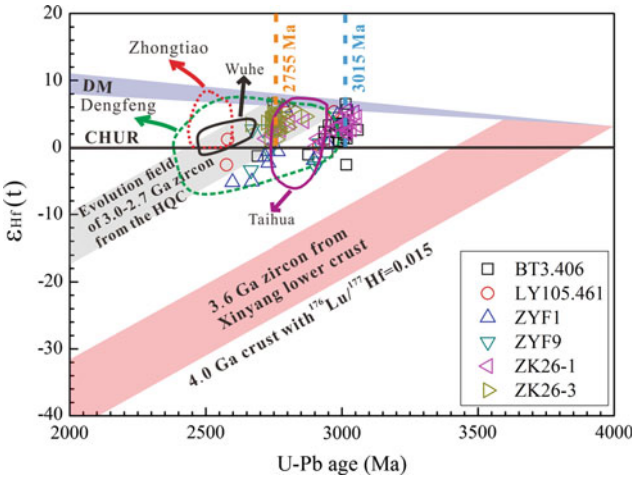

Fig. 6.12 Plots of $\varepsilon_{Hf}(t)$ versus $^{207}Pb/^{206}Pb$ ages of all detrital zircons from the HQC. *CHUR* chondrite uniform reservoir, *DM* depleted mantle. *HQC* Huoqiu complex. 3.0–2.7 Ga zircon evolution field occupied by zircons from metaigneous rocks from Liu et al. (2015). Data for 3.6 Ga zircons from Xinyang lower crust are taken from Zheng et al. (2004). Data sources: Dengfeng Complex (Liu et al. 2012a; Zhang et al. 2014); Zhongtiao Complex (Liu et al. 2012b); Taihua Complex (Liu et al. 2009; Diwu et al. 2010); Wuhe Complex (Wang et al. 2012). In addition, the Hf isotope and age data of ZK26-1 and ZK26-3 from the HQC are taken from Wang et al. (2014). Two major juvenile crustal growth episodes, represented by zircons with $\varepsilon_{Hf}(t)$ similar to DM at 2755 and 3015 Ma are also highlighted with *stippled lines*

whereby most detrital zircons have positive $\varepsilon_{Hf}(t)$ values (Fig. 6.12). By comparison with zircons from metaigneous rocks in the HQC, only the Neoarchean detrital zircons are fall within the same evolution field that is encompassed by zircons from amphibolites, TTG gneisses and K-rich granites from basement of the HQC (Liu et al. 2015). The Mesoarchean detrital zircons not only fall out the evolution field from the HQC, but also are different from other terranes, e.g., Taihua Complex, Wuhe Complex and Dengfeng Complex. Furthermore, they are also far away the ancient Xinyang lower crust evolution field at the Southern NCC (Fig. 6.12).

Previous work has documented the existence of Eo–Paleoarchean (4.0–3.2 Ga) rocks or crustal components from the NCC (Liu et al. 1992; Song et al. 1996; Zheng et al. 2004; Wan et al. 2005; Wilde et al. 2008; Diwu et al. 2013). In particular, the Eoarchean components, e.g., 4.0 Ga xenocrystic zircons from a felsic volcanic rock in the North Qinling Orogenic Belt, are regarded as representing the oldest basement of the NCC (Diwu et al. 2013), while 3.6 Ga zircons in the felsic granulite xenoliths from Xinyang have the lowest negative $\varepsilon_{Hf}(t)$ value of −41, corresponding to the oldest t_{DM} age up to 4.0 Ga (Zheng et al. 2004). All these ages combined with Hf isotopic constraints on the time-integrated evolution of their source demonstrate that the Eoarchean (as early as 4.0 Ga ago) components indeed

existed in the NCC. A single zircon (spot 14 from sample LY105.461) has a nearly concordant (concordance = 98 %) age as old as 3997 ± 8 Ma (1σ, unpublished data), and can therefore be regarded as a new record for Eoarchean terrestrial crust occurrence in the NCC. Additionally, the 3.8 Ga continental rocks are locally exposed in the Anshan and Eastern Hebei areas, e.g., Baijiafen gneisses and Dongshan trondhjemitic rocks in the Anshan area (Liu et al. 1992; Song et al. 1996; Wan et al. 2005), Caozhuang metaquartzites from Eastern Hebei (Liu et al. 1992; Wilde et al. 2008), but these ancient rocks are experienced episodic crustal reworking from the Archean to the Paleoproterozoic (e.g., Song et al. 1996; Wan et al. 2005).

Mesoarchean (3.2–2.8 Ga) rocks, especially 3.0–2.9 Ga rocks are rarely reported in the Eastern Block of the NCC, except for the Anshan-Benxi area (Wan et al. 1998), Qixia Complex (Jahn et al. 2008), Yishui terrane (Wu et al. 2013) and HQC (Liu et al. 2015). Moreover, the 3.0–2.9 Ga detrital zircons are mainly found in the southeastern NCC (e.g., Wan et al. 2010; Wang et al. 2014; Liu and Yang 2015). These zircons from metaigneous and metasedimentary rocks confirmed the existence of Mesoarchean rocks in the eastern block of the NCC. In particular for the HQC, apart from the first age peak of 2755 Ma in the detrital zircon age spectrum, the second peak is apparent at 3015 Ma, which is in agreement with the formation age obtained for amphibolite in this region (ZX84-3, 3012 Ma), indicating a magmatic event at 3.01 Ga (Wang et al. 2014). However, apart from this age determination, we have poor constraints on the nature of this magmatic event, including the geodynamic setting, the possible protoliths, and processes involved. As this 3.01 Ga event has not reported from other proximal Archean terranes, e.g., Taihua Complex, Dengfeng Complex and Wuhe Complex, a more detailed assessment of the data reported here will provide important insights into understanding the Mesoarchean crustal formation and evolution of the NCC. Mesoarchean detrital zircon Hf isotope compositions show that most zircons have positive $\varepsilon_{Hf}(t)$ values ranging from −2.1 to +6.5 and Hf model ages of 3.56–2.82 Ga with a prominent peak at 3.17 Ga (Figs. 6.14 and 6.5), suggesting that the Mesoarchean crust was derived mainly from juvenile sources and minor from the recycling of slightly older continental crust. In particular, several zircons of ca. 3.01 Ga with positive $\varepsilon_{Hf}(t)$ values close to the depleted mantle evolutional curve and their U–Pb ages are similar to or only slightly younger than the T_{DM1} model ages, hence indicating an episodes of juvenile crust accretion in this region.

Precambrian basement in the NCC consists of 85 % Neoarchean (2.8–2.5 Ga) lithotectonic assemblages and 15 % other rocks (Zhao and Zhai 2013). The Neoarchean basement was formed during two distinct periods of 2.8–2.7 and 2.6–2.5 Ga, but the rocks of the former are not widely exposed in the NCC, although basement of that age may be more extensive than now recognized (Jiang et al. 2010; Wan et al. 2011a). Regardless, there is consensus that the 2.8–2.7 Ga basement was derived mainly from juvenile crust (Zhao and Zhai 2013). In this regard, the NCC is fundamentally similar to other cratons in the world as a result of major Neoarchean accretion at 2.8–2.7 Ga, but the NCC underwent a regional-scale tectonothermal event at ~2.5 Ga that obscured much of the older record (Wu et al. 2013). The 2.8–2.7 Ga lithotectonic assemblages in the NCC are mainly exposed in the Eastern Block and in the adjacent TNCO. In the Eastern Block, the reported 2.8–2.7 Ga rocks are exposed in the Taishan Complex, Qixia Complex and HQC (Jahn et al. 1988, 2008; Wan et al. 2010, 2011a; Wang et al. 2014). Conventional methods revealing low initial $^{87}Sr/^{86}Sr$ ratio coupled with high positive $\varepsilon_{Nd}(t)$ values of whole rocks provide strong evidence for continental accretion sourced from depleted mantle, as identified in the Taishan Complex (Jahn et al. 1988). Recently, Wan et al. (2011a) published high positive $\varepsilon_{Hf}(t)$ values ranging from +4.7 to +10.0 for most zircons of supracrustal and TTG rocks from the western Shandong Province, and their T_{DM} ages are similar to their U–Pb ages, indicating that these rocks represent largely juvenile crustal additions derived from depleted mantle only a short time before. In the present study, in addition to most positive zircon $\varepsilon_{Hf}(t)$ values being positive, there are also minor negative values that fall within the evolution field defined by 3.0–2.7 Ga zircons from the HQC (Fig. 6.12). Therefore, the strong 2.8–2.7 Ga tectonothermal event in the HQC involved not only mostly juvenile addition to the continental crust but also minor intracrustal recycling of older components. As mentioned earlier, the intensive ~2.5 Ga tectonothermal event in the Eastern Block more or less overprinted the 2.8–2.7 Ga rocks. Thus, the Neoarchean record preserved in the HQC allows rare insights into this era of crustal growth. A major magmatic event in the HQC was previously dated at 2.75 Ga (Liu et al. 2015), which is also reflected in age spectrum of detrital zircons (Fig. 6.11). The dominant detrital zircon age peak at 2755 Ma is thus interpreted as recording the most important magmatic event in this region.

In summary, in combination with published data, the concordant age spectra of all detrital zircons yield $^{207}Pb/^{206}Pb$ ages of 2343–3997 Ma that cluster into two principal age populations with peaks at 3015 and 2755 Ma, and two minor age populations with peaks at 2965–2985 and 2875 Ma. Zircons $\varepsilon_{Hf}(t)$ values range from −5.2 to 6.5 and most (n = 31 of 47) are positive values, with two-stage Hf model ages (T_{DM2}) concentrate at 3.0–3.4 Ga. The ca. 3.01 and 2.75 Ga zircons with positive $\varepsilon_{Hf}(t)$ values plot close to the depleted mantle evolutional curve and their U–Pb ages

are similar to or only slightly younger than the T_{DM1} model ages, hence indicating at least two episodes of juvenile continental crustal accretions. The older episode finds only minor correspondence in other cratons, suggesting little juvenile crustal growth occurred globally at a time of subdued mantle-derived magmatism. In contrast, the younger episode is coincident with a global rise in superplume activity in the Neoarchean. According to the geochemical and geochronological data, the 3.01 Ga juvenile crust was likely generated in an island-arc subduction system, whereas the 2.75 Ga crustal rocks were probably formed during magmatic underplating and subsequent partial melting of lower crustal mafic rocks. Consequently, they record a tectonic transition from a compressive to an extensional setting on the southeastern margin of the NCC between 3.01 and 2.75 Ga. This sequence of the events heralds a shift, from a mixture of net crustal growth and crustal reworking during multiple short-lived magmatic pulses, to fragmentation and dispersal of the early continental nucleus within 250 Ma.

6.3.3 Comparing with Nearby Archean Terranes

In contrast to other Archean terranes in the NCC, the HQC is mainly composed of 2.8–2.7 Ga rocks and lacks evidence of the 2.5 Ga event based on the zircon age data (Fig. 6.12; Wan et al. 2010; Liu et al. 2015; Wang et al. 2014; Yang et al. 2012, 2014). Indeed, the zircon Hf isotope compositions from the 2.8–2.7 Ga rocks in this region are similar to those of other complexes in the NCC (e.g., Taihua Complex), in that they share the characteristics of most zircon $\varepsilon_{Hf}(t)$ values being positive, which is in accordance with their derivation from juvenile crust (Fig. 6.12). Additional insights come from comparison with the Qixia Complex,

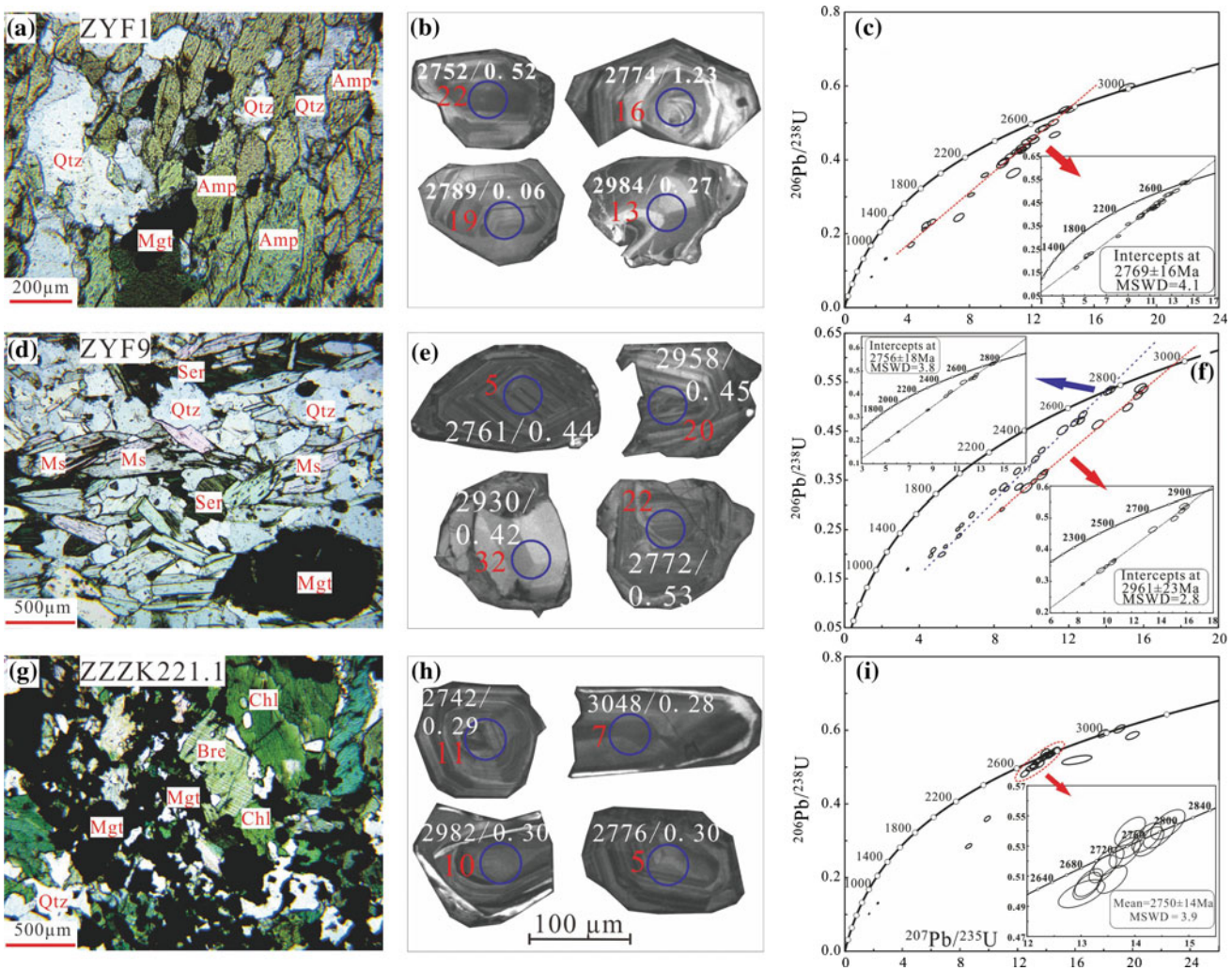

Fig. 6.13 Photomicrographs, zircon CL images and concordia diagrams for three BIF samples. **a–c** ZYF1; **d–f** ZYF9; **g–i** ZZZK221.1. The *white* number before slashes are the $^{207}Pb/^{206}Pb$ ages and the number after slashes are Th/U ratios. *Red* number near the *blue circle* (denotes the ablated location) are analyses spot number, see Table 6.5

which is part of the Archean Jiaobei terrane (Fig. 6.3a). Given the Early Cretaceous sinistral strike-slip along the TLF, with a displacement of ca. 500 km (Xu et al. 1987; Wan and Zhu 1996; Wang et al. 2001), it is probable that the HQC and the Qixia Complex share similar basement. Jahn et al. (2008) reported the existence of Mesoarchean continental crust represented by 2.9 Ga TTG gneiss from this region. They argued that the TTG gneiss was likely generated in an island-arc setting, which is in agreement with those of amphibolite in this region. Moreover, xenocrystic zircon from the Yishui terrane located within TLF has the concordant ages of 3073 ± 12 Ma, confirming the existence of a Mesoarchean crustal component in this region (Wu et al. 2013). Finally, magmatic zircon cores from biotite-plagioclase gneiss sample 10SD06-4 yielded a group of concordant ages of 2983–2840 Ma (Wu et al. 2013). Thus, we infer that the Mesoarchean crust are exposed along the southeastern margin of the NCC and the basement rocks of the HQC may be similar to those of the Yishui and Jiaobei Archean terrane, with additional records stored in deeply buried metasedimentary rocks, such as those that yielded the detrital zircons used from the HQC.

Compared with zircons from metaigneous rocks, integrated research on detrital zircons plays an increasingly important role in understanding the evolution of ancient basement, in reconstructing the paleogeographic history of denudational and drainage areas, and in revealing the tectonic affinity of different tectonic blocks (Veevers et al. 2005; Wan et al. 2011b and references therein). In the HQC, the whole rock compositions of 2.8–2.7 Ga TTG gneisses have been reported (Liu et al. 2015; Liu and Yang 2015). Combined with the corresponding detrital zircon Hf isotope compositions acquired, it is now possible to better unravel complexities of crustal growth and evolution.

The TTG gneisses in the HQC are characterized by strongly fractionated REE patterns, HFSE depletions, LREE and LILE enrichments, and elevated La/Yb and Sr/Y, indicating their Archean TTG affinity (Liu et al. 2015). Archean TTG are commonly products of partial melting of subducted oceanic crust (Foley et al. 2003; Rapp et al. 2003; Martin et al. 2005) or partial melting of metabasaltic rocks at the base of thickened crust (Smithies 2000; Smithies and Champion 2000; Nagel et al. 2012). In the HQC, the relative low MgO, Ni and Cr contents of the TTG gneisses are interpreted as evidence for the absence of any significant interaction between TTG magmas and peridotite within a mantle wedge (Liu et al. 2015). Moreover, most TTG samples fall outside the range of experimental melts produced by partial melting of subducted slab at 1–4 GPa and therefore, these features were suggested to indicate that their formation was related to underplating and subsequent partial melting of lower crustal mafic rocks (Liu et al. 2015). A very similar geologic model for 2.73–2.71 Ga TTG gneisses formation in the Qixia Complex has been identified by Jahn et al. (2008), although in detail, the chemical compositions of these rocks are different. Nevertheless, Nd isotope data for the Qixia gneisses also indicate that the Mesoarchean and Neoarchean rocks were mainly derived from juvenile sources with a limited amount of older crustal component (Jahn et al. 2008). This is consistent with the systematics of U–Pb ages and Hf isotope compositions for detrital zircons presented here. The third similarity between the Qixia Complex and the HQC is that there is no evidence for the formation of the ~2.5 Ga rocks in response to the extensive reworking events recorded in much of the NCC at that time. Therefore, it is probable that both complexes originally shared a unified Archean basement until the Mesozoic TLF separated them into two parts, lying at the eastern and western flanks, which are now at a >500 km distance from each other.

6.4 Huoqiu BIF Formation Age and Geochemistry

6.4.1 Temporal Significance of the Huoqiu BIF

Three BIF ore samples (ZYF1, ZYF9, and ZZZK221.1, see Figs. 6.16 and 6.17) were chosen for acquisition of U–Pb ages by LA-MC-ICPMS, and the results are listed in Table 6.5. Detrital zircon crystals recovered from three BIF samples are euhedral to subhedral, transparent to light yellow. The lengths of these grains range from 100 to 300 μm with aspect ratios from 1.5:1 to 2.5:1. Cathodoluminescence imaging reveals that these zircon crystals generally have oscillatory zoning (Fig. 6.13b, e, h), resembling zircons from the TTG gneiss in this region (Liu et al. 2015). Because oscillatory zonings and low to variable luminescence are characteristics of magmatic zircons (Hanchar and Rudnick 1995), we interpret that these detrital zircons were igneous in origin. Moreover, most detrital zircon grains have high Th/U ratios (>0.1) (Table 6.5). Eighty eight LA-MC-ICPMS U–Pb spot analyses on zircon cores were obtained from 88 zircon crystals (Fig. 6.13c, f, i). Twenty one zircon crystals from ZYF1 gave a discordia upper-intercept age of 2769 ± 16 Ma (MSWD = 4.1), yet sample ZYF9 yielded two discordia upper-intercept ages of 2756 ± 18 Ma (MSWD = 3.8, n = 11) and 2961 ± 23 Ma (MSWD = 2.8, n = 10). In addition, 13 spots with discordance of <10 % give a mean value of 2750 ± 14 Ma (1σ) in sample ZZZK221.1 (Fig. 6.13i). These ages agree within errors with the protolith ages of TTG gneiss (2752 ± 24 Ma in Liu et al. 2015; 2754 ± 13 Ma in Wan et al. 2010) and amphibolite (2966 ± 33 Ma in Liu et al. 2015; 2946 ± 41 Ma in Yang et al. 2012).

Table 6.5 Zircon LA-MC-ICPMS U–Pb data for the Huoqiu BIF samples

Sample	Concentrations (ppm)			Isotopic ratios								Isotopic ages (Ma)						Concordance (%)
Spot	Pb	U	Th/U	$^{206}Pb/^{238}U$	1σ	$^{207}Pb/^{235}U$	1σ	$^{207}Pb/^{206}Pb$	1σ	$^{232}Th/^{238}U$	1σ	$^{206}Pb/^{238}U$	1σ	$^{207}Pb/^{235}U$	1σ	$^{207}Pb/^{206}Pb$	1σ	
ZYF1																		
1	391	741	0.62	0.4499	0.0032	11.6872	0.1379	0.1884	0.0015	0.6318	0.0011	2395	17	2580	30	2728	13	88
2	398	1443	1.53	0.2314	0.0033	5.5788	0.1052	0.1749	0.0015	1.5745	0.0029	1342	19	1913	36	2605	14	52
3	344	1647	3.64	0.1702	0.0031	4.2676	0.0862	0.1818	0.0014	3.7388	0.0077	1013	19	1687	34	2669	13	38
4	525	1106	0.87	0.4225	0.0034	10.9818	0.1217	0.1885	0.0014	0.8928	0.0010	2272	18	2522	28	2729	13	83
5	451	1813	2.35	0.2130	0.0020	5.1151	0.0661	0.1742	0.0013	2.4122	0.0127	1245	11	1839	24	2598	13	48
6	343	1069	0.63	0.2439	0.0044	7.3289	0.1333	0.2180	0.0016	0.6447	0.0006	1407	25	2152	39	2966	12	47
7	1160	2254	1.12	0.4348	0.0035	11.6287	0.1255	0.1940	0.0014	1.1460	0.0143	2327	19	2575	28	2776	12	84
8	415	2696	2.25	0.1322	0.0013	2.6431	0.0356	0.1450	0.0011	2.3064	0.0013	800	8	1313	18	2288	13	35
9	905	1781	1.22	0.4255	0.0036	11.3811	0.1266	0.1940	0.0015	1.2543	0.0019	2285	19	2555	28	2776	12	82
10	801	2075	1.68	0.3054	0.0022	8.1094	0.0897	0.1926	0.0017	1.7285	0.0011	1718	12	2243	25	2764	14	62
11	1442	2653	0.85	0.4526	0.0035	12.1689	0.1265	0.1950	0.0014	0.8721	0.0007	2407	18	2618	27	2785	12	86
12	1398	3065	1.04	0.3895	0.0049	10.1283	0.1514	0.1886	0.0014	1.0639	0.0045	2121	27	2447	37	2730	12	78
13	2010	2945	0.27	0.5960	0.0043	18.1123	0.1978	0.2204	0.0017	0.2729	0.0002	3014	22	2996	33	2984	13	101
14	716	1484	0.98	0.3958	0.0042	10.2176	0.1361	0.1872	0.0014	1.0035	0.0022	2150	23	2455	33	2718	12	79
15	371	725	1.00	0.4330	0.0034	11.5683	0.1307	0.1938	0.0014	1.0216	0.0022	2319	18	2570	29	2774	12	84
16	776	1252	1.23	0.5008	0.0036	13.3754	0.1398	0.1937	0.0015	1.2660	0.0063	2617	19	2707	28	2774	12	94
17	681	1608	1.26	0.3641	0.0053	10.8315	0.1806	0.2157	0.0016	1.2968	0.0021	2002	29	2509	42	2949	12	68
18	1272	2338	0.63	0.4679	0.0033	13.4765	0.1405	0.2089	0.0015	0.6469	0.0046	2474	18	2714	28	2897	12	85
19	995	1762	0.06	0.5370	0.0038	14.4749	0.1518	0.1955	0.0015	0.0628	0.0001	2771	20	2781	29	2789	12	99
20	1505	2998	1.86	0.4287	0.0032	11.3224	0.1212	0.1915	0.0014	1.9046	0.0101	2300	17	2550	27	2755	12	83
21	761	1413	0.65	0.4593	0.0033	12.0388	0.1343	0.1901	0.0014	0.6715	0.0004	2436	17	2607	29	2743	12	89
22	1378	2253	0.52	0.5353	0.0038	14.1093	0.1557	0.1912	0.0014	0.5289	0.0012	2764	20	2757	30	2752	12	100
23	1331	2742	0.76	0.4109	0.0031	10.6030	0.1234	0.1871	0.0016	0.7826	0.0010	2219	17	2489	29	2717	14	82
24	1770	3072	0.90	0.4833	0.0036	12.6100	0.1516	0.1892	0.0015	0.9258	0.0004	2542	19	2651	32	2735	13	93
25	143	1413	2.97	0.0831	0.0006	1.7278	0.0208	0.1507	0.0012	3.0442	0.0057	515	4	1019	12	2354	14	22
26	555	1216	1.07	0.3937	0.0030	10.1134	0.1171	0.1863	0.0015	1.1027	0.0051	2140	16	2445	28	2710	13	79
27	1499	2642	0.94	0.4868	0.0038	12.7949	0.1466	0.1906	0.0014	0.9596	7.7438	2557	20	2665	31	2748	12	93
28	885	1754	1.21	0.4348	0.0031	11.3081	0.1235	0.1886	0.0014	1.2385	0.0004	2327	16	2549	28	2730	13	85
30	634	2268	1.64	0.2236	0.0038	5.2362	0.1142	0.1699	0.0014	1.6819	0.0045	1301	22	1859	41	2556	14	51
31	635	1228	1.23	0.4246	0.0031	11.2010	0.1180	0.1913	0.0014	1.2615	0.0025	2281	16	2540	27	2754	12	83
32	800	1875	1.19	0.3588	0.0026	8.9926	0.0952	0.1818	0.0014	1.2181	0.0023	1977	14	2337	25	2669	12	74
ZYF9																		
1	80	212	0.48	0.3342	0.0039	9.7296	0.1221	0.2111	0.0012	0.4921	0.0017	1859	22	2410	30	2914	9	64
2	97	228	0.51	0.3683	0.0028	9.2375	0.0732	0.1819	0.0010	0.5253	0.0007	2021	16	2362	19	2671	9	76
3	63	160	0.71	0.3322	0.0021	8.6521	0.0656	0.1889	0.0013	0.7294	0.0027	1849	12	2302	17	2733	11	68
4	58	146	0.71	0.3471	0.0023	10.1265	0.0675	0.2116	0.0012	0.7285	0.0100	1921	13	2446	16	2918	10	66

(continued)

Table 6.5 (continued)

Sample	Concentrations (ppm)			Isotopic ratios								Isotopic ages (Ma)						Concordance (%)
Spot	Pb	U	Th/U	$^{206}Pb/^{238}U$	1σ	$^{207}Pb/^{235}U$	1σ	$^{207}Pb/^{206}Pb$	1σ	$^{232}Th/^{238}U$	1σ	$^{206}Pb/^{238}U$	1σ	$^{207}Pb/^{235}U$	1σ	$^{207}Pb/^{206}Pb$	1σ	
5	60	97	0.44	0.5317	0.0033	14.0918	0.0877	0.1922	0.0011	0.4463	0.0011	2749	17	2756	17	2761	9	100
6	60	106	0.57	0.4833	0.0034	12.7410	0.0915	0.1912	0.0011	0.5886	0.0041	2542	18	2661	19	2753	9	92
7	49	103	0.45	0.4106	0.0026	10.5508	0.0718	0.1864	0.0011	0.4590	0.0007	2217	14	2484	17	2710	9	82
8	44	97	0.73	0.3927	0.0030	10.2034	0.0772	0.1885	0.0011	0.7472	0.0035	2135	16	2453	19	2729	10	78
9	41	73	0.31	0.4986	0.0032	15.1503	0.1061	0.2204	0.0013	0.3144	0.0057	2608	17	2825	20	2984	9	87
10	86	224	0.37	0.3365	0.0027	9.3204	0.0863	0.2009	0.0012	0.3780	0.0007	1870	15	2370	22	2834	10	66
11	94	168	0.62	0.4676	0.0031	12.3258	0.0844	0.1912	0.0011	0.6365	0.0107	2473	16	2630	18	2752	9	90
12	77	215	0.91	0.2916	0.0017	8.4235	0.0542	0.2095	0.0012	0.9288	0.0026	1650	10	2278	15	2902	9	57
13	68	253	1.33	0.2158	0.0015	5.3966	0.0400	0.1814	0.0010	1.3687	0.0087	1259	9	1884	14	2666	9	47
14	49	77	0.43	0.5226	0.0031	15.6978	0.1001	0.2179	0.0012	0.4376	0.0034	2710	16	2859	18	2965	9	91
15	86	189	0.79	0.3599	0.0036	10.5740	0.1073	0.2131	0.0012	0.8131	0.0028	1982	20	2486	25	2929	9	68
16	86	136	0.73	0.4714	0.0030	12.6298	0.0863	0.1943	0.0011	0.7495	0.0017	2490	16	2652	18	2779	9	90
17	69	156	0.50	0.3665	0.0023	10.7064	0.0708	0.2119	0.0012	0.5100	0.0051	2013	12	2498	17	2920	9	69
18	90	246	0.87	0.2801	0.0024	6.8016	0.0549	0.1761	0.0010	0.8934	0.0029	1592	14	2086	17	2617	10	61
19	74	283	0.06	0.2512	0.0017	6.0623	0.0441	0.1751	0.0010	0.0628	0.0005	1444	10	1985	14	2607	9	55
20	80	127	0.45	0.5341	0.0032	15.9751	0.1045	0.2169	0.0012	0.4613	0.0011	2759	17	2875	19	2958	9	93
21	84	259	1.00	0.2594	0.0018	6.2654	0.0478	0.1752	0.0010	1.0290	0.0193	1487	10	2014	15	2608	9	57
22	56	87	0.53	0.5338	0.0032	14.2388	0.1024	0.1934	0.0012	0.5406	0.0013	2758	17	2766	20	2772	10	99
23	59	145	0.96	0.3261	0.0020	7.9504	0.0620	0.1768	0.0011	0.9798	0.0033	1819	11	2225	17	2623	10	69
24	87	160	0.71	0.4522	0.0039	11.6718	0.1138	0.1872	0.0012	0.7269	0.0009	2405	21	2578	25	2718	10	88
25	65	295	1.50	0.1996	0.0020	5.2125	0.0765	0.1894	0.0015	1.5428	0.0048	1173	12	1855	27	2737	13	43
26	80	319	1.43	0.2082	0.0022	4.7470	0.0553	0.1653	0.0010	1.4677	0.0162	1219	13	1776	21	2511	10	49
27	50	215	1.18	0.1967	0.0018	4.6106	0.0449	0.1700	0.0010	1.2059	0.0103	1158	10	1751	17	2558	10	45
28	96	183	0.44	0.4636	0.0038	13.5540	0.1236	0.2121	0.0012	0.4490	0.0066	2455	20	2719	25	2921	9	84
29	99	346	1.40	0.2380	0.0019	6.1324	0.0518	0.1869	0.0011	1.4370	0.0029	1376	11	1995	17	2715	9	51
30	82	442	0.61	0.1695	0.0012	3.3735	0.0244	0.1443	0.0008	0.6277	0.0103	1010	7	1498	11	2280	10	44
31	85	210	1.06	0.3361	0.0031	8.4948	0.0829	0.1833	0.0010	1.0870	0.0040	1868	17	2285	22	2683	9	70
32	19	31	0.42	0.5385	0.0035	15.8263	0.1264	0.2132	0.0014	0.4276	0.0013	2777	18	2866	23	2930	11	95
ZZZK221.1																		
1	5	200	0.41	0.0235	0.0002	0.1960	0.0073	0.0605	0.0022	0.4224	0.0032	150	1	182	7	622	78	24
2	21	33	0.33	0.5442	0.0041	14.6131	0.1298	0.1948	0.0015	0.3371	0.0013	2801	21	2790	25	2783	13	101
3	45	77	0.35	0.5148	0.0037	13.4055	0.1048	0.1889	0.0013	0.3571	0.0014	2677	19	2709	21	2732	11	98
4	60	154	0.07	0.3598	0.0030	9.8993	0.0845	0.1995	0.0014	0.0681	0.0026	1981	16	2425	21	2822	11	70
5	38	62	0.30	0.5330	0.0040	14.2565	0.1141	0.1940	0.0013	0.3030	0.0029	2754	20	2767	22	2776	11	99
6	99	885	0.32	0.1020	0.0008	1.6890	0.0134	0.1201	0.0009	0.3290	0.0010	626	5	1004	8	1958	13	32
7	38	54	0.28	0.6036	0.0044	19.0920	0.1571	0.2294	0.0016	0.2900	0.0012	3044	22	3046	25	3048	11	100
8	49	89	0.23	0.5035	0.0036	13.1132	0.1065	0.1889	0.0013	0.2383	0.0017	2629	19	2688	22	2732	12	96
9	29	48	0.29	0.5382	0.0039	14.4489	0.1188	0.1947	0.0014	0.2972	0.0011	2776	20	2780	23	2783	12	100
10	38	56	0.30	0.5911	0.0043	17.9410	0.1452	0.2201	0.0015	0.3122	0.0006	2994	22	2987	24	2982	11	100

(continued)

Table 6.5 (continued)

Sample	Concentrations (ppm)			Isotopic ratios							Isotopic ages (Ma)						Concordance (%)
Spot	Pb	U	Th/U	$^{206}Pb/^{238}U$	1σ	$^{207}Pb/^{235}U$	1σ	$^{207}Pb/^{206}Pb$	1σ	$^{232}Th/^{238}U$	1σ	$^{206}Pb/^{238}U$	1σ	$^{207}Pb/^{235}U$	1σ	$^{207}Pb/^{206}Pb$	1σ	
11	33	55	0.29	0.5310	0.0038	13.9130	0.1104	0.1900	0.0013	0.3012	0.0009	2746	20	2744	22	2742	11	100
12	19	283	0.27	0.0667	0.0005	0.5347	0.0066	0.0581	0.0007	0.2788	0.0032	416	3	435	5	535	26	78
13	23	42	0.23	0.4828	0.0041	12.5198	0.1202	0.1881	0.0016	0.2331	0.0018	2540	21	2644	25	2725	14	93
14	47	81	0.36	0.5057	0.0038	13.1440	0.1060	0.1885	0.0013	0.3707	0.0046	2638	20	2690	22	2729	11	97
15	101	276	0.46	0.2856	0.0026	8.6061	0.0864	0.2185	0.0016	0.4702	0.0012	1620	15	2297	23	2970	12	55
16	54	380	0.18	0.1306	0.0009	2.2943	0.0191	0.1274	0.0010	0.1848	0.0012	791	6	1211	10	2063	13	38
17	37	63	0.32	0.5198	0.0039	13.5132	0.1154	0.1886	0.0013	0.3284	0.0044	2698	20	2716	23	2730	12	99
18	67	99	0.49	0.5192	0.0051	16.1260	0.4251	0.2253	0.0039	0.4992	0.0039	2696	26	2884	76	3019	28	89
19	77	139	0.06	0.5255	0.0041	13.8144	0.1184	0.1907	0.0013	0.0628	0.0003	2723	21	2737	23	2748	11	99
20	32	54	0.30	0.5079	0.0038	13.5760	0.1139	0.1939	0.0014	0.3116	0.0021	2648	20	2721	23	2775	12	95
21	27	48	0.28	0.4984	0.0038	13.0120	0.1763	0.1894	0.0022	0.2904	0.0010	2607	20	2681	36	2737	19	95
22	53	88	0.32	0.5356	0.0040	14.2196	0.1126	0.1925	0.0013	0.3295	0.0010	2765	21	2764	22	2764	11	100
23	31	52	0.21	0.5396	0.0039	13.9109	0.1159	0.1870	0.0013	0.2149	0.0021	2782	20	2744	23	2716	12	102
24	85	103	0.72	0.5856	0.0043	19.9861	0.1919	0.2475	0.0020	0.7431	0.0007	2972	22	3091	30	3169	13	94

Data from Liu and Yang (2015)
Concordance defines as ($^{206}Pb/^{238}U$ age)/($^{207}Pb/^{206}Pb$ age)*100

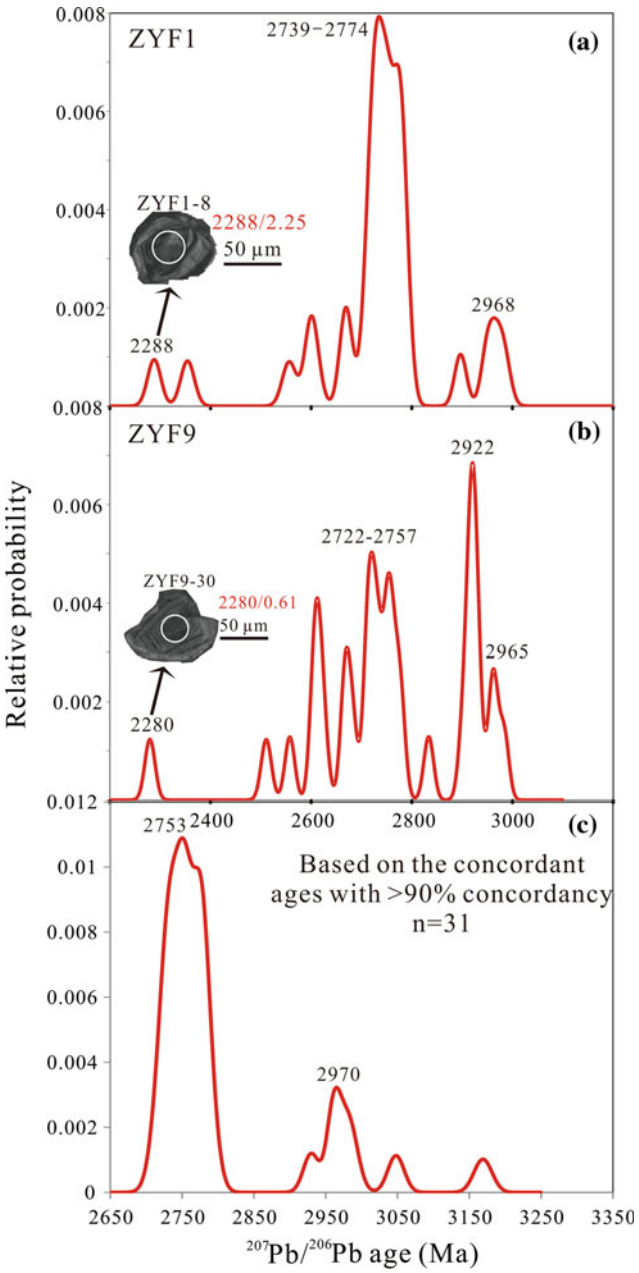

Fig. 6.14 Probability density of U–Pb ages for detrital zircons. **a** Ore sample ZYF1 and **b** ore sample ZYF9, inserts are the minimum $^{207}Pb/^{206}Pb$ age of zircon CL images, *red* number before slashes are the $^{207}Pb/^{206}Pb$ ages and the number after slashes are Th/U ratios; **c** based on the concordant ages with >90 % concordance, the age spectrum of all detrital zircons (ZYF1, ZYF2 and ZZZK221.1) from three BIF samples

In zircon $^{207}Pb/^{206}Pb$ ages population spectrums without considering age concordance, all zircons together can be divided into two major populations: 2722–2774 and 2922–2968 Ma (Fig. 6.14a, b). However, based on the concordant ages with >90 % concordance (n = 31), the peak age can be further constrained at 2753 and 2970 Ma (Fig. 6.14c), which agree well with the protolith ages of TTG gneiss and

amphibolite in the HQC within uncertainty (Liu et al. 2015). As for trace elements, zircon crystals from ZYF1 generally have more U (725–3072 ppm), Th (108–6062 ppm), and Pb (143–2010 ppm) concentrations than those in ZYF9 (31–442, 13–485 and 19–99 ppm, respectively). Zircons from sample ZZZK221.1 have similar U (33–885 ppm), Th (9–283 ppm), and Pb (5–101 ppm) concentrations to sample ZYF9 (Table 6.5).

Geochronological studies of Huoqiu BIF were conducted by the Rb–Sr isotopic system (Ying et al. 1984). The ages varied from 2681 to 2963 Ma (peak age: 2700 Ma) with errors above 5 % due to high-grade metamorphism leading to isotopic resetting (e.g., Faure 1977). In contrast, accompanying the advancement in analysis method, the more robust U–Pb system and the higher precision dating were applied to zircon crystals from HQC granitoids and amphibolites (Wan et al. 2010; Yang et al. 2012; Liu et al. 2015; Wang et al. 2014). Wan et al. (2010) identified two periods of granitoid formation, i.e., 2.75 and 2.56 Ga. The former age was confirmed by many later works (Yang et al. 2012; Liu et al. 2015; Wang et al. 2014). In order to constrain the age of BIF precipitation, U–Pb ages for zircons from associated meta-volcanic rocks are commonly determined (e.g., Trendall et al. 1997; Vavra et al. 1999), for BIF precipitation commonly does not form juvenile zircons, in particular for Superior-type BIF. In the HQC, the detrital zircon grains from BIF samples are sourced from proximal rocks. They gave the ages similar to the TTG gneiss and amphibolite ages as mentioned above. Furthermore, zircons with the same age show similar zonation patterns in CL images (Liu et al. 2015; Wan et al. 2010). In addition, there are good linear correlations between Al_2O_3 and TiO_2 for BIF and their wall rocks (Liu and Yang 2013), suggesting that at least a few terrigenous clastic sediments contributed to BIF formation, and thus constrained the upper limited age of BIF deposition at 2.75 Ga.

Although U, Th, and Pb concentrations of two samples shown considerable difference, their $^{207}Pb/^{206}Pb$ age spectrum is similar to each other (Fig. 6.14a, b). For example, the oldest age population is 2968 Ma in ZYF1, which agrees well with counterpart in ZYF9 (2965 Ma). Furthermore, the similar consistence also applies for the youngest age populations (2288 and 2280 Ma for ZYF1 and ZYF9, respectively). However, unfortunately their minimum ages have poor concordance (Table 6.5). Furthermore, they fall on a discordia, which indicates significantly Pb loss (Fig. 6.13c, f). Thus, the minimum apparent $^{207}Pb/^{206}Pb$ age cannot be interpreted as the age of Huoqiu BIF deposition, even if the zircons display apparently magmatic feature (Fig. 6.13). Recently, Wang et al. (2014) revealed three magmatic events at ~3.02, ~2.77, and ~2.71 Ga from this region, and the 2.71 Ga was identified by zircons from a granitoid, and 30 zircon analyses define a good discordia with an upper-intercept age of 2709 ± 21 Ma (Fig. 5c in their article). Moreover, detrital zircon age spectrum from paragneiss gave two peak ages of 2.77 and 3.02 Ga in their study, which is consistent with those from BIF ore samples in our study (Fig. 6.14c vs. Fig. 6 in Wang et al. 2014). Therefore, we infer that the lower limit age of the BIF formation was probably constrained at 2.71 Ga.

6.4.2 Environmental and Tectonic Significance of the Huoqiu BIF

Within the HQC, plagioclase amphibolite is one of basement rocks for BIF ore body. Most amphibolite samples fall into the continental basalt field (Fig. 6.15a). Both Ti and V tend to be immobile during metamorphism and alteration, which makes them good candidates for discriminating between different tectonic environments (Shervais 1982; Zhai et al. 1990). The Ti/V ratios of all amphibolites range from 20 to 50 except for one sample (Fig. 6.15b). Most samples plotted fall within the continental basalt field (Fig. 6.15b). In the triangular plot of MgO–FeOT–Al_2O_3 of Pearce et al. (1977), they are distributed into two fields, arc basalt and continental basalt (Fig. 6.15c). Therefore, we suggest that these amphibolite protoliths formed in a continental arc setting (Liu and Yang 2013; Liu et al. 2015; Wang et al. 2014).

The arc and continent characteristics of the amphibolites are also reflected in trace element compositions. They are clearly displayed HFSE depletion, LILE and LREE enrichment (Fig. 6.6). In the chondrite-normalized diagram, LREE are significantly fractionated from HREE, especially in Bantaizi samples (Fig. 6.6f), which is consistent with retention of HREE by residual garnet in the melt source (Foley et al. 2002; Spandler et al. 2003). Most samples exhibit weakly negative Eu anomalies, suggesting slight plagioclase fractional crystallization. Conversely, a few samples with marked positive Eu anomalies may point to considerable plagioclase accumulation.

In summary, the geochemical characteristics of these amphibolites, including relatively high HREE/LREE ratios with negative Eu anomalies, and high LILE (e.g., Rb, Cs and Ba) concentrations but low HFSE concentrations, suggest that their protoliths probably formed by partial melting of a subduction-modified (selective enrichment of LILE relative to HFSE), garnet-bearing subcontinental lithosphere mantle source (SCLM), then erupted or was emplaced in a continental arc setting. Similar geodynamic backgrounds have also been proposed for Neoarchean amphibolites of the Dengfeng Group, Henan Province (Zhou et al. 2009) and Anshan area in the NCC (Zhai et al. 1990).

The protoliths of most TTG gneisses are classified as orogenic granitoids, which includes island-arc granitoids

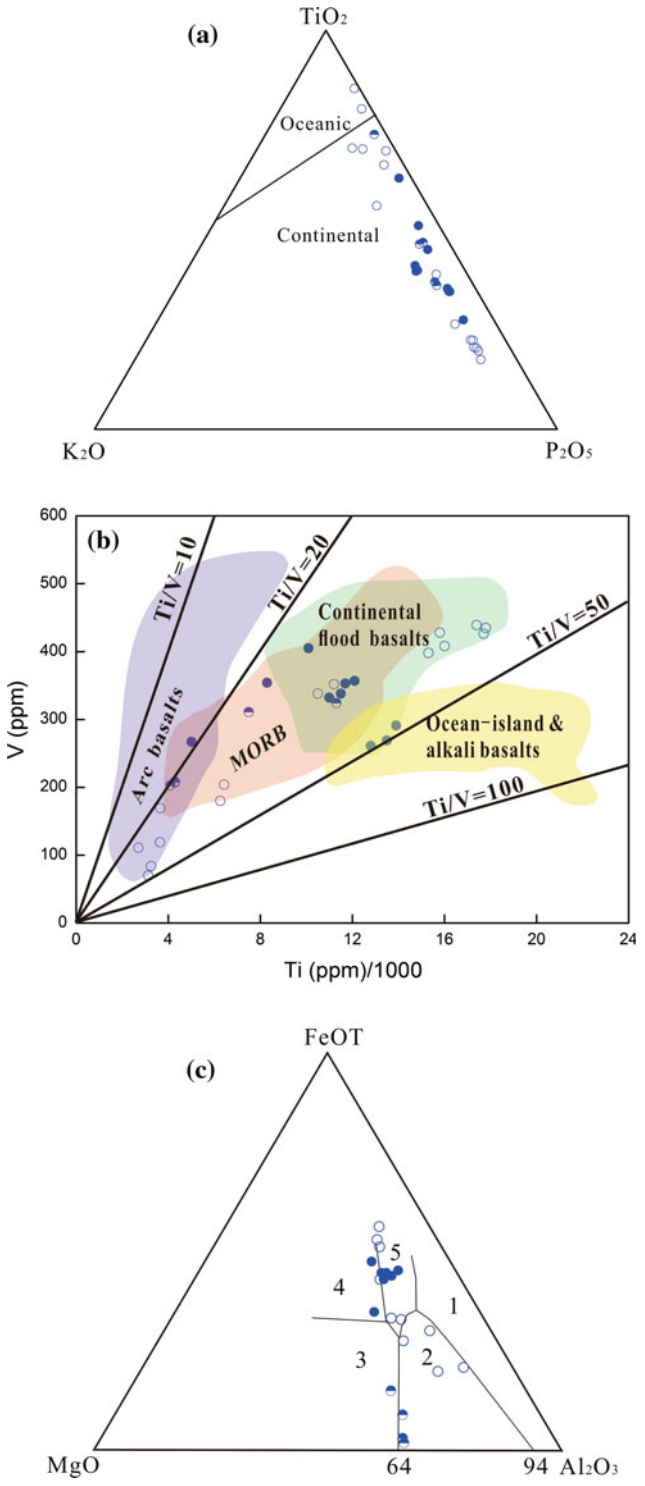

Fig. 6.15 Amphibolites from the Huoqiu BIF iron deposit plotted on the **a** P_2O_5–TiO_2–K_2O triangular diagram (after Pearce et al. 1975), **b** V-Ti/1000 diagram (after Shervais 1982) and **c** the Al_2O_3–FeOT–MgO triangular diagram (after Pearce et al. 1977). *1* Island of spreading center; *2* arc and active continental margin; *3* MORB; *4* OIB; *5* continental basalt

(IAG), continental arc granitoids (CAG), continental collision granitoids (CCG) and post orogenic granitoids (POG) (Fig. 6.16a, b) (Maniar and Piccoli 1989). Their trace element compositions are characterized by highly enriched LILE (e.g., Rb, Ba, Th and K) and LREE ($(La/Yb)_N$ = 3.1–154.6, Ave. = 63.3), as well as strongly depleted HFSE (e.g., Nb, Ta, Zr, Hf and Ti) and the HREE (Fig. 6.7), suggesting arc affinities (Condie 1986; Hergt et al. 1991; Pin and Paquette 1997). Rubidium, Y and Nb are commonly chosen to discriminate different tectonic settings of granitic rocks (Pearce et al. 1984). The Nb–Y diagram shows that all gneisses fall into the field of volcanic arc granite (VAG) + syn-collision granite (syn-COLG) (Fig. 6.16c), while the Rb-(Y + Nb) diagram can effectively distinguish between VAG and syn-COLG, and results show that the protoliths of most gneisses belong to VAG (Fig. 6.16d). However, they are different with typical arc rocks in that most gneisses are characterized by high Sr/Y ratio with low Y and high Sr concentrations with variable $(La/Yb)_N$ ranging from 3.1 to 155. Because of geochemical similarities between TTG and modern adakites, they are commonly assumed to have similar petrogenesis (Drummond and Defant 1990; Martin 1999), although some others argued against this hypothesis (Condie 2005; Smithies 2000). The fundamental conflict between the two groups is whether the subducted slab or thickened crust is suffered partial melting. Given the low Mg# and high SiO_2 contents in most gneiss samples, in particular their high K_2O contents and K_2O/Na_2O ratios, we infer that they are formed by partial melting of thickened crust in an arc setting. Given that a subduction model has been demonstrated for Neoarchean potassic high Ba–Sr granites in the Taishan granite–greenstone terrane (Peng et al. 2013), which is near the HQC, and that gneisses in the HQC have an arc affinities, thus subduction thickening is probably.

In our study, the well-preserved banding displays meso-bands, which tend to have an average thickness of less than an inch (25 mm) (Trendall and Blockley 1970). Moreover, the magnetite crystal generally occur as 0.05–0.25 mm in size, and is commonly present as discrete subhedral and as anhedral to subhedral granoblastic aggregates. These texture and banded features need a secular stable environment. The strata column of the HQC records well a flysch rhythmic structure (Fig. 6.3c), which generally reflects a sedimentary texture. Carbonate minerals such as breunnerite are commonly associated with magnetite (Fig. 6.13), implying they were once precipitates. In addition, no volcanism record within the Huoqiu BIF ore body or the adjacent rocks have been identified thus far, which preclude volcanic direct contribution for the Huoqiu BIF precipitation. The most

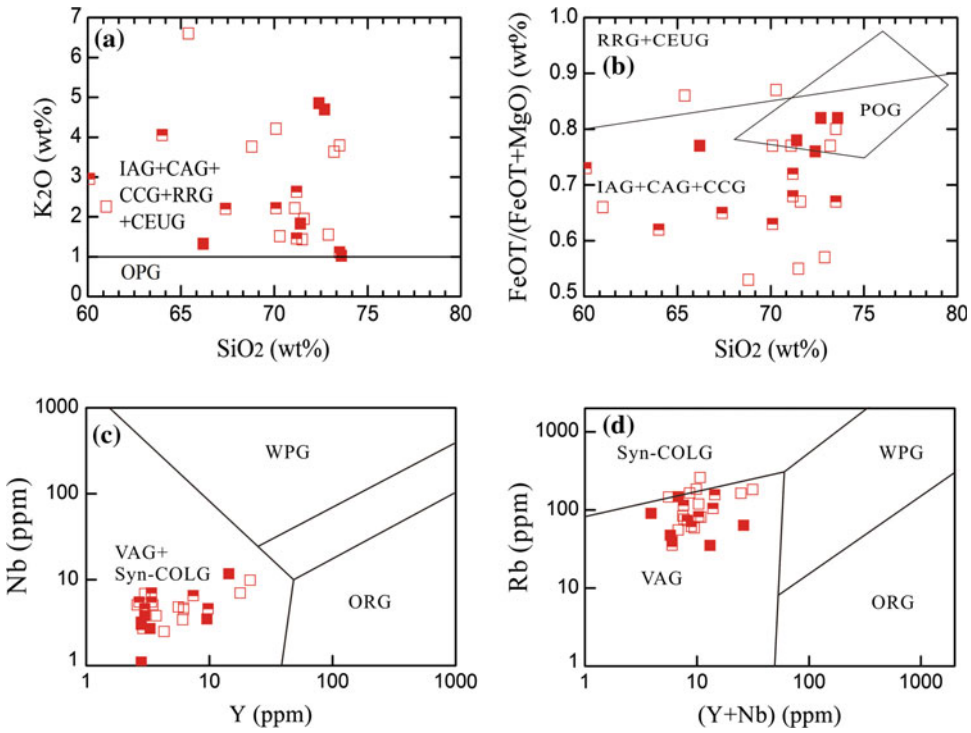

Fig. 6.16 K_2O–SiO_2 diagram (**a**) and FeOT/(FeOT + MgO)-SiO_2 diagram (**b**) of gneisses in the Huoqiu iron deposit (after Pearce et al. 1984; Maniar and Piccoli 1989, respectively). Nb–Yb diagram (**c**) and Rb–Y + Nb diagram (**d**) of gneisses (after Pearce et al. 1984). See text for granitic rock abbreviations

important piece of evidence is that the detrital zircons from wall rocks have been identified in three BIF ore samples, indicating the Huoqiu BIF deposited in continental marginal sea and belong to Superior-type.

6.4.3 Provenance of the Huoqiu BIF

Cloud (1973) and Holland (1973) first suggested that iron and silica, the main components of BIF, were derived from seawater. Recent research proposes that the sources of Fe and Si were derived from deep ocean hydrothermal activity admixing with seawater, to account for the fact that the REE patterns of almost all BIF have pronounced positive Eu anomalies (Huston and Logan 2004; Klein 2005). In our study, the ore samples from Zhouyoufang and Lilaozhuang exhibit extremely low Al_2O_3 and TiO_2 contents (<0.5 wt% in Liu and Yang 2013 and Huang et al. 2013b), which indicates few contributions of terrigenous clastic materials (Kato et al. 1996). Moreover, all ore samples also have extremely low concentrations of HFSE (Zr, Hf, Th and Sc), which normally are enriched in evolved continental crust. Thus, it seems unlikely that terrigenous clastic materials were a significant contribution to the parent material of the Huoqiu BIF.

According to Bekker et al. (2010), when the hydrothermal flux overwhelmed the oceanic oxidation state, reduced iron was transported and deposited from hydrothermal vents; where the hydrothermal flux was insufficient to overwhelm the oceanic redox state, iron was quickly oxidized and deposited only proximally. Because Mn is more mobile than iron (Bekker et al. 2010), it can be an indicator of hydrothermal flux, as discussed below.

REE + Y (REY) are particularly useful as geochemical fingerprints because of their immobility during post-depositional processes (Taylor and McLennan 1985). PAAS normalized REY patterns for BIF ores are shown in Fig. 6.17. For comparison, the average compositions of hydrothermal fluids and field of modern seawater are also displayed in the plot. When discussing the material sources of the Huoqiu BIF, it is necessary to briefly summarize the REY characteristics of modern seawater and hydrothermal fluids. Modern seawater is characterized by depletion of the LREE over HREE, superchondritic Y/Ho ratios of 40–90 (Bau and Dulski 1996), positive La and Gd anomalies and a negative Ce anomaly (Thurston et al. 2012). The Eu/Eu* values for modern seawater range from 0.8 to 1.2 (Kamber 2010; Schmidt et al. 2007). In contrast, high-temperature hydrothermal fluids vented along spreading ridges can have Eu/Eu* up to ca. 70 (Douville et al. 1999, 2002; Schmidt et al. 2007, 2011). Moreover, they exhibit flat REE pattern with relatively high REE concentrations (Fig. 6.17), and the Y/Ho ratios fall between 26 and 28 (Bau and Dulski 1996; Nozaki et al. 1997).

In the HQC, the ore samples can be divided into two types of high and low $(Eu/Eu^*)_{SN}$ BIF. The Bantaizi ores have relatively higher REE concentrations than those from Zhouyoufang and Lilaozhuang, but also contain the lowest Y/Ho ratios (31.1–38.6) and $(Eu/Eu^*)_{SN}$ (1.57–1.82) relative to Zhouyoufang (43.3–56.7 and 2.97–3.41) and Lilaozhuang

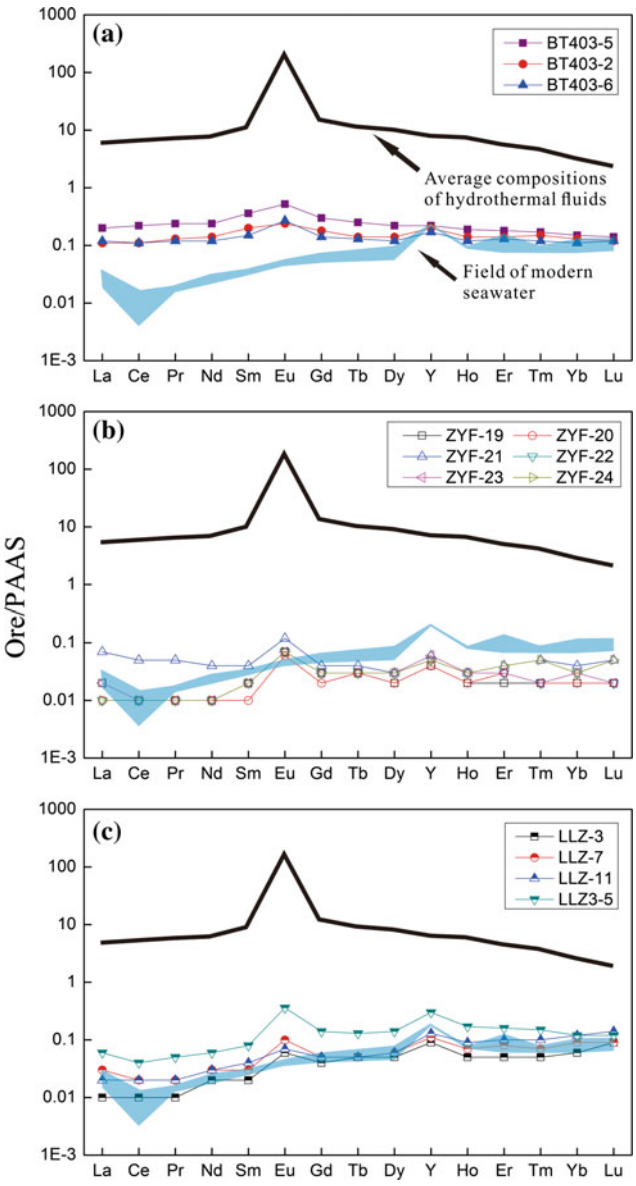

Fig. 6.17 PAAS-normalized REY pattern of iron ore samples. **a** Iron ore samples from Bantaizi; **b** iron ore samples from Zhouyoufang, and **c** iron ore samples from Lilaozhuang. Note that the data of Lilaozhuang are from Huang et al. (2013b). *Black line* denotes the average compositions of hydrothermal fluids (Bau and Dulski 1999). *Light blue* field denotes range of modern seawater composition (including data of South Pacific, Southern Ocean and Black Sea from Bolhar et al. 2004)

(37.6–47.9 and 1.65–3.37). The $(Eu/Eu^*)_{SN}$ of Bantaizi ores are comparable to those of Superior-type BIF (<1.8, Huston and Logan 2004). Furthermore, as an indicator of hydrothermal flux, their MnO contents also are the highest among these samples from three deposits (ca. 0.07 vs. ca. 0.01). Since Mn is an indicator of hydrothermal flux (Bekker et al. 2010), we infer that the Bantaizi BIF formed at a higher hydrothermal flux than the other two deposits. The Bantaizi ores also have relatively high Al_2O_3 and TiO_2 contents, ranging from 1.84 to 2.39 wt% and from 0.08 to 0.15 wt%, respectively. In the Al_2O_3–TiO_2 diagram of the Bantaizi gneisses, amphibolites and ores, they show marked linear relationship, indicating terrigenous clastic sediments also contributed to the Bantaizi BIF generation (Liu and Yang 2013; Yang et al. 2014). In addition, the consistent ages between ore and wall rocks also support this point.

6.5 The Regional Tectonic Evolution, Iron Mineralization and Genesis of Huoqiu BIF

6.5.1 Formation of the Huoqiu BIF and "Huo–Ying Tectonic Movement"

Archean is the most important period to form BIFs in China with mineralization ages from 3.3 to 2.5 Ga, which favorably occurred in the greenstone belt closely associated with metamorphic volcanic rocks (Zhai et al. 1990; Zhai and Windley 1990; Zhai 2010). Sang et al. (1981) obtained ages of 2681 ± 65 to 2963 ± 798 Ma with majorities of 2700 Ma in the Huoqiu BIF by whole rock Rb–Sr dating; Wan et al. (2010) measured the oldest zircon age of 2.7 Ga by SHRIMP. Those ages are slight younger than our results through LA-ICPMS (Yang et al. 2012). We obtained the oldest age of 2846 ± 82 Ma for amphibolite and an age of 2746 ± 91 Ma for gneiss. According to regional metamorphism and errors of measurements, we estimate that the oldest age for the Huoqiu BIF should be ca. 2.7 Ga, and the age of 1.8 Ga represented activity of migmatization which caused massive metamorphism in this region resulting from the Fengyang Tectonic Movement in eastern Anhui (BGMRA 1987). This 1.8 Ga age is well in accord with the $^{40}Ar/^{39}Ar$ age of muscovite acquired from the Wuhe Complex.

When the discussion is on the Huoqiu regional metamorphic event, it always refers to the Bengbu Tectonic Movement to account for tectonic evolution/history in this region. In this study, we recheck materials of regional geological sections, ages, and mineralization, and confirmed that the BIF, metamorphism, and iron mineralization in both Huoqiu and Bengbu regions are quite different. There are no accurate zircon ages in the Wuhe Group thus far, however, the metamorphism in the Wuhe Group in Bengbu region can reach granulite facies without or few iron mineralization (Fig. 6.4), the Huoqiu Group mostly underwent metamorphism of green schist to low amphibolite facies, part of reached to upper amphibolite facies, the whole BIF has rich in iron mineralization along Huoqiu–Shouxian–Yingshang and Lixin regions. From these aspects, we proposed a concept of Huoqiu–Yingshang (Huo–Ying) Tectonic Movement to account for the regional BIFs, iron mineralization and

their metamorphism in the HQC. Thereafter, the Fengyang tectonic movement occurred in ca. 1.8 Ga made the tectonic uniform in both Northwestern and Northeastern Anhui Province (Huoqiu vs. Bengbu).

A model accounting for the geological-sedimentary-metamorphic history in the Huoqiu region as well as formation of Huoqiu BIF and iron deposit is proposed based on the above discussion (Fig. 6.18).

6.5.2 Genesis of Huoqiu BIF

From the regional geological background, the Huoqiu Group consisting of volcanic-sedimentary metamorphic rock series has undergone migmatization. The lower part is consisting of argillaceous rocks, argillaceous sandstone and greywacke, marble, iron siliceous rocks, and magnesium carbonate. According to the mineral assemblages, we indicate that hornblende + almandine + plagioclase + quartz combination may have been equivalent to low amphibolite facies of regional metamorphism during metallogenic stages. In addition, local disseminated type ore formation and the emergence of the serpentine (Lilaozhuang deposit) shows that metallogenic stage had undergone hydrothermal metasomatic metamorphism (Sun 2007), similar to those reported hydrothermal reformation in Anshan, Benxi BIFs deposits in northeastern China (Li and Zhao 1999; Li 2003; Zhang 2005).

Superior-type BIF has close relationship with sedimentary formation, forming at stable shallow sea environment with depositional transgression sequence, its sedimentary environment belongs to passive continental margin (Trendall and Blockley 1970; Beukes 1983). From this point, the Huoqiu BIF developed obvious rhythmic sequences. According to drilling exploration, from bottom to top, the unit of rhythmic sequence is composed of biotite-amphibole granulitite sandwiched between thin-layered mica-quartz schist-amphibolite and amphibole schist. Wu (1979) identified this unit of rhythmic sequence is composed of turbidite, which can correspond to the Baoma turbidite layers with BCE sequences, parts of them are ABCE, CE, and AE sequences. From bottom to top of drilling profiles, the colors of rhythmic sequences become darker with increase of flake and columnar minerals, decrease of granular minerals, indicating that the Huoqiu BIF has characterized as flysch deposition. In some parts, this sequence is composed of biotite-plagioclase gneiss sandwiched between schist and amphibolites, reflecting flysch deposition feature. Looking around the whole Huoqiu BIF sequence, it appears to be composed of a huge rhythmic deposition, especially in the Zhouji Fm., equally to terrigenous clastic rocks-argillaceous shale-carbonate rocks sandwiched between ferrosilicon sedimentary formations (Qi and Yao 1982).

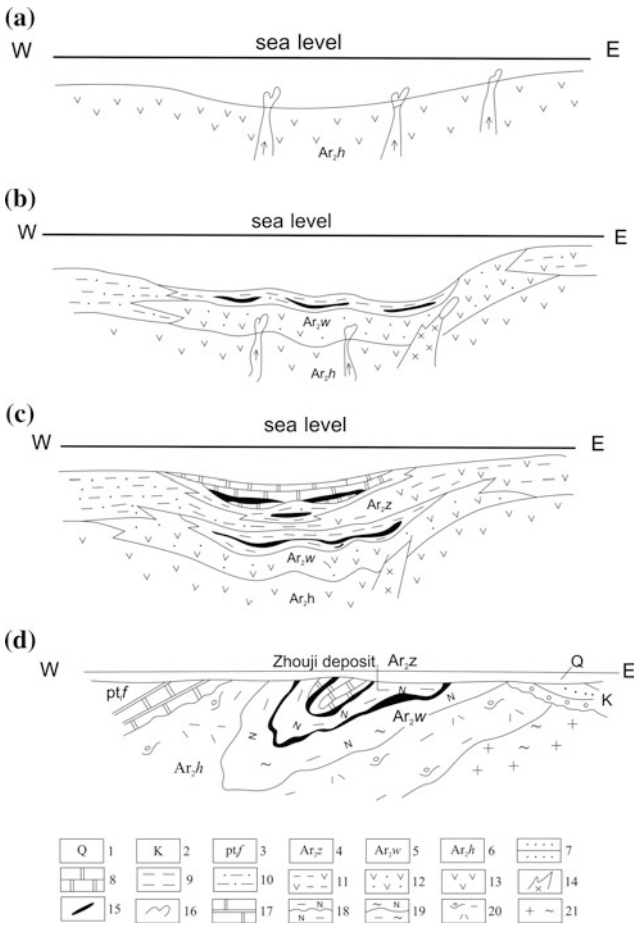

Fig. 6.18 The geological-tectonic evolution history in Huoqiu region and formation of Huoqiu BIF and iron deposit (after No. 313 Geol. Team 1991). **a** Formations of the acid volcanic rocks, clastic rocks and ferrosilicon rocks in Wuji Fm; **b** formations of the clastic rock and ferrosilicon rocks in Wuji Fm; **c** Huoqiu BIF iron ore field after Huo–Ying tectonic movement (Ar_2) and Fengyang tectonic movement (Pt_1); **d** iron ore evolution model of sedimentary basin pattern in the Huoqiu BIF iron ore field. *1* Quaternary; *2* Cretaceous; *3* Fengyang Group; *4* Zhouji Fm.; *5* Wuji Fm.; *6* The Huayuan Fm.; *7* greywacke; *8* dolomite; *9* mudstone; *10* muddy graywacke; *11* volcanic-sedimentary graywacke; *12* intermediate-acid volcanic rock; *13* basic volcanic rock; *14* sub-volcanic rock; *15* iron ore belt; *16* volcanic activity; *17* dolomite marble; *18* Biotite-plagioclase gneiss; *19* migmatization biotite plagioclase gneiss; *20* Augen-like migmatite; *21* migmatization granite

The significant geochemical discrepancies between A-type and S-type BIF are commonly ascribed to variations in volcanic-related hydrothermal fluid fluxes, which show a much larger contribution in the former, but less input in the latter (Huston and Logan 2004). Thus, A-type BIF commonly have more similar REY characteristics to hydrothermal fluids than S-type, whereas S-type BIF have more similar REY characteristics to the seawater (Huston and Logan 2004). The Huoqiu BIF samples exhibit slightly LREE depletion over HREE with totally low REE contents,

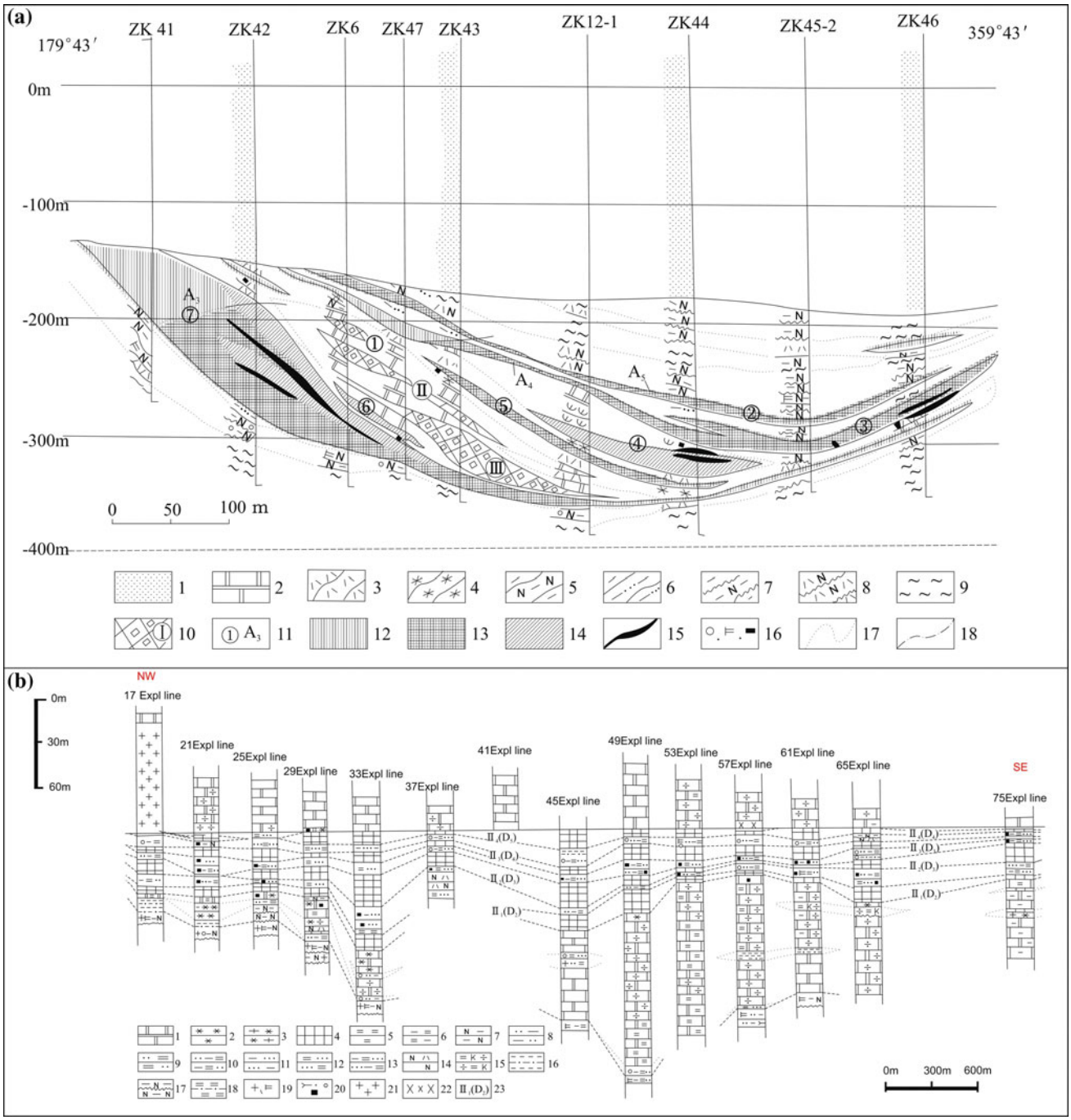

Fig. 6.19 Exploration section in the Huoqiu region (according to No. 337 Geol. Team 1986; No. 313 Geol. Team 1991; Yang et al., 2014). **a** The exploration in the Lilaozhuang ore deposit, showing extinctive anticline structure. *1* Quaternary; *2* magnesite dolomite marble; *3* amphibolite; *4* actinolite schists; *5* plagioclase—biotite schist; *6* biotite-quartz schist; *7* biotite-plagioclase gneiss; *8* amphibole-plagioclase gneiss angle; *9* migmatite; *10* magnesite body with number; *11* iron ore body; *12* Quartz-type oxidized iron ore; *13* quartz-type magnetite iron ore; *14* carbonate type iron ore; *15* rich iron ore body; *16* garnet, kyanite, magnetite; *17* geological boundaries; *18* boundaries between oxidized ore with native ore. **b** The D_3 drilling section in the Huoqiu region. *1* dolomite marble; *2* actinolite schist; *3* tremolite-actinolite schist; *4* iron ore body; *5* schist; *6* biotite-muscovite schist; *7* plagioclase biotite schist; *8* quartz biotite schist; *9* quartz muscovite schist; *10* quartz-biotite-muscovite schist; *11* biotite-quartz schist; *12* muscovite-quartz schist; *13* biotite-muscovite-quartz schist; *14* plagioclase amphibolite; *15* phlogopite potassium feldspar tremolite schist/phlogopite potassium feldspar gneiss; *16* dark granulitite; *17* biotite plagioclase gneiss; *18* phlogopite granulitite; *19* grenatite-kyanite rock; *20* Bucholzite-garnet-magnet ore; *21* pegmatite; *22* diabase; *23* ore body number

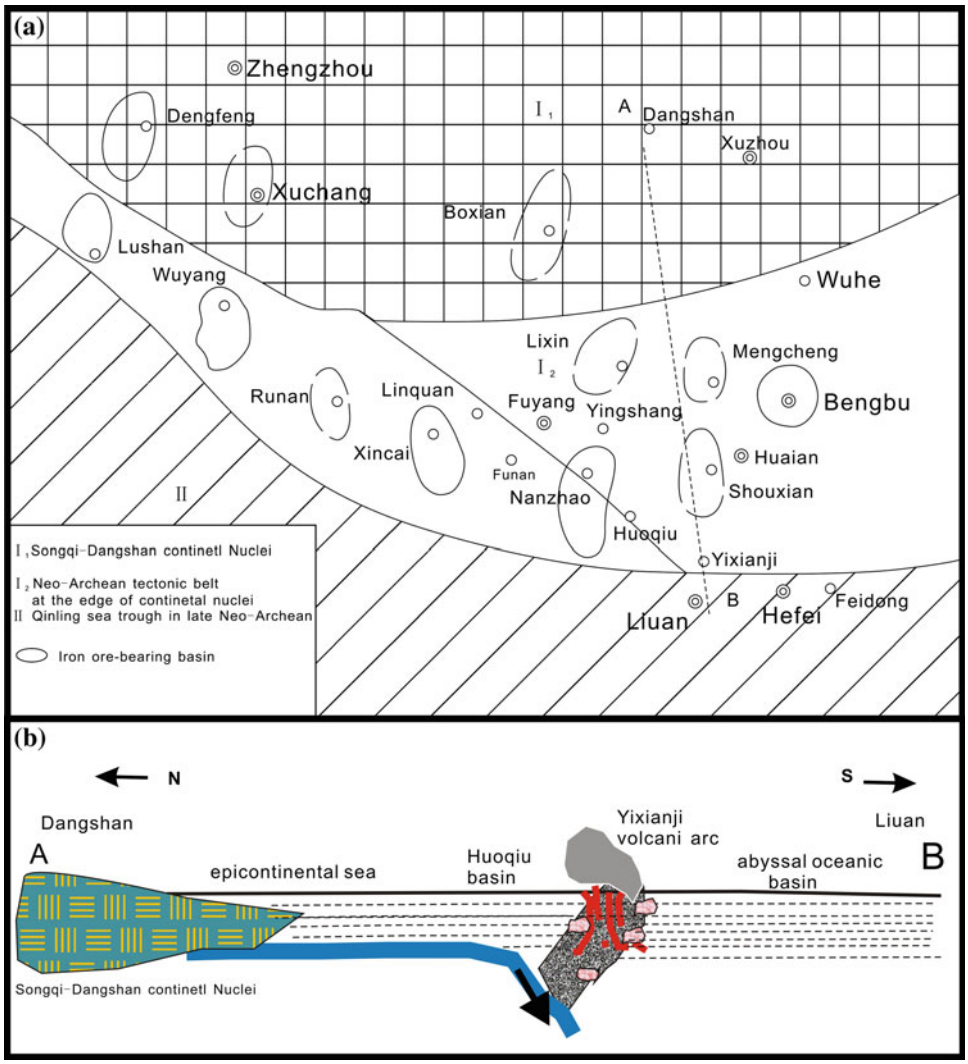

Fig. 6.20 Tectonic evolution and iron ore formation model in late Neoarchean and Paleoproterozoic in the Huoqiu iron deposit and its nearby region (after No. 313 Geol. Team 1991). **a** Plane map; **b** profile graph

similar to modern seawater (Fig. 6.17). In particular, their Y/Ho ratios and Eu anomalies are close to those of seawater (Liu and Yang 2013; Huang et al. 2013b; Yang et al. 2014). However, it is worth noting that hydrothermal fluids also exerted some marginal effect on the BIF deposition, as inferred from their significantly elevated $(Eu/Eu^*)_{SN}$, reduced Y/Ho relative to seawater. Therefore, we suggest that the sources contributing to the Huoqiu BIF deposition are predominantly seawater, and subordinately volcanic hydrothermal fluids and terrigenous clastic sediments, which agree well with the characteristics of S-type BIF.

Overall, the Huoqiu BIF should belong to the flysch-jasper iron formation, it developed around 500 m thickness of carbonate rocks on the top (Fig. 6.19). Figure 26 illustrates correction profiles of the Huoqiu BIFs and Hamersley, west Australia, showing that both Huoqiu BIF and Hamersley BIF have distinctive carbonate formation associated with iron ore formations as well as both iron ores consist of martite, thus they most likely have a supergene origin (Harmsworth et al. 1990). Compared to Hamersley, Huoqiu BIF has not a black shale formation, however, it has more a combination of magnesite on the top sequence in the Lilaozhuang deposit, reflecting slight different oxidation environment during their formations. According to these characteristics, we temporarily summed up the Huoqiu BIF into in Superior-type iron formation, different from the former called Algoma-type. Moreover, this BIF had undergone intensive metamorphism compared to other typical Superior types.

The Huo–Ying Tectonic Movement occurred around 2.7 Ga made the Neoarchaean Huoqiu BIF to undergo regional metamorphism at middle-high temperature and middle pressure conditions along Huoqiu–Yingshang regions, leading to recrystallization of former sedimentation of hematite, magnetite, flint and minerals, formed specularite, coarse magnetite, jade, or recrystallized quartz strips. In A + B ore belt, it commonly appears pieces of graphite and organic carbon fragments, which could be reduction materials in reducing hematite into magnetite. In fact, there are

some residual plate structures found in magnetite grains, proving function of reduction during formation of iron ores. A model of tectonic evolution and iron ore formation in late Neoarchean and Paleoproterozoic in the Huoqiu iron deposit and nearby region is proposed as shown in Fig. 6.20.

6.6 Summary

The whole rock compositions, zircon U–Pb and Hf isotopic data obtained for the HQC place important constraints on the timing of formation of TTG gneisses and amphibolites, and, importantly, provide new insights into understanding the Neoarchean continental growth and evolution of the southeastern margin of the NCC. The Huoqiu TTG gneisses with steep REE patterns and low HREE contents share the mineralogical and geochemical characteristics of typical Neoarchean TTG. The major and trace element characteristics of these rocks suggest that they were produced by partial melting of the basaltic protoliths of the spatially amphibolites at the base of a thickened mafic continental crust, leaving a rutile-bearing eclogite residue during 2.76–2.71 Ga. This conclusion has been verified by their zircon U–Pb ages, Hf isotopic compositions as well as multi-element geochemical modeling. Zircon Hf model ages of TTG gneisses suggest that this process mainly involved reworking of older continental crust.

The age spectrum of all available detrital zircons (n = 204) from the HQC consists of two peaks at 3.0–2.9 and 2.75 Ga, suggesting two principal magmatic events happened at the southeastern margin of the NCC. The two peaks also record at least two major episodic continental crustal growth processes, in particular the former is rarely reported in the NCC, whereas the latter is received widespread attentions wherever from the NCC or other cratons in the world. On the basis of detrital zircon Hf isotope compositions, it is believed that the two periods of continental crustal growth are not only involved mostly juvenile crustal additions but also minor crustal reworking. The geochronological and geochemical data from the HQC lead to the conclusion as follows: the former crust-forming event (3.0–2.9 Ga) was likely generated in an island-arc subduction system, whereas the latter crustal rocks (2.8–2.7 Ga) were probably formed at the setting of underplating subsequent partial melting of lower crustal mafic rocks. The island-arc subduction system implied a compressive setting, whereas the underplating and subsequent emplacement of the TTG magmas are suggested an extensional setting, thus they record a tectonic transition at the southeastern margin of the NCC during 3.01–2.75 Ga.

According to the characteristics of Huoqiu BIF, we can infer the following: (1) The Huoqiu BIF deposit in a continental marginal sea environment; (2) The upper limit age of the Huoqiu BIF precipitation has been constrained at 2.75 Ga; whereas the lower limit age is probably at 2.71 Ga; (3) The REY characteristics of the Huoqiu BIF sample indicate that their material sources were dominated by seawater, with minor contributions from the volcanic hydrothermal fluids and terrigenous sediments; (4) Based on precipitating environment, flysch rhythmic structure occurrence, and widespread carbonate mineral paragenesis with primary magnetite, we suggest that the Huoqiu BIF belongs to Superior-type.

Acknowledgments This study was supported by the State Key Basic Research Development Program of China (2012CB416602), Natural Science Foundation of China (41090372), the Fundamental Research Funds for the Central Universities and the China Postdoctoral Science Foundation (2014M561832). We are appreciate Academician Mingguo Zhai, Prof. Yue Zhao and Taiping Zhao originating this book and inviting us to participate in. We are indebted to Academician Chang Yinfo and Prof. Yao Zhenbiao for their kind guidance. We are grateful for the expert advice of Mr./Mrs. Li Y.X., Li C.S., Ma L.M., Bu M.K., Chen B.Q., Wu Z.L., Huang X.F., Xu L., Zang W.L., and Tu Z.B. from the No. 313 Geological Team who generously provided complete support in field. Yurong Cui, Jianzhen Geng, Jianghong Deng, Zilong Hu, Geng Chu, and Shuang Li are specially acknowledged for their help with the zircon U–Pb and Hf isotopic analyses.

References

Allègre, C. J., & Rousseau, D. (1984). The growth of the continent through geological time studied by Nd isotope analysis of shales. *Earth and Planetary Science Letters, 67*, 19–34.

Armstrong, R. L. (1981). Radiogenic isotopes: The case for crustal recycling on a steady-state no-continental-growth Earth. *Philosophical Transactions of the Royal Society of London Series A, 301*, 443–472.

Arndt, N., & Davaille, A. (2013). Episodic Earth evolution. *Tectonophysics, 609*, 661–674.

Barth, M. G., Foley, S. F., & Horn, I. (2002). Partial melting in Archean subduction zones: Constraints from experimentally determined trace element partition coefficients between eclogitic minerals and tonalitic melts under upper mantle conditions. *Precambrian Research, 113*(3–4), 323–340.

Bau, M., & Dulski, P. (1996). Distribution of yttrium and rare-earth elements in the Penge and Kuruman iron-formations, Transvaal Supergroup, South Africa. *Precambrian Research, 79*(1–2), 37–55.

Bau, M., & Dulski, P. (1999). Comparing yttrium and rare earths in hydrothermal fluids from the Mid-Atlantic Ridge: implications for Y and REE behaviour during near-vent mixing and for the Y/Ho ratio of Proterozoic seawater. *Chemical Geology, 155*, 77–90.

Bekker, A., Slack, J. F., Planavsky, N., Krapež, B., Hofmann, A., Konhauser, K. O., et al. (2010). Iron formation: The sedimentary product of a complex interplay among mantle, tectonic, oceanic, and biospheric processes. *Economic Geology, 105*(3), 467–508.

Belousova, E. A., Kostitsyn, Y. A., Griffin, W. L., Begg, G. C., O'Reilly, S. Y., & Pearson, N. J. (2010). The growth of the continental crust: Constraints from zircon Hf-isotope data. *Lithos, 119*, 457–466.

Beukes, N. J. (1983). Palaeoenvironmental setting of iron-formations in the depositional basin of the Transvaal Supergroup, South Africa. In A. F. Trendall & R. C. Morris (Eds.), *Iron formations: Facts and problems* (pp. 131–209). Amsterdam: Elsevier.

BGMRA (Bureau of Geology Mineral Resources of Anhui). (1987). *The regional geology of Anhui province* (pp. 548–558). Beijing: Geological Publishing House (in Chinese with detailed English illustrations).

BGMRA (Bureau of Geology Mineral Resources of Anhui). (1997). *Rock Strata in Anhui Province* (pp. 1–271). Wuhan: China University of Geosciences Press (in Chinese with detailed English illustrations).

BGMRH (Bureau of Geology Mineral Resources of Henan) (1989) *The regional geology of Anhui Province* (pp. 5–94). Beijing: Geological Publishing House (in Chinese with detailed English illustrations).

Bolhar, R., Kamber, B. S., Moorbath, S., Fedo, C. M., & Whitehouse, M. J. (2004). Characterisation of early Archaean chemical sediments by trace element signatures. *Earth and Planetary Science Letters, 222*, 43–60.

Cawood, P. A., Hawkesworth, C. J., & Dhuime, B. (2013). The continental record and the generation of continental crust. *Geological Society of America Bulletin, 125*(1–2), 14–32.

Cloud, P. (1973). Paleoecological significance of the banded iron formation. *Economic Geology, 68*, 1135–1143.

Condie, K. C. (1986). Geochemistry and tectonic setting of early Proterozoic supracrustal rocks in the southwestern United States. *The Journal of Geology, 94*, 845–864.

Condie, K. C. (2000). Episodic continental growth models: Afterthoughts and extensions. *Tectonophysics, 322*(1–2), 153–162.

Condie, K. C. (2005). TTG and adakites: Are they both slab melts? *Lithos, 80*(1–4), 33–44.

Condie, K. C., & Aster, R. C. (2010). Episodic zircon age spectra of orogenic granitoids: The supercontinent connection and continental growth. *Precambrian Research, 180*(3–4), 227–236.

Condie, K. C., Bickford, M. E., Aster, R. C., Belousova, E., & Scholl, D. W. (2011). Episodic zircon ages, Hf isotopic composition, and the preservation rate of continental crust. *Geological Society of America Bulletin, 123*(5–6), 951–957.

Condie, K. C., & Kröner, A. (2013). The building blocks of continental crust: Evidence for a major change in the tectonic setting of continental growth at the end of the Archean. *Gondwana Research, 23*(2), 394–402.

Dhuime, B., Hawkesworth, C. J., Cawood, P. A., & Storey, C. D. (2012). A change in the geodynamics of continental growth 3 billion years ago. *Science, 335*(6074), 1334–1336.

Diwu, C., Sun, Y., Wilde, S. A., Wang, H. L., Dong, Z. C., Zhang, H., et al. (2013). New evidence for similar to 4.45 Ga terrestrial crust from zircon xenocrysts in Ordovician ignimbrite in the North Qinling Orogenic Belt, China. *Gondwana Research, 23*(4), 1484–1490.

Diwu, C. R., Sun, Y., Ling, C. L., & Wang, H. L. (2010). LA-(MC)-ICPMS U-Pb zircon geochronology and Lu-Hf isotope compositions of the Taihua complex on the southern margin of the North China Craton. *Chinese Science Bulletin, 55*, 2557–2571.

Douville, E., Bienvenu, P., Charlou, J. L., Donval, J. P., Fouquet, Y., Appriou, P., et al. (1999). Yttrium and rare earth elements in fluids from various deep-sea hydrothermal systems. *Geochimica et Cosmochimica Acta, 63*, 627–643.

Douville, E., Charlou, J. L., Oelkers, E. H., Bienvenu, P., Jove Colon, C. F., Donval, J. P., et al. (2002). The rainbow vent fluids (36°14′N, MAR): The influence of ultramafic rocks and phase separation on trace metal content in Mid-Atlantic Ridge hydrothermal fluids. *Chemical Geology, 184*, 37–48.

Drummond, M. S., & Defant, M. J. (1990). A model for trondhjemite-tonalite-dacite genesis and crustal growth via slab melting: Archean to modern comparisons. *Journal of Geophysical Research, 95*, 21503–21521.

Faure, G. (1977). *Smith and Wyllie Intermediate Geology Series. Principles of isotope geology* (475 p.). New York, NY, United States: Wiley.

Foley, S. F. (2008). Rejuvenation and erosion of the cratonic lithosphere. *Nature Geoscience, 1*(8), 503–510.

Foley, S. F., Buhre, S., & Jacob, D. E. (2003). Evolution of the Archaean crust by delamination and shallow subduction. *Nature, 421*(6920), 249–252.

Foley, S. F., Tiepolo, M., & Vannucci, R. (2002). Growth of early continental crust controlled by melting of amphibolite in subduction zones. *Nature, 417*(6891), 837–840.

Gastil, G. (1960). The distribution of mineral dates in time and space. *American Journal of Science, 258*, 1–35.

Geng, Y. S., Du, L., & Ren, L. (2012). Growth and reworking of the early Precambrian continental crust in the North China Craton: Constraints from zircon Hf isotopes. *Gondwana Research, 21*(2–3), 517–529.

Griffin, W. L., Pearson, N. J., Belousova, E., Jackson, S. E., van Achterbergh, E., O'Reilly, S. Y., & Shee, S. R. (2000). The Hf isotope composition of cratonic mantle: LAM-MC-ICPMS analysis of zircon megacrysts in kimberlites. *Geochimica et Cosmochimica Acta, 64*(1), 133–147.

Goodwin, A. M. (1996). *Principles of Precambrian geology* (327 pp.). London: Academic Press.

Gross, G. A. (1980). A classification of iron-formation based on depositional environments. *Canadian Mineralogist, 18*, 215–222.

Gross, G. A. (1983). Tectonic systems and the deposition of iron-formation. *Precambrian Research, 20*, 171–187.

Gross, G. A. (1993). Industrial and genetic models for iron ore in iron-formations. In R. V. Kirkham, W. D. Sinclair, R. I. Thorpe, & J. M. Duke (Eds.), *Mineral deposit modeling* (pp. 151–170). Geological Association of Canada, Special Paper 40.

Hanchar, J. M., & Rudnick, R. L. (1995). Revealing hidden structures: The application of cathodoluminescence and back-scattered electron imaging to dating zircons from lower crustal xenoliths. *Lithos, 36*, 289–303.

Harmsworth, R. A., Kneeshaw, M., Morris, R. C., Robinson, C. J., & Shrivastava, P. K. (1990). BIF derived iron ores of the Hamersley Province. In: F. E. Hughes (Ed.), *Geology of the mineral deposits of Australia and Papua New Guinea* (Vol. 14, pp. 617–642). Melbourne (Aust. Inst. Min. Metall. Monogr.).

Hawkesworth, C. J., Cawood, P., & Dhuime, B. (2013). Continental growth and the crustal record. *Tectonophysics, 609*, 651–660.

Hawkesworth, C. J., Dhuime, B., Pietranik, A. B., Cawood, P. A., Kemp, A. I. S., & Storey, C. D. (2010). The generation and evolution of the continental crust. *Journal of the Geological Society, 167*(2), 229–248.

Hawkesworth, C. J., & Kemp, A. I. S. (2006). Evolution of the continental crust. *Nature, 443*(7113), 811–817.

Heimann, A., Johnson, C. M., Beard, B. L., Valley, J. W., Roden, E. E., Spicuzza, M. J., & Beukes, N. J. (2010). Fe, C, and O isotope compositions of banded iron formation carbonates demonstrate a major role for dissimilatory iron reduction in ~2.5 Ga marine environments. *Earth and Planetary Science Letters, 294*(1–2), 8–18.

Hergt, J. M., Peate, D. W., & Hawkesworth, C. J. (1991). The petrogenesis of Mesozoic Gondwana low-Ti flood basalts. *Earth and Planetary Science Letters, 105*, 134–148.

Hoffmann, J. E., Münker, C., Næraa, T., Rosing, M. T., Herwartz, D., Garbe-Schönberg, D., et al. (2011). Mechanisms of Archean crust formation inferred from high precision HFSE systematics in TTG. *Geochimica et Cosmochimica Acta, 75*, 4157–4178.

Holland, H. D. (1973). The oceans: A possible source of iron in iron-formation. *Economic Geology, 68*, 1169–1172.

Huang, H., Polat, A., & Fryer, B. J. (2013a). Origin of Archean tonalite–trondhjemite–granodiorite (TTG) suites and granites in the Fiskenæsset region, southern West Greenland: Implications for continental growth. *Gondwana Research, 23*(2), 452–470.

Huang, H., Zhang, L. C., Liu, X. F., Li, H. Z., & Liu, L. (2013b). Geological and geochemical charateristics of the Lee Laozhuang iron mine in Huoqiu iron deposti: Implications for sedimentary environment. *Acta Petrologica Sinica, 29*, 2593–2605 (in Chinese with English abstract).

Hurley, P. M., & Rand, J. R. (1969). Predrift continental nuclei. *Science, 164*, 1229–1242.

Huston, D. L., & Logan, G. A. (2004). Barite, BIFs and bugs: Evidence for the evolution of the Earth's early hydrosphere. *Earth and Planetary Science Letters, 220*, 41–55.

Ilyin, A. V. (2009). Neoproterozoic banded iron formations. *Lithology and Mineral Resources, 44*(1), 87–95.

Jahn, B. M., Auvray, B., Shen, Q. H., Liu, D. Y., Zhang, Z. Q., Dong, Y. J., et al. (1988). Archean crustal evolution in China: The Taishan complex, and evidence for juvenile crustal addition from long-term depleted mantle. *Precambrian Research, 38*(4), 381–403.

Jahn, B. M., Liu, D. Y., Wan, Y. S., Song, B., & Wu, J. S. (2008). Archean crustal evolution of the Jiaodong Peninsula, China, as revealed by zircon SHRIMP geochronology, elemental and Nd-isotope geochemistry. *American Journal of Science, 308*(3), 232–269.

Jiang, N., Guo, J., Zhai, M., & Zhang, S. (2010). $\sim$2.7 Ga crust growth in the North China Craton. *Precambrian Research, 179*(1–4), 37–49.

Jiao, Y. L., Wang, Y., Yao, Y., Tong, L. X. (2013). Can partial melting of the hydrous intermediate-basic lower continental crust generate C-type adakites?—Comment on Zhang et al. (2012). *Geological Journal of China Universities, 19*(2), 373–380 (in Chinese with English abstract).

Johnson, C. M., Beard, B. L., Beukes, N. J., Klein, C., & O'Leary, J. M. (2003). Ancient geochemical cycling in the Earth as inferred from Fe isotope studies of banded iron formations from the Transvaal Craton. *Contributions to Mineralogy and Petrology, 144*(5), 523–547.

Johnson, C. M., Beard, B. L., & Roden, E. E. (2008). The iron isotope fingerprints of redox and biogeochemical cycling in the modern and ancient Earth. *Annual Review of Earth Planetary Science, 36*, 457–493.

Johnson, C. M., Ludois, J. M., Beard, B. L., Beukes, N. J., & Heimann, A. (2013). Iron formation carbonates: Paleoceanographic proxy or recorder of microbial diagenesis? *Geology, 41*(11), 1147–1150.

Kamber, B. S. (2010). Archean mafic–ultramafic volcanic landmasses and their effect on ocean–atmosphere chemistry. *Chemical Geology, 274*, 19–28.

Kamber, B. S. (2015). The evolving nature of terrestrial crust from the Hadean, through the Archaean, into the Proterozoic. *Precambrian Research, 258*, 48–82.

Kato, Y., Kawakami, T., Kano, T., Kunugiza, K., & Swamy, N. S. (1996). Rare-earth element geochemistry of banded iron formations and associated amphibolite from the Sargur belts, south India. *Journal of Southeast Asian Earth Sciences, 14*, 161–164.

Klein, C. (2005). Some Precambrian banded iron-formations (BIFs) from around the world: Their age, geologic setting, mineralogy, metamorphism, geochemistry, and origin. *American Mineralogist, 90*(10), 1473–1499.

Klein, C., & Beukes, N. J. (1992). Time distribution, stratigraphy, and sedimentology, and sedimentologic setting, and geochemistry of Precambrian iron formation. In J. W. Schopf & C. Klein (Eds.), *The proterozoic biosphere: A multidisciplinary study* (pp. 139–146). New York: Cambridge University Press.

Klein, C., & Beukes, N. J. (1993). Sedimentology and geochemistry of the glaciogenic late proterozoic rapitan iron-formation in canada. *Economic Geology and the Bulletin of the Society of Economic Geologists, 88*(3), 542–565.

Kretz, R. (1983). Symbols for rock-forming minerals. *American Mineralogist, 68*(1–2), 277–279.

Li, D. L. (2003). Research of tectonics and ore-controlling factors in the iron ore in the Waitou Mountains, Liaoning. *Geological Prospectives Review, 18*(2), 882–894. (in Chinese with English abstract).

Li, H. Y., & Zhao, X. D. (1999). Study on Anshan type ironmine geological structure. *Precambrian Research Progress, 22*(3), 222–229. (in Chinese with English abstract).

Li, W., Beard, B. L., & Johnson, C. M. (2015). Biologically recycled continental iron is a major component in banded iron formations. *Proceedings of the National Academy of Sciences, 112*(27), 8193–8198.

Liu, C. H., Zhao, G., Sun, M., Zhang, J., & Yin, C. (2012b). U–Pb geochronology and Hf isotope geochemistry of detrital zircons from the Zhongtiao Complex: Constraints on the tectonic evolution of the Trans-North China Orogen. *Precambrian Research, 222–223*(0), 159–172.

Liu, C. H., Zhao, G., Sun, M., Zhang, J., Yin, C., & He, Y. (2012a). Detrital zircon U–Pb dating, Hf isotopes and whole-rock geochemistry from the Songshan Group in the Dengfeng Complex: Constraints on the tectonic evolution of the Trans-North China Orogen. *Precambrian Research, 192–195*(0), 1–15.

Liu, D. Y., Nutman, A. P., Compston, W., Wu, J. S., & Shen, Q. H. (1992). Remnants of $\geq$3800 Ma crust in the Chinese part of the Sino-Korean Craton. *Geology, 20*(4), 339–342.

Liu, D. Y., Wilde, S. A., Wan, Y., Wang, S., Valley, J. W., Kita, N., et al. (2009). Combined U–Pb, hafnium and oxygen isotope analysis of zircons from meta-igneous rocks in the southern North China Craton reveal multiple events in the Late Mesoarchean-Early Neoarchean. *Chemical Geology, 261*(1–2), 140–154.

Liu, L., & Yang, X. Y. (2013). Geochemical characteristics of the Huoqiu BIF ore deposit in Anhui province and their metallogenic significance: Taking the Bantaizi and Zhouyoufang deposits as examples. *Acta Petrologica Sinica, 29*(7), 2551–2566. (in Chinese with English abstract).

Liu, L., & Yang, X. (2015). Temporal, environmental and tectonic significance of the Huoqiu BIF, southeastern North China Craton: Geochemical and geochronological constraints. *Precambrian Research, 261*, 217–233.

Liu, L., Yang, X., Santosh, M., & Aulbach, S. (2015). Neoarchean to Paleoproterozoic continental growth in the southeastern margin of the North China Craton: Geochemical, zircon U–Pb and Hf isotope evidence from the Huoqiu complex. *Gondwana Research, 28*(3), 1002–1018.

Maniar, P. D., & Piccoli, P. M. (1989). Tectonic discrimination of granitoids. *Geological Society of America Bulletin, 101*, 635–643.

Martin, H. (1999). Adakitic magmas: Modern analogues of Archaean granitoids. *Lithos, 46*(3), 411–429.

Martin, H., Smithies, R. H., Rapp, R., Moyen, J. F., & Champion, D. (2005). An overview of adakite, tonalite–trondhjemite–granodiorite (TTG), and sanukitoid: Relationships and some implications for crustal evolution. *Lithos, 79*(1–2), 1–24.

Mcdonough, W. F., & Sun, S. S. (1995). The composition of the Earth. *Chemical Geology, 120*(3–4), 223–253.

Moyen, J. F., & Martin, H. (2012). Forty years of TTG research. *Lithos, 148*, 312–336.

Moyen, J. F., Stevens, G. (2006). Experimental constraints on TTG petrogenesis: Implications for Archean Geodynamics. In K. Benn, J. C. Mareschal, & K. C. Condie (Eds.), AGU *Geophysical Monograph Series*: *Vol. 164. Archean geodynamics and environments* (pp. 149–175).

Nagel, T. J., Hoffmann, J. E., & Münker, C. (2012). Generation of Eoarchean tonalite-trondhjemite-granodiorite series from thickened mafic arc crust. *Geology, 40*(4), 375–378.

No. 313 Geol. Team. (1991). A Report of the Regional 1:50000 Geological Survey in Huoqiu Iron Ore Field. Anhui Bureau of Geology and Mineral Resources, (in Chinese).

No. 337 Geol. Team (1986) A report of 1:50000 Geological Survey of the Sanhejian-Yunheji, Qiaogou-Gaotangji and Jiangji-Liuji Regions. Anhui Bureau of Geology and Mineral Resources, (in Chinese).

Nowell, G. M., Kempton, P. D., Noble, S. R., Fitton, J. G., Saunders, A. D., Mahoney, J. J., et al. (1998). High precision Hf isotope measurements of MORB and OIB by thermal ionisation mass spectrometry: Insights into the depleted mantle. *Chemical Geology, 149*, 211–233.

Nozaki, Y., Zhang, J., & Amakawa, H. (1997). The fractionation between Y and Ho in the marine environment. *Earth and Planetary Science Letters, 148*, 329–34.

Pearce, J. A., Harris, N. B. W., & Tindle, A. G. (1984). Trace element discrimination diagrams for the tectonic interpretation of granitic rocks. *Journal of Petrology, 25*, 956–983.Pearce, T.H., Gorman, B. E., & Birkett, T.C. (1975). The TiO2-K2O-P2O5 diagram: a method of discrimination between oceanic and non-oceanic basalts. *Earth and Planetary Science Letters*, 24, 419-426.

.Pearce, T.H, Gorman, B.E, & Birkett, T.C. (1975). The TiO2-K2O-P2O5 diagram: a method ofdiscrimination between oceanic and non-oceanic basalts. *Earth and Planetary Science Letters*, *24*, 419–426.

Pearce, T. H., Gorman, B. E., & Birkett, T. C. (1977). The relationship between major element chemistry and tectonic environment of basic and intermediate volcanic rocks. *Earth and Planetary Science Letters, 36*, 121–132.

Peng, T., Wilde, S. A., Fan, W., & Peng, B. (2013). Late Neoarchean potassic high Ba–Sr granites in the Taishan granite–greenstone terrane: Petrogenesis and implications for continental crustal evolution. *Chemical Geology, 344*, 23–41.

Pin, C., & Paquette, J. L. (1997). A mantle-derived bimodal suite in the Hercynian Belt: Nd isotope and trace element evidence for a subduction-related rift origin of the late Devonian Brévenne metavolcanics, Massif Central (France). *Contributions to Mineralogy and Petrology, 129*, 222–238.

Planavsky, N., Rouxel, O. J., Bekker, A., Hofmann, A., Little, C. T. S., & Lyons, T. W. (2012). Iron isotope composition of some Archean and Proterozoic iron formations. *Geochimica et Cosmochimica Acta, 80*, 158–169.

Polat, A. (2012). Growth of Archean continental crust in oceanic island arcs. *Geology, 40*(4), 383–384.

Qi, R. Z. (1987). A discussion on the genesis of BIF of the Precambrian Huoqiu complex. *Bulletin of Nanjing Institute of Geology and Mineral Resources, 8*(1), 1–20. (in Chinese with English abstract).

Qi, R. Z., & Yao, G. Y. (1982). The metamorphism of HQC. *Bulletin of Nanjing Institute of Geology and Mineral Resources, 3*(3), 30–46. (in Chinese with English abstract).

Rapp, R. P., Shimizu, N., & Norman, M. D. (2003). Growth of early continental crust by partial melting of eclogite. *Nature, 425*(6958), 605–609.

Rapp, R. P., Shimizu, N., Norman, M. D., & Applegate, G. S. (1999). Reaction between slab-derived melts and peridotite in the mantle wedge: Experimental constraints at 3.8 GPa. *Chemical Geology, 160*(4), 335–356.

Rapp, R. P., & Watson, E. B. (1995). Dehydration melting of metabasalt at 8–32 kbar: Implications for continental growth and crust-mantle recycling. *Journal of Petrology, 36*, 891–931.

Rapp, R. P., Watson, E. B., & Miller, C. F. (1991). Partial melting of amphibolite/eclogite and the origin of Archean trondhjemites and tonalites. *Precambrian Research, 51*(1–4), 1–25.

Rouxel, O. J., Bekker, A., & Edwards, K. J. (2005). Iron isotope constraints on the Archean and Paleoproterozoic ocean redox state. *Science, 307*(5712), 1088–1091.

Rudnick, R. L., & Gao, S. (2003). Composition of the continental crust. In R. L. Rudnick (Ed.), *Treatise on geochemistry* (Vol. 3, pp. 1–64)., The Crust Amsterdam: Elsevier.

Sang, B. L., Xing, F. M., & Chen, Y. Z. (1981). The Precambrian metamorphic iron ore characteristics and prospecting. *Anhui Institute of Geological Science, 1*, 10–20. (in Chinese with English abstract).

Schmidt, K., Garbe-Schönberg, D., Koschinsky, A., Strauss, H., Jost, C. L., Klevenz, V., et al. (2011). Fluid elemental and stable isotope composition of the Nibelungen hydrothermal field (8°18′S, Mid-Atlantic Ridge): Constraints on fluid-rock interaction in heterogeneous lithosphere. *Chemical Geology, 280*, 1–18.

Schmidt, K., Koschinsky, A., Garbe-Schönberg, D., de Carvalho, L. M., & Seifert, R. (2007). Geochemistry of hydrothermal fluids from the ultramafic-hosted Logatchev hydrothermal field, 15°N on the Mid-Atlantic Ridge: Temporal and spatial investigation. *Chemical Geology, 242*, 1–21.

Shervais, J. W. (1982). Ti-V plots and the petrogenesis of modern and ophiolitic lavas. *Earth and Planetary Science Letters, 59*, 101–118.

Skjerlie, K. P., & Douce, A. E. P. (2002). The fluid-absent partial melting of a zoisite-bearing quartz eclogite from 1 center dot 0 to 3 center dot 2 GPa; implications for melting in thickened continental crust and for subduction-zone processes. *Journal of Petrology, 43*(2), 291–314.

Smithies, R. H. (2000). The Archaean tonalite–trondhjemite–granodiorite (TTG) series is not an analogue of Cenozoic adakite. *Earth and Planetary Science Letters, 182*(1), 115–125.

Smithies, R. H., & Champion, D. C. (2000). The Archaean high-Mg diorite suite: Links to tonalite–trondhjemite–granodiorite magmatism and implications for early Archaean crustal growth. *Journal of Petrology, 41*(12), 1653–1671.

Song, B. A., Nutman, A. P., Liu, D. Y., & Wu, J. S. (1996). 3800 to 2500 Ma crustal evolution in the Anshan area of Liaoning Province, northeastern China. *Precambrian Research, 78*(1–3), 79–94.

Spandler, C., Hermann, J., Arculus, R., & Mavrogenes, J. (2003). Redistribution of trace elements during prograde metamorphism from lawsonite blueschist to eclogite facies; implications for deep subduction-zone processes. *Contributions to Mineralogy and Petrology, 146*, 205–222.

Stein, M., & Hofmann, A. W. (1994). Mantle plumes and episodic crustal growth. *Nature, 372*, 63–68.

Sun, S. S., & McDonough, W. F. (1989). Chemical and isotopic systematics of oceanic basalts: Implications for mantle composition and processes. *Geological Society, London, Special Publications, 42*(1), 313–345.

Sun, Y. B. (2007). Geological characteristics and metallogenic types of the Lilaozhuang iron-magnesite deposit in Huoqiu. *Anhui Mineral Resources of Geology, 21*(5), 532–537. (in Chinese with English abstract).

Taylor, S. R., & McLennan, S. M. (1985). *The continental crust: Its composition and evolution* (312 pp.). Oxford: Blackwell Scientific Publications.

Thurston, P. C., Kamber, B. S., & Whitehouse, M. (2012). Archean cherts in banded iron formation: Insight into Neoarchean ocean chemistry and depositional processes. *Precambrian Research, 214–215*, 227–257.

Trendall, A. F., & Blockley, J. G. (1970). The iron-formations of the Precambrian Hamersley Group, Western Australia. *Geological Survey Western Australia Bulletin, 119*, 366.

Trendall, A. F., de Laeter, J. R., Nelson, D. R., & Mukhopadhyay, D. (1997). A precise zircon U-Pb age for the base of the BIF of the Mulaingiri Formation (Bababudan Group, Dharwar Supergroup) of

the Karnataka Craton. *Journal of the Geological Society of India, 50*, 161–170.

Vavra, G., Schmidt, R., & Gebauer, D. (1999). Internal morphology, habit and U-Th–Pb microanalysis of amphibolite-to-granulite facies zircons: Geochronology of the Ivrea Zone (Southern Alps). *Contributions to Mineralogy and Petrology, 134*, 380–404.

Veevers, J. J., Saeed, A., Belousova, E. A., & Griffin, W. L. (2005). U-Pb ages and source composition by Hf-isotope and trace-element analysis of detrital zircons in Permian sandstone and modern sand from southwestern Australia and a review of the paleogeographical and denudational history of the Yilgarn Craton. *Earth Science Review, 68*, 245–279.

Wan, T., & Zhu, H. (1996). The maximum sinisrtra strike-slip displacement and formation time of the Tan-Lu fault zone. *Geological Journal of China Universities, 2*, 14–27. (in Chinese with English abstract).

Wan, Y. S., Dong, C., Wang, W., Xie, H., & Liu, D. (2010). Archean basement and a Paleoproterozoic Collision Orogen in the Huoqiu area at the southeastern margin of North China Craton: Evidence from sensitive high resolution ion micro-probe U-Pb zircon geochronology. *Acta Geologica Sinica, 84*(1), 91–104. (English Edition).

Wan, Y. S., Liu, D., Song, B., Wu, J., Yang, C., Zhang, Z., et al. (2005). Geochemical and Nd isotopic compositions of 3.8 Ga meta-quartz dioritic and trondhjemitic rocks from the Anshan area and their geological significance. *Journal of Asian Earth Sciences, 24*(5), 563–575.

Wan, Y. S., Liu, D., Wang, S., Yang, E., Wang, W., Dong, C., et al. (2011a). ~2.7 Ga Juvenile crust formation in the North China Craton (Taishan-Xintai area, western Shandong Province): Further evidence of an understated event from U–Pb dating and Hf isotopic composition of zircon. *Precambrian Research, 186*(1–4), 169–180.

Wan, Y. S., Liu, D., Wang, W., Song, T., Kröner, A., Dong, C., et al. (2011b). Provenance of Meso to Neoproterozoic cover sediments at the Ming Tombs, Beijing, North China Craton: An integrated study of U–Pb dating and Hf isotopic measurement of detrital zircons and whole-rock geochemistry. *Gondwana Research, 20*(1), 219–242.

Wan, Y. S., Liu, D. Y., Wu, J. S., Zhang, Z. Q., & Song, B. (1998). The origin of Mesoarchean granitic rocks from Anshan-Benxi area: Constraints of geochemistry and Nd isotopes. *Acta Petrologica Sinica, 14*, 278–288. (in Chinese with English abstract).

Wang, A.-D., Liu, Y.-C., Gu, X.-F., Hou, Z.-H., & Song, B. (2012). Late-Neoarchean magmatism and metamorphism at the southeastern margin of the North China Craton and their tectonic implications. *Precambrian Research, 220–221*, 65–79.

Wang, Q. Y., Zheng, J., Pan, Y., Dong, Y., Liao, F., Zhang, Y., et al. (2014). Archean crustal evolution in the southeastern North China Craton: New data from the Huoqiu complex. *Precambrian Research, 255*, Part 1(0), 294–315.

Wang, X., Li, Z., Chen, B., Chen, X., Dong, S., & Zhang, Q. (2001). *On Tan-Lu fault zone* (pp. 15–59). Beijing: Geological Publishing House (in Chinese).

Wang, Z. H., Wilde, S. A., Wang, K., & Yu, L. (2004). A MORB-arc basalt–adakite association in the 2.5 Ga Wutai greenstone belt: Late Archean magmatism and crustal growth in the North China Craton. *Precambrian Research, 131*(3–4), 323–343.

Wilde, S. A., Valley, J. W., Kita, N. T., Cavosie, A. J., & Liu, D. Y. (2008). SHRIMP U–Pb and CAMECA 1280 oxygen isotope results from ancient detrital zircons in the Caozhuang quartzite, Eastern Hebei, North China Craton: Evidence for crustal reworking 3.8 Ga ago. *American Journal of Science, 308*, 185–199.

Wu, F. Y., Zhang, Y. B., Yang, J. H., Xie, L. W., & Yang, Y. H. (2008). Zircon U–Pb and Hf isotopic constraints on the early Archean crustal evolution in Anshan of the North China Craton. *Precambrian Research, 167*(3–4), 339–362.

Wu, M. L., Zhao, G., Sun, M., Li, S., He, Y., & Bao, Z. (2013). Zircon U–Pb geochronology and Hf isotopes of major lithologies from the Yishui Terrane: Implications for the crustal evolution of the Eastern Block, North China Craton. *Lithos, 170–171*, 164–178.

Wu, Y. C. (1979). A report on Anhui BIF. *Anhui Institute of Geological Science, 1*, 1–8. (in Chinese with English abstract).

Xia, Q.-X., Zheng, Y.-F., & Hu, Z. (2010). Trace elements in zircon and coexisting minerals from low-T/UHP metagranite in the Dabie orogen: Implications for action of supercritical fluid during continental subduction-zone metamorphism. *Lithos, 114*(3–4), 385–412.

Xia, Q.-X., Zheng, Y.-F., Yuan, H., & Wu, F.-Y. (2009). Contrasting Lu–Hf and U–Th–Pb isotope systematics between metamorphic growth and recrystallization of zircon from eclogite-facies metagranites in the Dabie orogen, China. *Lithos, 112*(3–4), 477–496.

Xiao, W. J., & Santosh, M. (2014). The western Central Asian Orogenic Belt: A window to accretionary orogenesis and continental growth. *Gondwana Research, 25*, 1429–1444.

Xiong, X. L. (2006). Trace element evidence for growth of early continental crust by melting of rutile-bearing hydrous eclogite. *Geology, 34*(11), 945–948.

Xiong, X. L., Adam, J., & Green, T. H. (2005). Rutile stability and rutile/melt HFSE partitioning during partial melting of hydrous basalt: Implications for TTG genesis. *Chemical Geology, 218*(3–4), 339–359.

Xu, J. W., Zhu, G., Tong, W., Cui, K., & Liu, Q. (1987). Formation and evolution of the Tancheng-Lujiang wrench fault system: a major shear system to the northwest of the Pacific Ocean. *Tectonophysics, 134*(4), 273–310.

Yang, X. Y., Liu, L., Lee, I., Wang, B., Du, Z., Wang, Q., et al. (2014). A review on the Huoqiu banded iron formation (BIF), southeast margin of the North China Craton: Genesis of iron deposits and implications for exploration. *Ore Geology Reviews, 63*, 418–443.

Yang, X. Y., Wang, B. H., Du, Z. B., Wang, Q. C., Wang, Y. X., Tu, Z. B., et al. (2012). On the metamorphism of the HQC, formation ages and BIF forming mechanism of the Huoqiu iron deposit, South margin of the North China Craton. *Acta Petrological Sinica, 28*, 3476–3496. (in Chinese with English abstract).

Ying, J. L., Wang, Y. D., Zhao, F. Y., Lin, X. L., Sang, B. L., Xin, F. M., et al. (1984). The geochronology study on Precambrian metamorphic rock from West Anhui. *Geochimica, 2*, 145–152. (in Chinese).

Yoshiya, K., Sawaki, Y., Hirata, T., Maruyama, S., & Komiya, T. (2015). In-situ iron isotope analysis of pyrites in ~3.7 Ga sedimentary protoliths from the Isua supracrustal belt, southern West Greenland. *Chemical Geology, 401*, 126–139.

Zhai, M. G., & Windley, B. F. (1990). The Archaean and early Proterozoic banded iron formations of North China: Their characteristics, geotectonic relations, chemistry and implications for crustal growth. *Precambrian Research, 48*, 267–286.

Zhai, M. G., Windley, B. F., & Sills, J. D. (1990). Archaean gneisses, amphibolites and banded iron-formations from the Anshan area of Liaoning Province, NE China: Their geochemistry, metamorphism and petrogenesis. *Precambrian Research, 46*(3), 195–216.

Zhai, M. G. (2010). Tectonic evolution and metallogenesis of the North China Craton. *Mineral Deposit, 29*(1), 24–36. (in Chinese with English abstract).

Zhai, M. G., & Santosh, M. (2013). Metallogeny of the North China Craton: Link with secular changes in the evolving Earth. *Gondwana Research, 24*(1), 275–297.

Zhang, G. C. (2005). Geological characteristics and iron ore prospecting direction of the Anshan type iron deposits, in the upper part of the Yanglushan River, Sunan. *Geological Prospecting Review, 20* (Suppl.), 129–138 (in Chinese with English abstract).

Zhang, H.-F., Wang, J.-L., Zhou, D.-W., Yang, Y.-H., Zhang, G.-W., Santosh, M., et al. (2014). Hadean to Neoarchean episodic crustal growth: Detrital zircon records in Paleoproterozoic quartzites from the southern North China Craton. *Precambrian Research, 254*, 245–257.

Zhang, H. F., Zhai, M. G., Santosh, M., Diwu, C. R., & Li, S. R. (2011a). Geochronology and petrogenesis of Neoarchean potassic meta-granites from Huai'an Complex: Implications for the evolution of the North China Craton. *Gondwana Research, 20*(1), 82–105.

Zhang, L. C., Zhai, M. G., Wan, Y. S., Guo, J. H., Dai, Y. P., Wang, C. L., et al. (2012b). Study of the Precambrian BIF-iron deposits in the North China Craton: Progresses and questions. *Acta Petrologica Sinica, 28*(11), 3431–3445 (in Chinese with English abstract).

Zhang, L. C., Zhai, M. G., Zhang, X., Xiang, P., Dai, Y., Wang, C., et al. (2012a). Formation age and tectonic setting of the Shirengou Neoarchean banded iron deposit in eastern Hebei Province: Constraints from geochemistry and SIMS zircon U–Pb dating. *Precambrian Research, 222–223*(0), 325–338.

Zhang, X. J., Zhang, L., Xiang, P., Wan, B., & Pirajno, F. (2011b). Zircon U–Pb age, Hf isotopes and geochemistry of Shuichang Algoma-type banded iron-formation, North China Craton: Constraints on the ore-forming age and tectonic setting. *Gondwana Research, 20*(1), 137–148.

Zhao, G. C., Sun, M., Wilde, S. A., & Sanzhong, L. (2005). Late Archean to Paleoproterozoic evolution of the North China Craton: Key issues revisited. *Precambrian Research, 136*(2), 177–202.

Zhao, G. C., Wilde, S. A., Sun, M., Guo, J., Kröner, A., Li, S., et al. (2008). SHRIMP U–Pb zircon geochronology of the Huai'an complex: Constraints on late Archean to Paleoproterozoic magmatic and metamorphic events in the Trans-North China Orogen. *American Journal of Science, 308*(3), 270–303.

Zhao, G. C., & Zhai, M. (2013). Lithotectonic elements of Precambrian basement in the North China Craton: Review and tectonic implications. *Gondwana Research, 23*(4), 1207–1240.

Zheng, J. P., Griffin, W. L., O'Reilly, S. Y., Lu, F. X., Wang, C. Y., & Zhang, M. (2004). 3.6 Ga lower crust in central China: New evidence on the assembly of the North China craton. *Geology, 32*(3), 229–232.

Zhou, M. F., Zhao, J. H., Jiang, C. Y., Gao, J. F., Wang, W., & Yang, S. H. (2009). OIB-like, heterogeneous mantle sources of Permian basaltic magmatism in the western Tarim Basin, NW China: Implications for a possible Permian large igneous province. *Lithos, 113*(3–4), 583–594.

Part II
Paleoproterozoic Rifting-Subduction-Collision

Paleoproterozoic Gneissic Granites in the Liaoji Mobile Belt, North China Craton: Implications for Tectonic Setting

7

Mingchun Yang, Bin Chen, and Cong Yan

Abstract

Voluminous Paleoproterozoic gneissic granites occur in the Liaoji belt in the North China Craton (NCC), which were intruded by mafic dykes, and experienced a late-stage amphibolite facies metamorphism. These granites were thought by some researchers to be A-type granites and formed in a continental rifting setting. We propose a different model for the origin of these granites and the tectonic setting, based on the integrated field, petrographic, geochronological, and geochemical studies on a couple of gneissic granite plutons. The gneissic granites were emplaced at 2173–2203 Ma, and the mafic dykes at ca. 2159 Ma, followed by an amphibolite facies metamorphism at ca. 1.9 Ga. The gneissic granites contain mafic microgranular enclaves (MMEs), calcium hornblendes, magnesio-horblendes, accessory titanite, and pyrrhotite. They show calc-alkaline arc magma affinity, with A/CNK = 0.9 − 1.2 (mostly less than 1.1), A/NK = 0.9 − 1.4, SiO_2 = 68.3 − 76.9 wt %, low contents of TiO_2 (<0.3 wt%), enrichment of LILEs, such as K, Rb, Sr, Cs, depletion of some HFSEs, such as Nb, Ti. These characteristics suggest that these gneissic granites are I-type granites formed probably in a subduction zone. The A-type-like characteristics for some granites (the Dafangshen granite) are attributable to the highly evolved nature of the pluton as shown by the high SiO_2 contents (76.7–77.1 wt%), which could have been caused by the high boron contents of the pluton, because addition of boron in magma system tends to prolong magma evolution and lead to significant differentiation. The large variation of whole-rock $\varepsilon_{Nd}(t)$ values (−8.6 to 1.5) and zircon $\varepsilon_{Hf}(t)$ values (−1.3 to 5.6), together with the existence and petrographic features of the MMEs, and oscillatory zoning in plagioclase, suggest that mixing/mingling of lower crust-derived felsic magma with enriched mantle-derived mafic magma might have resulted in formation of these gneissic granites. The existence of Archean inherited zircons in these granites together with the arc affinity suggests a northward subduction for the JLJB in the Paleoproterozoic times.

Keywords

Gneissic granites • Subduction • Arc magmatism • Paleoproterozoic • North China Craton

M. Yang
China Ocean Press, State Oceanic Administration, Beijing, 100081, People's Republic of China

B. Chen (✉)
School of Resources and Environmental Engineering, Hefei University of Technology, Hefei, 230009, Anhui, China
e-mail: binchen@pku.edu.cn

C. Yan
Sinochem Petroleum Exploration & Production Co., LTD, Sinochem Group, Beijing, 100031, People's Republic of China

7.1 Geological Setting of the Liaoji Belt

The Liaoji orogenic belt is one of the three Paleoproterozoic mobile belts on the NCC, located in the eastern part of the Eastern Block (Fig. 7.1; Luo et al. 2008; Zhao et al. 2005). The belt consists of greenschist to lower amphibolite facies metasedimentary, metavolcanic successions, meta-granitic

M. Zhai et al. (eds.), *Main Tectonic Events and Metallogeny of the North China Craton*, Springer Geology, DOI 10.1007/978-981-10-1064-4_7

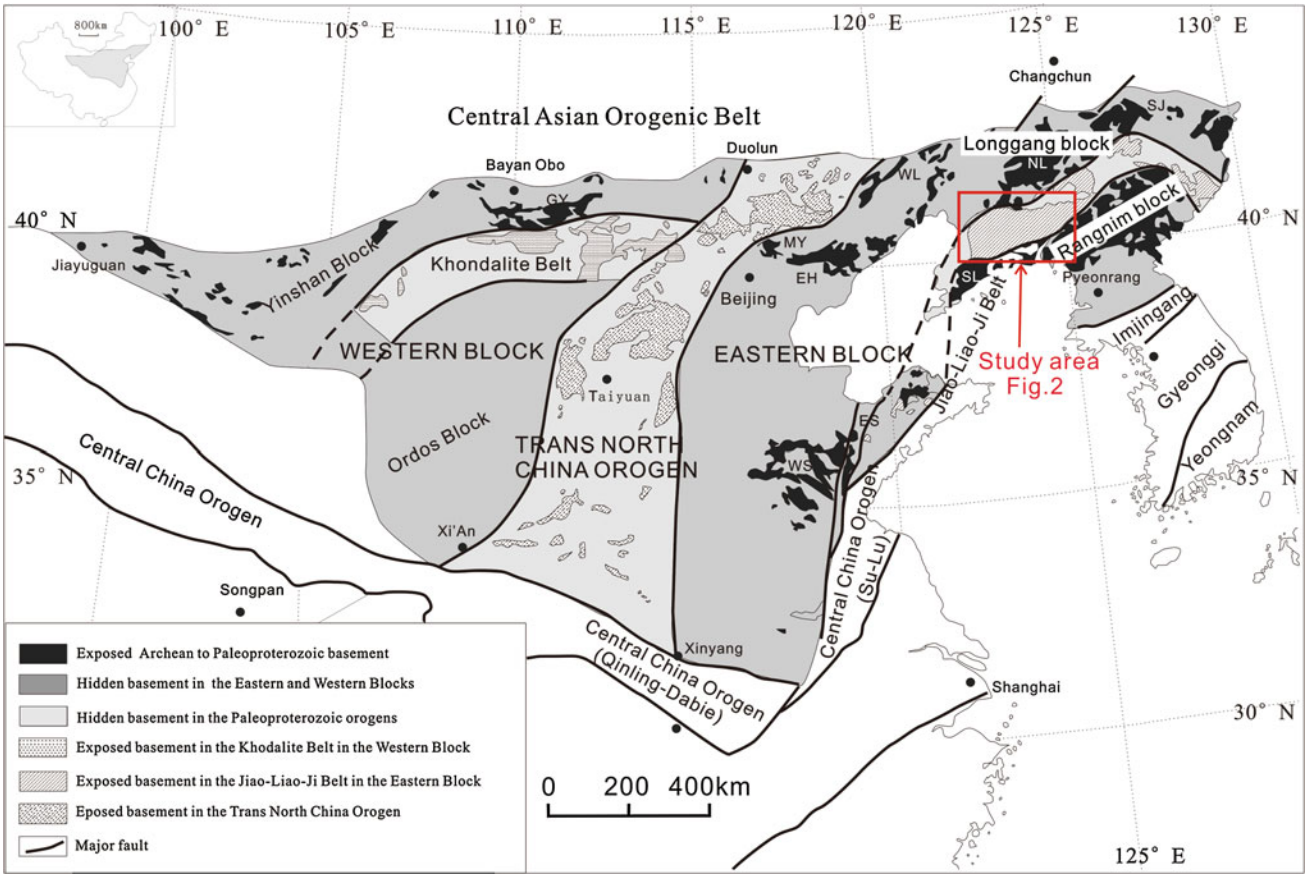

Fig. 7.1 The tectonic subdivision of the North China Craton (after Zhao et al. 2005); also shown is the Jiao-Liao-Ji Paleoproterozoic belt

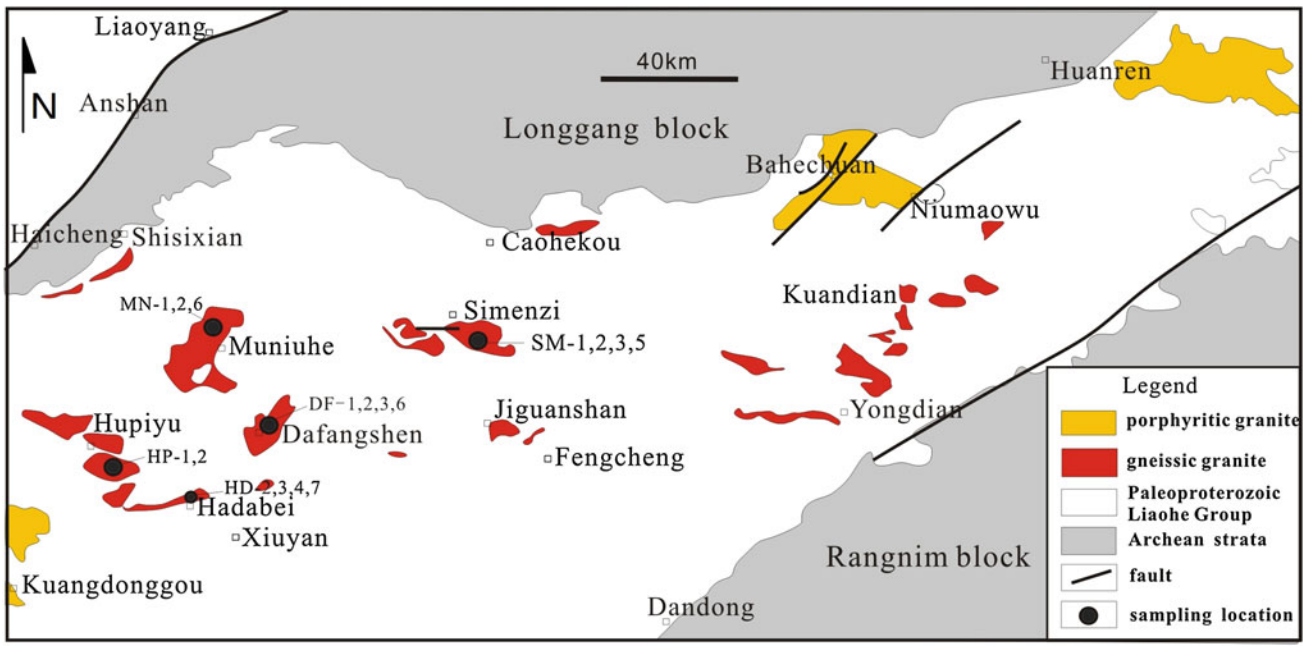

Fig. 7.2 Sketch geological map of the Paleoproterozoic granites in the Jiao-Liao-Ji Belt (after Hao et al. 2004), with sampling localities

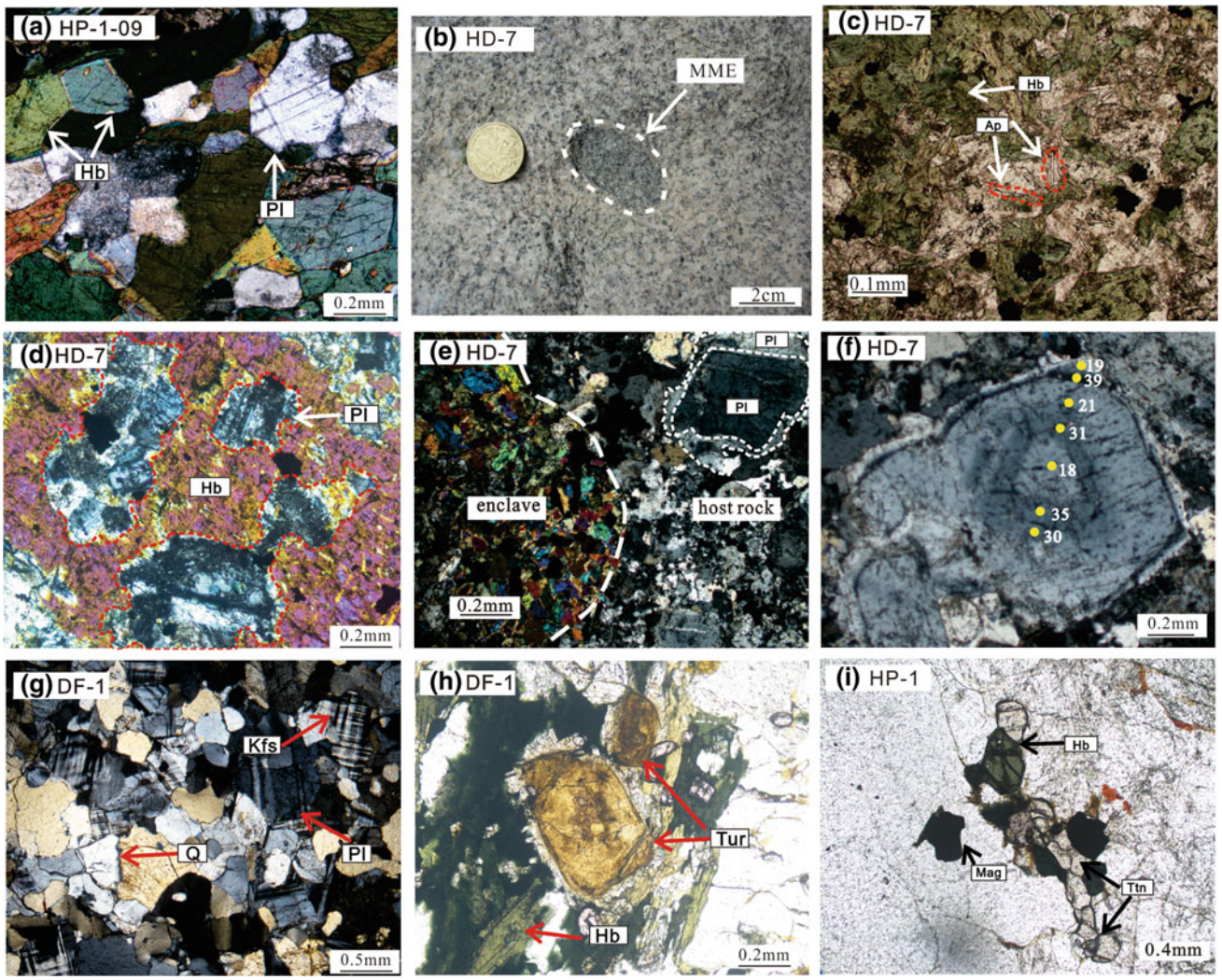

Fig. 7.3 **a** Microphotograph of amphibolite intruded into the Hupiyu gneissic granite pluton; **b** field photo of a mafic enclave from the Hadabei pluton; **c** inner structure of MME, showing hornblende and needle-like apatites; **d** plagioclases included in the hornblende from the MME; **e** textural disequilibrium of plagioclase near the MME; **f** compositional and textural disequilibrium of plagioclase from the gneissic granite; also shown are the An contents; **g** microphotographs of the Dafangshen granite; **h** microphotograph of tourmaline from the Dafangshen pluton; **i** accessory minerals of the Hupiyu pluton. *Kfs* potash feldspar; *Pl* plagioclase; *Q* quartz; *Hb* hornblende; *Mag* magnetite; *Ttn* titanite; *Tur* tourmaline; *Ap* apatite

and mafic intrusions with metamorphic age of ca. 1.9 Ga (Yin and Nie 1996; Luo et al. 2004; Lu et al. 2006). These rocks are called the Liaohe Group in the eastern Liaoning Peninsula, which are further divided into the North Liaohe Group and the South Liaohe Group (Zhang 1984) by the Qinglongshan-Zaoerling ductile shear zones and faults (Li et al. 2005). The North Liaohe Group is characterized by the abundance of clastic and carbonate rocks, whereas the South Liaohe Group contains much more volcanic rocks (Fig. 7.2; Zhang and Yang 1988; Bai 1993; Lu et al. 1996; Bai and Dai 1998), including a volcanic-rich sequence in the lower part (the Lieryu and Gaojiayu Formations), a carbonate-rich sequence in the middle (the Dashiqiao Formation), and a pelitic sequence in the upper part (the Gaixian Formation). The well-known Paleoproterozoic boron deposits are hosted in the Lieryu Formation (~1300 m thick) that comprises metamorphosed boron-bearing volcano-sedimentary successions (Zhang 1984; Peng and Palmer 1995).

There are two groups of Paleoproterozoic granites in the Liaoji Belt, including dominantly metamorphosed gneissic granodiorite-granite with zircon ages from 2.2 to 2.1 Ga (Hao et al. 2004; Lu et al. 2006), and subordinate un-metamorphosed syenite-granite with zircon ages of ca. 1.84–1.87 Ga (Li et al. 2003; Cai et al. 2002; Lu et al. 2004). The latter are post-collisional, showing cross-cut contact with the metasedimentary and volcanic successions (the Liaohe Group). The gneissic granites typically contain foliated minerals such as hornblende and magnetite due to the

regional metamorphism (Hao et al. 2004). In this paper, we select five typical gneissic granite plutons for petrological and geochemical studies, trying to clarify their origin and geodynamic setting (Fig. 7.2). Petrological descriptions of these plutons are as below.

7.2 Petrological Descriptions of the Gneissic Granites

The Hupiyu gneissic pluton is composed mainly of 30 % microcline, 15 % perthite, 15 % plagioclase, 25 % quartz, and small amounts of biotite and hornblende, and accessory epidote, magnetite, zircon, apatite, and sphene. Lineation of hornblende, magnetite, and sphene forms the gneissic structure. No obvious compositional zoning is observed in plagioclase grains that have An contents of 0.47–1.14. Mafic dikes are present in the pluton, which have been metamorphosed into amphibolites (Fig. 7.3a). In addition, a few mafic microgranular enclaves (MME) of dioritic composition can be seen in the pluton.

The Hadabei monzonite pluton (Fig. 7.2) shows similar mineralogy to the Hupiyu pluton, with 40 % plagioclase, 25 % perthite, 30 % quartz, small amounts of hornblende and biotite, and accessory pyrrhotite, zircon, titanite, epidote, magnetite, and apatite. The pluton is also intruded by mafic dykes that have been transformed into amphibolites during the metamorphism. In addition, gabbroic diorite enclaves are common in the granite (Fig. 7.3b, c) and some plagioclase crystals are included by the hornblende in the MME (Fig. 7.3d). Plagioclases are characterized by compositional zoning (Fig. 7.3e, f): those far away from the MMEs show normal compositional zoning with An contents decreasing from core to rim, and those near the MMEs show reversal and complicated zoning textures (Fig. 7.3f).

The Muniuhe pluton (Fig. 7.2) is a gneissic hornblende biotite granite pluton, composed mainly of 35 % plagioclase, 15 % K-feldspar (perthite and small amounts of microline), 30 % quartz, 8 % biotite (partially altered to chlorite), and 7 % hornblende. Accessory minerals are zircon, sphene, and magnetite. The hornblende is euhedral. The biotite is foliated, and the plagioclase is kaolinised. Zonal texture of plagioclase is rare in the Muniuhe granite. Again, some dioritic dykes intruded into the granite.

The Dafangshen pluton is a gneissic K-feldspar granite pluton with metamorphic equilibrium textures (Fig. 7.3g), composed of 25 % microline, 15 % perthite, 5 % plagioclase, 40 % quartz, 10 % hornblende, and small amounts of biotite. Accessory minerals are tourmaline, zircon, zoisite, titanite, and magnetite. Banded distribution of hornblende, magnetite, and sphene forms the gneissic structure. The tourmaline is euhedral with obvious zonal structure (Fig. 7.3h).

The Simenzi pluton is a hornblende monzogranite pluton, composed mainly of 35 % microline, 25 % plagioclase, 25 % quartz and 10 % hornblende, and accessory zircon, sphene, and epidote. The hornblende is subhedral to euhedral. There are some dioritic dykes intruding into the granite.

7.3 Geochronology

The Liaoji Belt consists of Paleoproterozoic meta-volcano-sedimentary rocks, and granitic intrusions (Li et al. 2011). Previous studies have shown that the metasedimentary and volcanic rocks were formed at 2.2–2.0 Ga (Luo et al. 2004, 2008; Lu et al. 2006; Wan et al. 2006) and underwent greenschist to amphibolite facies metamorphism at ca. 1.9–1.93 Ga (Luo et al. 2004, 2008; Lu et al. 2006; Wan et al. 2006; Tam et al. 2011, 2012a, b). A few age data have been reported for the Paleoproterozoic gneissic granites. The gneissic granites in Haicheng and Kuandian have been dated at 2140 and 2070 Ma, respectively (Zhang and Yang 1988; Sun et al. 1993). The Qianzhuogou gneissic granite in the south of Liaonan was dated at 2160 Ma by Lu et al. (2005). Lu et al. (2004) reported a zircon U-Pb age of 2160 Ma for the Hupiyu gneissic granite.

Our new experimental data gained by LA-ICP-MS U-Pb zircon dating method shows that the Hupiyu gneissic granite was emplaced at 2183 Ma and the Hadabei pluton at 2173 Ma (Table 7.1), consistent with previous age data (Wu and Zheng 2004; Li and Zhao 2007). The Muniuhe pluton was formed at 2201 Ma and the Simenzi pluton at 2203 Ma. In summary, the gneissic granites in the JLJB were formed at ca. 2.17–2.20 Ga (Fig. 7.4). It should be stressed that we found inherited Archean zircons both in the gneissic granites and the amphibolite dykes intruding into the granites, such zircon inheritance was scarcely reported by previous researchers (Lu et al. 2004, 2005; Luo et al. 2004; Zhao et al. 2005; Li and Zhao 2007; Li et al. 2011). The ages of those inherited Archean zircons cluster at around 2.5 Ga and 2.7–2.8 Ga, in accordance with the ages of the two main Archean volcanisms within the NCC (Peuct et al. 1986; Liu et al. 1992; Wang et al. 1997; Geng et al. 2002; Zhao et al. 2002; Lu et al. 2004). These zircons of Archean ages suggest an Archean basement for the main source of the gneissic granites. The metamorphosed mafic dykes that intruded into the gneissic granites have been dated at 2159 Ma, indicating the intrusion happened shortly after the emplacement of the granites. U-Pb dating of the zircon overgrowth rims from the amphibolite yields an age of ca. 1.9 Ga, which coincides with the published metamorphic ages (Luo et al. 2004, 2008; Lu et al. 2006; Li et al. 2005; Li and Zhao 2007; Zhou et al. 2008; Tam et al. 2011) and is interpreted as the metamorphism age of the gneissic granites.

Table 7.1 In situ zircon U-Pb isotopic dating for the gneissic granites

Component/$\times 10^{-6}$			Th/U	Ratio				Age					
30 μm	Th	U		$^{206}Pb/^{238}U$	$^{206}Pb/^{238}U$	$^{207}Pb/^{235}U$	$^{207}Pb/^{235}U$	$^{206}Pb/^{238}U$	$^{206}Pb/^{238}U$	$^{207}Pb/^{235}U$	$^{207}Pb/^{235}U$	$^{207}Pb/^{206}Pb$	$^{207}Pb/^{206}Pb$
	ppm	pmm		Ratio	1sigma	Ratio	1sigma	Age (Ma)	1sigma	Age (Ma)	1sigma	Age (Ma)	1sigma
HD-2-1	103	107	1	0.37601	0.002	7.0823	0.0526	2057.6	9.2	2121.8	6.6	2184.3	9.1
HD-2-2	156	146	1.1	0.376342	0.004	7.0613	0.1051	2059.2	18.9	2119.2	13.2	2188.9	19.9
HD-2-3	110	104	1.1	0.357948	0.004	6.7274	0.097	1972.4	19.1	2076.2	12.7	2180.6	13.1
HD-2-4	97	123	0.8	0.362335	0.0018	6.7721	0.0377	1993.2	8.5	2082.1	4.9	2172.2	4.6
HD-2-5	110	100	1.1	0.365257	0.0061	6.9069	0.1106	2007	28.7	2099.5	14.2	2192.3	5.7
HD-2-6	74	83	0.9	0.365011	0.0024	6.8603	0.0501	2005.9	11.5	2093.5	6.5	2180.6	4.6
HD-2-7	37	50	0.7	0.366977	0.0025	6.9404	0.0515	2015.2	11.8	2103.8	6.6	2191.1	5.6
HD-2-8	87	130	0.7	0.362557	0.0024	6.7932	0.0465	1994.3	11.5	2084.8	6.1	2175.9	3.5
HD-2-9	40	54	0.7	0.360724	0.0022	6.8111	0.0489	1985.6	10.6	2087.2	6.4	2188.0	5.7
HD-2-10	52	61	0.9	0.366016	0.0025	6.8979	0.0481	2010.6	11.6	2098.4	6.2	2184.9	5.4
HD-2-11	33	44	0.8	0.379136	0.0036	7.0991	0.0827	2072.2	16.7	2123.9	10.4	2173.2	9.1
HD-2-12	51	58	0.9	0.374443	0.0021	7.0099	0.0539	2050.3	9.7	2112.7	6.8	2173.2	9.3
HD-2-13	73	67	1.1	0.36889	0.0019	6.8969	0.0369	2024.2	9	2098.3	4.7	2172.2	3.6
HD-2-14	57	62	0.9	0.383221	0.0035	7.1764	0.0871	2091.3	16.5	2133.6	10.8	2173.2	9.4
HD-2-15	90	85	1.1	0.384555	0.0018	7.189	0.0397	2097.5	8.6	2135.1	4.9	2172.2	6.5
HD-2-16	48	53	0.9	0.397158	0.0056	7.446	0.1074	2155.9	25.6	2166.5	12.9	2176.2	9.3
HD-2-17	62	62	1	0.384441	0.0033	7.2219	0.0644	2097	15.2	2139.2	8	2179.9	7.4
HD-2-18	62	65	1	0.364533	0.0058	6.8571	0.1157	2003.6	27.2	2093.1	15	2181.2	8.5
HD-2-19	62	65	1	0.386326	0.0078	7.2305	0.1467	2105.8	36.1	2140.3	18.1	2173.2	9.1
HD-2-20	46	56	0.8	0.386781	0.0043	7.2364	0.0814	2107.9	19.7	2141	10	2171.9	4.2
HD-2-21	31	44	0.7	0.378658	0.0058	7.0928	0.11	2070	27.1	2123.1	13.8	2175.9	9.9
HD-2-22	59	70	0.8	0.366921	0.0077	6.8706	0.1326	2014.9	36.1	2094.9	17.1	2175.9	8.3
HD-2-23	127	113	1.1	0.383248	0.003	7.1738	0.0582	2091.4	13.9	2133.2	7.2	2173.2	4.6
HD-2-24	93	95	1	0.380753	0.0028	7.1345	0.0531	2079.8	12.8	2128.4	6.6	2175.9	4.6
HD-2-25	97	102	1	0.365976	0.0024	6.8656	0.0483	2010.4	11.3	2094.2	6.2	2176.9	4.6
HD-2-26	72	77	0.9	0.378709	0.0031	7.1076	0.0609	2070.3	14.3	2125	7.6	2177.5	5.6
HD-2-27	87	93	0.9	0.381092	0.0026	7.1538	0.0511	2081.4	12.2	2130.8	6.4	2188.9	5.6
HD-2-28	114	114	1	0.375289	0.0033	7.0709	0.0654	2054.2	15.5	2120.4	8.2	2184.3	0.8
HD-2-29	99	106	0.9	0.362595	0.005	6.8371	0.1013	1994.5	23.6	2090.5	13.1	2187.0	8.6
HD-2-30	22	134	0.2	0.348026	0.0102	6.601	0.1985	1925.2	48.9	2059.5	26.5	2196.0	12.5
HP-1-1	168	176	1	0.38062	0.0056	7.1302	0.1015	2079.2	26.3	2127.8	12.7	2175.9	11.3
HP-1-3	152	153	1	0.37865	0.0022	7.1325	0.0473	2070	10.3	2128.1	5.9	2184.9	0.8

(continued)

Table 7.1 (continued)

Component/$\times 10^{-6}$			Th/U	Ratio				Age					
30 μm	Th	U		$^{206}Pb/^{238}U$	$^{206}Pb/^{238}U$	$^{207}Pb/^{235}U$	$^{207}Pb/^{235}U$	$^{206}Pb/^{238}U$	$^{206}Pb/^{238}U$	$^{207}Pb/^{235}U$	$^{207}Pb/^{235}U$	$^{207}Pb/^{206}Pb$	$^{207}Pb/^{206}Pb$
	ppm	pmm		Ratio	1sigma	Ratio	1sigma	Age (Ma)	1sigma	Age (Ma)	1sigma	Age (Ma)	1sigma
HP-1-4	31	50	0.6	0.3784	0.0028	7.095	0.0543	2068.8	13.3	2123.4	6.8	2177.5	9.3
HP-1-5	37	55	0.7	0.38753	0.0025	7.2494	0.0513	2111.4	11.7	2142.6	6.3	2173.2	6.8
HP-1-6	45	53	0.9	0.3825	0.0058	7.199	0.1122	2087.9	27.2	2136.4	13.9	2183.6	11.9
HP-1-7	95	105	0.9	0.37729	0.0028	7.0837	0.0592	2063.6	12.9	2122	7.4	2188.9	6.2
HP-1-8	80	104	0.8	0.38136	0.003	7.1642	0.0593	2082.7	14	2132.1	7.4	2179.9	5.6
HP-1-9	65	74	0.9	0.38791	0.0053	7.2808	0.111	2113.1	24.4	2146.5	13.6	2188.9	11.1
HP-1-10	96	104	0.9	0.39777	0.0052	7.486	0.0563	2158.8	24	2171.3	6.7	2183.6	20.4
HP-1-11	95	109	0.9	0.3857	0.0038	7.2585	0.0808	2102.9	17.4	2143.7	9.9	2183.0	11.4
HP-1-12	131	137	1	0.40724	0.0028	7.6978	0.0572	2202.3	13	2196.3	6.7	2190.4	4.2
HP-1-14	71	86	0.8	0.39649	0.0024	7.4251	0.0474	2152.9	10.9	2164	5.7	2175.9	4.9
HP-1-15	40	62	0.7	0.39157	0.0063	7.3859	0.1198	2130.1	29.2	2159.3	14.5	2187.4	15.1
HP-1-16	79	76	1	0.40826	0.0185	7.562	0.324	2207	84.5	2180.4	38.4	2166.7	9.7
HP-1-17	88	90	1	0.38247	0.0052	7.1666	0.1182	2087.8	24.1	2132.4	14.7	2175.9	9.9
HP-1-18	31	45	0.7	0.38975	0.0043	7.3218	0.2315	2121.7	19.9	2151.5	28.3	2188.9	38.9
HP-1-19	97	97	1	0.38381	0.0107	7.2137	0.212	2094.1	49.8	2138.2	26.2	2179.9	11.9
HP-1-20	97	99	1	0.39497	0.0039	7.3768	0.0785	2145.8	18.2	2158.2	9.5	2169.4	7.7
HP-1-21	60	71	0.8	0.38727	0.0039	7.1797	0.0792	2110.2	18.1	2134	9.8	2166.7	7.4
HP-1-22	101	120	0.9	0.3961	0.0034	7.3448	0.0678	2151	15.7	2154.3	8.2	2166.7	7.6
HP-1-23	89	109	0.8	0.41435	0.0034	7.7489	0.0709	2234.8	15.6	2202.3	8.2	2172.2	12.2
HP-1-25	66	103	0.6	0.39129	0.0025	7.3017	0.0504	2128.8	11.6	2149	6.2	2168.5	3.6
HP-1-26	108	123	0.9	0.38057	0.0053	7.1638	0.1046	2079	24.7	2132	13	2183.3	7.6
HP-1-27	122	142	0.9	0.39396	0.0036	7.4201	0.0687	2141.1	16.6	2163.4	8.3	2184.3	0.9
HP-1-28	74	117	0.6	0.39185	0.0027	7.3768	0.0559	2131.4	12.5	2158.2	6.8	2183.0	6.9
HP-1-29	78	130	0.6	0.39211	0.0029	7.3731	0.0555	2132.6	13.3	2157.7	6.7	2183.3	5.1
MN-6-2	92	122	0.8	0.38311	0.0061	7.2438	0.1208	2090.8	28.6	2141.9	14.9	2190.7	7.3
MN-6-3	88	95	0.9	0.38587	0.003	7.3303	0.0577	2103.7	13.8	2152.5	7	2199.1	7.7
MN-6-4	94	96	1	0.37955	0.0036	7.126	0.1631	2074.2	16.8	2127.3	20.4	2188.9	24.2
MN-6-5	58	205	0.3	0.38012	0.0025	9.0303	0.0687	2076.9	11.9	2341.1	7.0	2579.3	6.9
MN-6-7	68	81	0.8	0.38058	0.0033	7.2253	0.0677	2079	15.3	2139.6	8.4	2197.8	7.3
MN-6-8	85	84	1	0.40105	0.0041	7.6002	0.0839	2173.9	19	2184.9	9.9	2194.8	8.0
MN-6-9	232	248	0.9	0.35614	0.0034	7.5034	0.1165	1963.8	16.3	2173.4	13.9	2376.9	15.4
MN-6-13	36	63	0.6	0.37665	0.0048	7.156	0.0964	2060.6	22.3	2131	12	2199.7	9.7

(continued)

Table 7.1 (continued)

Component/×10^{-6}			Th/U	Ratio				Age					
30 μm	Th	U		$^{206}Pb/^{238}U$	$^{206}Pb/^{238}U$	$^{207}Pb/^{235}U$	$^{207}Pb/^{235}U$	$^{206}Pb/^{238}U$	$^{206}Pb/^{238}U$	$^{207}Pb/^{235}U$	$^{207}Pb/^{235}U$	$^{207}Pb/^{206}Pb$	$^{207}Pb/^{206}Pb$
	ppm	pmm		Ratio	1sigma	Ratio	1sigma	Age (Ma)	1sigma	Age (Ma)	1sigma	Age (Ma)	1sigma
MN-6-15	65	83	0.8	0.3822	0.0039	7.2569	0.0777	2086.6	18.2	2143.5	9.6	2198.5	11.4
MN-6-16	34	59	0.6	0.36895	0.0057	7.012	0.1177	2024.4	26.8	2113	14.9	2199.7	9.3
MN-6-17	103	107	1	0.36921	0.0047	7.0431	0.0936	2025.7	22.1	2116.9	11.8	2206.5	6.8
MN-6-18	54	83	0.7	0.38117	0.0085	7.23	0.1558	2081.7	39.7	2140.2	19.2	2198.2	11.1
MN-6-19	190	254	0.8	0.32966	0.0060	7.1472	0.0628	1836.7	29.2	2129.9	7.8	2427.8	17.4
MN-6-20	54	74	0.7	0.38243	0.003	7.2776	0.0628	2087.6	13.8	2146.1	7.7	2202.2	7.7
MN-6-21	23	38	0.6	0.3808	0.0068	7.2217	0.1654	2080	31.8	2139.2	20.4	2195.4	20.4
MN-6-22	73	104	0.7	0.36891	0.0098	7.0747	0.1966	2024.3	46.1	2120.9	24.7	2216.7	11.1
MN-6-23	95	105	0.9	0.38476	0.0081	7.3037	0.1788	2098.5	37.6	2149.3	21.9	2198.2	9.9
MN-6-24	31	48	0.6	0.37664	0.0077	7.1484	0.1658	2060.6	35.9	2130.1	20.7	2198.2	14.8
MN-6-25	100	115	0.9	0.40095	0.0044	7.6424	0.0943	2173.4	20.2	2189.9	11.1	2205.2	9.6
MN-6-27	13	20	0.6	0.38206	0.0156	7.2557	0.3212	2085.9	72.7	2143.4	39.5	2195.4	12.0
MN-6-28	69	69	1	0.38313	0.0027	7.2747	0.0555	2090.9	12.7	2145.7	6.8	2198.5	6.6
MN-6-29	142	108	1.3	0.39435	0.0067	7.5213	0.1366	2143	31.1	2175.5	16.3	2205.9	8.0
MN-6-30	107	92	1.2	0.3865	0.0058	7.3614	0.1138	2106.6	26.8	2156.3	13.8	2205.6	8.5
SM-1-1	212	258	0.8	0.33405	0.0032	7.4993	0.0884	1858.0	15.6	2172.9	10.6	2484.9	9.7
SM-1-2	275	351	0.8	0.28189	0.0032	7.5642	0.1068	1600.9	15.8	2180.6	12.7	2783.0	20.4
SM-1-5	52	64	0.8	0.388	0.0046	7.3765	0.0933	2113.5	21.3	2158.1	11.3	2201.5	10.6
SM-1-6	47	69	0.7	0.38806	0.0040	7.3832	0.0807	2113.8	18.8	2158.9	9.8	2202.8	5.6
SM-1-7	302	287	1.0	0.33138	0.0040	7.5057	0.1134	1845.0	19.5	2173.7	13.5	2501.9	11.1
SM-1-8	107	148	0.7	0.39855	0.0169	7.5511	0.3511	2162.4	78	2179.1	41.7	2194.8	7.4
SM-1-10	145	143	1	0.38787	0.0042	7.4333	0.0999	2112.9	19.6	2165	12	2214.5	7.7
SM-1-11	6	265	0	0.32835	0.0018	6.2716	0.0626	1830.4	8.7	2014.5	8.7	2205.6	11.1
SM-1-13	136	163	0.8	0.38145	0.0042	7.2821	0.0887	2083	19.8	2146.6	10.9	2207.1	5.4
SM-1-14	39	57	0.7	0.37393	0.007	7.1042	0.1108	2047.8	32.6	2124.6	13.9	2202.2	19.0
SM-1-15	38	44	0.9	0.37387	0.0167	7.1397	0.2156	2047.6	78.6	2129	26.9	2213.9	80.2
SM-1-16	45	56	0.8	0.39203	0.0188	7.4385	0.3365	2132.2	87.2	2165.6	40.5	2198.5	17.9
SM-1-17	59	73	0.8	0.38639	0.0174	7.2986	0.4113	2106.1	81.1	2148.6	50.4	2188.6	20.5
SM-1-19	119	155	0.8	0.3877	0.0043	7.4067	0.0892	2112.2	19.9	2161.8	10.8	2209.3	5.6
SM-1-20	100	136	0.7	0.40806	0.0116	7.7928	0.2731	2206	53.2	2207.4	31.5	2207.1	12.7
SM-1-21	207	267	0.7	0.36318	0.0112	7.9811	0.2758	1997.2	53.1	2228.9	31.2	2449.1	33.2
SM-1-23	40	51	0.8	0.36798	0.0089	7.0206	0.2069	2019.9	42.1	2114	26.2	2205.9	14.0

(continued)

Table 7.1 (continued)

Component/$\times 10^{-6}$			Th/U	Ratio				Age					
30 μm	Th	U		$^{206}Pb/^{238}U$	$^{206}Pb/^{238}U$	$^{207}Pb/^{235}U$	$^{207}Pb/^{235}U$	$^{206}Pb/^{238}U$	$^{206}Pb/^{238}U$	$^{207}Pb/^{235}U$	$^{207}Pb/^{235}U$	$^{207}Pb/^{206}Pb$	$^{207}Pb/^{206}Pb$
	ppm	pmm		Ratio	1sigma	Ratio	1sigma	Age (Ma)	1sigma	Age (Ma)	1sigma	Age (Ma)	1sigma
SM-1-24	279	349	0.8	0.30652	0.0062	7.8182	0.1218	1723.6	30.7	2210.3	14.0	2712.7	36.9
SM-1-26	226	270	0.8	0.33777	0.0096	7.7597	0.2229	1875.9	46.1	2203.6	25.8	2525.6	25.6
SM-1-27	57	68	0.8	0.37929	0.0053	7.1906	0.1036	2073	24.8	2135.3	12.8	2196.0	5.7
SM-1-28	57	73	0.8	0.38772	0.0029	7.3878	0.0586	2112.3	13.5	2159.5	7.1	2205.6	-0.9
SM-1-29	27	45	0.6	0.37515	0.004	7.093	0.1199	2053.6	18.9	2123.2	15	2191.1	29.6
HP-9-02	2056	1133	1.81	0.36318	0.0051	6.792	0.117	1997	24	2085	15	2172	14
HP-9-03	13716	2911	4.71	0.36769	0.0052	6.912	0.119	2019	24	2100	15	2181	14
HP-9-06	*76*	*208*	*0.36*	*0.36755*	*0.0052*	*5.916*	*0.106*	*2018*	*25*	*1966*	*16*	*1907*	*15*
HP-9-07	*593*	*626*	*0.95*	*0.37312*	*0.0059*	*6.312*	*0.206*	*2044*	*28*	*2020*	*29*	*1996*	*66*
HP-9-10	1142	987	1.16	0.40078	0.0057	7.524	0.133	2173	26	2176	16	2178	14
HP-9-11	1749	1168	1.50	0.36773	0.0052	6.844	0.121	2019	24	2091	16	2164	14
HP-9-12	606	538	1.13	0.44459	0.0063	8.309	0.148	2371	28	2265	16	2171	14
HP-9-14	482	434	1.11	0.35517	0.0051	6.591	0.119	1959	24	2058	16	2158	15
HP-9-15	1259	1070	1.18	0.36503	0.0052	6.708	0.120	2006	24	2074	16	2141	14
HP-9-16	1215	1046	1.16	0.37457	0.0053	6.983	0.127	2051	25	2109	16	2166	15
HP-9-20	80	966	0.08	0.46455	0.0065	10.702	0.190	2460	28	2498	16	2529	19
HP-9-21	684	164	4.18	0.36209	0.0053	6.026	0.115	1992	25	1980	17	1966	16
HP-9-22	1493	441	3.39	0.38343	0.0055	6.870	0.127	2092	26	2095	16	2097	15
HP-9-23	836	839	1.00	0.38144	0.0055	7.022	0.130	2083	25	2114	16	2144	15
HP-9-25	348	915	0.38	0.38378	0.0055	6.951	0.129	2094	26	2105	16	2116	15
HP-9-30	1368	771	1.78	0.39731	0.0057	7.374	0.139	2157	26	2158	17	2159	15
HP-9-32	324	343	0.94	0.42185	0.0061	7.730	0.148	2269	28	2200	17	2136	16
HP-9-35	1765	1632	1.08	0.34916	0.005	6.525	0.125	1931	24	2049	17	2171	16
HP-9-37	1463	884	1.65	0.30702	0.0045	5.257	0.102	1726	22	1862	17	2017	16
HP-9-38	405	349	1.16	0.39281	0.0057	7.168	0.142	2136	27	2133	18	2129	16
HP-9-40	13	57	0.23	0.36077	0.0057	6.108	0.140	1986	27	1991	20	1997	20

HD-2: the Hadabei granite;
HP-1: the Hupiyu granite;
MN-6: the Muniuhe granite;
SM-1: the Simenzi granite;
HP-9: the mafic dyke

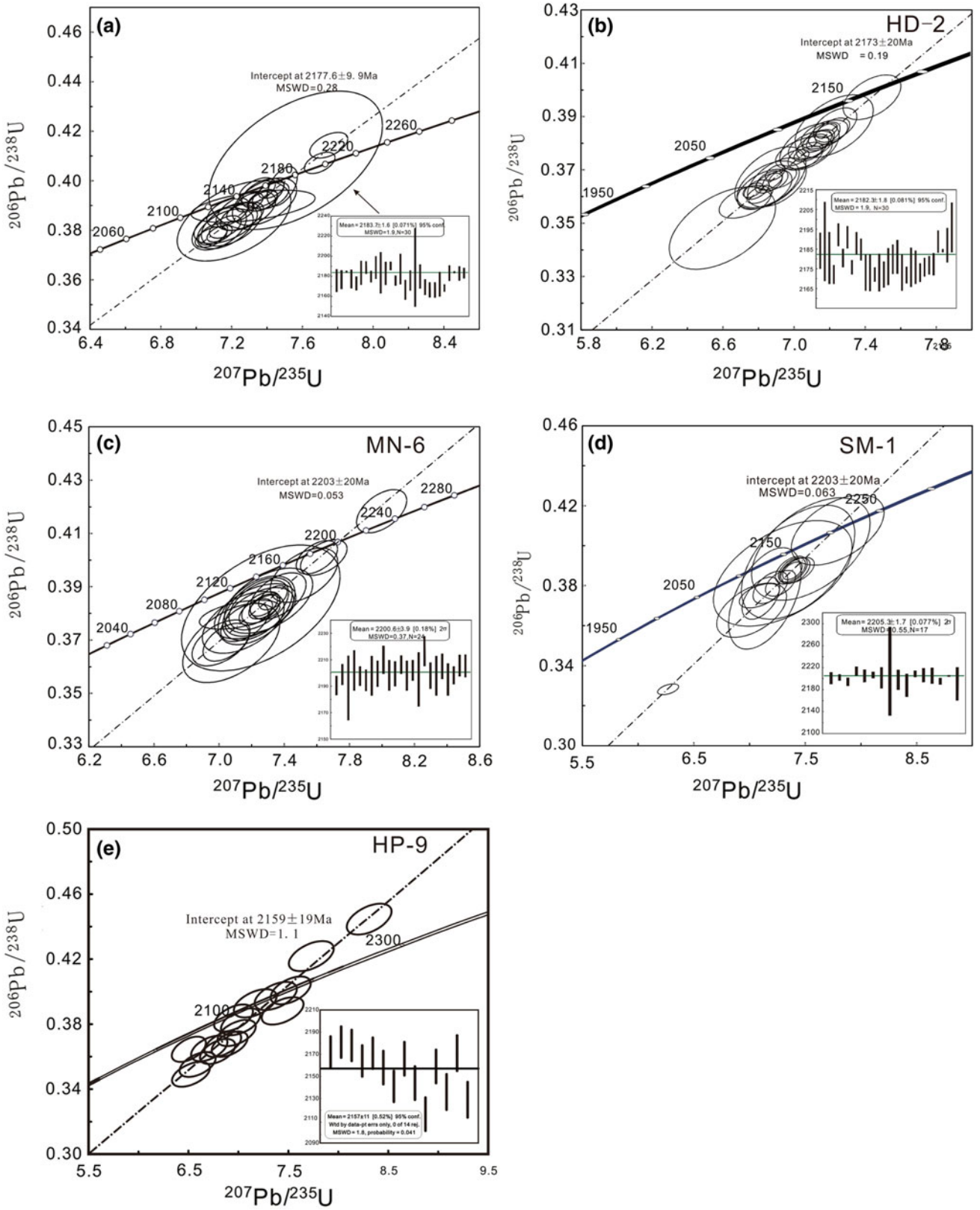

Fig. 7.4 Zircon U-Pb isotope concordia diagrams; **a** the Hupiyu granite; **b** the Hadabei granite; **c** the Muniuhe granite; **d** the Simenzi granite; **e** mafic dyke

7.4 A-type Granites?

The gneissic granites have been regarded as A-type granite in previous studies (Wu and Zheng 2004; Hao et al. 2004; Zhao et al. 2005), mainly based on limited data plotted in some geochemical diagrams such as Zr + Nb + Ce + Y versus FeO/MgO.

In this paper, we suggest that the gneissic granites are calc-alkaline I-type granites based on the following lines of evidences. (1) A-type granite commonly formed in an anorogenic setting and shows water-deficient and alkaline characteristics (e.g., Whalen et al. 1987). Hornblendes in A-type granites, if any, are generally Na-rich alkaline ones (Whalen et al. 1987). We saw no alkali hornblende or sodium hornblende in these gneissic granite samples, rather, the hornblendes within these rocks are mainly euhedral calcium hornblendes and magnesiohornblendes (Figs. 7.3i, c and 7.5; Table 7.2). (2) Lots of titanites and magnetites occur in these granites (Fig. 7.3i), which, along with the abundance of calcium hornblende and some MMEs (Fig. 7.3b), suggest a calc-alkaline, H_2O-rich, and high fO_2 affinity of the parental magma, typical of I-type granites. (3) The major elements show medium potassium calc-alkaline features (Fig. 7.6). These granites are enriched in LILEs, such as K, Rb, Sr, and Cs, and depleted in some HFSEs that are otherwise enriched in A-type granites, such as Nb, Ta, and Th. The chondrite-normalized REE patterns of these granites are different from those of A-type granites which are commonly characterized by significant negative Eu anomalies and tetrad effects. (4) Negative Ba anomalies are not so significant as in many A-types (Whalen et al. 1987), which may be caused by the enrichment of H_2O in the magma system. Because water-saturated felsic magma tends to show high oxygen fugacity and high internal water pressure due to exsolution of discrete vapor phases and the thermal breakdown of H_2O (Bonin 1990). As a consequence, alkali feldspar fractionation and, thus, negative Ba anomalies, are reduced. In addition, the contents of Fe and Ti are also lower than those of typical A-type granites, which may also be caused by the H_2O-enrichment in the magma system, because titanomagnetite and Nb-Mn ilmenite precipitate in an early stage, decreasing the contents of Fe and Ti in residual magma (Bonin 1990). These data suggest that the Paleoproterozoic gneissic granites could be basically water-enriched I-type granites (Tables 7.3 and 7.4).

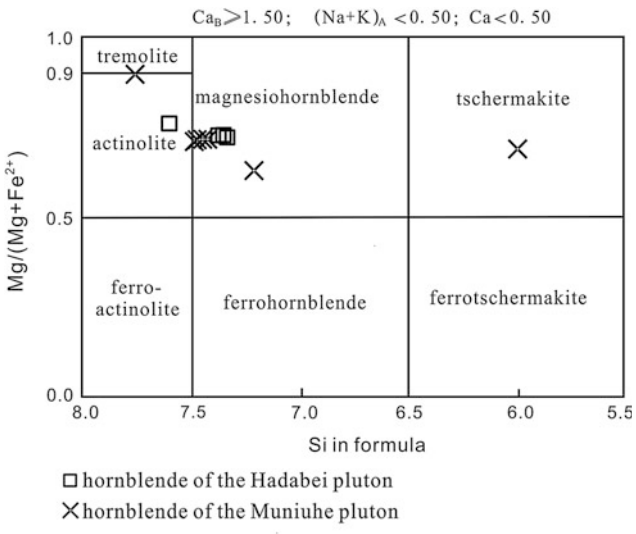

Fig. 7.5 Classfication diagram of hornblende from the Hadabei and Muniuhe granites (after Leake et al. 1997)

However, some samples from the Dafangshen pluton show A-type features. As shown in Fig. 7.7, these samples have significant negative Eu anomalies (Eu/Eu* = 0.1), slight REE tetrad effect ($TE_{1,3}$ = 0.12–0.21) and lower Zr/Hf ratios (30.5–33.7) than in normal granites (35–40, Jahn et al. 2001; Chen et al. 2014). We suggest that the A-type-like characteristics are attributable to the highly evolved nature of the pluton as shown by the high SiO_2 contents (76.7–77.1 wt%), which could have been caused by the high boron contents of the pluton, because tourmaline (texturally in equilibrium with other rock-forming minerals) is common in this pluton (Fig. 7.3h). The B-rich feature of the Dafangshen granite (>1 wt% boron for the crystallization of tourmaline; Lukkari and Holtz 2007) could have lowered the solidus temperature and viscosity of the magma system (Chen et al. 2014), and thus prolong the process of magma evolution and strengthen the melt-rock interaction, leading to high silica, non-CHARAC characteristics (e.g., low Zr/Hf ratios) and the slight REE tetrad effect of the pluton (Bau 1996; Chen et al. 2014). This is also supported by the occurrence of extremely Ab-rich plagioclase in the Dafangshen pluton (with Ab = 71.1–98.3), a feature typical of highly evolved (A-type) granites (Whalen et al. 1987). The Ab-rich feature could have been related with addition of boron in the magma system, which was proved to shift the ternary minimum composition towards the Ab apex in the phase relations of Ab-Or-Qtz (Manning 1981).

7.5 Role of Magma Mixing/Mingling

According to the petrography and geochemical characteristics of these gneissic granites, we suggest that they formed through a mingling/mixing process between dominant crustal melts and subordinate mantle-derived mafic magmas. This is supported by the following lines of evidence.

First, MMEs are common in the gneissic granites (Fig. 7.3b, c). Although MMEs have been suggested as early crystallized mineral cumulates from magma chamber (Noyes et al. 1983), or as residual phases after partial melting of source rocks (White et al. 1999; Chappell et al. 2000), we

Table 7.2 Microprobe analysis for representative hornblende from the Liao-Ji gneissic granites

Pluton	Hadabei				Muniuhe							
Spot no.	HD-7.1	HD-7.2	HD-7.3	HD-7.4	MN-4.1	MN-4.2	MN-4.3	MN-4.4	MN-4.5	MN-4.6	MN-4.7	MN-4.8
SiO_2	54.8	51.84	52.63	52.1	52.72	30.47	53.36	53.3	52.83	56.82	50.06	42.59
TiO_2	0.1	0.35	0.16	0.15	0.29	37.62	0.06	0.17	0.08	0.03	0.43	1.89
Al_2O_3	1.49	3.1	2.95	3.03	2.66	1.42	2.5	2.85	2.24	0.33	3.1	12.72
Cr_2O_3	0	0.07	0.02	0.03	0.05	0.12	0.06	0.17	0	0.09	0.01	0.08
Fe_2O_3	4.87	4.87	4.87	4.87	4.87	4.87	4.87	4.87	4.87	4.87	4.87	4.87
FeO	9.88	11.08	11.13	10.97	10.18	0.31	10.68	10.29	10.66	4.23	16.47	10.27
MnO	0.33	0.37	0.34	0.36	0.18	0.01	0.25	0.23	0.19	0.24	0.44	0.11
MgO	18.36	16.75	17.25	17.15	17.17	0.04	16.93	16.87	17.36	22.9	13.23	15.49
CaO	12.35	12.37	12.28	12.25	13.27	30.17	13.32	13.16	13.39	12.48	12.1	11.85
Na_2O	0.42	0.82	0.84	0.87	0.29	0	0.3	0.36	0.32	0.11	0.56	2.52
K_2O	0.1	0.23	0.2	0.22	0.14	0	0.13	0.15	0.12	0.07	0.33	0.96
Totals	102.7	101.86	102.68	102.01	101.82	105.06	102.46	102.42	102.06	102.17	101.61	103.36
Oxygens	23	23	23	23	23	23	23	23	23	23	23	23
Si	7.525	7.27	7.308	7.286	7.349	4.426	7.401	7.381	7.367	7.63	7.226	5.986
Ti	0.01	0.037	0.017	0.016	0.03	4.11	0.006	0.018	0.008	0.003	0.047	0.2
Al	0.241	0.513	0.483	0.5	0.437	0.243	0.409	0.465	0.368	0.052	0.528	2.108
Cr	0	0.008	0.002	0.003	0.006	0.014	0.007	0.019	0	0.01	0.001	0.009
Fe^{3+}	0.504	0.514	0.509	0.513	0.511	0.533	0.509	0.508	0.512	0.493	0.53	0.516
Fe^{2+}	1.135	1.299	1.292	1.283	1.187	0.038	1.239	1.192	1.243	0.475	1.988	1.207
Mn	0.038	0.044	0.04	0.043	0.021	0.001	0.029	0.027	0.022	0.027	0.054	0.013
Mg	3.757	3.501	3.57	3.574	3.567	0.009	3.5	3.482	3.608	4.583	2.846	3.245
Ca	1.817	1.859	1.827	1.836	1.982	4.696	1.98	1.953	2.001	1.796	1.871	1.785
Na	0.112	0.223	0.226	0.236	0.078	0	0.081	0.097	0.087	0.029	0.157	0.687
K	0.018	0.041	0.035	0.039	0.025	0	0.023	0.027	0.021	0.012	0.061	0.172
Sum	15.157	15.308	15.309	15.328	15.195	14.071	15.183	15.167	15.238	15.11	15.307	15.927
Mg#	0.77	0.73	0.73	0.74	0.75	0.19	0.74	0.74	0.74	0.91	0.59	0.73

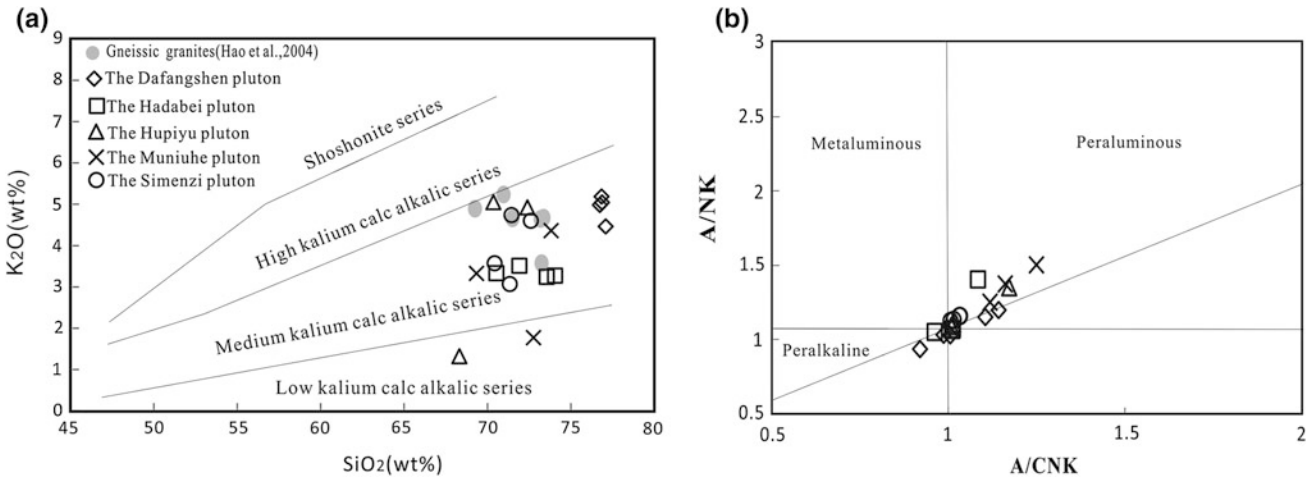

Fig. 7.6 **a** K_2O-SiO_2 diagram (after Peccerillo and Taylor 1976) and **b** A/NK-A/CNK diagram for the granites

Table 7.3 Microprobe analysis for representative plagioclase from the gneissic granites

Pluton	Hupiyu						Hadabei					
Spot no.	HP-1.3	HP-1.4	HP-1.5	HP-6.1	HP-6.2	HP-6.3	HD-2.1	HD-2.2	HD-2.3	HD-2.4	HD-1.1	HD-1.2
SiO_2	67.86	65.73	66.49	67.93	66.56	69.08	59.55	59.46	62.10	58.13	58.70	58.82
TiO_2	0.07	0.04	0.00	0.04	0.02	0.02	0.08	0.06	0.00	0.00	0.00	0.05
Al_2O_3	19.01	20.54	20.29	20.82	20.58	19.37	24.64	24.47	22.47	25.31	25.50	24.78
Cr_2O_3	0.07	0.00	0.03	0.00	0.01	0.02	0.02	0.00	0.07	0.04	0.00	0.00
Fe_2O_3	0.00	0.00	0.00	0.00	0.00	0.00	0.00	0.00	0.00	0.00	0.00	0.00
FeO	0.00	0.00	0.00	0.00	0.00	0.00	0.00	0.00	0.00	0.00	0.00	0.00
MnO	0.00	0.00	0.00	0.05	0.00	0.00	0.01	0.00	0.00	0.06	0.00	0.00
MgO	0.00	0.01	0.00	0.00	0.00	0.01	0.01	0.00	0.00	0.00	0.01	0.00
CaO	0.23	1.30	1.26	1.36	1.32	0.11	6.08	6.62	3.95	6.87	6.88	6.78
Na_2O	11.03	12.37	11.97	11.19	12.21	12.57	8.83	8.42	10.16	7.94	8.14	8.15
K_2O	0.08	0.30	0.08	0.12	0.19	0.06	0.53	0.45	0.56	0.49	0.38	0.47
Total	98.35	100.29	100.12	101.51	100.89	101.24	99.75	99.48	99.31	98.84	99.61	99.05
Si	3.01	2.90	2.92	2.93	2.91	2.99	2.67	2.67	2.78	2.63	2.64	2.66
Ti	0.00	0.00	0.00	0.00	0.00	0.00	0.00	0.00	0.00	0.00	0.00	0.00
Al	0.99	1.07	1.05	1.06	1.06	0.99	1.30	1.30	1.19	1.35	1.35	1.32
Cr	0.00	0.00	0.00	0.00	0.00	0.00	0.00	0.00	0.00	0.00	0.00	0.00
Fe^{3+}	0.00	0.00	0.00	0.00	0.00	0.00	0.00	0.00	0.00	0.00	0.00	0.00
Fe^{2+}	0.00	0.00	0.00	0.00	0.01	0.00	0.01	0.01	0.01	0.01	0.01	0.01
Mn	0.00	0.00	0.00	0.00	0.00	0.00	0.00	0.00	0.00	0.00	0.00	0.00
Mg	0.00	0.00	0.00	0.00	0.00	0.00	0.00	0.00	0.00	0.00	0.00	0.00
Ca	0.01	0.06	0.06	0.06	0.06	0.01	0.29	0.32	0.19	0.33	0.33	0.33
Na	0.95	1.06	1.02	0.94	1.04	1.06	0.77	0.73	0.88	0.70	0.71	0.71
K	0.01	0.02	0.00	0.01	0.01	0.00	0.03	0.03	0.03	0.03	0.02	0.03
An	1.14	5.37	5.45	6.26	5.60	0.47	26.79	29.56	17.21	31.47	31.17	30.68
Ab	98.34	93.13	94.18	93.05	93.41	99.25	70.46	68.03	79.89	65.88	66.76	66.79
Or	0.52	1.50	0.37	0.70	0.99	0.28	2.75	2.41	2.90	2.65	2.07	2.53

Pluton	Hadabei											Dafangshen
Spot no.	HD-1.3	HD-1.4	HD-1.5	HD-1.6	HD-7.1	HD-7.2	HD-7.3	HD-7.4	HD-7.5	HD-7.6	HD-7.7	DF-8.1
SiO_2	57.61	58.40	58.66	59.63	59.26	57.97	63.46	59.43	64.43	56.60	62.87	59.82
TiO_2	0.01	0.04	0.00	0.01	0.03	0.00	0.04	0.01	0.03	0.00	0.00	0.00
Al_2O_3	25.61	25.60	24.88	25.02	24.42	25.48	22.37	24.96	22.69	27.16	22.67	25.48

(continued)

Table 7.3 (continued)

Pluton	Hadabei											Dafangshen
Spot no.	HD-1.3	HD-1.4	HD-1.5	HD-1.6	HD-7.1	HD-7.2	HD-7.3	HD-7.4	HD-7.5	HD-7.6	HD-7.7	DF-8.1
Cr_2O_3	0.03	0.00	0.02	0.00	0.00	0.00	0.01	0.00	0.00	0.01	0.00	0.00
Fe_2O_3	0.00	0.00	0.00	0.00	0.18	0.09	0.21	0.17	0.18	0.15	0.14	0.00
FeO	0.00	0.00	0.00	0.00	0.00	0.00	0.00	0.00	0.00	0.00	0.00	0.00
MnO	0.00	0.00	0.03	0.01	0.04	0.00	0.03	0.01	0.01	0.00	0.01	0.02
MgO	0.01	0.04	0.01	0.01	0.03	0.00	0.01	0.02	0.00	0.03	0.01	0.02
CaO	7.65	7.55	7.16	5.89	6.63	7.54	3.85	6.62	3.97	8.83	4.13	6.25
Na_2O	7.84	7.90	8.40	8.57	7.94	7.42	9.26	7.87	7.98	7.38	9.26	9.10
K_2O	0.38	0.42	0.34	0.48	0.72	0.47	0.27	0.63	0.36	0.26	0.54	0.38
Total	99.14	99.95	99.50	99.62	99.25	98.98	99.51	99.73	99.66	100.42	99.62	101.07
Si	2.61	2.62	2.64	2.67	2.67	2.63	2.82	2.67	2.84	2.54	2.80	2.65
Ti	0.00	0.00	0.00	0.00	0.00	0.00	0.00	0.00	0.00	0.00	0.00	0.00
Al	1.37	1.35	1.32	1.32	1.30	1.36	1.17	1.32	1.18	1.44	1.19	1.33
Cr	0.00	0.00	0.00	0.00	0.00	0.00	0.00	0.00	0.00	0.00	0.00	0.00
Fe^{3+}	0.00	0.00	0.00	0.00	0.01	0.00	0.01	0.01	0.01	0.01	0.01	0.00
Fe^{2+}	0.01	0.01	0.01	0.00	0.00	0.00	0.00	0.00	0.00	0.00	0.00	0.00
Mn	0.00	0.00	0.00	0.00	0.00	0.00	0.00	0.00	0.00	0.00	0.00	0.00
Mg	0.00	0.00	0.00	0.00	0.00	0.00	0.00	0.00	0.00	0.00	0.00	0.00
Ca	0.37	0.36	0.35	0.28	0.32	0.37	0.18	0.32	0.19	0.43	0.20	0.30
Na	0.69	0.69	0.73	0.74	0.70	0.65	0.80	0.68	0.68	0.64	0.80	0.78
K	0.02	0.02	0.02	0.03	0.04	0.03	0.02	0.04	0.02	0.02	0.03	0.02
An	34.32	33.80	31.45	26.85	30.34	35.06	18.37	30.64	21.10	39.28	19.20	27.00
Ab	63.64	63.97	66.73	70.59	65.69	62.36	80.12	65.90	76.54	59.33	77.88	71.09
Or	2.04	2.23	1.82	2.56	3.97	2.59	1.51	3.47	2.36	1.39	2.92	1.91

Pluton	Dafangshen			Muniuhe									
Spot no.	DF-8.2	DF-8.3	DF-8.4	MN-3.2	MN-3.3	MN-3.4	MN-3.5	MN-4.1	MN-4.2	MN-4.3	MN-7.1	MN-7.2	MN-7.3
SiO_2	66.58	66.35	68.14	49.37	49.32	51.44	51.69	67.67	65.03	68.85	67.67	65.03	68.85
TiO_2	0.04	0.06	0.03	0.00	0.00	0.00	0.00	0.01	0.02	0.06	0.01	0.02	0.06
Al_2O_3	19.67	20.26	18.56	31.77	32.89	31.17	30.86	18.89	20.66	18.51	18.89	20.66	18.51
Cr_2O_3	0.00	0.00	0.00	0.02	0.00	0.00	0.00	0.04	0.04	0.00	0.04	0.04	0.00
Fe_2O_3	0.00	0.00	0.00	0.00	0.00	0.00	0.00	0.00	0.00	0.00	0.00	0.00	0.00
FeO	0.00	0.00	0.00	0.00	0.00	0.00	0.00	0.00	0.00	0.00	0.00	0.00	0.00

(continued)

Table 7.3 (continued)

Pluton	Dafangshen			Muniuhe									
Spot no.	DF-8.2	DF-8.3	DF-8.4	MN-3.2	MN-3.3	MN-3.4	MN-3.5	MN-4.1	MN-4.2	MN-4.3	MN-7.1	MN-7.2	MN-7.3
MnO	0.02	0.02	0.00	0.00	0.01	0.03	0.02	0.03	0.00	0.02	0.03	0.00	0.02
MgO	0.01	0.00	0.03	0.01	0.01	0.01	0.03	0.00	0.03	0.00	0.00	0.03	0.00
CaO	1.52	2.35	0.31	14.76	15.48	12.85	13.05	0.84	1.27	0.86	0.84	1.27	0.86
Na_2O	11.58	10.63	11.97	4.10	3.56	5.02	4.98	11.73	11.92	12.15	11.73	11.92	12.15
K_2O	0.05	0.07	0.06	0.01	0.04	0.10	0.08	0.18	0.05	0.06	0.18	0.05	0.06
Total	99.47	99.74	99.10	100.04	101.31	100.62	100.71	99.39	99.02	100.51	99.39	99.02	100.51
Si	2.94	2.92	3.01	2.26	2.23	2.33	2.34	2.99	2.90	3.01	2.99	2.90	3.01
Ti	0.00	0.00	0.00	0.00	0.00	0.00	0.00	0.00	0.00	0.00	0.00	0.00	0.00
Al	1.03	1.05	0.97	1.71	1.75	1.66	1.65	0.98	1.08	0.95	0.98	1.08	0.95
Cr	0.00	0.00	0.00	0.00	0.00	0.00	0.00	0.00	0.00	0.00	0.00	0.00	0.00
Fe^{3+}	0.00	0.00	0.00	0.00	0.00	0.00	0.00	0.00	0.00	0.00	0.00	0.00	0.00
Fe^{2+}	0.00	0.00	0.00	0.00	0.00	0.00	0.00	0.00	0.00	0.00	0.00	0.00	0.00
Mn	0.00	0.00	0.00	0.00	0.00	0.00	0.00	0.00	0.00	0.00	0.00	0.00	0.00
Mg	0.00	0.00	0.00	0.00	0.00	0.00	0.00	0.00	0.00	0.00	0.00	0.00	0.00
Ca	0.07	0.11	0.02	0.72	0.75	0.62	0.63	0.04	0.06	0.04	0.04	0.06	0.04
Na	0.99	0.91	1.03	0.36	0.31	0.44	0.44	1.00	1.03	1.03	1.00	1.03	1.03
K	0.00	0.00	0.00	0.00	0.00	0.01	0.01	0.01	0.00	0.00	0.01	0.00	0.00
An	6.74	10.85	1.44	66.48	70.49	58.22	58.85	3.80	5.58	3.73	3.81	5.50	3.74
Ab	92.98	88.76	98.27	33.43	29.32	41.21	40.69	95.26	94.14	95.99	95.24	94.50	96.26
Or	0.28	0.39	0.29	0.09	0.19	0.56	0.47	0.95	0.27	0.28	0.95	0.00	0.00

Note Ion number is calculated based on eight oxygen atoms

Table 7.4 Whole-rock chemical compositions of the gneissic granites in the Jiao-Liao-Ji Belt

Pluton	Dafangshen				Hadabei				Hupiyu		Muniuhe			Simenzi			
Sample	DF-1	DF-2	DF-3	DF-6	HD-2	HD-3	HD-4	HD-7	HP-1	HP-2	MN-1	MN-2	MN-6	SM-1	SM-2	SM-3	SM-5
(wt%)																	
SiO_2	76.7	77.1	76.8	77	73.6	74.1	71.9	70.5	72.4	70.4	72.8	73.8	69.4	72.6	71.5	70.4	71.3
K_2O	5	4.5	5.2	5	3.2	3.3	3.5	3.3	4.9	5	1.8	4.4	3.3	4.6	4.7	3.6	3.1
TiO_2	0.2	0.1	0.1	0.1	0.3	0.3	0.3	0.3	0.3	0.3	0.1	0.3	0.1	0.2	0.3	0.1	0.1
Al_2O_3	10.8	11.2	10.6	11	12.5	11.9	12.4	13.8	12.6	13.1	15.4	12.1	17.1	12.9	13	15	15.2
TFe_2O_3	2.8	2.5	2.1	2	3.7	3.4	5.2	2.1	3.6	4.2	0.6	3.6	1.2	3.4	3.9	1.8	0.8
MgO	0.03	0.01	0.06	0.04	0.06	0.07	0.06	1.41	0.08	0.15	0.27	0.18	0.46	0.12	0.09	0.30	0.32
MnO	0.02	0.02	0.02	0.01	0.01	0.02	0.01	0.04	0.04	0.03	0.01	0.04	0.02	0.04	0.05	0.03	0.02
CaO	0.4	0.5	0.5	0.2	0.69	1.14	0.65	3.16	1.1	1	2.2	1.2	2.5	1.5	1.5	1.6	1.7
Na_2O	2.4	2.8	2.8	3.2	5	4.74	4.8	3.8	3.7	4	5.7	3	4.7	3.7	3.7	5.7	6.2
P_2O_5	b.d.	b.d.	0.08	b.d.	b.d.	0.008	0.007	0.011	0.074	0.01	0.07	0.014	0.02	0.016	0.017	0.01	0.04
LOl	0.6	0.2	0.6	0.4	0	0	0.2	0.5	0.2	0.8	0.3	0.3	0.3	-0.1	0.3	0.3	0.3
Total	98.9	98.9	98.9	99	99	99	99	99	99	99	99	98.9	99	99	99	99	99
A/NK	1.2	1.2	1.0	1.0	1.1	1.0	1.1	1.4	1.1	1.1	1.4	1.2	1.5	1.2	1.2	1.1	1.1
A/CNK	1.1	1.1	0.9	1.0	1.0	0.9	1.0	0.9	0.9	0.9	1.0	1.0	1.1	0.9	0.9	0.9	0.9
K_2O/Na_2O	2.1	1.6	1.9	1.6	0.6	0.7	0.7	0.9	1.3	1.3	0.3	1.5	0.7	1.2	1.3	0.6	0.5
Mg#	4.2	1.7	11.7	8.2	7.1	8.4	5.1	74.9	8.9	13.7	66.7	18.2	63.2	13.6	9.1	42.5	64.2
(ppm)																	
Sc	1.7	1.5	1.6	1	3.2	3.7	4	5.6	4.2	5.7	1	4.8	2.6	3.4	5.8	0.9	0.8
Ti	1011	761	839	822	1672	1980	1967	1961	1887	2354	401	1964	607	1387	2388	474	475
V	1.8	1.7	1.7	1.3	7	5	7	40.8	2.8	3.7	4.7	6.8	10.6	3.2	2.7	2	3.7
Cr	1	0.5	1.6	1.1	4	1.2	1.8	46	4.7	2.1	2.6	4.7	3.6	3	2.1	3.1	2.4
Mn	207	176	133	64	97.3	141.4	122.7	310.6	350.2	233	83.9	350.6	164	370.8	443.6	250	200
Co	0.2	0.1	0.3	0.2	1.4	0.9	3.3	4.8	0.5	0.7	0.8	1.4	1.8	0.7	1.3	0.4	0.8
Ni	0.8	0.4	1	0.9	2.4	3.9	2.3	11.9	3	1.9	2	2.9	1.3	0.8	1.4	2.6	2.3
Cu	1	0.4	0.8	1	1.9	3.4	5.7	0.9	3.4	4.1	1.4	2.3	6.8	1.5	4.4	0.9	1.3
Zn	34.3	27.1	40.3	22	25.6	22.7	42.7	59.6	29.9	60.5	29.3	60.7	42.5	32.6	45.6	46.3	58.5
Ga	21.9	21.2	20.9	24	19.5	21.4	22	18.6	21	24.1	15.3	21.8	19.7	21.3	24	16.8	15.6
Rb	247	191	237	200	81.9	99.2	92.5	87.9	136	161	56.2	180.4	173	131.1	146.9	86.5	79.5
Sr	22	28.7	29.8	16	89.6	116.5	102.7	609.8	52.3	55.5	880	136.5	389	167.6	190.1	280	570
Y	46.6	74.2	48.3	60	38	50.9	38.7	8.1	57.2	47.2	3	35.3	5.5	34.3	76.7	9	8.6
Zr	349	323	364	326	379.2	439.8	409.4	148.5	374	460	63.9	391.6	29.4	278.4	569.3	57.9	73.8
Nb	27.1	16.6	20.5	37	21.2	27.9	19.1	9.9	24.7	35.1	2	23.6	8.3	17.7	33.7	5	3.6

(continued)

Table 7.4 (continued)

Pluton	Dafangshen				Hadabei				Hupiyu		Muniuhe			Simenzi			
Sample	DF-1	DF-2	DF-3	DF-6	HD-2	HD-3	HD-4	HD-7	HP-1	HP-2	MN-1	MN-2	MN-6	SM-1	SM-2	SM-3	SM-5
Cs	1.6	0.8	1.7	0.6	0.5	0.4	0.4	0.8	1.6	3.9	1.1	2.5	5.5	0.4	0.4	0.1	0.2
Ba	188	167	203	122	1057	1194	1032	1282	821.8	779	970	1114	1911	1099	1344	965	1169
La	66	123	160	74	24.1	49.1	32.7	26.7	11.2	7.3	4.9	54.3	1.8	14.3	106	2.8	4.2
Ce	195	253	256	155	66.7	109.3	85.1	50.5	31.9	21	9.6	115.2	3.4	40.2	185.4	7.4	6.2
Pr	16.8	31.9	35.9	19	9.2	13.3	11.4	5.4	5.5	3.9	1.2	13.7	0.4	5.9	20.3	1.1	1
Nd	58.1	114	124	65	35.8	49.3	43	17.8	26.3	20	4.2	48.9	1.7	24.1	72.2	4.4	3.8
Sm	11.4	23.9	24.7	13	7.5	10.1	8.6	2.8	8.2	6.8	0.8	9.3	0.5	5.8	14.9	1.1	0.9
Eu	0.3	0.7	0.7	0.4	1.6	1.9	1.6	1	1.4	1.3	0.5	1.6	0.6	1.2	2.4	0.6	0.5
Gd	10.2	22.4	21.4	12	7.3	9.9	7.9	2.3	9.2	7.7	0.7	8.6	0.7	6	14.6	1.2	1
Tb	1.6	3.3	2.7	1.9	1.1	1.5	1.2	0.3	1.6	1.3	0.1	1.2	0.1	1	2.2	0.2	0.2
Dy	10.2	19	13.2	12	7.2	9.6	7.1	1.6	10.3	8.4	0.5	7.2	0.8	6.3	13.9	1.3	1.1
Ho	2.1	3.4	2.1	2.5	1.5	2	1.5	0.3	2.2	1.7	0.1	1.4	0.2	1.3	2.9	0.3	0.3
Er	6.2	8.2	4.6	7.3	4.3	5.7	4.3	0.9	6.5	5	0.3	3.8	0.6	3.9	8.4	0.9	0.9
Tm	0.9	0.9	0.5	1	0.6	0.8	0.6	0.1	0.9	0.7	0	0.5	0.1	0.6	1.2	0.1	0.1
Yb	5.3	5	2.7	6.6	4.1	5	4.1	0.9	6.2	4.9	0.3	3.1	0.7	3.8	8	1.1	1
Lu	0.7	0.6	0.4	0.9	0.6	0.7	0.6	0.1	0.9	0.7	0	0.4	0.1	0.6	1.1	0.2	0.2
Hf	10.8	10.6	10.8	11	9.5	10.5	9.8	3.9	8.8	11.5	1.8	9.9	1	6.7	13.2	1.7	1.9
Ta	1.5	1.1	1.3	2	1.4	1.7	1.4	0.6	1.4	2.1	0.1	1.4	0.8	1	2.5	0.3	0.3
Pb	13.9	14.8	17.1	10	7.8	8	9.1	11.3	6.1	7.4	18	9.9	38.7	4.9	9.3	4	7.3
Th	37.6	49	48.4	33	6.7	12.7	4.9	7.2	20.5	13.5	1.3	21	0.9	5.3	25.1	0.5	0.4
U	2.6	4.3	2.9	3.1	1.8	1.7	2.7	2.4	2.7	3	0.4	4.3	2.5	1.6	2.8	0.7	0.7
Sr/Y	0.5	0.4	0.6	0.3	2.4	2.3	2.7	75.3	0.9	1.2	293.5	3.9	70.7	4.9	2.5	31.1	66.3
ΣREE	385	609	649	371	171.7	268.2	209.6	110.8	122.2	90.8	23.1	269.2	11.6	115	453.6	22.7	21.3
La_N/Yb_N	8.9	17.6	41.9	8	4.2	7	5.7	22.1	1.3	1.1	11.7	12.4	2	2.7	9.5	1.9	2.9
Eu/Eu*	0.1	0.1	0.1	0.1	0.7	0.6	0.6	1.1	0.5	0.5	1.9	0.5	3.3	0.6	0.5	1.5	1.7
K/Ta	####	####	####	###	18187	15446	19892	43763	27849	####	####	25008	####	36602	14959	####	####
Ba/La	2.8	1.4	1.3	1.6	43.9	24.3	31.6	48.0	73.4	####	198.0	20.5	####	76.9	12.7	344.7	278.2
Zr/Hf	32.3	30.5	33.7	30.4	39.9	41.9	41.8	38.1	42.5	40.0	35.5	39.6	29.4	41.6	43.1	34.1	38.8
$TE_{1,3}$	0.12	0.21	0.19	0.12	0.07	0.09	0.07	0.03	0.06	0.04	0.01	0.08	0.00	0.05	0.14	0.01	0.01
T_{Zr} (°C)	870	870	870	870	870.3	870.3	870.3	870.3	870.3	870	870	870.3	870	870.3	870.3	870	870

Note $Eu/Eu^* = Eu_N/((Sm_N + Gd_N)/2)$

T_{Zr} (°C)—zircon saturation temperature, calculated using the geothermometer of Watson and Harrison (1983)

$TE_1 = (((Ce/Ce^* \times Pr/Pr^*)^{0.5} \times (Tb/Tb^* \times Dy/Dy^*)^{0.5})^{0.5}$,—the degree of the tetrad effect (Irber 1999)

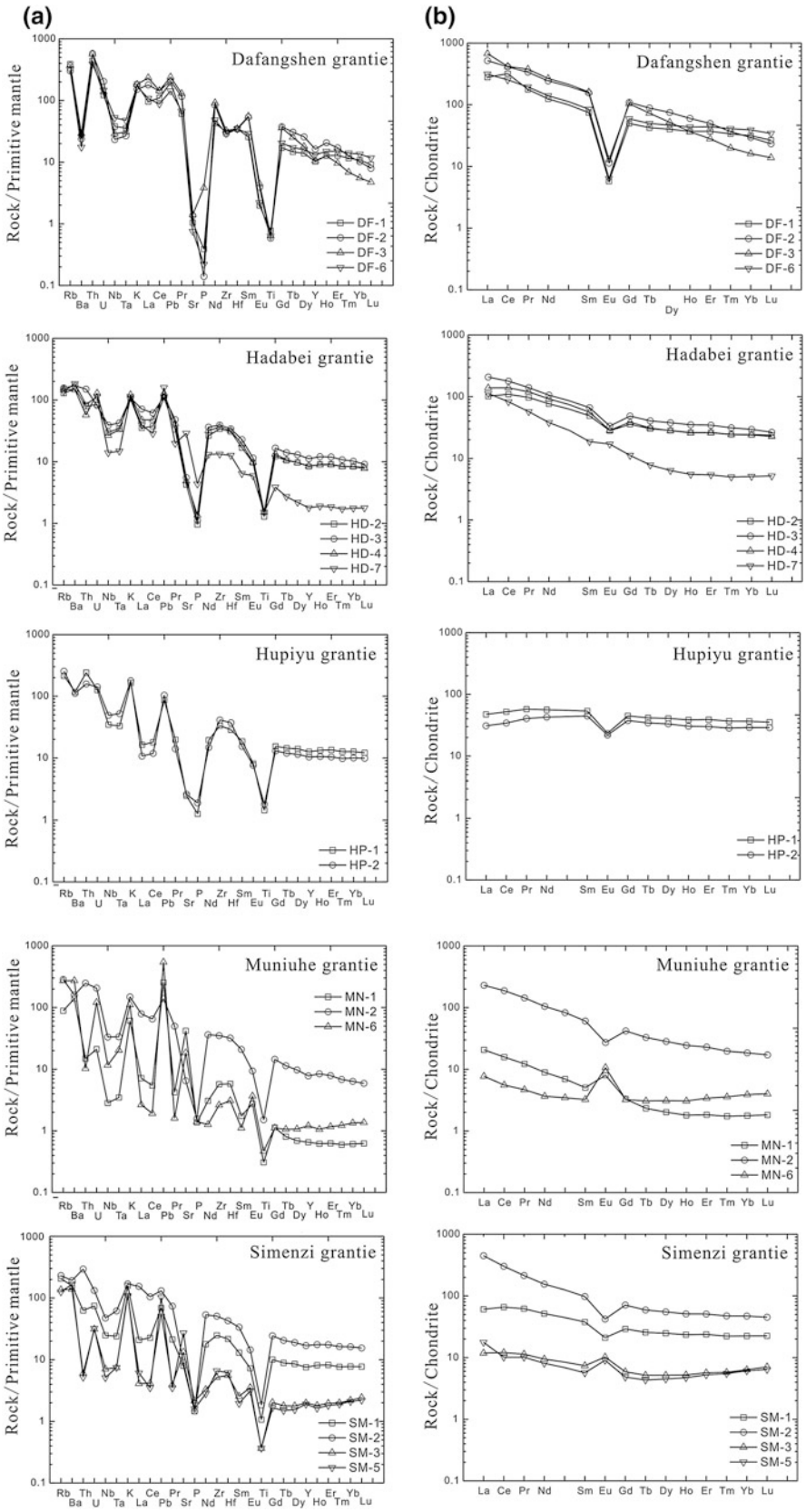

Fig. 7.7 **a** Chondrite-normalized REE patterns of ths gneissic granites. Normalization values of chondrite are from Sun and McDonough (1989). **b** Primitive mantle (PM)-normalized spidergrams of the granites. PM values are from Sun and McDonough (1989). *DF* Dafangshen; *HD* Hadabei; *HP* Hupiyu; *MN* Muniuhe; *SM* Simenzi

suggest that they are originally mantle-derived mafic magma and then modified by mixing/mingling with surrounding felsic melts (Holden et al. 1987; Vernon et al. 1988; Bonin 2004; Sklyarov and Fedorovsky 2006; Chen et al. 2008, 2009; Feeley et al. 2008; Ma et al. 2013) for evidence as below. (1) MMEs are elongated in shape without solid-stated deformation (Fig. 7.3b), due to stretching plastically within a partially crystallized, convective magma (Chen et al. 2008, 2009). (2) There are some plagioclase inclusions in the hornblende crystal from the MME (Fig. 7.3d), indicating that the mafic magma injected into the felsic magma and captured the plagioclase crystallized in the early period. (3) MMEs show more fine-grained and equigranular textures than host rocks (Fig. 7.3c) and many needle-like apatites can be seen in the MMEs (Fig. 7.3c), suggesting that the hot mafic magma has undergone a quenching process when injected into the felsic magma with lower temperatures. The existence of MMEs is typical of a mingling/mixing process for the genesis of the host magma (Clynne 1999; Kemp 2004; Chen et al. 2009).

Second, some plagioclases near the MMEs in the host rock show complicated compositional and textural disequilibrium (Fig. 7.3e, f), which commonly results from magma mixing between intermediate-mafic and felsic melts (Anderson 1976; Janoušek et al. 2004; Chen et al. 2009). As shown in Fig. 7.3h, the Na-rich plagioclase core (An_{18}) was crystallized from felsic magma, and the relatively Ca-rich overgrowths (An_{35} and An_{39}) may result from two pulses of input of mafic magma into the magma system and subsequent magma mixing (Chen et al. 2013).

Third, the whole-rock Nd isotopic compositions vary significantly ($\varepsilon_{Nd}(t) = -8.6$ to 1.5; Fig. 7.8), even for samples from a single pluton. This argues against a process of closed system magma evolution (Griffin et al. 2002; Kemp and Hawkesworth 2006), rather, a magma mixing process between two end members with distinct Nd isotopic compositions is required. This is consistent with the large variation of $\varepsilon_{Hf}(t)$ values (from −1.27 to 5.58; Fig. 7.9) of zircons from each pluton. Large Hf isotopic variation is also considered as having been resulted from a mixing/mingling process between magmas with distinct sources by some other researchers (Kemp and Hawkesworth 2006; Yang et al. 2008; Zhang et al. 2011) (Tables 7.5 and 7.6).

7.6 Source Characteristics

Potential end members that may have contributed to the formation of these granites are felsic magma derived from partial melting of the basement and mafic magma from the mantle. The gneissic granites have a wide range of whole-rock $\varepsilon_{Nd}(t)$ values (−8.6 to 1.5). The very negative $\varepsilon_{Nd}(t)$ values of some samples (as low as −8) suggest that the felsic end member should have been originated from partial melting of Archean basement rocks. This is supported by the ages of the inherited zircons from these gneissic granites mentioned above (2.53–2.78 Ga), and is compatible with the protolith ages (2.5–2.6 Ga) obtained by Kröner et al. (1988) and Zhao et al. (2001) for the basement rocks beneath the East Block. The Archean basement of the North China Craton is composed mainly of intermediate-mafic granulite/amphibolite and TTG gneisses (Jahn and Ernst 1990; Liu et al. 1992; Zhao et al. 2005). The Dafangshen, Hupiyu and Simenzi granites are rich in potassium, with

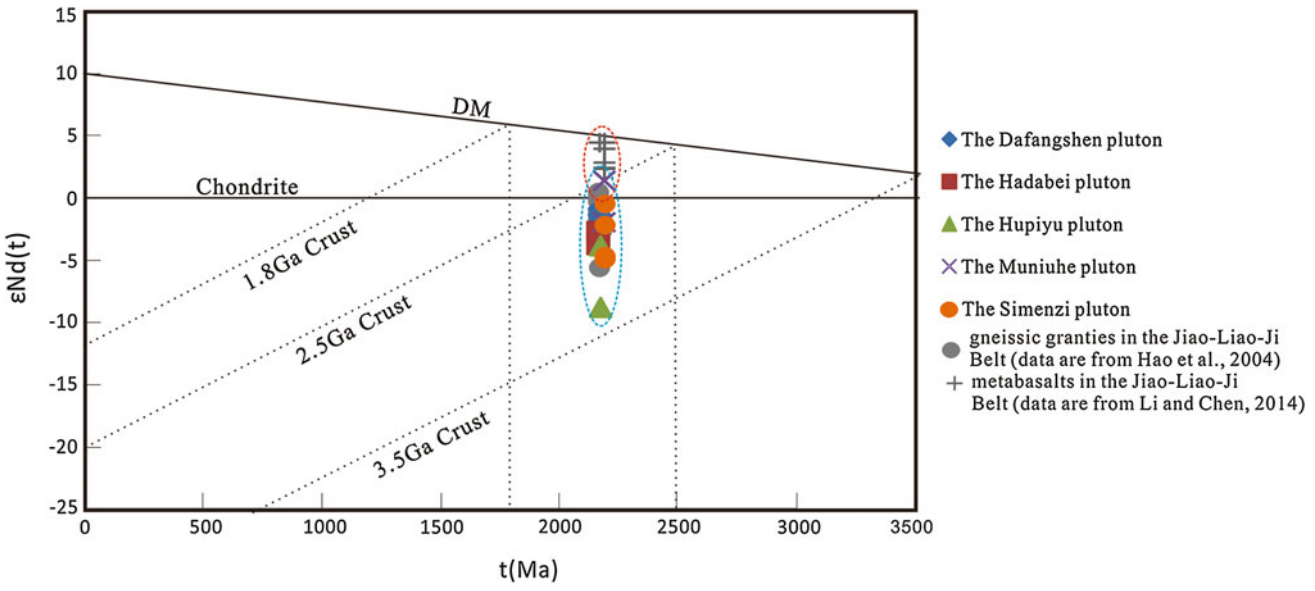

Fig. 7.8 Whole-rock Nd isotopic data of the gneissic granites

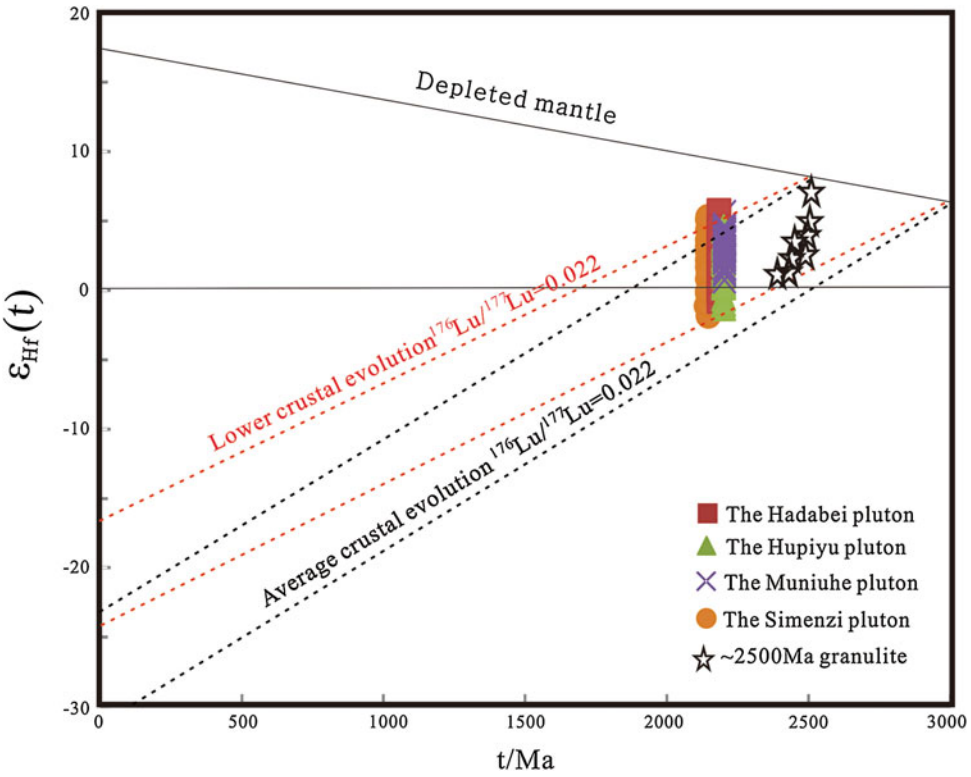

Fig. 7.9 Zircon Hf isotopic compositions of the granites. Zircon $\varepsilon_{Hf}(t)$ values were calculated at the crystallization ages of these granites. Values of ~2500 Ma granulite are from Jiang et al. (2013)

Table 7.5 In-situ Hf isotopic data for zircons of the gneissic granites

Spot	$^{176}Yb/^{177}Hf$	$^{176}Lu/^{177}Hf$	$^{176}Hf/^{177}Hf$	2σ	Age	$\varepsilon_{Hf}(t)$	$f_{Lu/Hf}$	T_{DM1}(Hf)(Ma)	T_{DM2}(Hf)(Ma)
Hadabei									
HD-2-1	0.081416	0.001535	0.281519	0.000024	2173	2.1	−0.95	2467	2636
HD-2-2	0.077523	0.001437	0.281426	0.000028	2173	−1.1	−0.96	2590	2831
HD-2-3	0.090094	0.001663	0.281543	0.000026	2173	2.7	−0.95	2442	2595
HD-2-4	0.065516	0.001235	0.281535	0.000028	2173	3.1	−0.96	2425	2574
HD-2-5	0.072699	0.001355	0.281602	0.000027	2173	5.3	−0.96	2340	2437
HD-2-6	0.100365	0.002538	0.281534	0.000023	2173	1.1	−0.92	2513	2694
HD-2-7	0.071790	0.001327	0.281517	0.000025	2173	2.3	−0.96	2456	2622
HD-2-8	0.087769	0.001598	0.281482	0.000028	2173	0.7	−0.95	2523	2723
HD-2-9	0.082085	0.001457	0.281488	0.000026	2173	1.1	−0.96	2505	2697
HD-2-10	0.046407	0.000861	0.281402	0.000029	2173	−1.1	−0.97	2584	2832
HD-2-11	0.047838	0.000954	0.281466	0.000024	2173	1.0	−0.97	2502	2700
HD-2-12	0.066753	0.001304	0.281563	0.000025	2173	4.0	−0.96	2391	2519
HD-2-13	0.057992	0.001174	0.281491	0.000023	2173	1.6	−0.96	2482	2665
HD-2-14	0.068398	0.001366	0.281439	0.000022	2173	−0.5	−0.96	2567	2796
HD-2-15	0.092179	0.001819	0.281481	0.000025	2173	0.3	−0.95	2539	2745
HD-2-16	0.061374	0.001243	0.281488	0.000023	2173	1.4	−0.96	2491	2678
HD-2-17	0.093567	0.001855	0.281514	0.000024	2173	1.4	−0.94	2495	2676
HD-2-18	0.073175	0.001458	0.281475	0.000025	2173	0.6	−0.96	2523	2726
HD-2-19	0.051215	0.000997	0.281452	0.000025	2173	0.5	−0.97	2524	2734
HD-2-20	0.044025	0.000835	0.281434	0.000026	2173	0.1	−0.97	2538	2759
HD-2-21	0.055230	0.001028	0.281477	0.000030	2173	1.3	−0.97	2492	2682

(continued)

Table 7.5 (continued)

Spot	$^{176}Yb/^{177}Hf$	$^{176}Lu/^{177}Hf$	$^{176}Hf/^{177}Hf$	2σ	Age	$\varepsilon_{Hf}(t)$	$f_{Lu/Hf}$	T_{DM1}(Hf)(Ma)	T_{DM2}(Hf)(Ma)
HD-2-22	0.057294	0.001066	0.281465	0.000026	2173	0.8	−0.97	2511	2712
HD-2-23	0.084556	0.001544	0.281545	0.000027	2173	3.0	−0.95	2431	2580
HD-2-24	0.063984	0.001187	0.281489	0.000022	2173	1.5	−0.96	2486	2671
HD-2-25	0.071754	0.001606	0.281599	0.000024	2173	4.8	−0.95	2360	2467
HD-2-26	0.068927	0.001250	0.281434	0.000026	2173	−0.5	−0.96	2566	2797
HD-2-27	0.106870	0.001855	0.281486	0.000029	2173	0.4	−0.94	2534	2737
HD-2-28	0.070238	0.001215	0.281412	0.000024	2173	−1.3	−0.96	2594	2842
HD-2-29	0.099390	0.002123	0.281563	0.000025	2173	2.8	−0.94	2444	2593
HD-2-30	0.074455	0.001353	0.281508	0.000025	2173	1.9	−0.96	2470	2644
Hupiyu									
HP-1-1	0.074395	0.001386	0.281494	0.000021	2183.7	1.6	−0.96	2492	2671
HP-1-2	0.044793	0.000846	0.281464	0.000023	2183.7	1.4	−0.97	2498	2688
HP-1-3	0.050848	0.000967	0.281506	0.000026	2183.7	2.7	−0.97	2448	2607
HP-1-4	0.088921	0.001619	0.281475	0.000028	2183.7	0.6	−0.95	2534	2734
HP-1-5	0.053146	0.001007	0.281548	0.000026	2183.7	4.1	−0.97	2393	2518
HP-1-6	0.075915	0.001421	0.281539	0.000029	2183.7	3.2	−0.96	2432	2576
HP-1-7	0.071330	0.001294	0.281483	0.000025	2183.7	1.4	−0.96	2501	2687
HP-1-8	0.057529	0.001036	0.281498	0.000027	2183.7	2.3	−0.97	2464	2631
HP-1-9	0.074812	0.001346	0.281468	0.000026	2183.7	0.8	−0.96	2525	2725
HP-1-10	0.088741	0.001577	0.281476	0.00003	2183.7	0.7	−0.95	2530	2728
HP-1-11	0.099652	0.001774	0.281559	0.00003	2183.7	3.4	−0.95	2427	2564
HP-1-12	0.085097	0.001539	0.281535	0.00003	2183.7	2.9	−0.95	2445	2595
HP-1-13	0.069756	0.001278	0.281489	0.000027	2183.7	1.6	−0.96	2492	2672
HP-1-14	0.094813	0.001765	0.281519	0.00003	2183.7	2.0	−0.95	2482	2651
HP-1-15	0.035352	0.000687	0.281448	0.000025	2183.7	1.0	−0.98	2509	2709
HP-1-16	0.075686	0.001474	0.281545	0.000025	2183.7	3.3	−0.96	2427	2567
HP-1-17	0.089821	0.001733	0.28162	0.000026	2183.7	5.6	−0.95	2338	2426
HP-1-18	0.066379	0.001308	0.281495	0.000029	2183.7	1.8	−0.96	2485	2662
HP-1-19	0.071755	0.001419	0.281454	0.000029	2183.7	0.2	−0.96	2550	2762
HP-1-20	0.07638	0.001479	0.281483	0.000031	2183.7	1.1	−0.96	2513	2704
HP-1-21	0.046277	0.000901	0.281462	0.000026	2183.7	1.2	−0.97	2504	2697
HP-1-22	0.073131	0.001373	0.281446	0.000026	2183.7	−0.1	−0.96	2558	2775
HP-1-23	0.077632	0.001406	0.281431	0.000031	2183.7	−0.6	−0.96	2581	2811
HP-1-24	0.123147	0.002167	0.281567	0.000027	2183.7	3.1	−0.93	2441	2582
HP-1-25	0.067404	0.001282	0.28145	0.000028	2183.7	0.2	−0.96	2546	2758
HP-1-26	0.082199	0.001428	0.28145	0.000028	2183.7	0.0	−0.96	2556	2772
HP-1-27	0.09599	0.00169	0.281586	0.000024	2183.7	4.4	−0.95	2383	2497
HP-1-28	0.099401	0.001691	0.281481	0.000028	2183.7	0.7	−0.95	2530	2728
HP-1-29	0.067734	0.001195	0.281498	0.000022	2183.7	2.1	−0.96	2474	2645
HP-1-30	0.044159	0.000818	0.281477	0.000023	2183.7	1.9	−0.98	2478	2657
Muniuhe									
MN-6-1	0.068236	0.001302	0.281523	0.000019	2200.6	3.2	−0.96	2446	2590
MN-6-2	0.064231	0.001825	0.281468	0.000019	2200.6	0.4	−0.95	2558	2759
MN-6-3	0.064976	0.001227	0.281555	0.000029	2200.6	4.4	−0.96	2397	2513
MN-6-4	0.089113	0.001725	0.281519	0.000022	2200.6	2.4	−0.95	2479	2638

(continued)

Table 7.5 (continued)

Spot	$^{176}Yb/^{177}Hf$	$^{176}Lu/^{177}Hf$	$^{176}Hf/^{177}Hf$	2σ	Age	$\varepsilon_{Hf}(t)$	$f_{Lu/Hf}$	T_{DM1}(Hf)(Ma)	T_{DM2}(Hf)(Ma)
MN-6-6	0.036055	0.000868	0.28151	0.000019	2200.6	3.3	−0.97	2436	2579
MN-6-7	0.075335	0.001412	0.281455	0.000021	2200.6	0.6	−0.96	2548	2749
MN-6-8	0.089766	0.001845	0.281424	0.000021	2200.6	−1.2	−0.94	2621	2857
MN-6-9	0.07596	0.001384	0.281494	0.00002	2200.6	2.0	−0.96	2492	2661
MN-6-10	0.096975	0.001864	0.281491	0.00002	2200.6	1.2	−0.94	2528	2712
MN-6-12	0.069868	0.001299	0.281537	0.00003	2200.6	3.7	−0.96	2427	2559
MN-6-13	0.05172	0.000965	0.28149	0.000029	2200.6	2.5	−0.97	2470	2632
MN-6-14	0.056778	0.001194	0.281416	0.000028	2200.6	−0.5	−0.96	2587	2815
MN-6-15	0.066777	0.001233	0.281468	0.000029	2200.6	1.3	−0.96	2518	2704
MN-6-16	0.096858	0.001738	0.281519	0.000026	2200.6	2.4	−0.95	2480	2639
MN-6-17	0.04692	0.00087	0.281488	0.000022	2200.6	2.6	−0.97	2467	2627
MN-6-18	0.088128	0.001722	0.281559	0.000025	2200.6	3.8	−0.95	2423	2550
MN-6-19	0.096699	0.001725	0.28152	0.000026	2200.6	2.4	−0.95	2478	2636
MN-6-20	0.079048	0.001882	0.281582	0.000025	2200.6	4.4	−0.94	2401	2514
MN-6-21	0.039258	0.000737	0.281491	0.000026	2200.6	2.9	−0.98	2454	2609
MN-6-22	0.052304	0.001005	0.281522	0.000022	2200.6	3.6	−0.97	2429	2565
MN-6-23	0.060564	0.001121	0.28146	0.000027	2200.6	1.2	−0.97	2521	2712
MN-6-24	0.046786	0.001007	0.281397	0.000024	2200.6	−0.9	−0.97	2600	2839
MN-6-25	0.071917	0.001364	0.281481	0.000022	2200.6	1.6	−0.96	2509	2688
MN-6-26	0.098614	0.001963	0.281494	0.000019	2200.6	1.1	−0.94	2531	2714
MN-6-27	0.037522	0.000763	0.281455	0.000021	2200.6	1.5	−0.98	2505	2690
MN-6-28	0.074898	0.001485	0.281502	0.000025	2200.6	2.1	−0.96	2487	2653
MN-6-30	0.079432	0.001923	0.281469	0.000025	2200.6	0.3	−0.94	2563	2765
Simenzi									
SM-1-1	0.118087	0.001896	0.281571	0.000023	2203	4.0	−0.94	2418	2538
SM-1-2	0.082921	0.001361	0.281538	0.000018	2203	3.7	−0.96	2429	2561
SM-1-3	0.097105	0.001612	0.281547	0.000019	2203	3.6	−0.95	2433	2565
SM-1-4	0.123158	0.002059	0.281585	0.000023	2203	4.3	−0.94	2408	2522
SM-1-5	0.089992	0.001561	0.281544	0.000023	2203	3.6	−0.95	2434	2566
SM-1-6	0.146659	0.002533	0.281567	0.000022	2203	2.9	−0.92	2465	2605
SM-1-7	0.105565	0.001815	0.28155	0.00002	2203	3.4	−0.95	2442	2577
SM-1-8	0.075895	0.00138	0.281555	0.000021	2203	4.2	−0.96	2407	2526
SM-1-9	0.123441	0.002152	0.281624	0.00002	2203	5.5	−0.94	2359	2445
SM-1-10	0.078022	0.001429	0.281517	0.00002	2203	2.8	−0.96	2463	2614
SM-1-11	0.101877	0.001895	0.281563	0.00002	2203	3.7	−0.94	2429	2555
SM-1-12	0.139913	0.002588	0.281551	0.000019	2203	2.3	−0.92	2492	2645
SM-1-13	0.071504	0.00133	0.281563	0.000018	2203	4.6	−0.96	2393	2503
SM-1-14	0.085331	0.001575	0.281519	0.000024	2203	2.7	−0.95	2470	2623
SM-1-15	0.062735	0.001184	0.281512	0.000022	2203	3.0	−0.96	2454	2602
SM-1-16	0.05278	0.000967	0.281477	0.000021	2203	2.1	−0.97	2488	2659
SM-1-17	0.045639	0.000869	0.281436	0.000022	2203	0.8	−0.97	2538	2740
SM-1-18	0.118256	0.00207	0.28158	0.000024	2203	4.1	−0.94	2416	2534
SM-1-19	0.037631	0.000678	0.281455	0.000019	2203	1.7	−0.98	2499	2681
SM-1-20	0.11944	0.002047	0.28156	0.000023	2203	3.4	−0.94	2443	2576
SM-1-21	0.093779	0.00156	0.281489	0.000018	2203	1.6	−0.95	2510	2687

(continued)

Table 7.5 (continued)

Spot	$^{176}Yb/^{177}Hf$	$^{176}Lu/^{177}Hf$	$^{176}Hf/^{177}Hf$	2σ	Age	$\varepsilon_{Hf}(t)$	$f_{Lu/Hf}$	T_{DM1}(Hf)(Ma)	T_{DM2}(Hf)(Ma)
SM-1-22	0.116543	0.001937	0.281526	0.000023	2203	2.4	−0.94	2484	2640
SM-1-23	0.094341	0.001611	0.281539	0.000025	2203	3.3	−0.95	2444	2582
SM-1-24	0.105058	0.001704	0.281536	0.000017	2203	3.1	−0.95	2454	2597
SM-1-25	0.143297	0.002384	0.281599	0.000021	2203	4.3	−0.93	2410	2521
SM-1-26	0.099439	0.001666	0.281562	0.00002	2203	4.1	−0.95	2415	2537
SM-1-27	0.106738	0.001827	0.281494	0.000023	2203	1.4	−0.94	2521	2701
SM-1-28	0.035731	0.000676	0.281441	0.00002	2203	1.2	−0.98	2518	2711
SM-1-29	0.064531	0.001129	0.281551	0.000019	2203	4.5	−0.97	2397	2511
SM-1-30	0.097948	0.001748	0.281581	0.000024	2203	4.6	−0.95	2394	2502

Note $\varepsilon_{Hf}(0) = (((^{176}Hf/^{177}Hf)_S/(^{176}Hf/^{177}Hf)_{CHUR,0} - 1) \times 10{,}000$, $f_{Lu/Hf} = (^{176}Lu/^{177}Hf)_S/(^{176}Lu/^{177}Hf)_{CHUR} - 1$
$\varepsilon_{Hf}(t) = (((^{176}Hf/^{177}Hf)_S - (^{176}Lu/^{177}Hf)_S \times (e^{\lambda t} - 1))/((^{176}Hf/^{177}Hf)_{CHUR,0} - (^{176}Lu/^{177}Hf)_{CHUR} \times (e^{\lambda t} - 1)) - 1) \times 10{,}000$
$T_{DM1}(Hf) = 1/l \times (1 + ((^{176}Hf/^{177}Hf)_S - (^{176}Hf/^{177}Hf)_{DM})/((^{176}Lu/^{177}Hf)_S - (^{176}Lu/^{177}Hf)_{DM}))$
$T_{DM2}(Hf) = T_{DM1}(Hf) - (T_{DM1}(Hf) - t)((f_{CC} - f_S)/(f_{CC} - f_{DM}))$
where, $(^{176}Lu/^{177}Hf)_S$ and $(^{176}Hf/^{177}Hf)_S$ are the measured values of samples; $(^{176}Lu/^{177}Hf)_{CHUR} = 0.0332$ and $(^{176}Hf/^{177}Hf)_{CHUR,0} = 0.282772$; $(^{176}Lu/^{177}Hf)_{DM} = 0.0384$ and (176Hf/177Hf)DM = 0.28325; $f_{CC} = -0.548$ (average continental crust), $f_{DM} = 0.16$, t = crystallization time of zircon, $\lambda = 1.865 \times 10^{-11}$ $year^{-1}$ (Soderlund et al. 2004) are used in calculation

Table 7.6 Sm–Nd isotopic data of gneissic granites in the Jiao-Liao-Ji Belt

Sample	Sm (ppm)	Nd (ppm)	$^{147}Sm/^{144}Nd$	$^{143}Nd/^{144}Nd$	2σ	T (Ma)	I_{Nd}	$\varepsilon_{Nd}(0)$	$\varepsilon_{Nd}(T)$	$f_{Sm/Nd}$	T_{DM1}	T_{DM2}
Dafangshen												
DF-1	11.386	58.06	0.124421129	0.511536	2	2180	0.509749397	−21.497	−1.258	−0.3675	2740	2702
DF-2	23.86	113.74	0.13309361	0.51158452	3	2180	0.509673386	−20.55	−2.749	−0.3234	2941	2821
DF-3	24.66	124.24	0.125930701	0.51158202	5	2180	0.509773741	−20.599	−0.78	−0.3598	2708	2664
DF-6	12.943	65.25	0.125850349	0.51153065	1	2180	0.509723525	−21.601	−1.765	−0.3602	2793	2743
Hadabei												
HD-2	7.482	35.76	0.132745615	0.51158772	3	2173	0.509687748	−20.488	−2.646	−0.3251	2923	2807
HD-3	10.138	49.26	0.130574349	0.51150663	3	2173	0.509637735	−22.07	−3.627	−0.3362	2993	2886
HD-4	8.568	43	0.126418605	0.5115008	2	2173	0.509691385	−22.183	−2.575	−0.3573	2862	2802
Hupiyu												
HP-1	8.208	26.3	0.198007477	0.51221656	2	2184	0.509368053	−8.221	−8.636	0.00665	8835	3269
HP-2	6.828	19.962	0.217014849	0.51273939	3	2184	0.509617446	1.9778	−3.744	0.10328	####	2985
Muniuhe												
MN-1	0.771	4.156	0.117700641	0.51139916	22	2200	0.509693442	−24.166	−1.844	−0.4016	2764	2765
MN-6	0.495	1.712	0.18344312	0.51252019	4	2200	0.509861731	−2.2981	1.4576	−0.0674	3150	2500
Simenzi												
SM-1	5.766	24.14	0.151543517	0.51174952	5	2203	0.509550334	−17.332	−4.574	−0.2296	3407	2985
SM-2	14.874	72.197	0.13070994	0.5116597	3	2203	0.509762849	−19.084	−0.405	−0.3355	2721	2653
SM-3	1.13	4.414	0.162422468	0.51189613	29	2203	0.50953907	−14.472	−4.795	−0.1743	3694	3001
SM-5	0.864	3.78	0.145018007	0.51178192	4	2203	0.509677432	−16.7	−2.081	−0.2627	3016	2786

Note $\varepsilon_{Nd} = (((^{143}Nd/^{144}Nd)_S/(^{143}Nd/^{144}Nd)_{CHUR} - 1) \times 10{,}000$, $f_{Sm/Nd} = (^{147}Sm/^{144}Nd)_S/(^{147}Sm/^{144}Nd)_{CHUR} - 1$, $T_{DM1} = 1/\lambda \times \ln(1 + ((^{143}Nd/^{144}Nd)_S - (^{143}Nd/^{144}Nd)_{DM})/((^{147}Sm/^{144}Nd)_S - (^{147}Sm/^{144}Nd)_{DM}))$, $T_{DM2} = T_{DM1} - (T_{DM1} - t)((-0.4 - f_{Sm/Nd})(-0.4 - 0.08592))$, $^{143}Nd/^{144}Nd_{CHUR} = 0.512638$, $^{147}Sm/^{144}Nd_{CHUR} = 0.1967$, $^{143}Nd/^{144}Nd_{DM} = 0.51315$, $^{147}Sm/^{144}Nd_{DM} = 0.2137$; $\lambda_{Rb} = 1.42 \times 10^{-11}$/year, and $\lambda_{Sm} = 6.54 \times 10^{-12}$/year

K_2O/Na_2O ratios in the ranges of 1.6–2.1, 1.3 and 0.5–1.3, respectively. They also have relatively low $\varepsilon_{Nd}(t)$ values (−2.8 to −0.8, −8.6 to −3.7, −4.8 to −0.41, respectively), which are lower than that of the late Archean mafic-ultra mafic amphibolites at 2.2 Ga (−1.19 to 10.51), but in the range of TTG's ε_{Nd} (2.2 Ga) (−16.41 to 1.94). Hence, we suggest that the source of the felsic end member of the Dafangshen, Hupiyu and Simenzi plutons is dominated by the Archean TTG gneisses, which is consistent with the high contents of SiO_2 (70.4–77.1 wt%) of the these plutons. The Muniuhe and Hadabei plutons, however, show relatively low K_2O/Na_2O ratios (mostly <1) and high $\varepsilon_{Nd}(t)$ values (−3.6 to 1.46), suggesting that some amounts of the late Archean amphibolites could have been involved in the source of the felsic end member of the two granite plutons.

We suggest that the other end member having contributed to forming the gneissic granites is mafic magma derived from a mantle source that was previously metasomatized by subduction zone fluids/melts released from a down-going oceanic slab. This is first supported by the positive $\varepsilon_{Nd}(t)$ values (+1.5 for sample MN-6) and zircon $\varepsilon_{Hf}(t)$ values (+5.6 for sample HP-1) of some gneissic granite samples, which is indicative of involvement of mantle-derived magma in the source. The abundance of euhedral hornblende in MMEs (Fig. 7.3c) and in coeval meta-mafic rocks (Li et al. 2003) suggests that the parental magma of the MMEs should be a hydrous basaltic magma (Chen et al. 2009, 2013), possibly derived from a mantle source above a subduction zone. The coeval meta-mafic rocks show high LILEs, such as Sr, Ba, Th and depletion of HSFEs, such as Nb, Ta, and Ti, which, along with the typical calc-alkaline features of the basaltic rocks (Faure et al. 2004; Wang et al. 2012; Li and Chen 2014), suggest a metasomatized lithospheric mantle for the source of the basalts. In addition, the meta-mafic rocks have extremely high K/Ta (>20,000, data from Li and Chen 2014) and Ba/La ratios (1.3–1062). This is probably caused by the high mobility of K and Ba in subduction zone fluids (Huang et al. 2001).

7.7 Geodynamic Setting

Most researchers believe that the Paleoproterozoic Liaoji Belt was formed in an intra-continental rifting setting on the NCC (Zhang and Yang 1988; Peng and Palmer 1995; Chen et al. 2003; Li et al. 2003, 2005; Luo et al. 2004, 2008; Zhao et al. 2005; Li and Zhao 2007). Some others, however, suggested that the Paleoproterozoic Belt formed as a result of arc-continent collision at ca. 1.9 Ga (Bai 1993; He and Ye 1998a, b; Faure et al. 2004; Lu et al. 2006; Wang et al. 2011; Meng et al. 2013). Our new data on the Paleoproterozoic gneissic granites suggest a continental arc setting for these granites and thus for the Paleoproterozoic belt, and the arguments are as below.

Most gneissic granites in the Paleoproterozoic belt show calc-alkaline affinity, although some of them show features of A-types, e.g., the Dafangshen pluton, due probably to addition of boron in magma system. The calc-alkaline affinity is manifested by both the chemical compositions of I-type and the common occurrence of hornblende, apatite, magnetite and sphene, typical features of arc magmas. In addition, the arc affinity of the gneissic granites are strongly supported by the hydrous nature and mixed source characteristics (e.g., the presence of MMEs). The hydrous nature, as shown by the abundance of hydrous phases such as hornblende in the plutons, could be attributable to mixing of basaltic magma derived from a mantle- wedge previously metasomatized by subduction fluid/melt. Actually, the coeval metabasaltic rocks also show typical calc-alkaline affinity such as enrichment of LILEs (La, Th, Sr, Rb, etc.) and depletion of HSFEs (e.g., Nb, Ti) (Faure et al. 2004; Li and Chen 2014). Importantly, the gneissic granites show large variation in isotopic compositions with $\varepsilon_{Nd}(t) = -8.6$ to 1.5 and $\varepsilon_{Hf}(t) = -1.26$ to 5.59, which is consistent with the model of magma mixing between mantle-wedge derived basic magma and crustal melts in an arc setting.

As for the polarity of subduction, Bai (1993) proposed a northward subduction beneath the Longgang Block, while passive continental margin-type clastic sedimentary rocks were formed in the northern margin of the Rangnim Block. Final closure of the Paleoproterozoic ocean at ca. 1.9 Ga led to a continent-arc-continent collision and subsequent thrusting, forming the Liaoji Belt. In contrast, Faure et al. (2004) proposed a southward subduction beneath the Rangnim Block based on the fact that the South Liaohe Group is dominated by volcanic rocks. Our new zircon U-Pb data on the gneissic granites reveal the presence of some inherited zircons with ages of ~2500 and ~2700 Ma. These inherited zircons are in agreement with the age data reported for the TTG gneisses from the Longgang block that has received lots of U-Pb dating with ages ranging from 2500 to 3800 Ma but clustering at ~2500 and ~2700 Ma, which are commonly accepted as two major Archean crustal growth periods in the North China Craton (Zhao et al. 2001; Gao et al. 2004, 2005). By contrast, published data suggest that the Rangnim block contain rare rocks older than 2500 Ma (mainly 2440–2500 Ma; Wu et al. 2007a, b). So we can conclude that the source of the arc magmatism is mainly the lower crust beneath the Longgang Block in the north, which suggests a northward subduction in the Paleoproterozoic.

7.8 Conclusions

Most Paleoproterozoic gneissic granites in the Liaoji Belt are I-type granites, rather than A-type granites. The A-type features shown by some plutons (e.g., the Dafangshen pluton)

are attributable to extra addition of boron in the magma system, which have prolonged magma evolution, producing the highly evolved granites. The gneissic granites in the JLJB were formed at ca. 2.17–2.20 Ga, and were metamorphosed at ca. 1.9 Ga. These granites contain inherited zircons with Ahchean ages (ca. 2.5 Ga and 2.7–2.8 Ga). Based on the petrographical, mineralogical and geochemistry characteristics, we suggest that mixing/mingling of lower crust-derived felsic magma with enriched mantle-derived mafic magma might have resulted in formation of these gneissic granites. Overall, the petrology (common occurrence of hornblende, magnetite and sphene), geochemical data (the calc-alkaline affinity) and large variation of Nd–Hf isotopic data suggest that the Paleoproterozoic granites formed in a continental arc setting, rather than in a rifting setting as suggested by many other researchers.

References

Anderson, A. T. (1976). Magma mixing: Petrologicalprocess and volcanological tool. *Journal of Volcanologyand Geothermal Research, 1*, 3–33.

Bai, J. (1993). *The Precambrian geology and Pb–Zn mineralization in the northern margin of North China Platform*. Beijing: Geological Publishing House (in Chinese with English abstract).

Bai, J., & Dai, F.-Y. (1998). Archean crust of China. In X. Y. Ma, J. Bai (Eds.), *Precambrian crustal evolution of China* (pp. 15–86). Beijing: Springer Geological Publishing House (in Chinese with English abstract).

Bau, M. (1996). Controls on the fractionation of isovalent trace elements in magmatic and aqueous systems: Evidence from Y/Ho, Zr/Hf, and lanthanide tetrad effect. *Contribution to Mineralogy and Petrology, 123*, 323–333.

Bonin, B. (1990). From orogenic to anorogenic settings: Evolution of granitoid suites after a major orogenesis. *Geological Journal, 25*, 261–270.

Bonin, B. (2004). Do coeval mafic and felsic magmas in post-collisional to within-plate regimes necessarily imply two contrasting, mantle and crust, sources? A review. *Lithos, 78*, 1–24.

Cai, J.-H., Yan, G.-H., Mu, B.-L., Xu, B.-L., Shao, H.-X., & Xu, R.-H. (2002). U-Pb and Sm-Nd isotopic ages of an alkaline syenite complex body in Liangtun-Kuangdongguo, Gai County, Liaoning Province, China and their geological significance. *Acta Petrologica Sinica*, *18*, 349–354 (in Chinese with English abstract).

Chappell, B. W., White, A. J. R., Williams, I. S., Wyborn, D., & Wyborn, L. A. I. (2000). Lachlan Fold Belt granites revisited: High- and low-temperature granites andtheir implications. *Australian Journal of Earth Sciences, 47*, 123–138.

Chen, B., Chen, Z.-C., & Jahn, B.-M. (2009). Origin of mafic enclaves from the Taihang Mesozoic orogen, North China Craton. *Lithos*, *110*, 343–358.

Chen, B., Jahn, B.-M., & Suzuki, K. (2013). Petrological and Nd-Sr-Os isotopic constraints on the origin of high-Mg adakitic rocks from the North China Craton: Tectonic implications. *Geology, 41*, 91–94.

Chen, B., Ma, X.-H., & Wang, Z.-Q. (2014). Origin of the fluorine-rich highly differentiated granites from the Qianlishan composite plutons (South China) and implications for polymetallic mineralization. *Journal of Asian Earth Sciences, 93*, 301–314.

Chen, B., Tian, W., Jahn, B. M., & Chen, Z.-C. (2008). Zircon SHRIMP U-Pb ages and in-situ Hf isotopic analysis for the Mesozoic intrusions in South Taihang, North China Craton: Evidence for hybridization between mantle-derived magmas and crustal components. *Lithos, 102*, 118–137.

Chen, R.-D., Li, X.-D., & Zhang, F.-S. (2003). Several problems about the Paleoproterozoic geology of eastern Liaoning. *Geology of China*, *30*, 207–213 (in Chinese with English abstract).

Clynne, M. A. (1999). A complex magma mixing origin for rocks erupted in 1915, Lassen Peak, California. *Journal of Petrology, 40*, 105–132.

Faure, M., Lin, W., Monie, P., & Bruguier, O. (2004). Palaeoproterozoic arc magmatism and collision in Liaodong Peninsula (north-east China). *Terra Nova*, *16*, 75–80.

Feeley, T. C., Wilson, L. F., & Underwood, S. J. (2008). Distribution and compositions of magmatic inclusions in the Mount Helen dome, Lassen Volcanic Center, California: Insights into magma chamber processes. *Lithos, 106*, 173–189.

Gao, S., Rudnick, R. L., Yuan, H.-L., Liu, X.-M., Liu, Y.-S., Xu, W.-L., et al. (2004). Recycling lower continental crust in the North China Craton. *Nature*, *432*, 892–897.

Geng, Y.-S., Wan, Y.-S., & Shen, Q.-H. (2002). Precambrian basic volcanism and crustal growth in the North China Craton. *Acta Geologica Sinica*, *76*(2), 199–208.

Griffin, W. L., Wang, X., Jackson, S. E., Pearson, N. J., O'Reilly, S. Y., Xu, X., et al. (2002). Zircon chemistry and magma mixing, SE China: In-situ analysis of Hf isotopes. *Tonglu and Pingtan igneous complexes. Lithos, 61*, 237–269.

Guo, J.-H., Sun, M., Chen, F.-K., & Zhai, M.-G. (2005). Sm-Nd and SHRIMP U-Pb zircon geochronology of high-pressure granulites in the Sanggan area, North China craton: Timing of Paleoproterozoic continental collision. *Journal of Asian Earth Sciences*, *24*, 629–642.

Hao, D.-F., Li, S.-Z., Zhao, G.-C., Sun, M., Han, Z.-Z., & Zhao, G.-T. (2004). Origin and its constraint to tectonic evolution of Paleoproterozoic granitoids in the eastern Liaoning and Jilin province, North China. *Acta Petrologica Sinica*, *20*, 1409–1416 (in Chinese with English abstract).

He, G.-P., & Ye, H.-W. (1998a). Compositions and main characteristics of Early Proterozoic metamorphic terrains in the eastern Liaoning and the southern Jilin areas. *Journal of Changchun University Science and Technology*, *28*, 121–126 (in Chinese with English abstract).

He, G.-P., & Ye, H.-W. (1998b). Two types of Early Proterozoic metamorphism in the Eastern Liaoning and Southern Jilin provinces and their tectonic implications. *Acta Petrologica Sinica*, *14*, 152–162 (in Chinese with English abstract).

Holden, P., Halliday, A. N., & Stephens, W. E. (1987). Neodymium and strontium isotope content of microdiorite enclaves points to mantle input to granitoid production. *Nature, 330*, 53–56.

Huang, D.-Z., Gao, J., & Dai, T.-G. (2001). Geochemical tracing of the fluid in subduction zones. *Earth Science Frontiers*, *8*(3), 131–139 (in Chinese with English abstract).

Irber, W. (1999). The lanthanide tetrad effect and its correlation with K/Rb, Eu/Eu*, Sr/Eu, Y/Ho, and Zr/Hf of evolving peraluminous granite suites. *Geochimica et Cosmochimica Acta, 63*, 489–508.

Jahn, B.-M., & Ernst, W. G. (1990). Late Archean Sm-Nd Isochron Age for mafic-ultramafic supracrustal amphibolites from the Northeastern Sino-Korean Craton, China. *Precambrian Research, 46*, 295–306.

Jahn, B.-M., Wu, F.-Y., Capdevila, R., Martineau, F., Zhao, Z.-H., & Wang, Y.-X. (2001). Highly evolved juvenile granites with tetrad REE patterns: The Woduhe and Baerzhe granites from the Great Xing'an Mountains in NE China. *Lithos, 59*, 171–198.

Janoušek, V., Braithwaite, C. J. R., Bowes, D. R., & Gerdes, A. (2004). Magma-mixing in the genesis of Hercynian calc-alkaline granitoids:

An integrated petrographic and geochemical study of the Sázava intrusion, Central Bohemian Pluton, Czech Republic. *Lithos, 78*, 67–99.

Jiang, N., Guo, J.-H., & Chang, G.-H. (2013). Nature and evolution of the lower crust in the eastern North China Craton: A review. *Earth-Science Reviews, 122*, 1–9.

Kemp, A. I. S. (2004). Petrology of high-Mg, low-Ti igneous rocks of the Glenelg River Complex (SE Australia) and the nature of their interaction with crustal melts. *Lithos, 78*, 119–156.

Kemp, A. I. S., & Hawkesworth, C. J. (2006). Using hafnium and oxygen isotopes in zircons to unravel the record of crustal evolution. *Chemical Geology, 226*, 144–162.

Kröner, A., Compston, W., Zhang, G.-W., Guo, A.-L., & Todt, W. (1988). Age and tectonic setting of Late Archean greenstone–gneiss terrain in Henan Province, China, as revealed by single-grain zircon dating. *Geology, 16*, 211–215.

Leake, B. E., Woolley, A. R., Aprs, C. E. S., et al. (1997). Nomenclature of amphiboles: Report of the subcommittee on amphiboles of the international mineralogical association, commission on new minerals and mineral names. *The Canadian Mineralogist, 35*, 219–246.

Li, S.-Z., & Zhao, G.-C. (2007). SHRIMP U-Pb zircon geochronology of the Liaoji granitoids: Constraints on the evolution of the Paleoproterozoic Jiao-Liao-Ji belt in the Eastern Block of the North China Craton. *Precambrian Research, 158*, 1–16.

Li, S.-Z., Zhao, G.-C., Santosh, M., Liu, X., & Dai, L.-M. (2011). Palaeoproterozoic tectonothermal evolution and deep crustal processes in the Jiao-Liao-Ji Belt, North China Craton: A review. *Geological Journal*, *46*, 525–543.

Li, S.-Z., Zhao, G.-C., Sun, M., Han, Z.-Z., Hao, D.-F., Luo, Y., et al. (2005). Deformation history of the Paleoproterozoic Liaohe Group in the Eastern Block of the North China Craton. *Journal of Asian Earth Sciences*, *24*(5), 659–674.

Li, S.-Z., Zhao, G.-C., Sun, M., Hao, D.-F., Luo, Y., & Yang, Z.-Z. (2003). Paleoproterozoic tectonothermal evolution and deep crustal processes of the Jiao–Liao Block. *Acta Geologica Sinica*, *73*, 328–340 (in Chinese with English abstract).

Li, Z., & Chen, B. (2014). Geochronology and geochemistry of the Paleoproterozoic meta-basalts from the Jiao-Liao-Ji Belt, North China Craton: Implications for petrogenesis and tectonic setting. *Precambrian Research, 255*, 653–667.

Liu, D.-Y., Nutman, A. P., Compston, W., Wu, J.-S., & Shen, Q.-H. (1992). Remmants of ≥3800 Ma crust in the Chinese part of the Sino- Korean Craton. *Geology, 20*, 339–342.

Lu, X.-P., Wu, F.-Y., Guo, J.-H., Wilde, S. A., Yang, J.-H., Liu, X.-M., et al. (2006). Zircon U-Pb geochronological constraints on the Paleoproterozoic crustal evolution of the Eastern block in the North China Craton. *Precambrian Research*, *146*, 138–164.

Lu, X.-P., Wu, F.-Y., Guo, J.-H., & Yin, C.-J. (2005). Late Paleoproterozoic granitic magmatism and crustal evolution in the Tonghua region, northeast China. *Acta Petrologica Sinica*, *21*(3), 721–736 (in Chinese with English abstract).

Lu, X.-P., Wu, F.-Y., Lin, J.-Q., Sun, D.-Y., Zhang, Y.-B., & Guo, L.-C. (2004). Geochronological framework of early Precambrian granitic magmatism in the eastern Liaoning Peninsular: Constraints on the early Precambrian evolution of the Eastern Block of the North China Craton. *Chinese Journal of Geology*, *39*, 123–138.

Lu, L.-Z., Xu, X.-C., & Liu, F.-L. (1996). *Early Precambrian Khondalite Series in North China*. Changchun: Changchun Publishing House.

Lukkari, S., & Holtz, F. (2007). Phase relations of a F-enriched peraluminous granite: An experimental study of the Kymi topaz granite stock, southern Finland. *Contribution to Mineralogy and Petrology, 153*, 273–288.

Luo, Y., Sun, M., Zhao, G.-C., Ayers, J. C., Li, S.-Z., Xia, X.-P., et al. (2008). A comparison of U-Pb and Hf isotopic compositions of detrital zircons from the North and South Liaohe Group: Constraints on the evolution of the Jiao-Liao-Ji Belt, North China Craton. *Precambrian Research*, *163*, 279–306.

Luo, Y., Sun, M., Zhao, G.-C., Li, S.-Z., Xu, P., Ye, K., et al. (2004). LA-ICP-MS U-Pb zircon ages of the Liaohe Group in the Eastern Block of the North China Craton: Constraints on the evolution of the Jiao-Liao-Ji Belt. *Precambrian Research*, *134*, 349–371.

Ma, X.-H., Chen, B., & Yang, M.-C. (2013). Magma mixing origin for the Aolunhua porphyry related to Mo-Cu mineralization, eastern Central Asian Orogenic Belt. *Gondwana Research, 24*, 1152–1171.

Manning, D. A. C. (1981). The effect of fluorine on liquidus phase relationships in the system Qz-Ab-Or with excess water at 1 kb. *Contributions to Mineralogy and Petrology, 76*, 206–215.

Meng, E., Liu, F.-L., Cui, Y., & Cai, J. (2013). Zircon U-Pb and Lu-Hf isotopic and whole-rock geochemical constraints on the protolith and tectonic history of the Changhai metamorphic supracrustal sequence in the Jiao-Liao-Ji Belt, southeast Liaoning Province, Northeast China. *Precambrian Research, 233*, 297–315.

Noyes, H., Frey, F. A., & Wones, D. R. (1983). A tale of two plutons: Geochemical evidence bearing on the origin and differentiation of the Red Lake and Eagle Peak plutons, central Sierra Nevada, California. *Journal of Geology, 91*, 487–509.

Peccerillo, A., & Taylor, A. R. (1976). Geochemistry of Eocene calc-alkaline volcanicrocks from the Kastamonu area, Northern Turkey. *Contributions to Mineralogy and Petrology, 58*, 63–81.

Peng, Q.-M., & Palmer, M. R. (1995). The Palaeoproterozoic boron deposits in eastern Liaoning, China—A metamorphosed evaporite. *Precambrian Research, 72*, 185–197.

Peuct, J. J., Jahn, B.-M., & Cornichet, J. (1986). Zircon U-Pb age of a tonalite within the Qingyuan granite greenstone belt in Northeast China. In Chinese Academy of Geological Sciences (Ed.), *Contributions to international symposium of precambrian crustal evolution* (Vol. 3, pp. 222–229). Beijing: Geological Publishing House.

Sklyarov, E. V., & Fedorovsky, V. S. (2006). Magma mingling: Tectonic and geodynamic aspects. *Geotektonika*, *2*, 47–64.

Soderlund, U., Patchett, P. J., Vervoort, J. D. & Isachsen, C. E. (2004). The 176Lu decay constant determined by Lu-Hf and U-Pb isotope systematics of Precambrian mafic intrusions. *Earth and Planetary Science Letters, 219*(3-4), 311–324.

Sun, M., Armstrong, R. L., Lambert, R. S. J., Jiang, C.-C., & Wu, J.-H. (1993). Petrochemistry and Sr, Pb and Nd isotopic geochemistry of the Paleoproterozoic Kuandian Complex, the eastern Liaoning province, China. *Precambrian Research, 62*, 171–190.

Sun, S. S., & McDonough, W. F. (1989). Chemical and isotopic systematics of oceanicbasalts: Implications for mantle composition and processes. In: A. D. Sauders & M. J. Norry (Eds.), *Magmatism in the Ocean Basins* (Vol. 42, pp. 313–345). Geological Special Publications.

Tam, P. Y., Zhao, G.-C., Liu, F.-L., Zhou, X.-W., Sun, M., & Li, S.-Z. (2011). SHRIMP U-Pb zircon ages of high-pressure mafic and pelitic granulites and associated rocks in the Jiaobei massif: Constraints on the metamorphic ages of the Paleoproterozoic Jiao-Liao-Ji Belt in the North China Craton. *Gondwana Research*, *19*, 150–162.

Tam, P. Y., Zhao, G.-C., Sun, M., Li, S.-Z., Wu, M.-L., & Yin, C.-Q. (2012b). Petrology and meta-morphic P–T path of high-pressure mafic granulites from the Jiaobei massif inthe Jiao–Liao–Ji Belt, North China Craton. *Lithos*, *155*, 94–109.

Tam, P. Y., Zhao, G.-C., Zhou, X.-W., Sun, M., Guo, J.-H., Li, S.-Z., et al. (2012a). Metamorphic P-T path and implications of high-pressure politic granulites from the Jiaobei massif in the Jiao-Liao-Ji Belt, North China Craton. *Gondwana Research*, *22*, 104–117.

Vernon, R. H., Etheridge, M. E., & Wall, V. J. (1988). Shape and microstructure of microgranitoidenclaves: Indicators of magma mingling and flow. *Lithos, 22*, 1–11.

Wan, Y.-S., Song, B., Liu, D.-Y., Wilde, S.A., Wu, J. –S., Shi, Y.-R., et al. (2006). SHRIMP U-Pb zircon geochronology of Palaeoproterozoic metasedimentary rocks in the North China Craton: Evidence for a major Late Palaeoproterozoic tectonothermal event. *Precambrian Research*, *149*, 249–271.

Wang, H.-C., Lu, S.-N., Chu, H., Xiang, Z.-Q., Zhang, C.-J., & Liu, H. (2011). Zircon U-Pb age and tectonic setting of meta-basalts of Liaohe Group in Helan area Liaoyang, Liaoning Province. *Journal of Jilin University (Earth Science Edition)*, *41*, 1321–1334.

Wang, R.-M., Chen, Z.-Z., & Lai, X.-Y. (1997). Conversion from mantle plum regime to plate tectonic regime in North China. *Earth Sciences, 22*(3), 28–50.

Wang, W., Liu, S.-W., Wilde, S.A., Li, Q.-G., Zhang, J., Bai, X., et al. (2012). Petrogenesis and geochronology of Precambrian granitoid gneisses in Western Liaoning Province: Constraints on Neoarchean to early Paleoproterozoic crustal evolution of the North China Craton. *Precambrian Research*, *222–223*, 290–311.

Watson, E. B., & Harrison, T. M. (1983). Zircon saturation revisited: Temperature and composition effects in a variety of crustal magma types. *Earth and Planetary Science Letters, 64*(2), 295–304.

Whalen, J. B., Currie, K. L., & Chappell, B. W. (1987). A-type granites: Geochemical characteristics, discrimination and petrogenesis. *Contributions to Mineralogy and Petrology, 95*, 407–419.

White, A. J. R., Chappell, B. W., Wyborn, D. (1999). Application of the restite model to the Deddick granodiorite and its enclaves—A reinterpretation of the observations and data of Maas et al. (1997). *Journal of Petrology*, *40*, 413–421.

Wu, F.-Y., Han, R.-H., Yang, J.-H., Wilde, S. A., Zhai, M.-G., & Par, S. C. (2007a). Initial constraints on the timing of granitic magmatism in North Korea using U-Pb zircon geochronology. *Chemical Geology*, *238*, 232–248.

Wu, F.-Y., Yang, J.-H., Wilde, S. A., Liu, X.-M., Guo, J.-H., & Zhai, M.-G. (2007b). Detrital zircon U–Pb and Hf isotopic constraints on the crustal evolution of North Korea. *Precambrian Research*, *159*, 155–177.

Wu, Y.-B., & Zheng, Y.-F. (2004). Genetic mineralogy study on zircon and its restrict to explanation of U-Pb ages. *Chinese Science Bulletin*, *49*(16), 1589–1604 (in Chinese).

Yang, J.-H., Wu, F.-Y., Wild, S. A., & Zhao, G.-C. (2008). Petrogenesis and geodynamics of Late Archean magmatism in eastern Hebei, eastern North China Craton: Geochronological, geochemical and Nd-Hf isotopic evidence. *Precambrian Research*, *167*, 125–149.

Yin, A., & Nie, S. (1996). Phanerozoic palinspastic reconstruction of China and its neigh-boring regions. In A. Yin & T. M. Harrison (Eds.), *The tectonic evolution of Asia* (pp. 285–442). New York: Cambridge University Press.

Zhang, H.-F., Zhai, M.-G., Santosh, M., Diwu, C. R., & Li, S.-R. (2011). Geochronology and petrogenesis of Neoarchean potassic meta-granites from Huai'an Complex: Implications for the evolution of the North China Craton. *Gondwana Research*, *20*, 82–105.

Zhang, Q.-S. (1984). *Geology and metallogeny of the early Precambrian in China*. Jiling: Jilin People's Press.

Zhang, Q.-S., & Yang, Z.-S. (1988). *Early crust and mineral deposits of Liaodong Peninsula, China*. Beijing: Geological Publishing House (in Chinese with English abstract).

Zhao, G.-C., Sun, M., Wilde, S. A., & Li, S.-Z. (2005). Late Archean to Paleoproterozoic evolution of the North China Craton: Key issues revisited. *Precambrian Research, 136*(2), 177–202.

Zhao, G.-C., Wilde, S. A., Cawood, P. A., & Sun, M. (2001). Archean blocks and their boundaries in the North China Craton: Lithological, geochemical, structural and P–T constraints and tectonic evolution. *Precambrain Research, 107*, 45–73.

Zhao, G.-C., Wilde, S. A., Cawood, P. A., & Sun, M. (2002). SHRIMP U-Pb zircon ages of the Fuping Complex: Implications for accretion and assembly of the North ChinaCraton. *American Journal of Science, 302*, 191–226.

Zhou, X.-W., Zhao, G.-C., Wei, C.-J., Geng, Y.-S., & Sun, M. (2008). Metamorphic evolution and Th-U-Pb zircon and monazite geochronology of high-pressure pelitic granulites in the Jiaobei massif of the North China Craton. *American Journal of Science*, *308*, 328–350.

Genetic Mechanism and Metamorphic Evolution of Khondalite Series Within the Paleoproterozoic Mobile Belts, North China Craton

8

Fu-Lai Liu, Ping-Hua Liu, and Jia Cai

Abstract

The Paleoproterozoic khondalite series rocks of the North China Craton, consisting mainly of graphite-bearing Al-rich gneiss/granulite, garnet quartzite, felsic paragneiss, calc-silicate rock, and marble, contain important information about the composition, tectonic evolution, and growth history of the early continental crust, and provide important insights into the formation and evolution of the North China Craton. Integrated analysis of petrography, geochemistry, mineral compositions, metamorphic reaction textures and history, thermobarometry and pseudosection modeling, and geochronology of these khondalite series rocks from the Wulashan-Daqingshan Complex within the Khondalite Belt and Jiaobei Complex within the Jiao-Liao-Ji Belt, combined with previous metamorphic and geochronological data, indicated the following sedimentary, metamorphic, magmatic, and tectonic processes. (i) The sedimentary protoliths of the khondalite series rocks in the Khondalite Belt and Jiao-Liao-Ji Belt were likely deposited in an active continental margin in the late Paleoproterozoic, ranging from 2200 to 2000 Ma and from 1950 to 1930 Ma, respectively. (ii) During the period from 2000 to 1950 Ma, the protoliths of the khondalite series rocks from the Khondalite Belt and Jiao-Liao-Ji Belt experienced a crustal thickening event due to subduction of the Paleoproterozoic oceanic crust. As a result of tectonic burial and heat conduction, a greenschist facies to amphibolite facies prograde metamorphism occurred in the upper and middle crust region of the Khondalite Belt and Jiao-Liao-Ji Belt, forming the early mineral assemblage of garnet (core) and inclusion-type minerals (e.g., biotite, quartz, and plagioclase). (iii) During the period from 1950 to 1900 Ma, accompanied by cessation of oceanic crust subduction, the aggregation between the Paleoproterozoic arc and Archean continent and the collision between the Archean continents caused regional middle- and high-pressure granulite-facies metamorphism, as represented by the mineral assemblage of garnet and matrix-type minerals (e.g., kyanite/sillimanite, K-feldspar, plagioclase, biotite, quartz, Fe–Ti oxide, and liquid) in the pelitic granulites of the Khondalite Belt and Jiao-Liao-Ji Belt, occurring in a region of ca. 35–45 km of the thickened lower crust or arc root at ca. 1950–1900 Ma. (iv) During the period from 1900 to 1800 Ma, after the main collision and peak middle- and high-pressure granulite-facies metamorphism, the Paleoproterozoic khondalite series rocks experienced post-peak retrogressive metamorphism in the post-collisional exhumation and extension stage. The post-peak metamorphic and tectonic processes can be divided into two stages. During the early fast tectonic exhumation stage, the pelitic granulites of the Paleoproterozoic khondalite series rocks from the Khondalite Belt and Jiao-Liao-Ji Belt experienced slight heating or a nearly isothermal decompression, which resulted in overprinting of the regional middle- and

F.-I. Liu (✉) · P.-H. Liu · J. Cai
Institute of Geology, Chinese Academy of Geological Sciences,
Beijing, China
e-mail: lfl0225@sina.com

M. Zhai et al. (eds.), *Main Tectonic Events and Metallogeny of the North China Craton*,
Springer Geology, DOI 10.1007/978-981-10-1064-4_8

low-pressure granulite-facies metamorphism, and the development of cordierite-bearing symplectite around the garnets. Meanwhile, emplacement of the ca. 1900–1850 mafic dyke/sill swarms and partial melting of the crustal rocks were caused by underplating of mantle-derived mafic magma in the early stage. After the temperature peak, the late retrogressive metamorphism was dominated by slow near-isobaric cooling processes, which resulted in overprinting of the regional amphibolite facies metamorphism and the development of biotite-bearing symplectites around garnets in the pelitic rocks. In summary, the Paleoproterozoic khondalite series rocks from the Khondalite Belt and Jiao-Liao-Ji Belt are characterized by clockwise *P–T–t* paths bearing isothermal decompression and isobaric cooling processes metamorphic processes, suggesting that they were involved in the rapid deposition-, subduction-, aggregation-, and collision-related tectonic processes in an active continental margin or continental arc setting during the period from 2200 to 1800 Ma.

Keywords
Metamorphic evolution • Khondalite series • Paleoproterozoic mobile belts

8.1 Introduction

The khondalite series is one of the major constituents of the Precambrian metamorphic complexes of high-grade metamorphic provinces worldwide, consisting mainly of graphite-bearing Al-rich gneiss/granulite, garnet quartzite, felsic paragneiss, calc-silicate rock, and marble (Walker 1902; Narayanaswami 1975; Bates and Jackson 1980; Dash et al. 1987). This terminology is derived from the Eastern Ghats Belt of India and has been used increasingly for similar rock assemblages that have been recognized in other Precambrian high-grade terranes, such as those in southern India (Chacko et al. 1987), Sri Lanka (Cooray 1962), and Lapland of Fennoscandia (Barbey et al. 1982). The khondalite series rocks have long been considered as alumina-rich, high-grade metamorphic supracrustal rocks that formed during the early stages of continental crustal development. More recently, they have also been identified in some Phanerozoic terranes (e.g., Xu et al. 2005a, b; Zeng et al. 2008), implying that their formation may not be correlated with the early Precambrian. These rocks have long been interpreted as metamorphosed platform or cratonic sediments, and their protoliths are deposited in cratonic or passive margin type basins (Shackleton 1976; Condie et al. 1992; Lu et al. 1992, 1996; Li et al. 1999; Wan et al. 2000a, b). On the other hand, some groups argued that they could also have been deposited in active continental margins (Barbey et al. 1982; Daly et al. 2001; Dan et al. 2012).

The early Precambrian khondalite series rocks also occurred in several areas of the North China Craton (NCC) and were well exposed in the Jining, Wulashan-Daqingshan, Qianlishan, and Helanshan Complexes within the Khondalite Belt, and the Jiaobei Complex (JBC) within the Jiao-Liao-Ji Belt (Fig. 8.1). They were previously thought to have been deposited and metamorphosed in the Archean (e.g., Lu et al. 1992, 1996; Li et al. 1999). Their protoliths were traditionally considered as a typical example deposited in cratonic or passive margin type basins (Condie et al. 1992; Lu et al. 1996; Li et al. 1999; Qian and Li 1999). On the other hand, the results of a number of recent studies were inconsistent with these previous suggestions. Detrital zircon age data from the khondalite series rocks of the NCC show that their protoliths were deposited at ca. 2000–1950 Ma (Luo et al. 2004, 2008; Wan et al. 2006, 2009; Xia et al. 2006a, b; Zhou and Geng 2009; Yin et al. 2009, 2011), not in the Neoarchean as previously thought (e.g., Lu et al. 1996; Li et al. 1999). Soon after their deposition, these rocks were metamorphosed to granulite-facies at ca. 1950 Ma, which led some groups to propose that the protoliths of these khondalite series rocks were likely deposited on an active continental margin (e.g., Wan et al. 2009; Dan et al. 2012). However, the nature of the protoliths of these khondalite series rocks is still unclear, which hampers a better understanding of the depositional setting of their protoliths. Meanwhile, the precise peak and post-peak timing of metamorphism of the khondalite series rocks within the Khondalite Belt and Jiao-Liao-Ji Belt remain unclear. To resolve these issues, we have carried out a detailed geochemical, metamorphic, and geochronological study of the khondalite series rocks from the Wulashan-Daqingshan Complex in the Khondalite Belt and Jiaobei Complex in the Jiao-Liao-Ji Belt. Combined with previous geological data, the results of this study provide important insights into the formation and evolution of the khondalite series in the North China Craton.

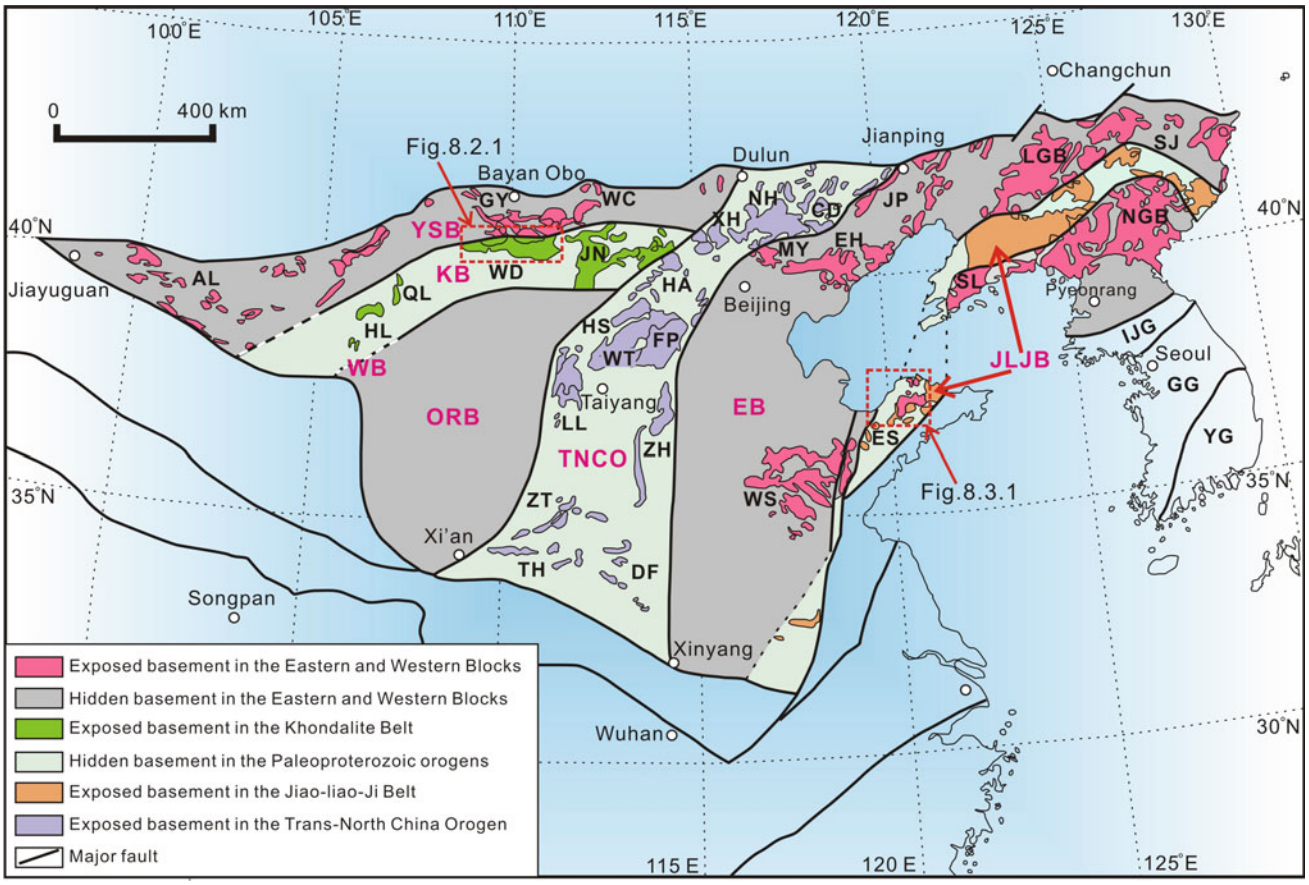

Fig. 8.1 Simplified geological map of the tectonic subdivisions of the NCC (after Zhao et al. 2005). Abbreviations of metamorphic complexes and tectonic unites: *KB* Khondalite Belt; *WS* Western Block; *ORB* Ordos Block; *YSB* Yinshan Block; *TNCO* Trans-North China Orogen; *EB* Eastern Block; *JLJB* Jiao-Liao-Ji Belt; *AL* Alashan; *CD* Chengde; *DF* Dengfu, *EH* Eastern Hebei; *ES* Eastern Shandong; *FP* Fuping; *GY* Guyang; *HA* Huai'an; *HL* Helanshan; *HS* Hengshan; *JN* Jining; *JP* Jianping; *LG* Langrim; *LL* Lvliang; *MY* Miyun; *NH* Northern Hebei; *NL* Northern Liaoning; *QL* Qianlishan; *SJ* Southern Jilin; *SL* South Liaoning; *TH* Taihua; *WD* Wulashan-Daqingshan; *WS* Western Shandong; *WT* Wutai, *XH* Xuanhua; *ZH* Zanhuang; *ZT* Zhongtiao

8.2 Khondalite Series of the Khondalite Belt in the Western Block

8.2.1 Geological Setting

The Wulashan-Daqingshan Complex is exposed in the central segment of the Paleoproterozoic Khondalite Belt in the Western Block of the NCC (Fig. 8.2). The complex is mainly composed of the late Neoarchean to Paleoproterozoic basement rocks and Mesozoic sedimentary rocks with minor Phanerozoic granitic rocks (Fig. 8.2).

In terms of metamorphic lithological association, structural style, metamorphism, and geochronology, the Neoarchean to Paleoproterozoic basement rocks in the Wulashan-Daqingshan Complex can be subdivided into two lithological units, i.e., basement reworked and Paleoproterozoic lithological series (Jin 1989; Jin et al. 1991; Liu et al. 1993a, b; Liu 1994, 1996; Yu 1994; Jin and Li 1994, 1996).

The basement reworked lithological series is made up of the late Neoarchean to early Paleoproterozoic banded iron formation (BIF)-bearing supracrustal rocks (also named the "lower Wulashan Subground," "Shangan Group," or "Xinhe Group"; Yang et al. 2000, 2003, 2006; Xu et al. 2003) and 2550–2450 Ma amphibolite- to granulite-facies metamorphic intrusive rocks in the Wulashan-Daqingshan Complex. The representative 2550–2450 Ma BIF-bearing supracrustal rocks are composed mainly of garnet-bearing banded granulites or amphibolites, and biotite- or garnet-bearing paragneisses, probably derived from a volcanic-sedimentary formation. The representative 2550–2450 Ma supracrustal rocks are mainly exposed in Saihutong, Deersutai, Hademenggou, Hujigou, Danangou, Jidengwan, Wudangzhao, Kunduigou, and Nalinggou within the Wulashan-Daqingshan Complex (Liu 1994; Yu 1994; Xu et al. 2003, 2005a, b; Ma et al. 2012a, b; Dong et al. 2014). The 2550–2450 Ma metamorphic intrusive rocks are composed predominantly of hypersthene-bearing dioritic–granodioritic orthogneisses (enderbitic–charnockitic orthogneisses), and meta-mafic dykes or sills with minor garnet-bearing granitic and K-rich granitic gneisses. These metamorphic intrusive rocks are

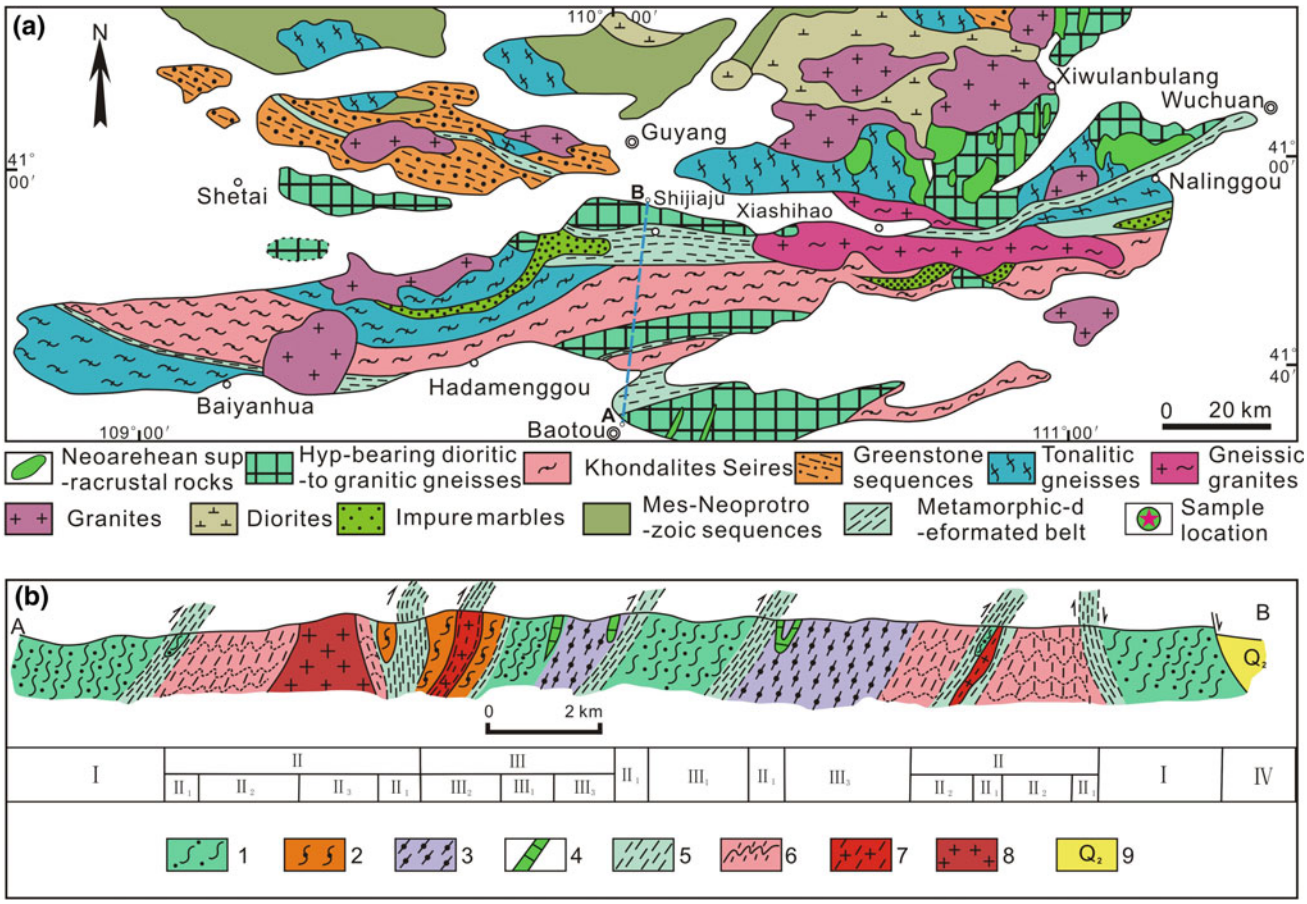

Fig. 8.2 **a** A simplified geological map of the Wulashan–Daqingshan Complex (modified by Li et al. 1994). **b** A cross-sectional map through the middle part of the WDC (modified by Yu 1994). In Fig. 8.2b, *1* mafic–dioritic–granitic gneisses, *2* Al-rich gneiss, *3* Calc-silicate rocks, *4* Marble, *5* Basement reworked rocks, *6* Amp-Pl gneiss, *7* Syn-tectonic granitic gneiss, *8* Post-tectonic granites, *9* Loess, *I* Archean basement, *II* High temperature metamorphic and deformed belt, II_1 Strong deformation belt, II_2 Weak deformation belt, II_3 Post-tectonic granites, *III* Nappe/Thrusting tectonic slices, III_1 Granulite–dioritic–granitic gneiss slices; III_2 Al-rich gneiss slices, III_3 Calc-silicate rock slices, *IV* Cenozoic loess

mainly exposed in Shadegai, Adaohai, and Hantonghui within the Wulashan-Daqingshan Complex (Liu 1994; Yu 1994; Xu et al. 2003, 2005a, b; Ma et al. 2012a, b; Wan et al. 2013a; Dong et al. 2014; Liu et al. 2014b). Recent new SHRIMP and LA-ICP-MS U–Pb zircon data indicate that the basement reworked lithological series not only recorded the 2500–2450 Ma metamorphic ages, but was also overprinted by the 1950–1850 Ma metamorphic ages (Ma et al. 2012a, b; Wan et al. 2013b; Dong et al. 2014; Liu et al. 2014b).

Paleoproterozoic lithological series are composed predominantly of the widespread Paleoproterozoic khondalite series rocks (also named the "upper Wulashan Subgroup" and "Meidaizhao Group") with some Paleoproterozoic igneous rocks (Jin 1989; Yu 1994; Yang et al. 2000, 2003, 2006; Xu et al. 2003, 2005a, b; Wan et al. 2009).

Similar to the khondalite series rocks exposed in the Jining, Qianlishan, and Helanshan Complexes, the widespread Paleoproterozoic khondalite series rocks within the Wulashan-Daqingshan Complex are also made up of Al-rich paragneisses, garnet quartzites, felsic paragneisses, calc-silicate rocks, and marble. They are mainly exposed in Liubagou, Xiaomiao, Hademengou, Taoerwan, Hujigou, Danangou, Qiandian, Wudangzhao, Jidengwan, Miaogou, Shuijiangou, Zhaoergou, and Dongpo within the Wulashan-Daqingshan Complex. In addition, the Paleoproterozoic khondalite series rocks contain minor graphite deposits in Miaogou and Hademenggou. Structural analysis and metamorphic reaction relations indicate that the Paleoproterozoic khondalite series rocks of the Wulashan-Daqingshan Complex are strongly deformed to produce an E–W trending fold belt and underwent early prograde (M_1), peak (M_2), post-peak decompression (M_3) and late cooling (M_4) metamorphism (Jin 1989; Liu et al. 1993a, b; Jin and Li 1994; Li et al. 1994; Yu 1994; Cai et al. 2014). The M_1 stage is represented by mineral inclusions of quartz + plagioclase + biotite + sillimanite/kyanite + ilmenite preserved in a core of garnet. The M_2 stage is marked by the growth of garnet and the matrix mineral assemblage of kyanite/sillimanite + K-feldspar + plagioclase + biotite + quartz + Fe–Ti oxide + liquid. The M_3 stage is represented by the cordierite +

sillimanite + K-feldspar ± plagioclase ± quartz ± Fe–Ti oxide ± spinel symplectites around garnet grains. The M_4 stage is represented by retrogressive biotite + muscovite + plagioclase + quartz. The P–T evolution shows a clockwise *P–T* path with isothermal decompression, indicating that the Daqingshan–Wulashan khondalite series rocks were involved in the late Paleoproterozoic orogenic event (the Luliang Movement in earlier Chinese literature). Recent metamorphic studies also showed that the Paleoproterozoic khondalite series rocks of the Wulashan-Daqingshan Complex contain sapphirine-bearing ultra-high temperature (UHT) granulites at Dongpo. These UHT granulites with the peak metamorphic condition of 910–980 °C are characterized by assemblages of garnet + sapphirine + spinel + sillimanite + biotite + plagioclase (Jin 1989; Guo et al. 2006, 2012; Jiao and Guo 2011; Jiao et al. 2011, 2013a; Tsunogae et al. 2011). At the same time, recent SHRIMP and LA-ICP-MS U–Pb zircon ages indicate that the khondalite series rocks in the Wulashan–Daqingshan Complex were also formed ca. 2000–1950 Ma, and were metamorphosed from 1950 to 1850 Ma (Wu et al. 2006; Xia et al. 2006a, b; Dong et al. 2007, 2012; Wan et al. 2009; Cai et al. 2015).

On the other hand, the Paleoproterozoic magmatic rocks are also a representative part of the Paleoproterozoic lithological units within the Wulashan-Daqingshan Complex. These include pre-, syn-, or post-tectonic granitic-dioritic-mafic small plutons or veins/sills with minor volcanic lavas and tuffs (Dong 2012). They underwent a regional high-grade metamorphism and were strongly deformed (Jin 1989; Liu et al. 1993a, b, 2013c, 2014c; Yu 1994; Ma et al. 2012b; Wan et al. 2013a). These Paleoproterozoic meta-magmatic rocks are mainly exposed in Wulabulianggou, Hademenggou, and Danuqi within Wulashan area, Aobaoshan, Banglianggou, Dengkouxigou, and Taoerwan within the Daqingshan area. In addition, the Paleoproterozoic granitic pegmatite veins contain minor muscovite deposits in Xiaomiaozi within the Wulashan area. Recently, new SHRIMP and LA-ICP-MS U–Pb zircon analyses revealed that the Paleoproterozoic meta-magmatic rocks were emplaced during the periods of ca. 2300–2000 Ma, 1970–1940 Ma, and ca. 1850 Ma, and were metamorphosed at 1950–1800 Ma (Dong et al. 2009a, b, 2012, 2014; Wan et al. 2009, 2013a; Dong 2012; Liu et al. 2012a, 2014b; Ma et al. 2012a, b).

In addition to the late Neoarchean to Paleoproterozoic basement rocks, the Wulashan-Daqingshan Complex also contains the Phanerozoic sedimentary rocks with minor Phanerozoic magmatic rocks. The Phanerozoic sedimentary rocks are chiefly composed of arkose-quartz, quartzites, and mudstones. They are exposed mainly in the Siguai and Menggou areas. Increasing numbers of structural studies have shown that the late Neoarchean to Paleoproterozoic basement rocks and the Phanerozoic sedimentary rocks are separated by regional-scale ductile shear zones (Liu 1996; Xu et al. 2003). In addition, the Phanerozoic granitoids that were intruded into the late Neoarchean to Paleoproterozoic basement rocks were emplaced mainly at 365–330 Ma and 245–220 Ma (Miao et al. 2001; Hou et al. 2011; Zhang 2012).

8.2.2 Whole-Rock Geochemistry

As mentioned above, the Paleoproterozoic khondalite series rocks of the Khondalite Belt can be subdivided into three different types: Al-rich paragneisses with high Al_2O_3 and low SiO_2 contents, garnet- or sillimanite-bearing felsic paragneisses or felsic granular rocks with high SiO_2 and low Al_2O_3 contents, and calc-silicate rocks and marble with high CaO and low SiO_2 contents. With the exception of calc-silicate rocks and marble, the major and trace element compositions of representative Paleoproterozoic khondalite series rocks within the Khondalite Belt are presented in Table 8.1.

8.2.2.1 Major Elements

As shown in Fig. 8.3 and Table 8.1, the Paleoproterozoic khondalite series rocks from the Helanshan Complex, Qianlishan Complex, Wulashan–Daqingshan Complex, Jining Complex, and Huai'an Complex within the Khondalite Belt and the adjacent region are characterized by significantly variable concentrations of SiO_2, Al_2O_3, FeO^T, MgO, CaO, Na_2O, and K_2O, with values ranging from 44.87 to 92.24 wt%, 3.39–27.39 wt%, 1.23–13.27 wt%, 0.21–13.87 wt%, 0.35–15.82 wt%, 0.10–4.65 wt%, and 0.21–9.34 wt%, respectively. In contrast, the concentrations of TiO_2 (0.09–1.49 wt%), MnO (0.01–0.27 wt%), and P_2O_5 (0.02–0.42 wt %) are low and exhibit restricted variations. The large variations in major element concentrations for all of the Paleoproterozoic khondalite series samples within the Khondalite Belt and the adjacent region are typical of weathered rocks. Chemistry is strongly correlated with grain size, because most elements show markedly linear trends on the Al_2O_3 variation diagram (Harker variation diagrams omitted). In general, most elements increase as Al_2O_3 increases from sandstone to argillites. The concentrations of TiO_2, Al_2O_3, Fe_2O_3, MgO, CaO, Na_2O, and K_2O decrease with increasing SiO_2 content, suggesting that samples increase in their mineralogical maturity or quartzose contents but decrease in immature detrital grains (e.g., feldspar and rock fragments). Cratonic and recycled sediments associated with passive margins are higher in silica (SiO_2: > 85 wt% and 65–95 wt%, respectively), whereas arc-derived sediments within active orogenic margins normally contain relatively lower and variable levels of silica (SiO_2: 47–82 wt %). Arc-derived sediments are also higher in Fe, Mg, Ti, and Al than cratonic and recycled sediments (Bhatia 1983). Most of the Paleoproterozoic khondalite series samples within the

Table 8.1 Whole rock analyses on the representative Khondalite Series rocks within the Wulashan-Daqingshan Complex

Sample no.	BT19-1	BT20-1	BT38-1	BT51-1	BH28-5	BH39-4	BH1-1	BH23-1	BH27-1	BH27-2
SiO_2	65.79	60.04	63.22	77.71	44.87	61.37	60.12	67.84	56.32	60.33
TiO_2	0.26	0.78	0.65	0.44	0.90	0.78	0.77	0.40	0.93	0.94
Al_2O_3	15.28	19.14	17.03	11.60	21.55	17.60	18.82	15.30	17.84	19.18
Fe_2O_3	1.10	1.47	2.01	1.10	2.27	1.71	1.54	1.09	0.75	1.55
FeO	6.45	5.05	4.33	0.84	11.23	5.62	4.72	1.99	7.74	5.69
MnO	0.11	0.07	0.11	0.01	0.01	0.06	0.06	0.04	0.07	0.09
MgO	2.57	3.54	2.90	1.09	5.68	3.27	3.32	1.32	4.67	2.63
CaO	0.91	2.35	2.71	0.86	0.49	1.66	1.12	1.94	3.44	0.93
Na_2O	1.86	3.15	3.26	2.07	1.18	1.63	2.45	2.77	3.02	2.00
K_2O	4.95	2.71	2.76	3.25	9.34	3.65	4.58	5.38	2.09	3.21
P_2O_5	0.05	0.10	0.08	0.06	0.12	0.12	0.10	0.14	0.07	0.08
LOI	0.31	1.46	0.51	0.69	0.83	1.69	1.35	0.66	0.97	1.59
Total	99.64	99.86	99.57	99.72	98.47	99.16	98.95	98.87	97.91	98.22
La	35.50	64.00	56.20	35.00	4.10	48.70	69.70	80.20	52.80	83.70
Ce	56.90	124.00	107.00	64.90	9.59	93.00	134.00	163.00	105.00	172.00
Pr	5.89	14.00	12.40	7.09	1.36	11.10	15.10	17.80	12.40	19.90
Nd	20.30	50.80	45.50	25.60	6.51	42.10	57.90	65.40	48.50	77.20
Sm	4.08	8.20	7.17	4.30	1.91	7.38	8.88	10.30	7.90	12.10
Eu	2.09	1.76	1.29	0.99	0.81	1.60	1.95	2.15	1.83	1.97
Gd	6.71	6.29	6.46	2.97	2.51	6.10	5.80	7.78	5.95	7.64
Tb	1.41	0.85	1.09	0.32	0.46	0.95	0.87	1.37	0.88	1.06
Dy	9.22	4.62	6.66	1.27	3.19	5.81	4.50	7.11	5.08	5.62
Ho	1.70	0.94	1.42	0.22	0.66	1.21	0.93	1.40	1.06	1.14
Er	4.46	2.90	4.21	0.61	2.02	3.78	2.64	3.60	3.18	3.18
Tm	0.56	0.45	0.67	0.10	0.28	0.58	0.40	0.50	0.51	0.46
Yb	3.34	2.84	4.16	0.66	1.88	3.93	2.55	2.84	3.45	2.90
Lu	0.46	0.44	0.67	0.10	0.30	0.63	0.42	0.43	0.56	0.45
Sc	47.20	22.60	26.20	4.58	46.30	22.10	18.30	10.60	27.20	27.00
V	66.80	152.00	119.00	64.20	243.00	139.00	135.00	67.60	193.00	200.00
Cr	164.00	319.00	205.00	96.60	262.00	129.00	207.00	97.00	191.00	155.00
Co	17.30	23.10	21.90	12.20	42.40	18.30	22.90	11.50	36.80	17.20
Ni	31.60	60.90	57.80	35.80	212.00	53.80	87.80	40.90	149.00	46.60
Cu	25.50	44.30	39.70	60.20	10.50	23.10	30.30	21.30	174.00	77.80
Zn	52.00	80.70	76.30	46.40	96.00	129.00	107.00	35.40	108.00	89.60
Ga	14.80	26.20	18.60	16.90	23.80	24.20	23.70	18.30	23.40	27.10
Rb	86.10	86.50	72.90	94.00	201.00	171.00	119.00	130.00	114.00	122.00
Sr	488.00	400.00	378.00	316.00	68.80	182.00	368.00	389.00	295.00	147.00
Y	45.80	25.20	38.10	5.60	17.50	32.60	22.10	32.90	25.50	27.90
Zr	266.00	226.00	298.00	159.00	45.20	231.00	224.00	166.00	193.00	174.00
Nb	2.23	9.26	4.85	6.95	2.11	14.40	10.10	9.85	13.80	17.90
Mo	0.13	0.43	0.17	0.79	0.10	0.48	0.38	1.24	1.55	0.57
Sn	0.79	0.49	0.54	1.01	0.85	1.04	0.59	0.46	0.42	0.53
Cs	0.32	0.85	0.4	1.35	23.4	8.04	1.5	1.66	2.26	1.11
Ba	1818	775	720	992	300	812	1492	1100	1275	699

(continued)

Table 8.1 (continued)

Sample no.	BT19-1	BT20-1	BT38-1	BT51-1	BH28-5	BH39-4	BH1-1	BH23-1	BH27-1	BH27-2
Hf	8.1	6.4	8.17	4.56	1.33	6.86	6.72	5.71	5.99	5.74
Ta	0.12	0.51	0.17	0.39	0.12	0.8	0.53	0.83	0.81	1.32
Pb	26.8	19.7	16.9	13.3	10.5	18.3	30.9	39.2	14	16
Th	4.52	12.3	18.8	9.47	0.52	15.5	24.6	31.6	13.3	23.6
U	0.56	1.16	1.07	1.27	0.4	1.92	1.4	4.55	1.46	2.07

Khondalite Belt and the adjacent region were plotted in the sandstone and argillites fields in the classification diagrams (Fig. 8.3). For example, the log (Fe_2O_3/K_2O) against log (SiO_2/Al_2O_3) plots (Herron 1988) fell mainly in the shale, wacke, and arkose fields with some in the subarkose, sublitharenite, and Fe-Sand fields (Fig. 8.3c).

8.2.2.2 Rare Earth Elements

Chondrite-normalized rare earth element (REE) patterns and representative data for all the Paleoproterozoic khondalite series rocks within the Khondalite Belt and the adjacent region are shown in Fig. 8.4 and Table 8.1, respectively. They display relatively variable REE concentrations (35.58–677.75 ppm) and relatively moderately fractionated REE patterns ($(La/Yb)_N$ = 1.19–5.87) with variable Eu anomalies (δEu = 0.62–1.26). It is worth noting that garnet- or sillimanite-bearing felsic paragneisses or felsic granular rocks (e.g., arkosite, quartzite, and leptite) have lower REE concentrations than metamorphic pelitic rocks. Compared with the 2200–2000 Ma K-rich granitic rocks from the NCC (e.g., Du et al. 2013; Liu et al. 2014b), these rocks have similar REE patterns.

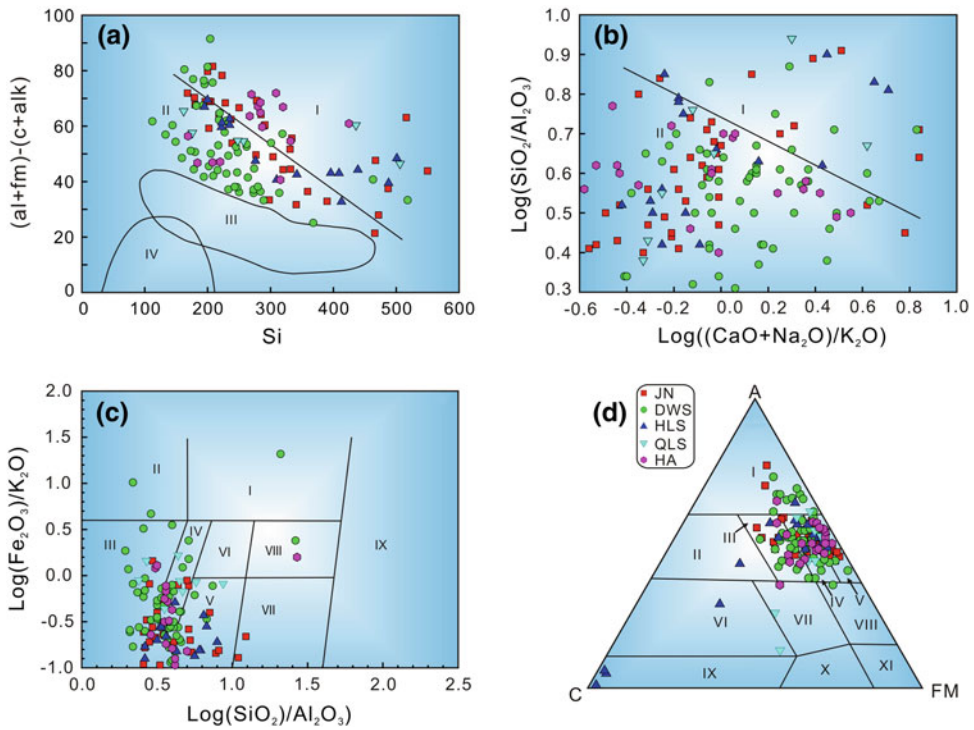

Fig. 8.3 Classification diagrams of the khondalite series rocks in the Khondalite Belt. **a** Si versus ((al + fm)-(c + alk)) (Simonen 1953), *I* Arenaceous sedimentary rocks, *II* Argillous sedimentary rocks, *III* Volcanic rocks, *IV* Calcareous. **b** Log((CaO + Na_2O)/K_2O) versus Log (SiO_2/Al_2O_3) (Garrels and Mackenzie 1971), *I* Arenaceous sedimentary rocks, *II* Argillous sedimentary rocks. **c** Log(Fe_2O_3/K_2O) versus Log (SiO_2/Al_2O_3) (Herron 1988), *I* Fe-Sand, *II* Fe-Shale, *III* Shale, *IV* Wacke, *V* Arkose, *VI* Litharenite, *VII* Subarkose, *VIII* Sublitharenite, *IX* Quartz arenite. **d** A-C-FM (secondary source from Wang et al. 1987), *I* Clay rock and acidic volcanic rock, *II* Arkose, *III* Graywacke, intermediate and alkaline volcanic rock, *IV* Wacke Overlay region of Graywacke, intermediate and alkaline volcanic rock, and Clay rock, *V* Clay rock and graywacke, *VI* Calc-silicate rock and quartzite, *VII* Basic volcanic rock and ferruginous and dolomitic marl, *VIII* tuffaceous siltstone, *IX* Calcareous carbonate, *X* Ultrabasic rock, *XI* Siliceous and ferruginous sedimentary rock and ultrabasic rock. Abbreviations of metamorphic complexes (the same below): *JN* Jining Complex; *DWS* Daqingshan-Wulashan Complex; *HLS* Helanshan Complex; *QLS* Qianlishan Complex; *HA* Huai'an Complex

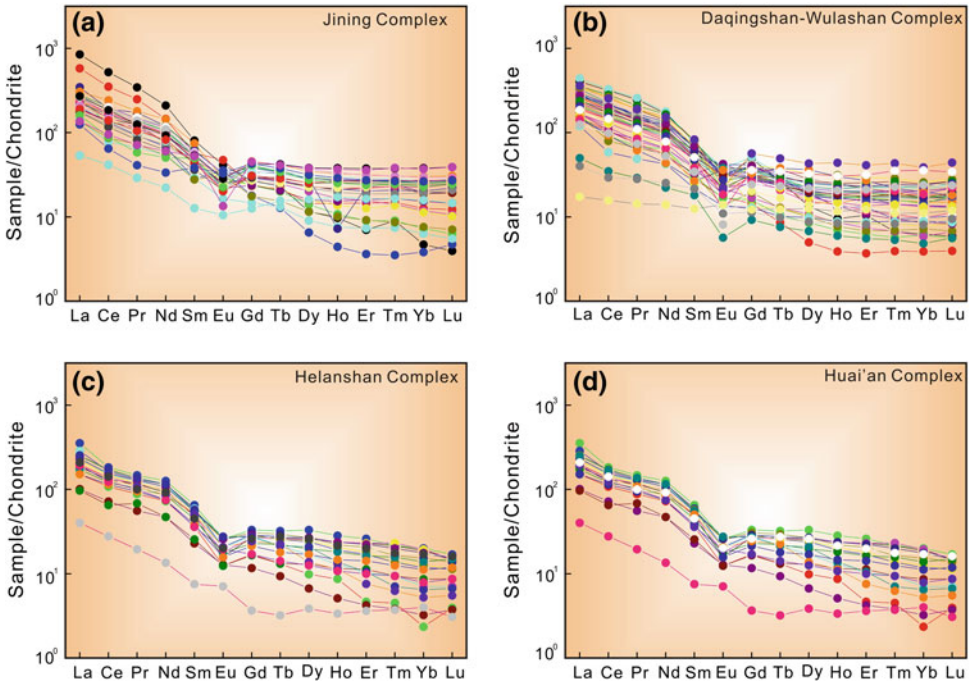

Fig. 8.4 Chondrite-normalized rare earth element (REE) patterns for the khondalite series rocks in the Khondalite Belt. Normalizing values are after Sun and McDonough (1989)

8.2.2.3 Trace Elements

The Paleoproterozoic khondalite series within the Khondalite Belt and the adjacent region are characterized by moderately to largely variable concentrations of Sc (1.19–37.80 ppm), Zr (34.50–485.00 ppm), Hf (1.28–12.8 ppm), Nb (0.55–132 ppm), and Ta (0.12–11.00 ppm). Furthermore, the concentrations are above or below those in the average upper continental crust (UCC) (Taylor and McLennan 1985). Similarly, concentrations of Co (2.00–42.40 ppm), Cr (6.80–386.00 ppm), Ni (1.51–212.00 ppm), Rb (6.96–220.00 ppm), Sr (39.2–707 ppm), Ba (76.80–2,188 ppm), Th (0.52–31.6 ppm), and U (0.22–4.55 ppm) exhibit large variations. In a primitive mantle-normalized trace element spidergram (Fig. 8.5), the Paleoproterozoic khondalite series rocks show marked depletions in high field strength elements (HFSE) with negative Nb, Ta, Ti, and Y anomalies.

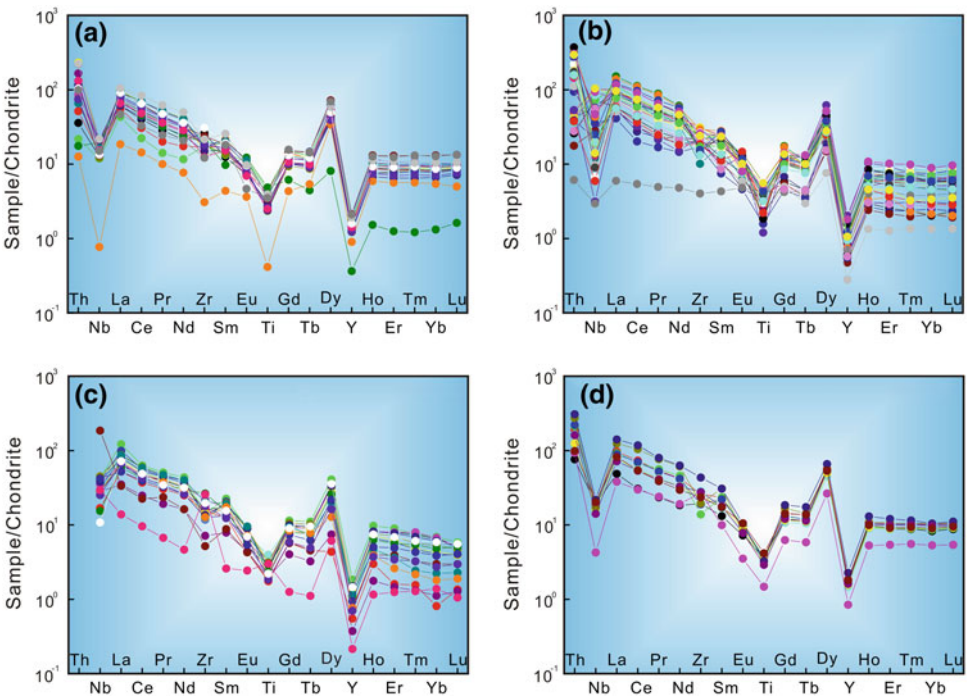

Fig. 8.5 Primitive mantle-normalized trace element patterns for the khondalite series rocks in the Khondalite Belt. Normalizing values are after Sun and McDonough (1989). **a** Jining complex. **b** Daqingshan-Wulashan complex. **c** Helanshan complex. **d** Huai'an complex

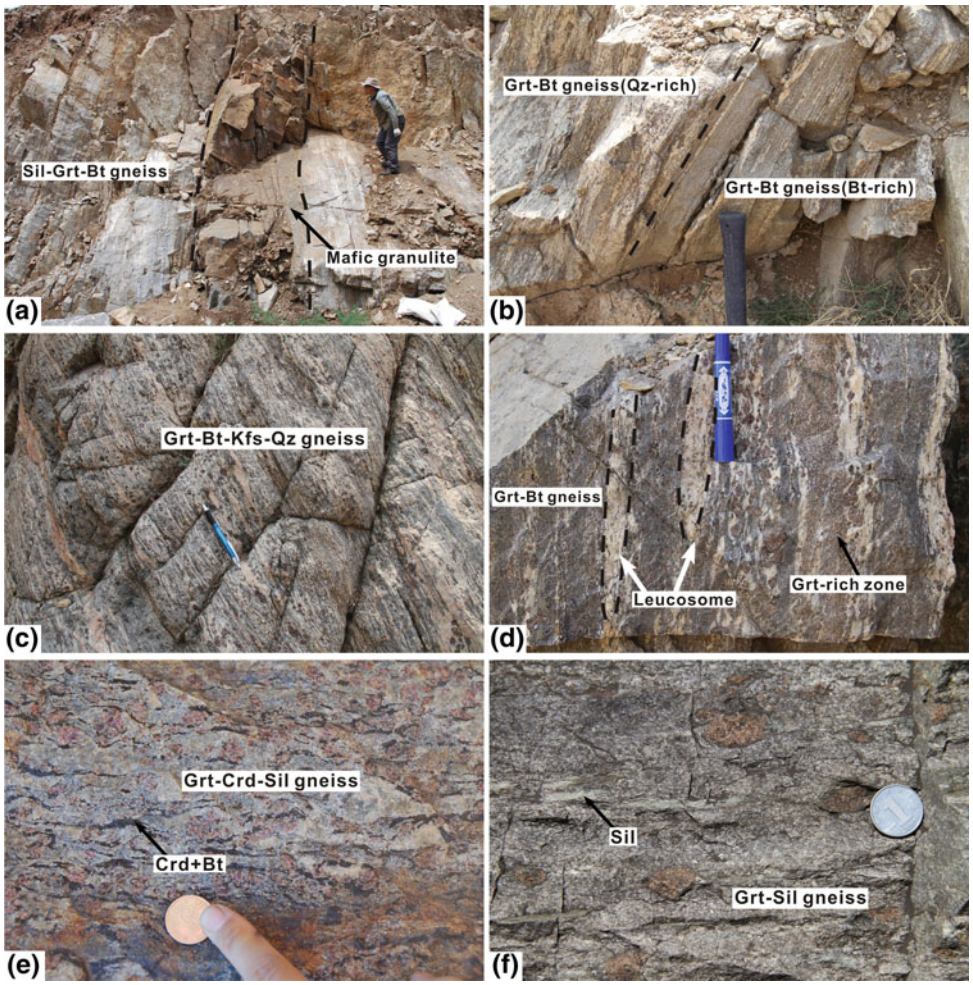

Fig. 8.6 Outcrops of meta-pelitic rocks in the Khondalite Belt. **a** Sillimanite–garnet–biotite gneiss and mafic granulites occur as interlayers. **b** Garnet–biotite (biotite-rich) and garnet–biotite (quartz-rich) occur as interlayers. **c** Occurrence of the garnet–biotite gneisses. **d** Garnet–biotite gneiss with quartzofeldspathic layers. **e** Cordierite distributed along garnet rim forming "black-eye-socket" structure. **f** Large garnet porphyroblast occur in the garnet–sillimanite gneiss (modified after Cai et al. 2014)

8.2.3 Petrography

The Sil–Grt–Bt and quartzofeldspathic Grt–Bt gneisses occur as interlayers with mafic granulites occurring as mafic dykes (Fig. 8.6a). The Grt–Bt gneisses (biotite-rich) and garnet-bearing quartzofeldspathic gneisses are interlayered with thicknesses ranging from several meters to tens of meters (Fig. 8.6b). Representative Grt–Crd–Sil gneisses are rich in cordierite, sillimanite, biotite, and garnet porphyroblasts. Banded quartzofeldspathic concordant layers or small-scale rootless folds consist of quartz, plagioclase, and K-feldspar with or without garnet (Fig. 8.6c–d), suggesting partial melting during high-grade metamorphism. Occasionally, garnet porphyroblasts (up to 2 cm) are surrounded by cordierite-biotite symplectites showing a "black-eye-socket" structure (Fig. 8.6e). Mineral inclusions of sillimanite, biotite, quartz, plagioclase, and ilmenite can be identified within the garnet. Thin layers rich in prismatic sillimanite and biotite in the matrix formed gneissosity (Fig. 8.6f).

Representative meta-pelitic rocks involving Sil–Grt–Bt gneisses (samples BT35-1 and P01-10), Crd–Grt–Bt gneisses (BH27-1, BH27-2, BH39-4 and BT16-6), and Ms–Sil–Grt gneiss (BT51-1) have mineral assemblages suitable for *P–T* calculations. The textural characteristics of these rocks are illustrated in Figs. 8.7, 8.8 and 8.9. Mineral abbreviations are after Whitney and Evans (2010). The detailed petrological observations reveal a multistage metamorphic evolution with microstructures and reaction textures revealing four stages of metamorphism; i.e., the prograde (M_1), peak (M_2), post-peak decompression (M_3), and late retrograde cooling (M_4) stages in the meta-pelitic rocks of the Khondalite Belt.

8.2.3.1 Prograde Stage (M_1)

Due to high diffusion rates under high-grade conditions and partial melting of the granulite-facies meta-pelitic rocks, evidence of the prograde segment (M_1) is often not preserved (Harley 1989). However, the M_1 metamorphic stage can be obtained from a garnet core ($\sim$7 mm) (Fig. 8.7a) containing

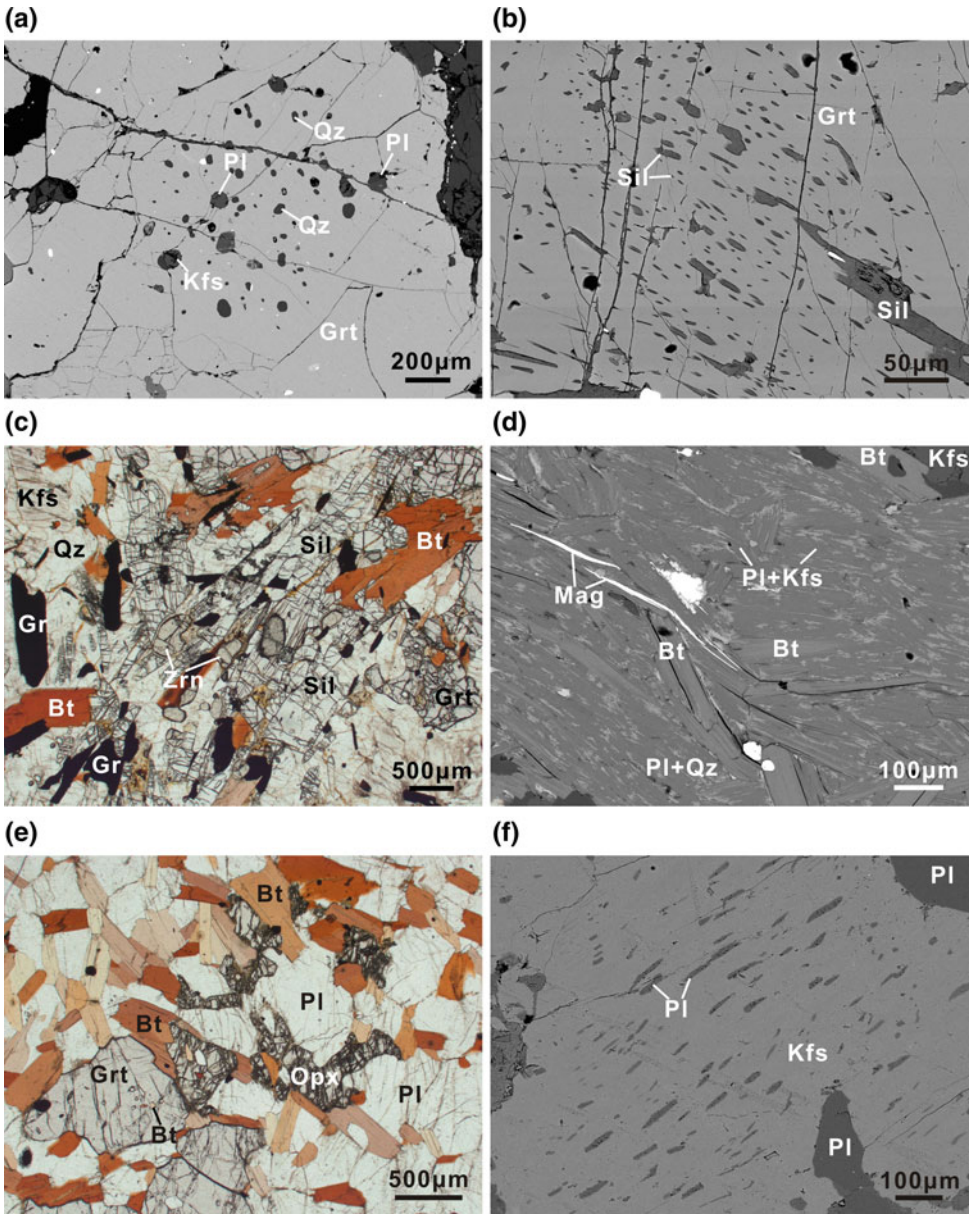

Fig. 8.7 Representative back-scattered electron (BSE) images and photomicrographs (plane-polarized light, PPL) showing microtextures of the meta-pelitic rocks in the Khondalite Belt. **a** BSE image of a garnet porphyroblast with minute mineral inclusions. **b** BSE image of oriented fibrolitic sillimanite within a garnet porphyroblast. **c** Photomicrograph (PPL) of coarse-grained matrix sillimanite and biotite with minor zircon and flaky graphite. **d** BSE image of biotite partially replaced by plagioclase and K-feldspar by biotite dehydration melting. **e** Photomicrograph (PPL) of garnet matrix, orthopyroxene, biotite, and plagioclase. **f** BSE image of perthite with plagioclase lamellae. (modified after Cai et al. 2014)

fibrolitic sillimanite (Fig. 8.7b), fine-grained plagioclase, K-feldspar, biotite, and magnetite, ranging from 5 to 50 μm. The representative mineral assemblage of the M_1 stage is garnet (core) + the included minerals plagioclase + biotite + sillimanite + quartz + K-feldspar ± magnetite.

8.2.3.2 Peak Stage (M_2)

The mineral assemblage of the peak metamorphism (M_2) is garnet (mantle) + K-feldspar + plagioclase + biotite + quartz ± sillimanite ± orthopyroxene ± ilmenite ± magnetite ± rutile (Fig. 8.7c). A foliation is defined by oriented biotite. Coarse-grained K-feldspar, plagioclase, quartz, and flaky graphite are observed in the matrix (Fig. 8.7c). Melt is produced by biotite dehydration melting crystallized to fine-grained K-feldspar + plagioclase (Fig. 8.7d). The garnet mantle continued to grow by consumption of sillimanite, biotite, and plagioclase due to the following biotite dehydration melting reaction (Patiño Douce and Johnston 1991):

$$|\mathrm{Bt}| + |\mathrm{Sil}| + |\mathrm{Qz}| \pm |\mathrm{Pl}| \rightarrow |\mathrm{Grt}| + |\mathrm{Kfs}| + |\mathrm{Melt} \quad (8.1)$$

8.2.3.3 Post-Peak Stage (M_3)

Peak mineral assemblages are commonly overprinted by the post-peak process, which is well preserved in various microstructures (Fig. 8.8). The post-peak stage is characterized by cordierite-bearing assemblages in microdomains. In samples lacking spinel, cordierite coronae containing sillimanite and quartz relicts form rims on the garnets (Fig. 8.8a, b, d, f), indicating the following decompressional reaction:

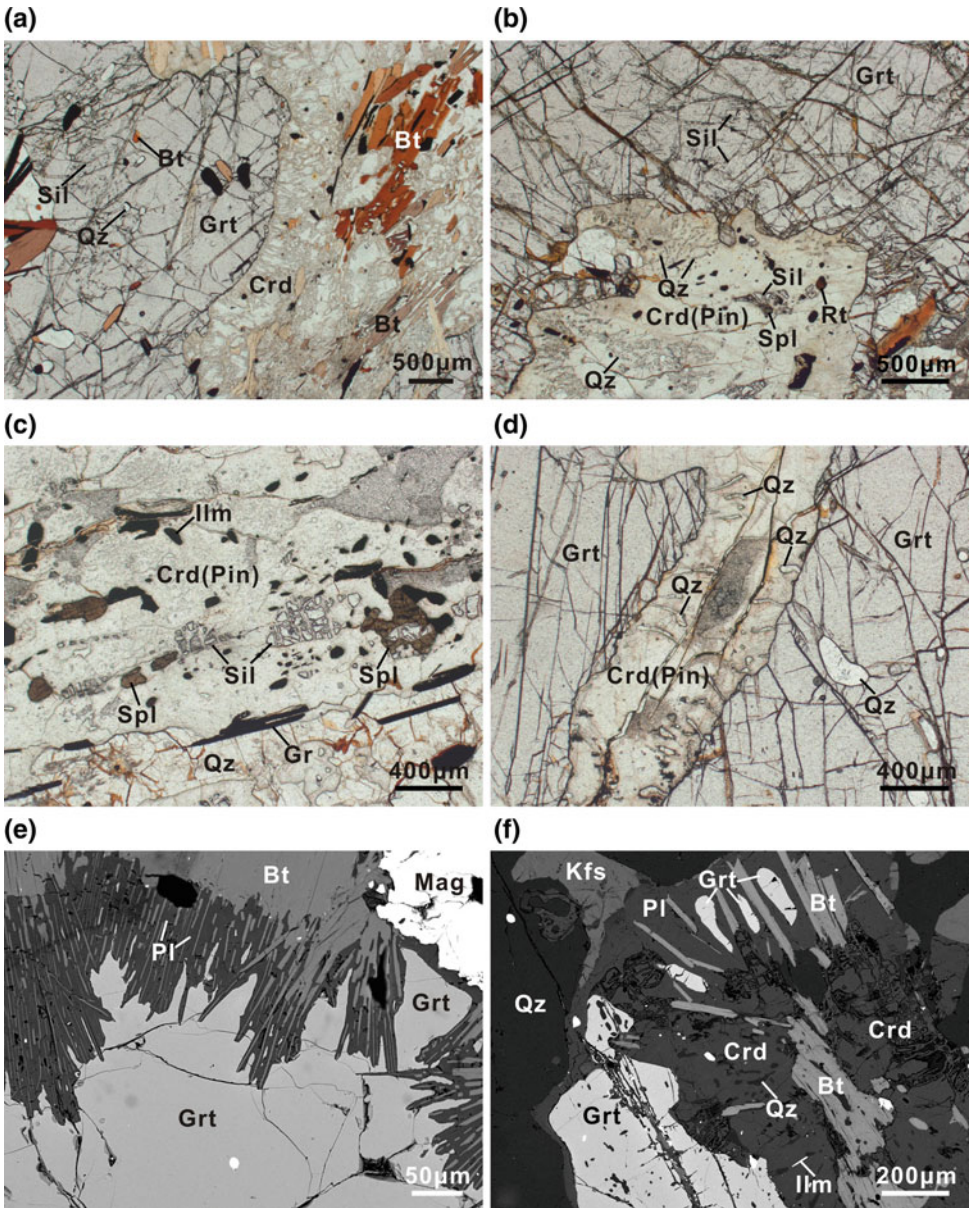

Fig. 8.8 Representative photomicrographs (PPL) and BSE images showing microtextures of the meta-pelitic rocks in the Khondalite Belt. **a** Photomicrograph (PPL) of garnet porphyroblast including fibrolitic sillimanite, biotite, and quartz surrounded by cordierite corona. **b** Photomicrograph (PPL) of a garnet porphyroblast mantled by cordierite containing vermicular quartz, sillimanite relicts, and brownish green spinel. **c** Photomicrograph (PPL) of brown spinel, sillimanite relicts, biotite, and ilmenite within cordierite matrix. Oriented flaky graphite occurs in the matrix. **d** Photomicrograph (PPL) of pinitized cordierite partially replacing garnet, and worm-like quartz vertically distributed along the garnet rim. **e** BSE image of porphyroblastic garnet surrounded by skeletal biotite–plagioclase intergrowths. **f** BSE image of garnet porphyroblast rimmed by cordierite-bearing symplectite (modified after Cai et al. 2014)

$$|\mathrm{Grt}| + |\mathrm{Sil}| + |\mathrm{Melt}| \rightarrow |\mathrm{Crd}| + |\mathrm{Bt}| + |\mathrm{Fe-oxide} \quad (8.2)$$

In silica-undersaturated domains, sillimanite relicts and spinel are included in cordierite (Fig. 8.8b, c), suggesting the following reaction (Harris 1981):

$$|\mathrm{Grt}| + |\mathrm{Sil}| \pm |\mathrm{Qz}| \rightarrow |\mathrm{Crd}| \pm |\mathrm{Spl} \quad (8.3)$$

Symplectites of biotite + plagioclase partially replaced garnet grains (Fig. 8.8e, f). The secondary plagioclase was probably formed by the release of grossular by the following garnet breakdown reaction (Vielzeuf and Montel 1994):

$$|\mathrm{Grt}| + |\mathrm{Melt}| \rightarrow |\mathrm{Bt}| + |\mathrm{Qz}| \pm |\mathrm{Pl} \quad (8.4)$$

In the Opx–Grt–Bt gneiss, symplectites of orthopyroxene + plagioclase + K-feldspar (Fig. 8.9a, b) were formed by the following garnet breakdown reactions:

$$|\mathrm{Grt}| + |\mathrm{Qz}| + |\mathrm{Bt}| \rightarrow |\mathrm{Opx}| + |\mathrm{Pl}| + |\mathrm{Kfs} \quad (8.5)$$

$$|\mathrm{Grt}| + |\mathrm{Qtz}| \rightarrow |\mathrm{Opx}| + |\mathrm{Pl} \quad (8.6)$$

8.2.3.4 Late Retrograde Cooling Stage (M_4)

The assemblage of the late retrograde cooling stage is chlorite + biotite + muscovite + plagioclase + quartz ± sillimanite ± garnet. Coarse sillimanite is rimmed by late muscovite in the quartz-rich domains (Fig. 8.9d), indicating the following reaction:

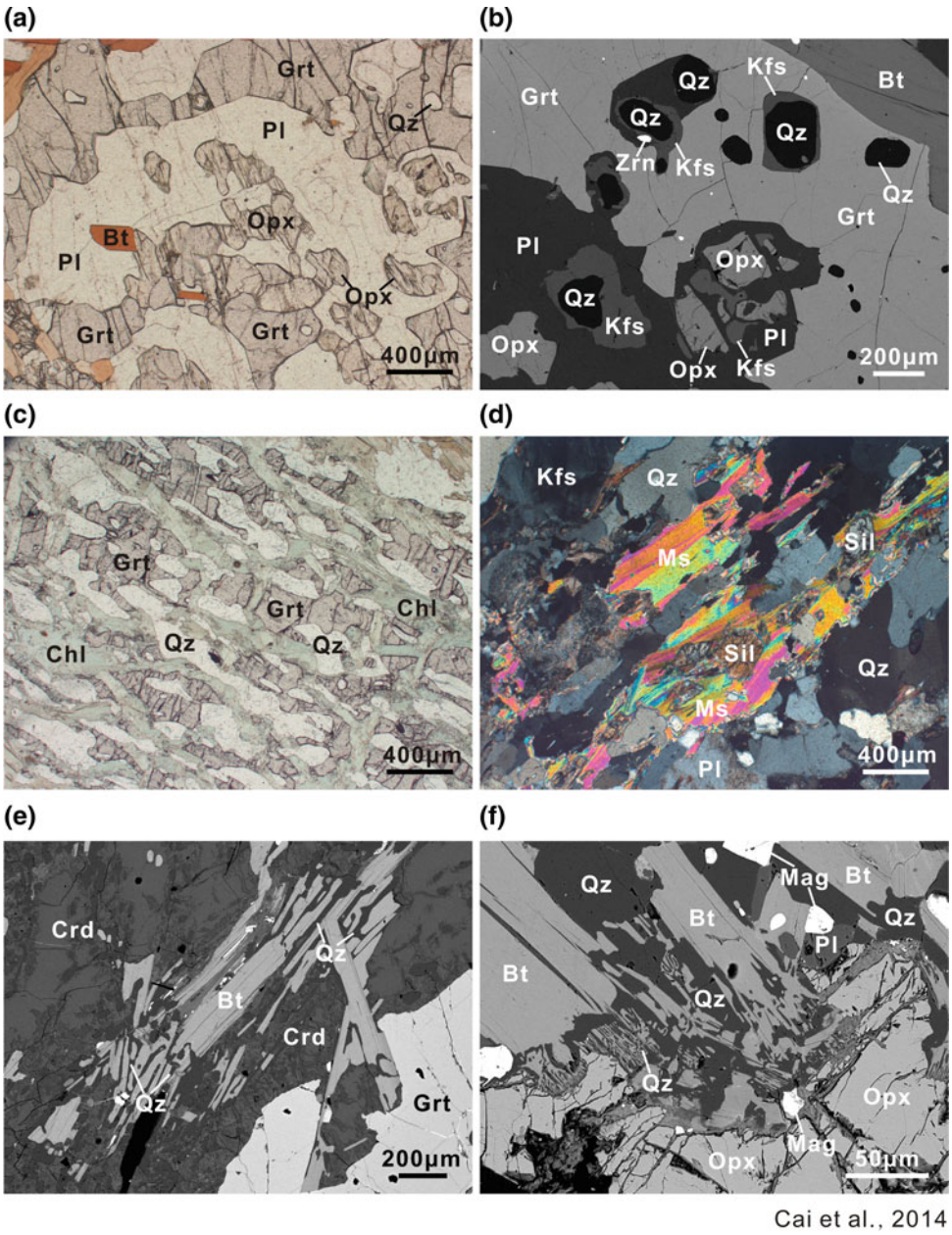

Fig. 8.9 Representative photomicrographs (PPL; cross-polarized light, CPL) and BSE images showing microtextures of the meta-pelitic rocks in the Khondalite Belt. **a** Photomicrograph (PPL) of symplectite of orthopyroxene + plagioclase replacing garnet. **b** BSE image of a garnet porphyroblast partially resorbed by orthopyroxene–plagioclase symplectites. Quartz separated from plagioclase by a thin film of K-feldspar. **c** Photomicrograph (PPL) of garnet retrogressed to chlorite + quartz. **d** Photomicrograph (CPL) of coarse-grained sillimanite surrounded by late muscovite. **e** BSE image of a porphyroblastic garnet rimmed by cordierite containing biotite + vermicular quartz. **f** BSE image of orthopyroxene rimmed by biotite + vermicular quartz (modified after Cai et al. 2014)

$$\text{Sil}| + |\text{Kfs}| + |\text{H}_2\text{O}| \rightarrow |\text{Ms}| + |\text{Pl}| + |\text{Qz} \quad (8.7)$$

Garnet is replaced by quartz + chlorite (Fig. 8.9c) due to the following reaction:

$$\text{Grt}| + |\text{H}_2\text{O}| \rightarrow |\text{Chl}| + |\text{Qz} \quad (8.8)$$

Biotite + quartz transecting cordierite and orthopyroxene grains (Fig. 8.9e, f) are indicative of late retrogression or rehydration by the following reaction:

$$\text{Crd/Opx}| + |\text{Kfs}| + |\text{H}_2\text{O}| \rightarrow |\text{Bt}| + |\text{Qz} \quad (8.9)$$

8.2.4 Mineral Chemistry

The chemical compositions of representative minerals were analyzed using an electron microprobe analyzer (EPM; JXA-8100, JEOL) at the Laboratory of Orogenic Belt and Crustal Evolution of Beijing University, China. The analyses were conducted under conditions of 15 kV acceleration voltage and 1.0×10^{-8} A probe current, and the data were regressed using the ZAF correction method. Representative chemical compositions of the minerals analyzed are listed in Tables 8.2, 8.3, 8.4, 8.5, 8.6 and 8.7.

Table 8.2 Representative compositional analyses of garnet from the Khondalite Series rocks within the Wulashan-Daqingshan Complex

Sample	BH27-1	BH27-1	BH27-2	BH27-2	BH27-3	BH27-3	BH27-3	BH39-4	BH39-4	BT16-6	BT51-1	P01-10
SiO_2	39.03	39.00	38.71	38.92	38.38	38.56	38.55	38.74	38.27	37.91	37.85	38.03
TiO_2	0.02	0.09	0.01	0.00	0.02	0.04	0.08	0.03	0.01	0.00	0.00	0.06
Al_2O_3	22.29	22.17	21.93	22.12	21.76	21.59	22.09	21.67	21.68	20.82	21.89	21.61
Cr_2O_3	0.03	0.00	0.00	0.05	0.08	0.06	0.05	0.00	0.03	0.09	0.08	0.00
FeO	27.18	27.66	27.78	27.68	26.71	27.94	27.73	30.85	32.41	30.92	30.88	30.34
MnO	0.40	0.46	0.40	0.35	0.83	0.86	0.78	0.32	0.46	0.70	0.69	0.63
MgO	10.04	9.51	9.90	10.42	7.79	8.22	8.07	7.43	6.37	7.57	8.32	8.47
CaO	1.31	1.18	1.45	1.42	3.54	2.26	2.15	1.07	1.58	1.20	0.91	0.97
Na_2O	0.03	0.00	0.00	0.01	0.00	0.08	0.09	0.00	0.01	0.02	0.03	0.01
Total	100.33	100.07	100.20	100.99	99.11	99.61	99.59	100.11	100.82	99.23	100.68	100.13
Si	2.978	2.995	2.965	2.950	2.994	2.995	2.993	3.021	2.985	2.986	2.924	2.950
Ti	0.001	0.005	0.001	0.000	0.001	0.002	0.005	0.002	0.001	0.000	0.000	0.003
Al	2.005	2.007	1.979	1.976	2.001	1.976	2.021	1.991	1.993	1.933	1.993	1.976
Cr	0.002	0.000	0.000	0.003	0.005	0.004	0.003	0.000	0.002	0.006	0.005	0.000
Fe^{3+}	0.039	0.000	0.089	0.123	0.004	0.038	0.000	0.000	0.035	0.094	0.159	0.120
Fe^{2+}	1.696	1.777	1.690	1.632	1.739	1.777	1.800	2.012	2.080	1.943	1.835	1.848
Mn	0.026	0.030	0.026	0.023	0.055	0.057	0.051	0.021	0.030	0.047	0.045	0.041
Mg	1.142	1.089	1.130	1.177	0.906	0.952	0.934	0.864	0.741	0.889	0.958	0.979
Ca	0.107	0.097	0.119	0.116	0.296	0.188	0.179	0.089	0.132	0.101	0.075	0.081
Na	0.004	0.000	0.000	0.002	0.000	0.012	0.014	0.000	0.002	0.003	0.005	0.002
Total	8.000	8.000	8.000	8.000	8.000	8.000	8.000	8.000	8.000	8.000	8.000	8.000
X_{Mg}	0.402	0.380	0.401	0.419	0.343	0.349	0.342	0.300	0.263	0.314	0.343	0.346
Grs	0.036	0.032	0.040	0.039	0.099	0.063	0.060	0.030	0.044	0.034	0.026	0.027
Prp	0.384	0.364	0.381	0.399	0.302	0.320	0.315	0.289	0.248	0.298	0.329	0.332
Alm	0.571	0.594	0.570	0.554	0.580	0.598	0.607	0.674	0.697	0.652	0.630	0.627
Sps	0.009	0.010	0.009	0.008	0.018	0.019	0.017	0.007	0.010	0.016	0.015	0.014

Notes (1) cations to 12 oxygens; (2) FeO^T is total FeO. (3) $X_{Mg} = Mg/(Mg + Fe)$; (4) $Grs = Ca/(Fe^{2+} + Mg + Mn + Ca)$; $Prp = Mg/(Fe^{2+} + Mg + Mn + Ca)$; $Alm = Fe^{2+}/(Fe^{2+} + Mg + Mn + Ca)$.; $Sps = Mn/(Fe^{2+} + Mg + Mn + Ca)$. The same below

Table 8.3 Representative compositional analyses of biotite from the Khondalite Series rocks within the Wulashan-Daqingshan Complex

Sample	BH27-1	BH27-1	BH27-1	BH27-2	BH27-3	BH27-3	BH27-3	BH39-4	BH39-4	BT35-1	BT35-1	BT35-1
SiO_2	36.49	37.32	36.48	36.51	36.54	37.01	36.05	35.67	35.21	36.06	36.18	35.90
TiO_2	6.78	4.84	6.65	6.84	4.29	4.40	4.34	6.03	6.05	5.89	4.78	5.19
Al_2O_3	15.18	16.50	15.72	15.66	16.24	16.22	16.00	16.52	16.86	17.40	17.12	16.36
Cr_2O_3	0.24	0.09	0.12	0.26	0.15	0.07	0.08	0.07	0.39	0.07	0.17	0.08
FeO^T	13.89	9.59	12.67	16.19	13.04	9.87	12.97	16.53	16.43	11.64	11.81	14.90
MnO	0.02	0.01	0.03	0.03	0.03	0.00	0.03	0.03	0.01	0.09	0.00	0.02
MgO	13.22	16.78	13.68	11.87	14.46	17.50	15.10	11.02	10.55	14.15	14.46	12.82
CaO	0.02	0.11	0.01	0.00	0.11	0.00	0.01	0.00	0.00	0.02	0.04	0.04
Na_2O	0.12	0.32	0.15	0.13	0.07	0.25	0.07	0.07	0.12	0.36	0.16	0.19
K_2O	9.75	9.57	9.95	9.55	9.74	10.05	9.97	9.91	10.04	9.86	9.98	10.00
ZnO	0.13	0.02	0.07	0.04	0.00	0.07	0.00	0.05	0.10	0.00	0.13	0.02
NiO	0.01	0.00	0.00	0.00	0.00	0.00	0.12	0.06	0.07	0.00	0.01	0.09
Total	95.85	95.15	95.52	97.08	94.67	95.44	94.74	95.95	95.83	95.54	94.84	95.61

(continued)

Table 8.3 (continued)

Sample	BH27-1	BH27-1	BH27-1	BH27-2	BH27-3	BH27-3	BH27-3	BH39-4	BH39-4	BT35-1	BT35-1	BT35-1
Si	2.710	2.723	2.703	2.699	2.729	2.706	2.699	2.679	2.654	2.655	2.687	2.689
Ti	0.379	0.266	0.371	0.380	0.241	0.242	0.244	0.341	0.343	0.326	0.267	0.293
Al	1.329	1.419	1.373	1.364	1.429	1.398	1.412	1.462	1.498	1.510	1.499	1.444
Cr	0.014	0.005	0.007	0.015	0.009	0.004	0.005	0.004	0.023	0.004	0.010	0.005
Fe^{2+}	0.863	0.585	0.785	1.001	0.814	0.604	0.812	1.038	1.036	0.717	0.734	0.933
Mn	0.001	0.001	0.002	0.002	0.002	0.000	0.002	0.002	0.001	0.006	0.000	0.001
Mg	1.464	1.825	1.511	1.308	1.610	1.908	1.685	1.234	1.186	1.553	1.601	1.432
Ca	0.002	0.009	0.001	0.000	0.009	0.000	0.001	0.000	0.000	0.002	0.003	0.003
Na	0.017	0.045	0.022	0.019	0.010	0.035	0.010	0.010	0.018	0.051	0.023	0.028
K	0.924	0.891	0.940	0.901	0.928	0.937	0.952	0.950	0.966	0.926	0.946	0.956
Zn	0.007	0.001	0.004	0.002	0.000	0.004	0.000	0.003	0.006	0.000	0.007	0.001
Ni	0.001	0.000	0.000	0.000	0.000	0.000	0.007	0.004	0.004	0.000	0.001	0.005
Total	7.710	7.768	7.718	7.691	7.780	7.838	7.830	7.727	7.734	7.750	7.776	7.785
X_{Mg}	0.629	0.757	0.658	0.567	0.664	0.760	0.675	0.543	0.534	0.684	0.686	0.605

Notes (1) cations to 11 oxygens; (2) FeO^T is total FeO. (3) X_{Mg} = Mg/(Mg + Fe), the same below

Table 8.4 Representative compositional analyses of feldspar from the Khondalite Series rocks within the Wulashan-Daqingshan Complex

Sample	BH27-1	BH27-1	BH27-2	BH27-3	BH27-3	BH27-3	BH27-3	BH39-4	BT35-1	BT35-1	BT51-1	P01-10
SiO_2	55.44	58.66	61.45	53.23	55.01	55.02	64.23	59.06	61.96	63.66	62.27	61.93
TiO_2	0.03	0.01	0.04	0.04	0.00	0.00	0.05	0.00	0.03	0.04	0.00	0.02
Al_2O_3	28.73	25.98	24.21	29.43	28.29	28.49	18.64	26.02	23.79	18.88	23.86	23.71
Cr_2O_3	0.00	0.00	0.00	0.01	0.00	0.00	0.07	0.00	0.00	0.02	0.04	0.00
FeO^T	0.31	0.00	0.00	0.55	0.09	0.04	0.04	0.01	0.00	0.05	0.06	0.03
MnO	0.02	0.00	0.01	0.03	0.02	0.00	0.01	0.04	0.00	0.00	0.02	0.01
MgO	0.02	0.00	0.01	0.09	0.02	0.00	0.00	0.01	0.00	0.00	0.00	0.01
CaO	9.48	6.60	5.21	11.12	9.75	9.52	0.04	6.81	4.43	0.01	4.82	4.95
Na_2O	6.71	8.49	8.55	5.36	5.94	6.20	1.16	7.26	9.52	1.45	9.02	8.62
K_2O	0.13	0.43	0.16	0.11	0.29	0.31	14.84	0.32	0.22	15.42	0.29	0.41
Total	100.87	100.17	99.63	99.97	99.41	99.58	99.07	99.53	99.95	99.53	100.38	99.67
Si	2.454	2.587	2.734	2.397	2.482	2.473	2.986	2.647	2.729	2.934	2.743	2.753
Ti	0.001	0.000	0.001	0.001	0.000	0.000	0.002	0.000	0.001	0.001	0.000	0.001
Al	1.499	1.350	1.270	1.562	1.504	1.509	1.021	1.374	1.235	1.025	1.239	1.242
Cr	0.000	0.000	0.000	0.000	0.000	0.000	0.003	0.000	0.000	0.001	0.001	0.000
Fe^{2+}	0.011	0.000	0.000	0.021	0.003	0.002	0.002	0.000	0.000	0.002	0.002	0.001
Mn	0.001	0.000	0.000	0.001	0.001	0.000	0.000	0.002	0.000	0.000	0.001	0.000
Mg	0.001	0.000	0.000	0.006	0.001	0.000	0.000	0.001	0.000	0.000	0.000	0.001
Ca	0.450	0.312	0.248	0.537	0.471	0.458	0.002	0.327	0.209	0.000	0.228	0.236
Na	0.576	0.726	0.737	0.468	0.520	0.540	0.105	0.631	0.813	0.130	0.770	0.743
K	0.007	0.024	0.009	0.006	0.017	0.018	0.880	0.018	0.012	0.907	0.016	0.023
Total	5.000	5.000	5.000	5.000	5.000	5.000	5.000	5.000	5.000	5.000	5.000	5.000
An	0.435	0.294	0.250	0.531	0.468	0.451	0.002	0.335	0.202	0.000	0.224	0.235
Ab	0.558	0.684	0.741	0.463	0.516	0.532	0.106	0.646	0.786	0.125	0.760	0.742
Or	0.007	0.023	0.009	0.006	0.017	0.017	0.892	0.019	0.012	0.875	0.016	0.023

Notes (1) cations to 8 oxygens; (2) FeO^T is total FeO;(3) An = 100* Ca/(Ca + Na + K); Ab = 100*Na/(Ca + Na + K); Or = 100* K/(Ca + Na + K), the same below (modified after Cai et al. 2014)

Table 8.5 Representative compositional analyses of cordierite from the Khondalite Series rocks within the Wulashan-Daqingshan Complex

Sample	BH27-1	BH27-1	BH27-1	BH39-4	BH39-4	BH39-4	BH39-4
SiO_2	49.06	50.11	49.96	49.92	49.88	49.74	49.54
TiO_2	0.06	0.00	0.00	0.02	0.00	0.00	0.00
Al_2O_3	34.73	33.90	34.11	34.40	34.24	33.99	34.01
Cr_2O_3	0.00	0.02	0.00	0.02	0.02	0.00	0.00
FeO^T	4.83	4.58	4.54	6.94	6.68	6.87	6.81
MnO	0.07	0.05	0.03	0.04	0.06	0.02	0.00
MgO	10.62	10.63	10.61	8.66	9.02	8.97	9.40
CaO	0.00	0.03	0.01	0.00	0.00	0.02	0.02
Na_2O	0.05	0.07	0.04	0.05	0.10	0.07	0.09
K_2O	0.00	0.00	0.01	0.00	0.02	0.00	0.04
ZnO	0.01	0.00	0.05	0.08	0.00	0.11	0.09
NiO	0.00	0.00	0.00	0.02	0.04	0.00	0.01
Total	99.43	99.38	99.35	100.15	100.05	99.80	100.00
Si	4.903	5.013	4.999	5.019	5.007	5.012	4.970
Ti	0.005	0.000	0.000	0.002	0.000	0.000	0.000
Al	4.091	3.997	4.022	4.076	4.051	4.036	4.021
Cr	0.000	0.002	0.000	0.002	0.002	0.000	0.000
Fe^{3+}	0.105	0.000	0.000	0.000	0.000	0.000	0.062
Fe^{2+}	0.299	0.383	0.380	0.583	0.561	0.579	0.509
Mn	0.006	0.004	0.003	0.003	0.005	0.002	0.000
Mg	1.582	1.585	1.583	1.298	1.350	1.347	1.406
Ca	0.000	0.003	0.001	0.000	0.000	0.002	0.002
Na	0.010	0.014	0.008	0.010	0.019	0.014	0.018
K	0.000	0.000	0.001	0.000	0.003	0.000	0.005
Zn	0.001	0.000	0.004	0.006	0.000	0.008	0.007
Ni	0.000	0.000	0.000	0.002	0.003	0.000	0.001
Total	11.000	11.000	11.000	11.000	11.000	11.000	11.000
X_{Mg}	0.841	0.805	0.806	0.690	0.706	0.699	0.731

Notes (1) cations to 18 oxygens; (2) FeO^T is total FeO. (3) X_{Mg} = Mg/(Mg + Fe). (modified after Cai et al. 2014)

Table 8.6 Representative compositional analyses of orthopyroxene from the Khondalite Series rocks within the Wulashan-Daqingshan Complex

Sample	BH27-3	BH27-3	BH27-3	BH27-3	BH27-3	BH27-3	BT38-1
SiO_2	50.68	51.02	50.43	51.50	51.03	51.47	50.08
TiO_2	0.07	0.06	0.09	0.12	0.10	0.07	0.02
Al_2O_3	2.66	3.45	3.75	3.20	2.71	2.82	3.71
Cr_2O_3	0.06	0.00	0.03	0.00	0.02	0.03	0.07
FeO^T	25.02	24.78	23.94	23.30	24.35	24.37	24.67
MnO	0.22	0.25	0.26	0.23	0.32	0.24	0.25
MgO	20.12	19.41	20.99	20.67	20.28	20.40	20.96
CaO	0.20	0.20	0.20	0.19	0.28	0.22	0.11
Na_2O	0.06	0.00	0.13	0.03	0.01	0.00	0.03
ZnO	0.12	0.00	0.06	0.05	0.14	0.00	0.05
NiO	0.02	0.00	0.06	0.04	0.00	0.08	0.00
Total	99.21	99.17	99.93	99.37	99.24	99.70	99.95
Si	1.922	1.940	1.884	1.939	1.933	1.939	1.875
Ti	0.002	0.002	0.003	0.003	0.003	0.002	0.001

(continued)

Table 8.6 (continued)

Sample	BH27-3	BH27-3	BH27-3	BH27-3	BH27-3	BH27-3	BT38-1
Al	0.119	0.155	0.165	0.142	0.121	0.125	0.164
Cr	0.002	0.000	0.001	0.000	0.001	0.001	0.002
Fe^{3+}	0.035	0.000	0.070	0.000	0.008	0.000	0.086
Fe^{2+}	0.759	0.788	0.678	0.734	0.764	0.768	0.687
Mn	0.007	0.008	0.008	0.007	0.010	0.008	0.008
Mg	1.138	1.100	1.169	1.160	1.145	1.146	1.170
Ca	0.008	0.008	0.008	0.008	0.011	0.009	0.004
Na	0.004	0.000	0.009	0.002	0.001	0.000	0.002
Zn	0.003	0.000	0.002	0.001	0.004	0.000	0.001
Ni	0.001	0.000	0.002	0.001	0.000	0.002	0.000
Total	4.000	4.000	4.000	4.000	4.000	4.000	4.000
X_{Mg}	0.600	0.583	0.633	0.613	0.600	0.599	0.630
Wo	0.004	0.004	0.004	0.004	0.006	0.005	0.002
En	0.587	0.580	0.607	0.610	0.594	0.596	0.601
Fs	0.409	0.416	0.389	0.386	0.400	0.399	0.397

Notes (1) cations to 6 oxygens; (2) FeO^T is total FeO. (3) X_{Mg} = Mg/(Mg + Fe) (modified after Cai et al. 2014)

Table 8.7 Representative compositional analyses of spinel from the Khondalite Series rocks within the Wulashan-Daqingshan Complex

Sample	BH39-4	BH39-4	BH27-2	BH27-2	BT16-6	BT38-1
SiO_2	0.12	0.04	0.05	0.06	0.16	0.15
TiO_2	0.02	0.00	0.03	0.05	0.02	0.24
Al_2O_3	58.72	58.85	56.57	56.93	53.92	55.73
Cr_2O_3	1.04	0.41	3.45	2.81	4.38	2.31
FeO^T	24.20	26.26	24.40	27.60	22.78	17.67
MnO	0.00	0.05	0.07	0.00	0.10	0.06
MgO	4.16	4.45	5.69	5.64	5.10	8.92
CaO	0.02	0.01	0.02	0.00	0.00	0.00
Na_2O	0.39	0.28	0.31	0.22	0.47	0.56
K_2O	0.00	0.00	0.02	0.00	0.01	0.02
ZnO	10.36	9.59	9.04	6.26	12.13	13.83
NiO	0.00	0.03	0.09	0.01	0.13	0.02
Total	99.02	99.98	99.73	99.58	99.20	99.51
Si	0.003	0.001	0.001	0.002	0.005	0.004
Ti	0.000	0.000	0.001	0.001	0.000	0.005
Al	1.977	1.963	1.890	1.900	1.835	1.836
Cr	0.023	0.009	0.077	0.063	0.100	0.051
Fe^{3+}	0.014	0.041	0.046	0.044	0.082	0.125
Fe^{2+}	0.564	0.580	0.532	0.609	0.468	0.288
Mn	0.000	0.001	0.002	0.000	0.002	0.001
Mg	0.177	0.188	0.240	0.238	0.220	0.372
Ca	0.001	0.000	0.001	0.000	0.000	0.000
Na	0.022	0.015	0.017	0.012	0.026	0.030
K	0.000	0.000	0.001	0.000	0.000	0.001
Zn	0.218	0.200	0.189	0.131	0.259	0.285
Ni	0.000	0.001	0.002	0.000	0.003	0.000
Total	3.000	3.000	3.000	3.000	3.000	3.000
X_{Mg}	0.239	0.244	0.311	0.281	0.319	0.563

Notes (1) cations to 4 oxygens; (2) FeO^T is total FeO. (3) X_{Mg} = Mg/(Mg + Fe) (modified after Cai et al. 2014)

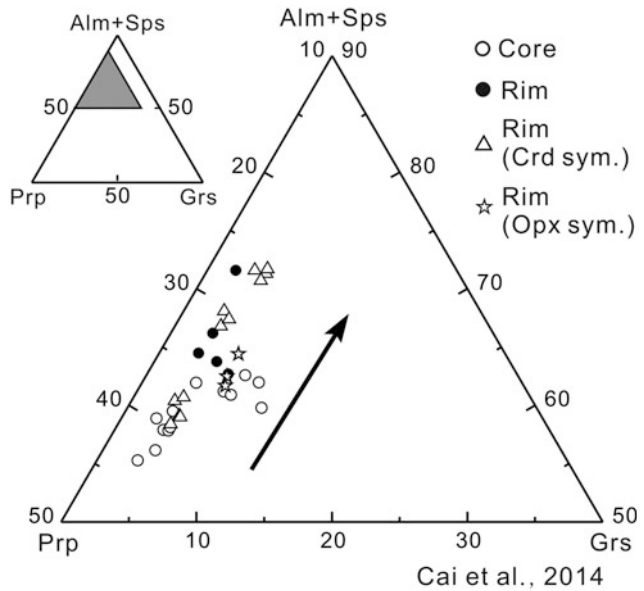

Fig. 8.10 Prp–Alm + Sps–Grs diagram showing garnet compositions (modified after Cai et al. 2014)

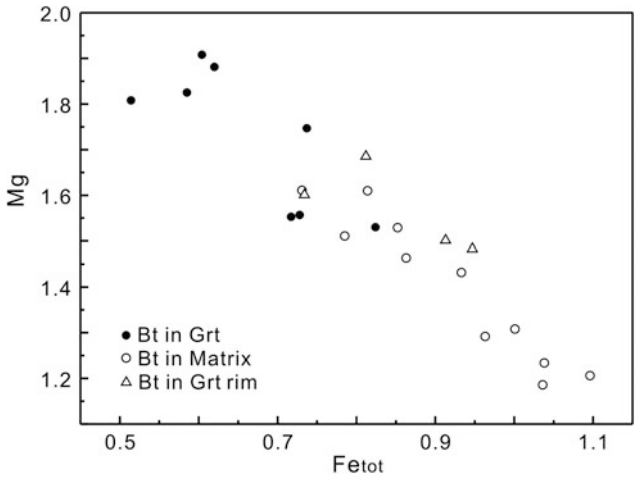

Fig. 8.11 Mg versus Fe^{tot} variation diagram for biotites (modified after Cai et al. 2014)

8.2.4.1 Garnet

The garnets are essentially almandine (55–70 mol%)–pyrope (25–40 mol%) solid solutions with low spessartine (0.7–1.9 mol%) and grossularite (2.1–9.9 mol%) contents (Table 8.2; Fig. 8.10). In general, the X_{Mg} = Mg/(Mg + Fe^{2+}) values of the garnets reduced from core to rim within an individual garnet due to cation diffusion after crystallization (Dallmeyer and Dodd 1971). In individual samples, garnet rims in contact with cordierite show low MgO and high FeO contents compared to the garnet core.

8.2.4.2 Mica

Representative compositions of biotite and muscovite are listed in Table 8.3. Matrix biotites are slightly less magnesian than those rimming garnets, and those included in garnet porphyroblasts show higher values of X_{Mg} (0.68–0.76), suggesting Fe–Mg exchange and late re-equilibration (Cesare et al. 2008). The Ti contents of the biotites varied from 2.38 to 6.84 wt%, indicating a high metamorphic grade (Spear et al. 1990; Henry and Guidotti 2002). A variation diagram of Mg versus Fe^{tot} for biotite (Fig. 8.11) defines a near-linear negative correlation relation indicating Mg–Fe substitutions within biotite (Aydin et al. 2003). Moreover, the X_{Mg} values of muscovite in the Ms–Sil–Grt gneiss are 0.46–0.48.

8.2.4.3 Feldspar

The composition of feldspar is shown in Table 8.4, and the chemical compositions of the plagioclases are largely controlled by the bulk rock composition. Plagioclases that occur as symplectites have lower anorthite contents than plagioclase included in the garnets and matrix plagioclase in an individual sample. The composition of the K-feldspar host of the perthite is approximately $Or_{88}Ab_{13}$.

8.2.4.4 Other Minerals

Cordierites display minor compositional variations of X_{Mg} in the range of 0.70–0.84 (Table 8.5). Cordierite rims adjacent to the garnet have lower values of X_{Mg} (0.69), whereas those close to spinel have slightly higher values of X_{Mg} (up to 0.73).

Orthopyroxenes (En 58–61) belong to the solid solution between enstatite and ferrosilite, displaying similar X_{Mg} values ranging from 0.58 to 0.63 (Table 8.6). The symplectite orthopyroxene has low Al_2O_3 contents (2.71–2.82 wt%) compared with orthopyroxene rimming garnet.

The spinels are primarily solid solutions between hercynite and Mg-spinel with high ZnO contents (6.26–12.13 wt%) and minor Cr_2O_3 (0.41–4.38 wt%) without compositional zoning. The X_{Mg} values of the spinels range from 0.24 to 0.32 (Table 8.7).

8.2.5 Metamorphic P–T Conditions

The metamorphic conditions during the polyphase thermal evolution of the meta-pelitic rocks in the Khondalite Belt have been investigated using quantitative *P–T* pseudosections. Using changes in the predicted mineral abundances, we have investigated the predicted peak and post-peak assemblages, and retrograde evolution on *P–T* pseudosections (Korhonen et al. 2010). Pseudosections were constructed for the bulk compositions of samples BH27-2, BH39-4, and BT51-1 using THERMOCALC 3.33 (Powell and Holland 1988; updated June 2009) and the internally consistent thermodynamic dataset of Holland and Powell (1998; dataset tcds55, created in November 2003). The calculations were

Table 8.8 Bulk compositions used for mineral equilibria modeling the representative Daqingshan Khondalite Series rocks

Sample	SiO_2	Al_2O_3	CaO	MgO	FeO	K_2O	Na_2O	TiO_2	Fe_2O_3	MnO	CO_2	LOI	Total
XRF whole rock analyses (wt%)													
BH39-4	61.37	17.6	1.66	3.27	5.62	3.65	1.63	0.78	1.71	0.06	0.34	1.69	97.35
BH27-2	60.33	19.18	0.93	2.63	5.69	3.21	2	0.94	1.55	0.09	0.34	1.59	96.55
BT51-1	77.71	11.6	0.86	1.09	0.84	3.25	2.07	0.44	1.1	0.01	0.1	0.69	99.76
Normalized molar proportion													
Sample	Figure	SiO2	Al_2O_3	CaO	MgO	FeO	K_2O	Na_2O	TiO_2	O	H_2O	Total	
BH27-2	Figure 8.12a	67.72	12.69	1.12	4.40	5.34	2.30	2.18	0.79	0.65	2.80	100.00	
BH39-4	Figure 8.12d	67.44	11.41	1.95	5.36	5.16	2.56	1.74	0.64	0.69	3.04	100.00	
BT51-1	Figure 8.12c	68.94	13.17	1.74	2.56	3.23	2.23	3.00	0.37	0.24	4.52	100.00	

Notes 1, XRF composition; 2, Calculated composition; 3, Melt-reintegrated composition (modified after Cai et al. 2014)

performed in the chemical system NCKFMASHTO (Na_2O–CaO–K_2O–FeO–MgO–Al_2O_3–SiO_2–H_2O–TiO_2–Fe_2O_3), which provides the most realistic compositional approximation to the meta-pelitic rocks so that suprasolidus conditions can be further calculated (White et al. 2001, 2003, 2007). The phases involved in modeling and the related a-*x* models include garnet (White et al. 2007), biotite and melt (White et al. 2007), hydrous cordierite (Holland and Powell 1998), orthopyroxene and spinel–magnetite (White et al. 2002), plagioclase and K-feldspar (Holland and Powell 2003), muscovite (Coggon and Holland 2002), and ilmenite–hematite (White et al. 2000). The aluminosilicates, quartz, and rutile are treated as pure end-member phases.

Bulk rock compositions for a suite of samples were determined by X-ray fluorescence analysis using a PW4400 X-ray fluorescence (XRF) spectrometer at the National Research Center of Geoanalysis, Beijing, China. FeO contents were analyzed by Fe^{2+} titration and the Fe_2O_3 contents were calculated by the difference method. MnO was neglected in the modeling as the MnO contents of these samples were low (<0.15 wt%; Table 8.8). MnO is considered to have less effect on the stability of ferromagnesian assemblages (Wei et al. 2004). However, pseudosections based on whole-rock compositions are quantitatively applicable only with fairly homogeneous rocks.

For sample BT51-1 (Ms–Sil–Grt gneiss), quartzofeldspathic and sillimanite sections are compositionally layered. In these cases, the measured bulk compositions are not effective (Hollis et al. 2006); consequently, calculated bulk compositions are applied for constructing the *P–T* pseudosection for BT51-1, using integrated data from the modal abundances of all phases relevant to the modal system and using microprobe analyses of the grains (Wei et al. 2003, 2007; White et al. 2003). Based on detailed petrological observations at the thin section scale, for the bulk composition calculation we used the modal proportions (vol %) for BT51-1; the values were garnet 6, biotite 10, muscovite 8, plagioclase 30, K-feldspar 10, quartz 25.5, sillimanite 10, magnetite 0.3, and ilmenite 0.2. These modal proportions were then combined with electron microprobe data. The proportion of Fe^{3+} to Fe^{2+} was retrieved from Fe-bearing minerals for which the Fe^{3+}/Fe^{2+} ratio was estimated using the stoichiometric charge balance. The measured bulk compositions and recalculated compositions of modeled samples are shown in Table 8.8.

Here, an appropriate H_2O content is determined by calculating the lower limit of the H_2O content contained in a given assemblage. For sample BT51-1, the H_2O content was used to produce a water-saturated solidus to discuss the *P–T* conditions of the M_4 metamorphic stage located just below the water-saturated solidus. The amount of H_2O used for suprasolidus assemblages was set such that assemblages were just H_2O-saturated at the solidus, at ~5 kbar. Subsolidus assemblages were calculated with H_2O in excess.

8.2.5.1 Peak Metamorphic Stage

The inferred peak mineral assemblage (M_2) consists of garnet +biotite + K-feldspar + sillimanite + plagioclase + ilmenite + quartz ± magnetite + liquid in the meta-pelitic rocks of the Khondalite Belt. The peak field is stable over a limited temperature range but a large pressure range covering a wide *P–T* range and must be further constrained using compositional isopleths or mineral modal proportions. Isopleths of x(grt) = $Fe^{2+}/(Mg + Fe^{2+})$, z(grt) = $Ca/(Ca + Mg + Fe^{2+})$ and ca(pl) = Ca/(Ca + Na + K) and mineral modal proportions are contoured to determine the peak *P–T* conditions. For sample BH27-2 (Fig. 8.12a), the isopleths for x(grt) and ca(pl) determine the peak conditions of 840–890 °C at 10.1–11.9 kbar. For sample BH39-4 (Fig. 8.12b), the isopleth for z(grt) and the modal proportions for garnet and plagioclase indicate predicted peak *P–T* conditions of 850–880 °C at 9.7–11.5 kbar.

8.2.5.2 Post-peak Metamorphic Stage

The cordierite symplectites rim garnet porphyroblasts suggest a stage of retrogression. Moreover, large cordierite with

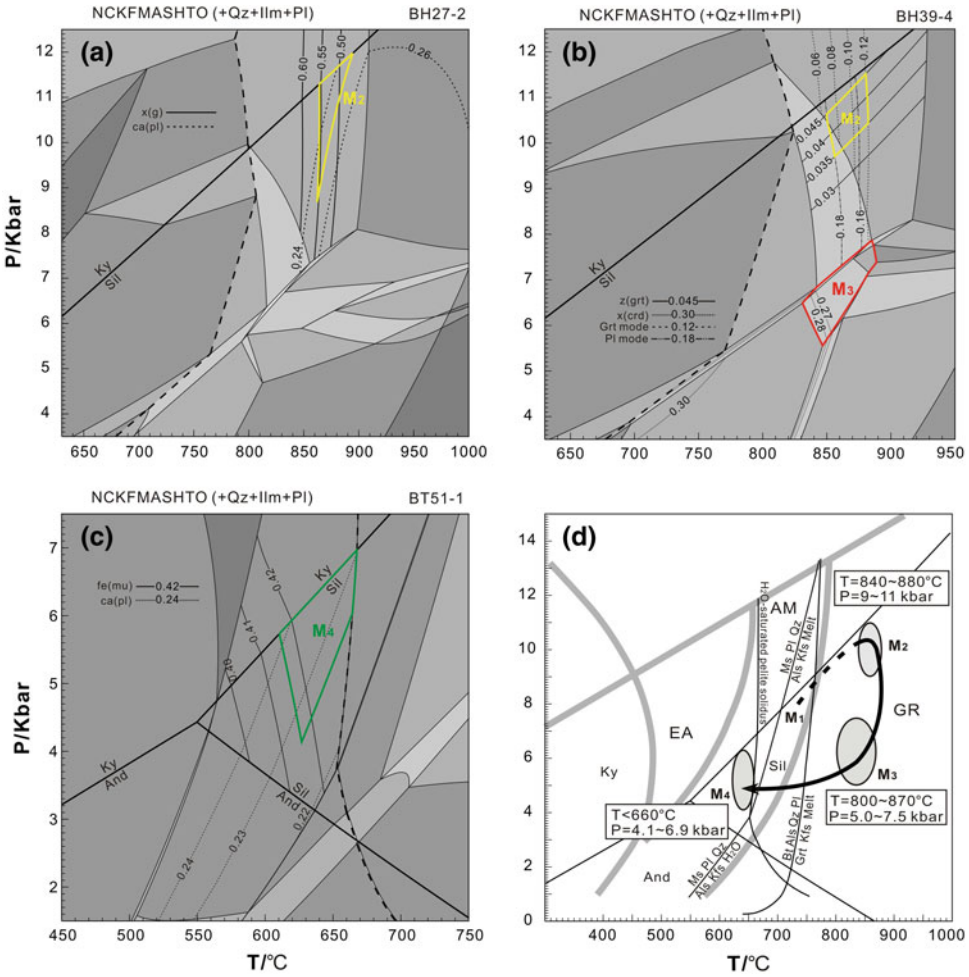

Fig. 8.12 *P–T* pseudosection for samples **a** BT27-2, **b** BH39-4, **c** BT51-1. Isopleths for garnet, z(grt) = Ca/(Ca + Mg + Fe) and x (grt) = Fe/(Mg + Fe), plagioclase, ca(pl) = Ca/(Ca + Na + K), cordierite, x(crd) = Fe/(Fe + Mg), and muscovite, fe(mu) = Fe/(Mg + Fe) are contoured in the predicted peak, post-peak, and late cooling field. Calculated garnet and plagioclase modal proportions are contoured for BH39-4. The *thick dashed line* represents the solidus. *Thick solid lines* delineate conditions of peak, post-peak and late cooling field metamorphism. **d** Inferred clockwise *P–T* path of meta-pelitic rocks in the Khondalite Belt based on phase equilibria modeling. The inferred prograde segment is shown by a *dashed line*. The division of metamorphic phases is after Spear et al. (1995). The melting reactions are from Le Breton and Thompson (1988) and Spear et al. (1995) (modified after Cai et al. 2014)

sillimanite, spinel, and ilmenite inclusions also occur in the matrix away from garnet. The inferred post-peak (M_3) mineral assemblage is biotite + cordierite + garnet + K-feldspar + plagioclase + ilmenite + quartz ± sillimanite ± spinel ± magnetite + liquid. For Crd–Grt–Bt gneiss (sample BH39-4), the predicted M_3 assemblage is stable under *P–T* conditions of 830–890 °C and 5.5–7.8 kbar (Fig. 8.12b).

8.2.5.3 Retrograde Cooling Stage

The *P–T* conditions for the late retrograde metamorphism are indicated in the pseudosection for Ms–Sil–Grt gneiss, sample BT51-1 (Figs. 8.12c). The predicted M_4 assemblage is biotite + muscovite + sillimanite + plagioclase + ilmenite + quartz + H_2O, which is consistent with the petrographic observations for BT51-1, where sillimanite is surrounded by late muscovite (Fig. 8.9d). The upper temperature of the inferred retrograde cooling (M_4) field is bounded by the water-saturated solidus. The lower pressure limit of the M_4 stage is constrained to >4.1 kbar at 628 °C by isopleths of muscovite, Fe(mu) = Fe/(Mg + Fe), and plagioclase, ca (pl) = Ca/(Ca + Na + K). The stability of sillimanite provides an upper pressure constraint of <6.9 kbar. The M_4 late retrograde assemblage is predicted to be stable at <660 °C and 4.1–6.9 kbar.

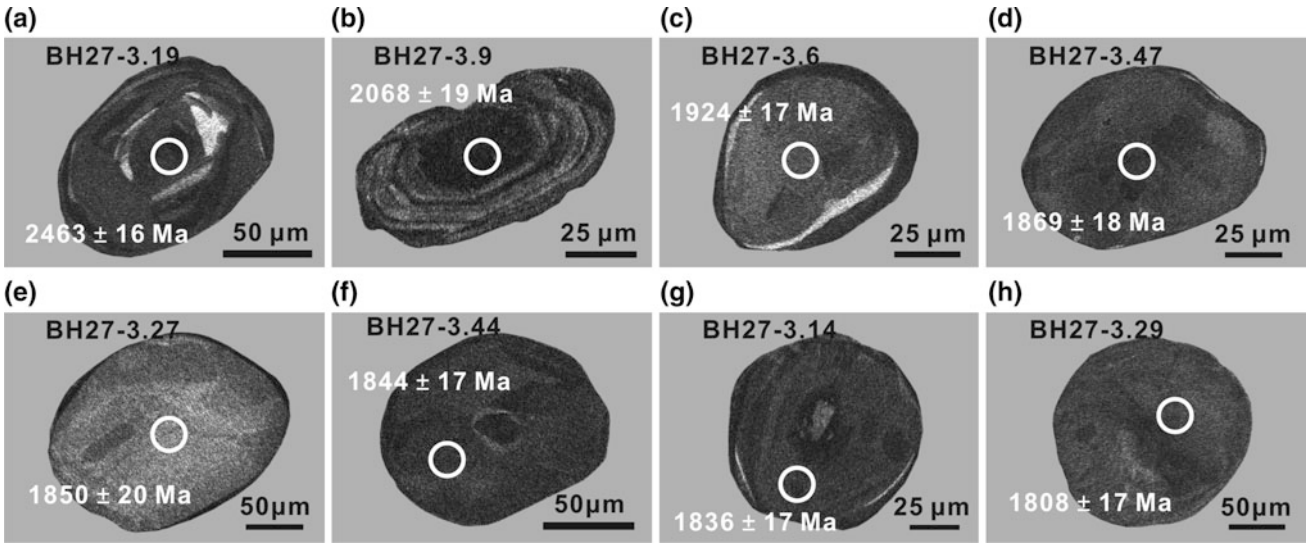

Fig. 8.13 Cathodoluminescent (CL) images and LA-ICP-MS U–Pb ages of zircons from the Hyp–Grt–Bt gneiss (BH27-3) (modified after Cai et al. 2015). **a** The zircon grain showing a middle-low-luminescent (*gray-grayish black*) magmatic zoning core, low-luminescent (*grayish black-black*) rim. **b** The elongated zircon grain showing middle-low-luminescent (*gray-grayish black*) magmatic zoning. **c**–**e** The zircon grains showing homogeneous middle-low-luminescence (*gray-black*). **f**, **g** The zircon grains showing a small grayish black-luminescent core and homogeneous low-luminescent (*grayish black-black*) rim. **h** The zircon grain showing homogeneous low-luminescence (*grayish black-black*)

8.2.6 U–Pb Dating of Zircons

8.2.6.1 Hyp–Grt–Bt Gneiss (BH27-3)

The detrital zircon of the sample BH27-3 showed a relatively high Th content ($96 \times 10^{-6} - 1002 \times 10^{-6}$). However, the content of U is variable ($185 \times 10^{-6} - 1145 \times 10^{-6}$). The ratio of Th/U is 0.23–1.46. In comparison, the metamorphic zircon has a lower Th content ($6 \times 10^{-6} - 616 \times 10^{-6}$) and Th/U ratio (0.01–0.49) with variable U content ($183 \times 10^{-6} - 1256 \times 10^{-6}$). The $^{207}Pb/^{206}Pb$ age could be divided into two groups: one is in the range of 2047–2463 Ma for the detrital zircon, and the other is 1808–1924 Ma for metamorphic zircon with a weighted average age of 1863 ± 11 Ma (MSWD = 2.9, n = 33; Fig. 8.13 and 8.17a).

8.2.6.2 Grt-Bearing Quartzofeldspathic Rock (BH28-1)

For the sample BH28-1, the detrital zircon exhibits a high content of Th ($35 \times 10^{-6} - 763 \times 10^{-6}$) and ratio of Th/U (0.12–1.56) with variable U content ($61 \times 10^{-6} - 1040 \times 10^{-6}$). Nevertheless, the metamorphic zircon has a low Th content ($5 \times 10^{-6} - 73 \times 10^{-6}$) and Th/U ratio (0.01–0.13). In the $^{207}Pb/^{235}U$-$^{206}Pb/^{238}U$ diagram (Fig. 8.17b), the detrital zircon records $^{207}Pb/^{206}Pb$ age of 2076–2502 Ma, the metamorphic zircon shows $^{207}Pb/^{206}Pb$ age of 1825–1922 Ma with weighted average age of 1858 ± 8 Ma (MSWD = 2.1, n = 28; Fig. 8.14).

8.2.6.3 Hyp–Grt–Bt Gneiss (BT38-1)

The detrital zircon in the sample BT38-1 displays variable Th content ($6 \times 10^{-6} - 614 \times 10^{-6}$), U content ($81 \times 10^{-6} - 1846 \times 10^{-6}$), and Th/U ratio (0.01–1.67). For the metamorphic zircon, the Th and U contents are relatively low ($31 \times 10^{-6} - 214 \times 10^{-6}$ and $73 \times 10^{-6} - 438 \times 10^{-6}$, respectively). $^{207}Pb/^{206}Pb$ age of the detrital zircon is 2115–2499 Ma, and that of metamorphic zircon is 1906–1962 Ma with a weighted average age of 1946 ± 5 Ma(MSWD = 0.76, n = 30; Figs. 8.15 and 8.17c).

8.2.6.4 Sil–Crd–Grt Gneiss (BT20-1)

The Th and U content of the detrital zircon in sample BT20-1 are variable, with values of $16 \times 10^{-6} - 239 \times 10^{-6}$ and $30 \times 10^{-6} - 360 \times 10^{-6}$, respectively. Similar to other samples, metamorphic zircon shows a low Th content ($28 \times 10^{-6} - 117 \times 10^{-6}$) and ratio of Th/U (0.11–0.43). The detrital zircon reveals $^{207}Pb/^{206}Pb$ age of 2033–2408 Ma, and the metamorphic zircon displays $^{207}Pb/^{206}Pb$ age of 1929–1966 Ma with a weighted average age of 1946 ± 12 Ma (MSWD = 2.9, n = 7; Figs. 8.16 and 8.17d).

8.2.7 Discussion

8.2.7.1 Age of Protoliths

The histogram of the detrital zircon from the meta-pelitic rocks in the Khondalite Belt show major peak ages

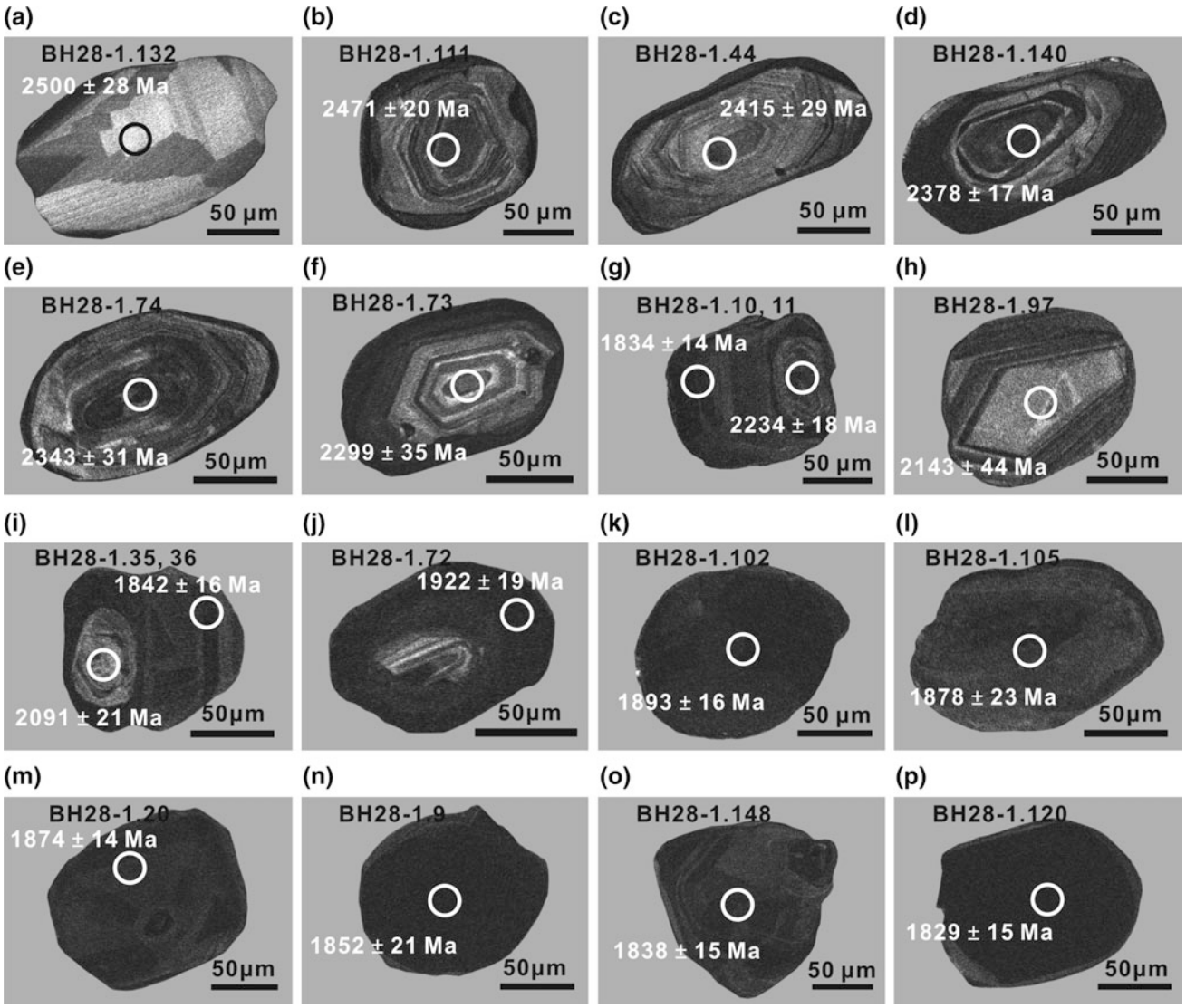

Fig. 8.14 CL images and LA-ICP-MS U–Pb ages of zircons from the Grt-bearing quartzofeldspathic rock (BH28-1) (modified after Cai et al. 2015). **A** Elongated zircon grain showing high-middle-luminescent (*grayish white-gray*) magmatic zoning structure. **b–j**, **o** The zircon grains showing a middle-luminescent (*gray-grayish black*) magmatic zoning core, low-luminescent (*grayish black-black*) rim relationship. **k–n**, **p** The zircon grains showing homogeneous low-luminescence (*grayish black-black*)

concentrated at 2400–2500 Ma, ~2300 Ma, and 2000–2100 Ma (Fig. 8.18). These results were consistent with previously published data (Wan et al. 2006, 2009; Wu et al. 2006; Xia et al. 2006a, b; Dong et al. 2007, 2012; Yin et al. 2009, 2011; Zhou and Geng 2009). It is therefore deduced that the deposition age of the meta-pelitic rocks from the Khondalite Belt after 2200–2000 Ma.

8.2.7.2 Tectonic Settings and Provenance of Protoliths

The geochemistries of sediments deposited in oceanic island arc, continental island arc, active continental margin, and passive margin tectonic settings have been investigated by many groups (e.g., Bhatia 1983; Bhatia and Crook 1986; Roser and Korsch 1986; McLennan et al. 1990; McLennan and Taylor 1991; Bhat and Ghosh 2001). Generally, Al_2O_3, $Fe_2O_3^T$ + MgO, TiO_2, and Al_2O_3/SiO_2 ratios decrease in sandstones from oceanic island arc settings to passive margins, while SiO_2 and K_2O/Na_2O ratios increase (Bhatia 1983). The meta-felsic rocks of the khondalite series rock samples in the Khondalite Belt have high SiO_2, and moderate Al_2O_3, TiO_2, and Al_2O_3/SiO_2 ratios. Most of these samples show strong affinity with graywackes from continental island arc or active continental margin settings (Fig. 8.19). The contents and ratios of trace elements (including REEs) in most of the meta-felsic rocks in the khondalite series rock samples within the Khondalite Belt and the adjacent region

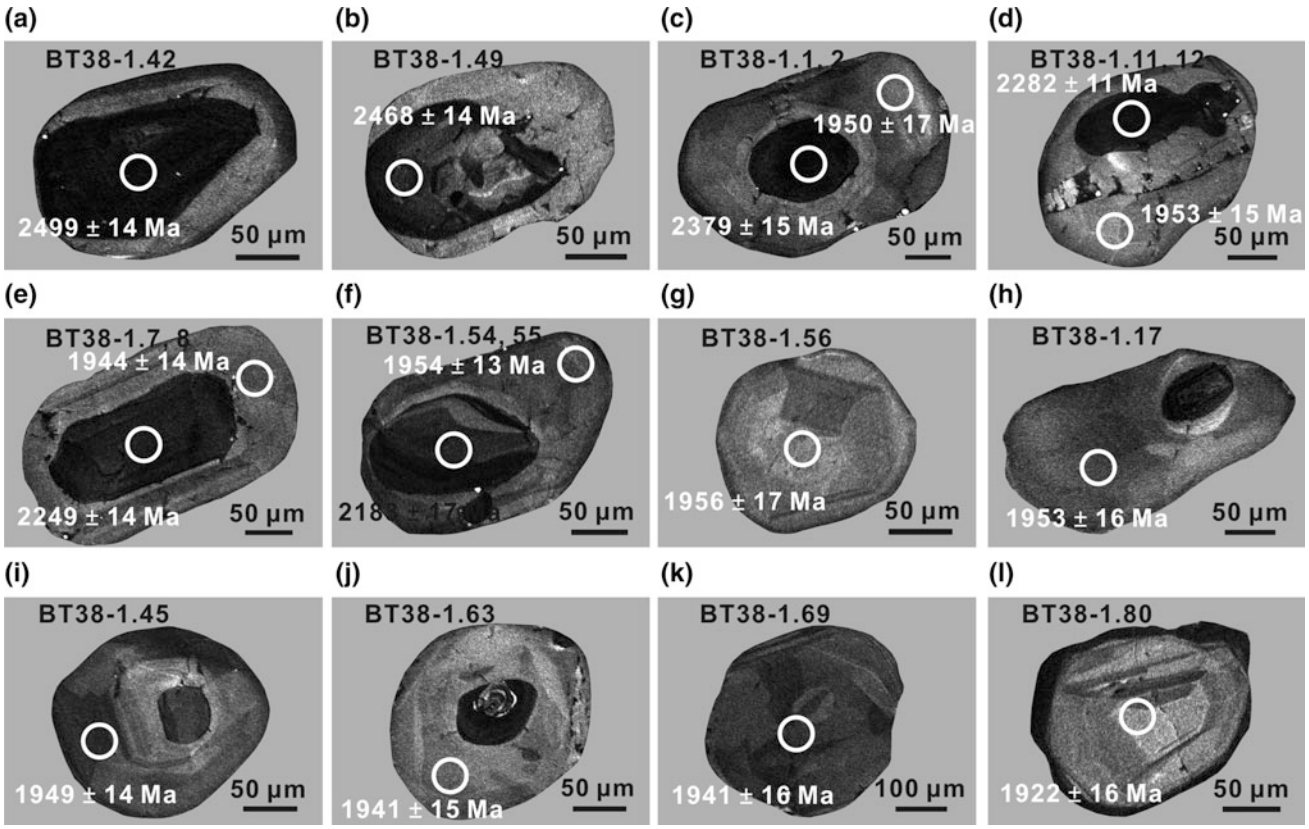

Fig. 8.15 CL images and LA-ICP-MS U–Pb ages of zircons from the Hyp–Grt–Bt gneiss (BT38-1) (modified after Cai et al. 2015). **a**–**f** The zircon grains showing a low-luminescent (*grayish black-black*) core, middle-low-luminescent (*gray-grayish black*) rim relationship. **g** The zircon grains showing homogeneous middle-luminescence (*gray*). **h**–**j** The zircon grains showing a middle-low-luminescent (*grayish black-black*) core and middle-low-luminescent (*gray-grayish black*) rim. **k**, **l** The zircon grains showing homogeneous middle-low-luminescence (*gray-grayish black*)

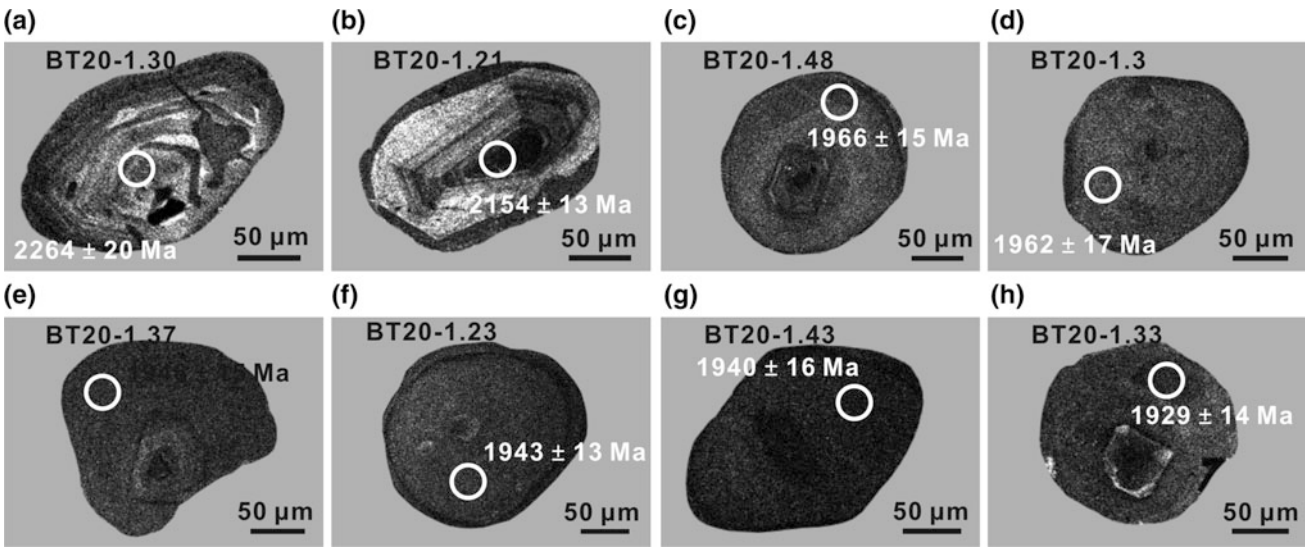

Fig. 8.16 CL images and LA-ICP-MS U–Pb ages of zircons from the Sil–Crd–Grt gneiss (BT20-1) (modified after Cai et al. 2015). **a**, **b** The zircon grains showing a middle-luminescent (*gray*) magmatic zoning core and middle-low-luminescent (*gray-grayish black*) metamorphic rim. **c** The zircon grains showing a low-luminescent core and homogeneous middle-luminescent (*grayish black*) rim. **d** The zircon grains showing homogeneous low-luminescence. **e** The zircon grains showing a low-luminescent (*grayish black-black*) core and rim. **f**, **g** The zircon grains showing homogeneous low-luminescence (*grayish black-black*). **h** The zircon grains showing a low-luminescent (*grayish black*) rim

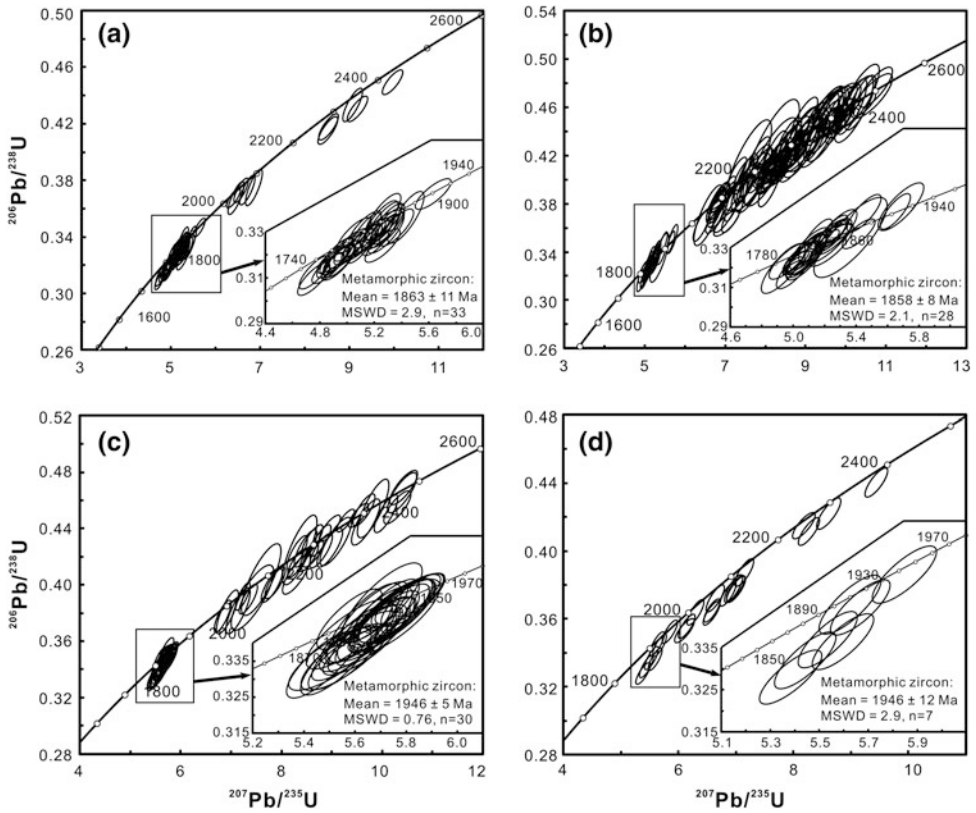

Fig. 8.17 $^{207}Pb/^{235}U$-$^{206}Pb/^{238}U$ diagrams showing U–Pb analyses for zircons of the khondalite rocks in the Wulashan–Daqingshan Complex (modified after Cai et al. 2015). **a** Hyp–Grt–Bt gneiss (BH27-3). **b** Grt-bearing quartzofeldspathic rock (BH28-1). **c** Hyp–Grt–Bt gneiss (BT38-1). **d** Sil–Crd–Grt gneiss (BT20-1)

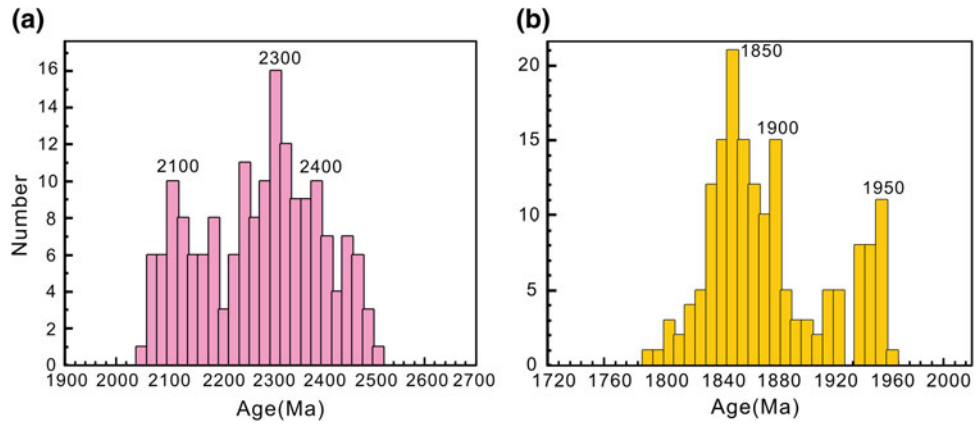

Fig. 8.18 Histogram of the $^{207}Pb/^{206}Pb$ ages of detrital and metamorphic zircons from the Wulashan-Daqingshan khondalite series rocks in the Khondalite Belt. Data from Cai et al. (2015). **a** Detrital zircons from the Wulashan-Daqingshan khondalite series rocks. **b** Metamorphic zircons from the Wulashan-Daqingshan khondalite series rocks

exhibit the greatest similarity to graywackes from continental island arcs or acid arcs (Fig. 8.35). In the discriminatory La–Th–Sc diagram (Bhatia 1985; Bhatia and Crook 1986), most samples plot in continental arc field (Fig. 8.19). Similar results were revealed by the other trace element diagrams (Bhatia and Crook 1986). These geochemical features, in combination with other geological data, suggest that the sedimentary protoliths of the khondalite series rocks in the Khondalite Belt were deposited in a basin adjacent to a Paleoproterozoic continental arc.

8.2.7.3 Metamorphic Ages and P–T–t Paths

Petrological observations, together with phase equilibria modeling, provide evidence that the meta-pelitic rocks in

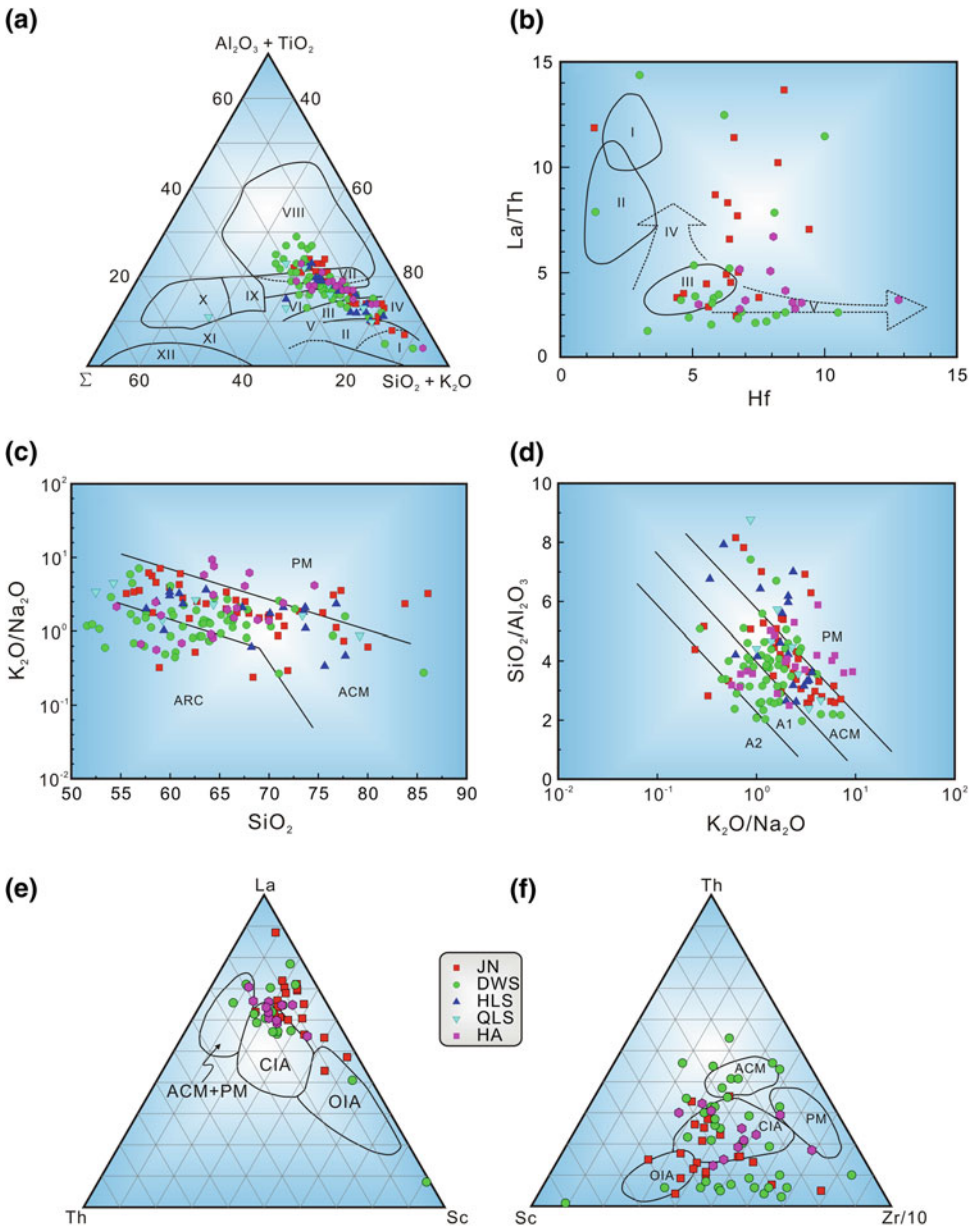

Fig. 8.19 Discrimination diagrams showing the protolith formation and source rock for the khondalite series rocks in the Khondalite Belt. **a** (second source from Wang et al. 1987): ∑ Residual components; *I* Quartz sandstone and quartzite; *II* Single-mineral sandstone and quartzitic sandstone, *III* Polymineral sandstone, *IV* Arkose, *V* Calcareous sandstone, *VI* Weakly differentiated chemical sedimentary rock, *VII* Marine and continental facies clay rock of frigid and temperate zones, *VIII* Strongly differentiated chemical clay rock of humid climate zones, *IX* Iron-bearing carbonate clay rock, *X* Marl, *XI* Siliceous marl and Iron-bearing sandstone, *XII*-Iron-bearing quartzite. **b** Floyd and Leveridge (1987): *I* Tholeiitic ocean island source; *II* Andesitic arc source, *III* acidic arc source. **c** Roser and Korsch (1986), **d** Maynard et al. (1982), e Bhitia and Crook(1986), and **f** Bhitia and Crook(1986): *PM* passive continental margin; *ACM* Active Continental Margin; *ARC A1* Island Arc; *A2* Evolved Island Arc; *CIA* Continental Island Arc; *OIA* Oceanic Island Arc

the Khondalite Belt, Inner Mongolia underwent a clockwise *P–T* path. This has been constructed from analyses of samples BH27-2 and BH39-4 (Fig. 8.12), and is consistent with the observed microstructures.

Mineral equilibria modeling indicated that the peak assemblage is garnet + biotite + K-feldspar + sillimanite + plagioclase + ilmenite + quartz ± magnetite + liquid with *P–T* conditions of 9–11 kbar and 840–880 °C (Fig. 8.15d). Further decompressional cooling (M_3) toward the inferred early retrograde field of cordierite + garnet + K-feldspar + plagioclase + ilmenite + quartz ± sillimanite ± biotite ± spinel ± magnetite + liquid at 5.0–7.5 kbar and 800–870 °C resulted in the growth of cordierite and the consumption of sillimanite, the latter mineral being observed occasionally as inclusions in cordierite or garnet. The retrograde cooling (M_4) assemblage of biotite + muscovite + sillimanite + plagioclase + ilmenite + quartz + H_2O is stable at <660 °C and 4.1–6.9 kbar. Growth zoning is not observed in the garnet porphyroblasts of the studied samples, and the prograde path inferred from the pseudosections should therefore be regarded with caution. In Fig. 8.12a, the prograde portion of the *P–T* path is shown as a dashed line because it is based on inclusions of biotite, quartz, plagioclase, and rare sillimanite in cores of garnet porphyroblasts, restricting it to relatively low temperatures and moderate pressures of <780 °C at <9 kbar in the bt–sil–kfs–pl–ilm–qz–liq-bearing field. The results from the *P–T* pseudosections are consistent with the observed mineral assemblages, and the clockwise

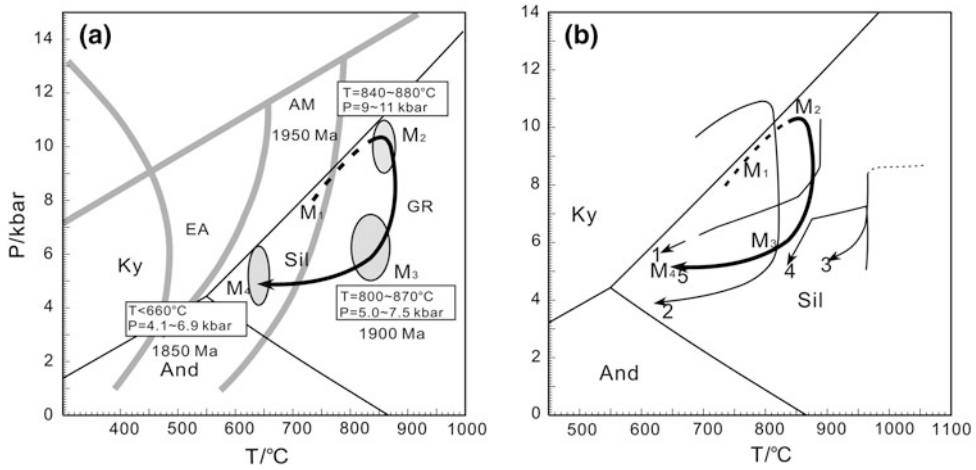

Fig. 8.20 Summarized metamorphic *P–T–t* paths of the Khondalite Belt (modified after Cai et al. 2014). **a** Middle pressure pelitic granulites (Cai et al. 2014). **b**: *1* Garnetites in Jining (Jiao et al. 2013a); *2* High-pressure meta-pelitic rocks in Helanshan (Yin et al. 2014); *3* Ultrahigh-temperature granulites in Dongpo, Daqingshan (Guo et al. 2012); *4* Ultrahigh-temperature granulites in Tuguiwula, Jining (Santosh et al. 2009); *5* Meta-pelitic rocks from the Daqingshan Complex (modified after Cai et al. 2014)

P–T path involved in the peak and decompressional cooling segment.

Zhao et al. (2005) suggested that the Khondalite Belt is the result of a continent-continent collision between the Yinshan Block in the north and the Ordos Block in the south, which formed the Western Block at around 1950 Ma. The age data reported for the Khondalite Belt show that the ages of detrital zircons in the khondalite series range from 2300 to 2000 Ma, and that the metamorphic zircon ages range from 1950 to 1920 Ma (e.g. Zhao et al. 2005; Wan et al. 2006, 2009; Xia et al. 2006a, b; Dong et al. 2007, 2012; Santosh et al. 2007; Yin et al. 2009; Yin 2010; Li et al. 2011; Ma et al. 2012a, b).

8.2.7.4 Tectonic Implications

The meta-pelitic rocks in the Khondalite Belt experienced multiple deformations and a multistage granulite-facies metamorphic evolution (Condie et al. 1992; Lu et al. 1992, 1996). As mentioned above, petrological observations, together with phase equilibria modeling, provide evidence that the meta-pelitic rocks from the Daqingshan Complex underwent a clockwise *P–T* path. Our *P–T* path is comparable with the paths documented by other groups (Fig. 8.20; Santosh et al. 2009; Guo et al. 2012; Jiao et al. 2013a; Yin et al. 2014). Our estimates of peak metamorphic temperatures (840–880 °C) and pressures (9–11 kbar) indicate a granulite-facies metamorphism comparable to those reported by some other groups (Zhao et al. 1999; Santosh et al. 2009; Guo et al. 2012; Jiao et al. 2013b; Yin et al. 2014) (Fig. 8.20b). The retrograde path, characterized by decompressional cooling, is in agreement with the paths defined previously by Liu et al. (1993a, b), Lu and Jin (1993), Zhou et al. (2010), Jiao et al. (2013a), and Yin et al. (2014).

It has been proposed that a near-isothermal decompressional path reflects continental collision or overthrusting processes (England and Richardson 1977; England and Thompson 1984; Thompson and England 1984; Harley 1989; Brown 1993). Our clockwise *P–T* path, involving the peak and subsequent near-isothermal decompressional stage, indicated that the rocks experienced a sequence of tectonothermal processes commencing with crustal thickening, followed by rapid crustal uplift and late cooling. It is inferred that the sedimentary rocks were taken down to lower crustal levels as a result of continental subduction and collision, where they experienced granulite-facies metamorphism. Taken together, these results and the *P–T* evolution (Fig. 8.20), along with the abovementioned age data, further support the tectonic model of Zhao et al. (2005), in which the Khondalite Belt is a continent-continent collisional belt of Paleoproterozoic age.

8.3 Khondalite Series of the Jiao-Liao-Ji Belt in the Eastern Block

8.3.1 Geological Setting

The Jiaobei Complex is exposed in the southern segment of the Jiao-Liao-Ji Belt in the Eastern Block of the NCC (Fig. 8.1), bordered by the Bohai Sea to the north, the West Shandong terrane to the west, with the Tan–Lu Fault forming the junction between the terrane and the Sulu high pressure to ultrahigh-pressure orogenic belt to the southeast, and bounded by the Yantai–Qingdao–Wulian Fault Belt (Fig. 8.21). The Jiaobei Complex is mainly composed of Early Precambrian basement rocks, Meso-Neoproterozoic

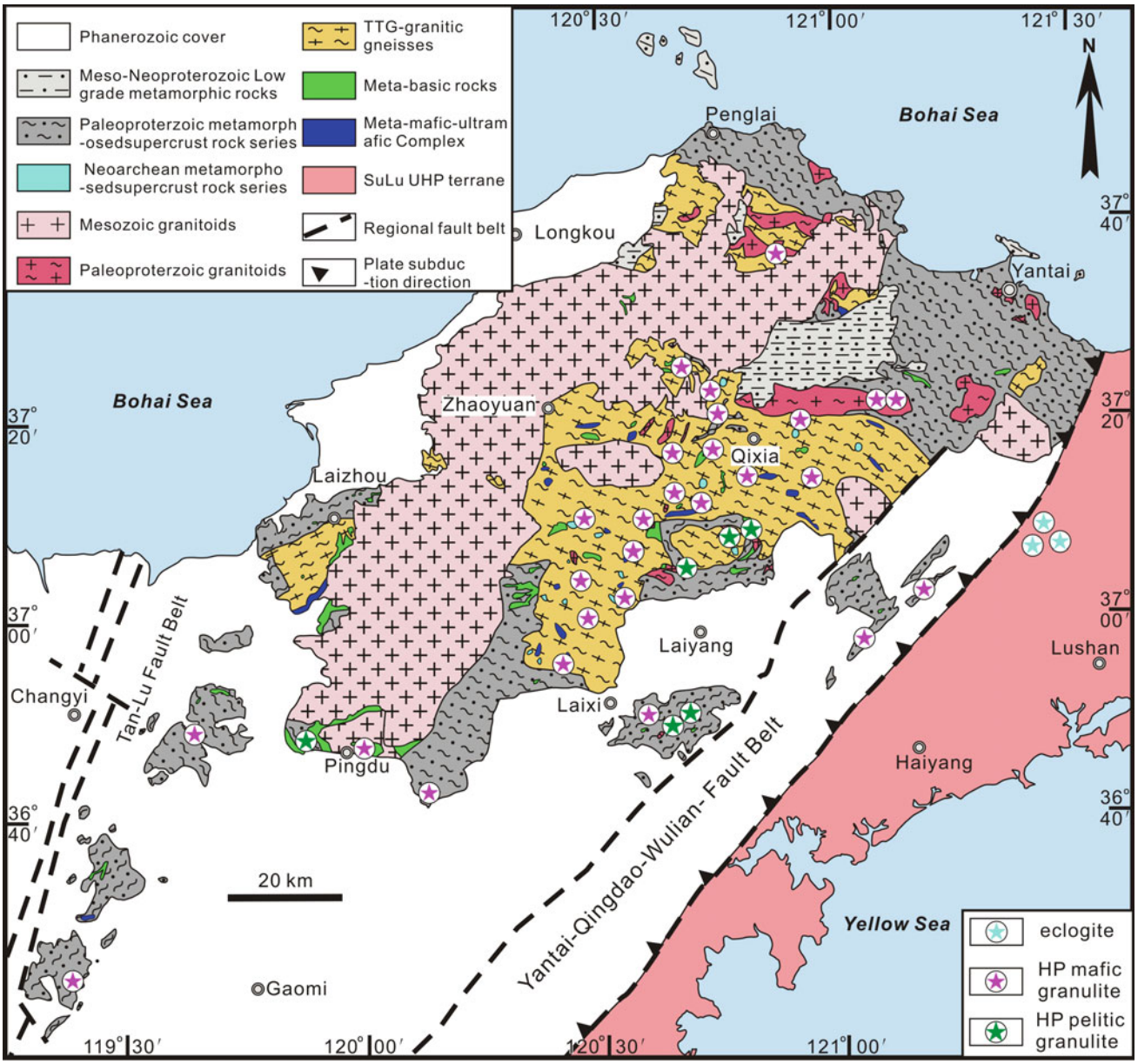

Fig. 8.21 Simplified geological map showing the Jiaobei Precambrian metamorphic basement rocks (modified after Lu et al. 1996)

Penglai and Zhifu Groups, Mesozoic sedimentary rocks, and voluminous Mesozoic igneous intrusions (Fig. 8.21). The early Precambrian rocks consist mainly of tonalite–trondhjemite–granodiorite (TTG) and granitic gneisses, BIF-bearing metamorphic supracrustal rocks (also named the "Tangjiazhuang Group" and "Jiaodong Group"), the Paleoproterozoic khondalite series rocks (also named the "Jingshan Group" and "Fenzishan Group"), with some lenses or sheets of metamorphic mafic-ultramafic rocks (Liu et al. 2015).

The TTG and granitic gneisses are widely exposed in the Jiaobei Complex from northern Qixia to southern Laixi–Laiyang. They are characterized by a strong ductile deformation, mylonitic fabrics, extensive migmatization, and amphibolite facies metamorphism, and they have segregations of light-colored granitic material (leucosomes) within dark-colored amphibole, biotite, and pyroxene-rich layers. The recently available precise geochronological data suggest that the Jiaobei TTG and granitic gneisses formed ca. 2900 Ma, ca. 2750 Ma, ca. 2550 Ma, and ca. 2100 Ma, and that they record two high-grade metamorphic events at ca. 2500 Ma and 1950–1800 Ma (Tang et al. 2007; Jahn et al. 2008; Zhou et al. 2008a; Liu et al. 2011a, 2013a; Wan et al. 2011; Xie et al. 2014).

The widespread Paleoproterozoic khondalite series rocks in the Jiaobei Complex are composed of the Jingshan and

Fenzishan Groups. The Jingshan Group has been divided into two lithological assemblages, i.e., a series of Al-rich gneisses and marble. The Al-rich gneisses are mainly sillimanite–garnet–biotite schist–gneisses, quartzofeldspathic gneisses, and biotite leptynite. There are also some intercalations of amphibolites and mafic granulites in the Jingshan Group. The marble contains serpentine marble and dolomitic marble with thin layers and lenses of amphibolites. SHRIMP zircon U–Pb apparent $^{207}Pb/^{206}Pb$ ages, obtained from detrital zircons in the Jingshan Group, range from 2900 to 2100 Ma, with metamorphic zircons in some samples recording apparent $^{207}Pb/^{206}Pb$ ages of 1950–1800 Ma (Wan et al. 2006; Zhou et al. 2008b; Liu et al. 2011b; Tam et al. 2011). The Fenzishan Group, chiefly found in Miaohou and Menlou within the Qixia area, and Fenzishan within the Laizhou area, are represented by serpentine and dolomitic marble, biotite leptynite, sillimanite–biotite schist–gneisses, and arkose–quartzite, all of which record an upper greenschist to low amphibolite facies metamorphism. Wan et al. (2006) reported SHRIMP zircon U–Pb apparent $^{207}Pb/^{206}Pb$ ages from detrital zircons in the Fenzishan Group ranging from 2800 to 2200 Ma, and with metamorphic zircons in the same samples recording 1950–1850 Ma $^{207}Pb/^{206}Pb$ ages, similar to the events recorded in the Jingshan Group. Therefore, it is suggested that the Fenzishan and Jingshan Groups are the same unit, but that they have different metamorphic histories.

Unconformably overlying the Paleoproterozoic Fenzishan and Jingshan Groups is the Meso-Neoproterozoic Penglai Group, chiefly composed of meta-limestone, slates, and quartzite. The Penglai Group is exposed mainly in the Penglai area and in the northern part of the Qixia area. SIMS zircon U–Pb ages obtained from detrital zircons in the Penglai Group range from 1700 to 1100 Ma, probably indicating Meso-Neoproterozoic deposition for the Penglai Group (Li et al. 2007; Chu et al. 2011). The Mesozoic granitoids that were intruded into the Precambrian metamorphic basement consist mainly of granodiorites and biotite granites, emplaced mainly at 160–150 Ma and 130–120 Ma (Miao et al. 1998; Wang et al. 1998; Zhang et al. 2003; Yang et al. 2012).

8.3.2 Whole-Rock Geochemistry

As mentioned above, the Paleoproterozoic khondalite series rocks of the LJLB can also be subdivided into three different types: Al-rich paragneisses with high Al_2O_3 and low SiO_2 contents, garnet- or sillimanite-bearing felsic paragneisses or felsic granular rocks with high SiO_2 and low Al_2O_3 contents, and calc-silicate rocks and marble with high CaO and low SiO_2. With the exception of calc-silicate rocks and marble, the major and trace element compositions of the representative Paleoproterozoic khondalite series rocks within the Jiao-Liao-Ji Belt are presented in Table 8.9.

8.3.2.1 Major Elements

As shown in Fig. 8.22 and Table 8.9, the studied Paleoproterozoic khondalite series rocks within the Jiao-Liao-Ji Belt are characterized by significantly variable concentrations of SiO_2, Al_2O_3, FeO^T, MgO, CaO, Na_2O, and K_2O, with values ranging from 39.45 to 93.75 wt%, 0.21–27.78 wt%, 0.22–15.71 wt%, 0.09–11.14 wt%, 0.12–19.68 wt%, 0.01–4.65 wt%, and 0.05–8.93 wt%, respectively. In contrast, concentrations of TiO_2 (0.02–1.55 wt%), MnO (0.01–0.50 wt%), and P_2O_5 (0.01–0.44 wt%), are low and exhibit restricted variations.

The large variation in major element concentrations for all of the Paleoproterozoic khondalite series samples within the Jiao-Liao-Ji Belt is typical of weathered rocks. The chemistry is strongly correlated with grain size, because most elements show marked linear trends on the Al_2O_3 variation diagram (Harker variation diagrams omitted). In general, the levels of most elements increase as Al_2O_3 increases from sandstone to argillites. The TiO_2, Al_2O_3, Fe_2O_3, MgO, CaO, Na_2O, and K_2O decrease with increasing SiO_2 content, suggesting that samples increase in their mineralogical maturity or quartzose contents but decrease in immature detrital grains (*e.g.*, feldspar and rock fragments). Cratonic and recycled sediments associated with passive margins are higher in silica (SiO_2: >85 wt% and 65–95 wt%, respectively), whereas arc-derived sediments within active orogenic margins normally contain relatively lower and variable levels of silica (SiO_2: 47–82 wt%). Arc-derived sediments are also higher in Fe, Mg, Ti, and Al than cratonic and recycled sediments (Bhatia 1983). Our samples fall in the range of arc-derived sediments within active orogenic margins. Most of the Paleoproterozoic khondalite series samples within the Jiao-Liao-Ji Belt were plotted in the sandstone and argillites fields in the classification diagrams (Fig. 8.22). For example, the log (Fe_2O_3/K_2O) against Log (SiO_2/Al_2O_3) plots (Herron 1988) falls mainly in the shale, wacke, and arkose fields with some in the subarkose, sublitharenite, and Fe-Sand fields (Fig. 8.22c).

8.3.2.2 Rare Earth Elements

Chondrite-normalized REE patterns and representative data for all the Paleoproterozoic khondalite series rocks of the Jiao-Liao-Ji Belt are shown in Fig. 8.23 and Table 8.9, respectively. They show relatively variable REE concentrations (14.63–454.65 ppm) and relatively moderately fractionated REE patterns ($(La/Yb)_N$ = 1.22–8.36) with variable Eu anomalies (δEu = 0.61–1.30). It is worth noting that Sil-bearing felsic granular rocks (mainly arkosite, quartzite, and leptite) have lower REE concentrations than metamorphic pelitic rocks. Compassed with 2200–2000 Ma K-rich

Table 8.9 Whole rock analyses on the representative Khondalite Series rocks within the Jiaobei Complex

Sample no.	PD-03c-02	PD-04a-02	PD-05a-02	PD-08a-02	PD-10a-03	PL11-1	PL12-1	TA15-1	TA15-2	TA19-1
SiO_2	59.35	54.37	52.79	59.19	55.73	53.03	57.11	56.63	58.14	58.10
TiO_2	0.68	0.79	0.80	0.73	0.74	0.71	0.75	0.78	0.74	0.64
Al_2O_3	19.23	22.35	21.71	19.78	20.48	21.94	20.74	21.49	20.41	19.41
Fe_2O_3	1.18	0.26	1.64	0.92	1.76	0.89	1.63	1.85	1.89	2.72
FeO	7.35	10.22	8.91	7.42	7.60	8.69	7.17	8.55	6.84	5.14
MnO	0.12	0.15	0.16	0.11	0.11	0.12	0.10	0.15	0.12	0.10
MgO	3.71	4.21	4.95	3.52	4.06	4.82	3.96	4.05	4.33	3.98
CaO	0.88	0.54	1.06	0.79	0.94	2.22	0.87	0.59	1.43	0.76
Na_2O	1.54	0.75	1.37	0.78	1.22	0.72	0.87	0.64	1.00	0.59
K_2O	4.13	4.17	5.11	4.15	4.61	5.14	4.03	3.91	4.33	5.22
P_2O_5	0.05	0.06	0.05	0.13	0.08	0.07	0.09	0.07	0.07	0.10
LOI	0.73	0.60	0.40	1.05	1.73	0.27	1.38	0.57	0.38	2.77
Total	98.95	98.47	98.95	98.57	99.06	98.62	98.70	99.28	99.68	99.53
La	62.74	76.99	54.17	67.32	80.23	55.90	66.00	70.60	67.30	53.70
Ce	127.10	151.30	115.70	127.90	152.50	108.00	129.00	143.00	134.00	108.00
Pr	12.91	15.17	11.03	13.29	15.08	12.00	14.30	15.40	14.60	11.90
Nd	45.71	55.18	41.27	48.63	54.39	43.80	50.90	57.00	54.70	45.10
Sm	7.97	9.79	7.25	9.09	9.67	7.52	9.37	9.92	9.11	7.96
Eu	1.85	1.57	1.36	1.15	1.82	1.33	1.33	1.45	1.30	1.26
Gd	6.94	8.29	7.42	8.09	7.82	6.74	7.59	7.88	7.20	6.57
Tb	1.08	1.21	1.30	1.20	1.16	0.92	1.04	1.23	1.10	0.94
Dy	6.37	7.58	8.58	7.57	6.75	5.65	6.01	7.17	6.23	5.43
Ho	1.23	1.50	1.69	1.47	1.23	1.10	1.17	1.43	1.26	1.07
Er	3.75	4.47	4.89	4.47	3.70	3.29	3.47	4.34	3.88	3.28
Tm	0.53	0.62	0.70	0.63	0.50	0.48	0.47	0.58	0.53	0.46
Yb	3.60	4.33	4.72	4.35	3.40	3.26	3.37	3.61	3.61	3.04
Lu	0.50	0.59	0.64	0.61	0.46	0.49	0.51	0.56	0.56	0.48
Sc	–	–	–	–	–	–	–	29.30	28.30	24.40
V	113.10	136.10	150.00	103.80	123.40	153.00	123.00	129.00	130.00	109.00
Cr	180.40	190.10	164.90	139.70	166.20	149.00	157.00	179.00	133.00	131.00
Co	26.56	29.85	30.69	22.73	27.75	27.40	24.90	29.90	26.20	21.60
Ni	27.13	68.04	53.09	54.89	67.49	53.70	64.70	72.80	50.30	51.40
Cu	24.79	55.03	9.12	20.40	35.44	13.00	12.90	51.50	25.10	3.12
Zn	113.60	138.80	145.70	116.90	75.06	114.00	70.40	143.00	137.00	116.00
Ga	27.45	31.88	30.96	27.68	30.53	27.00	25.30	30.90	31.50	30.00
Rb	132.60	129.40	214.60	182.10	207.50	219.00	214.00	156.00	211.00	243.00
Sr	150.70	90.06	68.19	76.18	118.30	74.50	102.00	92.50	57.30	77.10
Y	29.22	36.40	42.81	35.99	30.40	27.50	27.70	44.80	40.80	34.40
Zr	150.30	127.70	151.90	155.10	127.40	117.00	127.00	146.00	141.00	142.00
Nb	11.39	13.07	14.06	13.61	11.95	11.50	13.50	14.60	13.30	12.30
Mo	0.54	0.26	0.22	0.16	0.56	0.14	0.09	0.22	0.21	0.13
Sn	0.34	1.48	1.55	1.64	1.57	1.83	1.69	1.96	2.35	3.50
Cs	0.7	3.11	3.95	3.83	6.24	3.52	5.27	3.23	4.53	11.7
Ba	993.6	691.4	816.1	703.3	824.8	782	696	701	604	847

(continued)

Table 8.9 (continued)

Sample no.	PD-03c-02	PD-04a-02	PD-05a-02	PD-08a-02	PD-10a-03	PL11-1	PL12-1	TA15-1	TA15-2	TA19-1
Hf	4.27	3.67	4.32	4.36	3.86	3.87	4.45	4.21	4.09	4.22
Ta	0.77	0.74	0.92	0.64	0.76	0.85	1.17	0.92	0.97	0.9
Pb	22.95	15.3	13.68	10.82	4.98	24.8	4.43	19.5	16.5	14
Th	13.91	19.31	16.29	17.26	19.17	18.3	21.6	29	27.7	20
U	1.9	2.14	1.13	2.04	2.35	1.1	2.11	3.21	1.46	2.91

Notes –, below the test line of the elements

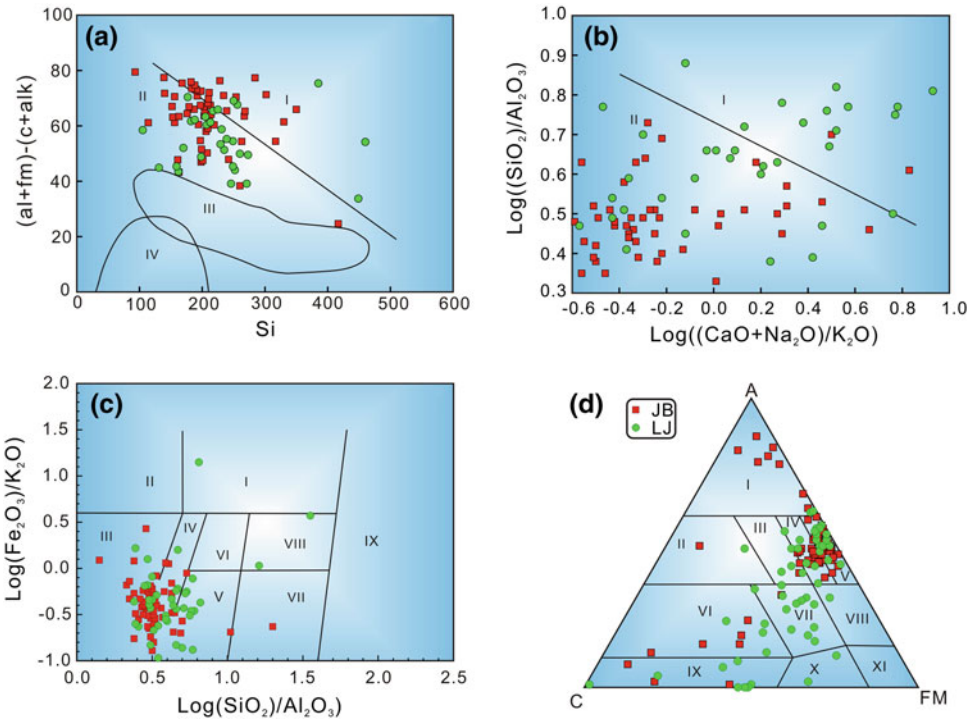

Fig. 8.22 Classification diagrams of the khondalite series rocks in the Jiao-Liao-Ji Belt. **a** Si versus ((al + fm) – (c + alk)) (Simonen 1953), *I* Arenaceous sedimentary rocks, *II* Argillous sedimentary rocks, *III* Volcanic rocks, *IV* Calcareous. **b** Log((CaO + Na_2O)/K_2O) versus Log (SiO_2/Al_2O_3) (Garrels and Mackenzie 1971), *I* Arenaceous sedimentary rocks, *II* Argillous sedimentary rocks. **c** Log(Fe_2O_3/K_2O) versus Log (SiO_2/Al_2O_3) (Herron 1988), *I* Fe-Sand, *II* Fe-Shale, *III* Shale, *IV* Wacke, *V* Arkose, *VI* Litharenite, *VII* Subarkose, *VIII* Sublitharenite, *IX* Quartz arenite. **d** A-C-FM (secondary source from Lu et al. 1996), *I* Clay rock and acidic volcanic rock, *II* Arkose, *III* Graywacke, intermediate and alkaline volcanic rock, *IV* Wacke overlay region of graywacke, intermediate and alkaline volcanic rock, and Clay rock, *V* Clay rock and graywacke, *VI* Calc-silicate rock and quartzite, *VII* Basic volcanic rock and ferruginous and dolomitic marl, *VIII* tuffaceous siltstone, *IX* Calcareous carbonate, *X* Ultrabasic rock, *XI* Siliceous and ferruginous sedimentary rock and ultrabasic rock. *JB* The khondalite series rock samples from the Jiaobei Complex, *LJ* The khondalite series rock samples from the Liaoji Complex

granitic rocks from the NCC (e.g., Du et al. 2013; Liu et al. 2014b), they have similar REE patterns.

8.3.2.3 Trace Elements

The Paleoproterozoic khondalite series within the Jiao-Liao-Ji Belt are characterized by moderately to largely variable concentrations of Sc (1.19–37.80 ppm), Zr (5.89–290 ppm), Hf (0.24–7.90 ppm), Nb (0.38–24.9 ppm), and Ta (0.09–2.45 ppm). Furthermore, these concentrations are above or below the average values in the UCC (Taylor and McLennan 1985). Similarly, concentrations of Co (1.62–331.00 ppm), Cr (1.62–311.00 ppm), Ni (1.69–163.00 ppm), Rb (21.1–394 ppm), Sr (9–1916 ppm), Ba (38–1599 ppm), Th (0.71–51.7 ppm), and U (0.31–5.41 ppm) exhibit large variations. In a primitive mantle-normalized trace element spidergram (Fig. 8.23b), the Paleoproterozoic khondalite series rocks within the Jiao-Liao-Ji Belt show marked depletions in HFSE with negative Nb, Ta, Ti, and Y anomalies.

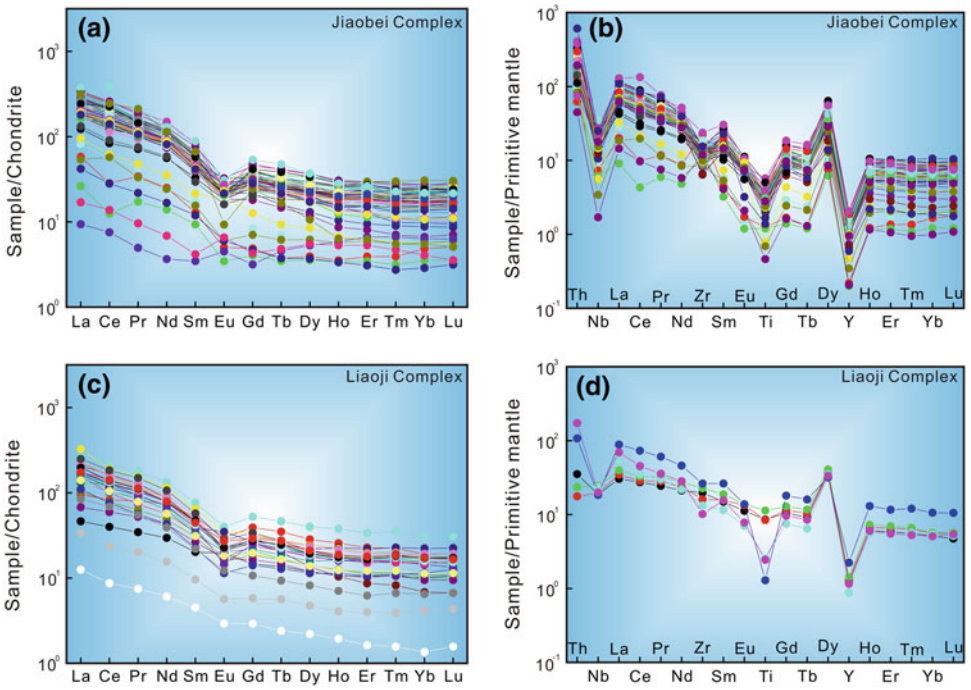

Fig. 8.23 Chondrite-normalized REE (**a**, **c**) and primitive mantle-normalized trace element patterns (**b**, **d**) for the khondalite series rocks in the Jiao-Liao-Ji Belt. Normalized values are after Sun and McDonough (1989)

8.3.3 Petrography

Only the petrography of the high pressure pelitic granulites (representative Paleoproterozoic khondalite series rocks within the Jiao-Liao-Ji Belt) is discussed due to length restrictions of the paper. The Jiaobei high-pressure pelitic granulite samples were collected from the Taipingzhuang area of the Jiaobei Complex (Figs. 8.24 and 8.25). They consist mainly of garnet (15–20 %), kyanite (5–8 %), sillimanite (5–8 %), biotite (25–30 %), plagioclase (10–15 %),

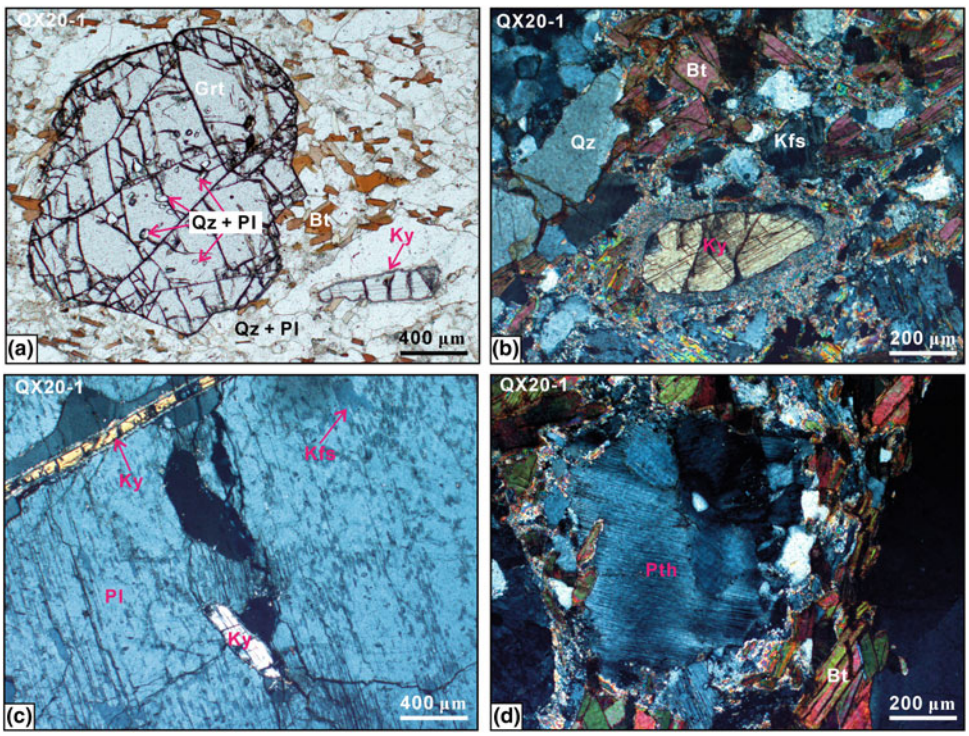

Fig. 8.24 Photomicrographs showing typical mineral assemblage and microtextures of the Jiaobei high-pressure pelitic granulites (Liu et al. 2015). **a**, **b** High-pressure granulite-facies mineral assemblage of garnet (Grt) + kyanite (Ky) + K-feldspar (Kfs) + plagioclase (Pl) + quartz (Qz) + biotite (Bt) identified in the pelitic granulite sample QX20-1, CPL. **c** Fine-grained kyanite (Ky) as inclusion preserved in the coarse-grained antiperthite, CPL. **d** Coarse-grained perthite surrounded by fine-grained biotite (Bt)

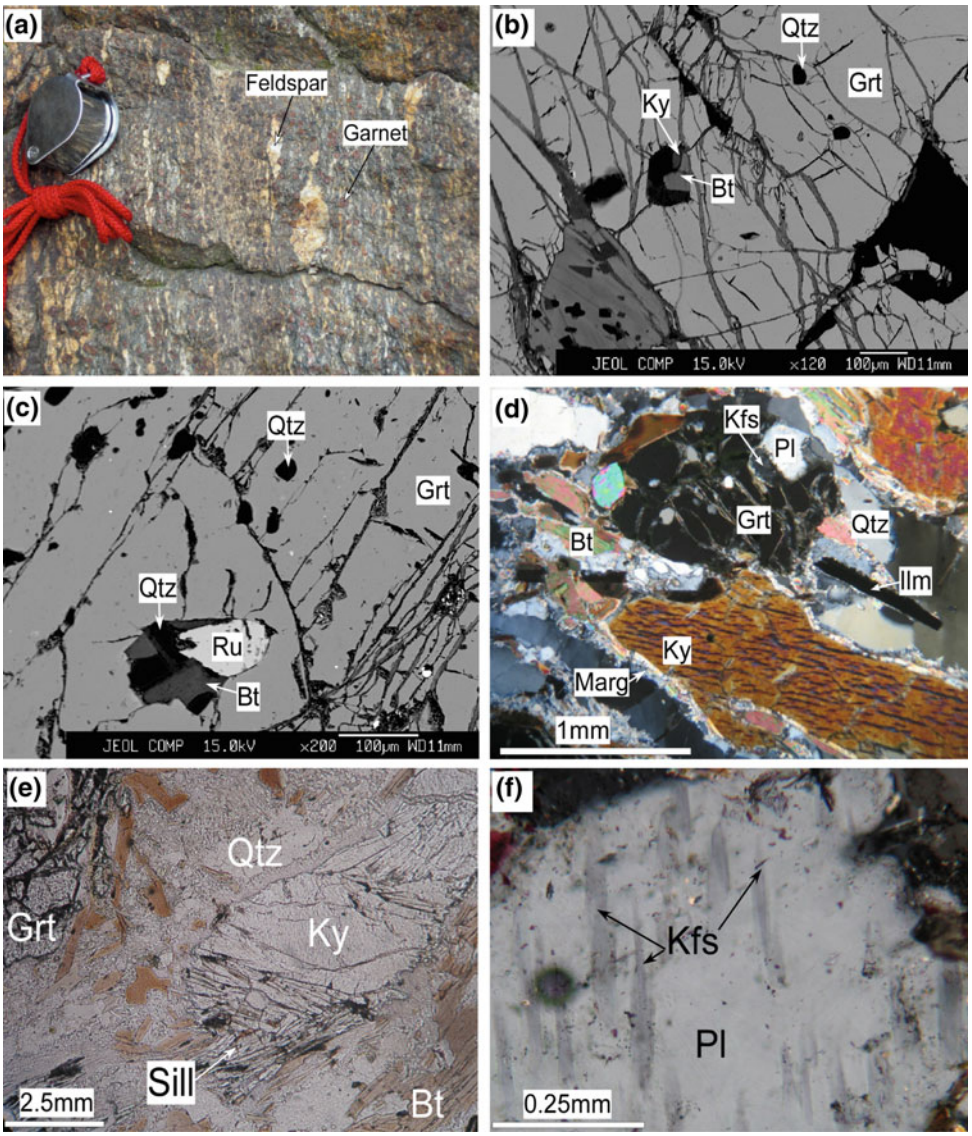

Fig. 8.25 Field photograph and photomicrographs showing typical mineral assemblage and microtextures of the Jiaobei high-pressure pelitic granulites (Tam et al. 2012a). **a** A field photograph showing the high-pressure pelitic granulite containing large amounts of garnet and strongly sheared feldspar grains. **b** Mineral inclusions of kyanite (Ky_1), quartz (Qz_1), and biotite (Bt_1) preserved in the cores of garnet (Grt_1) (BSE images). **c–d** Microscopic photographs (**c**, **d**, under cross-polarized light) showing a representative peak mineral assemblage of garnet (Grt_2) + K-feldspar (Kfs) + kyanite (Ky_2) + plagioclase (Pl_2) + biotite (Bt_2) + rutile (Ru) + ilmenite (Ilm_2) + quartz (Qz_2) in the studied high-pressure pelitic granulite, of which kyanite occurs as tabular grains with the rims replaced by margarite (Marg). **e** Photomicrograph (under plane-polarized light) showing "sillimanite + biotite" symplectite surrounded by fine-grained biotite crystals with a preferred orientation parallel to the foliation defined by sillimanite fibrolites. **f** Photomicrograph (under cross-polarized light) showing an antiperthite grain with the plagioclase-base and K-feldspar lamella

K-feldspar (3–4 %), muscovite (2–3 %), and quartz (20–25 %), with minor ilmenite, rutile, monazite, and zircon contents. Based on microstructures and reaction textures between mineral phases of the Jiaobei high-pressure pelitic granulites, three metamorphic stages are recognized: the pre-peak (M_1), peak (M_2), and post-peak (M_3) stages.

8.3.3.1 Pre-peak (M_1) Stage

The pre-peak (M_1) stage is characterized by a mineral assemblage of garnet core (Grt_1) + biotite (Bt_1) + quartz (Qz_1) + plagioclase (Pl_1) + ilmenite (Ilm_1). They exist as mineral inclusions within the garnet cores and are considered to develop coevally with the latter (Figs. 8.24 and 8.25).

Kyanite (Ky) and muscovite (Ms) were reported within garnet cores by Tam et al. (2012a) and are considered as being among the inclusion-type minerals.

8.3.3.2 Peak (M_2) Stage

The mineral assemblage of the peak (M_2) stage of the examined high-pressure pelitic granulites is garnet mantle (Grt_2) + kyanite (Ky_2) + K-feldspar + plagioclase (Pl_2) + biotite (Bt_2) + rutile (Rt) + ilmenite (Ilm_2) + quartz (Qz_2) (Figs. 8.24 and 8.25). Garnet mantle (Grt_2) without any other mineral inclusions (Figs. 8.24 and 8.25) is interpreted to grow after the pre-peak (M_1) stage, most likely at the peak (M_2) stage. Kyanite (Ky_2) occurs as coarse-grained tabular grains with the rims replaced by margarite (Figs. 8.24 and 8.25). K-feldspar is usually present as anhedral crystals in the matrix (Figs. 8.24 and 8.25), and most of the plagioclase (Pl_2) exhibits albite twining. The garnet mantle and K-feldspar may have developed from the reactions between inclusion-type minerals of kyanite + biotite + quartz (Spear et al. 1999; O'Brien and Rötzler 2003).

$$\text{biotite} + \text{kyanite} + \text{quartz} \rightarrow \text{garnet} + \text{feldspar} + \text{liquid} \tag{8.10}$$

$$\text{biotite} + \text{kyanite} + \text{quartz} + \text{ilmenite} \rightarrow \text{garnet} + \text{rutile} + \text{liquid}. \tag{8.11}$$

It is also possible that the growth of kyanite and K-feldspar was generated from the following reactions (Spear et al. 1999; White et al. 2001):

$$\text{muscovite} + \text{quartz} \rightarrow \text{kyanite} + \text{K} - \text{feldspar} + \text{H}_2\text{O} \tag{8.12}$$

$$\text{Pyrophyllite} \rightarrow \text{kyanite} + \text{quartz} + \text{H}_2\text{O}. \tag{8.13}$$

Table 8.10 Representative compositional analyses of garnet from the Khondalite Series rocks within the Jiaobei Complex

Sample no.	LY-7	JD16-3	JB07-1	PD08a-03-3.6	QX20-1-2.1	PD04a-01-4.29	PD03a-01-4.7	JB04-3	JB04-3
Type	C	C	C	C	C	C	C	C	C
SiO_2	38.71	38.32	37.80	38.04	38.33	38.51	39.37	38.69	38.96
TiO_2	0.00	0.00	0.00	0.05	0.02	0.03	0.00	0.13	0.09
Al_2O_3	21.36	21.30	21.66	21.93	21.40	21.80	22.77	22.33	22.02
FeO^T	24.59	30.53	29.28	31.85	29.50	32.07	26.21	29.66	31.08
MnO	0.40	0.59	1.70	0.62	0.43	0.76	0.33	0.65	0.50
MgO	7.34	5.96	6.34	5.36	7.38	6.54	10.73	6.77	6.93
CaO	6.65	2.86	2.89	3.02	3.11	1.16	0.83	1.64	1.76
Na_2O	0.02	0.00	0.04	0.05	0.00	0.00	0.00	0.02	0.00
K_2O	0.00	0.00	0.01	0.01	0.00	0.01	0.00	0.01	0.00
Total	99.07	99.56	99.72	100.93	100.17	100.88	100.24	99.90	101.33
Si	3.013	3.022	2.967	2.971	2.979	2.998	2.987	3.0240	3.0070
Ti	0.000	0.000	0.000	0.003	0.001	0.002	0.000	0.0080	0.0050
Al	1.960	1.980	2.003	2.019	1.961	2.001	2.037	2.0560	2.0020
Fe^{3+}	0.000	0.000	0.069	0.041	0.079	0.000	0.000	0.0000	0.0000
Fe^{2+}	1.601	2.014	1.853	2.039	1.838	2.088	1.663	1.9390	2.0060
Mn	0.026	0.039	0.110	0.041	0.028	0.050	0.021	0.0430	0.0320
Mg	0.852	0.701	0.742	0.624	0.855	0.759	1.213	0.7890	0.7970
Ca	0.555	0.241	0.243	0.253	0.259	0.097	0.067	0.1370	0.1460
Na	0.003	0.000	0.005	0.008	0.000	0.000	0.000	0.0030	0.0000
K	0.000	0.000	0.001	0.001	0.000	0.001	0.000	0.0010	0.0000
X_{Mg}	0.26	0.26	0.26	0.23	0.32	0.27	0.42	0.23	0.24
Grs	0.183	0.080	0.082	0.0856	0.0869	0.0324	0.0226	0.047	0.049
Prp	0.281	0.234	0.252	0.2110	0.2869	0.2535	0.4092	0.271	0.267
Sps	0.009	0.013	0.037	0.0139	0.0094	0.0167	0.0071	0.015	0.011
Alm	0.528	0.672	0.629	0.6896	0.6168	0.6974	0.5611	0.667	0.673

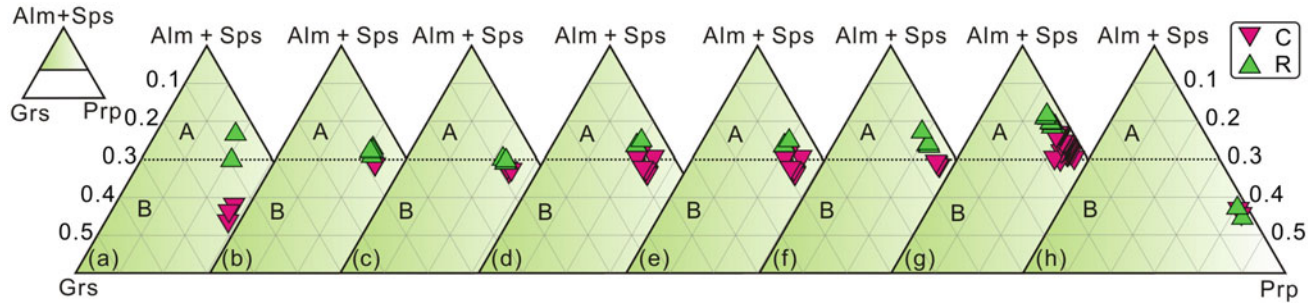

Fig. 8.26 Prp–(Alm + Spr)–Grs triangular diagram of the garnets from the Jiaobei pelitic granulites (Liu et al. 2015). *A* and *B* represent the regions of the garnet formed in granulite facies and amphibolite facies, respectively (secondary source from Liu 1995). **a–h** Jiaobei pelitic granulite samples LY-6, JD16, JB07, QX20-1, PD08a-03, JB04-3, PD04a-01, and PD03a-01, respectively. C: Cores of the garnets from the Jiaobei pelitic granulites; Rims of garnets from the Jiaobei pelitic granulites

8.3.3.3 Post-peak (M_3) Stage

The mineral assemblage of garnet rim (Grt_3) + sillimanite + plagioclase (Pl_3) + biotite (Bt_3) + ilmenite (Ilm_3) + quartz (Qtz_3) is a representative feature of post-peak metamorphism (M_3) (Fig. 8.25). The appearance of sillimanite in the matrix is interpreted as having formed at the post-peak (M_3) stage after the high-pressure granulite-facies metamorphism (M_2) because some sillimanite fibrolite occurs as reaction rims surrounding kyanite in the matrix (Figs. 8.24 and 8.25). Furthermore, Zhou et al. (2008a) reported that the sillimanite was transformed from kyanite, with Raman analysis revealing spectrum peaks of kyanite and sillimanite of the high-pressure pelitic granulites collected from the Taipingzhuang area. Thus, it is believed that some sillimanite of the high-pressure pelitic granulites was formed from kyanite. Antiperthite or/and perthite is interpreted as resulting from the exsolution of K-feldspar and plagioclase, respectively, during decompression with slow cooling (Philpotts 1989). Biotite (Bt_3) in contact with sillimanite and the garnet rims occurs as fine-grained crystals in the matrix forming during the post-peak metamorphism, showing a preferred orientation parallel to the foliation defined by oriented sillimanite fibrolite (Fig. 8.25). In addition, some biotite and sillimanite intergrow to form a symplectic texture (Tam et al. 2012a). The sillimanite, biotite, and the "sillimanite + biotite" symplectite are considered to result from the reverse reaction (1) (Tam et al. 2012a).

8.3.4 Mineral Chemistry

8.3.4.1 Garnet

Representative garnet analyses from the Jiaobei pelitic granulite samples are given in Table 8.10, and all garnet analyses are plotted in the grossular–(spessartine + almandine)–pyrope triangular diagrams (Fig. 8.26). The garnet of the examined samples is predominantly almandine (52.8–80.2 %), with grossular (2.26–18.29 %), pyrope (15.58–42.80 %), and minor amounts of spessartine (0.33–1.70 %). Among them, the maximum value of MgO contents of garnets from middle pressure pelitic granulite sample PD03a-1 was 10.68–11.30 %, which was consistent with the garnets from the granulite-facies Paleoproterozoic khondalite series rocks in the Khondalite Belt. Thus, they are plotted in the granulite-facies field in Fig. 8.27. However, most of the garnet from the Jiaobei pelitic granulites is plotted in the amphibolite facies to granulite-facies boundary field, as garnet compositions are affected by the post-peak decompression and cooling.

Microprobe and scanning electron microscopy (SEM) analyses revealed two types of variation of the individual garnets from the Jiaobei pelitic granulites: (i) most of the garnets are characterized from core to rim by decreases in pyrope, increases in spessartine and almandine, and a lack of variation in grossular (Fig. 8.26), which may reflect resetting by diffusion reaction during post-peak cooling; but (ii) a few of the garnets are characterized from core to rim by decreases in pyrope and grossular, and increases in spessartine and almandine (Fig. 8.26), reflecting resetting by diffusion and net transfer reaction during post-peak decompression and cooling.

8.3.4.2 Biotite

The chemical compositions of representative biotites from the Jiaobei pelitic granulites are summarized in Table 8.11. Three main kinds of biotite were analyzed: (i) biotite (Bt_1) as inclusions within the core of garnet. (ii) the core of biotite (Bt_2) in contact with felsic minerals in the matrix; and (iii) the rim of biotite (Bt_3) in the matrix growing next to sillimanite and garnet. Most of the biotites of the Jiaobei pelitic granulite samples are plotted in the biotite and magnesium-rich biotite fields in the classification diagrams (Fig. 8.27), indicating that the biotites from the Jiaobei pelitic granulites are characterized by magnesium-rich compositions. However, the three kinds of biotite show compositional variations, especially X_{Fe} ($X_{Fe} = Fe_{2+}/(Mg + Fe^{2+})$), MgO, and TiO_2 values. For example, the three kinds of biotite from the same sample have variable concentrations of TiO_2, ranging from 0.68 to 5.99, suggesting that they record different metamorphic *P–T* conditions.

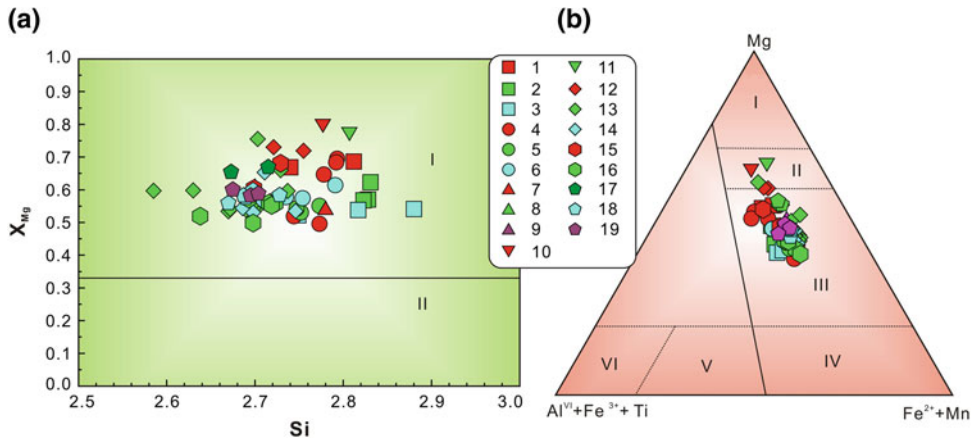

Fig. 8.27 Si versus X_{Mg} diagram (**a**; Deer et al. 1997) and Mg–(Al^{VI} + Fe^{3+}+Ti)–(Fe^{2+}+Mn) triangular diagram (**b**; Foster 1960) of the biotites from the Jiaobei pelitic granulites (Liu et al. 2015). *1* Inclusion-type biotites from sample JB04-4; *2* Matrix-type biotites from sample JB04-1; *3* Matrix-type biotites from samples JB04-4 and JB04-5; *4* Inclusion-type biotites from samples JB07-3, JB07-5, JB07-2 and JD16-4; *5* Cores of the matrix-type biotites from samples JB07-3, JB07-4 and JD16-4; *6* Rims of the matrix-type biotites from samples JB07-3 and JB07-5; *7* Inclusion-type biotites from sample LY-6; *8* Cores of the matrix-type biotites from samples LY-6 and LY-7; *9* Rims of the matrix-type biotites from sample LY-7; *10* Inclusion-type biotites from sample PD03a-01; *11* Matrix-type biotites from sample PD03a-01; *12* Inclusion-type biotites from sample PD04a-01; *13* Cores of the matrix-type biotites from sample PD04a-01; *14* Rims of the matrix-type biotites from sample PD04a-01; *15* Inclusion-type biotites from sample PD08a-03; *16* Matrix-type biotites from sample PD08a-03; *17* Inclusion-type biotites from sample QX20-1; *18* Cores of the matrix-type biotites from sample QX20-1; *19* Rims of the matrix-type biotites from sample QX20-1

Table 8.11 Representative compositional analyses of biotite from the Khondalite Series rocks within the Jiaobei Complex

Sample	JB04-4	JB07-5	JB07-2	JD16-4	LY-6	PD03a-01-6.1	PD04a-01-1.3	PD04a-01-1.3	PD08a-03-4.6	QX20-1-3.2
SiO_2	37.16	37.56	35.52	36.30	37.23	38.38	37.11	36.13	36.12	35.69
TiO_2	3.508	3.61	3.26	3.00	0.02	5.99	4.72	3.66	3.17	3.76
Al_2O_3	18.15	20.26	17.92	18.13	19.25	16.21	17.65	17.56	18.84	17.61
Cr_2O_3	0.075	0.04	0.12	0.05	0.00	0.20	0.17	0.18	0.06	0.01
FeO^T	11.87	11.66	18.72	17.20	17.56	7.37	14.51	16.20	14.44	13.40
MnO	0.015	0.09	0.09	0.03	0.06	0.00	0.01	0.00	0.00	0.04
MgO	14.59	14.30	10.37	11.49	11.56	16.61	12.02	12.01	12.38	14.33
CaO	0.014	0.08	0.03	0.02	0.00	0.05	0.00	0.01	0.03	0.09
Na_2O	0.176	0.24	0.14	0.26	0.10	0.17	0.14	0.10	0.26	0.28
K_2O	9.689	9.16	9.22	10.74	10.55	9.70	9.77	9.87	9.44	8.94
Total	95.25	97.00	95.37	97.24	96.32	94.71	96.20	95.85	94.82	94.20
Si	2.812	2.792	2.773	2.747	2.780	2.777	2.737	2.706	2.699	2.673
Ti	0.200	0.202	0.191	0.171	0.001	0.326	0.262	0.206	0.178	0.212
Al	1.619	1.776	1.649	1.617	1.694	1.383	1.534	1.550	1.659	1.555
Cr	0.004	0.002	0.007	0.003	0.000	0.011	0.010	0.011	0.004	0.001
Fe^{3+}	0.000	0.000	0.000	0.000	0.000	0.000	0.000	0.000	0.000	0.000
Fe^{2+}	0.751	0.725	1.222	1.089	1.097	0.446	0.895	1.015	0.902	0.839
Mn	0.001	0.006	0.006	0.002	0.004	0.000	0.001	0.000	0.000	0.003
Mg	1.645	1.585	1.207	1.296	1.286	1.791	1.321	1.340	1.378	1.600
Ca	0.001	0.006	0.002	0.002	0.000	0.004	0.000	0.001	0.002	0.007
Na	0.026	0.035	0.021	0.038	0.014	0.024	0.020	0.015	0.038	0.041
K	0.935	0.869	0.918	1.036	1.005	0.896	0.920	0.944	0.901	0.855
X_{Mg}	0.69	0.68	0.50	0.54	0.54	0.80	0.60	0.57	0.60	0.66

Table 8.12 Representative compositional analyses of feldspar from the Khondalite Series rocks within the Jiaobei Complex

Sample	PD08a-03-3.14	QX20-1-2.3	LY-6	LY-7	JB07-1	JB04-1	PD03a-01-4.2	PD03a-01-4.5	PD04a-01-3.6	PD04a-01-2.1
SiO_2	69.06	60.55	58.79	56.88	62.33	47.73	68.66	61.16	47.33	55.60
TiO_2	0.00	0.02	0.00	0.00	0.06	0.00	0.02	0.02	0.00	0.11
Al_2O_3	20.06	23.93	26.57	27.41	22.46	32.21	20.85	24.03	33.60	27.34
Cr_2O_3	0.00	0.01	0.00	0.00	0.00	0.00	0.03	0.01	0.00	0.00
FeO	0.03	0.00	0.10	0.08	0.13	0.55	0.10	0.09	0.61	0.22
MnO	0.01	0.03	0.02	0.00	0.03	0.03	0.02	0.09	0.07	0.04
MgO	0.00	0.00	0.00	0.00	0.00	0.00	0.03	0.01	0.00	0.00
CaO	0.26	5.53	7.87	9.76	3.59	16.42	0.33	5.39	16.43	9.94
Na_2O	10.72	8.84	7.10	6.07	9.56	2.26	8.55	8.30	2.42	6.32
K2O	0.04	0.09	0.20	0.15	0.19	0.00	0.90	0.05	0.04	0.35
Total	100.18	99.00	100.65	100.35	98.35	99.19	99.49	99.15	100.50	99.92
Si	2.9970	2.7210	2.611	2.546	2.804	2.2110	2.9910	2.7350	2.1650	2.5130
Ti	0.0000	0.0010	0.000	0.000	0.002	0.0000	0.0010	0.0010	0.0000	0.0040
Al	1.0260	1.2680	1.391	1.446	1.191	1.7590	1.0710	1.2670	1.8120	1.4570
Fe^{3+}	0.0010	0.0000	0.000	0.000	0.000	0.0000	0.0040	0.0030	0.0230	0.0080
Fe^{2+}	0.0000	0.0000	0.004	0.003	0.005	0.0210	0.0000	0.0000	0.0000	0.0000
Mn	0.0000	0.0010	0.001	0.000	0.001	0.0010	0.0010	0.0030	0.0030	0.0020
Mg	0.0000	0.0000	0.000	0.000	0.000	0.0000	0.0020	0.0010	0.0000	0.0000
Ca	0.0120	0.2660	0.375	0.468	0.173	0.8150	0.0150	0.2580	0.8050	0.4810
Na	0.9020	0.7700	0.612	0.527	0.834	0.2030	0.7220	0.7200	0.2150	0.5540
K	0.0020	0.0050	0.011	0.009	0.011	0.0000	0.0500	0.0030	0.0020	0.0200
Or	0	0	1	1	1	0	6	0	0	2
An	1	26	38	47	17	80	2	26	79	46
Ab	98	74	61	52	82	20	92	73	21	53

8.3.4.3 Feldspar

Representative feldspar analyses from the Jiaobei pelitic granulite samples are shown in Table 8.12 and all feldspar analyses are plotted in the Or–An–Ab triangular diagrams (Fig. 8.28). Feldspar can be classified into three compositional types: (i) plagioclase, (ii) k-feldspar, and (iii) albite. Among them, plagioclase can be classified into three textural types: (i) inclusion-type plagioclase (Pl_1) within the core of garnet, (ii) the core of plagioclase (Pl_2) in the matrix, and (iii) fine-grained new-grow matrix-type and rim of the coarse-grained matrix-type plagioclase (Pl_3). The three kinds of plagioclase exhibit significant variation in anorthite (An) contents. For example, in sample PD04a-1, inclusion-type and matrix plagioclases were plotted in the anorthite and bytownite fields, respectively (Fig. 8.28). It is worth noting that the matrix-type plagioclases from the high-pressure pelitic granulite sample JB04 have the highest anorthite values (An: 71–80), which may be related to migration of calcium from the peak to post-peak decompression stages (Tam et al. 2012a).

8.3.4.4 Other Minerals

Cordierites from the Jiaobei pelitic granulites can be classified into two textural types: (i) matrix-type cordierite ($Cord_1$) and (ii) symplectite-type cordierite ($Cord_2$). As shown in Fig. 8.29, both matrix-type and symplectite-type cordierites display similar compositional variations of X_{Mg}, ranging from 0.67 to 0.78, and are magnesium-rich cordierites (Wang et al. 2010; Tam et al. 2012a).

Muscovite is found within the garnet cores of the Jiaobei high-pressure pelitic granulites and exhibit large variation in X_{Fe} (Fe/(Fe + Mg)), ranging between 0.39 and 0.79, but restricted variations in contents of Si and Al, ranging from 3.765–3.990 to 2.730–2.746, respectively (Tam et al. 2012a).

8.3.5 Metamorphic P–T Conditions

8.3.5.1 Pre-peak Stage (M_1)

As mentioned above, in the Jiaobei high-pressure pelitic granulites, fine-grained mineral inclusions of biotite +

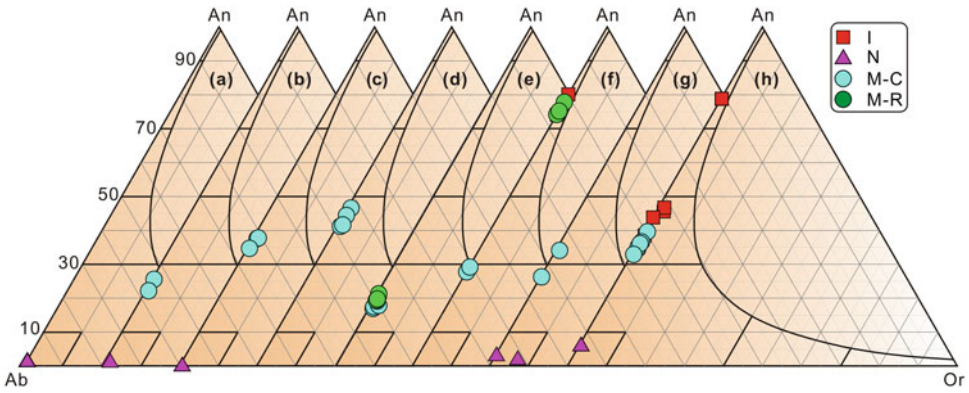

Fig. 8.28 Ab–Or–An triangular diagram of the plagioclases from the Jiaobei pelitic granulites (Liu et al. 2015). **a**–**h** Plagioclases from samples PD08a-03, b-QX20-1, c-LY6, d-LY7, JB07, JB04, PD03a-01, and PD04a-01, respectively; N: Albites-stripe from the coarse-grained perthites; *I* Inclusion-type plagioclases; *M-C* Cores of the matrix-type plagioclases; *M-R* Rims of the matrix-type plagioclases

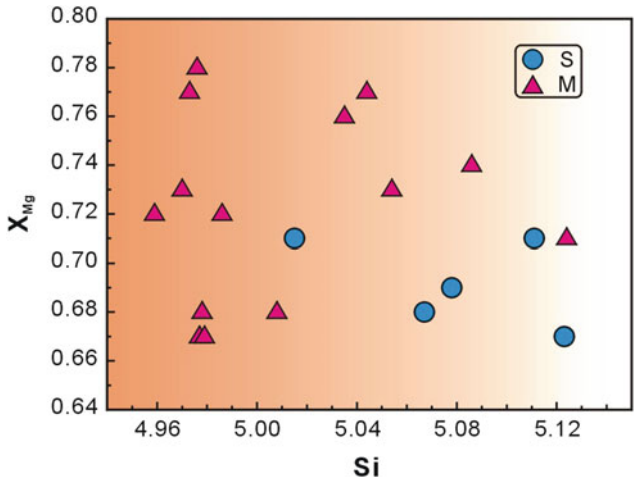

Fig. 8.29 Si-X_{Mg} diagram of the cordierites from the Jiaobei pelitic granulites. *I* Symplectite-type cordierite; *M* Matrix-type cordierites (Liu et al. 2015)

plagioclase (Pl_1) + quartz + kyanite (Ky_1) + muscovite (Ms) + ilmenite (Ilm_1), with the garnet cores, has been recognized as typical pre-peak prograde mineral assemblage. Accordingly, Wang et al. (2010) chose the core composition of garnet and fine-grained inclusions, used GB-GASP formulae, and yielded pre-peak *P–T* conditions of ca. 0.4 GPa and 550—590 °C. Meanwhile, Tam et al. (2012a) chose the NCKFMASHTO system, used the X_{Fe} isopleths of muscovite cores and the X_{Fe} isopleths of inclusion-type biotite (Bt_1), and determined similar *P–T* conditions of 0.93–1.07 GPa and 645–670 °C for the pre-peak prograde stage (M_1).

8.3.5.2 Peak Stage (M_2)

Matrix-type mineral assemblage of K-feldspar + kyanite (Ky_2) + plagioclase (Pl_2) + biotite (Bt_2) + rutile + ilmenite + quartz, with garnet mantle (Grt_2), was thought to be a characteristic peak mineral assemblage in the Jiaobei pelitic granulites. Wang et al. (2010) chose the peak mineral assemblage and corresponding mineral compositions, used the GB-GASP formulae, and yielded peak *P–T* conditions of ca. 1.0 GPa and ca. 780 °C (M_1). In addition, in the NCKFMASHTO system, Tam et al. (2012a) used the X_{Ca} values of garnet and X_{An} of plagioclase (Pl_2) in the matrix, and yielded peak *P–T* conditions of 1.48–1.62 GPa and 860–890 °C.

8.3.5.3 Post-peak Retrograde Stage (M_3)

As mentioned above, the post-peak *retrograde* stage (M_3) is characterized by the mineral assemblage of garnet rim (Grt_3) + sillimanite + plagioclase (Pl_3) + biotite (Bt_3) + ilmenite + quartz. In the NCKFMASHTO system, Tam et al. (2012a) used the X_{Fe} isopleths of garnet and biotite (Bt_3), and yielded post-peak *P–T* conditions of 0.63–0.85 GPa and 710–740 °C. In addition, Zhou et al. (2008a) chose the post-peak mineral assemblage and corresponding mineral compositions, used rims of the garnets and fine-grained plagioclase and biotite by the GB-GASP formulae, and obtained post-peak *P–T* conditions of 0.58–0.72 GPa and 620–680 °C.

8.3.6 U–Pb Dating of Zircons

8.3.6.1 Zircon CL Imaging

1. Zircons from high-pressure pelitic granulite

Zircons from the high-pressure pelitic granulite sample PD-8a-2 are mainly purple red in color, nearly round, equant or columnar in shape, and 50–100 μm in length with length-to-width ratios of ca. 1:1–2:1 (Fig. 8.30). These

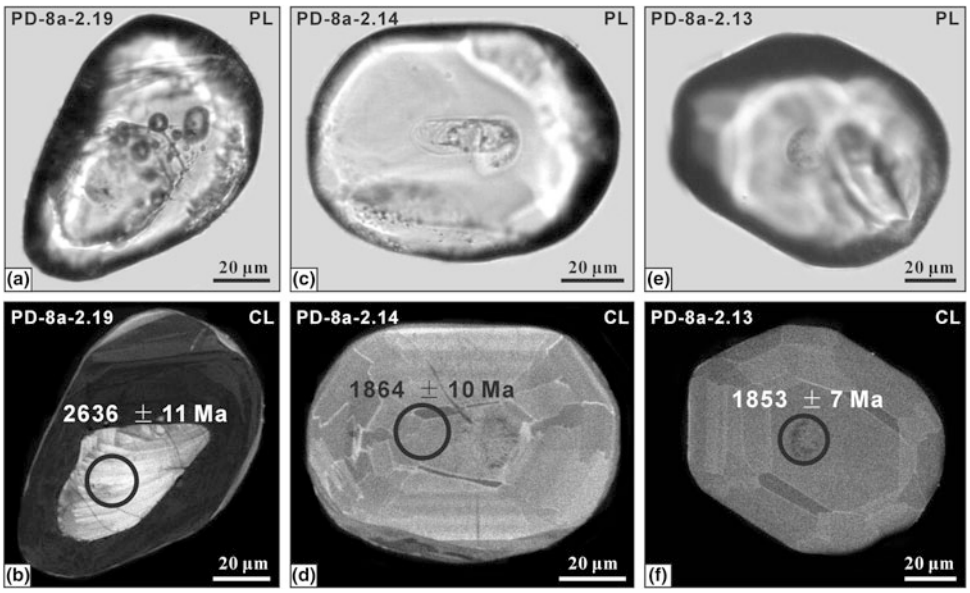

Fig. 8.30 PPL images, Cathodoluminescence (CL) images and SHRIMP U–Pb ages of the host zircons from the high-pressure pelitic granulite (PD-8a-2) (Liu et al. 2011c). **a** Zircon PD-8a-2.19 with rounded crystal shape. **b** CL image of the same zircon as in Fig. 8.30a showing a high-luminescent core and low-luminescent metamorphic rim, and $^{207}Pb/^{206}Pb$ age. **c** Zircon grain PD-8a-2.14 with rounded crystal shape. **d** CL image of the same metamorphic zircon as in Fig. 8.33c showing a high-luminescent CL image, and $^{207}Pb/^{206}Pb$ age. **e** Zircon PD-8a-2.13 with columnar crystal shape. **f** CL image of the same zircon as in Fig. 8.30e showing a middle (*gray*)-luminescent CL image, and $^{207}Pb/^{206}Pb$ age

zircon grains can be subdivided into two textural types based on CL imaging, crystal habits, and mineral inclusions. Type one zircon grains are characterized by entirely homogeneous medium-luminescence in CL images, and rare mineral inclusions of apatite. In contrast, Type-2 zircon grains are characterized by homogeneous high-luminescence metamorphic cores surrounded by relatively homogeneous low-luminescence metamorphic rims (Fig. 8.30). Laser Raman spectroscopy indicates the presence of rare inclusions of apatite + quartz in cores and rims of the Type-2 zircon grains. Luminescence of the cores and rims is homogeneous. CL image features and the crystal habits of Type-1 zircon grains and rims of the Type-2 zircon grains indicate a metamorphic origin.

2. Zircons from middle pressure pelitic granulite

Zircons separated from the middle pressure pelitic granulite sample PD-3c-2 are mainly nearly rounded, equant, or columnar in shape, and have lengths of 20–80 μm with length-to-width ratios of ca. 1:1–2:1 (Fig. 8.31). Based on CL imaging, crystal habits, and mineral inclusions, these zircon grains can be subdivided into two textural types. Type-1 zircon grains are characterized by clear and high- to middle-luminescent (black–gray) oscillatory-zoned magmatic cores surrounded by relatively homogeneous middle-luminescent (gray) metamorphic rims (Fig. 8.31). Laser Raman spectroscopy indicates the presence of rare inclusions of apatite in cores and rims of the zircon grains. Type-2 zircon grains are characterized by entirely homogeneous medium-luminescence (gray) in CL images, and rare mineral inclusions of apatite by laser Raman spectroscopy.

8.3.6.2 Zircon U–Pb Dating

1. Zircons from high-pressure pelitic granulite

Two significant age groups were identified in the different domains of the high-pressure pelitic granulite sample PD-8a-2 (Fig. 8.32a). One inherited core domain has a Th/U ratio of 0.59 and yields a concordant $^{207}Pb/^{206}Pb$ age of 2636 ± 11 Ma, which is interpreted as the age of the magmatic or metamorphic provenance of this pelitic granulite. In contrast, 26 overgrowth domains have lower Th/U ratios of 0.01–0.07 and yield younger and concordant $^{207}Pb/^{206}Pb$ ages ranging from 1879 ± 5 to 1847 ± 8 Ma, with a weighted mean age of 1868 ± 3 Ma. These older metamorphic ages are consistent with the peak metamorphic ages recorded by metamorphic zircon domains containing mineral inclusions of garnet + clinopyroxene + plagioclase + quartz in sample PD13d-02 of Liu et al. (2012b), interpreted as the timing of the peak metamorphism in the high-pressure pelitic granulite sample PD-8a-02.

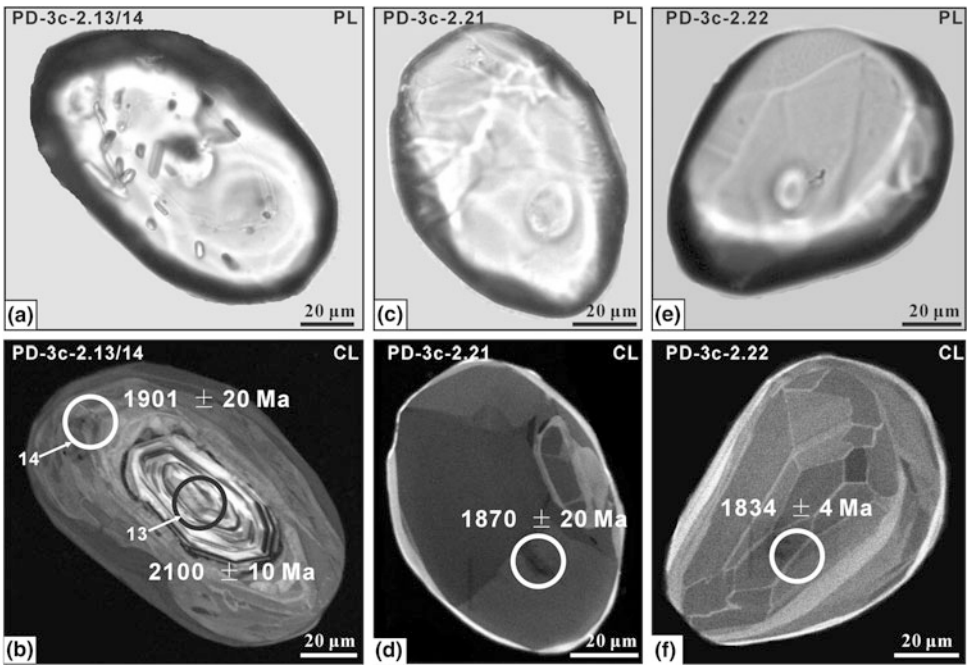

Fig. 8.31 PPL images, CL images, and SHRIMP U–Pb ages of host zircons from the pelitic granulite (PD-3c-2) (Liu et al. 2011c). **a** Zircon grain PD-3c-2.13 with columnar crystal shape. **b** CL image of the same zircon as in Fig. 8.31a showing a high-luminescent magmatic core and low-luminescent metamorphic rim, and $^{207}Pb/^{206}Pb$ ages. **c** Zircon grain PD-3c-2.21 with rounded crystal shape. **d** CL image of the same metamorphic zircon as in Fig. 8.31c showing a low-luminescent CL image, and $^{207}Pb/^{206}Pb$ age. **e** Zircon grain PD-3c-2.22 with rounded crystal shape. **f** CL image of the same zircon as in Fig. 8.31e showing a high-luminescent CL image, and $^{207}Pb/^{206}Pb$ age

2. Zircons from middle pressure pelitic granulite

Three significant age groups were identified in the different domains of the middle-pressure pelitic granulite sample PD-3c-2 (Fig. 8.32b). Four inherited core domains have variable Th/U ratios of 0.19–2.58 and yield $^{207}Pb/^{206}Pb$ ages ranging from 2216 ± 42 to 2100 ± 10 Ma. One analysis on the oscillatory-zoned magmatic cores yields a concordant $^{207}Pb/^{206}Pb$ age of 2100 ± 10 Ma, interpreted as the age of the magmatic provenance of this pelitic granulite. In contrast, seven metamorphic domains have lower Th/U ratios of 0.01–0.04, and yield younger $^{207}Pb/^{206}Pb$ ages ranging from 1922 ± 12 to 1868 ± 11 Ma, with a weighted mean age of 1881 ± 16 Ma. The older metamorphic ages are consistent with the peak metamorphic ages recorded in metamorphic zircon domains in sample PD13d-02 by Liu et al. (2012b). Thus, they are interpreted as the timing of the peak metamorphism in the middle pressure pelitic granulite specimen PD-3c-02. In addition, 16 metamorphic domains have lower Th/U ratios of 0.01–0.33 and yield the youngest $^{207}Pb/^{206}Pb$ ages ranging from 1855 ± 5 to 1833 ± 9 Ma, with a weighted mean age of 1842 ± 4 Ma. These metamorphic ages are similar to the retrogressive metamorphic ages (1839 ± 3 Ma) recorded in the Opx-bearing zircon metamorphic domains in sample PD16a-02 of Liu et al. (2012b). Thus, the relatively younger metamorphic ages should represent the timing of the retrogressive metamorphism in the middle pressure pelitic granulite sample PD-3c-02.

8.3.7 Discussion

8.3.7.1 Age of the Protoliths

The khondalite series rocks in the Jiao-Liao-Ji Belt were named as the Jingshan Group or Fenzishan Group in Jiaobei Complex, and as the Liaohe Group, Liaoling Group, or Ji'an Group in the Liaoji Complex. Many groups have carried out studies to date the timing of the sedimentary protoliths of the khondalite series rocks in the Jiao-Liao-Ji Belt. Among them, based on earlier isotopic data, including K–Ar and Rb–Sr whole-rock isochron dates and conventional multi-grain zircon ages, it was previously suggested that the khondalite series rocks in the Jiaobei Complex and Liaoji Complex were deposited between 2182 and 1906 Ma and 2400 and 2000 Ma, respectively (Zhang et al. 1988; Ji 1993; Wang 1995). However, conventional methods cannot give reliable constraints on the depositional ages of the khondalite series rocks in the Jiao-Liao-Ji Belt (Lu et al. 2006; Wan et al. 2006).

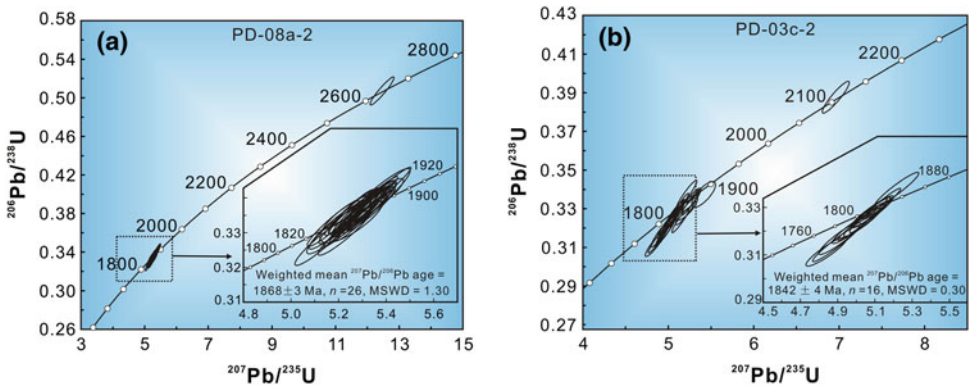

Fig. 8.32 $^{206}Pb/^{238}U$-$^{207}Pb/^{235}U$ diagrams showing U–Pb analyses of different zircon domains from the pelitic granulites within the Jiaobei terrane (modified after Liu et al. 2011c). **a** Sample PD-08a-2. **b** Sample PD-03c-2

Recently, many researchers have carried out LA-ICP-MS and SHRIMP zircon U–Pb dating (Luo et al. 2004, 2008; Lu et al. 2006; Wan et al. 2006; Zhou et al. 2008b; Tam et al. 2011; Liu et al. 2011c; Zhao et al. 2014; Xie et al. 2014). As shown in Fig. 8.33, detrital zircons from the representative khondalite series rocks within the Jiao-Liao-Ji Belt yielded concordant $^{207}Pb/^{206}Pb$ ages between 3420 and 1990 Ga and 3357–2000 Ma, respectively, reflecting that the protoliths of the khondalite series rocks in the Jiao-Liao-Ji Belt came mainly from the Archaean and Paleoproterozoic provenances. This also indicates that the maximum deposition ages of the protolith of the khondalite series rocks within the Jiao-Liao-Ji Belt is constrained to 2200–2000 Ma by their youngest detrital zircon ages (Luo et al. 2004, 2008; Wan et al. 2006; Lu et al. 2006; Zhou et al. 2008b; Tam et al. 2011; Liu et al. 2011c, 2015). Their minimum deposition age can be constrained by the oldest concordant age of 1950–1930 Ma for the metamorphic zircon overgrowths from the khondalite series rocks within the Jiao-Liao-Ji Belt (Tam et al. 2011; Luo et al. 2004, 2008; Lu et al. 2006; Wan et al. 2006; Liu et al. 2011c).

These new geochronological results indicate that the sedimentary protoliths of the khondalite series rocks in the Jiao-Liao-Ji Belt were deposited at some time between 2200 and 2000 and 1950–1930 Ma (Luo et al. 2004, 2008; Lu et al. 2006; Tam et al. 2011; Liu et al. 2015), not shortly after the end of the Late Archean, as previously considered (e.g. Zhang et al. 1988).

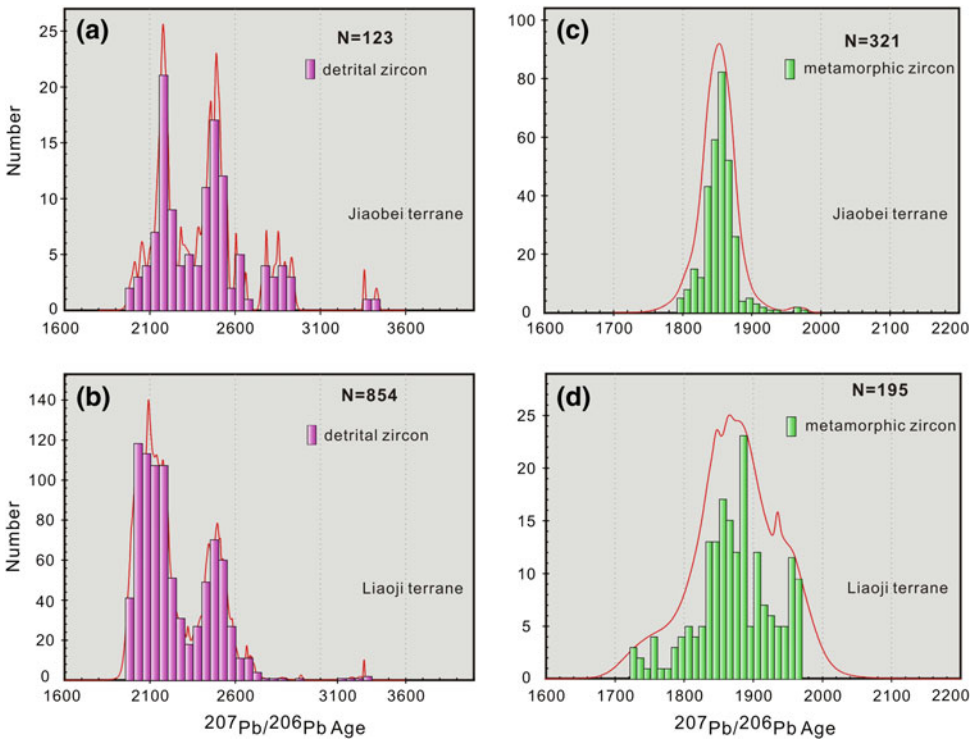

Fig. 8.33 Histograms of zircon $^{207}Pb/^{206}Pb$ ages for the khondalite series rocks within the JLIB showing detrital and metamorphic zircon ages with Mesoarchean–Late Paleoproterozoic magmatic-metamorphic thermal events. **a** Detrital zircon from the Jiaobei terrane, **b** metamorphic zircon from the Jiaobei terrane, **c** detrital zircon from the Liaoji terrane, **d** metamorphic zircon from the Liaoji terrane. Data are from Luo et al. (2004, 2008), Lu et al. (2006), Wan et al. (2006), Zhou et al. (2008b), Tam et al. (2011), Liu et al. (2011c), Zhao et al. (2014), and Xie et al. (2014)

8.3.7.2 Age of Metamorphism

There has been controversy regarding the metamorphic timing of the khondalite series rocks in the Jiao-Liao-Ji Belt. Yin and Nie (1996) obtained a biotite $^{40}Ar/^{39}Ar$ age of 1896 ± 7 Ma from a main detachment shear zone in the Liaohe Group, which was interpreted as the post-peak cooling age as biotite generally has a relatively low closure temperature (300 ± 50 °C).

Applying SIMS and LA-ICP-MS U–Pb zircon dating combined with CL imaging, numerous geochronological studies have been examined for the metamorphic timing of the khondalite series rocks in the Jiao-Liao-Ji Belt. As shown in Fig. 8.33, metamorphic zircons from the khondalite series rocks within the Jiao-Liao-Ji Belt yielded concordant $^{207}Pb/^{206}Pb$ ages between 1950–1800 Ma, reflecting that the khondalite series rocks in the Jiao-Liao-Ji Belt experienced regional metamorphism and deformation during 1950–1800 Ma. In addition, these metamorphic zircon domains can be divided into two textural types. The first type of metamorphic zircons yielded relatively older and concordant $^{207}Pb/^{206}Pb$ ages, mainly ranging from 1950 to 1900 Ma. For example, Luo et al. (2004) first recognized metamorphic zircons from the amphibolite facies schists of the Liaohe Group, which yielded a weighed mean $^{207}Pb/^{206}Pb$ age of 1929 ± 38 Ma and an upper intercept age of 1929 ± 26 Ma. Meanwhile, Tam et al. (2011) and Liu et al. (2011c) also reported that one metamorphic zircon with a low Th/U ratio (0.01, 0.04), from a fine-grained graphite-bearing garnet-sillimanite gneiss sample (08JB02-1 and PD-3C-2), also gives apparent $^{207}Pb/^{206}Pb$ ages of 1939 ± 15 Ma and 1922 ± 12 Ma, respectively. These metamorphic ages of 1950–1900 Ma are remarkably older than the emplacement ages of post-orogenic/anorogenic granites in the Jiao-Liao-Ji Belt (Lu et al. 2006; Li and Zhao 2007), and are consistent with the peak metamorphic ages recorded by metamorphic zircon domains containing mineral inclusions of garnet + clinopyroxene + plagioclase + quartz in sample PD13d-02 of Liu et al. (2012b). Thus, the metamorphic ages of 1950–1900 Ma, recorded by the first type of metamorphic zircons from the khondalite series rocks in the Jiao-Liao-Ji Belt, were usually thought of as the timing of peak metamorphism during the main collision or crustal thickening stage.

In contrast, as shown in Fig. 8.33, the second type of metamorphic zircons from the khondalite series rock samples in the Jiao-Liao-Ji Belt yielded similar and concordant $^{207}Pb/^{206}Pb$ ages of 1860–1820 Ma (ca. 1850 Ma). For example, Lu et al. (2006) applied the LA-ICP-MS U–Pb zircon dating technique to determine the metamorphic ages of the Laoling and Ji'an Groups in southern Jilin Province. Their results showed that the metamorphism of the Laoling and Ji'an Groups occurred at ca. 1850 Ma. Meanwhile, Tam et al. (2011) and Liu et al. (2011c) reported metamorphic ages of 1827 ± 8 and 1842 ± 4 Ma recorded by graphite-bearing garnet-sillimanite gneiss samples 08JB02-1 and PD-3c-2 within the Jiaobei terrane, respectively.

These younger metamorphic ages of 1860–1820 Ma are consistent with the ages of the partial melting of 1860–1830 Ma recorded by anatectic zircons from granitic leucosomes within the Jiaobei Complex (Liu et al. 2014a), the emplacement ages of post-orogenic/anorogenic mafic-granitic rocks in the Jiao-Liao-Ji Belt (Lu et al. 2006; Li and Zhao 2007; Dong et al. 2011), and $^{40}Ar/^{39}Ar$ age of 1803 ± 12 Ma recorded by the amphibole from the high-pressure mafic granulite sample in the Jiaobei area (Faure et al. 2003). These younger metamorphic ages are also consistent with the post-peak retrogressive metamorphic ages recorded by the opx-bearing metamorphic zircons from the high-pressure mafic granulites (Liu et al. 2013b, 2015). Therefore, the 1860–1820 Ma (ca. 1850 Ma) metamorphic ages, recorded by the khondalite series rocks in the Jiao-Liao-Ji Belt, were interpreted as the timing of the post-peak regional metamorphism during the post-collisional exhumation and extension stage.

8.3.7.3 Tectonic Settings and Provenance

Many groups have investigated the geochemistry of sediments deposited in oceanic island arc, continental island arc, active continental margin, and passive margin tectonic settings (e.g., Bhatia 1983; Bhatia and Crook 1986; Roser and Korsch 1986; McLennan et al. 1990; McLennan and Taylor 1991). Generally, Al_2O_3, $Fe_2O_3^T$ + MgO, TiO_2, and Al_2O_3/SiO_2 ratios decrease in sandstones from oceanic island arc settings to passive margins, while SiO_2 and K_2O/Na_2O ratios increase (Bhatia 1983). The meta-felsic rocks of the khondalite series rock samples in the Jiao-Liao-Ji Belt have high SiO_2 and moderate Al_2O_3, TiO_2, and Al_2O_3/SiO_2 ratios. Most of these samples show strong affinity with graywackes from continental island arc or active continental margin settings (Fig. 8.34). The contents and ratios of trace elements (including REEs) in most of the meta-felsic rocks of the khondalite series rock samples in the Jiao-Liao-Ji Belt exhibit the greatest similarity to graywackes from continental island arcs or acid arcs (Fig. 8.34). In the discriminatory La–Th–Sc diagram (Bhatia and Crook 1986), most samples plot in the continental arc field (Fig. 8.34). Similar results were obtained with the other trace element diagrams (Bhatia and Crook 1986). These geochemical features, in combination with other geological data, suggest that the sedimentary protoliths of the khondalite series rocks in the Jiao-Liao-Ji Belt were also deposited in a basin adjacent to a Paleoproterozoic continental arc.

8.3.7.4 P–T–T Paths and Tectonic Implications

As shown Fig. 8.35, based on integrated petrographic analysis with *P–T* thermobarometry and pseudosection

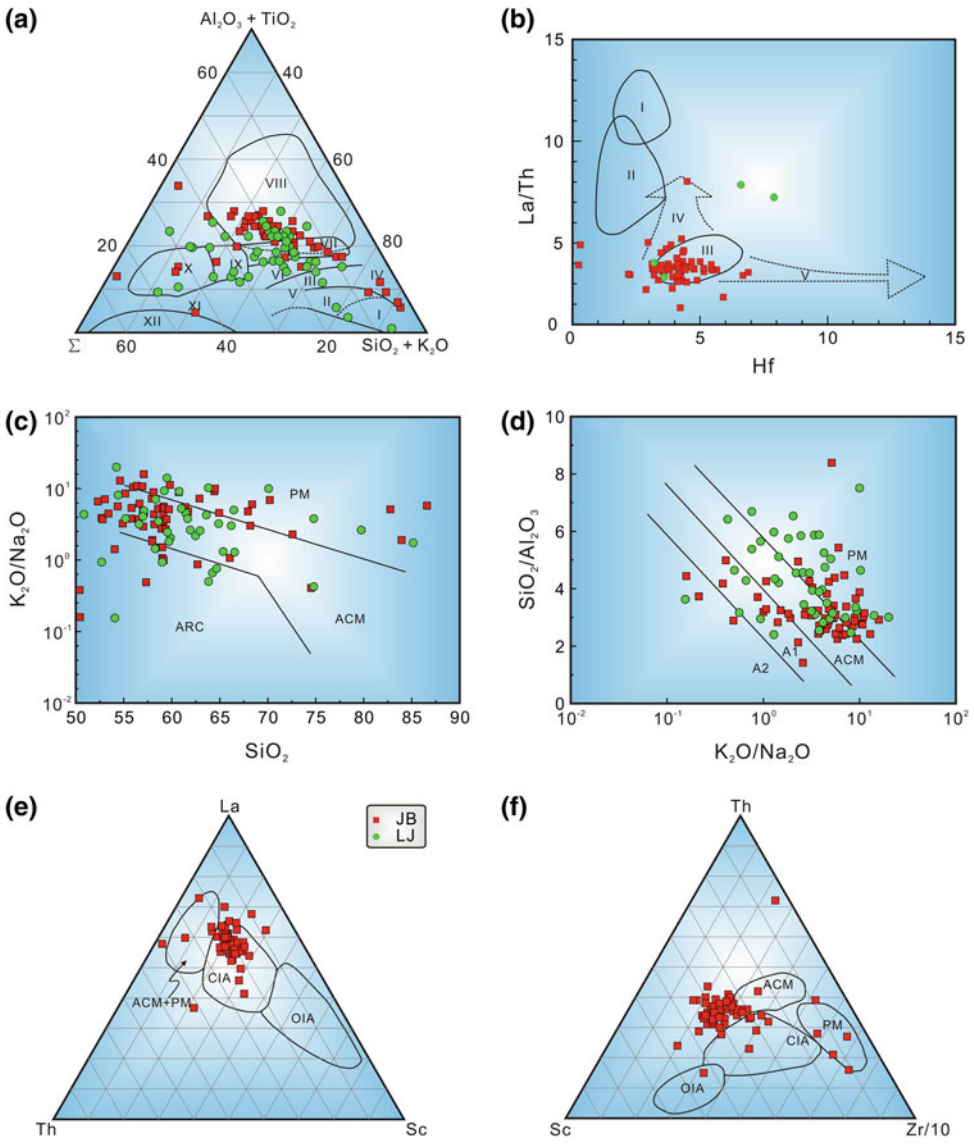

Fig. 8.34 Discrimination diagrams showing protolith formation and source rock for the khondalite series rocks in the Jiao-Liao-Ji Belt. **a** (second source from Lu et al. 1996): ∑ Residual components; *I* Quartz sandstone and quartzite; *II* Single-mineral sandstone and quartzitic sandstone, *III* Polymineral sandstone, *IV* Arkose, *V* Calcareous sandstone, *VI* Weakly differentiated chemical sedimentary rock, *VII* Marine and continental facies clay rock of frigid and temperate zones, *VIII* Strongly differentiated chemical clay rock of humid climate zones, *IX* Iron-bearing carbonate clay rock, *X* Marl, *XI* Siliceous marl and Iron-bearing sandstone, XII-Iron-bearing quartzite. **b** (Floyd and Leveridge 1987): *I* Tholeiitic ocean island source; *II* Andesitic arc source, *III* acidic arc source. **c** (Roser and Korsch 1986), **d** (Maynard et al. 1982), **e** (Bhitia and Crook 1986), and **f** (Bhitia and Crook 1986): *PM* passive continental margin; *ACM* Active Continental Margin; *ARC* *A1* Island Arc; *A2* Evolved Island Arc; *CIA* Continental Island Arc; *OIA* Oceanic Island Arc

modeling, combined with isotopic and other data, many groups have built *P–T–t* paths of the representative meta-pelitic and meta-mafic rocks within the Jiaobei Complex. The metamorphism of the meta-pelitic and meta-mafic is characterized by a clockwise *P–T–t* path, and belongs to the medium-pressure facies series that formed in the continental collisional orogenic belt (e.g., Migashiro 1961; England and Thompson 1984; Thompson and England 1984; Eillis 1987; Harley 1989; Brown 1993, 2006, 2007, 2008, 2014; Carswell and O'Brien 1993; Wei et al. 2014).

Among them, the Paleoproterozoic regional high-pressure granulite-facies metamorphism of the Jiao-Liao-Ji Belt is characterized by the clockwise *P–T–t* paths bearing a nearly isothermal decompression and near-isobaric cooling processes (e.g., Liu et al. 2010, 2013b, 2015; Tam et al. 2012a, b, c), suggesting that the Jiao-Liao-Ji Belt was involved in subduction-, aggregation-, and collision-related tectonic processes during 2000–1800 Ma, and the following metamorphic and tectonic processes are inferred:

1. During 2000–1950 Ma, the Jiao-Liao-Ji Belt experienced a crustal thickening event as a consequence of subduction of the Paleoproterozoic oceanic crust. As a result of tectonic burial and heat conduction, a greenschist facies to amphibolite facies prograde metamorphism occurred in the upper and middle crust region of the Jiao-Liao-Ji Belt. During 1950–1900 Ma, accompanied by cessation of oceanic crust subduction, the aggregation between the Paleoproterozoic arc and Archean continent and the collision between the Archean continents caused the development of the regional high-pressure granulite-facies metamorphism, as represented by the mineral assemblages of garnet + clinopyroxene + plagioclase ± amphibole ± Fe–Ti oxide ± quartz and garnet + kyanite + K-feldspar +

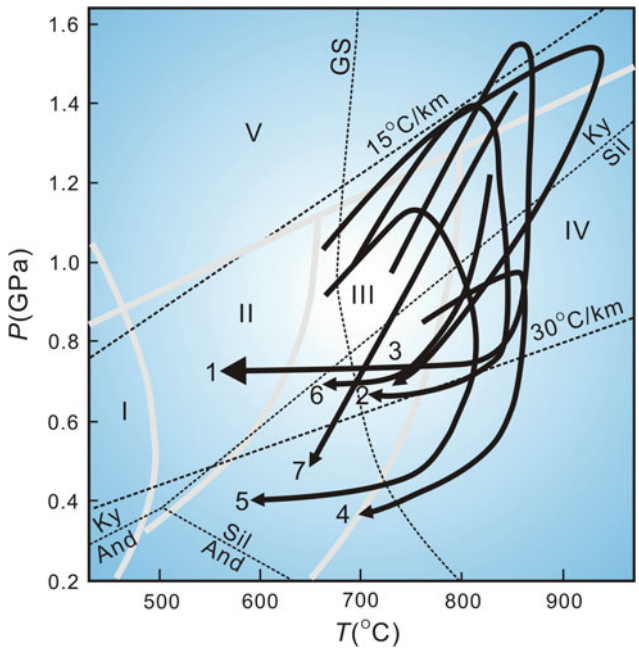

Fig. 8.35 Summary of metamorphic P–T paths of the Jiaobei terrane (modified after Liu et al. 2013b). *1* Jiaobei high-pressure mafic granulite (Liu et al. 2013b); *2* Jiaobei high-pressure mafic granulite (Tam et al. 2012c); *3* Jiaobei high-pressure pelitic granulite (Tam et al. 2012a); *4* Jiaobei MP pelitic granulite (Tam et al. 2012b); *5* Jiaobei high-pressure pelitic granulite (Wang et al. 2010); *6* Jiaobei high-pressure pelitic granulite (Zhou et al. 2004); *7* Jiaobei high-pressure mafic granulite (Liu et al. 1998). The granite solidus (GS) cited from Schliestedt and Johannes (1984). The boundary lines for metamorphic facies are cited from Brown (2001), I-Greenschist, II-Epidote-amphibolite facies, III-Amphibolite facies, IV-Granulite-facies, V-Eclogite facies. The transition lines of Al_2SiO_5 were from Salje (1986)

plagioclase + biotite + quartz + Fe–Ti oxide + liquid in the mafic granulites and pelitic granulites, respectively (e.g., Liu et al. 2010, 2013b, 2015; Tam et al. 2012a, b, c), that occurred in a region of ca. 50 km of the thickened lower crust or arc root at 1950–1900 Ma.

2. During 1900–1800 Ma, after the main collision and peak metamorphism, the Paleoproterozoic orogenesis of the Jiao-Liao-Ji Belt reached the post-collisional exhumation and extension stage. The post-collisional tectonic process can be divided into two stages. During the early fast tectonic exhumation stage, the high-pressure pelitic and mafic granulites experienced slight heating or a nearly ITD, which resulted in overprinting of the regional post-peak middle- and low-pressure granulite-facies metamorphism, and the development of orthopyroxene-bearing symplectites in the high-pressure mafic granulites (e.g., Liu et al. 2010, 2013b, 2015; Tam et al. 2012a, b, c).
3. Meanwhile, emplacement of the ca. 1850 Ma mafic dyke/sill swarms and partial melting of the crustal rocks were caused by the underplating of mantle-derived mafic magma during the early stage (e.g., Cai et al. 2002; Lu et al. 2006; Dong et al. 2011; Liu et al. 2014a). After the temperature peak, the late stage is dominated by slow isobaric cooling processes, which resulted in overprinting of the regional amphibolite facies metamorphism and the development of amphibole- or biotite-bearing symplectites or rims around garnet in the mafic and pelitic granulites, respectively. Finally, the end of the 2000–1800 Ma orogenesis of the Jiao-Liao-Ji Belt was marked by the regional development of ca. 1800 Ma tourmaline-bearing granitic pegmatites (Liu et al. 2014b).

8.4 Conclusions

The major conclusions of this study can be summarized as follows:

1. The sedimentary protoliths of the khondalite series rocks in the Khondalite Belt and Jiao-Liao-Ji Belt were likely deposited in an active continental margin in the late Paleoproterozoic, ranging from 2200–2000 Ma to 1950–1900 Ma.
2. During 2000–1950 Ma, the protoliths of the khondalite series rocks from the Khondalite Belt and Jiao-Liao-Ji Belt experienced a crustal thickening event due to subduction of the Paleoproterozoic oceanic crust. As a result of tectonic burial and heat conduction, a greenschist facies to amphibolite facies prograde metamorphism occurred in the upper and middle crust region of the Khondalite Belt and Jiao-Liao-Ji Belt, forming the early mineral assemblage of garnet (core) and inclusion-type minerals (biotite + quartz + plagioclase).
3. Accompanied by cessation of oceanic crust subduction, the aggregation between the Paleoproterozoic arc and Archean continent and the collision between the Archean continents caused the regional middle- and high-pressure granulite-facies metamorphism, as represented by the mineral assemblage of garnet + kyanite/sillimanite + K-feldspar + plagioclase + biotite + quartz + Fe–Ti oxide + liquid in the pelitic granulites, occurring in a region of ~50 km of the thickened lower crust or arc root at 1950–1900 Ma.
4. During 1900–1800 Ma, after the main collision and peak middle and high-pressure granulite-facies metamorphism, the Paleoproterozoic khondalite series rocks experienced post-peak retrogressive metamorphism in the post-collisional exhumation and extension stage.
5. In summary, the regional middle and high-pressure granulite-facies metamorphism of the Paleoproterozoic khondalite series rocks from the Khondalite Belt and Jiao-Liao-Ji Belt is characterized by clockwise

P–T–t paths bearing nearly isothermal decompression and near-isobaric cooling processes, suggesting that they have been involved in rapid deposition-, subduction-, aggregation-, and collision-related tectonic processes in an active continental margin or continental arc during 2200–1800 Ma.

Acknowledgments We are grateful to the members of the Research Department of Metamorphic and Precambrian Geology, Institute of Geology, Chinese Academy of Geological Sciences for the original manuscript preparation. We also thank Mingguo Zhai, Qihan Shen, Jinghui Guo, Guochun Zhao, Peng Peng, Lingling Xiao, Chaohui Liu, Fang Wang, and others for discussions and support during this research. We are particularly grateful to Academician Mingguo Zhai for originating this special issue. This paper presents a summary of the results of current and previous long-term studies in the Paleoproterozoic mobile belts in North China Craton, supported financially by the National Natural Science Foundation of China (41430210, 41372069, 41302153), the Major State Basic Research Program of the People's Republic of China (2012CB416603), and the China Geological Survey Project (DD20160121, 12120114061901, 1212011120150).

References

Aydin, F., Karsli, O., & Sadiklar, M.-B. (2003). Mineralogy and chemistry of biotites from Eastern Pontide granitoid rocks, NE-Turkey: Some petrological implications for granitoid magmas. *Chemie der Erde-Geochemistry, 63*, 163–182.

Barbey, P., Capdevila, R., & Hameurt, J. (1982). Major and transition trace element abundances in the khondalite suite of the granulite belt of Lapland (Fennoscandia): Evidence for an early Proterozoic flysch belt. *Precambrian Research, 16*, 273–290.

Bates, R.-L, & Jackson, J.-A (1980). *Glossary of geology* (2nd ed., p. 340). Falls Church, Virginia: American Geological Institute.

Bhat, M.-I., & Ghosh, S.-K. (2001). Geochemistry of the 2.51 Ga old Rampur group pelites, western Himalayas: implications for their provenance and weathering. *Precambrian Research, 108*, 1–16.

Bhatia, M.-R. (1983). Plate tectonics and geochemical composition of sandstones. *Journal of Geology, 91*, 611–627.

Bhatia, M.-R. (1985). Rare earth element geochemistry of Australian Paleozoic graywackes and mudrocks: Provenance and tectonic control. *Sedimentary Geology, 45*, 97–113.

Bhatia, M.-R., & Crook, K.-A.-W. (1986). Trace element characteristics of graywackes and tectonic setting discrimination of sedimentary basins. *Contributions to Mineralogy and Petrology, 92*, 181–193.

Brown, M. (1993). *P-T-t* evolution of orogenic belts and the causes of regional metamorphism. *Journal of the Geological Society, London, 150*(2), 227–241.

Brown, M. (2001). From microscope to mountain belt: 150 years of petrology and its contribution to understanding geodynamics, particularly the tectonics of orogens. *Journal of Geodynamics, 32*, 115–164.

Brown, M. (2006). A duality of thermal regimes is the distinctive characteristic of plate tectonics since the Neoarchean. *Geology, 34*, 961–964.

Brown, M. (2007). Metamorphic conditions in orogenic belts: A record of secular change. *International Geology Review, 49*, 193–234.

Brown, M. (2008). Characteristic thermal regimes of plate tectonics and their metamorphic imprint throughout Earth history. In K. Condie & V. Pease (Eds.), *When did plate tectonics begin*? (Vol. 440, pp. 97–128). Washington: Geological Society of America Special Papers.

Brown, M. (2014). The contribution of metamorphic petrology to understanding lithosphere evolution and geodynamics. *Geoscience Frontiers, 5*(4), 553–569.

Cai, J., Liu, F.-L., Liu, P.-H., Liu, C.-H., Wang, F., & Shi, J.-R. (2014). Metamorphic P-T path and tectonic implications of pelitic granulites from the Daqingshan Complex, North China Craton. *Precambrian Research, 241*, 161–184.

Cai, J., Liu, F.-L., Liu, P.-H., Wang, F., & Shi, J.-R. (2015). Geochronology of the Paleoproterozoic Khondalite rocks from the Wulashan-Daqingshan area, the Khondalite Belt. *Acta Petrologica Sinica, 31*(10), 3081–3106.

Cai, J.-H., Yan, G.-H., Mu, B.-L., Xu, B.-L., Shao, H.-X., & Xu, R.-H. (2002). U-Pb and Sm-Ndisotopic ages of an alkaline syenite complex body in Liangtun-Kuangdongguo, Gai County, Liaoning Province, China and their geological significance. *Acta Petrologica Sinica, 18*, 349–354.

Carswell, D.-A., & O'Brien, P.-J. (1993). Thermobarometry and geotectonic significance of high-pressure granulites: examples from the Moldanubian Zone of the Bohemian Massif in Lower Austria. *Journal of Petrology, 34*(3), 427–459.

Cesare, B., Satish-Kumar, M., Cruciani, G., Pocker, S., & Nodari, L. (2008). Mineral chemistry of Ti-rich biotite from pegmatite and metapelitic granulites of the Kerala Khondalite Belt (southeast India): Petrology and further insight into titanium substitutions. *American Mineralogist, 93*, 327–338.

Chacko, T., Ravindra, K.-G.-R., & Newton, R.-C. (1987). Metamorphic P-T conditions of Kerala (South India) khondalite belt: A granulite facies supracrustal terrain. *Journal of Geology, 95*, 343–358.

Chu, H., Lu, S.-N., Wang, H.-C., Xiang, Z.-Q., & Liu, H. (2011). U-Pb age spectrum of detrital zircons from the Fuzikuang Formaation, Penglai Group in Chandong Province. *Acta Petrologica Sinica, 27*(4), 1017–1028.

Coggon, R., & Holland, T.-J.-B. (2002). Mixing properties of phengitic micas and revised garnet-phengite thermobarometers. *Journal of Metamorphic Geology, 20*, 683–696.

Condie, K.-C., Boryta, M.-D., Liu, J.-Z., & Qian, X.-L. (1992). The origin of khondalites: Geochemical evidence from the Archean to early Proterozoic granulite belt in the North China craton. *Precambrian Research, 59*(3–4), 207–223.

Cooray, P.-G. (1962). Charnockites and their associated gneisses in the Precambrian of ceylon. *Quarterly. Journal of the Geological Society, 118*, 239–273.

Dallmeyer, R.-D., & Dodd, R.-T. (1971). Distribution and significance of cordierite in paragneisses of the Hudson Highlands, Southeastern New York. *Contributions to Mineralogy and Petrology, 33*, 289–308.

Daly, J.-S., Balagansky, V.-V., Timmerman, M.-J., Whitehouse, M.-J., de Jong, K., Guise, P., et al. (2001). Ion microprobe U-Pb zircon geochronology and isotopic evidence for a trans-crustal suture in the Lapland-Kola Orogen, northern Fennoscandian Shield. *Precambrian Reseach, 105*, 289–314.

Dan, W., Li, X.-H., Guo, J.-H., Liu, Y., & Wang, X.-C. (2012). Integrated in situ zircon U-Pb age and Hf-O isotopes for the Helanshan khondalites in North China Craton: Juvenile crustal materials deposited in active or passive continental margin? *Precambrian Research, 222–223*, 143–158.

Dash, B., Sahu, K.-N., & Bowes, D.-R. (1987). Geochemistry and original nature of Precambrian khondalites in the Eastern Ghats, Orissa, India. *Transactions of the Royal Society of Edinburgh: Earth Sciences, 78*, 115–127.

Deer, W.-A., Howie, R.-A., & Zussman, J. (1997). *Rock-forming minerals* (pp. 3–4). Second editon.Washington D.C.: Geological Society Publishing House.

Dong, X.–J. (2012). Composition and evolution of the early precambrian basement in Daqingshan Region, Inner Mongolia. Unpublished Ph.D. thesis. Jilin University, Changchun (in Chinese with English abstract).

Dong, C.-Y., Liu, D.-Y., Li, J.-J., Wan, Y.-S., Zhou, H.-Y., Li, C.-D., et al. (2007). Paleoproterozoic Khondalite Belt in the western North China Craton: New evidence from SHRIMP dating and Hf isotope composition of zircons from metamorphic rocks in the Bayan Ul-Helan Mountains area. *Chinese Science Bulletin, 52*(16), 2984–2994.

Dong, C.-Y., Liu, D.-Y., Wan, Y.-S., Xu, Z.-Y., Liu, Z.-H., & Yang, Z.-S. (2009a). Crustally derived carbonatite from the Daqingshan area: zircon features and SHRIMP dating. *Acta Geologica Sinica, 83*(3), 388–398. (in Chinese with English abstract).

Dong, C.-Y., Liu, D.-Y., Wan, Y.-S., Xu, Z.-Y., Wang, W., & Xie, H.-Q. (2009b). Hf isotope composition and REE pattern of zircons from early Precambrian metamorphic rocks in the Daqing Mountains. *Inner Mongolia. Geological Review, 55*(4), 509–520. (in Chinese with English abstract).

Dong, C.-Y., Wan, Y.-S., Wilde, S.-A., Xu, Z.-Y., Ma, M.-Z., Xie, H.-Q., & Liu, D.-Y. (2014). Ealiest Paleoproterozoic supracrustal rocks in the North China Craton recognized from the Daqingshan Area of the Khondalite Belt: Constraints on craton evolution. *Gondwana Research, 25*(4), 1535–1553.

Dong, C.-Y., Wan, Y.-S., Xu, Z.-Y., Liu, D.-Y., Yang, Z.-S., Ma, M.-Z., & Xie, H.-Q. (2012). SHRIMP zircon U-Pb dating of late Paleoproterozoic kondalites in the Daqing Mountains area on the North China Craton. *Science China Earth Sciences, 56*(1), 1–11.

Dong, C.-Y., Wang, S.-J., Liu, D.-Y., Wang, J.-G., Xie, H.-Q., Wang, W., et al. (2011). Late Palaeoproterozoic crustal evolution of the North China Craton and formation time of the Jingshan Group: Constraints from SHRIMP U-Pb zircon dating of meta-intermediate-basic intrusive rocks in eastern Shandong Province. *Acta Petrologica Sinica, 27*(6), 1699–1706.

Du, L.-L., Yang, C.-H., Wei, W., Ren, L.-D., Wan, Y.-S., Wu, J.-S., et al. (2013). Paleoproterozoic rifting of the North China Craton: Geochemical and zircon Hf isotopic evidence from the 2137 Ma Huangjinshan A-type granite porphyry in the Wutai area. *Journal of Asian Earth Sciences, 72*(4), 190–202.

Eills, D.-J. (1987). Origin and evolution of granulites in normal and thickened crusts. *Geology, 15*(2), 167–170.

England, P.-C., & Richardson, S.-W. (1977). The influence of erosion upon the mineral facies of rocks from different metamorphic environments. *Journal of the Geological Society of London, 134*, 201–213.

England, P.-C., & Thompson, A.-B. (1984). Pressure-temperature-time paths of regional metamorphism I. Heat transfer during the evolution of regions of thickened continental crust. *Journal of Petrology, 25*, 894–928.

Faure, M., Lin, W., Monid, P., Breton, N.-L., Poussineau, S., Panis, D., & Deloule, E. (2003). Exhumation tectonics of the ultrahigh-pressure metamorphic rocks in the Qinling orogen in east China: New petrological-structu ral-rad iometric insights from the Shandong Peninsula. *Tectonics, 22*(3), 1018–1040.

Floyd, P.-A., & Leveridge, B.-E. (1987). Tectonic environment of the Devonian Gramscatho basin, South Cornwall: Framework mode and geochemical evidence from turbiditie sandstones. *Journal of the Geological Society, 144*(4), 531–542.

Foster, M.-D. (1960). Interpretation of the composition of trioctahedral micas. *United States Geological Survey. Professional Paper, 354*, 11–48.

Garrels, R.-M., & Mackenzie, F.-T. (1971). *Evolution of sedimentary rocks* (p. 397). New York: Norton.

Guo, J.-H., Chen, Y., Peng, P., Liu, F., Chen, L., Zhang, L.-Q. (2006). Sapphirine-bearing granulite in Daqingshan, Inner Mongolia: 1.8 Ga UHT metamorphic events. In *Abstract Volume of 2006 Petrology and Earth dynamics in China* (pp. 215–218). Nanjing University, Nanjing (in Chinese with English abstract).

Guo, J.-H., Peng, P., Chen, Y., Jiao, S.-J., & Windley, B.-F. (2012). UHT sapphirine granulite metamorphism at 1.93–1.92 Ga caused by gabbronorite intrusions: Implications for tectonic evolution of the northern margin of the North China Craton. *Precambrian Research, 222–223*, 124–142.

Harley, S.-L. (1989). The origins of granulites: a metamorphic perspective. *Geological Magazine, 126*(3), 215–247.

Harris, N. (1981). The application of spinel-bearing metapelites to P/T determinations: An example from South India. *Contributions to Mineralogy and Petrology, 76*, 229–233.

Henry, D.-J., & Guidotti, C.-V. (2002). Titanium in biotite from metapelitic rocks: Temperature effects, crystal-chemical controls, and petrologic applications. *American Mineralogist, 87*, 375–382.

Herron, M.-M. (1988). Geochemical classification of terrigeneous sands and shales from core or log data. *Journal of Sedimentary Petrology, 58*, 820–829.

Holland, T.-J.-B., & Powell, R. (1998). An internally consistent thermodynamic data set for phases of petrological interest. *Journal of Metamorphic Geology*, *16*, 309–343.

Holland, T.-J.-B., & Powell, R. (2003). Activity-composition relations for phases in petrological calculations: An asymmetric multicomponent formulation. *Contributions to Mineralogy and Petrology, 145*, 492–501.

Hollis, J.-A., Harley, S.-L., White, R.-W., & Clarke, G.-L. (2006). Preservation of evidence for prograde metamorphism in ultrahigh-temperature, high-pressure kyanite-bearing granulites, South Harris, Scotland. *Journal of Metamorphic Geology, 24*, 263–279.

Hou, W.-R., Nie, F.-J., Hu, J.-M., Liu, Y.-F., Xiao, W., Liu, Y., & Zhang, K. (2011). Geochronology and geochemistry of Shadegai granites in Wulashan area, Inner Mongolia and its geological significance. *Journal of Jilin University (Earth Science Edition), 41*(6), 1914–1927. (in Chinese with English abstract).

Jahn, B.-M., Liu, D.-Y., Wan, Y.-S., Song, B., & Wu, J.-S. (2008). Archean crustal evolution of the Jiaodong Peninsula, China, as revealed by zircon SHRIMP geochronology, elemental and Nd-isotope geochemistry. *American Journal of Science, 308*(3), 232–269.

Ji, Z.-Y. (1993). New data on isotope age of the Proterozoic metamorphic rocks from northern Jiaodong and its geological significance. *Shandong Geology, 9*(1), 43–51. (in Chinese).

Jiao, S.-J., & Guo, J.-H. (2011). Application of the two-feldspar geothermometer to ultrahigh-temperature (UHT) rocks in the Khondalite belt, North China craton and its implications. *American Mineralogist, 96*, 250–260.

Jiao, S.-J., Guo, J.-H., Harley, S.-L., & Peng, P. (2013a). Geochronology and trace element geochemistry of zircon, monazite and garnet from the garnetite and/or associated other high-grade rocks: Implications for Palaeoproterozoic tectonothermal evolution of the Khondalite Belt, North China Craton. *Precambrian Research, 237*, 78–100.

Jiao, S.-J., Guo, J.-H., Harley, S.-L., & Windley, B.-F. (2013b). New constraints from garnetite on the P-T path of the Khondalite belt: Implications for the tectonic evolution of the North China Craton. *Journal of Petrology, 54*(9), 1725–1758.

Jiao, S.-J., Guo, J.-H., Mao, Q., & Zhao, R.-F. (2011). Application of Zr-in-rutile thermometry: a case study from ultrahigh-temperature

granulites of the Khondalite belt, North China Craton. *Contributions to Mineralogy and Petrology, 162*(2), 379–393.

Jin, W. (1989). Geological evolution and metamorphic dynamics of early Precambrian basement rocks along the northern boundary (central section) of the North China Craton. Unpublished Ph.D. thesis. Changchun College of Geology, Changchun (in Chinese with English abstract).

Jin, W., & Li, S.-X. (1994). The lithological association and geological features of early Proterozoic orogenic belt in Daqingshan, NeiMongol. In X.-L. Qian & R.-M. Wang (Eds.), *Geological evolution of granulite facies zone in northern North China* (pp. 32–41). Beijing: Sesimological Press. (in Chinese with English abstract).

Jin, W., & Li, S.-X. (1996). PTt path and crustal thermodynamic model of late Archean-Early Proterozoic high-grade metamorphic terrain in North China. *Acta Petrologica Sinica, 12*(2), 42–55. (in Chinese with English abstract).

Jin, W., Li, S.-X., & Liu, X.-S. (1991). A study on characteristics of early precambrian high-grade metamorphic rock series and their metamorphic dynamics. *Acta Petrologica Sinica, 11*(4), 27–35. (in Chinese with English abstract).

Korhonen, F.-J., Saito, S., Brown, M., & Siddoway, C.-S. (2010). Modeling multiple melt loss events in the evolution of an active continental margin. *Lithos, 116*, 230–248.

Le Breton, N., & Thompson, A.-B. (1988). Fluid-absent (dehydration) melting of biotite in metapelites in the early stages of crustal anatexis. *Contributions to Mineralogy and Petrology, 99*, 226–237.

Li, X.-H., Chen, F.-K., Guo, J.-H., Li, Q.-L., Xie, L.-W., & Siebel, W.-F. (2007). South China provenance of the lower-grade Penglai Group north of the Sulu UHP orogenic belt, eastern China: Evidence from detrital zircon ages and Nd-Hf isotopic composition. *Geochemical Journal, 41*(1), 29–45.

Li, J.-H., Qian, X.-L., & Liu, S.-W. (1999). Geochemistry of the Khondalite series in the central North China Craton and implications for the crustal cratonization. *Science in China (Series D), 29*, 193–203.

Li, S.-X., Xu, X.-C., Liu, X.-S., & Sun, Y.-D. (1994). Early precambrian geology of Wulashan region, Inner Mongolia. Geological Publishing House, Beijing (in Chinese with English abstract).

Li, X.-P., Yang, Z.-Y., Zhao, G.-C., Grapes, R., & Guo, J.-H. (2011). Geochronology of khondalite-series rocks of the Jining Complex: Confirmation of depositional age and tectonometamorphic evolution of the North China craton. *International Geology Review, 53*, 1194–1211.

Li, S.-Z., & Zhao, G.-C. (2007). SHRIMP U-Pb zircon geochronology of the Liaoji granitoids: constraints on the evolution of the Paleoproterozoic Jiao-Liao-Ji belt in the Eastern Block of the North China Craton. *Precambrian Research, 158*, 1–16.

Liu, X.-S. (1994). Characteristics of basement reworked complex and implication for Daqingshan orogenic belt. *Acta Pertologica Sinica, 10*(4), 413–426. (in Chinese with English abstract).

Liu, F.-L. (1995). Metamorphic minerals and fluid evolution and tectonic environment of granulite facies high-grade terrain in the Huai'an-Datong region. Unpublished Ph.D. thesis. Changchun College of Geology, Changchun (in Chinese with English abstract).

Liu, X.-S. (1996). Progressive metamorphic genesis of Archean granulites in Central Nei Mongol. *Acta Petrologica Sinica, 12*(2), 121–132. (in Chinese with English abstract).

Liu, S.-J., Dong, C.-Y., Xu, Z.-Y., Santosh, M., Ma, M.-Z., Xie, H.-Q., et al. (2013a). Palaeoproterozoic episodic magmatism and high-grade metamorphism in the North China Craton: evidence from SHRIMP zircon dating of magmatic suites in the Daqingshan area. *Geological Journal, 48*(5), 429–455.

Liu, X.-S., Jin, W., & Li, S.-X. (1993a). Low-pressure metamorphism of granulite facies in an Early Proterozoic orogenic event in Central Inner Mongolia. *Acta Geologica Sinica, 6*(1), 63–77.

Liu, X.-S., Jin, W., Li, S.-X., & Xu, X.-C. (1993b). Two types of Precambrian high-grade metamorphism, Inner Mongolia, China. *Journal of metamorphic Geology, 11*(4), 499–510.

Liu, J.-H., Liu, F.-L., Ding, Z.-J., Liu, P.-H., Guo, C.-L., & Wang, F. (2014a). Geochronology, petrogenesis and tectonic implications of Paleoproterozoic granitoid rocks in the Jiaobei Terrane, North China Craton. *Precambrian Research, 255*, 685–698.

Liu, J.-H., Liu, F.-L., Ding, Z.-J., Liu, C.-H., Yang, H., Liu, P.-H., et al. (2013b). The growth, reworking and metamorphism of early Precambrian crust in the Jiaobei terrane, the North China Craton: Constraints from U-Th-Pb and Lu-Hf isotopic systematics, and REE concentrations of zircon from Archean granitoid gneisses. *Precambrian Research, 224*, 287–303.

Liu, P.-H., Liu, F.-L., Liu, C.-H., Liu, J.-H., Wang, F., Xiao, L.-L., et al. (2014b). Multiple mafic magmatic and high-grade metamorphic events revealed by zircons from meta-mafic rocks in the Daqingshan-Wulashan Complex of the Khondalite Belt, North China Craton. *Precambrian Research, 246*, 334–357.

Liu, J.-H., Liu, F.-L., Liu, P.-H., Wang, F., & Ding, Z.-J. (2011a). Polyphase magmatic and metamorphic events from early Precambriam metamorphic basement in Jiaobei area: Evidences from the zircon U-Pb dating of TTG and granitic gneisses. *Acta Petrologica Sinica, 27*(4), 943–960.

Liu, P.-H., Liu, F.-L., Liu, C.-H., Wang, F., Liu, J.-H., Yang, H., et al. (2013c). Petrogenesis, P-T–t path, and tectonic significance of high-pressure mafic granulites from the Jiaobei terrane, North China Craton. *Precambrian Research, 233*, 237–258.

Liu, P.-H., Liu, F.-L., Wang, F., & Liu, J.-H. (2010). Genetic mineralogy and metamorphic evolution of mafic high-Pressure (HP) granulites from the Shandong Peninsula. *China. Acta Petrologica Sinica, 26*(7), 2039–2056. (in Chinese with English abstract).

Liu, P.-H., Liu, F.-L., Wang, F., & Liu, J.-H. (2011b). U-Pb dating of zircons from Al-rich paragneisses of Jinshan Group in Shandong peninsula and its geological significance. *Acta Petrologica Et Mineralogica, 30*(5), 829–843. (in Chinese with English abstract).

Liu, F.-L., Liu, P.-H., Wang, F., Liu, J.-H., Meng, E., Cai, J., & Shi, J.-R. (2014c). U-Pb dating of zircons from granitic leucosomes in migmatites of the Jiaobei Terrane, southwestern Jiao-Liao-Ji Belt, North China Craton: constraints on the timing and nature of partial melting. *Precambrian Research, 245*, 80–99.

Liu, P.-H., Liu, F.-L., Wang, F., Liu, C.-H., Yang, H., Liu, J.-H., et al. (2015). *P-T-t* paths of the multiple metamorphic events of the Jiaobei terrane in the southeastern segment of the Jiao-Liao-Ji Belt (JLJB), in the North China craton: Implication for formation and evolution of the JLJB. *Acta Petrologica Sinica, 31*(10), 2889–2941.

Liu, P.-H., Liu, F.-L., Yang, H., Wang, F., & Liu, J.-H. (2012a). Protolith ages and timing of peak and retrograde metamorphism of the high pressure granulites in the Shandong Peninsula, eastern North China Craton. *Geoscience Frontiers, 3*(6), 923–943.

Liu, S.-J., Tsunogae, T., Li, W.-S., Shimizu, H., Santosh, M., Wan, Y.-S., & Li, J.-H. (2012b). Paleoproterozoic granulites from Heling'er: Implications for regional ultrahigh-temperature metamorphism in the North China Craton. *Lithos, 148*, 54–70.

Liu, W.-J., Zhai, M.-G., & Li, Y.-G. (1998). Metamorphism of the high-pressure basic granulite in Laixi, Eastern Shandong. *China. Acta Petrologica Sinica, 14*(4), 449–459. (in Chinese with English abstract).

Lu, L.-Z., & Jin, S.-Q. (1993). P–T–t paths and tectonic history of an early Precambrian granulite facies terrane, Jining district, southeastern Inner Mongolia China. *Journal of Metamorphic Geology, 11*(4), 483–498.

Lu, L.-Z., Jin, S.-Q., Xu, X.-C., & Liu, F.-L. (1992). *Petrogenesis and mineralization of Khondalite Series in southeastern Inner Mongolia*. Changchun (in Chinese with English abstract): Jilin Science and Technology Press.

Lu, X.-P., Wu, F.-Y., Guo, J.-H., Wilde, S.-A., Yang, J.-H., Liu, X.-M., & Zhang, X.-O. (2006). Zircon U-Pb geochronological constraints on the Paleoproterozoic crustal evolution of the Eastern block in the North China Craton. *Precambrian Research, 146*(3–4), 138–164.

Lu, L.-Z., Xu, X.-C., & Liu, F, -L. (1996). Early precambrian khondalite series in North China. Changchun Publishing House, Changchun (in Chinese with English abstract).

Luo, Y., Sun, M., Zhao, G.-C., Li, S.-Z., Ayers, J.-C., Xia, X.-P., & Zhang, J.-H. (2008). A comparison of U-Pb and Hf isotopic compositions of detrital zircons from the North and South Liaohe Groups: constraints on the evolution of the Jiao-Liao-Ji Belt, North China Craton. *Precambrian Research, 163*, 279–306.

Luo, Y., Sun, M., Zhao, G.-C., Li, S.-Z., Xu, P., Ye, K., & Xia, X.-P. (2004). LA-ICP-MS U-Pb zircon ages of the Liaohe Group in the Eastern Block of the North China Craton: constraints on the evolution of the Jiao-Liao-Ji Belt. *Precambrian Research, 134*, 349–371.

Ma, M.-Z., Wan, Y.-S., Santosh, M., Xu, Z.-Y., Xie, H.-Q., Dong, C.-Y., et al. (2012a). Decoding multiple tectonothermal events in zircons from single rock samples: SHRIMP zircon U-Pb data from the late Neoarchean rocks of Daqingshan. *North China Craton. Gondwana Research, 22*(3–4), 810–827.

Ma, M.-Z., Wan, Y.-S., Xu, Z.-Y., Liu, S.-J., Xie, H.-Q., Dong, C.-Y., & Liu, D.-Y. (2012b). Late Paleoproterozoic K-feldspar pegmatite veins in Daqingshan area, North China Craton: SHRIMP age and Hf composition of zircons. *Geological Bulletin of China, 31*(6), 825–833. (in Chinese with English abstract).

Maynard, J.-B., Valloni, R., & Yu, H.-S. (1982). Composition of modern deep-sea sands from arc-related basins. *Geological Society, London, Special Publications, 10*(1), 551–561.

McLennan, S.-M., & Taylor, S.-R. (1991). Sedimentary rocks and crustal evolution: tectonic setting and secular trends. *Journal of Geology, 99*, 1–21.

McLennan, S.-M., Taylor, S.-R., McCulloch, M.-T., & Maynard, J.-B. (1990). Geochemical and Nd–Sr isotopic composition of deep-sea turbidites: crustal evolution and plate tectonic associations. *Geochimica et Cosmochimica Acta, 43*, 375–388.

Miao, L.-C., Luo, Z.-K., Guan, K., & Huang, J.-Z. (1998). The implications of the SHRIMP U-Pb age in zircon to the petrogenesis of the Linglong granite. *East Shandong Province. Acta Petrologica Sinica, 14*(2), 198–206. (in Chinese with English abstract).

Miao, L.-C., Qiu, Y.-M., Guan, K., McNaughton, N., Qiu, Y.-S., Luo, Z.-K., & Groves, D. (2001). A chronological study of SHRIMP U-Pb of zircon from the Dahuabei intrusion in the Wulashan area. *Inner Mongolia. Geological Review, 47*(2), 169–174. (in Chinese with English abstract).

Miyashiro, A. (1961). Evolution of Metamorphic Belts. *Journal of Petrology, 2*(3), 277–311.

Narayanaswami, S. (1975). Proposal for charnockite-khondalite system in the Archaean shield of Peninsular India. In "precambrian geology of peninsular India". *Geology. Survey India Miscellneous Publ., 23*, 1–16.

O'Brien, P.-J., & Rötzler, J. (2003). High-pressure granulites: formation, recovery of peak conditions and implications for tectonics. *Journal of Metamorphic Geology, 21*(1), 3–20.

Patiño Douce, A.-E., & Johnston, A.-D. (1991). Phase equilibria and melt productivity in the pelitic system: Implications for the origin of peraluminous granitoids and aluminous granulites. *Contributions to Mineralogy and Petrology, 107*, 202–218.

Philpotts, A.-R. (1989). Rock-forming minerals and their optical properties. In *Petrography of Igneous and Metamorphic Rocks* (pp. 43–46).

Powell, R., & Holland, T.-J.-B. (1988). An internally consistent dataset with uncertainties and correlations, pp 3 applications to geobarometry, worked examples and a computer program. *Journal of Metamorphic Geology, 6*, 173–204.

Qian, X.-L., & Li, J.-H. (1999). The discovery of NeoArchaean unconformity and its implication for continental cratonization of the North China Craton. *Sciences in China* (*Series D*), *42*, 401–407.

Roser, B.-P., & Korsch, R.-J. (1986). Determination of tectonic setting of sandstone-mudstone suites using SiO_2 content and K_2O/Na_2O ratio. *Journal of Geology, 94*, 635–650.

Salje, E. (1986). Heat capacities and entropies of andalusite and sillimanite; the influence of fibrolitization on the phase diagram of the Al_2SiO_5 polymorphs. *American Mineralogist, 71*(11–12), 1366–1371.

Santosh, M., Sajeev, K., Li, J.-H., Liu, S.-J., & Itaya, T. (2009). Counterclockwise exhumation of a hot orogen: The paleoproterozoic ultrahigh-temperature granulites in the North China Craton. *Lithos, 110*, 140–152.

Santosh, M., Tsunogae, T., Li, J.-H., & Liu, S.-J. (2007). Discovery of sapphirine-bearing Mg-Al granulites in the North China Craton: Implications for Paleoproterozoic ultrahigh temperature metamorphism. *Gondwana Research, 11*, 263–285.

Schliestedt, M., & Johannes, W. (1984). Melting and subsolidus reactions in the system K_2O-CaO-Al_2O_3-SiO_2-H_2O: Corrections and additional experimental data. *Contributions to Mineralogy and Petrology, 88*, 403–405.

Shackleton, R.-M. (1976). Shallow and deep-level exposures of the Archean crust in India and Africa. In B. F. Windley (Ed.), *The Early history of the earth* (pp. 317–321). London: Wiley.

Simonen, A. (1953). Stratigraphy and sedimentation of the Svecofennidie, early Archean supracrustal rocks in southwestern Finland. *Bulletin of the Geological Society of Finland, 160*, 1–64.

Spear, F.-S., Hickmott, D.-D., & Selverstone, J. (1990). Metamorphic consequences of thrust emplacement, Fall Mountain, New Hampshire. *Geological Society of America Bulletin, 102*, 1344–1360.

Spear, F.-S., Kohn, M.-J., & Cheney, J.-T. (1999). *P-T* paths from anatectic pelites. *Contributions to Mineralogy and Petrology, 134*, 17–32.

Spear, F.-S., Kohn, M.-J., & Paetzold, S. (1995). Petrology of the regional sillimanite zone, west-central New Hampshire, U.S.A., with implications for the development of inverted isograds. *American Mineralogist, 80*, 361–376.

Sun, S.-S., & McDonough, W.-F. (1989). Chemical and isotopic systematics of oceanic basalts: implications for mantle composition and processes. *Geological Society, London, Special Publications, 42*, 313–345.

Tam, P.-Y., Zhao, G.-C., Liu, F.-L., Zhou, X.-W., Sun, M., & Li, S.-Z. (2011). Timing of metamorphism in the Paleoproterozoic Jiao-Liao-Ji Belt: New SHRIMP U-Pb zircon dating of granulites, gneisses and marbles of the Jiaobei massif in the North China Craton. *Gondwana Research, 19*(1), 150–162.

Tam, P.-Y., Zhao, G.-C., Sun, M., Li, S.-Z., Iizuka, Y.-Y., Ma, G.-S.-K., et al. (2012a). Metamorphic PT path and tectonic implications of medium-pressure pelitic granulites from the Jiaobei massif in the Jiao-Liao-Ji Belt, North China Craton. *Precambrian Research, 220–221*, 177–191.

Tam, P.-Y., Zhao, G.-C., Sun, M., Li, S.-Z., Wu, M.-L., & Yin, C.-Q. (2012b). Petrology and metamorphic PT path of high-pressure mafic granulites from the Jiaobei massif in the Jiao-Liao-Ji Belt, North China Craton. *Lithos, 155*, 94–205.

Tam, P.-Y., Zhao, G.-C., Zhou, X.-W., Sun, M., Guo, J.-H., Li, S.-Z., et al. (2012c). Metamorphic P-T path and implications of high-pressure pelitic granulites from the Jiaobei massif in the Jiao-Liao-Ji Belt. *North China Craton. Gondwana Research, 22*(1), 104–117.

Tang, J., Zheng, Y.-F., Wu, Y.-B., Gong, B., & Liu, X.-M. (2007). Geochronology and geochemistry of metamorphic rocks in the Jiaobei terrane: Constraints on its tectonic affinity in the Sulu orogen. *Precambrian Research, 152*(1–2), 48–82.

Taylor, S.-R., & McLennan, S.-M. (1985). *The continental crust: its composition and evolution* (p. 312). Oxford, UK: Blackwell Scientific Publications.

Thompson, A.-B., & England, P.-C. (1984). Pressure–temperature–time paths of regional metamorphism II. Their inference and interpretation using mineral assemblages in metamorphic rocks. *Journal of Petrology, 25*, 929–955.

Tsunogae, T., Liu, S.-J., Santosh, M., Shimizu, H., & Li, J.-H. (2011). Ultrahigh-temperature metamorphism in Daqingshan, Inner Mongolia Suture Zone. *North China Craton. Gondwana Research, 20*(1), 36–47.

Vielzeuf, D., & Montel, J.-M. (1994). Partial melting of metagreywackes. Part I. Fluid-absent experiments and phase relationships. *Contributions to Mineralogy and Petrology, 117*, 375–393.

Walker, T.-L. (1902). The geology of Kalahandi State, Central Province. *Memoirs of the Geological Survey of India, 33*(3), 1–23.

Wan, Y.-S., Geng, Y.-S., Liu, F.-L., Shen, Q.-H., Liu, D.-Y., & Song, B. (2000a). Age and composition of the khondalite series of the North China Craton and its adjacent area. *Prog. Precambrian Res., 23*, 221–235. (in Chinese with English abstract).

Wan, Y.-S., Geng, Y.-S., Shen, Q.-H., & Zhang, R.-X. (2000b). Khondalite series—geochronology and geochemistry of the Jiehekou Group in Lüliang area. *Acta Petrologica Sinica, 16*, 49–58. (in Chinese with English abstract).

Wan, Y.-S., Liu, D.-Y., Dong, C.-Y., Liu, S.-J., Wang, S.-J., & Yang, E.-X. (2011). U-Th-Pb behavior of zircons under high-grade metamorphic conditions: A case study of zircon dating of meta-diorite near Qixia, eastern Shandong. *Geoscience Frontiers, 2*(2), 37–146.

Wan, Y.-S., Liu, D.-Y., Dong, C.-Y., Xu, Z.-Y., Wang, Z.-J., Wilde, S.-A., et al. (2009). The Precambrian Khondalite Belt in the Daqingshan area, North China Craton: evidence for multiple metamorphic events in the palaeoproterozoic era. *Geological Society, London, Special Publications, 323*(1), 73–97.

Wan, Y.-S., Song, B., Liu, D.-Y., Wilde, S.-A., Wu, J.-S., Shi, Y.-R., et al. (2006). SHRIMP U-Pb zircon geochronology of palaeoproterozoic metasedimentary rocks in the North China craton: Evidence for a major late palaeoproterozoic tectonothermal event. *Precambrian Research, 149*(3–4), 249–271.

Wan, Y.-S., Xie, H.-Q., Yang, H., Wang, Z.-J., Liu, D.-L., Kröner, A., et al. (2013a). Is the Ordos Block Archean or Paleoproterozoic in age? Implications for the Precambrian evolution of the North China Craton. *American Journal of Science, 313*, 683–711.

Wan, Y.-S., Xu, Z.-Y., Dong, C.-Y., Nutman, A., Ma, M.-Z., Xie, H.-Q., et al. (2013b). Episodic Paleoproterozoic (~2.45, ~1.95 and ~1.85 Ga) mafic magmatism and associated high temperature metamorphism in the Daqingshan area, North China Craton: SHRIMP zircon U-Pb dating and whole-rock geochemistry. *Precambrian Research, 224*, 71–93.

Wang, P.-C. (1995). New knowledge on the research about the relationships between the Fenzishan Group and Jingshan Group. *Journal of Stratigraphy*, *19*(1), 77–78 (in Chinese)

Wang, R.-M., He, G.-P., Chen, Z.-Z., Zhen, S.-Y., & Geng, Y.-S. (1987). *Graphic discrimination method of metamorphic protoliths*. Geological Publishing House, Beijing (in Chinese).

Wang, F., Liu, F.-L., Liu, P.-H., & Liu, J.-H. (2010). Metamorphic evolution of early Precambrian khondalite series in North Shangdong Province. *Acta Petrologica Sinica, 26*(7), 2057–2072.

Wang, L.-G., Qiu, Y.-M., McNaughton, N.-J., Groves, D.-I., Luo, Z.-K., Huang, J.-Z., et al. (1998). Constraints on crustal evolution and gold metallogeny in the Northwestern Jiaodong Peninsula, China, from SHRIMP U-Pb zircon studies of granitoids. *Ore Geology Reviews, 13*(1), 275–291.

Wei, C.-J., Clarke, G., Tian, W., & Qiu, L. (2007). Transition of metamorphic series from the Kyanite- to andalusite-types in the Altai orogen, Xinjiang, China: Evidence from petrography and calculated KMnFMASH and KFMASH phase relations. *Lithos, 96*, 353–374.

Wei, C.-J., Powell, R., & Clarke, G.-L. (2004). Calculated phase equilibria for low- and medium-pressure metapelites in the KFMASH and KMnFMASH systems. *Journal of Metamorphic Geology, 22*, 495–508.

Wei, C.-J., Powell, R., & Zhang, L.-F. (2003). Eclogites from the south Tianshan, NW China: petrological characteristic and calculated mineral equilibria in the Na_2O-CaO-FeO-MgO-Al_2O_3-SiO_2-H_2O system. *Journal of Metamorphic Geology, 21*, 163–179.

Wei, C.-J., Qian, J.-H., & Zhou, X.-W. (2014). Paleoproterozoic crustal evolution of the Hengshan-Wutai-Fuping redion, North China craton. *Geoscience Frontiers, 5*(4), 265–485.

White, R.-W., Powell, R., & Clarke, G.-L. (2002). The interpretation of reaction textures in Fe-rich metapelitic granulites of the Musgrave Block, central Australia: Constraints from mineral equilibria calculations in the system K_2O-FeO-MgO-Al_2O_3-SiO_2-H_2O-TiO_2-Fe_2O_3. *Journal of Metamorphic Geology, 20*, 41–55.

White, R.-W., Powell, R., & Clarke, G.-L. (2003). Prograde metamorphic assemblage evolution during partial melting of metasedimentary rocks at low pressures: Migmatites from Mt Stafford, Central Australia. *Journal of Petrology, 44*, 1937–1960.

White, R.-W., Powell, R., & Holland, T.-J.-B. (2001). Calculation of partial melting equilibria in the system Na_2O-CaO-K_2O-FeO-MgO-Al_2O_3-SiO_2-H_2O (NCKFMASH). *Journal of Metamorphic Geology, 19*, 139–153.

White, R.-W., Powell, R., & Holland, T.-J.-B. (2007). Progress relating to calculation of partial melting equilibria for metapelites. *Journal of Metamorphic Geology, 25*, 511–527.

White, R.-W., Powell, R., Holland, T.-J.-B., & Worley, B.-A. (2000). The effect of TiO_2 and Fe_2O_3 on metapelitic assemblages at greenschist and amphibolite facies conditions: Mineral equilibria calculations in the system K_2O-FeO-MgO-Al_2O_3-SiO_2-H_2O-TiO_2-Fe_2O_3. *Journal of Metamorphic Geology, 18*, 497–511.

Whitney, D. L., & Evans, B. W. (2010). Abbreviations for names of rock-forming minerals. *American Mineralogist, 95*(1), 185–187.

Wu, C.-H., Sun, M., Li, H.-M., Zhao, G.-C., & Xia, X.-P. (2006). LA-ICP-MS U-Pb zircon ages of the khondalites from the Wulashan and Jining high-grade terrain in northern margin of the North China Craton: constraints on sedimentary age of khondalite. *Acta Petrologica Sinica, 22*(11), 2639–2654.

Xia, X.-P., Sun, M., Zhao, G.-C., & Luo, Y. (2006a). LA–ICP–MS U–Pb geochronology of detrital zircons from the Jining Complex, North China Craton and its tectonic significance. *Precambrian Research, 144*(3), 199–212.

Xia, X.-P., Sun, M., Zhao, G.-C., Wu, F.-Y., Xu, P., Zhang, J.-P., et al. (2006b). U–Pb and Hf isotopic study of detrital zircons from the Wulashan khondalites: Constraints on the evolution of the Ordos Terrane, Western Block of the North China Craton. *Earth and Planetary Science Letters, 241*(3), 581–593.

Xie, S.-Y., Qie, H.-Q., Wang, S.-J., Kröner, A., Liu, S.-J., Zhou, H.-Y., et al. (2014). Ca. 2.9 Ga granitoid magmatism in eastern Shandong, North China craton: Zircon dating, Hf-in-zircon isotopic analysis and whole-rock geochemistry. *Precambrian Research, 255*, 534–562.

Xu, Z.-Y., Liu, Z.-H., & Yang, Z.-S. (2003). The discoverty of Zaoergou angular uncomformity and estalishment of Meidaizhao Group-complex in Daqing Mountains, Inner Mongolia-Paleaoproterzoic Low-grade metamorphic strata on the Khondalite series. *Geologica Bulletin of China, 22*(7), 480–486. (in Chinese with English abstract).

Xu, Z.-Y., Liu, Z.-H., & Yang, Z.-S. (2005a). Structures of early metamorphic strata in the khondalite series in the Daqingshan-Wulashan area. *Inner Mongolia: Jouranl of stratigraphy, 29*(S1), 423–432. (in Chinese with English abstract).

Xu, Z.-Q., Qi, X.-X., Liu, F.-L., Yang, J.-S., Zeng, L.-S., & Wu, C.-L. (2005b). A new Caledonian khondalites in West Kunlun, China: age constraints and tectonic significance. *International Geology Review, 47*, 986–998.

Yang, K.-F., Fan, H.-R., Santosh, M., Hu, F.-F., Wilde, S.-A., Lan, T.-G., et al. (2012). Reactivation of the Archean lower crust: Implications for zircon geochronology, elemental and Sr-Nd-Hf isotopic geochemistry of late Mesozoic granitoids from northwestern Jiaodong Terrane, the North China Craton. *Lithos, 146–147*, 12–127.

Yang, Z.-S., Xu, Z.-Y., & Liu, Z.-H. (2000). Khondalite event and Archean crust structure evolvement. *Progress in Precambrian Research, 23*(4), 206–212. (in Chinese with English abstract).

Yang, Z.-S., Xu, Z.-Y., Liu, Z.-H., & Wang, S.-L. (2006). Major progress in Early Precambrian research in the Daqingshan–Wulashan region, central Inner Mongolia, China, and some suggestions for stratigraphic work in high-grade metamorphic areas. *Geological Bulletin of China, 25*(4), 427–433 (in Chinese with English abstract)

Yang, Z.-S., Xu, Z.-Y., Liu, Z.-H., & Gu, X.-D. (2003). Consideration and practice of construction of litho stratigraphic systems in high-grade metamorphic terrains-acase study in the Daqingshan-Wulashan area. *Geology in China, 30*(4), 343–351. (in Chinese with English abstract).

Yin, C.-Q. (2010). *Metamorphism of the Qianlishan-Helanshan Complex and its implications for tectonic evolution of the Khondalite Belt in the Western Block, North China Craton*. Unpublished Ph.D. thesis. The University of Hong Kong, Hong Kong.

Yin, A., & Nie, S. (1996). Phanerozoic palinspastic reconstruction of China and its neighboring regions. In A. Yin & T. M. Harrison (Eds.), *The Tectonic Evolution of Asia* (pp. 285–442). New York: Cambridge University Press.

Yin, C.-Q., Zhao, G.-C., Guo, J.-H., Sun, M., Xia, X.-P., Zhou, X.-W., & Liu, C.-H. (2011). U-Pb and Hf isotopic study of zircons of the Helanshan complex: Constrains on the evolution of the Khondalite Belt in the Western Block of the North China Craton. *Lithos, 122* (3–4), 25–38.

Yin, C.-Q., Zhao, G.-C., Sun, M., Xia, X.-P., Wei, C.-J., Zhou, X.-W., & Leung, W.-H. (2009). LA-ICP-MS U-Pb zircon ages of the Qianlishan complex: Constrains on the evolution of the Khondalite Belt in the western block of the North China craton. *Precambrian Research, 174*(1–2), 78–94.

Yin, C.-Q., Zhao, G.-C., Wei, C.-J., Sun, M., Guo, J.-H., & Zhou, X.-W. (2014). Metamorphism and partial melting of high-pressure pelitic granulites from the Qianlishan complex: Constraints on the tectonic evolution of the Khondalite Belt in the North China craton. *Precambrian Research, 242*, 172–186.

Yu, H.-F. (1994). High temperature deformational-metamorphic zone and Early Proterozoic inner continental orogeny. Unpublished Ph. D. thesis. Changchun College of Geology, Changchun (in Chinese with English abstract).

Zeng, L.-S., Liang, F.-H., Xu, Z.-Q., & Qi, X.-X. (2008). Metapelites in the Himayan oregenic belt and their protoliths. *Acta Pertologica Sinica, 24*, 1517–1527. (in Chinese with English abstract).

Zhang, Y.-M. (2012). Metallogenesis, Ore-controlling factors and prospecting direction of the Liubagou-Hadamengou gold deposit, Inner Mongolia. Unpublished Ph.D. thesis. China University of Geosciences (Beijing) (in Chinese with English abstract).

Zhang, X.-O., Cawood, P.-A., Wilde, S.-A., Liu, R.-Q., Song, H.-L., Li, W., & Snee, L.-W. (2003). Geology and timing of mineralization at the Cangshang gold deposit, north-western Jiaodong Peninsula, China. *Mineralium deposita, 38*(2), 141–153.

Zhang, Q.-S, Yang, S.-Z., & Liu, L.-D. (1988). *Early crust and ore deposits in the Eastern Liaoning Peninsula* (pp. 218–322). Beijing: Geological Publishing House (in Chinese).

Zhao, G.-C., Sun, M., Wilde, S.-A., & Li, S.-Z. (2005). Late archean to paleoproterozoic evolution of the North China craton: Key issues revisited. *Precambrian Research, 136*, 177–202.

Zhao, L., Tiesheng Li, T.-S., Peng, P., Guo, J.-H., Wang, W., Wang, H.-Z., et al. (2014). Anatomy of zircon growth in high pressure granulites: SIMS U–Pb geochronology and Lu–Hf isotopes from the Jiaobei Terrane, eastern North China Craton. *Gondwana Research*, doi: 10.1016/j.gr.2014.10.009.

Zhao, G.-C., Wilde, S.-A., Cawood, P.-A., & Lu, L.-Z. (1999). Tectonothermal history of the basement rocks in the western zone of the North China craton and its tectonic implications. *Tectonophysics, 310*(1), 37–53.

Zhou, X.-W., & Geng, Y.-S. (2009). Metamorphic age of the khondalite series in the Helanshan region: Constraints on the evolution of the western block in the North China Craton. *Acta Pertologica Sinica, 25*(8), 1843–1852.

Zhou, X.-W., Wei, C.-J., Geng, Y.-S., & Zhang, L.-F. (2004). Discovery and implications of the high-pressure pelitic granulites from the Jiaobei massif. *Chinese Science Bulletin, 49*(14), 1942–1948.

Zhou, J.-B., Wilde, S.-A., Zhao, G.-C., Zheng, C.-Q., Jin, W., Zhang, X.-Z., & Cheng, H. (2008a). SHRIMP U-Pb zircon dating of the Neoproterozoic Penglai Group and Archean gneisses from the Jiaobei Terrane, North China, and their tectonic implications. *Precambrian Research, 160*(3–4), 323–340.

Zhou, X.-W., Zhao, G.-C., & Geng, Y.-S. (2010). Helanshan high pressure pelitic granulite: Petrologic evidence for collision event in the western block of the North China Craton. *Acta Petrologica Sinica, 26*, 2113–2121.

Zhou, X.-W., Zhao, G.-C., Wei, C.-J., Geng, Y.-S., & Sun, M. (2008b). EPMA U-Th-Pb monazite and SHRIMP U-Pb zircon geochronology of high-pressure pelitic granulites in the Jiaobei massif of the North China Craton. *American Journal of Science, 308*(3), 328–350.

9 Paleoproterozoic Copper System in the Zhongtiaoshan Region, Southern Margin of the North China Craton: Ore Geology, Fluid Inclusion, and Isotopic Investigation

Yuhang Jiang, Yan Zhao, and Hecai Niu

Abstract

The Zhongtiaoshan region is located in the south segment of the North China Craton and hosts a number of significant Paleoproterozoic copper deposits with a total metal endowment of approximately 400 Mt of metal Cu. Among these Cu deposits, the Tongkuangyu and Hujiayu Cu deposits constitute approximately 80 % of the total reserves. The Tongkuangyu Cu deposit, the largest copper deposit in the Zhongtiaoshan region, is hosted in quartz-monzonite porphyry ($\sim$2.1 Ga) and its wall rocks of the meta-quartz crystal tuffs of the Jiangxian Group. In contrast, the Hujiayu Cu deposit is hosted within reduced marine sedimentary sequence of the mid-Paleoproterozoic Zhongtiao Group. For decades, as these ancient deposits underwent subsequent metamorphism, the metallogenesis models of the two deposits are highly controversial. More importantly, the nature and origins of the ore-forming fluids and the mechanism of multistage fluid mineralization are still unclear. Summarizing previous researches, we systematically investigate the ore geology, fluid inclusions, and stable isotopes of the typical Tongkuangyu and Hujiayu Cu deposits. The main conclusions are as follows: (1) The oxygen fugacity of hydrothermal system of the Tongkuangyu Cu deposit fluctuates near the Magnetite–Hematite (MH) buffer line, corresponding to the redox state of typical oxidized porphyry copper deposits. The main ore-forming fluids of this deposit consist of magmatic–hydrothermal fluids with middle-high temperature and high salinity. Orebody spatial structure, mineralization types, and alteration features support a porphyry copper deposit model. The formation age of the quartz-monzonite porphyry is consistent with Cu mineralization. We propose that the Tongkuangyu Cu deposit is a porphyry copper deposit formed in an arc-related extension environment. (2) Fluid inclusion studies on the Hujiayu Cu deposit show that the ore-forming fluids of the early mineralization stage are mainly characterized by high salinity and moderate temperature basinal brines. The ore-forming fluids of the late mineralization stage are characterized by CO_2-rich and high salinity and high temperature metamorphic hydrothermal solutions, which obviously experience phase separation. Early stage mineralization of the Hujiayu Cu deposit may occur via interaction of oxidized Cu-bearing brines from the underlying red beds [formed after the Great Oxidation Event (GOE)] with the upper reducing carbonaceous shales. In contrast, late stage mineralization at the Hujiayu deposit is likely related to CO_2 escaping from metamorphic hydrothermal

Y. Jiang · Y. Zhao · H. Niu (✉)
Key Laboratory of Mineralogy and Metallogeny, Guangzhou Institute of Geochemistry, Chinese Academy of Sciences, Guangzhou, 510640, China
e-mail: niuhc@gig.ac.cn

Y. Jiang · Y. Zhao
University of Chinese Academy of Sciences, Beijing, 100049, China

M. Zhai et al. (eds.), *Main Tectonic Events and Metallogeny of the North China Craton*, Springer Geology, DOI 10.1007/978-981-10-1064-4_9

solutions. The Hujiayu copper deposit is a typical sediment-hosted stratiform copper deposit. The "Hu-Bi" type copper deposits can be comparable with Central Africa Copper Belt.

Keywords
Fluid inclusions • Genetic model • Zhongtiaoshan • Paleoproterozoic copper system • North China Craton

9.1 Introduction

The Zhongtiaoshan region, located in the south segment of the North China Craton (Sun et al. 1990; Fig. 9.1a), is one of the significant Cu-producing areas in China (Rui et al. 1984; Huang et al. 2001). More than 30 copper deposits, containing a total metal endowment of approximately 400 Mt of metal Cu, are supposed to occur in the Paleoproterozoic metamorphosed magmatic and sedimentary rocks of the Zhongtiaoshan region (Xu 2010). The deposits have been controlled by NW- or NE-trending basement fractures in this region (Fig. 9.1b). Among these Cu deposits, Tongkuangyu and Hujiayu Cu deposits constitute approximately 80 % of the total reserves (Huang et al. 2001). Tongkuangyu Cu deposit, the largest copper deposit in the Zhongtiaoshan region, is hosted in quartz-monzonite porphyry (~2.1 Ga) and its wall rocks of meta-quartz crystal tuffs of the Paleoproterozoic Jiangxian Group (Fig. 9.2), indicating that Cu mineralization is closely associated with magmatism. The Hujiayu Cu deposit is hosted within dolomitic marble and carbonaceous shales of the mid-Paleoproterozoic Zhongtiao Group (Sun and Hu 1993; Fig. 9.2), obviously showing that sedimentation diagenesis may provide metal materials for ore formation. For decades, as these ancient deposits underwent subsequent metamorphism (CGGCDZM 1978; Sun and Hu 1993), the genetic models and metallogenesis of those deposits are highly controversial (Wang and Wen 1957; Xie 1963; CGGCDZM 1978; Sun and Ge 1990; Sun and Hu 1993; Xu et al. 1995; Chen and Li 1998; Zhen and Shu 2006; Zhou 2007; Xu 2010; Zhang 2012; Li et al. 2013; Jiang et al. 2013, 2014a, b; Sun et al. 2014; Liu et al. 2015). More importantly, the nature and origins of ore-forming fluids and mechanism of multistage fluid mineralization are still unclear.

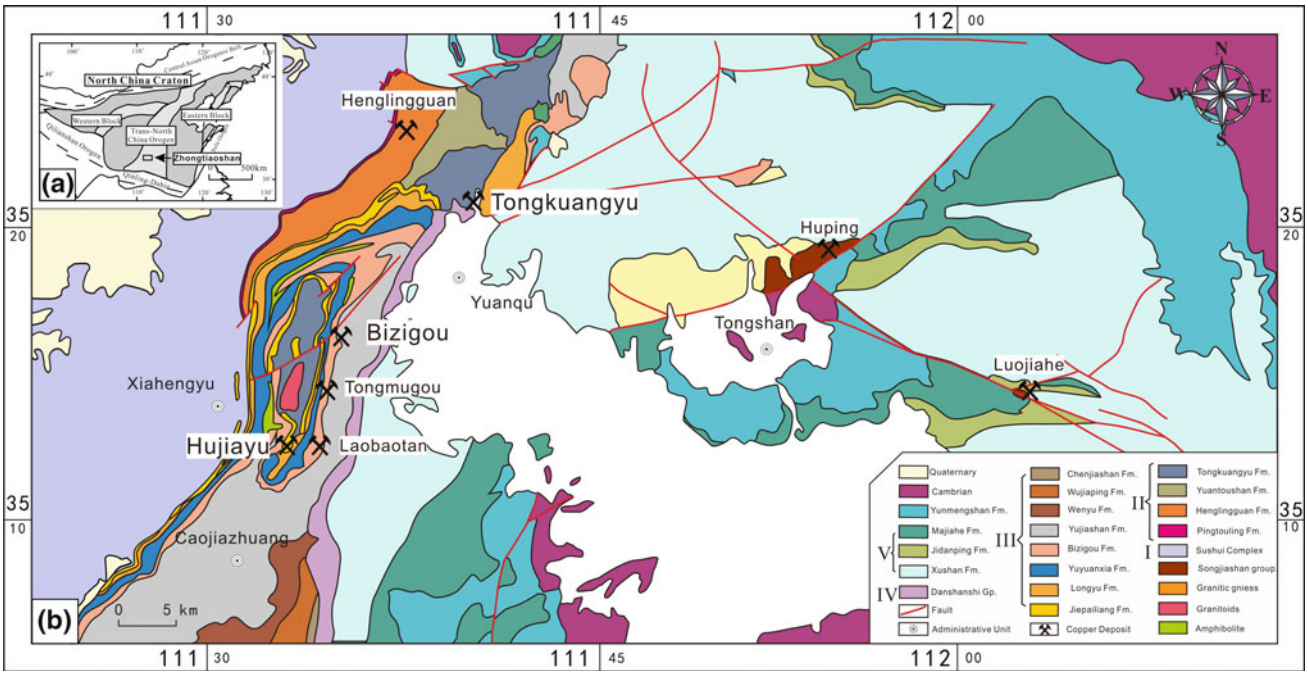

Fig. 9.1 Regional geological map of the Zhongtiaoshan area (**a**). Tectonic framework of the North China Craton and the location of Zhongtiaoshan (**b**). Regional geology of the Zhongtiaoshan area. *I* Sushui Complex; *II* Jiangxian Group; *III* Zhongtiao Group; *IV* Dashanshi Group; *V* Xiyanghe Group (modified after Sun and Hu (1993))

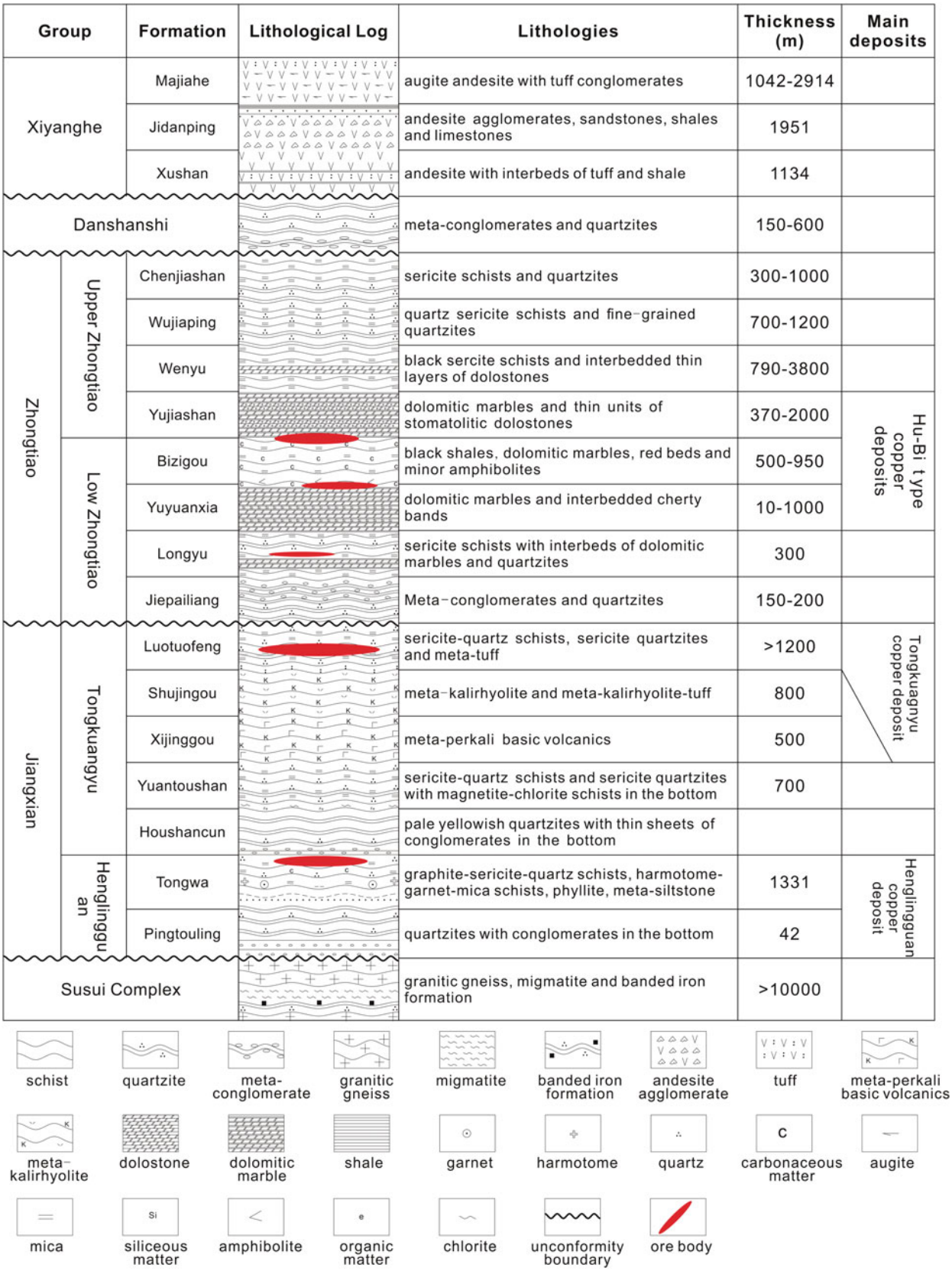

Fig. 9.2 Neoarchean–Paleoproterozoic stratigraphic chart and location of main Cu deposits in the Zhongtiao area (modified after Sun and Hu 1993)

In recent years, we carry out systematical studies on the ore geology, fluid inclusion, and stable isotopes of the typical Tongkuangyu and Hujiayu Cu deposits (Li et al. 2013; Jiang et al. 2014a, b). This investigation shows that (1) magnetite and hematite coexist within the ores and porphyry of Tongkuangyu, and (2) fluid inclusions with anhydrite, hematite and chalcopyrite daughter minerals are ubiquitous in the hydrothermal quartz of this deposit (Jiang et al. 2014a). It suggests that the oxygen fugacity fluctuation of hydrothermal system plays an important role in copper deposition. As for the Hujiayu Cu deposit, the evaporates, red beds are formed after the Great Oxidation Event (GOE), and black shales are documented to be closely associated with ore formation (Jiang et al. 2014b). The compositions, origins of the ore-forming fluids, and the redox potential control on the fluid evolution of the two typical Cu deposits as well as their implications on ore genesis are discussed in depth.

9.2 Paleoproterozoic Rock Units in the Zhongtiaoshan Region

The Paleoproterozoic rock units exposed in the Zhongtiaoshan area include, from the oldest to the youngest, Jiangxian Group, Zhongtiao Group, Danshanshi Group, and Xiyanghe Group (Hu and Sun 1987; Sun and Ge 1990; Bai 1997; Fig. 9.1b). During 2.2–2.1 Ga, the North China Craton as a whole was in an extensional regime (Zhai et al. 2010; Zhai and Santosh 2011, 2013), which lead to abundant extension-related magmatism in the Trans-North China Orogen (Du et al. 2010, 2012). The accumulation of potassic bimodal volcanic rocks and shallow facies clastic sedimentation in this period formed the Jiangxian Group, which hosts the Tongkuangyu Cu deposit (Jiang et al. 2014a). In the period of 2.1–1.9 Ga, the sedimentation was primarily terrigenous clastic, volcanic, and marine carbonate, forming the Zhongtiao Group (Sun and Ge 1990; Sun and Hu 1993). The Hujiayu Cu deposit is hosted by dolomitic marble and carbonaceous shales in this Group. During 1.90–1.85 Ga, the region has experienced a series of tectonic events, including crust uplifting, exhumation, granite intrusion and regional metamorphism, which eventually formed the molasse sequences of Danshanshi Group, responding the end of cratonization of the North China Craton (Sun et al. 1991; Zhai and Santosh 2013). In the late Paleoproterozoic, geological products in the middle-eastern part of the Zhongtiaoshan region is represented by the Xiyanghe Group, which is predominated by andesitic volcanic rocks, comparable to the Xiong'er Group on the southern margin of the North China Craton (Sun et al. 1990; Zhao et al. 2002; He et al. 2008).

9.3 Tongkuangyu Porphyry Copper Deposit

9.3.1 Ore Geology of the Tongkuangyu Copper Deposit

The Tongkuangyu porphyry Cu deposit is located in the northern part of the Zhongtiaoshan region, of which the ore bodies are hosted in the Paleoproterozoic quartz-monzonite porphyry and the Tongkuangyu Formation of the Paleoproterozoic Jiangxian Group (Fig. 9.2). Among seven ore bodies in the Tongkuangyu Cu deposit, No. 4 and 5 are economically viable. The two ore bodies contain 2,800,000 tons Cu metal at an average grade of 0.68 % (Xu 2010), accounting for more than 90 % of the total reserve. No. 5 orebody forms a lens of 1100 m long and 185 m thick.

The rocks exposed in the mining area include quartz-monzonite porphyries, sericite–quartz rocks, meta-potassic mafic volcanic rocks and sericite-schists (Fig. 9.3a). The orebodies are mainly hosted in meta-quartz crystal tuffs (Fig. 9.3b) and meta-quartz monzonite porphyries (Fig. 9.4d). The structure of the Tongkuangyu mine is highly complex. The Tongkuangyu Formation is intensely sheared and formed an overturned anticline, showing intense shear movements. The nearly N–S trending Dabaogou–Tongkuangyu translational normal fault offsets the No. 5 ore body (Fig. 9.3a). The faulted structures that postdate the Cu mineralization resulted from regional metamorphism whilst the destructive effect to the ore bodies is far from significant (CGGCDZM 1978).

Alteration zonation of the Tongkuangyu porphyry Cu deposit includes the quartz–K–feldspar-, quartz–sericite- and carbonate alterations (CGGCDZM 1978). Unlike the alteration and mineralization zoning for typical porphyry Cu deposits, the order of the alteration zonation is inconspicuous at Tongkuangyu. This is partly due to the overprinting of intense regional metamorphism (CGGCDZM 1978; Chen et al. 1998; Sillitoe 2010; Zhang 2012).

The mineralization processes in the Tongkuangyu porphyry Cu deposit are divided into three stages:

1. The early mineralization stage is characterized by quartz–potassium feldspar alteration with sparsely disseminated chalcopyrite and pyrite ores. Quartz veinlets, containing sparsely disseminated sulfides, are visible in some places. Minerals in the quartz–potassium feldspar alteration zone include potassium feldspar, biotite, quartz, magnetite, scapolite, and tourmaline.
2. The main mineralization stage, associated with quartz-sericite alteration, is characterized by veinlets (0.2–3 cm) containing disseminated chalcopyrite and minor molybdenite, pyrite, magnetite, hematite, bornite,

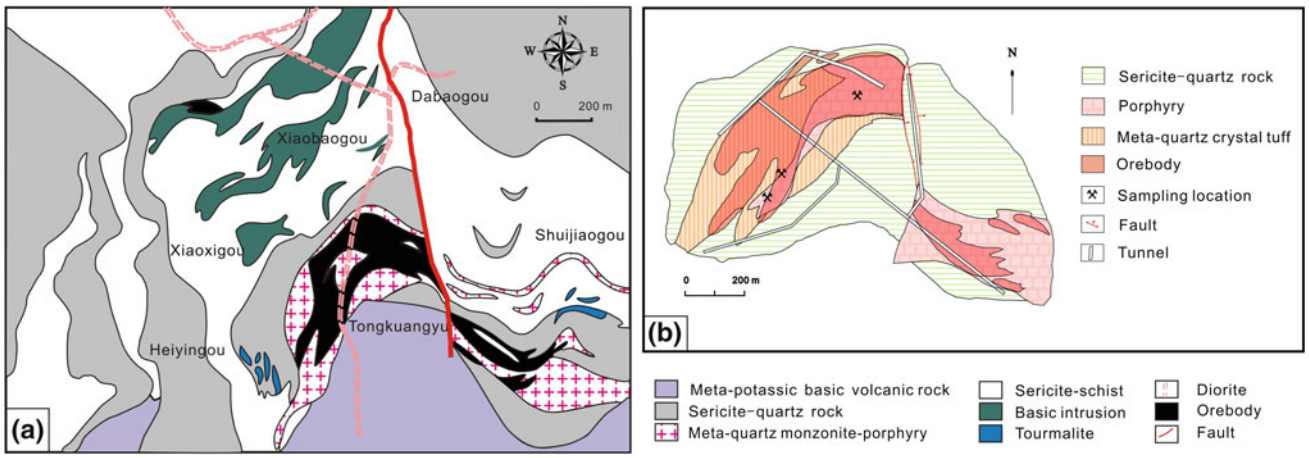

Fig. 9.3 Ore deposit geology map of the Tongkuangyu Cu deposit. **a** Geological map of the Tongkuangyu porphyry Cu deposit. **b** Mining tunnel plan of No. 5 orebody (modified after Sun and Hu 1993; Huang et al. 2001)

and chalcocite (Fig. 9.4a, c, f). Chalcopyrite–pyrite–molybdenite is the main ore mineral assemblage. Being the major gangue mineral, quartz occurs as veinlets associated with the ore minerals. Three sulfides zones are recognized in the main mineralization stage, namely (from the bottom up) the pyrite–chalcopyrite, molybdenite–chalcopyrite and bornite zones. Minerals in the quartz-sericite alteration zone include sericite, quartz, magnetite, hematite, carbonate, chlorite and scapolite. Orebodies mainly occur in the quartz-sericite zone surrounding the quartz–potassisum feldspar zone.

3. The late mineralization stage is characterized by vein-type ores, of which the quartz–calcite veins (3–10 cm) are thicker than those in the main mineralization stage (Fig. 9.4b, e). Ore minerals consist of chalcopyrite, pyrite, molybdenite, magnetite and specularite, accompanied with gangue quartz and calcite. Carbonate alteration also occurred in the late mineralization stage.

The main mineralization stage in Tongkuangyu is the predominant ore formation stage, which is responsible for the emplacement of massive quartz–sulfide veinlets. By contrast, the early- and late mineralization stages are much less significant in terms of the ore formation. Ores and mineralized porphyries from the Tongkuangyu porphyry Cu deposit were dated at 2108 and 2122 Ma by using molybdenite Re–Os and zircon U–Pb dating methods, respectively (Chen and Li 1998; Li et al. 2013; Liu et al. 2015). The similar ages between the porphyry crystallization and mineralization formation demonstrated that Cu mineralization may be genetically linked to the porphyry emplacement. Both of them may be formed in an extensional setting.

9.3.2 Metal Transport in the Ore-Forming Fluids of the Tongkuangyu Cu Deposit

Despite decades of research, the metal transport agents in magmatic–hydrothermal ore deposits are still controversial (Williams-Jones and Heinrich 2005). For more than a century, most researchers believed that the metals are transported as complexes in aqueous liquids (Roedder 1971; Holland 1972; Crerar and Barnes 1976). With the continuous development of experimental technology, high temperature and pressure simulated experiments indicate that Cu is preferentially partitioned into low-salinity magmatic vapor by complexation of Cu with sulfur-bearing ligands in sulfur-rich magmatic–hydrothermal systems (Henley and McNabb 1978; Audétat et al. 1998; Heinrich et al. 1999; Williams-Jones and Heinrich 2005; Heinrich 2007; Lai and Chi 2007). Recently, Lerchbaumer and Audétat (2012) have demonstrated that sulfur in quartz-hosted fluid inclusions has played an important role in determining the Cu diffusion from the external hydrothermal fluids to the internal fluid inclusions, resulting in the precipitation of $CuFeS_2$ in the fluid inclusions. Since sulfur fractionates preferentially into the vapor phase (Drummond and Ohmoto 1985; Suleimenov and Krupp 1994), sulfur-rich vapor inclusions may incorporate more Cu than the coexisting sulfur-poor brine inclusions after entrapment (Lerchbaumer and Audétat 2012).

Actually, based on the study of the fluid inclusions of the Tongkuangyu Cu deposit, Jiang et al. (2014a) has demonstrated that the brine phase might be the dominant Cu transport medium. The fluid inclusions in the quartz enclosed in chalcopyrite (hereafter referred to as B-type

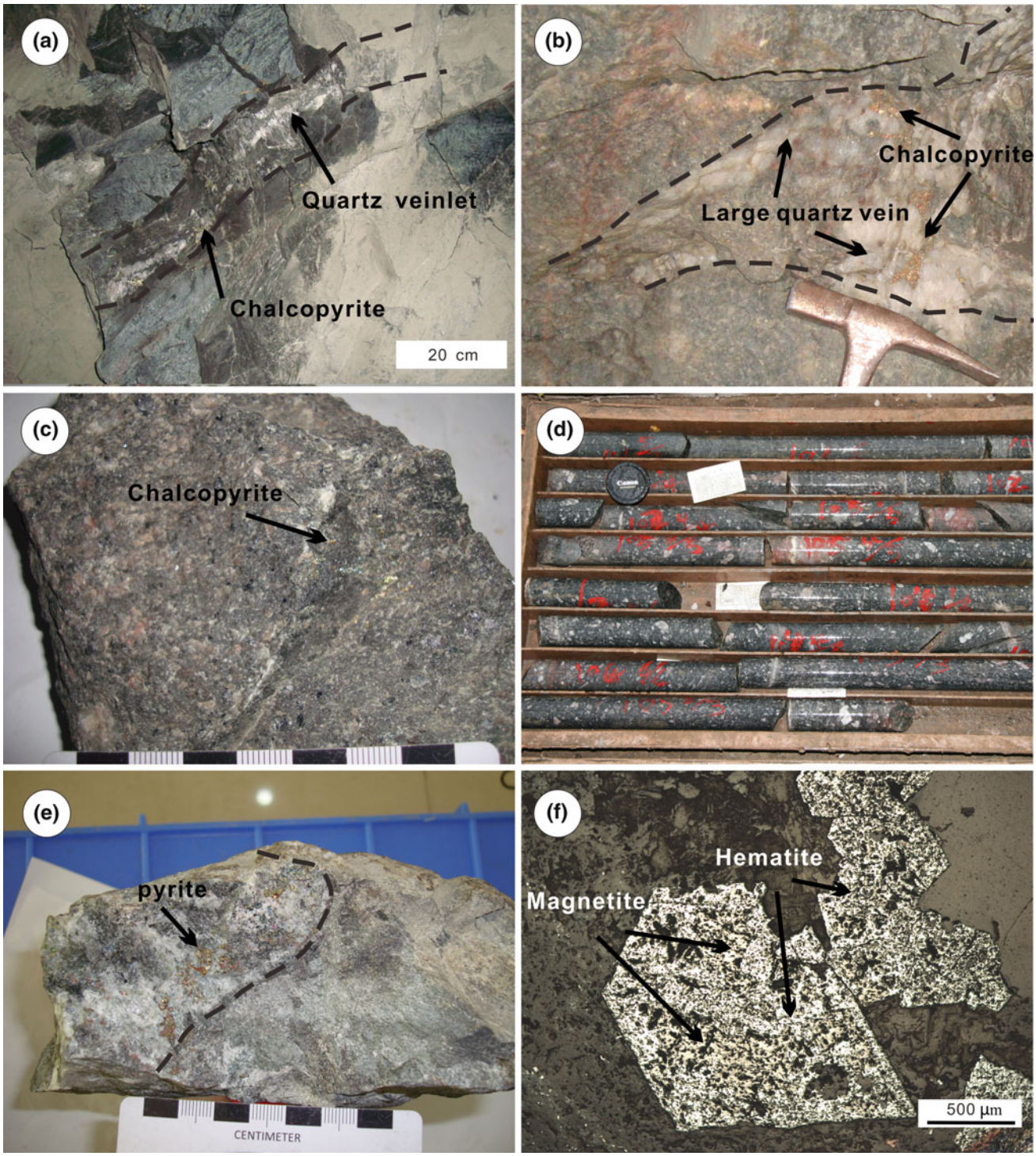

Fig. 9.4 Petrographic features of the ores, quartz–monzonite porphyry and the magnetite–hematite assemblage in the Tongkuangyu Cu deposit

quartz; Fig. 9.5b, c) are regarded as important objects of the study. The reason is that this type of quartz occurs as isolated grains and commonly shows a straight contact with chalcopyrite. Therefore, they are typical syn-ore quartz, and thus their fluid inclusions may be safely taken as a proxy for the primary ore-forming fluids.

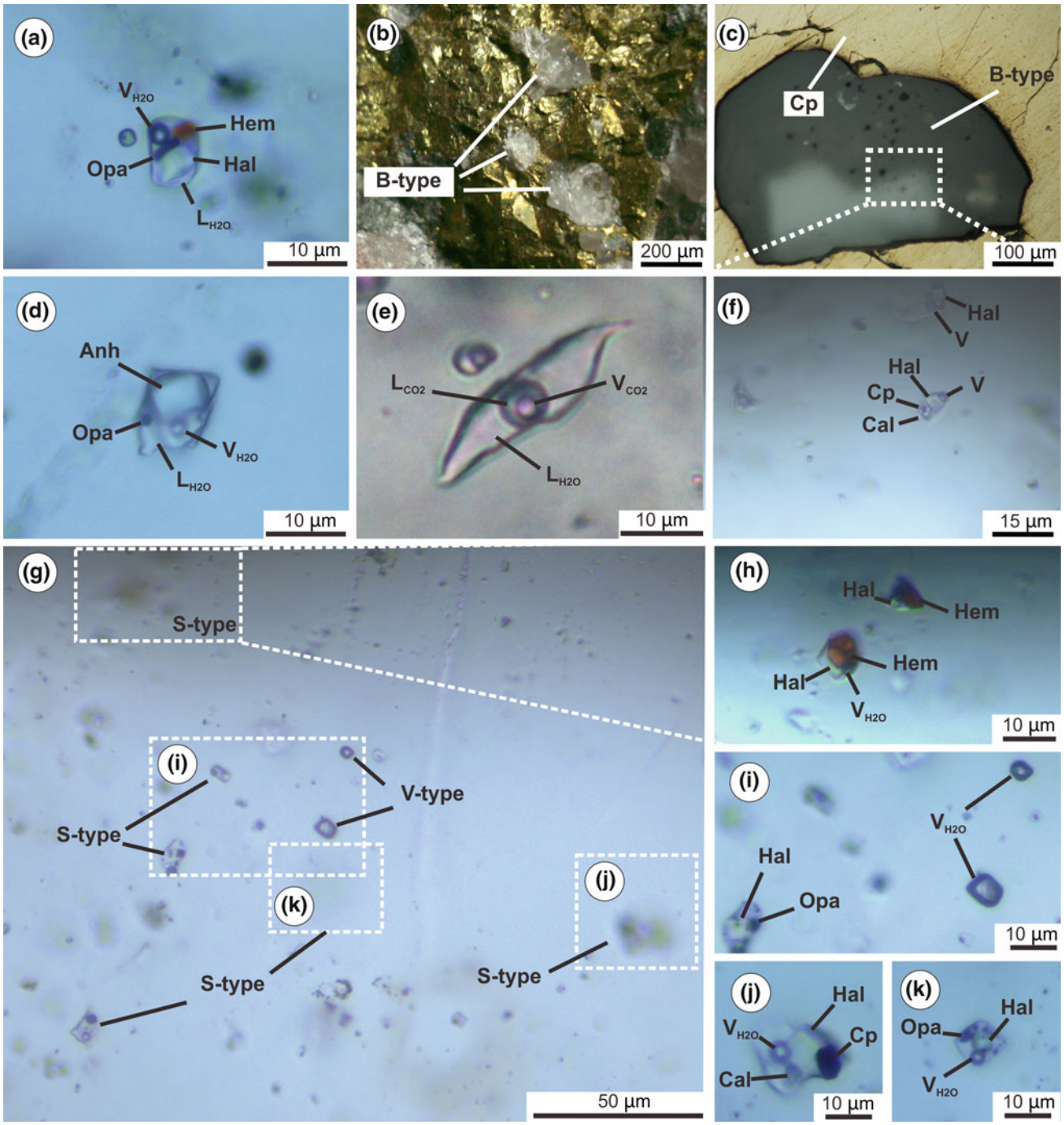

Fig. 9.5 The types and occurrence of fluid inclusions in the Tongkuangyu Cu deposit. *Abbreviations* V_{CO_2}: CO_2 vapor; L_{CO_2}: CO_2 liquid; V_{H_2O}: H_2O vapor; L_{H_2O}: H_2O liquid; *Hal* halite; *Cal* calcite; *Hem* hematite; *Cp* chalcopyrite; *Anh* anhydrite

1. Daughter mineral-bearing inclusions (S-type inclusion) dominate the main- and late stage B-type quartz (Fig. 9.5f). Given that B-type quartz is closely associated with ore minerals (Fig. 9.5b, c), the predominance of S-type inclusions provides direct evidence for brine to be the major metal transport medium.
2. S-type inclusions (with chalcopyrite and hematite daughter minerals) are ubiquitous in the main stage B-type quartz (Fig. 9.5a, h, j). In contrast, chalcopyrite daughter minerals are absent in the synchronic vapor-rich (V-type) inclusions, similarly, the early- and late stage S-type inclusions have no chalcopyrite daughter minerals

either. Hence, chalcopyrite in the S-type inclusions of the main stage was unlikely to be derived by selective Cu diffusion. Alternatively, we propose that the brine phase was the dominant Cu transport medium in the Tongkuangyu porphyry Cu deposit.

9.3.3 Redox Control on the Fluid Evolution of the Tongkuangyu Cu Deposit

Previous studies have suggested that highly oxidized magmas that were derived from the mantle or lower crust are crucial for chalcophile element enrichment (Sillitoe 1997; Mungall 2002). Actually, most ore-forming porphyries have abundant SO_4^{2-} (Mungall 2002; Liang et al. 2009; Sillitoe 2010; Sun et al. 2013), since sulfide undersaturation during the main magma evolution stage is advantageous for the enrichment of incompatible Cu (Sun et al. 2004, 2013). Ferrous ion plays a pivotal role in determining the reduction of sulfates, as it is the most effective and abundant reducing agent in magmas (Mungall 2002). Magnetite crystallizing from the magmas may lead to the reduction of SO_4^{2-} to S^{2-}, which provided an ideal condition for Cu to separate from the magma to enter the hydrothermal fluids (Sun et al. 2004), as illustrated by the following equation (Liang et al. 2009):

$$12[FeO] + H_2SO_4 = 4Fe_3O_4 + H_2S \quad (9.1)$$

Coincidentally, magnetite is ubiquitous in the quartz–potassium feldspar alteration of the Tongkuangyu Cu deposit, which occurs in the early mineralization stage. The homogenization temperatures of S-type inclusions in this stage range from 479 to 560 °C (Jiang et al. 2014a), consistent with the temperature of typical potassic alteration (420–700 °C) in porphyry Cu environment (Rui et al. 1984). It indicates that reduction of sulfates has occurred in the early stage, which promoted the formation of the lean Cu mineralization.

The ore bodies formed in the main mineralization stage are mainly hosted in the quartz-sericite alteration zone, where the coexistence of magnetite and hematite is common (Fig. 9.4f). The study of the fluid inclusion shows that hematite and chalcopyrite daughter minerals are ubiquitous in the S-type inclusions, whose homogenization temperatures vary in the range of 233–450 °C (Jiang et al. 2014a). It is noteworthy that the crystallization temperatures of chalcopyrite and pyrite in the porphyry Cu environment are in the range of 250–350 and 180–410 °C, respectively (Rui et al. 2003). Thus, temperature decrease of the ore-forming fluids apparently plays an important role in Cu deposition. On the one hand, fluid boiling in the temperature range of 233–450 °C promotes further Cu enrichment in the fluids with high salinity (Fig. 9.6). On the other hand, the coexistence of magnetite and hematite indicates that oxygen fugacity of the hydrothermal system fluctuates near the Magnetite–Hematite (MH) buffer line (Sun et al. 2013). With the fluid temperature decreases, magnetite is further oxidized to hematite by the reduction of SO_4^{2-}. Furthermore, the findings of S-type inclusions (with hematite, chalcopyrite and anhydrite daughter minerals) also show that hematite crystallization may lead to the reduction of sulfates and promote the oversaturation of S^{2-} and deposition of metal sulfides (modified after Sun et al. 2004):

$$8Fe^{2+} + 3SO_4^{2-} = 4Fe_2O_3 + 3S^{2-} \quad (9.2)$$

Magnetite and specularite were also observed in the late mineralization stage, indicating that the oxygen fugacity of

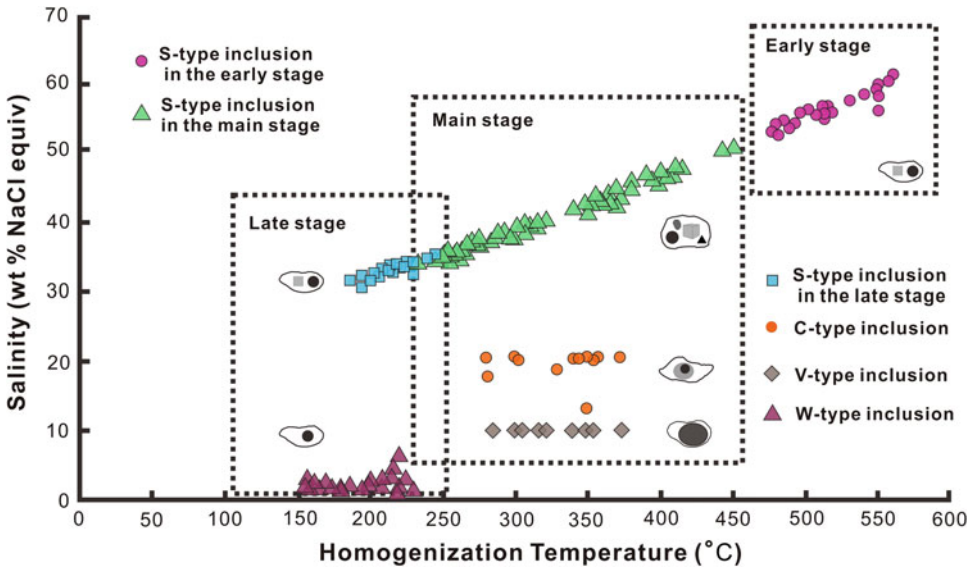

Fig. 9.6 Homogenization temperatures versus salinities of fluid inclusions in different stages (modified from Jiang et al. 2014a). The regions inside the dotted line show the entire range of salinities and homogenization temperatures measured for each inclusion type. Fluid boiling and the appearance of S-type inclusions with metal daughter minerals occur in the main mineralization stage, corresponding to the major phase of Cu deposition

hydrothermal system was still near the Magnetite–Hematite (MH) buffer line. However, the temperature of late mineralization stage dropped to the range of 186–245 °C. Besides, B-type quartz contains some Liquid-rich (L-type) inclusions. These characteristics suggest that the salinity of the late stage ore-forming fluids may have decreased with the influx of meteoric water. Importantly, lowering the fluids' salinity may have led to the decrease of its Cu transport capacity, corresponding to the absence of chalcopyrite daughter minerals in the late stage S-type inclusions. Furthermore, the lacking of hematite and anhydrite in the late stage S-type inclusions indicates that the reduction of SO_4^{2-} to S^{2-} was much less significant, as demonstrated by the very small-scale late stage vein-type mineralization.

9.3.4 H–O–C Isotopes Constraint on the Sources of Ore-Forming Fluids

Based on the study of the fluid inclusions of Jiang et al. (2014a), we investigate the characteristics of H and O isotopes of the fluid inclusions in the Tongkuangyu Cu deposit (Table 9.1). The result shows that the H–O isotope data

Table 9.1 Hydrogen and oxygen isotopic compositions of quartz from the three major types of copper deposits in the Zhongtiao area

Deposit	Sample	$\delta^{18}O$ (mineral)	δD (water)	$\delta^{18}O$ (water)	Source
Tongkuangyu	12TKY-2	13.00	−50.00	7.70	This study
	12TKY3-5	12.80	−42.60	7.50	This study
	12TKY3-2-3	12.10	−36.10	6.80	This study
	12TKYJ2-1	12.30	−48.10	7.00	This study
	810-5147-1	13.10	−64.30	7.80	Sun et al. (1995)
	870-5141-2	12.13	−52.80	6.83	Sun et al. (1995)
	930-2-5	14.25	−82.10	8.95	Sun et al. (1995)
	810-5139-2	16.30	−84.90	11.00	Sun et al. (1995)
	810-5153-11	13.26	−84.90	7.96	Sun et al. (1995)
	810-5153-13	13.80	−52.60	8.50	Sun et al. (1995)
	870-5141-6	12.39	−30.20	7.09	Sun et al. (1995)
	870-5147-11	12.11	−54.90	6.81	Sun et al. (1995)
	TSX-3	13.55	−46.80	11.31	Sun et al. (1995)
	TSX-l	12.77	−47.00	7.47	Sun et al. (1995)
	TSX-4	10.72	−58.80	5.42	Sun et al. (1995)
	TSX-6	11.91	−65.00	6.61	Sun et al. (1995)
	TSX-7	13.24	−65.00	7.94	Sun et al. (1995)
Bizigou	B579-TH6		−50.30	5.89	Sun et al. (1995)
	B579-Wb20		−45.70	4.64	Sun et al. (1995)
	B579-Wb21		−46.60	4.50	Sun et al. (1995)
	B579-Wb5		−70.70	5.28	Sun et al. (1995)
	B475		−72.20	4.73	Sun et al. (1995)
	B600		−36.30	3.88	Sun et al. (1995)
	B651		−41.00	4.72	Sun et al. (1995)
	B464		−31.30	6.07	Sun et al. (1995)
	T-77		−40.00	8.87	Sun et al. (1995)
	T-33		−37.00	5.55	Sun et al. (1995)
	T-47		−40.64	4.46	Sun et al. (1995)
Hujiayu	12HJ-1	−44.00	13.10	6.21	This study
	HUK	−61.00	13.40	6.51	This study
	14HUK4-6	−33.20	14.00	7.11	This study
	14HUK4-1	−47.90	14.40	7.51	This study

mainly distribute in the magmatic water box. Together with the previous H–O isotope data of this deposit, the ore-forming fluids of the Tongkuangyu Cu deposit are believed to be derived from magmatic fluids (Fig. 9.11). The result is consistent with the high temperature and salinity of S-type inclusions, which represent the characteristics of possible magmatic fluids. Furthermore, it seems that Cu mineralization is more closely associated with the porphyries.

We have summarized all the published C–O isotope data of hydrothermal calcite in the Tongkuangyu Cu deposits in Fig. 9.12a and Table 9.2, showing an elongated data distribution. Oxygen isotope values have a relatively narrow range

Table 9.2 Carbon and oxygen isotopic compositions of calcite for three major types of copper deposits in the Zhongtiao area

Sample	$\delta^{13}C_{V\text{-}PDB}$	$\delta^{18}O_{V\text{-}PDB}$	$\delta^{18}O_{V\text{-}SMOW}$	Source
Tongkuangyu *Mineralized carbonate* (*early stage*)				
930-2106	−0.62	−0.28	30.62	Sun et al. (1995)
930-2-9	−6.68	−17.33	13.04	Sun et al. (1995)
930-3-2	−4.89	−17.76	12.60	Sun et al. (1995)
930-3-4	−3.57	−17.72	12.64	Sun et al. (1995)
930-5145-1	−4.06	−18.08	12.27	Sun et al. (1995)
810-5139-30	−2.01	−14.16	16.31	Sun et al. (1995)
810-5139-10	−2.84	−16.28	14.13	Sun et al. (1995)
810-5153-12	−3.17	−13.41	17.09	Sun et al. (1995)
810-5135-23	−4.27	−13.76	16.72	Sun et al. (1995)
810-5147-8	−3.59	−18.25	12.10	Sun et al. (1995)
810-5141-7	−1.37	−18.18	12.17	Sun et al. (1995)
930-5145-2	−4.23	−17.96	12.39	Sun et al. (1995)
Mineralized carbonate (*late stage*)				
810-5139-4	1.05	−18.04	12.31	Sun et al. (1995)
810-5139-5	0.44	−17.92	12.44	Sun et al. (1995)
870-5147-9	1.04	−17.87	12.49	Sun et al. (1995)
870-5147-10	−0.96	−17.54	12.83	Sun et al. (1995)
Bizigou *Mineralized carbonate*				
B579-b22	−17.53	1.06	12.84	Sun et al. (1995)
B579-b30	−16.22	1.48	14.19	Sun et al. (1995)
B579-Wb20	−18.02	−2.53	12.33	Sun et al. (1995)
B579-Wb21	−17.55	−2.83	12.82	Sun et al. (1995)
B579-Wb27	−1.52	3.66	29.34	Sun et al. (1995)
B579-Wb37	−18.70	1.74	11.63	Sun et al. (1995)
B579-Wb32	−18.08	−3.69	12.27	Sun et al. (1995)
B579-Wb5	−16.81	−8.99	13.58	Sun et al. (1995)
BZG-339ZD-CM13-B24	−14.85	2.70	15.60	Zhang (2012)
BZG-339ZD-8 C-B3	−16.45	2.20	13.95	Zhang (2012)
BZG-339ZD-CM13-B27	−13.85	4.30	16.63	Zhang (2012)
BZG-339ZD-CM13-B23	−15.65	2.20	14.78	Zhang (2012)
BZG-339ZD-CM13-W15	−16.65	−9.60	13.75	Zhang (2012)
BZG-339ZD-CM13-H5	−17.45	−0.30	12.92	Zhang (2012)
TMG-ZD365-26 C-W2	−14.65	−0.50	15.81	Zhang (2012)
TMG-ZD365-29 C-B2	−13.85	−4.40	16.63	Zhang (2012)

(continued)

Table 9.2 (continued)

Sample	$\delta^{13}C_{V\text{-}PDB}$	$\delta^{18}O_{V\text{-}PDB}$	$\delta^{18}O_{V\text{-}SMOW}$	Source
Hujiayu				
Dolomitic marble (*Bizigou formation*)				
D209B-80	0.48	−7.66	23.01	Jiang et al. (2014b)
809-640-3	0.39	−7.86	22.80	Jiang et al. (2014b)
809-640-2	0.29	−7.97	22.70	Jiang et al. (2014b)
809-640-1	0.29	−8.11	22.55	Jiang et al. (2014b)
Dolomitic marble (*Yujiashan formation*)				
NHG-ZD240-4XC-B7	−1.2	−12.50	17.97	Huang et al. (2013)
NHG-ZD240-4XC-B6	−1.0	−13.90	16.53	Huang et al. (2013)
NHG-240ZD-CM2-B4	0.7	−9.20	21.38	Huang et al. (2013)
NHG-240ZD-CM96-B3	−0.6	−11.30	19.21	Huang et al. (2013)
Mineralized carbonate (*early stage*)				
HUK-CC-1	−2.01	−16.33	14.07	Jiang et al. (2014b)
D401-200	−3.97	−15.87	14.55	Jiang et al. (2014b)
13HJ3-3	−4.09	−16.60	13.80	Jiang et al. (2014b)
HUK439-04-1	−1.78	−17.29	13.09	Jiang et al. (2014b)
HUK439-04-2	−1.53	−16.83	13.56	Jiang et al. (2014b)
Mineralized carbonate (*late stage*)				
HUK240Z5-1-1	−2.86	−15.16	15.28	Jiang et al. (2014b)
HUK240Z5-1-2	−1.18	−15.15	15.29	Jiang et al. (2014b)
HUK	−5.91	−15.57	14.86	Jiang et al. (2014b)
D301-70	−10.50	−15.92	14.50	Jiang et al. (2014b)
D301-112	−2.73	−16.15	14.26	Jiang et al. (2014b)
D301-115	−4.39	−16.21	14.19	Jiang et al. (2014b)
D401-65	−8.60	−15.79	14.63	Jiang et al. (2014b)
Mineralized carbonate				
NHG-240ZD-CM94-B10	−3.9	−17.3	13.03	Huang et al. (2013)
NHG-240ZD-CM94-B10′	−2.2	−17.3	13.03	Huang et al. (2013)
NHG-240ZD-CM96-B1	−0.9	−16.8	13.54	Huang et al. (2013)
NHG-240ZD-CM96-B1′	−1.1	−16.4	13.95	Huang et al. (2013)
NHG-240ZD-CM94-B14	−0.2	−16.9	13.44	Huang et al. (2013)
NHG-240ZD-CM96-B4	−2.8	−16	14.37	Huang et al. (2013)
NHG-240ZD-CM94-B2	−0.4	−17	13.34	Huang et al. (2013)

$\delta^{18}O$ V-SMOW (‰) = 1.03091 × $\delta^{18}O_{V\text{-}PDB}$ (‰) + 30.91, according to Coplen et al. (1983)

of variation (12.10–17.09 ‰), with mostly varying from 12.10 to 14.50 ‰. In contrast, carbon isotope values have a considerably wider range of variation (−6.96 to −1.37 ‰). Coincidentally, the interval of carbon isotope values corresponds to two end members of magmatic carbon and marine carbon. Given that the orebodies are mainly hosted by marine volcanic-sedimentary sequence surrounding quartz-monzonite porphyry, the range of carbon isotope may result from mixing of magmatic carbon and marine carbon.

9.3.5 Genetic Models of the Tongkuangyu Copper Deposit

For decades, the genetic models of the Tongkuangyu copper deposit are highly controversial (Wang and Wen 1957; Xie 1963; CGGCDZM 1978; Sun and Ge 1990; Sun and Hu 1993; Xu et al. 1995; Chen and Li 1998; Zhen and Shu 2006; Zhou 2007; Xu 2010; Zhang 2012; Li et al. 2013; Jiang et al. 2014a; Sun et al. 2014; Liu et al. 2015). The main genetic

models include: (1) porphyry copper deposit, (2) metamorphosed sediment-hosted stratiform copper (SSC) deposit, and (3) iron oxide–copper–gold (IOCG) deposit.

Wang and Wen (1957) first found the Tongkuangyu copper deposit during mineral exploration and proposed a porphyry copper deposit model for this deposit. Their evidence is based on orebody spatial structure, mineralization types, and alteration features. First, the orebodies are spatial associated with porphyries, occurring in tuff around the porphyries. Second, the mineralization types of this deposit are dominated by disseminated to veinlet type mineralization. Third, some primary features of alteration are overprinted by subsequent metamorphism, but quartz–K–feldspar- and quartz–sericite-alterations have been identified. All these features of ore geology support a porphyry copper deposit model, which is widely accepted by a majority of subsequent researches (CGGCDZM 1978; Sun and Hu 1993; Xu et al. 1995; Chen and Li 1998; Zhen and Shu 2006; Xu 2010; Zhang 2012; Li et al. 2013; Jiang et al. 2014a; Sun et al. 2014).

Xie (1963) discussed the lithogenesis of the metamorphosed quartz-monzonite porphyry and proposed that the called "porphyry" was form by granitization of basement sedimentary rocks. Thus, Tongkuangyu copper deposit was supposed to be a metamorphosed stratiform copper deposit with volcano-sedimentary origin. This deposit is compared with the Central Africa Copper Belt (Xie 1963). The model is accepted and improved by some subsequent researches (Liu et al. 2015). However, a key problem for this model is that SSC-type deposits are mainly hosted in sedimentary rocks but the Tongkuangyu copper deposit is hosted within volcanic quartz crystal tuff and porphyry. Furthermore, typical rock units for SSC-type deposits, such as oxidized red beds, reduced organic matter-rich layers and evaporates, have not been found in Tongkuangyu.

According to the geological setting and geochemical characteristics of volcanic and granitic rocks, Zhou (2007) proposed that Tongkuangyu copper deposit was an IOCG deposit. However, iron oxide and gold are no economic significance in Tongkuangyu. The features of mineralization and rock assemblage are significantly different from typical IOCG deposit.

Recently, we investigate the ore geology, petrogenesis, fluid inclusion, and stable isotopes of the Tongkuangyu Cu deposits (Li et al. 2013; Jiang et al. 2014a). The results support the genetic model of porphyry copper deposit:

1. Ore geology study shows that orebody spatial structure, mineralization types, and alteration features are comparable to porphyry copper deposit. This is consistent with the investigations of Wang and Wen (1957).
2. The ubiquitous coexistence of magnetite and hematite in the porphyries, ores, and fluid inclusions of the Tongkuangyu Cu deposit indicates that the oxygen fugacity of hydrothermal system fluctuates near the Magnetite–Hematite (MH) buffer line. The redox state corresponds to typical oxidized porphyry copper deposits (Sun et al. 2013).
3. The fluid inclusion assemblages with the coexistence of S-type and vapor-rich type inclusions represent typical characteristics of the ore-forming fluids of porphyry copper deposits (Bodnar et al. 2014). The middle-high temperature and high salinity of the fluid inclusions in Tongkuangyu indicate an origin of magmatic–hydrothermal fluids, which are also documented by our H–O isotope analysis.
4. C–O isotopic investigation shows that ore-forming fluids may be derived from mixing of magmatic carbon and marine carbon. This can interpret the reason why orebodies are dominantly hosted within marine volcanic-sedimentary sequence, simultaneously indicating porphyries are closely associated with Cu mineralization.
5. Zircon U–Pb geochronology shows that quartz-monzonite porphyry was emplaced at ~2120 Ma (Sun and Hu 1993; Li et al. 2013). It is approximately consistent with molybdenite Re–Os ages of 2108–2120 Ma (Chen and Li 1998; Liu et al. 2015), which represent the formation age of Tongkuangyu Cu deposit.
6. Typical porphyry copper deposits are generally formed in oceanic subduction setting (Sillitoe 2010), however, continental collision-related environment, such as post-collision extension, also can form porphyry copper deposits (Hou et al. 2007, 2015; Yang et al. 2015). The bimodal volcanic rocks in the Tongkuangyu mine are located under the ore-bearing layers, indicating a local extensional tectonic setting. Liu et al. (2012) proposed that Jiangxian and Lower Zhongtiao Groups (2.2–2.1 Ga) are the products of a back-arc basin, whereas the Upper Zhongtiao and Danshanshi Groups are interpreted as molasses-type siliciclastic rocks deposited in a retro-arc foreland basin. Taken together, the Tongkuangyu porphyry copper deposit may be formed in an arc-related extension environment.

9.4 Hujiayu Sediment-Hosted Stratiform Copper Deposit

9.4.1 Ore Geology of the Hujiayu Copper Deposit

The Hujiayu copper deposit is located in the southwestern of the Zhongtiaoshan region. The deposit is geologically similar to the nearby Bizigou, Laobaotan, and Tongmugou

copper deposits (Fig. 9.1b) and is classified as a "Hu-Bi type" copper deposit in literature (CGGCDZM 1978; Sun and Hu 1993). The deposits are located in an approximately 20 km long belt (Fig. 9.1b). The majority of the deposits occur in silicic albitite and dolomitic marble between the lower parts of the Yujiashan Formation and the top of the Bizigou Formation (CGGCDZM 1978; Sun et al. 1995; Fig. 9.2).

The Hujiayu Cu deposit, containing 450,000 tons copper (average Cu grade: 1.07 %) and 1700 tons Co (average Co grade: 0.027 %), 1119 tons Au (average grade 0.19 g/t Au), and 10 tons Ag (average grade 1.25 g/t Ag), is the largest "Hu-Bi type" deposit (Huang et al. 2001; Zhang 2012). The Hujiayu deposit comprises of 167 orebodies. No. 3 orebody is the largest with 650 m long and 24 m thick (Sun et al. 1995).

The strata exposed in the Hujiayu mining area include the Yuyuanxia, Bizigou, and Yujiashan Formations (from the oldest to the youngest) (Figs. 9.2 and 9.7). The Yuyuanxia Formation is predominantly composed of stromatolite-bearing dolomitic marble. The orebodies are mainly hosted in the Bizigou Formation. The rocks of the Bizigou Formation are generally classified into six types (from the deepest to the shallowest): amphibolite, scapolite–biotite schist, red sandstone and dolomitic marble, gray dolomitic marble, silicic albitite, and carbonaceous shales (Fig. 9.8).

The orebodies are mainly hosted in the silicic albitite and gray dolomitic marble within the upper segment of the Bizigou Formation, but they locally extend into the uraninite and pyrite bearing carbonaceous shales (Figs. 9.7 and 9.8a) at the bottom of the Yujiashan Formation. The silicic albitite is spatially associated with dolomitic marble and carbonaceous shales, and is characterized by very fine stratification consisting of albite and quartz. The presence of red beds is ubiquitous in the Zhongtiao Group although their significances often got overlooked (Wei et al. 1984; Cen and Yang 1993). The red beds (red dolomitic marble and sandstone) occur discontinuously in the lower segment of the Bizigou Formation with a total thickness of up to one hundred meters (Wei et al. 1984; Fig. 9.8d), while a range of 6–20 m for the individual red beds (Fig. 9.8e). The occurrence of red beds is similar to other strata of the Bizigou Formation. Strongly limonitic dolomitic marble can be observed in some parts of the Bizigou Formation.

Fold and fault structures are well-developed in the Hujiayu mine area. The orebodies are mainly controlled by the Nanhegou-Xigou congruent inverted syncline (Fig. 9.7a). Common types of hydrothermal alteration products in the Hujiayu Cu deposit include albite, carbonate, biotite, and silica. However, as regional metamorphism significantly altered the rocks of Bizigou Formation, the alterations associated with mineralization are difficult to be identified (CGGCDZM 1978; Sun and Ge 1990).

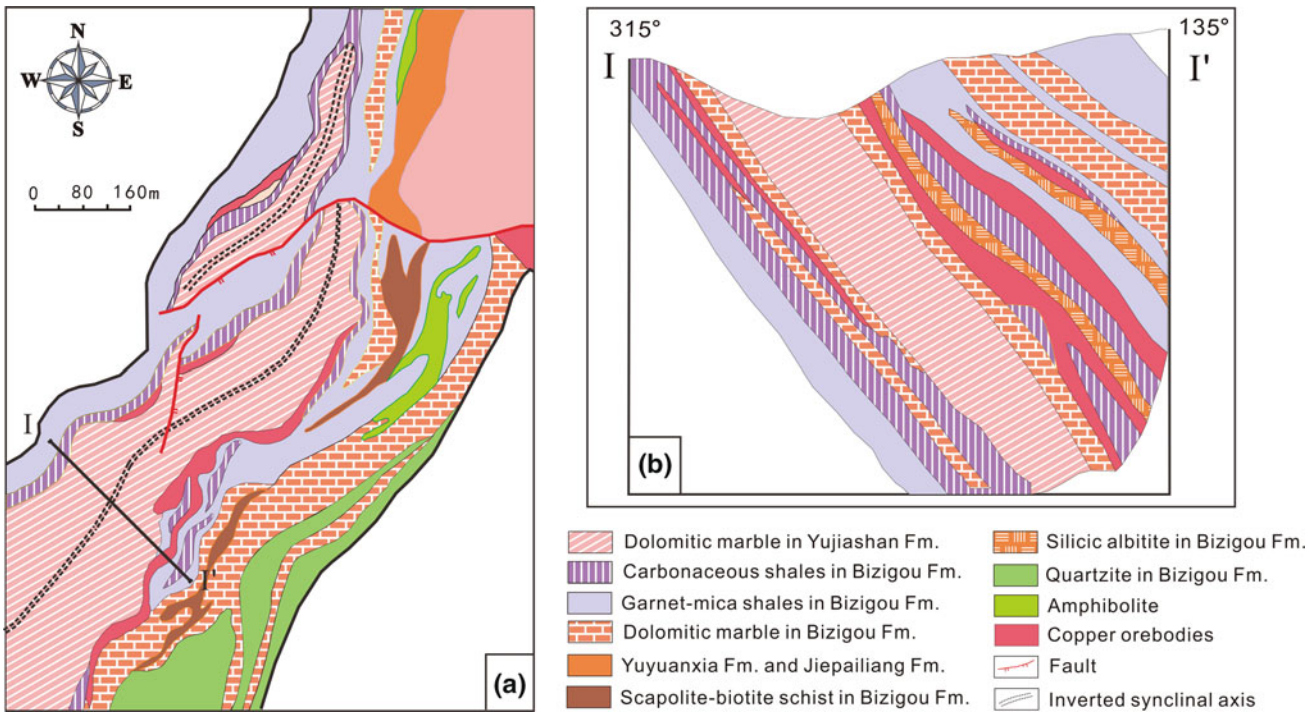

Fig. 9.7 Schematic geological map (**a**) and profile (**b**) of the Hujiayu Cu deposit (modified after CGGCDZM 1978; Sun and Hu 1993)

The mineralization observed in the Hujiayu Cu deposit can be divided into early stage (diagenetic stage) and late stage (metamorphic stage):

1. The early mineralization stage is the major ore-forming stage. It is characterized by disseminated to veinlet (<0.5 cm wide) metal sulfides in silicic albitite and dolomitic marble. The ore minerals are mainly chalcopyrite, pyrite, and pyrrhotite with accessory chalcocite, bornite, molybdenite, cobaltite, and lesser linneite. Gangue minerals are mainly dolomite, quartz, and albite. Bedding is deformed around metal sulfide nodules due to differential compaction, suggesting the nodules were emplaced early in diagenesis (Fig. 9.8c). The veinlets are thin and discontinuous with irregular boundaries against the host rocks (Fig. 9.8h). Almost all the nodules and veinlets are aligned parallel to the stratification of silicic albitite and dolomitic marble (Fig. 9.8a, c, g).
2. The late stage mineralization is hosted within quartz–dolomite veins (3–20 cm wide) that are more continuous and thicker than those of the early stage (Fig. 9.8b, f, i). The vein minerals consist of chalcopyrite, pyrite, pyrrhotite quartz, and dolomite. The ore veins are controlled by tectonic fractures and often crosscut the stratigraphy of the host rocks and the metal sulfide veinlets of the early stage (Fig. 9.8b, f, i). The grain size of metal sulfides and gangue minerals is much coarser in the late stage veins than the early stage.

9.4.2 Compositions and Nature of the Ore-Forming Fluids in the Hujiayu Cu Deposit

The L-type inclusions (Fig. 9.9a, g) from the two different stages exhibit distinct microthermometric behaviors under cooling. First melting temperatures for L-type inclusions of the early stage (varying from −61.8 to −47 °C) indicate a fluid system with H_2O–NaCl–$CaCl_2$ (Oakes et al. 1990; Chi

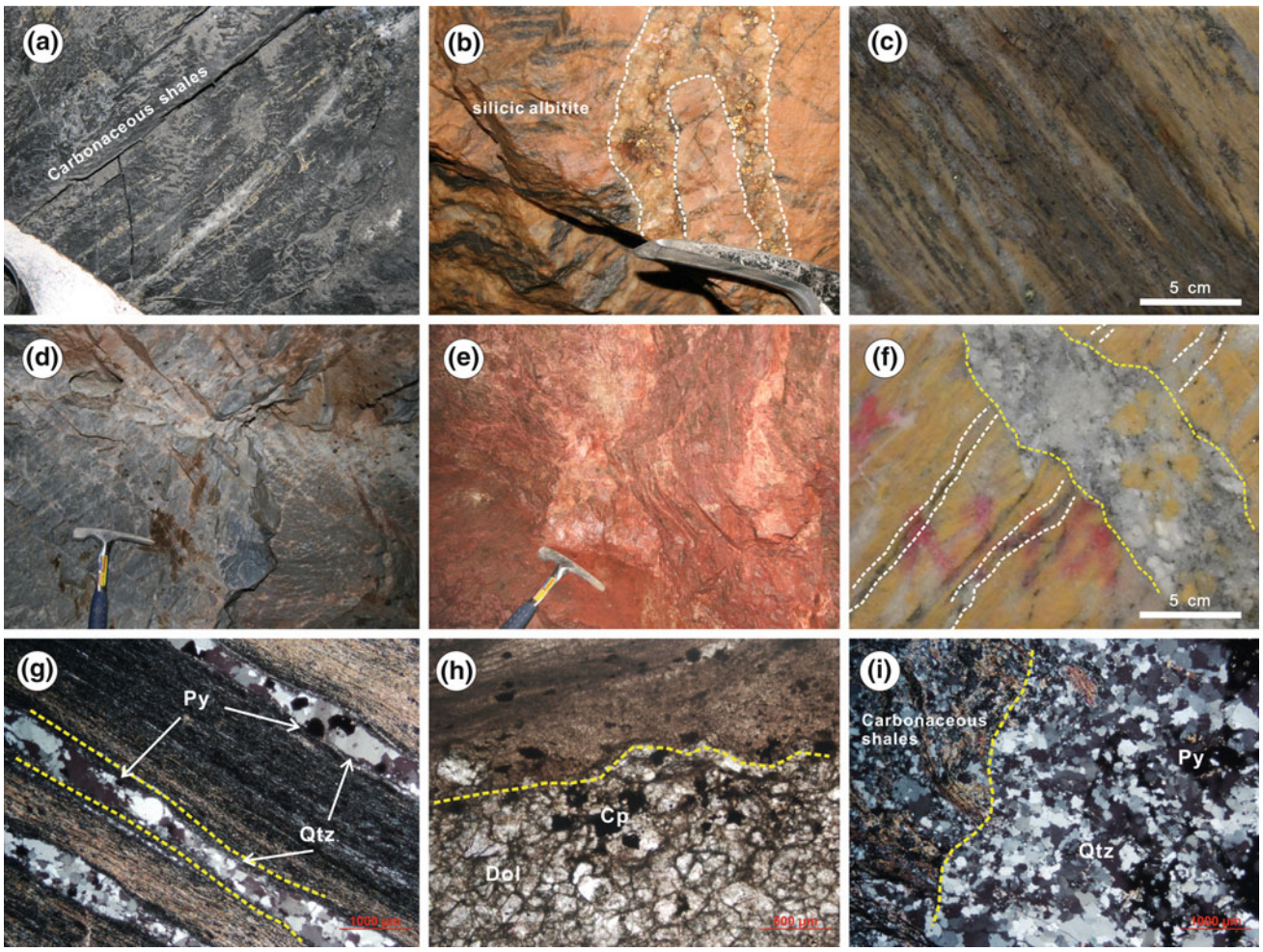

Fig. 9.8 Petrographic features of the ores, red beds, dolomitic marbles and black shales in the Hujiayu Cu deposit

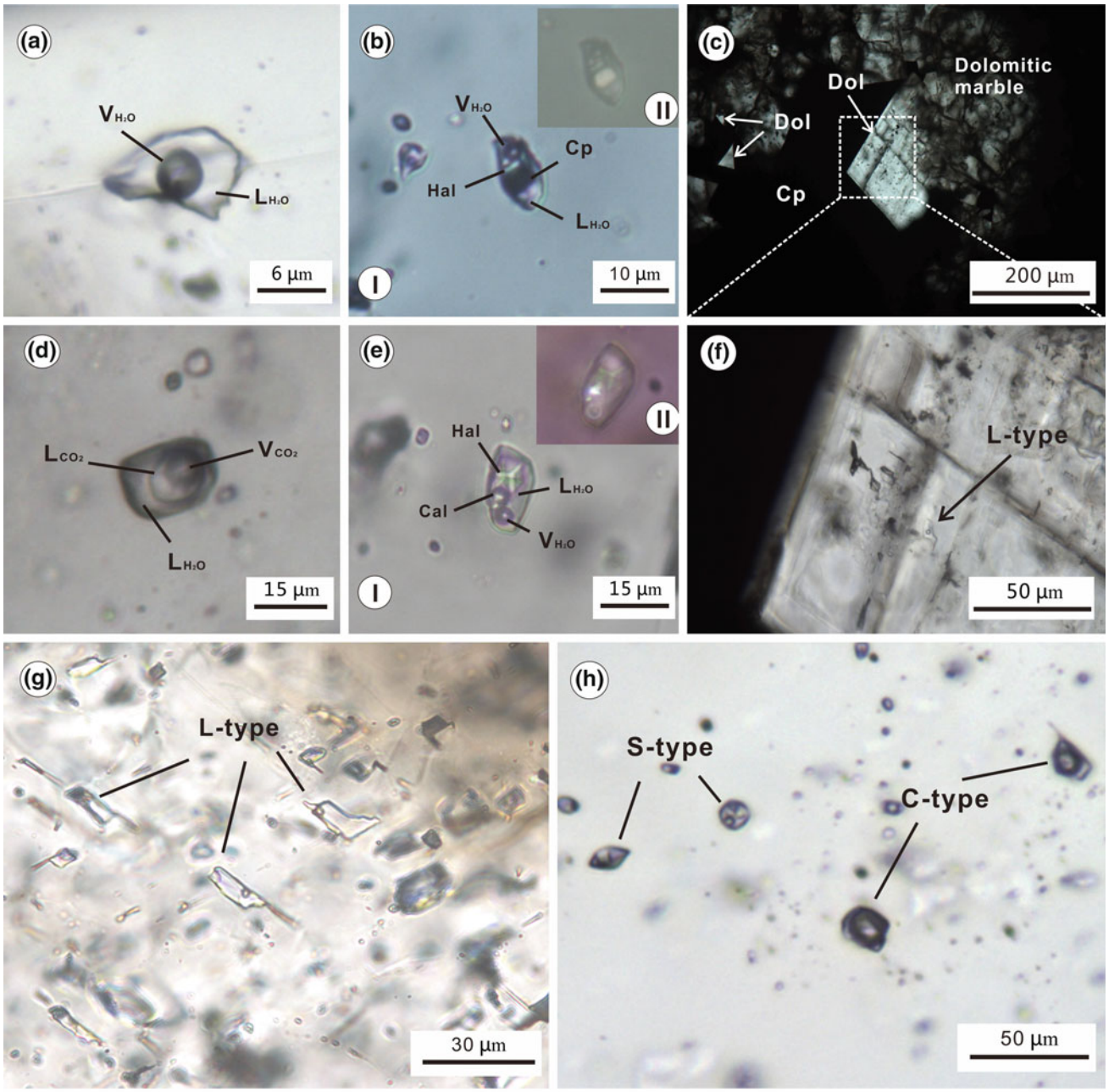

Fig. 9.9 The types and occurrence of fluid inclusions in the Hujiayu Cu deposit. *Abbreviations*: *Dol* dolomite

and Ni 2007; Jiang et al. 2014b). In contrast with the early stage, the L-type inclusions in the late stage are representative of a relatively simple H_2O–NaCl system. The striking difference of fluid systems between the early and late mineralization stages suggests that the two stages of mineralization are of different origins.

9.4.2.1 High Salinity Basinal Brines

As shown in the salinity–total homogenization temperature diagrams (Fig. 9.10a), the fluid inclusions of the early stage in the Hujiayu Cu deposit have salinities that mainly vary from 22 to 40 wt% NaCl equiv. The common occurrence of S-type inclusions, in particular, represents a high saline environment (Jiang et al. 2014b). Actually, previous study showed that silicic albitite in this deposit was formed in an evaporitic environment (Wei et al. 1984). A possible mechanism for massive albite formation is the reaction between detrital feldspar and dissolved evaporates (Land and Milliken 1981). The reaction can also release typical sedimentary basin brines (containing sodium, calcium, and

chloride), consistent with the compositions (primarily H_2O–NaCl–$CaCl_2$ systems) of the early stage ore-forming fluid in the Hujiayu Cu deposit (Jiang et al. 2014b).

This is also consistent with other sediment-hosted stratiform Cu deposits, which are commonly associated with evaporates units that are the main source of high salinity fluids (Brown 1997). Furthermore, scapolite is widespread in the dolomitic marble and biotite schist of the Zhongtiao Group (Sun and Hu 1993; Sun et al. 1995), indicative of the migration of high salinity fluids (Oliver et al. 1994; Pollard 2001; Moore 2010). The EMPA analysis of scapolite in the scapolite–biotite schist shows that the content of Cl is up to 2.5–3.0 % (Sun and Hu 1993). We infer that the rocks of the Bizigou Formation may have been affected by chlorine-rich fluids in the early stage of formation. The high salinity of the ore-forming fluids in the early stage may be derived from dissolve evaporate.

9.4.2.2 CO_2-Rich Metamorphic Hydrothermal Solutions

In the late stage mineralization, fluid unmixing can easily be discerned by the coexistence of CO_2-rich inclusions (C-type; Fig. 9.9d) and S-type inclusions (Fig. 9.9e, h) as well as microthermometric results (Fig. 9.10b), indicative of CO_2-rich facies unmixing with high salinity facies. Therefore, the escape of CO_2 from solutions results in the extensive change of pH, fluid pressure and salinity of the remaining fluids and promotes the precipitation of Cu (Lowenstern 2001; Robb 2013). In addition, the salinities of S-type inclusions of the late stage are significantly higher than those in the early stage (Fig. 9.10). This can be explained by significant fluid unmixing in the late stage.

Previous study shows that the occurrence of the late stage mineralization is closely related to regional metamorphism during the Zhongtiao Movement (Sun and Hu 1993; Jiang et al. 2014b). Furthermore, the homogenization temperatures of C-type and S-type inclusions representing extensive unmixing vary from 240 to 480 °C (Fig. 9.10b), consistent with the temperature of low-grade greenschist facies to high-grade greenschist facies metamorphism. Thus, the CO_2-rich ore-forming fluids are supposed to be metamorphic hydrothermal solutions produced by devolatilization of the host rocks (Jiang et al. 2014b).

9.4.3 H–O Isotopic Constraint on the Origins of Ore-Forming Fluids

According to the data of the fluid inclusion of Jiang et al. (2014b), we investigate the characteristics of H and O isotopes of the fluid inclusions in the Hujiayu Cu deposit (Table 9.1). The samples were mainly collected from quartz veins in the late stage. The result shows that the H–O isotopic

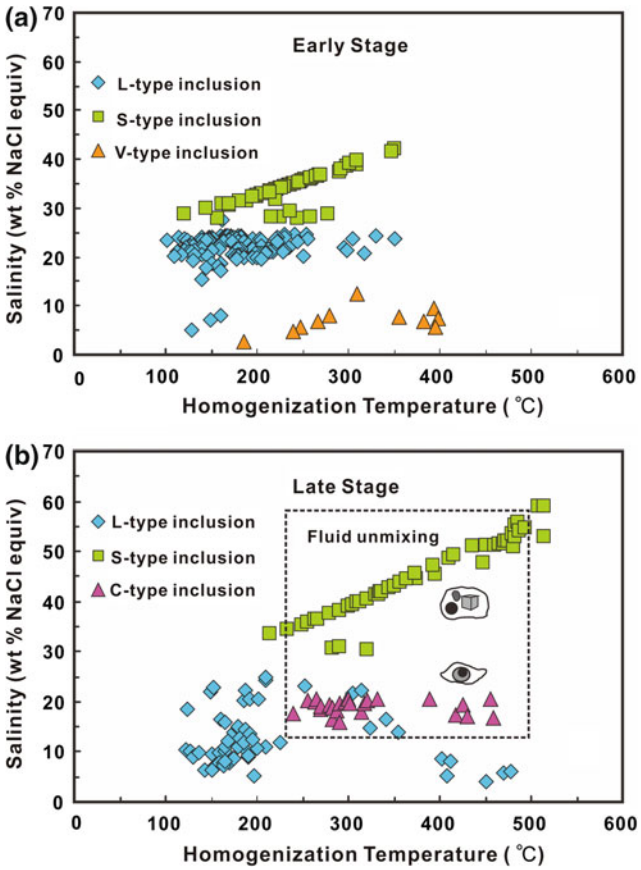

Fig. 9.10 Histograms of salinities and homogenization temperatures of fluid inclusions in both the early stage and the late stage of the Hujiayu Cu deposit (modified from Jiang et al. 2014b)

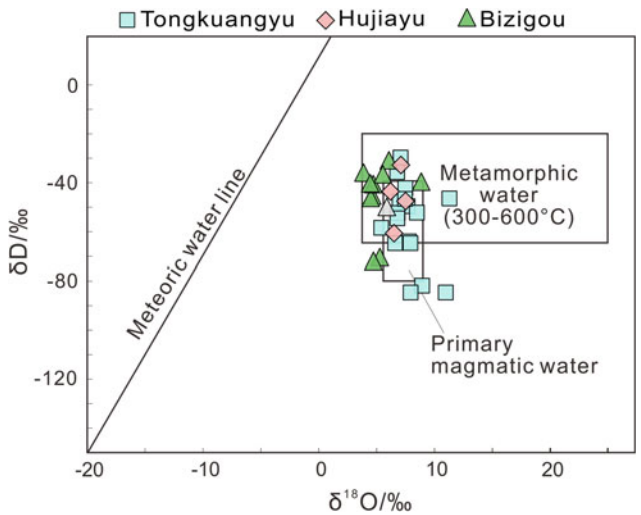

Fig. 9.11 Hydrogen and Oxygen isotopic compositions for the three major types of copper deposits in the Zhongtiao area. Also shown are the calculated fields of primary magmatic waters and metamorphic waters (Taylor 1974), and calculation of equilibrium oxygen isotopic fractionation between water and quartz (Clayton et al. 1972)

data were plotted in the magmatic and metamorphic water boxes (Fig. 9.11). Together with previous H–O isotopic data of the Hu-Bi type copper deposit, the late stage mineralization fluids of this type of copper deposit may mainly consist of metamorphic hydrothermal solutions (Fig. 9.8). As for the characteristics of magmatic water, Jiang et al. (2014b) give a reasonable interpretation by fluid inclusion. Because of metamorphism and deformation overprinting, some veinlets in the early stage are hardly discriminated with quartz veins in the late stage. Their study shows that the coexistence of S-type and V-type inclusions can be found in some quartz veinlets. Given that the two types of inclusions have approximately identical homogenization temperatures (Fig. 9.10a) but homogenize into different phases, it can be confirmed that unmixing occurred locally at this stage. The unmixing assemblage has relatively higher homogenization temperatures than the other inclusions of the early stage. Previous studies have shown that the Cu content of amphibolite near the orebodies is much lower than the amphibolite far away from the orebodies, which indicates that the amphibolite is a source of copper for the ore-forming fluids (Cen and Yang 1993). Hitzman et al. (2010) also propose that igneous activity can participate in the mineralization of sediment-hosted stratiform copper deposits. Therefore, the unmixing assemblage in the veinlets may represent the presence of magmatic fluids in the early stage. Alternatively, it can well interpret that some H–O isotopic compositions have characteristics of magmatic water.

9.4.4 C–O Isotopic Investigation on the Hujiayu Cu Deposit

The C–O isotopic data of hydrothermal calcite in the "Hu-Bi" type Cu deposits have been summarized in Fig. 9.12 and Table 9.2, showing an elongated data distribution. Oxygen isotopic values have a relatively narrow range of variation (13.09–14.55 ‰), while carbon isotopic values have a considerably wider range of variation (−10.5 to −0.70 ‰). Carbon isotopic fractionation between mineral–fluid does not depend on temperature significantly (O'Neil et al. 1969), so the range of carbon isotopic data may result from mixing of multiple fluids with different carbon isotopic compositions. This inference can be explained by ore-forming model of sediment-hosted stratiform Cu deposits (Hitzman et al. 2010). For this type of deposit, reductants within the rocks overlying the red beds are essential for the precipitation of Cu sulfides (Hitzman et al. 2010). The reductants act as a chemical trap for the reduction of oxidized copper-bearing brines and discharge of copper (Brown 1992; Hitzman et al. 2010). The reducing rocks are carbonaceous shales in most sediment-hosted stratiform Cu deposits (Hitzman et al. 2005; Zhao et al. 2012). For the Hujiayu Cu deposit, carbonaceous shales are ubiquitous in the strata between the top of the Bizigou Formation and the bottom of the Yujiashan Formation. Local mineralization can be observed in the carbonaceous shales (Fig. 9.7b). The interaction between the oxidized Cu-bearing brines and reduced carbonaceous shales would have resulted in the oxidation of organic matter (Selley et al. 2005; El Desouky et al. 2010), which may be the main reason for the significant variation of carbon isotopic values.

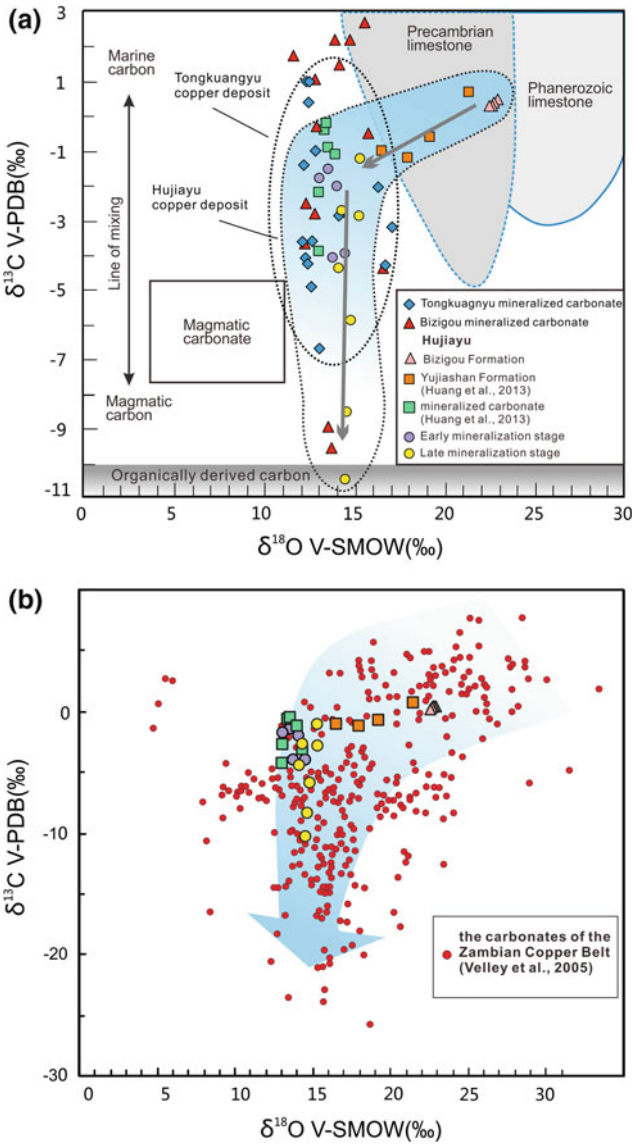

Fig. 9.12 Carbon and Oxygen isotopic compositions. **a** Carbon and Oxygen isotope compositions of major copper deposits in the Zhongtiao area. **b** The $\delta^{13}C$ and $\delta^{18}O$ data of 369 carbonate samples (whole rock, veins, and evaporate nodules) from 10 deposits in the Zambian Copperbelt compiled by Selley et al. (2005). The trends of $\delta^{13}C$ and $\delta^{18}O$ variations are similar to those of the Hujiayu deposit. The variation of Precambrian and Phanerozoic limestone is in accordance to those reported by Bell and Simonetti (2009). Field of organically derived carbon in (**a**) is from Longstaffe (1989)

The late stage mineralization overprints the early mineralization, and thus the carbon and oxygen isotopic values of the mineralized carbonates in the late stage veins have distribution characteristics similar to those in the early stage. However, two samples of the late stage mineralized carbonate have the carbon isotopic values of −8.6 and −10.5 ‰, respectively (Fig. 9.12a), which shows that the carbon isotopic values of the late stage mineralized carbonates have a wider range of variation than those in the early stage. The fluid inclusion study indicates that CO_2 degassing from hydrothermal solutions is common in the late stage, thus the heavy carbon isotope fractionating to CO_2 may produce more negative carbon isotopic values in the late stage mineralized carbonates than the early stage (Zheng and Chen 2000).

The carbon and oxygen isotope values of dolomitic marble in the Bizigou Formation exhibit a narrower range of variation comparable with the mineralized carbonates (Fig. 9.12a), indicating that these rocks are derived from marine carbonate. Huang et al. (2013) analyzed the C and O isotopic values of the mineralized carbonate veins in the Hujiayu Cu deposit and the marble in the Yujiashan Formation. The data of mineralized carbonate veins are consistent with the data of this paper, but the data of the Yujiashan Formation are different from those data of the Bizigou Formation (Fig. 9.12a). Combining the data of Huang et al. (2013) with this study, the C and O isotopic values show a gradually decrease from the unmineralized carbonates of the Bizigou Formation to the mineralized carbonates within the orebodies of Hujiayu. Carbon and oxygen isotopic data from 369 carbonate samples (whole rock, veins, and evaporate nodules) of 10 deposits in the Zambian Copper Belt were compiled by Selley et al. (2005). The $\delta^{13}C$ and $\delta^{18}O$ values shift from the Neoproterozoic marine carbonates in the unaltered sedimentary carbonates toward the hydrothermal carbonates sampled within or close to the orebodies (Fig. 9.12b). The trend of C and O isotopic variations in the Hujiayu deposit is quite similar to those reported by Selley et al. (2005) (Fig. 9.12b).

9.4.5 Ore Genesis Model for the Hujiayu Cu Deposit

The Hujiayu copper deposit experienced two mineralization stages, which are supported by many studies of ore geology and geochronology (CGGCDZM 1978; Sun and Ge 1990; Sun and Hu 1993; Zhang 2012). It is commonly accepted that the late stage mineralization is closely associated with the regional metamorphism during the Zhongtiao Movement (~1.9 Ga) (CGGCDZM 1978; Sun and Ge 1990; Sun and Hu 1993; Zhang 2012). However, the mechanism of early stage mineralization has been contentious. Sun and Ge (1990) proposed that the "Hu-Bi type" Cu deposits are hydrothermal exhalation sedimentary deposits (similar to SEDEX). Silicic albitite is regarded as exhalative sedimentary rock. Nevertheless, the economic metals of SEDEX-type deposits are mainly Pb and Zn, and lack of Cu (Goodfellow and Lydon 2007; Pirajno 2009; Leach et al. 2010). Furthermore, Wei et al. (1984) has documented that silicic albitite were derived from dissolved evaporates. Based on our field study and petrography observation, the Hujiayu Cu deposit has relatively complete spatial structure of the sediment-hosted stratiform Cu deposits, containing the red beds, reduced marble, albitite and black shales (Fig. 9.13). In fact, the oxidized red beds are a key component for the formation of sediment-hosted stratiform Cu deposits (Hitzman et al. 2010). The sedimentation of the Bizigou Formation started at 2.06 Ga (Sun and Hu 1993), subsequent to the Great Oxidation Event (GOE) (2.33–2.06 Ga, Melezhik et al. 1999; Tang et al. 2013).

In addition, El Desouky et al. (2009) studied the ore-forming fluids of two main Cu–Co sulfide stages in the Katanga Copperbelt of the Central African Copper Belt. In the first stage, early diagenetic stratiform mineralization was produced, which was related to a moderate temperature (115–220 °C) and moderate salinity (11.3–20.9 wt% NaCl equiv.) fluid (El Desouky et al. 2009). In the second stage, late syn-orogenic Cu mineralization was produced, which was related to a high temperature (270–385 °C) and high salinity (35–45.5 wt% NaCl equiv.) fluid (El Desouky et al. 2009). This is comparable with the microthermometric trend observed at the Hujiayu Cu deposit.

Taken together, we propose that the Hujiayu Cu deposit is a typical sediment-hosted stratiform copper deposit. The "Hu–Bi" type copper deposits can be comparable with Central Africa Copper Belt. Based on the ore geology, fluid inclusion and C–O isotopic analyses, we propose a model for the early stage hydrothermal mineralization in the Hujiayu Cu deposit as follow. High saline brines were released by the reaction between detrital feldspar and dissolved evaporates. Then, the brines leached copper and other metals through the red bed and formed oxidized Cu–chloride brines. As the Cu-bearing fluids migrated upwards along fractures and encountered organic-rich reducing carbonaceous shales, Cu was discharged in the form of sulfides. The basic intrusion at the bottom of the Bizigou Formation may also provide Cu and heat for the ore-forming fluids. In contrast, late stage mineralization is mainly characterized by metamorphic hydrothermal solutions, which is closely associated with Zhongtiao Movement. The discharge of Cu is most likely caused by CO_2 escaping from metamorphic hydrothermal solutions.

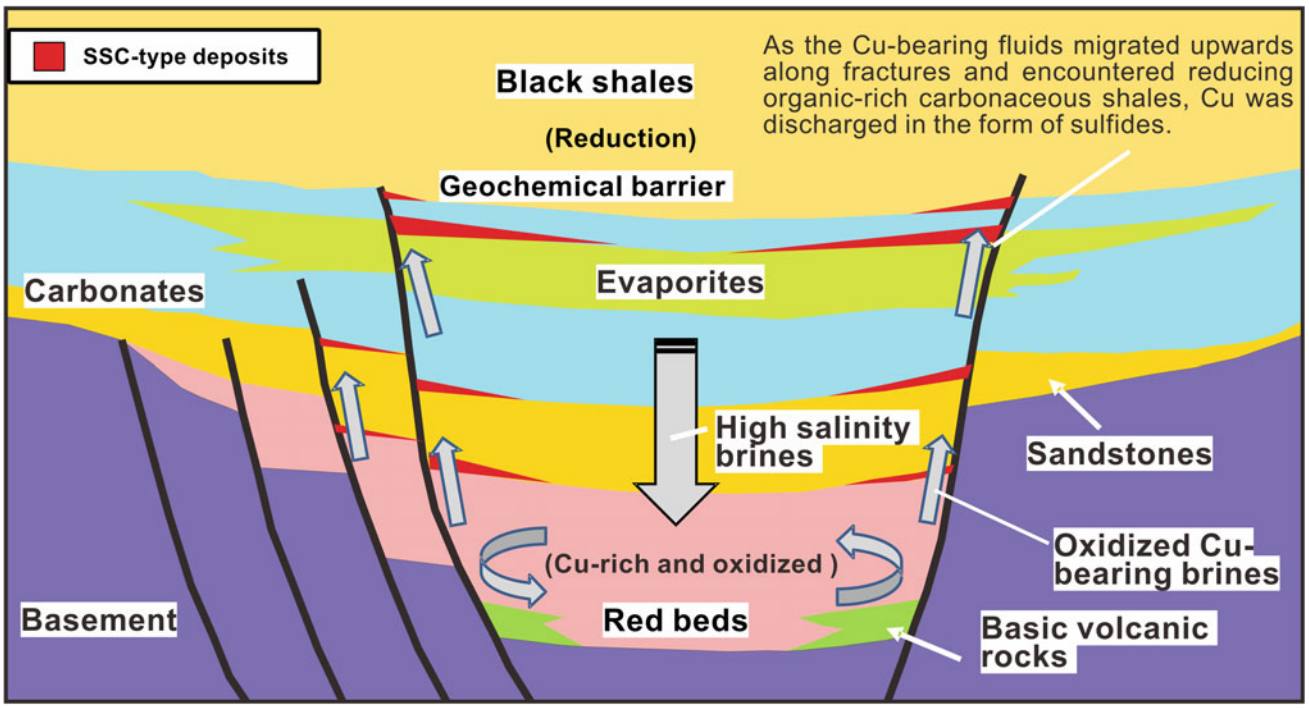

Fig. 9.13 Metallogenesis model for the Hujiayu sediment-hosted stratiform copper deposit (modified from Huston et al. 2010)

9.5 Summary

The copper deposits hosted in the Zhongtiaoshan region are mainly formed in the Paleoproterozoic period, which is an important metallogenic epoch in the North China Craton (Zhai and Santosh 2013). Based on systematical investigation on the ore geology, fluid inclusion, and stable isotopes of the Tongkuangyu and Hujiayu Cu deposits, we draw several conclusions as follows:

1. The oxygen fugacity of hydrothermal system of the Tongkuangyu Cu deposit fluctuates near the Magnetite–Hematite (MH) buffer line, corresponding to the redox state of typical oxidized porphyry copper deposits.
2. The main ore-forming fluids of the Tongkuangyu Cu deposit consist of magmatic–hydrothermal fluids with middle-high temperature and high salinity.
3. Orebody spatial structure, mineralization types, and alteration features are comparable with porphyry copper deposit. The formation age of the quartz-monzonite porphyry is consistent with Cu mineralization. We propose that the Tongkuangyu Cu deposit is a porphyry copper deposit formed in an arc-related extension environment.
4. In the Hujiayu Cu deposit, the ore-forming fluids of the early mineralization stage are mainly characterized by high salinity and moderate temperature basinal brines, whereas the ore-forming fluids of the late mineralization stage are characterized by CO_2-rich and high salinity and high temperature metamorphic hydrothermal solutions, which experienced obvious phase separation.
5. Early stage mineralization of the Hujiayu Cu deposit may occur via interaction of oxidized Cu-bearing brines from the underlying red beds (after the GOE event) with the upper reducing carbonaceous shales. Late stage mineralization at the Hujiayu deposit is likely related to CO_2 escaping from metamorphic hydrothermal solutions.
6. The Hujiayu copper deposit is a typical sediment-hosted stratiform copper deposit. The "Hu-Bi" type copper deposits can be comparable with Central Africa Copper Belt.
7. The formation of the Paleoproterozoic copper deposits in the Zhongtiaoshan region is closely associated with the regional metamorphism event during ~1.85 Ga. The mineralization at metamorphism stage has formed the main orebodies of the "Hu-Bi" type deposits, Henglingguan Cu deposit, and Huping Cu deposit.

Acknowledgments This study was financially supported by the National Basic Research Program of China (No. 2012CB416603). The Zhongtiaoshan Non-Ferrous Metals Group Co., Ltd. is thanked for the assistances during the field work. Special thanks are due to Prof. Chen Bin for his constructive comments. We also thank Prof. Sun Weidong and Prof. Chen Huayong from Guangzhou Institute of Geochemistry, Chinese Academy of Sciences for their constructive suggestions.

References

Audétat, A., Günther, D., & Heinrich, C. A. (1998). Formation of a magmatic-hydrothermal ore deposit: Insights with LA-ICP-MS analysis of fluid inclusions. *Science, 279*, 2091–2094.

Bai, J. (1997). Precambrian crustal evolution of the Zhongtiao Mountains. *Earth Science Frontiers, 4*, 281–289. (in Chinese).

Bell, K., & Simonetti, A. (2009). Source of parental melts to carbonatites—critical isotopic constraints. *Mineralogy & Petrology, 98*, 77–89.

Bodnar, R., Lecumberi-Sanches, P., Moncada, D., & Steele-MacInnis, M. (2014). Fluid inclusions in hydrothermal ore deposits. In *Treatise on geochemistry* (2nd ed., pp. 119–142).

Brown, A. C. (1992). Sediment-hosted stratiform copper deposits. *Geoscience Canada, 19*.

Brown, A. C. (1997). World-class sediment-hosted stratiform copper deposits: Characteristics, genetic concepts and metallotects. *Australian Journal of Earth Sciences, 44*, 317–328.

Cen, B. X., & Yang, Y. (1993). Analysis on time structure and regularity of mineralization evolution of Hu-Bi type copper deposits in Zhongtiao Mountains, Shanxi. *Earth Science—Journal of China University of Geosciences, 18*, 209–210. (in Chinese).

Chen, W. M., & Li, S. P. (1998). Rhenium-Osmium isotopic ages of sulfides from the Tongkuangyu porphyry copper deposit in the Zhongtiao Mountain. *Mineral Deposits, 17*, 224–228. (in Chinese).

Chen, W. M., Zhang, C. X., Lu, J. R., Cao, Y. J., Li, S. P., Cui, W. B., et al. (1998). Polygenetic mineralization of the early Proterozoic Tongkuangyu Metaporphyry copper deposit in the Zhongtiao Mountains, Shanxi Province. *Acta Geologica Sinica, 72*, 154–168. (in Chinese).

Chi, G. X., & Ni, P. (2007). Equations for calculation of NaCl/(Nacl + $CaCl_2$) ratios and salinities from hydrohalite-melting and ice-melting temperatures in the H_2O-NaCl-$CaCl_2$ system. *Acta Petrologica Sinica, 23*, 33–37.

Clayton, R. N., Mayeda, T. K., & O'Neil, J. R. (1972). Oxygen isotope exchange between quartz and water. *Journal of Geophysical Research Atmospheres, 77*, 3057–3067.

Compilation Group of the Geology of Copper Deposits of the Zhongtiao Mountains. (1978). *Geology of copper deposits in the Zhongtiao Mountains* (pp. 25–86). Beijing: Geological Publishing House (in Chinese).

Coplen, T. B., Kendall, C., & Hopple, J. (1983). Comparison of stable isotope reference samples. *Nature, 302*, 236–238.

Crerar, D. A., & Barnes, H. (1976). Ore solution chemistry; V, Solubilities of chalcopyrite and chalcocite assemblages in hydrothermal solution at 200 degrees to 350 degrees C. *Economic Geology, 71*, 772–794.

Drummond, S., & Ohmoto, H. (1985). Chemical evolution and mineral deposition in boiling hydrothermal systems. *Economic Geology, 80*, 126–147.

Du, L. L., Yang, C. H., Guo, J. H., Wang, W., Ren, L. D., Wan, Y. S., et al. (2010). The age of the base of the Paleoproterozoic Hutuo Group in the Wutai Mountains area, North China Craton: SHRIMP zircon U-Pb dating of basaltic andesite. *Chinese Science Bulletin, 55*, 1782–1789.

Du, L. L., Yang, C. H., Wang, W., Ren, L. D., Wan, Y. S., Wu, J. S., et al. (2012). Paleoproterozoic rifting of the North China Craton: Geochemical and zircon Hf isotopic evidence from the 2137 Ma Huangjinshan A-type granite porphyry in the Wutai area. *Journal of Asian Earth Sciences, 72*, 190–202.

El Desouky, H. A., Muchez, P., Boyce, A. J., Schneider, J., Cailteux, J. L., Dewaele, S., et al. (2010). Genesis of sediment-hosted stratiform copper–cobalt mineralization at Luiswishi and Kamoto, Katanga Copperbelt (Democratic Republic of Congo). *Mineralium Deposita, 45*, 735–763.

El Desouky, H. A., Muchez, P., & Cailteux, J. (2009). Two Cu–Co sulfide phases and contrasting fluid systems in the Katanga Copperbelt, Democratic Republic of Congo. *Ore Geology Reviews, 36*, 315–332.

Goodfellow, W., & Lydon, J. (2007). Sedimentary exhalative (SEDEX) deposits. Mineral deposits of Canada: A synthesis of major deposit types, district metallogeny, the evolution of geological provinces, and exploration methods. *Geological Association of Canada, Mineral Deposits Division, Special Publication*, 163–183.

He, Y., Zhao, G., Sun, M., & Wilde, S. A. (2008). Geochemistry, isotope systematics and petrogenesis of the volcanic rocks in the Zhongtiao Mountain: An alternative interpretation for the evolution of the southern margin of the North China Craton. *Lithos, 102*, 158–178.

Heinrich, C., Günther, D., Audétat, A., Ulrich, T., & Frischknecht, R. (1999). Metal fractionation between magmatic brine and vapor, determined by microanalysis of fluid inclusions. *Geology, 27*, 755–758.

Heinrich, C. A. (2007). Fluid-fluid interactions in magmatic-hydrothermal ore formation. *Reviews in Mineralogy and Geochemistry, 65*, 363–387.

Henley, R., & Mcnabb, A. (1978). Magmatic vapor plumes and ground-water interaction in porphyry copper emplacement. *Economic Geology, 73*, 1–20.

Hitzman, M., Kirkham, R., Broughton, D., Thorson, J., & Selley, D. (2005). The sediment-hosted stratiform copper ore system. *Economic Geology, 100* (*Anniversary Volume*), 609–642.

Hitzman, M. W., Selley, D., & Bull, S. (2010). Formation of sedimentary rock-hosted stratiform copper deposits through Earth history. *Economic Geology, 105*, 627–639.

Holland, H. D. (1972). Granites, solutions, and base metal deposits. *Economic Geology, 67*, 281–301.

Hou, Z., Yang, Z., Lu, Y., Kemp, A., Zheng, Y., Li, Q., et al. (2015). A genetic linkage between subduction-and collision-related porphyry Cu deposits in continental collision zones. *Geology, 43*, 247–250.

Hou, Z. Q., Pan, X. F., Yang, Z. M., & Qu, X. M. (2007). Porphyry Cu-(Mo-Au) deposits no related to oceanic-slab subduction: Examples from Chinese porphyry depositsin continental settings. *Geoscience, 21*, 332–351. (in Chinese).

Hu, W. X., & Sun, D. Z. (1987). Mineralization and evolution of the early proterozoic copper deposits in the Zhongtiao Mountains. *Acta Geologica Sinica,* 152–165 (in Chinese).

Huang, C. K., Bai, Y., Zhu, Y. S., Wang, H. Z., & Shang, X. Z. (2001). *Copper deposit of China* (pp. 142–152). Beijing: Geological Publishing House.

Huang, W. P., Sun, F. Y., Zhang, H., & Wang, J. L. (2013). Petrology and geochemistry characteristic of Hu-Bi copper deposit in Zhongtiao mountains of Shanxi Province. *Global Geology, 32*, 212–220. (in Chinese).

Huston, D. L., Pehrsson, S., Eglington, B. M., & Zaw, K. (2010). The geology and metallogeny of volcanic-hosted massive sulfide deposits: Variations through geologic time and with tectonic setting. *Economic Geology, 105*, 571–591.

Jiang, Y., Niu, H., Bao, Z., Li, N., Shan, Q., & Yang, W. (2014a). Fluid evolution of the Tongkuangyu porphyry copper deposit in the Zhongtiaoshan region: Evidence from fluid inclusions. *Ore Geology Reviews, 63*, 498–509.

Jiang, Y., Niu, H., Bao, Z., Li, N., Shan, Q., Yang, W., et al. (2014b). Fluid evolution of the Paleoproterozoic Hujiayu copper deposit in the Zhongtiaoshan region: Evidence from fluid inclusions and carbon–oxygen isotopes. *Precambrian Research, 255*, 734–747.

Jiang, Y. H., Luo, Y., Niu, H. C., Guo, S. L., & Li, N. B. (2013). Study on fluid inclusions from the Luojiahe copper deposit in Zhongtiaoshan region. *Acta Petrologica Sinica, 29*, 2583–2592. (in Chinese).

Lai, J., & Chi, G. (2007). CO_2-rich fluid inclusions with chalcopyrite daughter mineral from the Fenghuangshan Cu–Fe–Au deposit,

China: Implications for metal transport in vapor. *Mineralium Deposita, 42*, 293–299.

Land, L. S., & Milliken, K. L. (1981). Feldspar diagenesis in the Frio Formation, Brazoria County, Texas Gulf Coast. *Geology, 9*, 314–318.

Leach, D. L., Bradley, D. C., Huston, D., Pisarevsky, S. A., Taylor, R. D., & Gardoll, S. J. (2010). Sediment-hosted lead-zinc deposits in Earth history. *Economic Geology, 105*, 593–625.

Lerchbaumer, L., & Audétat, A. (2012). High Cu concentrations in vapor-type fluid inclusions: An artifact? *Geochimica et Cosmochimica Acta, 88*, 255–274.

Li, N. B., Luo, Y., Jiang, Y. H., Guo, S. L., & Niu, H. C. (2013). Zircon U-Pb geochronology and Hf isotopic characteristic of metamorphic quartz-monzonite porphyry from Tongkuangyu area, Zhongtiao Mountain and their geological implications. *Acta Petrologica Sinica, 29*, 2416–2424. (in Chinese).

Liang, H. Y., Sun, W. D., Su, W. C., & Zartman, R. E. (2009). Porphyry copper-gold mineralization at Yulong, China, promoted by decreasing redox potential during magnetite alteration. *Economic Geology, 104*, 587–596.

Liu, C. H., Zhao, G. C., Sun, M., Zhang, J., & Yin, C. (2012). U-Pb geochronology and Hf isotope geochemistry of detrital zircons from the Zhongtiao Complex: Constraints on the tectonic evolution of the Trans-North China Orogen. *Precambrian Research, 222–223*, 159–172.

Liu, X., Fan, H.-R., Santosh, M., Yang, K.-F., Qiu, Z.-J., Hu, F.-F., et al. (2015). Geological and geochronological constraints on the genesis of the giant Tongkuangyu Cu deposit (Palaeoproterozoic), North China Craton. *International Geology Review,* 1–16.

Longstaffe, F. J. (1989). Stable isotopes as tracers in clastic diagenesis. In I. E. Hutcheon1 (Ed.), *Short course in burial diagenesis: Mineral Association of Canada Short Course* (pp. 201–284).

Lowenstern, J. B. (2001). Carbon dioxide in magmas and implications for hydrothermal systems. *Mineralium Deposita, 36*, 490–502.

Melezhik, V. A., Fallick, A. E., Medvedev, P. V., & Makarikhin, V. V. (1999). Extreme $^{13}C_{carb}$ enrichment in ca. 2.0 Ga magnesite–stromatolite–dolomite–'red beds' association in a global context: a case for the world-wide signal enhanced by a local environment. *Earth-Science Reviews, 48*, 71–120.

Moore, J. (2010). Comparative study of the Onganja copper mine, Namibia: A link between Neoproterozoic mesothermal Cu (-Au) mineralization in Namibia and Zambia. *South African Journal of Geology, 113*, 445–460.

Mungall, J. E. (2002). Roasting the mantle: Slab melting and the genesis of major Au and Au-rich Cu deposits. *Geology, 30*, 915–918.

Oakes, C. S., Bodnar, R. J., & Simonson, J. M. (1990). The system NaCl-$CaCl_2$-H_2O: I. The ice liquidus at 1 atm total pressure. *Geochimica et Cosmochimica Acta, 54*, 603–610.

Oliver, N. H., Rawling, T. J., Cartwright, I., & Pearson, P. J. (1994). High-temperature fluid-rock interaction and scapolitization in an extension-related hydrothermal system, Mary Kathleen, Australia. *Journal of Petrology, 35*, 1455–1491.

O'Neil, J. R., Clayton, R. N., & Mayeda, T. K. (1969). Oxygen isotope fractionation in divalent metal carbonates. *The Journal of Chemical Physics, 51*, 5547.

Pirajno, F. (2009). *Hydrothermal processes and mineral systems* (pp. 581–726). Heidelberg: Springer.

Pollard, P. J. (2001). Sodic (–calcic) alteration in Fe-oxide–Cu–Au districts: An origin via unmixing of magmatic H_2O–CO_2–NaCl ± $CaCl_2$–KCl fluids. *Mineralium Deposita, 36*, 93–100.

Robb, L. (2013). *Introduction to ore-forming processes*. New York: Wiley.

Roedder, E. (1971). Fluid inclusion studies on the porphyry-type ore deposits at Bingham, Utah, Butte, Montana, and Climax, Colorado. *Economic Geology, 66*, 98–118.

Rui, Z. Y., Huang, C. K., Qi, G. M., Xu, J., Zhang, H. T. (1984). *Porphyry copper (molybdenum) deposits of China* (pp. 279–315). Beijing: Geological publishing house (in Chinese).

Rui, Z. Y., Li, Y. Q., Wang, L. S., & Wang, Y. T. (2003). Approach to ore-forming conditions in light of ore fluid inclusions. *Mineral Deposits, 22*, 13–23. (in Chinese).

Selley, D., Broughton, D., Scott, R., Hitzman, M., Bull, S., Large, R., et al. (2005). A new look at the geology of the Zambian Copperbelt. *Society of Economic Geologists Inc., 100 (Anniversary Volume)*, 965–1000.

Sillitoe, R. H. (1997). Characteristics and controls of the largest porphyry copper-gold and epithermal gold deposits in the circum-Pacific region. *Australian Journal of Earth Sciences, 44*, 373–388.

Sillitoe, R. H. (2010). Porphyry Copper Systems. *Economic Geology, 105*, 3–41.

Suleimenov, O., & Krupp, R. (1994). Solubility of hydrogen sulfide in pure water and in NaCl solutions, from 20 to 320 °C and at saturation pressures. *Geochimica et Cosmochimica Acta, 58*, 2433–2444.

Sun, D. Z., Hu, W. X. (1993). *Precambrian geochronology, chronotectonic framework and model of chronocrustal structure of the Zhongtiao Mountains* (1st ed., pp. 1–102). Beijing: Geological publishing house (in Chinese).

Sun, D. Z., Hu, W. X., Tang, M., Zhao, F. Q., & Condie, K. C. (1990). Origin of Late Archean and Early Proterozoic rocks and associated mineral deposits from the Zhongtiao Mountains, east-central China. *Precambrian Research, 47*, 287–306.

Sun, D. Z., Li, H. M., Lin, Y. X., Zhou, H. F., Zhao, F. Q., & Tang, M. (1991). Precambrian geochronology, chronotectonic framework and model of chronocrustal structure of the Zhongtiao Mountains. *Acta Petrologica Sinica, 3*, 216–231. (in Chinese).

Sun, H. T., & Ge, C. H. (1990). *Hydrothermal exhalative copper deposits in Zhongtiaoshan District, Shanxi Province* (1st ed., pp. 101–106). Beijing: Beijing Science and Technology Press (in Chinese).

Sun, J. G., Li, H. Y., Liu, X. H., Xie, K. Q., Li, B. L., & Yin, D. W. (2014). Alteration and mineralization characteristics of Tongkuangyu copper deposit in Zhongtiao Mountain, Shanxi Province. *Mineral Deposits, 33*, 1306–1324. (in Chinese).

Sun, J. Y., Ji, S. K., & Zhen, Y. Q. (1995). *The copper deposits in the Zhongtiao rift* (1st ed., pp. 84–140). Beijing: Geological publishing house (in Chinese).

Sun, W. D., Arculus, R. J., Kamenetsky, V. S., & Binns, R. A. (2004). Release of gold-bearing fluids in convergent margin magmas prompted by magnetite crystallization. *Nature, 431*, 975–978.

Sun, W. D., Liang, H. Y., Ling, M. X., Zhan, M. Z., Ding, X., Zhang, H., et al. (2013). The link between reduced porphyry copper deposits and oxidized magmas. *Geochimica et Cosmochimica Acta, 103*, 263–275.

Tang, H.-S., Chen, Y.-J., Santosh, M., Zhong, H., & Yang, T. (2013). REE geochemistry of carbonates from the Guanmenshan Formation, Liaohe Group, NE Sino-Korean Craton: Implications for seawater compositional change during the Great Oxidation Event. *Precambrian Research, 227*, 316–336.

Taylor, H. (1974). The application of oxygen and hydrogen isotope studies to problems of hydrothermal alteration and ore deposition. *Economic Geology, 69*, 843–883.

Wang, Z., & Wen, G. (1957). Zhongtiaoshan style Porphyry copper deposit. *Acta Geologica Sinica, 4*, 401–421. (in Chinese).

Wei, D. Y., Xing, S. C., & Liang, X. (1984). The implications of the Hu-Bi type copper deposits in the Zhongtiaoshan region. *Acta of Hebei Geological College, 25*, 30–41. (in Chinese).

Williams-Jones, A. E., & Heinrich, C. A. (2005). Vapor transport of metals and the formation of magmatic-hydrothermal ore deposits. *Society of Economic Geologists Inc*, *100* (*Anniversary Volume*), 1287–1312.

Xie, J. R. (1963). Problems pertaining to geology and ore deposits of a copper deposit in Shansi province. *Science in China, Series A,* 1345–1355.

Xu, Q. L. (2010). *Study on the geological characteristics and ore genesis of Tongkuangyu copper deposit in the Zhongtiaoshan Mountains, Shanxi Province* (pp. 59–71). Master thesis, Jilin University (in Chinese).

Xu, W. X., Guo, X. S., Ji, S. K., Lu, J. R., & Li, S. P. (1995). Geochemstry study of Tongkuangyu Cu deposit. *Mineral Resources Geology, 9*, 77–86. (in Chinese).

Yang, Z.-M., Lu, Y.-J., Hou, Z.-Q., & Chang, Z.-S. (2015). High-Mg diorite from Qulong in southern Tibet: Implications for the genesis of adakite-like intrusions and associated porphyry Cu deposits in collisional orogens. *Journal of Petrology,* egu076.

Zhai, M. G., Li, T. S., Peng, P., Hu, B., Liu, F., & Zhang, Y. (2010). Precambrian key tectonic events and evolution of the North China Craton. *Geological Society, London, Special Publications, 338*, 235–262.

Zhai, M. G., & Santosh, M. (2011). The early Precambrian odyssey of the North China Craton: A synoptic overview. *Gondwana Research, 20*, 6–25.

Zhai, M. G., & Santosh, M. (2013). Metallogeny of the North China Craton: Link with secular changes in the evolving Earth. *Gondwana Research, 24*, 275–297.

Zhang, H. (2012). *Metallogenesis of paleoproterozoic copper deposits in the northern Zhongtiaoshan Mountains, Shanxi Province* (pp. 119–123). PhD thesis, Jilin University (in Chinese).

Zhao, T. P., Zhou, M. F., Zhai, M. G., & Xia, B. (2002). Paleoproterozoic rift-related volcanism of the Xiong'er Group, North China Craton: Implications for the breakup of Columbia. *International Geology Review, 44*, 336–351.

Zhao, X.-F., Zhou, M.-F., Hitzman, M. W., Li, J.-W., Bennett, M., Meighan, C., et al. (2012). Late Paleoproterozoic to early Mesoproterozoic Tangdan sedimentary rock-hosted strata-bound copper deposit, Yunnan Province, Southwest China. *Economic Geology, 107*, 357–375.

Zhen, Y. Q., & Shu, Q. A. (2006). Oxygen isotope implications for the fluid of copper ore in Zhongtiaoshan area. *Geological Survey and Research, 29*, 30–37. (in Chinese).

Zheng, Y. F., & Chen, J. F. (2000). *Stable isotope geochemistry* (1st ed., pp. 291–296). Beijing: Science press.

Zhou, X. (2007). *Studies on Geologieal-geoehemical charaeteristies of Tongkuangyu iron oxide-copper-gold deposit in Zhongtiao Mountains, Shanxi Province*. Master thesis, Central South University (in Chinese).

The Paleoproterozoic Continental Evolution in the Southern North China Craton: Constrains from Magmatism and Sedimentation

10

Yanyan Zhou, Qianying Sun, Taiping Zhao, and Chunrong Diwu

Abstract

Recently, increasing lines of evidence for the 2.45–2.00 Ga magmatic rocks and Paleoproterozoic low-grade metasedimentary sequences have been identified, which can provide diagnostic constrains on the debate on the Paleoproterozoic (2.45–2.00 Ga) evolutional regime of the NCC. The widespread 2.45–2.20 Ga magmatisms occurred in the southern NCC mainly include TTG, dioritic-gabbroic gneiss, amphibolite, and high-K granites. The 2.45–2.20 Ga TTG or TTG-like gneisses show variable Mg# values, low Cr, Ni, and high Rb/Sr ratios, suggesting that they most likely derived from partial melting of basaltic lower crust with juvenile materials addition. The 2.45–2.20 Ga dioritic-gabbroic gneisses show the similar geochemical characteristics with adakitic rocks from thickened lower crust. Their $\varepsilon_{Hf}(t)$ and $\varepsilon_{Nd}(t)$ values are variable, and have weak Ta enrichment, and not obvious negative Nb anomalies, suggesting they were produced by partial melting of metasomatized lithospheric mantle. The 2.45–2.20 Ga amphibolites are consistent with magma derivation from MORB-like mantle wedge. The 2.45–2.20 Ga (high-K) calc-alkaline granites are representative of syn-collisional granites, and derived from older crust with variable mixing of a juvenile melt in a subduction-collision related setting. The 2.20–2.00 Ga magmatism reveals a major period of crustal reworking, rather than one of crustal addition. The 2.20–2.00 Ga monzonites have mixed IAB- and OIB-like geochemical signatures, possibly related to extension and thinning of the lithosphere and upwelling of asthenosphere. The 2.20–2.00 Ga potassic granites belong to highly fractionated aluminous A-type granite, and formed in an extensional-rift setting. As indicated by the zircon in situ Hf isotopic compositions, the injection of basaltic melt into the crust has been widely considered as an important mechanism to generate silicious melts. The 2.20–2.00 Ga tonalite would be derived from partial melting of delaminated lower crust. The temporal change from mostly 2.45–2.20 Ga low-K igneous rocks (TTG) to 2.20–2.0 Ga mostly high-K igneous rocks in the southern segment of the NCC indicates a tectonic transformation from accretionary orogenesis (ca. 2.30 Ga) to extensional

Y. Zhou (✉)
State Key Laboratory of Lithospheric Evolution,
Institute of Geology and Geophysics,
Chinese Academy of Sciences, Beijing, 100029, China
e-mail: llylz_b3@163.com

Q. Sun · T. Zhao
Key Laboratory of Mineralogy and Metallogeny,
Guangzhou Institute of Geochemistry,
Chinese Academy of Sciences, Guangzhou, 510640, China

C. Diwu
State Key Laboratory of Continental Dynamics,
Department of Geology, Northwest University,
Xi'an, 710069, China

M. Zhai et al. (eds.), *Main Tectonic Events and Metallogeny of the North China Craton*,
Springer Geology, DOI 10.1007/978-981-10-1064-4_10

regimes (ca. 2.10 Ga). On the other hand, provenances, depositional ages and tectonic settings of low-grade Paleoproterozoic metasedimentary units in the NCC can also provide rigorous constraints on the tectonic evolution in the period between 2.45 and 2.00 Ga. In the Henan-Shaanxi province on the southern NCC, the Paleoproterozoic sedimentary sequences include the Shangtaihua Group, the Songshan Group, the Yinyugou Group, and the Tietonggou Formation. The low-grade metasedimentary Songshan Group deposited after 2.35 Ga and before 1.78 Ga and sourced from felsic rocks including major 3.00–2.40 Ga TTG gneisses, 2.40–1.95 Ga granitoid plutons and meta-rhyolites of the Dengfeng, Zhongtiao and Taihua complexes in the southern NCC, and minor 3.70–3.00 Ga transported exotic Paleoarchean and Mesoarchean crustal materials because no lithologies or zircons with such age founded in study areas. The Tietonggou Formation deposited at 1.91–1.80 Ga, with detrital zircon age peak of ~2.10 Ga which possibly sourced from ~2.10 Ga lithologic units in the south of NCC. The depositional ages of the Paleoproterozoic low-grade metasedimentary units in the NCC are constrained at a certain period of 2.35–1.78 Ga, which overlaps with the stage of subduction-collision related 2.45–2.20 Ga magmatisms and rift setting related 2.20–2.00 Ga magmatisms. The detrital zircon Hf isotopes of the low-grade sediments varied mainly toward the reduction of the radiogenic Hf isotope and gradually show a similar trend of the isotope trajectories of crustal evolution. Like previous studies, all these groups were deposited in basin settings which were not simple long-lived foreland basins. Combining with 2.45–2.00 Ga igneous rocks, they may evolved from back-arc or intra-arc basins developing at the subduction-collision stage (from ~2.45 Ga) to rift stage (from ~2.20 Ga) and then to foreland basins at the collision stage (from ~1.85 to ~1.80 Ga).

Keywords
Continental evolution • Southern NCC • Magmatism • Low-grade metasedimentary sequences

10.1 Introduction

There is a broad consensus that the NCC does not have a uniform basement but formed by the assembly of several microcontinental blocks. However, the tectonic subdivision of the microcontinental blocks and the timing of their collision are still controversial. Zhao et al. (2001, 2005) divided the NCC into the Eastern Block (EB) and Western Block (WB) separated by the Trans-North China Orogen on the basis of tectonics, lithology and metamorphism. They suggested that the EB and WB developed independently during the Neoarchean (2.70–2.50 Ga), and then experienced long east-dipping subduction and collided to form the NCC at ca. 1.85 Ga (e.g., Guo et al. 2001; Zhao et al. 2005; Zhao et al. 2006b; Kröner et al. 2005; Kusky et al. 2007). However, other studies suggested that the main body of the NCC formed through amalgamation of seven micro-blocks at the end of the Neoarchean (ca. 2.50 Ga) (Kusky et al. 2001; Li et al. 2002; Kusky and Li 2003; Zhai and Liu 2003). The NCC behaved as a stable continental block in general during the interval of ~2.45–2.35 Ga (Condie 2004). Subsequently, continental rifting was initiated in the interval ~2.35–2.00 Ga, similar to the other cratons of the world (Condie and Kröner 2008), and then experienced subduction-accretion-collision tectonics (from 1.95 to 1.80 Ga) to form a uniform block (Kusky et al. 2001; Li et al. 2002; Kusky and Li 2003; Zhai and Liu 2003; Zhai 2004, 2008), which was followed by plume-triggered extension and rifting at ~1.75 Ga (Zhao et al. 2002). Therefore, the Paleoproterozoic (2.45–2.00 Ga) tectonic regime is important to provide diagnostic constraints on the debates on the Precambrian evolution models of the NCC aforementioned.

Nevertheless, although the original time framework and tectonic processes from 2.45 to 2.00 Ga have been hypothesized like mentioned above, the property of the tectonothermal events is still controversial, because the 2.45–2.00 Ga tectono-magmatic events have been occasionally reported from the NCC before, their distribution and petrogenesis are poorly understood due to lack of robust geochronological, petrological and geochemical data. In the last decades, an increasing lines of evidence for the 2.45–2.00 Ga plutonic and volcanic rocks, especially those aged of 2.20–2.00 Ga, have been identified (Fig. 10.1; e.g., the Liaoji granitoids and Nanying granitic gneiss in the eastern and northern NCC, respectively; Li and Zhao 2007; Zhao et al. 2008), and thus potentially could provide important

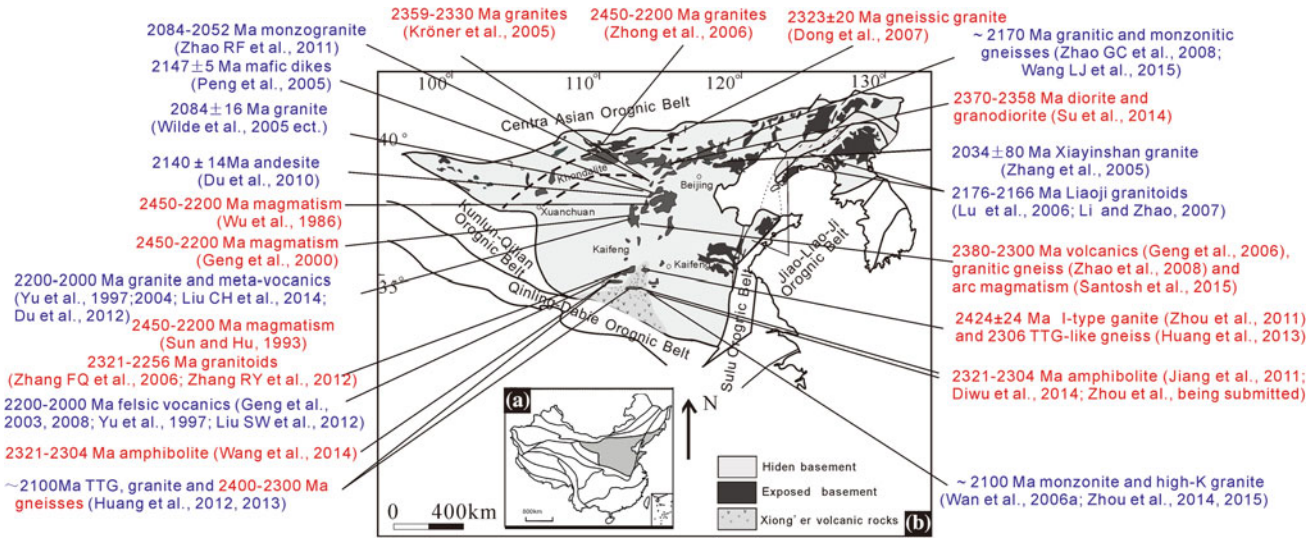

Fig. 10.1 The reported 2.45–2.00 Ga magmatism in the NCC

information for understanding the evolution process of the NCC in the possible geological age gap from 2.45 to 2.00 Ga (e.g., Condie et al. 2009). The petrogenesis and tectonic affinity of the ca. 2.45–2.00 Ga igneous rocks has long been controversial, partly resulting in the different models for the tectonic evolution of the craton. These rocks were previously suggested to have formed in a foreland basin along a passive margin (Zhai and Liu 2003; Peng et al. 2005), related to collision between a continent and an island arc (Hu 1992; Bai et al. 1993; Zhao et al. 2005, 2008; Liu et al. 2011a, b), or opening and closing of an intra-continental rift events after ~2.50 Ga cratonization of the NCC (e.g., Liu et al. 1997; Li et al. 1997, 1998, 2001a, b; Li and Yang 1997; Lu et al. 2004a, b, 2006; Yang et al. 2011; Peng and Palmer 2002; Li and Zhao 2007; Du et al. 2010, 2013), etc.

On the other hand, although most studies focused on high-grade metamorphic and igneous rocks to resolve the above controversy, provenances, depositional ages and tectonic settings of low-grade Paleoproterozoic metasedimentary units in the NCC (Fig. 10.2) can also provide rigorous constraints on the tectonic evolution in the period between 2.50 and 1.85 Ga. Zhai and Santosh (2013) reveal that the Paleoproterozoic (~2.35–2.00 Ga) rifts widened into ocean basins, following which subduction was initiated. As a result of rifting event, three main mobile belts formed, including the Jiaoliao, Jinyu and Fengzhen Mobile Belts in the northwestern NCC. The presentative volcanic-sedimentary sequences are the Liaohe and Fengzishan groups, the Lüliang, Hutuo and Zhongtiao groups, and the Fengzhen and Erdaowa groups, respectively. However, Li and Kusky (2007) considered that the lower part of the Hutuo Group has been the central sector of a Qinglong foreland basin related to the ~2.50 Ga collisional event, whereas the middle part has been deposited in a craton-wide graben system, and the upper part was formed in another foreland basin related to the collision of the northern margin of the NCC with part of the Columbia supercontinent at ~1.9 Ga. But for the 1.85 Ga collision model, the whole Hutuo Group was interpreted as a backarc and/or a retroarc foreland basin during the east-dipping subduction of the WB beneath the western margin of the EB from ~2.10 to ~1.85 Ga (Zhao et al. 2001; Wilde et al. 2004; Zhang et al. 2006; Liu et al. 2011b).

Our preliminary work on the Lushan, Wangwushan, Xiaoqinling and Xiong'ershan areas at the southern margin of the NCC has identified suites of magmatic rocks aged at 2.45–2.00 Ga, including granitoids, gabbro, diorite, monzonite, and metamorphic basaltic volcanics, undoubtedly providing key constraints on the early Paleoproterozoic evolution process of the NCC. In addition, similar to the Hutuo Group, the Songshan Group in Dengfeng Complex, the Zhongtiaoshan Group in Zhongtiao Complex and the Tietonggou Formation in Xiaoqinling area are low-grade metasedimentary units (Fig. 10.2, Sun et al. 1990; Sun and Hu 1993; Bai et al. 1997). Their detrital zircons can provide crucial information on the tectonic evolution of the NCC.

Combining to summarize previous systematic geochronology and geochemical data, this chapter plans to investigate the petrogenesis and genetic connections of the early Paleoproterozoic (2.45–2.00 Ga) igneous and low-grade metasedimentary rocks in the Songshan, Lushan, Xiong'ershan and Xiaoqinling areas in southern NCC. The ultimate aim is to explore the geodynamic background recorded in the magmatism and sedimentation during the period of 2.45–2.00 Ga and provide a better understanding of the early Paleoproterozoic crustal evolution in the NCC.

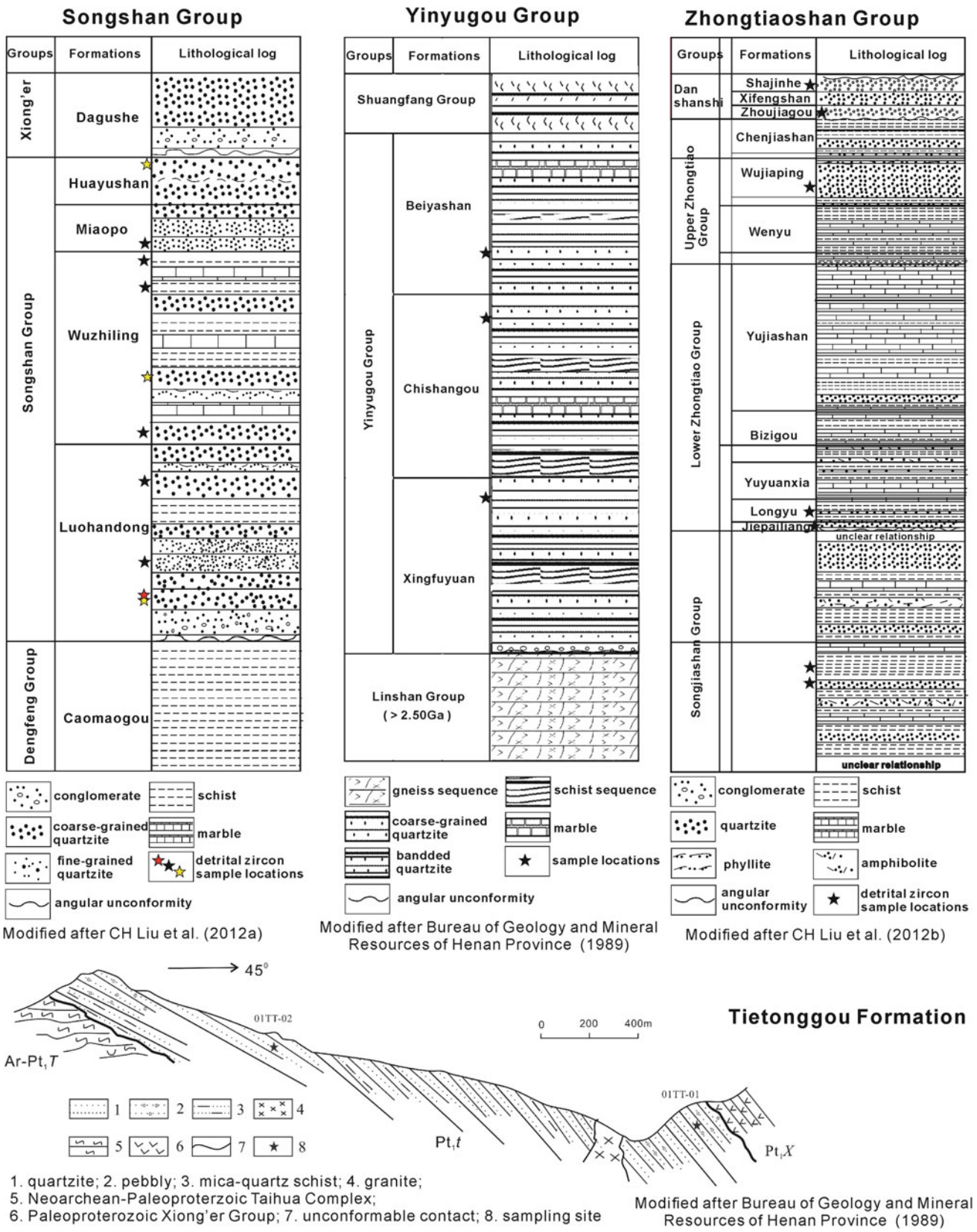

Fig. 10.2 Stratigraphic subdivision of the Songshan Group, Yinyugou Group, Zhongtiaoshan Group and Tietonggou Formation (detrital zircon samples in the Songshan area are from Diwu et al. 2008; Liu et al. 2012a; Zhang et al. 2014; in the Zhongtiaoshan area are from Liu et al. 2012a; in the Yinyugou area are from Sun et al. under review)

10.2 Regional Geology of the Southern NCC

The Precambrian basement in the southern NCC is composed of two distinct tectonic complexes: The Songshan Dengfeng Complex (Fig. 10.3) in the northeast and the Taihua Complex in the south (Fig. 10.4) (e.g., Zhang et al. 1985).

10.2.1 Dengfeng Complex

The Precambrian basement in the Songshan area (Fig. 10.3c) can be divided into Neoarchean (2.80–2.50 Ga) and Paleoproterozoic (2.50–1.80 Ga) basements (Fig. 10.3c) (Kröner et al. 1988; Xue et al. 1995, 2004; Wan et al. 2009; Zhou et al. 2009a, b). The Neoarchean basement is well exposed

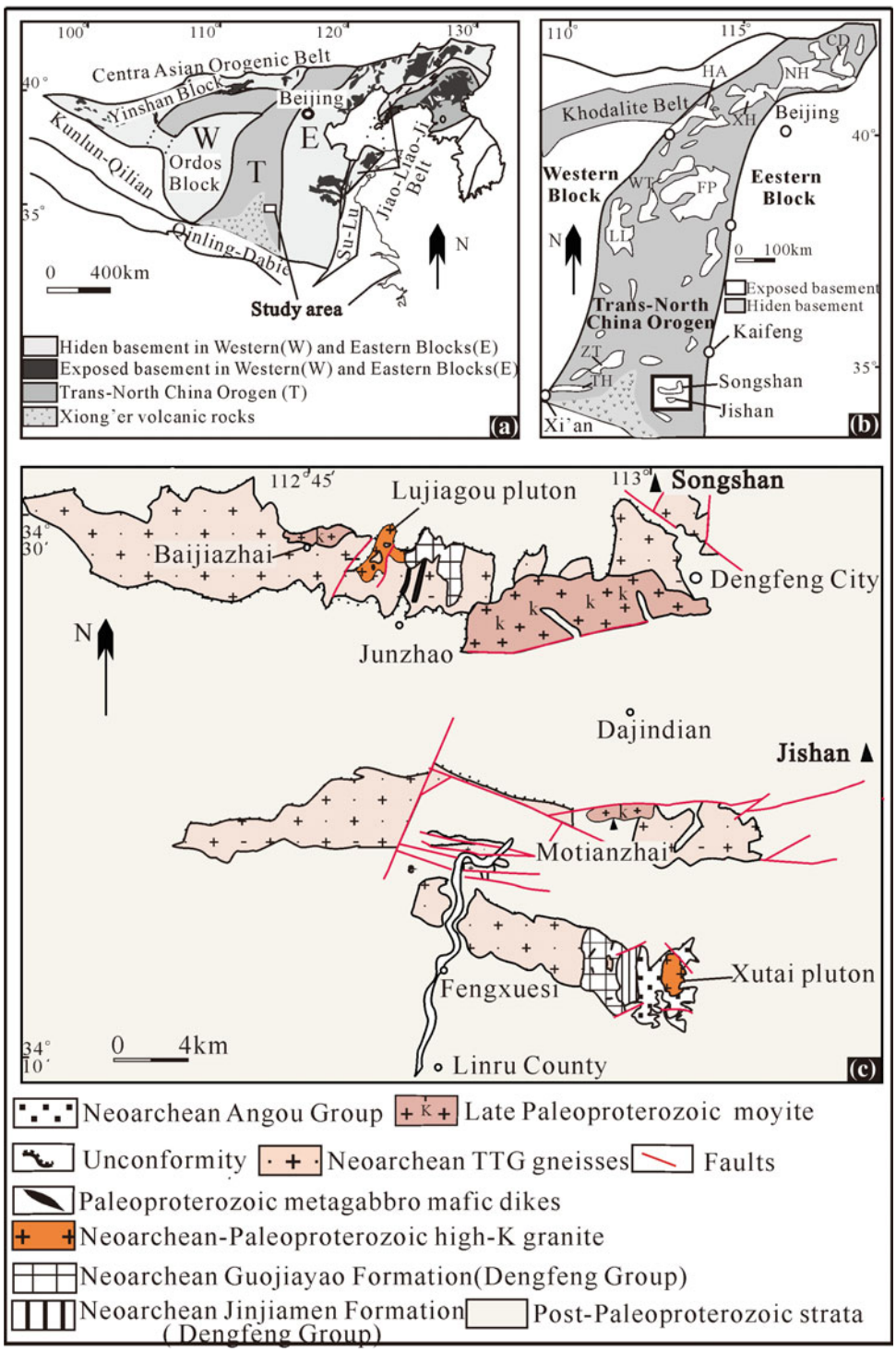

Fig. 10.3 **a** Tectonic framework of the NCC (modified after Zhao et al. 2005); **b** generalized geological map for the Trans-North China Orogen and **c** outcrop distribution map for the Dengfeng Complex (Modified after Regional Geology of Henan Province 1989)

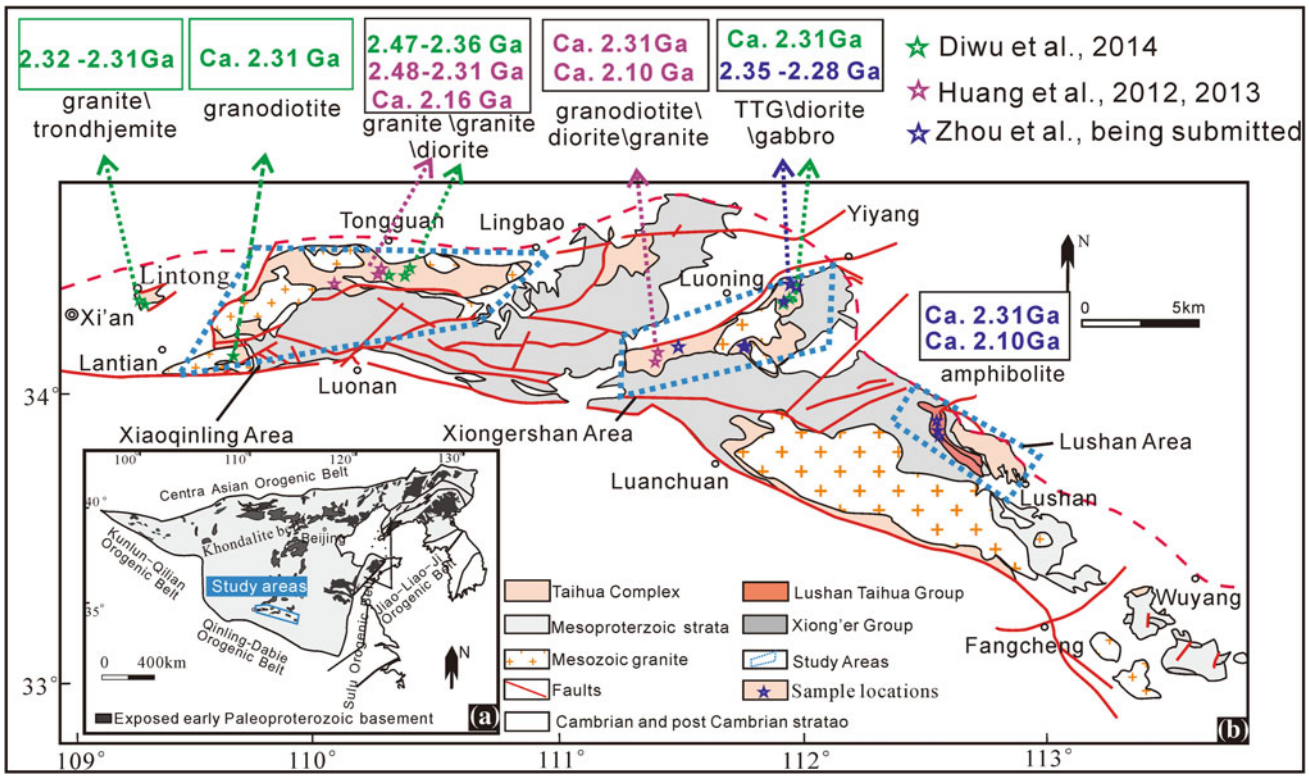

Fig. 10.4 Outcrop distribution map for the Taihua Complex (modified after Regional Geology of Henan Province 1989)

as a late Neoarchean granite–greenstone in the Dengfeng City (Zhang et al. 1985), and comprises 2.60–2.50 Ga plutonic rocks and supracrustal assemblages (Zhou et al. 2009a, b; Diwu et al. 2011). The Paleoproterozoic basement is composed of the Songshan Group, basaltic dyke swarms and granitoids (Guan 1996). The Songshan Group is a thick succession of green-schist facies metamorphosed clastic sedimentary rocks with thin layers of dolomites, and unconformably overlies the Dengfeng Group (Figs. 10.2 and 10.3; Ma et al. 1981). The group is subdivided into three formations, including Luohandong, Wuzhiling, Miaoposhan and Huayu formations (Fig. 10.2). The rocks have experienced strong fold deformation, forming a series overturned fold (Zhang 1951; Ma et al. 1981; Zhang et al. 1985). There are also two K-rich granite-granodiorite-monzonite (GGM) suites in the Songshan-Jishan area, including the 2399 ± 24 Ma Lujiagou pluton to the west of the Songshan area, and the other is the 2509 ± 33 Ma Xutai pluton to the east of the Jishan area (Zhou et al. 2011, Figs. 10.1 and 10.3).

10.2.2 Taihua Complex

The Taihua Complex crops out in several terranes distributing E-W-strikingly in the Lishan, Xiaoshan, Xiong'ershan, Lushan and Wuyang areas along the southern margin of the NCC, and extends to the east where Neoarchean Huoqiu Group in Anhui Province is outcropped (Fig. 10.4). The Taihua Complex is composed of gneisses and khondalite series, mainly including the early Precambrian medium–high- grade metamorphic rocks and a series of graphite-bearing gneisses, biotite gneisses, marbles and banded iron formations.

The Taihua Complex in the Lushan area is unconformably overlain by the Mesoproterozoic Ruyang Group and Neoproterozoic to Cambrian rock units in the northeast, and by the Mesoproterozoic Xiong'er Group in the southwest. The Taihua Complex in the Lushan area comprises >70 % TTG gneiss, supracrustal rocks and K-rich GGM suites (Xu et al. 1994; Shen 1994; Zhang et al. 2001). The TTG gneiss formed during 2.80–2.70 Ga is an indicator of the Archean tectonothermal events (e.g., Kröner et al. 1988; Sun et al. 1994; Liu et al. 2009; Diwu et al. 2010; Huang et al. 2010; Zhou et al. 2014a). The GGM suite includes at least two groups of granitoids aged at 2.76–2.57 Ga and ca. 2.10 Ga (Zhou et al. 2014a, 2015). The former intruded into the TTG gneiss and the latter intruded into the Shangtaihua Group. The supracrustal rocks are further subdivided into Neoarchean Xiataihua Group at the bottom (ca. 2.80 Ga, Kröner et al. 1988) and Paleoproterozoic Shangtaihua Group on the top (ca. 2.50–2.11 Ga, Shen 1994; Xue et al. 1995; Tu 1998). The Xiataihua Group comprises 2845–2620 Ma amphibolites (Liu et al. 2009;

Diwu et al. 2010; Huang et al. 2010) and gneisses occurring as enclaves in the widely distributed TTG gneiss. The Shangtaihua Group includes the Tieshanling, Shuidigou and Xuehuagou formations in ascending order, and is composed of graphite-bearing gneiss, marble, banded iron formation (BIF) and amphibolites (Zhang et al. 1985; Wu et al. 1998; Tu 1998; Wan et al. 2006a; Yang 2008), similar to the khondalite series of Southern India (Dash et al. 1987; Chacko et al. 1992). Graphite-garnet-sillimanite gneiss in the Shangtaihua Group contains detrital zircons yielding the age from 2.50 to 2.11 Ga with metamorphic rims of ca. 1.84 Ga (Wan et al. 2006a).

The Taihua Complex in the Xiong'ershan area was traditionally considered as a meta-volcano-sedimentary sequence (Zhang and Li 1998; Guan 1996; Ni et al. 2003), and was divided into the Caogou, Shiban'gou and Duan'gou "formations" from the bottom upwards (Zhang and Li 1998). The rock sequences are dominated by meta-mafic to intermediate magmatic rocks (amphibole-bearing gneiss and amphibolite), gray gneisses, subordinate meta-felsic magmatic rocks (biotite-plagioclase gneiss or granulite) and a suite of meta-felsic volcanic and sedimentary rocks (biotite ± garnet gneiss or granulite). Zircon U-Pb dating of the gray gneisses reveals at least two episodes of early Paleoproterozoic magmatism (2.30–2.32 and 2.07–2.19 Ga), each with distinct geochemical features (Huang et al. 2012b). The Taihua Complex in the Xiong'ershan area is unconformably or tectonically overlain by the widespread Xiong'er Group.

The Taihua Complex in the Xiaoqinling area was traditionally regarded as a meta-volcanic-sedimentary sequence, and was further subdivided into the Shangtaihua and Xiataihua "groups" according to rock types (Qi 1992; Guan 1996; Ding 1996), similar to those in the Lushan and Xiong'ershan areas (Huang et al. 2010; Huang et al. 2012b). The Shangtaihua "Group" consists of quartzite, metapelitic gneiss and schist, marble and iron formation, whereas the Xiataihua "Group" consists of meta-basic volcanic rocks (amphibolite) and intermediate to felsic gneisses (biotite–plagioclase gneiss and plagioclase–amphibole gneiss), with minor granulites (Qi 1992; Ding 1996). There is evidence of widespread migmatization in the Xiataihua "Group," and the amphibolite occurs as elongated enclaves in the gneisses, elongated parallel to the gneissic banding. The Taihua Complex in the Xiaoqinling area is unconformably covered by the Tietonggou Formation at Bayuan (Fig. 10.2), which consists dominantly of Paleoproterozoic metamorphosed clastic rocks. Mesozoic granites intrude the Taihua Complex in this area and are abundant throughout the eastern and western parts (Fig. 10.4).

10.3 Major Distribution of the Early Paleoproterozoic Magmatism in the Southern NCC and Their Geochronology and Geochemical Characteristics

10.3.1 The 2.45–2.20 Ga Magmatic Rocks

10.3.1.1 Major Distributions

During the interval of ~2.45–2.20 Ga, tectono-magmatic events have been occasionally reported from the NCC before the year of 2000, such as sporadically exposed 2.45–2.30 Ga magmatic rocks in the Wutai, Lüliang and Zhongtiaoshan areas (Wu et al. 1986; Sun and Hu 1993; Geng et al. 2000). But in recent years, magmatism is more widely discovered in the NCC than previously known (Fig. 10.1). For instance, the 2435 ± 16 Ma adakitic granite, 2426 ± 41 Ma sanukitoids, 2416–2330 Ma closepet granite and 2438–2231 Ma strongly peraluminous granite in the central segment of the northern NCC (Zhong 2006, Doctoral thesis). The 2358 ± 34 Ma dioritic gneiss and 2370 ± 24 Ma granodioritic gneiss in the Huan'an area (Su et al. 2014). The 2323 ± 20 Ma gneissic granite in the west segment of the Khondalite Belt (Dong et al. 2007). The 2359–2330 Ma granitic gneiss in the southern Hengshan Complex (Kröner et al. 2005). The 2364 ± 9 Ma Gaijiazhuang gneissic granite and volcanics (Geng et al. 2006), 2375 ± 10 Ma porphyritic granitic gneiss (Zhao et al. 2008) and 2.30–2.00 Ga arc magmatism (Santosh et al. 2015) from Lüliang area.

In addition to the northern and eastern NCC, the southern NCC also contains abundant Paleoproterozoic granitoids which mainly distributed around the Zhongtiaoshan, Lushan and Xiong'ershan areas, such as 2256 ± 35 Ma Hengling-guan granodioritic gneiss, 2321 ± 2 Ma Zhaizi tonalitic gneiss and Yanzhuang K-feldspar to monzonitic granitic gneisses (Zhao et al. 2006a; Zhang et al. 2012) in the Zhongtiaoshan area, 2424 ± 24 Ma high fractionated I-type ganite (Zhou et al. 2011) and 2306 ± 6 Ma TTG-like gneiss (Huang et al. 2013) in the Songshan area, 2321–2304 Ma amphibolite in the Xiong'ershan (Jiang et al. 2011) and Huanshan in Xiaoqinling areas (Wang et al. 2014), and 2.40–2.30 Ga gabbro-dioritic-TTG gneisses and granite (Huang et al. 2012a; Diwu et al. 2007; Huang et al. 2012b; Huang et al. 2013; Yu et al. 2013; Diwu et al. 2014, Figs. 10.1 and 10.4) from the Taihua Complex in the Lushan, Xiong'ershan and Xiaoqinling areas. In the western margin of the NCC, Dan et al. (2012) found 2.34–2.30 Ga basic-felsic magmatism in the Alxa area. In the year of 2015, the authors of this chapter also identified some new types of

igneous rocks aged from 2350 to 2270 Ma in the Xiong'ershan and Lushan areas, including trondhjemite, metabasic volcanic (amphibolite), quartz diorite, diorite, gabbro, and granitic gneisses (Zhou et al., being submitted, Figs. 10.1 and 10.4).

10.3.1.2 The Geochronology and Geochemical Characteristics and Rock Petrogenesis

TTG Gneisses

The ~2.45–2.20 Ga TTG gneisses are commonly associated with small mafic enclaves or sheets in the cores of domes or antiforms. They are represented by typical gray or banded gneisses with a mineral assemblage of plagioclase (45–60 %), quartz (25–30 %), biotite (5–10 %), K-feldspar (≤5 %), hornblende (1–5 %).

The TTG gneisses have undergone a complex history of high amphibolite- to granulite-facies metamorphism with strongly polyphase deformation and multiple foliations. The available geochemical data from the Taihua Complex in Xiong'ershan and Xiaoqinling areas and the Dengfeng Complex in Songshan area (Huang et al. 2012b, 2013; Zhou et al., being submitted) reveals that the trondhjemite and granodiorite show variable SiO_2 (57.68–75.31 wt%), moderate Al_2O_3 (13.65–17.37 wt%), CaO (1.11–6.56 wt%) and variable Mg# (11–53). The $Na_2O + K_2O$ are in range of 5.87–8.96 wt%. In the triangular diagram of normative feldspar composition, the rocks plot in the fields of trondhjemite, tonalite, and granodiorite (Fig. 10.5a). All the TTG, diorite, gabbro and granites show LREE enrichment (Huang et al. 2012b; Diwu et al. 2014; Zhou et al., being submitted). The Eu anomalies are variable (0.12–2.1), but mostly negative in the chondrite-normalized REE diagram (Fig. 10.6). The TTG rocks are characterized by pronounced negative Nb-Ta anomalies. Relative to HFSE, the LILE are rich with high Ba/Ta ratios. Their typical high Sr/Y and La/Yb ratios are indicative of various contributions of plagioclase, amphibole, or garnet during melting or fractional crystallization. They have low Cr and Ni concentrations and plot in the fields of thick lower crust-derived adakitic rocks (Fig. 10.7). In addition, typical slab melts generally have low Rb/Sr ratios (<0.05), in contrast to the wide range of Rb/Sr ratios (0.01–0.4) for adakites derived from thickened crust (Huang et al. 2009). The TTG gneisses in the Xiong'ershan and Dengfeng areas have high Rb/Sr ratios (0.07–1.06), thereby arguing against slab melting and indicating a large contribution from the thickened basaltic lower crust in their generation. Their low $\varepsilon_{Hf}(t)$ (−7.3–4.5) and $\varepsilon_{Nd}(t)$ values (−6.2–4.98; Diwu et al. 2007, 2014; Huang et al. 2012b, 2013) with Hf model ages varying from 3.22 to 2.72 Ga also support this model (Fig. 10.8). On the other hand, some samples have positive $\varepsilon_{Nd}(t)$ values, and the youngest Nd model age of 2.32 Ga is very close to the crystallization age, indicating the extensive participation of juvenile components in the source,

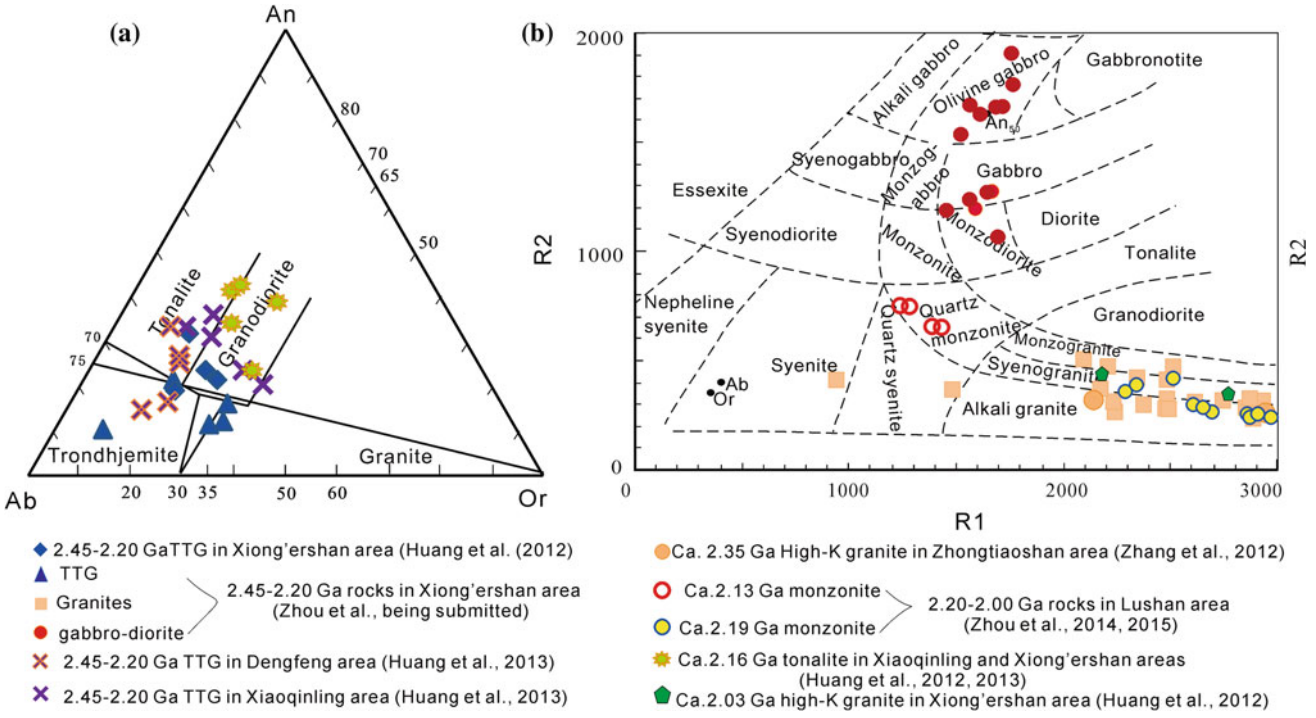

Fig. 10.5 Classification of the granitoids using **a** normative Anorthite (*An*), Albite (*Ab*), and Orthoclase (*Or*) and **b** Parameters R1 and R2 classification diagram of the potassic granite in the Southern NCC (after De La Roche et al. 1980). R1 = 4Si − 11(Na + K) − 2(Fe + Ti); R2 = 6Ca + 2 Mg + Al

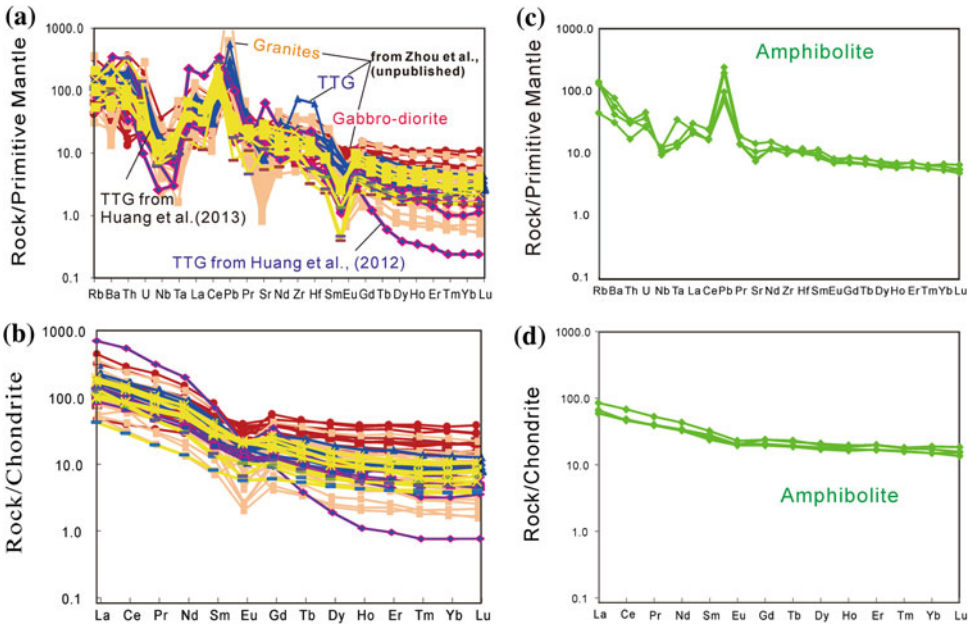

Fig. 10.6 **a** Chondrite-normalized REE and **b** primitive mantle-normalized trace elements patterns of the 2.45–2.20 Ga magmatism in the southern NCC (after Sun and McDonough 1989)

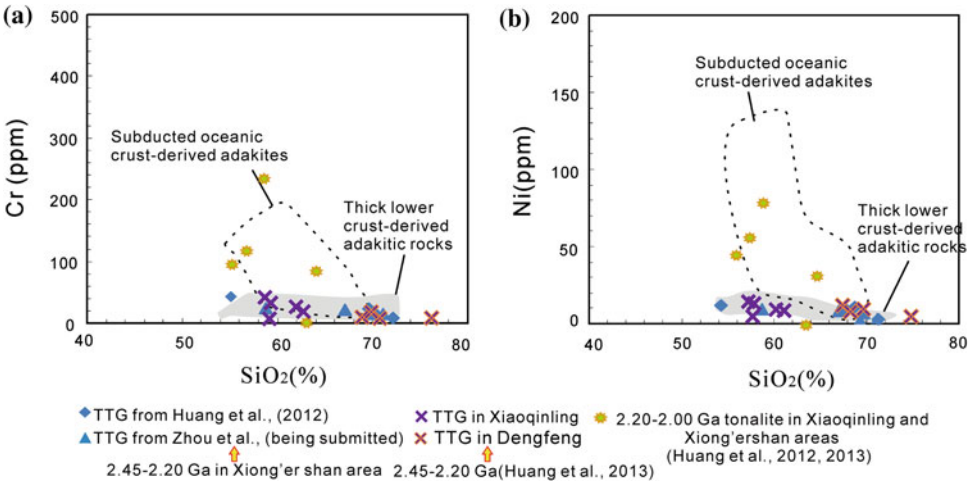

Fig. 10.7 **a** Plots of SiO_2 versus Cr and **b** SiO_2 versus Ni for the 2.45–2.00 Ga magmatism in the southern NCC. Fields of adakites are after Wang et al. (2006)

which could possibly be related to mafic magma underplating (Huang et al. 2012b). In the Rb-Y + Nb plot (Fig. 10.9a), all of the samples fall in the boundary field of VAG and post-COLG. In the Nb/Zr-Zr diagram (Fig. 10.9b), most samples are distributed within the boundary region between subduction and collision. Thus, the most effective thickening process is tectonic shortening at the convergence zone between two plates.

Dioritic-gabbroic Gneisses

The dioritic and gabbroic gneisses are commonly spatially associated with the TTG gneisses. The dioritic gneisses in the Xiong'ershan area are composed principally of plagioclase (50–60 %), hornblende (20–30 %), quartz (10–15 %), and biotite (<5 %). Apatite, zircon, magnetite, and allanite are accessory minerals (<1 %) found in both the dioritic and granitic gneisses. The gabbroic gneisses intruded into the TTG gneiss, and are composed principally of plagioclase (~45 %), pyroxenes (~45 %), hornblende (~5 %), and biotite (<5 %). Apatite, magnetite, and allanite are accessory minerals (<1 %). Both type of the rocks have SiO_2 (46.65–59.46 wt%), Al_2O_3 (11.95–18.38 wt%), and CaO (4.97–10.90 wt%), high TiO_2 (1.21 wt% on average). The total alkali is in range of 3.17–8.35 wt% with Mg number of 41–66 (Huang et al. 2012b; Zhou et al., being submitted). The diorite and gabbro also show the similar geochemical characteristics with adakitic rocks from thickened lower crust (Fig. 10.6, Zhou et al., being submitted). However, all of the gabbros have weak Ta enrichment, and not obvious negative Nb anomalies, arguing against subduction-zone setting and

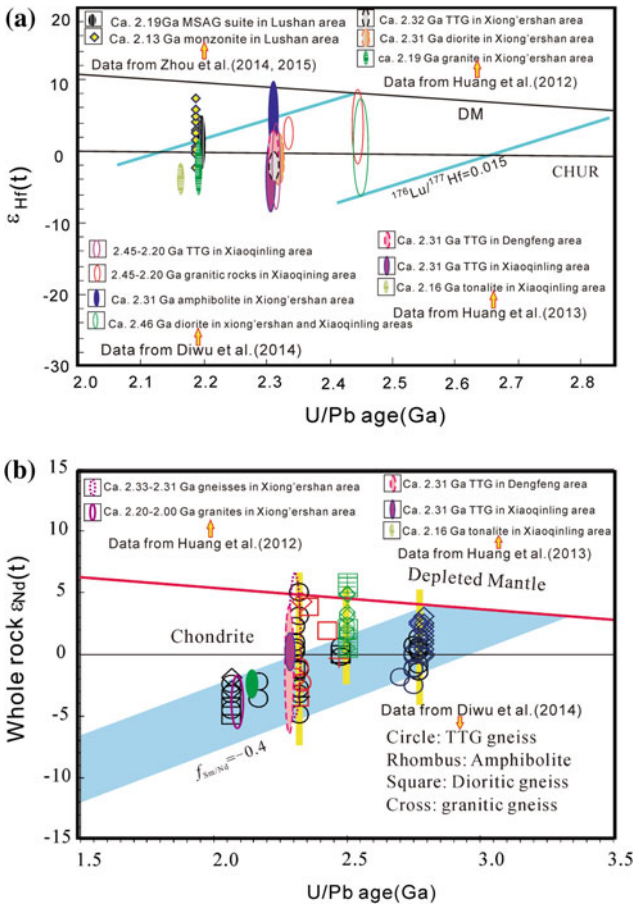

Fig. 10.8 **a** ε_{Hf} (t) versus U-Pb age (Ma) diagram and **b** ε_{Nd} (t) versus U-Pb age (Ma) of the 2.45–2.00 Ga magmatism in the southern NCC

crustal contamination. The rocks also have high La/Nb ratios. Zircons yield variable $^{176}Hf/^{177}Hf$ ratios with $\varepsilon_{Hf}(t)$ values varying from −4.6 to 6.2 and $\varepsilon_{Nd}(t)$ values of −3.4–0.3. The single-stage Hf model ages range from 2.42 to 3.06 Ga, but most zircons define a peak at 2.62 Ga (Fig. 10.8, Huang et al. 2012b; Diwu et al. 2014). Additionally, the diorite sample contains inherited zircons with ages of 2496 ± 4 to 3352 ± 14 Ma. All above data suggest they were produced by partial melting of metasomatized lithospheric mantle. To account for the partial melting of deep mantle to generate the high-Ti mafic rocks, an extensional setting is needed. In combination with synchronous developed TTG rocks in the region, these rocks might be produced in a back-arc extension under the subduction-collision related tectonic setting.

Amphibolites

The amphibolites are associated with the khondalite series or are interbedded with granitoid gneisses and appear to be of volcano-sedimentary origin. They are gray green, display a medium-coarse granular crystal texture, and have a mineral assemblage of hornblende (60–70 %), plagioclase (20–35 %), and quartz (5–10 %), with minor accessory minerals (<5 %) of zircon, apatite, and magnetite. The geochemical data is from the Lushan area (Zhou et al., being submitted). The rocks show SiO_2 (48.46–51.01 wt%), Al_2O_3 (11.95–18.38 wt%), and CaO (8.03–9.68 wt%). The $Na_2O + K_2O$ are in range of 3.73–5.04 wt%, with Mg number of 41–50, and belongs to sub-alkaline basalt. They have slightly fractionated REE patterns ($[La/Yb]_N$ = 4.95 − 7.39) with weak

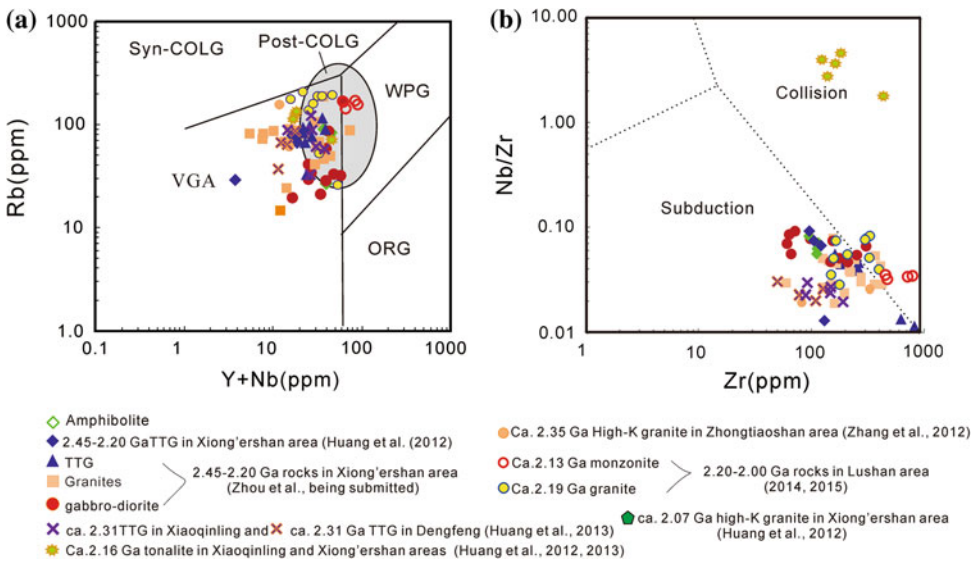

Fig. 10.9 **a** Plots of Y/Nb versus Rb and **b** Zr versus Nb/Zr of the 2.45–2.00 Ga magmatism in the southern NCC (after Eby 1992)

to negligible negative Eu anomalies (Fig. 10.6). On the primitive mantle-normalized multi-element spidergram, the amphibolites show negative Nb but weak negative to positive Ta anomalies. Their low Th/Ce ratios (<0.1) preclude any significant contribution from subducted sediments. They show positive $\varepsilon_{Hf}(t)$ values (up to 9.0) and a relatively high $\varepsilon_{Nd}(t)$ value (up to 4.2) with Hf T_{DM} model ages of 2.65–2.33 Ga (Fig. 10.8), the youngest Hf model age is close to the crystallization age (ca. 2.30 Ga; Jiang et al. 2011; Diwu et al. 2014). The results are consistent with magma derivation from OIB-like mantle wedge, without metasomatism by LILE–LREE-rich fluids derived through the dehydration of the subducted slab.

Granitic Gneisses

The granitic gneisses consist mainly of K-rich monzogranite-syenogranite-alkali granite-syenite in the Xiong'ershan area. The mineral assemblage of the monzonitic granite has equal amounts of plagioclase and alkali-feldspar (total as 40–60 %) with subsidiary quartz (25–35 %) and minor hornblende and biotite (~5 %). Syenogranite is mainly composed of microcline (45–55 %), quartz (25–35 %), and plagioclase (5–10 %). The alkali-granite is composed of alkali-feldspar (40–60 %), quartz (25–30 %), plagioclase (~5 %), and minor hornblende and biotite (~5 %). Accessory minerals of monzogranite-syenogranite-alkali-granite suite account for <1 % and include zircon, apatite, titanite, and Fe–Ti oxide. Geochemical data from Xiaoqinling and Xiong'ershan areas reveal that the rocks have SiO_2 (67.31–77.96 wt%), Al_2O_3 (11.65–17.88 wt%), CaO (0.16–2.49 wt%), Na_2O (0.48–4.99 wt%) and K_2O (1.64–9.37 wt%) (Huang et al. 2012b; Zhou et al., being submitted). A/CNK ratios are of 0.75–1.28 (1.05 on average). The major oxide contents suggest the potassic granite shares an affinity with high-alkaline peraluminous granite. The rocks show LREE enrichment with obviously negative Eu anomalies, high FeO^T/MgO ratios (22.5–85.5), Zr concentrations and negative Ba and Sr anomalies, characteristics of typical A-type granite (Fig. 10.10a, b, Whalen et al. 1987). Nevertheless, they have low Nb contents (1.86–19.7), variable Zr + Nb + Ce + Y concentrations (93.3–671 ppm), 10,000 Ga/Al ratios (1.54 and 3.00), and zircon saturation temperatures (703–926 °C). In the plots of Nb versus 10,000 × Ga/Al, and Nb versus 10,000 × Ga/Al (Fig. 10.10c, d, Whalen et al. 1987), many of the samples fall in the field of the I-, S-, and M-type granites. But anyhow, the rocks have high Rb/Sr ratios (0.57–5.67, 2.29 on average) and low P_2O_5 (0.01–0.10 wt%), contrasting to the features of S-type granite (Rb/Sr < 1; P_2O_5 mostly >0.14 wt%; King et al. 1997). Both Hf isotopic values in zircons and whole-rock $\varepsilon_{Nd}(t)$ values from the 2.45–2.20 Ga granitic gneisses are similar to coeval TTG gneisses, considerable variation, from negative to positive (−7.2 to 7.8; Diwu et al. 2014) (Fig. 10.8), indicating that these rocks were derived from a source that involved the melting of materials

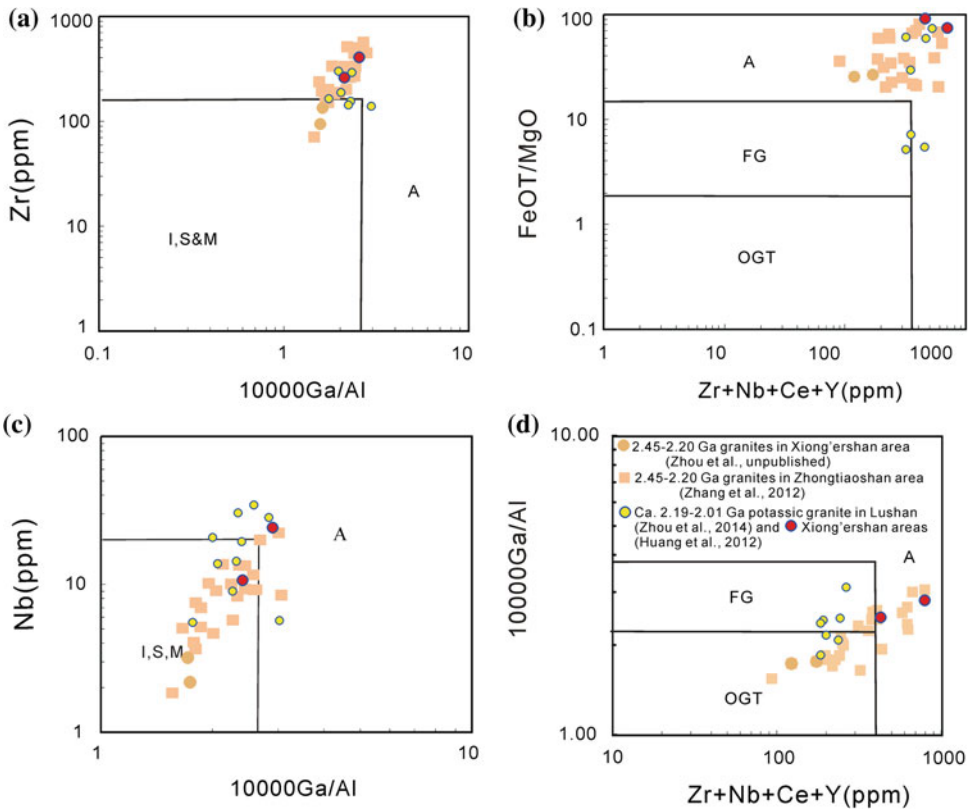

Fig. 10.10 **a** Zr versus 10,000 × Ga/Al, **b** FeOT/MgO versus Zr + Nb + Ce + Y, **c** Nb versus 10,000 × Ga/Al and **d** 10,000 × Ga/Al versus Zr + Nb + Ce + Y classification diagrams of the 2.20–2.00 Ga magmatism in the southern NCC (after Whalen et al. 1987). *FG* Fractionated felsic granites; *OGT* Unfractionated M-, I- and S-type granites

from old crust and depleted mantle. In the tectonic setting discriminated diagrams (Nb vs. Y and Y + Nb vs. Rb, Fig. 10.9), the rocks are plotted into the VAG or post-collision fields and subuction-colllision boundary field.

10.3.2 2.20–2.00 Ga Magmatic Rocks

10.3.2.1 Major Distributions

Recently, a number of granitic and volcanic rocks formed at ca. 2.20 Ga are identified within the whole NCC (Fig. 10.1). They are the Liaoji granitoids in the Jiao-Liao-Ji belt of the eastern NCC (2166 ± 14 to 2176 ± 11 Ma; Lu et al. 2004a, b, 2006; Li and Zhao 2007). Lingyunkou hornblende monzogranite and biotite monzogranite in the Hengshan terrane (2052 ± 17 and 2084 ± 4 Ma; Zhao et al. 2011). Nanying granitic gneiss (Zhao et al. 2008), and Gushan quartz monzonitic gneiss (ca. 2.17 Ga, Wang et al. 2015) in the Huai'an area of the northern NCC. Wangjiahui granite (Kröner et al. 2002; Zhao et al. 2002; Wilde et al. 2005), mafic dikes (2147 ± 5 Ma, Peng et al. 2005) and basaltic andesite (2140 ± 14 Ma, Du et al. 2010) in the Wutai-Fuping terrane. Granitoids, metamorphic basalt and rhyolite (2.2–2.1 Ga, Yu et al. 1997, 2004), and magnesian andesites, Nb-enriched basalt-andesites, and adakitic rocks (2188 ± 48 Ma, Liu et al. 2014) in the Lüliang Complex of the central NCC. Coeval basic and felsic bimodal magma (Geng et al. 2008; Yu et al. 1997; Geng et al. 2003) and rift-related felsic volcanic rocks in the Jiangxian Group in the Zhongtiao area and basalt in the Taihang Mountains of the southern NCC (Liu et al. 2012c). The high-K granite (2194 ± 29 Ma) and garnet-bearing monzonite (2134 ± 17 Ma) in the Lushan area (Zhou et al. 2014a, 2015). The tonalite (2065 ± 23 Ma) and granite (2013 ± 36 Ma) in Xiong'ershan area (Huang et al. 2012b). The TTG (2.16 Ga) in Xiaoqinling Taihua Complex (Huang et al. 2013). The widely exposed early Paleoproterozoic magmatism suggests that the ca. 2.20 Ga tectonothermal events were ubiquitous in the NCC. This is also supported by detrital zircon age distribution model from metasedimentary rocks of the Paleoproterozoic khondalite series widely present in the North China Craton (Wan et al. 2006b).

10.3.2.2 The Geochronology and Geochemical Characteristics and Rock Petrogenesis

Garnet-bearing Monzonite

The Lushan garnet-bearing quartz monzonite was emplaced into the western Taihua Complex at 2134 ± 17 Ma on the southern margin of the North China Craton (NCC) (Zhou et al. 2015). The rocks have nearly equal amounts of plagioclase and alkali-feldspar with a total of 65–75 wt%, quartz (5–20 %) and biotite (5–10 %), and are thus classified as quartz monzonite. The rocks contain SiO_2 contents of 56.98–59.05 wt%, with high $K_2O + Na_2O$ (7.46–9.14 wt%) and Al_2O_3 (15.87–17.58 wt%), and low CaO (2.38–2.77 wt %) and MgO (1.18–1.50 wt%) contents, and belong to an intermediate shoshonitic series. In the plot of R1 versus R2, samples lie in the field of quartz monzonite (Fig. 10.9b).

Magmatic garnet grains in the rocks are chemically homogeneous (Fig. 10.11), with relatively high CaO (6.36–7.92 wt%), but low MnO (1.45–1.94 wt%) and MgO (2.47–3.45 wt%) contents and high Fe/Mn ratios. They contain 61.94–66.39 mol% almandine, 18.60–23.40 mol% grossular, 10.06–15.11 mol% pyrope and 1.09–4.32 mol% spessartine, similar to high-pressure garnets formed from M-type magma but different from those found in S-type granites and metapelites (Harangi et al. 2001) (Fig. 10.12). Phase equilibrium diagrams (e.g., Green 1982, 1992; Conrad et al. 1988) in combination with trace element distribution coefficients between zircon and garnet suggest whole-rock zircon saturation temperatures varying from 891 to 951 °C (Fig. 10.13, Rubatto 2002; Hermann and Rubatto 2003; Whitehouse and Platt 2003; Hokada and Harley 2004; Kelly and Harley 2005; Buick et al. 2006; Rubatto et al. 2006) and the mineral assemblage of garnet + plagioclase + amphibole or biotite in these rocks is stable at >15 kbar and 890–950 °C with H_2O <3 wt% in the magma. This temperature range

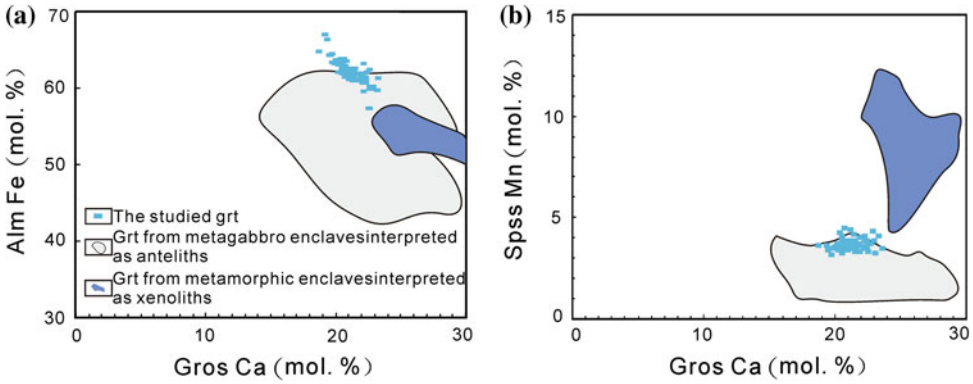

Fig. 10.11 End-member compositions of garnets in the Lushan quartz monzonite: **a** Gross Ca versus Alm Fe and **b** Gross Ca versus Spss Mn diagrams (data fields and related references can be seen in Zhou et al. 2015)

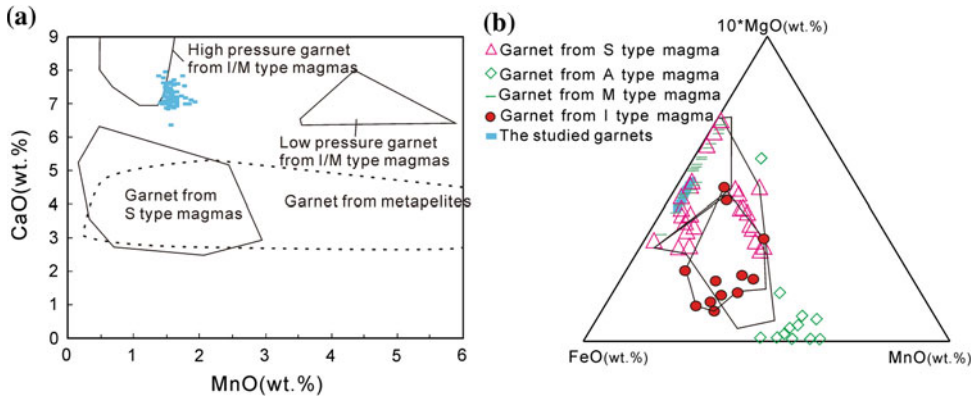

Fig. 10.12 **a** CaO versus MnO and **b** 10 × MgO versus FeO versus MnO diagrams of garnet from the garnet quartz monzonite in the Lushan area. (data fields and related references can be seen in Zhou et al. 2015)

permits the breakdown of biotite and Ca-amphibole ($T > 800$ °C).

All of the rocks are enriched in LILE and LREE with low Nb/La ratios (0.24–0.61), similar to those of lithospheric mantle, which has a Nb/La ratio of ~0.5 (Bradshaw and Smith 1994; Smith et al. 1999) (Fig. 10.14). Therefore, the garnet and whole-rock chemical compositions indicate that the Lushan quartz monzonite possibly formed by small degrees of partial melting of a phlogopite-bearing lithospheric mantle (Zhou et al. 2015). The variable zircon $\varepsilon_{Hf}(t)$ values (−3.5 to +4.1) with T_{DM}^{C} from 2.34 to 2.51 Ga suggest involvement of crustal materials (Fig. 10.8a). The

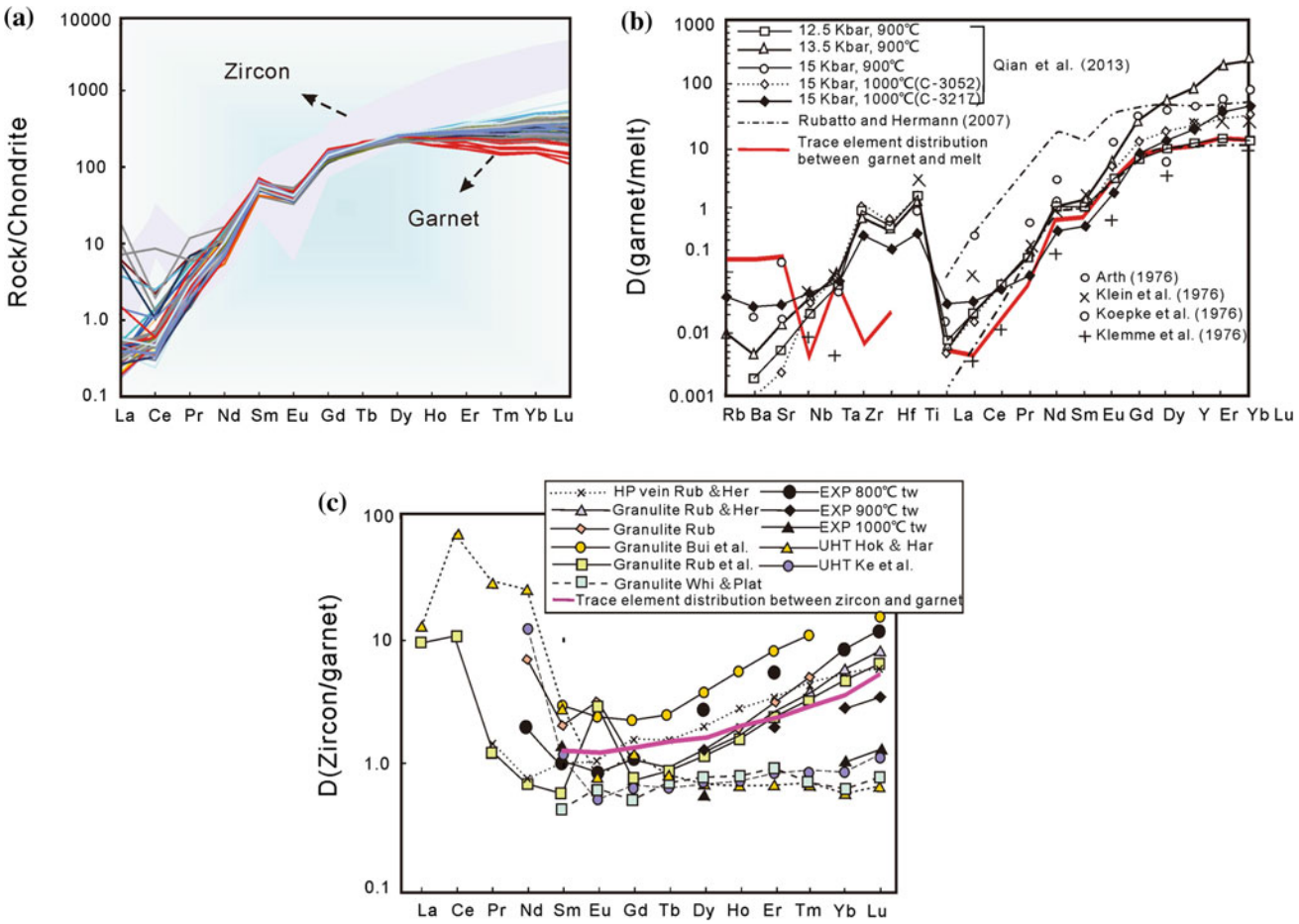

Fig. 10.13 **a** Garnet chondrite-normalized REE patterns, **b** Garnet-melt partition coefficients in dacitic melts (Arth 1976; Nath and Crecraft 1985; Severs et al. 2009), and **c** trace element distribution pattern between zircon and garnet from the Lushan quartz monzonite. (data fields and related references can be seen in Zhou et al. 2015)

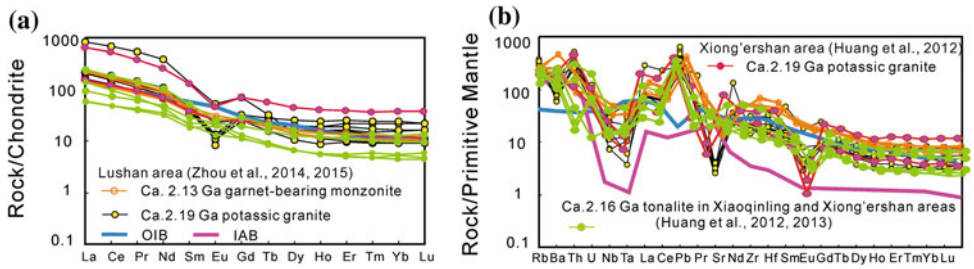

Fig. 10.14 **a** Chondrite-normalized REE and **b** primitive mantle-normalized trace elements patterns of the 2.20–2.00 Ga magmatism in the southern NCC (after Sun and McDonough 1989)

rocks have slightly negative Nb and Ta anomalies, characteristics of island arc basalts (IAB) (Fig. 10.14). However, their high Zr (598–926 ppm) and Zr/Y ratios (17.1–21.8) suggest an affinity with ocean island basalt (OIB). Hence, the mixed IAB- and OIB-like geochemical signatures are indicative of continental intraplate rifting, possibly related to extension and thinning of the lithosphere and upwelling of asthenosphere (Muller and Groves 1995).

Potassic Granite

The Paleoproterozoic potassic granites formed at 2.20–2.00 Ga (Huang et al. 2012b; Zhou et al. 2014a, b). In the Lushan area, the rocks intruded into the Shangtaihua Group and were unconformably overlain by the Mesoproterozoic Xiong'er Group with clear contact boundaries (Zhou et al. 2014a, Fig. 10.8). They mainly formed intrusive bodies with one to several km^2 in extension. The mineral assemblage is composed of alkali-feldspar (50–55 %) with subsidiary quartz (~30 %), minor plagioclase (~10 %), hornblende, and biotite (~5 %). K-feldspar is the main kind of alkali-feldspar.

The rocks are rich in SiO_2 (69.64–77.73 wt%), and K_2O (5.05–6.90 wt%) with high $K_2O + Na_2O$ contents from 7.56 to 8.48 wt%, but poor in CaO (0.10–1.65 wt%), P_2O_5 (0.0.2–0.07 wt%) and MgO (0.01–0.30 wt%, Mg# = 1.08 − 36.4), indicating they experienced fractional crystallization. Major element compositions suggest the potassic granites share an affinity with high K calc-alkaline granite. Even though the Lushan potassic granitic rocks have high A/CNK ratios (1.05–1.25), which can reach peraluminous feature, the very low P_2O_5 contents and negative correlation of P_2O_5 and SiO_2 ruling out they are S-type granite (e.g., Chappell 1999; Bonin 2007). Differ from peralkaline A-type granite, the Lushan and Xiong'ershan potassic granites have variable Zr concentrations and 10,000 Ga/Al ratios. Its low Zr concentrations might be contributed to fractionation, similar to highly fractionated aluminous A-type granite in the Lachlan Fold Belt (Fig. 10.15a, b, King et al. 2001). Together with high zircon saturation temperatures (T_{Zr} = 826–885 °C), indicating they are fractionated aluminous A-type granites (Fig. 10.10). Enriched LREE ($(La/Yb)_N$ = 9.72–24.1), negative Eu anomalies, and low Sr/Y with no correlations in Sr/Y and Sr/Zr versus CaO suggest the possible presence of Ca-rich plagioclase and absence of garnet in the residual. Magmatic zircon grains have variable $\varepsilon_{Hf}(t)$ values (−10.7 to +7.3) with zircon two-stage Hf model ages (T^C_{DM}) varying from 2848 to 2307 Ma (mostly around ca. 2.50 Ga), and are plotted in the evolution line of crustal felsic rock (Fig. 10.8a). In the tectonic setting discriminated diagrams (Y + Nb vs. Rb, Fig. 10.9a), the rocks are plotted into the post-collision field. Moreover, judging from field relationships and zircon U-Pb/T_{DM} ages, Paleoproterozoic quartz monzonite in the Lushan area formed successive and mostly contemporaneous to the potassic granites, suggesting that they developed in the same setting (ca. 2.13 Ga, Zhou et al. 2015). Furthermore, there are small volume of mafic rocks (mafic enclaves) present within the potassic granites. All of these allow us to favor the extensional setting in which formed the Lushan potassic granite.

Meanwhile, this model is also supported by a few lines of evidence in the Lushan area: (1) the presence of ca. 2.26 Ga metamorphosed tholeiite formed in an intra-continental setting (Yang 2008); (2) the presence of the geochemically and geochronologically similar late Archean TTG basement gneisses and mafic dyke swarms in the Lushan area; (3) the identification of the Archean detrital zircons from the Paleoproterozoic Shangtaihua Group, etc. Thus, a cartoon can be illustrated to show the evolution process of the ca. 2.19 Ga potassic granites in the southern margin of the NCC: The upwelling mantle-derived magma provided thermal flux into a localized area and caused the partial melting of the overlying tonalitic-granodioritic crust to form the 2.20–2.00 Ga potassic granites, and contemporaneously, it also provided source materials for them. As indicated by the zircon in situ Hf isotopic compositions of the potassic granites, the injection of basaltic melt into the crust has been widely considered as an important mechanism to generate silicious melts in the continental crust and basalt can act either as a parental source or as the thermal trigger for crustal melting.

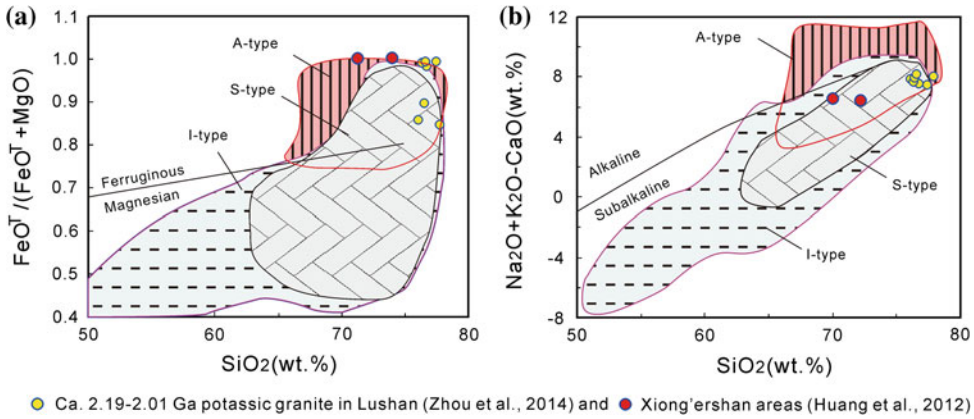

Fig. 10.15 **a** SiO_2 versus $FeO^T/(FeO^T + MgO)$ and **b** SiO_2 versus $K_2O + Na_2O$-CaO diagrams of the 2.20–2.00 Ga magmatism in the southern NCC. The data for composition fields come from Lachlan Fold Belt (after Frost et al. 2001)

Tonalite

The 2.20–2.00 Ga tonalite gneiss in the Xiong'ershan and Xiaoqinling areas are composed mainly of 5–20 % biotite, 3–20 % amphibole, 60–70 % plagioclase, 10–30 % quartz. The tonalities formed at 2.16–2.07 Ga in the Xiong'ershan (Huang et al. 2012b) and Xiaoqinling area (Huang et al. 2013) have low SiO_2 (57.11–64.33 wt%), high MgO (1.83–4.62 wt%) (Fig. 10.7). All rocks have relatively low contents of HREE (Yb_N = 5.00–14.35) and Y (9.71–25.4 ppm), with moderate $(La/Yb)_N$ (9.7–24.8) and Sr/Y (20.0–65.7) ratios, and show negative Ta-Nb and Ti anomalies and positive Sr and Pb anomalies (Fig. 10.14), which is consistent with partial melting of subducted oceanic crust or delaminated lower crust. Given that all samples show negative whole rock $\varepsilon_{Nd}(t)$ (−5.01 to −2.33) and zircon $\varepsilon_{Hf}(t)$ values (−10.7 to −1.99), corresponding to much older whole-rock Nd model ages (2.55–2.82 Ga) and zircon "crustal" model ages (2.86–3.33 Ga) than their crystallization age, the partial melting of delaminated lower crust is the preferred mechanism. Additionally, the high Rb/Sr ratios (0.12–0.35) also suggest a large contribution of the lower crust in their generation (Huang et al. 2009). The lower crust might form at ~2.30 Ga according to the ages of inherited zircons.

The 2.20–2.00 Ga tonalite has high MgO (Mg#), Ni and Cr, and would be derived from partial melting of delaminated lower crust (Huang et al. 2013). Delamination is a process where by a dense segment of the lower crust and lithospheric mantle sink into the convecting asthenosphere (Rudnick and Fountain 1995). If delamination occurs, the lower crust must undergo large density increases, which is always due to "eclogitic" phase transitions (Kay and Kay 1993; Lustrino 2005). The lower crust might have been thickened enough for partial melting to occur, with a restite of eclogite or garnet-clinopyroxenite (Kay and Kay 1993), and partial melts of TTG and adakitic affinity (Lustrino 2005). Extensive TTGs generated at ~2.40–2.20 Ga in Taihua and Dengfeng complexes suggest that the lower crust had been overall "eclogitic" character in the Early Paleoproterozoic, which would be responsible for delamination or detachment of the lower crust at the end of the Early Paleoproterozoic (such as the Bayuan TTG at ~2.16 Ga; Huang et al. 2013).

During sinking, the lower crust is likely to undergo partial melting, producing liquids of TTG or adakitic affinity (e.g., Zegers and van Keken 2001; Xu et al. 2002; Lustrino 2005). Considering the coeval A-type granite, we favor that the rocks formed by the partial melting of delaminated lower crust due to upwelling mantle-derived magma in an extensional setting. The magmatic episode at 2.20–2.00 Ga in the Lushan (Zhou et al. 2014a, 2015), Xiong'ershan and Xiaoqinling areas (Huang et al. 2012b, 2013; Diwu et al. 2014) of the Taihua Complex is mainly potassium-rich, suggesting an extensional regime at the end of the Early Paleoproterozoic.

10.3.3 Possible Genetic Relationships of the 2.45–2.00 Ga Magmatisms in the Southern NCC

Previously, based on Sm–Nd isochrons, depleted mantle Nd model ages and single-grain zircon evaporation Pb–Pb ages, it was previously suggested that the Taihua Complex in the Xiong'ershan and Xiaoqinling areas is similar to that in the Lushan area, and that it was formed during Neoarchean time and underwent metamorphism in the Paleoproterozoic (Guan 1996; Ni et al. 2003; Zhang and Li 1998). However, widespread occurrences of ~2.45–2.20 Ga TTG gneisses associated with coeval dioritic gneisses and granites have been reported in the Xiaoqinling and Xiong'ershan areas. Minor ~2.20–2.00 Ga TTG gneisses, K-feldspar granite gneisses, and granites have also been recognized (Huang et al. 2012b; Diwu et al. 2014; Zhou et al., being submitted). Zircons of the two age ranges in the Xiong'ershan and Xiaoqinling areas have negative $\varepsilon_{Hf}(t)$ values and their model ages (2.85–2.70 Ga) are similar to the crystallization ages of the Archean gneiss series in the Lushan area (Fig. 10.8), which

indicates that continental crustal materials as old as 2.85–2.70 Ga in the Lushan area probably preexisted in the Xiaoqinling and Xiong'ershan areas and constituted sources of the magmatic rocks.

10.4 Major Distribution of the Early Paleoproterozoic Sedimentation in the Southern NCC and Their Depositional Characteristics

As mentioned above, most previous studies focused on high-grade metamorphic and igneous rocks, and few investigations have been carried out on the widespread low-grade metasedimentary units. Conventional, the final amalgamation and cratonization of the NCC was considered to be related to the Lüliang movement at the late Paleoproterozoic (~1.80 Ga) (e.g., Ma and Wu 1981; Zhao 1993), which are characterized by unconformity between the Paleo-Mesoproterozoic sedimentary strata and metamorphosed Archean basement in different regions. For example, the Paleoproterozoic Yejishan, Hutuo, Zhongtiao, Yinyugou and Songshan groups, and Tietonggou Formation were deposited overlies the Neoarchean–Paleoproterozoic basement in the Lüliang, Wutai, Zhongtiao, Wangwushan, Songshan, and Xiaoqinling regions in the Trans-North China Orogen, respectively.

In the Henan-Shaanxi province on the southern NCC, the Neoarchean–Paleoproterozoic rocks extend in an E-W direction and consist of the Taihua and Dengfeng complexes, the Angou, Xiong'er, Yinyugou and Songshan groups and the Tietonggou Formation (Fig. 10.2). Of these, the lower subgroup of the original Taihua Group (Ma et al. 1981) (which disintegrated from the Taihua Complex), the Dengfeng Complex (Zhang et al. 1985; Diwu et al. 2011) and the Angou Group (Yang et al. 2009) developed in Neoarchean, whereas the upper subgroup of the Taihua Group (Diwu et al. 2010), Yinyugou Group (Bureau of Geology and Mineral Resources of Henan Province 1989; Sun et al. under review), Songshan Group (Diwu et al. 2008; Liu et al. 2012a), Xiong'er Group and the Tietonggou Formation were formed in Paleoproterozoic (Peng et al. 2008). So far, published detrital zircon ages and provenance analysis of the low-grade metasediments are focused on the Songshan Group and the Tietonggou Formation.

10.4.1 The Songshan Group

The Songshan Group mainly exposed in the Dengfeng and Linru areas, Henan Province, and is composed of low-grade metamorphic Songshan quartzite and Wuzhiling schist, suggesting a neritic-littoral facies terrigenous clastics and carbonate, in which sedimentary structures such as cross-bedding and slanting-bedding are well preserved (Zhang 1951; Ma et al. 1981). Zhang (1951) discovered two angular unconformities between the Archean Dengfeng Group and Proterozoic Songshan Group, and between Proterozoic Wuzhiling schist and Sinian strata, which were named as "Songyang Movement (Wutai Movement)" and "Zhongtiao Movement", respectively.

The REE patterns of the Songshan quartzite and schist are characterized by LREE enrichment, negative Eu anomalies and fractionated LREE (Liu et al. 2012a), indicating felsic to intermediate source rocks (Slack and Stevens 1994). Moreover, certain trace elemental ratios such as La/Sc, Th/Sc, La/Co, and Th/Co have also been used to distinguish between mafic and felsic source rocks and all values of these elemental ratios from the Songshan rocks are indicative of felsic sources (Liu et al. 2012a).

The depositional age of the Songshan Group was considered to be the same as the Wutai Group in terms of the similar structures of the two groups (Zhang 1951). Zhao (1956), on the other hand, considered the Songshan Group may have formed at the same time as the Hutuo Group according to the relationship of lithology and tectonics (Guan et al. 2002). Ma et al. (1981) argued that the Songshan Group started to deposit between ~2.00 and ~1.80 Ga. Diwu et al. (2008) reported that a single detrital zircon derived from a fine-grained quartzite in the Luohandong Formation yielded an age of 2337 ± 23 Ma, suggesting the Songshan Group has possibly deposited at some time after 2337 Ma. More recently, Liu et al. (2012a) analyzed detrital zircon grains from the Luohandong and Wuzhiling formations and obtained the youngest $^{207}Pb/^{206}Pb$ ages of ~2.35 and ~1.96 Ga, respectively (Fig. 10.16a). On the other hand, the minimum depositional age of the Songshan Group is constrained by the ~1780 Ma unmetamorphosed volcanic rocks from the overlying Xiong'er Group (Zhao et al. 2004; He et al. 2009) and ~1775 Ma undeformed Shicheng potassic granitoid crosscutting the group (Wan et al. 2009; Zhao and Zhou 2009). Therefore, the age of ~2.35 Ga as a more reliable constraint on the maximum depositional age of the Luohandong Formation, and the depositional age of the Wuzhiling, Miaoposhan, and Huayu formations can be constrained in the period of 1.96–1.78 Ga.

In this chapter, we collect 840 detrital zircon U-Pb ages from the Songshan Group (data from Diwu et al. 2008; Liu et al. 2012a; Zhang et al. 2014) and reveal that the ages can be divided into three age populations of 3700–3000, 3000–2400, and 2400–1950 Ma (Fig. 10.16a). Almost 80 % of detrital zircons from the quartzite samples and 10 % of them from the schist samples in the Songshan Group exhibit an age range between 3000 and 2400 Ma (Fig. 10.16). This age range is well consistent with the ages of the Huishansi,

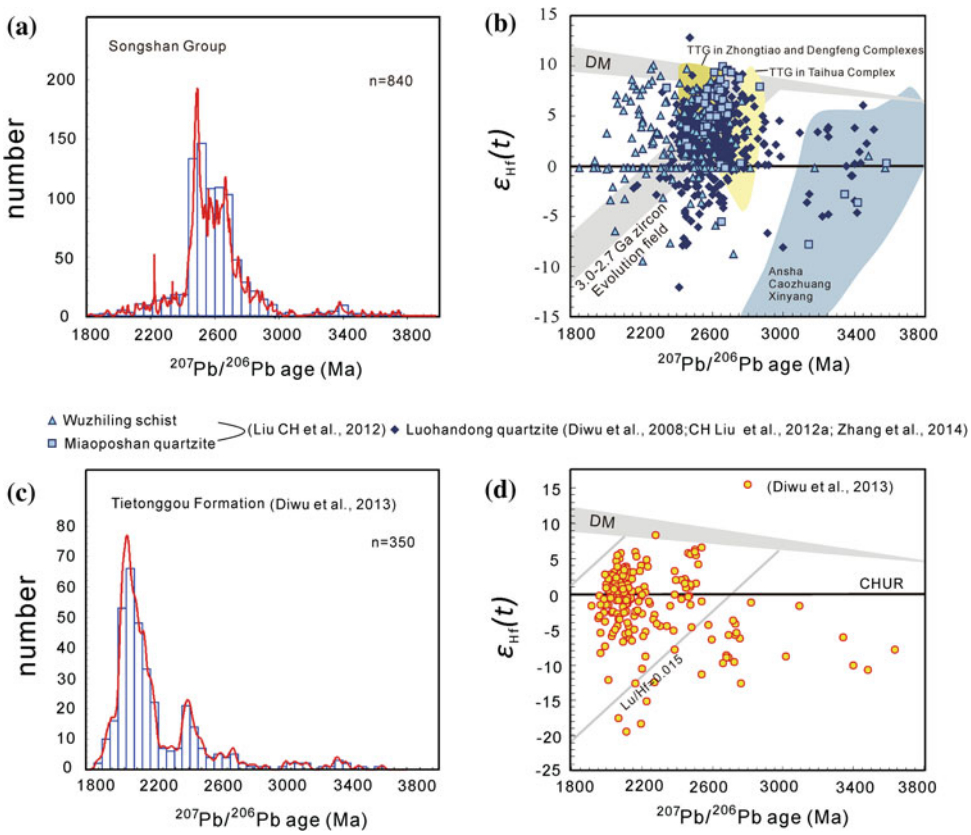

Fig. 10.16 *Left panels* show corresponding relative probability plots of $^{206}/^{207}$Pb ages for concordant detrital zircons from **a** the Songshan Group and **c** Tietonggou Formation; *right panels* show relationship between $\varepsilon_{Hf}(t)$ values and U-Pb ages for zircons from **b** the Songshan Group and **d** Tietonggou Formation

Niuwulan, Beigou, and Datasi TTG gneisses (2617–2509 Ma; Wan et al. 2009; Zhou et al. 2011), the Shipaihe diorites (2493 ± 7 Ma; Wan et al. 2009) and metavolcanic rocks of the Dengfeng Group (2547–2508 Ma; Wan et al. 2009; Diwu et al. 2011), the ages of the Xiyao and Zhaizi TTG gneisses (2560–2536 Ma; Guo et al. 2008; Yu et al. 2006) and the ages of 2832–2752 Ma obtained from the TTG gneisses in the adjacent Taihua Complex (Liu et al. 2009; Diwu et al. 2010). In addition, the Neoarchean TTG gneisses in the Dengfeng and Zhongtiao complexes mostly yielded positive zircon $\varepsilon_{Hf}(t)$ values ranging from 0 to +10 and those in the Taihua Complex gave $\varepsilon_{Hf}(t)$ values ranging from −5.8 to +8.9 (Guo et al. 2008; Diwu et al. 2011), which overlap with the $\varepsilon_{Hf}(t)$ value range of 3000–2400 Ma detrital zircons from the integrated samples (Fig. 10.16). In a word, such age and isotopic fits suggest that nearly all the detrital zircons within the age range between 3000 and 2400 Ma from the Songshan quartzites and schists were sourced from the TTG gneisses of the Dengfeng, Zhongtiao and Taihua complexes in the southern sector of the NCC.

The subordinate detrital zircons yield ages from 2400 Ma to 1950 Ma. The felsic rocks with this age range are presented by the meta-rhyolites (2330–2059 Ma; Sun and Hu 1993) and the Wulaofeng potassic granitoids (1968–1944 Ma; Tian et al. 2006) in the adjacent Zhongtiao Complex and the Xutai and Lujiagou granitoids (2509 ± 33, 2399 ± 24 Ma, Zhou et al. 2011) in the Dengfeng Complex. This suggests that the 2400–1950 Ma detrital zircons of the studied samples were most likely directly sourced from the Paleoproterozoic granitoid plutons and meta-rhyolites in the Zhongtiao and Dengfeng complexes. Whereas minor amounts of 3700–3000 Ma detrital zircons may have been derived from transported exotic Paleoarchean and Mesoarchean crustal materials, because no lithologies or zircons with such age founded in the Dengfeng and adjacent complexes in the south NCC. The felsic rocks with zircon ages of 3.85–2.85 Ga have been reported from the northern part of the Eastern Block, including fuchsite-bearing quartzites in the Caozhuang area and granitoids and metasedimentary rocks in the Anshan area (Liu et al. 1992, 2008; Wu et al. 2005, 2008; Fig. 10.16b). A closer and more possible source area for these ancient zircons is the basement of the Xinyang area in the southwestern part of the Eastern Block.

10.4.2 The Tietonggou Formation

The Tietonggou Formation outcrops in the Xiaoqinling area. In 1958, the Bureau of geology and mineral resources of Shanxi Province (BGMRSP) has established a typical

geologic section for the Tietonggou Formation in Bayuan area, Lantian country, Shaanxi Province (Bureau of Geology and Mineral Resources of Hean Province 1989). The formation consists of a succession of clastic sendiematry rocks 315–2850 m in thickness and unconformably overlies the Taihua Complex (Fig. 10.2), In the Bayuan region, the Tietonggou Formation was unconformably overlain by the Xiong'er Group. This unconformity present an orogeny, named the "Luanchuan Movement" by some Chinese geologists, which occurred coevally with the "Lüliang Movement" and "Zhongtiao Movement" in Lüliang and Zhongtiao area of Shanxi province, respectively. The Tietonggou Formation is composed mainly of quartzite, pebbly quartzite, and muscovite quartzite. Its protoliths were mature terrigenous clastic rocks. The ripple marks and cross–bedding structures still preserved in the quartzite, which was considered to have deposited in littoral sedimentary environment (Bureau of Geology and Mineral Resources of Hean Province 1989). The Tietonggou Formation differs from the underlying Taihua Complex and the overlying Xiong'er Group in rock assemblages and metamorphic grade.

Although the Tietonggou Formation is conventionally considered to have formed in Paleoproterozoic (Bureau of Geology and Mineral Resources of Hean Province 1989), the depositional age of the formation has not been well constrained. On the basis of the ages of the youngest detrital zircons from the quartzites and the ages of the Xiong'er Group, the depositional ages of the protoliths of the Tietonggou Formation were well constrained to be older than 1.91–1.80 Ga (Diwu et al. 2013). The detrital zircon ages from the two quartzite samples show broadly similar age patterns with one major age population of ~2.10 Ga, which are consistent with 2.20–2.00 Ga magmatisms in the NCC (see references in the part of 10.3 of this chapter). The majority of the ~2.10 Ga detrital zircons mostly have high $\delta^{18}O$ values (>6.5‰) and negative $\varepsilon_{Hf}(t)$ values (−7.8–0.0), with corresponding Hf model ages significantly greater than their crystallization ages, indicating that these zircons formed from the partial melting of ancient continental crust (Diwu et al. 2013; Fig. 10.16c, d). Microscopic observation show that the Tietonggou Formation quartzite does not have typical quartz grains in either volcanic or sedimentary rocks as mentioned above. In fact, these quartz grains mostly have suture-like contact boundaries or apparent wavy extinctions, indicating that they were derived from metagranitic rocks. The high compositional maturity of the quartz sandstone suggests the source materials have experienced long distance transportation. Taking into account the structural and compositional maturity of the Tietonggou Formation quartzite, the ~2.10 Ga lithologic units in the south NCC are interpreted as the major source of the Tietonggou Formation. In addition, a significant number of ~2.50 Ga detrital zircon occurs as a minor age population in some other two samples (Fig. 10.16c). The majority of the 2.80–2.70 and ~2.50 Ga detrital zircons from the Tietonggou Formation had positive $\varepsilon_{Hf}(t)$ values, and mantle-like $\delta^{18}O$ values, suggesting that the NCC has experienced two stages of significant crustal growth in the Neoarchaean at 2.70 and 2.50 Ga, respectively (Diwu et al. 2013).

10.5 Major Paleoproterozoic Magmatic Activity and Tectonic Evolution of the Southern NCC

The geochronology of the Dengfeng Complex (in the Dengfeng area) and the Taihua Complex (in the Lushan, Xiong'ershan, and Xiaoqinling areas) reveals at least four magmatic episodes in the southern segment of the NCC from the Late Mesoarchean to Early Paleoproterozoic (2.85–2.70, 2.60–2.50, 2.45–2.20, and 2.20–2.00 Ga). The depositional age of the low-grade metasedimentary sequences can be delimited to approximately 2.35–1.97 Ga. Of note, zircons with a peak metamorphic age of ~1.94 Ga occurred in both the TTG gneisses and the khondalite series rocks of the Taihua Complex.

10.5.1 During the Interval of 2.45–2.20 Ga

The database of global zircon ages from both granitoids and detrital sediments shows a marked age gap between 2.45 and 2.20 Ga characterized by the absence or near-absence of arc-type greenstones or TTG suites and banded iron formation (Condie et al. 2009), and a global glaciation (2.40–2.30 Ga) and an analogous 2.45–2.20 Ga basal unconformity can be observed on most cratons (Condie et al. 2009; Eriksson and Condie 2014). Condie et al. (2009) postulated that these geological records are possibly related to a global magmatic shutdown event between 2.45 and 2.20 Ga. However, recent studies suggest that the current Paleoproterozoic record does not favor the global magmatic shutdown (2.45–2.20 Ga) hypothesis (Condie 1998; Condie et al. 2009), as magmatic activities have been reported in the Karelian province of the Dharwa Craton (India), the Churchill Craton (Canada), the Tarim Craton (China), the Quanji Massif (northwestern China), and the NCC at this period, though less frequent than those in the 100 Ma prior to the quiet interval (Lauri et al. 2012; Strand and Köykkä 2012; Pehrsson et al. 2014). The scenario could involve subduction cessation following the global Archean cratonization, with contemporary initiation of subduction in the exterior ocean or within restricted small-scale ocean basins. But current data of tectono-magmatic events has not reached a sufficient mass to verify the model. Many researcheres suggest that the widespread early Paleoproterozoic (2.45–

2.20 Ga) mafic and felsic intrusions associated with volcanic-sedimentary rocks represent an episode of initial rifting of the late Archean craton in the eastern Fennoscandian Shield, which was related to the breakup of the inferred Kenorland supercontinent from 2.50 to 2.10 Ga (Lauri et al. 2012; Strand and Köykkä 2012). A ~2.30 Ga large igneous province in the Dharwar Craton (French and Heaman 2010) probably suggests that the mafic magmatism was linked with mantle plume sources and the breakup of one or more Archean continents. However, a suite of ~2.30 Ga granites has also been identified in the Arrowsmith Orogen, Western Churchill Craton. The geochemical and Nd isotopic signatures of these plutons suggest that the ~2.30 Ga magmatism was related to the thickening of continental crust and the magmatic activity occurred in a syn- to post-collisional orogenic setting (Harlaub et al. 2007).

In the NCC, many researchers considered the 2.45–2.20 Ga magmatic rocks to be subduction related at an Andean-style convergent margin or in a marginal arc-back-arc basin system after large volume of ~2.50 arc magmatism (Zhao et al. 2002, 2005, 2008; Liu et al. 2014; Su et al. 2014), such as the successive arc-type ~2360–2370, ~2180–2150 and ~1872–1850 Ma magmatic rocks in Lüliang (Zhao et al. 2008) and Huan'an areas (Su et al. 2014). However, many papers revealed that the NCC went through a unified rifting setting during the 2.45–2.20 Ga (Wang et al. 2005; Zhai and Peng 2007; Du et al. 2013). But some other researchers put forward that different magmatism are representative of different stages in the same orogenic event: (1) the 2.40–2.30 Ga early crustal extension stage (Wu et al. 1986; Sun and Hu 1993; Yu et al. 1997; Geng et al. 2000; 2006); (2) the transitory stage from extension to compression (2.20–2.10 Ga) (Wilde et al. 2005; Geng et al. 2000; Yu et al. 2004; Zhao et al. 2002; Guan et al. 2002); (3) the 2.00–1.85 Ga collision compression stage (Zhao et al. 2002; Guan et al. 2002); (4) the ~1.80 Ga post-collisional stage (Yu et al. 1997; Wu et al. 1998; Geng et al. 2003). Li et al. (1998) and Wan et al. (2000) suggested that there exists two stage of rift-collisional movement, and formed 2.40–2.30 Ga South Liaohe Group and 2.15–1.80 Ga North Liaohe Group, respectively. Zhai and Santosh (2013) proposed that the NCC records an important Paleoproterozoic event coincident with similar global GOE (Great Oxidation Event) during the interval 2.35–2.00 Ga, represented by the deposition of vast, thick magnesite–marble–graphite rocks in rifts that have been suggested to represent a worldwide rifting event following the 2.50–2.35 Ga glacial (Snowball) period (Condie and Kröner 2008).

Different from the Archean magmatism in the southern NCC, the 2.45–2.20 Ga magmatic activity differentiates the Taihua and Dengfeng complexes in the southern NCC from other complexes in the NCC. Overall, the 2.45–2.20 Ga TTG or TTG-like gneisses most likely derived from partial melting of basaltic lower crust with juvenile materials addition (Zhao et al. 2006a; Huang et al. 2012b; Diwu et al. 2014; Su et al. 2014) or subducted slab (Zhong 2006; doctoral thesis). In combination with their arc-related geochemical signatures (such as enriched LREE patterns and high La/Yb ratios) and synchronous developed dioritic and gabbroic plutons which might be produced in a subduction-collision-related tectonic setting during the Neoproterozoic crustal growth along the margins of NCC, we prefer that they formed in an Andean-type continental margin arc environment or accretionary orogenesis accompanied by basaltic underplating. The synchronous amphibolite are consistent with magma derivation from OIB-like mantle wedge, without metasomatism by LILE–LREE-rich fluids derived through the dehydration of the subducted slab. The typical calc-alkaline and high-K calc-alkaline granites are representative of syn-collisional or post-collisional granites (Zhao et al. 2006a; Zhou et al. 2011; Zhou et al., being submitted). In addition, in the $\varepsilon_{Hf}(t)$ versus age and $\varepsilon_{Nd}(t)$ versus age diagrams (Fig. 10.8), both Hf isotopic values in zircons and whole-rock $\varepsilon_{Nd}(t)$ values from the 2.45–2.20 Ga gneiss series of the southern NCC show considerable variation, from positive to negative. This isotopic pattern indicates that these rocks were derived from sources that involved the melting of materials from depleted mantle and old crust.

At the same time, previously research experience also brings us many key scientific issues, such as whether the 2.45–2.20 Ga magmatism in the NCC occurred episodically or in terms of small frequency successive pulse is still controversial. In addition, their temporal-spatial distribution, possibly rock genetic connection are also need to be further defined.

10.5.2 During the Interval of 2.20–2.00 Ga

The tectonic affinity of the 2.20–2.00 Ga igneous rocks has long been controversial. These rocks were previously suggested to have formed in a foreland basin along a passive margin (Zhai and Liu 2003; Peng et al. 2005), related to collision between a continent and an island arc (Hu 1992; Bai et al. 1993; Zhao et al. 2008; Liu et al. 2011b), or opening and closing of an intra-continental rift (e.g., Peng and Palmer 2002; Liu et al. 1997; Li et al. 1997, 1998, 2001a, b; Li and Yang 1997; Lu et al. 2004a, b, 2006; Li and Zhao 2007; Yang et al. 2011; Du et al. 2010, 2013). Peng et al. (2012) reported ~2.20 Ga igneous rocks in the central and eastern parts of the NCC which constitute a new Hengling magmatic belt (HMB) including the ~2.15 Ga Hengling mafic sill/dyke swarm, the ~2.06 Ga Yixiongzhai mafic dyke swarm, and the ~1.97 Ga Xiwangshan mafic dyke swarm. Together with A-type granites and other igneous associations in this belt,

these mafic rocks suggest formation in an intra-continental rift (e.g., Sun and Hu 1993; Lu et al. 2006; Yang et al. 2011). Trap et al. (2011) suggested that a 2.30–2.00 Ga tectonothermal event was responsible for the opening of the Taihang and Lüliang oceans in a proto-NCC, and that the Western, Fuping, and Eastern Blocks were separated by the two oceans. Zhai and Santosh (2011) proposed that there were several remnant ocean basins in the NCC that formed in the Late Neoarchean, followed by the formation of shallow rift basins in the Paleoproterozoic during 2.35–1.97 Ma. Alternatively, Wei et al. (2014) argued that the 2.35–2.00 Ga bimodal magmatism associated with sedimentary rocks (e.g., the Huhuo Group) probably due to development of back-arc extension on an Archean basement in the Hengshan–Wutai–Fuping region. Diwu et al. (2013) documented detrital zircons from the Tietongou Formation in the Xiaoqinling region, which show a major age peak at ~2.10 Ga, consistent with 2.20–2.00 Ga magmatism in the NCC.

According to the above studies of the 2.20–2.00 Ga igneous rocks, we favor that this episode of magmatism was contemporary with the breakup of the first proposed supercontinent that aggregated in the Late Archean or the assembly of the Early Proterozoic supercontinent (i.e., Columbia/Nuna) (Condie 1998). Magmatism reveals major of older crustal and minor juvenile materials which are characterized by mainly negative whole rock $\varepsilon_{Nd}(t)$ and zircon $\varepsilon_{Hf}(t)$ values (Fig. 10.8). It was thus a major period of crustal reworking, rather than one of crustal addition. In addition, the temporal change from mostly 2.45–2.20 Ga low-K igneous rocks (TTG) to 2.20–2.0 Ga mostly high-K igneous rocks in the southern segment of the NCC indicates a tectonic transformation from accretionary orogenesis (~2.30 Ga) to extensional regimes (~2.10 Ga).

10.6 Major Paleoproterozoic Low-Grade Sedimentary Sequences and Tectonic Evolution of the Southern NCC

The provenances of the low-grade metasedimentary units in the NCC show some similarities but also exhibit some differences. The major age range of detrital zircons from the Hutuo and Yejishan groups is 2560 and 1850 Ma, which is most likely sourced from the end-Archean TTG gneisses and the Paleoproterozoic intrusive rocks in the Hengshan–Wutai–Fuping belt and the Lüliang Complex (Liu et al. 2011a, b). However, detrital zircons in this age range are not the dominant components in the Upper Zhongtiao, Danshanshi, Yinyugou, and Songshan groups (Fig. 10.16) in the southern segment of the NCC and derived from the lithologic units of the Zhongtiao and Dengfeng Complexes (Liu et al. 2012a, b). On the other hand, the major ages of detrital zircons from the Tietonggou Formation are of ~2.10 Ga, and a significant number of ~2.50 Ga detrital zircon occurs as a minor age population (Diwu et al. 2013). These Paleoproterozoic to end-Archean detrital zircons show a large variation of $\varepsilon_{Hf}(t)$ values from −22.6 to +9.2, reflecting the mixing of an Archean crust with a juvenile crust (Liu et al. 2011a, b, 2012b). Possibly, the 2560–1850 Ma rocks in the NCC were the main sources of detritus of the low-grade metasedimentary units and the proportions of detrital zircons within this age range decrease from the north to the south (Liu et al. 2012a, b).

For the 2850–2600 Ma detrital zircons of the low-grade metasedimentary units. In the Wutai and Lüliang complexes, minor amounts of detrital zircons with this range age are suggested to come from the inherited/xenocrystic zircons recognized in the Wutai-Longquanguan granitoids and Hengshan and Fuping TTG gneisses (Liu et al. 2011a, b). In contrast, detrital zircons with these ages constitute 30 and 60 % of all the analyzed zircons in the Zhongtiao and Dengfeng complexes, and the TTG gneisses and amphibolites in the Taihua Complex are interpreted as their source rocks (Liu et al. 2012a, b). These Meso- to Neoarchean detrital zircons show negative to positive $\varepsilon_{Hf}(t)$ values, reflecting the mixing of a Eo- to Mesoarchean crust with a juvenile crust (Liu et al. 2011a, b, 2012a, b). For the minor populations of detrital zircons with ages older than 3100 Ma from the low-grade metasedimentary units, they were suggested to derive from the Paleo- and Mesoarchean crust of the Eastern Block due to their age and isotopic similarities (Liu et al. 2012a, b). These Paleo- and Mesoarchean detrital zircons display $\varepsilon_{Hf}(t)$ values ranging from −15.8 to +4.3, suggesting that they were originated from reworking of the Eoarchean crust.

For the depositional ages and tectonic setting of these low-grade metasedimentary units, the Songshan Group had been correlated with the Hutuo Group in the Wutai Complex and interpreted to have deposited in a rift basin (Du et al. 2009, 2010; Wan et al. 2009), but rift sedimentation and subsidence is primarily controlled by episodic faulting and basin subsidence, which result in lithostratigraphic replete with lateral and vertical facies changes (Wright and Troxel 1999). In addition, volcanic, evaporitic and lacustrine deposits are common in rift basins (Jackson et al. 2006). Neverthless, the Songshan Group exhibits none of these features and is characterized by >1.5 km vertically and >70 km horizontally similar siliciclastic sediments different to most rift basins. Li and Kusky (2007) interpreted the lower part of the Hutuo Group in the Wutai Complex and the Songshan Group in the Dengfeng Complex as the products of the Qinglong foreland basin which developed during the final collision between the Eastern and Western Blocks at ~2.50 Ga. However, some researchers suggest that the

lower part of the Hutuo Group was deposited after ~2100 Ma (Liu et al. 2011b), which is inconsistent with the above ~2.50 Ga collision model (Kusky and Li 2003; Li and Kusky 2007), but in accordance with collision between the Eastern and Western blocks along the Trans-North China Orogen at ~1.85 Ga (Zhao et al. 2001, 2005; Wilde et al. 2002; Kröner et al. 2005, 2006; Guo et al. 2005; Liu et al. 2005; Zhang et al. 2006, 2007, 2009). Similar results have also been produced from the upper part of the Yejishan Group in the Lüliang Complex and the Upper Zhongtiao and Danshanshi groups in the Zhongtiao Complex, suggesting that they were formed in foreland basins between ~1850 and ~1800 Ma (Liu et al. 2011a, 2012b).

However, the depositional ages of the Paleotroterozoic low-grade metasedimentary units in the NCC discussed in this chapter are constrained at a certain period after 2.35 Ga and before 1.80 Ga, which overlaps with the stage of subduction-collision related 2.45–2.20 Ga mamatisms and extensional setting related 2.20–2.00 Ga magmatisms. In addition, the Hf isotopic data of detrital zircons from Paleoproterozoic metasedimentary rocks varied mainly toward the reduction of the radiogenic Hf isotope and gradually show a similar trend of the isotope trajectories of crustal evolution (Diwu et al. 2013). This reveals that the NCC probably not has developed a long-lived subduction to complete the final assembly of the NCC. Alternatively, these maybe imply that the tectonic setting of the NCC substantially changed at ~2.10 Ga. Therefore, possibly, like previous studies, all these low-grade metasedimentary groups were deposited basin settings which were not simple foreland basins, they evolved from back-arc or intra-arc basins developing at the subduction-collision stage (from ~2.45 to 2.20 Ga) to rift stage (from ~2.20 to 2.00 Ga) and then to foreland basins at the collision stage (from ~1.85 to ~1.80 Ga; Liu et al. 2011a, b, 2012a).

10.7 Summary and Conclusions

1. The widespread 2.45–2.20 Ga magmatisms occurred in the southern NCC. The TTG or TTG-like gneisses of this age range most likely derived from partial melting of basaltic lower crust with juvenile materials addition or subducted slab. The 2.45–2.20 Ga dioritic-gabbroic gneisses were produced by partial melting of metasomatized lithospheric mantle. The amphibolites are consistent with magma derivation from OIB-like mantle wedge. The (high-K) calc-alkaline granites are representative of syn-collisional or post-collisional granites, and were produced by variable mixing of a juvenile melt with older crust in a continental margin arc or island arc setting.
2. The 2.20–2.00 Ga magmatism reveals a major period of crustal reworking, rather than one of crustal addition. The monzonite of this age range possibly formed related to extension and thinning of the lithosphere and upwelling of asthenosphere. The potassic granite belongs to highly fractionated aluminous A-type granite, and formed in a post-collisional setting, the injection of basaltic melt into the crust has been widely considered as an important mechanism to generate the A-type melt. The tonalite would be derived from partial melting of delaminated lower crust.
3. The temporal change from mostly 2.45–2.20 Ga low-K igneous rocks (TTG) to 2.20–2.0 Ga mostly high-K igneous rocks in the southern NCC indicates a tectonic transformation from accretionary orogenesis to extensional regimes.
4. The Songshan Group deposited after 2.35 Ga and before 1.80 Ga and sourced from felsic rocks. The major group of 3000–2400 Ma detrital zircons was sourced from the TTG gneisses of the Dengfeng, Zhongtiao, and Taihua complexes in the southern NCC. The minor amounts of 3700–3000 Ma detrital zircons derived from transported exotic Paleoarchean and Mesoarchean crustal materials. The 2400–1950 Ma detrital zircons were most likely sourced from the Paleoproterozoic granitoids and meta-rhyolites in the southern NCC.
5. The Tietonggou Formation deposited at 1.91–1.80 Ga, with major detrital zircon age peak of ~2.10 Ga. The minor group peaks of the detrital zircons are of 2.80–2.70 and ~2.50 Ga. All zircons possibly sourced from coeval lithologic units in the south NCC.
6. The provenances of the low-grade metasedimentary units in the NCC show some similarities but also exhibit some differences. They are constrained at a certain period of 2.35–1.80 Ga, overlapping with the subduction-collision stage (2.45–2.20 Ga) and rift setting stage (2.20–2.00 Ga).

Acknowledgments This study is supported by research grants from the National Basic Research Program of China (Grant No. 2012CB4166006), the National Science Foundation of China for Distinguished Young Scientists (Grant No. 41202139) and MOST Special Funds from the State Key Laboratory of Continental Dynamics. We thank senior engineer Shiyan Wang, Dr. Guohui Hu and Caiyuan Lan for field assistance and relevant academic discussion. We are very grateful to Prof. Chengli Zhang providing constructive and insightful comments to improve our manuscript.

References

Arth, J.-G. (1976). Behaviour of trace elements during magmatic processes-a summary of theoretical models and their applications. *Journal of Research U.S. Geological Survey, 4*, 41–47.

Bai, J., Huang, G.-X., Dai, F.-Y., & Wu, C.-H. (1993). *The Precambrian crustal evolution of China* (pp. 199–203). Beijing: Geological Publishing House (in Chinese).

Bai, J., Yu, Z.-X., Yan, Y.-Y., & Dai, F.-Y. (1997). *Precambrian geology of Zhongtiaoshan* (pp. 1–143). Tianjin: Tianjin Science and Technology Press (in Chinese with English abstract).

Bonin, B. (2007). A-type granites and related rocks: Evolution of a concept, problems and prospects. *Lithos, 97*, 1–29.

Bradshaw, T.-K., & Smith, E.-I. (1994). Polygenetic quaternary volcanism at Crater Flat, Nevada. *Journal of Volcanology and Geothermal Research, 63*, 165–182.

Buick, I.-S., Hermann, J., Williams, I.-S., Gibson, R.-L., & Rubatto, D. (2006). Age and petrogenesis of garnet–cordierite–orthoamphibole gneisses from the Central Zone of the Limpopo Belt, South Africa. *Lithos, 88*, 150–172.

Bureau of Geology and Mineral Resources of Henan Province. (1989). *Regional geology of Henan Province* (pp. 1–774). Beijing: Geological Publishing House (in Chinese).

Chacko, T., Ravindra Kumar, G.-R., Meen, J.-K., & Rogers, J.-J. (1992). Geochemistry of high-grade supracrustal rocks from the Kerala Khondalite Belt and adjacent massif charnockites, South India. *Precambrian Research*, *55*, 469–489.

Chappell, B.-W. (1999). Aluminium saturation in I and S-type granites and the characterization of fractionated haplogranites. *Lithos, 46*, 535–551.

Condie, K.-C. (1998). Episodic continental growth and supercontinents: A mantle avalanche connection? *Earth and Planetary Science Letters, 163*, 97–108.

Condie, K.-C. (2004). Supercontinents and superplume events: Distinguishing signals in the geologic record. *Physics of the Earth and Planetary Interiors, 146*, 319–332.

Condie, K.-C., & Kröner, A. (2008). When did plate tectonics begin? Evidence from the geologic record. *Geological Society of America Special Papers, 440*, 281–294.

Condie, K.-C., Belousova, E., Griffin, W.-L., & Sircombe, K.-N. (2009). Granitoid events in space and time: Constrains from igneous and detrital zircon age spectra. *Gondwana Research, 15*, 228–242.

Conrad, W.-K., Nicholls, I.-A., & Wall, V.-J. (1988). Water-saturated and undersaturated melting of metaluminous and peraluminous crustal compositions at 10 kb: Evidence for the origin of silicic magmas in the Taupo Volcanic Zone, New Zealand, and other occurrences. *Journal of Petrology, 29*, 765–803.

Dan, W., Li, X.-H., Guo, J.-H., Liu, Y., & Wan, C.-C. (2012). Paleoproterozoic evolution of the eastern Alxa Block, westernmost North China: Evidence from in situ zircon U-Pb dating and Hf-O isotopes. *Gondwana Research, 21*, 838–864.

Dash, B., Sahu, K.-N., & Bowes, D.-R. (1987). Geochemistry and original nature of Precambrian khondalites in the Eastern Ghats, Orissa, India. Transactions of the Royal Society of Edinburgh. *Earth Sciences, 78*, 115–127.

De La Roche, H., Letterier, J., Grandclaude, P., & Marchal, M. (1980). A classification of volcanic and plutionic rocks using R1-R2 diagram and major element analysis. Its relation with current nomenclature. *Chemical Geology, 29*, 183–210.

Ding, L.-F. (1996). New recognition to Group Taihua in the Mountain Small Qinling in the west of province Henan. *Journal of Xi'an College of Geology, 18*, 1–8 (in Chinese with English abstract).

Diwu, C.-R., Sun, Y., Gao, J.-F., & Fan, L.-G. (2013). Early Precambrian tectonothermal events of the North China Craton: Constrains from in situ detrital zircon U-Pb, Hf and O isotopic compositions in Tietonggou Formation. *Chinese Science Bulletin, 58*, 3760–3770.

Diwu, C.-R., Sun, Y., Guo, A.-L., Wang, H.-L., & Liu, X.-M. (2011). Crustal growth in the North China Craton at $\sim$2.5 Ga: Evidence from in situ zircon U-Pb ages, Hf isotopes and whole-rock geochemistry of the Dengfeng complex. *Gondwana Research, 20*, 149–170.

Diwu, C.-R., Sun, Y., Lin, C.-L., Liu, X.-M., & Wang, H.-L. (2007). Zircon U–Pb ages and Hf isotopes and their geological significance of Yiyang TTG gneisses from Henan province, China. *Acta Petrologica Sinica, 23*, 253–262 (in Chinese with English abstract).

Diwu, C.-R., Sun, Y., Lin, C.-L., & Wang, H.-L. (2010). LA-(MC)-ICPMS U-Pb zircon geochronology and Lu–Hf isotope compositions of the Taihua complex on the southern margin of the North China Craton. *Chinese Science Bulletin, 55*, 2557–2571.

Diwu, C.-R., Sun, Y., Yuan, H.-L., Wang, H.-L., Zhong, X.-P., & Liu, X.-M. (2008). U-Pb ages and Hf isotopes for detrital zircons from quartzite in the Paleoproterozoic Songshan Group on the southwestern margin of the North China Craton. *Chinese Science Bulletin, 53*, 2828–2839.

Diwu, C.-R., Sun, Y., Zhao, Y., & Lai, S.-C. (2014). Early Paleoproterozoic (2.45–2.20 Ga) magmatic activity during theperiod of global magmatic shutdown: Implications for the crustalevolution of the southern North China Craton. *Precambrian Research, 255*, 627–640.

Dong, C.-Y., Liu, D.-Y., Li, J.-J., Wan, Y.-S., Zhou, H.-Y., Li, C.-D., et al. (2007). Palaeoproterozoic Khondalite Belt in the western North China Craton: New evidence from SHRIMP dating and Hf isotope composition of zircons from metamorphic rocks in the Bayan Ul–Helan Mountains area. *Chinese Science Bulletin, 52*, 2984–2994.

Du, L.-L., Yang, C.-H., Guo, J.-H., Wang, W., Ren, L.-D., Wan, Y.-S., et al. (2010). The age of the base of the Paleoproterozoic Hutuo Group in the Wutai Mountains area, North China Craton: SHRIMP zircon U-Pb dating of basaltic andesite. *Chiese Science Bulletin, 55*, 1782–1789.

Du, L.-L., Yang, C.-H., Ren, L.-D., Wan, Y.-S., & Wu, J.-S. (2009). Petrology, geochemistry and petrogenesis of the metabasalts of the Hutuo Group, Wutai Mountains, Shanxi, China. *Geological Bulletin of China, 28*, 867–876 (in Chinese with English abstract).

Du, L.-L., Yang, C.-H., Wang, W., Ren, L.-D., Wan, Y.-S., Wu, J.-S., et al. (2013). Paleoproterozoic rifting of the North China Craton: Geochemical and zircon Hf isotopic evidence from the 2137 Ma Huangjinshan A-type granite porphyry in the Wutai area. *Journal of Asian Earth Sciences, 72*, 190–202.

Eby, G.-N. (1992). Chemical subdivision of the A-type granitoids: Petrogenetic and tectonic implications. *Geology, 20*, 641–644.

Eriksson, P.-G., & Condie, K.-C. (2014). Cratonic sedimentation regimes in the ca. 2450–2000 Ma period: Relationship to a possible widespread magmatic slowdown on Earth? *Gondwana Research, 25*, 30–47.

French, J.-E., & Heaman, L.-M. (2010). Precise U–Pb dating of Paleoproterozoic mafic dykes warms of the Dharwar craton, India: implications for the existence of the Neoarchean supercraton Sclavia. *Precambrian Research, 183*, 416–441.

Frost, B.-R., Barnes, C.-G., Collins, W.-J., Arculus, R.-J., Ellis, D.-J., & Frost, S.-D. (2001). A geochemical classification for granitic rocks. *Journal of Petrology, 42*, 2033–2048.

Geng, Y.-S., Wan, Y.-S., Shen, Q., Li, H., & Zhang, R. (2000). Chronological framework of the early Precambrian important events in the Lüliang Area. Shanxi Province. *Acta Geologica Sinica, 74*, 216–223 (in Chinese with English abstract).

Geng, Y.-S., Wan, Y.-S., & Yang, C.-H. (2003). The Paleoproterozoic rift-type volcanism in Lüliangshan area, Shanxi Province, and its geological significance. *Acta Geoscientia Sinica, 24*, 97–104 (in Chinese with English abstract).

Geng, Y.-S., Wan, Y.-S., & Yang, C.-H. (2008). Integrated research report on the establishment of Paleoproterozoic system of China—Determination of major Paleoproterozoic geological events and prelimary subdivision of Paleoproterozoic strata in the Lüliang area. In *Research Report on the Establishment of Major Stratigraphical*

Stages in China (2001–2005) (pp. 515–533). Beijing: Geological Publishing House (in Chinese).

Geng, Y.-S., Yang, C.-H., & Wan, Y.-S. (2006). Paleoproterozoic graniticmagmatismin the Luliang area, North China Craton: Constraint from isotopic geochronology. *Acta Petrologica Sinica, 22*, 305–314 (in Chinese with English abstract).

Green, T.-H. (1982). Anatexis of mafic crust and high pressure crystallization of andesite. In R. S. Thorpe (Ed.), *Andesites: Orogenic andesites and related rocks* (pp. 465–487). Chichester: JohnWiley.

Green, T.-H. (1992). Experimental phase equilibrium studies of garnet-bearing I-type volcanics and high-level intrusives from Northland, New Zealand. *Transactions of the Royal Society of Edinburgh: Earth Sciences, 83*, 429–438.

Guan, B.-D. (Ed.). (1996). *The Precambrian-Lower Cambrian geology and metallogensis in the south border of the North China platform in Henan Province* (pp. 1–328). Wuhan: Press of China University of Geosciences (in Chinese with English abstract).

Guan, H., Sun, M., Wilde, S.-A., Zhou, X.-H., & Zhai, M.-G. (2002). SHRIMP U-Pb zircon geochronology of the Fuping complex: Implications for formation and assembly of the North China Craton. *Precambrian Research, 113*, 1–18.

Guo, J.-H., Sun, M., Chen, F.-K., & Zhai, M.-G. (2005). Sm-Nd and SHRIMP U-Pb zircon geochronology of high-pressure granulites in the Sanggan area, North China Craton: Timing of Paleoproterozoic continental collision. *Journal of Asian Earth Sciences, 24*, 629–642.

Guo, J.-H., Zhai, M.-G., & Xu, R.-H. (2001). Timing of the granulite facies metamorphism in the Sanggan area, North China craton: Zircon U-Pb geochronology. *Science in China (Series D), 44*, 1010–1018.

Guo, L.-S., Liu, S.-W., Liu, Y.-L., Tian, W., Yu, S.-Q., Li, Q.-G., et al. (2008). Zircon Hf isotopic features of TTG gneissed and formation environment of Precambrian Sushui Complex in Zhongtiao mountains. *Acta Petrologica Sinica, 24*, 139–148.

Harangi, S.-Z., Downes, H., Kosa, L., Szabo, C.-S., Thirlwall, M.-F., Mason, P.-R.-D., et al. (2001). Almandine garnet in calc-alkaline volcanic rocks of the Northern Pannonian Basin (Eastern–Central Europe): Geochemistry, petrogenesis and geodynamic implications. *Journal of Petrology, 42*, 1813–1843.

Harlaub, R.-P., Heaman, L.-M., Chacko, T., & Ashton, K.-E. (2007). Circa 2.3-Ga Magmatismof the Arrowsmith Orogeny, Uranium City Region, Western Churchill Craton, Canada. *The Journal of Geology, 115*, 181–195.

He, Y.-H., Zhao, G.-C., Sun, M., & Xia, X.-P. (2009). SHRIMP and LA-ICP-MS zircon geochronology of the Xiong'er volcanic rocks: Implications for the Paleo-Mesoproterozoic evolution of the southern margin of the North China Craton. *Precambrian Research, 16*, 213–222.

Hermann, J., & Rubatto, D. (2003). Relating zircon and monazite domains to garnet growth zones: Age and duration of granulite facies metamorphism in the Val Malenco lower crust. *Journal of Metamorphic Geology, 21*, 833–852.

Hokada, T., & Harley, S.-L. (2004). Zircon growth in UHT leucosome: Constraints from zircon-garnet rare earth elements (REE) relations in Napier Complex, East Antarctica. *Journal of Mineralogical and Petrological Sciences, 99*, 180–190 (Special Issue).

Hu, G.-W. (1992). The basic structural characteristics of the early Proterozoic Liaohe Group. *Bulletin of Tianjin Institute of Geology and Mineral Resources, 26/27*, 179–188 (in Chinese with English Abstract).

Huang, D.-M., Zhang, D.-H., Wang, S.-Y., Zhang, Y.-X., Dong, C.-Y., Liu, D.-Y., et al. (2012a). 2.3 Ga magmatism and 1.94 Ga metamorphism in the Xiatang Area, southern margin of the North China Craton—Evidence from whole-rock geochemistry and zircon geochronology and Hf isotope. *Geological Review, 3*, 565–576.

Huang, X.-L., Niu, Y.-L., Yi, G.-X., Yang, Q.-J., & Zhong, J.-W. (2010). Geochemistry of TTG and TTG-like gneisses from Lushan-Taihua complex in the southern North China Craton: Implications for late Archean crustal accretion. *Precambrian Research, 182*, 43–56.

Huang, X.-L., Wilde, S.-A., Yang, Q.-J., & Zhong, J.-W. (2012b). Geochronology and petrogenesis of gray gneisses from the Taihua Complex at Xiong'er in the southern segment of the Trans-North China Orogen: Implications for tectonic transformation in the Early Paleoproterozoic. *Lithos, 134–135*, 236–252.

Huang, X.-L., Wilde, S.-A., & Zhong, J.-W. (2013). Episodic crustal growth in the southern segment of the Trans-North China Orogen across the Archean-Proterozoic boundary. *Precambrian Research, 233*, 337–357.

Huang, X.-L., Xu, Y.-G., Lan, J.-B., Yang, Q.-J., & Luo, Z.-Y. (2009). Neoproterozoic adakitic rocks from Mopanshan in the western Yangtze Craton: Partial melts of a thickened lower crust. *Lithos, 112*, 367–381.

Jackson, C.-A.-L., Gawthorpe, R.-L., Leppard, C.-W., & Sharp, I.-R. (2006). Rift-initiation development of normal fault blocks: Insights from the Hamman Faraun fault block, Suez Rift, Egypt. *Journal of the Geological Society, 163*, 165–183.

Jiang, Z.-S., Wang, G.-D., Xiao, L.-L., Diwi, C.-R., Lu, J.-S., & Wu, C.-M. (2011). Paleoproterozoic metamorphic P-T-t path and tectonic significance of the Luoning metamorphic complex at the southern terminal of the Trans-North China Orogen, Henan Province. *Acta Petrologica Sinina, 27*, 3701–3717 (in Chinese with English abstract).

Kay, R.-W., & Kay, S.-M. (1993). Delamination and delamination magmatism. *Tectonophysics, 219*, 177–189.

Kelly, N., & Harley, S. (2005). An integrated microtextural and chemical approach to zircon geochronology: Refining the Archean history of the Napier Complex, east Antarctica. *Contributions to Mineralogy and Petrology, 149*, 57–84.

King, P.-L., Chappell, B.-W., Allen, C.-M., & White, A.-J.-R. (2001). Are A-type granites the high-temperature felsic granites? Evidence from fractionated granites of the Wangrah Suite. *Australian Journal of Earth Sciences, 48*, 501–514.

King, P.-L., White, A.-J.-R., Chappell, B.-W., & Allen, C.-M. (1997). Characterization and origin of aluminous A-type granites from the Lachlan Fold Belt, southeastern Australia. *Journal of Petrology, 38*, 371–391.

Kröner, A., Compston, W., Zhang, G.-W., Guo, A. L., & Todt, W. (1988). Age and tectonic setting of late Archean greenstone-gneiss terrain in Henan province, China as revealed by single-grain zircon dating. *Geology, 16*, 211–215.

Kröner, A., Wilde, S.-A., & Li, J.-H. (2005). Age and evolution of a late Archean to Paleoproterozoic upper to lower crustal section in the Wutaishan/Hengshan/Fuping terrain of northern China. *Journal of Asian Earth Sciences, 24*, 577–595.

Kröner, A., Wilde, S.-A., Wang, K.-Y., & Zhao, G.-C. (2002). *Age and evolution of a late Archean to early Palaeozoic upper to lower crustal section in the Wutaishan/Hengshan/Fuping terrain of northern China, a field guide*. Geological Society of America Penrose Conference, Beijing, China (September).

Kröner, A., Wilde, S.-A., Zhao, G.-C., O'Brien, P., Sun, M., Liu, D.-Y., et al. (2006). Zircon geochronology and metamorphic evolution of mafic dykes in the Hengshan complex of Northern China: Evidence for late Paleoproterozoic extension and subsequent high-pressure metamorphism in the North China Craton. *Precambrian Research, 146*, 45–67.

Kusky, T.-M., & Li, J.-H. (2003). Paleoproterozoic tectonic evolution of the North China Cratons. *Journal of Asian Earth Sciences, 22*, 383–397.

Kusky, T.-M., Li, J.-H., & Santosh, M. (2007). The Paleoproterozoic North Hebei Orogen: North China Craton's collisional suture with the Columbia supercontinent. *Gondwana Research, 12*, 4–28.

Kusky, T.-M., Li, J.-H., & Tucker, R.-T. (2001). The Archean Dongwanzi ophiolite complex, North China Craton: 2.505 billion year old oceanic crust and mantle. *Science, 292*, 1142–1145.

Lauri, L.-S., Mikkola, P., & Karinen, T. (2012). Early Paleoproterozoic felsic and mafic magmatism in the Karelian province of the Fennoscandian shield. *Lithos, 151*, 74–82.

Li, J.-H., & Kusky, T.-M. (2007). A late Archean foreland fold and thrust belt in the North China craton: Implications for early collisional tectonics. *Gondwana Research, 12*, 47–66.

Li, J.-H., Kusky, T.-M., & Huang, X. (2002). Neoarchean podiform chromites and harzburgite tectonite in ophiolitic mélange, North China Craton remnants of Archean oceanic mantle. *GSA Today, 12*, 4–11.

Li, S.-Z., Han, Z.-Z., Liu, Y.-J., & Yang, Z.-S. (2001a). Constrains of Geology and Geochemistry on Palaeoproterozoic Pre-orogenic deep processes in the Jiao-Liao Massif. *Scientia Geologica Sinica, 36*, 189–195 (in Chinese with English abstract).

Li, S.-Z., Han, Z.-Z., Liu, Y.-J., Yang, Z.-S., & Ma, R. (2001b). Continental dynamics and regional metamorphism in the Liaohe Group. *Geological Review, 47*, 9–18 (in Chinese with English abstract).

Li, S.-Z., & Yang, Z.-S. (1997). Types and genesis of palaeoproterozoic granites in the Jiao-Liao Massif. *Northwest Geol, 43*, 21–27 (in Chinese with English abstract).

Li, S.-Z., Yang, Z.-S., & Liu, Y.-J. (1998). Stratification of metamorphic belts and its genesis in the Liaohe group. *Chinese Science Bulletin, 43*, 430–434.

Li, S.-Z., Yang, Z.-S., Liu, Y.-J., & Liu, J.-L. (1997). Emplacement model of paleoproterozoic early-granite in the Jiao-Liao-Ji area and its relation to layered gravitational sliding stucture. *Acta Petrologica Sinica, 13*, 189–202 (in Chinese with English abstract).

Li, S.-Z., & Zhao, G.-C. (2007). SHRIMP U-Pb zircon geochronology of the Liaoji granitoids: Constraints on the evolution of the Paleoproterozoic Jiao-Liao-Ji belt in the Eastern block of the North China Craton. *Precambrian Research, 158*, 1–16.

Liu, C.-H., Zhao, G.-C., Liu, F.-L., & Shi, J.-R. (2014). 2.2 Ga magnesian andesites, Nb-enriched basalt-andesites, and adakitic rocks in the Lüliang Complex: Evidence for early Paleoproterozoic subduction in the North China Craton. *Lithos, 208–209*, 104–117.

Liu, C.-H., Zhao, G.-C., Sun, M., Wu, F.-Y., Yang, J.-H., Yin, C.-Q., & Leung, W.-H. (2011a). U-Pb and Hf isotopic study of detrital zircons from the Yejishan Group of the Lüliang Complex: Constraints on the timing of collision between the Eastern and Western Blocks, North China Craton. *Sedimentary Geology, 236*, 129–140.

Liu, C.-H., Zhao, G.-C., Sun, M., Zhang, J., He, Y.-H., Yin, C.-Q., et al. (2011b). U-Pb and Hf isotopic study of detrital zircons from the Hutuo group in the Trans-North China Orogen and tectonic implications. *Gondwana Research, 20*, 106–121.

Liu, C.-H., Zhao, G.-C., Sun, M., Zhang, J., & Yin, C.-Q. (2012a). U-Pb geochronology and Hf isotope geochemistry of detrital zircons from the Zhongtiao Complex: Constraints on the tectonic evolution of the Trans-North China Orogen. *Precambrian Research, 222–223*, 159–172.

Liu, C.-H., Zhao, G.-C., Sun, M., Zhang, J., Yin, C.-Q., & He, Y.-H. (2012b). Detrital zircon U-Pb dating, Hf isotopes and whole-rock geochemistry from the Songshan Group in the Dengfeng Complex: Constraints on the tectonic evolution of the Trans-North China Orogen. *Precambrian Research, 192–195*, 1–15.

Liu, D.-Y., Nutman, A.-P., Compston, W., Wu, J.-S., & Shen, Q.-H. (1992). Remnants of 3800 crust in the Chinese part of the Sino-Korean craton. *Geology, 20*, 339–342.

Liu, D.-Y., Wilde, S.-A., Wan, Y.-S., Wang, S.-Y., Valley, J.-W., Kita, N., et al. (2009). Combined U-Pb, hafnium and oxygen isotope analysis of zircons from meta-igneous rocks in the southern North China Craton reveal multiple events in the Late Mesoarchean-Early Neoarchean. *Chemical Geology, 261*, 139–153.

Liu, D.-Y., Wilde, S.-A., Wan, Y.-S., Wu, J.-S., Zhou, H.-Y., Dong, C.-Y., et al. (2008). New U-Pb and Hf isotopic data confirm Anshan as the oldest preserved segment of the North China Craton. *American Journal of Science, 308*, 200–231.

Liu, J.-L., Liu, Y.-J., Chen, H., Sha, D.-M., & Wang, H.-C. (1997). The inner zone of the Liaoji Paleorift: Its early structural styles and structural evolution. *Journal of Asian Earth Sciences, 15*, 19–31.

Liu, S.-W., Pan, Y.-M., Xie, Q.-L., Zhang, J., Li, Q.-G., & Yang, B. (2005). Geochemistry of the Paleoproterozonic Nanying granitic gneisses in the Fuping Complex: Implications for the tectonic evolution of the Central Zone, North China Craton. *Journal of Asian Earth Sciences, 24*, 643–658.

Liu, S.-W., Zhang, J., Li, Q.-G., Zhang, L.-F., Wang, W., & Yang, P.-T. (2012c). Geochemistry and U-Pb zircon ages of metamorphic volcanic rocks of the Paleoproterozoic Lüliang Complex and constraints on the evolution of the Trans-North China Orogen, North China Craton. *Precambrian Research, 222–223*, 173–190.

Lu, X.-P., Wu, F.-Y., Guo, J.-H., Wilde, S.-A., Yang, J.-H., & Liu, X.-M. (2006). Zircon U-Pb geochronological constraints on the Paleoproterozoic crustal evolution of the Eastern Block in the North China Craton. *Precambrian Research, 146*, 138–164.

Lu, X.-P., Wu, F.-Y., Lin, J.-Q., Sun, D.-Y., Zhang, Y.-B., & Guo, C.-L. (2004a). Geochronological successions of the Early Precambrian granitic magmatism in southern Liaoning Peninsula and its constraints on tectonic evolution of the North China Craton. *Chinese Journal of Geology (Scientia Geologica Sinica), 39*, 123–139 (in Chinese with English abstract).

Lu, X.-P., Wu, F.-Y., Zhang, Y.-B., Zhao, C.-B., & Guo, C.-L. (2004b). Emplacement age and tectonic setting of the Paleoproterozoic Liaoji granites in Tonghua area, southern Jilin Province. *Acta Petrologica Sinica, 20*, 381–392 (in Chinese with English abstract).

Lustrino, M. (2005). How the delamination and detachment of lower crust can influence basaltic magmatism. *Earth-Science Reviews, 72*, 21–38.

Ma, X.-Y., Suo, S.-T., & You, Z.-D. (1981). *Tectonic deformation of the Songshan area, Henan Province, China: Gravitational tectonics, structural analysis*. Beijing: Geological Publishing House (in Chinese).

Ma, X.-Y., & Wu, Z.-W. (1981). Early tectonic evolution of China. *Precambrian Research, 14*, 185–202.

Muller, D., & Groves, D.-I. (1995). *Potassic igneous rocks and associated gold-copper mineralization* (pp. 1–144). Berlin: Springer.

Nath, W.-P., & Crecraft, H.-R. (1985). Partition coefficients for trace elements in silicic magmas. *Geochimica et Cosmochimica Acta, 49*, 2309–2322.

Ni, Z.-Y., Wang, R.-M., Tong, Y., Yang, C., & Dai, T.-M. (2003). $^{207}Pb/^{206}Pb$ age of zircon and $^{40}Ar/^{39}Ar$ of amphibole from plagioclase amphibolite in the Taihua Group, Luoning, Henan, China. *Geological Review, 49*, 361–366 (in Chinese with English abstract).

Pehrsson, S.-J., Buchan, K.-L., Eglington, B.-M., Berman, R.-M., & Rainbird, R.-H. (2014). Did plate tectonics shutdown in the Palaeoproterozoic? A view from the Siderian geologic record. *Gondwana Research, 26*, 803–815.

Peng, P., Guo, J.-H., Zhai, M.-G., Windley, B.-F., Li, T.-S., & Liu, F. (2012). Genesis of the Hengling magmatic belt in the North China Craton: Implications for Paleoproterozoic tectonics. *Lithos, 148*, 27–44.

Peng, P., Zhai, M.-G., Ernst, R.-E., Guo, J.-H., Liu, F., & Hu, B. (2008). A 1.78 Ga large igneous province in the North China craton: The Xiong'er Volcanic Province and the North China dyke swarm. *Lithos, 101*, 260–280.

Peng, P., Zhai, M.-G., & Guo, J.-H. (2005). Geochronological constraints on the Paleoproterozoic evolution of the North China Craton: SHRIMP Zircon ages of different types of Mafic Dikes. *International Geology Review, 47*, 492–508.

Peng, Q.-M., & Palmer, M.-R. (2002). The Paleoproterozoic Mg and Mg-Fe borate deposits of Liaoning and Jilin Provinces, Northeast China. *Economic Geology, 97*, 93–108.

Qi, J.-Y. (1992). Metamorphic rock series of Taihua Group and conditions for its formation in eastern Qinling. *Scientia Geologica Sinica, 27*, 94–107 (in Chinese with English abstract).

Rubatto, D. (2002). Zircon trace element geochemistry: Distribution coefficients and the link between U-Pb ages and metamorphism. *Chemical Geology, 184*, 123–138.

Rubatto, D., Hermann, J., & Buick, I.-S. (2006). Temperature and bulk composition control on the growth of monazite and zircon during low-pressure anatexis (Mount Stafford, central Australia). *Journal of Petrology, 47*, 1973–1996.

Rudnick, R.-L., & Fountain, D.-M. (1995). Nature and composition of the continental crust: A lower crustal perspective. *Reviews of Geophysics, 33*, 267–309.

Santosh, M., Yang, Q.-Y., Teng, X.-M., & Tang, L. (2015). Paleoproterozoic crustal growth in the North China Craton: Evidence from the Lüliang Complex. *Precambrian Research, 263*, 197–231.

Severs, M.-J., Beard, J.-S., Fedele, L., Hanchar, J.-M., Mutchler, S.-R., & Bodnar, R.-J. (2009). Partitioning behavior of trace elements between dacitic melt and plagioclase, orthopyroxene, and clinopyroxene based on laser ablation ICPMS analysis of silicate melt inclusions. *Geochimica et Cosmochimica Acta, 7*, 2123–2141.

Shen, F.-N. (1994). The discovery of unconformity within the Taihua Group and definition of its stratigraphic sequence in the Lushan area, Henan. *Regional Geology of China, 2*, 135–140.

Slack, J.-F., & Stevens, P.-J. (1994). Clastic metasediments of the Early Proterozoic Broken Hill Group, New South Wales, Australia: Geochemistry, provenance and metallogenic significance. *Geochimica et Cosmochimica Acta, 58*, 3633–3652.

Smith, E.-I., Sanchez, A., Walker, J.-D., & Wang, K. (1999). Geochemistry of mafic magmas in the Hurricane Volcanic field, Utah: Implications for small- and large-scale chemical variability of the lithospheric mantle. *Journal of Geology, 107*, 433–448.

Strand, K., & Köykkä, J. (2012). Early Paleoproterozoic rift volcanism in the eastern Fennoscandian Shield related to the breakup of the Kenorland supercontinent. *Precambrian Research, 214–215*, 95–105.

Su, Y.-P., Zheng, J.-P., Griffin, W.-L., Zhao, J.-H., Li, Y.-L., Wei, Y., et al. (2014). Zircon U-Pb ages and Hf isotope of gneissic rocks from the Huai'an Complex: Implications for crustal accretion and tectonic evolutionin the northern margin of the North China Craton. *Precambrian Research, 255*, 3335–3354.

Sun, D.-Z., & Hu, W.-X. (1993). *The geochronological framework and crustal structures of Precambrian basement in the Zhongtiaoshan Area* (pp. 108–117). Beijing: Geological Publishing House (in Chinese).

Sun, D.-Z., Hu, W.-X., Tang, M., Zhao, F.-Q., & Condie, K.-C. (1990). Origin of late Archean and early Proterozoic rocks and associated mineral deposits from the Zhongtiao Mountains, east-central China. *Precambrian Research, 47*, 287–306.

Sun, Q.-Y., Zhao, T.-P., & Zhou, Y.-Y. Detrital zircon U-Pb ages, Hf isotopes and whole-rock geochemistry of the Yinyugou Group in the Wang wushan area, southern region of the North China Craton: Implications for provenance study and the Paleo proterozoic tectonic evolution (Under review).

Sun, S.-S., & McDonough, W.-F. (1989). Chemical and isotopic systematics of oceanic basalts: Implications for mantle composition and processes. In S. D. Saunders & M. J. Norry (Eds.), *Magmatism in ocean basins* (Vol. 42, pp. 313–345). Geological Society of London.

Sun, Y., Yu, Z.-P., & Kröner, A. (1994). Geochemistry and single zircon geochronology of Archaean TTG gneisses in the Taihua high-grade terrain, Lushan area, central China. *Journal of South Asian Earth Science, 10*, 227–233.

Tian, W., Liu, S.-W., & Zhang, H.-F. (2006). Paleoproterozoic potassic granitoids in the Sushui complex from the Zhongtiao Mountains, Northern China: Geochronology, geochemistry and petrogenesis. *Acta Geologica Sinica, 80*, 875–885.

Trap, P., Faure, M., Lin, W., Augier, R., & Fouassier, A. (2011). Syn-collisional channel flow and exhumation of paleoproterozoic High Pressure rocks in the Trans- North China Orogen: The critical role of partial-melting and orogenic bending. *Gondwana Research, 20*, 498–515.

Tu, Y.-J. (1998). Geochimical comparing of two types of amphibolites within Taihua Group in Lushan County, Henan Province and their tectonic settings. *Geochimica, 27*, 412–421.

Wan, Y.-S., Geng, Y.-S., & Shen, Q.-H. (2000). Khondalite series—geochronology and geochemistry of the Jiehekou Group in Luliang area, Shanxi Province. *Acta Petologica Sinica, 1*, 49–58 (in Chinese with English abstract).

Wan, Y.-S., Liu, D.-Y., Dong, C.-Y., Xu, Z.-Y., Wang, Z.-J., Wilde, S., et al. (2009). The Precambrian Khondalite Belt in the Daqingshan area, North China Craton: Evidence for multiple metamorphic events in the Paleoproterozoic era. *Geological Society of London, Special Publications, 323*, 73–97.

Wan, Y.-S., Song, B., Liu, D.-Y., Wilde, S.-A., Wu, J.-S., Shi, Y.-R., et al. (2006a). SHRIMP U-Pb zircon geochronology of Palaeoproterozoic metasedimentary rocks in the North China Craton: Evidence for a major Late Palaeoproterozoic tectonothermal event. *Precambrian Research, 149*, 249–271.

Wan, Y.-S., Wilde, S.-A., Liu, D.-Y., Yang, C.-X., Song, B., & Yin, X.-Y. (2006b). Further evidence for 1.85 Ga metamorphism in the Central Zone of the North China Craton: SHRIMP U-Pb dating of zircon from metamorphic rocks in the Lushan area, Henan Province. *Gondwana Research, 9*, 189–197.

Wang, G.-D., Wang, H., Chen, H.-X., Lu, J.-S., & Wu, C.-M. (2014). Metamorphic evolution and zircon U-Pb geochronology of the Mts. Huashan amphibolites: Insights into the Palaeoproterozoic amalgamation of the North China Craton. *Precambrian Research, 245*, 100–114.

Wang, H.-C., Lu, S.-N., Zhao, F.-Q., & Zhong, C.-D. (2005). The paleoproterzoic geological records in North China Craton and their tectonic significance. *Geological Survey and Research, 3*, 129–143.

Wang, L.-J., Guo, J.-H., Peng, P., Liu, F., & Wubdketm, B.-F. (2015). Lithological units at the boundary zone between the Jining and Huai'an complexes (central-northern margin of the North China Craton): A Paleoproterozoic tectonic mélange? *Lithos, 227*, 205–224.

Wang, Y., Deng, T., & Biasatti, D. (2006). Ancient diets indicate significant uplift of southern Tibet after ca. 7 Ma. *Geology, 34*, 309–312.

Wei, C.-J., Qian, J.-H., & Zhou, X.-W. (2014). Paleoproterozoic crustal evolution of the Hengshan-Wutai-Fuping region, North China Craton. *Geoscience Frontiers, 5*, 485–497.

Whalen, J.-B., Currie, K.-L., & Chappell, B.-W. (1987). A-type granites: Geochemical characteristics, discrimination and petrogenesis. *Contributions to Mineralogy and Petrology, 95*, 407–419.

Whitehouse, M.-J., & Platt, J.-P. (2003). Dating high-grade metamorphism: Constraints from rare-earth elements in zircon and garnet. *Contributions to Mineralogy and Petrology, 145*, 61–74.

Wilde, S.-A., Cawood, P.-A., Wang, K.-Y., Nemchin, A., & Zhao, G.-C. (2004). Determining Precambrian crustal evolution in China: A case study from Wutaishan, Shanxi Province, demonstrating the application of precise SHRIMP U-Pb geochronology. *Geological Society of London Special Publication, 226*, 5–26.

Wilde, S.-A., Cawood, P.-A., Wang, K.-Y., & Nemchin, A.-A. (2005). Granitoid evolution in the late Wutai Complex, North China Craton. *Journal of Asian Earth Scieces, 2*, 597–613.

Wilde, S.-A., Zhao, G.-C., & Sun, M. (2002). Development of the North China Craton during the Late Archaean and its final amalgamation at 1.8 Ga: Some speculation on its position within a global Paleoproterozoic Supercontinent. *Gondwana Research, 5*, 85–94.

Wright, L.-A., & Troxel, B.-W. (1999). *Cenozoic Basins of the Death Valley Region* (p. 333). Geological Society of American, Special Papers.

Wu, F.-Y., Yang, J.-H., Liu, X.-M., Li, T.-S., Xie, L.-W., & Yang, Y.-H. (2005). Hf isotopes of the 3.8 Ga zircons in eastern Hebei Province, China: Implications for early crustal evolution of the North China Craton. *Chinese Science Bulletin, 50*, 2473–2480.

Wu, F.-Y., Zhang, Y.-B., Yang, J.-H., Xie, L.-W., & Yang, Y.-H. (2008). Zircon U-Pb and Hf isotopic constraints on the early Archean crustal evolution in Anshan of the North China Craton. *Precambrian Research, 167*, 339–362.

Wu, J.-S., Geng, Y.-S., Shen, Q.-H., Liu, D.-Y., & Song, B. (1998). *Archean geology characteristics and tectonic evolution of China-Korea Paleocontinent* (pp. 160–184). Beijing: Geological Publishing House (in Chinese).

Wu, J.-S., Liu, D.-Y., & Jin, L.-G. (1986). The zircon U-Pb age of metamorphosed basic volcanic lavas from the Hutuo Group in the Wutai mountain area, Shanxi Province. *Geological Review, 32*, 178–184 (in Chinese with English abstract).

Xu, J.-F., Shinjo, R., Defant, M.-J., Wang, Q., & Rapp, R.-P. (2002). Origin of Mesozoic adakitic intrusive rocks in the Ningzhen area of East China: Partial melting of delaminated lower continental crust? *Geology, 30*, 1111–1114.

Xu, Q.-D., Gao, S., & Liu, Q.-S. (1994). Geochemical constrains of granulite facies rocks in Taihua Group, Lushan County, Henan Province. *Acta Petrologica et Mineralogica, 13*, 214–226 (in Chinese with English abstract).

Xue, L.-W., Yuan, Z.-L., Zhang, Y.-S., & Qiang, L.-Z. (1995). The Sm-Nd isotope age of Taihua Group in the Lushan area and their implications. *Geochimica (Beijing), 24*(Suppl.), 92–97 (in Chinese with English abstract).

Xue, L.-W., Zhang, T.-Y., Xu, L., & Lu, X.-X. (2004). A discussion on the classification and dating of the Dengfeng Group. *Acta Geoscientica Sinica, 25*, 229–234 (in Chinese with English abstract).

Yang, C.-H., Du, L.-L., Ren, L.-D., Song, H.-X., Wan, Y.-S., Xie, H.-Q., et al. (2011). The age and petrogenesis of the Xuting granite in the Zanhuang Complex, Hebei Province: Constraints on the structural evolution of the Trans-North China Orogen, North China Craton. *Acta Petrologica Sinica, 27*, 1003–1016 (in Chinese with English abstract).

Yang, C.-H., Du, L.-L., & Ren, L.-D. (2009). SHRIMP U-Pb ages and stratigraphic correlation of the Angou group on the southern margin of the North China Craton. *Acta Petrol Sin, 25*, 1853–1862.

Yang, C.-X. (2008). Zircon SHRIMP U-Pb ages, geochemical characteristics and environmental evolution of the Early Precambrian metamorphic series in the Lushan area, Henan, China. *Geological Buletin of China, 27*, 517–533 (in Chinese with English abstract).

Yu, J.-H., Wang, D.-Z., & Wang, C.-Y. (1997). Geochemical characteristics and petrogenesis of the early Proterozoic bimodal volcanic rocks from Lüliang group, Shanxi Province. *Acta Petrologica Sinica, 13*, 59–70 (in Chinese with English abstract).

Yu, J.-H., Wang, D.-Z., Wang, C.-Y., & Wang, L.-J. (2004). Paleoproterozoic granitic magmatism and metamorphism in the middle Lüliang Mountain, Shanxi Province. *Geological Journal of China Universities, 10*, 500–512 (in Chinese).

Yu, S.-Q., Liu, S.-W., Tian, W., Li, Q.-G., & Feng, Y.-G. (2006). SHRIMP Zircon U-Pb Chronology and Geochemistry of the Hneglingguan and Beiyu Granitoids in the Zhongtiao Mountains, Shanxi Province. *Acta Geologica Sinica, 80*, 912–924.

Yu, X.-Q., Liu, J.-L., Li, C.-L., Chen, S.-Q., & Dai, Y.-P. (2013). Zircon U-Pb dating and Hf isotope analysis on the Taihua Complex: Constraints on the formation and evolution of the Trans-North China Orogen. *Precambrian Research, 230*, 31–44.

Zegers, T.-E., & van Keken, P.-E. (2001). Middle Archean continent formation by crustal delamination. *Geology, 29*, 1083–1086.

Zhai, M.-G. (2004). Precambrian geological events in the North China Craton. In J. Malpas, C. J. N. Fletcher, J. R. Ali, & C. Aitchison (Eds.), *Aspects on Tectonic Evolution of China* (Vol. 226, pp. 57–72). London: Geological Society Special Publication.

Zhai, M.-G. (2008). Lower crust and lithosphere beneath the North China Craton before the Mesozoic lithospheric disruption. *Acta Petrologica Sinica, 24*, 2185–2204 (in Chinese with English abstract).

Zhai, M.-G., & Liu, W.-J. (2003). Paleoproterozoic tectonic history of the North China Craton: A review. *Precambrian Research, 122*, 183–199.

Zhai, M.-G., & Peng, P. (2007). Paleoproterozoic events in the North China Craton. *Acta Petrologica Sinica, 23*, 2665–2682 (in Chinese with English abstract).

Zhai, M.-G., & Santosh., M. (2011). The early Precambrian odyssey of North China Craton: A synoptic overview. *Gondwana Research, 20*, 1–20.

Zhai, M.-G., & Santosh, M. (2013). Metallogeny of the North China Craton: Link with secular changes in the evolving Earth. *Gondwana Research, 24*, 275–297.

Zhang, B.-S. (1951). Songyang orogeny and Wutai formation in Songshan area (abstract). *Geological Review, 16*, 79–80 (in Chinese).

Zhang, G.-W., Bai, Y.-B., & Sun, Y. (1985). Composition and evolution of the Archean crust in central Henan, China. *Precambrian Research, 27*, 7–35.

Zhang, H.-F., Sun, M., Lu, F.-X., Zhou, X.-H., Zhou, M.-F., Liu, Y.-S., et al. (2001). Moderately depleted lithospheric mantle underneath the Yangtze Block: Evidence from a garnet lherzolite xenolith in the Dahongshan kimberlite. *Geochemical Journal, 35*, 315–331.

Zhang, H.-F., Wang, J.-L., Zhou, D.-W., Yang, Y.-H., Zhang, G.-W., Santosh, M., et al. (2014). Hadean to Neoarchean episodic crustal growth: Detrital zircon records in Paleoproterozoic quartzites from the southern North China Craton. *Precambrian Research, 254*, 245–257.

Zhang, J., Zhao, G.-C., Li, S.-Z., Sun, M., Liu, S.-W., Wilde, S.-A., et al. (2007). Deformation history of the Hengshan Complex: Implications for the tectonic evolution of the Trans-North China Orogen. *Journal of Structural Geology, 29*, 933–949.

Zhang, J., Zhao, G.-C., Li, S.-Z., Sun, M., Liu, S.-W., Xia, X.-P., et al. (2006). U-Pb zircon dating of the granitic conglomerates of the Hutuo Group: Affinities to the Wutai granitoids and significance to the tectonic evolution of the Trans-North China Orogen. *Acta Geologica Sinica-English Edition, 80*, 886–898.

Zhang, J., Zhao, G.-C., Li, S.-Z., Sun, M., Liu, S.-W., & Yin, C.-Q. (2009). Deformational history of the Fuping Complex and newU–Th–Pb geochronological constraints: Implications for the tectonic evolution of the Trans-North China Orogen. *Journal of Structural Geology, 31*, 177–193.

Zhang, R.-Y., Zhang, C.-L., Diwu, C.-R., & Sun, Y. (2012). Zircon U-Pb geochronology, geochemistry and its geological implications for the Precambrian granitoids in Zhongtiao Mountain, Shanxi

Province. *Acta Petrologica Sinina, 28*, 3559–3573 (in Chinese with English abstract).

Zhang, Z.-Q., & Li, S.-M. (1998). Sm–Nd, Rb–Sr age and its geological significance of Archean Taihua Group in Xiongershan, western Henan province. In Y. Q. Chen (Ed.), *Contributions of Early Precambrian Geology in North China Craton* (pp. 123–132). Beijing: Geological PublishingHouse (in Chinese).

Zhao, F.-Q., Li, H.-M., Zuo, Y.-C., & Xue, K.-Q. (2006a). Zircon U-Pb ages of Paleoproterozoic granitolds in the Zhongtiao mountains, southern Shanxi, China. *Geological Bulletin of China, 25*, 442–447 (in Chinese with English abstract).

Zhao, G.-C., Sun, M., Wilde, S.-A., & Li, S.-Z. (2005). Late Archean to Paleoproterozoic evolution of the North China Craton: Key issues revisited. *Precambrian Research, 136*, 177–202.

Zhao, G.-C., Sun, M., Wilde, S.-A., Li, S.-Z., Liu, S.-W., & Zhang, J. (2006b). Composite nature of the North China granulite-facies belt: Tectonothermal and geochronological constraints. *Gondwana Research, 9*, 337–348.

Zhao, G.-C., Wilde, S.-A., Cawood, P.-A., & Sun, M. (2001). Archean blocks and their boundaries in the North China craton: Lithological, geochemical, structural and P-T constraints and tectonic evolution. *Precambrian Research, 107*, 45–73.

Zhao, G.-C., Wilde, S.-A., Cawood, P.-A., & Sun, M. (2002). SHRIMP U-Pb zircon ages of the Fuping Complex: Implications for Late Archean to Paleoproterozoic accretion and assembly of the North China Craton. *American Journal of Science, 302*, 191–226.

Zhao, G.-C., Wilde, S.-A., Sun, M., Guo, J.-H., Kröner, A., Li, S.-Z., et al. (2008). Shrimp U-Pb zircon geochronology of the Huai'an Complex: Constraints on Late Archean to paleoproterozoic magmatic and metamorphic events in the Trans-North China Orogen. *American Journal of Science, 308*, 270–303.

Zhao, R.-F., Guo, J.-H., Peng, P., & Liu, F. (2011). 2.1 Ga crustal remelting event in Hengshan Complex: Evidence from zircon U-Pb dating and Hf-Nd isotopic study on potassic granites. *Acta Petrologica Sinica, 27*, 1607–1623 (in Chinese with English abstract).

Zhao, T.-P., Zhai, M.-G., Xia, B., Li, H.-M., Zhang, Y.-X., & Wan, Y.-S. (2004). Study on the zircon SHRIMP ages of the Xiong'er Group volcanic rocks: Constraint on the starting time of covering strata in the North China Craton. *Chinese Science Bulletin, 9*, 2495–2502 (in Chinese with English abstract).

Zhao, Z.-P. (1956). On the stratigraphic problems of the Hutuo and the Sinian systems in china. *Acta Geologica Sinica, 36*, 81–93 (in Chinese with English abstract).

Zhao, Z.-P. (1993). *Evolution of Precambrian crust of Sino-Korean platform* (pp. 366–368). Beijing: Scientific Press (in Chinese).

Zhao, T.-P., & Zhou, M.-F. (2009). Geochemical constraints on the tectonic setting of Paleoproterozoic A-type granites in the southern margin of the North China Craton. *Journal of Asian Earth Sciences, 36*, 183–195.

Zhong, C.-D. (2006). *Paleoproterozoic granitoids from central segment of North China Craton: Geochemistry, geochronology and tectonic significance*. Doctoral thesis.

Zhou, Y.-Y., Zhai, M.-G., Zhao, T.-P., Gao, J.-F., Lan, Z.-W., & Sun, Q.-Y. (2014a). Geochronological and geochemical constraints on the petrogenesis of the early Paleoproterozoic potassic granite in the Lushan area, southern margin of the North China Craton. *Journal of Asian Earth Sciences, 94*, 190–204.

Zhou, Y.-Y., Zhao, T.-P., Wang, C.-Y., & Hu, G.-H. (2011). Geochronology and geochemistry of Neoarchean to early Paleoproterozoic granitic plutons in the southern margin of the North China Craton: Implications for a tectonic transition from arc to post-collision setting. *Gondwana Research, 2*, 171–183.

Zhou, Y.-Y., Zhao, T.-P., Xue, L.-W., & Wang, S.-Y. (2009a). The Geochemistry and origin of Neoarchean plagio-amphibolites in Songshan, Hennan Province. *Acta Petrologica Sinica, 25*, 3043–3056 (in Chinese with English abstract).

Zhou, Y.-Y., Zhao, T.-P., Xue, L.-W., Wang, S.Y-., & Gao, J.-F. (2009b). Petrological, geochemical and chronological constraints for the origin and geological significance of Neoarchean TTG gneiss in the Songshan area, North China Craton. *Acta Petrologica Sinica, 25*, 331–347 (in Chinese with English abstract).

Zhou, Y.-Y., Zhao, T.-P., Zhai, M.-G., Gao, J.-F., Lan, Z.-W., & Sun, Q.-Y. (2015). Petrogenesis of the 2.1 Ga Lushan garnet-bearing quartz monzonite on the southern margin of the North China Craton and its tectonic implications. *Precambrian Research, 256*, 241–255.

Zhou, Y.-Y., Zhao, T.-P., Zhai, M.-G., Gao, J.-F., & Sun, Q.-Y. (2014b). Petrogenesis of the Archean tonalite-trondhjemite-granodiorite (TTG) and granites in the Lushan area, southern margin of the North China Craton: Implications for crustal accretion and transformation. *Precambrian Research, 255*, 514–537.

Part III
Great Oxidation Event

The Great Oxidation Event and Its Records in North China Craton

11

Yanjing Chen and Haoshu Tang

Abstract

In this chapter, we review the early Paleoproterozoic sedimentary records in North China Craton (NCC) and elsewhere in the world. We also propose a sequence framework for the subprime events happened in sedimentary sphere, biosphere, hydrosphere and atmosphere during the period of 2.5 to 1.8 Ga, and give an introduction to the Great Oxidation Event (GOE). These events are characteristic of the GOE, and are assigned to two main stages: (1) the early-stage hydrosphere oxidation (2.5–2.3 Ga), represented by the precipitation of the banded iron formations (BIFs), and (2) the late-stage atmospheric oxygenation (2.3–1.8 Ga), indicated by sediments of thick carbonate strata with 2.22–2.06-Ga $\delta^{13}C_{carb}$ positive excursion (Lomagundi Event), 2.25–1.95 Ga red beds, as well as the disappearance of BIFs at ca 1.8 Ga and prevail of black shales at 2.0–1.7 Ga. The 2.29–2.25-Ga Huronian Glaciation Event (HGE) demonstrated that the Earth's superficial system oxidation had entered from hydrosphere into atmosphere. The 2.3-Ga turnpoint is a better Archean-Proterozoic boundary in Geological Time Chart.

Keywords

Geological environment catastrophe • 2300 Ma • Geologic evolution • Ar–Pt boundary • Great oxidation event (GOE)

11.1 Discovery of the Environment Catastrophe at 2300 Ma

The significant change in sedimentary REE patterns at ca. 2300 Ma, characterized by pronounced Eu-depletion, was firstly discovered at the southern margin of North China Craton, which was proven universal in the whole North China Craton (NCC; Chen et al. 1988, 1989, 1990, 1991, 1992a, b, 1994, 1996, 1998; Chen and Fu 1991; Chen and Deng 1993; Chen and Zhao 1997; Chen and Su 1998). This was interpreted to have resulted from a dramatic change in oxygen fugacity of the hydrosphere and atmosphere (Chen 1988, 1989, 1990, 1996). If the discovery is a truth, the following phenomena could be speculated:

① The oxygen fugacity in hydrosphere and atmosphere increased globally, because the homogenization of oxygen fugacity or the diffusion of oxygen in atmosphere and hydrosphere are very swift;

② Due to the global increase in oxygen fugacity, sedimentary REE patterns changed worldwide at about 2300 Ma;

③ Increase in oxygen fugacity would inevitably result in many changes in the Earth's surficial system. For example, the type, valence and activity of ions in hydrosphere might be changed, which caused great influence on types and characteristics of sediments;

④ Changes in nature of biosphere, in composition and climate of atmosphere.

Y. Chen (✉)
Key Laboratory of Crustal and Orogenic Evolution, Peking University, Beijing, 100871, China
e-mail: yjchen@pku.edu.cn

H. Tang (✉)
State Key Laboratory of Ore Deposit Geochemistry, Institute of Geochemistry, Chinese Academy of Sciences, 99 Linchengxi Roud, Guiyang, 550081, China
e-mail: tanghaoshu@163.com

M. Zhai et al. (eds.), *Main Tectonic Events and Metallogeny of the North China Craton*,
Springer Geology, DOI 10.1007/978-981-10-1064-4_11

Table 11.1 Changes of the Earth's surface system around 2300 Ma (modified after Chen 1989, 1996; Chen et al. 1991)

Before 2300 Ma	After 2300 Ma (mainly before 1900 Ma)
Sporadic evidences of life	Universal stromatolites
Locally thin BIFs bearing pyrite, dominant of magnetite, with little hematite	Extensively thick BIFs dominantly composed by hematite and limonite, with no pyrite
No thick-bedded carbonate, no magnesite deposit	Extensively thick-bedded carbonate, superlarge magnesite deposits
Lack of phosphorite	Abundant phosphorite and phosphorus deposits
No evaporate	Appearance of evaporate
No graphite deposit, little graphite-bearing strata	Abundant graphite deposits and graphite-bearing strata
No red bed, no gypsum, but detrital pyrites can be observed in sediments	Red beds and gypsum beds are commonly observed
Well known giant Rand-type gold deposit, lack of gold placer	Lack of Rand-type gold deposits, frequently observed gold placers
Detrital uraninite in sediments hosting Rand-type uranium deposits	Absence of detrital uraninite, lots of weathering leaching-type uranium deposits
lack of weathering crust-or laterite-type deposit	A lot of weathering crust- or laterite-type deposits such as laterite-type gold and bauxite
Upward decreasing Fe_2O_3/FeO ratios in weathering crust	Upward increasing Fe_2O_3/FeO ratios in weathering crust
Sediments showing positive Eu-anomalies, low ΣREE and high $(La/Yb)_N$	Sediments showing negative Eu-anomalies, high ΣREE and low $(La/Yb)_N$
No REE-enriched sediment formation	REE-enriched iron sediment formation
Limited tillites in South Africa	A lot of tillites, global glaciation event
Lack of khondalite series and deposits of sillimanite, kyanite, etc.	Lots of khondalite series and deposits of sillimanite, kyanite, etc.
Intense volcanism, widespread greenstone belts	Volcanic gap, limited greenstone belt, many stable sedimentary basins
Organic carbon in sediments about 0.7 %	Organic carbon in sediments about 1.6 %
Low U, Th, La/Sc, Th/Sc, Th/U, K_2O/Na_2O, Fe_2O_3/FeO in sediments; low $^{87}Sr/^{86}Sr$ in carbonate	High U, Th, La/Sc, Th/Sc, Th/U, K_2O/Na_2O, Fe_2O_3/FeO in sediments; high $^{87}Sr/^{86}Sr$ in carbonate
Atmosphere rich in low valence gases (NH_3, CH_4, PH_3, H_2S, etc.); free oxygen absent	Atmosphere rich in high valence gases (NO_2, CO_2, SO_3, SO_2, etc.); flourished by free oxygen
Hydrosphere rich in low valence ions (Eu^{2+}, Fe^{2+}, Mn^{2+}, etc.) and anions(SCN^- CN^-, HS^-); low f_{O2} and pH	Hydrosphere rich in high valence ions (Eu^{3+}, Fe^{3+}, Mn^{4+}, etc.) and anions (SO_4^{2-}, CO_3^{2-}, NO_3^-, PO_4^{3-}, etc.); high f_{O2} and pH

Whether the above phenomena are reliable or not? What is responsible for the changes in the Earth's surficial environment? If this discovery is helpful to understand the Precambrian subdivision, geological evolution and formation of ore deposits? Obviously, they are important and open issues to study.

Since the discovery of the change in sedimentary REE patterns at about 2300 Ma, we have studied the changes in surficial environment around 2300 Ma comprehensively, and obtained a series of inspiring achievements which encourage us to exchange our research works and ideas with colleagues. Therefore, this Chapter tries to display evidences for the catastrophe at about 2300 Ma.

11.2 Paleoproterozoic Environment Change in NCC

Many aspects of the Earth's surficial system changed dramatically at about 2300 Ma, suggesting the occurrence of a catastrophe in geological environment at about 2300 Ma. All the changes are listed in Table 11.1, and some of them will be introduced in this chapter. As for related metallogenic explosion, such as graphite, phosphorite, the Superior Lake-type iron, boron (Tang et al. 2009a), magnesite (Tang et al. 2009b, c, 2013b), and lead–zinc deposits, will be discussed in Chap. 12 by Tang et al. (2016).

11.2.1 Volcanic Gap

High surface heat flow, intense volcanic eruption and magmatic intrusion in the early time of the Earth resulted in the widespread distribution of greenstone belts in the Archean (Condie 1981; Windley 1976; Eriksson and Truswell 1978), and the sediments account for less than 15 % of the Archean rocks. The global development of greenstone belt ceased at 2300 Ma on the whole (Eriksson and Truswell 1978), and were substituted by stable sedimentary basins. It is considered that from 2500 Ma when the Kenoran Movement ended, to the beginning of typical Wilson Cycle around 2000–1900 Ma, volcanic rocks were only developed in a few rift zones, companied by relatively intense sedimentation, forming the supracrustal lithologic assemblage composed of bimodal volcanic rocks, quarztites, quartz-feldspar sandstones and arkoses, such as the Angou, Xiaoshan and Jiangxian Groups in NCC. This assemblage accounted for about 20 % of the Paleoproterozoic supracrustal rocks and was termed Proterozoic supracrustal rock assemblage I (Condie 1982; Condie et al. 1992). Proterozoic spuracrustal rock assemblage II accounted for more than 60 % of the Paleoproterozoic lithostratigraphic sequences, and was composed of carbonate quartzite and shale, and mainly formed during the period of 2300–2000 Ma (Condie 1982), as exemplified by the Liaohe, Songshan, Fenzishan, Hutuo, Jingshan, Shuidigou and Fengzhen Groups of China, the Hamersley Group of Australia, the Huronian supergroup of Canada, the Krivoy Rog Series of Ukraine and Transvaal Supergroup of South Africa. These facts indicate a volcanic gap during the 2300–2000 Ma, which is in striking contrast with the pan volcanism in the Archean, reflecting a drastic change in Earth surficial system.

Kroner (1981) regarded the period of 2500–1900 Ma as the volcanic gap. Isley and Abbott (1999) argues that there is an absence of greenstone with age of 2450–2200 Ma. Several volcano-sedimentary formations such as the Elliot Lake Group of Canada, the Fortiscue Group of Western Australia, are thought to develop during this gap (Kroner 1981). Therefore, the volcanic gap was prolonged. In fact, those volcano-sedimentary formations are resulted from widespread Achean volcanism, not the products during Paleoproterozoic volcanic gap. However, in several areas, Paleoproterozoic volcanics are found in greenstones and rifting succession. For examples, in Svecokarelian Belt of the Baltic Shield, riftting volcanics (including komatiites) aged of 2.3–2.0 Ga are found within the Sumian-Sariolian Group and Upper Lapponian, Jatulian and Karelian sequences (Melezhik and Fallick 1996).

11.2.2 Global Glaciation

The temperature was very high before 2300 Ma due to high heat flow and extensive volcanism. After 2300 Ma, sharp drop of volcanism and temperature resulted in the formation of stable sedimentary basins over the world and the first global glaciation event in the Earth evolution (see Bekker and Kaufman 2007; Young 2014; and references therein). It is known as the 'Huronian Glaciation Event' (HGE, Tang and Chen 2013; Fig. 11.1), or the'Huronian-age glaciations' (Melezhik et al. 2013), or the Siderian Snowball Earth (SSE, Hoffman 2013). Tillites of the event had been showed and discussed in Tang and Chen (2013). It could be constrained in the duration time 2.32–2.22 Ga, and more concisely, to be 2.29–2.25 Ga and was a part of the GOE (Hoffman 2013; Tang and Chen 2013). In NCC, Paleoproterozic glaciogenic rocks have not been reported, however, the $\delta^{13}C_{carb}$ negative excursion in the Jianan-Daguan Fm., Dongye Subgroup, Hutuo Group (2.5–2.2 Ga, Wilde et al. 2004), might be respond of the NCC to the HGE (Kong et al. 2011).

11.2.3 Widespread Carbonate Sedimentation

Before 2300 Ma, volcanism was extremely intense, resulting in the formation of greenstone belts on every ancient continent. Stromatolitic carbonates and other bio-mediated carbonate units are unknown from pre-2.3 Ga strata, but occur in Late Archean sequence in Canada, Zimbabwe and elsewhere (Lowe 1994); insignificant thin-bedded pelitic dolomitic carbonates are found in a few areas. From the beginning of Proterozoic, i.e. after 2300 Ma, carbonates (especially thick-bedded carbonates) suddenly developed in large scale all over the world (Eriksson and Truswell 1978; Frakes 1979). It was estimated that carbonates and BIFs accounted for more than 15 % of the sediments with age of 2300–1900 Ma (Eriksson and Truswell 1978).

In the West Australian Shield, the unconformity between metamorphic basement of the Pilbara Block and its cover, the Mount Bruce Supergroup which is widespreadly exposed in Hamersley Basin, is usually accepted as the Archean-Proterozoic boundary (Taylor and Mclennan 1985). The Archean metamorphic strata (including the Warrawoona, the Gorge Creek and the Whim Creek groups) lack carbonate sediments. The Mount Bruce Supergroup was subdivided into the Fortescue, the Hamersley and the Turee Creek groups upward. The Fortescue Group yielded several isotopic ages older than 2500 Ma (Jahn and Simonson 1995; Bekker et al. 2003a, b; and references therein) and was

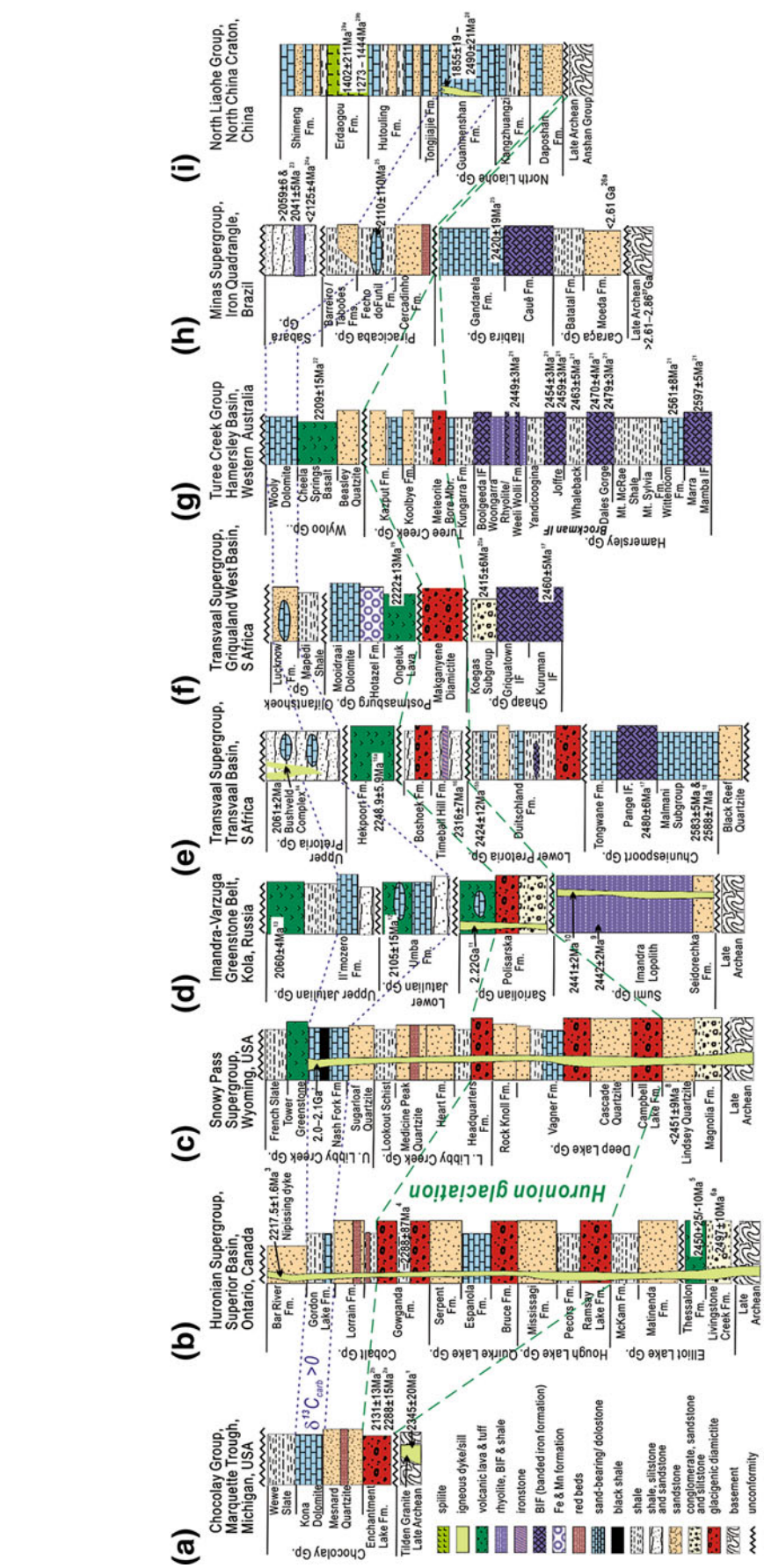

Fig. 11.1 Stratigraphic correlation of the Huronian glaciations and positive $\delta^{13}C_{carb}$ anomalies in the world (see Tang et al. 2011, Tang and Chen 2013; and references therein). Notations to ages: 1, zircon TIMS U–Pb age (Hammond 1976); 2a, detrital zircon U-Pb age, suggesting maximum age of deposition (Vallini et al. 2006); 2b, hydrothermal xenotime age, suggesting minimum age of deposition) (Vallini et al. 2006); 3, baddeleyite TIMS U–Pb age (Andrews et al. 1986); 4, argillaceous rocks Rb-Sr isochron (Fairbairn et al. 1969); 5, zircon TIMS U–Pb age for volcanic rocks (Krogh et al. 1984); 6, detrital zircon U–Pb age (Rainbird and Davis 2006); 7, zircon and baddeleyite TIMS U–Pb ages (Premo and Van Schmus 1989; Cox et al. 2000); 8, detrital zircon TIMS U–Pb age (Premo and Van Schmus 1989); 9, zircon TIMS U–Pb age for volcanic rocks (Amelin et al. 1995); 10, zircon SHRIMP U–Pb age for basalt lava (Puchtel et al. 1996); 11, cited from Hanski et al. (2001); 12, zircon U-Pb age (Huhma 1986); 13, zircon U-Pb age (Melezhik et al. 1997a); 14, zircon U–Pb age (Walraven 1997); 15a, zircon U–Pb age (Dorland 2004); 15b, detrital zircon U–Pb age (Dorland 2004); 16, diagenetic pyrite Re–Os isochron age (Hannah et al. 2004); 17, zircon SHRIMP U–Pb age for volcanic ash beds (Pickard 2003); 18, zircon SHRIMP U–Pb age for ash beds (Martin et al. 1998); 19, whole rock Pb–Pb isochron age (Cornell et al. 1996); 20, detrital zircon U–Pb age (Gutzmer and Beukes 1998); 21, zircon SHRIMP U–Pb age (Trendall et al. 1998); 22, zircon SHRIMP U–Pb age (Barley et al. 1997); 23, titanite U–Pb age (Noce et al. 1998); 24, detrital zircon U–Pb age (Machado et al. 1992); 25, carbonate Pb–Pb isochron age (Babinski et al. 1995); 26, zircon SHRIMP U–Pb age (Endo et al. 2002); 27, compiled from Machado et al. (1992, 1996), Machado and Carneiro (1992), Chemale et al. (1994), Noce et al. (1998), and Endo et al. (2002); 28, zircon $^{207}Pb/^{206}Pb$ age (Rui et al. 1991); 29a, Rb-Sr isochron age (Wang et al. 1989); 29b, K-Ar ages (Wang et al. 1989)

widely regarded as Archean strata (Plumb and James 1986). Ages of the Hamersley Group are confined between 2479 ± 3 Ma and 2449 ± 3 Ma by SHRIMP U-Pb zircon dating with tuffaceous mudrocks (Pickard 2002) and the Turee Creek Group was formed in the span of 2449 ± 3 Ma and 2222 ± 13 Ma (Nelson et al. 1999; Bekker et al. 2001). At the top of the Fortescue Group, there developed a few carbonates which were occasionally classified into Hamersley Group by some authors. The Hamersley Group was characterized by the well-known Hamersley BIFs and a huge amount of carbonates including dolomites and limestones. The Turee Creek Group was featured by tillites and contained lots of carbonate rocks. The Wyloo Group, unconformably overlying the Mount Bruce Supergroup, abounds with dolomites deposited during 2100–1900 Ma (Jahn and Simonson 1995; Plumb and James 1986). It has been reported that a considerable amount of dolomites of 2300–2000 Ma occur in the Norway, Finland and Russia (Melezhik and Fallick 1996). The Krivoy Rog series was divided into eight rock assemblage units, of which four were BIFs. Three of the four BIF units are paragenetic with carbonate rocks (Alexandrov 1973). Alexandrov (1973) also reported that a great deal of limestone was developed in the roof and the footwall of the BIF in the Odessa-Brusilov belt, whose age and characteristics are similar to those of Krivoy Rog Series. The overlying rocks of the BIF of Kursk metamorphic assemblage are calc-schists and limestones (Melezhik and Fallick 1996). The Kalstasin unmetamorposed dolomites were dated at 2150 ± 60 Ma (Pb-isochron), reflecting the time of sedimentation (Salop 1977). In Karelia and Finland, the Onega Group of the Karelian Complex is composed of 1500 m thick dolomites and siltstones with interbedded hematite ores (Salop 1977).

In Labrador Trough, the BIF is composed partly of carbonates such as siderite, and usually interbedded with dolomites; its underlying strata have thick dolomites and were dated between 2170 and 2140 Ma (Dimroth 1981; Melezhick et al. 1997a). The Huronian Supergroup surrounding Superior Lake, Ontario was developed during 2450–2217.5 Ma (Krogh et al. 1984; Andrews et al. 1986). Its middle–upper portion contains a huge amount of dolomites (Taylor and Mclennan 1985). The Paleoproterozoic Marquette Range Supergroup in Michigan and Wisconsin of USA is often regarded as the counterpart of the Huronian Supergroup; its bottom group, the Chocolay Group, is mainly composed of dolomites (Bayley and James 1973; Bekker et al. 2006) and developed between 2302 ± 4 and 2009 ± 7 Ma (Goldich 1973; Goldich and Fischer 1986; Vallini et al. 2006). Meanwhile, no carbonate could be found in the Archean strata underlying the Marquette Range Supergroup. In Montana, Paleoproterozoic BIF-bearing strata are abundant in carbonates, whereas Archean BIFs do not coexist with carbonates. The BIF in Ruby Greek is directly covered by 1000 ft thick dolomites which account for about 40 % of Paleoproterozoic assemblage. The footwall of the BIF in Tobacco Root Mountain is dolomites with several hundred feet in thickness, and in Kelly area, is more than 600 ft; they account for more than 37 % of all the host strata of BIFs (Bayley and James 1973). The country rocks of the BIFs in Cater Creek are almost carbonate rocks (Bayley and James 1973). The BIF in Hartville-Sunrise area of Wyoming was made up of iron-carbonates, with a footwall of dolomites (Bayley and James 1973). Enclosed in limestones, the Homestake BIF in Black Hills, South Dakota, is also made up mainly of carbonate facies. All the above strata are confined to the period of 2500–1650 Ma, most probably depositing during 2300–1900 Ma (especially at the period of 2300–2100 Ma).

In South America, the Itabira Group in Quadrilatero Ferrifero, Minas Gerais, Brazil, is the most important BIF-bearing sequence. Its upper portion is predominant of dolomites, and its lower portion major of itabirites (iron quartzite), being interbedded with carbonates and dolomitic itabirites. Additionally, some iron orebodies hosted in the Itabira Group are enveloped by pure dolomites. In Africa, both the roofwall and the footwall of BIF within Transvaal Supergroup are made up of dolomites, and the footwall of the BIF within the Griqualand West Supergroup is also composed of carbonate rocks (Eriksson and Truswell 1978; Buick et al. 1998; Bekker et al. 2001, 2006).

Limestones has been found under the Superior type BIF in Singhbhum area of India (Bose 1990). The Aravalli Group (~2.15 Ga) has two thick stromatolitic dolomitic limestone horizons (Chanhan 1979; Goodwin 1991; Sreenivas et al. 2001; Purohit et al. 2010).

In NCC, the high grade metamorphic carbonates were generally found very thick in khondalite series which widely developed around the margin of the NCC. For examples, the Shuidigou Group (also named as Huoqiu Group in Anhui) of the Taihua united terrain (Chen and Fu 1991; Chen and Zhao 1997), the Jingshan/Fenzishan Group of the Jiaobei terrain (Hu et al. 1997), the Fuping Group of the Fuping block, the Jianping Group of the West Liaoning block, the Fengzhen Group of the Central Inner Mongolia block (Condie et al. 1992), and the Ji'an Group of the South Jilin block. The isotopic ages for the above khondalite series have been documented no more than 2300 Ma, suggesting sedimentation occurred in the period of 2300–2000 Ma (Kröner et al. 2005; Liu et al. 2006; Wan et al. 2006; Yin et al. 2009; Xu et al. 2009), although those khondalite series had ever been classified into Archean strata by some geologists. Low grade metamorphic carbonate rocks were more extensively developed in the Songshan Group of the Songji block, the Hutuo Group of theWutaishan terrain, the Liaohe Group of the East Liaoning block. They yielded nearly same isotopic ages to the above mentioned high grade ones, or slightly later than the latter, and probably formed during the period of 2300–1850 Ma (Zhao

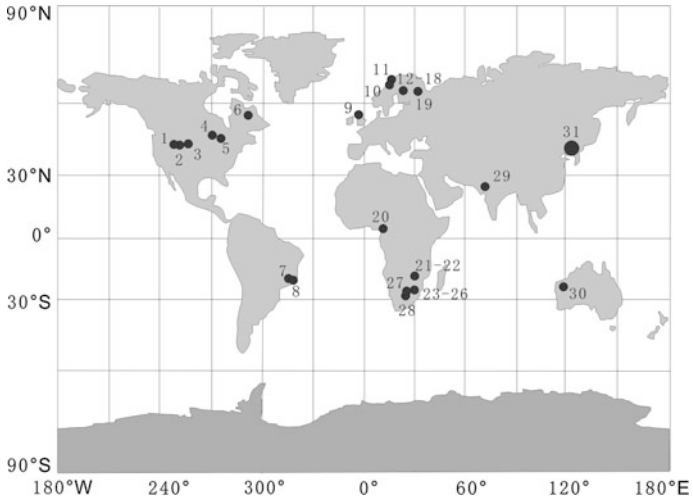

Fig. 11.2 Worldwide distribution of 2.33–2.06 Ga carbonates with positive $\delta^{13}C_{carb}$ excursions (after Tang et al. 2011; No. and data sources see Tang et al. 2011, and references therein)

et al. 2004; Lu et al. 2004a, b, 2006; Luo et al. 2004; Li et al. 2004, 2007, 2015; Meng et al. 2013, 2014; Li et al. 2015; Liu et al. 2015). The pre-2300 Ma strata, usually underlying khondalite series or their low grade equivalents, lack carbonate rocks.

From above, we can conclude that little carbonate rocks formed before 2500 Ma, carbonate platforms began to form during 2500–2300 Ma. On the contrary, after 2300 Ma, large-scale carbonates, especially thick carbonates, suddenly appeared worldwide. Due to carbonates are generally formed in normal sedimentary environment without or with weak volcanism (Siever 1977), the differences in the documents of carbonate between pre- and post-2300 Ma suggest that there exist a worldwide gap of volcanism during the period of 2300–1900 Ma, which coincides with the global development of thick carbonate strata during 2300–2000 Ma, and with the absence of greenstone belts aged of 2300–2000 Ma (Kroner 1981). Erriksson and Truswell (1978) therefore concluded that "the appearance of widespread stromatolitic carbonates at about 2300 Ma separates off the Archean from the Proterozoic".

In 1975, Schidlowski et al. reported a phenomenon by showing that the ~2000 Ma carbonates in the Karelia, Russia and the Fennoscandian Shields have positive $\delta^{13}C$ values. Dolomites in the Lomagundi Province, South Africa, with ages of 2.65–1.95 Ga, have $\delta^{13}C$ values up to 12 ‰. To explain this anomaly, they related this phenomenon to the oxidation of the atmosphere. In 1989, the International Commission on Stratigraphy recommended that 2.3 Ga be a defining boundary in the Precambrian Stratigraphy Chart. Thereafter positive $\delta^{13}C_{carb}$ excursions have been recognized in 2.33–2.06 Ga strata worldwide (Schidlowski 1988; Bekker et al. 2003a, b, 2006; GJ Tang et al. 2004; HS Tang et al. 2011; and references therein; Figs. 11.1 and 11.2). The excursion was genetically related to global environmental changes (Karhu 1993; Karhu and Holland 1996; Melezhik et al. 1999a, b), to the breakup of the Kenorland/Superia supercontinent (Bekker and Eriksson 2003), and to a 2.3 Ga catastrophe, which was shown by the contrasting REE geochemical signatures between pre- and post-2.3 Ga sediments (Chen 1988; Chen and Zhao 1997; Chen et al. 1991, 1994, 1996, 1998, 2000). This Paleoproterozoic positive $\delta^{13}C_{carb}$ excursion event variable termed the Lomagundi Event (Schidlowski et al. 1975, Schidlowski 1976; Baker and Fallick 1989a, b; Karhu and Holland 1996; Melezhik et al.; 1997a, 1999a, b; Buick et al. 1998; Bekker et al. 2001, 2003a, b, 2006; Tang et al. 2004; Aharon 2005; Tang et al. 2011; and references therein), the Jatulian Event (Melezhik and Fallick 1996; Melezhik et al. 1999b), or the GOE of the atmosphere (Karhu and Holland 1996; Anbar et al. 2007; Konhauser et al. 2009; Frei et al. 2009; Lyons and Reinhard 2009; Tang et al. 2013a, b).

This excursion is unique in terms of both duration (>250 Ma) and ^{13}C enrichment (up to +18 ‰ has been recorded in Jatulian carbonates) (Schidlowski 1988, 2001; Aharon 2005), and coincides with a maximum in the diversity and abundance of stromatolites (Semikhatov and Raaben 1994; Melezhik et al. 1997b, c). The highly positive $\delta^{13}C$ excursion may represent a major oxidation event (Karhu and Holland 1996) caused by accelerated burial of reduced carbon (Schidlowski et al. 1975; Schidlowski 1976; Melezhik and Fallick 1996; Melezhik et al. 1999a, b), and companied with global mineralization and developed voluminous giant deposits (Tu et al. 1985; Chen 1990; Chen et al. 1991; Huston and Logan 2004; Zhao 2010). Melezhik et al. (1999b) suggested that the Lomagundi Event consisted of several subsidiary events; but Bekker et al. (2003a) considered that it was a long-lasted single event.

The recognition of the GOE or environmental catastrophe was one of the most important progresses and hottest issues on the Precambrian research (Konhauser et al. 2009, 2011; Frei et al. 2009; Lyons and Reinhard 2009), and provided insights into understanding of the Precambrian evolution and mineralization during the early Earth history. In NCC, there was a carbon isotope shift (from negative to positive) between the Daguandong Fm. and its underlying Jian'ancun Fm. and overlying the Huaiyingcun Fm. carbonates of the Hutuo Group

in Shanxi (Zhong and Ma 1995). The Liaohe Group in Liaoning (Tang et al. 2008, 2009b, c, 2011, 2013a, b) and the Wuzhiling Fm. of Songshan Group in Henan (Lai et al. 2012) had been reported the positive $\delta^{13}C$ excursion in carbonate strata.

This unique $\delta^{13}C$ isotope, combined with other isotopic tracers, such as Sr and Pb, can be potentially utilized for stratigraphic correlations and "blind dating" (Chen et al. 2000; Tang et al. 2008; 2013a, b; Banner 2004; Melezhik et al. 2001a, b, 2002, 2005a, b, 2006, 2008; Ray et al. 2003). This is particularly important for the Precambrian which lacks a biostratigraphic framework (Walter et al. 2000).

11.2.4 Devoid of Rand-Type Au-U Deposit

As the most important type of gold resources in the world, the Rand-type Au-U deposits are hosted in conglomerate characterized by detrital pyrite and uraninite, representing a reductive sedimentary environment (Schidlowski 1976; Condie 1981; Mossman and Harron 1983; Bache 1987). The formation of large uraniferous conglomerates in Archean and early Proterozoic indicates that the oxygen partial pressure was below 10^{-6} times the present atmospheric level (PAL) to permit the survival of detrital uraninite (Roscoe and Minter 1993; Roscoe 1996; Bekker et al. 2005). The devoid of Rand-type Au-U deposit after Paleoproterozoic should indicate that the sedimentary environment turned into oxic.

The Witwatersrand in South Africa is a typical Rand-type gold deposit, hosted in the Witwatersrand Supergroup, in which well rounded pyrite and uraninite are well preserved (Schidlowski 1976), whose age is confined to the period of 2700–2340 Ma (Frakes 1979).

Numerous Rand-type gold deposits have been discovered in the Huronian Supergroup (Mossman and Harron 1983). The lower three groups (the Elliot Lake Group, the Hough Lake Group and Quirke Lake Group) and the lower portion of the Gowganda Formation of the Cobalt Group are levels containing Rand-type gold deposits, overlying iron-deficient paleosols (Fig. 11.1b). While the upper part of the Gowganda Formation, the Firstbrook Member is a reddish unit. Hence the oxygenation was well evidenced to be within the Gowganda Formation. Intruded by Nipissing Diabase dated at 2150 Ma, the Huronian Supergroup deposited 2450–2250 Ma. Due to the Creighton granite intruding the Elliot Lake Group yielded a U-Pb upper concordia intercept age of 2333 + 33/ -22 Ma on zircon (Frarey et al. 1982), which provides a minimum age for depositon of the Huronian Supergroup, and the argillaceous rocks of the Gowganda Formation yielded a Rb-Sr isochron of 2288 ± 87 Ma (Fairbairn et al. 1969; Mossman & Harron 1983), the oxygenation should occurred at about 2300 Ma.

Rand-type Au-U deposits have also been found in the Bababudan Group in Indian Craton (Bache 1987), the Beaton Greek conglomerate at the bottom of Fortescue Group, Hamersley Basin (Blockley 1975). The Tunguda-Nadvoitsa Group of Karelian Complex has pyritized quartz conglomerate (Salop 1977). All these strata formed in Archean, at least before 2300 Ma. The Jacobina Au-U deposit, Brazil, is the only one reported to be Rand-type gold deposit (Bache 1987) formed after 2300 Ma (ca. 2200 Ma) (Goodwin 1991).

Occurrence of detrital pyrite undoubtedly indicates that atmosphere is deficient in oxygen. Uraninite is unstable when oxygen partial pressure is more than 10^{-21} atm (Bekker et al. 2004), and presence of uraninite shows a reducing condition with $P_{O2} < 10^{-21}$ atm. Therefore, development of Rand-type Au-U deposits in pre-2300 Ma sediments suggests that atmosphere was lack of oxygen before 2300 Ma; devoid of Rand-type Au-U deposit in post-2300 Ma strata reflects free O_2 abundant in atmosphere and hydrosphere after 2300 Ma.

11.2.5 Oldest Red Beds in the World and NCC

It is widely accepted that red beds began to appear in the Proterozoic, reflecting the formation of oxic atmosphere. The exact appearance time, however, is still open to discuss. A large group of researchers suggest that the oldest red beds appeared after 2000 Ma (Schidlowski 1976; Frakes 1979). A few geologists consider the beginning time of red beds might be even earlier (Chen 1989; Mossman and Harron 1983).

Recently, some of reported red beds are proved earlier than 2000 Ma, while some red beds older than 2000 Ma are found in various continents (Fig. 11.1; Melezhik et al. 1999b; Bekker et al. 2005), exactly, peaking at 2.22–1.95 Ga. The Labrador Trough is the erosional remnant of a Paleoproterozoic geosyncline filled by sediments during 2300–1850 Ma (Dimroth 1981), although its age is not well-known. Its lower portion, the Chakonipau Formation, comprises thick red beds made up of arkose and arkosic gneiss pebble conglomerates. Its middle portion, including Portage, Lace Lake, Alder, Uve, Savigny and Otelnuk Formations, usually called as Cycle I, also has several levels of red beds interbedded with stromatolitic dolomites (dolarenites), BIFs, quartzites, and clastic sediments. The upper portion, called Cycle II (Dimroth 1981), is characterized by the Sokoman iron formation.

In North Canada, the detrital rocks of molasses facies of the upper portion of the Hurwitz Group (2400–2100 Ma) abound with hematite. The bottom of the Circum-Ungava geosyncline (2400–1900 Ma) is composed of red terrigenous arkoses and conglomerates. Red molasses in Coronation, Keroneising geosyncline, and red sediments in Cobalt Group (2300–2100 Ma) of Huronian Supergroup have been reported (Windley 1980; Mossman and Harron 1983; Taylor and Mclennan 1985). Mossman and Harron (1983) insisted that the red beds in Cobalt Group should accumulated during 2288–2250 Ma.

Red beds in the Waterberg Group (equivalents: Matsap Group, Umkondo Group, Soutpansberg Group), Southern Africa, are alluvial continental molasses facies (Windley 1980), their ages are constrained between 2025 ± 23 Ma ($^{40}Ar/^{39}Ar$ age for basalt) and 1785 ± 80 Ma (K-Ar age) (cf. Goodwin 1991).

Age of red sediments of Hogfonna Formation in Antarctic continent is older than 1700 Ma (Hambrey and Harland 1981). In Baltic Shield the bottom of Yatulian Group is composed of quartz conglomerates bearing hematite (2180 ± 60 Ma) (Hambrey and Harland 1981). From the description by Salop (1977), we can infer that the red sandstones and slates in the Vepsian Group at the top of Karelian Supergroup and the hematite ores in the Onega Group at the middle of the Karelian Supergroup are of age of 2300–2150 Ma.

In China, we find a lot of hematite-bearing quartz sandstones and conglomerates in the Luohandong Formation of the Songshan Group, in the Tietonggou Group, Henan, and in the Zhongtiao Group, Shanxi. Red conglomerate are recognized in the Fenzishan Group, Shandong (Hu et al. 1997). The red Doucun slates in Hutuo Group, Shanxi, are previously accepted red beds. All these strata experienced the Zhongyue Orogeny (also named as Luliang Orogeny) occurred at about 1850 ± 50 Ma, accumulated during 2300–1850 Ma.

The red bed at the top of the Bababudan greenstones of Indian craton is accepted as the oldest red bed in the world (Windley 1980). The Bababudan greenstone is argued between 2700 and 2300 Ma (Windley 1980) and 2600–2200 Ma (Naqvi et al. 1978), suggesting the red bed at its top should develop in a range of 2300–2200 Ma.

Clearly, we can conclude that the red beds began to appear universally in various continents from 2300 Ma.

11.2.6 Change in Sedimentary REE Patterns: A Redox Proxy

At the south margin of North China craton, the pre-2300 Ma sediments (the Beizi Group, Dangzehe Group, and Junzhao Group; Table 11.2) show positive Eu-anomalies, the post-2300 Ma ones (the Shuidigou Group, the Angou

Table 11.2 REE geochemical characteristics of khondalite series in North China Craton (normalized to Chondrite values reported by Masuda et al. 1973; cited from Chen et al. 1998)

Stratigraphy and location	Petrology	Num.	Eu_{CN}/Eu_{CN}^*	ΣREE	$(La/Yb)_{CN}$
Shuidgou Group, Huaxiong block	Graphite and, sillimanite-garnet gneiss	8	0.30–0.69 (0.59)	102.74–211.17 (141.7)	1.03–46.90 (11.28)
Shuidgou Group, Huaxiong block	Graphite-marble	1	0.72	74.35	17.27
Jingshan Group, Jiaodong block	Garnet gneiss, BIF, graphite gneiss	9	0.32–1.10 (0.67)	137.49–378.99 (212.6)	2.7–12.2 (7.0)
Jingshan Group, Jiaodong block	Marble	1	0.70	34.57	19.0
Jingshan Group, Jiaodong block	Kyanite gneiss	1	3.49	86.68	35.1
Fenzishan Group, Jiaodong block	Gneiss	6	0.43–1.08 (0.64)	107.67–219.91 (156.3)	3.5–14.6 (9.2)
Helanshan Group, Alashan block	Al-rich gneiss	9	0.30–0.65 (0.52)	150.7–280.5 (216.7)	8.3–54.0 (11.0)
Helanshan Group, Alashan block	Leptynites	8	0.53–1.27 (0.65)	36.3–240.1 (152.3)	8.4–32.3 (16.2)
Jining Group, Daqingshan area	Gneiss	4	0.47–0.88 (0.62)	272.80–333.0 (312.97)	?
Jining Group, Datong area	Sillimanite-garnet gneiss	6	0.43–0.78		
Sanggan Group, Wulashan area	Sillimanite-garnet gneiss	9	0.42–0.87 (0.64)	63.85–350.82 (205.67)	4.68–27.08 (15.03)
Fuping Group, Taihang Mountain	Marble	2	0.97–1.78 (1.38)	69.28–133.44 (101.36)	19.43–23.92 (19.42)
Fuping Group, Taihang Mountain	Felsic gneiss	13	0.42–1.37 (0.89)	53.81–1168.77 (222.55)	11.49–38.67 (18.38)
Fuping Group, Taihang Mountain	Amphibole gneiss	10	0.71–0.95 (0.85)	58.85–167.29 (112.40)	2.66–5.98 (4.75)

Averages in parentheses;
$Eu_{CN}^* = (Sm_{CN} + Gd_{CN})/2$

Group, and the Xiaoshan Group) show negative anomalies ($Eu_{CN}/Eu^*_{CN} < 0.80$; subscript CNstands for chondrite values reported by Masuda et al. 1973 or Taylor and McLennan 1985), reflecting oxygenation occurred at about 2300 Ma (Chen and Fu 1991; Chen and Zhao 1997; Chen et al. 1998).

Bai (1986) reported the sedimentary REE characteristics of the Wutai Group (2550–2200 Ma) in Wutai Mountains, Shanxi. Sediments from the Gaofan Subgroup (2300–2200 Ma) showed clear Eu-depletion and those from the Shizui Subgroup (2550–2300 Ma) showed positive Eu-anomalies. The Gaofan and the Shizui Subgroups are separated by the Taihuai Orogeny.

The upper portion of the Jining Group in central Inner Mongolia is accepted as typical khondalite series (Wang 1989), and newly named Fengzhen Group (Condie et al. 1992). Its isotopic ages by differing methods are confined to the period of 2316–1900 Ma, and accordingly regarded as Paleoproterozoic strata (Chen 1990; Condie 1993; Wu et al. 1994; Chen et al. 1996). Its sediments show clearly negative Eu-anomalies (Wang 1989), with Eu_{CN}/Eu_{CN}* ranging from 0.4 to 0.8 (Condie 1993; Wu et al. 1994).

In Daqingshan Mountains, Inner Mongolia, the Wulashan Group has been divided into Archean and Paleoproterozoic associations (Jin and Li 1994) since the discovery of an intragroup unconformity by Dong and Zhou (1984). The Paleoproterozoic association, with ages of 2303 Ma (whole rock Rb-Sr isochron) and 1962 Ma (U-Pb age for zircon), is also typical khondalite series and shows obvious Eu-depletion, with Eu_{CN}/Eu^*_{CN} ranging 0.47–0.88, total REE ranging 272.8–333 ppm.

The sediments in Hongtoushan greenstone belt were formed in the Archean, and the REE patterns of meta-conglomerates in this belt and BIF (including its wall rock) in Anben area are characterized by high $(La/Yb)_{CN}$, low ∑REE and Eu_{CN}/Eu_{CN}* > 1 (Zhang 1984). Ji et al. (1990) made a study on the sediments of Jiaodong (or Qishan) and Jingshan Groups, and found that Jiaodong Group showed a positive Eu-anomaly, Jingshan Group showed a negative Eu-anomaly. As for Songshan, Hutuo and Fenzishan Groups, REE patterns show a negative Eu-anomaly more clearly and will not be discussed in detail here. The data from Taylor and Mclenann (1985) indicated that Elliot Lake Group in Huronian Supergroup showed no clear Eu-depletion, but Hough Lake and Quirke Lake Groups overlying the Elliot Lake Group had a characteristic of clear Eu-depletion. Negative Eu-anomalies of Uru (overlying the Hamersley Group) and Hamersley Groups are very clear. However, underlying the Hamersley Group, the Fortescue Group has no clear Eu-depletion, and Archean sediments have a positive or no Euanomaly. Sediments in Womay orogenic belt and Pine Creek geosyncline have a characteristic similar to that above.

Many reports on the REE pattern of the sediments (especially iron formation, Frei et al. 2008) older than 2300 Ma indicated that they all showed a characteristic of positive Eu-anomaly and relatively low ΣREE, which will not be exemplified here.

The facts exemplified above suggest that sediments show a positive or no Eu-anomaly before 2300 Ma and negative Eu-anomaly after 2300 Ma (Fig. 11.3; Tang et al. 2013a), which reflects the change of global depositional environment from reduction to oxidation.

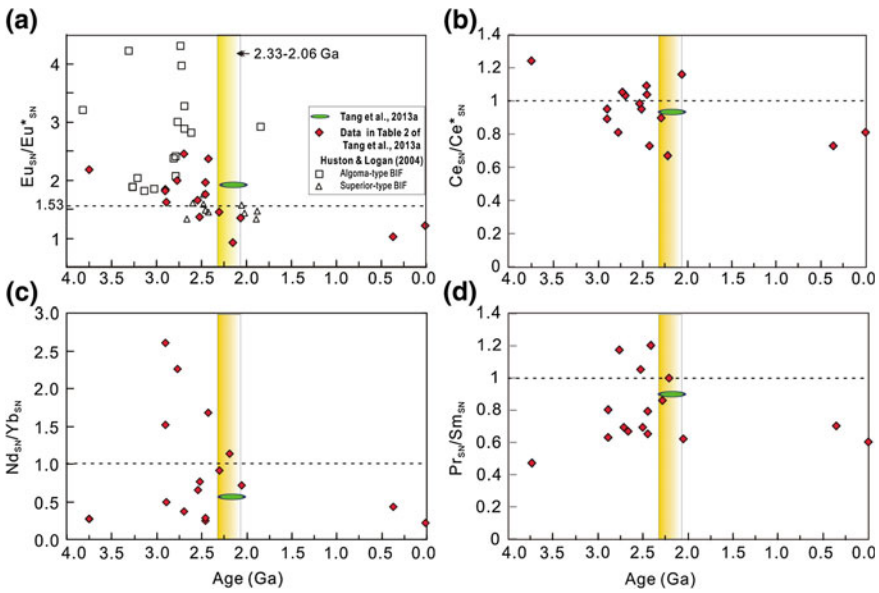

Fig. 11.3 Chemical sedimentary Eu_{SN}/Eu_{SN}* (**a**), Ce_{SN}/Ce_{SN}* (**b**), Nd_{SN}/Yb_{SN} (**c**), Pr_{SN}/Sm_{SN} (**d**) and their change with geologic time. Subscript SN means that the values are normalized to Post-Archean Australian Shale reported by McLennan (1989), and the $Eu_{SN}/Eu_{SN}^* = Eu_{CN}/Eu_{CN}^* + 0.53$. Data from Huston and Logan (2004) (n = 158) and Tang et al. (2013a) (n=205)

11.2.7 Changes of Elements and Isotopic Compositions of Sediments

In addition to the REE characteristics of sediments around 2300 Ma, geochemical characteristics of other element and isotope compositions in sediments also confirm the catastrophe at 2300 Ma. According to Condie (1982, 1993) and Taylor and Mclenann (1985), Th/U, Th/Sc, K_2O/Na_2O, Fe_2O_3/FeO, U, Th of the <2300-Ma detrital sediments are higher than those of the >2300-Ma sediments, by contrast, Cr, Ni, $MnO/(Fe_2O_3 + FeO)$ of the <2300 Ma sediments are lower than those of the >2300 Ma. According to Cameron and Jonasson (1972), Schidlowski (1976), the average of organic carbon contents in sediments changed from 0.7 % before 2300 Ma, through 1.6 % during 2300–1900 Ma, and to 0.5 % after 1900 Ma. Data documented by Lambert (1974) showed that the $^{87}Sr/^{86}Sr$ ratios of the <2300-Ma carbonate rocks were obviously higher than those of the > 2300-Ma carbonates. Researches by Kimberly and Dimroth (1976) indicated that the C, H, O and S isotopic compositions changed around 2300 Ma.

11.2.8 Explosion of Living Beings and Records in Sediments

The evidences of life have been rapidly accumulated since 2300 Ma (Knoll et al. 1988; Schopf 1977). Straomatolites (especially the stromatolites bearing blue-green algae) extensively developed in the world (Melezhik et al. 1997b, c). Furthermore, those stromatolite-bearing strata are often associated with graphite deposits, and carbon isotopic researches suggest that graphite deposits are organogenic.

The first period of global phosphorites and the first episode of worldwide graphite resources had developed during 2.5–1.85 Ga. The organic-rich "black shale" prevailed in ~2.0–1.7 Ga (see Tang et al. 2016; and references therein of Chap. 12 for details).

11.3 Some Problems and Discussion

11.3.1 Timing of the Environment Changes

The time of environment changes is tentatively determined at 2300 Ma, according to the facts below: (1) The strata over the boundary have not yet acquired convincing isotopic ages older than 2300 Ma. (2) The upper limit age of Witwatersrand Supergroup is 2340 Ma (Rb-Sr isochron) (Frakes 1979), and the Rb-Sr isochron age of the tuff interbeds in Elliot Lake Group in the bottom of Huronian supergroup is 2330 Ma (recited from Taylor and Mclennan 1985). Both stratigraphic units abound with Rand-type Au-U deposits, suggesting that the catastrophic event probably took place after 2330 Ma. (3) The Cobalt Group, the top unit of Huronian Supergroup, containing red beds, evaporates and carbonate rocks, and showing clear negative Eu-anomaly, was obviously formed after the catastrophe and yielded (Gowganda Fm.) isochron age of 2288 ± 77 Ma (Fairbairn et al. 1969; Mossman and Harron 1983; Fig. 11.1), which indicates that the catastrophe took place before 2288 Ma. Hence, the catastrophe might occur between 2330 Ma and 2288 Ma, i.e., 2300 ± 30 Ma.

The determination of 2300 Ma as the boundary age of the environment changes is on the basis of available dating techniques and age data, and it will be correspondingly modified with improvement of dating techniques and accumulation of age data. For example, Jahn and Simonson (1995) made a Pb-isotope dating on the carbonate rocks from Hamersley Group, and obtained ages for regional diagenesis (2541 ± 32 Ma), late diagenesis (2505 ± 37 Ma) and metasomatism (after diagenesis) (2340 ± 48 Ma). Jahn (1990) also reported a diagenetic age of 2557 ± 49 Ma for the Transvaal Supergroup of South Africa. However, these strata are considered to have formed after the environment changes. If the Pb-isotope age of carbonate rocks is proved to be more reliable in the future, the age of environment changes will be re-constrained at about 2550 Ma. Unfortunately, the outcomes acquired by Jahn (1990) and (Jahn and Simonson 1995) have not been widely accepted, and implications of Pb-isotopic age of carbonate rocks are not very clear either, and thus they are not adopted in this paper.

11.3.2 Why Carbonate Sedimentation began at 2300 Ma

The Archean was generally lack of carbonate rocks, except for some thin-bedded discontinuous carbonate rocks occasionally observed in later Archean. After 2300 Ma, thick-bedded carbonate strata developed all over the world (Eriksson and Truswell 1978). The atmosphere in Archean was rich in CO_2 (e.g., Chen and Zhu 1988), but why were carbonates absent before 2300 Ma? See Chap. 12 of Tang et al. (2016) for detail explanations.

11.3.3 Life Explosion and Reasons

Appearance of life was an important event in the geologic evolution. Sporadic evidences of life before 2300 Ma (Schopf 1977) indicate that the life activity was restrained in the Archean. Melezhik et al. (1997b) confirmed the observation of Semikhatov and Raaben (1994) that a rise in taxonomic diversity and abundance of stromatolite-forming organisms occurred during 2330–2060 Ma. There was an

abrupt rise at 2330 Ma and decline between 2060 and 1900 Ma in both abundance and taxonomic diversity of stromatolites. These data are in agreement with the systematics of the diversity and abundance of stromatolites from India and China (Semikhatov and Raaben 1994). It is suspected that the enhanced biomass fertility ('Broecker ratio'), namely a high level of diversity and abundance of stromatolite-forming bacteria, led to an increase in biological ^{12}C uptake from the inorganic carbon pool in Jatutian time (2330 to 2060 Ma). This resulted in surface water depletion in ^{12}C and probably caused the positive $\delta^{13}C_{carb}$ shift in the Jatulian carbonate precipitates (Jatulian heavy carbonate phenomenon). The decline of the stromatolites is linked with the first phase of 2000-Ma-old oceanisation of the Fennoscandian Shield leading to the formation of vast and relatively deep sea. All these changes were going on under oxygenated conditions, roughly synchronous with the first appearance of eukaryotic algae elsewhere. The explosion of Palaeoproterozoic stromatolites in taxonomic diversity and abundance (Schopf 1977; Semikhatov and Raaben 1994; Melezhik et al. 1997b) (especially those bearing blue-green algae) at 2330–2060 Ma suggests that the second leap in life evolution history took place at 2300 Ma. This life explosion event might be related to: (1) increase of weathering supplies plenty of nutriment for great propagation of organism; (2) oceanic nickel depletion at ca 2.5 Ga because Ni-compounds can restrain the organic evolution (Konhauser et al. 2009); and (3) removal of CN^- or SCN^- from the ocean, because of the oxygenation of the oceans (Chen 1990; Chen et al. 1991).

11.3.4 Occurrence of Atmosphere Rich in Oxygen

Occurrence of the atmosphere rich in oxygen on which human beings are living has been always a focus to study. Common viewpoints are: (1) $2H_2O$ (photodissociation) $\rightarrow 2H_2 + O_2$, H_2 ran away to the extraterrestrial place; and/or (2) CO_2 (+organism)$\rightarrow O_2$. Both models emphasized the oxygenation was a slow, long and continuous process, which began at the beginning of accreting of the Earth and ended at 1900 Ma (Frakes 1979; Schidlowski 1976). After 2300 Ma, Lake Superior type iron formation, red beds, gypsum, Eu-depletion of sediments and phosphorites appeared, and the development of Rand-type Au-U deposit ceased. These facts suggest that the atmosphere enriched in oxygen suddenly occurred in the period of 2330 Ma to 2288 Ma. It is easy to understand that the rapid oxygenation event contradicts the producing oxygen mechanism by H_2O photodissociation, and thus only the photosynthesis mechanism is reasonable. Rapid filling oxygen requires great propagation of organism after 2300 Ma, which is well consistent with the second leap of organic evolution mentioned above. Hence the filling oxygen was accomplished by intense photosynthesis resulting from the sudden great propagation of organism at 2300 Ma.

11.3.5 Compositional Evolution of Atmosphere and Hydrosphere

According to the principle of "the present is a key to the past", the components of paleoatmosphere and paleoseawater are consistent with those at present, in other words, present atmosphere and seawater which are rich in oxygen were formed in the gradual evolution of the Earth. In fact, component of atmosphere and seawater underwent mutational changes at 2300 Ma. The atmosphere is mainly composed of H_2O, CO_2, CH_4, H_2, N_2, CO, H_2S, NH_3 and some SO_2 and PH_3 before 2300 Ma; whereas, after 2300 Ma, it is similar to that at present, mainly of N_2, O_2, CO_2, H_2O, SO_2, SO_2, P_2O_5 and NO_2. Elements in the seawater before 2300 Ma were characterized by low valence anions and cations, mainly including HS^-, S^{2-}, $S_2O_3^{2-}$, Cl^-, F^-, CN^-, SCN^- and Na^+, Ca^{2+}, Mg^{2+}, NH^{4+}, Fe^{2+}, Mn^{2+}, K^+, Eu^{2+}, TR^{3+}, respectively. Seawater was acidic. After 2300 Ma, elements presented high valence anions, cations and neutral ions, mainly composed of CO_3^{2-}, HCO_3^-, OH^-, SO_4^{2-}, PO_4^{3-}, $H_2PO_4^-$, HPO_4^{2-}, NO_3^-, Cl^-, F^- and K^+, Na^+, Mg^{2+}, TR^{3+},respectively. Seawater was alkaline and showed high pH (in contrast with those before 2300 Ma).

The conclusions above are referred from the following convincing evidence: before 2300 Ma, carbonate, sulphate and phosphate rocks were absent, red beds were also absented, and well-rounded detrital pyrites and uraninites were usually seen, which are contrary to those after 2300 Ma (see Sect. 11.2 for detail and references).

11.3.6 Which is the First Global Glaciation Event

Some textbooks view the glacier in the Sinian period as the first global event. In fact, the first global glaciation event occurred during the period 2.29–2.25 Ga (HGE, Tang and Chen 2013), which is indicated by tillites recognised in all the continents (e.g., Hambrey and Harland 1981; Frakes 1979). Unfortunately, the tillites during this event have not yet been found in China, and researches on the event should be strengthened in the future (see Sect. 11.2.2 for detail and references).

The first glacier is one of a series of events resulting from the catastrophe at 2300 Ma. Intense photosynthesis after the catastrophe rapidly reduced the contents of CO_2 and CH_4, and increased the content of O_2, which cooled the

atmosphere system and resulted in the global Huronian Glaciation Event. Therefore, removal or drawdown of reducing components from the system is the prerequisite for a glaciation event (Tang and Chen 2013). As a result, the glacier event proved on the other side that greenhouse effect obviously appeared before 2300 Ma.

11.3.7 Time-Controlling on Sedimentary REE-Fe Deposit

Fryer (1977) pointed out that chemical sediments formed before 1900 Ma show Ce-nomality and positive Eu-anomaly, sediments and seawater after 800 Ma show clear Ce and Eu depletions, and sediments formed between 1900 Ma and 800 Ma range between these two end-members (Yuan 1981). Taylor and Mclenann (1985) pointed out that sediments before 2500 Ma showed positive or no Eu-anomaly, sediments after 2500 Ma showed negative Eu-anomaly, and the global development of kaligranite resulted in the changes in REE patterns of sediments around 2500 Ma. Discovery of catastrophe at 2300 Ma produces a series of new models (Chen 1990). Sediments before 2300 Ma in reducing condition are characterized by low ∑REE, high $(La/Yb)_{CN}$ and positive Eu-anomaly; on the contrary, sediments after 2300 Ma, formed in oxidizing conditions, are characterized by high ∑REE, low $(La/Yb)_{CN}$ and negative Eu-anomaly (Chen et al. 1998).

Most of REE resources in the world are related to the iron formations in the Precambrian. The well-known Bayan Obo REE deposit of China can be classified into this type. Identification of the 2300-Ma environmental catastrophe defines the earliest sedimentary REE-Fe formation to be younger than 2300 Ma. Before 2300 Ma, ligand anions in the seawater were mainly composed of soft bases, which are difficult to coordinate with the trivalent REE ions showing nature of hard acids, as a result, a lot of REE ions (TR^{3+}) accumulated in the seawater. After 2300 Ma, ligand anions were mainly composed of OH^-, SO_4^{2-}, CO_3^{2-}, PO_4^{3-}, and other hard bases, which have a tendency to coordinate with TR^{3+} and then precipitate to form REE deposit (see Chen and Zhao 1997; and references therein). REE and Fe are usually paragenetic with each other and the paragenesis is usually called "REE-Fe formation" because of their similar precipitating principle. The most favourable time of REE-Fe formation is in the early stage of the environment changes, i.e., 2300–1900 Ma. As a test, Chen and Deng (1993) conducted a REE study of the three BIF layers in the Lushan metamorphic terrane at the southern margin of the North China Craton. The BIFs with ages of 3000–2550 Ma, 2550–2300 Ma and 2300–2200 Ma have ΣREE contents of 25.21, 52.87 and 2176 ppm respectively. This confirms the inference above, and supplies new prospecting ideas.

11.3.8 Absence of Archean evaporite, laterite and Red Beds

Global lack of Archean evaporite is usually related to the destroy and disperse in late geological processes. The event at 2300 Ma clearly indicates that before 2300 Ma closed, oxidizing and hot condition required by depositing of salt deposits was not provided, so it is because there were no salt deposits formed in the Archaeozoic, instead of being destroyed by late geological processes. After 2300 Ma, a series of salt deposits were formed because of the conditions favourable for depositing of salt deposit, such as 2.3–1.9 Ga sulphate evaporites in siliciclastic and carbonate successions (Bekker et al. 2006). Evaporites and gypsum ores have been discovered in cobalt Group in the top of the Huronian Supergroup (Condie 1982) and in Li'eryu Formation of the Liaohe Group (Zhang 1988; Tang et al. 2013b) respectively.

Weathering crust deposits mainly include Bauxite, iron hat-type Fe, Au, Al, Cu deposits and red earth-type gold deposit. Most of them are found in modern weathering crust, and some in palaeo-weathering crust, however, the age of the oldest weathering crust is no more than 2300 Ma (Holland 1994). This is because weathering crust deposit is formed in the oxidizing condition, and it was merely after 2300 Ma when the oxidizing condition appeared.

Occurrence of red bed marks the formation of the atmosphere rich in oxygen. Generally, the oldest red bed is considered to appear at ~2000 Ma, Windley (1980) enumerated some red beds before 2000 Ma and furthermore pointed out the occurring possibility of Archaeozoic red beds. In fact, there were no red beds in the Archaeozoic, but the occurring time can trace back to 2300 Ma, peaking at 2.25–1.95 Ga (see 11.2.5 this chapter).

11.3.9 Forming Conditions and Time-Controlling Rules of Conglomerate-Type Gold Deposit and Placer Gold Deposit and Their Interrelations

Rand-type is representative of conglomerate-type gold deposit, characterized by well-rounded pyrite and uraninite detritus in ores and Au enriching with the accumulating of pyrite. Characteristics of conglomerate-type gold deposits restrict that they are merely formed in the reducing environment, namely the environment before 2300 Ma. Present conglomerate-type gold deposits found in South Africa, Canada, West Australia and Brazil, etc., exactly occurred in the strata before 2300 Ma. The sedimentary conglomerates before 2300 Ma in China were poorly developed and no earlier rock gold deposit was found, so it is impossible to find conglomerate-type gold deposit in China. Tu (1990)

definitely pointed out that the prospecting of Rand-type Au-U deposit was not inspiring.

Placer gold deposit is the second largest gold deposit, its importance is only secondly to conglomerate-type, and the ores occur in the coarse clastic sedimentary formations close to the rock gold deposits, such as residual materials and alluviums and so on. The ores, lacking of unstable mineral fragments such as pyrite, are the products of weathering, denuding, transporting and depositing in the oxidizing condition, and they are merely formed after 2300 Ma.

Summarily, conglomerate-type gold deposit and placer gold deposit are completely different in time, forming environment and enriching mechanism, and they belong to two types of gold deposit. That viewing conglomerate-type gold deposit as palaeo-placer gold deposit is a mistake, we can prospect placer gold deposits only in the strata after 2300 Ma and conglomerate-type gold deposits in the strata before 2300 Ma.

11.3.10 Ages of Khondalite Series

In the Precambrian petrogenic province, khondalite series, typically represented by those in Khonds area of India, are equally important as greenstone, granulite and TTG suite, and belong to hypometamorphic sedimentary formations bearing carbonate rocks, graphites, sillimanites and some iron formations. In a long time, they are considered to form in the Archaeozoic. Since Chen (1990) argued that most of the khondalite series in China formed during 2300–2050 Ma, nearly all the khondalite series have been universally accepted as Paleoproterozoic in age. In terms of present researches, all khondalite series show the characteristics of geologic formations after the 2300 Ma in rock assemblage, petrochemistry and geochemistry, and isotope dating also indicates that they are formed after 2300 Ma. For example, La Plaine series, in Scandinavian Peninsula, was formed at 2063ma (Wu 1988), and the age of the khondalite series in Ceylon area is 2100 Ma (Hapuarachchi 1972). And the age of the khondalite series in Central High Land of Sri Lanka, adjacent to the khondalite series in Khonds area, is 2.1–1.9 Ga (Cenki et al. 2004; Satish-Kumar et al. 2011). Khondalite rocks are also developed in NCC, widespreadly (Inner Mongolia, Shanxi, Shandong Liaoning Provinces, etc.), and massive evidences indicate that they are mainly formed 2.2–1.9 Ga (see Chen et al. 1998; Wu et al. 2006; Wang et al. 2010; Zhao et al. 2012; Cai et al. 2015; Liu et al. 2015; and references therein).

As for REE geochemistry of the khondalite series in various districts of the North China Craton (NCC), it had been studied and shown in Table 11.2. All of these khondalite series had been regarded as Archean for a long time. In China, most of the khondalite series formed during 2300–2050 Ma (Chen 1990), except for the Fuping Group in Taihang Mountains. The Fuping Group is distributed in the core of NCC, the others along the rim of NCC. Possessing less graphite and less BIF, the Fuping Group is differing from the Proterozoic khondalite series. Sedimentary rocks of different kinds from Proterozoic khondalite series show clear negative Eu-anomalies, with Eu_{CN}/Eu_{CN}^* averages ranging from 0.52 to 0.72, remarkably similar to PAAS or NS. Only one sample of kyanite gneiss from Jingshan Group, Jiaodong block, show strong positive Eu-anomaly ($Eu_{CN}/Eu_{CN}^* = 3.49$). The other geochemical features of REE and trace elements are also consistent with PAAS (Taylor and Mclennan 1985). Marbles of Archean khondalite series, Fuping Group, are characterized by positive Eu-anomaly. Neither felsic gneisses nor amphibole gneisses show clear Eu-depletion, their average Eu_{CN}/Eu_{CN}^* values are 0.89 and 0.85, respectively. The REE patterns are similar to Archean shales (Taylor and Mclennan 1985). The obvious differences in REE geochemistry between Archean and Proterozoic khondalite series of the NCC strongly support geochemical transition form Archean to Proterozoic (Taylor and Mclennan 1985). To explain this transition, most Chinese scholars appeal the theory advanced by Taylor and Mclennan (1985). The authors refer the Oxidation-Reduction Model (Chen and Fu 1991; Tang et al. 2013a), i.e. Archean reducing conditions result in the positive or slight Eu-anomalies of Archean sediments, and post-2300 Ma oxic environment led to sedimentary Eu-depletion (especially for chemical sediments). However, these two different explanations could not reveal the origin of the positive Eu-anomaly of kyanite gneiss from Jingshan Group (Chen et al. 1998).

11.4 An Evolution Framework for Earth's Superficial Change Events During the GOE

As mentioned above, during the GOE, there are many subprime events. It has an important question need to be answered, which one is before and which one is after, that is the sequence of these events.

The Archaean hydrosphere-atmosphere system was well accepted to be anoxic, although there was minor oxygen resulted from possibly local biological photosynthesis as revealed by the studies of S, Mo, Fe and Cr isotopes (Bekker et al. 2004; Anbar et al. 2007; Kaufman et al. 2007; Wille et al. 2007; Frei et al. 2009; Voegelin et al. 2010; Czaja et al. 2012). For examples, the timing of atmospheric $p(O_2)$ up to 10^{-5} times of the present atmospheric level (PAL) was proposed as between the second and third of the three-episodic Huronian Glaciation Event (Bekker et al. 2004), even > 50 Ma prior to the 2.45–2.32 Ga (Anbar et al. 2007; Kaufman et al. 2007) or prior to the first Palaeoproterozoic glacial

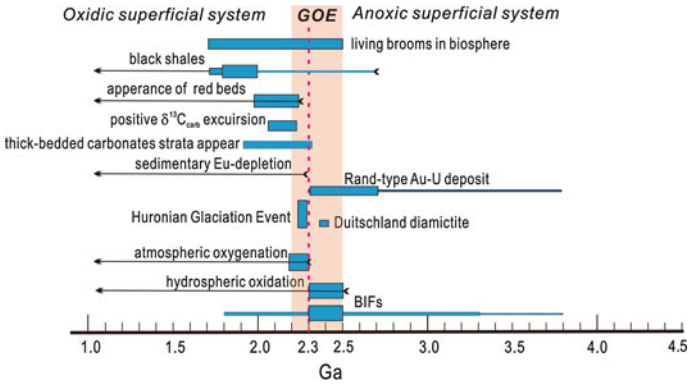

Fig. 11.4 A summary of framework for ca. 2.5–1.7 Earth's superficial change events and metallogenic explosion (modified after Tang and Chen 2013), see references in text for data source

episode (Wille et al. 2007; Voegelin et al. 2010; Czaja et al. 2012). However, the partisan sedimentary evidence supporting the GOE is the worldwide development of "red beds" (Holland 1994; Melezhik et al. 1999b; Eriksson et al. 2011), overlapped with the positive $\delta^{13}C_{carb}$ excursion. The latter showed that the level of oxygen in the atmosphere rose between 2.22 and 2.06 Ga from $<2 \times 10^{-3}$ atm (1 % of PAL) to >0.03 atm (15 % of PAL) (Holland 1994).

Tang and Chen (2013) propose a two-stage oxygenation model, i.e. the GOE mainly occurred in the period of 2.5–2.2 Ga, including the earlier hydrosphere oxidation stage during 2.5–2.3 Ga and then the later atmosphere oxygenation stage oxygenation during 2.3–2.2 Ga. In Tang and Chen (2013), authors gave a temporal evolution framework for 2.5–1.95 Earth's superficial changes event, including the widespread deposition of the Siderian banded iron formations (BIFs), slightly postdated by the 2.29–2.25 Ga global Huronian Glaciation Event (HGE, or the oldest Snowball Earth, Kirschvink et al. 2000), then, followed by the development of the 2.22–2.06 Ga carbonate strata with positive $\delta^{13}C_{carb}$ anomalies (Lomagundi/Jatulian Event, see Tang et al. 2011; and references therein) and 2.25–1.95 the oldest red beds in each continents (Sects. 11.2.5 and 11.3.8). These significant events, occurred in younging order with somewhat temporal overlap, together with other Earth's superficial changes, resulted from, or relate to, the GOE and recorded global changes in the atmosphere, biosphere, hydrosphere and lithosphere. And the GOE throughout overprinted by the early Paleoproterozoic metallogenic explosion in early Precambrian cratons, such as NCC (see Chap. 12).

Based on discussion above, here we give a further instruction that the oldest GOE influences the whole early Paleoproterozoic era (2.5–1.7 Ga) of the Earth and shown in Fig. 11.4:

1. Before 2.5 Ga, in reducing hydrosphere, the dissolved elements (anions or cations) must be present as low valences. For examples, the Fe, Eu, Mo, Cr and S will be dominated by Fe^{2+}, Eu^{2+}, Mo^{4+}, Cr^{2+} and S^{2+}, respectively, rather than by Fe^{3+}, Eu^{3+}, Mo^{6+}, Cr^{6+} and S^{6+} that stably exist in oxidizing environment. It can be visaged that a huge quantity of low-valent cations and anions were accumulated in the hydrosphere during a 2 Ga-long (from 4.5 to 2.5 Ga) reducing Earth's evolution.
2. In early stage of the GOE, i.e., 2.5–2.3 Ga, oxygen generated from biological photosynthesis should be instantly consumed during oxidation of the accumulated low-valent components, resulting in precipitation as typically represented by banded iron formations (Fig. 11.4; see Chap. 12 for further explaination).
3. After the oxidation of the majority of the low-valent ions in the oceans, the O_2 produced by biological photosynthesis gradually accumulated in the atmosphere at expense of CO_2, i.e. atmospheric oxygenation (Fig. 11.4). Along with increasing O_2 in atmosphere, drawdown of CO_2 and elimination of CH_4, the icehouse effect of O_2 cooled the climate and resulted in the 2.29–2.25 Ga HGE (Tang and Chen 2013), companied with the devoid of Rand-type Au-U deposits (Fig. 11.4).
4. The HGE was followed by widespread deposition of 2.22–2.06 Ga carbonates with positive $\delta^{13}C_{carb}$ anomalies (Fig. 11.4) due to the fixation of ^{12}C in organic debris and the CO_2 in hydrosphere-atmosphere system was relatively enriched in ^{13}C (Lomagundi/Jatulian Event, Schidlowski et al. 1975; Schidlowski 1988; Karhu and Holland 1996; Tang et al. 2011; Lai et al. 2012). The oldest red beds in each continent appeared during 2.25–1.95 Ga (Melezhik et al. 1999b). At the same time, with the rise of pH in seawater, there had a worldwide sudden sedimentation of carbonate strata and related carbonate deposits (e.g. marble, boron and magnesite deposits with graphite, phosphorite, lead-zinc deposits in NCC) during the 2.3–1.9 Ga (see Chap. 12).
5. Finally, the BIFs disappear ca. 1.8 Ga (Klein 2005) and the 2.0–1.7 Ga "black shale", succeeding the devoid of the BIFs and early Paleoproterozoic carbonate strata (Melezhik et al. 1997a, 1999b; Condie et al. 2001), indicated that the further elevated of seawater pH value (see Chap. 12).

11.5 Geological Episodic Division Significances of the Event at 2300 Ma —Some New Understandings of the Ar/Pt Boundary

Although the proposal that the Ar–Pt boundary is at 2500 Ma had been accepted in the 28th IGC, this does not mean that it is the best one for ever. In fact, the boundary age has been always indispute, and the proposal was an agreement, only meeting with 78 % approval. Further researches should be carried out on the age and its significances of the Ar–Pt boundary. The age will be revised with the improving of the research on Precambrian and developing of the Earth science theories. As author's point, a suitable age for the Ar–Pt boundary should be at 2300 Ma when a global catastrophic event took place in the geological environment.

11.5.1 Past Stratigraphic Division Involving 2300 Ma

In 1978, Eriksson and Truswell noted that the development of carbonate rocks and stromatolites before 2300 Ma was obviously different from that after 2300 Ma, and recommended 2300 Ma as the Ar–Pt boundary age. Smirnov (1984) advocated setting the boundary between North Sea period and Karel period should be 2300 Ma. Kroner et al. (1988) argued that 2300 Ma was an important turn in the African continent evolution. In spite of these, the proposal did not bring to the attention of IUGS (International Union of Geological Sciences) Subcommission on Precambrian Stratigraphy because of the lack of comprehensive information about the event at 2300 Ma. At first seven symposia sponsored by the IUGS Subcommission on Precambrian Stratigraphy during the last two decades, 2300 Ma has not been set as any boundary age (Table 11.3). In September, 1988, at the International Symposium on Geochemistry and Mineralization of Proterozoic Mobile Belts held in Tianjing, China, the authors proposed that, there occurred a catastrophe in the geologic environment at about 2300 Ma and presented a series of demonstrations for the catastrophe. Then, the IUGS Subcommission on Precambrian Stratigraphy, through discussing at its 8th symposium agreed to set 2300 Ma as the Siderian-Rhyacian boundary age to the Precambrian Stratigraphy chart (Table 11.3). The newly developed stratigraphic chart was accepted by the 28th IGC in 1989, which implicates that the importance and stratigraphic subdivision significances of the catastrophe at 2300 Ma has been gradually recognized by the international geological circles. However, it is a great pity that 2300 Ma is not determined as the Ar–Pt boundary age in the current stratigraphic chart, and that the time span of Siderian, 2500–2300 Ma, does not accord with the intensive developing time(2300–2000 Ma) of the well-known BIF in the world.

11.5.2 Principles of Geological Episodic Division

The purpose of the geological episodic division is to reveal the episodes and major events which occurred during the evolution of the earth. It is helpful to search for ore deposits on a worldwide scale and geological research. The Proterozoic-Phanerozoic division and some subdivisions for the Phanerozoic have been done successfully. The reason for these successes is that these divisions are carried out on the basis of great changes in the geologic environment including organic evolution; the significance of tectonic movements is not overemphasized. The Precambrian-Cambrian boundary is not marked by great worldwide tectonic movement, in addition, no obvious unconformity has been found around the boundary in the world, for instance, the Cambrian is conformably contacted with the Precambrian strata in South China. Around the boundary, vanishing of Ediacara fauna, extensive occurrence of fauna compiled by a lot of new species, transient drastic cold weather, extensive development of evaporates and phosphorites make the scientists accept the value and the logicality of the boundary. In recent two decade years, scientists (e.g. Hsu and Xu 1980; Hsu et al. 1986; Zhang et al. 1987; Feulner et al. 2015; and

Table 11.3 Progress in subdivision of early Precambrian by the IUGS subcommission on stratigraphy

Before ISGMB* (after Plumb 1988)	After ISGMB (after Sun 1990)
Proterozoic II	*Mesoproterozoic*
1600 Ma	1600 Ma
C	Statheria
1800 Ma	1800 Ma
Proterozoic I	*Palaeoproterozoic*
B	Orosirian
2050 Ma	2050 Ma
A	Rhyacian
2500 Ma	2300 Ma
	Siderian
	2500 Ma
Archean	Archean

**ISGMB* International Symposium on Geochemistry and Mineralization of Proterozoic Mobile Belts, hold in Tianjing, P.R. China, September, 1988. The left column is the recommended stratigraphic chart by IUGS Subcommission on Precambrian Stratigraphy represented by its Chairman, Plumb, at the ISGMB. The above column is the chart proposed by the 8th Symposium, and accepted by the 28th IGC in Washington

references therein) have proved that this boundary reflects a major catastrophic event. The reason of the biological revolution at the boundary of Pz-Mz and Mz-Kz have been also interpreted as catastrophe events in the environment (Hsu and Xu 1980; Berggren 1984), and none of these boundaries was determined in the light of tectonic movement. So important stratigraphic boundaries should be defined by transient drastic changes in the geologic environment which are usually caused by major events and lead to obvious variations in geologic processes, these variations were imprinted in the sediments and are helpful to the studying work in practice. Unfortunately, the current Ar–Pt boundary was defined by a "worldwide" tectonic movement around 2500 Ma rather than by a transient environmental change.

11.5.3 Defects of the Current Ar–Pt Boundary

Taking the tectonic movement around 2500 Ma as the Ar–Pt boundary possesses no less than the following shortcomings: (1) The implication of the boundary is to reflect a strong universal tectonic movement. But both a great number of first-hand data and the plate tectonic theory oppose that tectonic movements can take place worldwide, at least, contemporaneously in every region. Inevitably, the boundary as such is doubtable. (2) A large time span of 3000–2000 Ma is taken as the age of the Ar–Pt boundary in different countries, which results from the unsuitable implication of the current boundary. 3300 Ma, 2700–2600 Ma and 2500 Ma were taken by Taylor and Mclenann (1985) as the Ar–Pt boundary ages respectively for South Africa, West Australia and Superior Lake area. (3) There are unconformities in the stratigraphic column in every region, and that which exactly represents the Ar–Pt boundary is hard to be universally accepted, as a result, the Ar–Pt boundary and the ages of the strata have been always the points in debate. The Wutai Group in Shanxi Province, China, contacts unconformably with the underlying and overlying strata; it is now controversial and has been debated for decades that which unconformity, at the top or at the bottom of the Wutai Group, represents the Ar–Pt boundary. In eastern Hebei Province, Zhao (1980) has recommended the unconformity of about 2700 Ma as the Ar–Pt boundary, then, the others argue that the unconformity of about 2350 Ma should be the Ar–Pt boundary by himself (Zhao 1988). (4) Some strata were formed successively at about 2500 Ma, passing through the Ar–Pt boundary, and their ages are also ambiguous. The Dhawar series in South India is set between Archean and Proterozoic, which also has been in dispute. (5) As for the boundary, unconformity reflects a long-term sedimentary break which conflicts with the basis of stratotypes (without sedimentary break). (6) The sedimentary break at the boundary makes it difficult to study the boundary event in detail. (7) The principle to define the Ar–Pt boundary is incompatible with that of the Proterozoic-Phanerozoic boundary and subdivision boundaries within the Phanerozoic.

11.5.4 Logicality of Taking 2300 Ma as the Age of Ar–Pt Boundary

Based on the above discussion, we consider that an age of 2300 Ma is better than that of 2500 Ma to be defined as the age of the Ar–Pt boundary. This viewpoint can be supported by the following: (1) Drastic changes in the nature of the geologic environment occurred at about 2300 Ma, therefore, 2300 Ma can actually represent an age of an important transition in the evolution history of the Earth. (2) The implication of the boundary is clear enough to reflect the occurrence of a catastrophe in the geological environment. (3) The boundary event was mainly imprinted on the surficia geologic processes. In the surficial geologic processes such as cycling of the atmosphere, flowing of water and migrating of living things can proceed at high speed. Such changes in surficial geologic processes can be easily spread globally, which makes the boundary event happen consistently and contemporaneously all over the world. (4) The boundary event occurred in the time range from 2330 to 2288 Ma. Its duration is very short. Changing the geologic environment rather than bringing sedimentation to the end, it accords with the basement of stratotypes. (5) Strata underlying and overlying the boundary show different features in rock assemblage because they were formed under different conditions. So, it is easy to determine the boundary in practice, for example, taking the large-scale development of thick carbonate rocks as the beginning of deposition of the Proterozoic strata. (6) It is helpful to carry out effective prospecting and researches in geology, geochemistry and palaeontology, etc. (7) It is harmonious with the defined basement of the Proterozoic-Phanerozoic boundary and the subdivision boundaries within the Phanerozoic. The specific boundary of the event at 2300 Ma is the boundary between greenstone and khondalite series in the margin of the NCC (see Table 12.1 of Tang et al. 2016 of Chap. 12 for newly ages and references). It includes the boundaries of the Qishan-Jingshan in Jiaodong area, Dangzehe-Shuidigou in western Henan Province, Gehuyao-Fengzhen in Inne Mongolia and Jiapigou-Jian in South Jilin Province. In Canada, Australia and the Soviet Union, the specific boundary is equivalent to the boundaries between Elliot Lake Group and its overlying strata (in Superior Lake area), Fortescue Group and Hamersley Group, Krivoy Rog series and its underlying strata, respectively. Undoubtedly, more accurate definition of the boundary still requires more detailed researches.

Acknowledgements This study was funded by the National 973-Program (Project Nos. 2012CB416602, 2006CB403508) and National Natural Science Foundation of China (Nos. 40352003, 40425006, 40373007) and Frontier Field Project of the State Key Laboratory of Ore Deposit Geochemistry, Institute of Geochemistry, Chinese Academy of Sciences. Constructive suggestions, pertinent comments and careful corrections by Prof. Xiao-Yong Yang of the University of Science and Technology of China greatly improved the quality of the manuscript.

References

Aharon, P. (2005). Redox stratification and anoxia of the early Precambrian oceans: Implications for carbon isotope excursions and oxidation events. *Precambrian Research, 137*, 207–222.

Alexandrov, E. A. (1973). The precabrian banded iron-formations of the Soviet Union. *Economic Geology, 68*(7), 1035–1063.

Amelin, Yu. V., Heaman, L. M., & Semenov, V. S. (1995). U–Pb geochronology of layered mafic intrusions in the eastern Baltic Shield: implications for the timing and duration of Palaeoproterozoic continental rifting. *Precambrian Research, 75*, 31–46.

Anbar, A. D., Duan, Y., Lyons, T. W., Arnold, G. L., Kendall, B., Creaser, R. A., et al. (2007). A whiff of oxygen before the great oxidation event? *Science*, *317*, 1903–1906.

Andrews, A. J., Masliwec, A., Morris, W. A., Owsiacki, L., & York, D. (1986). The silver deposits at Cobalt and Gowganda, Ontario. II. An experiment in age determinations employing radiometric and paleomagnetic measurements. *Canadian Journal of Earth Sciences, 23*, 1507–1518.

Bache, J. J. (1987). *World gold peposits: A geological classification* (pp. 117–147). London: North Oxford Academic.

Bai, J. (1986). The *early precambrian geology of Wutaishan* (pp. 1–435). Tianjing: Tianjing Science and Technology Publishing House (in Chinese).

Banner, J. L. (2004). Radiogenic isotopes: Systematics and applications to earth surface processes and chemical stratigraphy. *Earth-Science Reviews, 65*, 141–194.

Bayley, R. W., & James, H. L. (1973). Precambrian iron-formations of the United States. *Economic Geology, 68*(7), 934–959.

Babinski, M., Chemale Jr., F., & Van Schmus, W. R. (1995). The Pb/Pb age of the Minas Supergroup carbonate rocks, Quadrilátero Ferrífero, Brazil. *Precambrian Research, 72*, 235–245.

Baker, A. J., & Fallick, A. E. (1989a). Evidence from Lewisian limestone for isotopically heavy carbon in two-thousand-million-year-old sea water. *Nature, 337*, 352–354.

Baker, A. J., & Fallick, A. E. (1989b). Heavy carbon in two-billion-year-old marbles from Lofoten-Vesteralen, Norway: implications for the Precambrian carbon cycle. *Geochimica et Cosmochimica Acta, 53*, 1111–1115.

Barley, M. E., Pickard, A. L., & Sylvester, P. L. (1997). Emplacement of a large igneousprovince as a possible cause of banded iron formation 2.45 billion years ago. *Nature, 385*, 55–58.

Bekker, A., & Eriksson, K. A. (2003). A Paleoproterozoic drowned carbonate platform on the southeastern margin of the Wyoming Craton: A record of the Kenorland breakup. *Precambrian Research, 120*, 327–364.

Bekker, A., Karhu, J. A., Eriksson, K. A., & Kaufman, A. J. (2003a). Chemostratigraphy of Palaeoproterozoic carbonate successions of the Wyoming Craton: Tectonic forcing of biogeochemical change? *Precambrian Research, 120*, 279–325.

Bekker, A., Karhu, J. A., & Kaufman, A. J. (2006). Carbon isotope record for the onset of the Lomagundi carbon isotope excursion in the Great Lakes area, North America. *Precambrian Research, 148*, 145–180.

Bekker, A., & Kaufman, A. J. (2007). Oxidative forcing of global climate change: A biogeochemical record across the oldest Paleoproterozoic ice age in North America. *Earth and Planetary Science Letters, 258*, 486–499.

Bekker, A., Kaufman, A. J., Karhu, J. A., Beukes, N. J., Swart, Q. D., Coetzee, L. L., & Eriksson, K. A. (2001). Chemostratigraphy of the Paleoproterozoic Duitschland Formation, South Africa: Implications for coupled climate change and carbon cycling. *American Journal of Science, 301*, 261–285.

Bekker, A., Kaufman, A. J., Karhu, J. A., & Eriksson, K. A. (2005). Evidence for Paleoproterozoic cap carbonates in North America. *Precambrian Research, 137*, 167–206.

Bekker, A., Sial, A. N., Karhu, J. A., Ferrerira, V. P., Noce, C. M., Kaufman, A. J., et al. (2003b). Chemostratigraphy of carbonates from the Minas Supergroup, Quadril´atero Ferr´ıfero (Iron Quadrangle), Brazil: A stratigraphic record of early Proterozoic atmospheric, biogeochemical and climatic change. *American Journal of Science, 303*, 865–904.

Bekker, A., Slack, J. F., Planavsky, N., Krapež, B., Hofmann, A., Konhauser, K. O., & Rouxel, O. J. (2010). Iron formation: The sedimentary product of a complex interplay among mantle, tectonic, oceanic, and biospheric processes. *Economic Geology, 105*, 467–508.

Bekker, A., Wang, P.-L., Rumble, D, I. I. I., Stein, H. J., Hannah, J. L., Coetzee, L. L., & Beukes, N. J. (2004). Dating the rise of atmospheric oxygen. *Nature, 427*, 117–120.

Berggren, W. A. (Ed.). (1984). *Catastrophe and earth history* (pp. 1–464). Princeton: Princeton University Press.

Blockley, J. G. (1975). *Hamersley basin: Economic geology of Australia and Pupua New Guiana* (pp. 413–414).

Bose, M. K. (1990). Growth of Precambrian continental crust—a study of the Singhbhum segment in the eastern Indian Shield. In S. M. Naqvi (Ed.), *Precambrian continental crust and its economic resources* (pp. 267–286). Amsterdam: Elsevier.

Buick, I. S., Uken, R., Gibson, R. L., & Wallmach, T. (1998). High & #x03B4;13C Paleoproterozoic carbonates from the Transvaal Supergroup, South Africa. *Geology, 26*, 875–878.

Cai, J., Liu, F.-L., Liu, P.-H., Wang, F., & Shi, J.-R. (2015). Geochronnlogy of the Paleoproterozoic khondalite rocks from the Wulashan-Daqingshan area, the Khondalite Belt. *Acta Petrologica Sinica, 31*(10), 3081–3106 (in Chinese with English abstract).

Cameron, E. M., & Jonasson, T. R. (1972). Mercury in Precambrian shales of the Canadian Shield. *Geochimica et Cosmochimica Acta, 36*, 985–1006.

Chanhan, D. S. (1979). Phosphate-bearing stromatolites of the Precambrian Arivalli Phosphorite deposits of the Udaipur region, their environmental significance and genesis of phosphorite. *Precambrian Research, 8*, 95–126.

Chen, Y.-J. (1988). Catastrophe of the geologic environment at 2300 Ma. In *Abstracts of International Symposium on Geochemistry and Mineralization of Proterozoic Mobile Belts* (p. 11). Tianjin, Sept 6–10.

Chen, Y.-J. (1989). Tentative study on Catastrophe in geological environment at 2300 Ma. In *Progress in comprehensive study on the relationship among life, earth and cosmos* (pp. 78–82). Beijing: Chinese Science & Technology Press (in Chinese).

Chen, Y.-J. (1990). Evidences for the catastrophe in geologic environment at about 2300 Ma and the discussions on several problems. *Journal of Stratigraphy, 14*, 178–186 (in Chinese with English abstract).

Chen, Y.-J. (Ed.). (1996). Progresses in application of sedimentary trace element geochemistry to probe crustal composition and environmental change. *Geology Geochemistry* (3), 1–125 (in Chinese).

Chen, Y.-J., & Deng, J. (1993). REE geochemical characteristics and evolution of early Preambrian sediments: Evidence from the southern margin of the northern China craton. *Geochimica (Beijing), 1*, 93–104 (in Chinese with English abstract).

Chen, Y.-J., & Fu, S.-G. (1991). Variation of REE patterns in early Precambrian sediments: Theoretical study and evidence from the southern margin of the northern China craton. *Chinese Science Bulletin 36*(13), 1100–1104.

Chen, Y.-J., Fu, S.-G., & Hu, S.-X. (1988). The main element character and its significance of different type greenstone belts at the southern margin of Northern-China craton. *Journal of Nanjing University (Earth Sciences), 1*, 70–83 (in Chinese with English abstract).

Chen, Y.-J., Fu, S.-G., Hu, S.-X., Chen, Z.-M., Zhou, S.-Z., Lin, Q.-L., & Fu, G.-H. (1989). Shipaihe movement and the dissection of "Dengfeng group". *Journal of Stratigraphy, 13*, 81–87 (in Chinese with English abstract).

Chen, Y.-J., Fu, S.-G., Hu, S.-X., & Zhang, Y.-Y. (1992a). The REE geochemical evolution and its significance of the Wuyang early Precambrian metamorphic terrain. *Chinese Journal of Geochemistry, 11*(2), 133–139 (in Chinese with English abstract).

Chen, Y.-J., Hu, S.-X., Fu, S.-G., Fu, C.-Y., & Zhang, S.-H. (1990). Unanimous distribution of auriferous districts with khondalite series and the prediction of new auriferous districts. *Gold Geology, 1*, 17–22 (in Chinese with English abstract).

Chen, Y.-J., Hu, S.-X., & Lu, B. (1998). Contrasting REE geochemical features between Archean and Proterozoic khondalite series of North China Craton. *Minralogical Magzine, 62A*, 318–319.

Chen, Y.-J., Ji, H.-Z., Zhou, X.-P., & Fu, S.-G. (1991). The challenge to the traditional geological theories from revelation of the catastrophe at 2300 Ma: New knowledge on several important geological subjects. *Advance in Earth Science, 6*(2), 63–68 (in Chinese with English abstract).

Chen, Y.-J., Liu, C.-Q., Chen, H.-Y., Zhang, Z.-J., & Li, C. (2000). Carbon isotope geochemistry of graphite deposits and ore-bearing khondalite series in North China: Implications for several geoscientific problems. *Acta Petrologica Sinica, 16*, 233–244 (in Chinese with English abstract).

Chen, Y.-J., Ouyang, Z.-Y., & Ji, H.-Z. (1992b). *A new understanding of the Archean-Proterozoic boundary. Contributions to 29th IGS* (pp. 334–341). Beijing: China Seismology Press.

Chen, Y.-J., Ouyang, Z.-Y., Yang, Q.-J., & Deng, J. (1994). A new understanding of the Archean-Proterozoic boundary. *Geologic Review, 40*, 483–488 (in Chinese with English abstract).

Chen, Y.-J., & Su, S.-G. (1998). Catastrophe in geological environment at 2300 Ma. *Mineralogical Magazine, 62A*(1), 320–321.

Chen, Y.-J., Yang, J.-Q., Deng, J., Ji, H.-Z., Fu, S.-G., Zhou, X.-P., & Lin, Q. (1996). An important change in Earth's evolution: An environmental catastrophe at 2300 Ma and its implications. *Geology-Geochemistry, 3*, 106–128 (in Chinese).

Chen, Y.-J., & Zhao, Y.-C. (1997). Geochemical characteristics and evolution of REE in the Early Precambrian sediments: Evidences from the southern margin of the North China Craton. *Episodes, 20*, 109–116.

Chen, F., & Zhu, X.-Q. (1988). Reconstruction of evolution of atmospheric CO_2 partial pressurebased on the sediment mineral assemblage. *Sci. China: Earth Sci., 7*, 747–755 (in Chinese).

Condie, K. C. (1981). *Archean greenstone belts* (pp. 1–434). Amsterdam: Elsevier Press.

Condie, K. C. (1982). *Plate tectonics & crustal evolution* (pp. 1–310). New York: Pergamon Press.

Condie, K. C. (1993). Chemical composition and evolution of the upper continental crust: Contrasting results from surface samples and shales. *Chemical Geology, 104*, 1–37.

Condie, K. C., Boryta, M. D., Liu, J.-Z., & Qian, X.-L. (1992). The origin of khondalites: Geochemical evidence from the Archean to early Proterozoic granulite belt in the North China craton. *Precambrian Research, 59*, 207–223.

Condie, K. C., DesMarais, D. J., & Abbott, D. (2001). Precambrian superplumes and supercontinents: A record in black shales, carbon isotopes, and paleoclimates? *Precambrian Research, 106*, 239–260.

Czaja, A. D., Johnson, C. M., Roden, E. E., Beard, B. L., Voegelin, A. R., Nägler, T. F., et al. (2012). Evidence for free oxygen in the Neoarchean ocean based on coupled ironemolybdenum isotope fractionation. *Geochimica et Cosmochimica Acta, 86*, 118–137.

Cenki, B., Braun, I., & Bröcker, M. (2004). Evolution of the continental crust in the Kerala Khondalite Belt, southernmost India: evidence from Nd isotope mapping, U–Pb and Rb–Sr geochronology. *Precambrian Research, 134(3–4)*, 275–292.

Chemale Jr., F., Rosie`re, C. A., & Endo, I. (1994). The tectonic evolution of the QuadriláteroFerrífero, Minais Gerais, Brazil. *Precambrian Research, 65*, 25–54.

Cornell, D. H., Schütte, S. S., & Eglington, B. L. (1996). The Ongeluk basaltic andesite formationin Griqualand West, South Africa: submarine alteration in a 2222 MaProterozoic sea. *Precambrian Research, 79*, 101–123.

Cox, D. M., Frost, C. D., & Chamberlain, K. R., (2000). 2.01-Ga Kennedy dike swarm, southeastern Wyoming: record of a rifted margin along the southern Wyoming province. *Rocky Mountain Geology, 35 (1)*, 7–30.

Dimroth, E. (1981). Labrador geosyncline: Type example of early Proterozoic cratonic reactivation. In A. Kroner (Ed.), *Precambrian plate tectonics* (pp. 1–238).

Dong, Q.-X., & Zhou, J.-C. (1984). Stratigraphic division of the original Wulashan Group in the Wula Mountains, Nei Monggol (Inner Mongolia). *Regional Geology of China, 10*, 19–37 (in Chinese with English abstract).

Dorland, H. C. (2004). Provenance ages and timing of sedimentation of selected Neoarchean and Paleoproterozoic successions on the Kaapvaal Craton. Ph.D.Thesis. Rand Afrikaans University, Johannesburg, South Africa, 326 pp.

Eriksson, P. G., Lenhardt, N., Wright, D. T., Mazumder, R., & Bumby, A. J. (2011). Late NeoarchaeanePalaeoproterozoic supracrustal basin-fills of the Kaapvaal craton: Relevance of the supercontinent cycle, the "Great Oxidation Event" and "Snowball Earth"? *Marine and Petroleum Geology, 28*, 1385–1401.

Eriksson, K. A., & Truswell, J. F. (1978). Geological process and atmospheric evolution in the Precambrian. In D. H. C. Tarling (Ed.), *Evolution of the Earth's Crust* (pp. 219–238). London: Academic Press.

Endo, I., Hartmann, L. A., Suita, M. T. F., Santos, J. O. S., Frantz, J. C., McNaughton, N. J., Barley, M. E., & Carneiro, M. A. (2002). Zircon SHRIMP isotopic evidence for Neoarchaeanage of the Minas Supergroup, Quadrilátero Ferrífero, Minas Gerais. In: Congresso Brasileiro de Geologia. Sociedade Brasileira de Geologia, João Pessoa. Anais, 518.

Fairbairn, H. W., Hurley, P. M., Card, K. D., & Knight, C. L. (1969). Correlation of radiometric ages of Nipissing Diabase and Huronian metasedinents with Proterozoic orogenic events in Ontario. *Canadian Journal of Earth Sciences, 6*, 489–497.

Feulner, G., Hallmann, C., & Kienert, H. (2015). Snowball cooling after algal rise. *Nature Geoscience, 8*(9), 659–662. doi:10.1038/ngeo2523

Frakes, L. A. (1979). *Climates throughout geologic time* (pp. 1–310). Amsterdam: Elsevier.

Frei, R., Dahl, P. S., Duke, E. F., Frei, K. M., Hansen, T. R., Frandsson, M. M., & Jensen, L. A. (2008). Trace element and isotopic characterization of Neoarchean and Paleoproterozoic iron formations in the Black Hills (South Dakota, USA): Assessment of chemical change during 2.9–1.9 Ga deposition bracketing the 2.4–2.2 Ga first rise of atmospheric oxygen. *Precambrian Research, 162*, 441–474.

Frei, R., Gaucher, C., Poulton, S. W., & Canfield, D. E. (2009). Fluctuations in Precambrian atmospheric oxygenation recorded by chromium isotopes. *Nature, 461*, 250–253.

Fryer, B. J. (1977). Rare earth evidence in iron-formations for changing Precambrian oxidation stage. *Geochimica et Cosmochimica Acta, 41*, 361–367.

Goldich, S. S. (1973). Ages of Precambrian banded iron-formation. *Economic Geology, 68*(7), 1126–1134.

Goldich, S. S., & Fischer, L. B. (1986). Air-abrasion experiments in U-Pb dating of zircon. *Chemical Geology, 58*, 195–215.

Goodwin, A. M. (1991). *Precambrian Geology* (pp. 1–521). London: Academic Press.

Gutzmer, J., & Beukes, N. J. (1998). High grade manganese ores in the Kalahari manganese field: characterization and dating of the oreforming 2 events. Unpublished Report. Rand Afrikaans University, Johannesburg, 221 pp.

Hambrey, M. J., & Harland, W. B. (Eds.). (1981). *Earth's pre-pleistocene glacial record* (pp. 1–1004). Cambridge: Cambridge University Press.

Hapuarachchi, D. J. A. C. (1972). Evolution of the granulites and sub-division of the granulite faces in Ceylon. *Ceological Magazine, 109*(5), 435–443.

Hoffman, P. F. (2013). The Great oxidation and a Siderian snowball Earth: MIF-S based correlation of Paleoproterozoic glacial epochs. *Chemical Geology, 263*, 143–156.

Hsu, K. J., Oberhansli, H., Gao, J.-Y., Sun, S., Chen, H.-H., & Krahenbuhl, U. (1986). Strangelove ocean before the Cambrian explosion. *Scientia Geologica Sinica, 1*, 1–6 (in Chinese with English abstract).

Hsu, K. J., & Xu, J.-H. (1980). The impact effect of Comet—the cause about producing catastrophe on the Earth in late Cretaceous. *Journal of the Changchun Geological Institute*, (2), 1–8 (in Chinese).

Hu, S.-X., Zhao, Y.-Y., Xu, J.-F., & Ye, Y., (1997). *Geology of gold deposits in north china platform* (pp. 7–55). Beijing, China Science Press (in Chinese).

Hammond, R. D. (1976). Geochronology and origin of Archean rocks in Marquette County, Upper Michigan. M.S. Thesis. University of Kansas, Lawrence, 108 pp.

Hannah, J. L., Bekker, A., Stein, H. J., Markey, R. J., & Holland, H. D. (2004). Primitive Os and 2316 Ma age for marine shale: implications for Paleoproterozoic glacial events and the rise of atmospheric oxygen. *Earth and Planetary Science Letters, 225*, 43–52.

Hanski, E., Huhma, H., & Vaasjoki, M. (2001). Geochronology of northern Finland: a summary and discussion. In: Vaasjoki, M. (Ed.), Radiometric Age Determination from Finnish Lapland and Their Bearing on the Timing of Precambrian Volcanosedimentary Sequences. Geological Survey of Finland Bulletin Special Paper, 33, pp. 255–279.

Holland, H. D., 1994. Early Proterozoic atmospheric change. In: Bengston, S. (Ed.), *Early Life on Earth. Nobel Symposium No. 84* (pp. 237–244). New York: Columbia University Press.

Huhma, H. (1986). SmeNd and Pb–ePb isotopic evidence for the origin of the Early Proterozoic Svecokarelian crust in Finland. *Geological Survey of Finland Bulletin, 337*, 48.

Huston, D. L., & Logan, G. A. (2004). Barite, BIFs and bugs: evidence for the evolution ofthe Earth's early atmosphere. *Earth and Planetary Science Letters, 220*, 41–55.

Isley, A.E., & Abbott, D. H. (1999). Plume-related mafic volcanism and the deposition of banded iron formation. *Journal of Geophysical Research. B: Solid Earth Planets*, *104*, 15461–15477.

Jahn, B.-M. (1990). Direct dating of stromatolitic carbonates from the Schmidsrif Formation (Transvaal Dolomite), South Africa, with implications on the age of the Ventersdorp Supergroup. *Geology, 18*, 1211–1214.

Jahn, B.-M., & Simonson, B. M. (1995). Carbonate Pb-Pb ages of the Wittenoom formation and Carawine dolomite, Hamersley basin, western Australia (with implications for their correlation with the Transvaal dolomite of South Africa). *Precambrian Research, 72*, 247–261.

Ji, H.-Z., & Chen, Y.-J. (1990). Khondalite series and their related mineral resources. *Geology and Prospecting, 11*, 11–13 (in Chinese).

Ji, H.-Z., Chen, Y.-J., & Zhao, Y.-Y. (1990). Khondalite Series and graphite deposits. *Nonmetallic Geology, 6*, 9–11 (in Chinese).

Jin, W., & Li, S.-X. (1994). The lithological association and geological features of early Proterozoic orogenic belt in Daqingshan, Nei Mongol. In X.-L. Qian & R.-M. Wang (Eds.), *Geological evolution of the granulite terrain in north part of the North China Craton* (pp. 32–42). Beijing: China Seismological Press (in Chinese with English abstract).

Karhu, J. A. (1993). Palaeoproterozoic evolution of the carbon isotope ratios of sedimentary carbonates in the Fennoscandian Shield. *Geological Survvey of Finland Bulletin, 371*, 1–87.

Karhu, J. A., & Holland, H. D. (1996). Carbon isotopes and the rise of atmospheric oxygen. *Geology, 24*(10), 867–870.

Kaufman, A. J., Johnston, D. T., Farquhar, J., Masterson, A. L., Lyons, T. W., Bates, S., et al. (2007). Late Archean biospheric oxygenation and atmospheric evolution. *Science, 317*, 1900–1903.

Kimberly, M. M., & Dimroth, E. (1976). Basic similarity of Archean to subsequent atmospheric and hydrospheric compositions as evidenced in the distributions of sedimentary carbon, sulphur, uranium and iron. In B. F. Windly (Ed.), *The early history of the earth* (pp. 579–585). London: Wiley Press.

Kirschvink, J. L., Gaidos, E. J., Bertani, L. E., Beukes, N. J., Gutzmer, J., Maepa, L. N., et al. (2000). Paleoproterozoic snowball Earth: Extreme climatic and geochemical global change and its biological consequences. *Proceedings of the National Academy of Sciences of the United States of America*, *97*, 1400–1405.

Klein, C. (2005). Some Precambrian banded iron-formations (BIFs) from around the world: Their age, geologic setting, mineralogy, metamorphism, geochemistry, and origin. *American Mineralogist, 90*, 1473–1499.

Knoll, A. H., Strother, P. K., & Rossi, S. (1988). Distribution and diagenesis of microfossils from the lower Proterozoic Duck Creek Dolomite, Western Australia. *Precambrian Research, 38*, 257–279.

Kong, F.-F., Yuan, X.-L., Zhou, C.-M. (2011). Paleoproterozoic glaciation: Evidence from carbon isotope record of the Hutuo Group, Wutai Mountain area of Shanxi Province, China. *Chinese Science Bulletin*, *56*, 2922–2930.

Konhauser, K. O., Lalonde, S. V., Planavsky, N. J., Pecoits, E., Lyons, T. W., Mojzsis, S. J., et al. (2011). Aerobic bacterial pyrite oxidation and acid rock drainage during the Great Oxidation Event. *Nature, 478*, 369–373.

Konhauser, K. O., Pecoits, E., Lalonde, S. V., Papineau, D., Nisbet, E. G., Barley, M. E., et al. (2009). Oceanic nickel depletion and a methanogen famine before the Great Oxidation Event. *Nature, 458*, 750–753.

Krogh, T. E., Davis, D. W., & Corfu, F. (1984). Precise U–Pb zircon and badelleyite ages for the Sudbury area. In E. G. Pye, A. J. Naldrett & P.E. Giblin (Eds.), *The geology and ore deposits of the sudbury structure. ontario geological survey specialists* (Vol. 1, pp. 431–446).

Kroner, A. (1981). Precambrian plate tectonics. In A. Kroner (Ed.), *Precambrian plate tectonics* (pp. 57–90). Amsterdam: Elsevier.

Kroner, A., Compston, W., Zhang, G.-W., Guo, A.-L., & Todt, W. (1988). Age and tectonic setting of late Archean greenstone-gneiss terrain in Henan province, China, as revealed by single-grain zircon dating. *Geology, 16*, 211–215.

Kröner, A., Wilde, S. A., Li, J. H., & Wang, K. Y. (2005). Age and evolution of a late Archean to early Palaeozoic upper to lower crustal section in the Wutaishan/Hengshan/Fuping terrain of northern China. *Journal of Asian Earth Sciences, 24*, 577–595.

Lai, Y., Chen, C., & Tang, H.-S. (2012). Paleoproterozoic positive $\delta^{13}C$ excursion in Henan, China. *Geomicrobiology Journal, 29*, 287–298.

Li, Z., Chen, B., Liu, J.-W., Zhang, L., & Yang, C. (2015). Zircon U-Pb ages and their implications for the South Liaohe Group in the Liaodong Peninsula, Northeast China. *Acta Petrologica Sinica, 31* (6), 1589–1605 (in Chinese with English abstract).

Li, S.-Z., & Zhao, G.-C. (2007). SHRIMP U-Pb zircon geochronology of the Liaoji granitoids: Constraints on the evolution of the Paleoproterozoic Jiao-Liao-Ji belt in the Eastern Block of the North China Craton. *Precambrian Research, 158*, 1–16.

Li, S.-Z., Zhao, G.-C., Sun, M., Wu, F.-Y., Liu, J.-Z., Hao, D.-F., et al. (2004). Mesozoic, not Paleoproterozoic SHRIMP U-Pb zircon ages of two Liaoji granites, Eastern Block, North China Craton. *International Geology Review, 46*, 162–176.

Liu, F.-L., Liu, P.-H., Wang, F., Liu, C.-H., & Cai, J. (2015). Progresses and overviews of voluminous meta-sedimentary series within the Paleoproterozoci Jiao-Liao-Ji orogenic/ mobile belt, North China Craton. *Acta Petrologica Sinica, 31*(10), 2816–2846 (in Chinese with English abstract).

Liu, S.-W., Zhao, G.-C., Wilde, S. A., Shu, G.-M., Sun, M., Li, Q.-G., et al. (2006). Th-U-Pb monazite geochronology of the Lüliang and Wutai Complexes: Constraints on the tectonothermal evolution of the Trans-North China Orogen. *Precambrian Research, 148*, 205–224.

Lowe, D. R. (1994). Archean greenstone-related sedimentary rocks. In K. C. Condie (Ed.), *Archean crustal evolution* (pp. 121–170). Amsterdam: Elsevier.

Lu, X.-P., Wu, F.-Y., Guo, J.-H., Wilde, S.-A., Yang, J.-H., Liu, X.-M., & Zhang, X.- O. (2006). Zircon U-Pb geochronological constraints on the Paleoproterozoic crustal evolution of the Eastern Block in the North China Craton. *Precambrian Research, 146*, 138–164.

Lu, X.-P., Wu, F.-Y., Lin, J.-Q., Sun, D.-Y., Zhang, Y.-B., & Guo, C.-L. (2004a). Geochronological successions of the Early Precambrian granitic magmatism in southern Liaoning Peninsula and its constraints on tectonic evolution of the North China Craton. *Chinese Journal of Geology, 39*, 123–138 (in Chinese with English abstract).

Lu, X.-P., Wu, F.-Y., Zhang, Y.-B., Zhao, C.-B., & Guo, C.-L. (2004b). Emplacement age and tectonic setting of the Paleoproterozoic Liaoji granites in Tonghua area, southern Jilin Province. *Acta Petrologica Sinica, 20*, 381–392 (in Chinese with English abstract).

Luo, Y., Sun, M., Zhao, G.-C., Li, S.-Z., Xu, P., Ye, K., & Xia, X.-P. (2004). LA ICP-MS U-Pb zircon ages of the Liaohe Group in the Eastern Block of the North China Craton: Constraints on the evolution of the Jiao-Liao-Ji Belt. *Precambrian Research, 134*, 349–371.

Lyons, T. W., & Reinhard, C. T. (2009). Eraly earth: Oxygen for heavy-metal fans. *Nature, 461*, 179–181.

Masuda, A., Nakamura, N., & Tanaka, T. (1973). Fine structures of lanthanide elements and an attempt to analyse separation-index patterns of some minerals. *Journal of Earth Sciences. Nayoya University, 10*, 173–187.

McLennan, S. M. (1989). Rare earth elements in sedimentary rocks: Influence of provenance and sedimentary processes. In B. R. Lipin & G. A. McKay (Eds.), *Geo-chemistry and mineralogy of rare earth elements*, *Review mineralogy society American* (Vol. 21, pp. 169–200).

Melezhik, V. A., Bingen, B., Fallick, A. E., Gorokhov, I. M., Kuznetsov, A. B., Sandstad, J. S., et al. (2008). Isotope chemostratigraphy of marbles in northeastern Mozambique: apparent depositional ages and tectonostratigraphic implications. *Precambrian Research, 162*, 540–558.

Melezhik, V. A., & Fallick, A. E. (1996). A widespread positive & #x03B4;13Ccarb anomaly at 2.33–2.06 Ga on the Fennoscandian Shield: A paradox? *Terra Nova Research, 8*, 141–157.

Melezhik, V. A., Fallick, A. E., & Clark, A. (1997a). Two billion year old isotopically heavy carbon: Evidence from the Labrador Trough, Canada. *Canadian Journal of Earth Sciences, 34*, 271–285.

Melezhik, V. A., Fallick, A. E., Filippov, M. M., & Larsen, O. (1999a). Karelian shungite–an indication of 2.0-Ga-old metamorphosed oil-shale and generation of petro-leum: Geology, lithology and geochemistry. *Earth-Science Reviews, 47*, 1–40.

Melezhik, V. A., Fallick, A. E., Makarikhin, V. V., & Lubtsov, V. V. (1997b). Links between Palaeoproterozoic palaeogeography and rise and decline of stromatolites: Fennoscandian Shield. *Precambrian Research, 82*, 311–348.

Melezhik, V. A., Fallick, A. E., Medvedev, P. V., & Makarikhin, V. V. (1999b). Extreme $^{13}C_{carb}$ enrichment in ca. 2.0 Ga magnesite–stromatolite–dolomite–'red beds' association in a global context: A case for the worldwide signal enhanced by a local environment. *Earth-Science Reviews, 48*, 71–120.

Melezhik, V. A., Fallick, A. E., Rychanchik, D. V., & Kuznetsov, A. B. (2005a). Paleoproterozoic evaporites in Fennoscandia: Implications for seawater sulfate, the rise of atmospheric oxygen and local amplification of the $\delta^{13}C$ excursion. *Terra Nova, 17*, 141–148.

Melezhik, V. A., Fallick, A. E., & Semikhatov, M. A. (1997c). Could stromatolite-forming cyanobacteria have influenced the global carbon cycle at 2300–2060 Ma? *Norges Geologiske Undersøkelse Bulletin, 433*, 30–31.

Melezhik, V. A., Gorokhov, I. M., Fallick, A. E., & Gjelle, S. (2001a). Strontium and carbon isotope geochemistry applied to dating of carbonate sedimentation: An example from high-grade rocks of the Norwegian Caledonides. *Precambrian Research, 108*, 267–292.

Melezhik, V. A., Gorokhov, I. M., Kuznetsov, A. B., & Fallick, A. E. (2001b). Review article: Chemostratigraphy of Neoproterozoic carbonates: Implications for 'blind dating'. *Terra Nova, 13*, 1–11.

Melezhik, V. A., Kuznetsov, A. B., Fallick, A. F., Smith, R. A., Gorokhov, I. M., Jamal, D., & Catuane, F. (2006). Depositional environments and an apparent age for the Geci meta-limestones: Constraints on the geological history of northern Mozambique. *Precambrian Research, 148*, 19–31.

Melezhik, V. A., Roberts, D., Fallick, A. E., Gorokhov, I. M., & Kuznetsov, A. B. (2005b). Geochemical preservation potential of high-grade calcite marble versus dolomite marble: Implication for isotope chemostratigraphy. *Chemical Geology, 216*, 203–224.

Melezhik, V. A., Roberts, D., Gorokhov, I. M., Fallick, A. E., Zwaan, K. B., Kuznetsov, A. B., & Pokrovsky, B. G. (2002). Isotopic evidence for a complex Neoproterozoic to Silurian rock assemblage in the North-Central Norwegian Caledonides. *Precambrian Research, 114*, 55–86.

Melezhik, V. A., Young, G. M., Eriksson, P. G., Altermann, W., Kump, L. R., & Lepland, A. (2013). Huronian-age glaciation. Chapter 7.2. In: V. A. Melezhik, L. R. Kump, A. E. Fallick, H. Strauss, E. J. Hanski, R. Prave, A. Lepland (Eds.), *Reading the archive of Earth's oxygenation. Global events and the Fennoscandian Arctic Russia–Drilling Early Earth Project* (Vol. 3, pp. 1059–1109). Berlin: Springer.

Meng, E., Liu, F.-L., Cui, Y., Liu, P.-H., Liu, C.-H., & Shi, J.-R. (2013). Depositional ages and tectonic implications for the Kuandian South Liaohe Group in Northeast Liaodong Peninsula, Northeast China. *Acta Petrologica Sinica, 29*(7), 2465–2480 (in Chinese with English abstract).

Meng, E., Liu, F.-L., Liu, P.-H., Liu, C.-H., Yang, H., Wang, F., et al. (2014). Petrogenesis and tectonic implications of Paleoproterozoic meta-mafic rocks from central Liaodong Peninsula, Northeast China: Evidence from zircon U-Pb dating and in situ Lu-Hf isotopes, and whole-rock geochemistry. *Precambrian Research, 247*, 92–109.

Mossman, D. J., & Harron, G. A. (1983). Origin and distribution of gold in the Huronian supergroup, Canada—the case for Witwatersrand-type paleoplacers. *Precambrian Research, 20*, 543–583.

Machado, N., & Carneiro, M. A. (1992). U–Pb evidence of late Archean tectono-thermalactivity in the southern São Francisco shield, Brazil. *Canadian Journal of Earth Sciences, 29*, 2341–2346.

Machado, N., Noce, C. M., Ladeira, E. A., & Belo de Oliveira, O. (1992). U–Pb geochronology of Archean magmatism and Proterozoic metamorphism in the QuadriláteroFerrífero, southern São Francisco craton, Brazil. *Geological Society of America Bulletin, 104*, 1221–1227.

Machado, N., Schrank, A., Noce, C. M., & Gauthier, G. (1996). Ages of detrital zircon from Archean–Paleoproterozoic sequences: implications for greenstone belt settingand evolution of a Transamazonian foreland basin in Quadrilátero Ferrífero, southeast Brazil. *Earth and Planetary Science Letters, 141*, 259–276.

Martin, D. M., Clendenin, C. W., Krapez, B., & McNaughton, N. J. (1998). Tectonic andgeochronological constraints on late Archaean and Palaeoproterozoic stratigraphic correlation within and between the Kaapvaal and Pilbara Cratons.*Journal of the Geological Society of London, 155*, 311–322.

Naqvi, S. M., Divakara, R. V., & Narain, H. (1978). The primitive crust: Evidence from the Indian Shield. *Precambrian Research, 6*, 323–345.

Nelson, D. R., Trendall, A. F., & Altermann, W. (1999). Chronological correlations between the Pilbara and Kaapvaal cratons. *Precambrian Research, 97*, 165–189.

Noce, C. M., Machado, N., & Teixeira, W. (1998). U–Pb geochronology of gneisses andgranitoids in the Quadrilátero Ferrífero (southern São Francisco craton): age constraints from Archean and Paleoproterozoic magmatism and metamorphism. *Revista Brasileira de Geociências, 28*, 95–102.

Pickard, A. L. (2002). SHRIMP U-Pb zircon ages of tuffaceous mudrocks in the Brockman iron formation of the Hamersley Range, Western Australia. *Australian Journal of Earth Sciences, 49*, 491–507.

Plumb, K. A. (1988). Tectonic subdivision of the Prorerozoic proposals by the Subcommission on Precambrian Stratigraphy. In S. Dazhong (Ed.), *Abstracts of International Symposium on Geochemistry and Mineralization of Proterozoic Mobile Belts* (pp. 73–74). Tianjin.

Plumb, K. A., & James, H. L. (1986). Subdivision of Precambrian time: Recommendations and suggestions by the Subcomission on Precambrain Stratigraphy. *Precambrian Research, 32*, 65–92.

Purohit, R., Sanyal, P., Roy, A. B., & Bhattacharya, S. K. (2010). ^{13}C enrichment in the Palaeoproterozoic carbonate rocks of the Aravalli Supergroup, northwest India: Influence of depositional environment. *Gondwana Research, 18*, 538–546.

Pickard, A. L. (2003). SHRIMP U–Pb zircon ages for the Palaeoproterozoic KurumanIron Formation, Northern Cape Province, South Africa: evidence for simultaneous BIF deposition on Kaapvaal and Pilbara Cratons. *Precambrian Research, 125 (3/4)*, 275–315.

Premo, W. R., & Van Schmus, W. R. (1989). Zircon geochronology of Precambrian rocks in southeastern Wyoming and northern Colorado. In: Grambling, J. A., Tewksbury, B. J. (Eds.), Proterozoic Geology of the Southern Rocky Mountains. Geological Society of America Special Paper, 235, pp. 1–12.

Puchtel, I. S., Hofmann, A. W., Mezger, K., Schipansky, A. A., Kulikov, V. S., & Kulikova, V. V. (1996). Petrology of a 2.41 Ga remarkably fresh komatiitic basalt lava lake in Lion Hills, central Vetreny Belt, Baltic Shield. *Contributions to Mineralogy and Petrology, 124*, 273–290.

Ray, J. S., Veizer, J., & Davis, W. J. (2003). C, O, Sr and Pb isotope systematics of carbonate sequences of the Vindhyan Supergroup, India: Age, diagenesis, correlations and implications for global events. *Precambrian Research, 121*, 103–140.

Roscoe, S. M. (1996). Paleoplacer uranium, gold. In O. R. Eckstrand, W. D. Sinclair & R. I. Thorpe (Eds.), *Geology of Canadian mineral deposit types. Geological society of America, The Geology of North America* (Vol. P-1, pp. 10–23).

Roscoe, S. M., Minter, W. E. L. (1993). Pyritic paleoplacer gold and uranium deposits. In R. V. Kirkham, W. D. Sinclair, R. I. Thorpe & J. M. Duke (Eds.), *Mineral deposit modeling* (Vol. 40, pp. 103–124). Geological Association Canada Special Paper.

Rainbird, R. H., & Davis, W. J. (2006). Sampling superior: detrital zircon geochronology of the Huronian. Geological Association of Canada Abstracts with Programs 31, 125.

Rui, Z.-Y., Li, N., & Wang, L.-S. (1991). Lead and zinc deposits of Guanmenshan (pp. 1–208). Beijing: Geological Publishing House (in Chinese with English abstract).

Salop, L. J. (1977). *Precambrian of the northern hemisphere* (pp. 1–378). Amsterdam: Elsevier Press.

Satish-Kumar, M., Yurimoto, H., Itoh, S., & Cesare, B. (2011). Carbon isotope anatomy of a single graphite crystal in a metapelitic migmatite revealed by high-spatial resolution SIMS analysis. *Contributions to Mineralogy and Petrology, 162*(4), 821–834.

Schidlowski, M. (1976). Archean atmosphere and evolution of the terrestrial oxygen. In B. F. Windley (Ed.), *The early history of the earth* (pp. 525–535). London: Wiley.

Schidlowski, M. (1988). A 3800-million-year isotopic record of life from carbon in sedimentary rocks. *Nature, 333*, 313.

Schidlowski, M. (2001). Carbon isotopes as biogeochemical recorders of life over 3.8 Ga of Earth history: Evolution of a concept. *Precambrian Research, 106*, 117–134.

Schidlowski, M., Eichmann, R., & Junge, C. E. (1975). Precambrian sedimentary carbonates: carbon and oxygen isotope geochemistry and implications for the terrestrial oxygen budget. *Precambrian Research, 2*, 1–69.

Schopf, J. W. (1977). Evidences of Archean life. In: C. Ponnamperuam (Ed), Chemical Evolution of the Early Precambrian (pp. 101–105). New York: Academic Press.

Semikhatov, M. A., & Raaben, M. E. (1994). Dynamics of the global diversity of Proterozoic stromatolites. Article I: Northern Eurasia, China and India. *Stratigraphy and Geological Correlation, 2*(6), 10–32.

Siever, R. (1977). Early Precambrian weathering and sedimentation: An impressionistic view. In C. Ponnamperuam (Ed.), *Chemical evolution of the early Precambrian* (pp. 13–23). New York: Academic Press.

Sreenivas, B., Sharma, D. S., Kumar, B., Patil, D. J., Roy, A. B., & Srinivasan, R. (2001). Positive $\delta^{13}C$ excursion in carbonate and organic fractions from the Paleoproterozoic Aravalli Supergroup, Northwestern India. *Precambrian Research, 106*, 277–290.

Sun, D.-Z. (1990). A discussion on Precambrian geochronology. *Regional Geology of China, 4*, 289–300.

Tang, H.-S., & Chen, Y.-J. (2013). Global glaciations and atmospheric change at ca. 2.3Ga. *Geoscience Frontiers, 4*, 583–596.

Tang, G.-J., Chen, Y.-J., Huang, B.-L., & Chen, C.-X. (2004). Paleoprotoerozoic δ13Ccarb positive excursion event: Research progress on 2. 3 Ga catastrophe. *Journal of Mineralogy and Petrology*, *24*(3), 103–109 (in Chinese with English abstract).

Tang, H.-S., Chen, Y.-J., Santosh, M., & Yang, T. (2013a). REE geochemistry of carbonates from the Guanmenshan Formation, Liaohe Group, NE Sino-Korean Craton: Implications for seawater compositional change during the Great Oxidation Event. *Precambrian Research, 227*, 316–336.

Tang, H.-S., Chen, Y.-J., Santosh, M., Zhong, H., Wu, G., & Lai, Y. (2013b). C-O isotope geochemistry of the Dashiqiao magnesite belt, North China Craton: Implications for the Great Oxidation Event and ore genesis. *Geological Journal, 48*, 467–483.

Tang, H.-S., Chen, Y.-J., & Wu, G. (2009a). ^{40}Ar-^{39}Ar dating and its geological implication of the Houxianyu boron deposit. *Liangning province. Acta Petrologica Sinica, 25*(11), 2752–2762 (in Chinese with English abstract).

Tang, H.-S., Chen, Y.-J., Wu, G., & Lai, Y. (2008). The C-O isotope composition of the Liaohe Group, northern Liaoning province and its geologic implications. *Acta Petrologica Sinica, 24*(1), 129–138 (in Chinese with English abstract).

Tang, H.-S., Chen, Y.-J., Wu, G., & Lai, Y. (2011). Paleoproterozoic positive $\delta^{13}C_{carb}$ excursion in northeastern Sino-Korean craton: evidence of the Lomagundi Event. *Gondwana Research, 19*, 471–481.

Tang, H.-S., Chen, Y.-J., Wu, G., & Yang, T. (2009b). Rare earth element geochemistry of carbonates of Dashiqiao Formation, Liaohe Group, eastern Liaoning province: Implications for Lomagundi Event. *Acta Petrologica Sinica, 25*(11), 3075–3093 (in Chinese with English abstract).

Tang, H.-S., Wu, G., & Lai, Y. (2009c). The C-O isotope geochemistry and genesis of the Dashiqiao magnesite deposit, Liaoning province. *NE China. Acta Petrologica Sninca, 25*(2), 455–467 (in Chinese with English abstract).

Taylor, S. R., & Mclennan, S. M. (1985). *The continental crust: Its composition and evolution* (pp. 1–312). Oxford: Blackwell.

Tu, G.-Z., Zhao, Z.-H., & Qiu, Y.-Z. (1985). Evolution of Precambrian REE mineralization. *Precambian Research, 27*, 131–151.

Turner, P. (1980). *Continental red beds* (pp. 1–562). Amsterdam: Elsevier.

Tang, H.-S., Chen, Y.-J., Li, K.-Y., Chen, W.-Y., Zhu, X.-Q., Ling, K.-Y., Sun, X.-H. (2016). Early Paleoproterozoic metallogenic explosion in North China Craton. In: M.-G. Zhai, et al. (Eds), Main Tectonic Events and Metallogeny of the North China Craton (Chapter 12). Singapore, Springer.

Trendall, A. F., Nelson, D. R., de Laeter, J. R., & Hassler, S. W. (1998). Precise zircon U–Pb ages from the Marra Mamba Iron Formation and the Wittenoom Formation, Hamersley Group, Western Australia. *Australian Journal of Earth Sciences, 45*,137–142.

Tu, G.-Z. (1990). Classification of primary gold ore deposit and prospect analysis of different type gold ore deposit in China-Report in inaugural meeting of mineral, lithogeochemical society of Guanxi. *Mineral Resources and Geology, 4(1)*, 1–10 (in Chinese with English abstract).

Vallini, D. A., Cannon, W. F., & Schulz, K. J. (2006). New constraintson the timing of Paleoproterozoic glaciation, Lake Superior region: Detrital zircon and hydrothermal xenotime ages on the Chocolay Group, Marquette Range Supergroup. *Canadian Journal of Earth Sciences, 43*, 571–591.

Voegelin, A. R., Nägler, T. F., Beukes, N. J., & Lacassie, J. P. (2010). Molybdenum isotopes in late Archean carbonate rocks: implications for early Earth oxygenation. *Precambrian Research, 182*, 70–82.

Walter, M. R., Veevers, J. J., Calver, C. R., Gorjan, C. R., & Hill, A. C. (2000). Dating the 840–544 Ma Neoproterozoic interval by isotopes of strontium, carbon, and sulfur in seawater, and some interpretative models. *Precambrian Research, 100*, 371–433.

Wan, Y.-S., Song, B., Liu, D.-Y., Wilde, S. A., Wu, J.-S., Shi, Y.-R., et al. (2006). SHRIMP U-Pb zircon geochronology of Palaeoproterozoic metasedimentary rocks in the North China Craton: Evidence for a major Late Palaeoproterozoic tectonothermal event. *Precambrian Research, 149*, 249–271.

Wang, S.-Q. (1989). The geological features of host rocks and metallogenesis of the Xinghe graphite deposit. *Nei Mongol. Mineral Deposit, 8*(1), 85–96 (in Chinese with English abstract).

Wang, F., Liu, F.-L., Liu, P.-H., & Liu, J.-H. (2010). Metamorphic evolution of Early Precambrian khondalite series in North Shandong Province. *Acta Petrologica Sinica, 26*(7), 2057–2072 (in Chinese with English abstract).

Wilde, S. A., Zhao, G.-C., Wang, K.-Y., & Sun, M. (2004). First precise SHRIMP U-Pb zircon ages for the Hutuo Group, Wutaishan: Further evidence for the Palaeoproterozoic amalgamation of the North China Craton. *Chinese Science Bulletin, 49*, 83–90.

Wille, M., Kramers, J. D., Nägler, T. F., Beukes, N. J., Schröder, S., Meisel, Th, et al. (2007). Evidence for a gradual rise of oxygen between 2.6 and 2.5 Ga from Mo isotopes and Re-PGE signatures in shales. *Geochimica et Cosmochimica Acta, 71*, 2417–2435.

Windley, B. F. (1976). *The Early History of the Earth*. London: Wily.

Windley, B. F. (1980). Evidence for land emergence in the early to middle Precambrian. *Proceedings of Geological Assosiation*, *91*, 13–23.

Windley, B. F. (1983). Banded iron formation in Proterozoic greenstone belts: Call for further studies. *Precambrian Research, 20*, 585–588.

Windley, B. F. (1984). The evolving continents (pp. 1–399, 2nd edn.). Chichester: Wiley.

Wu, C.-H. (1988). The age of khondalite series in Jiaodong (Fenzishan Group in Pindu County) and its comparison with khondalite series in China and overseas. In *Abstracts of the Symposium on Geochemistry and Mineralization of Proterozoic Mobile Belts* (p. 70). Tianjin.

Wu, C.-H., Gao, Y.-D., Mei, H.-L., & Zhong, C.-T. (1994). Structural fetures and unconformity arguments between the khondalite suite and the granulite complex in Huangtuyao area, Nei Mongol, North China. In X.-L. Qian & R.-M. Wang (Eds.), *Geological evolution of the granulite terrain in North Part of the North China Craton* (pp. 145–156). Beijing: China Seismological Press (in Chinese with English abstract).

Wu, C.-H., Sun, M., Li, H.-M., Zhao, G.-C., & Xia, X.-P. (2006). LA-ICP-MS U-Pb zircon ages of the khondaites from the Wulashan and Jining high-grade terrain in northern margin of the North China Craton: Constraints on sedimentary age of the khondalite. *Acta Petrologica Sinica, 22*(11), 2639–2654 (in Chinese with English abstract).

Walraven, F. (1997). Geochronology of the Rooiberg Group, Transvaal Supergroup, South Africa. Economic Geology Research Unit, University of the Witwatersrand, Johannesburg, South Africa. Inf. Circ. 316, 21 pp.

Wang, C.-Q., Fan, Y.-B., & Luo, J.-M. (1989). The geological characteristics of Proterozoic marine volcanic rocks—spilite in the Xunhe area, Northern Liaoning. *Regional Geology of China, 30 (3)*, 237–242 (in Chinese with English abstract).

Xu, X.-S., Griffin, W. L., Ma, X., O'Reilly, S. Y., He, Z.-Y., & Zhang, C.-L. (2009). The Taihua group on the southern margin of the North China craton: Further insights from U-Pb ages and Hf isotope compositions of zircons. *Mineralogy and Petrology, 97*, 43–59.

Yin, C.-Q., Zhao, G.-C., Sun, M., Xia, X.-P., Wei, C.-J., & Leung, W.-H. (2009). LA-ICP-MS U-Pb zircon ages of the Qianlishan Complex: constrains on the evolution of the Khondalite Belt in the Western Block of the North China Craton. *Precambrian Research, 174*, 78–94.

Young, G. M. (2014). Contradictory correlations of Paleoproterozoic glacial deposits: Local, regional or global controls? *Precambrian Research, 247*, 33–44.

Yuan, J.-Q. (1981). *Mineral deposits*. Beijing: Geology Publishing House (in Chinese).

Zhang, Q.-S. (1984). *The early Precambrian geology and metallogeny* (pp. 1–223). Changchun: Jilin Publishing House (in Chinese).

Zhang, Q.-S. (1988). *The early crust evolution and mineral deposits in eastern Liaoning Province Peninsula* (pp. 1–213). Beijing: Geological Publishing House (in Chinese with English abstract).

Zhang, W.-Z., Wang, H.-N., & Wang, M.-Y. (1987). *Coordination chemistry and its applications in geology* (pp. 1–429). Beijing: Geological Publishing House (in Chinese).

Zhao, Z.-H. (2010). Banded iron formation and great oxidation event. *Earth Science Frontiers, 17*, 1–12 (in Chinese with English abstract).

Zhao, G.-C., Cawood, P. A., Li, S.-Z., Wilde, S. A., Sun, M., Zhang, J., et al. (2012). Amalgamation of the North China Craton: Key issues and discussion. *Prcambrian Research, 222–223*, 55–76.

Zhao, Y.-Y., & Yan, M.-C. (1993). Geochemical record of the climate effect in sediments of the China shelf sea. *Chemical Geology, 107*, 267–269.

Zhao, T.-P., Zhai, M.-G., Xia, B., Li, H.-M., Zhang, Y.-X., & Wan, Y.-S. (2004). Study on the zircon SHRIMP ages of the Xiong'er Group volcanic rocks: Constraint on the starting time of covering strata in the North China Craton. *Chinese Science Bulletin, 9*(23), 2495–2502.

Zhao, Z.-P. (1980). Formation and evolution of the crystalline basement of the North China Fault-Block. In: W.-Y. Zhang (Ed.), Formation and Development of the North China Fault-Block (pp. 59–61). Beijing: Science Press (in Chinese).

Zhao, Z.-P. (1988). Subdivision of Precambrian time and rock-stratigraphic units of eastern China: inference from Precambrian crustal evolution of eastern Hebei Province. *Scientia Geologica Sinica, 4*, 301–323 (in Chinese with English abstract).

Zhong, H., & Ma, Y.-S. (1995). Discovery of early Proterozoic carbon isotope shifts. *Acta Geologica Sinica, 69*, 2185–2191 (in Chinese with English abstract).

Early Paleoproterozoic Metallogenic Explosion in North China Craton

12

Haoshu Tang, Yanjing Chen, Kaiyue Li, Weiyu Chen, Xiaoqing Zhu, Kunyue Ling, and Xiaohui Sun

Abstract

This chapter compiles the geology and geochronology of numerous ores, including graphite, phosphorite, the Lake Superior type BIFs, marble, boron, magnesite, and lead-zinc deposits, hosted in 2.5–1.8 Ga stata from the North China Craton (NCC) and elsewhere, and thereby provides insights into understanding the mineralization of the early Paleoproterozoic metallogenic explosion in NCC. These mineralized records, accompanied with the blooms of biological photosynthesis (indicated by graphite, phosphorite deposits, organics in black shale), suggested different mineralizations, which responded to different stages of dramatic Earth's environmental changes characteristic of the Great Oxidation Event (GOE). These changes includes that the early-stage hydrosphere oxidation (2.5–2.3 Ga), indicated by numerous development of the Lake Superior type BIFs; through the turnpoint from hydrosphere to atmosphere oxidation (2.3–2.25 Ga), indicated by the 2.29–2.25 Ga Huronnian Glaciation Event (HGE) and devoid of Rand-type Au–U deposits, to the late-stage atmospheric oxygenation, followed by 2.25–1.8 Ga sediments of thick-bedded carbonates strata and related deposits (e.g., marble, magnesite, boron, and lead-zinc deposits), the 2.25–1.95 Ga red beds, 2.22–2.06 Ga $\delta^{13}C_{carb}$ positive excursion (Lomagundi/Jatulian Event), as well as the prevail of black shales at 2.0–1.7 Ga and disappear of BIFs at ca. 1.8 Ga.

Keywords

Mineralization • Great Oxidation Event (GOE) • Early paleoproterozoic living bloom • Ph of seawater • Earth's environmental changes

H. Tang (✉) · X. Zhu · K. Ling · X. Sun
State Key Laboratory of Ore Deposit Geochemistry,
Institute of Geochemistry, Chinese Academy of Sciences,
99 Linchengxi Roud, Guiyang, 550081, China
e-mail: tanghaoshu@163.com

Y. Chen (✉) · K. Li · W. Chen
Key Laboratory of Crustal and Orogenic Evolution,
Peking University, Beijing, 100871, China
e-mail: yjchen@pku.edu.cn

X. Sun
School of Earth Science and Resources,
Chang'an University, Xi'an, 710054, China

M. Zhai et al. (eds.), *Main Tectonic Events and Metallogeny of the North China Craton*,
Springer Geology, DOI 10.1007/978-981-10-1064-4_12

12.1 Introduction

The Siderian/Rhyacian transition (2.3 Ga) witnessed dramatic environmental changes (e.g., Chen 1990; Chen and Su 1998; Holland 2009; Chen and Tang 2016, in Chap. 11; and references therein) in Earth's history characteristic of the Great Oxidation Event (GOE), which mainly occurred in the period of 2.5–2.2 Ga and includes the pre-2.3 Ga earlier hydrosphere oxidation stage and the post-2.3 Ga later atmosphere oxygenation stage (Tang and Chen 2013). The tectonic processes and global environmental changes during the Palaeoproterozoic from 2.5 to 1.6 Ga have been the focus of numerous studies in the past decades (e.g., Chen 1990, 1996b; Bekker et al. 2010; Holland 2009; Konhauser et al. 2009, 2011; Lyons and Reinhard 2009; Young 2012, 2013; Zhai and Santosh 2013; Zheng et al. 2013; Li et al. 2015a; and references therein). Particularly in the early paleoproterozoic (2.3–1.8 Ga) period, voluminous red beds, evaporites, stromatolite-bearing carbonates (Chen 1990; Melezhik et al. 1999a; Bekker et al. 2006; Tang et al. 2009a, b, c, 2011, 2013a; Lai et al. 2012), Superior type banded iron formations (Huston and Logan 2004; Zhao 2010; and references therein), phosphate, graphite (Melezhik et al. 1999b; Chen et al. 2000a), lead-zinc, uranium, talcum, boron, and magnesite deposits (e.g., the Dashiqiao magnesite belt deposits; Tang et al. 2013b) evolved rapidly. However, there are several questions remaining unanswered including whether these Palaeoproterozoic stratum record the GOE, and whether the sedimentary–metamorphic deposits are genetically related to the GOE. A key to these problems is important in understanding the Precambrian evolution and mineralizations during the early Earth history but have rarely studies (Chen 1996b; Chen et al. 2000a; Tang et al. 2009a, b, c, 2013a, b).

The North China Craton (NCC) is an Early Precambrian continental block with widespread early Palaeoproterozoic strata (see Zhai et al. 2010; Zhai and Santosh 2011; Zheng et al. 2013), which hosts numerous ore deposits. In this study, therefore, we compile early paleoproterozoic ores or host rock geology and geochronological data obtained for the NCC (Table 12.1; Figs. 12.1, 12.2), and evaluate the scientific problems related to the GOE, and the implications of the mineralization in the NCC.

12.2 Early Paleoproterozoic Metallogenic Explosion and Records in NCC

Many aspects of the Earth's surficial system changed dramatically at about 2300 Ma (for detail see Chap. 11), suggesting the occurrence of a catastrophe in geological environment at about 2300 Ma. What is responsible for the changes in the Earth's surficial environment? How can we appeal this discovery to understand the Precambrian geological evolution, and mineralization of ore deposits? Every item of those changes includes lots of detailed data, which makes us only introduce few sections here instead of all of them.

12.2.1 The First Episode of Worldwide Graphite Resources and Record in NCC

Schopf (1977) pointed out that if sporadic evidences of life were preserved in the Archaeozoic, the data about paleontologic activities would increase greatly in the Proterozoic. Schopf (1977) further pointed out that the reports on the threadlike and ultramicro fossils as the evidences of life were not reliable, more convincing evidences in the Precambrian were stromatolites. It has been reported that the Archaeozoic stromatolites were discovered in four areas, and only the stromatolites in limestones of the Bulawayan Group in the southern part of Africa are more widely accepted, which suggest that organic activities were extremely weak before 2300 Ma. Researches of life in the Archaeozoic have made great development since 1976 (Awramik et al. 1983), however, convincing evidences of life are still deficient. The evidences of life have been rapidly accumulated since 2300 Ma (Knoll et al. 1988; Schopf 1977), and stromatolites (especially the stromatolites bearing blue-green algae) were extensively developed in the world (Melezhik et al. 1997a, b). Ferrobacteria fossils have been discovered in the iron ores in Krivoy Rog, Kazakstan, and Siberia areas, and the ages of these strata are confined to the period of 2300–1900 Ma. Carbonate rocks (2300–2000 Ma) in Baihai Group had been interacting with bacteria during the precipitating, and in Kola peninsula, carbonatized germ microfossils have been reported in the calcite grains in some marbles (Melezhik et al. 1997a, 1999a; and references therein). Moreover, both diversity of taxa and abundance of Palaeoproterozoic stromatolites are sharply increased (Melezhik et al. 1997a). Karelian shungite even gave an indication of 2.0-Ga-old metamorphosed oil-shale and generation of petroleum (Melezhik et al. 1999a).

Well preserved threadlike blue-green algae, medusoid fossils have been discovered in the strata during Huronian period in Ontario area, and Gruneria binabikin have been discovered in the Biwabik and Gunflint iron formations in Minnesota and Ontario areas, respectively (Cloud and Semikhatov 1969). All kinds of stromatolites, such as *Katernia africana*, were reported to be in the dolomite series of 2000 Ma in north Cape Province of the southern part of Africa, and in the Transvaal dolomite series, other stromatolites (2300–1950 Ma) were also found (Cloud and Semikhatov 1969). Hamersley and Uru Groups abounded

Table 12.1 The geology and geochronology of graphite, phosphorite, the Lake Superior type BIFs, marble, boron, magnesite, and lead-zinc deposits hosted in ca 2.5–1.8 Ga stata from the North China Craton (NCC)

No.	Country	Locality or host rock assemblage	Characteristics of ores or host rocks	Age of ores or host rocks	References
Graphite ore					
1	Jilin, China	Ji'an city; Ji'an Group, Huangchagou Fm	Graphite biotite granulite; C% = 2.8–6.67 %	1916–1906	Zhang and Liu (2014), Wu et al. (2011)
2	Liaoning, China	Huanren county; Taizihe-Hunjiang trap; Liaohe Group,Gaojiayu Fm	Graphite tremolite monzogranulite, graphite tremolite; C% = 9.75 %	2200–1860	Wu and Qu (1994)
3	Liaoning, China	Heigou town; Liaohe Group	Graphite tremolite granulite; graphite tremolite; C% = 4.62-10.41 %	2191–1850	Sun et al. (1995)
4	Shandong, China	Nanshu town, Laixi city; Jingshan Group	Garnet plagioclase gneiss type, diopsidite type, marble type	2100–1900	Zhang et al. (2014b), Chen et al. (2000), Liu et al. (2011), Liu et al. (2015b)
5	Shandong, China	Jingcun deposit, Mingcun town, Pingdu city; Douya Fm., Jingshan Group	Graphite biotite monzogneiss, biotite granulite, diopside marble; C% = 2.5–5 %	2100-1900	Li (2014), Liu et al. (2011), Liu et al. (2015b)
6	Shandong, China	Zhangshe deposit, east Xishiling country, Zhangshe town, Pingdu city; Douya Fm., Jingshan Group	8.534×10^5tons, graphite diopside plagiogneiss, graphite biotite plagiogneiss, coarse grain graphitegranulite biotite and muscovite plagiogneiss	2100–1900	Wan et al. (2006), Liu et al. (2011), Liu et al. (2015a), Liu et al. (2015b), Li et al. unpublicated; Tang et al. unpublicated
7	Henan, China	Neixiang county; Wuyangshan deposit; Yanlinggou Fm; Shicaogou Fm., Qinling Group	Plagiogneiss type; marble type; broken crack rock type; C% = 3–25 %	2226–1987	Zhang (2013)
8	Henan, China	Beizi deposit, Lushan county, Henan; Shuidigou Fm., Lushan (Upper Taihua) Group	Graphite biotite plagiogneiss, graphite diopside plagiogneiss, graphite plagiogneiss, graphite tremolite plagiogneiss; layered, stratoid, lentoid, 58 ore bodys; 940–2370 m in length, 2.04–22.88 m in thickness, crystal graphite deposit; C% = 3–25 %	2250–1850	Wan et al. (2006), Yang (2008), Diwu et al. (2010), Wang and Xue (2010), Shen and Song (2014), Li et al. (2015b)
9	Hebei, China	Kangbao county, Chicheng county; Hongqiyingzi Group	Graphite-bearing granulite, graphite-bearing garnet amphibole biotite plagioclase gneiss; C% = 2.57–4.57 %	2350–2330	Fu (2014)
10	Inner Mongolia, China	Huangtuyao county; Huai'an terrain	Gray gneiss, metasedimentary rocks (khondalites) and mafic (high-pressure) granulites	2150–1850	Zhang et al. (2014a), Yang et al. (2014)
11	Inner Mongolia, China	Jining city, Zhuozi county; Jijing Group	Graphite gneiss, biotite graphite plagioclase gneiss; C% = 2–8 %	~2300	Liu et al. (1989)
Phosphorite deposits					
12	North Korea	Chengjin Fm, Macheonryeong Series	Equivalent to the Laoling Group in South Jilin	2100–1700	Li et al. (1994)

(continued)

Table 12.1 (continued)

No.	Country	Locality or host rock assemblage	Characteristics of ores or host rocks	Age of ores or host rocks	References
13	North Korea	Yongrou; Hanchuan; Napu	Kondalite series, Nangnim Group, equivalent to the Kuandian Group in South Jilin	2035–1885	Li et al. (1994), Wu et al. (2007a, b), Meng et al. (2013, 2014)
14	S Jilin, China	Hunjiang (Baishan)	P_2O_5 = 14.00 %, Laoling Group	2100–1950	Li et al. (1994), Liu et al. (2015a)
15	S Jilin, China	Shangqinggou, Ji'an	P_2O_5 = 3.64 %, Ji'an Group	2100–1950	Li et al. (1994), Liu et al. (2015a)
16	S Jilin, China	Banshigou; Yangmuchuan, Kuandian	Zhuanmiao Fm. of the Kuandian Gp., Coexist with boron deposits	2035–1885	Zhu (1982), Zhang (1984), Li et al. (1994), Meng et al. (2013, 2014)
17	E Liaoning, China	Tianshui, Langzishan, Dashiqiao, Zhenzhumen and Luotun deposits, hosted in the Gaojiayu Fm. of the Liaohe Gp	7 million tons with P_2O_5 = 12.98 % (Tianshui), associations of P, P-B-REE, P-Mg, P-V, and P-Fe respectively	2050–1950	Li et al. (1994), Liu et al. (2015a)
18	W Liaoning, China	Wulanwusu, Jianping; Gongguanyingzi, Fuxin	P_2O_5 > 4 %. Xiaotazigou Fm. of Jianping Gp. khondalite series	2450–1900; ca. 2250	Zhu (1982), Li et al. (1994), Lu et al. (1996)
19	Shandong, China	Yexian (Laizhou city, including three occurrences), Jiaodong	Jingshan and Fenzishan Groups	2100–1900	Ji and Chen (1990), Hu et al. (1997), Wan et al. (2006), Liu et al. (2015a, 2015b)
20	Hebei, China	Zhaobinggou, Fengning	P_2O_5 = 5.25 %. Coexist with V, Fe. Baimiao Fm. of Dantazi Gp. khondalite Series	2.55–2.45 Ga	Zhu (1982), Li et al. (1994), Xia and Wei (2005), Liu et al. (2007a)
21	Inner Mongolia, China	Hohhot-Jining-Fengzhen-Hunyuanyao	P_2O_5 > 4 %. Huangtuyao khondalite Series. Coexist with graphite, Mn, Fe etc.	<2316 or 2270–1892; 2150–1850	Zhu (1982), Guo et al. (1994), Wu et al. (1998, 2006), Yang et al. (2014), Zhang et al. (2014a)
22	Wutaishan of Shanxi, China	Baijiashan and several other occurrences of Dongjiao type	P_2O_5 = 13.95 %, Biancun Formation in Dongye Subgroup of Hutuo Group	2200–1820	Zhao (1982), Goodwin (1991), Li et al. (1994), Widle et al. (2004), Wan et al. (2010b), Du et al. (2015)
23	Zhongtiaoshan, Shanxi	Danshanshi Group		1848–1800	Li et al. (1994), Liu et al. (2012)
24	Henan, China	Huayu, Songshan	Huayu Formation, Songshan Group	2337 ± 23 −2000	Hu (1988), Li et al. (1994), Diwu et al. (2008), Wan et al. (2009)
Lake Superior type BIFs					
25	Shandong, China	Changyi-Anqiu iron-ore belt, Xiaosong Fm., Fengzishan Group, Jiaobei terrain	~20 middle/little size ore deposits, shallow-water, high-energy environment; 1.253 × 10^8 tons, Fe^T = 29.2 %	2240–2193	Lan et al. (2012), (2014a, b), (2015b)
26	Anhui, China	Huoqiu iron-ore field, Zhouji and Chongxingji towns, north-west Hefei ctiy, Anhui Province	>17.12 × 10^8 tons, Zhouji and Wuji Fm., Huoqiu Group	2700–1850	Wan et al. (2010a), Yang et al. (2012), Liu and Yang (2013), (2015)

(continued)

Table 12.1 (continued)

No.	Country	Locality or host rock assemblage	Characteristics of ores or host rocks	Age of ores or host rocks	References
27	Henan, China	Wuyang-Xingcai iron ore-field, Henan	Tieshan (2.47 × 10^8 tons), Jingshanshi (2.24 × 10^8tons), layered, stratoid, lentoid, hosted in the No. 2–3 Section of Tieshanmiao Fm. (overlying on the Zhao'anzhuang Fm.), Upper Taihua Group	2250–1850	Wan et al. (2006), Yang (2008), Diwu et al. (2010), Wang and Xue (2010), Li and Zhang (2011), Li et al. (2012), Li et al. (2013b), Liu et al. 2014, Shen and Song (2014), Li et al. (2015b)
28	Shanxi, China	Yuanjiachun,Lvliang, Shanxi	>1.2 billion tons, three occurrences, hosted in metasedimentary rock succession of the 840–1200 mYuanjiacun Formation, lower Lüliang Group	2380–2210	Zhu and Zhang (1987), Shen et al. (2010), Zhang et al. (2012), Wang et al. (2015a, b, c)
Boron deposits					
29	Jilin, China	Ji'an county; Ji'an Group	Serpentinite; Biotite granulite; Marble	2100–1950	Wang and Han (1989), Feng et al. (2008), Liu et al. (2015a)
30	Liaoning, China	Kuandian county, Zhuanmiao deposit, Li'eryu Fm., Liaohe Group	large-size Ludwigite deposit, hosted in banding magnesite-marbles or near-banding serpentinized Mg-olivine rocks, volcanic–sedimentary formations; serpentined marble; B2O3 = 10.52–16.02 %	2170–1869	Hu et al. (2014), Xie et al. (2015)
31	Liaoning, China	Fengcheng city; Kuandian county; Liaohe Group	magnesium peridotite; serpentinization peridotite; Pyroclastic rock; B2O3 = 0.51–36.97 %	2191–1829	Liu et al. (2005a), Wang et al. (2008)
32	Liaoning, China	Wengquangou deposit, Fengcheng city; Li'eryu Fm., Liaohe Group	large-size Ludwigite deposit, hosted in banding magnesite-marbles or near-banding serpentinized Mg-silicate rocks, biotite-granulite; plagio-leucogranulitite; amphibolite; B2O3 = 3.98–11.94 %	2050–1950	Peng et al. (1998), Wen and Teng (2014), Liu et al. (2015a)
33	Liaoning, China	Houxianyu deposit, Yingkou city; Li'eryu Fm., Liaohe Group	large-size szaibelyite deposit, hosted in banding magnesite-marbles or near-banding serpentinized Ultra-magnesium peridotite, biotite granulite, tourmaline rock; B2O3 = 17.61–41.51 %	2050-1950	Jiang et al. (1997), Wang et al. (2006), Tang et al. (2009a), Liu et al. (2015a)
34	Liaoning, China	Dashiqiao deposit, Yingkou city; Li'eryu Fm., Liaohe Group	Serpentined marble, granulite, tourmaline-granulite	2050–1950	Luo et al. (2004), Liu et al. (2005b, 2015a)
Magnesite deposits					
35	Liaoning, China	Dashiqiao magnesite belt, including the Shengshuishi, Qingshanhuai, Shuiquan, Huaziyu, Pailou, Jinjiabao, Xiafangsheng and Fanjiabaozi deposits, Dashiqiao and Haicheng countries, Dashiqiao Fm., Liaohe Group	Controlled by the third member of the Dashiqiao Fm. dolomites with bedded or lens-type occurrence, and comprise an important part of the Dashiqiao strata; proven reserve ca. 2.987 billion tons	2050–1950	Jiang et al. (2004), Tang et al. (2009b, c, 2013a), Liu et al. (2015a)

(continued)

Table 12.1 (continued)

No.	Country	Locality or host rock assemblage	Characteristics of ores or host rocks	Age of ores or host rocks	References
36	Shandong, China	Laizhou city, Jiaodong, Fenzishan Group	ca. 0.18 billion tons, seven occurrences, hosted in the Fengzishan Group	2100–1900	Wan et al. (2006), Liu et al. (2015a), Liu et al. 2015, Tang et al. unpublicated
Pb-Zn deposits					
37	Liaoning, China	Tieling city, Fanhe Basin, Liaobei terrain, intermediate-acidic volcanic rocks, feldspathic quartzarenite and carbonates	>57.3 × 10^4tons, stromatolitic clastic sediments, shales, and limestones and dolomites, Guanmenshan Fm., North Liaohe Group	2330–2060	Rui et al. (1991), Tang et al. (2008; 2011)
38	Liaoning, China	Qingchengzi Pb–Zn (Ag–Au) ore-field, East Liaoning	stromatolitic clastic sediments, shales, and limestones and dolomites, Pb–Zn > 150 × 10^4tons hosted in Langzishan and Dashiqiao Fms., Liaohe Group; Au > 200 tons, and Ag > 1100 tons, hosted in Dashiqiao and Gaixian Fms., Liaohe Group	2050–1950	Jiang (1988), Jiang and Wei (1989), Chen (2002), Duan et al. (2012), Liu et al. (2013), Liu et al. (2015a)

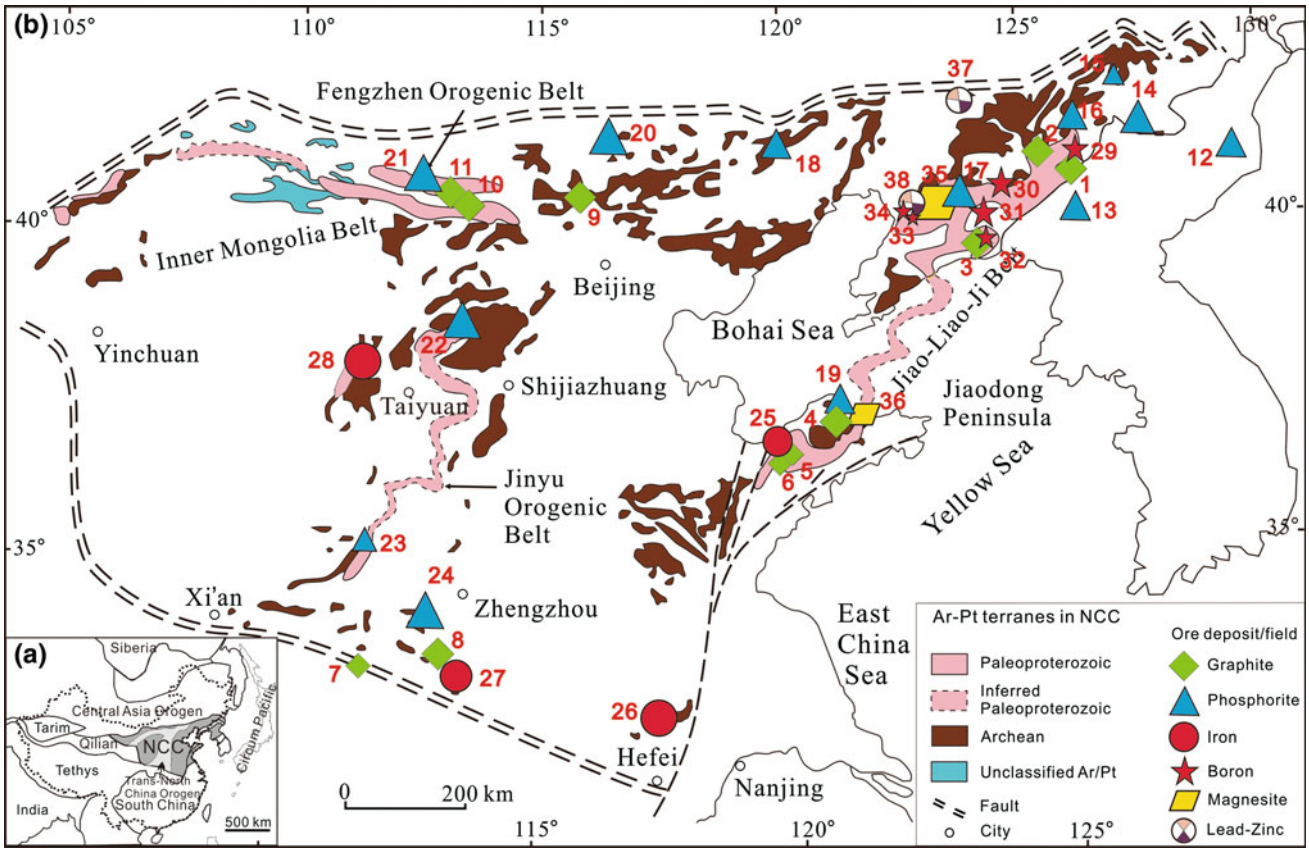

Fig. 12.1 The distribution and size of the part early Paleoproterozoic sedimentary ores in North China Craton (NCC). See Table 12.1 for the number of ore deposit/belt and references source. Archaean-Palaeoproterozoic terranes of the NCC (modified after Zhai and Santosh 2011). Ar/Pt = Archaean/Proterozoic

with algae fossils (Knoll et al. 1988). In the Onega Group, and locally in the Segozero Group, large amount of various stromatolitic bioherms, and in some cases, oncolites are found (Salop 1977). Furthermore, those stromatolite-bearing strata are often associated with graphite deposits, and carbon isotopic researches suggest that graphite deposits are organogenic. For instances, carbon isotopes of graphite deposits in 2.5–2.2 Ga Eastern Ghats Mobile Belt, Orissa, India, are −26.6 to −2.4 ‰ (Sanyal et al. 2009), in ~1.9 Ga Kerala Khondalite Belt (KKB) of southern India, are −18.06 to −17.87 ‰ (Cenki et al. 2004; Satish-Kumar et al. 2011); and in 2.45–2.3 Ga Sargur Area, Western Dharwar Craton, India, are −25.2 to −20.5 ‰ (Maibam et al. 2015).

In NCC, Liaohe, Songshan, Hutuo, and Feizishan Groups also abound with stromatolites (Cao et al. 1982; Cao 2003; Cao and Yuan 2003, 2009; Gao et al. 2009; Lai et al. 2012). Many graphite deposits are hosted in these 2.3–1.85 Ga early paleoproterozoic strata (Figs. 12.1, 12.2; Table 12.1). Carbon isotope researches suggest that Lushan of Henan (Chen and Deng 1993), Nanshu of Jiaodong (Lan 1981) and Xinhe of the Inner Mongolia graphite deposits are all organogenic, organic activities are very intense (Chen et al. 2000; Zhang 2013; Yang et al. 2014).

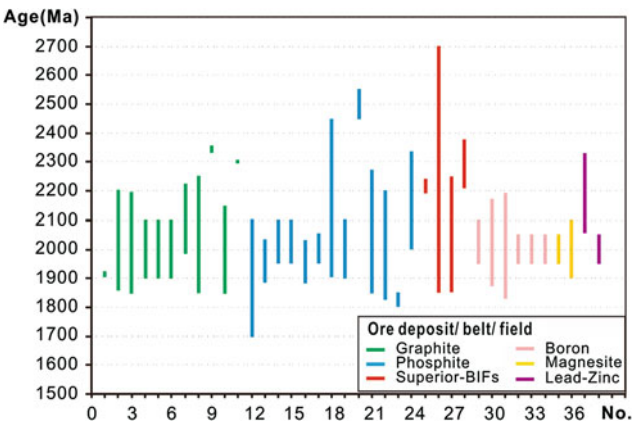

Fig. 12.2 The ages of the part early Paleoproterozoic sedimentary ores in North China Craton (NCC). See Table 12.1 for the number of ore deposit/belt and references source

In sum, sudden increase of organic activities at 2300 Ma resulted in a leap in the living beings evolution.

12.2.2 The First Period of Global Phosphorites and Record in NCC

"As recently as 1962, Geijer argued that there was an almost total absence of phosphorites in the Precambrian" (recited from Cook and Mcelhinny 1979). Davidson (1963), Cook and Mcelhinny (1979) documented the Precambrian phosphorites (including Archean) and denied Geijer's view. However, Windley (1980, 1984) pointed out that "phosphorite are phosphorus-rich sedimentary rocks that did not form in the Archean; minor phosphorites began to appear in the early Proterozoic, but major deposits not until the late Proterozoic".

Based on statistics of phosphorites in NCC (Table 12.1), all the authors indicated that Paleoproterozoic phosphorites and significant phosphorus deposits are documented widespread in the strata formed during 2500–1850 Ma (Fig. 12.2).

In China, phosphorites also occurred as the Dongjiao-type phosphorus deposits in the Songshan, Hutuo, and Liaohe Groups (Zhao 1982), which are Paleoproterozoic cratonic sediments on the NCC and experienced low-grade metamorphism at about 2100–1850 Ma.

It should be emphasized that, in the NCC (including North Korea) and its adjacent Jiamus Block, a lot of significant phosphorus deposits have been found in Khondalite series with age of 2300–1900 Ma (Figs. 12.1, 12.2; Table 12.1). The Shichang phosphorus deposit of Heilongjiang Province is located in the Paleoproterozoic Mashan Group, the Jiamus block, whose P_2O_5 content is 5 % in average (Liu 1988; Lu et al. 1996). Three phosphorus deposits have been found between 2100 and 1900 Ma Jingshan Group (Hu et al. 1997; Wan et al. 2006; Xie et al. 2014; Liu et al. 2015a), Yexian country, Shandong province (Ji and Chen 1990). The 2450–1900 Ma Zhaobinggou phosphorus deposit (Zhu 1982; Li et al. 1994; Xia and Wei 2005) occurs in the Baimiaozi Formation of 2.55–2.45 Ga Dantazi Group (Liu et al. 2007a, b) in Hebei Province. The Wulawusu phosphorus deposit is located in the Jianping Group in the west of Liaoning Province (Li et al. 1994). The borate-phosphorite formation was found paragenetic with marbles in 2035–1885 Ma Kuandian Group (Meng et al. 2013, 2014), Eastern Liaoning terrain (Zhang 1988). In the Inner Mongolia block, there is a 200 km long Paleoproterozoic phosphorite belt; it includes all the deposits in Hohhot, Jining, Fengzhen, and Hunyuanyao, etc. (Zhu 1982; Yang et al. 2014). In North Korea, the Macheonayeong Series and Nangnim Group (Li et al. 1994) also have economic metamorphic phosphorites (Table 12.1).

In Udaipur region of NW India, there are wave-brecciated stromatolite-bearing phosphorites in early Proterozoic Aravalli Group (~2.15 Ga, Purohit et al. 2010). The Aravalli Group contains two distinct phosphate-bearing horisons and huge reserves of rock phosphate. The lower phosphorite horizon is more or less close to the base of the Aravalli Group and well known for several important phosphorite deposits, i.e., Jhamar Kotra (50 milliontons with 15–39 % of P_2O_5, 16 million tons with P_2O_5 > 30 %), Maton (9.2 million tons with P_2O_5 16–26 %), Dakan Kotra, Kararia-Ka-Gurha, and Kanpur (the latter three with P_2O_5 contents varying from 12 to 25 %). The upper horizon comprises the small phosphorite deposits of Sismarma, Nimach Mata, and Baragaon, with P_2O_5 content ranging from 5 to 23 %. In addition, phosphorus ores are also found in Indian Khondalite series, coexisting with rocks bearing Mn-garnet (Zhu 1982).

In Finland, the U-bearing phosphatic sediments have been found within the supracrustal series metamorphosed during the Svecokarelian Orogeny about 1900–1850 Ma ago, deposited during 2080–1900 Ma (Karhu 1993; Melezhik and Fallick 1996).

Khondalite series in Scandinavian Peninsula, Ceylon (Sri Lanka), North Korea, Russia and Madras and East Ghats of India abound with phosphorus ores (Ji and Chen 1990; Jiang 1990; Lu et al. 1996). Phosphorites about 2000 Ma occur at Rum Jungle in northern Australia, in the Marquette Range of Michigan (phosphoritic pebbles in conglomerates), the Hamersley Group of W Australia and at Broken Hill in SE Australia (Schneider et al. 2002; Bekker et al. 2010; and references therein).

Phosphorites precipitate in strong oxidizing condition because phosphorus should exist as PO_4^{3-} (P^{5+}) in water. Intense biotic agency is another important factor resulting in the formation of phosphorites (e.g., Zhang et al., 2015). Global devoid of Archean phosphorus deposit suggests weak biologic activities and low oxygen fugacity of sedimentary environment before 2300 Ma. On the contrary, widespread development of phosphorites after 2300 Ma suggests a condition with prevailed biomass activities and high oxygen fugacity.

12.2.3 Fast Global Development of the Lake Superior-Type Banded Iron Formations and Record in NCC

It was statistic that more than 90 % of iron ores developed at Precambrian (Isley and Abbott 1999; Shen et al. 2006). Most of those iron ores are banded iron formations (BIFs) and prosperously developed during the period of 2500–1850 Ma (Trendall and Blockley 1970; Trendall 2002). Furthermore, most resource of iron is concentrated on a few Precambrian

superlarge deposits, which are giant sizes (up to 1.0×10^8 Mt for a single deposit, Huston and Logan 2004) and have unique geological features and genesis. Most of the deposit types are not (or few) developed any more at later geological history and nearly disappear at Mesoproterozoic. And just a few BIFs are developed during "Snowball Event" of ca. 800 Ma (Gaucher et al. 2008; Frei et al. 2009; Bekker et al. 2010).

It is considered that the development of BIFs reflected the comprehensive coupling results from both geological tectonic and environmental geochemistry evolutions, as well as organism activities of earth early history (Frei et al. 2008). Precambrian BIFs are generally classified into the Algoma- and Lake Superior-types (Gross 1980, 1983) and mainly formed in Paleoproterozoic when the fO_2 in seawater was high enough to oxidize Fe^{2+} into Fe^{3+} to form voluminous BIFs (Huston and Logan 2004). The Algoma-type BIFs are dominant magnetite (F_3O_4), minor pyrite and devoid of hematite, deposited under reducing conditions with a P_{O2} (partial pressure of oxygen) less than 10^{-65} atm (1 atm = 1.01325×10^5 Pa) (calculated by Garrels et al. 1973). They are mainly developed in the Archean-Paleoproterozoic volcanic–sedimentary formation and associated with greenstone belts (Zhang et al. 2012), represented by the BIFs in the Abitibi greenstone belts (Isley and Abbot 1999). The Lake Superior type BIFs are dominated by hematite (Fe_2O_3) and deposited in oxidic milieu. They were mainly developed in Paleoproterozoic clastic-carbonate formation and associated with the stable sedimentary basins and cratonic margins (Huston and Logan 2004), e.g., the lake superior area of Canada, the Hamersley area of Australia, the Carajas area of Brazil, and the Krivoy Rog area of Ukraine are all the famous source areas of numerous world-class superlarge BIFs (Trendall 2002).

The Hamersley BIFs is 2500 m in thickness and extent up to 4×10^4 km^2 and developed between 2480 and 2450 Ma (Pickard, 2002). It is over 35.6 billion tons in size and more than 24 billion ton rich ores with grade of 50–69 % (Trendall and Morris 1983). The Krivoy Rog Series, Ukranian Shield, is well known BIF-bearing succession. The Sksagan Suite ore field, producing about 85 % of the Krivoy Rog basin output, has the greatest commercial importance. The sedimentation time of Krivoy Rog Series is bracket in 2.6–1.9 Ga, most likely in the range of 2.3–2.0 Ga. Kursk Group marked as Kursk Magnetic Anomaly and composed of metamorphic rocks, is a major iron formation of the Voronezh Massif (Goodwin 1991), Russian, having 42.6 billion tons of iron ores with grade of 32–62 %, including ca. 26.1 billion tons of 54–62 %, and most likely developed during 2300–2000 Ma (Alexandrov 1973). The Karelian Complex (or Supergroup), widely distributed in the eastern part of the Baltic Shield, especially in Russian Karelia and Finland, may serve as a world stratotype of Paleoproterozoic. Overlying uncomformly on Archean greenstone-granite belt dated at 2800–2600 Ma (granite), it comprises upward the Tunguda-Nadvoitsa, Sariolian (with tillite), Segozero, Onega (BIF, dolomite, stromatolites), Bessovets, and Vepsian (with red bed) Groups (Salop 1977). Metamorphic minerals from the Karelian Complex and syn-Karelian Orogeny granites yield an age of 1900 Ma by different isotopic methods. Therefore, the Karelian Complex is bracket in range 2600–1900 Ma. Carbonate rocks of the Onega Group have been dated at 2300 ± 120 Ma by the Pb-isochron method, while the pre-tectonically intrusive basic dikes give a Pb-isotopic and K–Ar age of 2000–2150 Ma (cf. Salop 1977), suggesting at least the upper portion of the Karelian Complex sedimentated during 2300–2150 Ma. Significant hematite ores are found in the Onega Group which is up to 2000 m in thickness.

The Kaniapiskau Supergroup in the Labrador Trough, Canada is well known of Sokoman BIFs (Dimroth 1981), possessing more than 20.6 billion tons of ores. Dimroth (1981) divided it into three major stratigraphic units, from bottom to top, i.e., the Red Bed Basins (Chakonipau Formation), the Cycle I, and the Cycle II (including the Sokoman BIFs). Because a Rb–Sr isochron of 2.3 Ga has been obtained from volcanics of the easternmost Cape-Smith belt older than the Labrador Trough, Dimroth (1981) suggests the Labrador Trough is of Paleoproterozoic age and younger than 2.3 Ga. A Rb–Sr isochron age of 1.85 Ga for low-grade shales and a K–Ar age also of 1.85 Ga may place the major metamorphism of the Labrador Trough into the Penokean Orogeny that occurred during 1850 Ma, roughly contemporaneous with the Hudson Orogeny assumed to terminate at about 1800 Ma in the rest of the Circum-Superior Belt. However, the age of Kaniapiskau Supergroup is also controversial, for example, Trendall and Morris (1983) argued to be 2400–1800 Ma.

Lake Superior Region including Minnesota, Michigan, and Wisconsin is the most important iron-producing areas in USA, where the BIFs are hosted in Animike Series. The region has shipped 4.6 billion metric tons since 1848. In 1978, the region produced 75 million metric tons of ore or 89 % of the total ore produced in USA and 10 % of the total produced in the world (Morey and Southwick 1995). The Animike Series still contain vast resources; it has been estimated that more than 271 billion metric tons of crude iron ore or 36 billion metric tons of iron-ore concentrate are recoverable (Morey and Southwick 1995). The Animike Series experienced the Penokean Orogeny at about 1850 Ma (Bayley and James 1973; Goodwin 1991) and accumulated during 1930–1850 Ma (Morey and Southwick 1995; Schneider et al. 2002; Canfield 2005). As well known for Homestake Au–Fe formation, the BIFs in the northern Rocky Mountains were confined in Paleoproterozoic

sediments of 2500–1650 Ma, and possibly deposited during 2300–2100 Ma because they were also suggested to be consistent with those in Lake Superior area.

Discovered in 1967, the Carajas iron deposit in Brazil possesses no less than 16 billion tons of high-grade ores (>64 % Fe, averaged at 66.7 %) (Tolbert et al. 1971). Ores were accumulated in the Carajas layer itabirites (iron quartzites) which experienced the Trans-Amazonian Orogeny occurred in the period of 2100–1750 Ma (Goodwin 1991) and is dated around 2000 Ma. The high-grade ores (>60 %) of Itabira Group of Minas Supergroup in the Quadrilatero Ferrifero (Iron Quadrangle) district, Brazil, are estimated to exceed 10×10^9 tons (Goodwin 1991). The Minas Supergroup unconformably covers the granitoid dated of 2500 Ma, and is intruded by pegmatites dated at 2080 Ma (Rb–Sr) as well as the large Cristais pluton dated at 2050 Ma (Rb–Sr) (Goodwin 1991). The Gandarela formation carbonate, under Minas Supergroup, yielded a 2420 ± 19 Ma Pb–Pb isotope age (Babinski et al. 1995). Detrital zircons from a metagreywacke at the top of the Minas Supergroup provide a U–Pb date of 2125 ± 4 Ma (Goodwin 1991). Supporting minimum dates from sphene and zircon in pegmatite intrusion plays the main metamorphism of the Minas Supergroup between 2060 and 2030 Ma. In Guiana Shield, BIFs in Trans-Amazonian greenstone belts are dated at about 2250 Ma (Windley 1983; Klein and Ladiera 2000).

Iron ores in the Singhbhum district, India, bracketed in the period of 2700–2100 Ma, most possible age of 2200–2100 Ma, or of 2300 Ma (Goodwin 1991), are similar with Lake Superior type BIF. The Aravalli Group (~2.15 Ga) in NW India has Lake Superior type BIFs, in addition to phosphorite, manganese, copper, uranium deposits (Sreenivas et al. 2001; Ray et al. 2003; Purohit et al. 2010). The Transvaal Supergroup (up to 1.0×10^8 Mt, Trendall and Morris 1983) and correlated Griqualand West Supergroup iron deposits of South Africa were formed at 2480–2322 Ma (Bekker et al. 2001).

It is needed to mention that the pre-GOE Ga BIFs are mainly Algoma-type whereas the post-GOE Ga BIFs are dominated by Lake Superior type. The size of Superior Lake type BIF Fe deposits generally range 10^5–10^8 Mt, far larger than the Algoma-type of 10^3–10^7 Mt (Huston and Logan, 2004). The development time and geological characteristics of these two contrasting types of BIFs strongly demonstrate that the geological environment was rapidly changed during 2.33–2.06 Ga. After 1800 Ma, BIFs were relatively absent and far less in sizes and commercial value than those of pre-1800 Ma. And those intimate related with volcanics are called Rapidan-type BIFs (Gaucher et al. 2008; Frei et al. 2009), which are called volcanic hydrothermal fluid type or volcano rock type in China, while those less related with volcanism or volcanics are named Xinyu type (in South China) or Xuanlong type (in North China).

In China, Algoma-type BIFs are called Anshan type iron ores, and mainly distributed in the Anshan-Benxi area, Liaoning Province, Eastern Hebei, and the North Shanxi Provinces. Those BIFs are mostly hosted in the Neo-Archean volcanic–sedimentary sequences (Zhai et al. 1990; Shen et al. 2005; Zhai 2010; Zhai et al. 2010; Wan et al. 2012; Zhang et al. 2012; Zhai and Santosh 2013), their ore genesises, deposital sizes, and potential prospections, as well as the distributions of BIFs in space and time are closely related to the development of green rock belt. However, most world-class superlarge BIFs belong to the Lake Superior type. Where are the Lake Superior type BIF deposits in China? It is one of important suspended issues for research on iron ore resource of Chinese.

Recently, the 2.38–2.21 Ga Paleoproterozoic Yuanjiachun iron deposit in Lvliang area, Shanxi Province, NCC, has been identified as a representative Lake Superior type BIF in NCC (Fig. 12.1, Table 12.1; Zhu and Zhang 1987; Shen et al. 2010; Zhang et al. 2012; Wang et al. 2015a, b, c; see detail in Chap. 13 and references therein). Another example is the 2.7–1.85 Ga Paleoproterozoic Huoqiu iron deposit belt in Huoqiu area, Anhui Province, it has also been identified as a Lake Superior type BIF (Figs. 12.1, 12.2; Table 12.1; Yang et al. 2014; Liu and Yang 2013, 2015; and references therein). In Laizhou-Anqiu iron deposit belt, Jiaodong Peninsula of eastern China, the Paleoproterozoic BIF deposits in Changyi area have some geological and geochemical characteristics similar to the Superior Lake type BIF (Lan et al. 2012, 2014a, b; 2015). At the southern margin of the NCC, the Tieshanmiao, Hupanling, Malou, Tieshanling iron deposits in "Lushan Group" (Upper Taihua Group) were formed after or at about 2300 Ma (Chen et al. 1996; Wan et al. 2006; Yang 2008; Diwu et al. 2010; Li et al. 2013b; Shen and Song 2014; and references therein). Potential prospections of the Lake Superior type BIFs would be deserved expectation in those areas.

12.2.4 Early Paleoproterozoic Boron Mineralization in NCC

According to incomplete statistics, it has ~46.41×10^6 tons boron explored reserves in China (The ministry of Land and Resources P.R.C The ministry of Land and Resources P.R.C 2001), and about 91 % production of boron each year comes from Mg-rich borate deposits in Liaoning-Jilin area, NCC (Liu 1996, 2006; Figs. 12.1, 12.2, 12.3; Table 12.1).

The Liao-Ji giant boron belt is a world-class nonmetallic ore province and distributes at the Dashiqiao-Fengchengkuangdian area. It trends near east–west direction and about 300 km length and 100 km width with more than 100 large to small size deposits or ore spots, including large-sized boron deposits such as the Houxianyu ore (szaibelyite) in

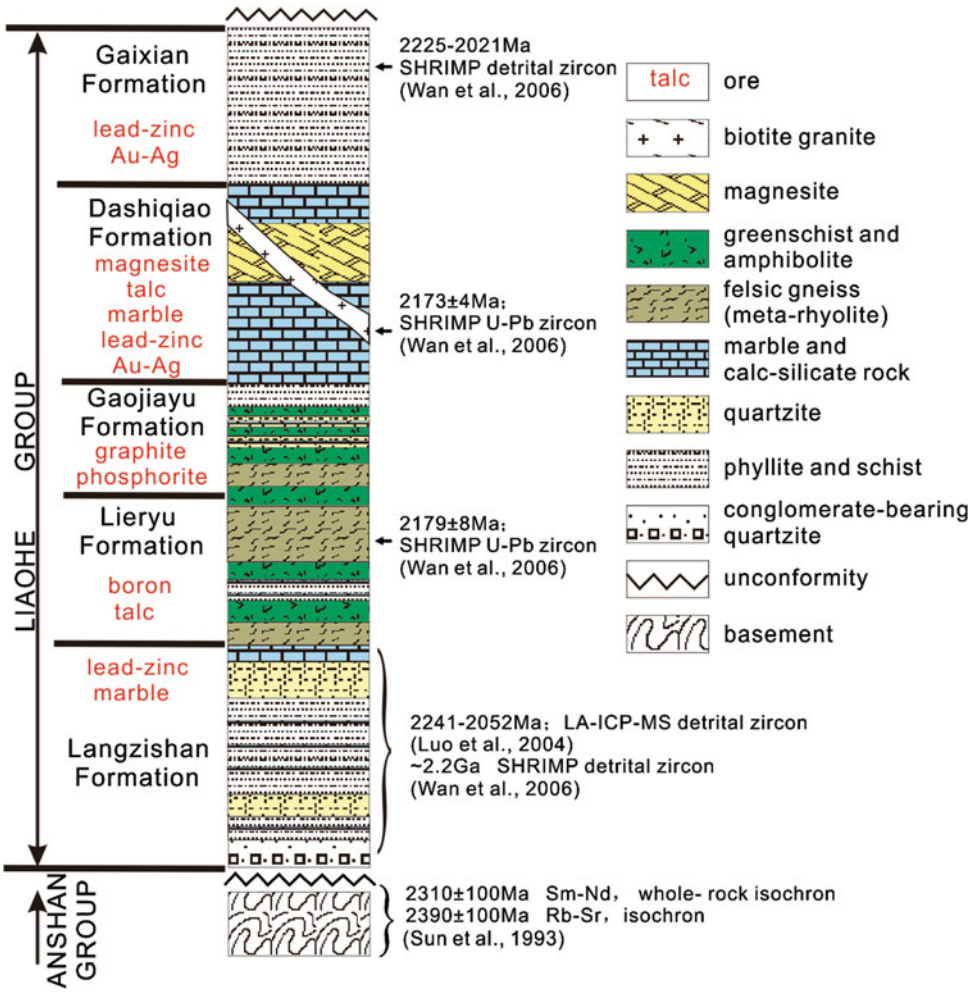

Fig. 12.3 The stratigraphic units of the Liaohe Group in the Jiao-Liao-Ji Belt (see Tang et al. 2013b, and references therein). Data source of ages from Sun et al. (1993) and Wan et al. (2006)

Dashiqiao city, Wengquangou ore (Ludwigite) in Fengcheng city, and Zhuanmiao ore (szaibelyite + ludwigite) in Kuandian area (Figs. 12.1, 12.2; Table 12.1; Qu et al. 2005). Boron ore-bodies mainly hosted in banding magnesite-marbles or near-banding serpentinized Mg-olivine rocks (Feng and Zou 1994; Feng et al. 1998).

These deposits are hosted in the early Paleoproterozoic Lieryu Formation (developed before 2179 Ma, Wan et al. 2006, Li et al. 2015a), Liaohe Group (Jiang et al. 1997, 2004; Xiao et al. 2003; Tang et al. 2009a), which underwent several times intense regional metamorphisms during about 1930–1850, 1450–1400, 885, 386.5, 250–220 Ma (for details see Tang et al. 2009a; and references therein). For example, phlogopite grains yield $^{40}Ar/^{39}Ar$ plateau age of 1918 ± 113 Ma, of 1918 ± 219 separated from the Zhuanmiao deposit, and $^{40}Ar/^{39}Ar$ plateau age of 1923 ± 115 Ma, isochron age of 1924 ± 215 Ma from the Wengquangou deposit, respectively (Lu et al. 2005). Pb–Pb-isochron ages for minerals are 1902 ± 12 Ma of the Zhuanmiao and 1852 ± 9 Ma of the Wenquangou deposits, respectively. These data recorded about 1930–1850 Ma regional metamorphisms in Liao-Ji giant boron belt, which responded to the Columbia supercontinent aggregation event (Zhao et al. 2004, 2005, 2012; Wan et al. 2015; Liu et al. 2015a; and references therein).

Carbon isotopes of Mg-rich marbles from hosting-rock of boron deposits (Gaojiayu Formation) exhibit clearly positive $\delta^{13}C$ anomalies. For example, the $\delta^{13}C$ of magnesit marbles from the Er'rengou boron deposit are +3.8 − +5.2 ‰ (4.8 ± 0.6 ‰, n = 5), and those of dolomitic marbles from the (Wang et al. 2008) Luanjiagou boron deposit are +4.6 − +5.6 ‰ (5.0 ± 0.4 ‰, n = 6). It shows that the Palaeoproterozoic Lieryu Formaton boron-bearing rock series in Liao-Ji area, NCC, records the global GOE.

12.2.5 Early Paleoproterozoic Magnesit Deposits in NCC

In China, world-class magnesit deposits are mainly distributed in the Jiao-Liao-Ji Belt (2.2–1.9 Ga, Li et al. 2015a; Liu et al. 2015a; and references therein) of the NCC

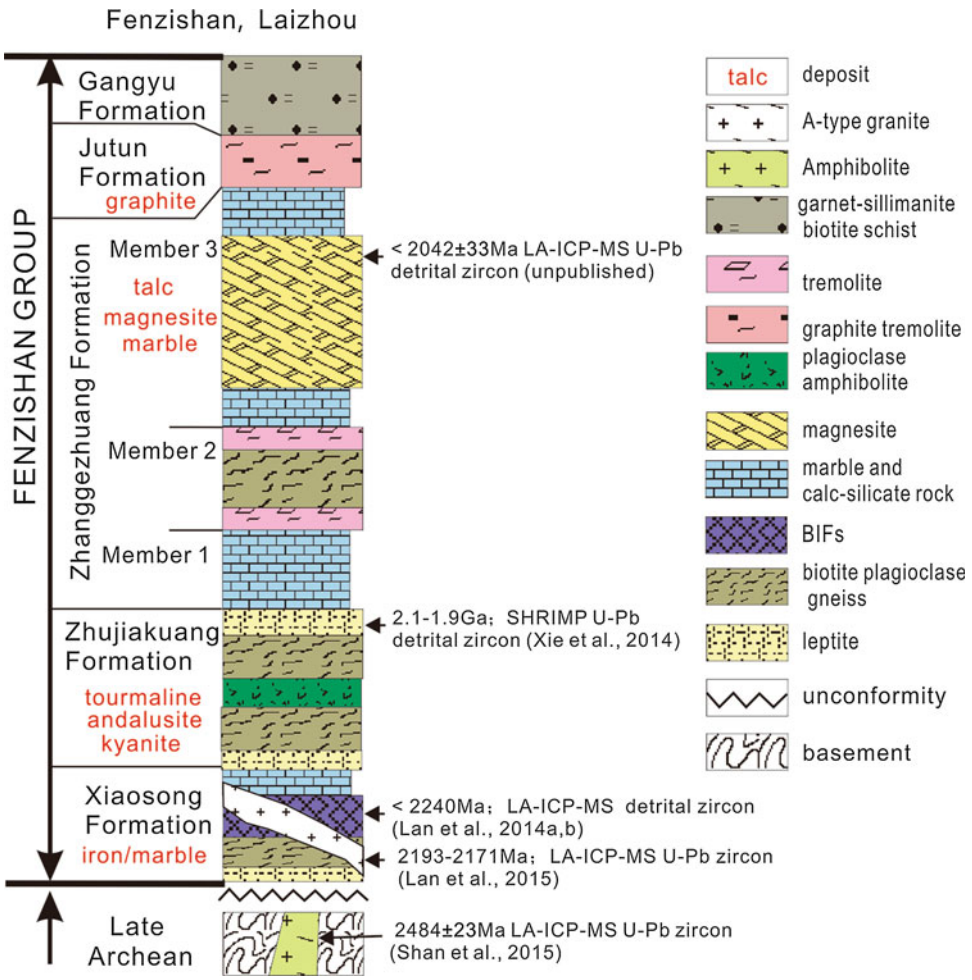

Fig. 12.4 The stratigraphic units of the Fengzishan Group in the Jiao-Liao-Ji Belt (modified after Li et al. 2013a, and references therein). Data source of ages from Shan et al. 2015; Lan et al. 2014a, b; 2015; Xie et al. 2014; and our unpublished paper

(Figs. 12.1, 12.2, 12.3, 12.4; Table 12.1). A number of important magnesite deposits, including the Shengshuishi, Qingshanhuai, Shuiquan, Huaziyu, Pailou, Jinjiabao, Xiafangsheng, and Fanjiabaozi deposits (Table 12.1; Tang et al. 2013a), occur in the Dashiqiao magnesite belt (Fig. 12.1), and are mainly located in the Haicheng and Dashiqiao counties, Liaoning Province. These deposits are controlled by the third member of the Dashiqiao Formation with bedded or lens-type occurrence, and comprise an important part of the 2.2–2.174 Ga Dashiqiao strata (Jiang et al. 2004; Wan et al. 2006; Tang et al. 2013a), Liaohe Group (2.2–1.9 Ga, Li et al. 2015a,b), in the northeastern NCC. The proven reserve of magnesite in this belt is 2.987 billion tons (The ministry of Land and Resources P.R.C 2001), accounting for >80 % of the total magnesite reserves in China and up to 30 % of the world reserves (Chen et al. 2003a). The Dashiqiao magnesite belt has been an important topic for the IGCP443 (International Geology and Environment Comparison of Magnesite and Talc) project (Chen and Cai 2000; Chen et al. 2003b; Jiang et al. 2004). Carbon and oxygen isotopes from magnesite orebody, hosting-rock (dolomitic marble) of this belt exhibit clearly positive $\delta^{13}C$ anomalies (Tang et al. 2013a; and references therein), it is estimated that the primary sediments of the Dashiqiao Formation might possess $\delta^{13}C$ values of >4.2 ‰, and $\delta^{18}O$ values of >21.5 ‰. These Palaeoproterozoic carbonate strata, therefore records the global GOE. The formation of the Dashiqiao magnesite deposits involved primary sedimentation (the Palaeoproterozoic evaporate sedimentation in a high-Mg lagoon), diagenesis, regional metamorphism, hydrothermal replacement and local post-ore fluid–rock interaction and records a multistage and polygenetic history (Tang et al. 2013a).

In Jiaodong Peninsula of eastern China, the large Fenzishan magnesit deposit (Figs. 12.1, 12.2, 12.4, Table 12.1) hosted in Paleoproterozoic Zhuanggezhuang Fm., Fengzishan Group (2.1–1.9 Ga; Xie et al. 2014; Tang et al. unpublicated). Carbon isotopes from magnesite orebody, hosting-rock (dolomitic marble) of this deposit are 0.4–2.3 ‰ (1.3 ± 0.6 ‰, n = 30) and also exhibit clearly positive $\delta^{13}C$ anomalies (our unpublished data).

The massive sedimentary rocks are mainly sourced from the Paleoproterozoic granitic rocks within the orogenic/mobile belt and the metamorphic basement of the

surrounding ancient blocks, and the protoliths were intensively developed between 2.15 and 1.95 Ga (Liu et al. 2015a).

The massive Palaeoproterozoic sedimentary strata in the Jiao-Liao-Ji Belt, NCC, therefore, record the global GOE.

12.3 Some Problems About Geological Environment Changes and Mineralize Record at 2300 Ma

12.3.1 Formation of Graphite Deposit and Its Time-Controlling

Carbon isotope research has verified that graphite deposit is organogenic, and this suggests that the depositing of ore-bearing formation was accompanied by intense biologic activity (Ji and Chen 1990). Graphite-bearing thin beds had occurred in sedimentary stratum at ca. 2.5 Ga, but graphite deposit is mainly hosted in the strata after 2300 Ma because intense biologic activity occurred only after 2300 Ma. The development of high-grade graphite deposits require that ore-bearing formations must be underwent high-grade metamorphism. Therefore, graphite deposits should be found in the medium–high-grade metamorphic sedimentary formations after 2300 Ma.

We know that Khondalite series are the most favourable host formations, so the margin of NCC and Korean peninsula, where Khondalite series are universally seen, are the most important areas producing graphites.

12.3.2 Occurring Time of Phosphorite and the First Period of Global Phosphorus Deposit

Why did the first period of global phosphorus deposit appear after 2300 Ma? This is because that phosphrite precipitates as phosphate, requiring strong oxidizing condition which at least can assure phosphorus of showing positive five valences. Before 2300 Ma, phosphorus, showing positive five valences, was unstable and merely existed as PH_3 (negative three valences) (indicating supergene condition) because of the reducing supergene environment, at the same time, organic activity was extremely weak and no conditions favourable for the forming of phosphorite were provided, as a result, sedimentary phosphorus ores before 2300 Ma could not be discovered. After 2300 Ma, intense organic activity and formation of the atmosphere rich in oxygen presented some favourable conditions for the depositing phosphorite; thus phosphorite appeared. A lot of PH_3 accumulated in the Earth surface system before 2300 Ma and they suddenly oxidized into phosphate rocks (P^{5+}) after 2300 Ma, therefore, which led to the first period (2300–1900 Ma) of global phosphorus deposit after 2300 Ma.

It should be mentioned that, the researches of phosphorus deposits of China, Ye (1989) pointed out that formations of phosphorus deposits were related to extraterrestrial factor, and weathering crust viewed extraterrestrial factor as one of three backgrounds of forming the phosphorus deposits. This is consistent with the event at 2300 Ma.

12.3.3 Time-Controlling Rules of Lake Superior Type Iron Deposit

A lot of Fe^{2+} accumulated in the reducing seawater before 2500 Ma. After 2500 Ma, sudden increase of oxygen fugacity resulted in Fe^{2+} being oxidized into Fe^{3+}, and the hydrolysis of Fe^{3+} produced hydroxide precipitates, at last a great number of iron deposits were formed globally, such as Lake Superior area of Canada, Kursk iron ore area of the Soviet Union, and Hamersley area of Australia and so on. Statistical data suggest that Lake Superior type iron deposits account for 60 % of all the iron resources, and 70 % of the rich resources (e.g., Information Division of CAGS 1975; Huston and Logan 2004).

It is obvious that gradualism can never reasonably explain the sudden development of Lake Superior type iron formation during 2500–2300 Ma Siderian and 2050–1800 Ma Orosirian, and why iron formations before 2500 Ma and after 1900 Ma are not so important as those a little after 2500 Ma. This problem would never be understood properly if the event at 2300 Ma had not been recognized scientifically.

12.3.4 Sudden Sedimentation of Carbonates Strata and Related Deposits

Before 2300 Ma, all the continents lacked carbonate rocks, except for some thin-bedded discontinuous carbonate rocks found in very few areas, however, after 2300 Ma, there was a great development of carbonate rocks over the world (Eriksson and Truswell 1978; see Sect. 11.2.3 of Chap. 11). The atmosphere of Archean was rich in CO_2 (e.g., Chen and Zhu 1988), but why were carbonates absent before 2300 Ma? It is generally explained as follows: in the Archaeozoic, weak organic activity and photosynthesis and high CO_2 partial pressure resulted in the reaction $CaCO_3 + CO_2 + H_2O \rightarrow Ca^{2+} + 2HCO_3^-$, and $CaCO_3$ was unstable and uneasy to precipitate (Wang 1989). But after Archean, organic activity increased and photosynthesis consumed a great deal of CO_2, as a result, the reaction $Ca^{2+} + CO_3^{2-} \rightarrow CaCO_3$ occurred. However, this explanation cannot answer the lack of other carbonates strata, such as $FeCO_3$, $MnCO_3$,

and $MgCO_3$, as they can precipitate at high CO_2 partial pressure. Another explanation is that the pH of seawater in Archean was too low to bring about the precipitating a lot of carbonate rocks (e.g., Chen and Zhu, 1985), as carbonate minerals were unstable in acid seawater. The weathering of terrestrial silicate minerals can increase the pH of seawater (Chen 1996a), e.g., $7Na[AlSi_3O_8]$(Albite) + $26H_2O \rightarrow 3Na_{0.33}Al_{2.33}Si_{3.67}O_{10}(OH)_2$ (Smectite) + $10H_4SiO_4$ (Hydrated silica) + $6Na^+ + 6OH^-$, $2KAl_3Si_3O_{10}(OH)_2$ (Muscovite) + $20H_2O \rightarrow 3Al_2O_3.3H_2O$ (Gibbsite) + $2K^+ + 6H_4SiO_4$ (Hydrated silica) $+2OH^-$, and $2Ca[Al_2Si_2O_8]$ (Anorthite) + $6H_2O \rightarrow [Al_4Si_4O_{10}](OH)_8$ (Kaolinite) + $2Ca^{2+} + 4OH^-$. However, the rate of weathering is slow and cannot explain that the sharp sediment of thick-bedded carbonate strata. The living bloom would be the best answer, with increase of the pH up to some point (see Sect. 12.4), a huge amount of thick-bedded carbonate rocks bearing stromatolites were formed globally (Chen 1990; Chen et al. 1991, 1994).

12.4 Linkage Between Early Paleoproterozoic Metallogenic Explosion in NCC and the GOE

The majority of mineralize records mentioned above (Table 12.1; Figs. 12.1, 12.2, 12.3, 12.4), indicate that there was a 2.5–1.85 Ga early Paleoproterozoic metallogenic explosion in NCC, with the blooms of biogeochemical oxygenic photosynthesis and can be related to the significant atmospheric change events during the GOE. Based on Tang and Chen (2013), Chen and Tang (2016) of Chap. 11 gave a further evolution sequence of these events for ca. 2.5–1.7 Ga Earth's superficial change events, including the widespread deposition of the Siderian banded iron formations (BIFs), slightly postdated by the 2.29–2.25 Ga global Huronian Glaciation Event (HGE, or the oldest Snowball Earth, Kirschvink et al. 2000), then, followed by the development of the 2.22–2.06 Ga carbonate strata with positive $\delta^{13}C_{carb}$ anomalies (Lomagundi/Jatulian Event, see Tang et al. 2004; Tang et al. 2011; and references therein), 2.25–1.95 Ga the oldest red beds in each continents (Melezhik et al. 1997b), as well as the disappearance of BIFs at ca 1.8 Ga and prevalence of black shales at 2.0–1.7 Ga. These significant events, occurred in younging order with somewhat temporal overlap, together with other Earth's superficial changes, resulted from, or relate to the GOE and recorded global changes in the atmosphere, biosphere, hydrosphere, and lithosphere. And the GOE throughout overprinted by the early Paleoproterozoic metallogenic explosion in early Precambrian cratons, such as NCC (Table 12.1; Figs. 12.1; 12.2).

The early Earth's hydrosphere–atmosphere system was obviously anoxic from 4.5 to 2.5 Ga (Cloud 1968, 1973; Holland 1994; Rye and Holland 1998). Such a long anoxic history made the Archaean hydrosphere enriched with a large amount of low-valent ions represented by Fe^{2+}. However, in the geological record, BIFs first appeared at 3.8 Ga but peaked at ca. 2.5 Ga and disappeared at ca. 1.8 Ga (e.g., Klein 2005; Huston and Logan 2004). Experimental simulations (Zhu et al. 2014; and references therein) indicate that the basic requirements for forming BIFs are adequate amounts of Fe^{2+} and the fit seawater pH of 1.25–5.5. If the pH is lower than 1.25, only amorphous colloidal silica would precipitate, no matter whether the solution was heated or not. Therefore, it would precipitate thick layer of siliceous rock rather than BIFs in this period. It suggests an anoxia environment or active volcanism (besides H_2O, the volcanic gas components are acidic gases and reduced gases, including CO_2, H_2, HCl, HF, SO_2, H_2S, CH_4, NH_3, N_2, Cl_2 and others, and H_2 and Cl_2 easily react to form HCl; Chen and Zhu 1985, 1987; Kump and Barley 2007). Otherwise, if the pH is higher than 5.5, silicic acid would highly dissociate and combine with cations to form ferrosilicates (clay minerals, such as black shale or iron-manganese concretion) rather than amorphous silica precipitates (Chen and Zhu 1984; Zhu et al., 2014). In acid seawater ($1.25 < pH < 5.5$) conditions, the precipitation of iron oxide is just opposite to that of amorphous silica. The higher the pH of the solution, the greater iron precipitation can be obtained. But in any case, Fe^{2+} did not precipitate continuously to produce a thick layer of "iron ore" (Zhu et al. 2014). It suggests that the Algoma-type BIFs developed in relative anoxia seawater (meaning low pH near 1.25), while the Superior Lake type BIFs developed in relative oxidic seawater (meaning high pH near 5.5), which was in accordance with the indication of Eu anomalies from Precambrian BIFs (Huston and Logan 2004) or other sediments (Chen and Zhao 1997; Chen et al. 1998; Tang et al. 2013a). And a high pH condition need a more oxidic environment or quiescent times with severer terrestrial weathering, the latter is in accordance with the 2.5–2.3 Ga quiescent time of the Earth (e.g., Condie et al. 2001; Zhai and Santosh 2011, 2013) and the worldwide high CIA values Khondalite series (see previous Sect. 11.3.4). And the former needs biological photosynthesis to give off O_2.

Based on records and discuss mentioned above, as well as Chen and Tang (2016) in Chap. 11, Here we give a summary of framework to explain the relation between early Paleoproterozoic era (2.5–1.8 Ga) metallogenic explosions, such as in NCC, and 2.5–1.7 Ga Earth's superficial change events during the GOE and shown in Fig. 12.5:

1. Since the beginning of the Palaeoproterozoic era, biological photosynthesis was enhanced (Melezhik et al.

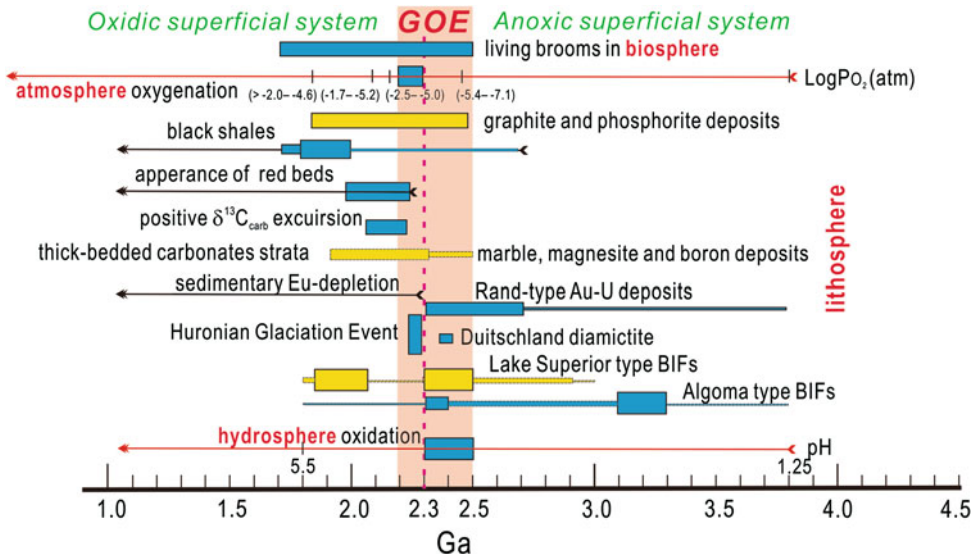

Fig. 12.5 A summary framework for ca. 2.5–1.7 Ga Earth's superficial changes events and metallogenic explosion during the GOE (modified after Tang and Chen 2013; Chen and Tang 2016 in Chap.11 and Tang et al. unpublicated). References: pH of seawater (Zhu et al. 2014); Algoma and Lake Superior types BIFs (Huston and Logan 2004); Huronnian Glaciation Event (HGE, Tang and Chen 2013); Rand-type Au-U deposits (Bekker et al. 2005; and references therein); sedimentary Eu-depletion (Tang et al. 2013a); thick-bedded carbonates strata (Eriksson and Truswell 1978); positive $\delta^{13}C_{carb}$ excursion (Karhu and Holland 1996); red beds (see Melezhik et al. 1997a; Bekker et al. 2005; and references therein); black shales (Condie et al. 2001); PO_2 in the Paleoproterozoic (Kanzaki and Murakami 2016), other ores see references in text for data source

1997a, b; Chen et al. 2000a; this paper), which fiercely transferred CO_2 into organic debris and release O_2; the O_2 was consumed in oxidation of the accumulated Fe^{2+}, CH_4 and elevated the pH value of seawater in the ways of $4Fe^{2+} + O_2 + 4H^+ \rightarrow 4Fe^{3+} + 2\,H_2O$, and $CH_4 + 2O_2 \rightarrow CO_2 + 2H_2O$, as well as $O_2 + H_2O + 4e^- \rightarrow 4OH^-$. During these processes, organic debris was deposited (graphite and phosphorite deposits, organism in black shale, even oil resources), and Lake Superior type BIFs were deposited (e.g., Huston and Logan 2004; Frei et al. 2008; Wang et al. 2015a, b, c), as well as atmospheric CO_2 drawdown occurred, CH_4 was eliminated (Fig. 12.5).

2. After removal of the majority of reducing components from the oceans which is indicated by widespread deposition of BIFs (Bekker et al. 2010; Tang and Chen 2013), the O_2 produced by biological photosynthesis gradually began to accumulate in atmosphere with the devoid of Rand-type Au–U deposits. The 2.29–2.25 Ga global Huronian Glaciation Event slightly postdated the widespread deposition of the Siderian BIFs (mainly Lake Superior type BIFs, Fig. 12.5), due to the icehouse effect of O_2 instead of greenhouse effect of CO_2 and CH_4 (Tang and Chen 2013). And the 0.8–0.6 Ga Snowball Earth was also after algal rise (Feulner et al. 2015).
3. The HGE was followed by widespread deposition of 2.22–2.06 Ga carbonates with positive $\delta^{13}C_{carb}$ anomalies due to the fixation of ^{12}C in organic debris and the CO_2 in hydrosphere–atmosphere system was relatively enriched in ^{13}C (Lomagundi/Jatulian Event, Schidlowski et al. 1975; Schidlowski 1988; Karhu and Holland 1996; Tang et al. 2011; Lai et al. 2012; Salminen et al. 2013). And the oldest red beds in each continent appeared during 2.25–1.95 Ga (Melezhik et al. 1997a).
4. At the same time, with the rise of pH in seawater, those carbonates can began to precipitate in the ways of $CO_2 + 2OH^- \rightarrow CO_3^{2-} + H_2O$, $CO_3^{2-} + Fe^{2+} \rightarrow FeCO_3(\downarrow)$ (Siderite), $CO_3^{2-} + Mg^{2+} \rightarrow MgCO_3(\downarrow)$(Magnesite), $2CO_3^{2-} + Ca^{2+} + Mg^{2+} \rightarrow CaMg\,(CO_3)_2\,(\downarrow)$ (Dolomite), $CO_3^{2-} + Ca^{2+} \rightarrow CaCO_3(\downarrow)(Calcite)$, $CO_3^{2-} + Mn^{2+} \rightarrow MnCO_3(\downarrow)$ (Rhodochrosite) etc., as these minerals are unstable in acid seawater (e.g., Chen and Zhu 1985). So, there had been a worldwide sudden sedimentation of carbonate strata and related carbonate deposits (e.g., marble, boron, and magnesite deposits with graphite, phosphorite, and Lead-Zinc deposits in NCC; Figs. 12.1, 12.2, 12.3, 12.4, 12.5) during the 2.3–1.9 Ga (e.g., Chen et al. 2000a; Tang et al. 2009c, 2013b; see previous sections in this paper). And the CO_2 in atmosphere rapidly entered into biosphere (organics), hydrosphere (CO_3^{2-}, HCO_3^-) and lithosphere (carbonates), thereby sharply decline.
5. With the O_2 was accumulated in the hydrosphere, the majority of the low-valent ions in the oceans were oxidation (e.g., $Fe^{2+} \rightarrow Fe^{3+}$), the pH value of seawater

further elevated ($O_2 + H_2O + 4e^+ \rightarrow 4OH^-$). Gradually, when the pH raised high enough (pH > 5.5), the two basic requirements for forming BIFs (adequate amounts of Fe^{2+} and the fit seawater pH of 1.25–5.5, Zhu et al. 2014) would be not available (Fig. 12.5). Consequently, the BIFs disappear ca. 1.8 Ga (Klein 2005).

6. As for the 2.0–1.7 Ga "black shale", succeeding the withdraw of the BIFs and early Paleoproterozoic carbonate strata (Melezhik et al. 1997a; Condie et al. 2001), its high CIA indexes and contained varying amounts of organic carbon (Condie et al. 2001) indicated that the provenance of black shale underwent severely weathering and long distance transport, and the sedimentation was under an peace with plenty living active environment, which might be the product of ferrosilicates precipitation (clay minerals) with terrestrial weathered materials (see Sect. 12.3.4) and organic remains deposited at higher pH (>5.5, means more oxidic condition) seawater (Fig. 12.5), as these shale showed negative Eu anomalies (Condie 1993; Chen and Zhao 1997; Chen et al. 1998).

12.5 Concluding Remarks

The geology and geochronology of numerous ores, including graphite, phosphorite, the Lake Superior type BIFs, marble, boron, magnesite, and Lead-Zinc deposits, hosted in 2.5–1.8 Ga stata from the NCC and elsewhere, have been complied in this paper. It indicated that there has an early Paleoproterozoic metallogenic explosion in NCC.

The early Paleoproterozoic metallogenic explosion is resulted from the significant Earth's environmental change related to the blooms of biogeochemical oxygenic photosynthesis in biosphere (graphite, phosphorite deposits), which result in hydrosphere (pH increase with dissolved element oxidation from low into high valences, e.g., Lake Superior type BIFs, REE deposits), atmosphere (e.g., CO_2, CH_4 withdraw and HGE), sedimentary sphere (e.g., BIFs, Glacial diamictite, Carbonates strata, Red beds, Black shales) rapidly changes and brought out the 2.5–1.8 Ga Great Oxygen Event (GOE). Different deposits responded to different stage events of the GOE.

The GOE includes the early-stage hydrosphere oxidation (2.5-2.3 Ga) and the late-stage atmospheric oxygenation (2.3–2.2 Ga). A pre-2.3 Ga reducing hydrosphere prevented atmosphere from oxygenation, because of the consumption of O_2 generated from biological photosynthesis in the oxidation of Fe^{2+} and precipitation of BIFs. After 2.3 Ga, increasing O_2 and decreasing CH_4 and CO_2 cooled the hydrosphere–atmosphere system and resulted in the global Huronian Glaciation Event, which was followed by sudden sedimentation of carbonate strata and $\delta^{13}C_{carb}$ positive excursion (Lomagundi Event), red beds, as well as the disappear of BIFs and prevail of black shales. The biogeochemical oxygenic photosynthesis plays a key role and operates throughout the process.

Acknowledgements This study was funded by the National 973-Program (Project Nos. 2012CB416602, 2006CB403508) and National Natural Science Foundation of China (Nos. 40,352,003, 40425006, 40373007) and Frontier Field Project of the State Key Laboratory of Ore Deposit Geochemistry, Institute of Geochemistry, Chinese Academy of Sciences. Constructive suggestions, pertient comments and careful corrections by Prof. Xiao-Yong Yang of the University of Science and Technology of China greatly improved the quality of the mamuscript.

References

Alexandrov, E. A. (1973). The precabrian banded iron-formations of the Soviet Union. *Economic Geology, 68*(7), 1035–1063.

Awramik, S. M., Schopf, J. W., & Walter, M. R. (1983). Filamentous fossil bacteria from the Archean of western Australia. *Precambrian Research, 20*, 357–374.

Babinski, M., Chemale, F, Jr., & Van Schmus, W. R. (1995). The Pb/Pb age of the Minas Supergroup carbonate rocks, Quadrilátero Ferrífero, Brazil. *Precambrian Research, 72*, 235–245.

Bayley, R. W., & James, H. L. (1973). Precambrian iron-formations of the United States. *Economic Geology, 68*(7), 934–959.

Bekker, A., Karhu, J. A., & Kaufman, A. J. (2006). Carbon isotope record for the onset of the Lomagundi carbon isotope excursion in the Great Lakes area, North America. *Precambrian Research, 148*, 145–180.

Bekker, A., Kaufman, A. J., Karhu, J. A., Beukes, N. J., Swart, Q. D., Coetzee, L. L., & Eriksson, K. A. (2001). Chemostratigraphy of the Paleoproterozoic Duitschland Formation, South Africa: Implications for coupled climate change and carbon cycling. *American Journal of Science, 301*, 261–285.

Bekker, A., Kaufman, A. J., Karhu, J. A., & Eriksson, K. A. (2005). Evidence for Paleoproterozoic cap carbonates in North America. *Precambrian Research, 137*, 167–206.

Bekker, A., Slack, J. F., Planavsky, N., Krapež, B., Hofmann, A., Konhauser, K. O., & Rouxel, O. J. (2010). Iron formation: the sedimentary product of a complex interplay among mantle, tectonic, oceanic, and biospheric processes. *Economic Geology, 105*, 467–508.

Canfield, D. E. (2005). The early history of atmospheric oxygen: homage to Robert M. Garrels. *Annual Review of Earth and Planetary Sciences, 33*, 1–36.

Cao, R.-J. (2003). History and current status of study on stromatolitic nomenclature and classification in the Precambrian. *Geological Survey and Research, 26*(2), 80–83 (in Chinese with English abstract).

Cao, R.-J., & Yuan, X.-L. (2009). Advances of stromatolite study in China. *Acta Palaeontologica Sinica, 48*(3), 314–321 (in Chinese with English abstract).

Cao, R.-J., Zhao, W.-J., & Xiao, Z.-Y. (1982). Subdivision and correlation of the Precambrian in China. In: Nanjing Institute of Geology and Paleontology (Ed.), *Stratigraphic correlation chart in China with explanatory text* (pp. 1–27). Beijing: Science Press (in Chinese).

Cenki, B., Braun, I., & Bröcker, M. (2004). Evolution of the continental crust in the Kerala Khondalite Belt, southernmost India: evidence from Nd isotope mapping, U–Pb and Rb–Sr geochronology. *Precambrian Research, 134*(3–4), 275–292.

Chen, Y.-J. (1990). Evidences for the catastrophe in geologic environment at about 2300 Ma and the discussions on several problems. *Journal of Stratigraphy, 14*, 178–186 (in Chinese with English abstract).

Chen, F. (1996a). Origin and evolution of the Earth's atmosphere and hydrosphere. In G.-Z. Tu & Z.-Y. Ouyang (Eds.), *Developments in geochemistry* (pp. 225–233). Guizhou: Guizhou Science and Technology Publishing House (in Chinese).

Chen, Y.-J. (1996b). Progresses in application of sedimentary trace element geochemistry to probe crustal composition and environmental change. *Geology Geochemistry, 3*, 1–125 (in Chinese).

Chen, J. (2002). The black shale series and ore deposit in Qingchengzi Liaoning Province. *Geology and Resources, 11*(3), 188–192 (in Chinese with English abstract).

Chen, C.-X., & Cai, K.-Q. (2000). Minerogenic system of magnesian nonmetalliic deposits in early Proterozoic Mg-rich carbonate formations in eastern Liaoning Province. *Acta Geologica Sinica, 74*, 623–631.

Chen, Y.-J., & Deng, J. (1993). REE geochemical characteristics and evolution of early Preambrian sediments: Evidence from the southern margin of the northern China craton. *Geochimica, 1*, 93–104 (in Chinese).

Chen, Y.-J., & Tang, H.-S. (2016). The Great Oxidation Event and its records in North China Craton. In M.-G. Zhai, et al. (Eds.), *Main Tectonic Events and Metallogeny of the North China Craton* (pp. xx–xx). Singapore: Springer.

Chen, Y.-J., Hu, S.-X., & Lu, B. (1998). Contrasting REE geochemical features between Archean and Proterozoic khondalite series of North China Craton. Goldschmidt Conference Toulouse 1998. *Minralogical Magzine, 62A*, 318–319.

Chen, Y.-J., Ji, H.-Z., Zhou, X.-P., & Fu, S.-G. (1991). The challenge to the traditional geological theories from revelation of the catastrophe at 2300 Ma: New knowledge on several important geological subjects. *Advance in Earth Science, 6*(2), 63–68 (in Chinese with English abstract).

Chen, C.-X., Jiang, S.-Y., Cai, K.-Q., & Ma, B. (2003a). Metallogenic conditions of magnesite and talc deposits in early Proterozoic Mg-rich carbonate formations, eastern Liaoning province. *Mineral Deposits, 22*(2), 166–176 (in Chinese with English abstract).

Chen, Y.-J., Liu, C.-Q., Chen, H.-Y., Zhang, Z.-J., & Li, C. (2000). Carbon isotope geochemistry of graphite deposits and ore-bearing khondalite series in North China: Implications for several geoscientific problems. *Acta Petrologica Sinica, 16*, 233–244 (in Chinese with English abstract).

Chen, C.-X., Ni, P., Cai, K.-Q., Zhai, Y.-S., & Deng, J. (2003b). The minerogenic fluids of magnesite and talc deposits in the Paleoproterozoic Mg-rich carbonate formations in eastern Liaoning Province. *Geological Review, 49*(6), 646–651 (in Chinese with English abstract).

Chen, Y.-J., Ouyang, Z.-Y., Yang, Q.-J., & Deng, J. (1994). A new understanding of the Archean-Proterozoic boundary. *Geologic Review, 40*, 483–488 (in Chinese with English abstract).

Chen, Y.-J., & Su, S.-G. (1998). Catastrophe in geological environment at 2300 Ma. *Mineralogical Magazine, 62A*(1), 320–321.

Chen, Y.-J., Yang, J.-Q., Deng, J., Ji, H.-Z., Fu, S.-G., Zhou, X.-P., & Lin, Q. (1996). An important change in Earth's evolution: An environmental catastrophe at 2300 Ma and its implications. *Geology-Geochemistry, 3*, 106–128 (in Chinese).

Chen, Y.-J., & Zhao, Y. C. (1997). Geochemical characteristics and evolution of REE in the Early Precambrian sediments: Evidences from the southern margin of the North China Craton. *Episodes, 20*, 109–116.

Chen, F., & Zhu, X.-Q. (1984). Simulating experiments on the mechanism of formation of banded iron–silica formation: Weathering–leaching of basalts. *Geochimica, 4*, 341–349 (in Chinese with English abstract).

Chen, F., & Zhu, X. Q. (1985). pH-evolution of Archaean seawater and its relations to ore deposition. *Acta Sedimentologica Sinica, 3*, 1–15 (in Chinese with English abstract).

Chen, F., & Zhu, X.-Q. (1987). The evolution of supergene weathering and its ability of oreforming elements. *Geochimica, 4*, 341–350 (in Chinese with English abstract).

Chen, F., & Zhu, X.-Q. (1988). Reconstruction of evolution of atmospheric CO_2 partial pressure based on the sediment mineral assemblage. *Science China- Earth Sciences, 7*, 747–755 (in Chinese).

Cloud, P. E. (1968). Atmospheric and hydrospheric evolution on the primitive earth. *Science, 160*, 729–736.

Cloud, P. E. (1973). Paleoecological significance of banded iron-formation. *Economic Geology, 68*, 1135–1143.

Cloud, J. P. E., & Semikhatov, M. A. (1969). Proterozoic stromatolite zonation. *American Journal of Science, 267*(9), 1017–1061.

Condie, K. C. (1993). Chemical composition and evolution of the upper continental crust: contrasting results from surface samples and shales. *Chemical Geology, 104*, 1–37.

Condie, K. C., DesMarais, D. J., & Abbott, D. (2001). Precambrian superplumes and supercontinents: A record in black shales, carbon isotopes, and paleoclimates? *Precambrian Research, 106*, 239–260.

Cook, P. J., & Mcelhinny, M. W. (1979). A reevaluation of the spatial and temporal distribution of sedimentary phosphate deposits in the light of plate tectonics. *Economic Geology, 74*, 315–330.

Davidson, C. F. (1963). Phosphate deposits of Precambrian age. *Mining Mag., 109*, 205–342.

Dimroth, E. (1981). Labrador Geosyncline: Type example of early Proterozoic cratonic reactivation. In: A. Kroner (Ed.), *Precambrian Plate Tectonics* (pp. 1–238).

Diwu, C.-R., Sun, Y., Lin, C.-L., & Wang, H.-L. (2010). LA-(MC)-ICP-MS U-Pb zircon geochronol-ogy and Lu–Hf isotope compositions of the Taihua complex on the southern margin of the North China Craton. *Chinese Science Bulletin, 55*, 2557–2571.

Diwu, C.-R., Sun, Y., Yuan, H.-L., Wang, H.-L., Zhong, X.-P., & Liu, X.-M. (2008). The U–Pb chronology of detrital zircon of quartzite and its geological significance of Songshan, Denfeng area of Henan Province. *Chinese Science Bulletin, 53*(16), 1923–1934 (in Chinese).

Du, L.-L., Yang, Z.-H., Lu, Z.-L., Zhao, L., Geng, Y.-S., Diwu, C.-R., et al. (2015). The Sijizhuang Formation at Jiangcun Area of Wutai Mountains: Further Constraints on the Age of the Hutuo Group. *Acta Geoscientica Sinica, 36*(5), 599–612 (in Chinese with English abstract).

Duan, X.-X., Liu, J.-M., Wang, Y.-B., Zhou, L.-L., Li, Y.-G., Li, B., et al. (2012). Geochronology, geochemistry and geological significance of Late Triassic magmatism in Qingchengzi orefield Liaoning. *Acta Petrologica Sinica, 28*(2), 595–606 (in Chinese with English abstract).

Eriksson, K. A., & Truswell, J. F. (1978). Geological process and atmospheric evolution in the Precambrian. In D. H. C. Tarling (Ed.), *Evolution of the Earth's Crust* (pp. 219–238). London: Academic Press.

Feng, B.-Z., Lu, J.-W., Zou, R., Ming, H.-L., & Xie, H.-Y. (1998). Ore-forming conditions for the early proterozoic large-superlarge boron deposits in Liaoning and Jilin Provinces, China. *Journal of Changchun University of Science and Technoly, 28*(1), 1–15 (in Chinese with English abstract).

Feng, X.-Z., Xiao, Y., & Liu, C.-X. (2008). Geology and geochemistry of the Gaotaigou boron deposit in southern Jilin China. *Geology of Chemical Minerals, 30*(4), 207–217 (in Chinese with English abstract).

Feng, B.-Z., & Zou, R. (1994). The characteristics and genesis of Houxianyu doron deposits, Yinkou Liaoning Province. *Earth Science Frontiers, 1*(3–4), 235–237 (in Chinese with English abstract).

Feulner, G., Hallmann, C., & Kienert, H. (2015). Snowball cooling after algal rise. *Nature Geoscience, 8*(9), 659–662. doi:10.1038/ngeo2523.

Frei, R., Dahl, P. S., Duke, E. F., Frei, K. M., Hansen, T. R., Frandsson, M. M., & Jensen, L. A. (2008). Trace element and isotopic characterization of Neoarchean and Paleoproterozoic iron formations in the Black Hills (South Dakota, USA): Assessment of chemical change during 2.9–1.9 Ga deposition bracketing the 2.4–2.2Ga first rise of atmospheric oxygen. *Precambrian Research, 162*, 441–474.

Frei, R., Gaucher, C., Poulton, S. W., & Canfield, D. E. (2009). Fluctuations in Precambrian atmospheric oxygenation recorded by chromium isotopes. *Nature, 461*, 250–253.

Fu, M.-Y. (2014). The prospecting direction of the graphite deposit in Hebei Province. *China Non-metallic Minerals Industry, 109*, 50–52 (in Chinese with English abstract).

Gao, W.-Y., Li, J.-H., Bai, X., & Mao, X. (2009). Structural characterister of a huge Paleoproterozoic stromatolite in Mt. Wutai and its genetic implication. *Acta Petrologica Sinica, 25*(3), 667–674 (in Chinese with English abstract).

Garrels, R. M., Perry, E. A. Jr., & Mackenzie, F. T. (1973). Genesis of Precambrian Iron-formation and the development of atmospheric oxygen. *Economic Geology, 68*, 1173–1179.

Gaucher, C., Blanco, G., Chiglino, L., Poiré, D., & Germs, G. J. B. (2008). Acritarchs of Las Ventanas Formation (Ediacaran, Uruguay): Implications for the timing of coeval rifting and glacial events in western Gondwana. *Gondwana Research, 13*, 488–501.

Goodwin, A. M. (1991). *Precambrian Geology* (pp. 1–521). London: Academic Press.

Gross, G. A. (1980). A classification of iron formations based on depositional environments. *Can. Mineral., 18*, 215–222.

Gross, G. A. (1983). Tectonic systems and the deposition of iron-formation. *Precambrian Research, 20*, 171–187.

Guo, J.-H., Zhai, M.-G., & Li, Y.-G. (1994). Isotopic ages and their tectonic significance of metamorphic rocks from middle part of the early Precambrian granulite belt, North China craton. In X.-L. Qian & R.-M. Wang (Eds.), *Geological evolution of the granulite terrain in north part of the North China Craton* (pp. 130–144). Beijing: China Seismological Press (in Chinese with English abstract).

Holland, H. D. (1994). Early Proterozoic atmospheric change. In: S. Bengston (Ed.), *Early Life on Earth. Nobel Symposium No. 84* (pp. 237–244). New York: Columbia University Press.

Holland, H. D. (2009). Why the atmosphere became oxygenated: A proposal. *Geochimica et Cosmochimica Acta, 73*, 5241–5255.

Hu, S.-X. (1988). *Geology and metallogeny of the collision belts between the Southern and the Northern China Plate* (pp. 1–558). Nanjing: Nanjing University Press (in Chinese).

Hu, G.-Y., Li, Y.-H., Fan, R.-L., Wang, T.-H., Fan, C.-F., & Wang, Y.-B. (2014). The formaiton age of the borate deposit in Kuandian area, eastern Liaoning Province: Constrains from the SHRIMP U–Pb data and boron istopic composition. *Acta Geologica Sinica, 88* (10), 1932–1943.

Hu, S.-X., Zhao, Y.-Y., Xu, J.-F., & Ye, Y. (1997). *Geology of gold deposits in North China platform* (pp. 7–55). Beijing: China Science Press (in Chinese).

Huston, D. L., & Logan, G. A. (2004). Barite BIFs and bugs: Evidence for the evolution of the Earth's early hydrosphere. *Earth Planetary Science Letters, 220*, 41–55.

Information Division of CAGS. (1975). Selections of overseas geologic data (20) (pp. 1–200). Unpublished (in Chinese).

Isley, A. E., & Abbott, D.H. (1999). Plume-related mafic volcanism and the deposition of banded iron formation. *Journal of Geophysical Resarch. B: Solid Earth Planets* 104, 15461–15477.

Ji, H.-Z., & Chen, Y.-J. (1990). Khondalite series and their related mineral resources. *Geology and Prospecting, 11*, 11–13 (in Chinese).

Jiang, S.-Y. (1988). Stable isotope geological characteristics of Oxygen, Carbon, Lead, and Sulfur and metllogenesis of the Qingchengzi Lead-Zinc deposit Liaoning. *Geologic Review, 34*(6), 515–523 (in Chinese with English abstract).

Jiang, J.-S. (1990). Khondalite series and its research progress. *Journal of Changchun University of Earth Sciences, 20*(2), 167–176 (in Chinese with English abstract).

Jiang, S.-Y., Chen, C.-X., Chen, Y.-Q., Jiang, Y.-H., Dai, B.-Z., & Ni, P. (2004). Geochemistry and genetic model for the giant magnesite deposits in the eastern Liaoning province China. *Acta Petrologica Sinica, 20*(4), 765–772.

Jiang, S.-Y., Palmer, M.-R., Peng, Q.-M., & Yang, J.-H. (1997). Chemical and stable isotopic compositions of Proterozoic metamorphosed evaporites and associated tourmalines from the Houxianyu borate deposit, eastern Liaoning, China. *Chemical Geology, 135*, 189–211.

Jiang, S.-Y., & Wei, J.-Y. (1989). Geochemistry of the Qingchengzi Lead-Zinc deposit. *Mineral Deposits, 8*(4), 20–28 (in Chinese with English abstract).

Kanzaki, Y., & Murakami, T. (2016). Estimates of atmospheric O_2 in the Paleoproterozoic from paleosols. *Geochimica et Cosmochimica Acta, 174*, 263–290.

Karhu, J. A. (1993). Palaeoproterozoic evolution of the carbon isotope ratios of sedimentary carbonates in the Fennoscandian Shield. *Geological Survvey of Finland Bulletin, 371*, 1–87.

Karhu, J. A., & Holland, H. D. (1996). Carbon isotopes and the rise of atmospheric oxygen. *Geology, 24*(10), 867–870.

Kirschvink, J. L., Gaidos, E. J., Bertani, L. E., Beukes, N. J., Gutzmer, J., Maepa, L. N., & Steinberger, R. E. (2000). Paleoproterozoic snowball Earth: Extreme climatic and geochemical global change and its biological consequences. *Proceedings of the National Academy of Sciences of the United States of America, 97*, 1400–1405.

Klein, C. (2005). Some Precambrian banded iron-formations (BIFs) from around the world: their age, geologic setting, mineralogy, metamorphism, geochemistry, and origin. *American Mineralogist, 90*, 1473–1499.

Klein, C., & Ladiera, E. A. (2000). Geochemistry and petrology of some Proterozoic banded iron-formations of the Quadrilátero Ferrífero, Minas Gerais, Brazil. *Economic Geology, 95*, 205–428.

Knoll, A. H., Strother, P. K., & Rossi, S. (1988). Distribution and diagenesis of microfossils from the lower Proterozoic Duck Creek Dolomite, Western Australia. *Precambrian Research, 38*, 257–279.

Konhauser, K. O., Lalonde, S. V., Planavsky, N. J., Pecoits, E., Lyons, T. W., Mojzsis, S. J., et al. (2011). Aerobic bacterial pyrite oxidation and acid rock drainage during the Great Oxidation Event. *Nature, 478*, 369–373.

Konhauser, K. O., Pecoits, E., Lalonde, S. V., Papineau, D., Nisbet, E. G., Barley, M. E., et al. (2009). Oceanic nickel depletion and a methanogen famine before the Great Oxidation Event. *Nature, 458*, 750–753.

Kump, L. R., & Barley, M. E. (2007). Increased subaerial volcanism and the rise of atmospheric oxygen 2.5 billion years ago. *Nature, 448*, 1033–1036.

Lai, Y., Chen, C., & Tang, H.-S. (2012). Paleoproterozoic positive $\delta^{13}C$ excursion in Henan, China. *Geomicrobiology Journal, 29*, 287–298.

Lan, X.-Y. (1981). Study on genesis of the Nanshu graphite deposit and on feature of Precambrian graphite-bearing rock association, Shandong. *Journal of Changchun University of Earth Sciences, 3*, 30–42 (in Chinese with English abstract).

Lan, T.-G., Fan, H.-R., Hu, F.-F., Yang, K.-F., Cai, Y.-C., & Liu, Y.-S. (2014a). Depositional envi-ronment and tectonic implications of Paleoproterozoic BIF in the Changyi area, eastern North China Craton: evidence from geochronology and geochemistry ofwall-rocks. *Ore Geology Reviews, 61*, 52–72.

Lan, T.-G., Fan, H.-R., Hu, F.-F., Zheng, X.-L., & Zhang, H.-D. (2012). Geological and geochemical characteristics of Paleoproterozoic Changyi banded iron formation deposit, Jiaodong Peninsula of eastern China. *Acta Petrologica Sinica, 28*(11), 3595–3611.

Lan, T.-G., Fan, H.-R., Santosh, M., Hu, F.-F., Yang, K.-F., Yang, Y.-H., & Liu, Y.-S. (2014b). U-Pbzircon chronology, geochemistry and isotopes of the Changyi banded iron forma-tion in eastern Shandong Province: Constraints on BIF genesis and implications for Paleoproterozoic tectonic evolution of the North China Craton. *Ore Geology Reviews, 56*, 472–486.

Lan, T.-G., Fan, H.-R., Yang, K.-F., Cai, Y.-C., Wen, B.-J., & Zhang, W. (2015). Geochronology, mineralogy and geochemistry of alkali-feldspargranite and albite granite association from the Changyi area of Jiao-Liao-Ji Belt: Implications for Paleoproterozoic rifting of eastern North China Craton. *Precambrian Research, 266*, 86–107.

Li, Z.-L. (2014). The geological characteristics and utilization prospect of the Jingcun graphite deposit, Pingdu city, Shandong Province. *China Non-metallic Minerals Industry, 112*, 45–46 (in Chinese with English abstract).

Li, Z., Chen, B., Liu, J.-W., Zhang, L., & Yang, C. (2015a). Zircon U–Pb ages and their implications for the South Liaohe Group in the Liaodong Peninsula Northeast China. *Acta Petrologica Sinica, 31* (6), 1589–1605 (in Chinese with English abstract).

Li, N., Chen, Y.-J., McNaughton, N. J., Ling, X.-X., Deng, X.-H., Yao, J.-M., & Wu, Y.-S. (2015b). Formation and tectonic evolution of the khondalite series at the Southern margin of the North China Craton: Geochronological Constraints from a 1.85-Ga Mo deposit in the Xiong'ershan area. *Precambrian Research, 269*, 1–17.

Li, H.-K., Li, Y.-F., Geng, K., Zhuo, C.-Y., Zhang, Y.-B., Liang, T.-T., & Wang, F. (2013a). Palaeoprpterozoic Tectonic Setting in the Eastern Shandong Province. *Geological Survey and Research, 36* (2), 114–130 (in Chinese with English abstract).

Li, Y.-Y., Luo, Y.-Q., Dongye, M.-X., Bi, R.-F., Zhou, M.-J., Wang, C.-W., et al. (1994). Phosphous deposits in China. In: S, H. Song. (Ed.), *Ore deposits of China* (Vol. 3, pp. 1–59). Beijing: China Geological Publishing House (in Chinese).

Li, H.-Q., Sheng, L.-S., & Jia, X.-J. (2012). Study on the Prospecting Direction in the External of Jingshansi Deposit in Wuyang Iron Ore Field Henan Province. *Gold Science & Technology, 20*(1), 54–60 (in Chinese with English abstract).

Li, Y.-F., Xie, K.-J., Luo, Z.-Z., & Li, J.-P. (2013b). Geochemistry of Tieshan iron deposit in the Wuyang area, Henan Province and its environmental implications. *Acta Geoligical Sinica, 87*(9), 1377–1398.

Li, H.-Q., & Zhang, Y.-L. (2011). Evaluation on deep prospecting potential of the iron mountain mine in Wuyang Henan. *Mineral Exploration, 2*(5), 487–493 (in Chinese with English abstract).

Liu, J.-L. (1988). Study on Precambrian geology of the Jiamusi block. *Journal of Changchun University of Earth Sciences, 18*(2), 147–156 (in Chinese with English abstract).

Liu, J.-D. (1996). Geological characteristics and genesis of early Proterozoic borate deposits in east Liaoning-Shouth Jili. *Geology of Chemical Minerals, 18*(3), 207–212 (in Chinese with English abstract).

Liu, J.-D. (2006). *Mineralization model and survey & evaluation of early Proterozoic Mg-borate deposits in east Liaoning (doctor candidate paper)* (pp. 1–114). Beijing: China University of Geoscience (in Chinese with English abstract).

Liu, Q.-Q., Li, Y.-F., Luo, Z.-C., Xie, K.-J., & Huang, Z.-L. (2014). Geochemical characteristics of Jingshansi iron deposit in Wuyang, Henan Province, and their geological significance. *Mineral Deposits, 33*(4), 697–712 (in Chinese with English abstract).

Liu, P.-H., Liu, F.-L., Wang, F., & Liu, J.-H. (2011). U–Pb dating of zircons from Al-rich paragneisses of Jingshan Group in Shandong peninsula and its geological significance. *Acta Petrologica et Mineralogica, 30*(5), 829–843 (in Chinese with English abstract).

Liu, F.-L., Liu, P.-H., Wang, F., Liu, C.-H., & Cai, J. (2015a). Progresses and overviews of voluminous meta-sedimentary series within the Paleoproterozoci Jiao-Liao-Ji orogenic/mobile belt, *Norht China Craton. Acta Petrologica Sinica, 31*(10), 2816–2846 (in Chinese with English abstract).

Liu, P.-H., Liu, F.-L., Wang, F., Liu, C.-H., Yang, H., Liu, J.-H., et al. (2015b). P-T-t paths of the multiple metamorphic events of the Jiaobei terrane in the southeastern segment of the Jiao-Liao-Ji Belt (JLJB), in the North China Craton: Implication for formation and evolution of the JLJB. *Acta Petrologica Sinica, 31*(10), 2889–2941 (in Chinese with English abstract).

Liu, S.-W., Lv, Y.-J., Feng, Y.-G., Liu, X.-M., Yan, Q.-R., Zhang, C., & Tian, W. (2007a). Zircon and monazite geochronology Hongqiy-ingzi complex, northern Hebei. *China. Geological Bulletin of China, 26*(9), 1086–1100 (in Chinese with English abstract).

Liu, S.-W., Lv, Y.-J., Feng, Y.-G., Zhang, C., Tian, W., Yan, Q.-R., & Liu, X.-M. (2007b). Geology and zircon U–Pb isotopic chronology of Dantazi Complex, Northern Hebei Province. *Geological Journal of China Universities, 13*(3), 484–497 (in Chinese with English abstract).

Liu, J.-Z., Qian, R.-X., & Chen, Y.-P. (1989). The tectonic orgin of graphite deposits in the khondalite group, the middle part of inner Mongolia China. *Geotectonica et Metallogenia, 13*(2), 162–167 (in Chinese with English abstract).

Liu, H.-J., Sha, D.-X., & Li, G.-S. (2013). Genetic connection between the Lead-Zinc and Gold-Silver deposits in the Qingchengzi ore concentration area in eastern Liaoning. *Geology and Resources, 22* (4), 299–303 (in Chinese with English abstract).

Liu, J.-D., Xiao, R.-G., Wang, S.-Z., & Wang, C.-Z. (2005a). Geological characteristics and exploration of Zhuanmiao borate deposit Liaoning Province. *Geology and Resources, 14*(2), 126–131 (in Chinese with English abstract).

Liu, J.-D., Xiao, R.-G., Wang, C.-Z., Zhou, H.-C., & Fei, H.-C. (2005b). Genesis of the Dashiqiao granite and its significance in Borate mineral exploration. *Journal of Jilin University (Earth Science Edition), 35*(6), 714–719 (in Chinese with English abstract).

Liu, L., & Yang, X.-Y. (2013). Geochemical characteristics of the Huoqiu BIF ore deposit in Anhui Province and their metallogenic significance: Taking the Bantazi and Zhouyoufang deposits as examples. *Acta Petrologica Sinica, 29*(7), 2551–2566 (in Chinese with English abstract).

Liu, L., & Yang, X.-Y. (2015). Temporal, environmental and tectonic significance of the Huoqiu BIF, southeastern North China Craton: Geochemical and geochronological constraints. *Precambrian Research, 261*, 217–233.

Liu, C.-H., Zhao, G.-C., Sun, M., Zhang, J., & Yin, C.-Q. (2012). U-Pb geochronology and Hf isotope geochemistry of detrital zircons from the Zhongtiao Complex: Constraints on the tectonic evolution of the Trans-North China Orogen. *Precambrain Research, 222–223*, 159–172.

Lu, Y.-F., Chen, Y.-C., Li, H.-Q., Xue, C.-J., & Chen, F.-W. (2005). Metallogenic chronology study of boron deposits in early proterozoic rift in east Liaoning. *Acta Geologica Sinia, 79*(2), 287.

Lu, L.-Z., Xu, X.-C., & Liu, F.-L. (1996). *The Early Precambrian khondalite Series in North China* (pp. 1–276). Changchun: Changchun Publishing House (in Chinese).

Luo, Y., Sun, M., Zhao, G.-C., Li, S.-Z., Xu, P., Ye, K., & Xia, X.-P. (2004). LA ICP-MS U-Pb zircon ages of the Liaohe Group in the Eastern Block of the North China Craton: Constraints on the evolution of the Jiao-Liao-Ji Belt. *Precambrian Research, 134*, 349–371.

Lyons, T. W., & Reinhard, C. T. (2009). Early Earth: Oxygen for heavy-metal fans. *Nature, 461*, 179–181.

Maibam, B., Sanyal, P., & Bhattacharya, S. (2015). Geochronological study of metasediments and carbon isotopes in associated graphites from the Sargur area, Dharwar craton: Constraints on the age and nature of the protoliths. *Journal of the Geological Society of India*, *85*.

Melezhik, V. A., & Fallick, A. E. (1996). A widespread positive δ^{13}Ccarb anomaly at 2.33-2.06 Ga on the Fennoscandian Shield: A paradox? *Terra Nova Research, 8*, 141–157.

Melezhik, V. A., Fallick, A. E., Filippov, M. M., & Larsen, O. (1999a). Karelian shungite–an indication of 2.0-Ga-old metamorphosed oil-shale and generation of petro-leum: geology, lithology and geochemistry. *Earth-Science Reviews, 47*, 1–40.

Melezhik, V. A., Fallick, A. E., Makarikhin, V. V., & Lubtsov, V. V. (1997a). Links between Palaeoproterozoic palaeogeography and rise and decline of stromatolites: Fennoscandian Shield. *Precambrian Research, 82*, 311–348.

Melezhik, V. A., Fallick, A. E., Medvedev, P. V., & Makarikhin, V. V. (1999b). Extreme $^{13}C_{carb}$ enrichment in ca. 2.0 Ga magnesite–stromatolite–dolomite–'red beds' association in a global context: A case for the worldwide signal enhanced by a local environment. *Earth-Science Reviews, 48*, 71–120.

Melezhik, V. A., Fallick, A. E., & Semikhatov, M. A. (1997b). Could stromatolite-forming cyanobacteria have influenced the global carbon cycle at 2300-2060 Ma? *Norges Geologiske Undersøkelse Bulletin, 433*, 30–31.

Meng, E., Liu, F.-L., Cui, Y., Liu, P.-H., Liu, C.-H., & Shi, J.-R. (2013). Depositional ages and tectonic implications for the Kuandian South Liaohe Group in Northeast Liaodong Peninsula. *Northeast China. Acta Petrologica Sinica, 29*(7), 2465–2480 (in Chinese with English abstract).

Meng, E., Liu, F.-L., Liu, P.-H., Liu, C.-H., Yang, H., Wang, F., et al. (2014). Petrogenesis and tectonic implications of Paleoproterozoic meta-mafic rocks from central Liaodong Peninsula, Northeast China: Evidence from zircon U–Pb dating and in situ Lu-Hf isotopes, and whole-rock geochemistry. *Precambrian Research, 247*, 92–109.

Morey, G. B., & Southwick, D. L. (1995). Allostratagraphic relationships of Early Proterozoic iron-formations in the Lake Superior region. *Economic Geology, 90*, 1983–1993.

Peng, Q.-M., Palmer, M. R., & Lu, J.-W. (1998). Geology and geochemistry of the Paleoproterozoic borate deposits in Liaoning-Jilin, northeastern China: Evidence of metaevaporites. *Hydrobiologia, 381*, 51–57.

Pickard, A. L. (2002). SHRIMP U-Pb zircon ages of tuffaceous mudrocks in the Brockman Iron Formation of the Hamersley Range, Western Australia. *Australian Journal of Earth Sciences, 49*, 491–507.

Purohit, R., Sanyal, P., Roy, A. B., & Bhattacharya, S. K. (2010). 13C enrichment in the Palaeoproterozoic carbonate rocks of the Aravalli Supergroup, northwest India: Influence of depositional environment. *Gondwana Research, 18*, 538–546.

Qu, H.-X., Guo, W.-J., Zhang, Y., Tan, W.-G., Chen, S.-L., Li, Q.-L., & Bian, X.-F. (2005). Genesis study and prospective prediction for boron deposits in eastern Liaoning. *Geology and Resoures, 14*(2), 131–138 (in Chinese with English abstract).

Ray, J. S., Veizer, W. J., & Davis, (2003). C, O, Sr and Pb isotope systematics of carbonate sequences of the Vindhyan Supergroup, India: Age, diagenesis, correlations and implications for global events. *Precambrian Research, 121*, 103–140.

Rui, Z.-Y., Li, N., & Wang, L.-S. (1991). *Lead and zinc deposits of Guanmenshan* (208 pp). Beijing: Geological Publishing House (in Chinese with English abstract).

Rye, R., & Holland, H. D. (1998). Paleosols and the evolution of atmospheric oxygen: A critical review. *American Journal of Science, 298*, 621–672.

Salop, L. J. (1977). *Precambrian of the northern hemisphere* (pp. 1–378). Amsterdam: Elsevier Press.

Salminen, P. E., Karhu, J. A., Melezhik, V. A. (2013). Tracking lateral δ13Ccarb variation in the Paleoproterozoic Pechenga Greenstone Belt, the north eastern Fennoscandian Shield. *Precambrian Research, 228*, 177–193.

Sanyal, P., Acharya, B. C., Bhattacharya, S. K., Sarkar, A., Agrawal, S., & Bera, M. K. (2009). Origin of graphite, and temperature of metamorphism in Precambrian Eastern Ghats Mobile Belt, Orissa, India: A carbon isotope approach. *Journal of Asian Earth Sciences, 36*(2–3), 252–260.

Satish-Kumar, M., Yurimoto, H., Itoh, S., & Cesare, B. (2011). Carbon isotope anatomy of a single graphite Crystal in a metapelitic migmatite revealed by high-spatial resolution SIMS analysis. *Contributions to Mineralogy & Petrology, 162*(4), 821–834.

Schidlowski, M. (1988). A 3800-million-year isotopic record of life from carbon in sedimentary rocks. *Nature, 333*, 313.

Schidlowski, M., Eichmann, R., & Junge, C. E. (1975). Precambrian sedimentary carbonates: carbon and oxygen isotope geochemistry and implications for the terrestrial oxygen budget. *Precambrian Research, 2*, 1–69.

Schneider, D. A., Bickford, M. E., Cannon, W. F., Schulz, K. J., & Hamilton, M. A. (2002). Age of volcanic rocks and syndepositional iron formations, Marquette Range Supergroup: Implications for the tectonic setting of Paleoproterozoic iron formations of the Lake Superior region. *Canadian Journal of Earth Sciences, 39*, 999–1012.

Schopf, J. W. (1977). Evidences of Archean life. In C. Ponnamperuam (Ed.), *Chemical evolution of the early Precambrian* (pp. 101–105). New York: Academic Press.

Shan, H.-X., Zhai, M.-G., Oliveira, E. P., Santosh, M., & Wang, F. (2015). Convergent margin magmatism and crustal evolution during Archean-Proterozoic transition in the Jiaobei terrane: Zircon U–Pb ages, geochemistry, and Nd isotopes of amphibolites and associated grey gneisses in the Jiaodong complex, North China Craton. *Precambrian Research, 264*, 98–118.

Shen, Q.-H., & Song, H.-X. (2014). Redefiniton of the Taihua Group, Lushan. *Hunan. Journal of stratigraphy, 38*(1), 1–7 (in Chinese with English abstract).

Shen, B.-F., Zhai, A.-M., Miao, P.-S., Sima, X.-Z., & Li, J.-J. (2006). Geological character and potential resources of iron deposits in the North China block. *Geological Survey and Research, 29*(4), 244–325 (in Chinese with English abstract).

Shen, B.-F., Zhai, A.-M., & Yang, C.-L. (2010). Paleoproterozoic animportant metallogenic epoch in China. *Geoligical Survey and Research, 33*(4), 241–256 (in Chinese with English abstract).

Shen, B.-F., Zhai, A.-M., Yang, C.-L., & Cao, X.-L. (2005). Temporal–spatialdistribution and evolutional characters of Precambrian iron deposits in China. *Geological Survey and Research, 28*(4), 196–206 (in Chinese with English abstract).

Sreenivas, B., Sharma, D. S., Kumar, B., Patil, D. J., Roy, A. B., & Srinivasan, R. (2001). Positive δ^{13}C excursion in carbonate and organic fractions from the Paleoproterozoic Aravalli Supergroup, Northwestern India. *Precambrian Research, 106*, 277–290.

Sun, M., Armstrong, R. L., Lambert, R. S., Jiang, C.-C., & Wu, J.-H. (1993). Petrochemistry and Sr, Pb and Nd isotopic geochemistry of Paleoproterozoic Kuandian Complex, the eastern Liaoning Province, China. *Precambrian Research, 62*, 171–190.

Sun, H.-J., Wu, C.-L., & Qu, Y.-Y. (1995). Khondalite and graphite deposits from Liaohe Group. *Mineral Resources and Geology, 9*(3), 208–212 (in Chinese with English abstract).

Tang, H.-S., & Chen, Y.-J. (2013). Global glaciations and atmospheric change at ca. 2.3Ga. *Geoscience Frontiers, 4*, 583–596.

Tang, G.-J., Chen, Y.-J., Huang, B.-L., & Chen, C.-X., (2004). Paleoprotoerozoic $\delta^{13}C_{carb}$ positive excursion event: research progress on 2. 3 Ga catastrophe. *Journal of Mineralogy and Petrology 24*(3), 103–109 (in Chinese with English abstract).

Tang, H.-S., Chen, Y.-J., Santosh, M., & Yang, T. (2013a). REE geochemistry of carbonates from the Guanmenshan Formation, Liaohe Group, NE Sino-Korean Craton: Implications for seawater compositional change during the Great Oxidation Event. *Precambrian Research, 227*, 316–336.

Tang, H.-S., Chen, Y.-J., Santosh, M., Zhong, H., Wu, G., & Lai, Y. (2013b). C–O isotope geochemistry of the Dashiqiao magnesite belt, North China Craton: implications for the Great Oxidation Event and ore genesis. *Geological Journal, 48*, 467–483.

Tang, H.-S., Chen, Y.-J., & Wu, G. (2009a). ^{40}Ar-^{39}Ar dating and its geological implication of the Houxianyu boron deposit Liangning province. *Acta Petrologica Sinica, 25*(11), 2752–2762 (in Chinese with English abstract).

Tang, H.-S., Chen, Y.-J., Wu, G., & Yang, T. (2009b). Rare earth element geochemistry of carbonates of Dashiqiao Formation, Liaohe Group, eastern Liaoning province: Implications for Lomagundi event. *Acta Petrologica Sinica, 25*(11), 3075–3093 (in Chinese with English abstract).

Tang, H.-S., Wu, G., & Lai, Y. (2009c). The C-O isotope geochemistry and genesis of the Dashiqiao magnesite deposit, Liaoning province, *NE China. Acta Petrologica Sninca, 25*(2), 455–467 (in Chinese with English abstract).

Tang, H.-S., Chen, Y.-J., Wu, G., & Lai, Y. (2008). The C–O isotope composition of the Liaohe Group, northern Liaoning province and its geologic implications. *Acta Petrologica Sinica, 24*(1), 129–138 (in Chinese with English abstract).

Tang, H.-S., Chen, Y.-J., Wu, G., & Lai, Y. (2011). Paleoproterozoic positive $\delta^{13}C_{carb}$ excursion in northeastern Sino-Korean craton: evidence of the Lomagundi Event. *Gondwana Research, 19*, 471–481.

The ministry of Land and Resources P.R.C. (2001). *Reporting the Land and Resources of China in 2000* (pp. 1–157). Beijing: Geological Publishing House (in Chinese).

Tolbert, G. E., Tremaine, J. W., Melcher, C. C., & Gomes, C. B. (1971). The recently discovered Serra dos Carajas iron depositsNorthern Briazil. *Economic Geology, 66*(7), 895–994.

Trendall, A. F. (2002). The significance of iron-formation in the Precambrian stratigraphic record. *Special Publications International Association of Sedimentology, 33*, 33–66.

Trendall, A. F., & Blockley, J. G. (1970). The iron formations of the Precambrian Hamersley Group, Western Australia with special reference to the crocidolite. *Geological Survey of Western Australia Bulletin 119*, 366 p.

Trendall, A. F., & Morris, R. C. (Eds.). (1983). *Transvaal Supergroup, South Africa, Iron formation: facts and problems* (pp. 471–490). Amsterdam: Elsevier.

Wan, Y.-S., Dong, C.-Y., Wang, W., Xie, H.-Q., & Liu, D.-Y. (2010a). Archean basement and a Paleoproterozoic collision orogen in the Huoqiu Area at the Southeastern marginof North China Craton: Evidence from sensitive high resolution ion micro-probe U–Pb zircon geochronology. *Acta Geologica Sinica, 84*, 91–104.

Wan, Y.-S., Dong, C.-Y., Xie, H.-Q., Wang, S.-J., Song, M.-C., Xu, Z.-Y., et al. (2012). Formation ages of Early Precambrian BIFs in the North China Craton: SHRIMP zircon U–Pb dating. *Acta Petrologica Sinica, 86*(9), 1447–1478 (in Chinese with English abstract).

Wan, Y.-S., Liu, D.-Y., Wang, S.-Y., Zhao, X., Dong, C.-Y., Zhou, H.-Y., et al. (2009). Early Precambrian crustal evolution in the Dengfeng Area, Henan Province (eastern China): Constraints from Geochemistry and SHRIMP U–Pb Zircon Dating. *Acta Geologica Sinica, 83*(7), 982–999.

Wan, Y.-S., Miao, P.-S., Liu, D.-Y., Yang, C.-H., Wang, W., Wang, H.-C., et al. (2010b). Formation ages and source regions of the Paleoproterozoic Gaofa, Hutuo and Dongjiao groups in the Wutai and Dongjiao areas of the North China Craton from SHRIMP U–Pb dating of detrital zircons: Resolution of debates over their stratigraphic relationships. *Chinese Science Bulletin, 55*(13), 1278–1284.

Wan, Y.-S., Song, B., Liu, D.-Y., Wilde, S. A., Wu, J.-S., Shi, Y.-R., et al. (2006). SHRIMP U-Pb zircon geochronology of Palaeoproterozoic metasedimentary rocks in the North China Craton: evidence for a major Late Palaeoproterozoic tectonothermal event. *Precambrian Research, 149*(3–4), 249–271.

Wan, B., Windly, B. F., Xiao, W.-J., Feng, J.-Y., & Zhang, J.-E. (2015). Paleoproterozoic high-pressure metamorphism in the northern North China Craton and implications for the Nuna supercontinent. *Nature Communications, 6*, 8344. doi:10.1038/ncomms9344.

Wang, S.-Q. (1989). The geological features of host rocks and metallogenesis of the Xinghe graphite deposit Nei Mongol. *Mineral Deposit, 8*(1), 85–96 (in Chinese with English abstract).

Wang, X.-W., & Han, X. (1989). A stady on metallogenic regularity of boron deposits in the Ji'an area, Jilin Province. *Jilin Geology, 1*, 72–76 (in Chinese with English abstract).

Wang, C.-Z., Xiao, R.-G., & Liu, J.-D. (2008). Ore-controlling factors and metallogenesis of borate deposits in eastern Liaoning and Southern Jilin. *Mineral Deposits, 27*(6), 727–741 (in Chinese with English abstract).

Wang, C.-Z., Xiao, R.-G., Liu, J.-D., Fei, H.-C., Wang, W.-W., Zhou, H.-C., & Liu, J.-Q. (2006). Ore control role of ultra_magnesium peridotite in Houxianyu boron ore district, Yingkou Liaoning Province. *Mineral Deposits, 25*(6), 683–692 (in Chinese with English abstract).

Wang, F.-R., & Xue, J.-Q. (2010). Geological characteristics and genesis of Beizi crystal graphite deposit in LusanHenan Province. *Mineral Exploration, 1*(3), 248–253 (in Chinese with English abstract).

Wang, C.-L., Konhauser, K. O., & Zhang, L.-C. (2015a). Depositional Environment of the Paleoproterozoic Yuanjiacun Banded Iron Formation in Shanxi Province, China. *Economic Geology, 110*, 1515–1539.

Wang, C.-L., Zhang, L.-C., Dai, Y.-P., & Lan, C.-Y. (2015b). Geochronological and geochemical constraints on the origin of clastic meta-sedimentary rocks associated with the Yuanjiacun BIF from the Lüliang Complex, North China. *Lithos, 212–215*, 231–246.

Wang, C.-L., Zhang, L.-C., Lan, C.-Y., Li, H.-Z., & Huang, H. (2015c). Analysis of sedimentary facies and depositional environment of the Yuanjiachun banded iron formation in the Lvliang area. *Shanxi Province. Acta Petrologica Sinica, 31*(6), 1671–1693 (in Chinese with English abstract).

Wen, D.-J., & Teng, S.-R. (2014). Preliminary discussion on the geochemical prospecting model for the Wengquangou ironoboron deposit in Liaoning Province. *Geology and Resources, 23*(3), 256–260 (in Chinese with English abstract).

Wilde, S. A., Zhao, G.-C., Wang, K.-Y., & Sun, M. (2004). First precise SHRIMP U-Pb zircon ages for the Hutuo Group, Wutaishan: further evidence for the Palaeoproterozoic amalgamation of the North China Craton. *Chinese Science Bulletin, 49*, 83–90.

Windley, B. F. (1980). Evidence for land emergence in the early to middle Precambrian. *Proceeding of the Geologists Association, 91*, 13–23.

Windley, B. F. (1983). Banded iron formation in Proterozoic greenstone belts: Call for further studies. *Precambrian Research, 20*, 585–588.

Windley, B. F. (1984). The evolving continents (pp. 1–399). Chichester: Wiley (second edition).

Wu, F.-Y., Han, R.-H., Yang, J.-H., Wilde, S. A., Zhai, M.-G., & Park, S. C. (2007a). Initial constrains on the timing of granitic magmatism in North Korea using U–Pb zircon geochronology. *Chemical Geology, 238*(3–4), 232–248.

Wu, C.-H., Li, H.-M., Zhong, C.-T., & Chen, Q.-A. (1998). The ages of zircon and rutile (cooling) from khondalite in Huangtuyao, inner Mongolia. *Geological Review, 44*(6), 618–626 (in Chinese with English abstract).

Wu, C.-L., & Qu, Y.-Y. (1994). The geological characteristics and the genesis of the heigoushi graphite deposit, Huanren county Liaoning Provinces. *Nonmetallic Geology, 74*(4), 25–27 (in Chinese with English abstract).

Wu, C.-H., Sun, M., Li, H.-M., Zhao, G.-C., & Xia, X. P. (2006). LA-ICP-MS U-Pb zircon ages of the khondaites from the Wulashan and Jining high-grade terrain in northern margin of the North China Craton: Constraints on sedimentary age of the khondalite. *Acta Petrologica Sinica, 22*(11), 2639–2654 (in Chinese with English abstract).

Wu, Y.-L., Xie, L.-F., Zhang, Y.-L., Fu, M., Ma, J.-C., & Wang, J.-M. (2011). Geological features and prospecting direction of Quanyan crystalline graphite deposit, Ji'an CityJilin Province. *Jilin Geology, 74*(4), 25–27 (in Chinese with English abstract).

Wu, F.-Y., Yang, J.-H., Wilde, S. A., Liu, X.-M., Guo, J.-H., & Zhai, M.-G. (2007b). Detrital zircon U–Pb and Hf isotopic constraints on the crustal evolution of North Korea. *Precambrian Research, 159* (3–4), 155–177.

Xia, X.-H., & Wei, X.-S. (2005). Comprehensive utilization and its geology of zhaobinggou iron/ phosphate deposit in Fengning Hebei Province. *Geology of Chemical Minerals, 27*(1), 1–5 (in Chinese with English abstract).

Xiao, R.-G., Takao, O., Fei, H.-C., & Nomura, M. (2003). Sedimentary-metamorphic boron deposits and their boron isotopic compositions in eastern Liaoning Province. *Geoscience, 17*(2), 137–142 (in Chinese with English abstract).

Xie, S.-W., Wang, S.-J., Xie, H.-Q., Liu, S.-J., Dong, C.-Y., Ma, M.-Z., et al. (2014). SHRIMP U-Pb dating of detrital zircons from the Fenzhishan Group in eastern Shandong Norht China Craton. *Acta Petrologica Sinica, 30*(10), 2989–2998 (in Chinese with English abstract).

Xie, Z., Zhang, H.-T., Chu, X.-Q., Liu, G.-H., Liu, X.-W., & Zhi, Y.-Q. (2015). The regional metallogenic characteritics and prospecting criteria of boron deposit in Kuandian area of Liaoning province. *Chine Mining Magazine, 24*(8), 79–83 (in Chinese with English abstract).

Yang, C.-X. (2008). Zircon SHRIMP U–Pb ages, geochemical characteristics and environmental evolution of the Early Pr ecambrian metamorphic series in the Lushan area, Henan China. *Geological Bulletin of China, 27*(4), 517–533 (in Chinese with English abstract).

Yang, Q.-Y., Santosh, M., & Wada, H. (2014). Graphite mineralization in Paleoproterozoic khondalites of the North China Craton: A carbon isotope study. *Precambrian Research, 255*, 641–652.

Yang, X.-Y., Wang, B.-H., Du, Z.-B., Wang, Q.-C., Wang, Y.-X., Tu, Z.-B., et al. (2012). On the metamorphism of the Huoqiu Group, forming ages and mechanism of BIF and iron deposit in the Huoqiu region, southern margin if North China craton. *Acta Petrologica Sinica, 28*(11), 3476–3496 (in Chinese with English abstract).

Ye, L.-J. (1989). *Phosphorus deposits of China* (pp. 286–311). Beijing: China Science Press (in Chinese).

Young, G. M. (2012). Secular changes at the Earth's surface: evidence from palaeosols, some sedimentary rocks, and palaeoclimatic perturbations of the Proterozoic Eon. *Gondwana Research, 24*(2), 453–467.

Young, G. M. (2013). Precambrian supercontinents, glaciations, atmospheric oxygenation, metazoan evolution and an impact that may have changed the second half of Earth history. *Geoscience Frontiers, 4*, 247–261.

Cao R.-J., & Yuan, X.-L. (2003). Brief history and current status of stromatolite study in China. *Acta Micropalaeontologica Sinica 20* (1), 5–14 (in English with Chinese abstract).

Zhai, M.-G. (2010). Tectonic evolution and metallogenesis of North China Craton. *Mineral Deposits, 29*(1), 24–36 (in Chinese with English abstract).

Zhai, M.-G., Li, T.-S., Peng, P., Hu, B., Liu, F., Zhang, Y.-B., et al. (2010). Precambrian key tectonic events and evolution of the North China Craton. In: T. M. Kusky, M.-G. Zhai, & W.-J. Xiao (Eds.), *The Evolving Continents: Understanding Processes of Continental Growth* (Vol. 338, pp. 235–262). London: Geological Society of London, Special Publication.

Zhai, M.-G., & Santosh, M. (2011). The early Precambrian odyssey of the North China Craton: A synoptic overview. *Gondwana Research, 20*, 6–25.

Zhai, M.-G., & Santosh, M. (2013). Metallogeny in the North China Craton: Secular changes in the evolving Earth. *Gondwana Research, 24*, 275–297.

Zhai, M.-G., Windly, B. F., & Sills, J. D. (1990). Archean gneisses, amphibolites and banded iron formations from the Anshan area of Liaoning Province, NE China: Their geochemistry, metamorphism and petrogenesis. *Precambrian Research, 46*, 195–216.

Zhang, Q.-S. (Ed.). (1984). Geology and metallogeny of the early Precambrian in China (pp. 536). Jilin Peoples' Press, Changchun (in Chinese with English abstract).

Zhang, Q.-S., (1988). *The early crust evolution and mineral deposits in eastern Liaoning Province Peninsula* (pp. 1–213). Beijing: Geological Publishing House (in Chinese with English abstract).

Zhang, Q.-S. (2013). From Neixiang county, Henan Province, the Wuyangshan mining area graphite mine geology and genesis of ore deposits. *Geology of Chemical Minerals, 35*(3), 175–178 (in Chinese with English abstract).

Zhang, Q., & Liu, S. (2014). Ore deposit features and prospecting criteria of crystalline graphite mine in Ji'an area Jilin Province. *Jilin Geology, 33*(3), 60–62 (in Chinese with English abstract).

Zhang, W., Yang, R.-G., Mao, T., Ren, H.-L., Gao, J.-B., & Chen, J.-Y. (2015). Sedimentary environment and mineralization mechanism of the stromatolitic phosphorite in the Ediacaran Dengying Formation, Weng' an County of Guizhou Province China. *Geological Journal of China Universities, 21*(2), 186–195 (in Chinese with English abstract).

Zhang, H.-F., Zhai, M.-G., Santosh, M., Wang, H.-Z., Zhao, L., & Ni, Z.-Y. (2014a). Paleoproterozoic granulites from the Xinghe graphite mine, North China Craton: Geology, zircon U–Pb geochronology and implications for the timing of deformation, mineralization and metamorphism. *Ore Geology Reviews, 63*, 478–497.

Zhang, L.-C., Zhai, M.-G., Wan, Y.-S., Guo, J.-H., Wang, C.-L., & Liu, L. (2012). Study of the Precambrian BIF-iron deposits in the North China Craton: Progresses and questions. *Acta Petrologica Sinica, 28*(11), 3431–3445 (in Chinese with English abstract).

Zhang, T.-Y., Zhang, Z.-L., & Li, J.-Q. (2014b). Summary of research status on regional metamorphic graphite deposit in China. *China Non-metallic Minerals Industry, 111*, 36–38 (in Chinese with English abstract).

Zhao, D.-X. (1982). The age and genesis of phosphorous deposits of the Dongjiao Type. *Scientia Geologica Sinica, 4*, 386–394 (in Chinese with English abstract).

Zhao, Z.-H. (2010). Banded iron formation and great oxidation event. *Earth Science Frontiers, 17*, 1–12 (in Chinese with English abstract).

Zhao, G.-C., Cawood, P. A., Li, S.-Z., Wilde, S. A., Sun, M., Zhang, J., et al. (2012). Amalgamation of the North China Craton: Key issues and discussion. *Prcambrian Research, 222–223*, 55–76.

Zhao, G.-C., Sun, M., Wilde, S. A., & Li, S.-H. (2004). A Paleo-Mesoproterozoic supercontinent: Assembly, growth and breakup. *Earth-Science Reviews, 67*, 91–123.

Zhao, G.-C., Sun, M., Wilde, S. A., & Li, S.-Z. (2005). Late Archean to Paleoproterozoic evolution of the North China Craton: key issues revisited. *Precambrian Research, 136*, 177–202.

Zheng, Y.-F., Xiao, W.-J., & Zhao, G.-C. (2013). Introduction to tectonics of China. *Gondwana Research, 23*, 1189–1206.

Zhu, S.-Q. (1982). The geological features of the stratiform phosphate deposits of China. *Earth Sciences*, *1*:157–166 (in Chinese with English abstract).

Zhu, X.-Q., Tang, H.-S., & Sun, X.-H. (2014). Genesis of banded iron formations: A series of experimental simulations. *Ore Geology Reviews, 63*, 465–469.

Zhu, J.-C., & Zhang, F.-S. (1987). The formation condition of the Precambrian iron ores in Yuanjiachun ore deposit Shanxi Province. *Mineral Deposits, 6*(1), 11–21 (in Chinese with English abstract).

A Genetic Link Between Paleoproterozoic Yuanjiacun BIF and the Great Oxidation Event in North China Craton

13

Changle Wang and Lianchang Zhang

Abstract

The Paleoproterozoic (~2.38–2.21 Ga) Yuanjiacun banded iron formation (BIF), located in Shanxi Province, is a Superior-type BIF in the North China Craton (NCC). This BIF is within a metasedimentary rock succession of the Yuanjiacun Formation in the lower Lüliang Group. The clastic metasediments associated with the BIF are mainly represented by well-bedded meta-pelites (chlorite schists and sericite-chlorite phyllites) and meta-arenites (sericite schists), which have undergone greenschist-facies metamorphism. The Yuanjiacun Formation had been originally deposited in a passive margin setting, most probably on a stable continental shelf. Iron oxide (magnetite and hematite), carbonate, and silicate facies are all present within the iron-rich layers. Integration of petrographic and isotopic evidence indicates that the most likely precursor materials were comprised predominantly of probably hydrous, Fe-silicate gels of stilpnomelane-type composition, amorphous silica gels, and ferrihydrite. The $P_{O_2}-P_{CO_2}$ and pH-Eh fields of the mineral assemblages (and/or their precursors) in the Yuanjiacun BIF indicate anoxic and near-neutral to slightly alkaline conditions for the original depositional environment except for the hematite precursor field (that of $Fe(OH)_3$), which is very small and exists only at relatively high P_{O_2} values. The eastward transition from carbonate- into oxide-facies iron formations is accompanied by a change in mineralogical composition from siderite in the west through magnetite-ankerite and magnetite-stilpnomelane assemblages in the transition zone to magnetite and then hematite in the east. These distinct lateral facies are also observed vertically within the BIF, i.e., the iron mineral assemblage changes up section from siderite through magnetite into hematite-rich iron formation. The oxide-facies BIF formed near shore, whereas carbonate (siderite)- and silicate-facies assemblages formed in deeper waters. Based on detailed analyses of these variations on a basinal scale, the BIF precipitated during a transgressive event within an environment that ranged from deep waters below storm-wave base to relatively shallow waters. The BIF samples display distinctively seawater-like REE + Y profiles that are characterized by positive La and Y anomalies and HREEs enrichment relative to LREEs in Post-Archean Australian shale-normalized diagrams. Consistently positive Eu anomalies are also observed, which are typical of reduced, high-temperature hydrothermal fluids. In addition, slightly negative to positive Ce anomalies, and a large range in ratios of light to heavy REEs and Y/Ho, are present in the oxide-facies BIF. These characteristics, in combination with consistently positive $\delta^{56}Fe$ values, suggest that deposition of the BIF took place along the chemocline

C. Wang (✉) · L. Zhang
Key Laboratory of Mineral Resources, Institute of Geology and Geophysics, Chinese Academy of Sciences, Beijing, 100029, China
e-mail: wcl19875210@126.com

M. Zhai et al. (eds.), *Main Tectonic Events and Metallogeny of the North China Craton*, Springer Geology, DOI 10.1007/978-981-10-1064-4_13

where upwelling of deep, anoxic, iron- and silica-rich hydrothermal fluids mixed with shallower and slightly oxygenated seawater. The ankerite displays highly depleted $\delta^{13}C$ values and the carbonate-rich BIF has a high content of organic carbon, suggesting dissimilatory Fe(III) reduction of a ferric oxyhydroxide precursor during burial of biomass deposited from the water column; that same biomass was likely tied to the original oxidation of dissolved Fe(II). The fact that the more ferric BIF facies formed in shallower waters suggests that river-sourced nutrients would have been minimal, thus limiting primary productivity in the shallow waters and minimizing the organic carbon source necessary for reducing the hematite via dissimilatory Fe(III) reduction. By contrast, in deeper waters more proximal to the hydrothermal vents, nutrients were abundant, and high biomass productivity was coupled to increased carbon burial, leading to the deposition of iron-rich carbonates. The deposition of the Yuanjiacun BIF during the onset of the Great Oxidation Event (GOE; ca. 2.4–2.2 Ga) confirms that deep marine waters during this time period were still episodically ferruginous, but that shallow waters were sufficiently oxygenated that Fe(II) oxidation no longer needed to be tied directly to proximal cyanobacterial activity.

Keywords

BIF facies • Depositional environment • Great oxidation event • Yuanjiacun • North China Craton

13.1 Introduction

Banded iron formations (BIFs) are chemical sedimentary rocks (TFe > 15 %) comprising alternating layers of iron-rich and silica-rich minerals that precipitated predominantly throughout Archean and early Paleoproterozoic (James 1954; Trendall 2002; Bekker et al. 2010). BIFs reach a maximum abundance between 2700 and 2400 million years ago, and then a second prominent peak of BIF deposition occurs at ~1.88 Ga after a significant gap (~2.4–2.1 Ga) of large BIF deposition. It is precisely this time frame which may have witnessed profound changes in the redox states of the oceans and atmosphere, such as the 'Great Oxidation Event' (GOE) (ca. 2.4–2.2 Ga) (Holland 2006). The deposition of BIFs has thereby been linked to significant compositional changes in the Earth's atmosphere and hydrosphere, and, by inference, the diversification of the biosphere (Konhauser et al. 2009).

BIFs can be divided into the Algoma and Superior types on the basis of the sedimentary and tectonic environments in which they were deposited (Gross 1980, 1996). The former are relatively small in size and thickness, and are often formed in arc/back-arc basins or intracratonic rift zones with a close affiliation with mafic/ultramafic to felsic volcanic rocks or volcaniclastic rocks and greywackes, whereas the latter, which are associated with clastic-carbonate rocks, are larger and their deposition occurred in relatively shallow-marine conditions under transgressing seas, perhaps on the continental shelves of passive tectonic margins or in intracratonic basins.

BIFs and BIF-hosted high-grade iron ore deposits are the principal source of iron for the global steel industry (Clout and Simonson 2005). Given their economic importance, BIFs have been extensively studied, but many aspects of their origin still remain enigmatic. In China, BIFs occur extensively throughout the Archean units of the North China Craton (NCC), and six major iron metallogenic provinces have been recognized: (1) Anshan–Benxi in the northeast; (2) Eastern Hebei in the north; (3) Wutai-Lüliang in the central part; (4) Xuchang-Wuyang-Huoqiu in the south; (5) Wuchuan-Guyang in the west; and (6) Western Shandong in the east. BIFs within these metallogenic provinces account for more than 60 % of iron ore production in China. Many researchers have focused primarily on their geology, geochemistry, and tectonic settings (e.g., Zhai and Windley 1990; Shen et al. 2009; Zhang et al. 2011, 2012a; Dai et al. 2012; Wan et al. 2012; Zhai and Santosh 2013). Overall, the BIFs in the NCC have five distinctive characteristics (1) most are Archean in age, with a peak in the Neoarchean (2.55–2.50 Ga); (2) they commonly occur in successions of supracrustal rocks, mostly in close association with mafic meta-volcanic rocks; (3) they have generally undergone amphibolite-facies metamorphism, even up to granulite facies, and display strong deformational features; (4) iron oxide, quartz, and various silicate minerals are dominant in nearly all of the BIFs, accompanied by rare carbonates and

sulfides; and (5) they generally formed in association with island arc or back-arc basins (Zhang et al. 2012b).

The Lüliang area is located in the western part of Shanxi Province, where large amounts of BIFs are exposed, including Jianshan, Hugushan, and Yuanjiacun BIFs. Previous work (Shen et al. 1982; Tian et al. 1986; Zhu and Zhang 1987; Yao 1993) on the geological characteristics of BIFs suggested that BIFs occur mainly in the transitional horizon from clastic deposits to chemical sediments (Shen 1998). These BIFs are thus considered as potential examples of Superior-type BIFs in China. In addition, based on detailed geochronological studies of the overlying meta-volcanic rocks and interbedded clastic metasedimentary rocks (Liu et al. 2012; Liu et al. 2013; Wang et al. 2015a), the depositional age of the Yuanjiacun BIF can be constrained to ~2.38–2.21 Ga, which contrasts with the general paucity of giant BIF deposition worldwide during the time interval of 2.4–2.0 Ga (Isley and Abbott 1999; Bekker et al. 2010). Therefore, this terrane offers the possibility to directly study the geochemical characteristics of BIF that formed during the pronounced rise of atmospheric oxygen between 2.4 and 2.2 Ga (Bekker et al. 2004; Hannah et al. 2004; Konhauser et al. 2011a).

13.2 Geological Background

The NCC is one of the oldest cratonic blocks in the world, containing rocks as old as ~3.85 Ga (Liu et al. 2008). The NCC consists of Archean to Paleoproterozoic basement overlain by Mesoproterozoic to Cenozoic cover. The basement of the NCC can be divided into the eastern and western blocks and the intervening Trans-North China Orogen (TNCO; Zhao et al. 2005). Basement rocks of the orogen consist of Neoarchean to Paleoproterozoic Tonalite-Trondhjemite-Granite (TTG) gneisses, supracrustal rocks (metamorphosed sedimentary and volcanic rocks), syn- to post-tectonic granites, and mafic dikes (Liu et al. 2011; Zhao and Zhai 2013). The Lüliang Complex is situated in the western portion of the TNCO, where large amounts of Paleoproterozoic supracrustal rocks and granitoid intrusions are exposed. These supracrustal rock sequences can be divided into four main groups, consisting of, from bottom to top, the Jiehekou, Lüliang, Yejishan, and Heichashan or Lanhe groups (Fig. 13.1). These sequences were intruded by the 2182–2151 Ma Guandishan-Chijianling TTG gneiss and the ~1800 Ma Luyashan charnockite (Zhao et al. 2008).

The Lüliang Group, occurring as the west wing of an overturned anticline, strikes roughly S-N and dips to the E. It is distributed only in the Jinzhouyu area and consists predominantly of greenschist to amphibolite-facies metamorphosed sedimentary rocks with BIFs in the lower sequence and volcanic rocks in the upper sequence (Liu et al. 2012). Regionally, the Lüliang Group is not in direct contact with the Jiehekou Group, but both the two groups are tectonically overlain by the Yejishan and Heichashan groups. Major lithological assemblages in the Lüliang Group include amphibolites, fine-grained felsic gneisses, schists, BIFs, and tremolite-actinolite marbles. The Lüliang Group is divided into four major units: the lower Yuanjiacun Formation, the middle Peijiazhuang and Jinzhouyu formations, and the upper Dujiagou Formation.

Yu et al. (1997a) obtained single-grain zircon U–Pb ages of 2051 ± 68 and 2099 ± 41 Ma for mafic meta-volcanic rocks in the Jinzhouyu Formation and meta-rhyolite in the Dujiagou Formation, respectively. In addition, three radiometric ages were reported by Geng et al. (2000, 2008), including zircon U–Pb ages of 2360 ± 95 Ma for interlayered intermediate-felsic volcanic tuff in the Jinzhouyu Formation and 2175 Ma for meta-rhyolite in the Dujiagou Formation, and a whole-rock Sm–Nd isochron age of 2351 ± 56 Ma for mafic meta-volcanic rocks in the Jinzhouyu Formation. Liu et al. (2012) reported a LA-ICP-MS U–Pb zircon age of 2213 ± 47 Ma for a mafic volcanic rock within the Jinzhouyu Formation. Most recently, Liu et al. (2014) obtained the youngest detrital zircon age of ~2205 Ma for metasedimentary rocks in the upper part of the Yuanjiacun Formation, and crystallization ages of 2209–2178 Ma for mafic meta-volcanic rocks of the Jinzhouyu and Dujiagou formations. Moreover, Wang et al. (2015a) conducted a similar geochronological study on the metasedimentary rocks intercalated with the Yuanjiacun BIF and obtained the youngest zircon age (n = 5) of 2384 ± 45 Ma. Considering that there exists a potential depositional gap characterized by a disconformity between the Peijiazhuang and Jinzhouyu formations (Tian et al. 1986; Yu et al. 1997a), we suggest that the age of the Yuanjiacun Formation is thus constrained to the Paleoproterozoic (~2.38–2.21 Ga).

13.3 Geology and Stratigraphy of the Yuanjiacun BIF

Exposed strata in the Yuanjiacun area include Paleoproterozoic metamorphosed sedimentary rocks of the Yuanjiacun Formation of the Lüliang Group and Cambrian–Ordovician carbonate strata (Fig. 13.2a). The Yuanjiacun BIF and associated metasedimentary rocks have undergone lower greenschist-facies metamorphism (Tian et al. 1986; Yu et al. 1997a). The BIF is commonly interbedded with chlorite schist, and contacts between them are sharp and well defined with no sign of grading, erosion, or intermixing.

The Yuanjiacun BIF is distributed in a NNE-NEE orientation, extending 20.5 km in length and 5.8 km in width. Figure 13.2a, b only depict the middle part of this long belt where the BIF is well developed and exposed. It strikes N–S

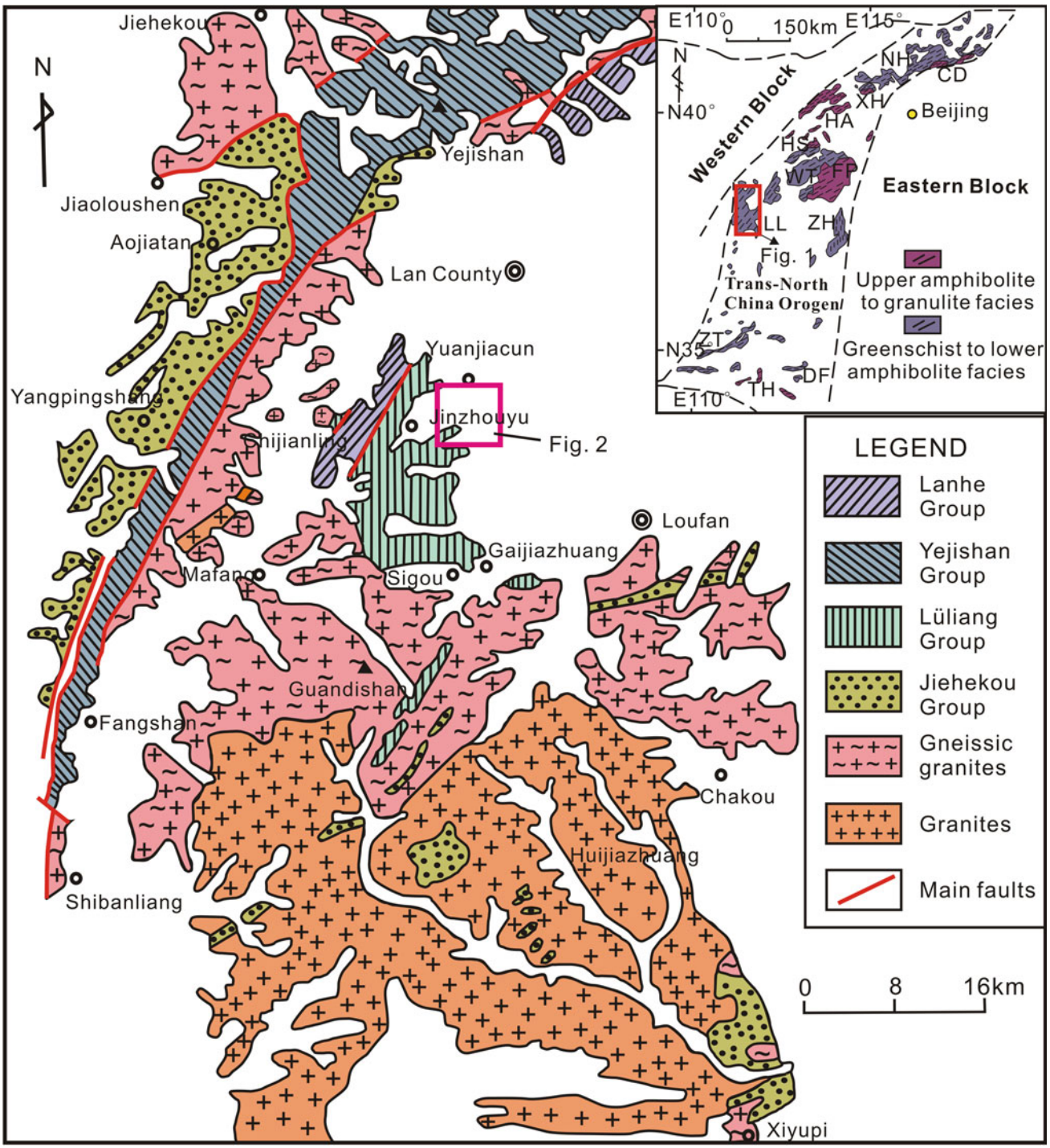

Fig. 13.1 Geologic sketch of the Paleoproterozoic Lüliang Complex (modified from Wan et al. 2000). *Insert* map shows location of the Lüliang Complex in the North China Craton (revised after Zhao et al. 2005). Abbreviations for metamorphic complexes: *CD* Chengde; *DF* Dengfeng; *FP* Fuping; *HA* Huai'an; *HS* Hengshan; *LL* Lüliang; *NH* Northern Hebei; *TH* Taihua; *WT* Wutai; *XH* Xuanhua; *ZH* Zanhuang; *ZT* Zhongtiao

and N–NE, dips steeply SE or E at 70–80°. Individual layers of the BIF vary commonly from less than 1 m to tens of meters in the section. Three distinctive sedimentary facies are recognized in the Yuanjiacun BIF on the basis of predominant iron minerals within the iron-rich layers: (1) oxide facies, composed of magnetite and hematite; (2) silicate facies, containing different iron silicate minerals due to varying metamorphic conditions; and (3) carbonate

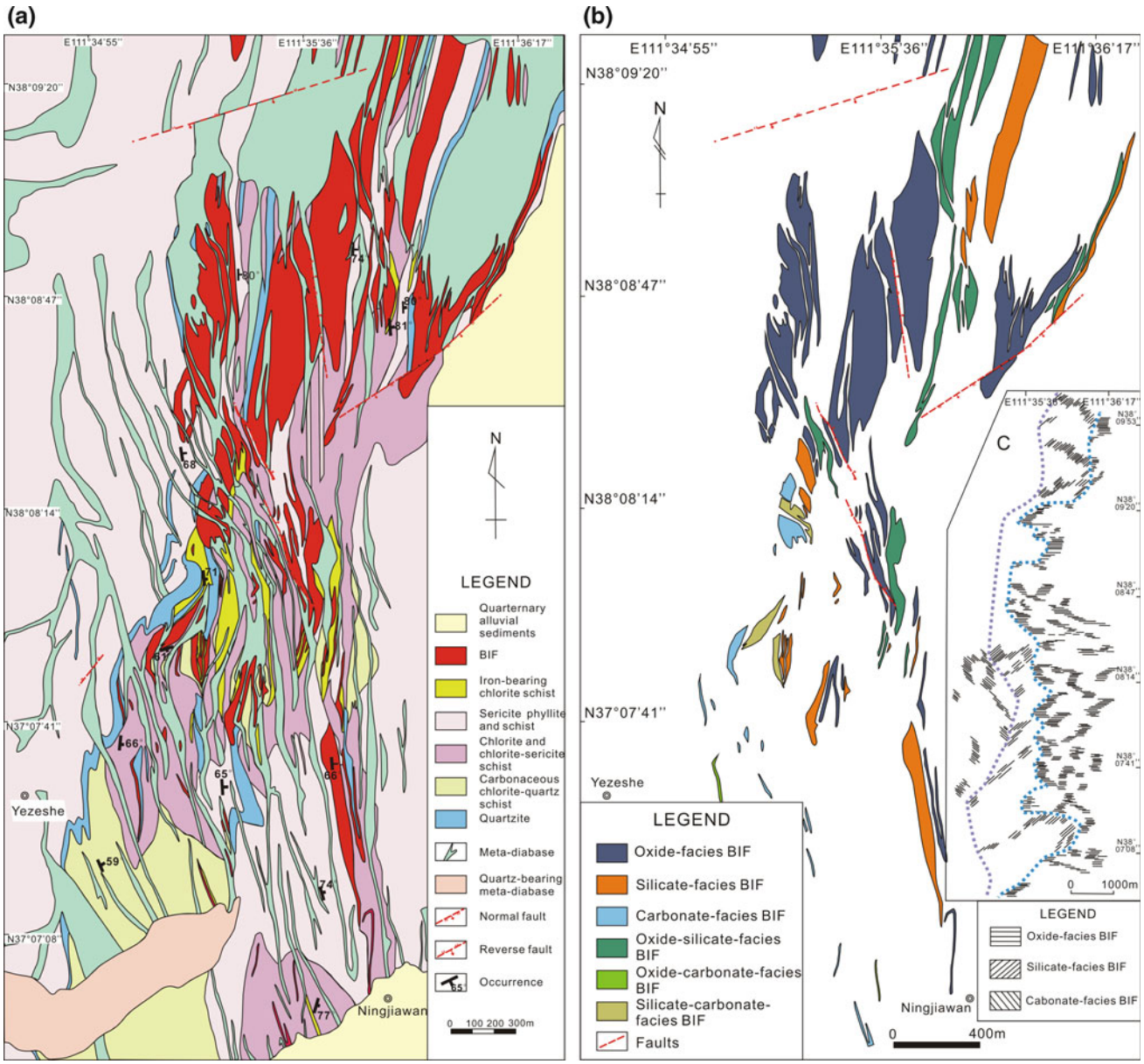

Fig. 13.2 **a** Geologic map of the Yuanjiacun BIF showing distribution of the BIF and associated clastic and chemical metasedimentary rocks (modified from Yao 1993). **b** Geologic sketch showing the distribution of various sedimentary facies of the BIF (modified from Tian et al. 1986); **c** Palinspastic map of sedimentary facies in the BIF (modified from Tian et al. 1986). Scope of this map is restricted at both ends (longitude and latitude) by exploration data for prospecting line IV. To highlight the distribution regularity, we merge the transition facies between oxide and silicate facies into oxide facies, and merge the transition facies (oxide-carbonate facies and silicate-carbonate facies) into carbonate facies

facies, in which the most prominent carbonate minerals are siderite and ankerite. As the predominant constituent (>60 vol%) of the Yuanjiacun BIF, the oxide-facies BIF occurs mainly in the north of the study area (Fig. 13.2b), and is here subdivided into two subfacies: hematite (>24 vol%) and magnetite (>36 vol%) iron formations. The silicate-facies BIF is scattered throughout the region and makes up ca. 30 vol% of the total BIF, whereas the minor carbonate-facies BIF (<10 vol%) is found commonly in the south. In addition to these three main BIF facies, there are transitional facies. Figure 13.2c, restored based on features of the regional tectonic framework (Tian et al. 1986), depicts the original distribution of various sedimentary facies in the Yuanjiacun area. The Yuanjiacun BIF is distributed in a N–S direction with an eastward transition from carbonate facies through silicate facies to oxide facies.

Overall, the Yuanjiacun Formation in the study area is a 1.5-km-thick succession of metasedimentary rocks

(Shen et al. 1982). Previous detailed field measurement of stratigraphic sections and compilation of drill hole data for several localities have spanned over twenty years (1960–1984). In conjunction with laboratory determinations and analyses and our current investigation, a newly synthesized stratigraphic sequence of the BIF has been constructed. From the base upwards, this sequence is divided into three transgressive-regressive cycles (Fig. 13.3). Within each cycle, the major lithologies commence with coarse- to medium-grained clastic sedimentary rocks, i.e., weakly

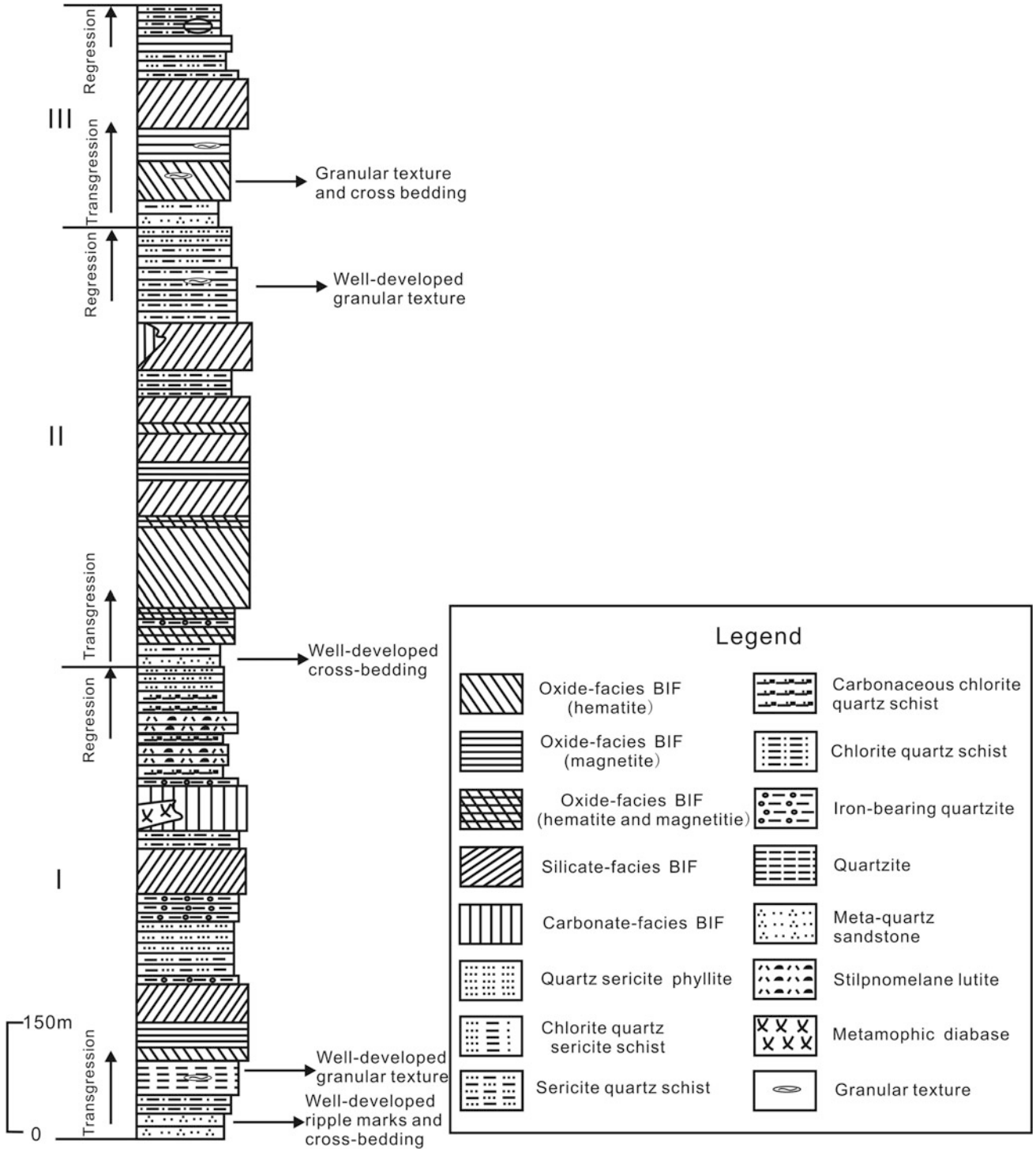

Fig. 13.3 Stratigraphic column of the Yuanjiacun Formation in the Yuanjiacun area, showing three transgressive and regressive cycles (modified after Shen et al. 1982)

metamorphosed quartz sandstone or arkose, where ripple marks and trough cross-beddings are well developed, indicating deposition above wave base. Stratigraphically upwards, the grain size of these units becomes finer, where the metasedimentary rocks consist mainly of fine-grained meta-pelite (quartz-sericite phyllite and chlorite schist), which then grade upward into chemical sedimentary rocks represented by iron-bearing quartzite and the BIF with chlorite schist and lesser amounts of interlayered quartz-sericite schist. In particular, the quartz grains of these schists are very small (<0.05 mm) relative to those of metasedimentary rocks in other units (>0.5 mm; Shen et al. 1982). The chlorite schist overlying the BIF underlies an upward-coarsening succession of interlaminated chlorite schist, quartz-sericite phyllite, and sericite schist. A conformable but sharp contact between the BIF and these metasediments is common.

13.4 Petrography of the BIF Facies

13.4.1 Oxide-Facies BIF

Hematite-rich units: On a microscopic scale, layering in the Yuanjiacun iron formation is diffuse, and, in the hematite-rich oxide facies, consists of alternating quartz- and hematite-rich microbands (0.05–7 mm thick). The individual microbands are generally straight and continuous, although deformation is present locally. Contacts between these two types of microbands are commonly sharp (Fig. 13.4a). Typically, the hematite-rich layers contain a high concentration of small (0.02–0.1 mm) crystals of microplaty hematite that are interconnected to form irregular aggregates intergrown with quartz. The quartz-rich layers are dominated by euhedral to subhedral quartz crystals (0.2 mm), and subordinate fine-grained, dusty hematite (<2 μm). The dusty hematite crystals form individual grains located at the triple point of quartz grains (Fig. 13.4b), or larger isolated tabular crystals truncating quartz grains (Fig. 13.4c). In addition, micrometer-sized hematite inclusions occur in places within quartz crystals (Fig. 13.4b). Specularite (metamorphic recrystallization product of hematite) is present locally, parallel to or truncating the layering.

Some megascopic hematite crystals (granules?) (0.1–1 mm in diameter) are observed locally in the BIF, iron-bearing quartzite, and/or chlorite schist (Fig. 13.4d). These crystals occur parallel to the layering or schistosity as defined by chlorite. Tian et al. (1986) and Zhu et al. (1988) recognized oolitic and granular iron oxides (hematite and magnetite), 0.2–8 mm in diameter, in some outcrops, including close-packed and lithified mass of ooliths or granules that constitute some iron-rich layers of the BIF. The interstices of these masses are typically filled by chert, but generally with a lower iron content. Cross-bedding and graded bedding are present in some of these BIF samples. Overall, such features are similar to those typically found in granular iron formation (GIF). It should be also noted that martite (pseudomorphs of magnetite after hematite) commonly forms individual crystals within the hematite-rich microbands. In some cases, martite, together with quartz, constitute microbands that alternate with hematite-rich microbands (Wang et al. 2015c).

Magnetite-rich units: Textures and sedimentary structures in the magnetite-rich oxide facies are very similar to those in the hematite-rich units. Magnetite microbands alternate with quartz microbands, and in places quartz microbands contain very fine-grained, magnetite-rich laminae (Fig. 13.4e). Magnetite occurs in two forms (1) subhedral grains interconnected to form irregular aggregates, and (2) very-fine-grained anhedral to subhedral grains intergrown with mosaic quartz in the iron-poor microbands. Euhedral quartz grains are locally truncated by disseminated, coarse-grained magnetite crystals (Fig. 13.4f). Sedimentary features such as tabular cross-bedding (Fig. 13.4g, i) is rare in the magnetite-rich units. In places, 1–2 mm euhedral magnetite crystals are aligned parallel to the layering (Fig. 13.4h).

13.4.2 Silicate-Facies BIF

The mineralogy of the silicate-facies BIF varies both in content and proportion due to the presence of various iron-bearing silicate minerals including stilpnomelane, minnesotaite, chlorite, cummingtonite, and actinolite. Pure magnetite and quartz layers are rare, but locally the quartz layers contain discontinuous laminations composed of fine-grained euhedral magnetite. Large amounts of ankerite occur in the silicate-carbonate- and oxide-carbonate-facies iron formations. It is noteworthy that some chert pods are found in these types of BIF (Fig. 13.5a), having a flat and lenticular form with internal microbanding. The ends of the pods are not sharply terminated but diffuse into the laminations, as is characteristic of the iron oxide-rich facies. Compared with chert pods in the Hamersley and Kuruman BIFs that have rounded terminations (e.g., Trendall and Blockley 1970; Beukes and Gutzmer 2008), the chert pods in the Yuanjiacun BIF pinch out as sharp terminations, which was likely attributed to postdepositional deformation. Ankerite is abundant in compacted silica-rich microbands that occur outside of the pods (Fig. 13.5b, c).

Stilpnomelane is the most common iron silicate within the BIF. This mineral ranges in length from 0.05 to 0.1 mm and has a width of 0.01 mm and forms thin, continuous laminations (Fig. 13.5d) or very-fine-grained sheaves and needles in iron-poor microbands (Fig. 13.5e). It is closely

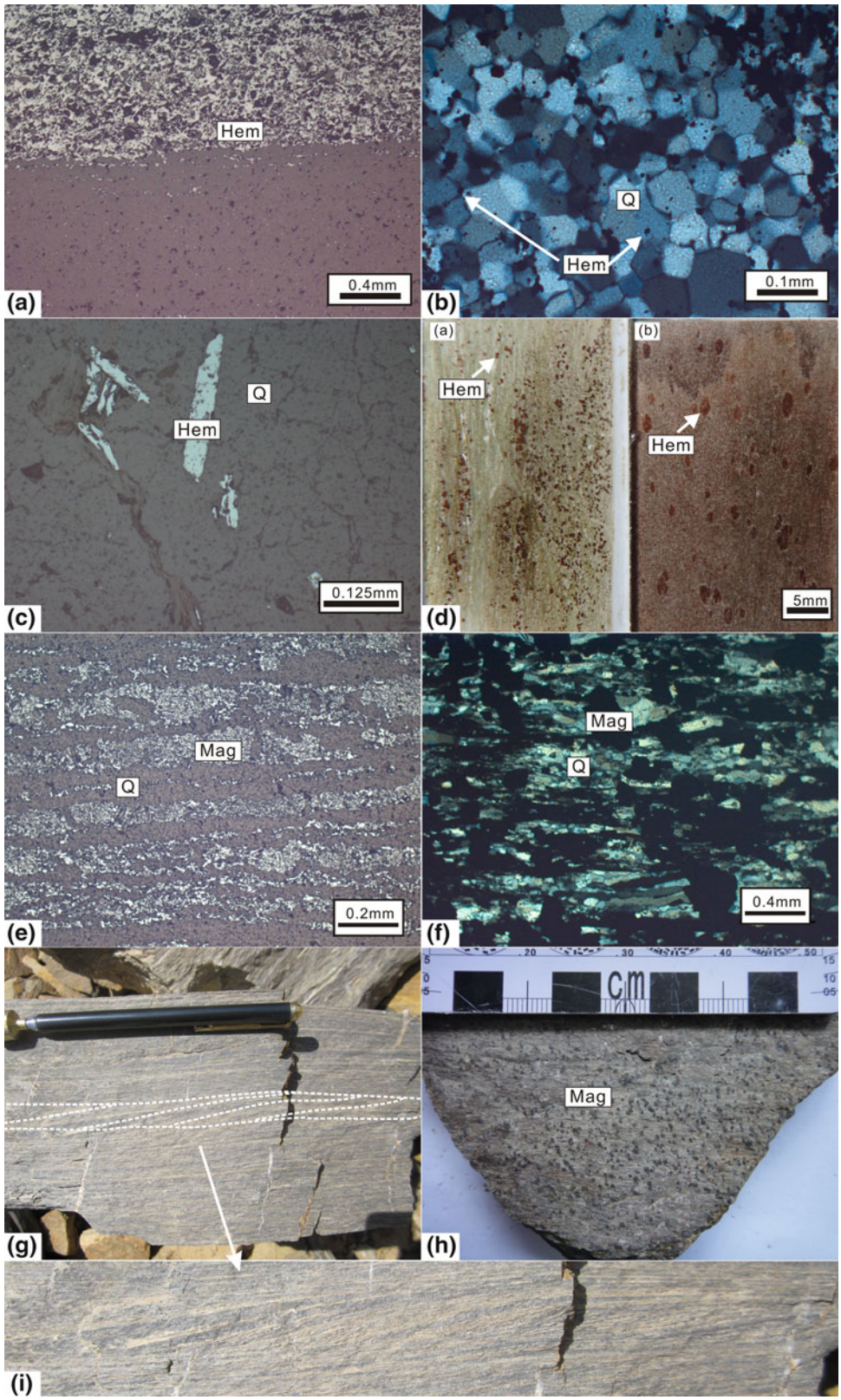

Fig. 13.4 Photomicrographs and field photos showing representative textures and petrographic relationships among main mineral phases in the oxide-facies BIF (Wang et al. 2015b). **a** Quartz-rich microbands with scattered crystals of dusty hematite (*Hem*) (2 μm in size) and contact between the quartz- and iron-rich microbands that are commonly sharp (reflected light). **b** Small hematite grains found either within or located at triple junctions of quartz (*Q*) crystals (crossed polarizers). **c** Quartz-rich microband with microplaty hematite crystals cutting quartz grains (reflected light). **d** Photographs of chlorite schist in two thin sections showing hematite granules (?) occurring parallel to schistosity defined by chlorite. **e** Magnetite (*Mag*) crystals forming either irregular aggregates in iron-rich microbands or small dispersed grains in quartz-rich microbands (reflected light). **f** Large euhedral and isolated magnetite crystals truncating the banding (crossed polarizers). **g** Tabular cross-bedding within the BIF (enhanced with *white dashed lines*) with small dip angles; pen is 15.5 cm long. **h** Macroscopic magnetite crystals (1–2 mm in size) occurring parallel to banding. **i** Close-up view of cross-bedding shown in **g**

associated with quartz, magnetite, and ankerite. Detailed examination of quartz microbands reveals the presence of numerous minute and spherical structures or granules (Fig. 13.6a). The granules are remarkably uniform in size, typically ~0.5 mm in diameter (range 0.4–1.0 mm). They are composed mainly of stilpnomelane, with some quartz and magnetite inclusions, but nearly all have been completely replaced by carbonate minerals and only

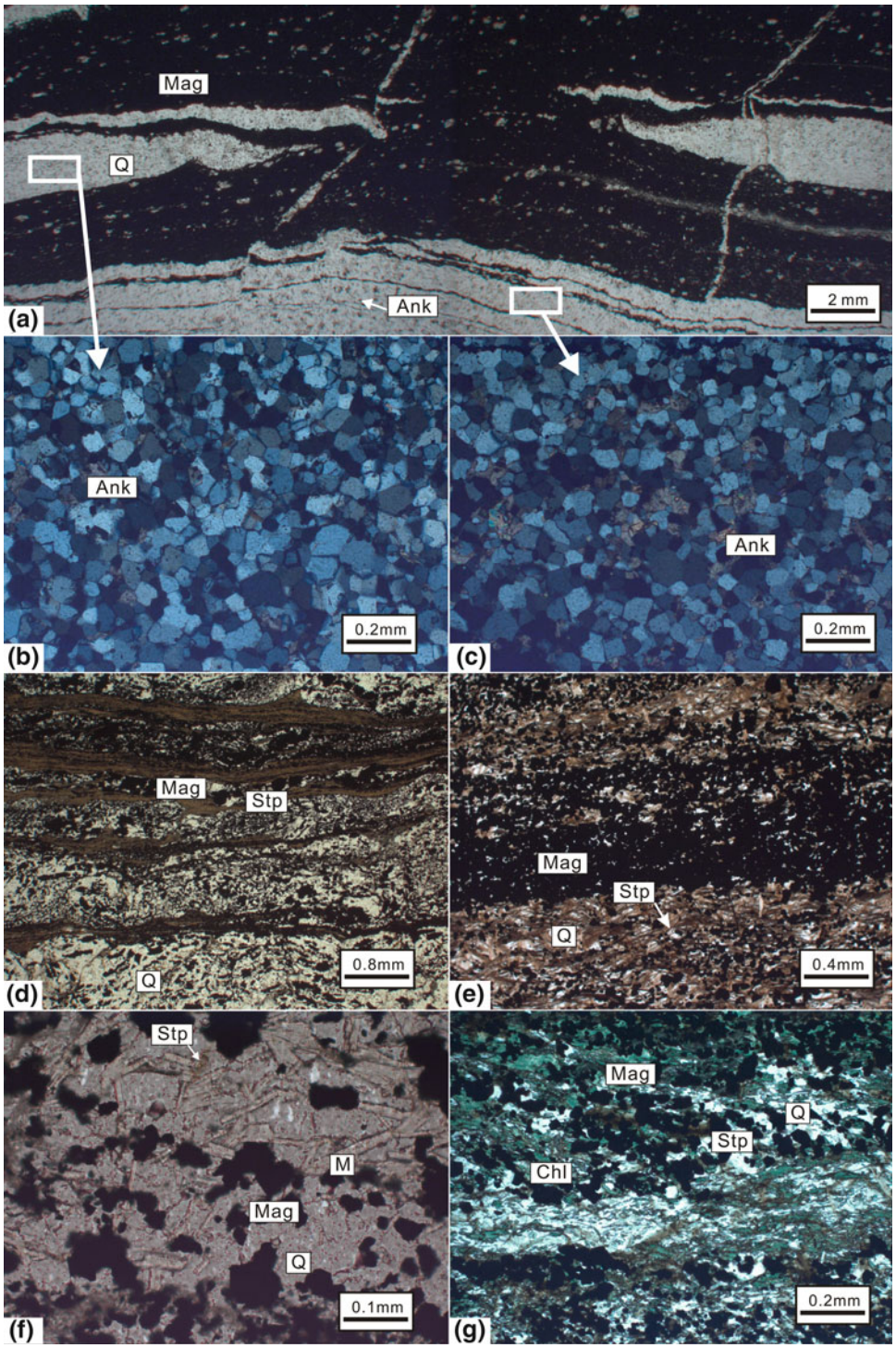

Fig. 13.5 Photomicrographs showing typical textures of chert pods in the BIF (Wang et al. 2015b). **a** Discontinuous chert pods in iron-rich mesobands containing finely laminated magnetite (*Mag*) (plane-polarized light). **b** Very small amount of ankerite (*Ank*) occurs within the chert pods (crossed polarizers). **c** Large numbers of ankerite grains occur in quartz-rich microbands outside of chert pods (crossed polarizers). Photomicrographs under plane-polarized light showing representative textures of stilpnomelane (*Stp*), ferro-talc-minnesotaite (*M*), and chlorite (*Chl*) in the silicate-facies iron formation. **d** Stilpnomelane microbands truncating quartz (*Q*) and magnetite microbands. **e** Stilpnomelane bundles intergrown with quartz and magnetite, occurring along edges of subhedral quartz crystals. **f** Minnesotaite intergrown with magnetite and quartz in quartz bands, and tabular stilpnomelane replaced by minnesotaite. **g** Chlorite intergrown with magnetite and quartz, occurring either as microbands comprising mainly magnetite and stilpnomelane or scattered anhedral crystals in quartz bands; *note* tabular stilpnomelane is locally replaced by chlorite

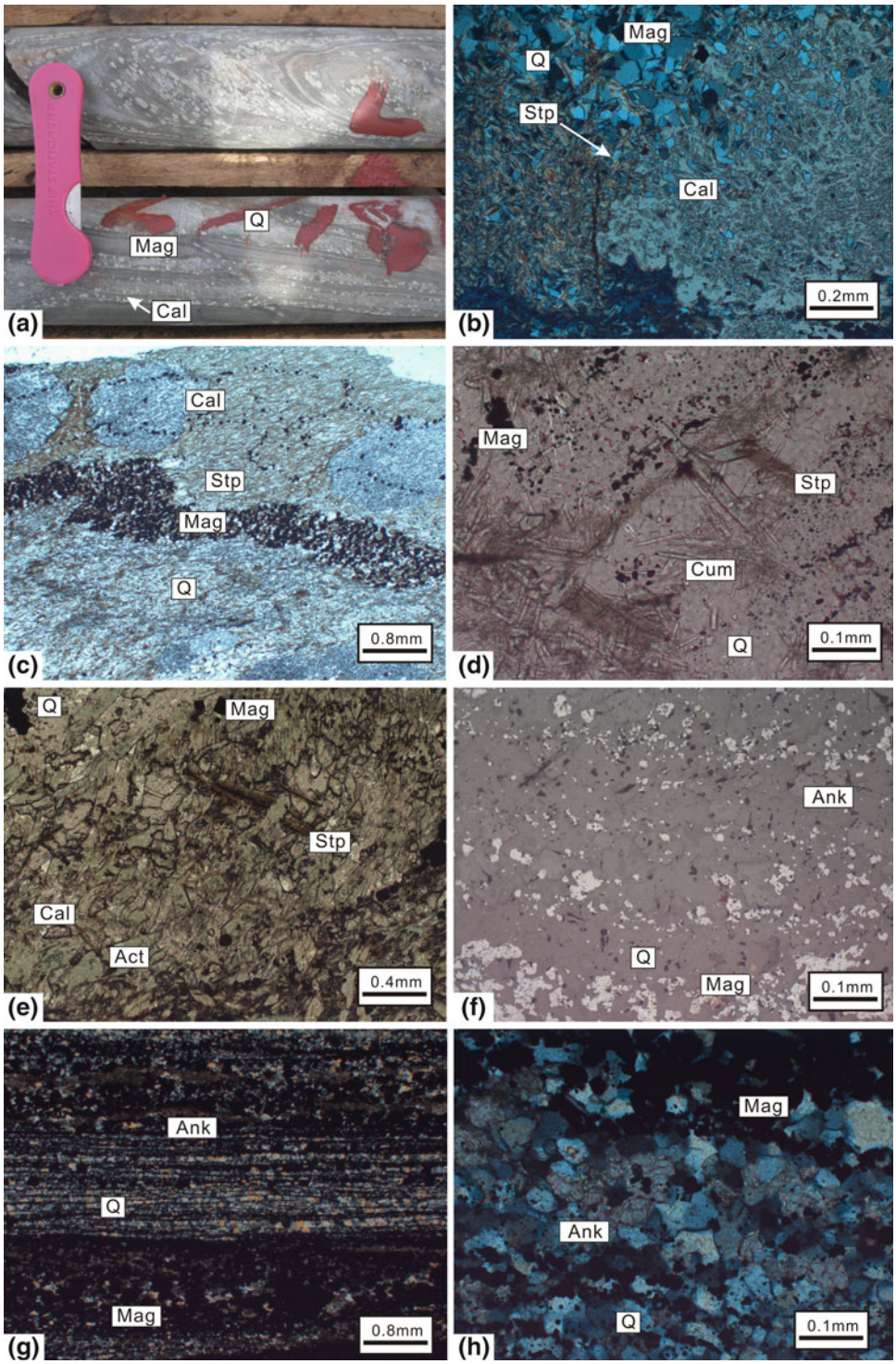

Fig. 13.6 Photomicrographs and field photos of stilpnomelane (*Stp*) granules found locally in quartz-rich microbands, nearly all stilpnomelane granules are replaced by carbonate (*Cal*) (Wang et al. 2015b). **a** Calcite grains of relatively uniform size, typically ~1 mm in diameter, along edges of quartz microbands. **b** Relicts of stilpnomelane preserved at edges of calcite grains, and stilpnomelane granules containing quartz (*Q*) and magnetite (*Mag*) inclusions (crossed polarizers); *note* tabular stilpnomelane is replaced by carbonate. **c** Finely laminated magnetite penetrating stilpnomelane granules (plane-polarized light). Photomicrographs showing representative textures of cummingtonite (*Cum*), actinolite (*Act*), and ankerite (*Ank*) in the silicate-facies iron formation. **d** Cummingtonite bundles intergrown with magnetite and quartz, and replacing early stilpnomelane (plane-polarized light). **e** Cummingtonite bundles truncating the banding (crossed polarizers). **f** Euhedral actinolite intergrown with magnetite, quartz, and calcite, and replacing early stilpnomelane (plane-polarized light). **g** Subhedral ankerite evenly distributed in quartz microbands; subhedral-euhedral magnetite crystals occur along edges of ankerite (reflected light). **h** Microbands comprising anhedral aggregates of anhedral ankerite and magnetite alternating with quartz microbands (crossed polarizers). **i** Ankerite forming euhedral rhomboids with edges commonly displaying corrosion, and containing magnetite inclusions (crossed polarizers)

stilpnomelane relicts are preserved at the edge of these granules (Fig. 13.6b). The granules are individually surrounded by quartz (Fig. 13.6a). Similar occurrences have been reported in the Brockman BIF, Western Australia (Rasmussen et al. 2013a); the only difference being the size of silicate granules in the Yuanjiacun BIF is substantially larger than that of the microgranules (5–20 μm) in the Brockman BIF. They argued that the microgranular texture developed due to clumping of amorphous mud (the precursor mineral of stilpnomelane), forming silt-sized floccules. Those microgranules were resedimented by density currents and deposited in lamina sets as the precursor sediments to the BIF (Rasmussen et al. 2013a). In our samples, some fine-grained magnetite laminations transect these granules (Fig. 13.6c), indicating their secondary origin with regards to the granules.

Minnesotaite is generally not as abundant as stilpnomelane. It occurs as fine- to medium-grained needles (0.05–0.2 mm in length) scattered within quartz microbands (Fig. 13.5f), and typically coexists with quartz, magnetite, and stilpnomelane, and locally cuts the fine-grained stilpnomelane sheaves (Fig. 13.5f). Chlorite is much more common than minnesotaite, displays a tabular to platy habit, and occurs with magnetite in thin laminations that alternate with quartz microbands that contain lesser amounts of chlorite. Chlorite and relics of stilpnomelane coexist in places (Fig. 13.5g).

Amphibole is a minor constituent of the silicate-facies BIF, and commonly coexists with quartz, magnetite, and calcite. In places, amphibole grains cut stilpnomelane. Cummingtonite occurs as fine-grained sprays and patches (Fig. 13.6d), as well as fine needles that truncate the layering. Euhedral actinolite grains form clustered arrangements in quartz microbands (Fig. 13.6e).

Ankerite is present mainly as angular, rhomb-shaped grains (0.05 mm diameter) that are evenly distributed in quartz-rich microbands (Fig. 13.6f). Less common are small ankerite aggregates, which are generally rounded and range from 0.01 to 0.02 mm in diameter (Fig. 13.6g). The ankerite is locally overgrown by fine-grained magnetite crystals (Fig. 13.6f), and also contains inclusions of magnetite (Fig. 13.6h). Veins composed of remobilized ankerite grains in places truncate the microbanding.

13.4.3 Carbonate-Facies BIF

The carbonate-facies BIF is only found in the southern part of the Yuanjiacun area. Toward the surface, this lithology changes to limonite and goethite because of strong weathering. As a consequence, fresh outcrops of carbonate-facies BIF are virtually absent, and the only information comes from previous studies (Tian et al. 1986; Zhu et al. 1988). The carbonate-facies BIF is interlayered with carbonaceous chlorite schist and stilpnomelane lutite beds, having a thickness from 5 to 20 m. It typically consists of light gray to brownish gray quartz microbands that alternate between darker brownish gray, carbonate-rich (siderite and ankerite) microbands. Iron oxide minerals are generally absent, but organic matter and pyrite are common trace constituents. The siderite crystals form as subhedral rhomboids, locally showing the development of weathered rims.

13.5 Mineral Paragenesis and Evolution

13.5.1 Paragenetic Sequence

Petrographic and geochemical data presented here for the Yuanjiacun BIF allow us to establish different generations of mineral formation during diagenesis and metamorphism. As in most BIFs, microcrystalline quartz is the most abundant mineral. This is not surprising, given that silica concentrations in the Precambrian oceans would have been much higher ($\sim$2 mM) than today ($\sim$0.1 mM), due to the absence of silica-secreting organisms before the Phanerozoic (Siever 1992; Konhauser et al. 2007). Silica precipitation in the Precambrian oceans could have been induced by evaporative or temperature-induced supersaturation (Garrels 1987; Posth et al. 2008) or coprecipitation with iron minerals (Ewers 1983; Konhauser et al. 2007). In the case of the latter, Fischer and Knoll (2009) proposed a model whereby dissolved silica ($Si(OH)_4$) was absorbed onto ferric oxyhydroxides, such as ferrihydrite ($Fe(OH)_3$), to form a siliceous ferric hydroxide precursor that sank to the sea floor, together with organic matter. At the seafloor, oxidation of that organic matter coupled to dissimilatory Fe(III) reduction (DIR), could have liberated some iron, leading to the formation of iron-poor layers (Nealson and Myers 1990) (reaction 13.1).

$$CH_3COO^- + 8Fe(OH)_3 \rightarrow 8Fe^{2+} + 2HCO_3^- + 15OH^- + 5H_2O \quad (13.1)$$

During burial diagenesis, there also may have been vertical escape of silica, which re-precipitated at sediment-water interface, yielding BIF with a higher silica content (Trendall and Blockley 1970). Alternatively, Krapež et al. (2003) and Pickard et al. (2004) have suggested that all chert in BIF is the siliceous equivalent of modern-day seafloor hardgrounds, in which silica replaced precursor sediment at or below the sediment-water interface. The presence of three-dimensional and micro-scale lenticularity of chert and relics of precursor sediment within lamina sets and discontinuous bands, as well as erosion surfaces on bedded cherts, shows that chert has a replacement origin and formed during early diagenesis, prior to compaction. In either case, high seawater

concentrations of silica are needed for incorporation into the original sediment to yield the high SiO_2 observed in the Yuanjiacun BIF.

Hematite displays textural diversity, including anhedral aggregates, xenomorphic, and microplaty grains (Fig. 13.4a, b). In iron-rich marine environments, the biotic or abiotic oxidation of dissolved Fe(II) leads to the production of Fe (III) oxyhydroxides (Konhauser et al. 2011b). These poorly crystalline Fe phases (e.g., ferrihydrite) can transform into hematite (via dehydration), and goethite and lepidocrocite (through Fe(II)-catalyzed transformation), depending on pH and solution chemistry (Posth et al. 2014). As previously observed by Schwertmann and Murad (1983), crystallization of ferrihydrite at pH 7–8 is the major pathway for hematite formation. The euhedral hematite crystals in the Yuanjiacun BIF (Fig. 13.4c) are interpreted as having formed from the low-grade metamorphic crystallization of smaller hematite grains. In general, the preservation of hematite-rich units represents sediment buried in which molar Fe(III):C_{org} ratios far exceeded the 4:1 molar ratio associated with DIR, because only a small amount of organic carbon, along with sufficient primary $Fe(OH)_3$, was required for the magnetite formation during diagenesis (Konhauser et al. 2005). Consequently, either (1) all of the biomass was oxidized, leaving behind a residue of ferric oxyhydroxide (Konhauser et al. 2005); or (2) there was minimal burial of organic carbon when the precursor ferric oxyhydroxide phases precipitated (Beukes et al. 1990). Based on the low TOC content in the hematite-rich unit (<0.1 wt%, Wang et al. 2015b), either option is possible.

Two main types of magnetite are found in the Yuanjiacun BIF, namely minute subhedral crystals that form aggregates or massive monomineralic laminae (Fig. 13.4e), and larger euhedral and isolated crystals that truncate quartz grains (Fig. 13.4f). The euhedral magnetite is paragenetically late, and is regarded as a metamorphic recrystallization product, whereas the aggregates may have formed earlier during diagenesis. In either case, the magnetite is unlikely to represent a primary precipitate. There are at least three plausible mechanisms responsible for the formation of magnetite:

1. Reduction of Fe(III) oxyhydroxide via DIR, which is the generally accepted model based on theoretical, experimental, and petrographic support (Lovley 1993; Frost et al. 2007; Johnson et al. 2008; Pecoits et al. 2009; Li et al. 2011, 2013). DIR can produce large Fe isotope fractionations between $Fe(III)_{solid}$ and $Fe(II)_{aq}$ with variably depleted $\delta^{56}Fe$ values in the generated dissolved phase (Beard et al. 1999; Crosby et al. 2007). Laboratory experiments of magnetite formation by DIR also demonstrate that isotopic exchange between magnetite and $Fe(II)_{aq}$ may be rapid, and that on a mass-balance basis, the bulk $\delta^{56}Fe$ value of magnetite is largely inherited from the precursor ferric oxyhydroxide minerals (Johnson et al. 2005). In general, partial Fe(III) reduction by DIR would likely produce low $\delta^{56}Fe$ values, typically −0.5 and −2.5 ‰ lower than those of the initial ferric oxyhydroxides (Johnson et al. 2008). However, if complete conversion occurs, the $\delta^{56}Fe$ values of magnetite produced by DIR will be identical to those of the ferric oxyhydroxide precursors. Interestingly, magnetite in the Yuanjiacun oxide-facies BIF has consistently positive $\delta^{56}Fe$ values (0.35–0.89 ‰, Hou et al. 2014; Wang et al. 2015b), similar to those of hematite (0.40–1.09 ‰, Hou et al. 2014; Wang et al. 2015b). This pattern suggests that the magnetite may have inherited the isotopic composition of the ferric oxyhydroxide precursors, followed by complete conversion to magnetite through DIR. The low organic carbon content in the oxide-rich BIF samples (<0.1 wt%, Wang et al. 2015b) further supports the premise that any oxidizable organic carbon deposited with the ferric oxyhydroxide precipitates was consumed during DIR.
2. Magnetite can be the metamorphic by-product of a reaction between hematite and siderite, at temperatures of 480–650 °C and pressures of 4 and 15 kbar (Koziol 2004) (reaction 13.2):

$$FeCO_{3(siderite)} + Fe_2O_{3(hematite)} = Fe_3O_{4(magnetite)} + CO_2 \quad (13.2)$$

Tian et al. (1986) suggested that the peak P–T conditions for the formation of the chlorite schist associated with the BIF are 2–3 kbar and 400–450 °C, which would have been insufficient for the above reaction to take place. However, the oxidation of dissolved Fe(II), or of Fe(II) minerals such as siderite, could also drive magnetite production and possibly produce methane in the process (French 1971) under burial conditions of 450 °C and 2 kbar (McCollom 2003) (reaction 13.3):

$$12FeCO_3 + 2H_2O \rightarrow 4Fe_3O_4 + 11CO_2 + CH_4 \quad (13.3)$$

Accordingly, this process could be responsible for the formation of the magnetite overgrowths on ankerite (Fig. 13.6f).
3. The reactions between Fe(II)-rich hydrothermal fluids (<200 °C and H_2S poor) and preexisting hematite could form magnetite (Ohmoto 2003) in environments of limited organic carbon supply. Reaction of dissolved Fe(II) with ferric oxyhydroxide has been shown to yield isotopically heavy oxide phases through the preferential sorption of ^{56}Fe onto Fe-oxide surfaces (Icopini et al. 2004). In a similar manner, low $\delta^{56}Fe$ values predicted for Archean seawater may reflect preferential

sequestration of ^{56}Fe on ferric oxyhydroxides (e.g., Rouxel et al. 2005). Therefore, it is also possible that the positive $\delta^{56}Fe$ values observed in magnetite from the Yuanjiacun BIF were generated via a hydrothermal Fe^{2+} component ($\delta^{56}Fe \approx 0$ ‰) reacting with precursor ferric oxyhydroxide precipitates ($\delta^{56}Fe > 0$ ‰).

Ankerite is commonly associated with the silica-rich microbands. Although some ankerite may have formed penecontemporaneously with early ferric oxyhydroxide precipitates, petrographic evidence suggests that ankerite growth occurred during diagenesis. For example, ankerite is not found within hematite and magnetite grains, whereas small magnetite grains occur as inclusions within the ankerite (Fig. 13.6h). Ankerite is also preferentially concentrated where several Fe-oxide layers coalesce due to burial compaction, forming irregular aggregates that distort the primary microlamination (Fig. 13.6g). Furthermore, the edges of ankerite commonly display corrosion gulfs resulting in a xenomorphic morphology (Fig. 13.6h). These features imply a late-stage growth of the mineral. One possible reaction is via siderite dissolution and ankerite precipitation (Pecoits et al. 2009; Li 2014) (reaction 13.4):

$$2FeCO_3 + Ca^{2+} \rightarrow CaFe(CO_3)_2 + Fe^{2+} \quad (13.4)$$

The highly negative $\delta^{13}C$ values of ankerite (average −6.91 ‰, Wang et al. 2015b) in the Yuanjiacun BIF, which are consistent with previously determined $\delta^{13}C$ values of siderite in the Yuanjiacun carbonate-facies BIF (average −7.1 ‰; Tian et al. 1986), strongly suggest that precursor siderite formed by DIR (e.g., Kaufman 1996; Beukes and Gutzmer 2008). Moreover, the Fe-oxide facies BIF in the Yuanjiacun sequence contains similar Al_2O_3 concentrations but less organic carbon than the carbonate-rich BIF (Wang et al. 2015b), which is attributed to effective degradation of organic matter in an oxygen-bearing water column before it could be incorporated into the sediment. An alternative interpretation is that hematite-rich BIF was only preserved if the organic carbon influx was low relative to ferric oxyhydroxide accumulation. Under conditions of complete ferric oxyhydroxide reduction, two sources of C are required for siderite formation (reaction 13.5):

$$4Fe(OH)_3 + CH_2O + 3HCO_3^- \rightarrow 4FeCO_3 + 3OH^- + 7H_2O \quad (13.5)$$

The excess HCO_3^- required in this reaction likely came from seawater infiltration into soft sediment, below the seawater/sediment interface (Heimann et al. 2010). If HCO_3^- is not adequate, complete reduction would produce Fe^{2+} in addition to siderite (reaction 13.6)

$$4Fe(OH)_3 + CH_2O + 2HCO_3^- \rightarrow 3FeCO_3 + 4OH^- + 6H_2O + Fe^{2+} \quad (13.6)$$

The isotopic composition of HCO_3^- in seawater is assumed to have a $\delta^{13}C$ value of 0 ‰ (Faure 1986; Fischer et al. 2009; Bekker et al. 2013; Smith et al. 2013), and we assume that organic carbon (CH_2O) input to the seafloor had a $\delta^{13}C$ value of −24 ‰, based on the average $\delta^{13}C$ value for organic carbon in the Yuanjiacun BIF (Wang et al. 2015b). For the above reaction (13.5) and (13.6), the lowest possible $\delta^{13}C$ value is ca. −6 and −8 ‰, respectively, for siderite whose Fe was entirely sourced by DIR. The majority of $\delta^{13}C$ values for ankerite (−7.84 to −6.04 ‰, Wang et al. 2015b) in transition-facies BIF scatter about the $\delta^{13}C$ value predicted by these reactions, suggesting near-complete reduction of $Fe(OH)_3$ by abundant HCO_3^-.

The most common iron silicates in the BIF are stilpnomelane and chlorite. Stilpnomelane is a characteristic mineral of iron formations that have undergone low- to medium-grade metamorphism (Klein 2005). It is likely that stilpnomelane was derived from an Fe-rich, but Al-poor silicate precursor such as nontronite, which is itself readily synthesized at low temperature from amorphous ferric oxyhydroxides and dissolved silica under anoxic conditions (Dekov et al. 2007; Rasmussen et al. 2013a; Bekker et al. 2013) (reaction 13.7).

$$2Fe(OH)_3 + 4Si(OH)_4 \rightarrow Fe_2Si_4O_{10}(OH)_2 \cdot 10H_2O \quad (13.7)$$

Precursors to chlorite may have been aluminous detrital clay minerals that recrystallized to chlorite during metamorphism. The coexistence of some chlorite and relics of stilpnomelane (Fig. 13.5g) further suggests that chlorite can be produced by the reaction between stilpnomelane and original Al-rich detritus.

Among the Fe-rich silicates in the Yuanjiacun BIF, minnesotaite and amphibole are generally not as abundant as stilpnomelane. These two minerals typically cut fine-grained sheaves of stilpnomelane (Figs. 13.5f and 13.6d, e), suggesting that stilpnomelane became unstable and was then partially transformed into late-stage minnesotaite and amphibole during metamorphism (reaction 13.8).

$$\begin{aligned} &Fe_{2.7}(Si, Al)_4(O, OH)_{12} \cdot xH_2O \ (\text{stilpnomelane-like}) \\ &+ 0.33Fe^{2+} \rightarrow Fe_3Si_4O_{10}(OH)_2 (\text{minnesotaite}) \\ &+ 2H_2O + Al + \text{minor } (Na,\ K) \end{aligned} \quad (13.8)$$

In addition, calcite is commonly intergrown with amphibole (Fig. 13.6e). Thus, it is possible that amphibole is also a reaction product of iron-rich carbonates (e.g., fer-

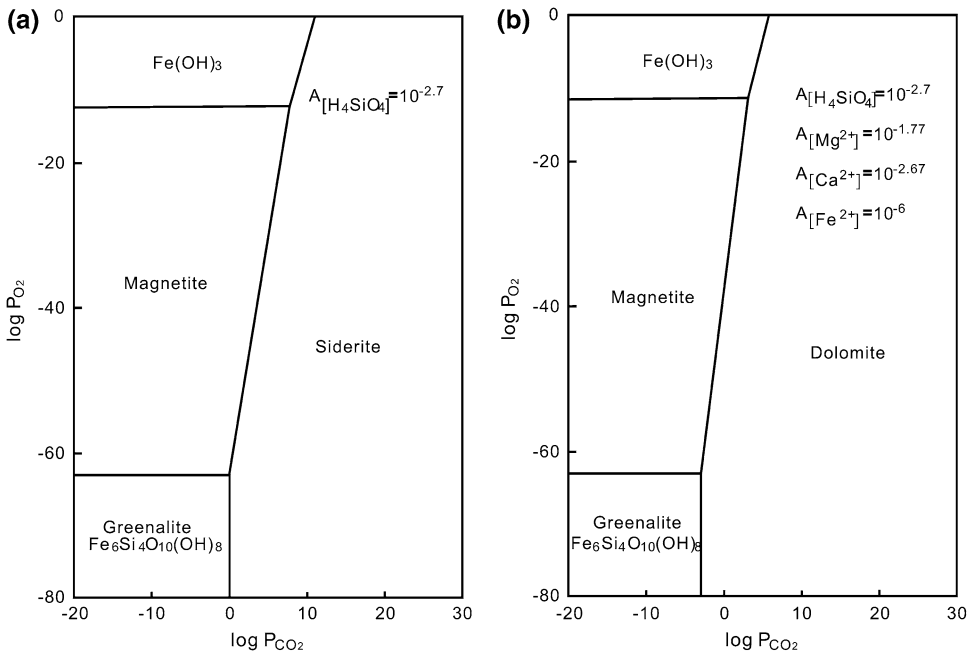

Fig. 13.7 Stability relations among greenalite-$Fe(OH)_3$-magnetite-siderite/dolomite as a function of P_{O_2} and P_{CO_2} at saturation with respect to amorphous silica at 25 °C (Klein and Bricker 1977). $A_{[H_4SiO_4]}$ = thermodynamic activity of H_4SiO_4

rodolomite) and quartz, together with calcite (Klein 2005). If the chemical potential of H_2O is high, while the chemical potential of CO_2 is low during metamorphism, the following type of reaction occurs (reaction 13.9):

$$\begin{aligned} &5Ca(Fe,Mg)(CO_3)_2 + 8SiO_2 + H_2O \\ &\quad \rightarrow Ca_2(Fe,Mg)_5Si_8O_{22}(OH)_2(\text{actinolite}) \\ &\quad + 3CaCO_3(\text{calcite}) + 7CO_2 \end{aligned} \tag{13.9}$$

13.5.2 Physical and Chemical Conditions of Iron-Formation Diagenesis and Low-Grade Metamorphism

The minerals described above from the Yuanjiacun BIF have typically been associated with diagenesis and low-grade metamorphism. Some of the physicochemical conditions of the environment of deposition can be evaluated in light of the above observations. Silica concentrations in Precambrian oceans would have been possibly close to saturation with respect to amorphous silica (Siever 1992). Decreasing temperature would decrease the solubility of silica whereas increasing temperatures would enhance its solubility. The maximum value of dissolved silica in equilibrium with amorphous silica is $10^{-2.7}$ (Klein and Bricker 1977). Under these conditions, Fig. 13.7 delineates the stability field of magnetite and $Fe(OH)_3$ relative to those of greenalite and siderite or dolomite (Klein and Bricker 1977). Formation of siderite (now ankerite), relative to magnetite, is favored at high P_{CO_2}. The close spatial relationship between these two minerals in the carbonate-rich BIF (Fig. 13.6h) suggests that pore water P_{CO_2} may have fluctuated locally between the stability fields of magnetite and siderite. In addition, it is also in open diagenetic environments of the compacted meso-bands that the excess organic carbon may be available, such that DIR could easily take place, thus explaining the presence of considerable amounts of ankerite in outside of chert pods (Fig. 13.5c). In places, martite crystals are intergrown with fine hematite within the iron-rich microbands (Wang et al. 2015c). The coexistence magnetite-$Fe(OH)_3$ (or hematite) requires a much higher partial pressure of oxygen (10^{-12}). Hematite-carbonates coexistences, however, are not observed in the Yuanjiacun BIF, suggesting that primary iron oxide might have been reduced completely under conditions of excess CH_2O.

To evaluate mineral equilibria in aqueous media, it is convenient to use the variables pE (or Eh) and pH. Figure 13.8 shows Eh-pH diagrams for several of the common mineral assemblages in the Yuanjiacun BIF, at 25 °C and 1 atm pressure; superimposed on the diagram are calculated values of P_{O_2} (Klein 2005). This aqueous, Fe-rich system is saturated with respect to amorphous silica ($A[H_4SiO_4] = 10^{-2.7}$). The hematite precursor field (that of $Fe(OH)_3$) is very small and exits only at relatively high P_{O_2} values. The presence of a relatively oxidized stilpnomelane-like phase ($Fe^{2+}/Fe^{3+} \approx 2{:}1$) (Wang et al. 2015c) nearly eliminates the greenalite field and greatly reduces the magnetite field (Fig. 13.9). Stilpnomelane coexists with magnetite in the silicate facies and is abundantly present in magnetite-carbonate assemblages. The magnetite field is stable only

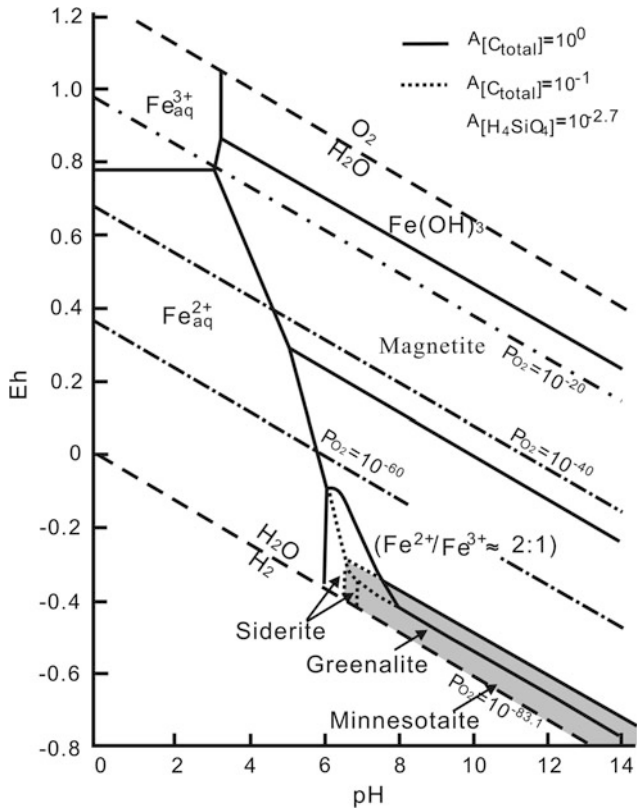

Fig. 13.8 Eh-pH diagrams depicting the stability fields of some minerals (or their precursors) in the system Fe-H_2O-O_2-SiO_2-dissolved C with the ratio of Fe^{2+}/Fe^{3+} in stilpnomelane approximating 2, at 25 °C and 1 atm total pressure. Boundaries between aqueous species and solids at $A_{[aqueous\ species]} = 10^{-6}$. Contours show partial pressure of oxygen. This diagram illustrates that at 25 °C minnesotaite (the shaded field) is the stable and greenalite the metastable phase (modified from Klein, 2005)

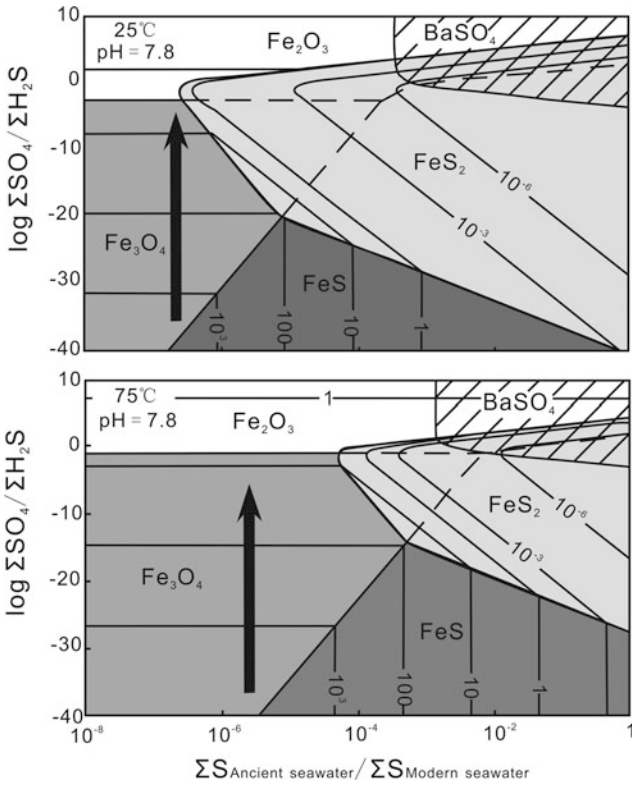

Fig. 13.9 $\sum SO_4/\sum H_2S$ versus total sulfur diagrams calculated at 25 and 75 °C at modern oceanic pH and salinity showing Fe–Ba–S–O mineral stabilities and Fe solubilities (Huston and Logan 2004)

at substantially lower values of P_{O_2} and the carbonate-silicate-rich mineral assemblages observed commonly in the Yuanjiacun BIF reflect even lower P_{O_2}. Such highly reducing environmental conditions for the BIF are to be expected because large amounts of Fe^{2+} must have been transported in solution. Iron solubility is possible only under highly reducing conditions, regardless of whether the solution is saturated with respect to amorphous silica or quartz. The siderite field disappears when the activity of total dissolved carbon is less than 10^{-1}. The common occurrence of minnesotaite, having formed at the expense of earlier stilpnomelane or Fe-carbonates in the BIF, is explained by the minnesotaite stability field (Fig. 13.10). This field reduces the stilpnomelane and siderite stability fields. At increasing temperatures, the minnesotaite field would expand further into the stilpnomelane field (Klein 2005).

Figure 13.9 illustrates the stability of Fe-S-O minerals and barite, and the solubility of iron as a function of sulfur content and redox at pH (7.8) and salinity of modern seawater (3 % NaCl) under 25 and 75 °C, respectively (Huston and Logan 2004). At 25 and 75 °C, magnetite is only stable at sulfur levels below 10^{-5} and 10^{-3} that of modern seawater. Iron is most soluble in the magnetite stability field and least soluble in the pyrite field. Although iron solubility exceeds 1 ppm at the base of the hematite field, it decreases with increasing $\Sigma SO_4/\Sigma H_2S$. Therefore, magnetite is only stable under reduced conditions, and high iron solubility is only possible under very low ambient sulfur concentrations.

13.6 Marine Redox Structure

The REE patterns of relatively siliciclastic-free BIF have frequently been used as a qualitative proxy of paleoseawater redox conditions (Bau 1999; Slack et al. 2007; Pecoits et al. 2009; Planavsky et al. 2010; Haugaard et al. 2013). Moreover, the REE + Y in BIF are generally regarded as being immobile during most geological processes (e.g., Bingen et al. 1996), and effects of metamorphism on the REE distribution in BIF have been found to be only of minor importance in most cases (Bau and Dulski 1996). Accordingly, the distribution of Y and REEs (REY) observed in the detritus-free Yuanjiacun BIF samples reflects those present in the primary marine precipitates (Wang et al. 2014, 2015b). In this context, the BIF samples display consistently positive La and Y anomalies, depletion of LREE and MREE relative

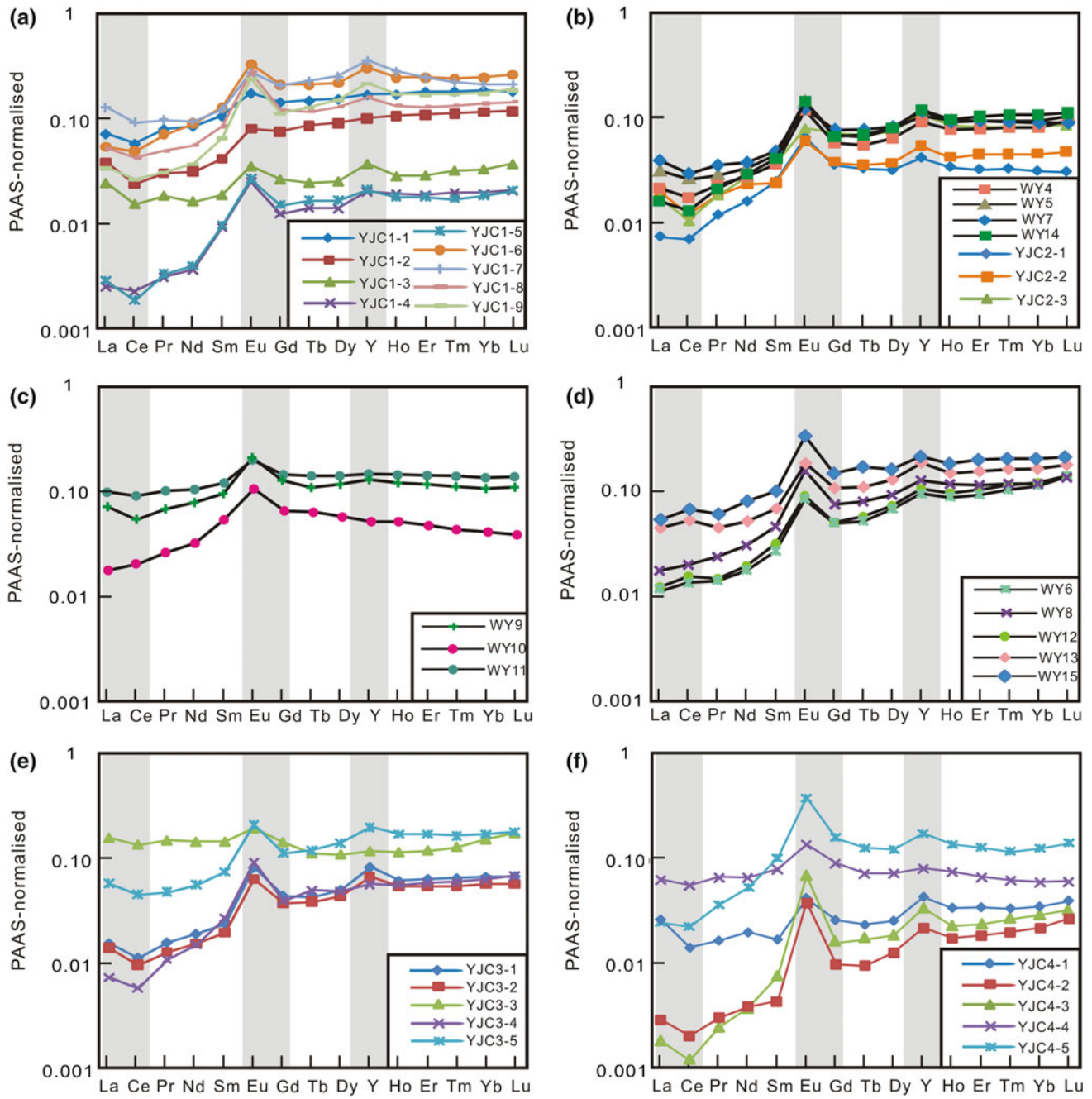

Fig. 13.10 PAAS-normalized REE + Y distributions of Yuanjiacun BIF samples (Wang et al. 2014, 2015b). **a** Hematite iron formation; **b–d** Magnetite iron formation; **e** Silicate-facies iron formation; **f** Carbonate-rich facies iron formation. PAAS data from McLennan (1989)

to HREE, and superchondritic Y/Ho ratios (>26); these collectively are features typical of modern seawater (Fig. 13.10). The positive Y anomalies in the BIF are distinct from those of slowly growing, modern marine hydrogenetic ferromanganese deposits that have negative Y anomalies, instead being more similar to rapidly precipitated, modern marine hydrothermal ferromanganese deposits. We thus infer that BIF precipitation occurred very rapidly and that the scavenged REY were not in exchange equilibrium with ambient seawater (see Bau and Dulski 1996). Rapid precipitation strongly favors a scenario for deposition of the BIF in which precipitation occurred due to upwelling of reduced ferruginous waters into an oxygenated shallow-water setting.

In contrast to modern seawater, the various Yuanjiacun BIF facies display positive Eu anomalies (Fig. 13.10) (Wang et al. 2014, 2015b), which were sourced from high-temperature (>250 °C) hydrothermal fluids effused after alteration of ocean-floor basalt (Beukes et al. 1990;

Bau 1993; Bau and Dulski 1996; Kato et al. 1998). This process suggests one of the following scenarios: (1) much of water column in the basin contained hydrothermally derived REE; (2) the hydrothermal fluids upwelled onto the shelf, perhaps as part of a plume (Isley 1995), which facilitated BIF precipitation, i.e., the BIF did not precipitate from ambient seawater; or (3) hydrothermal vents were proximal to the site of BIF deposition. In any case, enhanced magmatic activity (e.g., during eruption of large igneous provinces) would have created the ferruginous redox conditions in the oceans that promoted large-scale transport of dissolved iron (Bekker et al. 2010, 2013). In addition, such processes would have caused marked sea-level rise and transgressions, that in turn favored deposition of BIF on drowned, sediment-starved, continental shelves (e.g., Isley and Abbott 1999).

The redox-sensitive REEs, Eu and Ce, are often used to provide insights into the redox state of ancient seawater, and also the level of atmospheric oxygenation at that time (e.g., Frei et al. 2008). Modern oxygenated seawater shows a strong negative Ce anomaly and LREE depletion relative to HREE, using REE data that are normalized to the composition of average shale. By comparison, suboxic and anoxic waters lack negative Ce anomalies (German and Elderfield 1990; Byrne and Sholkovitz 1996), and display elevated LREE to HREE ratios. The cause of REE patterns in oxygenated seawater is oxidation of trivalent Ce that greatly reduces Ce solubility, resulting in preferential removal onto Mn–Fe oxyhydroxides, organic matter, and clay particles. Additionally, light REEs relative to heavy REEs are preferentially removed onto Mn–Fe oxyhydroxides and other reactive surfaces due to differential REE particle reactivity linked with REE carbonate complexation (Planavsky et al. 2010). In suboxic and anoxic waters, negative Ce anomalies are absent, or are locally positive due to the reductive dissolution of Mn–Fe oxyhydroxides below the redoxcline, resulting in an increased ratio of LREE to HREE (German et al. 1991; Sholkovitz et al. 1992). Moreover, based on experimental results, there is negligible oxidative scavenging of Ce onto ferric oxyhydroxide surfaces, unlike Mn(III/IV) oxides at pH conditions >5 (Bau 1999; Ohta and Kawabe 2001). Therefore, ferric oxyhydroxides qualitatively record Ce anomalies from the water column from which they precipitated, whereas Mn(III/IV) oxides are influenced by preferential Ce scavenging (Planavsky et al. 2009). In addition, Y/Ho ratios (>44) in marine environments are much higher than in shale composites (26) because of the difference in Y and Ho particle reactivity expressed in metal oxides. In suboxic and anoxic waters, Y/Ho ratios would likely decrease as Mn–Fe-rich particles dissolve, resulting in an increase in Ho relative to Y (Nozaki et al. 1997).

The discrimination and identification of Ce anomalies are complicated by possibly anomalous abundances of La. Bau and Dulski (1996) established a discrimination diagram, based on combined $(Ce/Ce^{*})_{SN}$ and $(Pr/Pr^{*})_{SN}$ values, to distinguish "real" from "false" anomalies of Ce within BIF. In Fig. 13.13, plots for late Paleoproterozoic (2.0–1.8 Ga) (field A) and Archean/early Paleoproterozoic (>2.4 Ga) BIF (field B) (Planavsky et al. 2010; Zhang et al. 2011; Dai et al. 2012) are also included. It is worth noting that except for the slightly negative Ce anomalies (Fig. 13.11), the REE patterns of the Yuanjiacun BIF (Wang et al. 2014, 2015b) are similar to those of late Paleoproterozoic (<2.0 Ga) iron formations, but differ from those in iron formations prior to the GOE (Planavsky et al. 2010). The large range of Ce anomalies and ratios of LREE to HREE and Y/Ho ratios in the BIF (Fig. 13.10) might reflect varying effects of the precipitation/dissolution of a Mn-oxyhydroxide shuttle, from shallow-water oxidized settings to deeper water reducing environments (Fig. 13.12). Especially, during the GOE, the atmospheric oxygen level might have been increasing. Ce and Mn were then all oxidized due to their similar redox potential, and large amounts of Ce(IV), LREE, and Ho were preferentially removed onto Mn-oxyhydroxide particles in the upper oxic waters. BIF precipitating in the oxic zone would display a LREE depletion relative to HREE, superchondritic Y/Ho ratios, and negative Ce anomalies. Subsequently, dissolution of these metal oxyhydroxides, occurring across a redoxcline and in deeper anoxic–suboxic waters would have increased dissolved Ce, LREE, and Ho contents of the local seawater (Fig. 13.12). These elements would be transferred to the sedimentary record when Fe oxyhydroxide precipitation occurred in these suboxic–anoxic waters. Thus, small amounts of positive Ce anomalies, higher LREE/HREE ratios, and lower Y/Ho ratios would appear. If Fe oxyhydroxide precipitation occurred in the transition zone between oxic and anoxic waters, where significant variation was likely in Ce anomalies, light to heavy REE, and Y/Ho ratios induced by oxidative scavenging and reductive dissolution, iron formations would show nearly flat aqueous REE patterns and low Y/Ho ratios (Fig. 13.10a–d).

Iron isotopes in BIF have been used to trace Fe cycling and fingerprint redox processes that led to deposition of BIF (Johnson et al. 2003, 2008; Rouxel et al. 2005; Anbar and Rouxel 2007). The most common mechanism proposed for accumulation of iron-rich components in BIF is the oxidation of hydrothermally sourced $Fe(II)_{aq}$ (Klein 2005), which should produce a $\delta^{56}Fe$ value of ca. 0 ‰, or slightly negative (−0.5 ‰) (Johnson et al. 2008; Planavsky et al. 2012a). Iron oxyhydroxides that precipitated under fully oxygenated conditions are expected to have the same $\delta^{56}Fe$ value as the dissolved iron sources, because of nearly complete Fe(II) oxidation and Fe(III) mineral precipitation. In contrast, partial Fe(II) oxidation produces iron oxyhydroxides with positive $\delta^{56}Fe$ values relative to the Fe(II) source. The presence of positive $\delta^{56}Fe$ values for hematite and magnetite

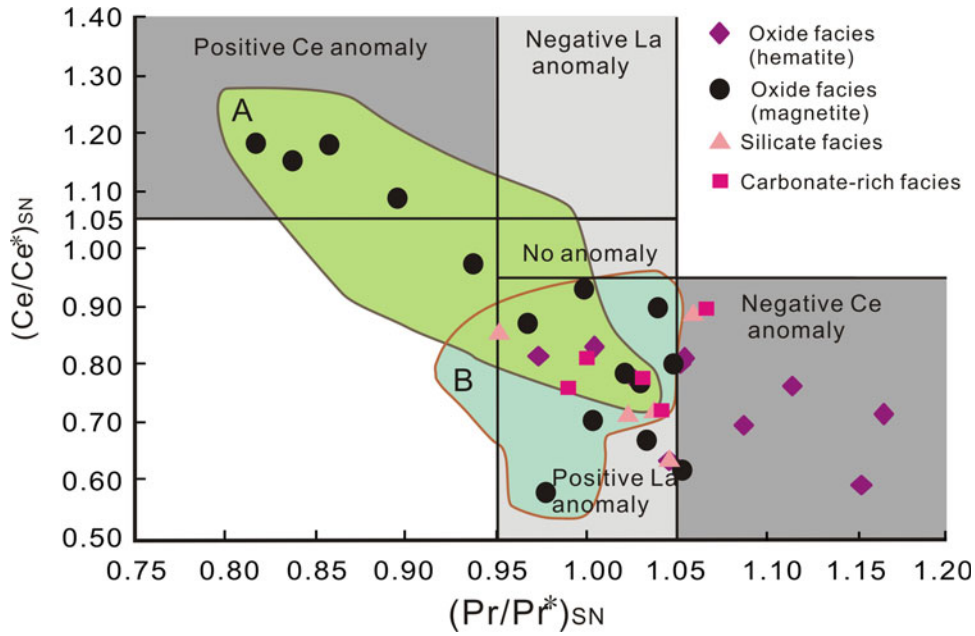

Fig. 13.11 Plot of Ce and Pr anomalies normalized to PAAS for Yuanjiacun BIF samples (Wang et al. 2014, 2015b), discriminating between positive La anomalies and true Ce anomalies (Bau and Dulski 1996). Plots of late Paleoproterozoic (<2.0 Ga) (field A) (after Planavsky et al. 2010) and Archean and early Paleoproterozoic (>2.4 Ga) (field B) (after Planavsky et al. 2010; Zhang et al. 2011; Dai et al. 2012) iron formations are also included

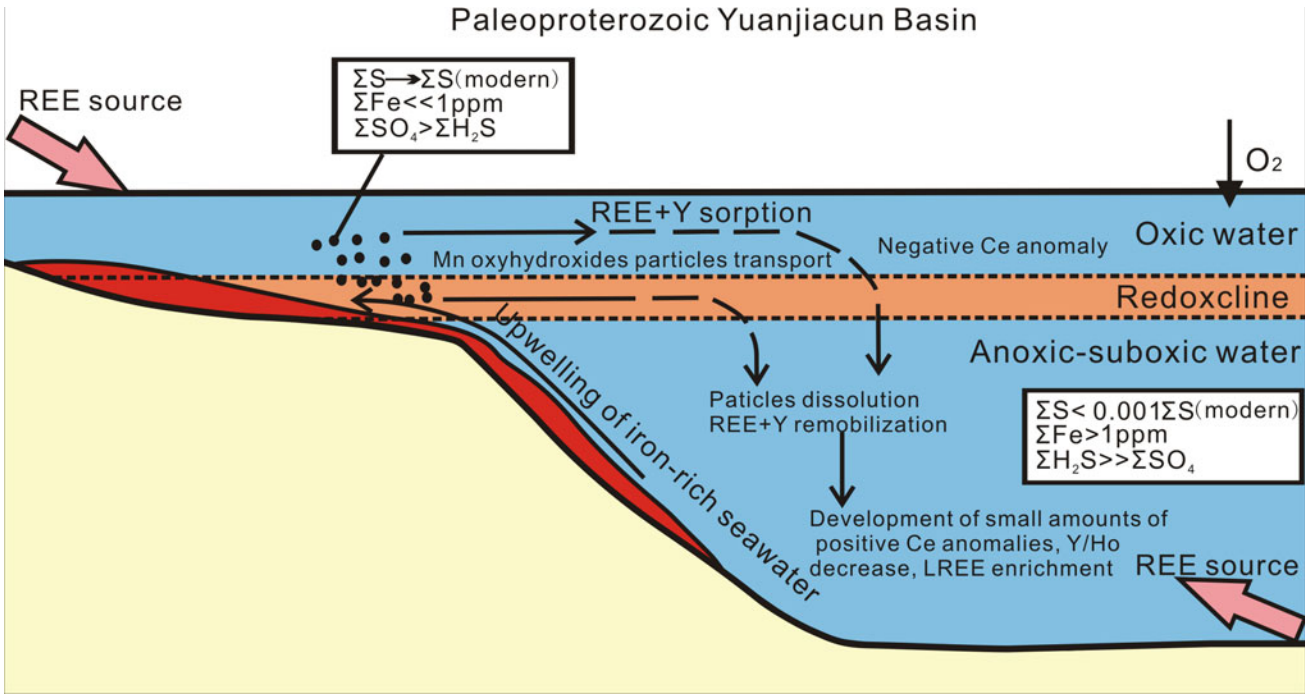

Fig. 13.12 Redox structure of seawater in Paleoproterozoic Yuanjiacun basin (modified from Wang et al. 2014)

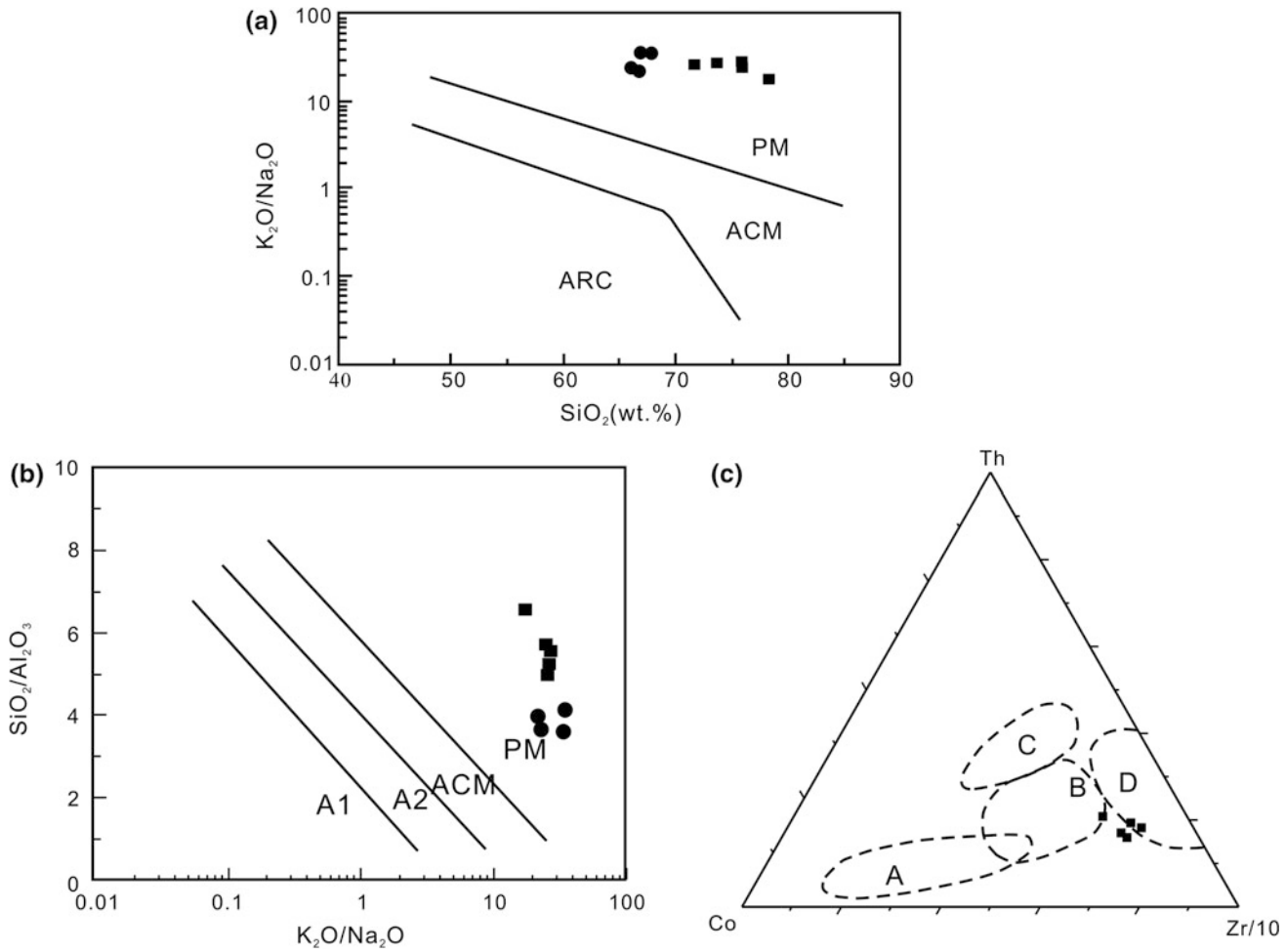

Fig. 13.13 Tectonic discrimination diagrams for the Yuanjiacun Formation metasediments including (**a**), (**b**) and (**c**) (modified from Wang et al. 2015a). **a** K_2O/Na_2O versus SiO_2 and **b** SiO_2/Al_2O_3 versus K_2O/Na_2O (after Roser and Korsch 1986). **c** Th–Co–Zr/10 (after Bhatia and Crook 1986)

in the Yuanjiacun oxide-facies BIF (Wang et al. 2015b) thus points to incomplete Fe(II) oxidation, which by extension, suggests deposition under conditions of low oxygenation.

13.7 BIF Depositional Model

13.7.1 Tectonic Setting of the BIF

Geochemical and Nd isotopic data from clastic sedimentary rocks associated with the BIF have been used to constrain the tectonic and sedimentary setting of the BIF. The Yuanjiacun metasedimentary rocks consist predominantly of low-Al and high-Al metapelites and meta-arenites. Considering that the low-Al pelites represent the mixing of compositions of normal pelites and typical BIFs, they are precluded from the following discussion (Wang et al. 2015a). The high-Al pelites and arenites are thought to be deposited as multicycled sediments or under tropical conditions with low relief and sedimentation rates based on their geochemical features. Moreover, these samples display high Th/Sc (≈1), and high Th/U (>3.8) and evolved major element compositions [e.g., high Si/Al and CIA (>70)] and low $\varepsilon_{Nd}(t)$ values (<0), as low as −4.3, which are most similar to those of old Upper Continental Crust (McLennan et al. 1995). These characteristics suggest that they are likely to form in a stable cratonic setting.

Roser and Korsch (1986) have shown that sandstone-mudstone suits from different tectonic settings can be distinguished on the basis of the K_2O/Na_2O and SiO_2/Al_2O_3 values and SiO_2 contents. On the K_2O/Na_2O versus SiO_2 and SiO_2/Al_2O_3 versus K_2O/Na_2O plots (Fig. 13.13a, b), all samples of high-Al pelites and arenites from the Yuanjiacun Formation plot in the passive continental margin (PM). Several immobile elements, such as Co, Th, and Zr, are more useful in distinguishing the tectonic environment than the major elements (Bhatia and Crook 1986; McLennan et al. 1993). The most widespread tectonic discriminatory plots

for the clastic sediments were compiled by Bhatia and Crook (1986) based on detailed geochemical study of graywacke. For the studied meta-arenites, petrographical indications, such as the low content of poorly sorted, angular quartz grains, the presence of well-defined bedding, and the oriented mica-flakes all point toward the meta-arenites not being an immature meta-graywacke, although geochemical data indicate that some meta-arenite samples belong to the graywacke. Therefore, these plots are not suitable for the meta-arenite samples, but can only provide some reference information. For example, the studied meta-arenite samples on the Th–Co–Zr ternary diagram (Fig. 13.13c, Bhatia and Crook 1986) are plotted in and close to the passive continental margin field.

Moreover, a few Yuanjiacun BIF samples contain distinct signatures of terrigenous input, as reflected by the high modal content of chlorite, and by high but variable concentrations of Al_2O_3, HFSEs (e.g., Zr, Hf), and strong positive correlations between Al_2O_3, TiO_2, and HFSEs (Wang et al. 2015b). These detrital components within the silicate-facies BIF exclude an abyssal plain fraction because of the low expected influx of allochtonous detritus in such settings (Haugaard et al. 2013). Moreover, the presence of oolitic/granular hematite (Tian et al. 1986) argues for a shallow-water environment. Therefore, a favored depositional site for these samples is more proximal to the palaeo-shoreline, possible on the shallow shelf.

In conclusion, we suggest a passive margin setting for the depositional basin of these sediments and BIFs. The absence of syn-depositional igneous rocks in the Lüliang area provides further evidence (Zhao et al. 2008). This setting obviously contrasts with the volcanic arc setting (Liu et al. 2012) or a continental rift environment (Yu et al. 1997b; Geng et al. 2003) for the overlying meta-basalts in the Jinzhouyu Formation and meta-rhyolites in the Dujiagou Formation. Thus, we strongly suggest that the Yuanjiacun BIF belongs to a Superior-type BIF, because they are laterally extensive and closely associated with clastic sedimentary rocks, and likely formed on passive margins.

13.7.2 Controls on Various BIF Facies Deposition

Detailed lithostratigraphic information (Shen et al. 1982; Tian et al. 1986; Zhu et al. 1988) in combination with geochemical data permit us to reconstruct a potential depositional model for the Yuanjiacun BIF (Fig. 13.14). The system tract for this BIF begins near shore with thickly bedded, wave-rippled, and cross-stratified quartz sandstone that was deposited above normal wave base (Fig. 13.5). The distribution of lithological units in upward-fining increments indicates that hematite-magnetite (oxide facies) BIF and associated meta-arenites and shales mark the beginning of transgression, whereas the oolitic/granular hematite (Zhu et al. 1988) is indicative of deposition in near-shore, shallow waters. The fact that the iron formations form the base of coarsening-upward progradational increments of sedimentation also implies that they were

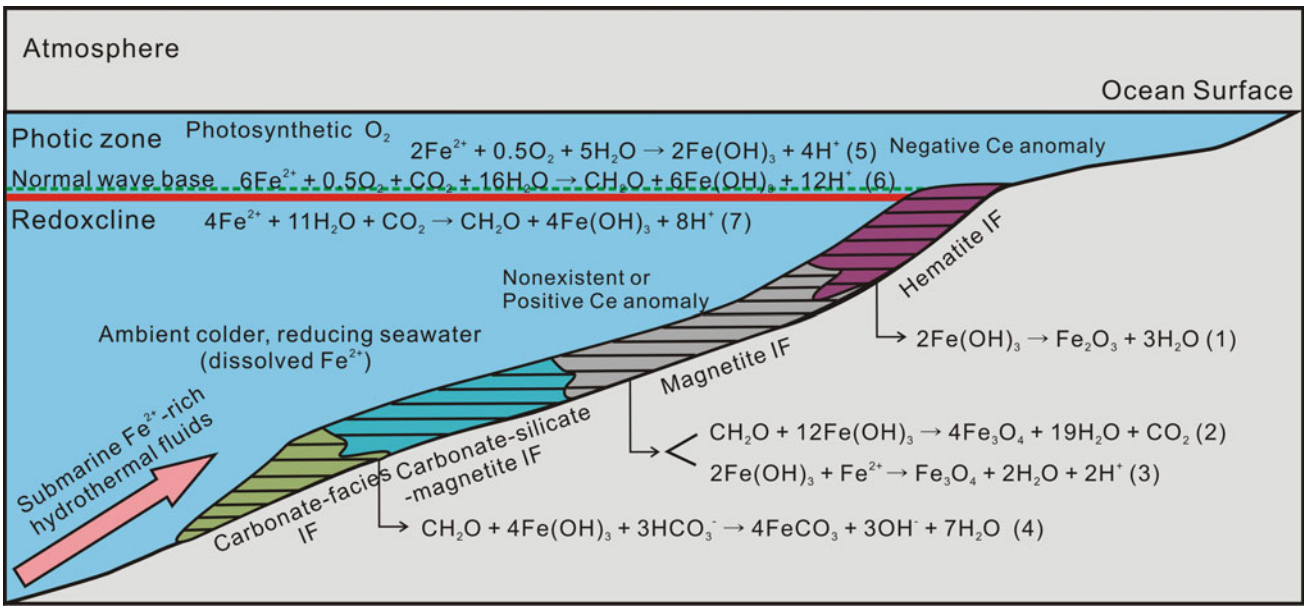

Fig. 13.14 Conceptual depositional model for the Paleoproterozoic Yuanjiacun BIF (Wang et al. 2015b). Reactions 13.2 and 13.3 are adapted from Beukes and Gutzmer (2008) and Ohmoto (2003), respectively; reaction 13.4 is modified from Heimann et al. (2010). Reaction 13.6 is from Konhauser et al. (2002) and reaction 13.7 is adapted from Kappler et al. (2005)

likely deposited most distal from siliciclastic input during transgression. Close examination of the vertical facies of the Yuanjiacun BIF reveals that the hematite-magnetite facies typically grades upward into magnetite-silicate and silicate-siderite facies, indicating that carbonate-rich iron formation was likely deposited in the most distal part of the depositional basin, during peaks of transgression, followed shoreward by hematite-magnetite facies iron formation. This distinct vertical facies change is also observed laterally, from west to east, i.e., the iron mineral assemblage changes from siderite through silicate into magnetite and hematite iron formations (Fig. 13.3c).

The alternating iron- and silica-rich microbands in the BIF, without indication of current activity, could reflect stable basinal conditions with precipitation occurring below storm-wave base (ca. 200 m), which is the average depth of the modern storm-wave base (Boggs 1995). However, the local presence of current-generated structures in the Yuanjiacun oxide-facies BIF, such as cross-bedding and granular textures (Tian et al. 1986), indicates that this facies formed in somewhat shallower environments at depths where storm-wave currents could occasionally rework bottom sediments. It should be noted that the carbonate-facies BIF is closely associated with the beds of stilpnomelane lutite (Fig. 13.5), which may represent ferruginized felsic pyroclastic material (Zhu et al. 1988). Additionally, positive Eu anomalies in the carbonate-rich iron formation are more pronounced than those in the oxide- and silicate-facies BIFs (Fig. 13.10). This pattern suggests that hydrothermal fluids related to volcanic events influenced the entire depositional environment for iron, and that the carbonate-facies BIF was more likely to have been deposited closer to submarine hydrothermal vents.

The Yuanjiacun BIF displays a clear REE signature indicative of basin-scale redox stratification and Fe(III) formation under varying redox conditions (Fig. 13.14). Specifically, a wide range of true Ce anomalies, varying from slightly negative to positive, or nonexistent, and range of LREE to HREE ratios present in the oxide-facies BIF, indicate that this facies formed in both mildly oxic shallow seawater and deeper anoxic waters, in contrast to the silicate- and carbonate-facies BIFs that lack Ce anomalies and thus likely formed in relatively deep, reducing waters. A dynamic redoxcline must have separated the oxic upper part of the water column from suboxic to anoxic deeper parts.

The actual mechanism of Fe(II) precipitation to form the ferric oxyhydroxide precursors to BIF remains a subject of debate. One possibility is the abiotic oxidation of Fe(II) by the O_2 produced by cyanobacteria (Cloud 1968; Klein and Beukes 1993), which may have played a role in depositing ferric oxyhydroxides in parts of the Yuanjiacun oxide-facies BIF in shallow oxic environments. Alternatively, the direct oxidation of Fe(II) by ancient microorganisms could have taken place, by microaerophilic Fe(II)-oxidizers using cyanobacterially produced O_2 as an electron acceptor (Emerson and Revsbech 1994; Konhauser et al. 2002) or anoxygenic phototrophic Fe(II)-oxidizers that use light to oxidize Fe(II) in the absence of O_2 (Kappler et al. 2005; Posth et al. 2008). The stratigraphy and lateral facies reconstruction of the Yuanjiacun BIF suggest that most of this iron-rich sequence was deposited below storm-wave base, but this model does not constrain where the initial Fe (II) oxidation took place. In other words, Fe(II) would have been oxidized in the photic zone, and the resultant ferric oxyhydroxide particles would then fall through the water column to the seafloor, irrespective of whether that setting represented very shallow or deep waters. However, a biologically mediated Fe(II) oxidation process requires sufficient nutrients to support the microbial biomass.

Within iron formation beds, the lateral facies changes are well represented by the presence of ferric oxyhydroxides with minor silica occurring most distal from volcanic centers or hydrothermal vents, versus the carbonate (siderite)- and silicate-rich assemblages that formed more proximal to the inferred vent sites (Fig. 13.14). The decrease in carbonates and increase in magnetite and hematite toward the former shoreline (i.e., more distal from hydrothermal vents) suggests that the supply of organic carbon to the sediment decreased in this direction (Beukes and Gutzmer 2008; Köhler et al. 2013). This interpretation is in contrast to previous models of BIF deposition, such as for the 2.46 Ga Kuruman Iron Formation in South Africa, in which hematite represents the most deep-water facies where organic carbon supply was so low that DIR did not occur, while siderite precipitated in a near-shore setting where organic carbon supply was abundant (Beukes et al. 1990). These different models can be explained by the location of primary productivity. In the Kuruman Iron Formation, the BIF conformably underlies shallow-water, organic-rich carbonates and shales, suggesting that the carbon source came from areas of high photosynthetic primary productivity and abundant nutrients on the shallow carbonate shelf, and by extension, that the nutrients for the microbial mats (e.g., chemolithoautotrophic iron-oxidizing bacteria) had a terrestrial source. By contrast, primary productivity in the Yuanjiacun basin seems to have been more prevalent in deeper water settings, implying that nutrients (e.g., V, Fe, Co, and Zn) were most likely sourced from marine hydrothermal vents (Beukes and Gutzmer 2008). Therefore, in settings proximal to vent sites, organic matter supply outpaced degradation, and more organic matter thus reached the sediment surface, resulting in effective DIR and the formation of early diagenetic siderite and magnetite. By contrast, depositional areas more distal from vent sites had very low primary organic productivity, allowing ferric oxyhydroxides to accumulate on the seafloor of the depository, to be later

transformed into hematite and/or magnetite (Fig. 13.14). Perhaps the most intriguing aspect of this model is that the shallow waters did not contain an abundant plankton biomass, and if this was the case, then the most likely oxidant for the oolitic/granular hematite (Tian et al. 1986) and parts of hematite-rich BIF, was O_2. This interpretation suggests that oxidation of Fe(II) was indirectly linked to cyanobacteria, and that the cyanobacteria were not necessarily abundant at the site of Fe(II) oxidation. In other words, the shallow waters were sufficiently oxygenated at this time such that any shallow-water Fe(II) was rapidly oxidized.

Silica would have been introduced together with ferrous iron from hydrothermal deep water (Bekker et al. 2013; Hou et al. 2014), and its precipitation is brought about by a decrease in temperature in the zone where the slightly warmer water mixes with cold ambient seawater (Beukes and Gutzmer 2008). However, continental weathering as a relevant source of silica to the shallow-marine water column cannot be excluded. In addition, we propose that in environments of low organic carbon burial, nontronite (precursor to stilpnomelane) is readily precipitated from mixtures of amorphous iron oxyhydroxides and silica under low-temperature anoxic conditions, in the presence of dissolved Fe(II) (Harder 1976, 1978), resulting in a scattered distribution of the silicate-facies BIF between the oxide- and carbonate-facies BIFs.

13.8 The Yuanjiacun BIF and Global Environmental Conditions

It is generally accepted that pre-GOE BIFs (>2.4 Ga) are often comprised of magnetite, iron-bearing silicates, and carbonates. But during the time interval 2.60–2.40 Ga, the BIF deposits begin containing intervals having granular textures as well as micro- and nanospheres of hematite (e.g., Ayres 1972; Beukes and Klein 1990; Spier et al. 2007). However, most granules consist of iron silicates and carbonates with only rare hematite granules; no hematite-coated grains have been documented (Bekker et al. 2013). Moreover, whether these hematite grains are primary still remains controversial. Hematite in the unmineralized BIF sediments is widely regarded as a dehydration product of a ferrihydrite precursor (e.g., Ahn and Buseck 1990; Pecoits et al. 2009; Sun et al. 2015). Yet in some cases, hematite is a result of postlithification fluid circulation during which the infiltrated O_2-bearing meteoric fluids oxidized ferrous iron to hematite (Rasmussen et al. 2014a, b).

Shale-normalized REE + Y patterns of detritus-poor pre-GOE BIFs are remarkably similar to those of Archean-Paleoproterozoic marine carbonates (Kamber and Webb 2001; Bau and Alexander 2006) and modern seawater, exhibiting positive La, Gd and Y anomalies and enrichment of the heavy REEs over the light REEs (e.g., Bau and Dulski 1996; Bolhar et al. 2004; Planavsky et al. 2010). The most salient differences between the REE + Y distribution in modern seawater and BIFs are that the latter have consistently positive Eu anomalies and lack the characteristic strongly negative Ce anomalies of modern seawater. The former indicates significant contributions from high-temperature (>250 °C) hydrothermal fluids emanating from submarine venting systems (Bau and Dulski 1999), while the latter reflects consistently reducing oceans (Holland 1984). However, some geochemical indexes indicate transient atmospheric oxygenation before the GOE (Frei et al. 2009; Crowe et al. 2013; Planavsky et al. 2014). For instance, based on Cr isotope values in BIF through time, Frei et al. (2009) found that cyanobacterial activity may already have been abundant by 2.8 Ga ago, and that their production of oxygen may have led to Earth's first oxidative weathering of the continents. However, relative to the GOE, the oxidative weathering during the Mesoarchean may not have been very profound as suggested by generally lower authigenic Cr supply to oceans (Konhauser et al. 2011a).

Previous studies have concluded that giant iron formations ($\geq$10,000 Gt; total amounts of iron formations) were not deposited between ca. 2.4 and 2.0 Ga (e.g., Bekker et al. 2010). Iron formations of this time period are distinctly different in scale (i.e., smaller), and in most cases their depositional settings are similar to those of Archean BIF. It seems that from ca. 2.4 to 2.0 Ga, either the deep-ocean redox state was too oxidized, relative to the magnitude of hydrothermal input, to have the ferruginous deep waters needed to promote the formation of giant BIFs, or that marine sulfate levels were high enough so that the sulfide produced during bacterial sulfate reduction exceeded the hydrothermal Fe(II) supply, with the result that iron sulfides precipitated instead of iron oxides (see Kump and Seyfried 2005). Several independent lines of evidence point toward high sulfate levels (>2.5 mM) during the Lomagundi Event at 2.22–2.11 Ga (Bekker et al. 2006; Schröder et al. 2008; Planavsky et al. 2012b; Scott et al. 2014), consistent with the idea that growth of the marine sulfate reservoir challenged the hydrothermal iron flux, and ultimately exerted a first-order control on the distribution and abundance of iron formations.

Oolitic hematitic ironstones of the Paleoproterozoic Timeball Hill Formation in South Africa were deposited in shallow-water, above fair-weather wave base (Schweigart 1965; Dorland 1999). Few geochemical data are available for this unit, partly because it contains significant amounts of siliciclastic material. Its deposition at ca. 2.32 Ga (Hannah et al. 2004; Rasmussen et al. 2013b) may coincide with a magmatic event at that time (e.g., Berman et al. 2005; Hartlaub et al. 2007). However, the significance of this magmatic event is poorly known. Another possible BIF that was deposited in this time interval is the 2.3 Ga Hotazel

Formation in South Africa, although its depositional age remains controversial (Gutzmer and Beukes 1997). Tsikos and Moore (1997) conducted geochemical studies on 12 samples of iron formation from this BIF and found an absence of positive Eu anomalies and negative Ce anomalies. However, by using the approach of Bau and Dulski (1996) to discriminate true Ce anomalies, we find that only two of the 12 Hotazel BIF samples have Ce anomalies, both of which are slightly negative. Because most of the data for these samples lack Tb values, we cannot calculate Eu anomalies. Nonetheless, the original calculation method indicates that some samples have slightly positive Eu anomalies (shale-normalized basis). Hence we suggest that the REE patterns of the Hotazel BIF are similar to those of the Kuruman BIF, except for lower Eu anomalies in the former (Bau and Dulski 1996). The presence of these Eu anomalies implies a dilute hydrothermal signature rather than an oxygenated state for the coeval deep ocean at ca. 2.3 Ga.

The ~2.38–2.21 Ga Yuanjiacun BIF is likely to be the largest (>1000 Gt; total amounts of iron formations) and most extensive BIF known during this globally, BIF-poor time interval. This BIF is likewise associated with transgression and consists of three upward-deepening to upward-shallowing sequences that were deposited in a continental shelf environment. Significantly, a certain amount of oolitic and granular hematite are present in the Yuanjiacun BIF (Tian et al. 1986; Zhu et al. 1988), and the BIF displays prominent positive and negative Ce anomalies and large shale-normalized ratios of LREE to HREE, which are essentially absent in pre-GOE iron formations (Planavsky et al. 2010). These features suggest that the ancient ocean at that time was redox-stratified, from oxic shallow waters to deeper anoxic waters. This marked redox stratification contrasts with the widespread, low-oxidizing potential that existed in the pre-GOE ocean. The presence of consistently positive Eu anomalies is also important, indicating that the global ocean was dominated by a high-temperature hydrothermal flux at that time (Wang et al. 2014, 2015b). Episodic delivery of Fe from hydrothermal fluids into the oceans could have had dramatic impacts on ocean productivity and ecosystem structure.

Deposition of the Yuanjiacun BIF occurred sometime during the GOE, but predates the largest positive carbon isotope excursion in Earth's history, the 2.22–2.11 Ga Lomagundi Event, which appears to be related to high burial rates of organic carbon and associated oxygen release to the atmosphere (e.g., Schidlowski et al. 1976; Karhu and Holland 1996; Bekker et al. 2001; Bekker and Holland 2012). The gaps in the record of major Superior-type iron formations deposition at 2.3–2.2 Ga closely coincide with inferred pauses in global plate tectonic activity (Silver and Benn 2008; Condie et al. 2009). The diagnostic REE pattern and geological features observed in the Yuanjiacun BIF may, therefore, indicate that significant parts of the shallow oceans were already oxygenated by ~2.3 Ga and that Fe(II) was soluble only in lower reduced waters of local basins overwhelmed by a relatively intense hydrothermal flux of reduced components such as Fe, Mn, and H_2S.

During the Lomagundi carbon isotope excursion, sedimentary sequences such as those containing hematitic oolites and hematite-rich sandstones in South Africa (e.g., Silverton Formation; Schweigart 1965) and on the Kola Peninsula in Russia (Kuetsjärvi Sedimentary Formation; Akhmedov 1972a), were attributed to be deposited in shallow-marine environments. The BIFs deposited during the 2.22–2.11 Ga Lomagundi excursion include those within the Ijil Group, Mauritania (Bronner and Chauvel 1979) and the Lomagundi Group, Zimbabwe (Master 1991). During the same time period, several volcanic-hosted iron formations were deposited in Brazil (e.g., Aimbė Formation, Guarinos Group; Resende and Jost 1995; and Itapicuru Complex of the Rio Itapicuru greenstone belt; Dalton de Souza et al. 2003) and Norway (Iddjajav'ri Group, Karasjok greenstone belt; Often 1985).

Immediately after the Lomagundi carbon isotope excursion, small, volcanic-hosted iron formations in North America (e.g., Homestake Iron Formation, Black Hills, South Dakota; Frei et al. 2008) and Finland (Paakola 1971; Laajoki and Saikkonen 1977), were deposited in several basins. Oolitic hematitic ironstone also formed within the Kolasjoki Formation, Kola Peninsula, Russia (Akhmedov 1972b). Taken together, these data are tentatively interpreted as recording dynamic ocean redox conditions that were constructed in the aftermath of the GOE, with periodic upwelling of iron into shallow-water settings above storm and fair-weather wave base. Interestingly, the 2.1–2.0 Ga BIF in the Black Hills displays REE patterns similar to those of the Yuanjiacun BIF, in which both positive and negative Ce anomalies are present (Frei et al. 2008). These features in the Black Hills BIF have been attributed to supergene oxidative processes and the oxygenation of bottom seawaters (Frei et al. 2008). This explanation has not been tested so far, and requires further consideration.

Extensive and large BIFs reappear at about 1.88 Ga. These are most common at the margins of the Superior craton and in Western Australia. These post-GOE oxide-facies IFs often contain hematite as the iron-bearing mineral within granules and on coated grains (Miller and Reading 1993; Hoffman 2011). The oxide facies commonly grades downward to finely laminated, sub-storm base Fe-silicate and carbonate-facies types (Bekker et al. 2013). In contrast, within the pre-GOE BIFs, hematite-magnetite facies iron formation was deposited in the most distal part of the depositional basin, followed shoreward by carbonate-magnetite facies iron formation (Beukes and Gutzmer 2008; Smith et al. 2013). Moreover, late Paleoproterozoic

BIFs show significant ranges in light to heavy REE, Ce anomalies, and Y/Ho ratios, which contrast markedly with data for the pre-GOE BIFs (Planavsky et al. 2009, 2010; Raye et al. 2015). Combined, these data suggest that after the GOE, there was a dynamic redoxcline between continuously oxic shallow waters and ferruginous deeper waters on the continental shelves. Differences between BIFs deposited before and after the GOE, in terms of original textures, the distribution of BIF facies, and depositional settings, are closely linked to oxygenation of the shallow ocean and the formation of a discrete redoxcline (Bekker et al. 2013).

Acknowledgments This research was financially supported by the Major State Basic Research Programme of the People's Republic of China (No. 2012CB416601) and the CPSF-CAS Joint Foundation for Excellent Postdoctoral Fellows (No. 2015LH0004). We would like to thank Xindi Jin, Lianjun Feng, Zhuyin Chu, Chaofeng Li, Wenjun Li, and Bingyu Gao for laboratory assistance, and Hongdi Pan, Mingtian Zhu, Yanpei Dai, Caiyun Lan, Hongzhong Li, Hua Huang, Mengtian Zheng, and Zhiquan Li for help with field work and lab analyses. We are much appreciated that Yusheng Wan, Houmin Li, Kurt Konhauser, Andrey Bekker, Bruce Simonson, John Slack, and Larry Meinert provided detailed and insightful comments.

References

Ahn, J.-H., & Buseck, P.-R. (1990). Hematite nanospheres of possible colloidal origin from a Precambrian banded iron formation. *Science, 250*, 111–113.

Akhmedov, A.-M. (1972a). Iron-rich metasedimentary rock of Pechenga Complex and their genesis: Materials on geology and metallogeny of Kola Peninsula. *Apatity, 4*, 125–131. (in Russian with English abstract).

Akhmedov, A.-M. (1972b). Hematite oolites in sedimentary rocks of the Pechenga Complex: Materials on mineralogy of the Kola Peninsula. *Nauka, 9*, 135–137. (in Russian with English abstract).

Anbar, A.-D., & Rouxel, O. (2007). Metal stable isotopes in paleoceanography. *Annual Review of Earth and Planetary Sciences, 35*, 717–746.

Ayres, D.-E. (1972). Genesis of iron-bearing minerals in banded iron formation mesobands in the Dales Gorge Member, Hamersley Group, Western Australia. *Economic Geology, 67*, 1214–1233.

Bau, M. (1993). Effects of syn- and post-depositional processes on the rare-earth element distribution in Precambrian iron-formations. *European Journal of Mineralogy, 5*, 257–267.

Bau, M. (1999). Scavenging of dissolved yttrium and rare earths by precipitating Fe oxyhydroxide: Experimental evidence for Ce oxidation, Y-Ho fractionation, and lanthanide tetrad effect. *Geochimica et Cosmochimica Acta, 63*, 67–77.

Bau, M., & Alexander, B. (2006). Preservation of primary REE patterns without Ce anomaly during dolomitization of Mid-Paleoproterozoic limestone and the potential reestablishment of marine anoxia immediately after the "Great Oxidation Event". *South African Journal of Geology, 109*, 81–86.

Bau, M., & Dulski, P. (1996). Distribution of yttrium and rare-earth elements in the Penge and Kuruman iron formations, Transvaal Supergroup, South Africa. *Precambrian Research, 79*, 37–55.

Bau, M., & Dulski, P. (1999). Comparing yttrium and rare earths in hydrothermal fluids from the Mid-Atlantic Ridge: Implications for Y and REE behaviour during near-vent mixing and for the Y/Ho ratio of Proterozoic seawater. *Chemical Geology, 155*, 77–90.

Beard, B.-L., Johnson, C.-M., Cox, L., Sun, H., Nealson, K.-H., & Aguilar, C. (1999). Iron isotope biosignatures. *Science, 285*, 1889–1892.

Bekker, A., & Holland, H.-D. (2012). Oxygen overshoot and recovery during the early Paleoproterozoic. *Earth and Planetary Science Letters, 317–318*, 295–304.

Bekker, A., Holland, H.-D., Wang, P.-L., Rumble, D, I. I. I., Stein, H.-J., Hannah, J.-L., et al. (2004). Dating the rise of atmospheric oxygen. *Nature, 427*, 117–120.

Bekker, A., Karhu, J.-A., & Kaufman, A.-J. (2006). Carbon isotope record for the onset of the Lomagundi carbon isotope excursion in the Great Lakes area. *Precambrian Research, 148*, 145–180.

Bekker, A., Kaufman, A.-J., Karhu, J.-A., Beukes, N.-J., Swart, Q.-D., Coetzee, L.-L., et al. (2001). Chemostratigraphy of the Paleoproterozoic Duitschland Formation, South Africa: Implications for coupled climate change and carbon cycling. *American Journal of Science, 301*, 261–285.

Bekker, A., Planavsky, N.-J., Krapež, B., Rasmussen, B., Hofmann, A., Slack, J.-F., et al. (2013). Iron formation: Their origins and implications for ancient seawater chemistry. In F. T. Mackenzie (Ed.), *Sediments, diagenesis, and sedimentary rocks: Treatise on geochemistry* (2nd ed., Vol. 7, pp. 561–628). Amsterdam: Elsevier.

Bekker, A., Slack, J.-F., Planavsky, N., Krapež, B., Hofmann, A., Konhauser, K.-O., et al. (2010). Iron formation: The sedimentary product of a complex interplay among mantle, tectonic, oceanic, and biospheric processes. *Economic Geology, 105*, 467–508.

Berman, R.-G., Sanborn-Barrie, M., Stern, R.-A., & Carson, C.-J. (2005). Tectonometamorphism at ca. 2.35 and 1.85 Ga in the Rae domain, western Churchill Province, Nunavut, Canada: Insights from structural, metamorphic and in situ geochronological analysis of the southwestern Committee Bay belt. *Canadian Mineralogist, 43*, 409–442.

Beukes, N.-J., & Gutzmer, J. (2008). Origin and paleoenvironmental significance of major iron formations at the Archean-Paleoproterozoic boundary. *Reviews in Economic Geology, 15*, 5–47.

Beukes, N.-J., & Klein, C. (1990). Geochemistry and sedimentology of a facies transition-from microbanded to granular iron-formation-in the early Proterozoic Transvaal Supergroup, South Africa. *Precambrian Research, 47*, 99–139.

Beukes, N.-J., Klein, C., Kaufman, A.-J., & Hayes, J.-M. (1990). Carbonate petrography, kerogen distribution, and carbon and oxygen isotope variations in an Early Proterozoic transition from limestone to iron-formation deposition: Transvaal Supergroup, South Africa. *Economic Geology, 85*, 663–690.

Bhatia, M.-R., & Crook, K.-A.-W. (1986). Trace element characteristics of graywackes and tectonic setting discrimination of sedimentary basins. *Contributions to Mineralogy and Petrology, 92*, 181–193.

Bingen, B., Demaiffe, D., & Hergoten, J. (1996). Redistribution of REE, thorium and uranium over accessory minerals in the course of amphibolite to granulite facies metamorphism: The role of apatite and monazite in orthogneisses from south-eastern Norway. *Geochimica et Cosmochimica Acta, 60*, 1341–1354.

Boggs, S. (1995). *Principles of sedimentology and stratigraphy* (pp. 1–784). New Jersey: Prentice-Hall.

Bolhar, R., Kamber, B.-S., Moorbath, S., Fedo, C.-M., & Whitehouse, M.-J. (2004). Characterisation of early Archaean chemical sediments by trace element signatures. *Earth and Planetary Science Letters, 222*, 43–60.

Bronner, G., & Chauvel, J.-J. (1979). Precambrian banded iron-formations of the Ijil Group (Kediat Ijil, Reguibat Shield, Mauritania). *Economic Geology, 74*, 77–94.

Byrne, R., & Sholkovitz, E. (1996). Marine chemistry and geochemistry of the lanthanides. In K. A. Gschneider & L. Eyring (Eds.), *Handbook on the physics and chemistry of the rare earths* (pp. 497–593). Amsterdam: Elsevier.

Cloud, P. (1968). Atmospheric and hydrospheric evolution on the primitive earth: Both secular accretion and biological and geochemical processes have affected earth's volatile envelope. *Science, 160*, 729–736.

Clout, J.-M., & Simonson, B.-M. (2005). Precambrian iron formations and iron formation-hosted ore deposits. In: *Economic geology. 100th Anniversary. Society of Economic Geologists*, 643–679.

Condie, K.-C., O'Neill, C., & Aster, R. (2009). Evidence and implications for a widespread magmatic shutdown for 250 My on Earth. *Earth and Planetary Science Letters, 282*, 294–298.

Crosby, H.-A., Roden, E.-E., Johnson, C.-M., & Beard, B.-L. (2007). The mechanisms of iron isotope fractionation produced during dissimilatory Fe(III) reduction by Shewanella putrefaciens and Geobacter sulfurreducens. *Geobiology, 5*, 169–189.

Crowe, S.-A., Døssing, L.-N., Beukes, N.-J., Bau, M., Kruger, S.-J., Frei, R., et al. (2013). Atmospheric oxygenation three billion years ago. *Nature, 501*, 535–538.

Dai, Y.-P., Zhang, L.-C., Wang, C.-L., Liu, L., Cui, M.-L., Zhu, M.-T., et al. (2012). Genetic type, formation age and tectonic setting of the Waitoushan banded iron formation, Benxi, Liaoning Province. *Acta Petrologica Sinica, 28*, 3574–3594. (in Chinese with English abstract).

Dalton de Souza, J., Kosin, M., Melo, R.-C., Oliveira, E.-P., Carvalho, M.-J., & Leite, C.-M. (2003). Guia de excursão—Geologia do segmento norte doorógeno itabuna-salvador-curaçá. *Revista Brasileira de Geociências, 33*, 27–32.

Dekov, V.-M., Kamenov, G.-D., Stummeyer, J., Thiry, M., Savelli, C., Shanks, W.-C., et al. (2007). Hydrothermal nontronite formation at Eolo Seamount (Aeolian volcanic arc, Tyrrhenian Sea). *Chemical Geology, 245*, 103–119.

Dorland, H.-C. (1999). *Paleoproterozoic laterites, red beds and ironstones of the Pretoria Group with reference to the history of atmospheric oxygen* (pp. 1–147) (Unpublished M.Sc. thesis). Rand Afrikaans University, Johannesburg.

Emerson, D., & Revsbech, N.-P. (1994). Investigation of an iron-oxidizing microbial mat community located near Aarhus, Denmark: Laboratory studies. *Applied and Environmental Microbiology, 60*, 4032–4038.

Ewers, W.-E. (1983). Chemical factors in the deposition and diagenesis of banded iron-formation. In A. F. Trendall & R. C. Morris (Eds.), *Banded iron-formation: Facts and problems* (pp. 491–512). Amsterdam: Elsevier.

Faure, G. (1986). *Principles of isotope geology* (pp. 1–589). New York: Wiley.

Fischer, W.-W., & Knoll, A.-H. (2009). An iron shuttle for deep-water silica in Late Archean and early Paleoproterozoic iron formation. *Geological Society of America Bulletin, 121*, 222–235.

Fischer, W.-W., Schroeder, S., Lacassie, J.-P., Beukes, N.-J., Goldberg, T., Strauss, H., et al. (2009). Isotopic constraints on the Late Archean carbon cycle from the Transvaal Supergroup along the western margin of the Kaapvaal Craton, South Africa. *Precambrian Research, 169*, 15–27.

Frei, R., Dahl, P.-S., Duke, E.-F., Frei, K.-M., Hansen, T.-R., Frandsson, M.-M., et al. (2008). Trace element and isotopic characterization of Neoarchaean and Paleoproterozoic iron formations in the Black Hills (South Dakota, USA): Assessment of chemical change during 2.9–1.9 Ga deposition bracketing the 2.4–2.2 Ga first rise of atmospheric oxygen. *Precambrian Research, 162*, 441–474.

Frei, R., Gaucher, C., Poulton, S.-W., & Canfield, D.-E. (2009). Fluctuations in Precambrian atmospheric oxygenation recorded by chromium isotopes. *Nature, 461*, 225–250.

French, B.-M. (1971). Stability relations of siderite ($FeCO_3$) in the system Fe–CO. *American Journal of Science, 271*, 37–78.

Frost, C.-D., von Blankenburg, F., Schoenberg, R., Frost, B.-R., & Swapp, S.-M. (2007). Preservation of Fe isotope heterogeneities during diagenesis and metamorphism of banded iron formation. *Contributions to Mineralogy and Petrology, 153*, 211–235.

Garrels, R.-M. (1987). A model for the deposition of the micro-banded Precambrian iron formations. *American Journal of Science, 287*, 81–106.

Geng, Y.-S., Wan, Y.-S., Shen, Q.-H., Li, H.-M., & Zhang, R.-X. (2000). Chronological framework of the Early Precambrian important events in the Lüliang area, Shanxi Province. *Acta Petrologica Sinica, 74*, 216–223. (in Chinese with English abstract).

Geng, Y.-S., Wan, Y.-S., & Yang, C.-H. (2003). The Palaeoproterozoic rift-type volcanism in Lüliangshan area, Shanxi Province, and its geological significance. *Acta Geoscientia Sinica, 24*, 97–104. (in Chinese with English abstract).

Geng, Y.-S., Wan, Y.-S., & Yang, C.-H. (2008). Integrated research report on the establishment of Paleoproterozoic system of China: Determination of major Paleoproterozoic geological events and preliminary subdivision of Paleoproterozoic strata in the Lüliang area. In National Stratigraphy Commission (Eds.), *Research report on the establishment of major stratigraphical stages in China (2001–2005)* (pp. 515–533). Beijing: Geological Publishing House (in Chinese).

German, C.-R., & Elderfield, H. (1990). Application of the Ce anomaly as a paleoredox indicator: The ground rules. *Paleoceanography, 5*, 823–833.

German, C.-R., Holliday, B.-P., & Elderfield, H. (1991). Redox cycling of rare earth elements in the suboxic zone of the Black Sea. *Geochimica et Cosmochimica Acta, 55*, 3553–3558.

Gross, G. (1980). A classification of iron formations based on depositional environments. *Canadian Mineralogist, 18*, 215–222.

Gross, G. (1996). Algoma-type iron-formation. In D. Lefebure & T. Hõy (Eds.), *Selected British Columbia mineral deposits profiles* (Vol. 2, pp. 25–28). Ottawa: British Columbia Ministry of Employment and Investment (Open File 1996–13).

Gutzmer, J., & Beukes, N.-J. (1997). Effects of mass transfer, compaction and secondary porosity on hydrothermal upgrading of Paleoproterozoic sedimentary manganese ore in the Kalahari manganese field, South Africa. *Mineralium Deposita, 32*, 250–256.

Hannah, J.-L., Bekker, A., Stein, H.-J., Markey, R.-J., & Holland, H.-D. (2004). Primitive Os and 2316 Ma age for marine shale: Implications for Paleoproterozoicglacial events and the rise of atmospheric oxygen. *Earth and Planetary Science Letters, 225*, 43–52.

Harder, H. (1976). Nontronite synthesis at low temperatures. *Chemical Geology, 18*, 169–180.

Harder, H. (1978). Synthesis of iron layer silicate minerals under natural conditions. *Clays and Clay Minerals, 26*, 65–72.

Hartlaub, R.-P., Heaman, L.-M., Chacko, T., & Ashton, K.-E. (2007). Circa 2.3-Ga magmatism of the Arrowsmith orogeny, Uranium City region, western Churchill Craton, Canada. *Journal of Geology, 115*, 181–195.

Haugaard, R., Frei, R., Stendal, H., & Konhauser, K. (2013). Petrology and geochemistry of the ~2.9 Ga Itilliarsuk banded iron formation and associated supracrustal rocks, West Greenland: Source characteristics and depositional environment. *Precambrian Research, 229*, 150–176.

Heimann, A., Johnson, C.-M., Beard, B.-L., Valley, J.-W., Roden, E.-E., Spicuzza, M.-J., et al. (2010). Fe, C, and O isotope compositions of banded iron formation carbonates demonstrate a major role for dissimilatory iron reduction in ~2.5 Ga marine environments. *Earth and Planetary Science Letters, 294*, 8–18.

Hoffman, P.-F. (2011). Birth date for the Coronation paleocean: Age of initial rifting in Wopmay orogen, Canada. *Canadian Journal of Earth Sciences, 48*, 281–293.

Holland, H.-D. (1984). *The chemical evolution of the atmosphere and oceans* (pp. 1–582). New York: Princeton University Press.

Holland, H.-D. (2006). The oxygenation of the atmosphere and oceans. *Philosophical Transactions of the Royal Society of London B: Biological Sciences, 361*, 903–916.

Hou, K., Li, Y., Gao, J., Liu, F., & Qin, Y. (2014). Geochemistry and Si–O–Fe isotope constraints on the origin of banded iron formations of the Yuanjiacun Formation, Lvliang Group, Shanxi, China. *Ore Geology Reviews, 57*, 288–298.

Huston, D.-L., & Logan, G.-A. (2004). Barite, BIFs and bugs: Evidence for the evolution of the Earth's early hydrosphere. *Earth and Planetary Science Letters, 220*, 41–55.

Icopini, G.-A., Anbar, A.-D., Ruebush, S.-S., Tien, M., & Brantley, S.-L. (2004). Iron isotope fractionation during microbial reduction of iron: The importance of adsorption. *Geology, 32*, 205–208.

Isley, A.-E. (1995). Hydrothermal plumes and the delivery of iron to banded iron formation. *The Journal of Geology, 103*, 169–185.

Isley, A.-E., & Abbott, D.-H. (1999). Plume-related mafic volcanism and the deposition of banded iron formation. *Journal of Geophysical Research, 104*, 15461–15477.

James, H.-L. (1954). Sedimentary facies of iron-formation. *Economic Geology, 49*, 235–293.

Johnson, C.-M., Beard, B.-L., Beukes, N.-J., Klein, C., & O'Leary, J.-M. (2003). Ancient geochemical cycling in the Earth as inferred from Fe isotope studies of banded iron formations from the Transvaal craton. *Contributions to Mineralogy and Petrology, 144*, 523–547.

Johnson, C.-M., Beard, B.-L., Klein, C., Beukes, N.-J., & Roden, E.-E. (2008). Iron isotopes constrain biologic and a biologic processes in banded iron formation genesis. *Geochimica et Cosmochimica Acta, 72*, 151–169.

Johnson, C.-M., Roden, E.-E., Welch, S.-A., & Beard, B.-L. (2005). Experimental constraints on Fe isotope fractionation during magnetite and Fe carbonate formation coupled to dissimilatory hydrous ferric oxide reduction. *Geochimica et Cosmochimica Acta, 69*, 963–993.

Kamber, B.-S., & Webb, G.-E. (2001). The geochemistry of Late Archaean microbial carbonate: Implications for ocean chemistry and continental erosion history. *Geochimica et Cosmochimica Acta, 65*, 2509–2525.

Kappler, A., Pasquero, C., Konhauser, K.-O., & Newman, D.-K. (2005). Deposition of banded iron formations by anoxygenic phototrophic Fe(II)-oxidizing bacteria. *Geology, 33*, 865–868.

Karhu, J.-A., & Holland, H.-D. (1996). Carbon isotopes and the rise of atmospheric oxygen. *Geology, 24*, 867–870.

Kato, Y., Ohta, I., Tsunematsu, T., Watanabe, Y., Isozaki, Y., Maruyama, S., et al. (1998). Rare earth element variations in mid-Archean banded iron formations: Implications for the chemistry of ocean and plate tectonics. *Geochimica et Cosmochimica Acta, 62*, 3475–3497.

Kaufman, A.-J. (1996). Geochemical and mineralogic effects of contact metamorphism on banded iron-formation: An example from the Transvaal Basin, South Africa. *Precambrian Research, 79*, 171–194.

Klein, C. (2005). Some Precambrian banded iron-formations (BIFs) from around the world: Their age, geologic setting, mineralogy, metamorphism, geochemistry, and origin. *American Mineralogist, 90*, 1473–1499.

Klein, C., & Beukes, N.-J. (1993). Proterozoic iron-formations. In K. C. Condie (Ed.), *Proterozoic crustal evolution* (pp. 383–418). Amsterdam: Elsevier.

Klein, C., & Bricker, O.-P. (1977). Some aspects of the sedimentary and diagenetic environment of Proterozoic banded iron-formations. *Economic Geology, 72*, 1457–1470.

Köhler, I., Konhauser, K.-O., Papineau, D., Bekker, A., & Kappler, A. (2013). Biological carbon precursor to diagenetic siderite with spherical structures in iron formations. *Nature Communications, 4*, 1741.

Konhauser, K.-O., Amskold, L., Lalonde, S.-V., Posth, N.-R., Kappler, A., & Anbar, A. (2007). Decoupling photochemical Fe (II) oxidation from shallow-water BIF deposition. *Earth and Planetary Science Letters, 258*, 87–100.

Konhauser, K.-O., Hamade, T., Morris, R.-C., Ferris, F.-G., Southam, G., Raiswell, R., et al. (2002). Could bacteria have formed the Precambrian banded iron formations? *Geology, 30*, 1079–1082.

Konhauser, K.-O., Kappler, A.-K., & Roden, E.-E. (2011b). The microbial role in iron redox and biomineralization reactions. *Elements, 7*, 89–93.

Konhauser, K.-O., Lalonde, S.-V., Planavsky, N., Pecoits, E., Lyons, T, Mojzsis, S., et al. (2011a). Chromium enrichment in iron formations record Earth's first acid rock drainage during the Great Oxidation Event. *Nature, 478*, 369–373.

Konhauser, K.-O., Newman, D.-K., & Kappler, A. (2005). The potential significance of microbial Fe (III)-reduction during Precambrian banded iron formations. *Geobiology, 3*, 167–177.

Konhauser, K.-O., Pecoits, E., Lalonde, S.-V., Papineau, D., Nisbet, E.-G., Barley, M.-E., et al. (2009). Oceanic nickel depletion and a methanogen famine before the great oxidation event. *Nature, 458*, 750–753.

Koziol, A.-M. (2004). Experimental determination of siderite stability and application to Martian Meteorite ALH84001. *American Mineralogist, 89*, 294–300.

Krapež, B., Barley, M.-E., & Pickard, A.-L. (2003). Hydrothermal and resedimented origins of the precursor sediments to banded iron formation: Sedimentological evidence from the early Palaeoproterozoic Brockman Supersequence of Western Australia. *Sedimentology, 50*, 979–1011.

Kump, L.-R., & Seyfried, W.-E. (2005). Hydrothermal Fe fluxes during the Precambrian: Effect of low oceanic sulfate concentrations and low hydrostatic pressure on the composition of black smokers. *Earth and Planetary Science Letters, 235*, 654–662.

Laajoki, K., & Saikkonen, R. (1977). On the geology and geochemistry of the Precambrian iron formations, Väyrylänkylä, South Puolanka area, Finland. *Geological Survey of Finland Bulletin, 292*, 1–137.

Li, Y.-L. (2014). Micro-and nanobands in Late Archean and Palaeoproterozoic banded-iron formations as possible mineral records of annual and diurnal depositions. *Earth and Planetary Science Letters, 391*, 160–170.

Li, Y.-L., Konhauser, K.-O., Cole, D.-R., & Phelps, T.-J. (2011). Mineral ecophysiological data provide growing evidence for microbial activity in banded iron formations. *Geology, 39*, 707–710.

Li, Y.-L., Konhauser, K.-O., Kappler, A., & Hao, X.-L. (2013). Experimental low-grade alteration of biogenic magnetite indicates microbial involvement in generation of banded iron formations. *Earth and Planetary Science Letters, 361*, 229–237.

Liu, D.-Y., Wilde, S.-A., Wan, Y.-S., Wu, J.-S., Zhou, H.-Y., Dong, C.-Y., et al. (2008). New U–Pb and Hf isotopic data confirm Anshan as the oldest preserved segment of the North China Craton. *American Journal of Science, 308*, 200–231.

Liu, S.-W., Zhang, J., Li, Q.-G., Zhang, L.-F., Wang, W., & Yang, P.-T. (2012). Geochemistry and U–Pb zircon ages of metamorphic volcanic rocks of the Paleoproterozoic Lüliang Complex and constraints on the evolution of the Trans-North China Orogen, North China Craton. *Precambrian Research, 222*, 173–190.

Liu, C.-H., Zhao, G.-C., Liu, F.-L., & Shi, J.-R. (2014). Geochronological and geochemical constraints on the Lüliang Group in the Lüliang Complex: Implications for the tectonic evolution of the Trans-North China Orogen. *Lithos, 198*, 298–315.

Liu, C.-H., Zhao, G.-C., Sun, M., Wu, F.-Y., Yang, J.-H., Yin, C.-Q., & Leung, W.-H. (2011). U-Pb and Hf isotopic study of detrital zircons from the Yejishan Group of the Lüliang Complex: Constraints on the timing of collision between the eastern and western blocks, North China Craton. *Sedimentary Geology, 236*, 129–140.

Lovley, D.-R. (1993). Dissimilatory metal reduction. *Annual Reviews in Microbiology, 47*, 263–290.

Master, S. (1991). *Stratigraphy, tectonic setting, and mineralization of the early Proterozoic Magondi Supergroup, Zimbabwe: A review* (Vol. 238, pp. 1–75). Johannesburg: University of Witwatersrand Economic Geology Research Unit (Information Circular).

McCollom, T.-M. (2003). Formation of meteorite hydrocarbons from thermal decomposition of siderite ($FeCO_3$). *Geochimica et Cosmochimica Acta, 67*, 311–317.

McLennan, S.-M. (1989). Rare earth elements in sedimentary rocks: Influence of provenance and sedimentary processes. In: B. R. Lipin & G. A. McKay (Eds.), *Geochemistry and mineralogy of rare earth elements* (Vol. 21, pp. 169–200) (Reviews in Mineralogy and Geochemistry).

McLennan, S.-M., Hemming, S., McDaniel, D.-K., & Hanson, G.-N. (1993). Geochemical approaches to sedimentation, provenance and tectonics. In: M. J. Johnsson & A. Basu (Eds.), *Processes controlling the composition of clastic sediments* (Vol. 284, pp. 21–40). Geological Society of America Special Paper.

McLennan, S.-M., Hemming, S., Taylor, S.-R., & Eriksson, K.-A. (1995). Early proterozoic crustal evolution: Geochemical and Nd–Pb isotopic evidence from metasedimentary rocks, southwestern North America. *Geochimica et Cosmochimica Acta, 59*, 1153–1177.

Miller, A.-R., Reading, K.-L. (1993) Iron-formation, evaporite, and possible metallogenetic implications for the Lower Proterozoic Hurwitz Group, District of Keewatin, Northwest Territories. Current Research, Part C, *Geological Survey of Canada, Paper 93-1C*, 179–185. Ottawa, ON: Natural Resources Canada.

Nealson, K.-H., & Myers, C.-R. (1990). Iron reduction by bacteria: A potential role in the genesis of banded iron formations. *American Journal of Science, 290*, 35–45.

Nozaki, Y., Zhang, J., & Amakawa, H. (1997). The fractionation between Y and Ho in the marine environment. *Earth and Planetary Science Letters, 148*, 329–340.

Often, M. (1985). The early proterozoic Karasjok greenstone belt, Norway: A preliminary description of lithology, stratigraphy and mineralization. *Norges Geologiske Undersøkelse Bulletin, 403*, 75–88.

Ohmoto, H. (2003). Nonredox transformations of magnetite-hematite in hydrothermal systems. *Economic Geology, 98*, 157–161.

Ohta, A., & Kawabe, I. (2001). REE (III) adsorption onto Mn dioxide (δ-MnO_2) and Fe oxyhydroxide: Ce (III) oxidation by δ-MnO_2. *Geochimica et Cosmochimica Acta, 65*, 695–703.

Paakola, J. (1971). The volcanic complex and associated manganiferous iron formation of the Porkonen-Pahtavaara area in Finnish Lapland. *Bulletin dela Commission géologique de Finlande, 247*, 1–82.

Pecoits, E., Gingras, M.-K., Barley, M.-E., Kappler, A., Posth, N.-R., & Konhauser, K.-O. (2009). Petrography and geochemistry of the Dales Gorge banded iron formation: Paragenetic sequence, source and implications for palaeo-ocean chemistry. *Precambrian Research, 172*, 163–187.

Pickard, A.-L., Barley, M.-E., & Krapež, B. (2004). Deep-marine depositional setting of banded iron formation: Sedimentological evidence from interbedded clastic sedimentary rocks in the early Palaeoproterozoic Dales Gorge Member of Western Australia. *Sedimentary Geology, 170*, 37–62.

Planavsky, N.-J., Asael, D., Hofmann, A., Reinhard, C.-T., Lalonde, S.-V., Knudsen, A., et al. (2014). Evidence for oxygenic photosynthesis half a billion years before the Great Oxidation Event. *Nature geosciences, 7*, 283–286.

Planavsky, N.-J., Bekker, A,. Hofmann, A., Owens, J.-D., & Lyons, T.-W. (2012b). Sulfur record of rising and falling marine oxygen and sulfate levels during the Lomagundi event. *Proceedings of the National Academy of Sciences, 109*, 18,300–18,305.

Planavsky, N., Bekker, A., Rouxel, O.-J., Kamber, B., Hofmann, A., Knudsen, A., et al. (2010). Rare earth element and yttrium compositions of Archean and Paleoproterozoic Fe formations revisited: New perspectives on the significance and mechanisms of deposition. *Geochimica et Cosmochimica Acta, 74*, 6387–6405.

Planavsky, N., Rouxel, O.-J., Bekker, A., Hofmann, A., Little, C.-T.-S., & Lyon, T.-W. (2012a). Iron isotope composition of some Archean and Proterozoic iron formations. *Geochimica et Cosmochimica Acta, 80*, 158–169.

Planavsky, N., Rouxel, O.-J., Bekker, A., Shapiro, R., Fralick, P., & Knudsen, A. (2009). Iron-oxidizing microbial ecosystems thrived in late Paleoproterozoic redox-stratified oceans. *Earth and Planetary Science Letters, 286*, 230–242.

Posth, N.-R., Canfield, D.-E., & Kappler, A. (2014). Biogenic Fe (III) minerals: From formation to diagenesis and preservation in the rock record. *Earth-Science Reviews, 135*, 103–121.

Posth, N.-R., Hegler, F., Konhauser, K.-O., & Kappler, A. (2008). Alternating Si and Fe deposition caused by temperature fluctuations in Precambrian oceans. *Nature Geoscience, 1*, 703–708.

Rasmussen, B., Bekker, A., & Fletcher, I.-R. (2013b). Correlation of Paleoproterozoic glaciations based on U–Pb zircon ages for tuff beds in the Transvaal and Huronian Supergroups. *Earth and Planetary Science Letters, 382*, 173–180.

Rasmussen, B., Krapež, B., & Meier, D.-B. (2014a). Replacement origin for hematite in 2.5 Ga banded iron formation: Evidence for postdepositional oxidation of iron-bearing minerals. *Geological Society of America Bulletin, 126*, 438–446.

Rasmussen, B., Krapež, B., & Muhling, J.-R. (2014b). Hematite replacement of iron-bearing precursor sediments in the 3.46-by-old Marble Bar Chert, Pilbara Craton, Australia. *Geological Society of America Bulletin, 126*, 1245–1258.

Rasmussen, B., Meier, D.-B., Krapež, B., & Muhling, J.-R. (2013a). Iron silicate microgranules as precursor sediments to 2.5-billion-year-old banded iron formations. *Geology, 41*, 435–438.

Raye, U., Pufahl, P.-K., Kyser, T.-K., Ricard, E., & Hiatt, E.-E. (2015). The role of sedimentology, oceanography, and alteration on the δ^{56}Fe value of the Sokoman iron formation, labrador trough, Canada. *Geochimica et Cosmochimica Acta, 164*, 205–220.

Resende, M.-G., & Jost, H. (1995). Petrogênese de formações ferríferas emetahidrotermalitos da formação aimbé, Grupo Guarinos (Arqueano), Goiás. *Revista Brasileira de Geociencias, 25*, 41–50.

Roser, B.-P., & Korsch, R.-J. (1986). Determination of tectonic setting of sandstone-mudstone suites using SiO_2 content and K_2O/Na_2O ratio. *Journal of Geology, 94*, 635–650.

Rouxel, O., Bekker, A., & Edwards, K. (2005). Iron isotope constraints on the Archean and Paleoproterozoic ocean redox state. *Science, 307*, 1087–1091.

Schidlowski, M., Eichmann, R., & Junge, C.-E. (1976). Carbon isotope geochemistry of the Precambrian Lomagundi carbonate province, Rhodesia. *Geochimica et Cosmochimica Acta, 40*, 449–455.

Schröder, S., Bekker, A., Beukes, N.-J., Strauss, H., & van Niekerk, H.-S. (2008). Rise in seawater sulphate concentration associated with the Paleoproterozoic positive carbon isotope excursion: Evidence from sulphate evaporites in the 2.2–2.1 Gyr shallow-marine Lucknow formation, South Africa. *Terra Nova, 20*, 108–117.

Schweigart, H. (1965). Genesis of the iron ores of the Pretoria Series, South Africa. *Economic Geology, 60*, 269–298.

Schwertmann, U., & Murad, E. (1983). Effect of pH on the formation of goethite and hematite from ferrihydrite. *Clays and Clay Minerals, 31*, 277–284.

Scott, C., Wing, B.-A., Bekker, A., Planavsky, N.-J., Medvedev, P., Bates, S.-M., et al. (2014). Pyrite multiple-sulfur isotope evidence for rapid expansion and contraction of the early Paleoproterozoic seawater sulfate reservoir. *Earth and Planetary Science Letters, 389*, 95–104.

Shen, B.-F., Song, L.-S., & Li, H.-Z. (1982). An analysis of the sedimentary facies and the formation condition of the Yuanjiacun iron formation, Lanxian County, Shanxi Province, China. *Journal of Changchun Geological Institution, 25*, 31–51. (in Chinese with English abstract).

Shen, Q.-H. (1998). The geological characteristics and forming geological background of the Early Precambrian banded itabirite in North China platform. In: Y.Q. Cheng (Ed.), *Precambrian geology study of North China platform*. Beijing, Geological Publishing House (in Chinese), 1–30.

Shen, Q.-H., Song, H.-X., & Zhao, Z.-R. (2009). Characteristics of rare earth elements and trace elements in Hanwang Neo-Archaean banded iron formations, Shandong Province. *Acta Geoscientica Sinica, 30*, 693–699. (in Chinese with English abstract).

Sholkovitz, E.-R., Shaw, T., & Schneider, D.-L. (1992). The geochemistry of rare earth elements in the seasonally anoxic water column and pore waters of Chesapeake Bay. *Geochimica et Cosmochimica Acta, 56*, 3389–3402.

Siever, R. (1992). The silica cycle in the Precambrian. *Geochimica et Cosmochimica Acta, 56*, 3265–3272.

Silver, P.-G., & Behn, M.-D. (2008). Intermittent plate tectonics? *Science, 319*, 85–88.

Slack, J.-F., Grenne, T., Bekker, A., Rouxel, O.-J., & Lindberg, P.-A. (2007). Suboxic deep seawater in the late Paleoproterozoic: Evidence from hematitic chert and iron formation related to seafloor-hydrothermal sulfide deposits, central Arizona, USA. *Earth and Planetary Science Letters, 255*, 243–256.

Smith, A.-J., Beukes, N.-J., & Gutzmer, J. (2013). The composition and depositional environments of Mesoarchean iron formations of the West Rand Group of the Witwatersrand Supergroup, South Africa. *Economic Geology, 108*, 111–134.

Spier, C.-A., de Oliveira, S.-M.-B., Sial, A.-N., & Rios, F.-J. (2007). Geochemistryand genesis of the banded iron formations of the Cauê Formation, Quadrilátero Ferrífero, Minas Gerais, Brazil. *Precambrian Research, 152*, 170–206.

Sun, S., Konhauser, K.-O., Kappler, A., & Li, Y.-L. (2015). Primary hematite in Neoarchean to Paleoproterozoic oceans. *Geological Society of America Bulletin, B31122*, 1–12.

Tian, Y.-Q., Yuan, G.-P., Lu, J.-R., Jing, Y., Yu, J.-H., & Li, M.-M. (1986). *Research on formation conditions and tectonic characteristics of Precambrian Yuanjiacun metamorphic-sedimentary iron deposits in Lan County, Shanxi Province* (pp. 1–270). Shanxi: Geology and Mineral Resources Bureau Press (in Chinese).

Trendall, A.-F. (2002). The significance of iron-formation in the Precambrian stratigraphic record. *Special Publication International Association of Sedimentologists, 33*, 33–66.

Trendall, A.-F., & Blockley, J.-G. (1970). The iron-formations of the Precambrian Hamersley Group, Western Australia. *Geological Survey of Western Australia Bulletin, 119*, 1–366.

Tsikos, H., & Moore, J.-M. (1997). Petrography and geochemistry of the Paleoproterozoic Hotazel iron-formation, Kalahari manganese field, South Africa: Implications for Precambrian manganese metallogenesis. *Economic Geology, 92*, 87–97.

Wan, Y.-S., Dong, C.-Y., Xie, H.-Q., Wang, S.-J., Song, M.-C., Xu, Z.-Y., et al. (2012). Formation ages of Early Precambrian BIFs in the North China Craton: SHRIMP zircon U-Pb dating. *Acta Geologica Sinica, 86*, 1447–1478. (in Chinese with English abstract).

Wan, Y.-S., Geng, Y.-S., Shen, Q.-H., & Zhang, R.-X. (2000). Khondalite series-geochronology and geochemistry of the Jiehekou Group in Lüliang area, Shanxi Province. *Acta Petrologica Sinica, 16*, 49–58. (in Chinese with English abstract).

Wang, C.-L., Konhauser, K.-O., & Zhang, L.-C. (2015b). Depositional environment of the Paleoproterozoic Yuanjiacun banded iron formation in Shanxi Province, China. *Economic Geology, 110*, 1515–1539.

Wang, C.-L., Zhang, L.-C., Dai, Y.-P., & Lan, C.-Y. (2015a). Geochronological and geochemical constraints on the origin of clastic meta-sedimentary rocks associated with the Yuanjiacun BIF from the Complex, North China. *Lithos, 212–215*, 231–246.

Wang, C.-L., Zhang, L.-C., Lan, C.-Y., & Dai, Y.-P. (2014). Rare earth element and yttrium compositions of the Paleoproterozoic Yuanjiacun BIF in the Lüliang area and their implications for the Great Oxidation Event (GOE). *Science China Earth Sciences, 57*, 2469–2485.

Wang, C.-L., Zhang, L.-C., Lan, C.-Y., Li, H.-Z., & Huang, H. (2015c). Analysis of sedimentary facies and depositional environment of the Yuanjiacun banded iron formation in the Lüliang, Shanxi Province. *Acta Petrologica Sinica, 31*, 1671–1693 (in Chinese with English abstract).

Yao, P.-H. (1993). *Records of Chinese iron ore deposits* (pp. 1–662). Beijing: Metallurgical Industry Press (in Chinese).

Yu, J.-H., Wang, D.-Z., & Wang, C.-Y. (1997a). Ages of the Lüliang Group and its main metamorphism in the Lüliang Mountains, Shanxi—Evidence from single-grain zircon U–Pb ages. *Geological Review, 43*, pp. 403–408 (in Chinese with English abstract).

Yu, J.-H., Wang, D.-Z., & Wang, C.-Y. (1997b). Geochemical characteristics and Petrogenesis of the early Proterozoic bimodal volcanic rocks from Lüliang group, Shanxi Province. *Acta Petrologica Sinica, 13*, 59–70 (in Chinese with English abstract).

Zhai, M.-G., & Santosh, M. (2013). Metallogeny of the North China Craton: Link with secular changes in the evolving Earth. *Gondwana Research, 24*, 275–297.

Zhai, M.-G., & Windley, B.-F. (1990). The Archaean and early Proterozoic banded iron formations of North China: Their characteristics geotectonic relations, chemistry and implications for crustal growth. *Precambrian Research, 48*, 267–286.

Zhang, L.-C., Zhai, M.-G., Wan, Y.-S., Guo, J.-H., Dai, Y.-P., C.-L., et al. (2012b). Study of the Precambrian BIF-iron deposits in the North China Craton: Progresses and questions. *Acta Petrologica Sinica, 28*, 3431–3445 (in Chinese with English abstract).

Zhang, L.-C., Zhai, M.-G., Zhang, X.-J., Xiang, P., Dai, Y.-P., Wang, C.-L., et al. (2012a). Formation age and tectonic setting of the Shirengou Neoarchean banded iron deposit in eastern Hebei Province: Constraints from geochemistry and SIMS zircon U–Pb dating. *Precambrian Research, 222*, 325–338.

Zhang, X.-J., Zhang, L.-C., Xiang, P., Wan, B., & Pirajno, F. (2011). Zircon U–Pb age, Hf isotopes and geochemistry of Shuichang Algoma-type banded iron-formation, North China Craton: Constraints on the ore-forming age and tectonic setting. *Gondwana Research, 20*, 137–148.

Zhao, G.-C., Sun, M., Wilde, S.-A., & Li, S.-Z. (2005). Late Archean to Paleoproterozoic evolution of the North China Craton: Key issues revisited. *Precambrian Research, 136*, 177–202.

Zhao, G.-C., Wilde, S.-A., Sun, M., Li, S.-Z., Li, X.-P., & Zhang, J. (2008). SHRIMP U–Pb zircon ages of granitoid rocks in the Lüliang Complex: Implications for the accretion and evolution of the Trans-North China Orogen. *Precambrian Research, 160*, 213–226.

Zhao, G.-C., & Zhai, M.-G. (2013). Lithotectonic elements of Precambrian basement in the North China Craton: Review and tectonic implications. *Gondwana Research, 23*, 1207–1240.

Zhu, J.-C., & Zhang, F.-S. (1987). The formation condition of the Precambrian iron ores in Yuanjiacun ore deposit, Shanxi Province. *Mineral Deposita-CH, 6*, 11–21. (in Chinese with English abstract).

Zhu, J.-C., Zhang, F.-S., & Xu, K.-Q. (1988). Depositional environment and metamorphism of Early Proterozoic iron formation in the Lüliangshan region, Shanxi Province, China. *Precambrian Research, 39*, 39–50.

Part IV

Meso-Neoproterozoic Multiple Rifting and Metallogeny

14 Magmatic Records of the Late Paleoproterozoic to Neoproterozoic Extensional and Rifting Events in the North China Craton: A Preliminary Review

Shuan-Hong Zhang and Yue Zhao

Abstract

The North China Craton (NCC) is characterized by multistages of extensional and continental rifting and deposition of thick marine or interactive marine and terrestrial clastic and carbonate platform sediments without angular unconformity during Earth's middle age of 1.70–0.75 Ga. Factors controlling these multistages of extensional and continental rifting events in the NCC can be either from the craton itself or from the neighboring continents being connected during these periods. Two large igneous provinces including the ca. 1.32 Ga mafic sill swarms in Yanliao rift (aulacogen) in the northern NCC and the ca. 0.92–0.89 Ga Xu-Huai–Dalian–Sariwon mafic sill swarms in southeastern and eastern NCC, have recently been identified from the NCC. Rocks from these two large igneous provinces exhibit similar geochemical features of tholeiitic compositions and intraplate characteristics. Formation of these two large igneous provinces was accompanied by pre-magmatic uplift as indicated by the field relations between the sills and their hosted sedimentary rocks. The Yanliao and Xu-Huai–Dalian–Sariwon large igneous provinces represent two continental rifting events that have led to rifting to drifting transition and breakup of the northern margin of the NCC from the Columbia (Nuna) supercontinent and the southeastern margin of the NCC from the Rodinia supercontinent, respectively. As shown by the ca. 200 Ma Central Atlantic Magmatic Province related to breakup of the Pangea supercontinent and initial opening of the Central Atlantic Ocean and the ca. 180 Ma Karoo-Ferrar large igneous province related to initial breakup of Gondwana, magmatism related to continental breakup and rifting to drifting transition can occur as mafic dykes, sills, and/or lavas across the neighboring continents and is mainly tholeiitic in chemical composition. This kind of magmatism should be large in volume and constitute a large igneous province. In many cases, eruption or/and emplacement of breakup-related magmatism were accompanied by pre-magmatic uplift. Large volumes of mafic sill swarms near continental margins and accompanied pre-magmatic uplift in marginal rift basins can most likely be used as important indicators for continental breakup and paleogeographic reconstruction.

Keywords

Late Paleoproterozoic to Meso-Neoproterozoic • Earth's middle age • Continental breakup • Continental rifting • Rodinia supercontinent • Columbia (Nuna) supercontinent • North China Craton

S.-H. Zhang (✉) · Y. Zhao
Institute of Geomechanics, Chinese Academy of Geological Sciences, Beijing, 100081, China
e-mail: tozhangshuanhong@163.com

Y. Zhao
e-mail: yue_zhao@cags.ac.cn

S.-H. Zhang · Y. Zhao
Key Laboratory of Palaeomagnetism and Tectonic Reconstruction, Ministry of Land and Resources, Beijing, 100081, China

M. Zhai et al. (eds.), *Main Tectonic Events and Metallogeny of the North China Craton*, Springer Geology, DOI 10.1007/978-981-10-1064-4_14

14.1 Introduction

The period 1.70–0.75 Ga is Earth's middle age that is characterized by environmental, evolutionary, and lithospheric stability that contrasts with the dramatic changes in preceding and succeeding eras (Cawood and Hawkesworth 2014). Two supercontinents, namely Columbia (Nuna) and Rodinia, existed during this period (e.g., Hoffman 1991; Dalziel 1991; Zhao et al. 2002, 2004a, 2011; Rogers and Santosh 2002; Evans 2013). The North China Craton (NCC) during this period is characterized by deposition of thick marine or interactive marine and terrestrial clastic and carbonate platform sediments. Although several disconformities have been identified, no regional angular unconformities have been recognized, indicating no deformation during the deposition of these thick sequences of sedimentary rocks. Except for the high-potassium alkaline mafic-intermediate volcanic rocks in the Dahongyu Formation and the upper part of the Tuanshanzi Formation in Pinggu and Jixian areas within the Yanliao rift (aulacogen) in the northern NCC (e.g., Liu 1991; Yu et al. 1994; Ding et al. 2005; Hu et al. 2007; Zhang et al. 2013b, 2015; Wang et al. 2015a), volcanic rocks are rare within the late Paleoproterozoic to Meso-Neoproterozoic sedimentary sequences. In recent years, many layers of tuffs and K-bentonite beds have been identified from the sedimentary rocks in the Yanliao rift (aulacogen) in the northern NCC and Ruzhou area in southern margin of the NCC, which provide important constraints on ages of the strata of the NCC (Gao et al. 2007, 2008a, b; Su et al. 2008, 2010, 2012; Li et al. 2010a, 2014a; Tian et al. 2015).

Traditionally, the lower boundary age of the Mesoproterozoic period in China has been regarded as 1.80 Ga based on the lower boundary age of the Changzhougou Formation in the Yanliao rift (aulacogen) in the northern NCC (e.g., China National Commission on Stratigraphy 2001; Wang 2014). This boundary age of 1.80 Ga is 200 Ma earlier than that of the Mesoproterozoic period of 1.60 Ga in the International Stratigraphic Chart (e.g., Gradstein et al. 2004; Walker and Geissman 2009; International Commission on Stratigraphy 2012). The lower boundary age of the Changzhougou Formation in the Yanliao rift (aulacogen) was traditionally regarded as 1.80 Ga. However, recently results show that the lower boundary age of the Changzhougou Formation in the Yanliao rift (aulacogen) is likely ca. 1.70 Ga (Wang et al. 1995; Peng et al. 2012) or ca. 1.66–1.65 Ga (Li et al. 2011, 2013; He et al. 2011a, b; Zhang et al. 2013b). Moreover, regional geological mapping results show that the contact between the 1.79–1.76 Ga volcanic rocks of Xiong'er Group and the late Paleoproterozoic to Mesoproterozoic Yunmengshan Formation or Gaoshanhe Formation (BGMRHNP 1989; BGMRSP 1989; GSIHNP 2003, GSISXP 2007; Zhao et al. 2015) is an angular unconformity, indicating that the Xiong'er Group is very different from the late Paleoproterozoic to Meso-Neoproterozoic sedimentary sequences in the NCC and may belong to another structural layer beneath the late Paleoproterozoic to Meso-Neoproterozoic sedimentary rocks in the NCC. A regional deformation event likely occurred between deposition of the Xiong'er Group and the Yunmengshan Formation or Gaoshanhe Formation during ca. 1.75–1.70 Ga. Therefore, the tectonic setting of the Xiong'er Group in the southern NCC is likely very different from that of the other late Paleoproterozoic to Meso-Neoproterozoic sedimentary rocks in the NCC. In this chapter, we will give a preliminary review on the magmatic records of the late Paleoproterozoic to Neoproterozoic (Meso-Neoproterozoic according to the Stratigraphic Chart of China using 1.80 Ga as the lower boundary age of the Mesoproterozoic period) extensional and rifting events in the NCC from ca. 1.75–1.70 Ga.

14.2 Late Paleoproterozoic Magmatism, Extension, and Continental Rifting

14.2.1 The 1.75–1.68 Ga Magmatism and Extension in the NCC

The 1.75–1.68 Ga magmatic rocks are mainly distributed in the northern NCC with minor in the southern margin of the NCC (Table 14.1; Fig. 14.1). Most of them are located within or near the Trans-North China Orogen of the NCC as shown by Zhao et al. (2005). One small alkaline intrusion (Wayao quartz syenite, Wang et al. 2012a) is located in the khondalite belt between the Yinshan and Ordos blocks (Fig. 14.1). Formation of the 1.75–1.68 Ga magmatic rocks is lightly later than eruption of the 1.79–1.76 Ga volcanic rocks of Xiong'er Group in the southern NCC and emplacement of the 1.79–1.77 Ga mafic dyke swarms in the central NCC (e.g., Zhao et al. 2002; Peng et al. 2008; He et al. 2009; Peng 2015). However, their emplacement is earlier than deposition of the Meso-Neoproterozoic sedimentary sequences in the NCC, as indicated by the conformity between the 1.73 Ga Guandaokou quartz syenite porphyry and the Gaoshanhe Formation in the southern margin of the NCC (Ren et al. 2000) and conformity between the 1.68 Ga Shachang rapakivi granite and the Changzhougou Formation in the Yanliao rift (aulacogen) in the northern NCC (He et al. 2011a, b).

The 1.75–1.68 Ga magmatic rocks consist mainly of norite, mangerite, anorthosite, charnockite, gabbro, syenite, monzonite, rapakivi granite, alkaline granite, diorite and mafic (diabase) dykes (Table 14.1). The above rock associations indicate their emplacement in an extensional tectonic

Table 14.1 Summary of zircon U–Pb and $^{40}Ar/^{39}Ar$ ages of the 1.75–1.68 Ga magmatic rocks in the NCC

Location/intrusion name	Longitude (E)	Latitude (N)	Rock type	Age (Ma)	Method	References
Damiao, northern Hebei	117°42′–118°15′	41°08′–41°19′	Norite	1693 ± 7	Zircon TIMS	Zhao et al. (2004b)
			Mangerite	1715 ± 6	Zircon TIMS	Zhao et al. (2004b)
			Mangerite	1718 ± 26	Zircon TIMS	Ren et al. (2006)
			Light anorthosite	1726 ± 9	Zircon SHRIMP	Zhang et al. (2007)
			Mangerite	1739 ± 14	Zircon SHRIMP	Zhao et al. (2009)
			Norite	1742 ± 17	Zircon LA-ICP-MS	Zhao et al. (2009)
			Noritic gabbro	1725 ± 13	Zircon LA-ICP-MS	Teng and Santosh (2015)
			Norite	1687 ± 18	Zircon LA-ICP-MS	Teng and Santosh (2015)
			Leuconorite	1751 ± 15	Zircon LA-ICP-MS	Teng and Santosh (2015)
			Leuconorite	1693 ± 24	Zircon LA-ICP-MS	Teng and Santosh (2015)
			Gabbronorite	1721 ± 17	Zircon LA-ICP-MS	Teng and Santosh (2015)
			Gabbroic anorthosite	1729 ± 14	Zircon LA-ICP-MS	Teng and Santosh (2015)
			Ferroan charnockite	1749 ± 6	Zircon LA-ICP-MS	Yang et al. (2014)
			Ferroan charnockite	1747 ± 10	Zircon LA-ICP-MS	Yang et al. (2014)
			Magnesian charnockite	1756 ± 3	Zircon LA-ICP-MS	Yang et al. (2014)
			Magnesian charnockite	1757 ± 9	Zircon LA-ICP-MS	Yang et al. (2014)
			Magnesian charnockite	1731 ± 17	Zircon LA-ICP-MS	Yang et al. (2014)
			Gabbro	1732 ± 8	Zircon LA-ICP-MS	Yang et al. (2014)
			Gabbroic anorthosite	1747 ± 7	Zircon LA-ICP-MS	Yang et al. (2014)
			Magnetite	1763 ± 22	Zircon LA-ICP-MS	Liu et al. (2016)
			Magnetite	1768 ± 39	Zircon LA-ICP-MS	Liu et al. (2016)
			Magnetite	1752 ± 53	Zircon LA-ICP-MS	Liu et al. (2016)
Changsaoying, northern Beijing	116°46′–117°00′	40°45′–40°49′	K-feldspar granite	1753 ± 23	Zircon SHRIMP	Zhang et al. (2007)
Gubeikou, northern Beijing	117°07′–117°31′	40°40′–40°45′	K-feldspar granite	1692 ± 19	Zircon LA-ICP-MS	Zhang et al. (2007)
Lanying, northern Beijing	116°29′–116°44′	40°45′–40°49′	Anorthosite	1739 ± 43	Zircon LA-ICP-MS	Zhang et al. (2007)
			Quartz syenite	1712 ± 15	Zircon LA-ICP-MS	Zhang et al. (2007)
Pingquan, northern Hebei	118°31′–118°44′	41°02′–41°11′	Clinopyroxene syenite	1726 ± 13	Zircon TIMS	Ren et al. (2006)

(continued)

Table 14.1 (continued)

Location/intrusion name	Longitude (E)	Latitude (N)	Rock type	Age (Ma)	Method	References
Shachang, Miyun, northern Beijing	116°58′–117°07′	40°22′–40°25′	Rapakivi granite	1706 ± 15	Zircon TIMS	Song (1992)
			Rapakivi granite	1715 ± 35	Zircon TIMS	Song (1992)
			Rapakivi granite	1716 ± 21	Hornblende $^{40}Ar/^{39}Ar$	Hu et al. (1990)
			Rapakivi granite	1711 ± 6	Hornblende $^{40}Ar/^{39}Ar$	Song (1992)
			Rapakivi granite	1683 ± 4	Zircon TIMS	Ramo et al. (1995)
			Rapakivi granite	1681 ± 10	Zircon LA-ICP-MS	Yang et al. (2005)
			Rapakivi granite	1679 ± 10	Zircon LA-ICP-MS	Yang et al. (2005)
			Rapakivi granite	1685 ± 15	Zircon SHRIMP	Gao et al. (2008c)
Wenquan, Zhangjiakou, NW Hebei	115°41′–115°50′	40°52′–40°57′	A-type granite	1697 ± 7	Zircon LA-ICP-MS	Jiang et al. (2011)
Miyun, northern Beijing	117°01′–117°09′	40°32′–40°39′	Mafic dyke	1731 ± 4	Baddeleyite TIMS	Peng et al. (2012)
Jianping, western Liaoning	119°33′–119°40′	40°25′–40°35′	Magnetite	1694 ± 12	Zircon LA-ICP-MS	Liu et al. (2011)
			Magnetite diorite	1721 ± 9	Zircon LA-ICP-MS	Wang et al. (2013a)
			Clinopyroxene monzonite	1724 ± 10	Zircon LA-ICP-MS	Wang et al. (2013a)
			Clinopyroxene monzonite	1720 ± 8	Zircon LA-ICP-MS	Wang et al. (2013a)
			Quartz syenite	1717 ± 9	Zircon LA-ICP-MS	Wang et al. (2013a)
			Syenite	1701 ± 9	Zircon LA-ICP-MS	Wang et al. (2013a)
			Quartz syenite	1698 ± 13	Zircon LA-ICP-MS	Wang et al. (2013a)
			Magnetite	1725 ± 26	Zircon LA-ICP-MS	Liu et al. (2016)
Wayao, Guyang, Inner Mongolia	110°33′–110°41′	40°54′–40°57′	Quartz syenite	1702 ± 32	Zircon SHRIMP	Wang et al. (2012a)
Yanyaozhai, Luanchuan, Henan	110°29′	34°05′	Syenite	1750 ± 65	Zircon TIMS	Ren et al. (2000)
Guandaokou, Lushi, Henan	110°04′	34°18′–34°19′	Quartz syenite porphyry	1731 ± 29	Zircon TIMS	Ren et al. (2000)

setting. Although some researchers considered the 1.75–1.68 Ga anorthosite-mangerite-alkali granitoid-rapakivi granite suite in the northern NCC as anorogenic magmatism in continental rifting (e.g., Ramo et al. 1995; Yu et al. 1994, 1996; Ren et al. 2006; Zhai et al. 2014, 2015), others proposed that the 1.75–1.68 Ga magmatic rocks in the NCC were generated in a postcollisional/post-orogenic extensional tectonic environment after continent–continent collision between the Western and Eastern continental blocks of the NCC at ca. 1.85 Ga (Zhang et al. 2007; Wang et al. 2013a; Yang et al. 2014; Teng and Santosh 2015; Liu et al. 2016). Since the 1.75–1.68 Ga magmatic rocks in the NCC are mainly distributed within or near the Trans-North China Orogen of the NCC and their emplacement occurred prior to deposition of the Meso-Neoproterozoic sedimentary sequences, we believe that the 1.75–1.68 Ga magmatism in the NCC occurred in a postcollisional/post-orogenic extensional tectonic environment and represents a long extension period in the NCC after continent–continent collision between the Western and Eastern continental blocks at ca. 1.85 Ga, as

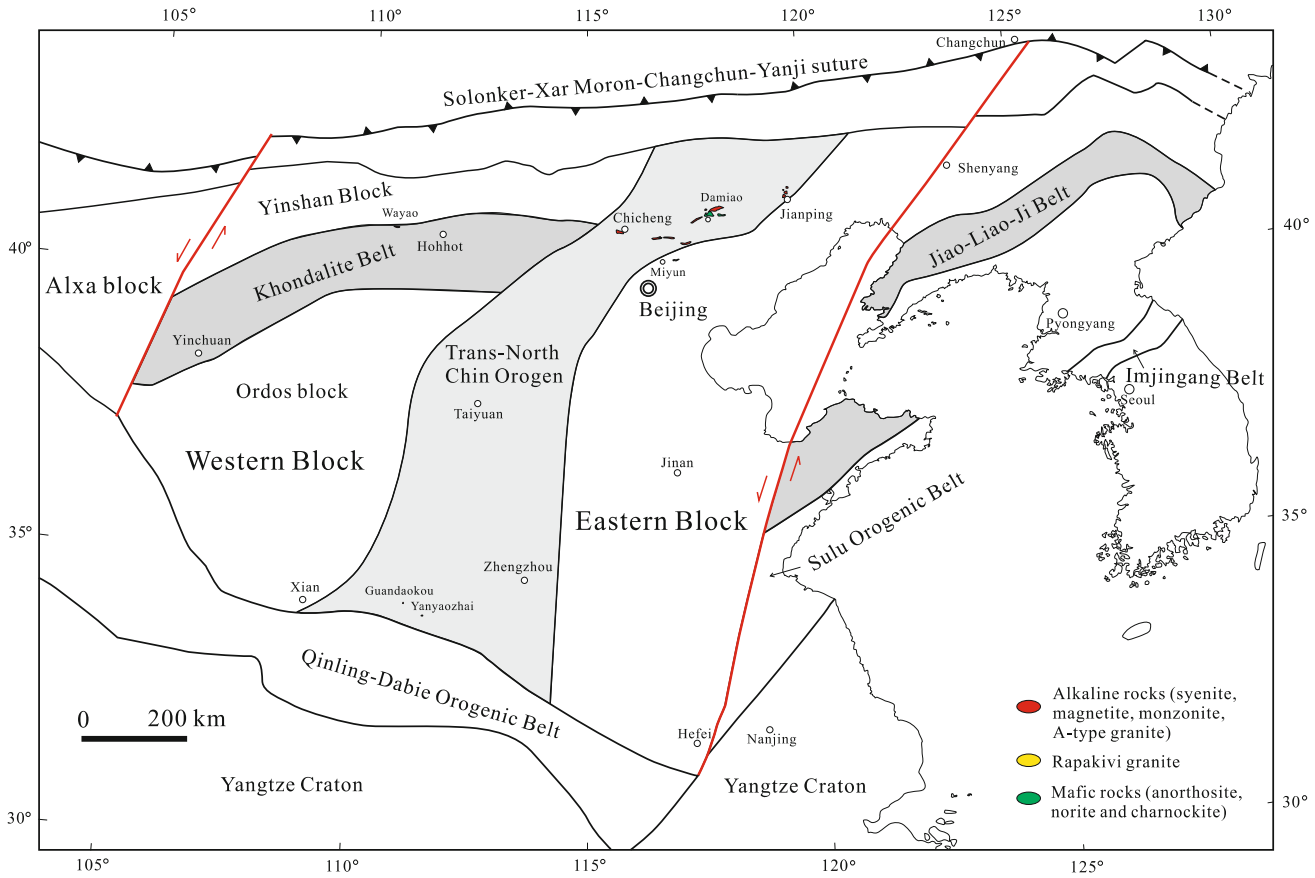

Fig. 14.1 Sketch map showing distribution of the 1.75–1.68 Ga magmatic rocks in the NCC. Boundaries of the late Paleoproterozoic (1.95–1.85 Ga) orogens are from Zhao et al. (2005), Zhao and Zhai (2013)

suggested by our previous study on the 1.75–1.68 Ga anorthosite-mangerite-alkali granitoid-rapakivi granite suite from the northern North China Craton (Zhang et al. 2007).

14.2.2 The 1.64–1.62 Ga Volcanic Rocks in the Yanliao Rift (Aulacogen)

The 1.64–1.62 Ga volcanic rocks are located within the Dahongyu Formation and the upper part of the Tuanshanzi Formation in Pinggu, Jixian, Zunhua, and Luanxian areas in the Yanliao rift (aulacogen) (Figs. 14.2 and 14.3). They are distributed in a SEE-trending zone that is 150 km long and 20 km wide. The volcanic eruption centers are located near Pingpu and Jixian areas with thickness ranging from 60 to 450 m (BGMRHBP 1989). In the Zunhua and Luanxian areas, their thickness is about 2–16 m (BGMRHBP 1989). Zircon LA-ICP-MS (laser ablation-inductively coupled mass spectrometry) U–Pb dating on a potassium-rich volcanic rock in the upper part of the Tuanshanzi Formation in Pinggu area yielded a weighted mean $^{207}Pb/^{206}Pb$ age of 1637 ± 15 Ma and a concordia age of 1641 ± 4 Ma, indicating eruption of the volcanic rocks of the Tuanshanzi Formation at ca. 1.64 Ga (Zhang et al. 2013b). Volcanic rocks from the Dahongyu Formation in Pinggu and Jixian areas yielded zircon $^{207}Pb/^{206}Pb$ ages from 1626 ± 9 to 1622 ± 23 Ma (Lu and Li 1991; Lu et al. 2008b; Gao et al. 2008a; Zhang et al. 2015).

The 1.64–1.62 Ga volcanic rocks are composed mainly of olivine basalt, trachybasalt, trachyandesite, trachyte, phonolite, and some volcanic-clastic rocks. Most of them are classed as alkaline volcanic rocks in the total alkali ($K_2O + Na_2O$) versus silica (SiO_2) classification diagram (Liu 1991; Yu et al. 1994; Ding et al. 2005; Hu et al. 2007; Wang et al. 2015a; Zhang et al. 2015). They are characterized by low contents of SiO_2 and high contents of K_2O and exhibit slightly negative to positive $\varepsilon_{Nd}(t)$ and $\varepsilon_{Hf}(t)$ values from −2.1 to 4.3 (Hu et al. 2007; Wang et al. 2015a), indicating that they were likely produced by partial melting of the asthenosphere with assimilation of crustal materials. Most researchers agree that the 1.64–1.62 Ga volcanic rocks in the Yanliao rift (aulacogen) were formed in an intracontinental rift setting (Liu 1991; Yu et al. 1994; Ding et al. 2005; Hu et al. 2007; Wang et al. 2015a; Zhang et al. 2015). Some researchers proposed that the 1.64–1.62 Ga volcanic rocks represent the rifting to drifting (or spreading) transition

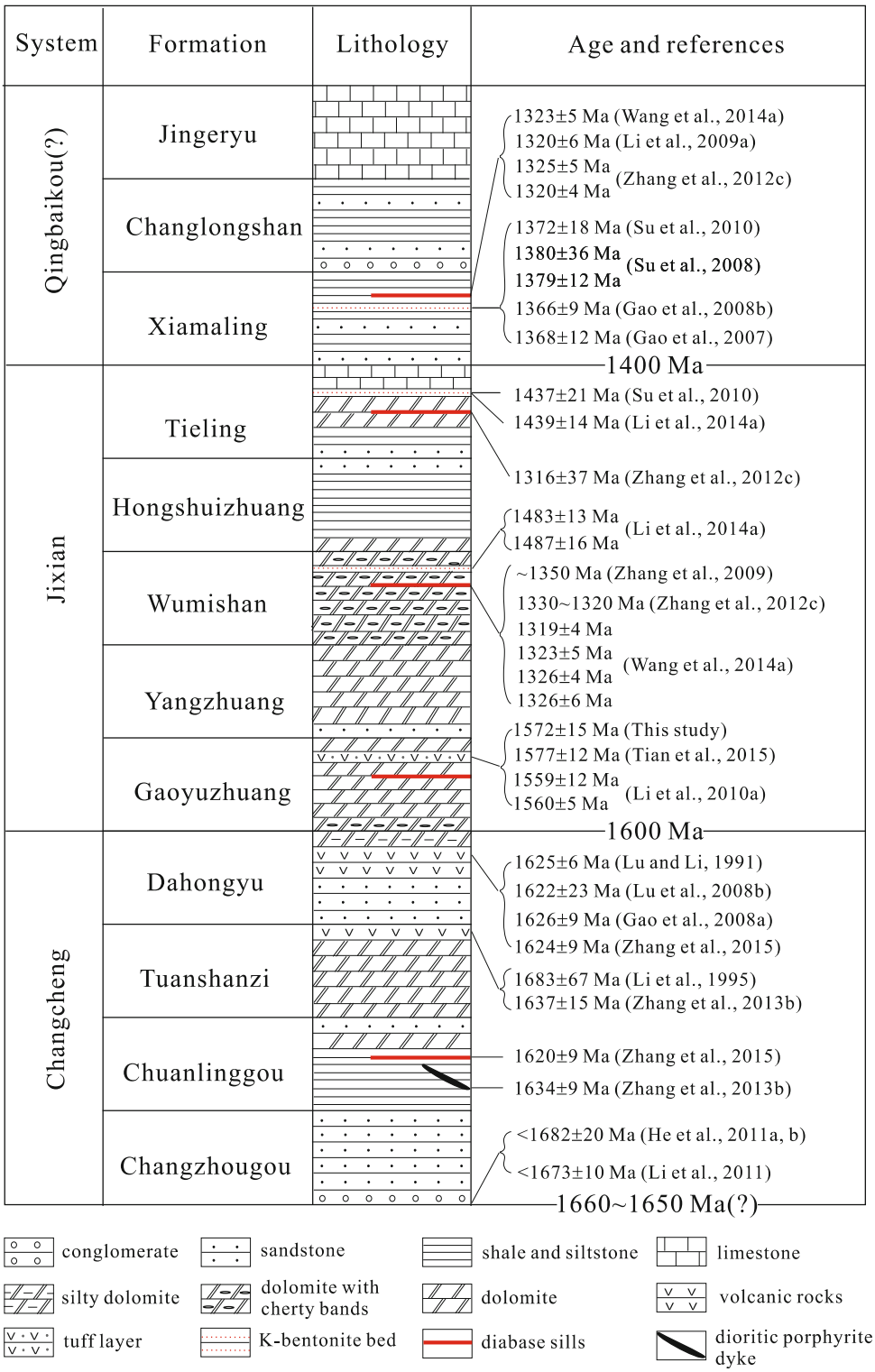

Fig. 14.2 Subdivision and zircon U–Pb age constraints on the late Paleoproterozoic to Mesoproterozoic strata in the Yanliao rift (aulacogen) in the northern NCC (modified after Zhang et al. 2013b)

of the northern NCC from the Columbia supercontinent (Meng et al. 2011; Zhang et al. 2015); others proposed that the continental rifting was aborted shortly after the beginning and has not resulted in rifting to drifting transition (Ding et al. 2005). Since the 1.64–1.62 Ga volcanic rocks are only distributed in a very small area in the Yanliao rift (aulacogen) and are characterized by alkaline geochemical compositions, we propose the 1.64–1.62 Ga volcanic rocks were formed in a failed intracontinental rift that has not developed into a rifting to drifting transition.

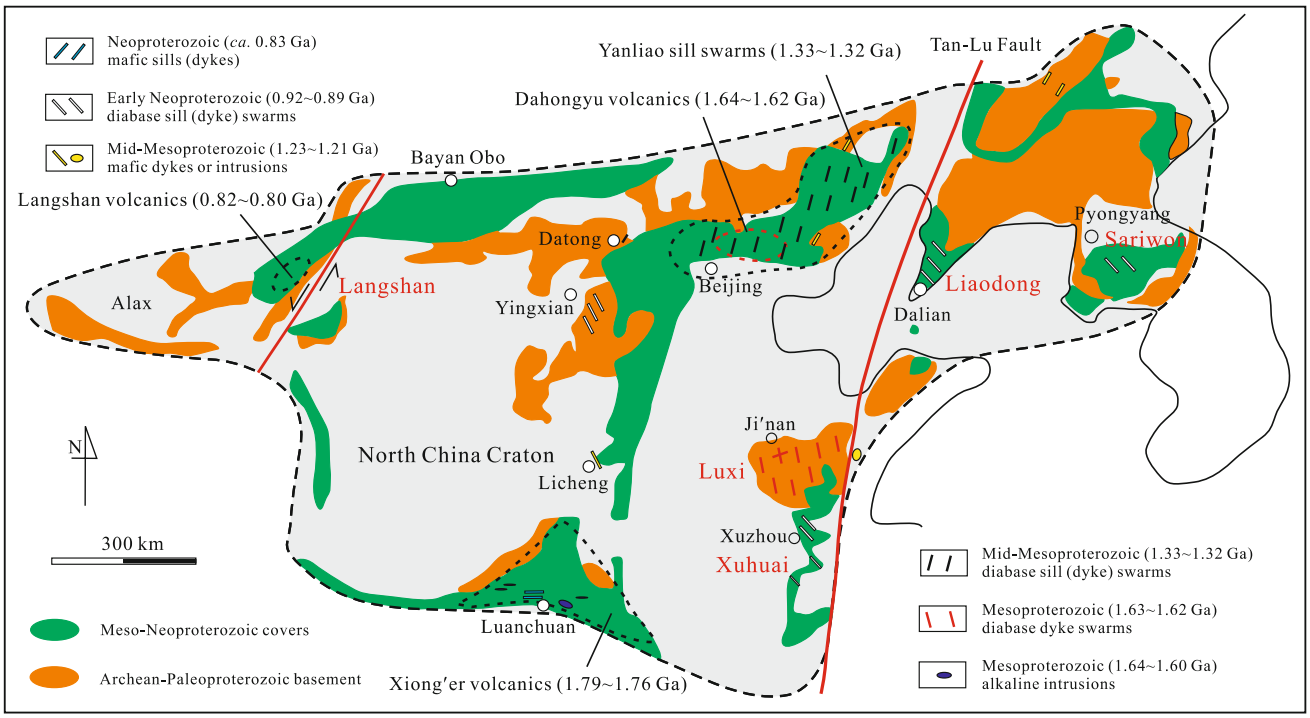

Fig. 14.3 Sketch map showing distribution of the Meso-Neoproterozoic magmatic rocks in the NCC (modified after Peng et al. 2011a)

14.2.3 The 1.68 Ga Laiwu Mafic Dykes in the Eastern NCC

A secondary ion mass spectrometry (SIMS) baddeleyite $^{207}Pb/^{206}Pb$ age of 1680 ± 5 Ma was reported for a NNW-trending mafic dyke from Zoujialanzi village, Laiwu in the Luxi area in the eastern NCC (Li et al. 2015b). The Laiwu mafic dykes are NNW in strike with steeply dipping angles of 65°–85°. They are typical diabase with a mineral assemblage of clinopyroxene and plagioclase, with minor amounts of ilmenite, magnetite, and quartz (Li et al. 2015b). Compared with the 1.63–1.62 Ga mafic dykes in the Luxi area, the 1.68 Ga mafic dykes contain more volumes of plagioclase and Fe–Ti oxides are slightly rich in TiO_2 (Li et al. 2015b). Since these dykes are spatially associated with the 1.63–1.62 Ga mafic dykes, more researches are needed to determine their volumes and relations to the 1.63–1.62 Ga mafic dykes.

14.2.4 The 1.63–1.62 Ga Mafic Dyke Swarms in Luxi Area in the Eastern NCC

The Luxi area in the eastern NCC is characterized by emplacement of large volumes of mafic dyke swarms into the Archean-Paleoproterozoic metamorphic basement rocks (Fig. 14.4). They are generally NW–NNW in strike with a steeply dipping angle. A few of them are NE–NNE in strike. They are unconformably overlain by the Neoproterozoic or Early Cambrian sedimentary rocks. The mafic dykes are less than half a meter to 2–5 m wide and their lengths ranging from several ten meters to >20 km. Most of them are very fresh without deformation and metamorphism. Early zircon SHRIMP (sensitive high-resolution ion micro-probe) U–Pb dating on the NW–NNW-trending mafic dykes from Taishan and Mengyin yielded $^{207}Pb/^{206}Pb$ ages of 1837 ± 18 Ma (Hou et al. 2006) and 1841 ± 17 Ma (Wang et al. 2007), respectively. Recent baddeleyite thermal ionization mass spectrometer (TIMS) and SIMS U–Pb dating on the NW–NNW-trending mafic dykes from Taishan yielded $^{207}Pb/^{206}Pb$ ages of 1621 ± 9 Ma (Lu et al. 2008a) and 1632 ± 4 Ma (Xiang et al. 2012), respectively. These baddeleyite $^{207}Pb/^{206}Pb$ ages are similar to our newly obtained baddeleyite ages of the mafic dykes from Taishan and Zoucheng. Therefore, emplacement of the large volumes of mafic dyke swarms in the Luxi area in the eastern NCC occurred mainly during 1.63–1.62 Ga.

The 1.63–1.62 Ga mafic dykes in the Luxi area consist mainly of gabbro, diabase, or diabase porphyrite with a main mineral assemblage of clinopyroxene and plagioclase (some occur as phenocrysts); other minerals include biotite, hornblende, ilmenite, magnetite, and/or quartz. They are tholeiitic in composition and are characterized by low contents of SiO_2 and MgO, enrichment in large-ion lithophile elements (LILEs) and light rare earth elements (REEs) and depletion in high-field strength elements (HFSEs) and heavy REEs

Fig. 14.4 Field photos of the 1.63–1.62 Ga mafic dykes in the Luxi area in the eastern NCC. **a** Cylindrical columnar joints in the NNW-trending Taishan mafic dyke. **b** NE-trending mafic dyke in eastern Taishan. **c** NNW-trending mafic dyke in eastern Laiwu. **d** NNW-trending mafic dyke in western Laiwu. **e** Diabase porphyrite from a NNW-trending mafic dyke in Fangcheng, Linyi. **f** Intrusive contact between the NNW-trending mafic dyke and Archean gneissic granite in Xiayandian, Linyi

(Hou et al. 2006; Wang et al. 2007; Xiang et al. 2012; Li et al. 2015b). Emplacement of large volumes of mafic dyke swarms in the Luxi area indicates that the eastern NCC experienced widespread extension during 1.63–1.62 Ga. However, it is still uncertain what caused the above widespread extension during 1.63–1.62 Ga in the eastern NCC.

14.2.5 The 1.64–1.60 Ga Alkaline Rocks in the Southern NCC

Several 1.64–1.60 Ga intrusions (Miaoling, Longwangzhuang, and Maping) have been identified from the southern margin of the NCC (Ren et al. 2000; Lu et al. 2003; Bao et al. 2011; Liu 2011; Wang et al. 2013b; Deng et al. 2015; Fig. 14.3). The Miaoling aegirine-augite syenite occurs as dykes or small intrusions within the Xiong'er Group near Songxian in southern Henan Province and zircon TIMS U–Pb dating yielded a upper intercept age of 1644 ± 14 Ma (Ren et al. 2000). The Longwangzhuang granite pluton is located near Luanchuan County in southern Henan Province with an area of 120 km^2. It intruded into the Archean metamorphic basement rocks and its eastern side was intruded by an Early Cretaceous granitoid pluton. It is composed mainly of syenogranite with a main mineral assemblage of K-feldspar (mainly microcline, 40–60 vol.%), quartz (20–35 vol.%), biotite (1–10 vol.%), albite (5–10 vol.%), and hornblende (0–5 vol.%). Zircon U–Pb dating of different samples from the Longwangzhuang pluton by TIMS, SHRIMP, and LA-ICP-MS methods yielded weighted mean $^{207}Pb/^{206}Pb$ ages from 1625 ± 16 to 1602 ± 7 Ma (Lu et al. 2003; Bao et al. 2011; Wang et al. 2013a), indicating its emplacement during 1.63–1.60 Ga. The Maping alkaline complex is located 5 km northwest to Luonan in Shaanxi Province. It occurs as E–W-trending intrusions intruded into the Guandaokou Group in an area that is 5 km long and 500 m wide. It consists mainly of granite porphyry and syenogranite with a main mineral assemblage of K-feldspar, quartz and biotite, and is characterized by high SiO_2 and alkaline ($Na_2O + K_2O$) contents (Liu 2011; Deng et al. 2015). Zircon LA-ICP-MS dating on two granite porphyry samples yielded weighted mean $^{207}Pb/^{206}Pb$ ages of 1600 ± 24 and 1583 ± 28 Ma, respectively (Deng et al. 2015). Zircon SHRIMP U–Pb dating of a syenogranite sample yielded a weighted mean $^{207}Pb/^{206}Pb$ ages of 1598 ± 9 Ma (Liu 2011). Therefore, emplacement of the Maping alkaline complex occurred during ca. 1.60 Ga.

Compared with the 1.64–1.62 Ga volcanic rocks in the Yanliao rift (aulacogen) and 1.63–1.62 Ga mafic dyke swarms in the Luxi area, the 1.64–1.60 Ga alkaline rocks in the southern NCC are small in volume and are only distributed in a narrow belt that is 180 km long along the middle segment of the southern margin of the NCC (Fig. 14.3). Their high alkaline and A-type granitic compositions indicate their formation in an extensional environment. The 1.64–1.60 Ga extension in the southern margin of the NCC might be related to an identified tectonic event represented by the angular unconformity between the 1.79–1.76 Ga volcanic rocks of Xiong'er Group and the Mesoproterozoic sedimentary rock (Yunmengshan Formation or Gaoshanhe Formation). The above inference is consistent with the spatial distribution of the 1.64–1.60 Ga alkaline rocks in the areas with exposure of the Xiong'er volcanic rocks in the southern NCC.

14.3 Mesoproterozoic Magmatism, Large Igneous Province, and Continental Breakup

14.3.1 The ca. 1.32 Ga Yanliao Large Igneous Province and Continental Breakup in the Northern Margin of the NCC

The Yanliao rift (aulacogen) in the northern NCC is characterized by deposition of thick marine clastic and carbonate platform sedimentary rocks from the late Paleoproterozoic to Meso-Neoproterozoic periods (Fig. 14.2). Large volumes of diabases occur as sill swarms within these sedimentary rocks and are especially common within the Xiamaling, Wumishan, Gaoyuzhuang, and Tieling formations (Fig. 14.2). No diabase sills have been identified from the Changlongshan and Jingeryu formations. Usually, three to five layers of diabse sills can be observed within the Xiamaling Formation from western Bejing to Chaoyang in the northern NCC (Fig. 14.5). The sills are several meters to several hundred meters thick and few kilometers to several tens of kilometers long. Due to difficulties in dating mafic-ultramafic rocks such as diabase, these sills were previously regarded as Late Paleozoic (Li and Li 2005), Triassic (BGMRLNP 1965, 1967; BGMRHBP 1969) or Jurassic (BGMRLNP 1969) in age. However, recent baddeleyite and zircon U–Pb/Pb–Pb dating results (Zhang et al. 2009, 2012c, 2016a; Li et al. 2009a; Wang et al. 2014a) on the diabase sills emplaced into the Xiamaling, Tieling, Wumishan, and Gaoyuzhuang formations indicate their simultaneous emplacement during the Mesoproterozoic period at ca. 1.32 Ga (Table 14.2).

The Yanliao diabase sills display typical diabasic texture with similar mineral compositions of pyroxene, plagioclase, magnetite, and hornblende. They are characterized by very similar petrological and geochemical compositions with low contents of SiO_2, high contents of TiO_2, Fe_2O_3T, and MgO and exhibit geochemical features of tholeiitic compositions and intraplate characteristics (Zhang et al. 2012c, 2016a; Wang et al. 2014b). Field investigation results show that the sill swarms are distributed in an area that is >600 km long

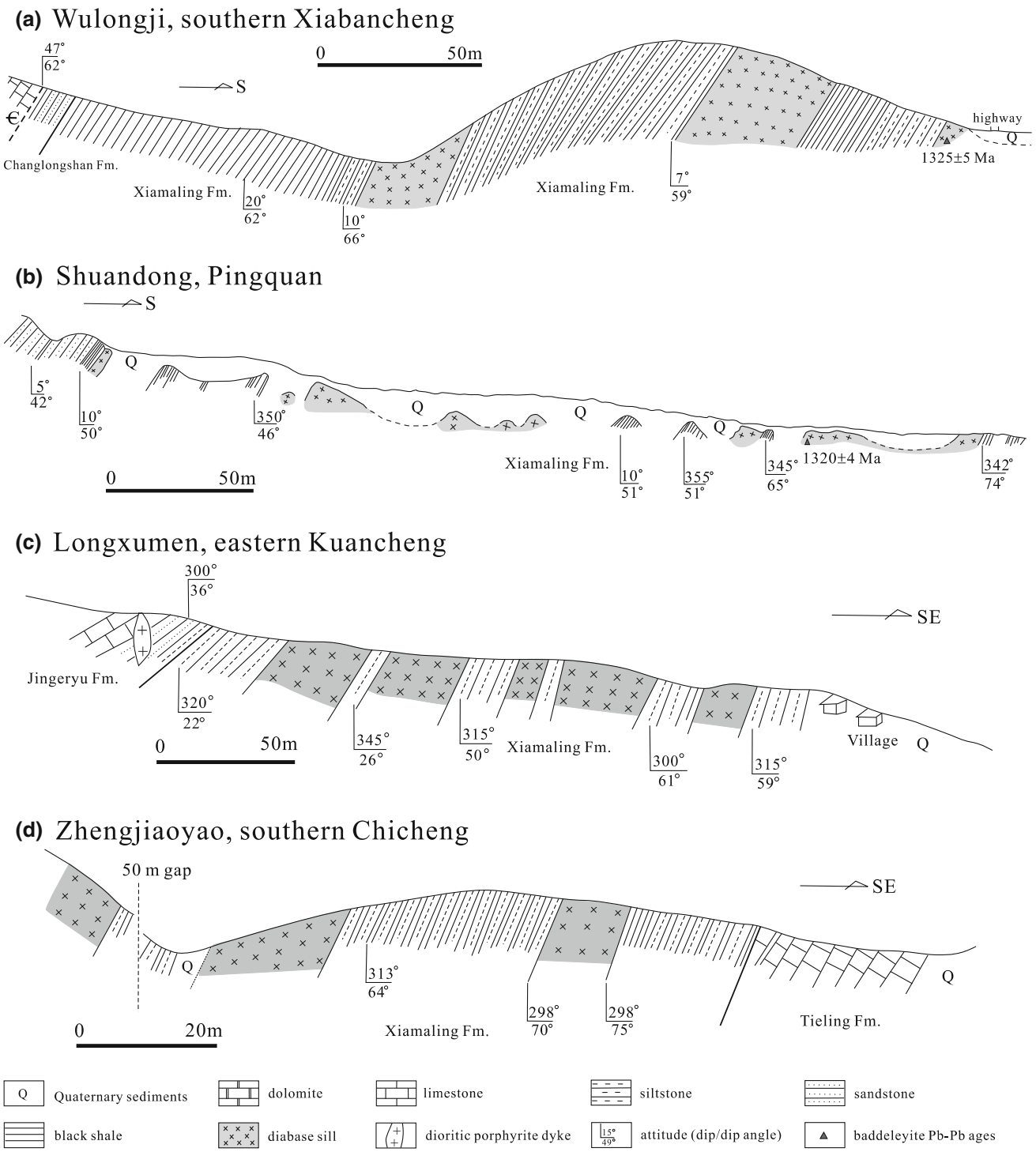

Fig. 14.5 Cross sections showing the diabase sills emplaced into the Xiamaling Formation in the Yanliao rift (aulacogen) in the northern NCC (modified after Zhang et al. 2009, 2012c)

and >200 km wide with areal extent >1.2 × 10^5 km^2 (Fig. 14.3). The cumulative thickness of the sills ranges from 50 m at the margins to >1800 m (Zhang et al. 2016a). Therefore, the diabase sill swarms in the Yanliao rift (aulacogen) constitute a Mid-Mesoproterozoic large igneous province in the northern NCC. If the newly identified ca. 1.32 Ga diabase dykes in Datong in northern Shanxi Province in the north-central NCC are considered together (Peng 2015), the areal extent of the Yanliao large igneous province is much larger 1.2 × 10^5 km^2. The Yanliao diabase sills are

Table 14.2 Summary of zircon and baddeleyite U–Pb ages of the *ca.* 1.32 Ga magmatic rocks in the NCC

Location/intrusion name	Longitude (E)	Latitude (N)	Rock type	Age (Ma)	Method	References
Kuancheng/sill within Xiamaling Fm.	118°21.4′	40°34.8′	Diabase	1320 ± 6	Baddeleyite TIMS	Li et al. (2009a)
Chaoyang/sill within Wumishan Fm.	120°18.4′	41°24.7′	Diabase	1314 ± 6	Zircon SHRIMP	Zhang et al. (2012c)
Chaoyang/sill within Wumishan Fm.	120°18.7′	41°23.7′	Diabase	1323 ± 11	Zircon LA-ICP-MS	Zhang et al. (2012c)
Chaoyang/sill within Wumishan Fm.	120°18.4′	41°24.7′	Diabase	1324 ± 5	Baddeleyite SIMS	Zhang et al. (2012c)
Chaoyang/sill within Tieling Fm.	120°14.2′	41°14.1′	Diabase	1316 ± 37	Baddeleyite SIMS	Zhang et al. (2012c)
Pingquan/sill within Xiamaling Fm.	118°45.5′	40°58.6′	Diabase	1320 ± 4	Baddeleyite SIMS	Zhang et al. (2012c)
Xiabancheng/sill within Xiamaling Fm.	118°08.0′	40°41.2′	Diabase	1325 ± 5	Baddeleyite SIMS	Zhang et al. (2012c)
Kazuoqi/sill within Wumishan Fm.	120°01′ 35.1″	41°06′ 26.9″	Diabase	1319 ± 4	Baddeleyite SIMS	Wang et al. (2014a)
Lingyuan/sill within Xiamaling Fm.	119°34′ 48.1″	41°15′ 31.5″	Diabase	1323 ± 5	Baddeleyite SIMS	Wang et al. (2014a)
Kazuoqi/sill within Wumishan Fm.	119°58′ 00.2″	41°09′ 26.9″	Diabase	1323 ± 5	Baddeleyite SIMS	Wang et al. (2014a)
Kazuoqi/sill within Wumishan Fm.	120°00′ 23.9″	41°05′ 26.5″	Diabase	1326 ± 4	Baddeleyite SIMS	Wang et al. (2014a)
Chaoyang/sill within Wumishan Fm.	120°18′ 19.2″	41°24′ 26.2″	Diabase	1326 ± 6	Baddeleyite SIMS	Wang et al. (2014a)
Kuancheng/sill within Xiamaling Fm.	118°18.6′	40°37.2′	Diabase	1315 ± 11	Baddeleyite SIMS	Zhang et al. (2016a)
Lingyuan/sill within Xiamaling Fm.	119°30.7′	41°13.3′	Diabase	1305 ± 11	Baddeleyite SIMS	Zhang et al. (2016a)
Chaoyang/sill within Gaoyuzhuang Fm.	120°31.2′	41°38.6′	Diabase	1327 ± 6	Baddeleyite SIMS	Zhang et al. (2016a)
Chaoyang/sill within Gaoyuzhuang Fm.	120°31.8′	41°39.8′	Diabase	1321 ± 4	Baddeleyite SIMS	Zhang et al. (2016a)
Lingyuan/sill within Xiamaling Fm.	119°31.9′	41°15.7′	Diabase	1318 ± 4	Baddeleyite SIMS	Zhang et al. (2016a)
Lingyuan/sill within Xiamaling Fm.	119°40.6′	41°02.5′	Diabase	1313 ± 6	Baddeleyite SIMS	Zhang et al. (2016a)
Yixian/sill within Gaoyuzhuang Fm.	121°11.4′	41°39.7′	Diabase	1330 ± 4	Baddeleyite SIMS	Zhang et al. (2016a)
Pingquan/sill within Tieling Fm.	118°42.2′	40°57.3′	Diabase	1324 ± 5	Baddeleyite SIMS	Zhang et al. (2016a)
Shangdu-Huade/granite pluton	113°46.9′	41°47.0′	Granite	1331 ± 11	Zircon LA-ICP-MS	Zhang et al. (2012c)
Shangdu-Huade/granite pluton	113°45.9′	41°44.6′	Granite	1313 ± 17	Zircon LA-ICP-MS	Zhang et al. (2012c)
Shangdu-Huade/granite pluton	113°46.9′	41°47.0′	Granite	1324 ± 14	Zircon LA-ICP-MS	Zhang et al. (2012c)
Shangdu-Huade/granite pluton	113°47.7′	41°48.6′	Granite	1330 ± 12	Zircon LA-ICP-MS	Zhang et al. (2012c)
Wulanhada/granite dyke	113°08′ 07.0″	41°39′ 45.5″	Granite	1318 ± 7	Zircon SHRIMP	Shi et al. (2012)
Wulanhada/granite dyke	113°08′ 07.0″	41°39′ 45.5″	Granite porphyry	1321 ± 15	Zircon SHRIMP	Shi et al. (2012)

characterized by similar Nd and Hf isotopic compositions with positive whole-rock $\varepsilon_{Nd}(t)$ values of 0.40–1.96 and zircon and baddeleyite $\varepsilon_{Hf}(t)$ values of 2.0–8.5 and were likely generated by partial melting of the depleted asthenosphere mantle coupled with slight crustal assimilation (Zhang et al. 2012c). Formation of the Yanliao large igneous province is related to continental rifting events in the northern NCC that have led to the final breakup of the Columbia (Nuna) supercontinent.

The Changlongshan and Jingeryu formations overlaid upon the Xiamaling Formation are only limitedly distributed in the western and southern margins of the Yanliao rift (aulacogen). In most other places, the Xiamaling Formation and sometimes the diabase sills within this formation were disconformably overlain by the Early Cambrian sedimentary rocks. Therefore, formation of the Yanliao large igneous province was accompanied by pre-magmatic uplift as indicated by the absence of sedimentation after Xiamaling Formation in most areas and erosion of some sills near surface. Since uplift of continental margins prior to breakup is typical and an expected process accompanying continental breakup (e.g., Esedo et al. 2012; Frizonde de Lamotte et al. 2015), the above pre-magmatic uplift provides solid evidence for linking the Yanliao large igneous province to breakup the northern margin of the NCC from the Columbia (Nuna) supercontinent.

Laurentia, Siberia, and Baltica are considered as the core of the Columbia supercontinent (Evans and Mitchell 2011). Extension-related magmatism at ca. 1.40–1.25 Ga is widespread around parts of Laurentia, Baltica, and Siberia and is ascribed to Columbia breakup (Evans 2013). Several continental mafic large igneous provinces during this period have been recognized in Laurentia, Baltica, Siberia, Congo, Kalahari, West Africa, North Australia, and East Antarctica cratons (Ernst et al. 2013; Ernst 2014 and references therein). Comparisons of the late Paleoproterozoic to Meso-Neoproterozoic sedimentary rocks and their tuff and K-bentonite beds in the Yanliao rift (aulacogen) in the northern NCC (Fig. 14.2) with the late Paleoproterozoic to Mesoproterozoic strata in other cratons suggest a close relation of the NCC with the Laurentia, Baltica, Siberia and India cratons. Paleomagnetic results on the NCC suggest connections of the NCC with Laurentia, Siberia, Baltica, India, and North Australian cratons in the Columbia (Nuna) supercontinents (Halls et al. 2000; Wu et al. 2005; Pei et al. 2006; Piper et al. 2011; Zhang et al. 2012b; Chen et al. 2013a; Xu et al. 2014). Therefore, the NCC has a close connection with the Siberia, Laurentia, Baltica, India, and North Australian cratons during the Mesoproterozoic period and was likely served as the core of the Columbia (Nuna) supercontinent. The ca. 1.32 Ga Yanliao large igneous province and the accompanying pre-magmatic uplift represent rifting to drifting transition and breakup of the northern NCC from the core of the Columbia (Nuna) supercontinent and initiation of the passive continental margin of the northern NCC.

Except for the large volumes of diabase sill swarms in the Yanliao rift (aulacogen), some Mid-Mesproterozoic granitic plutons and dykes have been identified from the east edge of the Zha'ertai-Bayan Obo-Huade rift zone in the northern NCC (Zhang et al. 2012c; Shi et al. 2012). They emplaced into the Bayan Obo Group (or Huade Group) that composed mainly of sedimentary rocks subjected to low-grade metamorphism. Zircon SHRIMP and LA-ICP-MS U–Pb on six samples yielded emplacement ages of ca. 1.32 Ga, similar to those of the Yanliao diabase sill swarms (Table 14.2). The ca. 1.32 Ga granites are characterized by high contents of SiO_2 (70–76 wt %) and alkaline ($Na_2O + K_2O$ = 6–9 wt%) and exhibit negative whole-rock $\varepsilon_{Nd}(t)$ values of −6.9 to −6.3 and zircon $\varepsilon_{Hf}(t)$ values of −15.9 to −3.6, indicating that they were generated mainly through partial melting of the ancient continental crust, probably induced by the upwelling of hot asthenosphere mantle during continent rifting processes (Zhang et al. 2012c). These granitic plutons and dykes, together with the Yanliao diabase sill swarms, constitute a typical bimodal magmatic association rifting events that are considered to have led to the final breakup of the Columbia supercontinent (Zhang et al. 2012c). However, the present day volume of the ca. 1.32 Ga granites is much smaller than that of the ca. 1.32 Ga diabase sill swarms in the northern NCC.

14.3.2 The 1.23–1.21 Ga Mafic Magmatism in the Eastern and Central NCC

Some 1.23–1.21 Ga mafic intrusions or dykes have been identified from the eastern and central NCC (Pei et al. 2013; Peng et al. 2013; Peng 2015; Wang et al. 2015b; Fig. 14.3). In contrast to the ca. 1.32 Ga mafic rocks occur mainly as sills within the Mesoproterozoic sedimentary rocks, the 1.23–1.21 Ga mafic rocks in the NCC occur mainly as intrusions or dykes in the Archean-Paleoproterozoic metamorphic basement rocks. The 1.23–1.21 Ga magmatic rocks in the NCC include the Tonghua diabase dykes with zircon U–Pb upper intercept age of 1244 ± 28 Ma in the northeastern NCC (Pei et al. 2013), the Yishui gabbro intrusions with zircon $^{207}Pb/^{206}Pb$ age of 1209 ± 6 Ma (Peng et al. 2013), the Jianping mafic dykes with zircon $^{207}Pb/^{206}Pb$ ages of 1231 ± 16 to 1229 ± 10 Ma (Wang et al. 2015b), the Qinglong mafic dykes with zircon $^{207}Pb/^{206}Pb$ age of 1208 ± 24 Ma (Wang et al. 2015b), the Qingyuan mafic dykes with zircon $^{207}Pb/^{206}Pb$ age of 1226 ± 11 Ma (Wang et al. 2015b) and the Licheng mafic dykes with baddeleyite $^{207}Pb/^{206}Pb$ age of 1226 ± 11 Ma (Peng 2015).

The 1.23–1.21 Ga mafic rocks in the eastern and central NCC are composed of gabbro and diabase with a major

mineral assemblage of plagioclase, clinopyroxene, and hornblende, and minor orthopyroxene, alkaline feldspar, biotite, quartz, and magnetite (Pei et al. 2013; Peng et al. 2013; Peng 2015; Wang et al. 2015b). They are characterized by low contents of SiO_2 and high contents of Fe_2O_3T and TiO_2 and classified as subalkaline or alkaline basalts in major and trace element classification diagrams and were considered to be derived from partial melting of a depleted asthenospheric mantle or a subduction-modified enriched lithospheric mantle (Pei et al. 2013; Peng et al. 2013; Wang et al. 2015b). Some researchers suggest that 1.23–1.21 Ga mafic magmatism in the NCC is related to a prolonged superplume that led to the final breakup of the Columbia supercontinent (Peng et al. 2013). However, their emplacement ages are younger than those of the Mackenzie and Bear River radiating dyke swarms in the Laurentia (ca. 1.27 Ga, LeCheminant and Heaman 1989; Schwab et al. 2004) that are considered to be related to a mantle plume leading to final of breakup of the Columbia supercontinent (e.g., Zhao et al. 2004a, b; Evans and Mitchell 2011; Ernst 2014). Moreover, evidence for assembly of Rodinia supercontinent as indicated by worldwide orogenic events is very clear after ca. 1.30 Ga (e.g., Li et al. 2008; Ernst et al. 2008; Aitken et al. 2015). Some mafic–ultramafic magmatic events of extensional origin after ca. 1.25 Ga may be related to back arc extension during assembly of the Rodinia supercontinent (Ernst et al. 2008). Recent researches on the 0.92–0.89 Ga mafic sill swarms and Neoproterozoic sedimentary rocks suggested that the southeastern margin of the NCC was probably connected to some other continents that are characterized by strong Grenville magmatism in the Rodinia supercontinent (e.g., Peng et al. 2011b; Zhang et al. 2016b). Therefore, the 1.23–1.21 Ga mafic magmatism represents another intense extension event in the eastern NCC, which may be related to a far-field continental back arc extension during subduction-assembly of the Rodinia supercontinent in its eastern side.

14.3.3 Mesoproterozoic Tuff Layers and K-Bentonite Beds in the Northern NCC

Thin tuff layers and K-bentonite beds are produced by explosive felsic-intermediate volcanism. Since the volcanic components in these rocks can be transported for hundreds of kilometers in the air before deposition in marine basins, they are very useful for stratigraphic correction and paleogeographic reconstruction. In recent years, several tuff layers, including the 1.38–1.37 Ga K-bentonite beds within the Xiamaling Formation (Gao et al. 2007, 2008b; Su et al. 2008, 2010), the 1.44 Ga K-bentonite beds within the Tieling Formation (Su et al. 2010; Li et al. 2014a), the 1.49 Ga K-bentonite beds within the Wumishan Formation (Li et al. 2014a), and the 1.58–1.56 Ga tuff beds within the Gaoyuzhuang Formation (Li et al. 2010a; Tian et al. 2015; Fig. 14.6c and Table 14.3), have been identified from the sedimentary rocks in the Yanliao rift (aulacogen) in the northern NCC (Fig. 14.2). The K-bentonite beds within the Xiamaling, Tieling, and Wumishan formations are usually 1–10 cm thick and can be traced in a large areas in western Beijing, Zhangjiakou, Jixian, Chengde, and Pingquan (Gao et al. 2007, 2008b; Su et al. 2008, 2010; Li et al. 2014a). The tuff layer within the Gaoyuzhuang Formations in the Yanqing area in northern Beijing is about 1.4 m thick (Fig. 14.6a, b) and that in the Jixian area is about 15 cm thick (Tian et al. 2015). The above thickness variations suggest that the volcanic materials came from some areas north to the Yanliao rift (aulacogen) in the northern NCC.

Although tuff layers and K-bentonite beds of 1.58–1.56 to 1.38–1.37 Ga are common in the Yanliao rift (aulacogen) in the northern NCC, no contemporaneous volcanism has been identified in the NCC yet. Therefore, the source areas for these rocks may locate in some other continents near neighbors to the northern margin of the NCC during the Mesoproterozoic period. Explosive felsic-intermediate volcanisms of 1.58–1.56 Ga, 1.49 Ga, 1.44 Ga, and 1.38–1.37 Ga are especially common in Laurentia, Siberia, Baltica, and North and South Australian cratons (Sweet et al. 1999; Ernst et al. 2008, 2013; Ernst 2014 and references therein), which may serve as the sources for the K-bentonite and thin tuff beds in the northern NCC. The above fact supports our paleogeographic reconstruction that the NCC has a close connection with the Siberia, Laurentia, Baltica, India, and North Australian cratons during the Mesoproterozoic period and was likely served as the core of the Columbia (Nuna) supercontinent (Zhang et al. 2016a).

14.4 Neoproterozoic Magmatism, Large Igneous Province, and Continental Breakup

14.4.1 The 0.92–0.89 Ga Large Igneous Province and Continental Breakup in the Southeastern Margin of the NCC

In recent years, some Neoproterozoic mafic magmatism was recognized from the central and eastern NCC (Sino-Korean Craton) (Fig. 14.3; Liu et al. 2006; Gao et al. 2009; Peng et al. 2011a, b; Wang et al. 2012b; Zhang et al. 2016b). These include the Xu-Huai diabase sill swarms in the southeastern NCC (Liu et al. 2006; Gao et al. 2009; Wang et al. 2012b), the Dalian diabase sill swarms in the Liaodong

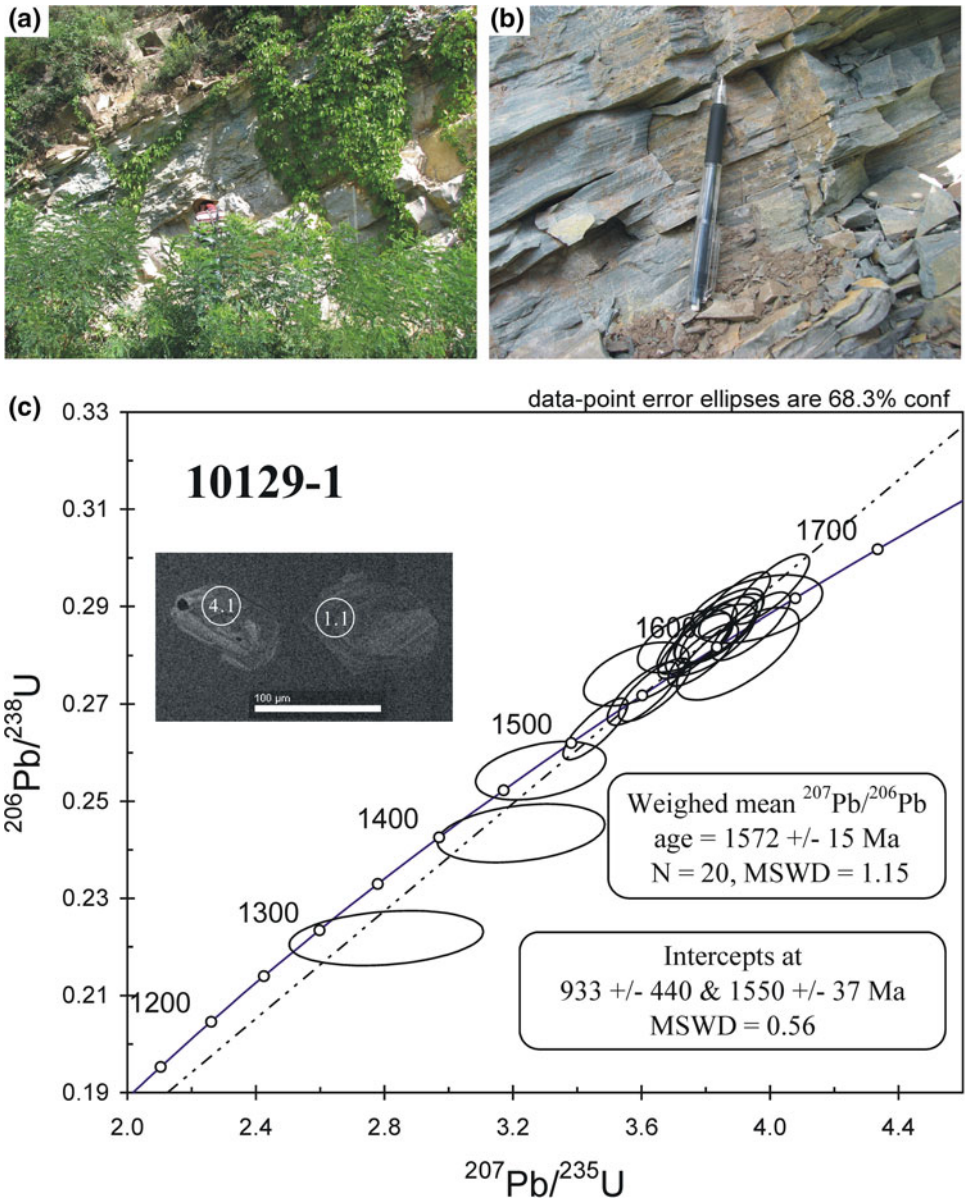

Fig. 14.6 Field photos of tuff layers within the Guangyuzhuang Formation in northern Beijing (**a**, **b**) and its zircon U–Pb concordia diagram and CL images (**c**)

Peninsula (Zhang et al. 2016b), the Sariwon diabase sill swarms in North Korea (2011b) and the Dashigou mafic dykes in the central NCC (Peng et al. 2011a). If corrected the effect of the sinistral strike-slip motion of the Tan-Lu fault zone during the Triassic–Jurassic period, they are distributed in an area that is ca. 700 km long and 100–200 km wide and may constitute an early Neoproterozoic large igneous province along the southeastern margin of the NCC (Fig. 14.7).

The Sariwon diabase sill swarms in North Korea are located in the Pyongnam basin in the southern part of the Nangrim massif (Fig. 14.3). They occur as sills intruded the Songwon System and the Archean-Paleoproterozoic metamorphic basement rocks and are overlain by the upper Neoproterozoic Kuhyon System and the Phanerozoic strata (Peng et al. 2011b). The sills are several meters to 150 m thick and several kilometers to over 10 km long (Peng et al. 2011b). Baddeleyite SIMS dating on a diabase sample yielded a weighed mean $^{207}Pb/^{206}Pb$ age of 899 ± 7 Ma, indicating its emplacement during the early Neoproterozoic at ca. 0.90 Ga (Peng et al. 2011b).

Diabase swarms are very common in the Liaodong Peninsula in eastern NCC and occur mainly as sills within the Neoproterozoic Yongning, Qiaotou, Changlingzi, Nanguanling, Ganjingzi, Yingchengzi, Cuijiatun, and Xingmincun formations. The diabase sills are usually several meters to several hundred meters thick and several hundred meters to over ten kilometers long (Zhang et al. 2016b). They were previously considered as Late Triassic based on zircon U–Pb dating (Yang et al. 2007; Liu et al. 2013). However, our recent zircon U–Pb and baddeleyite Pb–Pb results on five

Table 14.3 SHRIMP U–Pb dating results of zircons from a tuff layer within the Gaoyuzhuang Formation

Grain spot	$^{206}Pb_c$ (%)	U (ppm)	Th (ppm)	Th/U	$^{204}Pb/^{206}Pb$	$^{207}Pb^*/^{206}Pb^*$	±1σ (%)	$^{207}Pb^*/^{235}U$	±1σ (%)	$^{206}Pb^*/^{238}U$	±1σ (%)	$^{207}Pb^*/^{206}Pb^*$ Age (Ma)	±1σ	$^{207}Pb^*/^{235}U$ Age (Ma)	±1σ	$^{206}Pb^*/^{238}U$ Age (Ma)	±1σ
Sample 10129-1 (collected from Xiamalugou village, Yanqing, northern Beijing, GSP position: E116°12.88′; N40°44.28′)																	
1.1	0.06	140	107	0.79	0.00003	0.0982	1.2	3.791	1.9	0.2801	1.5	1590	22	1591	15	1592	21
2.1	0.00	135	100	0.77	0.00000	0.0968	1.3	3.641	2.0	0.2729	1.6	1562	24	1559	16	1556	22
3.1	0.15	157	165	1.09	0.00008	0.0958	2.2	3.735	2.6	0.2828	1.5	1543	40	1579	21	1606	21
4.1	0.13	117	102	0.90	0.00007	0.0969	1.2	3.764	2.0	0.2819	1.6	1565	23	1585	16	1601	22
5.1	0.11	73	72	1.03	0.00006	0.0974	1.7	3.840	2.4	0.2861	1.7	1574	31	1601	19	1622	25
6.1	0.33	86	71	0.85	0.00018	0.1009	2.3	3.898	3.2	0.2802	2.2	1641	43	1613	26	1592	31
7.1	0.00	105	98	0.96	0.00000	0.0961	1.3	3.605	2.0	0.2722	1.6	1549	24	1551	16	1552	22
8.1	4.37	138	157	1.17	0.00242	0.0960	5.1	3.207	5.3	0.2422	1.7	1548	95	1459	41	1398	21
9.1	0.00	149	107	0.74	0.00000	0.0946	1.1	3.457	1.9	0.2649	1.6	1521	21	1517	15	1515	21
10.1	0.00	133	80	0.62	0.00000	0.0521	3.8	0.323	4.2	0.0450	1.8	289	86	284	10	284	5
11.1	0.28	108	90	0.87	0.00016	0.0974	1.5	3.830	2.2	0.2851	1.6	1576	29	1599	18	1617	22
12.1	2.15	134	111	0.85	0.00119	0.0930	3.8	3.278	4.1	0.2557	1.6	1487	71	1476	32	1468	20
13.1	1.23	125	124	1.03	0.00068	0.0941	2.6	3.579	3.0	0.2758	1.6	1510	49	1545	24	1570	22
14.1	0.00	102	76	0.77	0.00000	0.0999	1.3	3.940	2.1	0.2860	1.6	1623	24	1622	17	1621	23
15.1	0.14	108	78	0.74	0.00008	0.0978	1.4	3.849	2.2	0.2854	1.6	1583	27	1603	18	1619	24
16.1	0.00	81	52	0.67	0.00000	0.0966	1.4	3.773	2.2	0.2833	1.7	1559	27	1587	17	1608	24
17.1	0.14	78	57	0.75	0.00008	0.0977	1.7	3.814	2.4	0.2831	1.7	1581	32	1596	20	1607	24
18.1	5.66	159	217	1.41	0.00314	0.0917	6.9	2.786	7.1	0.2205	1.7	1460	131	1352	53	1284	20
19.1	0.06	137	115	0.87	0.00003	0.0989	1.2	4.002	2.0	0.2936	1.6	1603	22	1635	16	1659	23
20.1	0.96	119	91	0.79	0.00053	0.0991	3.0	3.953	3.4	0.2892	1.6	1608	57	1625	28	1637	23
21.1	0.00	142	101	0.73	0.00000	0.0971	1.1	3.889	1.9	0.2904	1.5	1570	21	1612	15	1644	22

Errors are 1σ; Pb_c and Pb* indicate the common and radiogenic portions, respectively; Common Pb corrected using measured ^{204}Pb

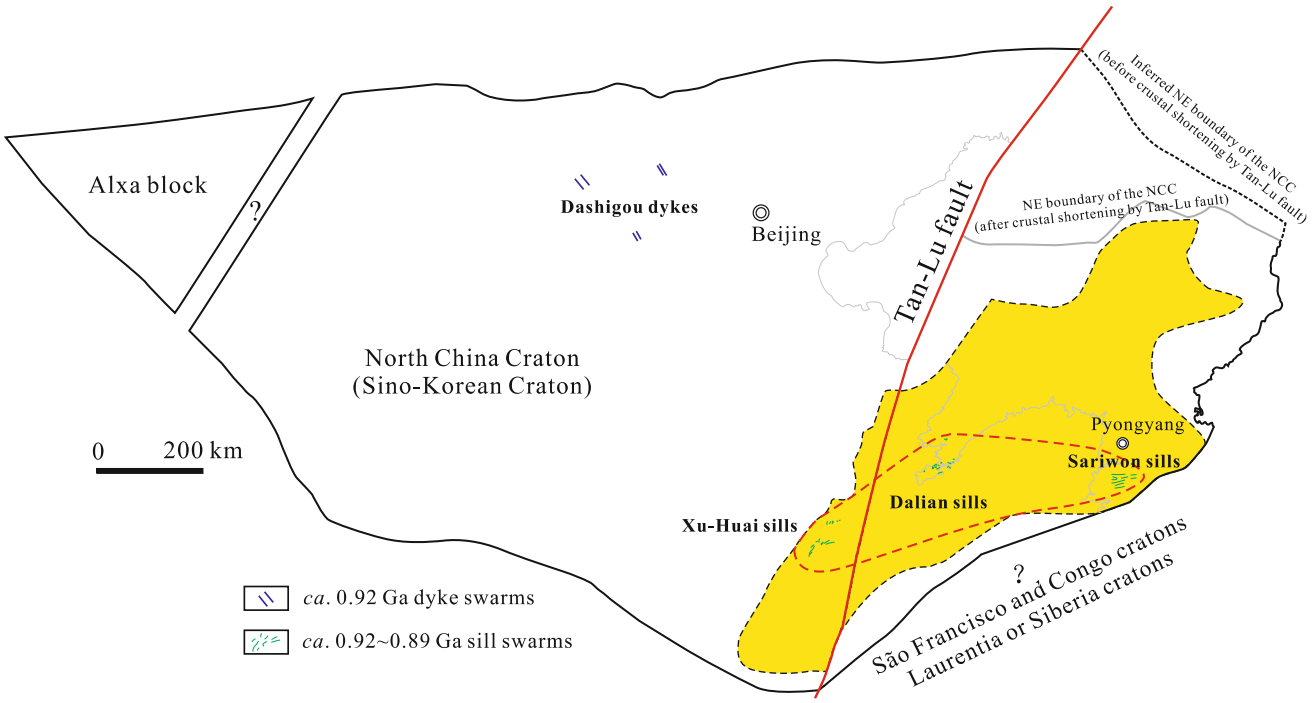

Fig. 14.7 A reconstruction map showing distribution of the early Neoproterozoic mafic sill (dyke) swarms in the NCC (Sino-Korean Craton) during the early Neoproterozoic period (after Zhang et al. 2016b). The southeastern and northeastern boundaries of the NCC are reconstructed by considering the sinistral strike-slip motion of the Tan-Lu fault zone during the Triassic–Jurassic period and possibly crustal shortening in northeastern NCC induced by Tan-Lu fault. *Yellow-shaded area* shows distribution of the early Neoproterozoic sedimentary rocks in the southeastern NCC. *Red dashed line* shows the boundary of the 0.92–0.89 Ga large igneous province inferred by diabase sill swarms

samples emplaced into the Qiaotou, Cuijiatun, and Xingmincun formations indicate their emplacement during the early Neoproterozoic at ca. 0.92–0.89 Ga (Zhang et al. 2016b).

Diabases in Xu-Huai area in the southeastern NCC occur mainly as sills emplaced into the Neoproterozoic Xinxing, Jushan, Jiayuan, Zhaoyu, Niyuan, Jiudingshan, Zhangqü, Shijia, Wangshan, and Jinshanzhai formations (BGMRAHP 1977; BGMRJSP 1978). They are usually several meters to several hundred meters thick and few kilometers to several tens of kilometers long. Zircon SHRIMP and LA-ICP-MS U–Pb dating by several groups yielded weighted mean $^{206}Pb/^{238}U$ ages of 933 ± 14 to 890 ± 14 Ma (Liu et al. 2006; Gao et al. 2009; Wang et al. 2012b), indicating their emplacement during ca. 0.93–0.90 Ga.

Except for the diabase sill swarms in the southeastern and eastern NCC, some early Neoproterozoic mafic dykes (Dashigou dyke swarm) have been identified from the central part of the NCC (Peng et al. 2011a). They are generally NW–NNW in strike and are typically 10–50 m (up to ~100 m) wide and up to 10–20 km long (Peng et al. 2011a). Baddeleyite TIMS U–Pb dating on three mafic dyke samples from Dashigou, Yangjiaogou, and Taohuagou yielded weighed mean $^{207}Pb/^{206}Pb$ ages of 926 ± 2 to 922 ± 3 Ma, indicating their emplacement during ca. 0.92 Ga (Peng et al. 2011a).

Because the Xingmincun Formation in the topmost part of the Neoproterozoic strata in the Liaodong Peninsula and Jinshanzhai and Wangshan Formations in the topmost part of the Neoproterozoic strata in the Xu-Huai area were intruded by the 0.92–0.89 Ga diabase sills, sedimentation of the Neoproterozoic strata had ended prior to ca. 0.92–0.89 Ga and the southeastern and eastern NCC has undergone significant uplift prior to ca. 0.92–0.89 Ga. Therefore, formation of the 0.92–0.89 Ga large igneous province was accompanied by pre-magmatic uplift (Zhang et al. 2016b).

The ca. 0.92–0.89 Ga mafic rocks in the NCC are characterized by similar mineral assemble of clinopyroxene, plagioclase, and Fe–Ti oxides and belong to the tholeiitic series (Peng et al. 2011a, b; Wang et al. 2012b; Zhang et al. 2016b). Most of them fall into the field of within-plate basalt on the Zr/Y versus Zr and Ti–Zr–Y discrimination diagrams and exhibit an evolution trend from within-plate basalt to mid-ocean ridge basalt on the Zr/Y versus Zr discrimination diagram (Wang et al. 2012b; Zhang et al. 2016b). They are characterized by slightly negative to positive $\varepsilon_{Nd}(t)$ values of −1.9 to 4.5 and young Nd isotopic T_{DM} model ages of 1.9–1.1 Ga (Peng et al. 2011a, b; recalculated data from Yang

et al. 2007; Liu et al. 2013) and were likely generated by partial melting of the depleted asthenosphere mantle coupled with differential crustal assimilation in a continental rifting setting that have led to breakup of southeastern NCC from some other continents in the Rodinia supercontinent. Breakup of the NCC from the Rodinia supercontinent at around 0.92–0.89 Ga is also supported by pre-magmatic regional uplift of the southeastern NCC prior to ca. 0.92–0.89 Ga and evolution trend of the Dalian and Xu-Huai diabase sills from within-plate basalt to mid-ocean ridge basalt on the Zr/Y versus Zr discrimination diagram (Zhang et al. 2016b).

14.4.2 The ca. 0.83 Ga Mafic Magmatism in the Southern NCC

The ca. 0.83 Ga mafic magmatism (Zenghekou sill swarms; Peng 2015) occurs mainly as sills emplaced into the Meso-Neoproterozoic Guandaokou and Luchuan groups (Fig. 14.3). It is distributed in a NWW-trending zone that is 50 km long and 1 km to 8 km wide from Lushi to Luanchuan counties along the southern margin of the NCC (GSIHNP 2002). It consists mainly of meta-gabbro with a main mineral assemblage of pyroxene (40–60 vol.%, altered to ouralite) and plagioclase (30–50 vol.%); other minerals include biotite, chlorite, epidote, apatite, magnetite, titanite, and zircon. Zircon U–Pb dating on three gabbros yielded weighted mean $^{206}Pb/^{238}U$ ages of 830 ± 6, 830 ± 7, and 826 ± 34 Ma, respectively (Wang et al. 2011), indicating their emplacement during the Mid-Neoproterozoic (Cryogenian) at ca. 0.83 Ga. They are characterized by high contents of TiO_2 and LREE, with negative Zr-Hf and Ti anomalies but without Nb-Ta anomalies and exhibit geochemical features of within-plate alkaline basalt (Wang et al. 2011). They were considered to be generated in a within-plate extensional setting by the low-degree partial melting of the carbonated asthenospheric mantle and interacted with the subduction-metasomatized lithospheric mantle (Wang et al. 2011).

Although the Zenghekou sill swarms were considered as part of the 925–900 Ma Sariwon-Dalian-Xuhuai mafic sill swarms by some researchers (Peng 2015), their ages of ca. 830 Ma (Wang et al. 2011) are younger than those of the Sariwon-Dalian-Xuhuai mafic sill province (925–890 Ma; Liu et al. 2006; Gao et al. 2009; Peng et al. 2011a, b; Wang et al. 2012b; Zhang et al. 2016b). Moreover, their alkaline basaltic compositions (Wang et al. 2011) are very different from the subalkaline tholeiitic compositions of the Sariwon-Dalian-Xuhuai mafic sills (Peng et al. 2011a, b; Wang et al. 2012b; Zhang et al. 2016b). Therefore, the ca. 0.83 Ga mafic sills in the southern NCC might represent a Mid-Neoproterozoic (Cryogenian) extension event in the southern margin of the NCC and are not belong to the Sariwon-Dalian-Xuhuai mafic sill province in the southeastern part of the NCC.

14.4.3 The 0.82–0.80 Ga Magmatism in the Langshan Area

The 0.82–0.80 Ga magmatism in the Langshan area in the eastern margin of the Alax block occurs as meta-felsic volcanic or volcanoclastic layers within the Langshan Group. The volcanic layers are several meters to 20 m thick and several kilometers long (Peng et al. 2010). The Langshan Group in the Alax block is considered as Mesoproterozoic in age and with the Zha'ertai Group in the northwestern margin of the NCC (e.g., BGMRNMAR 1991). However, zircon SHRIMP U–Pb dating on two quartz keratophyre samples from the volcanic layers within the Langshan Group yielded weighted mean $^{206}Pb/^{238}U$ ages of 817 ± 5 and 805 ± 5 Ma, respectively (Peng et al. 2010). Zircon LA-ICP-MS U–Pb dating of a meta-volcanoclastic sample collected from another layer yielded a weighted mean $^{206}Pb/^{238}U$ age of 804 ± 4 Ma (Hu et al. 2014). These new geochronological results clearly indicate that the Langshan Group in the Alax block is Neoproterozoic in age, not Mesoproterozic as previously regarded (e.g., BGMRNMAR 1991).

Although the Alax block is traditionally considered as part of the NCC (e.g., BGMRNMAR 1991), many recent results show that evolution of the Alxa block is very different from the NCC, especially during the Neoproterozoic period (e.g., Geng et al. 2002; Dan et al. 2014) and amalgamation of North China Craton with the Alxa block may occur during latest Early Paleozoic to Late Paleozoic (e.g., Li et al. 2012; Zhang et al. 2012a, 2013a; Yuan and Yang 2015a, b). Intensive Neoproterozoic magmatism in the Alax block (e.g., Geng et al. 2002; Geng and Zhou 2011; Dan et al. 2014), different ages of the Langshan Group in the Alax block, and Zha'ertai Group in the NCC (Peng et al. 2010; Hu et al. 2014) and different detrital zircon age patterns of sedimentary rocks from the Alxa block and the western NCC suggest that the Alxa block may share similar tectonic affinity to the Tarim or South China (Yangtze) cratons, which is very similar to that of the Precambrian microcontinents in the Central Asian Orogenic Belt (e.g., Wang et al. 2001; Zhao et al. 2006; Demoux et al. 2009; Levashova et al. 2010, 2011; Rojas-Agramonte et al. 2011; Han et al. 2011; Kröner et al. 2011, 2014) and the Bainaimiao arc terrain in the northern margin of the North China block (Zhang et al. 2014). Therefore, the 0.82–0.80 Ga magmatism in the Langshan area should be excluded in discussing the evolution of the NCC.

14.5 Late Paleoproterozoic to Neoproterozoic Mineralization and Ore Deposits in the NCC

14.5.1 Damiao Fe–Ti–P Ore Deposit

The Damiao Fe–Ti–P ore deposit is hosted in the 1.74–1.70 Ga Damiao massif-type anorthosite complex in the northern margin of the NCC. It has been mined since the 1960s at an annual production of 2 million tons of ores with an average grade of about 36 wt% Fe_2O_3t, 7.0 wt% TiO_2, 0.3 wt % V_2O_5, and 2.0 wt% P_2O_5 (Chen et al. 2013b). The Damiao massif-type anorthosite complex is the only one unique massif-type anorthosite in China with an exposure area of 120 km^2 (e.g., Xie 2005). The Damiao complex is composed of anorthosite (85 vol.%), norite (10 vol.%), mangerite (4 vol.%), and minor troctolite (<1 vol.%), accompanied by oxide-apatite gabbronorites, ferrodioritic, gabbroic, felsic dikes, and abundant Fe–Ti–(P) ores (Ye et al. 1996; Zhao et al. 2009; Chen et al. 2013b). Field relations indicate an emplacement sequence from anorthosite, norite to mangerite. Norite occurs as irregular veins or lenses, and fills fractures within the anorthosite and displays sharp boundaries with the anorthosite. Anorthosite xenoliths widely enveloped within the norite dykes (Li et al. 2014b). Fe–Ti–(P) ore bodies occur as irregular lenses, veins or pods crosscutting the anorthosite (Sun et al. 2009; Chen et al. 2013b; Li et al. 2014b; Fig. 14.8). Usually, Fe–Ti ores are spatially associated with Fe–Ti–P ores in the deposit (Chen et al. 2013b). Ore minerals consist mainly of vanadium–titanium magnetite, vanadium-bearing magnetite, ilmenite and apatite (Sun et al. 2009). Formation of the Damiao Fe–Ti–(P) ore deposit is considered as a result of accumulation and fractional crystallization of Fe–Ti oxides and apatite from late immiscible nelsonitic melts in the ferrodioritic parental magma formed under low-pressure condition during diapiric emplacement of the Damiao anorthosite complex (Chen et al. 2013b). Hydrothermal remobilization of

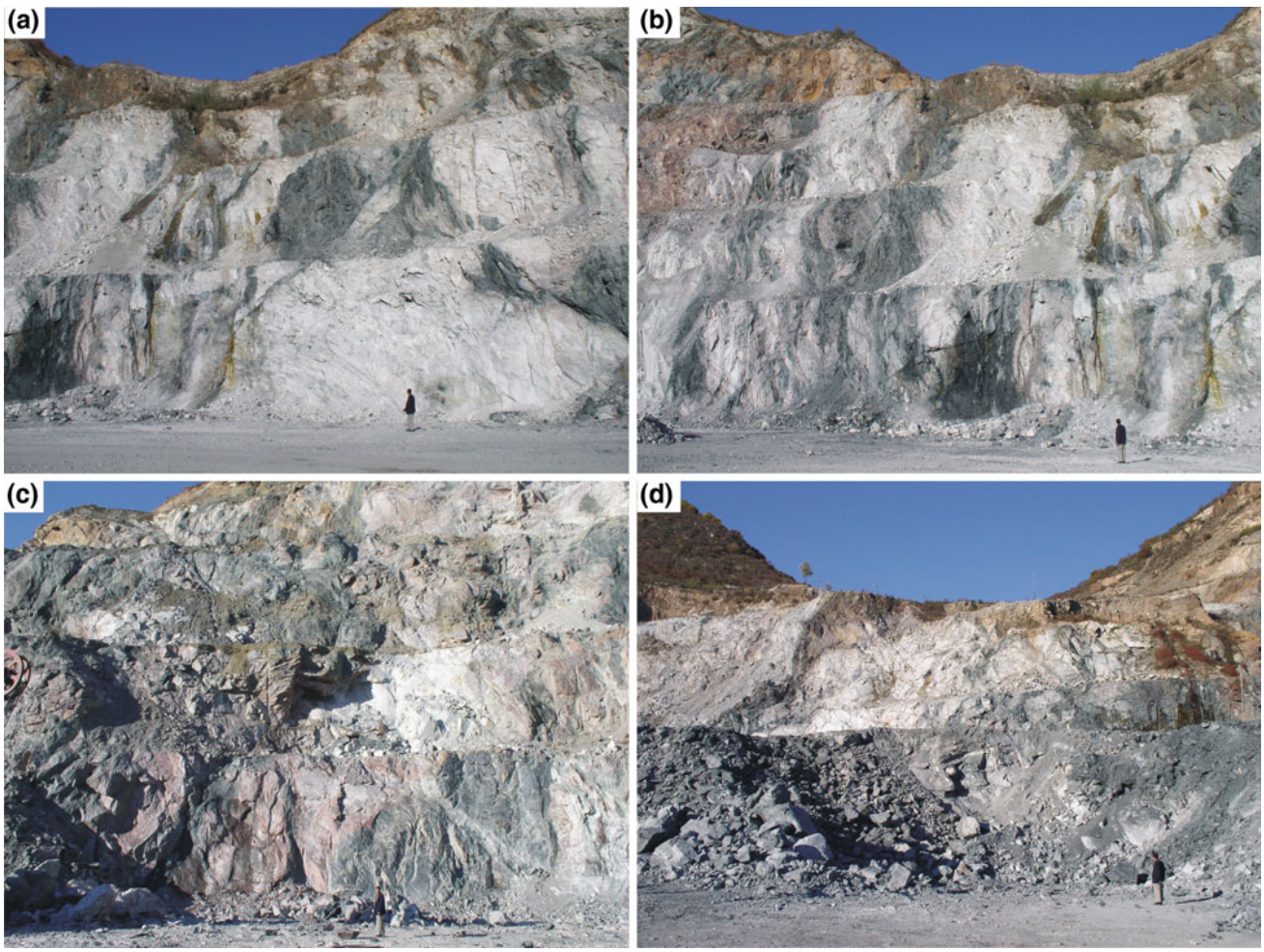

Fig. 14.8 Field photos of the open pit showing occurrences of ore bodies (*dark in color*) within the massive anorthosite (*white in color*) in the Damiao Fe–Ti–P ore deposit in the northern NCC. Post-mineralization faults are very common and cut and moved the ore bodies

Fe and Ti from the host altered anorthosite has also been suggested for the formation of the massive Fe and Fe–P orebodies (Li et al. 2014b).

14.5.2 Xuanlong-Type Iron Deposit

The Xuanlong-type iron deposit is one of the most important neritic facies sedimentary iron deposit in China. It is located in Xuanhua, Longguan, and Chicheng areas in northwestern Hebei Province and is near the western edge of the Yanliao rift (aulacogen). The iron deposit is distributed in an area that is 130 km from east to west and 150 km from north to south with a total of iron resources 300 Mt with an average grade of 40–45 % TFe (Liang et al. 2013; Zhang et al. 2014; Li et al. 2015a). Iron ores occur as layers within the Chuanlinggou Formation (Fig. 14.9). They generally include 1–4 layers of 0.5–3 m thick hematite ores and one layer of 0.35–0.4 thick siderite ore (Zhang et al. 2014). The ore-hosting Chuanlinggou Formation is 11–91 m thick and composed of shale, siltstone, and fine-grained sandstone. Primary ore minerals consist mainly of hematite, with minor siderite, magnetite, and limonite (Li and Zhu 2012; Li et al. 2015a). Textures of the ores are oolitic, kidney-shaped, and massive. Among them, the oolitic texture occurs in the upper part, and the kidney texture occurs in the lower part of the mineralized zone (Li et al. 2015a). Microbial activity probably played a key role during Fe accumulation in the near-shore environments (Du et al. 1992; Zhao 1994; Liu et al. 1995, 1997, 1999; Li and Zhu 2012). Geochemical and Fe–Nd isotopic results show that the iron sources of the Xuanlong-type iron deposit are mainly from detrital input and were mainly derived from iron-bearing formations in continents (Li and Zhu 2012). The Xuanlong-type iron deposit was deposited in a shallow marine environment with relatively low oxygen fugacity (Li and Zhu 2012).

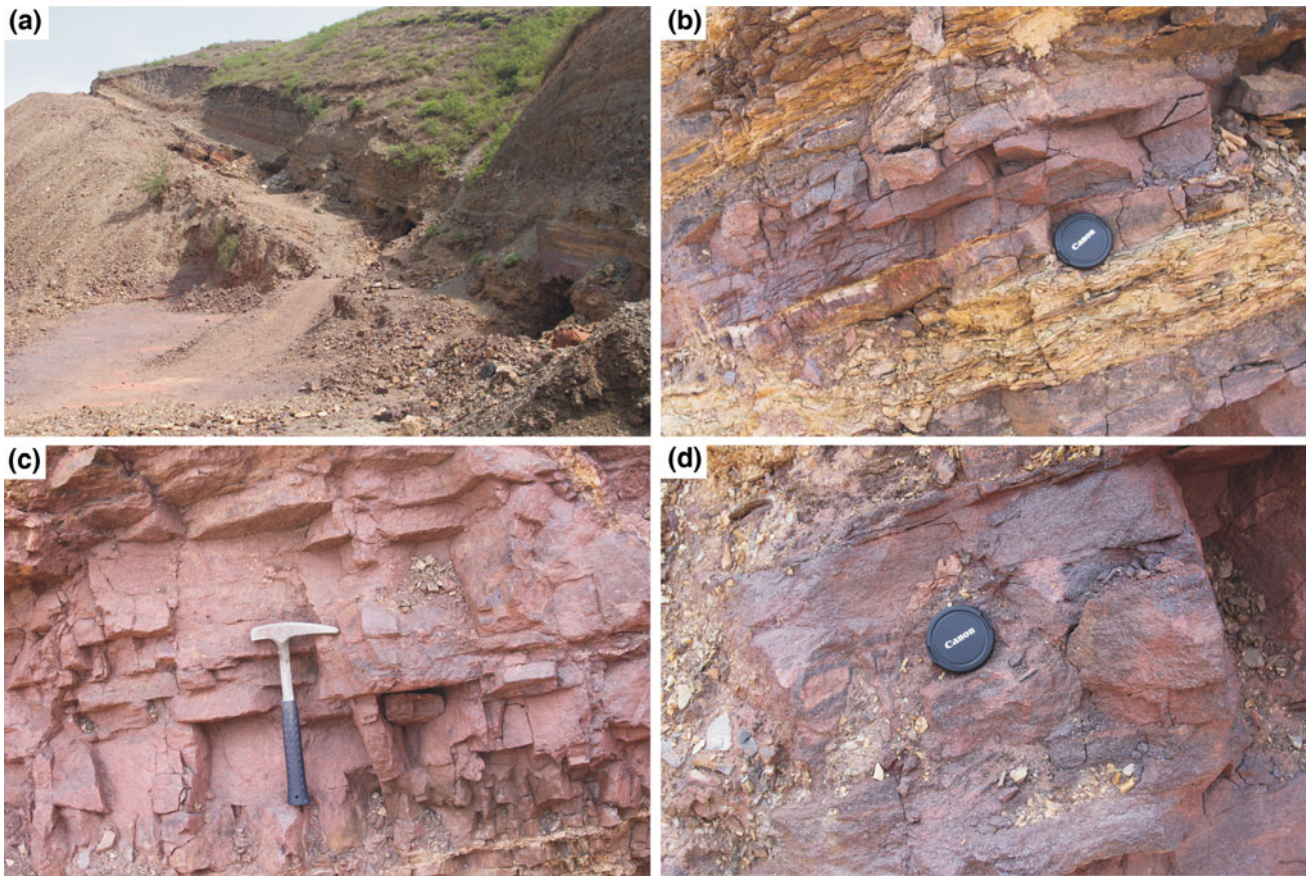

Fig. 14.9 Field photos of the Xuanlong-type iron deposit in the northern NCC. **a** Xuanlong-type iron layer within the Chuanlinggou Formation. **b** Iron layers interbedded with slate and siltstone of the Chuanlinggou Formation. **c** Massive iron ores of the Xuanlong-type iron deposit. **d** Oolitic iron ores of the Xuanlong-type iron deposit

14.5.3 Giant Bayan Obo Fe-REE-Nb Ore Deposit in the Northern Margin of the NCC

The Bayan Obo in the northern margin of the NCC is the world's largest light rare earth element (LREE) deposit and the largest niobium (Nb) and thorium (Th) deposit in China. It is hosted in the late Paleoproterozoic to Mesoproterozoic sediments of the Bayan Obo Group which are distributed in the Zhaertai-Bayan Obo-Huade rifting zone along the northern margin of the NCC (Fig. 14.3). The ore deposit is located in an east–west-trending syncline and is divided into the Main, East, and West ore bodies, which lies along an east–west zone more than 20 km long and 2–3 km wide. The REE and Nb ores occur throughout the Boluotu dolomite (or 'H8' dolomite marble), and Fe ores mainly in the Main, East, and West ore bodies. Although the ore-hosting dolomite marble in the Bayan Obo deposit was considered as sedimentary in origin by some researchers (e.g., Meng 1982; Zhang et al. 2008), most researchers believe that the main component of ore-hosting dolomite marble is magmatic in origin (e.g., Le Bas et al. 2007; Ling et al. 2013; Yang et al. 2011; Sun et al. 2013; Fan et al. 2014; Campbell et al. 2014; Smith et al. 2015; Zhu et al. 2015). Both field relations and geochemical evidence show a close petrogenetic link between the carbonatites and the Bayan Obo REE-Nb mineral deposit (e.g., Bai and Yuan 1985; Le Bas et al. 1992, 2007; Yuan et al. 1992; Wang et al. 2002; Yang et al. 2003, 2009, 2011; Fan et al. 2014; Campbell et al. 2014; Smith et al. 2015; Zhu et al. 2015). Most REE-Nb-rich carbonatites occur as sills emplaced into the slate, sandstone, and minor sedimentary dolomite and limestone of the Jianshan Formation of the Bayan Obo Group (Fig. 14.10); others occur as sills or dykes within the Dulahala Formation of the Bayan Obo Group and the latest Archean to Paleoproterozic metamorphic basement rocks (GSIIMAR 2003). The REE-Nb-rich carbonatites in the Bayan Obo deposit exhibit fine- to coarse-graded massive or banded structure and are composed mainly of dolomite and calcite (>80 vol.%); other minerals include apatite, monazite, barite, bastnäsite, magnetite, hematite, pyrite, fluorite, riebeckite, aegirine, phlogopite, allanite, etc.

Mineralization ages, tectonic setting, and genesis of the deposits have been the subject of much debate for many years (e.g., Ren et al. 1994; Liu et al. 2004; Wu 2008; Zhang et al. 2008). Although the ages of mineralization obtained from the REE-Nb deposit range from the Mesoproterozoic to Early Paleozoic, many results show that the Mid-Mesoproterozoic (1.4–1.2 Ga) is a very important period for REE-Nb mineralization (e.g., Nakai et al. 1989; Conrad and Mckee 1992; Wang et al. 1994; Zhang et al. 1994, 2001; Liu et al. 2004, 2005; Yang et al. 2011; Fan et al. 2014; Campbell et al. 2014; Smith et al. 2015; Zhu et al. 2015). Although the carbonatite rocks in the Bayan Obo REE-Nb-Fe ore deposit have not be precisely dated, their Sm–Nd isochron and zircon U–Pb ages are mainly around 1.4–1.2 Ga (e.g., Zhang et al. 2001; Fan et al. 2006, 2014; Le Bas 2006; Le Bas et al. 2007; Yang et al. 2011; Campbell et al. 2014), indicating their emplacement in the Mid-Mesoproterozoic, probably around 1.3 Ga, which is similar to the emplacement age of the Yanliao large igneous province and the Mid-Mesoproterozoic granite rocks in the Zha'ertai-Bayan Obo-Huade rift zones in the northern NCC. Since there is increasing evidence that many carbonatites are linked both spatially and temporally with large igneous provinces (Ernst and Bell 2009), the Bayan Obo carbonatites and REE-Nb mineralization are closely related to the Yanliao large igneous province leading to rifting to drifting transition and final breakup of the northern margin of the NCC from the Columbia (Nuna) supercontinent.

14.6 Discussion

14.6.1 Magmatism Leading to Continental Breakup or Rifting to Drifting Transition

As shown by the ca. 200 Ma Central Atlantic Magmatic Province related to breakup of the Pangea supercontinent and initial opening of the Central Atlantic Ocean (Fig. 14.11), breakup-related magmatism can occur as tholeiitic mafic dykes, sills or basalt lava flows across the neighboring continents (North America, South America, Africa, and Europe) and can be used as geological records for continental reconstruction (e.g., Deckart et al. 1997; Wilson 1997; Marzoli et al. 1999, 2011; Cirilli et al. 2009; Whalen et al. 2015). This magmatic province could be related to a mantle plume (e.g., Oyarzun et al. 1997; Wilson 1997) or non-plume continental rifting (e.g., McHone 2000; Hole 2015) leading to Pangea breakup. Since continental breakup is mainly developed from intracontinental rifting (e.g., Courtillot 1982; Frizonde de Lamotte et al. 2015), magmatism, and sedimentation in continental margin rift basins can be well correlated (e.g., Cirilli et al. 2009; Marzoli et al. 2011) and used for evidence for paleogeographic reconstruction. Moreover, the ca. 180 Ma Karoo-Ferrar large igneous province related to initial breakup of Gondwana is also characterized by tholeiitic mafic dykes, sills or basalt lava flows across the neighboring continents including southern Africa, the Dronning Maud Land sector of East Antarctica, the Transantarctic Mountains, southern Australia (Tasmania), and New Zealand (e.g., Encarnación et al. 1996; Elliot and Fleming 2000; Jourdan et al. 2008; Neumann et al. 2011; Svensen et al. 2012; Burgess et al. 2015).

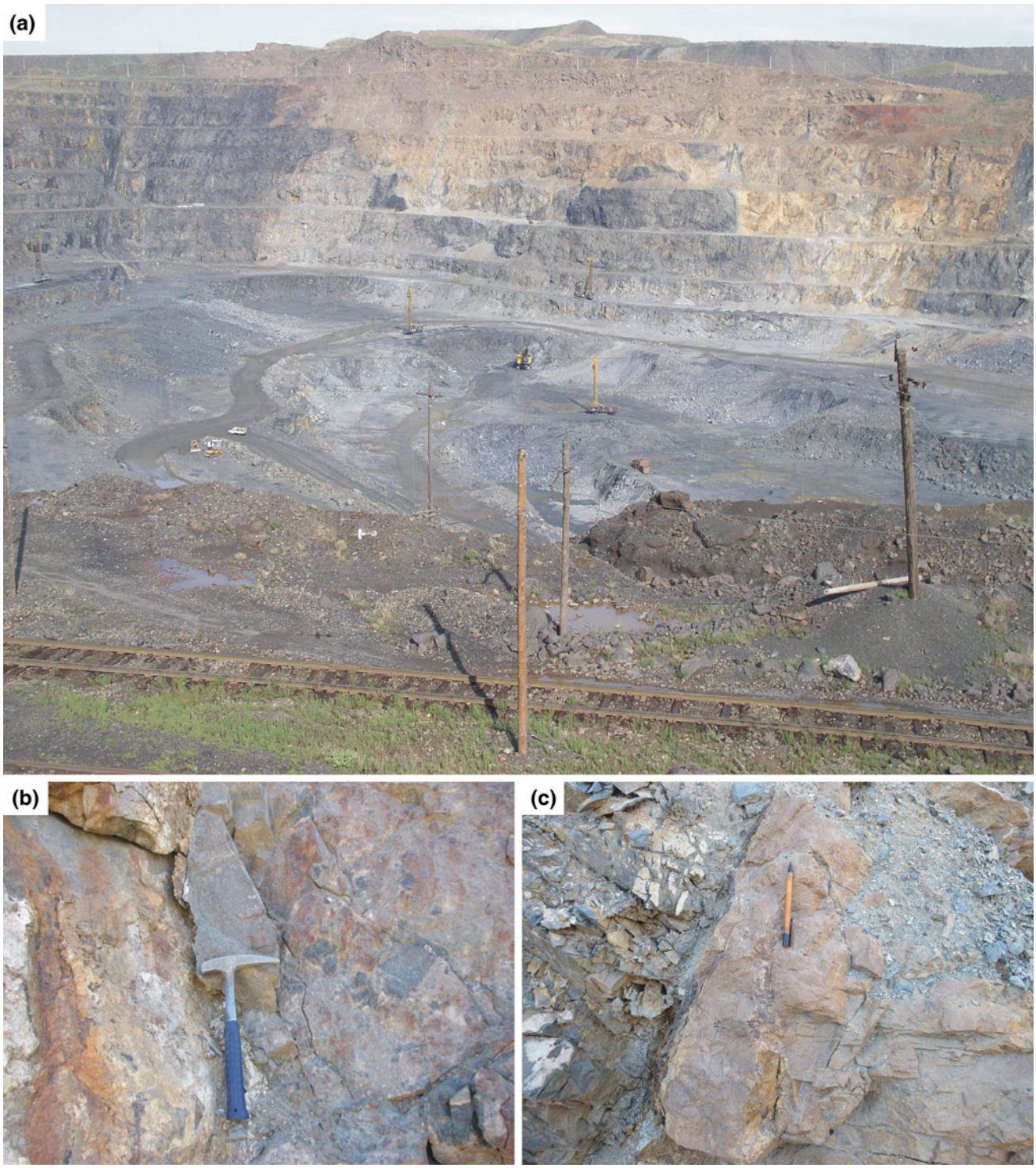

Fig. 14.10 Field photos of the giant Bayan Obo Fe-REE-Nb ore deposit in the northern margin of the NCC. **a** Open pit of the Bayan Obo deposit. **b** Black slate xenoliths of the Jianshan Formation of the Bayan Obo Group within the REE-Nb-rich carbonatites. **c** Intrusive contact between slate of Jianshan Formation and the REE-Nb-rich carbonatites

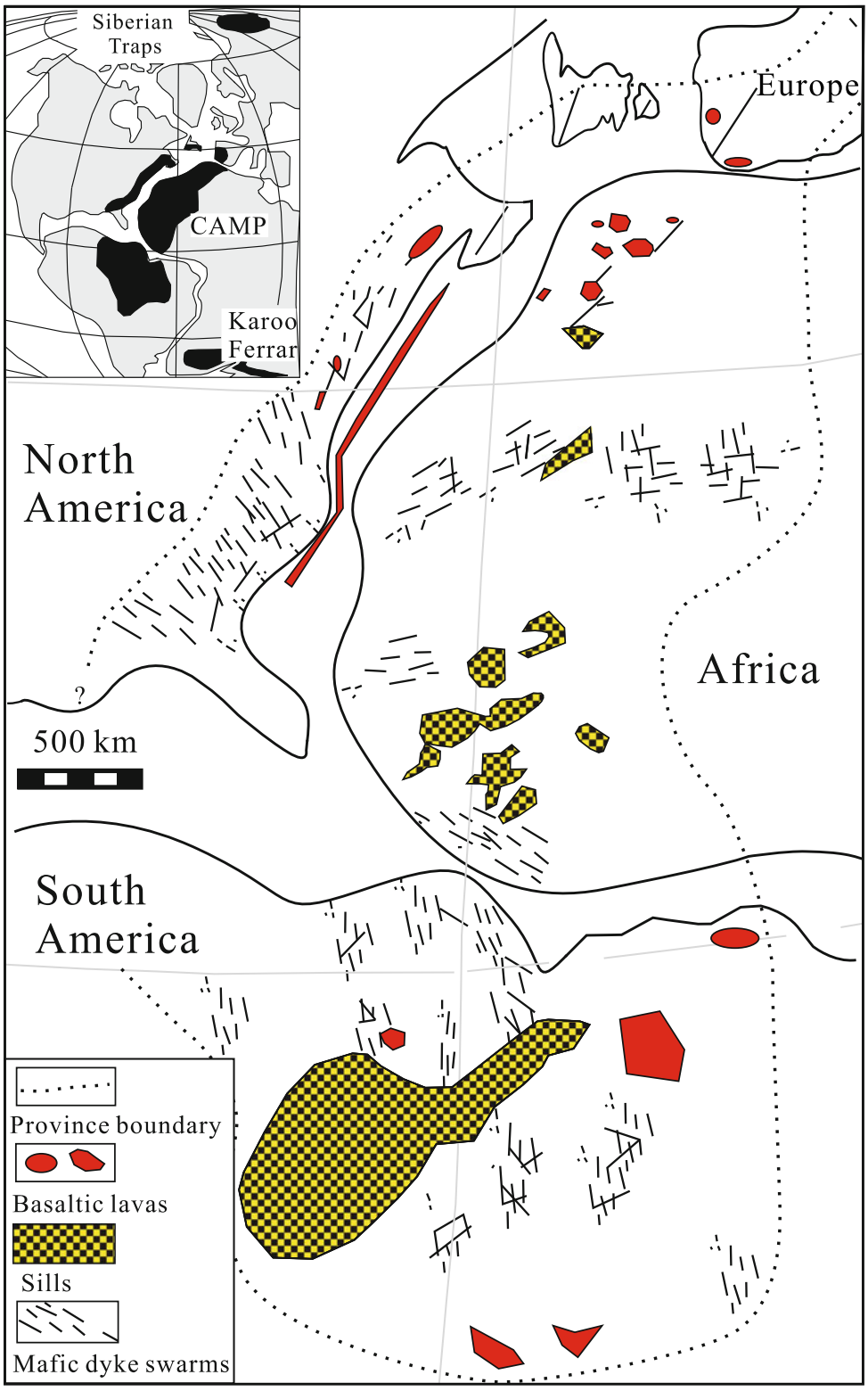

Fig. 14.11 The ca. 200 Ma Central Atlantic Magmatic Province (CAMP) associated with the breakup of Pangea (modified after Marzoli et al. 1999)

However, for the Precambrian continents suffered from long-term erosion and Phanerozoic crustal crustal growth and destruction, the above geological records (mafic dykes, sills or basalt lava flows) can only be partially preserved.

Mafic dyke swarms are especially useful for continental reconstruction, mainly because of their field geometry which can easily identified from geological maps or satellite images (e.g., Ernst and Baragar 1992; Ernst et al. 1995, 2001; Peng et al. 2008, 2011a; Peng 2010). Most of the giant (radiating, linear, and arcuate) mafic dyke swarms are considered as products of mantle plumes and their geochemistry is used to locate the plume centers (e.g., Ernst et al. 1995, 2001; Peng et al. 2008, 2011a; Peng 2010). For mafic sill swarms in continental margin rift basins, a main advantage for continental reconstruction is that both the mafic sills and their host rocks (including the volcanic layers, tuffs, K-bentonite beds, macroscopic fossils and microfossils, etc.) can be used for correlation. Moreover, unconformities or disconformities in the rift basin sequences and their contact relations with mafic sills will provide important information for uplift or subsidence during formation of the mafic sill swarms.

Recent results have revealed that all rifts undergo a phase of uplift before the lithosphere ruptures (Esedo et al. 2012; Frizonde de Lamotte et al. 2015). The signature of this uplift can be a sedimentary hiatus or a rapid change of the paleoenvironment from deep marine to subaerial (Campbell 2007; Frizonde de Lamotte et al. 2015). As talked above, both the ca. 1.32 and 0.92–0.89 Ga mafic large igneous provinces in the NCC were accompanied by pre-magmatic uplift and represent two breakup (rifting to drifting transition) events along its northern and southeastern margins, respectively. Therefore, large volumes of mafic sill swarms continental margins and accompanied pre-magmatic uplift in marginal rift basins can most likely be used as important indicators for continental breakup and reconstruction.

14.6.2 Complexity of the Mafic Dyke Swarms in the NCC

The late Paleoproterozoic to Meso-Neoproterozoic mafic dykes, which emplaced into the Archean-Paleoproterozoic metamorphic basement rocks and have not been affected by regional metamorphism, are very common in the NCC, especially in the central part of the NCC and the Luxi area in the eastern NCC (Fig. 14.3). The non-metamorphosed mafic dyke swarms in the central NCC (North China dyke swarm, Peng et al. 2007, 2008) were previously regarded mainly as ca. 1.78 or 1.80 Ga in age (mainly by zircon U–Pb dating results) and were considered to be related to a mantle plume located at the south-central part (Xiong'er) of the NCC leading to rifting and initial breakup of the NCC from the Columbia (Nuna) supercontinent (Zhai et al. 2000; Peng et al. 2006, 2007, 2008; Hou et al. 2008; Peng 2010; Hou 2012). However, recent baddeleyite U–Pb/Pb–Pb dating results show the North China dyke swarms are really very complex and were emplaced during several stages from late Paleoproterozoic to Neoproterozoic (Peng et al. 2011a; Peng 2015). Emplacement of the non-metamorphosed mafic dykes in the central NCC occurred at least during five stages at ca. 1.78, 1.73, 1.32, 1.23, and 0.92 Ga, respectively (Peng et al. 2011a; Peng 2015). The mafic dykes in the Luxi area in the eastern NCC were emplaced during 1.68 Ga and 1.63–1.62 Ga (Lu et al. 2008a; Xiang et al. 2012; Li et al. 2015b). Some mafic dykes in northern Beijing, eastern Hebei, western Liaoning, and central Jilin Province in the northern NCC were dated at two stages of 1.73 Ga and 1.23–1.21 Ga (Peng et al. 2012; Pei et al. 2013; 2015b). Most of the late Paleoproterozoic to Meso-Neoproterozoic mafic dykes are hosted in the Archean-Paleoproterozoic metamorphic basement rocks of the NCC and are characterized by similar field geometry with strikes mainly in NW–NNW, NEE or E–W (Peng 2015). Complexity of the late Paleoproterozoic to Meso-Neoproterozoic mafic dyke swarms in the NCC indicate that not all of them can be linked with mantle plumes or continental breakup events and some of dyke swarms are likely related to intracontinental extensions resulted either from the NCC itself or the neighboring continents connected with the NCC. Moreover, since the eastern-central NCC is characterized by intense structural deformation and lithospheric destruction (decratonization) from Mesozoic period (e.g., Zhu et al. 2011), intracontinental block rotations in eastern-central NCC during the Mesozoic period as revealed by paleomagnetic results (e.g., Sun et al. 1998; Zhu et al. 2002; Shi et al. 2004; Huang et al. 2007) should be considered when using geometry of the late Paleoproterozoic to Meso-Neoproterozoic mafic dykes for paleocontinental reconstructions.

14.6.3 Zircons and Precisely Dating of Mafic Rocks

Recent advance in dating of mafic rocks (e.g., Heaman and LeCheminant 1993; Söderlund et al. 2005; Heaman 2009; Li et al. 2009b, 2010b; Schmitt et al. 2010) makes it possible to obtain precise crystallization ages of Precambrian mafic dyke (sill) swarms for paleocontinental reconstruction (e.g., Ernst et al. 2013; Ernst 2014 and references therein). Although it is not easy to separate zircons from the silica-unsaturated rocks such as diabase and gabbro for high precise in situ U–Pb dating, it is still possible to obtain synmagmatic zircons from these rocks and yield reliable ages (e.g., Kamo et al. 1989; Wingate et al. 1998; Holm et al. 2006; Liu et al. 2006; Gao et al. 2009; Zhang et al. 2009, 2012c, 2016b; Wang et al. 2012b). However, in some

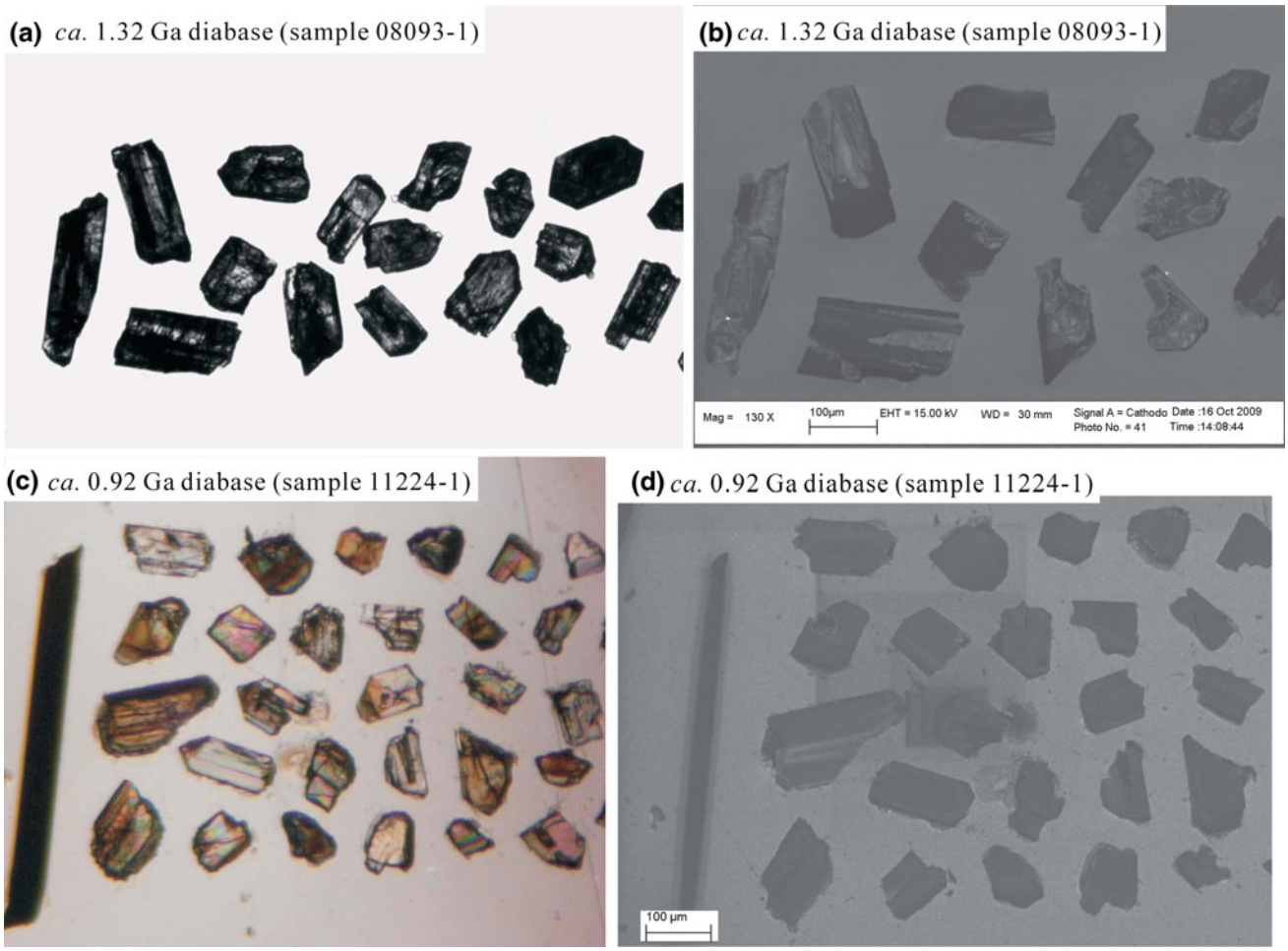

Fig. 14.12 Transmitted-light (**a**, **c**) and CL images (**b**, **d**) of synmagmatic zircons separated from diabase samples in the NCC

cases zircons in mafic rocks can be inherited from their country rocks or contaminated from other rocks during zircon separation processes and therefore yield unreliable ages. For example, the Laiwu mafic dykes in Luxi area were previously dated at 1.16–1.14 Ga by zircon SHRIMP U–Pb method (Hou et al. 2005); however, recent baddeleyite Pb–Pb dating yielded a emplacement of 1.68 Ga (Li et al. 2015b). Emplacement age of the Taishan mafic dykes was previously considered as 1.83 Ga by zircon SHRIMP U–Pb method (Hou et al. 2006); however, recent badeleyite TIMS and SIMS U–Pb dating results indicating their emplacement at 1.63–1.62 Ga (Lu et al. 2008a; Xiang et al. 2012). The Dalian sill swarms were previously considered as 0.21 Ga (Liu et al. 2012) or ca. 2.50 Ga (Liu et al. 2013) by zircon LA-ICP-MS U–Pb method; however, recent zircon LA-ICP-MS U–Pb and baddeleyite Pb–Pb dating results indicate their emplacement at 0.92–0.89 Ga (Zhang et al. 2016b). Different to synmagmatic zircons from intermediate-felsic rocks characterized by strong oscillatory zoning in cathodoluminescence (CL) images (e.g., Corfu et al. 2003; Wu and Zheng 2004), synmagmatic zircons separated from diabase samples are quite homogeneous euhedral to subhedral prisms or irregular broken fragments and exhibit weak oscillatory zoning in CL images and thin schlieren parallel to their long axis in transmitted-light images (e.g., Liu et al. 2006; Gao et al. 2009; Zhang et al. 2009, 2012c, 2016b; Wang et al. 2012; Fig. 14.12). Therefore, much attention should be paid to zircon CL images, morphology, and internal textures as well as field occurrences when using zircons to date the crystallization ages of mafic dyke (sill) swarms.

Compared with zircons, baddeleyites are particularly useful in confirming the emplacement age of mafic-ultramafic rock, as baddeleyites are not inherited (e.g., Heaman and LeCheminant 1993; Wingate 2001; Heaman 2009). Moreover, baddeleyite has the advantage of being apparently less susceptible than zircon to the effects of Pb loss and alteration (Wingate and Compston 2000). Therefore, baddeleyites (TIMS, SIMS, or LA-ICP-MS) have been widely used to date crystallization ages of mafic dyke (sill) swarms (e.g., Wingate 2001; Zhang et al. 2009, 2012c, 2016a, b; Peng et al. 2011a, b; Peng 2015; Ernst 2014 and

references therein). In many cases, TIMS method can yield precise baddeleyite U–Pb/Pb–Pb ages to constrain the crystallization ages of mafic rocks, especially when the ages are concordant or nearly concordant (e.g., Söderlund et al. 2005; Li et al. 2009a; Peng et al. 2011a; Gumsley et al. 2015; Teixeira et al. 2015). Since baddeleyite can fully or partially transform into zircon even at low grade metamorphism and some baddeleyite can be surrounded by polycrystalline zircon (e.g., Davidson and van Breemen 1988; Rioux et al. 2010; Söderlund et al. 2008, 2013), CL and back-scattered electron (BSE) images are very important during U–Pb/Pb–Pb dating of baddeleyites. This is really important especially when the baddeleyite U–Pb data obtained by TIMS method are moderately to strongly discordant (e.g., El Bahat et al. 2013). In contrast to mechanisms causing discordance in primary zircon which is commonly attributed to Pb-loss, recrystallization, overgrowth or the presence of a xenocrystic component (e.g. Corfu et al. 2003; Mezger and Krogstad 1997; Söderlund et al. 2013), moderately to strongly discordant baddeleyite data obtained by TIMS U–Pb method are normally caused by mixing between two end members of an older igneous (baddeleyite) and a younger (polycrystalline zircon) component and yield a upper intercept age younger than the crystallization age of the baddeleyite-hosting mafic rocks (e.g. Davidson and van Breemen 1988; Rioux et al. 2010; Söderlund et al. 2013). In this case, SIMS or LA-ICP-MS methods are much better than TIMS method in obtaining precise ages of mafic rocks (e.g., Söderlund et al. 2013).

14.7 Summary and Concluding Remarks

1. The NCC is characterized by multistages of extension and continental rifting and deposition of thick marine or interactive marine and terrestrial clastic and carbonate platform sediments without angular unconformity during Earth's middle age of 1.70–0.75 Ga. Factors leading to these multistages of extension and continental rifting events came either from the NCC itself or from the neighboring continents connected with the NCC during these periods.
2. Two large igneous provinces including the ca. 1.32 Ga mafic sill swarms in Yanliao rift (aulacogen) in the northern NCC and the 0.92–0.89 Ga Xu-Huai–Dalian–Sariwon mafic sill swarms in southeastern and eastern NCC have been identified from the NCC recently. They are characterized by similar geochemical features of tholeiitic compositions and intraplate characteristics. Formation of these two large igneous provinces was accompanied by pre-magmatic uplift. The Yanliao and Xu-Huai–Dalian–Sariwon large igneous provinces represent two continental rifting events that have led to rifting to drifting transition and breakup of the northern margin of the NCC from the Columbia (Nuna) supercontinent and the southeastern margin of the NCC from the Rodinia supercontinent, respectively.
3. Magmatism related to continental breakup and rifting to drifting transition can occur as mafic dykes, sills and/or lavas and is mainly tholeiitic in chemical composition. It should be large in volumes and constitute a large igneous province. In many cases, the breakup-related magmatism was accompanied by pre-magmatic uplift. Large volumes of mafic sill swarms near continental margins and accompanied pre-magmatic uplift in marginal rift basins can most likely be used as important indicators for continental breakup and paleocontinental reconstruction.

Acknowledgments This research was financially supported by the National Basic Research Program of China (2012CB416604). We thank Hangqiang Xie for help during zircon SHRIMP U–Pb analysis. We are grateful to Peng Peng for thoughtful and helpful comments on the manuscript.

References

Aitken, A. R. A., Betts, P. G., Young, D. A., Blankenship, D. D., Roberts, J. L., & Siegert, M. J. (2015). The Australo-Antarctic Columbia to Gondwana transition. *Gondwana Research, 29*, 136–152.

Bai, G., & Yuan, Z. (1985). Carbonatites and related mineral resources. *Bulletin of the Institute of Mineral Deposits, Chinese Academy of Geological Sciences, 13*, 107–140. (in Chinese with English abstract).

Bao, Z., Wang, Q., & Du, F. (2011). Geochemistry and geodynamic significance of the rare-earth mineralized Paleoproterozoic Longwangzhuang granite on the southern margin of the North China Craton. *Chinese Journal of Geochemistry, 30*, 270–279.

Bureau of Geology and Mineral Resources of Anhui Province (BGMRAHP). (1977). Geological map of Lingbi (I-50-22). *Scale,* 1:200000. (in Chinese).

Bureau of Geology and Mineral Resources of Hebei Province (BGMRHBP). (1969). Geological map of Qinglong (K-50-35). *Scale,* 1:200000. (in Chinese).

BGMRHBP. (1989). *Regional geology of Hebei Province, Beijing Municipality and Tianjin Municipality, geological memoirs* (Series 1, Number 15, pp. 1–741). Beijing: Geological Publishing House (in Chinese with English abstract).

Bureau of Geology and Mineral Resources of Henan Province (BGMRHNP). (1989). *Regional geology of Henan Province, geological memoirs* (Series 1, Number 17, pp. 1–772). Beijing: Geological Publishing House (in Chinese with English abstract).

Bureau of Geology and Mineral Resources of Jiangsu Province (BGMRJSP). (1978). Geological map of Xuzhou (I-50-16). *Scale,* 1:200000. (in Chinese).

Bureau of Geology and Mineral Resources of Liaoning Province (BGMRLNP). (1965). Geological map of Lingyuan (K-50-30). *Scale,* 1:200000. (in Chinese).

BGMRLNP. (1967). Geological map of Chaoyang (K-51-19). *Scale,* 1:200000. (in Chinese).

BGMRLNP. (1969). Geological map of Jinxi (K-51-25). *Scale,* 1:200000. (in Chinese).

Bureau of Geology and Mineral Resources of Nei Mongol Autonomous Region (BGMRNMAR). (1991). *Regional geology of Shanxi Province, geological memoirs* (Series 1, Number 25, pp. 1–725). Beijing: Geological Publishing House (in Chinese with English abstract).

Bureau of Geology and Mineral Resources of Shanxi Province (BGMRSXP). (1989). *Regional geology of Shanxi Province, geological memoirs* (Series 1, Number 18, pp. 1–780). Beijing: Geological Publishing House (in Chinese with English abstract).

Burgess, S. D., Bowring, S. A., Fleming, T. H., & Elliot, D. H. (2015). High-precision geochronology links the Ferrar large igneous province with early-Jurassic ocean anoxia and biotic crisis. *Earth and Planetary Science Letters, 415*, 90–99.

Campbell, I. H. (2007). Testing the plume theory. *Chemical Geology, 241*, 153–176.

Campbell, L. S., Compston, W., Sircombe, K. N., & Wilkinson, C. C. (2014). Zircon from the east orebody of the Bayan Obo Fe–Nb–REE deposit, China, and SHRIMP ages for carbonatite-related magmatism and REE mineralization events. *Contributions to Mineralogy and Petrology, 168*, 1041. doi:10.1007/s00410-014-1041-3.

Cawood, P. A., & Hawkesworth, C. J. (2014). Earth's middle age. *Geology, 42*, 503–506.

Chen, L., Huang, B., Yi, Z., Zhao, J., & Yan, Y. (2013a). Paleomagnetism of ca. 1.35 Ga sills in northern North China Craton and implications for paleogeographic reconstruction of the Mesoproterozoic supercontinent. *Precambrian Research, 228*, 36–47.

Chen, W., Zhou, M.-F., & Zhao, T.-P. (2013b). Differentiation of nelsonitic magmas in the formation of the ~1.74 Ga Damiao Fe–Ti–P ore deposit, North China. *Contributions to Mineralogy and Petrology, 165*, 1341–1362.

China National Commission on Stratigraphy. (2001). *Guide book and explanation of China stratigraphy* (Revised Edition, pp. 1–59). Beijing: Geological Publishing House (in Chinese).

Cirilli, S., Marzoli, A., Tanner, L., Bertrand, H., Buratti, N., Jourdan, F., et al. (2009). Latest Triassic onset of the Central Atlantic magmatic province (CAMP) volcanism in the Fundy basin (Nova Scotia): New stratigraphic constraints. *Earth and Planetary Science Letters, 286*, 514–525.

Conrad, I. E., & Mckee, E. H. (1992). $^{40}Ar/^{39}Ar$ dating of vein amphibole from the Bayan Obo iron-rare earth element-niobium deposit, China: Constraints on mineralization and deposition of the Bayan Obo Group. *Economic Geology, 87*, 185–188.

Corfu, F., Hanchar, J. M., Hoskin, P. W. O., & Kinny, P. (2003). Atlas of Zircon textures. *Reviews in Mineralogy and Geochemistry, 53*, 469–500.

Courtillot, V. (1982). Propagating rifts and continental breakup. *Tectonics, 1*, 239–250.

Dalziel, I. W. D. (1991). Pacific margins of Laurentia and East Antarctica-Australia as a conjugate rift pair: Evidence and implications for an Eocambrian supercontinent. *Geology, 19*, 598–601.

Dan, W., Li, X. H., Wang, Q., Wang, X. C., & Liu, Y. (2014). Neoproterozoic S-type granites in the Alxa block, westernmost north China and tectonic implications: In-situ zircon U-Pb–Hf–O isotopic and geochemical constraints. *American Journal of Science, 314*, 110–153.

Davidson, A., & van Breemen, O. (1988). Baddeleyite-zircon relationships in coronitic metagabbro, Grenville Province, Ontario: Implications for geochronology. *Contributions to Mineralogy and Petrology, 100*(3), 291–299.

Deckart, K., Féraud, G., & Bertrand, H. (1997). Age of Jurassic continental tholeiites of French Guyana, Surinam, and Guinea: Implications for the initial opening of the Central Atlantic Ocean. *Earth and Planetary Science Letters, 150*, 205–220.

Demoux, A., Kröner, A., Liu, D., & Badarch, G. (2009). Precambrian crystalline basement in southern Mongolia as revealed by SHRIMP zircon dating. *International Journal of Earth Sciences, 98*, 1365–1380.

Deng, X. Q., Zhao, T. P., Peng, T. P., Gao, X. Y., & Bao, Z. W. (2015). Petrogenesis of 1600 Ma Maping A-type granite in the southern margin of the North China Craton and its tectonic implications. *Acta Petrologica Sinica, 31*(6), 1621–1635. (in Chinese with English abstract).

Ding, J. H., Xiao, C. D., & Qin, Z. Y. (2005). Petrological and geochemical research on Dahongyu ultra-potassic volcanic rocks in Dongzigou area, Hebei Province. *Geological Survey and Research, 28*(2), 100–105. (in Chinese with English abstract).

Du, R. L., Li, F. C., Li, P. J., Liang, X., Lin, M., & Hu, H. B. (1992). Discovery and Significance of microfossils from the Changchengian Xuanlong-type Iron formations in northwestern Hebei. *Geological Review, 38*(2), 184–188. (in Chinese with English abstract).

El Bahat, A., Ikenne, M., Söderlund, U., Cousens, B., Youbi, N., Ernst, R., et al. (2013). U-Pb baddeleyite ages and geochemistry of dolerite dykes in the Bas Drâa Inlier of the Anti-Atlas of Morocco: Newly identified 1380 Ma event in the West African Craton. *Lithos, 174*, 85–98.

Elliot, D. H., & Fleming, T. H. (2000). Weddell triple junction: The principal focus of Ferrar and Karoo magmatism during the initial breakup of Gondwana. *Geology, 28*, 539–542.

Encarnación, J., Fleming, T. H., Elliot, D. H., & Eales, H. V. (1996). Synchronous emplacement of Ferrar and Karoo dolerites and the early break-up of Gondwana. *Geology, 24*, 535–538.

Ernst, R. E. (2014). *Large igneous provinces* (pp. 1–653). Cambridge, UK: Cambridge University Press.

Ernst, R. E., & Baragar, W. R. A. (1992). Evidence from magnetic fabric for the flow pattern of magma in the Mackenzie giant radiating dyke swarm. *Nature, 356*, 511–513.

Ernst, R. E., & Bell, K. (2009). Large igneous provinces (LIPs) and carbonatites. *Mineralogy and Petrology, 98*, 55–76.

Ernst, R. E., Bleeker, W., Söderlund, U., & Kerr, A. C. (2013). Large igneous provinces and supercontinents: Toward completing the plate tectonic revolution. *Lithos, 174*, 1–14.

Ernst, R. E., Grosfils, E. B., & Mège, D. (2001). Giant dike swarms: Earth, Venus and Mars. *Annual Reviews Earth and Planetary Science, 29*, 489–534.

Ernst, R. E., Head, J. W., Parfitt, E., Grosfils, E., & Wilson, L. (1995). Giant radiating dyke swarms on earth and venus. *Earth-Science Reviews, 39*, 1–58.

Ernst, R. E., Wingate, M. T. D., Buchan, K. L., & Li, Z. X. (2008). Global record of 1600–700 Ma large igneous provinces (LIPs): Implications for the reconstruction of the proposed Nuna (Columbia) and Rodinia supercontinents. *Precambrian Research, 160*, 159–178.

Esedo, R., van Wijk, J., Coblentz, D., & Meyer, R. (2012). Uplift prior to continental breakup: Indication for removal of mantle lithosphere? *Geosphere, 8*, 1078–1085.

Evans, D. A. D. (2013). Reconstructing pre-Pangean supercontinents. *Geological Society of America Bulletin, 125*, 1735–1751.

Evans, D. A. D., & Mitchell, R. N. (2011). Assembly and breakup of the core of Paleoproterozoic-Mesoproterozoic supercontinent Nuna. *Geology, 39*, 443–446.

Fan, H. R., Hu, F. F., Chen, F. K., Yang, K. F., & Wang, K. Y. (2006). Intrusive age of No.1 carbonatite dyke from Bayan Obo REE-Nb-Fe deposit, Inner Mongolia: With answers to comment of Dr. Le Bas. *Acta Petrologica Sinica, 22*, 519–520. (in Chinese with English abstract).

Fan, H. R., Hu, F. F., Yang, K. F., Pirajno, F., Liu, X., & Wang, K. Y. (2014). Integrated U-Pb and Sm–Nd geochronology for a REE-rich carbonatite dyke at the giant Bayan Obo REE deposit, Northern China. *Ore Geology Reviews, 63*, 510–519.

Frizonde de Lamotte, D., Fourdan, B., Leleu, S., Leparmentier, F., & de Clarens, P. (2015). Style of rifting and the stages of Pangea breakup. *Tectonics, 34*, 1009–1029. doi:10.1002/2014TC003760.

Gao, L., Zhang, C., Yin, C., Shi, X., Wang, Z., Liu, Y., et al. (2008a). SHRIMP zircon ages: Basis for refining the chronostratigraphic classification of the Meso-and Neoproterozoic strata in North China Old Land. *Acta Geoscientica Sinica, 29*, 366–376. (in Chinese with English abstract).

Gao, L. Z., Zhang, C. H., Shi, X. Y., Zhou, H. R., & Wang, Z. Q. (2007). Zircon SHRIMP U-Pb dating of the tuff bed in the Xiamaling formation of the Qingbaikouan system in North China. *Geological Bulletin of China, 26*, 249–255. (in Chinese with English abstract).

Gao, L. Z., Zhang, C. H., Shi, X. Y., Song, B., Wang, Z. Q., & Liu, Y. M. (2008b). Mesoproterozoic age for Xiamaling formation in North China plate indicated by zircon SHRIMP dating. *Chinese Science Bulletin, 53*, 2665–2671.

Gao, L. Z., Zhang, C. H., Liu, P. J., Tang, F., Song, B., & Ding, X. Z. (2009). Reclassification of the Meso- and Neoproterozoic chronostratigraphy of North China by SHRIMP zircon ages. *Acta Geologica Sinica, 83*, 1074–1084. (English Edition).

Gao, W., Zhang, C. H., Gao, L. Z., Shi, X. Y., Liu, Y. M., & Song, B. (2008c). Zircon SHRIMP U-Pb age of rapakivi granite in Miyun, Beijing, China, and its tectono-stratigraphic implications. *Geological Bulletin of China, 27*(6), 793–798. (in Chinese with English abstract).

Geng, Y. S., Wang, X. S., & Shen, Q. H. (2002). The discovery of Neoproterozoic Jinningian deformed granites in Alxa area and its significance. *Acta Petrologica et Mineralogica, 21*(4), 412–420. (in Chinese with English abstract).

Geng, Y. S., & Zhou, X. W. (2011). Characteristics of geochemistry and zircon Hf isotope of the Early Neoproterozoic granite in Alax area, Inner Mongolia. *Acta Petrologica Sinica, 27*(4), 908–987. (in Chinese with English abstract).

Geological Survey Institute of Henan Province (GSIHNP). (2002). Geological map of Neixiang County (I49C003003). *Scale,* 1:250000. (in Chinese).

Geological Survey Institute of Henan Province (GSIHNP). (2003). Geological map of Pingdingshan (I49C003004). *Scale,* 1:250000. (in Chinese).

Geology Survey Institute of Inner Mongolia Autonomous Region (GSIIMAR). (2003). Geological map of Bayan Obo (K49C003002). *Scale,* 1:250000. (in Chinese).

Geological Survey Institute of Shanxi Province (GSISXP). (2007). Geological map of Houmashi (I49C001003). *Scale,* 1:250000. (in Chinese).

Gradstein, F. M., Ogg, J. G., Smith, A. G., Bleeker, W., & Lourens, L. J. (2004). A new Geological Time Scale, with special reference to Precambrian and Neogene. *Episodes, 27*(2), 83–100.

Gumsley, A., Olsson, J., Söderlund, U., de Kock, M., Hofmann, A., & Klausen, M. (2015). Precise U-Pb baddeleyite age dating of the Usushwana Complex, southern Africa—Implications for the Mesoarchaean magmatic and sedimentological evolution of the Pongola Supergroup, Kaapvaal Craton. *Precambrian Research, 267*, 174–185.

Halls, H. C., Li, J. H., Davis, D., Hou, G., Zhang, B. X., & Qian, X. L. (2000). A precisely dated Proterozoic palaeomagnetic pole from the North China craton, and its relevance to palaeocontinental reconstruction. *Geophysical Journal International, 143*, 185–203.

Han, G., Liu, Y., Neubauer, F., Genser, J., Li, W., Zhao, Y., et al. (2011). Origin of terranes in the eastern Central Asian Orogenic Belt, NE China: U-Pb ages of detrital zircons from Ordovician-Devonian sandstones, North Da Xing'an Mts. *Tectonophysics, 511*, 109–124.

He, Y., Zhao, G., Sun, M., & Xia, X. P. (2009). SHRIMP and LA-ICP-MS zircon geochronology of the Xiong'er volcanic rocks: implications for the Paleo-Mesoproterozoic evolution of the southern margin of the North China Craton. *Precambrian Research, 168*, 213–222.

He, Z. J., Niu, B. G., Zhang, X. Y., Zhao, L., & Liu, R. Y. (2011a). Discovery of the paleo-weathered mantle of the rapakivi granite covered by the Proterozoic Changzhougou formation in the Miyun area, Beijing and their detrital zircon dating. *Geological Bulletin of China, 30*(5), 798–802. (in Chinese with English abstract).

He, Z. J., Zhang, X., Niu, B., Liu, R., & Zhao, L. (2011b). The paleo-weathering mantle of the Proterozoic rapakivi granite in Miyun County, Beijing and the relationship with the Changzhougou formation of Changchengian system. *Earth Science Frontiers, 18*(4), 123–130. (in Chinese with English abstract).

Heaman, L., & LeCheminant, A. N. (1993). Paragenesis and U-Pb systematics of baddeleyite (ZrO_2). *Chemical Geology, 119*, 95–126.

Heaman, L. M. (2009). The application of U-Pb geochronology to mafic, ultramafic and alkaline rocks: An evaluation of three mineral standards. *Chemical Geology, 261*, 43–52.

Hoffman, P. F. (1991). Did the breakout of Laurentia turn Gondwanaland inside-out? *Science, 252*, 1409–1412.

Hole, M. J. (2015). The generation of continental flood basalts by decompression melting of internally heated mantle. *Geology, 43*, 311–314.

Holm, P. M., Heaman, L. M., & Pedersen, L. E. (2006). Baddeleyite and zircon U-Pb ages from the Kaerven area, Kangerlussuaq: Implications for timing of Paleogene continental breakup in the North Atlantic. *Lithos, 92*, 238–250.

Hou G. T. (2012). *Mafic dyke swarms of North China* (pp. 1–177). Beijing: Science Press (in Chinese).

Hou, G. T., Liu, Y. L., Li, J. H., & Jin, A. W. (2005). The SHRIMP U-Pb chronology of mafic dyke swarms: A case study of Laiwu diabase dykes in western Shandong. *Acta Petrologica et Mineralogica, 24*, 179–185. (in Chinese with English abstract).

Hou, G. T., Liu, Y. L., & Li, J. H. (2006). Evidence for ~1.8 Ga extension of the Eastern Block of the North China Craton from SHRIMP U-Pb dating of mafic dyke swarms in Shandong Province. *Journal of Asian Earth Sciences, 27*, 392–401.

Hou, G. T., Santosh, M., Qian, X. L., Lister, G. S., & Li, J. H. (2008). Configuration of the Late Palaeoproterozoic supercontinent Columbia: Insights from radiating mafic dyke swarms. *Gondwana Research, 14*, 395–409.

Hu, J., Gong, W., Wu, S., Liu, Y., & Liu, S. (2014). LA-ICP-MS zircon U-Pb dating of the Langshan Group in the northeast margin of the Alxa block, with tectonic implications. *Precambrian Search, 255*, 756–770.

Hu, J. L., Zhao, T. P., Xu, Y. H., & Chen, W. (2007). Geochemistry and petrogenesis of the high-K volcanic rocks in the Dahongyu Formation, North China Craton. *Journal of Mineralogy and Petrology, 27*, 70–77.

Hu, S. L., Wang, S. S., Sang, H. Q., Qiu, J., Ye, D. H., Chui, R. H., et al. (1990). The isotopic ages and REE geochemistry of Damiao anorthosite and their geological implications. *Scientia Geologica Sinica, 25*, 332–343. (in Chinese with English abstract).

Huang, B., Piper, J. D. A., Zhang, C., Li, Z., & Zhu, R. (2007). Paleomagnetism of Cretaceous rocks in the Jiaodong Peninsula, eastern China: Insight into block rotations and neotectonic deformation in eastern Asia. *Journal of Geophysical Research, 112*, B03106. doi:10.1029/2006JB004462.

International Commission on Stratigraphy. (2012). *International chronostratigraphic chart*. http://www.stratigraphy.org/ICSchart/ChronostratChart2012.jpg

Jiang, N., Guo, J., & Zhai, M. (2011). Nature and origin of the Wenquan granite: Implications for the provenance of Proterozoic A-type granites in the North China craton. *Journal of Asian Earth Sciences, 42*, 76–82.

Jourdan, F., Féraud, G., Bertrand, H., Watkeys, M. K., & Renne, P. R. (2008). The 40Ar/39Ar ages of the sill complex of the Karoo large igneous province: Implications for the Pliensbachian–Toarcian climate change. *Geochemistry Geophysics Geosystem, 9*, 1–20. doi:10.1029/2008GC001994

Kamo, S. L., Gower, C. F., & Krogh, T. E. (1989). Birthdate for the Iapetus Ocean? A precise U-Pb zircon and baddeleyite age for the Long Range dikes, southeast Labrador. *Geology, 17*, 602–605.

Kröner, A., Demoux, A., Zack, T., Rojas-Agramonte, Y., Jian, P., Tomurhuu, D., et al. (2011). Zircon ages for a felsic volcanic rock and arc-related early Palaeozoic sediments on the margin of the Baydrag microcontinent, central Asian orogenic belt, Mongolia. *Journal of Asian Earth Sciences, 42*, 1008–1017.

Kröner, A., Kovach, V., Belousova, E., Hegner, E., Armstrong, R., Dolgopolova, A., et al. (2014). Reassessment of continental growth during the accretionary history of the Central Asian Orogenic Belt. *Gondwana Research, 25*, 103–125.

Le Bas, M. J. (2006). Re-interpretation of zircon date in a carbonite dyke at the Bayan Obo giant REE-Fe-Nb deposit, China. *Acta Petrologica Sinica, 22*, 517–518.

Le Bas, M. J., Keller, J., Tao, K. J., Wall, F., Williams, C. T., & Zhang, P. S. (1992). Carbonatite dykes at Bayan Obo, Inner Mongolia, China. *Mineralogy and Petrology, 46*, 195–228.

Le Bas, M. J., Xueming, Y., Taylor, R. N., Spiro, B., Milton, J. A., & Peishan, Z. (2007). New evidence from a calcite-dolomite carbonatite dyke for the magmatic origin of the massive Bayan Obo ore-bearing dolomite marble, Inner Mongolia, China. *Mineralogy and Petrology, 90*, 223–248.

LeCheminant, A. N., & Heaman, L. M. (1989). Mackenzie igneous events, Canada: Middle Proterozoic hotspot magmatism associated with ocean opening. *Earth and Planetary Science Letters, 96*, 38–48.

Levashova, N. M., Kalugin, V. M., Gibsher, A. S., Yff, J., Ryabinin, A. B., Meert, J. G., et al. (2010). The origin of the Baydaric Microcontinent, Mongolia: Constraints from paleomagnetism and geochronology. *Tectonophysics, 485*, 306–320.

Levashova, N. M., Meert, J. G., Gibsher, A. S., Grice, W. C., & Bazhenov, M. L. (2011). The origin of microcontinents in the Central Asian Orogenic Belt: Constraints from paleomagnetism and geochronology. *Precambrian Research, 185*, 37–54.

Li, H. K., Li, H. M., & Lu, S. N. (1995). Grain zircon U-Pb age for volcanic rocks from Tuanshanzi Formation of Changcheng System and their geological implication. *Geochimica (Beijing), 24*(10), 43–47. (in Chinese with English abstract).

Li, H. K., Lu, S. N., Li, H. M., Sun, L. X., Xiang, Z. Q., Geng, J. Z., et al. (2009a). Zircon and baddeleyite U-Pb precision dating of basic rock sills intruding Xiamaling Formation, North China. *Geological Bulletin of China, 28*, 1396–1404. (in Chinese with English abstract).

Li, H. K., Lu, S. N., Su, W. B., Xiang, Z. Q., Zhou, H. Y., & Zhang, Y. Q. (2013). Recent advances in the study of the Mesoproterozoic geochronology in the North China Craton. *Journal of Asian Earth Sciences, 72*, 216–227.

Li, H. K., Su, W., Zhou, H., Geng, J., Xiang, Z., Cui, Y., et al. (2011). The base age of the Changchengian System at the northern North China Craton should be younger than 1670: Constraints from zircon U-Pb LA-MC-ICPMS dating of a granite-porphyry dike in Miyun County, Beijing. *Earth Science Frontiers, 18*(3), 108–120. (in Chinese with English abstract).

Li, H. K., Su, W., Zhou, H., Xiang, Z., Tian, H., Yang, L., et al. (2014a). The first precise age constraints on the Jixian system of the Meso- to Neoproterozoic standard section of China: SHRIMP zircon U-Pb dating of bentonites from the Wumishan and Tieling formations in the Jixian Section, North China Craton. *Acta Petrologica Sinica, 30*, 2999–3012. (in Chinese with English abstract).

Li, H. K., Zhu, S. X., Xiang, Z. Q., Su, W. B., Lu, S. N., Zhou, H. Y., et al. (2010a). Zircon U-Pb dating on tuff bed from Gaoyuzhuang Formation in Yanqiang, Beijing: Further constraints on the new subdivision of the Mesoproterozoic stratigraphy in the northern North China Craton. *Acta Petrologica Sinica, 26*, 2131–2140. (in Chinese with English abstract).

Li, H. M., Li, L., Zhang, Z., Santosh, M., Liu, M., Cui, Y., et al. (2014b). Alteration of the Damiao anorthosite complex in the northern North China Craton: Implications for high-grade iron mineralization. *Ore Geology Review, 57*, 574–588.

Li, H. M., Li, L. X., Yang, X. Q., & Cheng, Y. B. (2015a). Types and geological characteristics of iron deposits in China. *Journal of Asian Earth Sciences, 103*, 2–22.

Li, J. Y., Zhang, J., & Qu, J. F. (2012). Amalgamation of North China Craton with Alxa Block in the late of Early Paleozoic: Evidence from sedimentary sequences in the Niushou Mountain, Ningxia Hui Autonomous Region, NW China. *Geological Review, 58*, 208–214. (in Chinese with English abstract).

Li, Q. L., Li, X. H., Liu, Y., Tang, G. Q., Yang, J. H., & Zhu, W. G. (2010b). Precise U-Pb and Pb-Pb dating of Phanerozoic baddeleyite by SIMS with oxygen flooding technique. *Journal of Analytical Atomic Spectrometry, 25*, 1107–1113.

Li, W. P., & Li, X. H. (2005). Geochemical characteristics of the Late Paleozoic diabase dyke swarms of Changmaohezi from western Liaoning, Northeast China. *Earth Science, 30*, 761–770. (in Chinese with English abstract).

Li, X. H., Liu, Y., Li, Q. L., Guo, C. H., & Chamberlain, K. R. (2009b). Precise determination of Phanerozoic zircon Pb/Pb age by multi-collector SIMS without external standardization. *Geochemistry Geophysics Geosystem, 10*, Q04010. doi:10.1029/2009GC002400.

Li, Y., Peng, P., Wang, X., & Wang, H. (2015b). Nature of 1800–1600 Ma mafic dyke swarms in the North China Craton: Implications for the rejuvenation of the sub-continental lithospheric mantle. *Precambrian Research, 257*, 114–123.

Li, Z. H., & Zhu, X. K. (2012). Geochemical features of Xuanlong type iron ore deposit in Hebei Province and their geological significances. *Acta Petrologica Sinica, 28*(9), 2903–2911. (in Chinese with English abstract).

Li, Z. X., Bogdanova, S. V., Collins, A. S., Davidson, A., De Waele, B., Ernst, R. E., Fitzsimons, I. C. W., Fuck, R. A., Gladkochub, D. P., Jacobs, J., Karlstrom, K. E., Lu, S., Natapov, L. M., Pease, V., Pisarevsky, S. A., Thrane, K. & Vernikovsky, V. (2008). Assembly, configuration, and break-up history of Rodinia: a synthesis. *Precambrian Research, 160*, 179–210.

Liang, R., Zhang, X. Y., Zhao, J., & Li, X. H. (2013). Geological characteristics and genesis of the "Xuanlong-type" iron deposit. *Huabei Land and Resources, 52*(1), 135–140. (in Chinese).

Ling, M. X., Liu, Y. L., Williams, I. S., Teng, F. Z., Yang, X. Y., Ding, X., et al. (2013). Formation of the world's largest REE deposit through protracted fluxing of carbonatite by subduction-derived fluids. *Scientific Reports, 3*(1776), 1–8. doi:10.1038/srep01776.

Liu, J. F., Li, J. Y., Qu, J. F., Hu, Z. C., Feng, Q. W., & Guo, C. L. (2016). Late Paleoproterozoic tectonic setting of the northern margin of the North China Craton: Constraints from the geochronology and geochemistry of the mangerites in the Longhua and Jianping areas. *Precambrian Research, 272*, 57–77.

Liu, M., Chen, Z. M., & Chen, Q. Y. (1997). The role of organic matter in the genesis of siderite from the Xuanlong area. *Acta Sedmentologica Sinica, 15*(3), 96–102. (in Chinese with English abstract).

Liu, M., Ye, L. J., Xu, S. Y., Chen, Z. M., & Chen, Q. Y. (1999). The organic Geochemistry characteristics and genetic significance of microbial ironstones from the Xuanlong area, Hebei Province. *Acta Sedmentologica Sinica, 17*(1), 24–29. (in Chinese with English abstract).

Liu, S., Hu, R., Gao, S., Feng, C., Coulson, I. M., Feng, G., et al. (2012). U-Pb zircon age, geochemical and Sr-Nd isotopic data as constraints on the petrogenesis and emplacement time of the Precambrian mafic dyke swarms in the North China Craton (NCC). *Lithos, 140–141*, 38–52.

Liu, S., Hu, R., Gao, S., Feng, C., Coulson, I. M., Feng, G., et al. (2013). Zircon U-Pb age and Sr–Nd–Hf isotopic constraints on the age and origin of Triassic mafic dikes, Dalian area, Northeast China. *International Geology Review, 55*, 249–262.

Liu, S. W., Santosh, M., Wang, W., Bai, X., & Yang, P. T. (2011). Zircon U-Pb chronology of the Jianping Complex: Implications for the Precambrian crustal evolution history of the northern margin of North China Craton. *Gondwana Research, 20*(1), 48–63.

Liu, W. X. (1991). The geochemical characteristics and the magma evolution of the Mid-Proterozoic volcanic rock in Yanshan mountain area. *Journal of Tianjin Geological Society, 9*(2), 46–55. (in Chinese with English abstract).

Liu, X. Y. (2011). *Chronological, petrological and geochemical characteristics of the Paleo-Mesoproterozoic alkali-rich intrusive rocks along the southern part of the North China Craton* (pp. 1–94). Master degree thesis. Beijing: Chinese Academy of Geological Sciences (in Chinese with English summary).

Liu, Y. L., Yang, G., Chen, J. F., Du, A. D., & Xie, Z. (2004). Re-Os dating of pyrite from giant Bayan Obo REE-Nb-Fe deposit. *Chinese Science Bulletin, 24*, 2627–2631.

Liu, Y. L., Chen, J. F., Li, H. M., Qian, H., Xiao, G. W., & Zhang, T. R. (2005). Single-grain U-Th-Pb-Sm-Nd dating of monazite from dolomite type ore of the Bayan Obo deposit. *Acta Petrologica Sinica, 21*, 881–888. (in Chinese with English abstract).

Liu, Y. Q., Gao, L. Z., Liu, Y. X., Song, B., & Wang, Z. X. (2006). Zircon U-Pb dating for the earliest Neoproterozoic mafic magmatism in the southern margin of the North China Block. *Chinese Science Bulletin, 51*, 2375–2382.

Liu, Z. L., Liu, X. X., Li, P. F., & Du, R. L. (1995). Biomarkes (alkanes) of the Xuanlong-type iron deposits. *Acta Geologica Sinica, 69*(2), 138–144. (in Chinese with English abstract).

Lu, S. N., Chen, Z. H., & Xiang, Z. Q. (2008a). *Geochronological framework of the Precambrian intrusive rocks in the Mountain Tai World Geopark* (pp. 1–90). Beijing: Geological Publishing House (in Chinese).

Lu, S. N., Li, H. K., Li, H. M., Song, B., Wang, S., Zhou, H., et al. (2003). U-Pb isotopic ages and their significance of alkaline granite in the southern margin of the North China Craton. *Geological Bulletin of China, 22*, 762–768. (in Chinese with English abstract).

Lu, S. N., & Li, H. M. (1991). A precise U-Pb single zircon age determination for the volcanics of Dahongyu Formation, Changcheng System in Jixian. *Bulletin of Chinese Academy of Geological Science, 22*, 137–145. (in Chinese with English abstract).

Lu, S. N., Zhao, G. C., Wang, H. C., & Hao, G. J. (2008b). Precambrian metamorphic basement and sedimentary cover of the North China Craton: A review. *Precambrian Research, 160*, 77–93.

Marzoli, A., Jourdan, F., Puffer, J. H., Cuppone, T., Tanner, L. H., Weems, R. E., et al. (2011). Timing and duration of the Central Atlantic magmatic province in the Newark and Culpeper basins, eastern U.S.A. *Lithos, 122*, 175–188.

Marzoli, A., Renne, P. R., Piccirillo, E. M., Ernesto, M., Bellieni, G., & De Min, A. (1999). Extensive 200 million-year-old continental flood basalts of the central Atlantic magmatic province. *Science, 284*, 616–618.

McHone, J. G. (2000). Non-plume magmatism and rifting during the opening of the central Atlantic Ocean. *Tectonopysics, 316*, 287–296.

Meng, Q. (1982). The genesis of the host rock dolomite of the Bayan Obo iron ore deposits and the analysis of its sedimentary environment. *Geological Review, 28*, 481–489. (in Chinese with English abstract).

Meng, Q. R., Wei, H. H., & Qu, Y. Q. (2011). Stratigraphic and sedimentary records of the rift to drift evolution of the northern North China craton at the Paleo- to Mesoproterozoic transition. *Gondwana Research, 20*, 205–218.

Mezger, K., & Krogstad, E. J. (1997). Interpretation of discordant U-Pb zircon ages: An evaluation. *Journal of Metamorphic Geology, 15*, 127–140.

Nakai, S., Masuda, A., Shimizu, H., & Qi, L. (1989). La-Ba dating and Nd and Sr isotope studies on Baiyun Obo rare earth element ore deposits, Inner Mongolia, China. *Economic Geology, 84*, 2296–2299.

Neumann, E. R., Svensen, H., Galerne, C. Y., & Planke, S. (2011). Multistage evolution of dolerites in the Karoo Large Igneous Province, Central South Africa. *Journal of Petrology, 52*, 959–984.

Oyarzun, R., Doblas, M., López-Ruiz, J., & Cebriá, J. M. (1997). Opening of the central Atlantic and asymetric mantle upwelling phenomena: implications for long-lived magmatism in western North Africa and Europe. *Geology, 25*, 727–730.

Pei, J., Yang, Z., & Zhao, Y. (2006). A Mesoproterozoic paleomagnetic pole from the Yangzhuang formation, North China and its tectonics implications. *Precambrian Research, 151*, 1–13.

Pei, F. P., Ye, Y. F., Wang, F., Cao, H. H., Lu, S. M., & Yang, D. B. (2013). Discovery of Mesoproterozoic diabase dyke in Tonghua region, Jilin Province and its tectonic implications. *Journal of Jilin University (Earth Science Edition), 43*, 110–118. (in Chinese with English Abstract).

Peng, P. (2010). Reconstruction and interpretation of giant mafic dyke swarms: A case study of 1.78 Ga magmatism in the North China craton. In T. M. Kusky, M.-G. Zhai, & W. Xiao (Eds.), *The evolving continents: Understanding processes of continental growth* (Vol. 338, pp. 163–178). London: Geological Society of London, Special Publication.

Peng, P. (2015). Precambrian mafic dyke swarms in the North China Craton and their geological implications. *Science China Earth Sciences, 58*, 649–675.

Peng, P., Bleeker, W., Ernst, R. E., Söderlund, U., & McNicoll, V. (2011a). U-Pb baddeleyite ages, distribution and geochemistry of 925 Ma mafic dykes and 900 Ma sills in the North China craton: Evidence for a Neoproterozoic mantle plume. *Lithos, 127*, 210–221.

Peng, P., Liu, F., Zhai, M., & Guo, J. (2012). Age of the Miyun dyke swarm: Constraints on the maximum depositional age of the Changcheng system. *Chinese Science Bulletin, 57*, 105–110.

Peng, P., Zhai, M. G., Ernst, R. E., Guo, J. H., Liu, F., & Hu, B. (2008). A 1.78 Ga large igneous province in the North China craton: the Xiong'er Volcanic Province and the North China dyke swarm. *Lithos, 101*, 260–280.

Peng, P., Zhai, M. G., & Guo, J. H. (2006). 1.80–1.75 Ga mafic dyke swarms in the central North China craton: Implications for a plume-related break-up event. In E. Hanski, S. Mertanen, T. Ramö, & J. Vuollo (Eds.), *Dyke swarms—Time markers of crustal evolution* (pp. 99–112). London, UK: Taylor & Francis Group plc.

Peng, P., Zhai, M.-G., Guo, J.-H., Kusky, T., & Zhao, T.-P. (2007). Nature of mantle source contributions and crystal differentiation in the petrogenesis of the 1.78 Ga mafic dykes in the central North China craton. *Gondwana Research, 12*, 29–46.

Peng, P., Zhai, M., Li, Q., Wu, F., Hou, Q., Li, Z., et al. (2011b). Neoproterozoic (~900 Ma) Sariwon sills in North Korea: Geochronology, geochemistry and implications for the evolution of the south-eastern margin of the North China Craton. *Gondwana Research, 20*, 243–254.

Peng, R. M., Zhai, Y. S., Wang, J. P., Chen, X. F., Liu, Q., Lv, J. Y., et al. (2010). Discovery of Neoproterozoic acid volcanic rock in the western section of Langshan, Inner Mongolia, and its geological significance. *Chinese Science Bulletin, 55*, 2611–2620. (in Chinese).

Peng, T. P., Wilde, S. A., Fan, W. M., Peng, B. X., & Mao, Y. S. (2013). Mesoproterozoic high Fe–Ti mafic magmatismin western Shandong, North China Craton: Petrogenesis and implications for the final breakup of the Columbia supercontinent. *Precambrian Research, 235*, 190–207.

Piper, J. D. A., Zhang, J. S., Huang, B., & Roberts, A. P. (2011). Palaeomagnetism of Precambrian dyke swarms in the North China shield: The ~1.8 Ga LIP event and crustal consolidation in late Palaeoproterozoic times. *Journal of Asian Earth Sciences, 41*, 504–524.

Ramo, O. T., Haapala, I., Vaasjoki, M., Yu, J. H., & Fu, H. Q. (1995). The 1700 Ma Shachang complex, northeast China: Proterozoic rapakivi granite not associated with Paleoproterozoic orogenic crust. *Geology, 23*(9), 815–818.

Ren, F. G., Li, H. M., Yin, Y. J., Li, S. B., Ding, S. Y., & Chen, Z. H. (2000). The upper chronological limit of the Xiong'er Group's volcanic rock series, and its geological significance. *Progress in Precambrian Research, 23*(3), 140-146 (in Chinese with English abstract).

Ren, K. X., Yan, G. H., Cai, J. H., Mu, B. L., Wang, Y. B., & Chu, Z. Y. (2006). Chronology and geological implication of the Paleo-Mesoproterozoic alkaline-rich intrusions belt from the northern part in North China Craton. *Acta Petrologica Sinica, 22*(2), 377–386. (in Chinese with English abstract).

Ren, Y. C., Zhan, Y. C., & Zhang, Z. Q. (1994). Study on heat events of ore-forming Bayan Obo deposit. *Acta Geoscientia Sinica, 15*, 95–101. (in Chinese with English abstract).

Rioux, M., Bowring, S., Dudás, F., & Hanson, R. (2010). Characterizing the U-Pb systematics of baddeleyite through chemical abrasion: Application of multi-step digestion methods to baddeleyite geochronology. *Contributions to Mineralogy and Petrology, 160*, 777–801.

Rogers, J. J. W., & Santosh, M. (2002). Configuration of Columbia, a Mesoproterozoic supercontinent. *Gondwana Research, 5*, 5–22.

Rojas-Agramonte, Y., Kroner, A., Demoux, A., Xia, X., Wang, W., Donskaya, T., et al. (2011). Detrital and xenocrystic zircon ages from Neoproterozoic to Palaeozoic arc terranes of Mongolia: Significance for the origin of crustal fragments in the Central Asian Orogenic Belt. *Gondwana Research, 19*, 751–763.

Schmitt, A. K., Chamberlain, K. R., Swapp, S. M., & Harrison, T. M. (2010). In situ U-Pb dating of micro-baddeleyite by secondary ion mass spectrometry. *Chemical Geology, 269*, 386–395.

Schwab, D. L., Thorkelson, D. J., Mortensen, J. K., Creaser, R. A., & Grant Abbott, J. (2004). The Bear River dykes (1265–1269 Ma): Westward continuation of the Mackenzie dyke swarm into Yukon, Canada. *Precambrian Research, 133*, 175–186.

Svensen, H., Corfu, F., Polteau, S., Hammer, Ø., & Planke, S. (2012). Rapid magma emplacement in the Karoo Large Igneous Province. *Earth and Planetary Science Letters, 325–326*, 1–9.

Shi, R., Huang, B., Zhu, R., & Ren, S. (2004). Paleomagnetic study on the Early Triassic red beds from Jiaocheng, Shanxi Province—Local rotation and tectonic significance. *Science in China* (*Series D*) *Earth Sciences, 47*, 108–114.

Shi, Y. R., Liu, D. Y., Kröner, A., Jian, P., Miao, L. C., & Zhang, F. Q. (2012). Ca. 1318 Ma A-type granite on the northern margin of the North China Craton: Implications for intraplate extension of the Columbia supercontinent. *Lithos, 148*, 1–9.

Smith, M. P., Campbell, L. S., & Kynicky, J. (2015). A review of the genesis of the world class Bayan Obo Fe-REE-Nb deposits, Inner Mongolia, China. *Ore Geology Reviews, 64*, 459–476.

Söderlund, U., Hellström, F., & Kamo, S. E. (2008). Geochronology of high-pressure mafic granulite dykes in SW Sweden: Tracking the P-T-t path of metamorphism using Hf isotopes in zircon and baddeleyite. *Journal of Metamorphic Geology, 26*, 539–560.

Söderlund, U., Isachsen, C., Bylund, G., Heaman, L., Jonathan Patchett, P., Vervoort, J., et al. (2005). U-Pb baddeleyite ages and Hf, Nd isotope chemistry constraining repeated mafic magmatism in the Fennoscandian Shield from 1.6 to 0.9 Ga. *Contributions to Mineralogy and Petrology, 150*, 174–194.

Söderlund, U., Ibanez-Mejia, M., El Bahat, A., Ernst, R. E., Ikenne, M., Soulaimani, A., et al. (2013). Reply to Comment on "U-Pb baddeleyite ages and geochemistry of dolerite dykes in the Bas-Drâa Inlier of the Anti-Atlas of Morocco: Newly identified 1380 Ma event in the West African Craton" by André Michard and Dominique Gasquet. *Lithos, 174*, 101–108.

Song, B. (1992). Isotope geochronology, REE geochemistry and petrogenesis of the Miyun rapakivi granites. *Earth Science Research–Bulletin of the Institute of Geology, Chinese Academy of Geological Sciences,* (No. 25), 137–157 (Beijing: Geological Publishing House; in Chinese with English abstract).

Su, W., Zhang, S., Huff, W. D., Li, H., Ettensohn, F. R., Chen, X., et al. (2008). SHRIMP U-Pb ages of K-bentonite beds in the Xiamaling formation: Implications for revised subdivision of the Meso- to Neoproterozoic history of the North China Craton. *Gondwana Research, 14*, 543–553.

Su, W., Li, H., Huff, W. D., Ettensohn, F. R., Zhang, S., Zhou, H., et al. (2010). SHRIMP U-Pb dating for a K-bentonite bed in the Tieling formation, North China. *Chinese Science Bulletin, 55*(29), 3312–3323.

Su, W., Li, H., Xu, L., Jia, S., Geng, J., Zhou, H., et al. (2012). Luoyu and Ruyang Group at the south margin of the North China Craton (NCC) should belong in the Mesoproterozoic Changchengian system: Direct constraints from the LA-ICP-MS U-Pb age of the tuffite in the Luoyukou Formation, Ruzhou, Henan, China. *Geological Survey and Research, 35*, 96–108. (in Chinese with English abstract).

Sun, Z., Yang, Z., Ma, X., & Zhao, Y. (1998). Paleomagnetic result of the Lower-Cretaceous from Luanping basin, Hebei Province and its tectonic implications. *Science in China* (*Series D*) *Earth Sciences, 41*(Supp.), 43–50.

Sun, J., Du, W., Wang, D., Li, J., Xu, G., & Han, Y. (2009). Geological characteristic and genesis of the Heishan V-Ti magnetite deposit in Damiao, Chengde Hebei Province. *Acta Geologica Sinica, 83*, 1344–1363. (in Chinese with English abstract).

Sun, J., Zhu, X., Chen, Y., & Fang, N. (2013). Iron isotopic constraints on the genesis of Bayan Obo ore deposit, Inner Mongolia, China. *Precambrian Research, 235*, 88–106.

Sweet, I. P., Brakel, A. T., Rawlings, D. J., Haines, P. W., Plum, K. A., & Wygralak, A. S. (1999). *Mount Marumba, Northern Territory, 1:250,000 geological map series explanatory notes, SD 53-6* (pp. 1–84). Darwin: Australian Geological Survey Organization, Canberra and Northern Territory Geological Survey.

Teixeira, W., Hamilton, M. A., Lima, G. A., Ruiz, A. S., Matos, R., & Ernst, R. E. (2015). Precise ID-TIMS U-Pb baddeleyite ages (1110–1112 Ma) for the Rincón del Tigre-Huanchaca large igneous province (LIP) of the Amazonian Craton: Implications for the Rodinia supercontinent. *Precambrian Research, 265*, 273–285.

Teng, X., & Santosh, M. (2015). A long-lived magma chamber in the Paleoproterozoic North China Craton: Evidence from the Damiao gabbro-anorthosite suite. *Precambrian Research, 256*, 79–101.

Tian, H., Zhang, J., Li, H., Su, W., Zhou, H., Yang, L., et al. (2015). Zircon LA-MC-ICPMS U-Pb dating of tuff from Mesoproterozoic Gaoyuzhuang formation in Jixian County of North China and its geological significance. *Acta Geoscientica Sinica, 36*, 647–658. (in Chinese with English abstract).

Walker, J. D., & Geissman, J. W. (2009). 2009 GSA geologic time scale. *GSA Today, 19*, 60. doi:10.1130/2009.CTS004R2C.

Wang, H. C., Xiang, Z. Q., Zhao, F. Q., Li, H. M., Yuan, G. B., & Chu, H. (2012a). The alkaline plutons in eastern part of Guyang County, Inner Mongolia: Geochronology, petrogenesis and tectonic implications. *Acta Petrologica Sinica, 28*(9), 2843–2854. (in Chinese with English abstract).

Wang, J., Tatsumoto, M., Li, X., Premo, W. R., & Chao, E. C. T. (1994). A precise ^{232}Th-^{208}Pb chronology of fine grained monazite: Age of the Bayan Obo REE-Fe-Nb ore deposit, China. *Geochimica et Cosmochimica Acta, 58*, 3155–3169.

Wang, Q. H., Yang, D. B., & Xu, W. L. (2012b). Neoproterozoic basic magmatism in the southeast margin of North China Craton: Evidence from whole-rock geochemistry, U-Pb and Hf isotopic study of zircons from diabase swarms in the Xuzhou-Huaibei area of China. *Science China Earth Sciences, 55*, 1461–1479.

Wang, Q. H., Yang, H., Yang, D. B., & Xu, W. L. (2014a). Mid-Mesoproterozoic (~1.32 Ga) diabase swarms from the western Liaoning region in the northern margin of the North China Craton: Baddeleyite Pb–Pb geochronology, geochemistry and implications for the final breakup of the Columbia supercontinent. *Precambrian Research, 254*, 114–128.

Wang, S. S., Sang, H. Q., Qiu, J., Chen, M. E. & Li, M. R. (1995). The metamorphic age of pre-Changcheng System in Beijing-Tianjin area and a discussion about the lower limit age of Changcheng System. *Scientia Geologica Sinica, 30*, 348–354 (in Chinese with English abstract).

Wang, T., Zheng, Y. D., Gehrels, G. E., & Mu, Z. G. (2001). Geochronological evidence for existence of South Mongolian microcontinent—A zircon U-Pb age of grantoid gneisses from the Yagan-Onch Hayrhan metamorphic core complex. *Chinese Science Bulletin, 46*, 2005–2008.

Wang, W., Liu, S. W., Bai, X., Li, Q. G., Yang, P. T., Zhao, Y., et al. (2013a). Geochemistry and zircon U-Pb–Hf isotopes of the late Paleoproterozoic Jianping diorite–monzonite–syenite suite of the North China Craton: Implications for petrogenesis and geodynamic setting. *Lithos, 162–163*, 175–194.

Wang, W., Liu, S. W., Santosh, M., Deng, Z. B., Guo, B. R., Zhao, Y., et al. (2015a). Late Paleoproterozoic geodynamics of the North China Craton: Geochemical and zircon U-Pb-Hf records from a volcanic suite in the Yanliao rift. *Gondwana Research, 27*, 300–325.

Wang, W., Liu, S. W., Santosh, M., Zhang, L. F., Bai, X., Zhao, Y., et al. (2015b). 1.23 Ga mafic dykes in the North China Craton reconstruct the Columbia supercontinent. *Gondwana Research, 27*, 1407–1418.

Wang, X., Hao, Z., Li, Z., Xiao, G., & Zhang, T. (2002). A typical alkaline rock-carbonatite complex in Bayan Obo, Inner Mongolia. *Acta Geologica Sinica, 76*, 501–524. (in Chinese with English abstract).

Wang, X. L., Jiang, S. Y., Dai, B. Z., Griffin, W. L., Dai, M. N., & Yang, Y. H. (2011). Age, geochemistry and tectonic setting of the Neoproterozoic (ca 830 Ma) gabbros on the southern margin of the North China Craton. *Precambrian Research, 190*, 35–47.

Wang, X. L., Jiang, S. Y., Dai, B. Z., & Kern, J. (2013b). Lithospheric thinning and reworking of Late Archean juvenile crust on the southern margin of the North China Craton: Evidence from the Longwangzhuang Paleoproterozoic A-type granites and their surrounding Cretaceous adakite-like granites. *Geological Journal, 48*(5), 498–515.

Wang, Y., Zhao, G., Fan, W., Peng, T., Sun, L., & Xia, X. (2007). LA-ICP-MS U-Pbzircon geochronology and geochemistry of Paleoproterozoic mafic dykesfrom western Shandong Province: Implications for back-arc basin magmatism in the Eastern Block, North China Craton. *Precambrian Research, 154*, 107–124.

Wang, Z. J., Huang, Z. G., Yao, J. X., & Ma, X. L. (2014b). Characteristics and main progress of "the stratigraphic chart of China and directions". *Acta Geoscientica Sinica, 35*, 271–276. (in Chinese with English abstract).

Whalen, L., Gazel, E., Vidito, C., Puffer, J., Bizimis, M., Henika, W., et al. (2015). Supercontinental inheritance and its influence on supercontinental breakup: The Central Atlantic Magmatic Province and the break up of Pangea. *Geochemistry Geophysics Geosystem, 16*. doi:10.1002/2015GC005885

Wilson, M. (1997). Thermal evolution of the central Atlantic passive margins: Continental break-up above a Mesozoic super-plume. *Journal of the Geological Society London, 154*, 491–495.

Wingate, M. T. D., Campbell, I. H., Compston, W., & Gibson, G. M. (1998). Ion microprobe U-Pb ages for Neoproterozoic basaltic magmatism in south-central Australia and implications for the breakup of Rodinia. *Precambrian Research, 87*, 135–159.

Wingate, M. T. D., & Compston, W. (2000). Crystal orientation effects during ion microprobe U-Pb analysis of baddeleyite. *Chemical Geology, 168*, 75–97.

Wingate, M. T. D. (2001). SHRIMP baddeleyite and zircon ages for an Umkondo dolerite sill, Nyanga Mountains, Eastern Zimbabwe. *South African Journal of Geology, 104*, 13–22.

Wu, C. (2008). Bayan Obo controversy: Carbonatites versus iron oxide-Cu-Au-(REE-U). *Resource Geology, 58*, 348–354.

Wu, H. C., Zhang, S., Li, Z. X., Li, H., & Dong, J. (2005). New paleomagnetic results from the Yangzhuang Formation of the Jixian System, North China, and tectonic implications. *Chinese Science Bulletin, 50*, 1483–1489.

Wu, Y. B., & Zheng, Y. F. (2004). Genesis of zircon and its constraints on interpretation of U-Pb age. *Chinese Science Bulletin, 49*, 1554–1569.

Xiang, Z., Li, H., Lu, S., Zhou, H., Li, H., Wang, H., et al. (2012). Emplacement age of the gabbro-diabase dike in the Hongmen scenic region of Mount Tai, Shandong Province, North China: Baddeleyite U-Pb precise dating. *Acta Petrologica Sinica, 28*, 2831–2842. (in Chinese with English abstract).

Xie, G. H. (2005). *Petrology and geochemistry of the Damiao anorthosite and the Miyun rapakivi granite* (pp. 1–195). Beijing: Science Press (in Chinese).

Xu, H., Yang, Z., Peng, P., Meert, J. G., & Zhu, R. (2014). Paleo-position of the North China craton within the supercontinent Columbia: Constraints from new paleomagnetic results. *Precambrian Research, 255*, 276–293.

Yang, J. H., Sun, J. F., Chen, F. K., Wilde, S. A., & Wu, F. Y. (2007). Sources and petrogenesis of Late Triassic dolerite dikes in the Liaodong Peninsula: Implications for post-collisional lithosphere thinning of the eastern North China Craton. *Journal of Petrology, 48*, 1973–1997.

Yang, J. H., Wu, F. Y., Liu, X. M., & Xie, L. W. (2005). Zircon U-Pb ages and Hf isotopes and their geological significance of the Miyun rapakivi granites from Beijing, China. *Acta Petrologica Sinica, 21*(6), 1633–1644. (in Chinese with English abstract).

Yang, K. F., Fan, H. R., Santosh, M., Hu, F. F., & Wang, K. Y. (2011). Mesoproterozoic mafic and carbonatitic dykes from the northern-margin of the North China Craton: Implications for the final breakup of Columbia supercontinent. *Tectonophysics, 498*, 1–10.

Yang, Q. Y., Santosh, M., Rajesh, H. M. & Tsunogae, T. (2014). Late Paleoproterozoic charnockite suite within post-collisional setting from the North China Craton: Petrology, geochemistry, zircon U–Pb geochronology and Lu–Hf isotopes. *Lithos, 208–209*, 34–52.

Yang, X. M., Yang, X. Y., Zheng, Y. F., & Le Bas, M. J. (2003). A rare earth element-rich carbonatite dyke at Bayan Obo, Inner Mongolia, North China. *Mineralogy and Petrology, 78*, 93–110.

Yang, X. Y., Sun, W. D., Zhang, Y. X., & Zheng, Y. F. (2009). Geochemical constraints on the genesis of the Bayan Obo Fe-Nb-REE deposit in Inner Mongolia, China. *Geochimica et Cosmochimica Acta, 73*, 1417–1435.

Ye, D. H., Yang, Q. W., & Xing, J. R. (1996). *The Damiao anorthosite and vanadic-titano magnetite and apatite deposits associated with the anorthosite in Chengde, Hebei. Field trip guide T216* (pp. T216.1–T216.15). In 30th International Geological Congress, Beijing, China.

Yu, J., Fu, H., Zhang, F., & Wan, F. (1994). Petrogenesis of potassic alkaline volcanics associated with rapakivi granites in the Proterozoic rift of Beijing, China. *Mineralogy and Petrology, 50*, 83–96.

Yu, J. H., Fu, H. Q., Zhang, F. L., Wan, F. X., Haapala, I., Ramo, O. T., et al. (1996). *Anorogenic rapakivi granite and related rocks in the northern part of North China craton* (pp. 1–189). Beijing: China Science and Technology Press (in Chinese with English abstract).

Yuan, W., & Yang, Z. Y. (2015a). The Alashan Terrane was not part of North China by the Late Devonian: Evidence from detrital zircon U-Pb geochronology and Hf isotopes. *Gondwana Research, 27*, 1270–1282.

Yuan, W., & Yang, Z. Y. (2015b). The Alashan Terrane did not amalgamate with North China block by the Late Permian: Evidence from Carboniferous and Permian paleomagnetic results. *Journal of Asian Earth Sciences, 104*, 145–159.

Yuan, Z., Bai, G., Wu, C., Zhang, Z., & Ye, X. (1992). Geological features and genesis of the Bayan Obo REE ore deposit, Inner Mongolia, China. *Applied Geochemistry, 7*, 429–442.

Zhai, M. G., Bian, A. G., & Zhao, T. P. (2000). The amalgamation of the supercontinent of North China craton at the end of the Neoarchaean, and its break-up during the late Palaeoproterozoic and Mesoproterozoic. *Science in China* (*Series D*), *43*(Supp.), 219–232.

Zhai, M. G., Hu, B., Peng, P., & Zhao, T. P. (2014). Meso-Neoproterozoic magmatic events and multi-stage rifting in the NCC. *Earth Science Frontiers, 21*(1), 100–119. (in Chinese with English abstract).

Zhai, M. G., Hu, B., Zhao, T. P., Peng, P., & Meng, Q. R. (2015). Late Paleoproterozoic-Neoproterozoic multi-rifting events in the North China Craton and their geological significance: A study advance and review. *Tectonophysics, 662*, 153–166.

Zhang, J., Li, J. Y., Liu, J. F., Qu, J. F., & Feng, Q. W. (2012a). The relationship between the Alxa Block and the North China Plate during the Early Paleozoic: New information from the Middle Ordovician detrial zircon ages in the eastern Alxa Block. *Acta Petrologica Sinica, 28*, 2912–2934. (in Chinese with English abstract).

Zhang, J., Li, J. Y., Xiao, W. X., Wang, Y. N., & Qi, W. H. (2013a). Kinematics and geochronology of multistage ductile deformation along the eastern Alxa block, NW China: New constraints on the relationship between the North China Plate and the Alxa block. *Journal of Structural Geology, 57*, 38–57.

Zhang, J., Tian, H., Li, H. K., Su, W. B., Zhou, H. Y., Xiang, Z. Q., et al. (2015). Age, geochemistry and zircon Hf isotope of the alkaline basaltic rocks in the middle section of the Yan-Liao aulacogen along the northern margin of the North China Craton: New evidence for the breakup of the Columbia Supercontinent. *Acta Petrologica Sinica, 31* (10), 3129–3146. (in Chinese with English abstract).

Zhang, S., Li, Z. X., Evans, D. A. D., Wu, H., Li, H., & Dong, J. (2012b). Pre-Rodinia supercontinent Nuna shaping up: A global synthesis with new paleomagnetic results from North China. *Earth and Planetary Science Letters, 353–354*, 145–155.

Zhang, S. H., Liu, S. W., Zhao, Y., Yang, J. H., Song, B., & Liu, X. M. (2007). The 1.75–1.68 Ga anorthosite-mangerite-alkali granitoid-rapakivi granite suite from the northern North China Craton: Magmatism related to a Paleoproterozoic orogen. *Precambrian Research, 155*(3–4), 287–312.

Zhang, S. H., Zhao, Y., Yang, Z. Y., He, Z. F., & Wu, H. (2009). The 1.35 Ga diabase sills from the northern North China Craton: Implications for breakup of the Columbia (Nuna) supercontinent. *Earth and Planetary Science Letters, 288*, 588–600.

Zhang, S. H., Zhao, Y., & Santosh, M. (2012c). Mid-Mesoproterozoic bimodal magmatic rocks in the northern North China Craton: Implications for magmatism related to breakup of the Columbia supercontinent. *Precambrian Research, 222–223*, 339–367.

Zhang, S. H., Zhao, Y., Ye, H., Hu, J. M., & Wu, F. (2013b). New constraints on ages of the Chuanlinggou and Tuanshanzi Formations of the Changcheng System in the Yan-Liao area in the northern North China Craton. *Acta Petrologica Sinica, 29*(7), 2481–2490. (in Chinese with English abstract).

Zhang, S. H., Zhao, Y., Li, X. H., Ernst, R. E., & Yang, Z. Y. (2016a). *The 1.32 Ga Yanliao large igneous province in the North China Craton: Implications for reconstruction of the Columbia (Nuna) supercontinent*. Geology (in revision).

Zhang, S. H., Zhao, Y., Ye, H., & Hu, G. (2016b). Early Neoproterozoic emplacement of the diabase sill swarms in the Liaodong Peninsula and pre-magmatic uplift of the southeastern North China Craton. *Precambrian Research, 272*, 203–225.

Zhang, Y. X., Jiang, S. Q., Zhang, Q. L., Lai, X. D., Peng, Y., & Yang, X. Y. (2008). A discussion on forming time of the Bayan Obo Group and ore-forming time of the Bayan Obo giant REE-Nb-Fe deposit, Inner Mongolia. *Geology in China, 35*, 1129–1137. (in Chinese with English abstract).

Zhang, Z. C., Hou, T., Santosh, M., Li, H. M., Li, J. W., Zhang, Z. H., et al. (2014). Spatio-temporal distribution and tectonic settings of the major iron deposits in China: An overview. *Ore Geology Review, 57*, 247–263.

Zhang, Z. Q., Tang, S. H., Wang, J. H., Yuan, Z. X., & Bai, G. (1994). New data for ore-forming age of the Bayan Obo REE ore deposit. *Acta Geoscientia Sinica, 15*, 85–94. (in Chinese with English abstract).

Zhang, Z. Q., Tang, S. H., Yuan, Z. X., Bai, G., & Wang, J. H. (2001). The Sm-Nd and Rb-Sr isotopic systems of the dolomite in the Bayan Obo ore deposit, Inner Mongolia, China. *Acta Petrologica Sinica, 17*, 637–642. (in Chinese with English abstract).

Zhao, D. X. (1994). Microstructures of ferruginous oolite and their genetic characteristics in the Xuanlong iron deposit, Hebei Province. *Scientia Geologica Sinica, 29*(1), 71–77. (in Chinese with English abstract).

Zhao, G. C., Cawood, P. A., Wilde, S. A., & Sun, M. (2002). A review of the global 2.1–1.8 Ga orogens: Implications for a pre-Rodinian supercontinent. *Earth-Science Reviews, 59*, 125–162.

Zhao, G. C., Li, S. Z., Sun, M., & Wilde, S. A. (2011). Assembly, accretion, and break-up of the Palaeo-Mesoproterozoic Columbia supercontinent: Record in the North China Craton revisited. *International Geology Review, 53*, 1331–1356.

Zhao, G. C., Sun, M., Wilde, S. A., & Li, S. (2004a). A Paleo-Mesoproterozoic supercontinent: Assembly, growth and breakup. *Earth-Science Reviews, 67*, 91–123.

Zhao, G. C., Sun, M., Wilde, S. A., & Li, S. Z. (2005). Late Archean to Paleoproterozoic evolution of the North China Craton: Key issues revisited. *Precambrian Research, 136*, 177–202.

Zhao, G. C., & Zhai, M. G. (2013). Lithotectonic elements of Precambrian basement in the North China Craton: Review and tectonic implications. *Gondwana Research, 23*, 1207–1240.

Zhao, T. P., Chen, F. K., Zhai, M. G., & Xia, B. (2004b). Single zircon U-Pb ages and their geological significance of the Damiao

anorthosite complex, Heibei Province, China. *Acta Petrologica Sinica, 20*(3), 685–690. (in Chinese with English abstract).

Zhao, T. P., Chen, W., & Zhou, M. F. (2009). Geochemical and Nd-Hf isotopic constraints on the origin of the ~1.74-Ga Damiao anorthosite complex. North China Craton. *Lithos, 113*, 673–690.

Zhao, T. P., Deng, X. Q., Hu, G. H., Zhou, Y. Y., Peng, P., & Zhai, M. G. (2015). The Paleoproterozoic-Mesoproterozoic boundary of the North China Craton and the related geological issues: A review. *Acta Petrologica Sinica, 31*(6), 1495–1508. (in Chinese with English abstract).

Zhao, Y., Song, B., & Zhang, S. H. (2006). The Central Mongolian microcontinent: Its Yangtze affinity and tectonic implications. In B. M. Jahn & S. L. Chung (Eds.), *Abstract volume of symposium on continental growth and orogeny in Asia* (pp. 135–136), Taipei, March 19–26.

Zhu, R. X., Chen, L., Wu, F. Y., & Liu, J. L. (2011). Timing, scale and mechanism of the destruction of the North China Craton. *Science China Earth Science, 54*, 789–797.

Zhu, R. X., Shao, J. A., Pan, Y. X., Shi, R. P., Shi, G. H., & Li, D. M. (2002). Paleomagnetic data from Early Cretaceous volcanic rocks of West Liaoning: Evidence for intracontinental rotation. *Chinese Science Bulletin, 47*, 1832–1837.

Zhu, X.-K., Sun, J., & Pan, C. (2015). Sm–Nd isotopic constraints on rare-earth mineralization in the Bayan Obo ore deposit, Inner Mongolia, China. *Ore Geology Reviews, 64*, 543–553.

Meso-Neoproterozoic Stratigraphic and Tectonic Framework of the North China Craton

15

Jianmin Hu, Zhenhong Li, Wangbin Gong, Guohui Hu, and Xiaopeng Dong

Abstract

The Meso-Neoproterozoic sedimentary strata of the North China Craton (NCC) occur mainly in the Xiong'er Rift in the southern marginal part of the craton, the Yanliao Rift in the central region, and the Zhaertai–Bayan Obo Rift on the northern margin. In recent years, high-precision zircon U-Pb dating ages from several crucial stratums in Yanliao rift system provided a strong foundation for reconstruction of Meso-Neoproterozoic stratigraphic framework in NCC. These revolutionary progresses require new recognitions for tectonic evolution of NCC in Meso-Neoproterozoic. Among these progresses, the most important breakthrough is that Neoproterozoic Xiamaling formation in former research is redivided into Mesoproterozoic stratums and redefined as building system. In the latest standard scheme of China stratigraphic chart, Changcheng system, Jixian system, building system, Qingbaikou system, Nanhua system, and Sinian system are, respectively, limited into 1.8–1.6 Ga, 1.6–1.4 Ga, 1.4–1.0 Ga, 1.0–0.78 Ga, 780–635 Ma, 635–541 Ma. Under the new stratigraphic framework, the Mesoproterozoic Changcheng System consists of clastic rocks of the tidal flat–littoral facies, and the Jixian System contains carbonate rocks of the neritic facies in the lower section and clastic rocks of the tidal flat–littoral facies in the upper section. Therefore, the sedimentary sequences of these systems record a complete sedimentary sequence from transgression to regression. The Neoproterozoic Qinbaikou and Nanhua systems are transgressive sequences consisting of clastic rocks of the tidal flat–littoral facies in lower sections and carbonate rocks of the neritic facies in upper sections. These changes in lithology indicate increasing water depth over time. The Sinian System is composed of tillite, which occurs along the western and southern margins of the NCC and in the Longshoushan area, on the southern margin of the Alxa Block. Based on the sedimentary characteristics of the Meso-Neoproterozoic strata, as well as multiple magmatic events, we identify five phases in the evolution of the NCC during this period: (1) continental rifting during the early Mesoproterozoic, (2) a passive continental margin during the middle Mesoproterozoic, (3) an active continental margin during the late Mesoproterozoic, (4) extrusion and uplift, and (5) continental rifting at the end of the

J. Hu (✉) · Z. Li · W. Gong · G. Hu · X. Dong
Institute of Geomechanics, Chinese Academy of Geological Sciences, Beijing, China
e-mail: jianminhu@vip.sina.com

J. Hu · Z. Li · W. Gong
Key Laboratory of Paleomagnetism and Tectonic Reconstruction of Ministry of Land and Resources, Beijing, China

M. Zhai et al. (eds.), *Main Tectonic Events and Metallogeny of the North China Craton*, Springer Geology, DOI 10.1007/978-981-10-1064-4_15

Mesoproterozoic and beginning of the Neoproterozoic. The first two stages likely record the final break-up of the Columbia supercontinent, whereas stages three to five may have been linked to the assembly and break-up of the Rodinia supercontinent.

Keywords
North China Craton • Meso-Neoproterozoic • Stratigraphic framework • Lithofacies paleogeography • Tectonic evolution

15.1 Introduction

After the final amalgamation of the North China Craton (NCC) at ~1.8 Ga, a continental rift started to develop during the Meso-to Neoproterozoic. Multi-stage tectono-magmatic events (Zhai et al. 2014) recorded the evolution of the rift, including a 1.78 Ga Large Igneous Province (LIP; Wang et al. 2004; Peng et al. 2007, 2008), 1.72–1.62 Ga anorogenic magmatism (Zhao et al. 2004a, b, 2009; Zhang et al. 2007b), 1.35–1.32 Ga diabase sill swarms (Sun et al. 2010; Li et al. 2009; Zhang et al. 2009, 2012), and 0.9 Ga mafic dike swarms in the Dashigou area (Liu et al. 2005; Peng et al. 2011; Wang et al. 2011a, b). All of these magmatic events have been linked to the development and break-up of supercontinents (Hoffman 1991; Li 1989, 1991; Xu 2001; Dalziel 1991, 1997; Karlstrom et al. 1997; Li et al. 2002, 2003; Hoffmann et al. 2004; Rogers and Santosh 2004; Zhang et al. 2005; Lu et al. 2004, 2005, 2008; Rino et al. 2008; Hu et al. 2013). The first three events have been suggested to relate to the break-up of the Columbia supercontinent (Zhao et al. 2002a; Li et al. 2007), and the last event has been linked to the break-up of Rodinia supercontinent (Peng et al. 2010, 2011; Peng 2010). However, no geological evidence, such as volcanic rocks associated with the amalgamation of Rodinia, has been documented in the NCC. Therefore, the following issues remain unresolved: (1) whether the NCC was involved in the amalgamation of Rodinia; and (2) the tectonic setting of the NCC during the period between the break-up of Columbia and the formation of Rodinia.

There are three Meso-Neoproterozoic rift systems in the NCC: the Zhaertai–Bayan Obo Rift in the north, the Yanliao Rift in the east, and the Xiong'er Rift in the south. Thick clastic, volcanic clastic, and carbonate rocks developed in these rifts (Fig. 15.1). The Zhaertai–Bayan Obo Rift comprises the Mesoproterozoic Zhaertai, Bayan Obo, and Huade groups, and the Neoproterozoic Langshan Group. The Yanliao and Xiong'er Rifts consist of the Mesoproterozoic Changcheng, Jixian, and Qingbaikou systems. In addition, there is a remnant of the Neoproterozoic Nanhua System exposed on the eastern margin of the NCC. The Neoproterozoic Sinian tillite occurs on the western and northern margins of the NCC and at Longshoushan, along the southwestern margin of the Alxa Block. These strata record important information on continent evolution during the Meso-Neoproterozoic. The ages of these Meso-Neoproterozoic strata have recently been refined based on abundant high-precision zircon U–Pb ages for mafic dikes and volcanic interlayers in the sedimentary strata (Liu et al. 2005; Gao et al. 2008a, b, 2011; Li et al. 2010, 2011; Sun et al. 2010; Su et al. 2012; Zhang et al. 2009, 2012; Wang et al. 2011a, b; Hu et al. 2014). In this study we define new stratigraphic age with the latest research results, reconstruct the lithofacies paleogeography, discuss the relationship between the NCC and the processes of amalgamation and break-up of supercontinents, and propose a model of multi-stage extension for the Meso-Neoproterozoic NCC.

15.2 Regional Geological Background

The NCC is one of the oldest cratons in the world (Liu et al. 1992; Song et al. 1996; Gao et al. 2005; Shen et al. 2005; Wan et al. 2005; Diwu et al. 2008; Chen et al. 2009; Geng 2009) and it records nearly all the important tectonic events during the initial stages of crust development in this region (Wan et al. 2000; Wu et al. 2008a, b; Zhai 2010).

The NCC is composed of several microcontinents, such as the Alxa terrane, the Jining terrane, the Fuping terrane, the Qianhuai terrane, and the Xuchang (or Jiaoliao) terrane (Zhai 2001; Zhai et al. 2005; Geng et al. 2006; Wan et al. 2009). The NCC is divided into the Western Block and the Eastern Block, separated by the Central Orogenic Belt (Zhao et al. 2000, 2005; Guo et al. 2001, 2005; Liu et al. 2002, 2005; Wilde et al. 2002; Kusky and Li 2003; Wang et al. 2004; Li and Kusky 2007; Trap et al. 2007). However, there is still no agreement on the timing of collision of the two blocks. The proposed amalgamation period for the NCC includes a 2.5 Ga crust-building event (Kusky and Li 2003; Polat et al. 2005; Li and Kusky 2007), a 1.85 Ga collision (Guo et al. 2001, 2005; Zhao et al. 2005), and collisions at 2.1 and 1.85 Ga (Trap et al. 2007, 2009).

From the late Paleoproterozoic to the Paleozoic, thick sedimentary sequences were deposited in the NCC with

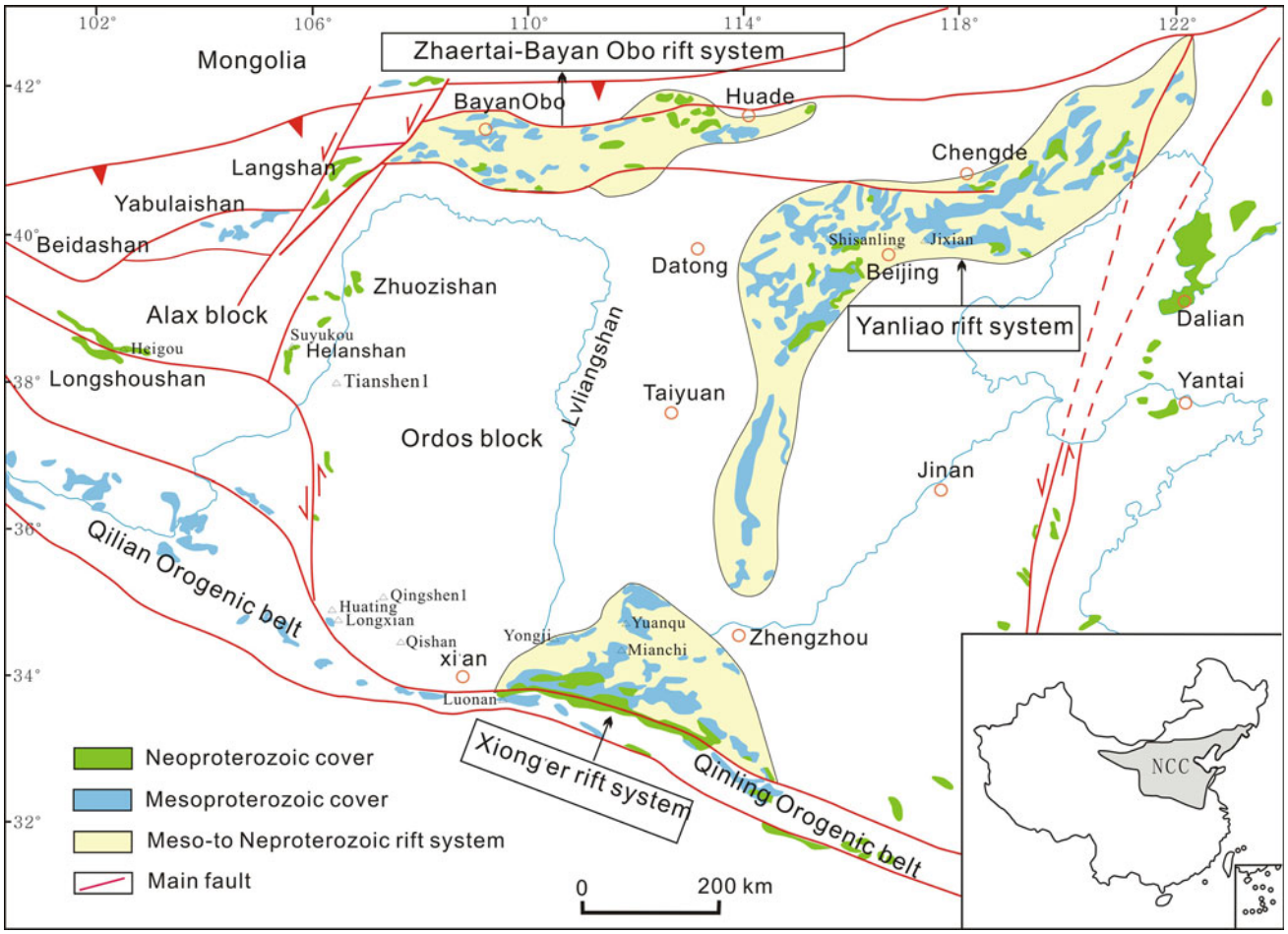

Fig. 15.1 Distribution of Meso-Neoproterozoic strata in the NCC (modified after Hu et al. 2014)

limited magmatism (Zhao, 1993; Lu et al. 2002, 2008; Zhai and Peng 2007; Zhai 2010). Only the southern rim of the NCC was modified by tectonic activity in the Qinling Orogenic Belt, and the northern rim of the NCC was modified by tectonic activity in the Central Asian Orogenic Belt (CAOB; Swisher et al. 2001; Cope, 2003; Gao et al. 2004; Niu et al. 2004; Zhao et al. 2004a, b; Liu et al. 2006a, b; Li et al. 2014a, b). The break-up of the NCC occurred in the Mesozoic when the tectonic stress in this region shifted from compression to extension and caused large-scale lithospheric thinning. Large-scale magmatic events and intense deformation occurred at the eastern margin of the NCC in the Late Cretaceous. The peak of magmatism was at 132–120 Ma (Wu et al. 2005, 2008; Zhu and Zheng 2009; Zhu et al. 2012). In the Cenozoic, the tectonic features on the eastern margin of the NCC were controlled by activity in the Circum-Pacific tectonic domain (CPD; Li et al. 2015).

15.3 Meso-Neoproterozoic Stratigraphy of the NCC

The Meso-Neoproterozoic strata of the NCC are distributed mainly in the Xiong'er Rift, the Yanliao Rift, the Zhaertai–Bayan Obo Rift, and the central–southern part of the Ordos Basin (Fig. 15.1). In addition, localized exposures of Meso-Neoproterozoic strata are documented at Lang Shan, Bayanxibie Shan, and Longshou Shan in the Alxa Block; in the Liaodong and Penglai peninsulas of Shandong Province, Southwest Shandong; and in the Xuhuai area.

15.3.1 Yanliao Rift

The Yanliao Rift is located in the Yanshan–West Liaoning area, in the north-central part of the NCC (Fig. 15.2). The

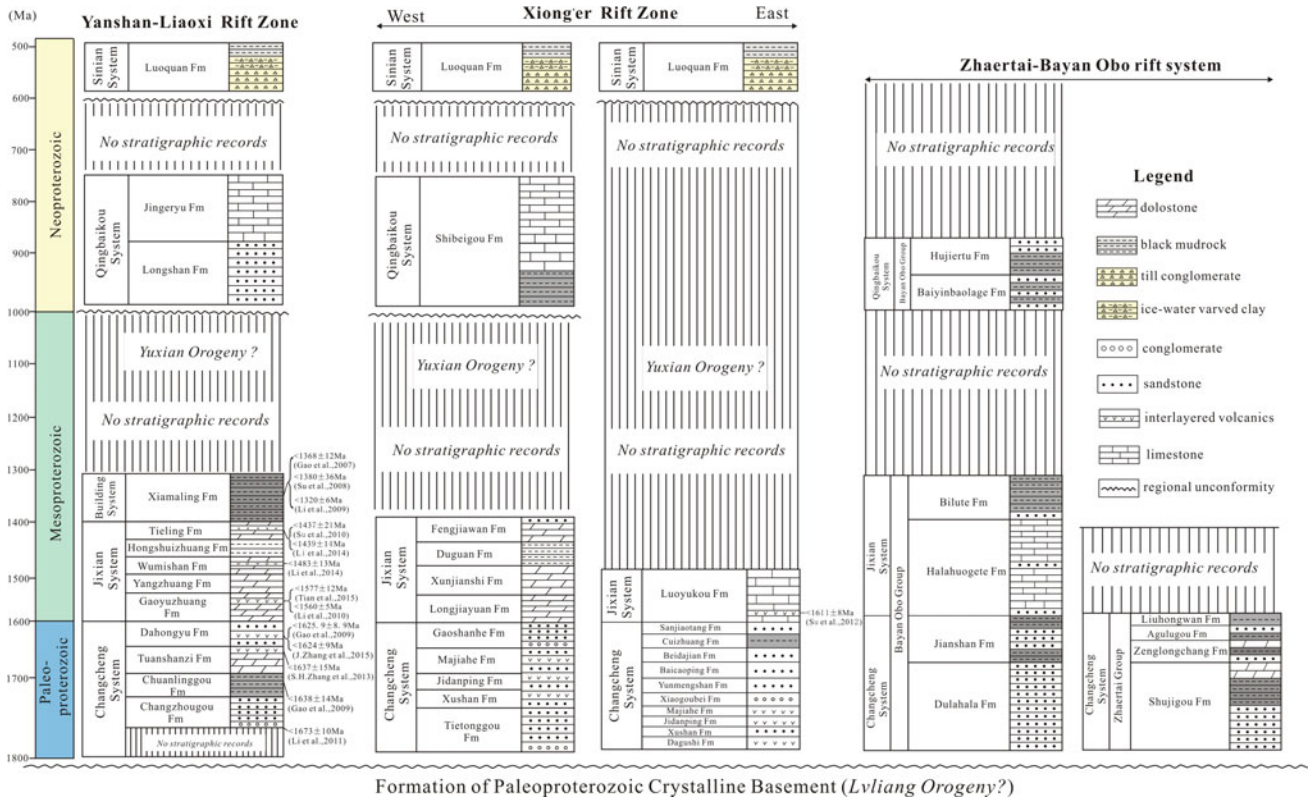

Fig. 15.2 Stratigraphy and correlation of Meso-Neoproterozoic strata in the Yanliao, Xiong'er, and Zhaertai–Bayan Obo rifts, North China Craton

thickest Meso-Neoproterozoic strata (~9000 m thick) are exposed in the Jixian area of Hebei Province. Using Jixian as a central reference point, the remnant Meso-Neoproterozoic strata pinch out toward the east from Huanghua to Qinhuangdao, toward the west from Datong to Yangquan, and toward the south to Shijiazhuang. In recent years, high-precision zircon U-Pb dating ages from several crucial stratums in Yanliao rift system provided a strong foundation for reconstruction of Meso-Neoproterozoic stratigraphic framework in NCC. The most revolutionary progress is the discovery of K-bentonites with 1368 ± 12 Ma and 1380 ± 16 Ma zircon U-Pb age and basic sill with 1320 ± 6 Ma zircon and baddeleyite U-Pb dating, and it provide strong foundation for redividing former Neoproterozoic Xiamaling formation into Mesoproterozoic (Gao et al. 2008a, b; Su et al. 2008, Sun et al. 2010; Li et al. 2009; Zhang et al. 2012). The 1673 ± 10 Ma granite-porphyry dykes overlied unconformably by pebbly sandstone of Changzhougou formation in Miyun area provide an accurate age limitation for the lower boundary of Changcheng system in Yanshan area (Li et al. 2011). Besides that, some volcanic interlayers play a vital role in stratum age determination, such as 1625 ± 8.9 Ma potassium-rich trachyte in Dahongyu formation, 1559 ± 12 Ma tuff in Gaoyuzhuang formation, 1437 ± 61 Ma tuff in Tieling formation.

Under the new stratigraphic framework, the exposed strata include Mesoproterozoic Changcheng System, Jixian System, Unnamed System, and Neoproterozoic Qingbaikou System. The Changcheng System has previously been separated into four formations (from bottom to top): the Changzhougou, Chuanlinggou, Tuanshanzi, and Dahongyu formations. The Changzhougou Formation is composed of off-white quartz sandstone and glauconite- and hematite-bearing sandstone. The Chuanlinggou Formation is composed of black to green shale and siltstone, along with thin quartz sandstone and grayish-yellow stromatolite reef-bearing dolomite layers. This formation is intruded by 1638 ± 14 Ma diabase (SHRIMP U–Pb zircon age; Gao et al. 2009). The Tuanshanzi Formation consists of thickly bedded to massive carbonate rocks. The Dahongyu Formation is composed of volcanic and sedimentary rocks, including quartz sandstone, arkose quartzite, conglomerate, dolomite, stromatolite-bearing dolomite, silexite, alkali trachyte, and alkali tuff. The Dahongyu Formation is only exposed in the Jixian, Pinggu, and Miyun areas. Dahongyu volcanic breccias and agglomerates dated at 1625 ± 8.9 Ma

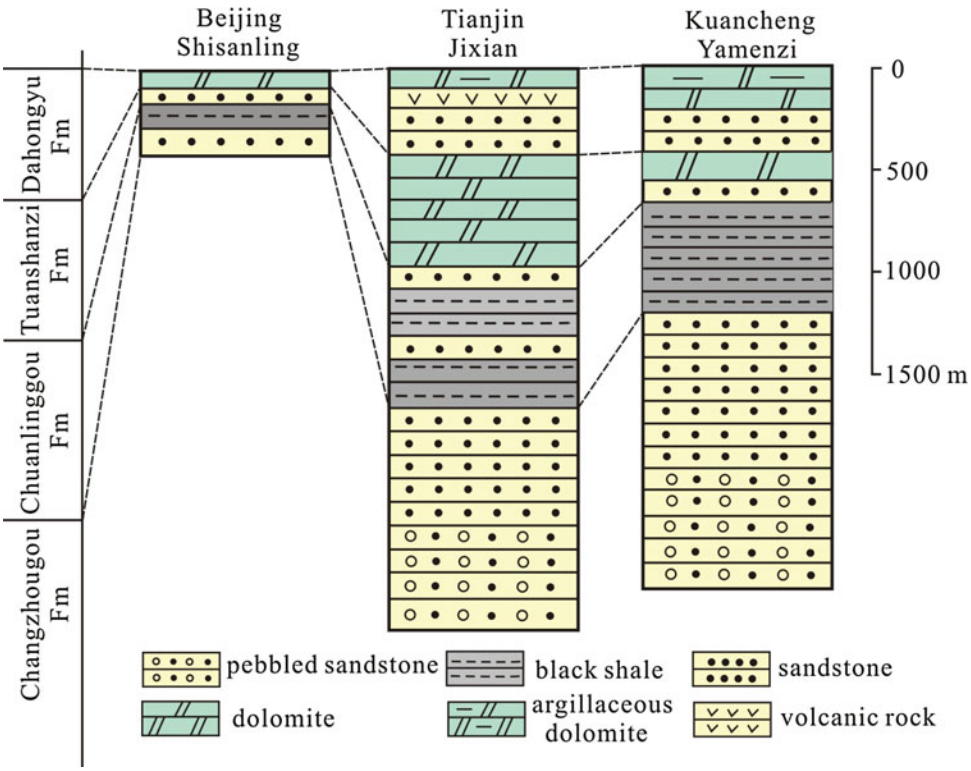

Fig. 15.3 Strata of the Mesoproterozoic Changcheng System in different areas of the Yanliao Rift

(SHRIMP U–Pb zircon age) are found in the Xinglong area (Li et al. 2009; Fig. 15.3).

The Jixian System is composed of five formations (from bottom to top): the Gaoyuzhuang, Yangzhuang, Wumishan, Hongshuizhuang, and Tieling formations (Fig. 15.4). The Gaoyuzhuang Formation consists of chert dolomite and dolomite, with numerous conophyton stromatolites in the lower parts. The middle to lower parts of the formation contain black dolomitic shale, manganese-bearing dolomite, and thickly bedded dolomite. SHRIMP U–Pb zircon ages for the tuffs in the Gaoyuzhuang Formation are 1559 ± 12 Ma and 1560 ± 5 Ma (Li et al. 2009). The Yangzhuang Formation consists of purple micrite dolomite, dolomite, chert dolomite, dolomitic limestone, and bituminous dolomite. The Wumishan Formation is composed of a stable lithofacies of thick stromatolite-bearing dolomite. The dolomite also contains discrete rhythmic interlayers of carbonate and massive microbes. Zircon and baddeleyite from the diabase cross-cutting the Wumishan Formation give ages of 1353 ± 14 Ma and 1345 ± 12 Ma, respectively (Zhang et al. 2009). The Hongshuizhuang Formation is composed mainly of black carbonaceous shale, with thin layers of siltstone in the upper part and microscopically thin layers of dolomite in the lower part. The Tieling Formation, composed of stromatolite-bearing dolomite, has an upper part comprising a cap of calcareous, pyritic, and manganese dolomites, and a lower part with columnar stromatolites at its top. The SHRIMP U–Pb zircon age of the tuff in the Tieling Formation is 1437 ± 61 Ma (Sun et al. 2010).

The Xiamaling Formation in the Building System is composed of grayish-green and black shale, clay rock, and pyritic siltstone. This formation is characterized by lenticular iron deposits, pyritic siltstone, and basal conglomerate in the bottom part of the formation, pancake marl in the middle part, and carbon-bearing siliceous shale in the top part. A zircon age of 1320 ± 6 Ma for diabase intrusions in the Xiamaling Formation indicates that the formation was deposited in the Mesoproterozoic rather than the Neoproterozoic (Li et al. 2009; Fig. 15.3).

The Neoproterozoic Qingbaikou System is composed of the Changlongshan Formation in the lower parts and the Jingeryu Formation in the upper parts. The Changlongshan Formation consists of conglomerate, quartz sandstone, quartz–feldspar sandstone, calcareous siltstone, and shale. The Jingeryu Formation is composed of medium to thin layers of microcrystalline limestone. There is a regional unconformity between the Changlongshan Formation and the underlying Xiamaling Formation (Qu et al. 2010; Meng et al. 2011).

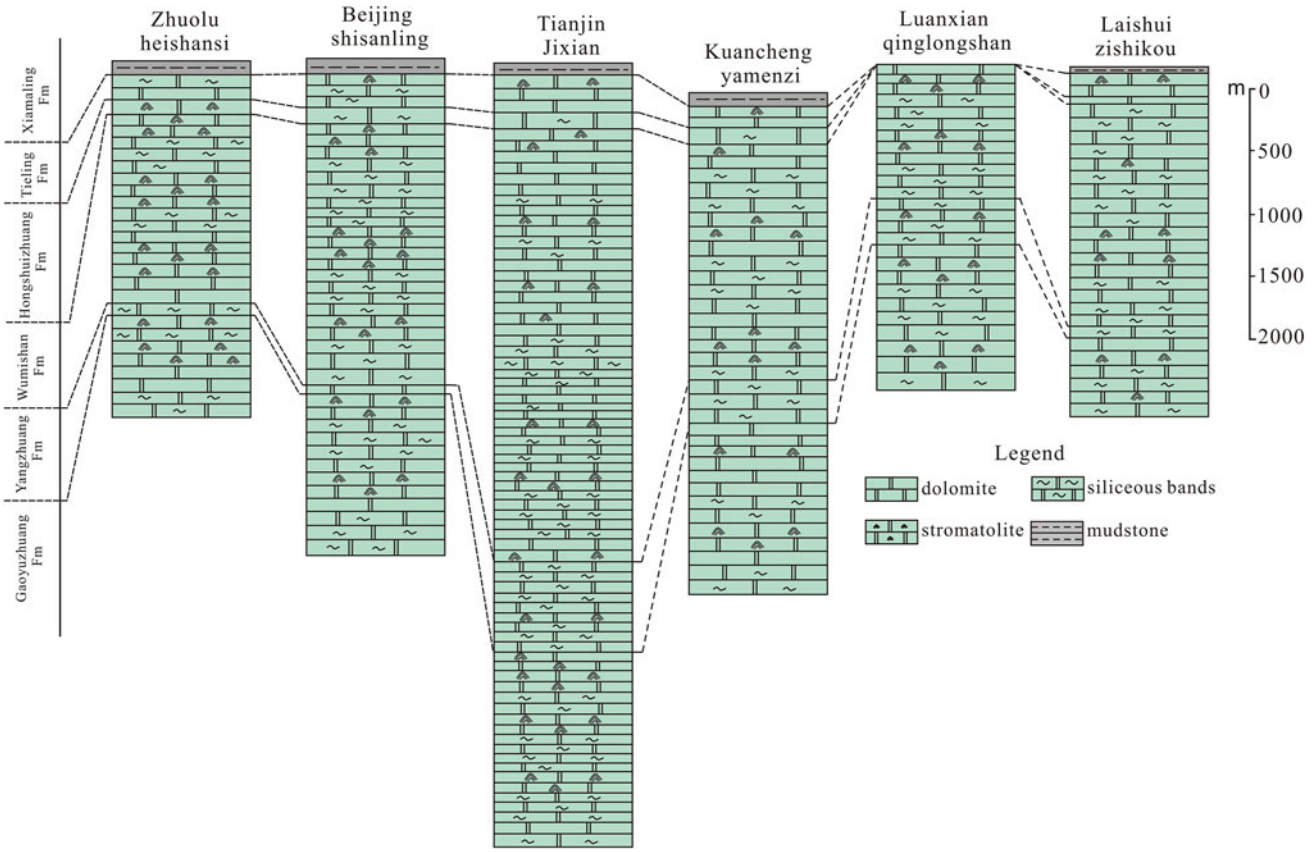

Fig. 15.4 Correlation of the Mesoproterozoic Jixian Group between different areas of the Yanliao Rift

15.3.2 Xiong'er Rift

The Xiong'er Rift, located on the southern margin of the NCC, is composed of volcanic sediments of the Mesoproterozoic Xiong'er Group, which are overlain by Meso-Neoproterozoic strata. The Xiong'er Group formed at 1800–1750 Ma, and peak volcanism occurred at ~1780 Ma (Zhao et al. 2002c; Cui et al. 2010, 2011; Zhai et al. 2014). In the Yingchi and Queshan areas of West Henan Province, the Ruyang Group, including (from bottom to top) the Xiaogoubei, Yunmengshan, Beidajian, and Baicaoping formations, is equivalent to the Jixian System. The Luoyu Group, which includes (from bottom to top) the Cuizhuang, Sanjiaotang, and Luoyukou formations, is equivalent to the Qingbaikou System. However, the Luoxu Group of the Qingbaikou System and the middle to lower part of the Ruyang Group of the Jixian System have been assigned to the Mesoprotezoic Changcheng System, based on a U–Pb zircon age of 1611 ± 8 Ma for a tuff in the central part of the Luoyukou Formation (Su et al. 2012). Therefore, the Luoyukou Formation in the upper part of the Ruyang Group is assigned to the Jixian System, based on regional lithostratigraphic correlations. Remnants of the Changcheng, Jixian, Qingbaikou, and Sinian systems are exposed in the Luonan area of Shann'xi Province. The Changcheng System in this area is composed of the Xiong'er Group in the lower part and the Gaoshanhe Group in the upper part; the Jixian System contains (from bottom to top) the Longjiayuan, Xunjiansi, Duguan, and Fengjiawan formations, and the Sinian System is represented by the Luoquan Formation.

The Xiong'er Group in West Henan Province can be divided into four formations (from bottom to top): the Dagushi, Xushan, Jidanping, and Majiahe formations. The Dagushi Formation, composed mainly of fluvial and lacustrine facies celadonite-bearing sandy conglomerate, arkose, purple sandy shale, and mudstone, is localized in distribution and tens of meters thick. The Xushan Formation consists of andesite and basaltic andesite, intercalated with dacitic rhyolite. The Jidanping Formation consists of rhyolite and dacitic rhyolite. The Majiahe Formation is composed of andesite and characterized by multiple interlayers of sedimentary and volcaniclastic rock. The Ruyang Group can be divided into (from bottom to top) the Yunmengshan, Baicaoping, and Beidajian formations. The Yunmengshan Formation occurs mainly in West Henan Province, and locally in Zhongtiao Shan, Shanxi Province. This formation

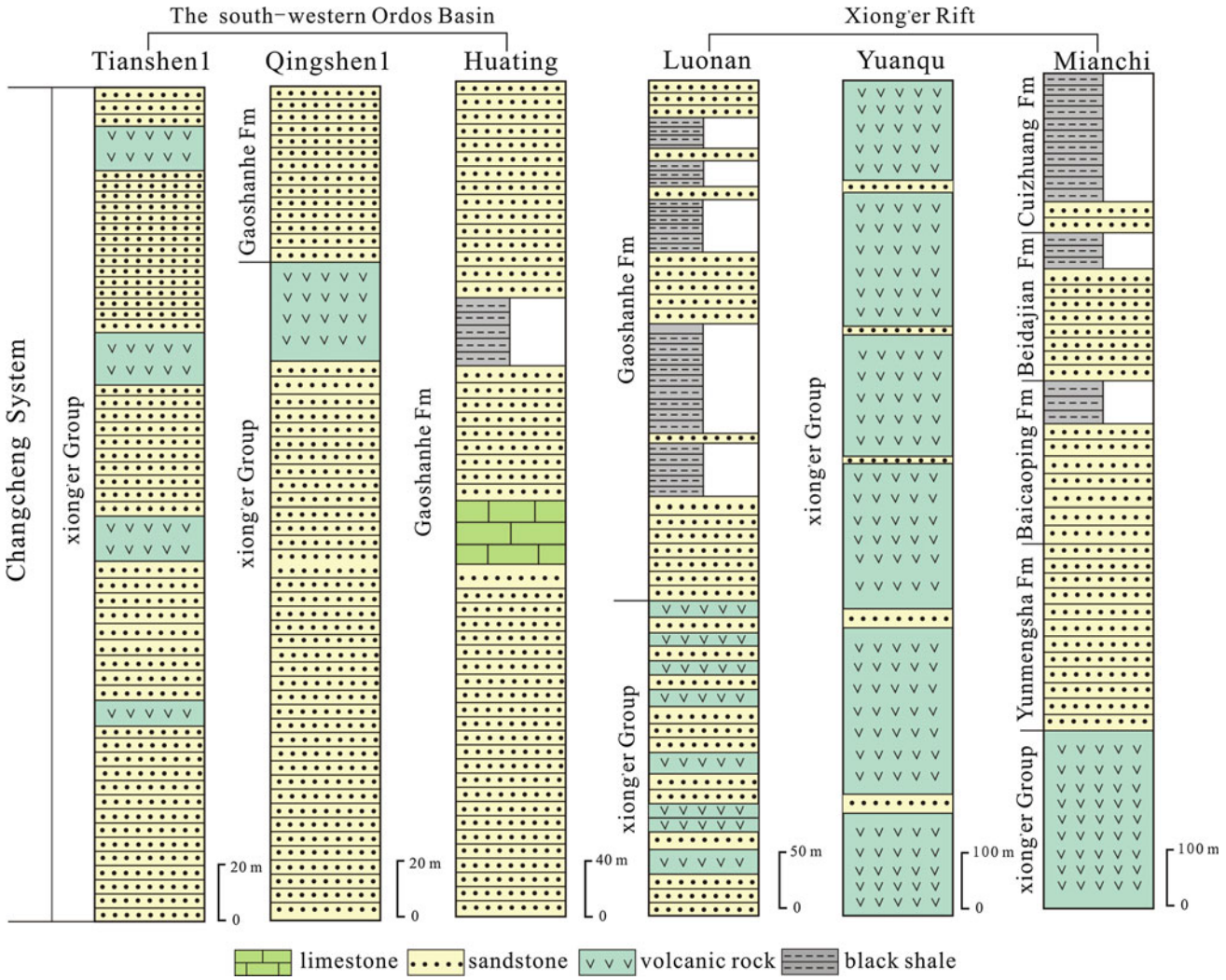

Fig. 15.5 Correlation between the Changcheng System and the Xiong'er Rift Group in different areas

is composed of purple quartz sandstone intercalated with gray quartz sandstone. The formation is thickest in the center of the rift trough and pinches out laterally. The Baicaoping Formation onlaps the underlying Yunmengshan Formation and consists of purple shale and silty shale, intercalated with thinly layered quartz sandstone, siltstone, and silty dolomite containing columnar and radial stromatolites. The Bedajian Formation is composed of quartz sandstone and quartz–feldspar sandstone. The upper part of the formation is intercalated with phosphorus-mineralized, grayish-green, silty shale rocks and glauconitic silty shale, which represent a marker unit for regional stratigraphic correlation. The Cuizhuang Formation of the Luoyu Group is composed of black–green shale and silty shale. The Sanjiaotang Formation consists of highly mature quartz sandstone. The upper part of the formation consists of glauconitic quartz sandstone; the lower part consists of ferruginous, spotted, ripple marked, and cross-bedded sandstone (Fig. 15.5). The Luoquan Formation of the Jixian System is composed of pink, thickly bedded dolomitic limestone with mud bands and massive *chert*. The Luoquan Formation of the Sinian System is characterized by tillite, which can be divided into three members: a till conglomerate in the lower section, tillite with morainic laminae in the middle section, and black shale at the top.

The Xiong'er Group in the Luonan area of Shann'xi Province has been correlated with its equivalent in West Henan Province. The Xiong'er Group is unconformably overlain by the Gaoshan Group. The latter occurs mainly in the Huanglongpu and Xiyuhe areas of Luonan, Shann'xi Province. The lower part of the group is characterized by intercalated sandstone and argillite, which occur together with conglomerate, quartz sandstone, silty sericite slate, siltstone, and quartz–feldspar sandstone. The middle section consists of quartz sandstone and quartz–feldspar sandstone. The upper section is composed of dolomite and sandy dolomite.

The Jixian System can be divided into four formations. The Longjiayuan formation at the bottom occurs in the Luonan, Longxian, and Lantian areas in Shann'xi Province, and extends eastward to the Lingbao, Lushi, Luanchuan, and Luoning areas in Henan Province. The Longjiayuan Formation is stable in lateral and consists of shallow marine magnesian limestone intercalated with clastic rocks in the lower parts of the formation. The major rock types include griseous to charcoal gray, moderate to very thick, powdery to finely crystalline dolomite with chert bands and abundant stromatolites, as well as pebbly sandstone and conglomerate in the lower sections, and local hematite lenses. The Longjiayuan Formation unconformably overlies the Gaoshanhe Formation. The Xunjiansi Formation is a griseous, medium to thickly bedded, chert-banded dolomite that contains a few stromatolites and fossil microflora; it conformably overlies the Longjiayuan Formation, which generally consists of dolomite with stromatolites and microflora. The Duguan Formation is composed of varicolored, thinly layered dolomitic carbonate, and unconformably overlies the Xunjiansi Formation. The Fengjiawan Formation consists of argillaceous dolomite intercalated with dolomitic slate; tawny, grayish-purple and shallow, celadonite-bearing, thinly layered dolomite intercalated with slate; and stromatolite reef dolomite in the lower parts of the section. The middle sections comprise grayish-white and grayish-purple thickly bedded dolomite with argillaceous stromatolite reefs. Grayish-white striped dolomite, and stromatolite-rich, chert-banded dolomite are intercalated with oolitic siliceous rocks in the upper part of the formation (Fig. 15.6).

The Shibeigou Formation of the Qingbaikou System can be divided into upper and lower members. The lower member is composed of silty slate and sericite slate; the upper member is composed of medium to thickly bedded siliceous limestone. Unconformities divide the Shibeigou Formation into the overlying Luoquan Formation and underlying Fengjiawan Formation.

15.3.3 Zhaertai–Bayan Obo Rift

The Zhaertai–Bayan Obo Rift is composed of the Mesoproterozoic Zhaertai Group in the west and the Bayan Obo Group in the east. The Mesoproterozoic Zhaertai Group of the Changcheng System is located in the east–west extending belt of the Zhaertai Shan–Lang Shan, and unconformably overlies the late Archean Serertengshan Group. The Zhaertai Group can be separated into four formations (from bottom to top): the Shujigou, Zenglongchang, Agulugou, and Liuhongwan formations. The Shujigou Formation comprises terrigenous clastic rock, with coarse-grained conglomerate, conglomeratic quartz sandstone, and quartz sandstone in the lower parts; and siltstone and mudstone intercalated with coarse-grained quartz sandstone, siltstone intercalated with mudstone, and minor basic volcanic rocks in the upper parts. The Zenglongchang Formation consists of quartz sandstone intercalated with marlite in the lower part, and carbonaceous strata in the upper part. The Agulugou Formation is composed of black slate and carbonaceous silty slate in the lower part, and argillaceous crystalline limestone in the upper part. The Liuhongwan Formation is composed mainly of pebbly quartz sandstone, medium to thinly layered quartzite, and quartz–feldspar sandstone, intercalated with minor dolomitic limestone and microcrystalline dolomite (Fig. 15.2).

The Bayan Obo Group occurs to the north of the Zhaertai Group and forms an east–west-trending belt from Bayan Obo to Guyang. The Bayan Obo Group unconformably overlies the late Archean Serertengshan Group. The Bayan Obo Group is divided into the Dulahala and Jianshan formations of the Changcheng System, the Halahuogete and Bilute formations of the Jixian System, and the Baiyinbulage and Hujiertu formations of the Qingbaikou System (Zhang et al. 2015). The Halahuogete Formation unconformably underlies the Jianshan Formation and overlies the Bilute Formation. The Dulahala Formation of the Changcheng System consists of coarse-grained, quartz–feldspar sandstone in the lower part, and quartzite in the upper part.

The Jianshan Formation is composed of carbonaceous, pyritic–manganic, silty slate intercalated with quartzite, quartz sandstone, and calcic sandstone. The Halahuogete Formation of the Jixian System is composed of quartz–feldspar sandstone, and quartzite intercalated with limestone and slate. The Bilute Formation consists of mudstone, siltstone, and carbonaceous slate, intercalated with minor siltstone, with slump breccias and associated turbidites. The Baiyinbulage Formation of the Qinbaikou Group is composed of grayish-white, medium- to fine-grained quartz sandstone, andalusite-bearing sericite slate, silty slate, metasiltstone, and sericite-bearing spotted slate. The Hujiertu Formation, conformably overlain by the Baiyinbulage Formation, is composed mainly of pale gray siltstone, meta-quartz–feldspar graywacke, laminar algal powdery to crystalline limestone, sericite slate, and silty slate (Fig. 15.2).

15.3.4 Ordos Block

The Meso-Neoproterozoic strata are covered by thick Paleozoic to Mesozoic sediments in the Ordos Block. The distribution and sedimentary framework of the Meso-Neoproterozoic strata are defined based on drilling and seismic data. According to interpretations of north–south and east–west seismic profiles across the Ordos Block, only the Changcheng and Jixian systems are present; the Qingbaikou and Sinian systems are absent. The Mesoproterozoic deposits are controlled by a series of deep NE–SW

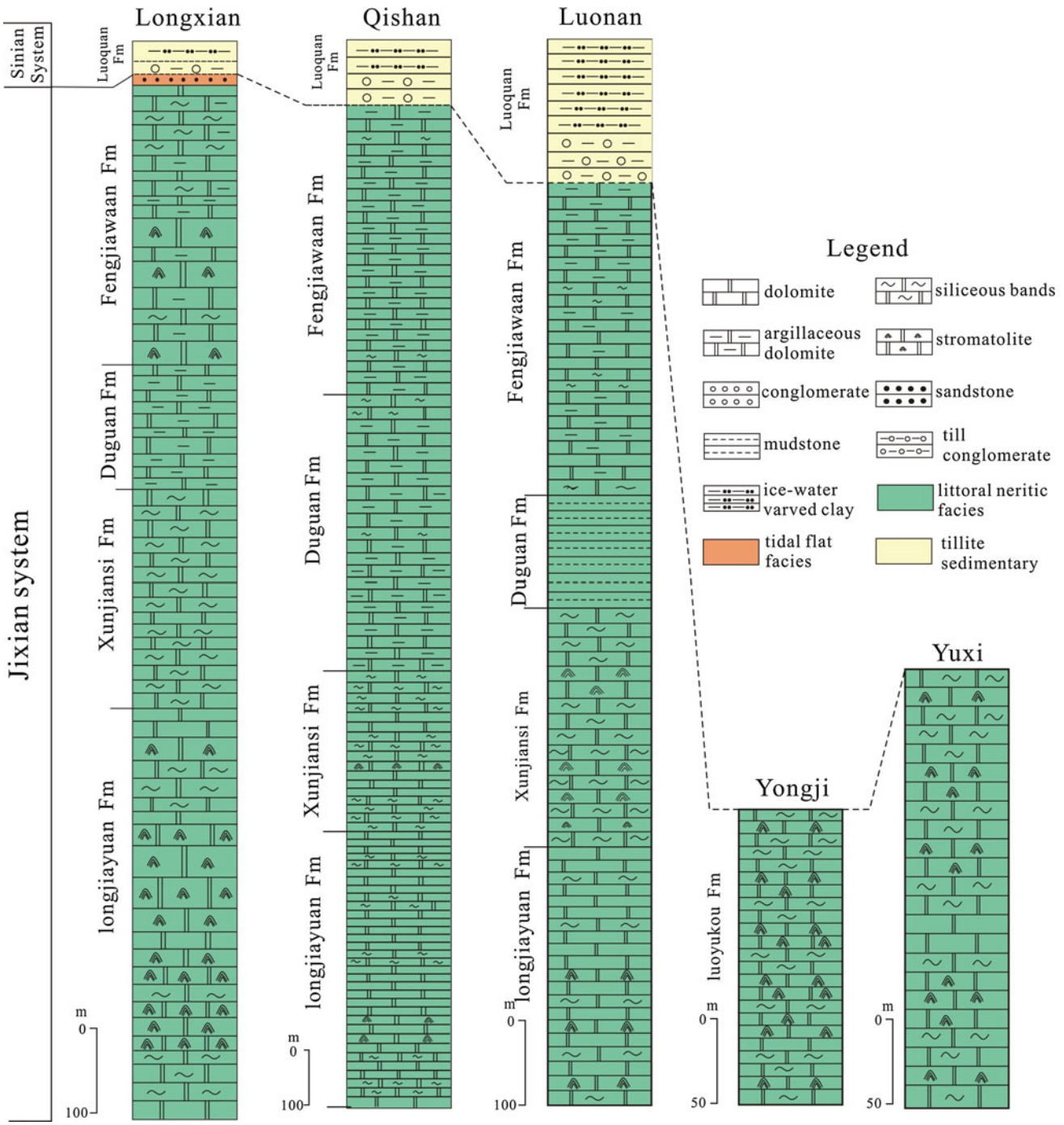

Fig. 15.6 Correlation between the Jixian System and the Xiong'er Rift Group in different areas

extensional faults (Fig. 15.7). These faults only developed in the Changcheng and Jixian systems; the overlying Cambrian strata are not disturbed. These faults generated a series of NE–SW-extending depressions that are evident as thick sedimentary columns in the Changcheng System. The thickness of the Changcheng System is about 0–2400 m, and increases from NE to SW. Three E–W extensional belts formed in the Changcheng System, concordant with the Xiong'er Rift (Fig. 15.8a). The thickness of the Jixian System is 0–1600 m, and it has a similar pattern to the Changcheng System. There is no clear variation in thickness in the Jixian System, which indicates that fault activity was minimal during this period (Fig. 15.8b). The Qingbaikou System is absent in the inner Ordos Block. The Sinian System only developed on the western and southern margins of the Ordos Block, with a thickness of 0–120 m. The Sinian

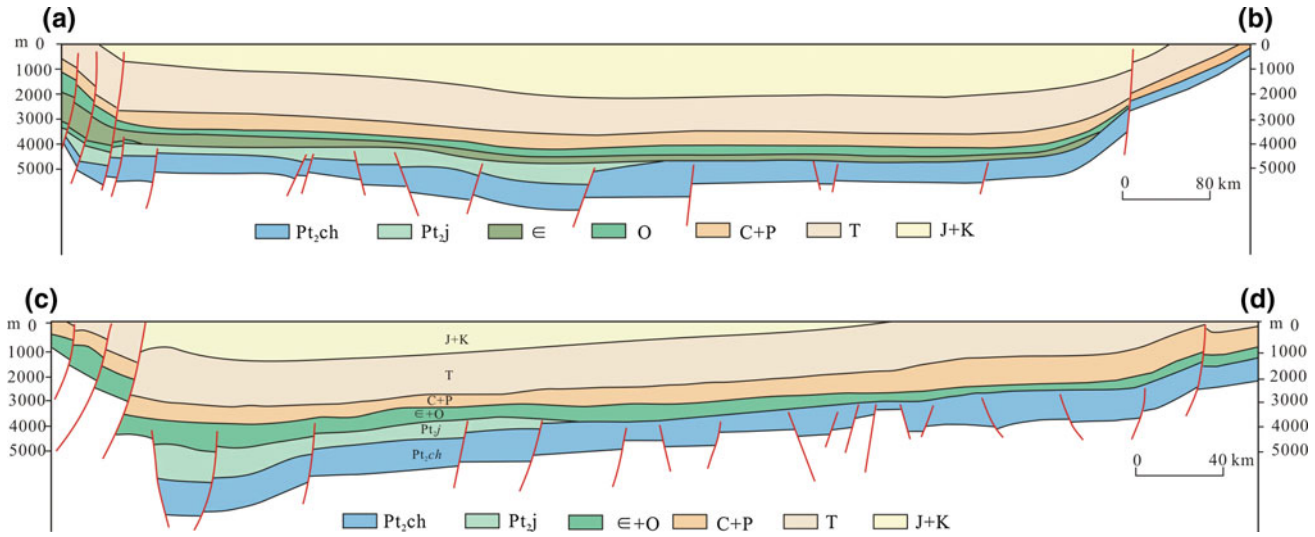

Fig. 15.7 Regional seismic profiles across the Ordos Block (see Fig. 15.8a for locations)

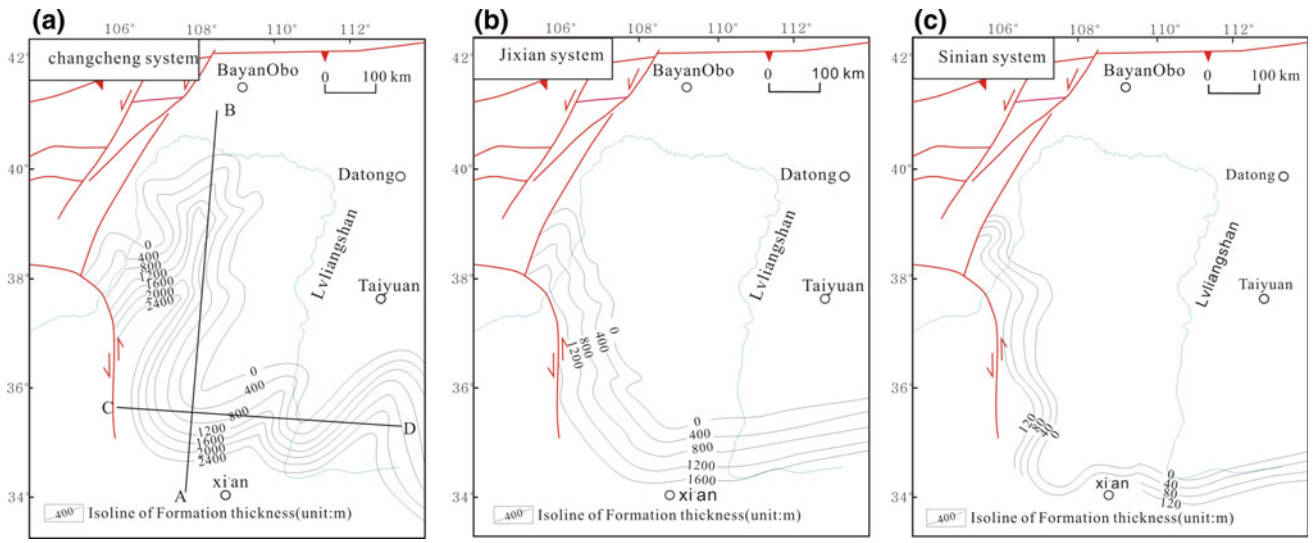

Fig. 15.8 Stratigraphic thickness maps for Meso-Neoproterozoic strata in the Ordos Basin

System can be divided into three members (from bottom to top): till conglomerate in the lower part, morainic laminated *tillite* in the middle part, and black slate intercalated with thinly layered quartzite in the upper part. The thickest remnants of the Sinian System are located in the Suyukou profile of the Helan Shan on the western margin of the Ordos Block, and the Luohua Road profile of Luonan on the southern margin (Figs. 15.8c and 15.9).

15.3.5 Alxa Block

The Meso-Neoproterozoic strata of the Alxa Block are located in the Lang Shan, Bayanxibie Shan, and Longshou Shan areas. The Langshan Group in the Lang Shan area has been correlated with the Zhaertai Group in the Zhaertai Shan area, and was suggested to be Mesoproterozoic. However, new U–Pb zircon ages indicate that the Langshan Group formed in the Neoproterozoic, and its depositional age is younger than 810 Ma (Hu et al. 2014). The underlying Baoyintu Group was previously thought to comprise Paleoproterozoic sediments, and consists of volcanic–marine facies clastic and carbonate rocks, including mica schist, two-mica–quartz schist, quartzite, granulite, and marble. However, the detrital zircon U–Pb ages give a peak of 1000–1200 Ma; therefore, the Baoyintu Group should be Mesoproterozoic (Teng et al., pers. comm.). The Langshan Group, with a thickness of more than 6860 m, can be divided into

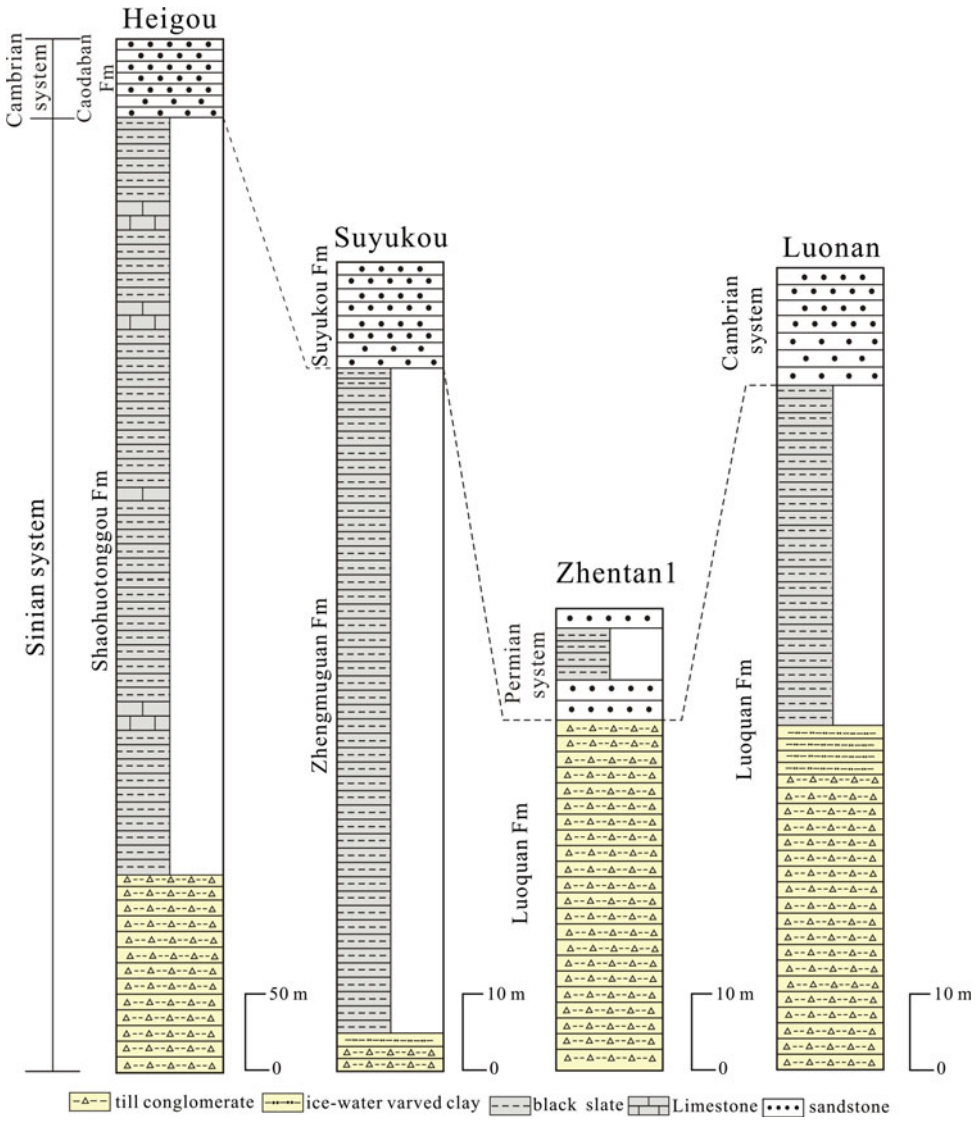

Fig. 15.9 Correlation of the Neoproterozoic Sinian System in different areas of the North China Craton

four formations (from bottom to top): quartz sandstone, phyllite, marlite, and quartzite; crystalline limestone intercalated with quartz sandstone, sandy slate, or basalt; carbonaceous slate and sandy slate, intercalated with crystalline limestone and sandy shale; and quartz–mica schist, quartzite, and marble (Fig. 15.10).

The Bayinxibie Shan area hosts the Mesoproterozoic Jixian System and the Neoproterozoic Qingbaikou System. Both these systems form E–W-trending elongat rift basins, 50 × 20 km in size. The Bayinxibie Formation of the Jixian System is composed of thickly bedded crystalline limestone. The Qingbaikou System comprises the Haishenghala Formation and the Zhulazhagamaodao Formation. The Haishenghala Formation can be divided into lower and upper members. The lower member consists of varicolored slate and quartzite, intercalated with argillaceous limestone lenses that include tawny stromatolite. Hematite and manganese lenses occur in the slate. The upper member is composed of three parts. The lower part consists of unstable conglomerate and varicolored slate, which includes small lenses of manganese and iron ore. The middle part consists of coarse-grained quartz sandstone and grayish-green slate, interbedded with argillaceous nodular limestone, including two layers of lenticular or stratiform manganese minerals. The upper part consists of argillaceous limestone interbedded with varicolored slate. The Zhulazhagamaodao Formation is composed of interbedded gray to grayish-green meta-sandstone, argillaceous limestone, black siliceous slate, and griseous argillaceous limestone. The Shaohuotonggou Formation of the Neoproterozoic Sinian System in the Longshoushan area can be correlated with the Zhengmuguan Formation of the Sinian System in the Helanshan area. Both of these formations are composed of thickly bedded moraine-breccia at the base, grading up into lamellar phyllite and carbonaceous phyllite.

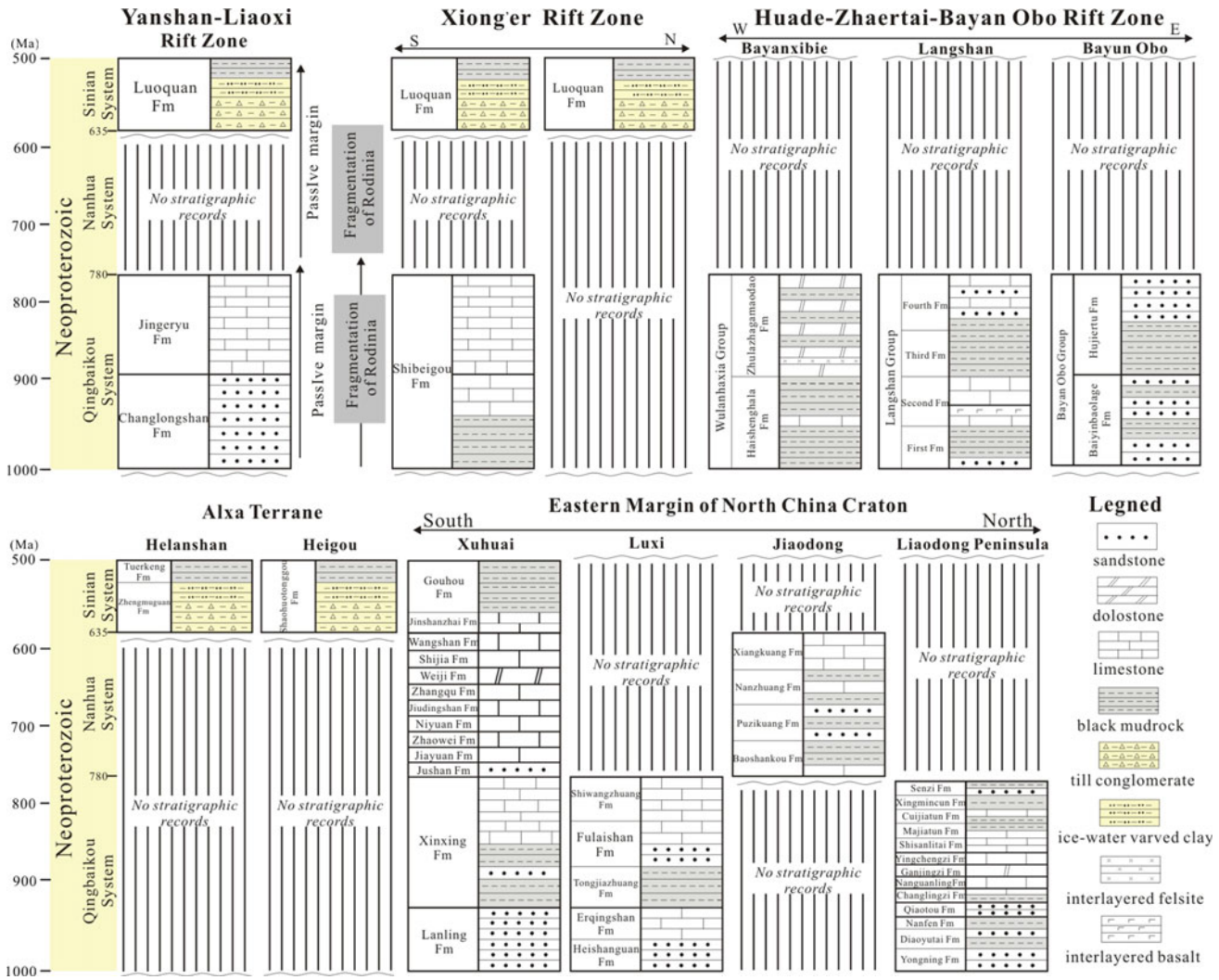

Fig. 15.10 Correlation of Neoproterozoic strata throughout the NCC

15.3.6 Eastern Part of the NCC

The Qingbaikou System and Nanhua System in the eastern NCC are locally distributed in the Liaodong Peninsula, and in the southwestern Shandong, Xuhuai, and Jiaodong areas (Fig. 15.10).

The Qingbaikou System is exposed in the Fuzhou–Dalian area of Liaodong Peninsula. The Qingbaikou System can be divided into thirteen formations (from bottom to top): the Yongning, Diaoyutai, Nanfen formations, Qiaotou, Changlingzi, Nanguanling, Ganjingzi, Yingchengzi, Shisanlitai, Majiatun, Cuijiatun, Xingmincun, and Senzi formations. The Yongning Formation is composed of thick sandstone and conglomerate, and is unconformably overlain by Archean migmatite. The Diaoyutai Formation comprises gray, medium to thickly bedded, medium- to fine-grained quartz sandstone and gravel-bearing, coarse-grained quartz sandstone in the lower parts; yellow to purple, thinly layered, fine-grained quartz sandstone and glauconite-bearing quartz sandstone and siltstone interbedded with yellow-green shale in the middle parts; and white or gray thickly bedded quartz sandstone in the upper parts (Fig. 15.11). The Nanfen Formation consists of grayish-green, flavovirens-bearing, purple silty shale intercalated with thinly layered siltstone in the lower part; pale blue to purple micrite with pyrite nodules and copper mineralization, and sandy micrite intercalated with purple calcareous shale in the middle part; and flavovirens-bearing purple shale, silty shale, and calcareous silty shale, intercalated with minor fine-grained quartz sandstone lenses in the upper part. The Qiaotou Formation consists of a lower member of gray, medium to thickly bedded quartzite, interbedded with slate that contains hematite lenses; and an upper member composed of grayish-white, medium to thickly bedded quartzite intercalated with slate. The Changlingzi Formation consists of three members. The lower member consists of flavovirens-bearing

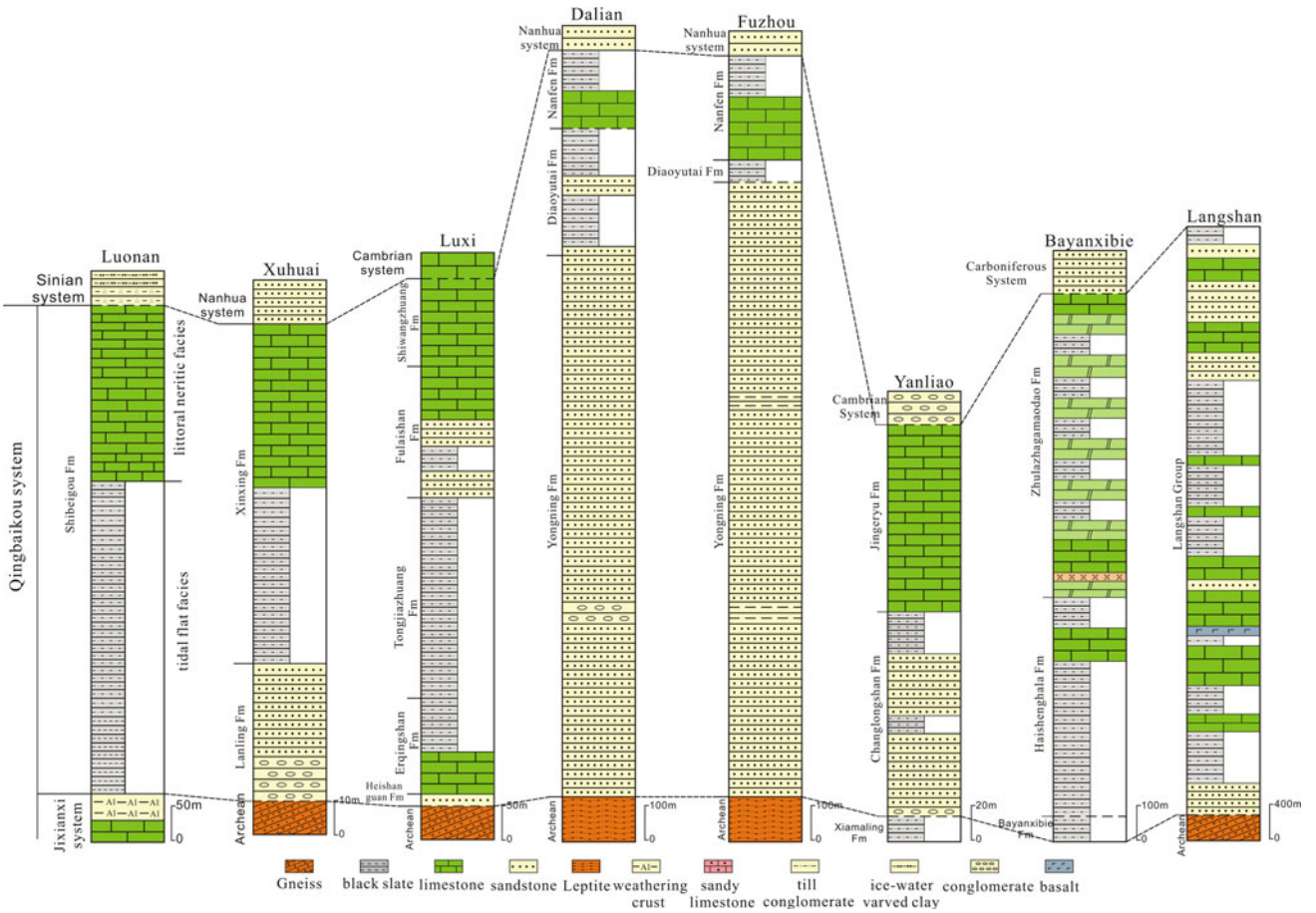

Fig. 15.11 Correlation of the Neoproterozoic Qingbaikou System throughout the NCC

shale and silty shale intercalated with thinly layered quartz sandstone. The middle member consists of flavovirens-bearing, thinly layered, fine-grained quartz sandstone, glauconite-bearing quartz sandstone, and siltstone, intercalated with shale. The upper member consists of gray to yellowish-gray, medium-bedded calcareous gritstone, and glauconite-bearing calcareous gritstone interbedded with micrite and sandy micrite. The Ganjingzi Formation can be divided into three members. The lower member includes griseous and pinkish, medium to thickly bedded stromatolitic limestone, intercalated with limy dolarenite. The middle member includes charcoal gray, medium to thickly bedded limy dolomicrite and limy dolarenite, intercalated with limy calcite dolomite, with siliceous layers and quartz sandstone lenses. The upper member is composed of griseous to grayish-white, medium to thickly bedded limy dolomite, intercalated with stromatolite dolomite. The Yingchengzi Formation consists of charcoal-colored, medium to thickly bedded micrite and stromatolite limestone in the lower section, and charcoal-gray, powdery to crystalline limestone in the upper section. The Shisanlitai Formation is composed of black, medium-bedded stromatolitic limestone in the lower section, and yellow-green to purple shale and purple stromatolitic limestone intercalated with shale in the upper section. The Cuijiatun Formation consists of grayish-green silty shale and grayish-green to purple, thinly layered siltstone, intercalated with shale. The Xingmingcun Formation is composed of grayish-green, gray, or brown, glauconite-bearing quartz sandstone, and ore-bearing quartz sandstone intercalated with grayish-green to purple shale. The Senzi Formation is composed of three parts. The lower part consists of black shale and gray, medium to thickly bedded, fine-grained quartz sandstone, intercalated with silty shale. The middle part is composed of purple and gray, thinly layered, medium-grained quartz sandstone, quartz–feldspar sandstone, and ferromanganese mudstone, intercalated with purple shale, silty shale, and siltstone. The upper part is composed of gray, purple, and yellow thinly layered micrite, micrite calcisilte limestone, micrite calcarenite, ferromanganese micrite, and calcisilte limy dolomite, intercalated with shale, calcareous shale, siltstone, calcareous siltstone, quartz–feldspar sandstone, dolomite, and collapse-breccia.

In southwestern Shandong, the Qingbaikou System is represented by the Tumen Group. This group can be divided

into five formations (from bottom to top): the Heishanguan, Erqingshan, Dongjiazhuang, Fulaishan, and Shiwang formations (Fig. 15.11). The Heishanguan Formation is composed of grayish-purple to grayish-green silty shale, thinly layered, glauconite-bearing gritstone, and medium-bedded pebbly sandstone. The Erqingshan Formation is composed of gray to lilac, thickly bedded glauconite-bearing quartz sandstone in the lower section; purple-gray to pale blue laminated aphanitic limestone in the middle section; and carmine calcareous shale intercalated with marl in the upper section. The Tongjiazhuang Formation is composed of chartreuse, medium to thinly layered silt to fine quartz sandstone, intercalated with silty shale, calcareous siltstone, and medium-bedded quartz sandstone, or gray medium-bedded pebbly quartz–feldspar sandstone with fine sandstone in the lower section, and chartreuse shale intercalated with carmine shale and thinly layered marl in the upper section. The Fulaishan Formation is composed of chartreuse, medium to thinly layered, medium to thickly bedded, glauconite-bearing fine-grained quartz sandstone, siltstone intercalated with shale, and thinly layered silty marl in the lower section; and cinereous, glauconite-bearing calcareous quartz siltstone or sandy limestone intercalated with thinly layered marl *in the upper section*. The Shiwangzhuang Formation is composed of calcite dolomite and dolomitic limestone.

The Qingbaikou, Nanhua, and Sinian systems occur in the Xuhuai area. The Qingbaikou System can be divided, from bottom to top, into the Lanling, Xinlan, and Jushan formations (Fig. 15.11). The Lanling Formation consists of off-white, medium- to coarse-grained glauconite-bearing quartz sandstone. The Xinxing Formation is composed of chartreuse marl and shale, intercalated with glauconite-bearing fine-grained quartz sandstone. The Jushan Formation consists of off-white, medium to thickly bedded quartz sandstone, intercalated with silty shale with minor glauconite.

The Nanhua System can be divided into nine formations (from bottom to top): the Jiayuan, Zhaowei, Niyuan, Jiudingshan, Zhangqu, Weiji, Shijia, Wangshan, and Jinshanzhai formations (Fig. 15.12). The Jiayuan Formation is composed of chartreuse, thinly layered silty mudstone, argillaceous siltstone intercalated with silty limestone, and calcareous fine-grained quartz sandstone in the lower section; and silty limestone intercalated with calcareous quartz sandstone and stromatolitic limestone in the upper section.The Zhaowei Formation includes thickly bedded limestone, argillaceous limestone, and stromatolitic limestone. The Niyuan Formation is dominated by dolomite. The Jiudingshan Formation is primarily limestone, intercalated with dolomite. The Zhangqu Formation is composed of gray, medium- to thinly bedded limestone, intercalated with atropurpureus-bearing laminated marl and minor wormkalk lenses in the lower section, and gray medium-bedded dolomite in the upper section. The Weiji Formation is composed of interbedded gray, medium-bedded dolomite and dolomitic limestone, intercalated with chartreuse to cinereous shale and stromatolitic limestone lenses in the lower section, and grayish-purple stromatolitic limestone in the upper section. The Shijia Formation consists of chartreuse shale, chartreuse laminated marl, calcareous shale, and medium-bedded quartz sandstone with ferruginous nodules, intercalated with gray, laminated to thinly layered stromatolitic limestone. The Wangshan Formation is composed of gray, laminated to thinly layered marl and calcareous shale in the lower section; gray, medium to thinly bedded argillaceous zebra limestone and dolomitic limestone in the middle section; and gray medium-grained limestone and dolomitic limestone with siliceous sand and chert nodules, intercalated with stromatolitic limestone lenses in the upper section. The Jinshanzhai Formation is composed of gray shale, intercalated with thinly layered fine-grained sandstone in the lower section; gray-yellow thickly bedded limestone intercalated with stromatolitic limestone lenses in the middle section; and gray medium-bedded limestone interbedded with chartreuse shale in the upper section.

The Gouhou Formation of the Sinian System is composed of three members. The lower member consists of grayish-black and chartreuse shale, intercalated with gray, thinly layered medium-grained quartz sandstone and limonite lenses, with limestone gravel at the bottom. The middle member is dominated by gray-yellow to lilac marl and carmine to gray-yellow calcareous shale. The upper member is dominated by gray, thinly layered to medium-bedded dolomite.

The Nanhua System in the Jiaodong area is represented by the Penglai Group, which can be divided into (from bottom to top) the Baoshankou, Puzikuang, Nanzhuang, and Xiangkuang formations. The Baoshankou Formation consists of slate and marble. The Puzikuang Formation is composed of interbedded, thinly layered medium to thickly bedded quartzite and slate. The Nanzhuang Formation is composed of varied slate and marble, including slate and limestone lenses with minor marl in the lower section, and slate and calcareous slate in the upper section. The Xiangzhuang Formation is composed of cinereous, medium to thickly bedded limestone, argillaceous dolomitic zebra limestone, thinly layered to medium-bedded argillaceous limestone, marl and slate.

15.4 Meso-Neoproterozoic Lithofacies Paleogeography of the North China Craton

15.4.1 Changcheng Period (1.8–1.6 Ga)

The sedimentary sequences of the Changcheng System contain mainly volcanic rocks and tidal flat–coastal clastic

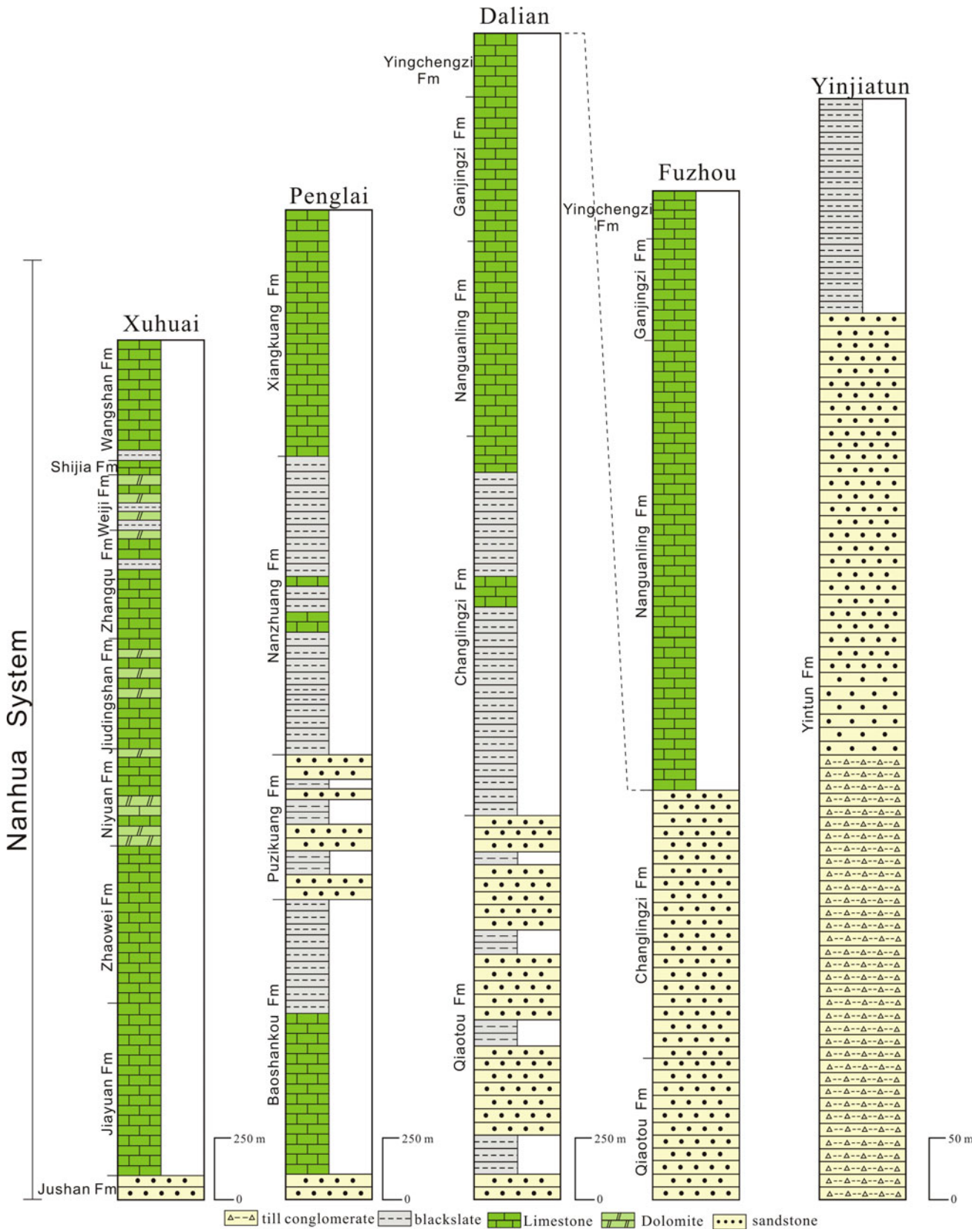

Fig. 15.12 Stratigraphic correlation of the Neoproterozoic Nanhua System in the North China Craton

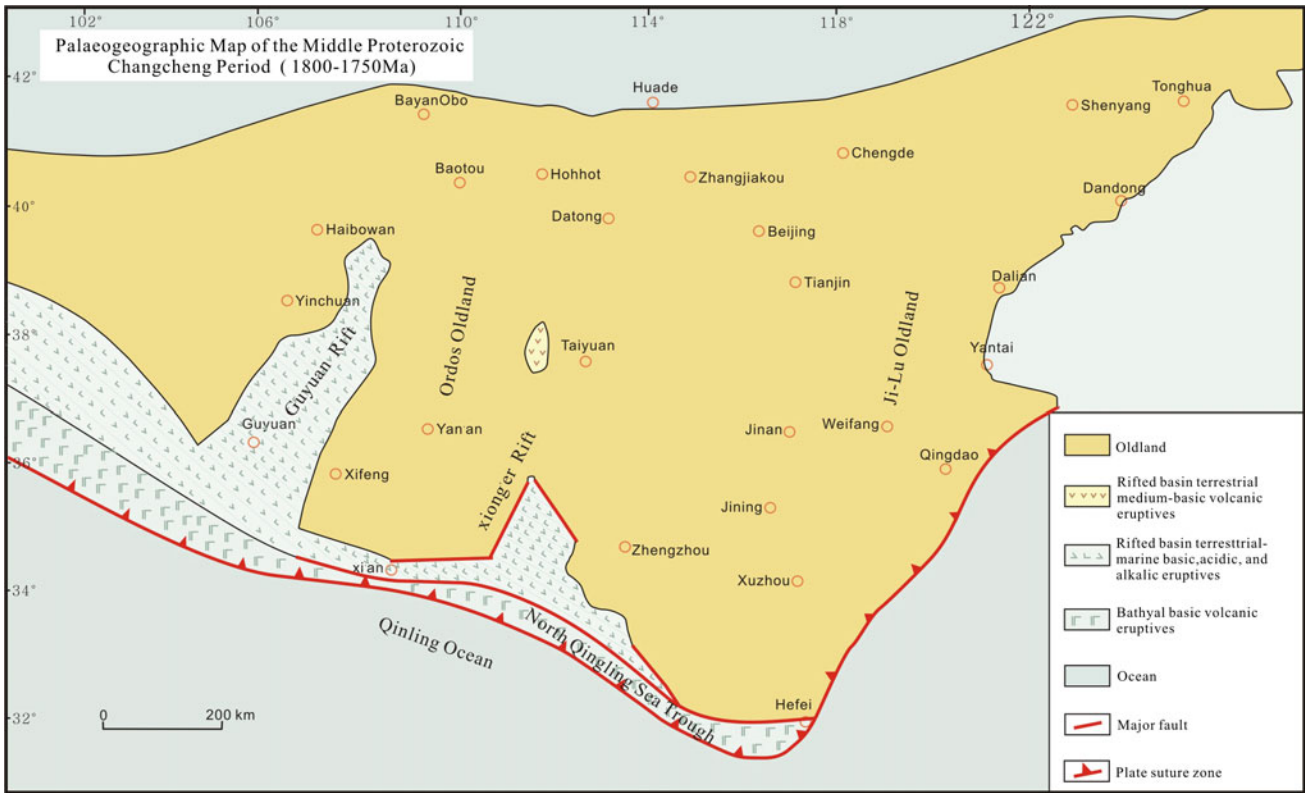

Fig. 15.13 Lithofacies paleogeography of the Changcheng Period (1800–1750 Ma) in the North China Craton (modified after Wang 1985)

sediments (Fig. 15.13). Typical cross sections of early-stage volcanic series can be observed in the Xiong'er Rift. The sedimentary section has been confirmed by drilling in the southwestern margin of the Ordos Block. Four sets of basic volcanic rocks were identified in drilling section Tianshen-1 and one set in drilling section Qingshen-1. The drill logs show that the rift is NE–SW trending and that the thickness of the sedimentary sections of the Changcheng System is constrained by the shape of the Xiong'er Rift. The development of the volcanic facies of the Yanliao Rift System, which contains volcanic breccia, lava, volcanic tuff, lamprophyre, and syenite porphyry veins, is inferred to post-date the Xiong'er Rift System. The Yanliao Rift System is interpreted to be contemporaneous with the Tuanshanzi–Dahongyu Formation. In the Zhaertai–Bayan Obo Rift System, metamorphic andesite, actinolite–chlorite–quartz schist, and chlorite–mica–quartz schist are documented in the Shujigou Formation of the Zhaertai Group in the Zhaertai Shan area. The protoliths of the metamorphic phases are proposed to be tholeiitic to calc-alkalic basalt series rocks (Wang et al. 1989).

The clastic rock series of the Changcheng System consist mainly of tidal flat–coastal facies (Fig. 15.14). The sedimentary series in the Xiong'er Rift in the southern part of the NCC include the Xiaogoubei, Yunmengshan, Baicaoping, and Beidajian formations of the Ruyang Group, and the Cuizhuang and Sanjiaotang formations of the Luoyu Group. The Xiaogoubei Formation is represented by a series of terrestrial conglomerates. The Yunmengshan Formation is composed of clastic rocks of the coastal facies, and conglomerates and quartz sandstones of the tidal flat–beach facies. The Baicaoping, Beidajian, Cuizhuang, and Sanjiaotang formations are characteristic of the clastic tidal flat facies, and contain subtidal–supratidal and foreshore–shore sediments (Dong et al. 1999; Gao et al. 2011). In the Yanliao Rift, the correlated strata are the Changzhougou, Chuanlinggou, Tuanshanzi, and Dahongyu formations. The Changzhougou Formation is characterized by tidal–dynamic-type clastic rocks with meter-scale cyclic sequences (Fig. 15.15). The Changzhougou Formation is composed of several sedimentary sequences: gravel-bearing gritstone and fine sand-bearing conglomerate of the subtidal flat facies; fine mud-bearing gritty conglomerate of the intertidal flat facies; and argillaceous sandstone of the supratidal flat facies (Mei et al. 2000). The Chuanlinggou Formation is characterized by wave–dynamic-type meter-scale cyclic bedding sequences, and the shale of the continental shelf facies thickens upward. The Tuanshanzi Formation is composed of carbonate rocks with peritidal-type meter-scale cyclic carbonate sequences, which include subtidal stromatolite-bearing dolomite, intertidal mud-sized crystalline dolomite, and supratidal argillaceous dolomite

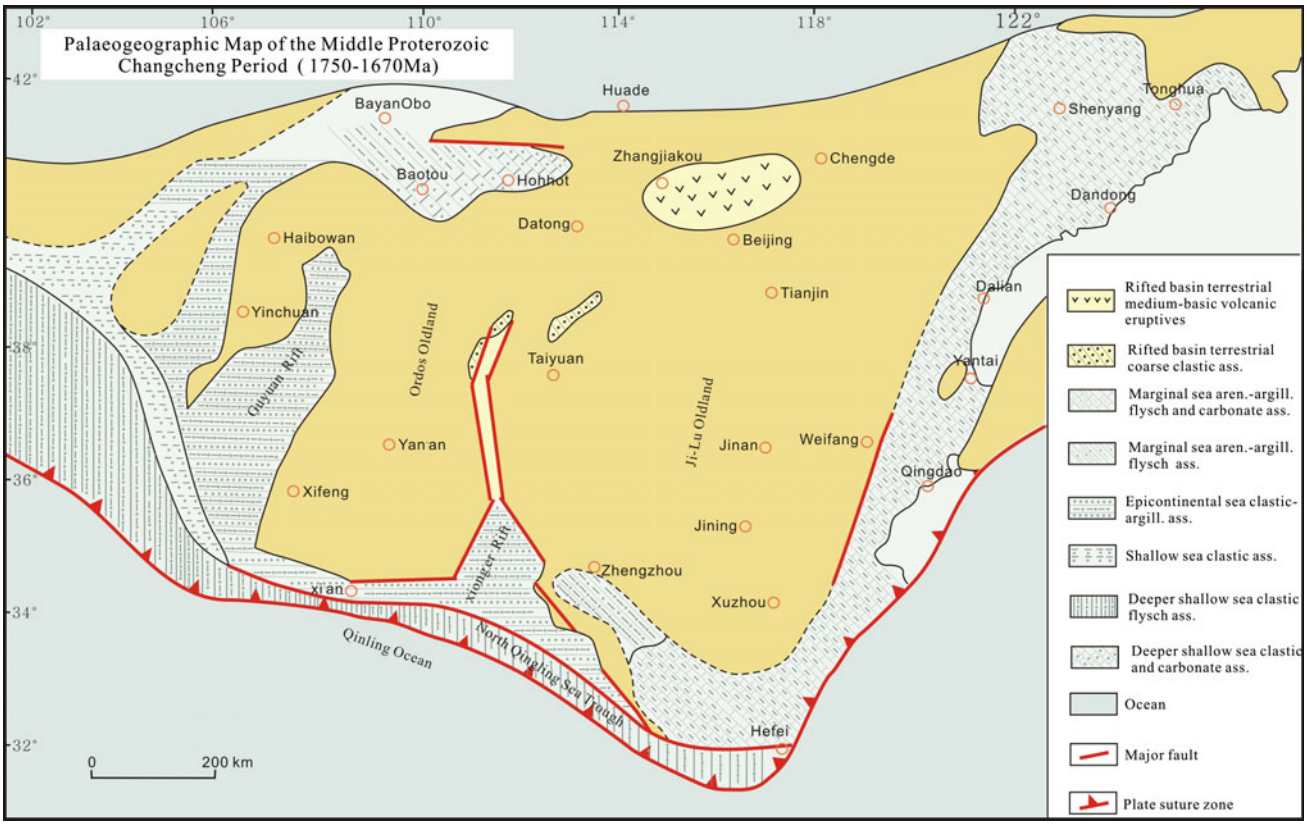

Fig. 15.14 Lithofacies paleogeography of the Changcheng Period (1750–1670 Ma) in the North China Craton (modified after Wang 1985)

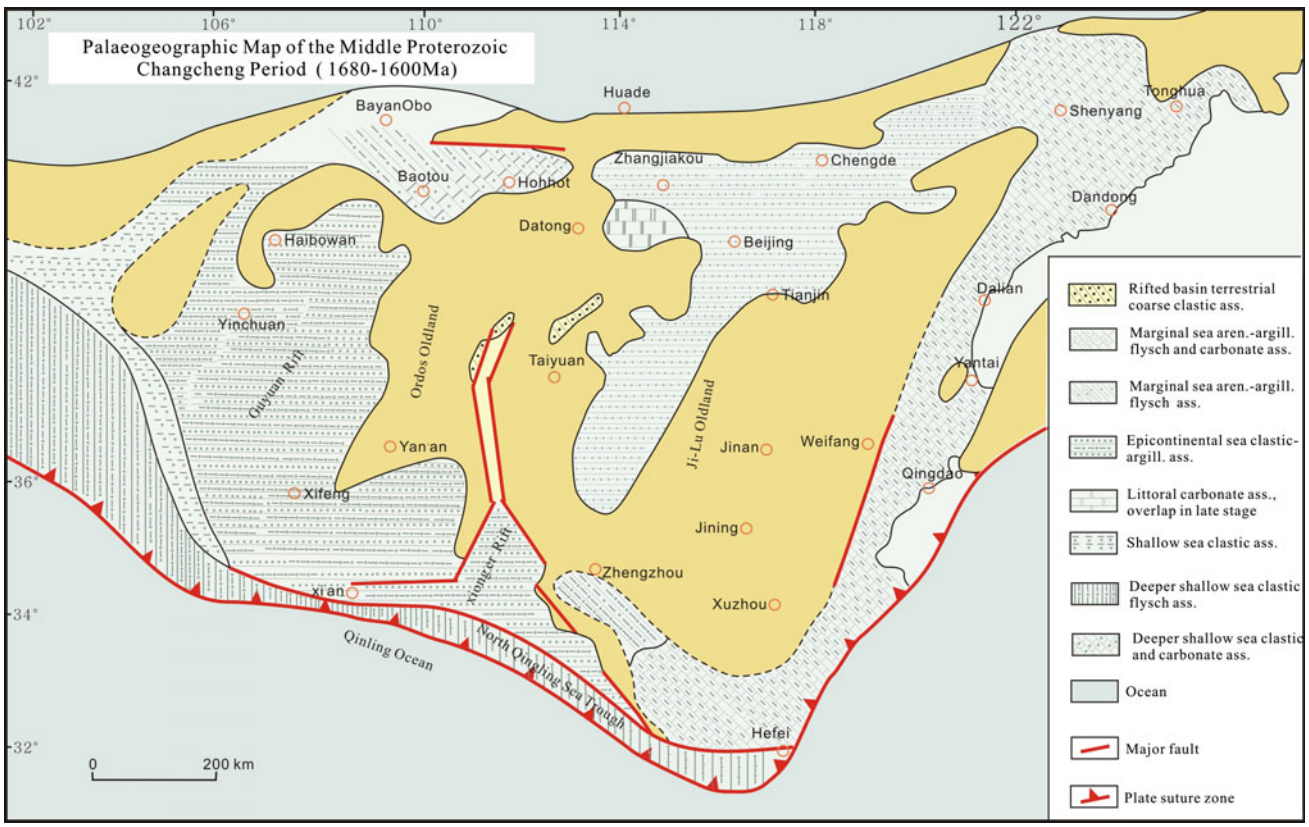

Fig. 15.15 Lithofacies paleogeography of the Changcheng Period (1670–1600 Ma) in the North China Craton (modified after Wang 1985)

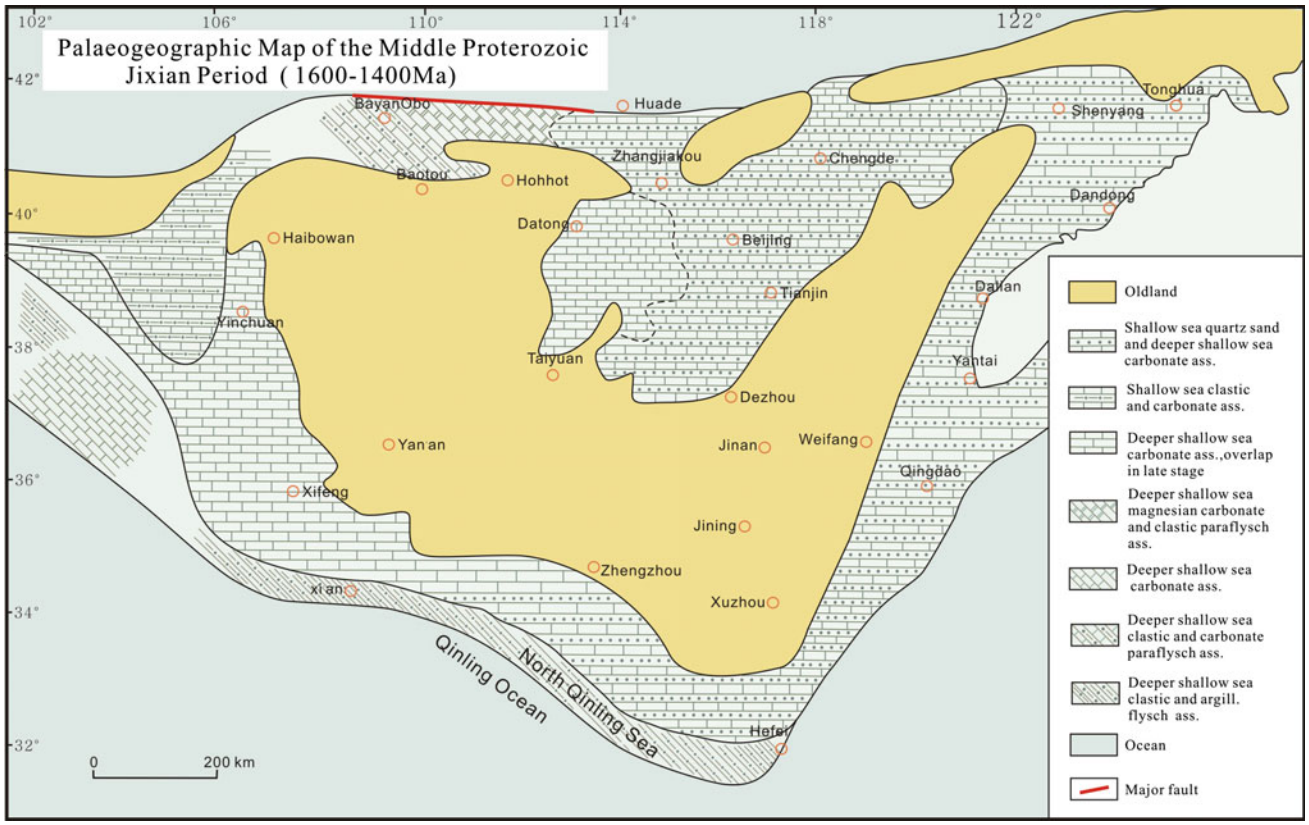

Fig. 15.16 Lithofacies paleogeography of the Jixian Period (1600–1400 Ma) in the North China Craton (modified after Wang 1985)

(Mei 1993, 1995). The Dahongyu Formation is mainly supratidal clastic rocks, with lesser carbonate rocks, lavas, and breccia.

15.4.2 Jixian Period (1.6–1.4 Ga)

Sedimentary sequences of the Jixian System can be divided into two parts: the lower part contains neritic facies with mainly carbonaceous rocks, and the upper part contains tidal–littoral facies with clastic rocks (Fig. 15.16). The carbonates formed mainly in the Xiong'er, Yanliao, and Zhaertai–Bayan Obo rifts.

The Jixian System in the Xiong'er Rift can be divided into the Longjiayuan, Xunjiansi, Duguan, and Fengjiawan formations that constitute a regressive sedimentary sequence (Li 1989). This sedimentary sequence contains stromatolite-bearing dolomite at the bottom and grades into debris dolomite and mud-sized crystalline dolomite upward, with wavy bedding, lenticular bedding, and coarse to fine laminae increasing in abundance. The Jixian System in the Yanliao Rift comprises the Gaoyuzhuang, Yangzhuang, Wumishan, Hongshuizhuang, and Tieling formations. The Gaoyuzhuang Formation is composed mainly of dolomite, in which the content of chert increases toward the ancient continent, and which grades into a coastal–neritic chert-bearing dolomite facies. In the Yangzhuang Formation, the sedimentary rocks are dominated by purplish-red argillaceous dolomite of the drought lagoon facies, which is uniformly thin across the lateral extent of the formation. The argillaceous dolomite is characterized by wave cross-stratification and ripple marks containing pseudomorphic halite crystals. The sedimentary environment grades from coastal–neritic to coastal–neritic sandstone–mudstone facies toward the ancient continent. The Wumishan Formation is dominated by sediments of the neritic dolomite facies, and is laterally continuous. The dolomite contains abundant stromatolites and microfossils of ancient plants. The different structural patterns of the stromatolites suggest hydrodynamic conditions of the sub-neritic facies. This dolomite grades into the coastal–neritic chert-bearing dolomite facies (Wen 1989). The sediments in the lower part of the Hongshuizhuang Formation are mainly celadonite-bearing shale and dolomite, and in particular, celadonite-bearing gray-black shale. The horizontal bedding and dispersed pyrite in the shale suggest a submarine environment with a flat terrain, a stable water body, a lack of coarse debris, and strong reducing conditions. The sediments in the Tieling Formation are mainly dolomite and dolomitic limestone with abundant stromatolites. These observations indicate a flat terrain, a warm climate, and flourishing algae.

15.4.3 Building Period (1.4–1.0 Ga)

The strata of the lower Xiamaling Formation in the Yanliao Rift record a sedimentary environment alternating between intertidal sand flat, intertidal mud–sand flat, and supratidal mud flat conditions (Fig. 15.17). In the Shuiyan Village section in Long County, on the southwestern margin of the Ordos Basin, 0.5-m-thick remnants of quartz sandstone are preserved on top of the argillaceous dolomite of the Fengjiawan Formation of the Jixian System. The sandstone contains wave structures and conformably overlies the sediments of the Fengjiawan Formation. The Fengjiawan Formation correlates with the section of the Xiamaling Formation exposed in the Yanliao Rift; its sedimentary environment is interpreted as intertidal sand flat facies. The Bi'telu Formation is exposed in the Zhaertai–Bayan Obo Rift System at the northern margin of the North China Craton. This formation is equivalent to the Xiamaling Formation in stratigraphic age, and is inferred to have been deposited in an intertidal mud–sand-flat setting.

15.4.4 Qingbaikou Period (1.0–0.78 Ga)

The sedimentary sequences of the Qingbaikou System can be divided into two parts: the lower part is tidal flat–coastal facies sediment that consists mainly of clastic rocks, and the upper part is neritic facies sediment dominated by carbonate rocks (Fig. 15.18). These sediments occur mainly in the Yanliao Rift, the Xiong'er Rift, and in the Langshan area, in east Liaoning Province and west Shandong Province. Strata in the Yanliao Rift corresponding to this sedimentation stage include the Changlongshan Formation and the Jing'eryu Formation. The sediments of the Changlongshan Formation are mainly a series of terrigenous clastic rocks consisting of sandstone, siltstone, and mudstone of the tidal flat–coastal facies. There is no clear spatial differentiation across the facies; however, this formation clearly onlaps the surrounding area. There was continuous deposition from the Jing'eryu Formation to the Changlongshan Formation. The boundary between these two formations is a layer of chlorite-bearing sandstone, which suggests a neritic facies

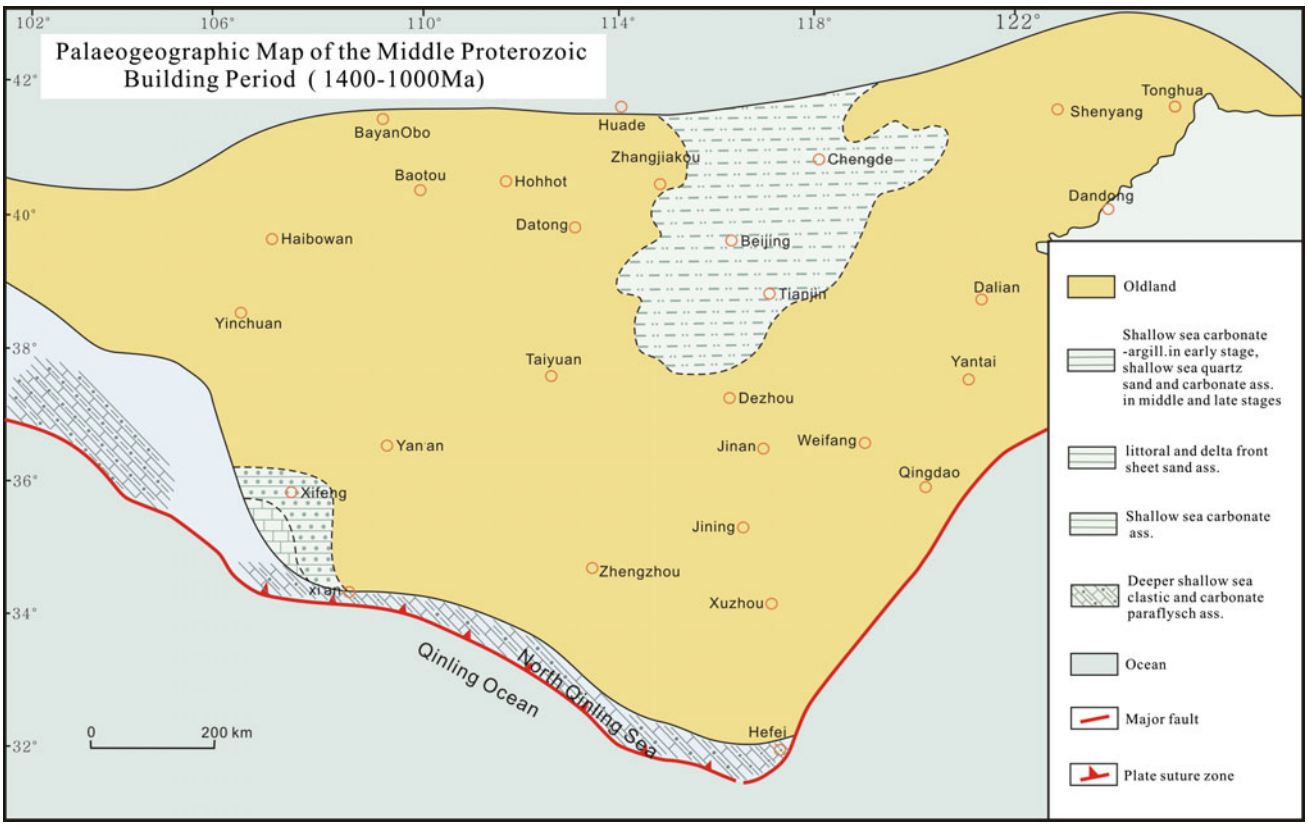

Fig. 15.17 Lithofacies paleogeography of the Building Period (1400–1000 Ma) in the North China Craton (modified after Wang 1985)

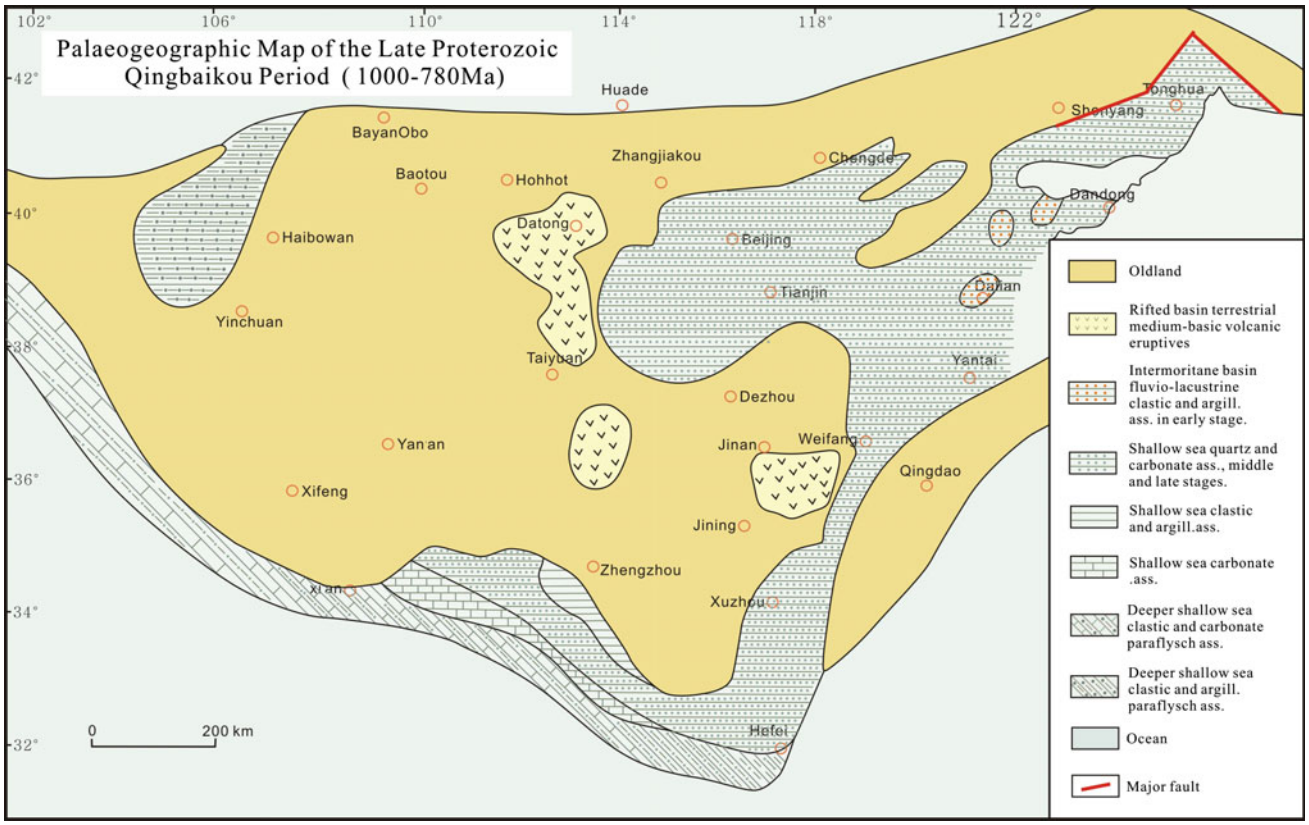

Fig. 15.18 Lithofacies paleogeography of the Qingbaikou Period (1000–780 Ma) in the North China Craton (modified after Wang 1985)

sedimentary environment. The depositional features of the Jing'eryu Formation include limited high-energy sedimentary marks and neritic carbonate rocks that formed under low-energy conditions (Zhou et al. 2006).

Strata of the Xiong'er Rift correlate with the Shibeigou Formation and can be divided into two sections: the lower section is a series of tidal flat–coastal facies sediments consisting primarily of silty slate, and the upper section is a series of neritic facies sediments consisting primarily of carbonate rocks.

The Langshan Group in the Langshan area can be divided into four lithologic members. The first member grades from quartz sandstone to phyllite, and then to marl. These changes indicate sea-level rise. There is an overall shift from coastal facies to neritic carbonate facies. The second member is dominated by crystalline limestone, which suggests that the water body was deep and had a low supply of terrigenous debris, whereas the isolated quartz sandstone and sandy slate in this member indicate that the sedimentary environment was intermittently agitated. The appearance of basalt in this member is a result of volcanic activity, which could also be the cause of the turbulence in the sedimentary environment. The overlying third member consists mainly of carbonaceous slate and sandy slate, indicating that the water body shallowed slightly and received terrigenous clastic input. The abundance of quartz–mica schist, quartzite, and marble in the uppermost fourth member indicates that the sedimentary environment changed from neritic shelf facies to coastal facies. In general, the sedimentary section of the Langshan Group suggests the evolution of the sedimentary environment from coastal facies to neritic shelf facies, and is a typical transgressive section.

15.4.5 Nanhua Period (780–635 Ma)

The distribution of the Nanhua System is sparse, exposed mainly in the Xuhuai area in the east of the NCC. The lower part of the system is a series of tidal flat–coastal facies sediments consisting primarily of clastic rocks, and the upper part is a series of neritic facies sediments consisting primarily of carbonate rocks. The formation shows a gradual sea-level rise from bottom to top (Fig. 15.19). Taking the Xuhuai area as an example, the strata of the sedimentary facies in this area include the Jiayuan, Zhaowei, Niyuan, Jiudingshan, Zhangqu, Weiji, Shijia, Wangshan, and Jinshanzhai formations. The Jiayuan Formation is a series of clastic rocks of the tidal flat facies, is dominated by siltstone. The Zhaowei and Jinshanzhai formations comprise carbonate rocks of the neritic facies.

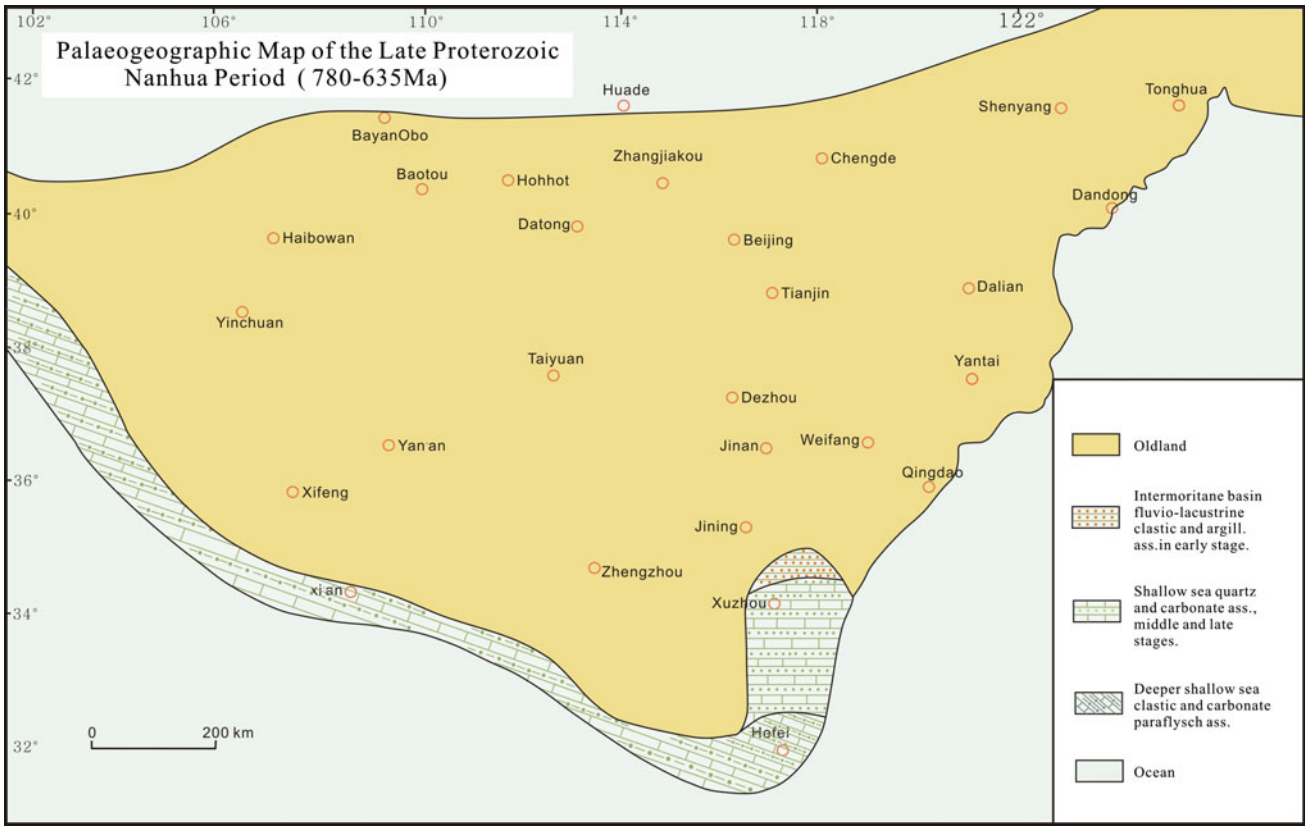

Fig. 15.19 Lithofacies paleogeography of the Nanhua Period (780–635 Ma) in the North China Craton (modified after Wang 1985)

15.4.6 Sinian Period (635–541 Ma)

In the NCC, Sinian tillite occurs mainly in the area from Huoqiu in An'hui Province, through the Linru, Lingbao, and Yiyang areas of He'nan Province, and Luonan and Liquan areas of Shanxi Province, to the middle part of the Helan Mountains in Ningxia Province and the Longshou Mountains in Gansu Province (Fig. 15.20). All of the Qingbaikou System underlying the tillite has been eroded. Phosphorus-containing sandstone of the Lower Cambrian overlies the tillite. There are two main types of tillite. The first is typified by the tillite of Linru, He'nan Province and Luonan, Shanxi Province, which has mauve to gray-yellow cement, with muddy moraine conglomerate, gravel-bearing moraine laminae, and evidence of glacial erosion. The second type is represented by the middle part of the Helan Mountains in the west of An'hui Province. These rocks have a mainly calcareous and dolomitic cement, are gray to dark gray, and show fewer traces of glacial erosion. The differences between these two tillites suggest that they formed in different sedimentary environments. The former type formed from offshore deposition by a continental glacier, and is characterized by both the sedimentary features of continental glaciers and microfossils of ancient marine plants. In contrast, the latter is a mixture of glacio-fluvial and carbonate deposition in the deep sea (Gu 1982).

15.5 Meso-Neoproterozoic Tectonic Framework and Sedimentary Evolution of the NCC

According to the sedimentary characteristics and magmatic events at different stages of its tectonic evolution, the tectonic events of the NCC can be summarized into five stages: (1) continental rift in the early Mesoproterozoic, (2) passive continental margin in the middle Mesoproterozoic, (3) active continental margin in the late Mesoproterozoic, (4) block amalgamation at the end of the Mesoproterozoic, and (5) rift reactivation in the Neoproterozoic (Fig. 15.21).

15.5.1 Continental Rift in the Early Mesoproterozoic

The amalgamation of the NCC has parallels with the Lüliang movement at the end of the Paleoproterozoic (Bai et al. 1993; Zhao 1993). A geochronological study of the

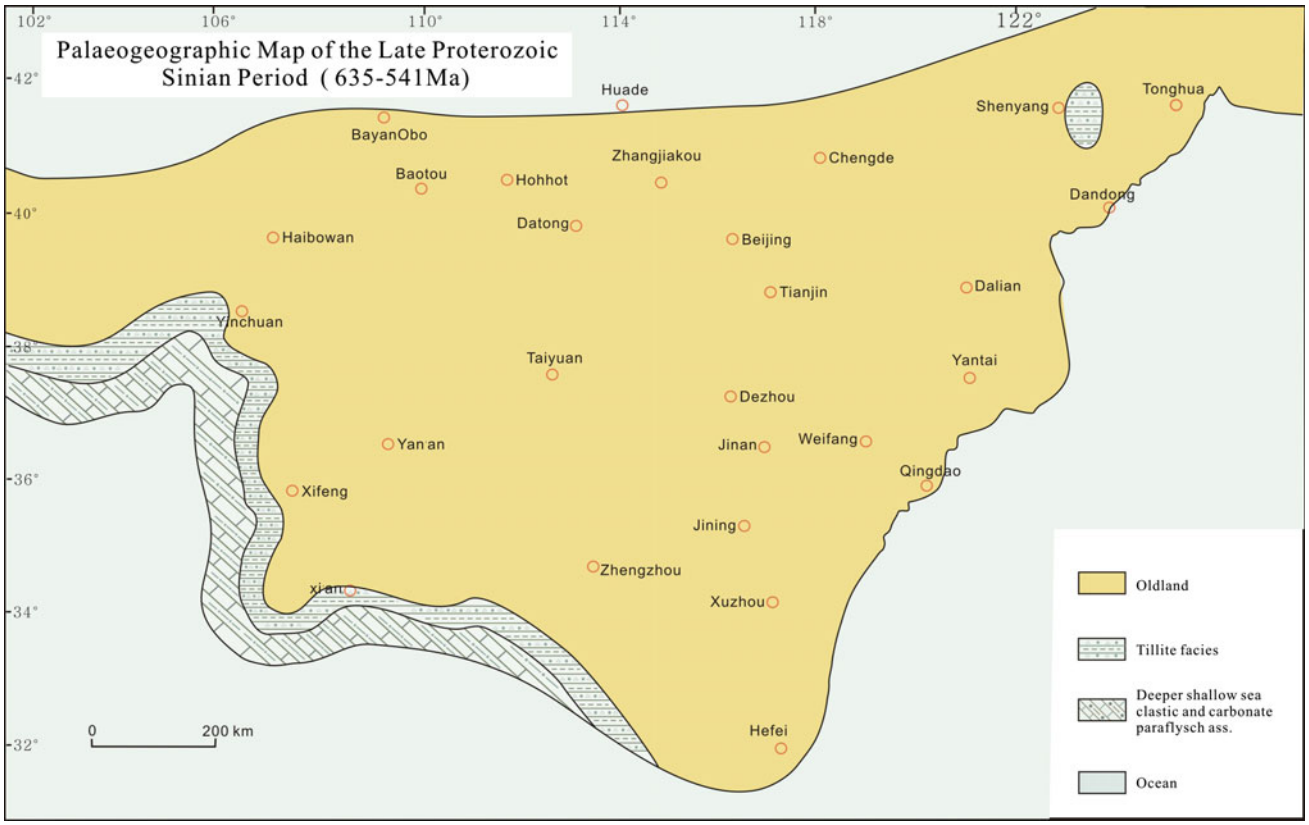

Fig. 15.20 Lithofacies paleogeography of the Sinian Period (780–635 Ma) in the North China Craton (modified after Wang 1985)

formation and metamorphism of the Precambrian basement indicates that this activity occurred at ca. 1.8 Ga (Zhai and Santosh 2011; Zhai and Santosh 2011, Zhai et al. 2014). After the Lüliang movement, Mesoproterozoic rift systems formed, inclusing the Xiong'er, Yanliao, and Zhaertai–Bayan Obo rifts.

At the beginning of the evolution of the Yanliao Rift System in the early Mesoproterozoic, the area was dominated by fluvial facies sediments of conglomerate, glutenite, and quartz graywacke, with a low degree of maturity. There is a set of thick conglomerate layers at the bottom of the Changzhougou Formation, in the Changcheng System. The conglomerate occurs on both sides of the main rift trough in a fan shape, and pinches out toward the interior of the rift. The gravels are well rounded, the maturity of the matrix is low, and the largest flat surfaces of the gravels, indicators of the paleocurrent direction, point toward the center of the main trough from both sides of the rift (Huang 2006). Immature glutenite and quartz graywacke in the main trough indicate rapid transportation and fast deposition. After the intermediate depositional phase of the Changzhougou Formation, a transgressive facies developed from NE to SW, and flat littoral sheet sands were deposited. The sands changed to tidal flat sediments at the end of deposition of the Changzhougou Formation. In the early depositional stage of the Chuanlinggou and Tuanshanzi formations, tidal flats expanded along both sides of the rift trough. Because most of the depositional areas were in a flat basin, there was a low supply of clastics, and intertidal and supratidal mud flat or carbonate flat sedimentation was dominant. Black shale and ferrocarbonates (hundreds of meters thick) were deposited in the center of the rift trough, and represent a closed to semi-closed reducing environment. With development of the rift, the Tuanshanzi–Dahongyu Formation was deposited, and volcanoes erupted in Pinggu, Jixian, and other sites. Periods of tectonic activity alternated with periods of relative tectonic stability. The depositional phases of the Changzhougou, Chuanlinggou, and Dahongyu formations represent tectonically active environments, whereas deposition in the Tuanshanzi Formation represents tectonic dormancy.

The Xiong'er Rift System records abundant early-stage volcanic activity and contains thick lava flows with a few interlayered thin sedimentary and volcaniclastic rocks. These volcanic rocks include basalt, basaltic andesite, andesite, dacite, and rhyolite, and can be classified as a bimodal tholeiitic series (Sun et al. 1985). The formation age of the Xiong'er Group volcanic rocks is generally agreed to be 1750–1800 Ma, with a peak at 1780 Ma. After the deposition of the Xiong'er Group, conglomerates at the bottom of the Yunmengshan Formation, which contain quartz gravels,

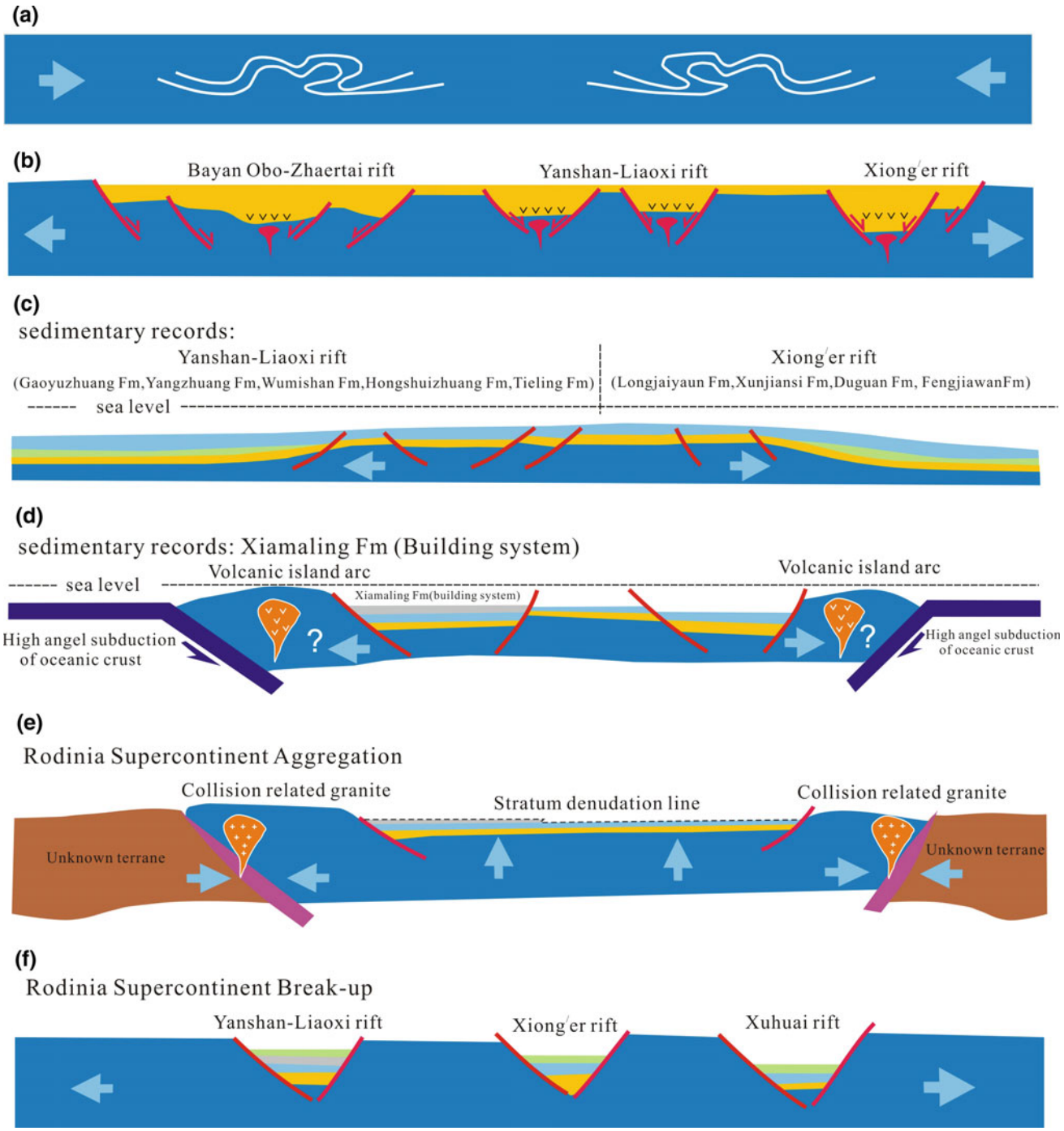

Fig. 15.21 Meso-Neoproterozoic tectonic evolution of the NCC. **a** Formation of North China Craton (1900 Ma). **b** Continental rifting stage (Changcheng system and its equivalents). **c** Passive continental margin stage. **d** Active continental margin stage. **e** Extrusion uplift stage (1200–900 Ma). **f** Continental rifting stage (Qingbaikou system and its equivalents)

were deposited. The clasts are well rounded and the sediments are low maturity, indicating rapid sedimentation. At this time, the Xiong'er Rift System evolved in a similar manner to the Yanliao Rift System. Deposition of the quartz sandstone of the Yunmengshan Formation and the shale of the Cuizhuang Formation occurred in three sandstone–shale sedimentary cycles and records fluctuations in tectonic activity. During the late depositional stage of the Beidajian

Formation, carbonates developed on its top, and these have similar sedimentary characteristics to the Tuanshanzi Formation in the Yanshan area.

Deposition of the Zhaertai–Bayan Obo Rift System was controlled by large-scale E–W-trending syn-tectonic basement fault. Sag sedimentation is typical of the Shujigou Formation, which is composed mainly of coarse clastics of the terrigenous delta facies. In the delta facies, the lithology is stable. Basaltic rocks are present in this formation (Shen et al. 2009). Controlled by the rift-related faulting during the deposition of the Zenglongchang Formation, sedimentation changed from transgressional to regressional, and epeiric carbonate platform sedimentation developed in an E–W direction. During the deposition of the Agulugou Formation, the rift-related faulting became more intense, semi-closed estuarine facies developed, and hydrothermal sedimentary sulfides were deposited in E–W-trending grabens outside the carbonate platform. At the same time, the movement of syn-sedimentary faults generated submarine volcanic eruptions, which provided enough mineralizing fluid to form large- to medium-sized polymetallic ore deposits.

15.5.2 Passive Continental Margin in the Middle Mesoproterozoic

The NCC entered a continental break-up stage in the Changcheng Period, and then became a passive continental margin in the early Jixian Period. The intensity of crustal movement decreased markedly in the Jixian Period. This period is characterized by marked reductions in volcanic activity and sedimentation rate, with the maximum sedimentation rate falling from 38.28 to 18.98 m/Ma, and the geometry of the basin changed from a linear graben to a short sag basin (Wen 1989). Large-scale transgression resulted in onlap of the Gaoyuzhuang Formation in the Yanliao Rift System and the Longjiayuan Formation in the Xiong'er Rift System onto metamorphic rocks of the Changcheng System. The neritic facies, which mostly consists of carbonate, developed with a geometry that changed from wedge to planar over time (Huang 2006). On the one hand, these carbonates were deposited in a basin where the sedimentary facies changed systematically from the margin to center of the basin. On the other hand, internal sedimentary structures indicate that the basin was very stable. Soft-sediment deformation is evident in the Wumishan Formation at the western margin of the Yanliao Rift System, in the Halahuogete Formation of the Bayan Obo Group at Bainaimiao in the Zhaertai–Bayan Obo Rift System, and in the Xunjiansi Formation at Qishan Mountain, on the southwestern margin of the Ordos Block (Qiao and Gao 1999; Zhang et al. 2007a; Jiao et al. 2011a, b). Soft-sediment deformation is an important indicator of paleo-earthquakes (McCaplin 1996; Obermeier 1996). All these contemporaneous strata can be compared laterally. Paleo-earthquake structures developed in different rift systems at the same time during the deposition of the Wumishan Formation. These observations indicate that an intense rifting event took place across the NCC at this time. There is currently consensus that the Columbia supercontinent amalgamated at ~1.8 Ga and broke up at 1.8 Ga or a little later (Wilde et al. 2002; Zhao et al. 2002b, 2009a, b). Therefore, the early to middle Mesoproterozoic strata in the NCC likely record sedimentary processes during the break-up of this supercontinent.

15.5.3 Active Continental Margin in the Late Mesoproterozoic

The tectonic setting of the NCC changed from a passive continental margin to an active continental margin during the Mesoproterozoic (Fig. 15.21). The sedimentary record of this stage is sparse, with only a few remnants preserved, such as the Xiamaling Formation (building system) in the Yanliao Rift System, the sandstone above the Fengjiawan Formation on the southwestern margin of the Ordos Basin, and the Bilute Formation in the Zhaertai–Bayan Obo Rift System. Among these remnants, the Xiamaling and Bilute formations (building system) are both dark shales deposited in deep water. However, the Xiamaling Formation contains bentonite, whereas the Bilute Formation does not. A 0.5-m-thick layer of quartz sandstone onlaps the carbonate of the Fengjiawan Formation of the Jixian System at the southwestern margin of the Ordos Basin. The abyssal shale, which typically overlies the quartz sandstone, had been eroded. This quartz sandstone layer is equivalent to the basal unit of the Xiamaling and Bilute formations. According to Nb–Y ratios and the inferred protoliths, the volcanic layers likely formed in an island arc environment at an active continental margin (Su et al. 2006), or in a back-arc basin behind a volcanic island arc (Qiao et al. 2007). The Mesoproterozoic Bainaimiao Group exposed near the Bainaimiao Temple in Inner Mongolia records a subduction-related volcanic series (Nie et al. 1995; Liu 1997). There are several diabase dike swarms (U–Pb age of 1365 Ma) at the junction of the provinces of Shanxi, Hebei, and Inner Mongolia. The chemical characteristics of the dikes indicate that the NCC underwent intense back-arc extension at ca. 1365 Ma (Zhang et al. 2009). Therefore, during the period of deposition of the Xiamaling Formation, the circum-NCC volcanic eruptions were contemporaneous with amalgamation of the Rodinia supercontinent. The presence of bentonite in the Xiamaling Formationis an indicator of volcanic eruptions in an intraplate syn-collisional setting (Su et al. 2006). This volcanic activity likely records the collision of the NCC with neighboring blocks and plates during the formation of Rodinia.

15.5.4 Block Collision at the End of the Mesoproterozoic

There is a discontinuity of 200–300 Myr between the Mesoproterozoic and Neoproterozoic strata. The discontinuity may correlate either with a lack of sediment supply or erosion after sediment deposition. If sedimentation was absent during this interval, the proposed paleo-environment of the NCC in the late Mesoproterozoic needs to be reconsidered. If the strata were eroded after deposition, this event needs to be investigated further to determine the transportation direction of the denuded materials, the time of erosion, and the tectonic setting. Previous research suggests that the northern margin of the NCC changed from an active continental margin to a collisional orogen at ca. 1.1 Ga. During the collisional orogeny, S-type granites formed and the sediments were deformed and metamorphosed (Zhang 2004). The ages of deformation and metamorphism have been constrained to 1054–1036 Ma, based on radiogenic isotope studies. For example, marble in the Weijiagou Group gives a Rb–Sr isochron age of 1036 Ma (Liu et al. 1999), quartz–mica schist and slate from Mesoproterozoic strata in the Langshan area give a Rb–Sr isochron age of 1198 Ma (Wang and Yang 1993), and Rb–Sr isochron ages for the Seluo Group have a range of 1054–1139 Ma. This combined evidence indicates that the paleo-Asian oceanic plate subducted beneath the northern margin of the NCC, accompanied by intense orogenic activity, after the deposition of the Xiamaling Formation. Suturing and ophiolite formation in the Wenduermiao area occurred during these orogenic subduction and collision events. In the North Qinling Orogenic Belt at the southern margin of the NCC, Neoproterozoic magmatism occurred primarily during the compressional events between 980 and 870 Ma. Extension started at ca. 840 Ma. The ca. 940 Ma highly deformed S-type syn-collisional granites, ca. 880 Ma weakly deformed I-type post-collisional granites, and ca. 840 Ma A-type intraplate alkaline rocks are the products of this Neoproterozoic magmatism (Liu et al. 2013). The S-type syn-collisional granites indicate that the southern margin of NCC underwent subduction and collision at ca. 940 Ma. Based on previous research, we infer that the southern and northern margins of the NCC both underwent intense subduction and collision at 1.1–0.94 Ga. The collision-related orogenic processes caused the erosion of late Mesoproterozoic strata in the NCC. The subduction and collision are suggested to be closely related to the assembly of the Rodinia supercontinent.

15.5.5 Rift Evolution in the Neoproterozoic

At the beginning of the Neoproterozoic, rifts started to develop in the NCC. In the Yanshan area, the Changlongshan Formation was deposited under shallow-water conditions. The carbonate of the Jingeryu Formation was deposited in a low-energy environment. There is no depositional hiatus between the Changlongshan and Jingeryu formations. The transgression increased in extent and the water became deeper over time. All these characteristics indicate that regional extension occurred at this time. Ultrabasic rocks scattered from Zhangjiakou to Chengde in the Yanshan area, and ultrabasic rocks in the Luojianggou area, yield Sm–Nd isochron ages of 881 Ma (Chen et al. 1991). The contact between the Shibeigou Formation and the underlying Fengjiawan Formation is a parallel unconformity, marked by a paleo-weathering surface. The rock types of the Shibeigou Formation indicate that the water deepened at this time, in response to regional extension. In the Langshan–Bayinnuoergong area of the northwestern NCC, the Neoproterozoic Langshan Group hosts a set of epimetamorphic rocks. The protolith was a sedimentary clastic and carbonate formation with minor volcanic interlayers that formed along the rift of the paleo-continental margin. The zircons from the volcanic interlayers give a mean U–Pb age of 804 ± 5 Ma (Hu et al. 2014). The chemical characteristics of the volcanic rocks, such as depletion in heavy rare earth elements, enrichment in light rare earth elements, a substantial negative Eu anomaly, enrichment in high field strength elements, and relative depletion in large ion lithophile elements, indicate an extensional rift volcanic environment (Peng et al. 2010). Some augen and banded gneisses occur in the western part of the Alxa terrane. Previous researchers interpreted these as the metamorphic basement of the Neoarchean–Paleoarchean Alxa Group. However, recent research has shown that the U–Pb zircon ages of the deformed orthogneisses range from 904 to 926 Ma; therefore, the protolith of the gneiss formed during the Neoproterozoic rifting period in the Alxa terrane. The rifting events in the Neoproterozoic NCC developed simultaneously with the break-up of Rodinia.

15.6 Conclusions

Based on recent high-precision dating, we have reanalyzed the Meso-Neoproterozoic sequences from different rift systems of the NCC, to reconstruct the lithofacies paleogeography of the Changcheng, Jixian, Qingbaikou, and Sinian systems, subdivide the sequences for several different sedimentary evolution phases, and re-evaluate the tectonic setting at different geological periods. Our conclusions are as follows.

1. In the early Mesoproterozoic, the NCC was in a rift stage of continental evolution. The Changcheng System is composed mainly of immature conglomerate, glutenite, quartz graywacke, volcanic rocks, and volcaniclastic

rocks. The formation and evolution of the continental rift were related to break-up of the Columbia supercontinent.
2. In the middle Mesoproterozoic, the NCC was a passive continental margin. A set of neritic-facies carbonatite sediments was continuously deposited in the trough of the rift and onlapped the ancient continent. The sedimentation in this stage records the final break-up of the Columbia supercontinent.
3. In the late Mesoproterozoic, the southern and northern margins of the NCC changed to an active continental margin, and back-arc extensional basins formed. The representative strata are the abyssal facies dark shale of the Xiamaling Formation, with bentonite interlayers in the Yanliao area, and massive diabase dikes intruded ito Mesoproterozoic strata in the NCC.
4. Several syn-collisional S-type granites were emplaced after the deposition of the Xiamaling Formation in the late Mesoproterozoic, related to intense subduction and collision along the southern and northern margins of the NCC. The collisional orogeny resulted in discontinuous sedimentary sequences in the NCC and lasted for 200–300 Myr.
5. In the Neoproterozoic, a continental rift started to develop within the NCC. The typical sedimentation in this period is transgressional sequences of the Changlongshan Formation and neritic carbonate platform sediments of the Jingeryu Formation. This extensional event may have been related to break-up of the Rodinia supercontinent.

Acknowledgments This work was funded by the National Basic Research Program of China (2012CB416604), the National Natural Science Foundation of China (41472211, 91114204), and the Geological Investigation Project of the China Geological Survey (1212011220259, DD20160060).

References

Bai, J., Huang, X.-G., Dai, F.-Y., & Wu, C.-H. (1993). *The precambrian evolution of China* (pp. 65–79). Beijing: Geological Publishing House (in Chinese).

Chen, L., Sun, Y., Diwu, C.-R., & Wang, H.-L. (2009). Crust formation in the Ordos block: Constraints from detrital zircons from Ordovician and Permian sandstones. In *Abstract with program of international discussion meeting on continental geology and tectonics* (p. 15). Xi'an: Northwest University Press.

Chen, S.-H., Liu, D.-R., Bao, Z.-W., Zhu, N.-J., Mao, C.-X., & Zhu, B.-Q. (1991). Emplacement ages and evolution of several ultrabasic rock belts on the Northern Margin of the North China Platform. *Geochimica, 2*, 128–133 (in Chinese).

Cope, T.-C. (2003). *Sedimentary evolution of the Yanshan fold-thrust belt, Northeast China* (pp. 1–230). Califonia: Stanford University.

Cui, M.-L., Zhang, B.-L., Peng, P., Zhang, L.-C., Shen, X.-L., Guo, Z.-H., & Huang, X.-F. (2010). Zricon/Baddeleyite U-Pb dating for the Paleo-proterozoic intermediate-acid intrusive rocks in Xiaoshan Mountains, west of Henan Province and their constrains on the age of the Xiong'er volcanic Province. *Acta Petrologica Sinica, 26*, 1541–1549 (in Chinese).

Cui, M.-L., Zhang, B.-L., & Zhang, L.-C. (2011). U-Pb dating of baddeleyite and zircon from the Shizhaogou diorite in the southern margin of the North China Craton: Constraints on the timing and tectonic setting of the Paleoproterozoic Xiong'er group. *Gondwana Research, 20*, 184–193.

Dalziel, I.-W.-D. (1991). Pacific margins of Laurentia and east Antarctica-Australia as a conjugate rift pair: Evidence and implications for an Eocambrian supercontinent. *Geology, 19*, 598–601.

Dalziel, I.-W.-D. (1997). Overview: Neoproterozoic-Paleozoic geography and tectonics: Review, hypothesis, environmental speculation. *Geological Society of America Bulletin, 109*, 16–42.

Diwu, C.-R., Sun, Y., Yuan, H.-L., Wang, H.-L., Zhong, X.-P., & Liu, X.-M. (2008). U-Pb ages and Hf isotopes for detrital zircons from quartzite in the Paleoproterozoic Songshan Group on the southwestern margin of the North China Craton. *Chinese Science Bulletin, 53*, 2828–2839.

Dong, W.-M., Shen, Y., Zhou, H.-R., & Cui, X.-S. (1999). Application of sequence stratigraphy to Precambrian strata—A case study on the Sinian in western Henan province. *Acta Sedimentologica Sinica, 17*, 742–746 (in Chinese).

Gao, L.-Z., Zhang, C.-H., Liu, P.-J., Ding, X.-Z., Wang, Z.-Q., & Zhang, Y.-J. (2009). Recognition of Meso- and Neoproterozoic stratigraphic framework in North and South China. *Acta Geoscientica Sinica, 30*, 433–446 (in Chinese).

Gao, L.-Z., Zhang, C.-H., Shi, X.-Y., Zhou, H.-R., & Wang, Z.-Q. (2008a). Mesoproterozoic age for Xiamaling formation in North China Plate indicated by zircon SHRIMP dating. *Science Bulletin, 53*, 2665–2671.

Gao, L.-Z., Zhao, T., Wan, Y.-S., Zhao, X., Ma, Y.-S., & Yang, S.-Z. (2005). Zircon SHRIMP U-Pb age of the Yuntaishan Precambrian metamorphic basement, Jiaozuo, Henan, China. *Geological Bulletin of China, 24*, 1089–1093 (in Chinese).

Gao, S., Rudnick, R.-L., Yuan, H.-L., Liu, X.-M., Liu, Y.-S., Xu, W.-L., et al. (2004). Recycling lower continental crust in the North China Craton. *Nature, 432*, 892–897.

Gao, W., Zhang, C.-H., Gao, L.-Z., Shi, X.-Y., Liu, Y.-M., & Song, B. (2008b). Zircon SHRIMP U-Pb age of rapakivigran in Miyun, Beijing, China and its tectono-stratigraphic implications. *Geological Bulletin of China, 27*, 793–798 (in Chinese).

Gao, W., Zhang, C.-H., & Wang, Z.-Q. (2011). The discovery of large-scale acanthomorphic acritarch assemblage on the southern margin of North China old land and an analysis of its paleogeographic environment. *Geology in China, 38*, 1232–1243 (in Chinese).

Geng, Y.-S. (2009). *The instructions of the early Precambrian in China*. Beijing: The Precambrian Stratigraphic Meeting (in Chinese).

Geng, Y.-S., Liu, F.-L., & Yang, C.-H. (2006). Magmatic event at the end of the Archean in eastern Hebei Province and its geological implication. *Acta Geologica Sinica, 80*, 819–833.

Gu, Q.-C. (1982). Late Precambrian Tillite in the Helan Mountains. *Journal of Stratigraphy, 6*, 156–157 (in Chinese).

Guo, J.-H., Sun, M., Chen, F.-K., & Zhai, M.-G. (2005). Sm-Nd and SHRIMP U-Pb zircon geochronology of high-pressure granulites in the Sanggan area, North China Craton: Timing of Paleoproterozoic continental collision. *Journal of Asian Earth Sciences, 24*, 629–642.

Guo, J.-H., Zhai, M.-G., & Xu, R.-H. (2001). Timing of the granulite facies metamorphism in the Sanggan area, North China Craton: Zircon U-Pb geochronology. *Science in China (Series D), 44*, 1010–1018.

Hoffman, P.-F. (1991). Did the breakout of Laurentia turn Gondwanaland inside-out? *Science, 252*, 1409–1412.

Hoffmann, K.-H., Condon, D.-J., Bowring, S.-A., & Crowley, J.-L. (2004). U-Pb zircon date from the Neoproterozoic Ghaub formation, Namibia: Constrains on Marinoan glaciation. *Geology, 32*, 815–820.

Hu, B., Zhai, M.-G., Peng, P., Liu, F., Diwu, C.-R., Wang, Z.-H., & Zhang, H.-D. (2013). Late Paleoproterozoic to Neoproterzoic geological events of the North China Craton: Evidences from LA-ICP-MS U-Pb geochronology of detrital zircons from the Cambrian and Jurassic sedimentary rocks in Western Hills of Beijing. *Acta Petrologica Sinica, 29*, 2508–2536 (in Chinese).

Hu, J.-M., Gong, W.-B., Wu, S.-J., Liu, Y., & Liu, S.-C. (2014). LA-ICP-MS zircon U-Pb dating of the Langshan Group in the northeast margin of the Alax block, with tectonic implications. *Precambrian Research, 255*, 756–770.

Huang, X.-G. (2006). Tectonic evolution of the Meso-Neoproterozoic sedimentary basin in Yanshan range. *Geological Survey and Research, 29*, 263–270 (in Chinese).

Jiao, D.-Y., Cui, X.-H., & Su, H.-W. (2011a). Seismites from Bayan Obo group in the Bainaimiao area of inner Mongolia and their tectonic implications. *Geoscience, 25*, 503–509 (in Chinese).

Jiao, P.-X., You, W.-F., Cao, X.-T., Hu, Y.-X., & Xie, C.-R. (2011b). Redefining of the Hanmushan Group in Longshoushan, central-western Gansu province. *Geological Bulletin of China, 30*, 1228–1232 (in Chinese).

Karlstrom, K.-E., Ahall, K.-I., Harlan, S.-S., Williams, M.-L., Mclelland, J., & Geissman, J.-W. (1997). Long-lived (1.8–1.0 Ga) convergent orogeny in southern Laurentia, its extensions to Australia and Baltica, and implications for refining Rodinia. *Precambrian Reseach, 111*, 5–30.

Kusky, T.-M., & Li, J.-H. (2003). Paleoproterozoic tectonic evolution of the North China Craton. *Journal of Asian Earth Sciences, 22*, 383–397.

Li, H.-K., Lu, S.-N., Li, H.-M., Sun, L.-X., Xiang, Z.-Q., Geng, J.-Z., & Zhou, H.-Y. (2009). Zircon and beddeleyite U-Pb precision dating of basic rock sills intruding Xiamaling Formation, North China. *Geological Bulletin of China, 28*, 1396–1404 (in Chinese).

Li, H.-K., Su, W.-B., Zhou, H.-Y., Geng, J.-Z., Xiang, Z.-Q., Cui, Y.-R., et al. (2011). The base age of the Changchengian System at the northern North China Craton should be younger than 1670 Ma: Constraints from zircon U-Pb LA-MC-ICPMS dating of a granite-porphyry dike in Miyun County, Beijing. *Earth Science Frontiers, 18*, 108–120 (in Chinese).

Li, H.-K., Zhu, S.-X., Xiang, Z.-Q., Su, W.-B., Lu, S.-N., Zhou, H.-Y., et al. (2010). Zircon U-Pb on tuff bed from Gaoyuzhuang Formation in Yanqing, Beijing: Further constraints on the new subdivision of the Mesoproterozoic stratigraphy in the northern North China Craton. *Acta Petrologica Sinica, 26*, 2131–2140 (in Chinese).

Li, H.-M., Li, L.-X., Zhang, Z.-C., Santosh, M., Liu, M.-J., Cui, Y.-H., et al. (2014a). Alteration of the Damiao anorthosite complex in the northern North China Craton: Implications for high-grade iron mineralization. *Ore Geology Review, 57*, 574–588.

Li, J.-H. (1991). Supercontinent cycle in the Precambrian and its implication for the plate tectonics. *Earth Science Frontiers, 5*, 141–151 (in Chinese).

Li, J.-H., & Kusky, T.-M. (2007). A late Archean foreland fold and thrust belt in the North China Craton: Implications for early collisional tectonics. *Gondwana Research, 12*, 47–66.

Li, S.-Z., Guo, L.-L., Xu, L.-Q., Somerville, I. D., Gao, X. Z., Yu, S., et al. (2015). Coupling and transition of Meso-Cenozoic intracontinental deformation between the Taihang and Qinling Mountains. *Journal of Asian Earth Sciences*. doi:10.1016/j.jseaes.2015.04.011

Li, W.-H. (1989). The Jixianian carbonate tidal flat sediments on the southern margin of the North China platform (Shanxi). *Journal of Palaeogeography, 42*, 20–26 (in Chinese).

Li, X.-H., Chen, F.-K., Guo, J.-H., Li, Q.-L., Xie, L.-W., & Siebel, W. (2007). South China provenance of the lower-grade Penglai Group north of the Sulu UHP orogenic belt, eastern China: Evidence from detrital zircon ages and Nd-Hf isotopic composition. *Geochemical Journal, 41*, 29–45.

Li, Z.-H., Dong, S.-W., & Qu, H.-J. (2014b). Timing of the initiation of the Jurassic Yanshan movement on the North China Craton: Evidence from sedimentary cycles, heavy minerals, geochemistry, and zircon U-Pb geochronology. *International Geology Review, 56*, 288–312.

Li, Z.-X., Li, X.-H., Kinny, P.-D., Wang, J., Zhang, S., & Zhou, H. (2003). Geochronology of Neoproterozoic syn-rift magmatism in the Yangtze Craton, South China and correlations with other continents: Evidence for a mantle superplume that broke up Rodinia. *Precambrian Research, 122*, 85–109.

Li, Z.-X., Li, X.-H., Zhou, H.-W., & Kinny, P.-D. (2002). Grenvillian continental collision in South China: New SHRIMP U-Pb zircon results and implications for the configuration of Rodinia. *Geology, 30*, 163–166.

Liu, B.-X., Nie, H., Qi, Y., Yang, L., Zhu, X.-Y., & Chen, F.-K. (2013). Genesis and geological significances of Neoproterozoic granitoids in the North Qinling terrain, SW Henan, China. *Acta Petrologica Sinica, 29*, 2437–2455 (in Chinese).

Liu, D.-Y., Nutman, A.-P., Compston, W., Wu, J.-S., & Shen, Q.-H. (1992). Remnants of 3800 Ma crust in the Chinese part of the Sino-Korean craton. *Geology, 20*, 339–342.

Liu, J., Zhao, Y., & Liu, X.-M. (2006a). Age of the Tiaojishan Formation volcanics in the Chengde Basin, northern Hebei Province. *Acta Petrologica Sinica, 22*, 2617–2630 (in Chinese).

Liu, S.-W., Pan, Y.-M., Li, J.-H., Li, Q.-G., & Zhang, J. (2002). Geological and isotopic geochemical constraints on the evolution of the Fuping Complex, North China Craton. *Precambrian Research, 117*, 41–56.

Liu, S.-W., Pan, Y.-M., Xie, Q.-L., Zhang, J., Li, Q.-G., & Yang, B. (2005). Geochemistry of the Paleoproterozonic Nanying granitic gneisses in the Fuping Complex: Implications for the tectonic evolution of the Central Zone, North China Craton. *Journal of Asian Earth Sciences, 24*, 643–658.

Liu, Y.-Q., Gao, L.-Z., Liu, Y.-X., Song, B., & Wang, Z.-X. (2006b). Zircon U-Pb dating for the earliest Neoproterozoic mafic magmatism in the southern margin of the North China Block. *Science Bulletin, 51*, 2375–2382.

Liu, Z.-H. (1997). *Middle Proterozoic tectonic mobile belt and mineralization in north continental margin of the North China Plateform*. Changchun: Changchun University of Science and Technology.

Liu, Z.-H., Xu, Z.-Y., & Yang, Z.-S. (1999). Establishment of the middle Proterozoic Weijiagou rock group and the geological significance in the northern margin of North China platform. *Journal of Changchun University of Science and Technology, 29*, 9–14 (in Chinese).

Lu, S.-N., Li, H.-K., Chen, Z.-H., Yu, H.-F., Jin, W., & Guo, K.-Y. (2004). Relationship between Neoproterozoic cratons of China and the Rodinia. *Earth Science Frontiers, 11*, 515–523 (in Chinese).

Lu, S.-N., Wang, H. C., & Li, H. K. (2005). Unscramble the ISC 2004 and special reference to Precambrian from 2004 to 2008. *Journal of Stratigraphy, 29*, 180–187 (in Chinese).

Lu, S.-N., Yang, C.-L., Li, H.-K., & Li, H.-M. (2002). A group of rifting events in the terminal Paleoproterozoic in the North China Craton. *Gondwana Research, 5*, 123–131.

Lu, S.-N., Zhao, G.-C., Wang, H.-C., & Hao, G.-J. (2008). Precambrian metamorphic basement and sedimentary cover of the North China Craton: A review. *Precambrian Research, 160*, 77–93.

McCaplin, J.-P. (1996). *Paleoseismology* (pp. 1–588). San Diego: Academic Press.

Mei, M.-X. (1993). Genetic types and mechanisms of the carbonate rock meter-scale cyclic sequences. *Journal of Palaeogeography, 13*, 34–45 (in Chinese).

Mei, M.-X. (1995). *Carbonate rock cycle and sequence* (pp. 1–245). Guiyang: Guizhou Science and Technology Press (in Chinese).

Mei, M.-X., Zhou, H.-R., Du, B.-M., & Luo, Z.-Q. (2000). Meso-and Neoproterozoic sedimentary sequences in Jixian, Tianjin, northern China: Division of the first-order sequences of the Cambrian strata (1800–600 Ma) and their correlation with the Phanerozoic strata. *Sedimentary Geology and Tethyan Geology, 20*, 47–59 (in Chinese).

Meng, Q.-R., Wei, H.-H., Qu, Y.-Q., & Ma, S.-X. (2011). Stratigraphic and sedimentary records of the rift to drift evolution of the northern North China craton at the Paleo-to Mesoproterozoic transition. *Gondwana Research, 20*, 205–218.

Nie, F.-J., Pei, R.-F., & Wu, L.-S. (1995). Nd- and Sr-isotope study on greenschist and granodiorite of the Bainaimiao district, Inner Mongolia, China. *Acta Geoscientia Sinica, 1*, 36–44 (in Chinese).

Niu, B.-G., He, Z.-J., Ren, J.-S., Song, B., & Xiao, W.-W. (2004). SHRIMP geochronology of volcanics of the Zhangjiakou and Yixian Formaitons, Northern Hebei Province, with a discussion on the age of the Xingpanling Group of the Great Hinggan Mountains and volcanic strata of the southeastern coastal area of China. *Acta Geologica Sinica (English edition), 78*, 1214–1228.

Obermeier, S.-F. (1996). Use of Liquefaction-induced features for paleoseismic analysis—An overview of how seismic liquefaction features can be distinguished from other features and how their regional distribution and properties of source sediment can be used to infer the location and strength of Holocene paleo-earthquakes. *English Geology, 44*, 1–74.

Peng, P. (2010). Reconstruction and interpretation of giant mafic dyke swarms: A case study of 1.78 Ga magmatism in the North China Craton. In: T. M. Kusky, M. G. Zhai, W. J. Xiao (Eds.), *The evolving continents: Understanding processes of continental growth* (Vol. 338, pp. 163–178). London: Geological Society (Special Publications).

Peng, P., Zhai, M.-G., Ernst, R.-E., Guo, J.-H., Liu, F., & Hu, B. (2008). A 1.78 Ga large igneous province in the North China Craton: The Xiong'er Volcanic Province and the North China dyke swarm. *Lithos, 101*, 260–280.

Peng, P., Zhai, M.-G., Guo, J.-H., Kusky, T., & Zhao, T.-P. (2007). Nature of mantle source contributions and crystal differentiation in the petrogenesis of the 1.78 Ga mafic dykes in the central North China Craton. *Gondwana Research, 12*, 29–46.

Peng, P., Zhai, M.-G., Li, Q.-L., Wu, F.-Y., Hou, Q.-L., Li, Z., et al. (2011). Neoproterozoic (~900 Ma) Sariwon sills in North Korea: Geochronology, geochemistry and implications for the evolutions of the south-eastern margin of the North China Craton. *Gondwana Research, 20*, 243–354.

Peng, R.-M., Zhai, Y.-S., Wang, J.-P., Chen, X.-F., Liu, Q., LV, J.-Y., et al. (2010). Discovery of Neoproterozoic acid volcanic rock in the western section of Langshan, Inner Mongolia, and its geological significance. *Chinese Science Bulletin*, *55*, 2611–2620 (in Chinese).

Polat, A., Kusky, T., Li, J.-H., Fryer, B., Kerrich, R., & Patrick, K. (2005). Geochemistry of Neoarchean (ca. 2.55–2.50 Ga) volcanic and ophiolitic rocks in the Wutaishan greenstone belt, central orogenic belt, North China Craton: Implications for geodynamic setting and continental growth. *Geological Society of America Bulletin, 117*, 1387–1399.

Qiao, X.-F., & Gao, L.-Z. (1999). Earthquake events in Neoproterozoic and Early Paleozoic and its relationship with supercontinental Rodinia in North China. *Chinese Science Bulletin, 44*, 1753–1758 (in Chinese).

Qiao, X.-F., Gao, L.-Z., & Zhang, C.-H. (2007). New idea of the Meso- and Neoproterozoic chronostratigraphic chart and tectonic environment in Sin-Korean Plate. *Geological Bulletin of China, 26*, 503–509 (in Chinese).

Qu, Y.-Q., Meng, Q.-R., Ma, S.-X., Li, L., & Wu, G.-L. (2010). Geological characteristics of unconformities in Mesoproterozoic successions in the northern margin of North China Block and their tectonic implications. *Earth Science Frontiers, 17*, 112–127 (in Chinese).

Rino, S., Kon, Y., Sato, W., Maruyama, S., Santosh, M., & Zhao, D. (2008). The Grenvillian and Pan-African orogens: World, S largest orogenies through geologic time, and their implications on the origin of superplume. *Gondwana Reseach, 14*, 51–72.

Rogers, J.-J.-W., & Santosh, M. (2004). *Continents and supercontinents* (pp. 1–289). New York: Oxford University Press.

Shen, C.-L., Zhang, M., & Yang, S.-S. (2009). The geological evidences significance of westward extension of Langshan-Zhaertaishan rift system, Northern margin of North China Terrane. *Geology and Exploration, 45*, 661–668 (in Chinese).

Shen, Q.-H., Geng, Y.-S., Song, B., & Wan, Y.-S. (2005). New information from the surface outcrops and deep crust of Archean rocks of the North China and Yangtze Blocks, and Qinling-Dabie Orogenic Belt. *Acta Geologica Sinica, 79*, 616–627 (in Chinese).

Su, W.-B., Li, H.-K., Xu, L., Jia, S.-H., Geng, J.-Z., Zhou, H.-Y., et al. (2012). Luoyu and Ruyang group at the south margin of the North China Craton (NCC) should belong in the Mesoproterozoic Changchengian system: Direct constraints from the LA-MC-ICPMS U-PB age of the tuffite in the Luoyukou Formation, Ruzhou, Henan, China. *Geological Survey and Research, 35*, 96–108 (in Chinese).

Su, W.-B., Li, Z.-M., Shi, X.-Y., Zhou, H.-R., Huang, S.-J., Liu, X.-M., et al. (2006). K-bentonites and black shales from the Wufeng Longmaxi formation (Early Paleozoic South China) and Xiamaling formation (Early Neoproterozoic North China)-implications for tectonic processes during two important transitions. *Earth Science Frontiers, 13*, 82–95 (in Chinese).

Su, W.-B., Zhang, S.-H., Huff, W. D., Li, H.-K., Ettensohn, F. R., Chen, X.-Y., et al. (2008). SHRIMP U-Pb ages of K-bentonite beds in the Xiamaling Formation: Implications for revised subdivision of the Meso- to Neoproterozoic history of the North China Craton. *Gondwana Research, 14*, 543–553.

Sun, W.-B., Li, H.-K., Huff, W.-D., Ettensohn, F.-R., Zhang, S.-H., Zhou, H.-Y., et al. (2010). SHRIMP U-Pb dating for a K-bentonite bed in the Tieling Formation, North China. *Chinese Science Bulletin, 55*, 3312–3323.

Sun, S., Zhang, G.-W., & Chen, Z.-M. (1985). *Precambrian geological evolution in South China Fault Block*. Beijing: The Publishing House of Metallurgical Industry (in Chinese).

Swisher, C.-C., Wang, X.-L., & Zhou, Z.-H. (2001). New evidence of the Yixian Formation isotope age and the ^{40}Ar-^{39}Ar dating of the Tuchengzi Formation. *Chinese Science Bulletin, 46*, 2009–2013.

Song, B., Nutman, A.-P., Liu, D.-Y., & Wu, J.-S. (1996). 3800 to 2500 Ma crustal evolution in the Anshan area of Liaoning Province, northeastern China. *Precambrian Research, 78*, 79–94.

Trap, P., Faure, M., Lin, W., Bruguier, O., & Monie, P. (2007). Late Paleoproterozoic (1900–1800 Ma) nappe stacking and polyphase understanding of the Trans-North-China Belt, North China Craton. *Precambrian Research, 156*, 85–106.

Trap, P., Faure, M., Lin, W., Monie, P., Meffre, S., & Melleton, J. (2009). The Zanhuang Massif, the second and eastern suture zone of the Paleoproterozoic Trans-North China Orogen. *Precambrian Research, 172*, 80–98.

Wan, Y.-S., Dong, C.-Y., Wang, W., Xie, H.-Q., & Liu, D.-Y. (2009). Archean basement and a Paleoproterozoic collision orogen in the Huoqiu area at the southeastern margin of North China Ctaton: Evidence from sensitive high resolution ion micro-probe U-Pb zircon Geochronology. *Acta Geologica Sinica, 84*, 91–104.

Wan, Y.-S., Geng, Y.-S., Liu, F.-L., Shen, Q.-H., Liu, D.-Y., & Song, B. (2000). Age and composition of the Khondalite series of the North China Craton and its adjacent area. *Progress in Precambrian Research, 23*, 221–237 (in Chinese).

Wan, Y.-S., Liu, D.-Y., Song, B., Wu, J.-S., Yang, C.-H., Zhang, Z.-Q., et al. (2005). Geochemical and Nd isotopic compositions of 3.8 Ga meta-quartz dioritic and trondhjemitic rocks from the Anshan area and their geological significance. *Journal of Asian Earth Sciences, 24*, 563–575.

Wang, H.-C., Yu, H.-F., Miao, P.-S., Zhao, F.-Q., & Xiang, Z.-Q. (2011a). Precambrian Research in China: New advances and perspectives. *Geological Survey and Research, 34*, 241–252 (in Chinese).

Wang H.-Z. (1985). *Alta of the Palaeogeography of China* (pp. 5–8). Beijing: Cartographic Publishing House (in Chinese).

Wang, J., Li, S.-Q., & Wang, B.-L. (1989). *The Langshan-Baiyunebo rift system* (pp. 1–132). Beijing: The Publishing House of Beijing University (in Chinese).

Wang, S.-Y., & Yang, H.-M. (1993). *Research on effusion metallogeny of the Langshan orogenic belt inner Mongolia* (pp. 115–152). Wuhan: The Publishing House of China University of Geosciences (in Chinese).

Wang, X.-L., Jiang, S.-Y., Dai, B.-Z., Griffin, W.-L., Dai, M.-N., & Yang, Y.-H. (2011b). Age, geochemistry and tectonic setting of the Neoproterozoic (ca. 830 Ma) gabbros on the southern margin of the North China Craton. *Precambrian Research, 190*, 35–47.

Wang, Y.-J., Fan, W.-M., Zhang, Y.-H., Guo, F., Zhang, H.-F., & Peng, T.-P. (2004). Geochemical $^{40}Ar/^{39}Ar$ geochronological and Sr-Nd isotopic constraints on the origin of Paleoproterozoic mafic dikes from the southern Taihang Mountains and implications for the Ca. 1800 Ma event of the North China Craton. *Precambrian Research, 135*, 55–77.

Wen, X.-D. (1989). Evolution of the sedimentary facies and Paleogeography in the northern of North China during Mid-Late Proterozoic. *Journal of the University of Petroleum (Natural Science Edition), 13*, 13–21 (in Chinese).

Wilde, S.-A., Zhao, G.-C., & Sun, M. (2002). Development of the North China Craton during the late Archaean and its final amalgamation at 1.8 Ga: Some speculations on its position within a global Palaeoproterozoic supercontinent. *Gondwana Research, 5*, 85–94.

Wu, F.-Y., Xu, Y.-G., Gao, S., & Zheng, J.-P. (2008a). Lithospheric thinning and destruction of the North China Craton. *Acta Petrologica Sinica, 24*, 1145–1174 (in Chinese).

Wu, F.-Y., Yang, J.-H., Wilde, S.-A., Zhang, X.-O., & Yang, J.-H. (2005). Nature and significance of the Early Cretaceous giant igneous event in Eastern China. *Earth and Planetary Science Letters, 233*, 103–119.

Wu, F.-Y., Zhang, Y.-B., Yang, J.-H., Xie, L.-W., & Yang, Y.-H. (2008b). Zircon U-Pb and Hf isotopic constrains on the Early Archean crustal evolution in Anshan of the North China Craton. *Precambrian Research, 167*, 339–362.

Xu, B. (2001). Recent study of the Rodinia supercontinent evolution and its main goal. *Geological Science and Technology Information, 20*, 15–19 (in Chinese).

Zhang, C. (2004). Hot-tectonic events and evolution of north margin of the North China Craton in Meso-Neoproterozoic. *Acta Scientiarum Naturalium Universitatis Pekinensis, 40*, 232–242 (in Chinese).

Zhang, C.-H., Wu, Z.-J., Gao, L.-Z., Wang, W., Tian, Y.-L., & Ma, C. (2007a). Earthquake-induced soft-sediment deformation structures in the Mesoproterozoic Wumishan Formation, North China, and their geologic implications. *Science China Earth Sciences, 50*, 350–358.

Zhang, J., Tian, H., Li, H.-K., Su, W.-B., Zhou, H.-Y., Xiang, Z.-Q., et al. (2015). Age, geochemistry and zircon Hf isotope of the alkaline basaltic rocks in the middle section of the Yan-Liao aulacogen along the northern margin of the North China Craton: New evidence for the breakup of the Columbia Supercontinent. *Acta Petrologica Sinica, 31*(10), 3129–3146 (in Chinese with English abstract).

Zhang, S., Jiang, J., Song, B., Kennedy, M.-J., & Christie-Blick, N. (2005). U-Pb sensitive high-resolution ion microprobe ages from the Doushantuo Formation in South China: Constraints on Late Neoproterozoic glaciations. *Geology, 33*, 473–476.

Zhang, S.-H., Liu, S.-W., Zhao, Y., Yang, J.-H., Song, B., & Liu, X.-M. (2007b). The 1.75–1.68 Ga anorthosite-mangerite-alkali granitoid-rapakivi granite suite from the northern North China Craton: Magmatism related to a Paleoproterozoic orogeny. *Precambrian Research, 155*, 287–312.

Zhang, S.-H., Zhao, Y., & Santosh, M. (2012). Mid-Mesoproterozoic bimodal magmatic rocks in the northern North China Craton: Implications for magmatism related to breakup of the Columbia supercontinent. *Precambrian Research, 222*(223), 339–367.

Zhang, S.-H., Zhao, Y., Yang, Z.-Y., He, Z.-F., & Wu, H. (2009). The 1.35 Ga diabase sills from the northern North China Craton: Implications for breakup of the Columbia (Nuna) supercontinent. *Earth and Planetary Science Letters, 288*, 588–600.

Zhang, S.-H., Zhao, Y., Ye, H., & Hu, G.-H. (2016). Early Neoproterozoic emplacement of the diabase sill swarms in the Liaodong Peninsula and pre-magmatic uplift of the southeastern North China Craton. *Precambrian Research,*. doi:10.1016/j.precamres.2015.11.005

Zhao, G.-C., Cawood, P.-A., Wilde, S.-A., & Sun, M. (2002a). Review of global 2.1–1.8 Ga orogens: Implications for a pre-Rodinia supercontinent. *Earth-Science Reviews, 59*, 125–162.

Zhao, G.-C., He, Y.-H., & Sun, M. (2009a). The Xiong, er volcanic belt at the southern margin of the North China Craton: Petrographic and geochemical evidence for its outboard position in the Paleo-Mesoproterozoic Columbia Supercontinent. *Gondwana Research, 16*, 170–181.

Zhao, T.-P., Chen, W., & Zhou, M.-F. (2009b). Geochemical and Nd-Hf isotopic constrains on the origin of the ~1.74 Ga Damiao anorthosite complex. *North China Craton. Lithos, 113*, 673–690.

Zhao, T.-P., Jin, C.-W., Zhai, M.-G., Xia, B., & Zhou, M.-F. (2002b). Geochemistry and petrogenesis of the Xiong'er group in the southern regions of the North China Craton. *Acta Petrologica Sinica, 18*, 59–69 (in Chinese).

Zhao, T.-P., Zhai, M.-G., Xia, B., Li, H.-M., Zhang, Y.-X., & Wan, Y.-S. (2004a). Zircon U-Pb SHRIMP dating for the volcanic rocks of the Xiong'er Group: Constraints on the initial formation age of the cover of the North China Craton. *Chinese Science Bulletin, 49*, 2342–2349 (in Chinese).

Zhao, Y., Xu, G., Zhang, S.-H., Yang, Z.-Y., Zhang, Y.-Q., & Hu, J.-M. (2004b). Yanshanian movement and conversion of tectonic regimes in East Asia. *Earth Science Frontiers, 11*, 319–328 (in Chinese).

Zhao, G.-C., Cawood, P.-A., Wilde, S.-A., Sun, M., & Lu, L.-Z. (2000). Metamorphism of basement rocks in the central zone of the North China Craton: Implications for Paleoproterozoic tectonic evolution. *Precambrian Research, 103*, 55–88.

Zhao, G.-C., Sun, M., Wilde, S.-A., & Li, S.-Z. (2005). Late Archean to Paleoproterozoic evolution of the North China Craton: Key issues revisited. *Precambrian Research, 136*, 177–202.

Zhao, G.-C., Wilde, S.-A., Cawood, P.-A., & Sun, M. (2002c). SHRIMP U-Pb zircon ages of the Fuping Complex: Implications for Late Archean to Paleoproterozoic accretion and assembly of the North China Craton. *American Journal of Science, 302*, 191–226.

Zhao, Z.-P. (1993). *Precambrian crust evolution of Sino-Korean platform* (pp. 3–384). Beijing: Science Press (in Chinese).

Zhai, M.-G. (2001). Signature of North China Block in supercontinent Rodinia. *Gondwana Research, 4*, 838–839.

Zhai, M.-G. (2010). Tectonic evolution and metallogenesis of North China Craton. *Mineral Deposits, 29*, 24–36 (in Chinese).

Zhai, M.-G., Guo, J.-H., & Liu, W.-J. (2005). Neoarchean to Paleoproterozoic continental evolution and tectonic history of the North China Craton: A review. *Journal of Asian Earth Sciences, 24*, 547–561.

Zhai, M.-G., Hu, B., Peng, P., & Zhao, T.-P. (2014). Meso-Neoproterozoic magmatic events and multi-stage rifting in the NCC. *Earth Science Frontiers, 21*, 100–119 (in Chinese).

Zhai, M.-G., & Peng, P. (2007). Paleoproterozoic events in the North China Craton. *Acta Petrologica Sinica, 23*, 2665–2682 (in Chinese).

Zhai, M.-G., & Santosh, M. (2011). The Early Precambrian odyssey of the North China Craton: A synoptic overview. *Gondwana Research, 20*, 6–25.

Zhou, H.-R., Mei, M.-X., Luo, Z.-Q., & Xing, K. (2006). Sedimentary sequence and stratigraphic framework of the Neoproterozoic Qingbaikou system in the Yanshan region, North China. *Earth Science Frontiers, 13*, 280–290 (in Chinese).

Zhu, R.-X., Yang, J.-H., & Wu, F.-Y. (2012). Timing of destruction of the North China Craton. *Lithos, 149*, 51–60.

Zhu, R.-X., & Zheng, T.-Y. (2009). Destruction geodynamics of the North China Craton and its paleoproterozoic plate tectonics. *Chinese Science Bulletin, 54*, 3354–3366.

16 Petrogenesis and Tectonic Significance of the Late Paleoproterozoic to Early Mesoproterozoic (~1.80–1.53 Ga) A-Type Granites in the Southern Margin of the North China Craton

Taiping Zhao and Xiaoqin Deng

Abstract

A-type granites are extremely rare before middle Paleoproterozoic but more frequent since late Paleoproterozoic globally, probably indicating a causal change of tectonics and deep geodynamic mechanism of the continents. The late Paleoproterozoic to early Mesoproterozoic tectonic transition is witnessed by the occurrence of the A-type granites in the southern margin of the North China Craton (NCC), including the 1.80 Ga Guijiayu and Motianzhai granites, 1.74 Ga Shicheng granite, 1.60 Ga Longwangzhuang and Maping granites, and 1.53 Ga Zhangjiaping granite. Most of the granites contain perthite, annite, and calcic amphibole but are lack of alkali mafic minerals. All of the granitic rocks show characteristics of typical A-type granites, with high silicon and total alkali, and HFSEs (i.e., Zr, Nb, Ce, Y) and low MgO, CaO, and P_2O_5, with negative Eu, Sr, and Ti anomalies and high FeOt/(FeOt + MgO) and Ga/Al ratios. Their geochemical characteristics, along with the negative zircon $\varepsilon_{Hf}(t)$ and whole-rock $\varepsilon_{Nd}(t)$ values, indicate that those A-type granites were derived from partial melting of ancient continental crust. Integrated with regional data, the late Paleoproterozoic to early Mesoproterozoic A-type granites in the southern margin of the NCC are most likely formed under post-collisional (1.80–1.78 Ga) to rifting regimes (1.78–1.53 Ga, or even younger), as Zhai and Peng (Acta Petrol Sinica, 23: 2665–2682, 2007) and Zhai et al. (Earth Sci Frontiers 21: 100–119, 2014, Tectonophysics, in press, 2015) proposed.

Keywords

Late Paleoproterozoic to early Mesoproterozoic • A-type granite • Petrogenesis • Tectonic regime • Southern margin of the North China Craton

16.1 Introduction

A-type granites are characterized by enrichment of iron, HFSEs (high field strength elements) contents and high Ga/Al ratios and commonly formed in an extensional environment (e.g., Eby 1992; Bonin 2007). They are quite rare before middle Paleoproterozoic but has been identified to occur extensively worldwide since the late Paleoproterozoic (e.g., Anderson and Bender 1989; Rämö et al. 1995; Dall'Agnol et al. 2012). Furthermore, the A-type granites are genetically related to continent crustal evolution (e.g., Collins et al. 1982; Bonin 2007) and are closely connected with tectonics and geodynamics of the Earth (e.g., Bonin 2007). Consequently, occurrence of A-type granites is indicative of a geodynamic transition of the Earth's continent crust evolution, and can be used to

T. Zhao (✉) · X. Deng
Key Laboratory of Mineralogy and Metallogeny, Guangzhou Institute of Geochemistry, Chinese Academy of Sciences, Guangzhou, 510640, China
e-mail: tpzhao@gig.ac.cn

X. Deng
University of Chinese Academy of Sciences, Beijing, 100049, China

M. Zhai et al. (eds.), *Main Tectonic Events and Metallogeny of the North China Craton*, Springer Geology, DOI 10.1007/978-981-10-1064-4_16

constrain the end of the syn-collisional compressional environment of orogeny (e.g., Loiselle and Wones 1979; Whalen et al. 1987; Eby 1992; Turner et al. 1992; Bonin 2007).

The North China Craton (NCC) is one of the oldest continental blocks in the world, containing rocks as old as 3.85 Ga (e.g., Song et al. 1996; Liu et al. 2009). It experienced a complicated evolutionary history and recorded multi-stage crustal growth and might bear imprints of almost all major Precambrian geological events (e.g., Zhai and Santosh 2011). Extensive structural, petrological, metamorphic, geochemical, and geochronological investigations suggested that almost all early Precambrian rocks in the NCC underwent extensive metamorphism and deformation during Paleoproterozoic and the NCC finally amalgamated at ~1.85 Ga (e.g., Zhao et al. 2001, 2003, 2005, 2008, 2010; Zhao and Cawood 2012). This late Paleoproterozoic metamorphic tectonothermal event was also called "Lvliang Movement" or "Zhongtiao Movement" in the early Chinese literatures (e.g., Wu and Xu 1982; Qiao and Wang 1984; Zhao 1993; Bai et al. 1996; Zhai and Liu 2003). Following the final amalgamation, the NCC underwent intensive extension, and developed volumetrically extension-related magmatic and sedimentary rocks, mainly including the Xiong'er volcanic rocks (~1.78 Ga), the Yan-Liao volcanic rocks (1.68–1.62 Ga) and coeval associated mafic dykes and sedimentary sequences; the anorthosite–mangerite–alkali granitoid–rapakivi granite suite (1.75–1.68 Ga) and the Jianping diorite–monzonite–syenite suite (1.72–1.69 Ga); and spatially and temporally associated granitoid rocks (Li et al. 1995; Rämö et al. 1995; Peng et al. 2004, 2005, 2008; Zhao et al. 2004, 2009; Zhang et al. 2007; Lu et al. 2008; Bao et al. 2009; Zhao and Zhou 2009; Hu et al. 2010; Wang et al. 2004, 2008, 2013a, b, 2015; Deng et al. 2015; Peng 2015).

The geodynamic mechanism of the ~1.8–1.60 Ga in the NCC remains controversial. A extensional regime has been suggested for the magmatism in the central, northern, and eastern parts of the NCC, and it was related to different geodynamic mechanisms, including post-collisional extensional setting (Zhao et al. 2001, 2002a, 2005; Zhang et al. 2007; Zhao and Cawood 2012; Wang et al. 2013a), mantle plume (Zhai and Liu 2003; Peng et al. 2008, 2015; Zhai et al. 2011) and intra-continental rift (Zhao et al. 2002b; Zhai et al. 2014, 2015; Wang et al. 2015). Moreover, in the case of the southern margin of the NCC, an alternative Andean arc setting has also been invoked to account for the Xiong'er volcanic rocks (e.g., Hu and Lin 1988; Chen et al. 1992; He et al. 2009, 2010; Zhao et al. 2009). Thus, the recognition of some late Paleoproterozoic to early Mesoproterozoic extension-related A-type granites in the southern margin of the NCC would provides important constraints on the geodynamic regime.

16.2 Geology and Petrography

16.2.1 The Guijiayu Granite (ca. 1.80 Ga)

The Guijiayu granitic pluton is located in the Xiaoqinling area (Fig. 16.1), which, as a small granitic pluton with an area of ~13 km^2, intruded into the Taihua Group that is composed mainly of the Paleoproterozoic gneiss series (2.45–2.20 Ga; e.g., Hu and Lin 1988; Diwu et al. 2014; Wang et al. 2014) and the Khondalite-dominated supracrustal rocks (2.35–1.97 Ga; e.g., Shen 1986; Hu and Lin 1988; Lu et al. 1995; Shi et al. 2011; Diwu et al. 2014).

The Guijiayu pluton is composed mainly of monzogranite with massive or gneissic structures. The mineral grain size in this pluton increases systematically from the margin to center. The monzogranites consist of K-feldspar (25–35 vol.%), plagioclase (20–30 vol.%), quartz (20–25 vol.%), biotite and amphibole (10–15 vol.%), with accessory minerals of apatite, zircon, and Fe–Ti oxide (~2 vol.%). K-feldspar is subhedral slabby to pin-stripe morphology, and is dominated by perthite and microcline (Fig. 16.2a). Biotite and hastingsite occur as mineral aggregates along the boundary of coarse-grained K-feldspar, plagioclase, and quartz (Fig. 16.2a, b). Most plagioclase grains have been altered to sericite (Fig. 16.2b). Biotite is partially altered to chlorite or spindle-shaped fibers of ilmenite.

Zircon U-Pb dating results for the Guijiayu pluton showed crystallization age of 1.80 Ga (1802 ± 27, 1803 ± 25 and 1797 ± 28 Ma; Deng et al. 2016a).

16.2.2 The Motianzhai Granite (ca. 1.80 Ga)

The Motianzhai pluton, covering an area of 4 km^2, is located in the Songshan area (Fig. 16.1b). It intruded into the Archean Dengfeng metamorphic complex (2.55–2.51 Ga? e.g., Wan et al. 2009; Zhao et al. 2012) and the Palaeoproterozoic quartzites of the Songshan Group (2.40–1.80 Ga? e.g., Diwu et al. 2008; Wan et al. 2009; Zhao et al. 2012). The Motianzhai pluton consists mainly of biotite granite with medium to coarse-grained and porphyritic texture. The mineral assemblage is microcline perthite (50–55 vol.%), quartz (35–40 vol.%), plagioclase (~5 vol.%; An = 27–29), and biotite (2–8 vol.%). SHRIMP zircon dating for the Motianzhai pluton yielded a weighted mean $^{207}Pb/^{206}Pb$ age of 1797 ± 14 Ma (e.g., Zhao and Zhou 2009).

16.2.3 The Shicheng Granite (ca. 1.74 Ga)

The Shicheng pluton, covering an area of 55 km^2, is located in the Songshan area (Fig. 16.1b). It intruded into the

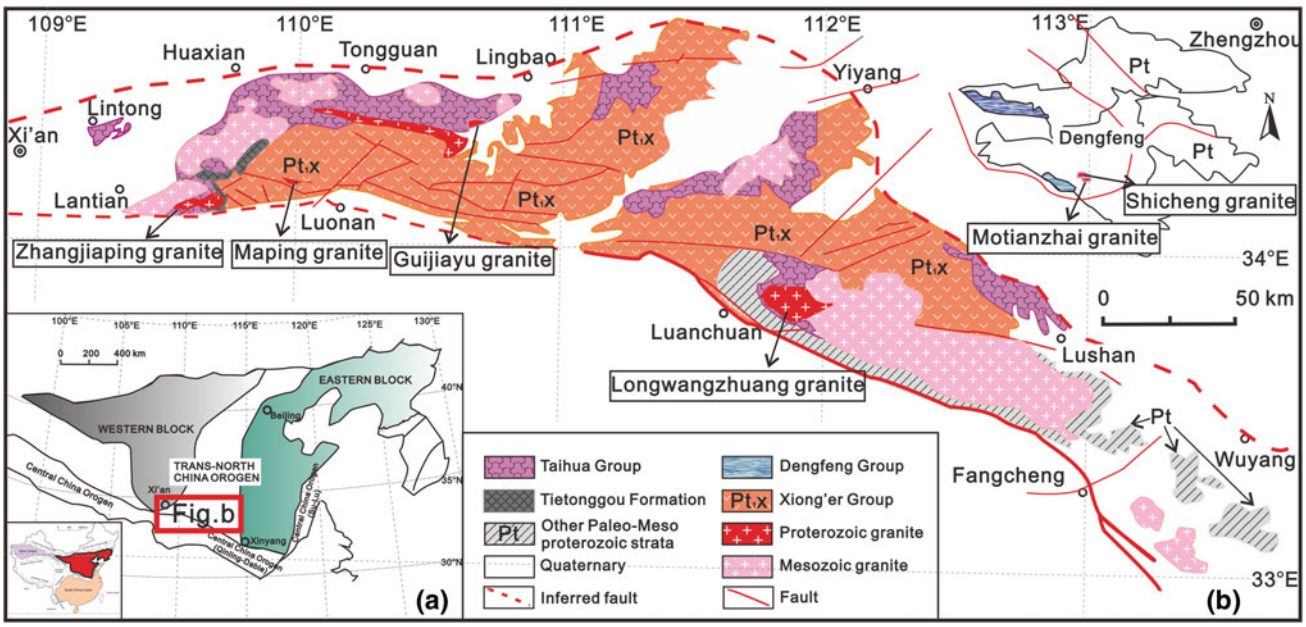

Fig. 16.1 **a** Tectonic subdivision of the North China Craton (modified from Zhao et al. 2005). **b** Simplified geological map of the southern margin of the NCC (modified from Diwu et al. 2014)

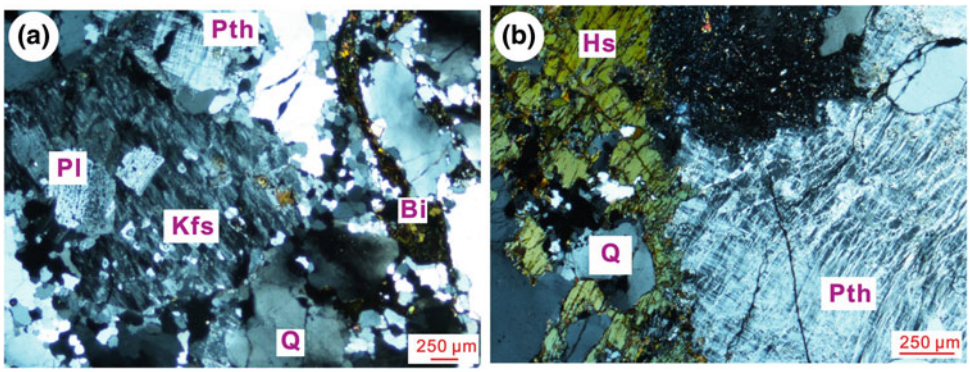

Fig. 16.2 Representative photomicrographs under cross-polarized light showing the petrographic characteristics of the Guijiayu granites. *Mineral abbreviations*: *Kfs* k-feldspar; *Pth* perthite; *Pl* plagioclase; *Q* quartz; *Bi* biotite; *Hs* hastingsite

quartzite of the Palaeoproterozoic Songshan Group (2.40–1.80 Ga? e.g., Diwu et al. 2008; Wan et al. 2009; Zhao et al. 2012). The mineral grain size in this pluton increases gradually from margin to center, whereas the mafic minerals decrease significantly.

The Shicheng pluton consists mainly of granodiorite and biotite granite. The biotite granites are medium to coarse-grained and porphyritic, and consist of microcline perthite (50–55 vol.%), quartz (35–40 vol.%), plagioclase (~5 vol.%; An = 27–29), and biotite (2–8 vol.%). The granodiorites are fine grained and aphyric in the margins but increase in grain size and become porphyritic toward the center. They are mainly composed of microcline (~20 vol.%), plagioclase (~50 vol.%; An = 30), quartz (~12 vol.%), and hornblende (~15 vol.%). The plagioclase shows well-developed oscillatory zoning (Zhao and Zhou 2009). Accessory minerals include magnetite, ilmenite, titanite, apatite, allanite, fluorite, and zircon. Magnetite is more abundant than ilmenite. SHRIMP zircon U–Pb dating gave forming age of 1775 ± 9 Ma from Wan et al. (2009) and 1743 ± 14 Ma from Zhao and Zhou (2009).

16.2.4 The Longwangzhuang Granite (ca. 1.60 Ga)

The Longwangzhuang pluton is the largest anorogenic intrusion in the southern NCC (Fig. 16.1b; e.g., Hu and Lin 1988; Lu 1989). It occurs ~20 km to the east of Luanchuan city, with an outcrop area covering 140 km^2. It is in fault contact with the Taihua Group on its northern margin, but intruded the Taihua Group to the west.

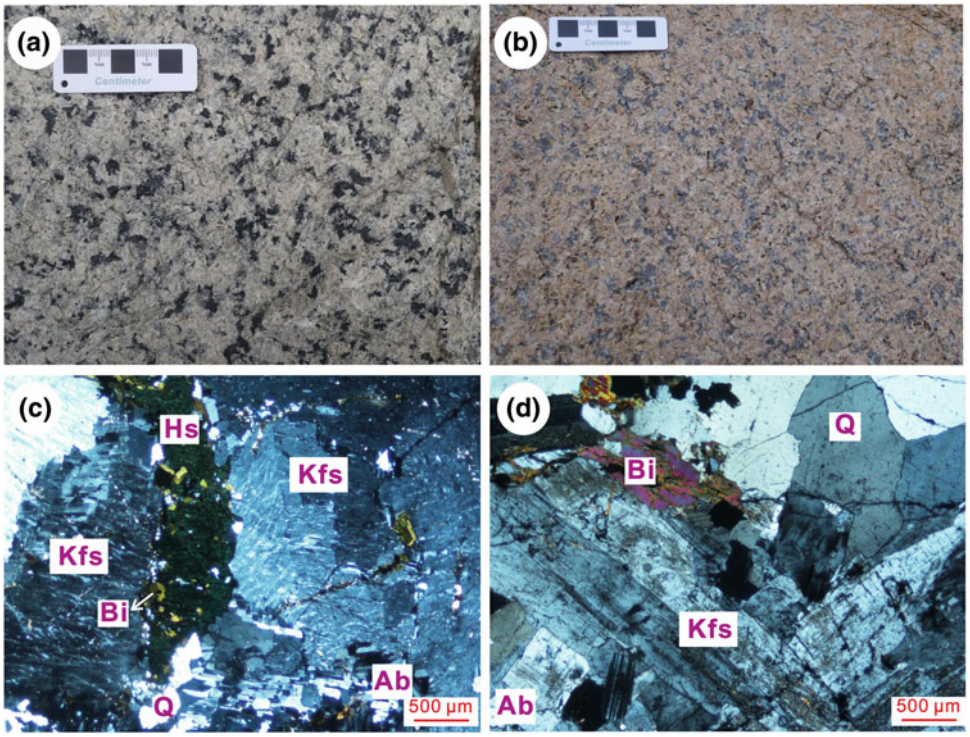

Fig. 16.3 Representative hand specimens (**a**–**b**) and photomicrographs under cross-polarized light (**c–d**) showing the petrographic characteristics of the Longwangzhuang granites. *Mineral abbreviations*: *Kfs* k-feldspar; *Ab* albite; *Q* quartz; *Bi* biotite; *Hs* hastingsite

Meanwhile, it was intruded by the early Cretaceous Funiushan biotite granites at the eastern margin (e.g., Hu and Lin 1988; Gao et al. 2014).

The Longwangzhuang pluton is composed mainly of hornblende granite (Fig. 16.3a) and K-feldspar granite (Fig. 16.3b). The hornblende granite is light gray, coarse-grained, and consists mainly of K-feldspar (55 vol.%), quartz (30 vol.%), albite (5 vol.%), and biotite and hornblende (5–10 vol.%) (Fig. 16.3c). K-feldspars are dominated by microcline. Albite is commonly anhedral or semi-euhedral and weakly sericitized. Biotite commonly occurs as aggregates of fine scale-like crystals. Quartz often occurs as granule aggregates with undulance extinction. Accessary minerals include magnetite, allanite, zircon, sphene, apatite, thorite, and bastnaesite. The K-feldspar granite is around the hornblende granite on the southern margin of the pluton, which is composed of quartz, K-feldspar, biotite, and albite without amphibole (Fig. 16.3d).

Previous study (e.g., Hu and Lin 1988; Lu 1989; Lu et al. 2003; Bao et al. 2009) considered that the alkali mafic minerals of the Longwangzhuang pluton are mainly sodic ferrogedrite, with few aegirine augite granites in some area. However, no micrographs and major element compositions of minerals support these alkali mafic minerals. Recently, major element compositions of the amphiboles of the Longwangzhuang granites analyzed by Wang et al. (2013b) showed they are not sodic amphiboles, but calcic amphiboles i.e., hastingsite, ferro-edenite, ferro-hornblende, ferro-actinolite, likely suggesting that the Longwangzhuang pluton is not alkali granite. Therefore, more mineralogical work would need to be done for the Longwangzhuang pluton.

Bao et al. (2009) and Wang et al. (2013b) reported LA-ICPMS zircon U-Pb date of 1602.1 ± 6.6 and 1616 ± 20 Ma, respectively, which are consistent with the published SHRIMP zircon age of 1625 ± 16 Ma (Lu et al. 2003).

16.2.5 The Maping Granite (ca. 1.60 Ga)

The Maping pluton is located in Luonan county, Shaanxi Province (Fig. 16.1b). It extended linearly across Siwa-Shijiagou in Maping town, 5 km long and 500 m wide. The Maping pluton intruded the Longjiayuan Formation of the Mesoproterozoic Guandaokou Group. The main rock types are syenite porphyry, aegirine syenite porphyry, and granite porphyry. The syenite porphyry consists of orthoclase (75–84 vol.%), plagioclase (10–14 vol.%), quartz (5–8 vol.%), and biotite (<5 vol.%), with accessory minerals of <1 vol.%. The phenocryst minerals include orthoclase and occasional quartz. The aegirine syenite porphyry has mineral compositions similar to the syenite porphyry, but contains aegirine. The aegirine occurs in both phenocryst and matrix. The granite porphyry (Fig. 16.4a) has the most abundant quartz in the Maping pluton, up to 20–25 vol.%. Its phenocryst minerals are K-feldspar and quartz (Fig. 16.4b). Zircon ages of 1598 ± 9 Ma (SHRIMP, Liu 2011), 1600 ± 24 Ma and 1583 ± 28 Ma (LA-ICPMS, Deng et al. 2015) have been obtained and considered as its crystallization age.

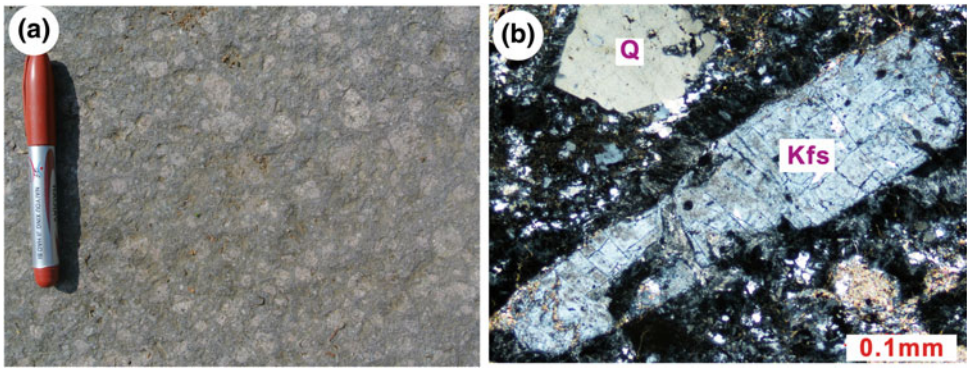

Fig. 16.4 Representative hand specimen (**a**) and photomicrograph under cross-polarized light (**b**) showing the petrographic characteristics of the Maping granite porphyry (modified from Deng et al. 2015). *Mineral abbreviations*: *Kfs* k-feldspar; *Q* quartz

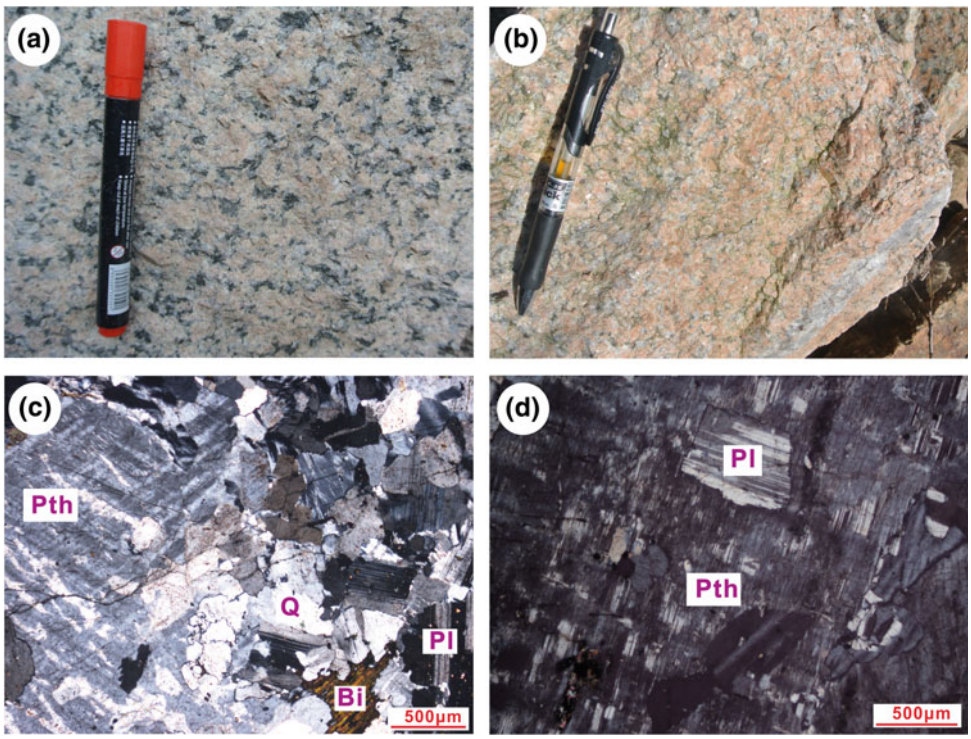

Fig. 16.5 Representative hand specimens (**a**–**b**) and photomicrographs under cross-polarized light (**c**–**d**) showing the petrographic characteristics of the Zhangjiaping granites (modified from Deng et al. 2016b). *Mineral abbreviations*: *Pl* plagioclase; *Pth* microcline perthite; *Q* quartz; *Bi* biotite

16.2.6 The Zhangjiaping Granite (ca. 1.53 Ga)

The Zhangjiaping granitic pluton is located in the Lantian county, Shaanxi Province (Fig. 16.1b), with an exposure area of ca. 46 km^2. It mainly intruded into the biotite plagiogneiss and mica-quartz schist of the Taihua Group, locally into the muscovite quartzite of the Tietonggou Formation (1.91–1.80 Ga, Diwu et al. 2013, 2014) to the southeast and the volcanic rocks of the Xiong'er Group to the south. The Zhangjiaping pluton varies gradually from margin to center in texture and composition.

The rocks in the margin are medium-fine-grained and gray-white in color, mainly composed of hypidiomorphic granular biotite granite (Fig. 16.5a), biotite–hornblende granite, and biotite monzogranite with gneissic, taxitic or massive textures. The mineral assemblages comprise plagioclase (20–40 vol.%), alkali-feldspar (30–60 vol.%), quartz (20–30 vol.%) with minor biotite (3–5 vol.%) and hornblende (2 vol.%) (Fig. 16.5c). Accessory minerals account for <2 vol.% and include allanite, fluorite, titanite, and Fe–Ti oxide.

The rocks in the center are dominantly medium to coarse-grained and gray-white or red in color, mainly composed of biotite granite and K-feldspar granite (Fig. 16.5b) with massive texture. The biotite granite is hypidiomorphic granular structure and consists of microcline (45–50 vol.%), quartz (~30 vol.%), plagioclase (20–25 vol.%), and minor biotite (5 vol.%) with accessory minerals (2 vol.%, i.e.,

Table 16.1 Major (wt%) and trace element concentrations (ppm) of the late Paleoproterozoic to early Mesoproterozoic granites in the southern NCC

	Guijiayu	Motianzhai	Shicheng	Longwangzhuang	Maping	Zhangjiaping
SiO_2	65.38–72.72	71.29–77.35	68.64–75.58	71.95–76.82	69.71–75.69	69.92–78.29
TiO_2	0.44–0.89	0.12–0.27	0.18–0.49	0.24–0.41	0.25–0.46	0.07–0.45
Al_2O_3	12.52–13.45	10.81–13.92	12.34–14.14	11.96–13.54	12.09–13.89	10.94–14.54
MgO	0.14–0.36	0.14–0.27	0.20–0.39	0.03–0.24	0.24–0.86	0.01–0.51
CaO	0.79–2.39	0.20–0.91	0.46–1.52	0.02–1.36	0.06–0.57	0.07–1.75
Fe_2O_3	3.81–9.33	1.64–3.09	2.22–4.78	1.41–3.78	0.56–5.14	1.02–4.54
Na_2O	2.44–3.43	2.73–3.71	3.02–3.70	2.57–3.70	0.13–2.75	2.84–4.06
K_2O	4.80–5.80	4.38–5.41	4.90–5.46	6.55–9.71	5.86–10.05	4.06–6.14
MnO	0.06–0.13	0.01–0.04	0.02–0.07	0.02–0.12	0.1–0.08	0.02–0.08
P_2O_5	0.06–0.19	0.00	<0.07	<0.10	<0.09	<0.09
FeOt/(FeOt + MgO)	0.93–0.97	0.87–0.94	0.87–0.93	0.92–0.99	0.59–0.91	0.85–0.99
∑REE	361–585	249–701	266–595	349–861	465–849	134–1111
(La/Yb)cn	9.86–17.1	7.22–11.2	5.67–14.4	14.0–54.4	13.2–18.0	1.60–23.1
Zr	335–631	198–371	240–541	136–966	319–671	108–518
t_{Zr}/°C	872–899	811–864	822–893	825–1002	870–953	753–890
10,000 Ga/Al	2.94–3.43	2.18–3.15	2.52–3.15	4.03–5.31	2.20–3.35	3.88–5.39

Note The data of the Guijiayu pluton from Deng et al. (2016a), Motianzhai pluton from Zhao and Zhou (2009), Shicheng pluton from Zhao and Zhou (2009), Longwangzhuang pluton from Bao et al. (2009) and Wang et al. (2013b), Maping pluton from Liu (2011) and Deng et al. (2015), Zhangjiaping pluton from Deng et al. (2016b). (La/Yb)cn is chondrite-normalized value

fluorite, Fe–Ti oxide). The K-feldspar granite is porphyritic in texture and consists of microcline (50–55 vol.%), quartz (~30 vol.%), plagioclase (~10 vol.%), and minor biotite (5 vol.%), mica (2 vol.%), with accessory minerals of fluorite and Fe–Ti oxide (<3 vol.%) (Fig. 16.5d).

Zircons from four granite samples from the Zhangjiaping pluton were dated at 1526 ± 17, 1532 ± 16, 1507 ± 18, 1508 ± 55 Ma (Deng et al. 2016b), indicating a crystallization age of ca. 1.53 Ga within errors.

16.3 Geochemistry

Major and trace element results of the late Paleoproterozoic to early Mesoproterozoic granites in the southern margin of the NCC are listed in Table 16.1.

Rocks from six plutons mentioned above are all rich in silica and total alkalis (Table 16.1). They have moderate Al_2O_3 contents (mostly <14 wt%) and low to moderate Fe_2O_3 contents (mostly <5 wt%), as well as low TiO_2, CaO, MnO, and P_2O_5 contents. Their A/CNK ratios range from 0.88 to 1.15, showing metaluminous to weakly peraluminous attribute (Fig. 16.6a), except that the Maping granites show strongly peraluminous signature with high aluminum saturation index (A/CNK > 1.11) (Fig. 16.6a). Most samples have low MgO contents (<0.51) and high FeOt/(FeOt + MgO) ratios (up to 0.99), showing an affinity to those of ferroan granites (Fig. 16.6b), whereas part of the Maping granites have low FeOt/(FeOt + MgO) ratios (even lower than 0.8).

Most granites show similar chondrite-normalized REE patterns with significant enrichment of LREE ($(La/Yb)_{cn} > 5.67$) except for the Zhangjiaping granites, which have variable $(La/Yb)_{cn}$ ratios (1.60–23.1) (Table 16.1). The Guijiayu and Motianzhai granites, Shicheng granite, Longwangzhuang, and Maping granites have high Zr contents (mostly >300 ppm, Table 16.1; Fig. 16.7a) and produce high zircon saturation temperatures (Table 16.1; Fig. 16.7b), higher than average A-type granite (839 °C, King et al. 1997).

16.4 Discussion

16.4.1 Petrogenesis

The high aluminum saturation index (A/CNK > 1.11) of the Maping granites show an affinity to that of strongly peraluminous granite, resembling S-type granite. However, their high Ga/Al ratios along with negative Eu, Sr, and Ti anomalies and high zircon saturation temperatures (870–953 °C) (Table 16.1), indicate that the Maping granite porphyry is similar to A-type granite (Deng et al. 2015). The other granitic rocks also show an affinity to A-type granites,

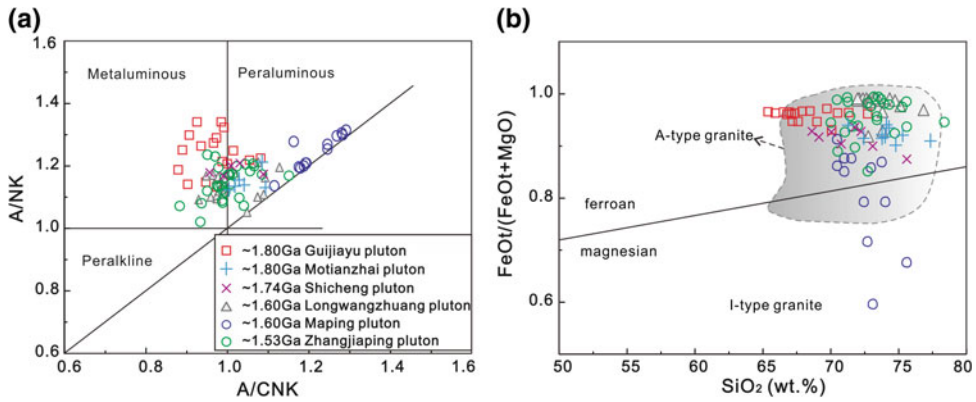

Fig. 16.6 **a** A/NK versus A/CNK; **b** FeOt/(FeOt + MgO) versus SiO_2 (wt%) plots (after Frost et al. 2001). The data of the Guijiayu pluton from Deng et al. (2016a), Motianzhai pluton from Zhao and Zhou (2009), Shicheng pluton from Zhao and Zhou (2009), Longwangzhuang pluton from Bao et al. (2009) and Wang et al. (2013b), Maping pluton from Liu (2011) and Deng et al. (2015), Zhangjiaping pluton from Deng et al. (2016b)

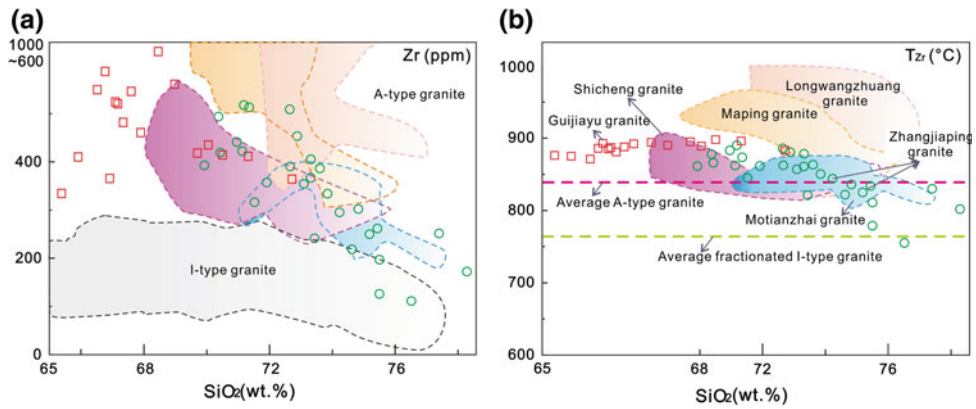

Fig. 16.7 **a** Zr (ppm) versus SiO_2 (wt%) (after King et al. 2001); **b** T_{Zr} (°C) versus SiO_2 (wt%), T_{Zr} (°C): the calculated Zr saturation temperatures; average A-type granite and fractionated I-type granite from King et al. (1997). Symbols of the Guijiayu and Zhangjiaping granites are as in Fig. 16.6

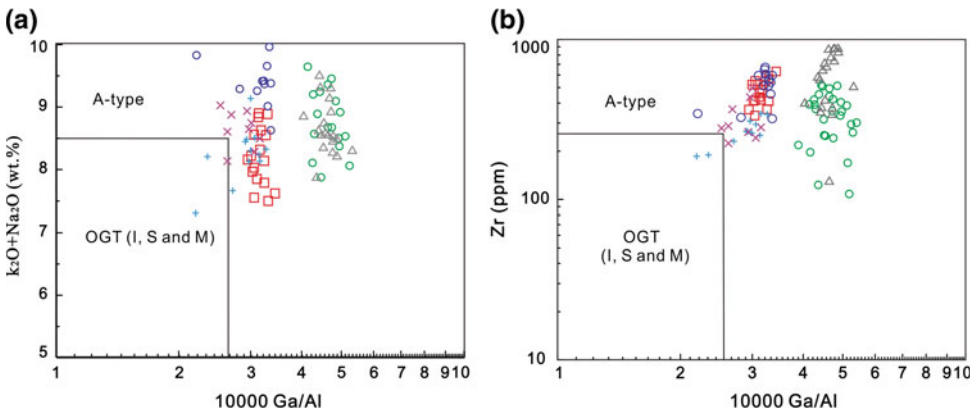

Fig. 16.8 **a** $(K_2O + Na_2O)/CaO$ and **b** Zr (ppm) versus 10,000 Ga/Al discrimination diagrams (after Whalen et al. 1987). I, S and M: unfractionated M-, I- and S-type granites. Symbols are as in Fig. 16.6

with enrichment in silicon and total alkali, and depletion in MgO, CaO, and P_2O_5 with negative Eu, Sr, and Ti anomalies, as well as high FeOt/(FeOt + MgO) and Ga/Al ratios (Table 16.1; Figs. 16.6b and 16.8). Moreover, the calculated zircon saturation temperatures (T_{Zr}) for the granites are high (mostly >830 °C), consistent with the range of T_{Zr} calculated from A-type granites (Table 16.1; Fig. 16.7b; Loiselle and Wones 1979; King et al. 1997). Petrological

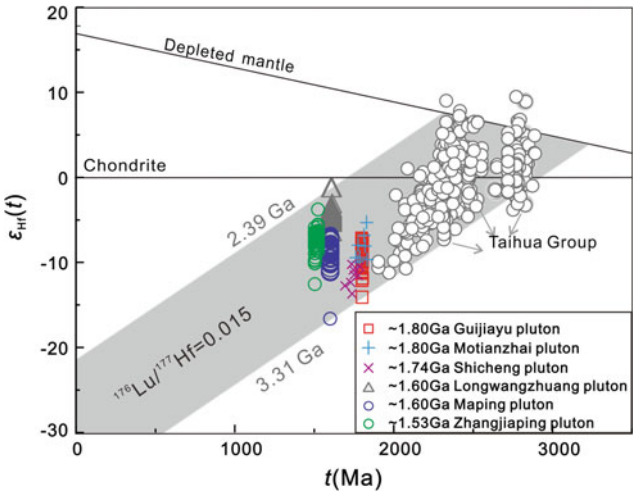

Fig. 16.9 Diagram of $\varepsilon_{Hf}(t)$ versus age. Taihua Group data are from Liu et al. (2009), Xu et al. (2009), Huang et al. (2010, 2012, 2013), Shi et al. (2011), Diwu et al. (2010, 2014)

characteristics of the late Paleoproterozoic to early Mesoproterozoic (1.80–1.53 Ga) granites in the southern NCC, including the occurrence of perthites, annite, and calcic amphibole (hastingsite) (Zhao and Zhou 2009; Wang et al. 2013b; Deng et al. 2015, 2016a, b), are consistent with aluminous A-type granites that usually contain annite and/or calcic- or sodic-calcic amphibole but are lack of alkali mafic minerals (e.g., Wu et al. 2002; Bonin 2007; Frost and Frost 2011). Consequently, these granites in the southern NCC are aluminous A-type granites.

The late Paleoproterozoic to early Mesoproterozoic (1.80–1.53 Ga) A-type granites in the southern NCC have negative zircon $\varepsilon_{Hf}(t)$ values (Fig. 16.9; e.g., Bao et al. 2009; Zhao and Zhou 2009; Wang et al. 2013b; Deng et al. 2015, 2016a, b) that overlap with the evolution of the basement rocks from the Taihua Group (Fig. 16.9), indicating that they were derived from partial melting of the ancient basement rocks. Furthermore, as shown in the Fig. 16.9, the $\varepsilon_{Hf}(t)$ values of the A-type granites younger than ca. 1.6 Ga are relatively higher than those of the older ones. Therefore, different source materials from the Taihua Group might be inferred, and moreover, this may reflect different geodynamic processes involved in the petrogenesis.

16.4.2 Tectonic Settings

The tectonic settings responsible for the late Paleoproterozoic magmatism in the southern NCC are controversial and several geodynamic environments were proposed such as post-collisional/post-orogenic extensional setting (e.g., Zhao et al. 2002a; Zhao and Cawood 2012; Wang et al. 2013b; Wang et al. 2015), continental margin arc (e.g., Hu and Lin 1988; He et al. 2009, 2010; Zhao et al. 2009) and mantle plume (e.g., Zhai and Liu 2003; Peng et al. 2008; Zhai et al. 2011; Peng 2015) or intra-continental rift (e.g., Zhao et al. 2002b; Zhai and Liu 2003; Zhai et al. 2014, 2015; Peng 2015). Meanwhile, most tectonic settings (except for the continental margin arc) are all involved with an extensional regime, which can be closely defined by A-type granites (Whalen et al. 1987; Eby 1992; Rämö et al. 1995; King et al. 1997; Wu et al. 2002). A-type granites are rather enigmatic not only as regards their petrogenesis but also in terms of their tectonic setting and overall significance in the evolution of the Earth's lithosphere (e.g., Dall'Agnol et al. 2012). Generation of typical A-type granite is commonly related to extensional settings, including post-collisional/post-orogenic or anorogenic (c.f., rift, mantle plume) environments (Whalen et al. 1987; Eby 1992; Rämö et al. 1995; King et al. 1997; Wu et al. 2002). Therefore, the generation of the A-type granites in the southern NCC would provide an important insight into the tectonic evolution and the deep geodynamic processes during Paleo-Mesoproterozoic.

1. **1.80–1.78 Ga: Post-collisional/post-orogenic setting**

Clockwise P-T paths of the Paleoproterozoic rocks in the Taihua metamorphic complex (e.g., Shen 1986; Lu et al. 1995; Wan et al. 2006; Jiang et al. 2011; Wang et al. 2014) is generally related to the process of continental collision followed by rapid uplift or exhumation (e.g., England and Thompson 1984; Brown 1993; Zhao et al. 2000), indicating that the southern margin of the NCC was also involved in the subduction and continent–continent collision. Furthermore, available dating results from these metamorphosed rocks in the southern margin of the NCC revealed that the tectono-metamorphism lasted as late as 1.80 Ga (e.g., Shen 1986; Lu et al. 1995; Wan et al. 2006; Shi et al. 2011; Diwu et al. 2014; Wang et al. 2014). In this case, it is most likely that the continent–continent collision finished at least before ~1.80 Ga in the southern margin of the NCC (e.g., Wan et al. 2006; Deng et al. 2016a). The 1.8 Ga Guijiayu and Motianzhai plutons are characterized by high-K calc-alkaline, which are typical for granites in the continental collision orogenic belts particularly at the end of collision (Barbarin 1999), indicating a post-collisional extension environment.

2. **1.78–1.53 Ga: Continental rift**

The volcanic rocks of the Xiong'er Group are dated at ~1.78–1.75 Ga (e.g., Sun et al. 1981; Hu and Lin 1988; Zhao et al. 2002b, 2004, 2015; Peng et al. 2008), indicating that the rifting started at the southern margin of the NCC in the late Paleoproterozoic (e.g., Zhao et al. 2002b; Zhai and

Liu 2003; Zhai et al. 2014, 2015; Peng 2015). Post-collisonal environment had been suggested for the 1.74 Ga Shicheng granites because of their characteristic of A_2-type (e.g., Zhao and Zhou 2009). However, in a post-collisonal setting, the strong upwelling of the asthenospheric mantle may lead to partial melting of the overlying lithospheric components as well as the asthenospheric mantle itself (e.g., Bonin 2004). The Shicheng granitic samples have highly negative zircon $\varepsilon_{Hf}(t)$ values (−10.2 to −13.5; Fig. 16.9; Zhao and Zhou 2009), arguing against any involvement of depleted asthenospheric mantle materials. Moreover, combined with abundant 1.78 Ga mafic dyke swarms and Xiong'er Group sedimentary sequences in the southern NCC, post-collisonal environment should be precluded and the anorogenic environment would be responsible for the generation of the Shicheng granites.

The 1.60 Ga Longwangzhuang pluton (e.g., Lu et al. 2003; Bao et al. 2009; Wang et al. 2013b) is considered as the largest anorogenic intrusion in the southern NCC (e.g., Hu and Lin 1988; Lu 1989). Therefore, the Longwangzhuang (e.g., Lu et al. 2003; Bao et al. 2009; Wang et al. 2013), Maping (Liu 2011; Deng et al. 2015) and Zhangjiaping (Deng et al. 2016b) plutons are representatives of anorogenic magmatism in the southern NCC from 1.78 to 1.53 Ga.

16.4.3 Tectonic Implications

As mentioned above, some researchers considered that the 1.90–1.80 Ga metamorphic event in the southern margin of the NCC represented continental collision (e.g., Shen 1986; Lu et al. 1995; Zhao et al. 2001, 2003, 2010; Wan et al. 2006; Wang et al. 2014), following by the 1.80–1.78 Ga post-collisional event (i.e., Guijiayu and Motianzhai A-type granites) and the 1.78–1.53 Ga (or even younger) rifting event (i.e., Xiong'er volcanic rocks and coeval craton-scale mafic dyke swarms; the Shicheng, Longwangzhuang, Maping, and Zhangjiaping A-type granites). The rift system is also represented by late Paleoproterozoic–Neoproterozoic sedimentary sequences and magmatic activities in the whole NCC (e.g., Zhai and Peng 2007; Zhai et al. 2014, 2015). The major sedimentary basins include the Xiong'er aulacogen system in the southcentral NCC (e.g., Zhao et al. 2002b, 2004; Hu et al. 2014), the Yan-Liao aulacogen system in the northcentral NCC (e.g., Li et al. 1995, 2011, 2013; Gao et al. 2008a, b, 2009; Lu et al. 2008; Peng et al. 2012; Wang et al. 2015; Zhang et al. 2015), the Northern marginal rift system in the northwestern NCC (e.g., Zhao et al. 2003; Zhao and Cawood 2012; Liu et al. 2014; Zhong et al. 2015) and the Eastern marginal rift system (e.g., Peng et al. 2011; Hu et al. 2012). Five episodes of magmatism in the Late Paleoproterozoic to Neoproterozoic have been recognized: (1) ~1.78 Ga Xiong'er igneous province (XIP; Zhao et al. 2002b, 2004b; Peng et al. 2004, 2005, 2008; Hu et al. 2014; Peng 2015), (2) ~1.72–1.60 Ga anorogenic magmatism (e.g., Li et al. 1995; Rämö et al. 1995; Lu et al. 2003; Zhang et al. 2007; Bao et al. 2009; Wang et al. 2013a, b; Deng et al. 2015), (3) ~1.53 Ga A-type granites (Deng et al., 2016b), (4) ~1.35–1.32 Ga diabase sill swarms (e.g., Li et al. 2009; Zhang et al. 2009, 2012), and (5) ~0.90 Ga mafic dyke swarms (e.g., Peng et al. 2011).

The post-collisional (1.80–1.78 Ga) and the five anorogenic (1.78–0.90 Ga) magmatic events suggest that the NCC was in a long-term extensional tectonic setting. The multi-rifting magmatic activities with vast and thick sedimentary sequences suggest that the NCC evolved into a stable platform during the late Paleoproterozoic to Neoproterozoic era (e.g., Cawood and Hawkesworth 2014; Zhai et al. 2015; Zhao et al. 2015).

Acknowledgements We appreciate the helpful comments of Drs. Touping Peng, Xinyu Gao, and Yang Alexandra Yang on an early version of the manuscript. We also thank Prof. Chengli Zhang and Dr. Zhiwei Bao for their constructive suggestions. This study is financially supported by the National Basic Research Program of China (No. 2012CB416606).

References

Anderson, J. L., & Bender, E. E. (1989). Nature and origin of Proterozoic A-type granitic magmatism in the southwestern United States of America. *Lithos, 23*, 19–52.

Bai, J., Huang, X. G., Dai, F. Y., & Wu, C. H. (1996). *The Precambrian crustal evolution of China* (pp. 199–203). Beijing: Geological Publishing House (in Chinese).

Bao, Z. W., Wang, Q., Zi, F., Tang, G. J., Du, F. J., & Bai, G. D. (2009). Geochemistry of the Paleoproterozoic Longwangzhuang A-type granites on the southern margin of the North China Craton: Petrogenesis and tectonic implications. *Geochimica, 38*, 509–522 (in Chinese with English abstract).

Barbarin, B. (1999). A review of the relationships between granitoid types, their origins and their geodynamic environments. *Lithos, 46*, 605–626.

Bonin, B. (2004). Do coeval mafic and felsic magmas in post-collisional to within-plate regimes necessarily imply two contrasting, mantle and crustal, sources? A review. *Lithos, 78*, 1–24.

Bonin, B. (2007). A-type granites and related rocks: Evolution of a concept, problems and prospects. *Lithos, 97*, 1–29.

Brown, M. (1993). P-T-t evolution of orogenic belts and the causes of regional metamorphism. *Journal of the Geological Society, 150*, 227–241.

Cawood, P. A., & Hawkesworth, C. J. (2014). Earth's middle age. *Geology, 42*, 503–506.

Chen, Y. J., Fu, S. G., & Qiang, L. Z. (1992). The tectonic environment for the formation of the Xiong'er Group and the Xiyanghe Group. *Geological Review, 38*, 325–333 (in Chinese).

Collins, W. J., Beams, S. D., White, A. J. R., & Chappell, B. W. (1982). Nature and origin of A-type granites with particular reference to southeastern Australia. *Contributions to Mineralogy and Petrology, 80*, 189–200.

Dall'Agnol, R., Frost, C. D., & Rämö, O. T. (2012). IGCP project 510 "A-type granites and related rocks through time": Project vita, results, and contribution to granite research. *Lithos, 151*, 1–16.

Deng, X. Q., Zhao, T. P., Peng, T. P., Gao, X. Y., & Bao, Z. W. (2015). Petrogenesis of 1600 Ma Maping A-type granite in the southern margin of the North China Craton and its tectonic implications. *Acta Petrologica Sinica, 31*, 1621–1635 (in Chinese).

Deng, X. Q., Peng, T.P. & Zhao, T. P. (2016a). Geochronology and geochemistry of the late Paleoproterozoic aluminous A-type granite in the Xiaoqinling area along the southern margin of the North China Craton: Petrogenesis and tectonic implications. *Precambrian Research*. In revision.

Deng, X. Q., Zhao, T. P.& Peng, T. P. (2016b). Age and geochemistry of the early Mesoproterozoic A-type granites in the southern margin of the North China Craton: Constraints on their petrogenesis and tectonic implications. *Precambrian Research*. In revision.

Diwu, C. R., Sun, Y., Gao, J., & Fan, L. (2013). Early Precambrian tectonothermal events of the North China Craton: Constraints from in situ detrital zircon U-Pb, Hf and O isotopic compositions in Tietonggou Formation. *Chinese Science Bulletin, 58*, 3760–3770.

Diwu, C. R., Sun, Y., Lin, C. L., & Wang, H. L. (2010). LA-(MC)-ICPMS U-Pb zircon geochronology and Lu-Hf isotope compositions of the Taihua Complex on the southern margin of the North China Craton. *Chinese Science Bulletin, 55*, 2112–2123.

Diwu, C. R., Sun, Y., Yuan, H., Wang, H., Zhong, X., & Liu, X. (2008). U-Pb ages and Hf isotopes for detrital zircons from quartzite in the Paleoproterozoic Songshan Group on the southwestern margin of the North China Craton. *Chinese Science Bulletin, 53*, 2828–2839.

Diwu, C. R., Sun, Y., Zhao, Y., & Lai, S. C. (2014). Early Paleoproterozoic (2.45–2.20 Ga) magmatic activity during the period of global magmatic shutdown: Implications for the crustal evolution of the southern North China Craton. *Precambrian Research, 255*, 627–640.

Eby, G. N. (1992). Chemical subdivision of the A-type granitoids: Petrogenetic and tectonic implications. *Geology, 20*, 641–644.

England, P. C., & Thompson, A. B. (1984). Pressure–temperature–time paths of regionalmetamorphism I. Heat transfer during the evolution of regions of thickenedcontinental crust. *Journal of Petrology, 25*, 894–928.

Frost, B. R., Barnes, C. G., Collins, W. J., Arculus, R. J., Ellis, D. J., Frost, C. D. (2001). A geochemical classification for granitic rocks. *Journal of Petrology, 42*, 2033–2048.

Frost, C. D., & Frost, B. R. (2011). On Ferroan (A-type) granitoids: Their compositional variability and modes of origin. *Journal of Petrology, 52*, 39–53.

Gao, L. Z., Zhang, C. H., Liu, Y. M., Ding, X. Z., Wang, Z. Q., & Zhang, Y. J. (2009). Recognition of Meso- and Neoproterozoic stratigraphic framework in North and South China. *Acta Geoscientica Sinica, 30*, 433–446 (in Chinese).

Gao, L. Z., Zhang, C. H., Yin, C. Y., Shi, X. Y., Wang, Z. Q., Liu, Y. M., et al. (2008a). Shrimp zircon ages: Basis for refining the chronostratigraphic classification of the Meso- and Neoproterozoic strata in North China Old Land. *Acta Geoscientica Sinica, 29*, 366–376 (in Chinese).

Gao, W., Zhang, C. H., Gao, L. Z., Shi, X. Y., Liu, Y. M., & Song, B. (2008b). Zircon SHRIMP U-Pb age of rapakivi granite in Miyun, Beijing, China, and its tectono-stratigraphic implications. *Geological Bulletin of China, 27*, 793–798 (in Chinese).

Gao, X. Y., Zhao, T. P., & Chen, W. T. (2014). Petrogenesis of the early Cretaceous Funiushan granites on the southern margin of the North China Craton: Implications for the Mesozoic geological evolution. *Journal of Asian Earth Sciences, 94*, 28–44.

He, Y. H., Zhao, G. C., Sun, M., & Han, Y. (2010). Petrogenesis and tectonic setting of volcanic rocks in the Xiaoshan and Waifangshan areas along the southern margin of the North China Craton: Constraints from bulk-rock geochemistry and Sr-Nd isotopic composition. *Lithos, 114*, 186–199.

He, Y. H., Zhao, G. C., Sun, M., & Xia, X. P. (2009). SHRIMP and LA-ICP-MS zircon geochronology of the Xiong'er volcanic rocks: Implications for the Paleo-Mesoproterozoic evolution of the southern margin of the North China Craton. *Precambrian Research, 168*, 213–222.

Hu, G. H., Hu, J. L., Chen, W. & Zhao, T. P. (2010). Geochemistry and tectonic setting of the 1.78 Ga mafic dykes in the Mt. Zhongtiao and Mt. Song areas, the southern margin of the North China Craton. *Acta Petrologica Sinica, 26*, 1563–1576 (in Chinese with English abstract).

Hu, B., Zhai, M. G., Li Li, T. S., Li, Z., Peng, P., Guo, J. H., & Kusky, T. M. (2012). Mesoproterozoic magmatic events in the eastern North China Craton and their tectonic implications: Geochronological evidence from detrital zircons in the Shandong Peninsula and North Korea. *Gondwana Research, 22*, 828–842.

Hu, G. H., Zhao, T. P., & Zhou, Y. Y. (2014). Depositional age, provenance and tectonic setting of the Proterozoic Ruyang Group, southern margin of the North China Craton. *Precambrian Research, 246*, 296–318.

Hu, S. X., & Lin, Q. L. (1988). *Geology and metallogeny of the collision belt between the South China and North China plates* (pp. 71–346). Nanjing: Nanjing University Press (in Chinese).

Huang, X. L., Niu, Y. L., Xu, Y. G., Yang, Q. J., & Zhong, J. W. (2010). Geochemistry of TTG and TTG-like gneisses from Lushan-Taihua complex in the southern North China Craton: Implications for late Archean crustal accretion. *Precambrian Research, 182*, 43–56.

Huang, X. L., Wilde, S. A., Yang, Q. J., & Zhong, J. W. (2012). Geochronology and petrogenesis of gray gneisses from the Taihua Complex at Xiong'er in the southern segment of the Trans-North China Orogen: Implications for tectonic transformation in the Early Paleoproterozoic. *Lithos, 134–135*, 236–252.

Huang, X. L., Wilde, S. A., & Zhong, J. W. (2013). Episodic crustal growth in the southern segment of the Trans-North China Orogen across the Archean-Proterozoic boundary. *Precambrian Research, 233*, 337–357.

Jiang, Z. S., Wang, G. D., Xiao, L. L., Diwu, C. R., Lu, J. S., & Wu, C. M. (2011). Paleoproterozoic metamorphic P-T-t path and tectonic significance of the Luoning metamorphic complex at the southern terminal of the Trans-North China Orogen, Henan Province. *Acta Petrologica Sinica, 27*, 3701–3717 (in Chinese).

King, P. L., Chappell, B. W., Allen, C. M., & White, A. J. R. (2001). Are A-type granites the high-temperature felsic granites? Evidence from fractionated granites of the Wangrah Suite. *Australian Journal of Earth Sciences, 48*, 501–514.

King, P. L., White, A. J. R., Chappell, B. W., & Allen, C. M. (1997). Characterization and origin of aluminous A-type granites from the Lachlan Fold Belt, southeastern Australia. *Journal of Petrology, 38*, 371–391.

Li, H. K., Li, H. M., & Lu, S. N. (1995). Grain zircon U-Pb ages for volcanic rocks from Tuanshanzi formation of Changcheng system and their geological implications. *Geochimica, 24*, 43–48 (in Chinese).

Li, H. K., Lu, S. N., Li, H. M., Sun, L. X., Xiang, Z. Q., Geng, J. Z., et al. (2009). Zircon and baddeleyite U-Pb precision dating of basic rock sills intruding Xiamaling Formation, North China. *Geological Bulletin of China, 28*, 1396–1404 (in Chinese).

Li, H. K., Lu, S. N., Su, W. B., Xiang, Z. Q., Zhou, H. Y., & Zhang, Y. Q. (2013). Recent advances in the study of the Mesoproterozoic geochronology in the North China Craton. *Journal of Asian Earth Sciences, 72*, 216–227.

Li, H. K., Su, W. B., Zhou, H. Y., Geng, J. Z., Xiang, Z. Q., Cui, Y. R., et al. (2011). The base age of the Changchengian System at the northern North China Craton should be younger than 1670 Ma: Constraints from zircon U-Pb LA-MC-ICPMS dating of a granite-porphyry dike in Miyun county, Beijing. *Earth Science Frontiers, 18*, 108–120 (in Chinese).

Liu, C. H., Zhao, G. C., & Liu, F. L. (2014). Detrital zircon U-Pb, Hf isotopes, detrital rutile and whole-rock geochemistry of the Huade Group on the northern margin of the North China Craton: Implications on the breakup of the Columbia supercontinent. *Precambrian Research, 254*, 290–305.

Liu, D. Y., Wilde, S. A., Wan, Y. S., Wang, S. Y., Valley, J. W., Kita, N., et al. (2009). Combined U-Pb, hafnium and oxygen isotope analysis of zircons from meta-igneous rocks in the southern North China Craton reveal multiple events in the Late Mesoarchean-Early Neoarchean. *Chemical Geology, 261*, 140–154.

Liu, X.Y. (2011). *Chronological, petrological and geochemical characteristics of the Paleo-Mesoproterozoic alkali-rich intrusive rocks along the southern part of the North China Craton*. Article on master of sciences, Beijing: Chinese Academy of Geological Sciences (in Chinese).

Loiselle, M. C., & Wones, D. R. (1979). Characteristics and origin of anorogenic granites. *Geological Society of America Abstracts with Programs, 11*, 468.

Lu, S. N., Li, H. K., Li, H. M., Song, B., Wang, S. Y., Zhou, H. Y., et al. (2003). U-Pb isotopic ages and their significance of alkaline granite in the southern margin of the North China Craton. *Geological Bulletin of China, 22*, 762–768 (in Chinese).

Lu, S. N., Zhao, G. C., Wang, H. C., & Hao, G. J. (2008). Precambrian metamorphic basement and sedimentary cover of the North China Craton: A review. *Precambrian Research, 160*, 77–93.

Lu, X. X. (1989). The grological characteristics of Longwangzhuang A-type granite and its significance. *Acta Petrologica Sinica*, 67–77 (in Chinese).

Lu, Z., Xu, X., & Liu, F. (1995). The Precambrian Khondalite Series in the North of China (pp. 245–251). Changchun Publishing House, Changchun (in Chinese).

Peng, P. (2015). Precambrian mafic dyke swarms in the North China Craton and their geological implications. *Science China Earth Sciences, 58*, 649–675.

Peng, P., Liu, F., Zhai, M., & Guo, J. (2012). Age of the Miyun dyke swarm: Constraints on the maximum depositional age of the Changcheng System. *Chinese Science Bulletin, 57*, 105–110.

Peng, P., Wang, X. P., Lai, Y., Wang, C., & Windley, B. F. (2015). Large-scale liquid immiscibility and fractional crystallization in the 1780 Ma Taihang dyke swarm: Implications for genesis of the bimodal Xiong'er volcanic province. *Lithos, 236–237*, 106–122.

Peng, P., Zhai, M., Ernst, R. E., Guo, J., Liu, F., & Hu, B. (2008). A 1.78 Ga large igneous province in the North China craton: The Xiong'er volcanic province and the North China dyke Swarm. *Lithos, 101*, 260–280.

Peng, P., Zhai, M.-G., Li, Q., Wu, F., Hou, Q., Li, Z., et al. (2011). Neoproterozoic (~900 Ma) Sariwon sills in North Korea: Geochronology, geochemistry and implications for the evolution of the south-eastern margin of the North China Craton. *Gondwana Research, 20*, 243–254.

Peng, P., Zhai, M. G., Zhang, H. F., & Guo, J. H. (2005). Geochronological constraints on the paleoproterozoic evolution of the North China craton: SHRIMP zircon ages of different types of mafic dikes. *International Geology Review, 47*, 492–508.

Peng, P., Zhai, M. G., Zhang, H. F., Zhao, T. P., & Ni, Z. Y. (2004). Geochemistry and geological significance of the 1.8 Ga mafic dyke swarms in the North China Craton: An example from the juncture of Shanxi, Hebei and Inner Mongolia. *Acta Petrologica Sinica, 20*, 439–456 (in Chinese).

Qiao, X. F., & Wang, X. Y. (1984). New stipulation concerning the Lvliang orogeny. *Geological Review, 30*, 177–178 (in Chinese with English abstract).

Rämö, O. T., Haapala, I., Vaasjoki, M., Yu, J. H., & Fu, H. Q. (1995). 1700 Ma Shachang complex, northeast China: Proterozoic rapakivi granite not associated with Paleoproterozoic orogenic crust. *Geology, 23*, 815–818.

Shen, F. N. (1986). Discussion on the relational questions of Taihua Group in Minor Qinling rage. *Journal of Northwest University (Natural Science Edition), 6*, 42–51 (in Chinese).

Shi, Y., Yu, J. H., Xu, X. S., Tang, H. F., Qiu, J. S., & Chen, L. H. (2011). U-Pb ages and Hf isotope compositions of zircons of Taihua Group in Xiaoqinling area, Shaanxi Province. *Acta Petrologica Sinica, 27*, 3095–3108 (in Chinese).

Song, B., Nutman, A. P., Liu, D. Y., & Wu, J. S. (1996). 3800 to 2500 Ma crustal evolution in the Anshan area of Liaoning Province, northeastern China. *Precambrian Research, 78*, 79–94.

Sun, S., Cong, B. L., & Li, J. L. (1981). Meso-Neoproterozoic sedimentary basins in Henan and Shanxi Provinces. *Scientia Geologica Sinica, 16*, 314–322 (in Chinese).

Turner, S. P., Foden, J. D., & Morrison, R. S. (1992). Derivation of some A-type magmas by fractionation of basaltic magma; an example from the Padthaway Ridge, South Australia. *Lithos, 28*, 151–179.

Wan, Y. S., Liu, D. Y., Wang, S. Y., Zhao, X., Dong, C. Y., Zhou, H. Y., et al. (2009). Early precambrian crustal evolution in the Dengfeng area, Henan province (eastern China): Constraints from geochemistry and SHRIMP U-Pb zircon dating. *Acta Geologica Sinica, 83*, 982–999.

Wan, Y. S., Wilde, S. A., Liu, D. Y., Yang, C., Song, B., & Yin, X. (2006). Further evidence for ~1.85 Ga metamorphism in the Central Zone of the North China Craton: SHRIMP U-Pb dating of zircon from metamorphic rocks in the Lushan area. *Henan Province. Gondwana Research, 9*, 189–197.

Wang, G. D., Wang, H., Chen, H. X., Lu, J. S., & Wu, C. M. (2014). Metamorphic evolution and zircon U-Pb geochronology of the Mts. Huashan amphibolites: Insights into the Palaeoproterozoic amalgamation of the North China Craton. *Precambrian Research, 245*, 100–114.

Wang, W., Liu, S., Bai, X., Li, Q., Yang, P., Zhao, Y., et al. (2013a). Geochemistry and zircon U-Pb-Hf isotopes of the late Paleoproterozoic Jianping diorite-monzonite-syenite suite of the North China Craton: Implications for petrogenesis and geodynamic setting. *Lithos, 162–163*, 175–194.

Wang, W., Liu, S., Santosh, M., Deng, Z., Guo, B., Zhao, Y., et al. (2015). Late Paleoproterozoic geodynamics of the North China Craton: Geochemical and zircon U-Pb-Hf records from a volcanic suite in the Yanliao rift. *Gondwana Research, 27*, 300–325.

Wang, X. L., Jiang, S. Y., Dai, B. Z., & Kern, J. (2013b). Lithospheric thinning and reworking of Late Archean juvenile crust on the southern margin of the North China Craton: Evidence from the Longwangzhuang Paleoproterozoic A-type granites and their surrounding Cretaceous adakite-like granites. *Geological Journal, 48*, 498–515.

Wang, Y. J., Fan, W. M., Zhang, Y., Guo, F., Zhang, H., & Peng, T. (2004). Geochemical,40Ar/39Ar geochronological and Sr–Nd isotopic constraints on the origin of Paleoproterozoic mafic dikes from the southern Taihang Mountains and implications for the ca. 1800 Ma event of the North China Craton. *Precambrian Research, 135*, 55–77.

Wang, Y. J., Zhao, G. C., Cawood, P. A., Fan, W., Peng, T., Sun, L. (2008). Geochemistry of Paleoproterozoic (1770 Ma) mafic dikes from the Trans-North China Orogen and tectonic implications. *Journal of Asian Earth Sciences, 33*, 61–77.

Whalen, J. B., Currie, K. L., & Chappell, B. W. (1987). A-type granites: Geochemical characteristics, discrimination and petrogenesis. *Contributions to Mineralogy and Petrology, 95*, 407–419.

Wu, F. Y., Sun, D. Y., Li, H. M., Jahn, B. M., & Wilde, S. A. (2002). A-type granites in northeastern China: Age and geochemical constraints on their petrogenesis. *Chemical Geology, 187*, 143–173.

Wu, T. S., & Xu, C. L. (1982). On the Lvliang movement. *Geological Review, 28*, 240–244 (in Chinese with English abstract).

Xu, X. S., Griffin, W. L., Ma, X., O'Reilly, S. Y., He, Z. Y., & Zhang, C. L. (2009). The Taihua group on the southern margin of the North China craton: further insights from U-Pb ages and Hf isotope compositions of zircons. *Mineralogy and Petrology, 97*, 43–59.

Zhai, M. G., Hu, B., Peng, P., & Zhao, T. P. (2014). Meso-Neoproterozoic magmatic events and multi-stage rifting in the NCC. *Earth Science Frontiers, 21*, 100–119 (in Chinese).

Zhai, M. G., Hu, B., Zhao, T. P., Peng, P., & Meng, Q. R. (2015). Late Paleoproterozoic–Neoproterozoic multi-rifting events in the North China Craton and their geological significance: A study advance and review. *Tectonophysics* (in press).

Zhai, M. G., & Liu, W. J. (2003). Palaeoproterozoic tectonic history of the North China craton: A review. *Precambrian Research, 122*, 183–199.

Zhai, M.-G., & Peng, P. (2007). Paleoproterozoic events in the North China Craton. *Acta Petrologica Sinica, 23*, 2665–2682 (in Chinese).

Zhai, M. G., & Santosh, M. (2011). The early Precambrian odyssey of the North China Craton: A synoptic overview. *Gondwana Research, 20*, 6–25.

Zhai, M. G., Santosh, M., & Zhang, L. C. (2011). Precambrian geology and tectonic evolution of the North China Craton. *Gondwana Research, 20*, 1–5.

Zhang, S. H., Liu, S. W., Zhao, Y., Yang, J. H., Song, B., & Liu, X. M. (2007). The 1.75–1.68 Ga anorthosite-mangerite-alkali granitoid-rapakivi granite suite from the northern North China Craton: Magmatism related to a Paleoproterozoic orogen. *Precambrian Research, 155*, 287–312.

Zhang, S. H., Zhao, Y., & Santosh, M. (2012). Mid-Mesoproterozoic bimodal magmatic rocks in the northern North China Craton: Implications for magmatism related to breakup of the Columbia supercontinent. *Precambrian Research, 222–223*, 339–367.

Zhang, S. H., Zhao, Y., Yang, Z. Y., He, Z. F., & Wu, H. (2009). The 1.35 Ga diabase sills from the northern North China Craton: Implications for breakup of the Columbia (Nuna) supercontinent. *Earth and Planetary Science Letters, 288*, 588–600.

Zhang, Y.-B., Li, Q.-L., Lan, Z.-W., Wu, F.-Y., Li, X.-H., Yang, J.-H., et al. (2015). Diagenetic xenotime dating to constrain the initial depositional time of the Yan-Liao Rift. *Precambrian Research, 271*, 20–32.

Zhao, G. C., & Cawood, P. A. (2012). Precambrian geology of China. *Precambrian Research, 222–223*, 13–54.

Zhao, G. C., Cawood, P. A., Wilde, S. A., & Sun, M. (2002a). Review of global 2.1–1.8 Ga orogens: Implications for a pre-Rodinia supercontinent. *Earth-Science Reviews, 59*, 125–162.

Zhao, G. C., Cawood, P. A., Wilde, S. A., Sun, M., & Lu, L. Z. (2000). Metamorphism of basement rocks in the Central Zone of the North China Craton: Implications for Paleoproterozoic tectonic evolution. *Precambrian Research, 103*, 55–88.

Zhao, G. C., He, Y. H., & Sun, M. (2009). The Xiong'er volcanic belt at the southern margin of the North China Craton: Petrographic and geochemical evidence for its outboard position in the Paleo-Mesoproterozoic Columbia Supercontinent. *Gondwana Research, 16*, 170–181.

Zhao, G. C., Sun, M., & Wilde, S. A. (2003). Major tectonic units of the North China Craton and their Paleoproterozoic assembly. *Science in China, Series D: Earth Sciences, 46*, 23–38.

Zhao, G. C., Sun, M., Wilde, S. A., & Li, S. Z. (2005). Late Archean to Paleoproterozoic evolution of the North China Craton: Key issues revisited. *Precambrian Research, 136*, 177–202.

Zhao, G. C., Wilde, S. A., Cawood, P. A., & Sun, M. (2001). Archean blocks and their boundaries in the North China Craton: lithological, geochemical, structural and P-T path constraints and tectonic evolution. *Precambrian Research, 107*, 45–73.

Zhao, G. C., Wilde, S. A., Sun, M., Li, S. Z., Li, X. P., & Zhang, J. (2008). SHRIMP U-Pb zircon ages of granitoid rocks in the Lüliang Complex: Implications for the accretion and evolution of the Trans-North China Orogen. *Precambrian Research, 160*, 213–226.

Zhao, G. C., Wilde, S. A., Guo, J. H., Cawood, P. A., Sun, M., & Li, X. P. (2010). Single zircon grains record two continental collisional events in the North China craton. *Precambrian Research, 177*, 266–276.

Zhao, T. P., Deng, X. Q., Hu, G. H., Zhou, Y. Y., Peng, P., & Zhai, M. G. (2015). The Paleoproterozoic-Mesoproterozoic boundary of the North China Craton and the related geological issues: A review. *Acta Petrologica Sinica, 31*, 1495–1508 (in Chinese).

Zhao, T. P., Zhai, M. G., Xia, B., Li, H. M., Zhang, Y. X., & Wan, Y. S. (2004). Study on the zircon SHRIMP ages of the Xiong'er Group volcanic rocks: constraint on the starting time of covering strata in the North China Craton. *Chinese Science Bulletin, 9*, 2495–2502.

Zhao, T. P., Zhang, Z. H., Zhou, Y. Y., Wang, S. Y., Liu, C. S., & Liang, H. J., et al. (2012). *Precambrian geology of the Songshan area, Henan province, China* (pp. 36–85). Beijing: Geological Publishing House (in Chinese).

Zhao, T. P., & Zhou, M. F. (2009). Geochemical constraints on the tectonic setting of Paleoproterozoic A-type granites in the southern margin of the North China Craton. *Journal of Asian Earth Sciences, 36*, 183–195.

Zhao, T. P., Zhou, M. F., Zhai, M. G., & Xia, B. (2002b). Paleoproterozoic rift-related volcanism of the Xiong'er Group, North China Craton: Implications for the breakup of Columbia. *International Geology Review, 44*, 336–351.

Zhao, Z. P. (1993). *Precambrian crustal evolution of the Sino-Korean Paraplatform*. Beijing: Science Press (in Chinese).

Zhong, Y., Zhai, M. G., Peng, P., Santosh, M., & Ma, X. D. (2015). Detrital zircon U-Pb dating and whole-rock geochemistry from the clastic rocks in the northern marginal basin of the North China Craton: Constraints on depositional age and provenance of the Bayan Obo Group. *Precambrian Research, 258*, 133–145.

17 Insights into the Ore Genesis of the Giant Bayan Obo REE-Nb-Fe Deposit and the Mesoproterozoic Rifting Events in the Northern North China Craton

Kui-Feng Yang, Hong-Rui Fan, Fang-Fang Hu, Shuang Liu, and Kai-Yi Wang

Abstract

Bayan Obo ore deposit is the largest rare earth element (REE) resource and the second largest niobium (Nb) resource in the world. The REE enrichment mechanism and genesis of this giant deposit still remains intense debated. The deposit is hosted in the massive dolomite, and nearly one hundred carbonatite dykes occur in the vicinity of the deposit. The carbonatite dykes can be divided into three types from early to late: dolomite, coexisting dolomite–calcite, and calcite type, corresponding to different evolutionary stages of carbonatitic magmatism, and the latter always has higher LREE content. The origin of the ore-hosting dolomite at Bayan Obo has been addressed in various models, ranging from a normal sedimentary carbonate rocks to volcano-sedimentary sequence, and a large carbonatitic intrusion. More geochemical evidences and field interspersed relationship show that the coarse-grained dolomite represents a Mesoproterozoic carbonatite pluton and the fine-grained dolomite resulted from the extensive REE mineralization and modification of the former one. The ore bodies, distributed along an E-W striking belt, occur as large lenses and underwent more intense fluoritization and fenitization with wall rocks. The first episode mineralization is characterized by disseminated mineralization in the dolomite. The second or main-episode is banded or massive mineralization, cut by the third episode consisting of aegirine-rich veins. Various dating methods gave different mineralization ages at Bayan Obo, resulting in long and hot debates. Compilation of available data suggests that the mineralization is rather variable with two peaks at ~1400 and 440 Ma. The early mineralization peak closes in time to the intrusion of the carbonatite dykes. A significant thermal event at ca. 440 Ma resulted in the formation of late-stage veins with coarse crystals of REE minerals. Fluids involving in the REE-Nb-Fe mineralization at Bayan Obo might be REE-F-CO_2-NaCl-H_2O system. The presence of REE-carbonates as an abundant solid in the ores shows that the original ore-forming fluids are very rich in REE, and therefore, have the potential to produce economic REE ores at Bayan Obo. The Bayan Obo deposit is a product of mantle-derived carbonatitic magmatism at ca. 1400 Ma, which was likely related to the breakup of the supercontinent Columbia. Some remobilization of REE occurred due to subduction of the Palaeo-Asian oceanic plate in the Early Paleozoic, forming weak vein-like mineralization.

K.-F. Yang (✉) · H.-R. Fan · F.-F. Hu · S. Liu · K.-Y. Wang
Key Laboratory of Mineral Resources, Institute of Geology and Geophysics, Chinese Academy of Sciences, Beijing, 100029, China
e-mail: yangkuifeng@mail.iggcas.ac.cn

M. Zhai et al. (eds.), *Main Tectonic Events and Metallogeny of the North China Craton*, Springer Geology, DOI 10.1007/978-981-10-1064-4_17

Keywords
Geochemistry • Geochronology • Carbonatite • Dolomite • Bayan Obo REE-Nb-Fe deposit

17.1 Introduction

Bayan Obo ore deposit is the largest rare earth element (REE) deposit, the second largest niobium (Nb) deposit in the world, and also a large iron (Fe) deposit in China. More than 80 % light REE (LREE) resources in China are distributed in the Bayan Obo region, Inner Mongolia, Northern China (Wu et al. 1996; Yang and Woolley 2006; Fan et al. 2014). Since the discoveries of Fe ores in the Main Orebody in 1927, many studies have been carried out, particularly in the recent two decades, on the geological background, mineral constituents, geochronology and geochemistry. However, due to the complicated element/mineral compositions and several geological activity events at Bayan Obo, the genesis of this giant REE ore deposit, particularly with regard to the mechanism of REE enrichment, still remains intense debated (Yuan et al. 1992; Wang et al. 1994, 2002a; Bai et al. 1996; Le Bas et al. 1997, 2007; Li 2007; Smith et al. 2000, 2015; Yang et al. 2000, 2003, 2009, 2011a, b, 2012; Fan et al. 2004a, b, 2014; Yang and Le Bas 2004; Smith 2007; Liu et al. 2008; Ling et al. 2013; Zhu et al. 2015).

The main arguments have focused on the genesis of the ore-hosting dolomite marble. Chao et al. (1992, 1997) proposed that the dolomite marble is a sedimentary formation and the REE mineralization formed from fluids associated with granitic magmatism and metamorphism during the Paleozoic. Wang et al. (1992), Yuan et al. (1991) and Bai et al. (1996) suggested that the ore-hosting dolomite marble is a volcano-sedimentary formation and that the REE mineralization was derived from a mantle fluid. Drew et al. (1990), Le Bas et al. 1992, 1997, 2007), Yang and Le Bas (2004) and Yang et al. (2003, 2011a, b) argued that the ore-hosting dolomite marble is a carbonatite intrusion and that the REE mineralization was derived from a Mesoproterozoic carbonatitic magma. However, recent studies (Campbell et al. 2014; Lai et al. 2015; Ling et al. 2013; Smith et al. 2015; Xu et al. 2010, 2012; Yang et al. 2009) appear to favor the model of multiple mineralization.

In this paper, combined with accumulation of the broad scientific research results, especially those large numbers of petrochemistry and radiogenic isotopic data, we review the geological features of this giant deposit, focusing on formation of ore-hosting dolomites and carbonatite dykes and propose a possible process for the giant Bayan Obo REE-Nb-Fe deposit.

17.2 Regional and Ore Geology

The Bayan Obo deposit is located in the northern margin of the North China Craton (NCC), bordering on the Central Asian Orogenic Belt to the north (Xiao et al. 2003; Xiao and Kusky 2009) (Fig. 17.1). Gentle fold structures, composed mostly of the low grade meta-sedimentary units of the Mesoproterozoic Bayan Obo Group, are distributed from south to north in the region (Fig. 17.1). The famous Bayan Obo giant REE-Nb-Fe deposit, hosted in the massive dolomite, occurs in one of the syncline cores (Fig. 17.2). To the north of the ore body, a complete sequence of Bayan Obo Group is exposed in the Kuangou anticline, which is developed on the Paleoproterozoic basement rocks with a distinct angular unconformity (Fig. 17.2). The low grade clastic sequences of the Bayan Obo Group represent the sedimentary units deposited within the Bayan Obo marginal rift (Wang et al. 1992), which correlated with the Mesoproterozoic continental breakup event of the NCC (Zhai 2004; Zhao et al. 2004; Li et al. 2006; Hou et al. 2008a, b; Yang et al. 2011b; Zhai and Santosh 2011). The Bayan Obo REE-Nb-Fe deposit is just located in the Bayan Obo continental margin rift in the north of the NCC. The ore-hosting dolomites, covered by K-rich slate (H_9 term) and extended 18 km from east to west with approximately 2 km width (Fig. 17.1), was once considered as a component of Bayan Obo Group, called H_8 term. The origin of the dolomite is still disputed, and it has been proposed to be either sedimentary (Meng 1982; Chao et al. 1992; Yang et al. 2009; Lai et al. 2012), or carbonatite related (Yuan et al. 1992; Le Bas et al. 1992, 1997, 2007; Yang et al. 2000, 2003, 2011a, b; Hao et al. 2002; Wang et al. 2002a; Zhu et al. 2015).

Basement rocks at Bayan Obo are composed of Neoarchean mylonitic granite-gneiss (2588 ± 15 Ma), Paleoproterozoic syenite and granodiorite (2018 ± 15 Ma), and biotite granite-gneiss and garnet-bearing granite-gneiss (~1890 Ma) (Wang et al. 2002b; Fan et al. 2010). Dioritic-granitic plutons, composed of gabbro, gabbroic diorite, granitic diorite, adamellite, and biotite granite, are distributed within a large area in the south and east Bayan Obo mine (Fig. 17.1). These plutons were once regarded as intruding from Devonian to Jurassic. New geochronology

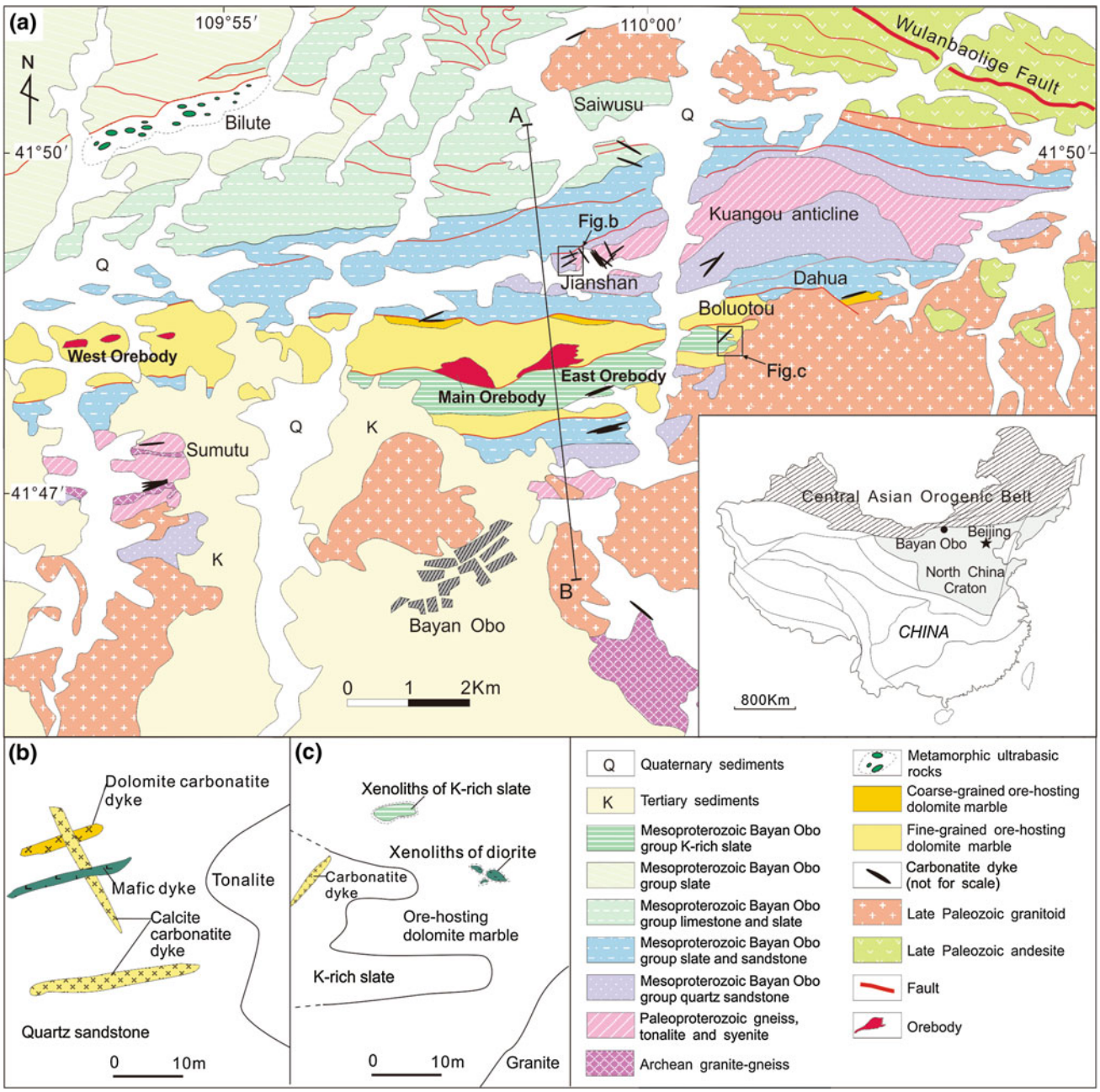

Fig. 17.1 Geological map of the Bayan Obo deposit (**a**). Intrusive contact between dolomite and calcite carbonatite dykes (**b**). Xenoliths of K-rich slate and diorite in fine-grained ore-hosting dolomite marble with extensive fenitization and flow structure around them (**c**), modified after Yang et al. (2011a)

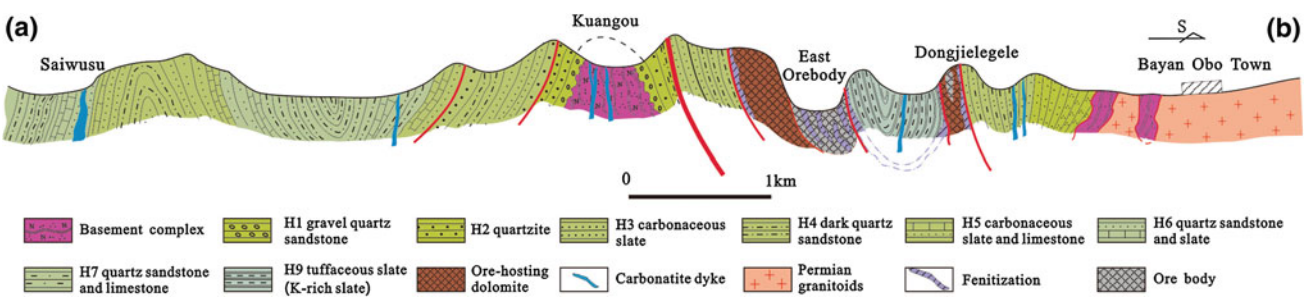

Fig. 17.2 Geological section of line *A*–*B* in Fig. 18.1, showing location of ore bodies

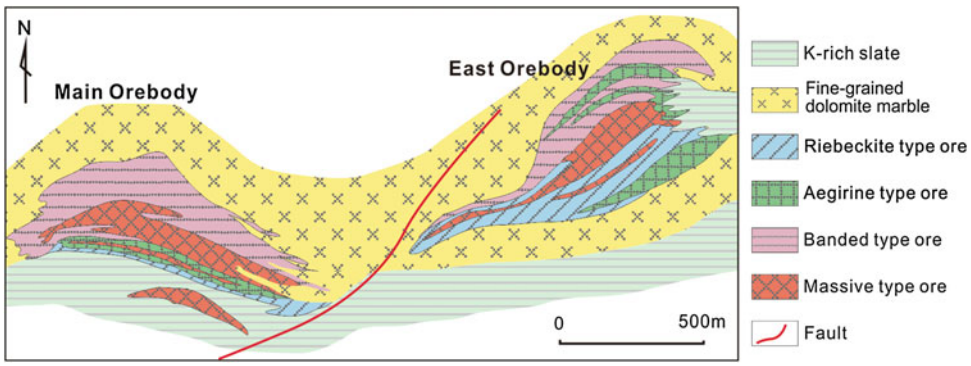

Fig. 17.3 Geological map of the main and east Orebody at Bayan Obo, modified after Institute of Geology and Guiyang Geochemistry, Chinese Academy of Sciences (1988)

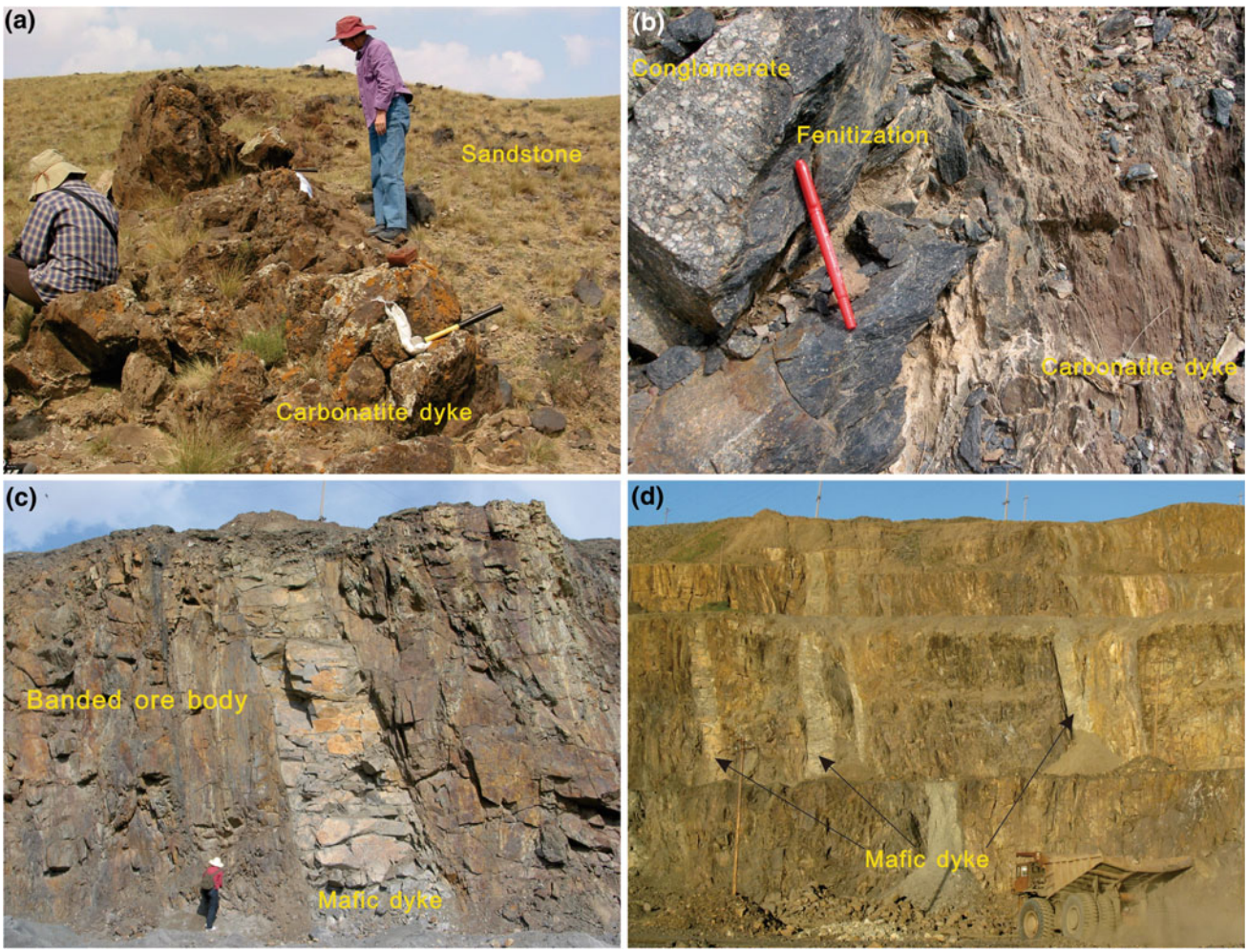

Fig. 17.4 Outcrop of mafic and carbonatite dykes at Bayan Obo. **a**, **b** Carbonatite dykes in the Dongjie and Dulahala showing strong fenitization developed around the wallrock quartz conglomerate; **c**, **d** mafic dykes cutting banded ore body in the Bayan Obo REE deposit

data reveal that these plutons were formed in a post-collisional tectonic regime at convergent margins in the late Paleozoic at a narrow time from 263 to 281 Ma with peak age of 269 Ma (Fan et al. 2009), which is consistent with the closure of the Palaeo-Asian Ocean (Ling et al. 2014). It has been proved that REE mineralization at Bayan Obo has no direct relation with these late Paleozoic granitoids (Fan et al. 2004b).

Detailed geological mapping showed that there are nearly one hundred carbonatite dykes occur in the vicinity of the Bayan Obo deposit (Figs. 17.1 and 17.4a). They intruded into the basement rocks and/or the Bayan Obo Group. The carbonatite dykes are usually 0.5–2.0 m wide and 10–200 m long, and strike generally to northeast or northwest (Le Bas et al. 1992; Tao et al. 1998; Yang et al. 2011a; Fan et al. 2014). It is significant that some dykes have metasomatized the country rocks on both sides of the contact zones, producing fenites characterized by the presence of sodic amphiboles and albite (Fig. 17.4b) (Le Bas et al. 1992; Yang et al. 2003; Yang and Le Bas 2004; Fan et al. 2014). The major constituent minerals in the dykes are dolomite and calcite, which are associated with subordinate apatite, monazite, barite, bastnaesite, and magnetite (Yang et al. 2003; Yang and Le Bas 2004). The REE contents in the different carbonatite dykes vary from ca. 0.02 to ca. 20 wt% (Tao et al. 1998; Yang et al. 2003).

The mine is composed of three major ore bodies, East, Main, and West Orebodies (Fig. 17.1). The East and Main Orebodies are distributed between the boundary of ore-hosting dolomite and Bayan Obo group K-rich slate. The West Orebody, including many small ore bodies, locates mainly in the massive dolomite. Relative to the West Orebody, the East and Main Orebodies occur as larger lenses (Fig. 17.3), underwent more intense fluoritization, fenitization, and hosted more abundant REE and Nb resource. The ores are distributed along an E-W striking belt. From south to north in the East and Main Orebodies, the REE ores are defined to be four types, namely, the riebeckite, aegirine, massive, and banded types (Fig. 17.3). The principal REE minerals are bastnaesite-(Ce) and monazite-(Ce), and accompanied with a various kinds of REE and Nb minerals, such as huanghoite, aeschynite-(Ce), felgusonite, apatite, and columbite. Iron minerals are magnetite and hematite. Main gangue minerals include fluorite, barite, alkali amphibole, quartz, and aegirine.

The paragenesis of the deposit is complex, according to Chao et al. (1992), with at least 11 stages from syngenetic sedimentary deposition, through metamorphism and mineralization, to the intrusion of late Paleozoic granitoids mainly to the southeast of the deposit. Based on ore occurrences and cross-cutting relations, three important REE mineralizing episodes can be indentified at the simplest level (Fig. 17.5). The first episode is characterized by disseminated mineralization which contains monazite associated with ferroan dolomite, ankerite, and magnetite, concentrated along grain boundaries in the relatively unaltered/massive dolomite (Fig. 17.5a). The second or main-episode is banded and/or massive mineralization (Fig. 17.5b), which shows a generalized paragenetic sequence of strongly banded REE and Fe ores showing alteration to aegirine, fluorite, and minor alkali amphibole. The banded and massive ores are cut by the third episode consisting of aegirine-rich veins containing fluorite, huanghoite, albite, calcite, biotite, and/or pyrite with coarser crystal (Fig. 17.5c, d).

17.3 Genesis of Carbonatite Dyke and Ore-Hosting Dolomite

Abundant carbonatite dykes occur adjacent to the eastern and southern of the Bayan Obo mine and particularly within the Kuangou anticline (Fig. 17.1). These dykes intruded into the Bayan Obo Group of low grade meta-sedimentary rocks, as well as the basement rocks, with fenitization of the wall rocks (Fig. 17.4a, b). Wang et al. (2002a) mentioned that carbonatite dykes at Bayan Obo can be divided into three types: dolomite, coexisting dolomite–calcite and calcite type. The latter always has higher LREE content. Wang et al. (2002a) also argued that these three types of carbonatite dykes might correspond with different evolutionary stages of carbonatitic magmatism based on the REE and trace element data. Yang et al. (2011a) found the outcrop of incision contact between dolomite type and calcite type dykes at Jianshan to the north of the East Orebody. Field evidence of incision contact shows that a dolomite carbonatite dyke was cut by a calcite one (Fig. 17.1b), showing that the emplacement of the calcite dyke is later than the dolomite one. Geochemical data (Yang et al. 2011a) show that Sr and LREE contents in the dykes gradually increase from dolomite type, through calcite-dolomite type, to calcite type. This trend might be resulted from the crystal fractionation of carbonatitic magma.

The origin of the ore-hosting dolomite at Bayan Obo has been addressed in various models, ranging from a normal sedimentary carbonate rocks (Chao et al. 1992) to volcano-sedimentary sequence (Wang et al. 1992), and a large carbonatitic intrusion (Le Bas et al. 1997, 2007; Yang et al. 2003, 2004). The possible presence of fossils (Meng 1982) has been cited to support the first argument, and the contact relationships and some internal features have been used to support the third one (Fig. 17.1c) (Le Bas et al. 1997, 2007; Yang et al. 2011a). All arguments have been supported with reference to the trace element and isotopic composition of the dolomite. It should be pointed that carbonate rocks with fossils are not found in the Bayan Obo area. Sun et al. (2012, 2014) systematically analyzed elemental geochemistry, and C, O, and Mg isotopic geochemistry of the ore-hosting dolomite and compared that with the nearby Sailinhudong micrite mound. They show that the Bayan Obo ore-hosting dolomite marbles are strongly enri-

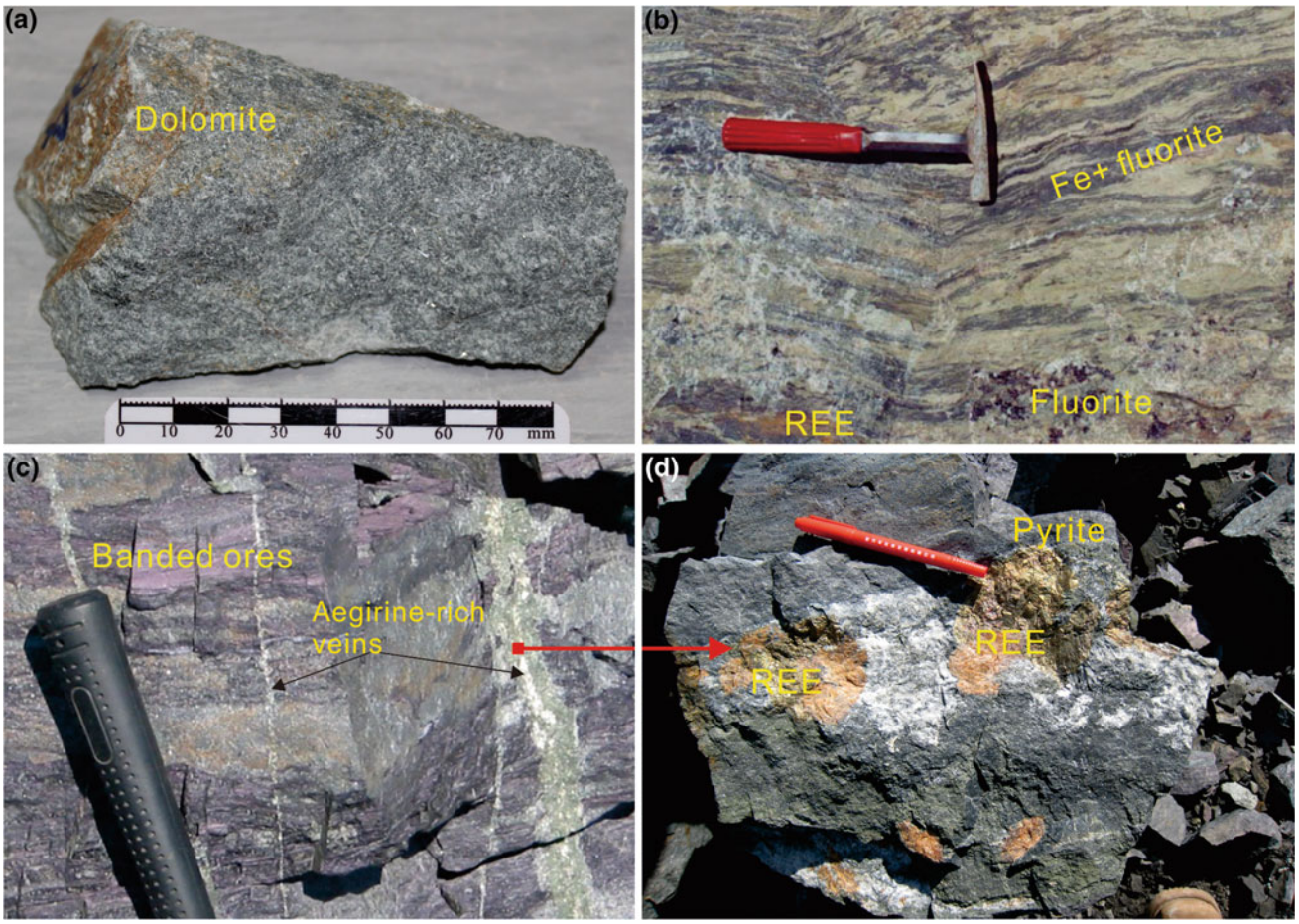

Fig. 17.5 Major mineralization types from the Bayan Obo deposit. **a** Fine-grained dolomite with disseminated mineralization; **b** banded REE–Nb–Fe mineralization; **c**, **d** late-stage vein cross-cutting banded REE–Nb–Fe ore

ched in LREEs, Ba, Th, Nb, Pb, and Sr, and have very different (PAAS)-normalized REE patterns, while Sailinhudong micrite carbonates have higher $\delta^{13}C_{PDB}$ and $\delta^{18}O_{SMOW}$ values, falling into the typical sedimentary field. The Bayan Obo ore-hosting dolomites are isotopically intermediate between primary igneous carbonatite and typical sedimentary limestone. The $\delta^{26}Mg$ values of the Sailinhudong micrite carbonates are lighter than those of normal Mesoproterozoic sedimentary dolostone, while those of the Bayan Obo ore-hosting dolomite marble are isotopically heavier, similar to $\delta^{26}Mg$ of mantle xenoliths and Bayan Obo intrusive carbonatite dyke. Sun et al. (2012, 2014) gave clear evidences that the ore-hosting dolomite at Bayan Obo was mainly derived from the mantle.

A relatively small volume of coarse-grained dolomite occurs in the Bayan Obo deposit mainly in the West Orebody, as well as in the northern part of the Main Orebody. The rocks are composed predominantly of coarse-grained euhedral–subhedral dolomite, associated with evenly distributed fine-grained apatite, magnetite, and monazite (Zhu et al. 2015). The fine-grained dolomites are distributed widely and constitute the main part of the deposit. It commonly also appears massive in outcrops, and consists predominantly of dolomite or ankerite, which is mostly fine-grained, ranging from 0.05 to 0.1 mm in diameter. The coarse-grained and fine-grained facies of the dolomite occurring at Bayan Obo introduced additional complexities in the interpretation of their genesis.

Le Bas et al. (2007) proposed that the coarse-grained dolomite represents a Mesoproterozoic carbonatite pluton and the fine-grained dolomite resulted from the extensive REE mineralization and modification of the coarse-grained variety. Yang et al. (2011a) showed the field observations in the northern part of the Main Orebody, and revealed that the coarse-grained dolomite intruded into the Bayan Obo group quartz sandstone as apophyses (Fig. 17.6a). However, the geochemical characteristics of the coarse-grained dolomite are not consistent with those of the fine-grained ones (Yang et al. 2011a). The major and trace element contents of the coarse-grained dolomite are very similar to the calcite-dolomite carbonatite dykes at Bayan Obo. Data from those samples overlap within the magnesio-carbonatite

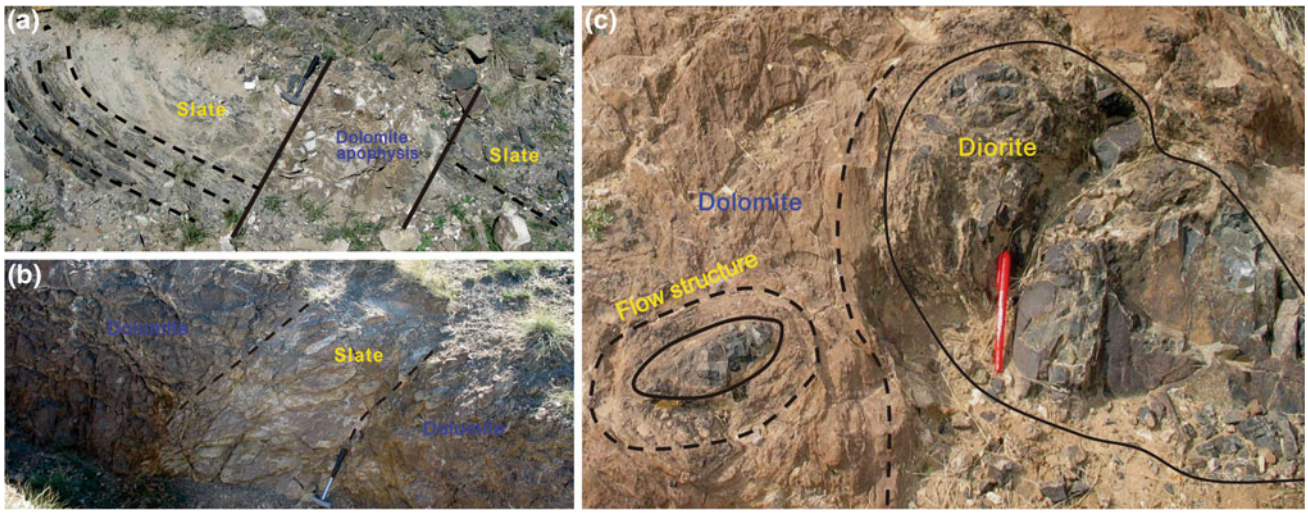

Fig. 17.6 Intrusion contact between dolomite and wallrocks. **a** A small apophysis, emanating from the dolomite, apparently intruded into the Bayan Obo group H_9 slate; **b** xenolith of H_9 slate in the ore-bearing dolomite; **c** xenoliths of diorite in the ore-bearing dolomite, and the flow structure around them

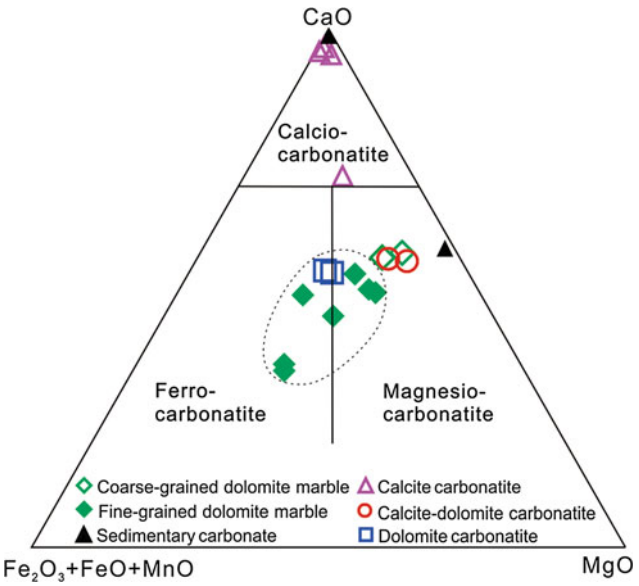

Fig. 17.7 CaO-MgO-(FeO + Fe_2O_3 + MnO) classification diagram (Woolley and Kempe 1989) for the carbonatite dykes, ore-hosting dolomite marble and sedimentary carbonate rocks from Bayan Obo district

region on the CaO-MgO-(FeO + Fe_2O_3 + MnO) classification diagram (Fig. 17.7) (Yang et al. 2011a), and show similar REE contents and distribution patterns on the chondrite-normalized abundance diagram (Yang et al. 2011a; Fig. 17.8a, b). The similar geochemical characteristics of coarse-grained dolomite and calcite-dolomite carbonatite dykes, and the intrusive contact between the coarse-grained dolomite and wallrocks (Fig. 17.6), indicate that the coarse-grained dolomite is likely an earlier phase of calcite-dolomite carbonatite stock, which did not witness the subsequent mineralization event from the residual carbonatitic melts, probably because it is located far from the main mineralized zone. The fine-grained dolomite from the Main, East, and West Orebody differs from the coarse-grained dolomite in their major, trace element and REE characteristics. The fine-grained dolomite shows major element compositions comparable to that of the dolomite carbonatite dykes. All the samples fall in the field of dolomite carbonatite dykes on the CaO-MgO-(FeO + Fe_2O_3 + MnO) classification diagram (Fig. 17.7) (Yang et al. 2011a). The REE content and distribution patterns of the fine-grained dolomite samples, however, are similar to those of the calcite carbonatite dykes (Fig. 17.8a, b). Therefore, the fine-grained dolomite cannot be compared with any specific type of carbonatite dykes at Bayan Obo as mentioned by Yang et al. (2011a).

The REE content in the dolomite carbonatite dykes is relatively low, as compared to the extreme accumulation in the calcite carbonatite dykes at Bayan Obo. Chao et al. (1992) noted that the REE minerals in the fine-grained dolomite occur as ribbon or aggregates. Wang et al. (2010) also found that the REE minerals are distributed around dolomite phenocryst in the fine-grained dolomite. Therefore, the REE minerals formed later than the formation of the dolomite phenocryst. These observations lead us to believe that the fine-grained dolomite represents an early stage large-scale dolomite carbonatite pluton, and the superposed REE mineralization was derived from the later calcite carbonatitic magma.

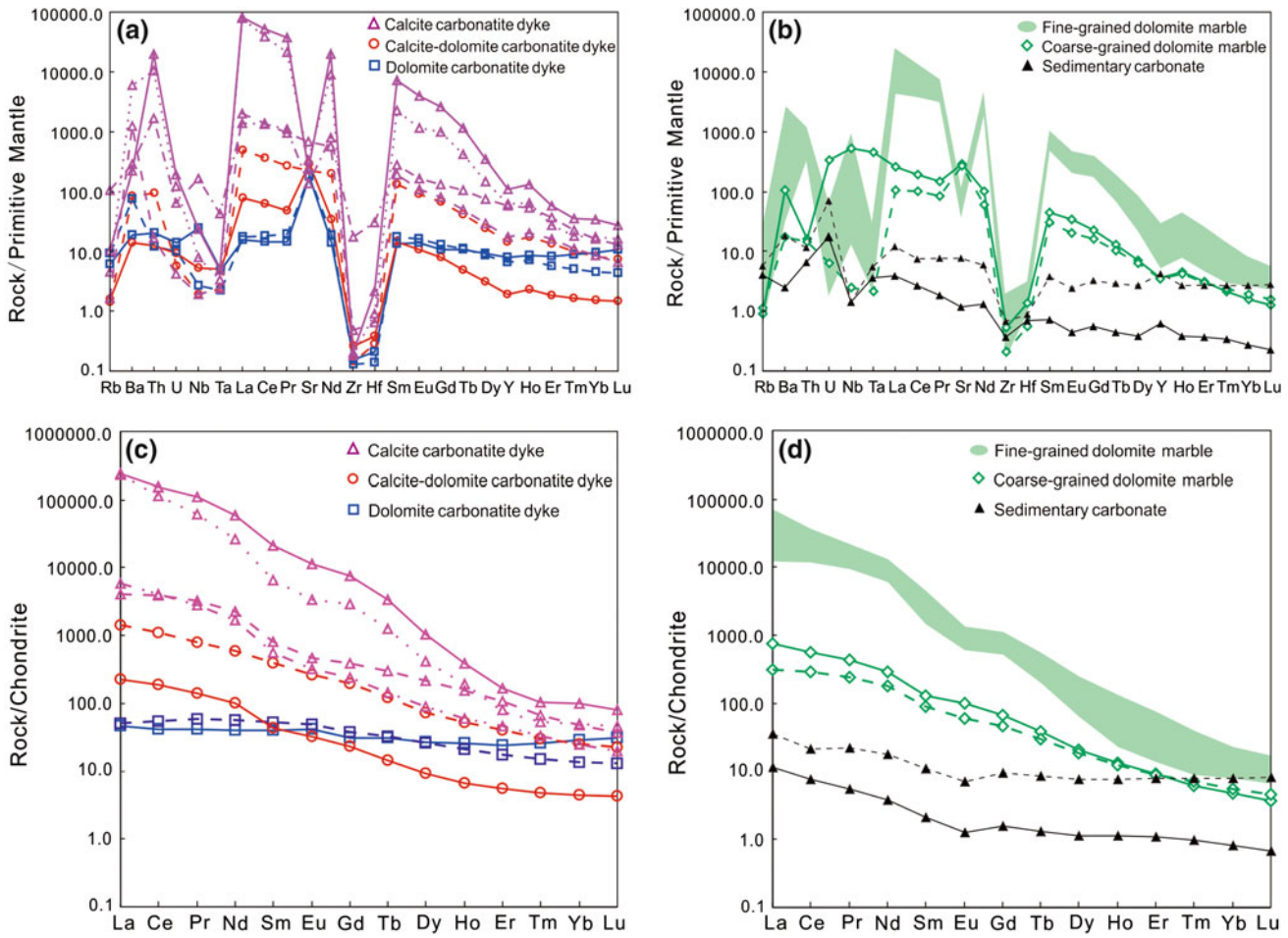

Fig. 17.8 **a**, **b** Primitive mantle-normalized trace element abundance pattern for carbonatite dykes, ore-hosting dolomite marble and sedimentary carbonate rocks at Bayan Obo; **c**, **d** chondrite-normalized REE abundance diagram for carbonatite dykes, ore-hosting dolomite marble, and sedimentary carbonate rocks at Bayan Obo, modified after Yang et al. (2011a)

17.4 REE Mineralizing Time

According to the occurrences of rocks/veins related with mineralization in the Bayan Obo deposit, the four types of REE mineralization are identified, including carbonatite dyke, ore-hosting dolomite, banded REE–Nb–Fe ore, and late-stage REE vein. Geochronology on these four type mineralizations, using U–Th–Pb, Sm–Nd, Rb-Sr, K-Ar, Ar–Ar, Re–Os, and La-Ba methods, have been reported in the last two decades (Nakai et al. 1989; Chao et al. 1992; Bai et al. 1996; Liu et al. 2004, 2008; Hu et al. 2009; Yang et al. 2011a, b; Campbell et al. 2014; Fan et al. 2014; Zhu et al. 2015). However, various dating methods gave different mineralization ages (Table 17.1; Fig. 17.9), resulting in long and hot debates. The compiled age data on Bayan Obo REE mineralization are rather variable, ranging from >1800 to ~390 Ma, with two peaks at ~1400 and 440 Ma. The earliest ages, reported from zircons in the carbonatite dykes by SHRIMP or ID-TIMS with ages >1.8 Ga, are largely thought to be inherited zircons derived from the Palaeoproterozoic basement in the area (Liu et al. 2008; Fan et al. 2014). There are three main opinions on mineralization ages.

17.4.1 Mesoproterozoic Mineralization

Nakai et al. (1989) first reported REE mineral La-Ba and Sm–Nd isochron date of 1350 ± 149 Ma and 1426 ± 40 Ma, respectively. In addition, Zhang et al. (2003) obtained mineral Sm–Nd isochron date from ores at Main and East Orebodies of 1286 ± 91 Ma and 1305 ± 78 Ma, respectively. Yang et al. (2011a) reported a whole-rock Sm–Nd isochron from of nine carbonatite dykes yielding a slightly older age of 1354 ± 59 Ma. Fan et al. (2014) analyzed zircons from a carbonatite dyke by conventional isotope dilution thermal ionization mass spectrometry (ID-TIMS), got an upper intercept age of 1417 ± 19 Ma. This age is confirmed by their SHRIMP

Table 17.1 A brief geochronology overview in the Bayan Obo deposit

Type	Material	Sample location	Methods	Age (Ma)	References
Carbonatite dyke	Carbonatite	Dulahala	Sm–Nd	1223	Zhang et al. (2003)
	Carbonatite dykes	Jianshan	Sm–Nd	1354	Yang et al. (2011a)
	Zircon in carbonatite	North of Main Orebody	U–Pb	1984	Liu et al. (2008)
	Zircon in carbonatite	–	U–Pb	1416	Campbell et al. (2000)
			U–Pb	2085	
			U–Pb	2035	
			U–Pb	1366	
	Carbonatite dykes	North of Main Orebody	U–Pb	1260	Liu et al. (2008)
			Pb–Pb	1236	
	Monazite in carbonatite	Dulahala	Sm–Nd	1320	Yang et al. (2008)
	Zircon in carbonatite	Dulahala	U–Pb	1418	Fan et al. (2014)
Ore-hosting dolomite marble, banded REE–Nb–Fe ore	Dolomite	Main and East Orebodies	Sm–Nd	1341	Yang et al. (2011a)
	Whole rock of ore	Main and East Orebodies	Sm–Nd	1592	Yuan et al. (1992)
	Monazite and bastaesite	Main Orebody	Sm–Nd	1580	Ren et al. (1994)
		North of Main and East Orebodies	Sm–Nd	1313	
	REE minerals	–	Sm–Nd	402	Cao et al. (1994)
	Allanite and riebeckite	–	Sm–Nd	422	Zhang et al. (2001)
	Dolomite	Main and East Orebodies	Sm–Nd	1273	
	REE minerals in dolomite	Main and East Orebodies	Sm–Nd	1250	Zhang et al. (1994)
	Whole rock	Main and East Orebodies	Sm–Nd	1286	
	Whole rock	Main and East Orebodies	Sm–Nd	1305	Zhang et al. (2003)
	Monazite	East Orebody	Sm–Nd	1013	Liu et al. (2005)
		West Orebody	Sm–Nd	809	
		ore	Sm–Nd	1060	
	REE minerals	Main and East Orebodies	Sm–Nd	1426	Nakai et al. (1989)
	monazite	North of Main Orebody	Th–Pb	445	Ren et al. (1994)
	Monazite	Main and East Orebodies	Th–Pb	461	Wang et al. (1994)
			Th–Pb	398-555	
	REE minerals	Main and East Orebodies	Th–Pb	407	Chao et al. (1991)
	Monazite	Dolomitic ore	Th–Pb	419	Chao et al. (1997)
	Bastaesite	Dolomitic ore	Th–Pb	555	Liu et al. (2005)
	monazite	ore	Th–Pb	1231	
	Apatite	Main and East Orebodies	U–Pb	1588	Institute of Geology and Guiyang Geochemistry, Chinese Academy of Sciences 1988)
	Whole rock	Main and East Orebodies	U–Pb	523	Zhang et al. (2003)
	REE minerals	East Orebody	SHRIMP U–Pb	820	Nakai et al. (1989)
		Contact zone	SHRIMP U–Pb	1002	
		Main and East Orebodies	La-Ba	1350	

(continued)

Table 17.1 (continued)

Type	Material	Sample location	Methods	Age (Ma)	References
	Whole rock	Main and East Orebodies	Pb–Pb	1500	Liu et al. (2001)
	Whole rock	West Orebody	Rb-Sr	391	Zhang et al. (2003)
	Alkali amphibole	Main and East Orebodies	Ar–Ar	820	Chao et al. (1991)
	Ore and dolomite	Main and East Orebodies	Nd DM model age	1544	Philpotts et al. (1991)
	Monazite in dolomite	Main and East Orebodies re	Nd DM model age	1656	Yang et al. (2008)
		East Orebody	Sm–Nd	860	
	Bastnaesite	Main Orebody	U–Th–Pb	425	Chao et al. (1991)
	Overgrowth of zircon in quartz dolomite	East Orebody	U–Pb	1325	Campbell et al. (2014)
	Overgrowth of zircon in quartz dolomite	East Orebody	U–Pb	455	Campbell et al. (2014)
Late-stage vein	Pyrite	–	Re–Os	439	Liu et al. (2004)
	Gangue mineral	Main Orebody	Sm–Nd	442	Hu et al. (2009)
	Gangue mineral	East Orebody	Rb-Sr	459	Hu et al. (2009)
	Huanghoite and aeschynite in aegirine vein	Main Orebody	U–Th–Pb	438	Chao et al. (1991)
	Huanghoite and aeschynite	–	Sm–Nd	420	Chao et al. (1991)
	Riebeckite vein	East of East Orebody	Ar–Ar	389	Lai et al. (2015)
	Molybdenite	–	Re–Os	439	Liu et al. (1996)

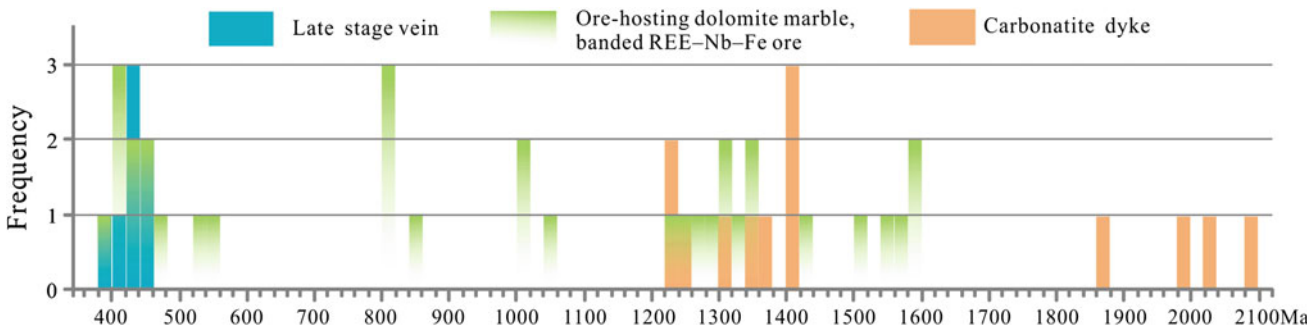

Fig. 17.9 Summary of published geochronological results of carbonatite dyke, ore-hosting dolomite marble, banded REE–Nb–Fe ore, and late-stage REE vein at Bayan Obo

U–Pb analysis of zircon from the same carbonatite dyke, which gave a $^{207}Pb/^{206}Pb$ weighted mean age of 1418 ± 29 Ma.

17.4.2 Early Paleozoic Mineralization

Wang et al. (1994) and Chao et al. (1997) made numerous Th–Pb dating of monazite and bastnaesite samples at Bayan Obo, and provided isochron ages for monazite mineralization ranging from 555 to 398 Ma. They proposed that intermittent REE mineralization of the Bayan Obo deposit started at about 555 Ma, and the principal mineralization occurred between 474 and 400 Ma. Hu et al. (2009) used Sm–Nd dating of REE mineral huanghoite and single-grain biotite Rb-Sr dating, showing concordant isochrons corresponding to 442 ± 42 and 459 ± 41 Ma, respectively.

17.4.3 Two-Stage Mineralization

Ren et al. (1994) obtained monazite and bastnaesite Sm–Nd isochron of 1313 ± 41 Ma from Main and East Orebody ores, and monazite Th–Pb isochron of 461 ± 62 Ma and 445 ± 11 Ma from carbonatite veins at Bayan Obo. SHRIMP analysis of monazite in the dolomite by Qiu (1997)

gave average $^{206}Pb/^{238}U$ age of 802 ± 35 Ma and average $^{208}Pb/^{232}Th$ age of 498.8 ± 2.9 Ma. Campbell et al. (2014) reported SHRIMP dating of extremely U-depleted (<1 ppm) zircons from banded ores in the East Orebody. Their $^{232}Th–^{208}Pb$ geochronological data reveal the age of zircon cores with Mesoproterozoic ages as 1325 ± 60 Ma and a rim alteration event with Caledonian ages as 455.6 ± 28.27 Ma. Zhu et al. (2015) reviewed Sm–Nd isotopic measurements which were undertaken to constrain the chronology of REE mineralization events at Bayan Obo, and considered that a series of ages between ca. 1400 and 400 Ma were resulted from thermal disturbance and do not imply the existence of additional mineralization events. They proposed that the earliest REE mineralization event was at 1286 ± 27 Ma using a Sm–Nd isochron of coarse-grained dolomite and the carbonatite dikes in their vicinity, and a significant thermal event at ca. 0.4 Ga resulted in the formation of late-stage veins with coarse crystals of REE minerals.

17.5 Nature of Ore-Forming Fluids and Sources

The study of the nature of ore-forming fluids at Bayan Obo is limited by the post depositional history of the ores, particularly in the earliest stages of the paragenesis like banded ores. Several possible sources of ore-forming fluids have been proposed for the Bayan Obo deposit, including deep source fluids (Institute of Geochemistry, Chinese Academy of Sciences 1988), anorogenic magma (Wang et al. 2002a), magmatic and metamorphic fluids (Chao et al. 1997), mantle fluids (Cao et al. 1994), and carbonatite magma/fluids (Bai et al. 1996; Le Bas et al. 2007). The source of ore-forming fluids best favor for REE mineralization is still disputed.

The available data on the oxygen, carbon, strontium and niobium isotope composition of the carbonatites, dolomites, and obviously sedimentary limestones at Bayan Obo are taken to indicate that the large and coarse-grained dolomite was an igneous carbonatite, and that the finer grained dolomite recrystallized under the influence of mineralizing solutions which entrained groundwater (Philpotts et al. 1991; Le Bas et al. 1997). Sun et al. (2013) systematically investigated the Fe isotope compositions of different types of rocks from the Bayan Obo deposit and related geological formations, such as carbonatites, mafic dykes, and Mesoproterozoic sedimentary iron formation and carbonates. The Fe isotope fractionation between magnetite and dolomite, and between hematite and magnetite at Bayan Obo is small, indicating that they formed in very high temperature conditions. Sun et al. (2013) proposed that the Fe isotope systematics for the Bayan Obo deposit is consistent with those of magmatic products, but different from those of sedimentary or hydrothermal products reported previously. They concluded that the Bayan Obo ore deposit is of magmatic origin. Huang et al. (2015) obtained trace elemental compositions of the magnetite and hematite from various ore types of the Bayan Obo deposit, using in situ LA-ICP-MS. Two generations of magnetite from Fe ores of the Bayan Obo deposit were identified, showing different trace element contents and origins. Magnetite of the first generation was sedimentary in origin and is rich in REEs, whereas that of the second generation was hydrothermal in origin and is relatively poor in REEs. Huang et al. (2015) concluded that sedimentary carbonates provided original REEs and were metasomatized by REE-rich hydrothermal fluids to form the giant REE deposit. This result is obviously different from that of above Fe isotope composition measurements, which imply a multiple process and hydrothermal fluids resources for REE mineralization.

Nature of ore-forming fluids is studied on fluid inclusions trapped in banded and vein ores at Bayan Obo (Smith et al. 2000; Fan et al. 2004a, 2006). Three types of fluid inclusions have been recognized: two or three phase CO_2-rich, three phase hypersaline liquid–vapor–solid, and two phase aqueous liquid-rich inclusions. Microthermometry measurements indicate that the carbonic phase in CO_2-rich inclusions is nearly pure CO_2. Fluids involving in the REE-Nb-Fe mineralization at Bayan Obo might be REE-F-CO_2-NaCl-H_2O system. Coexistences of hypersaline brine inclusion and CO_2-rich inclusion with similar homogenization temperatures give evidence that immiscibility was happened during REE mineralization. An unmixing of an original H_2O-CO_2-NaCl fluid with higher REE contents probably derived from carbonatite magma. The presence of REE-carbonates as an abundant solid in the ores shows that the original ore-forming fluids are very rich in REE, and therefore, have laid a foundation to produce economic REE ores at Bayan Obo (Fan et al. 2006).

17.6 Ore Genesis and Mesoproterozoic Rifting Events

Genesis of the Bayan Obo giant ore deposit has been subject to debate for over several decades. Several possible models of ore genesis have been proposed for the deposit as reviewed by Wu et al. (1996), including syngenetic sedimentary deposition (Meng 1982), metasomatism associated with granitic magmatism (Wang and Li 1973), and deposition from exhalative, possibly carbonatite related, hydrothermal fluids (Yuan et al. 1992). Chao et al. (1992) demonstrated an epigenetic origin for the deposit via multistage hydrothermal metasomatism. On this basis models involving metasomatism by fluids derived from either subduction (Chao et al. 1992; Wang et al. 1994), or carbonatite,

or alkaline, magmatism (Drew et al. 1990; Hao et al. 2002; Yang et al. 2003; Ling et al. 2013; Sun et al. 2013) have been proposed. The link between carbonatite magmatism and the Bayan Obo mineralization now seems firmly established. The interpretation of the carbonatite source for the metasomatic fluids is supported by the presence of carbonatite dykes cutting the metamorphic and sedimentary rocks around the deposit and the apparent carbonatitic affinities of the host dolomites (Le Bas et al. 1992, 1997, 2007; Yang et al. 2000, 2003, 2011a).

The Bayan Obo deposit is located in the north margin of the NCC, which experienced a major rifting event (the Langshan-Bayan Obo rift) in the Mesoproterozoic (Wang et al. 1992). The large Langshan-Bayan Obo continental rift, together with Yan-Liao rift in the east and Xiong'er rift in the south of NCC (Fig. 17.10), marked by swarm of mafic dykes between 1.75 and 1.79 Ga (Li et al. 2007; Peng et al. 2007; Santosh et al. 2010), correlate with the fragmentation of the Columbia supercontinent (Zhai et al. 2004; Zhao et al. 2004; Santosh et al. 2009).

The Bayan Obo deposit was likely associated in space and time with large-scale carbonatitic magmatic activity (ca. 1400–1300 Ma) in response to the long-term rifting and magma evolution in the north margin of North China Craton (Wang et al. 1992; Xiao and Kusky 2009). The depleted mantle model age (T_{DM}) from the Nd isotope data on carbonatite dyke and ore-hosting dolomite samples range from 1.61 to 1.79 Ga, which coincide with the initiation of the Bayan Obo rift (ca. 1.75 Ga, Li et al. 2007). Moreover Yang et al. (2011a) reported the coexistence of carbonatite and alkalic mafic rocks in the Bayan Obo region (Fig. 17.4c, d), which is usually related to continental rift environment. Extensive continental breakup and mantle-derived mafic and alkali magmatism during the middle Mesoproterozoic has been widely reported from various parts of the NCC in addition to the Bayan Obo region. Zhang et al. (2009) identified large volumes of 1.35 Ga diabase sills, emplaced into the Mesoproterozoic Wumishan Formation, indicates that the northern NCC underwent strong extension and mafic magmatism during the middle and late Mesoproterozoic (1.4–1.2 Ga), probably related to the final breakup of the supercontinent Columbia.

The mid–late Mesoproterozoic rifting within the NCC can be correlated to similar worldwide events associated with the breakup of the Columbia supercontinent (Rogers and Santosh 2002, 2009; Kusky and Li 2003; Kusky et al. 2007; Santosh et al. 2009). During its prolonged breakup history from ca. 1.8 to 1.2 Ga, the supercontinent probably witnessed two major episodes of fragmentation (e.g., Zhao et al. 2004, 2006). The early stage (1.8–1.6 Ga) is represented by the formation of several continental rifts accompanied by the emplacement of abundant mafic dyke swarms (Halls et al. 2000; Zhai et al. 2004; Li et al. 2006, 2007; Peng et al. 2007; Hou et al. 2008a, b). The second stage marked the final breakup (1.4–1.2 Ga), and witnessed the formation of several large mafic dyke swarms and anorogenic magmatic activity (Rogers and Santosh 2002; Zhao et al. 2004, 2006; Hou et al. 2008a).

The global anorogenic magmatism during Mesoproterozoic (mostly represented by alkaline mafic and ultramafic rocks) also include the kimberlites and carbonatites (1.6–1.2 Ga) in the margin of the Kaapvaal Craton (Phillips et al. 1989), the kimberlites (1.4–1.2 Ga) in the southwest margin of the West African (Haggerty 1982), the kimberlites

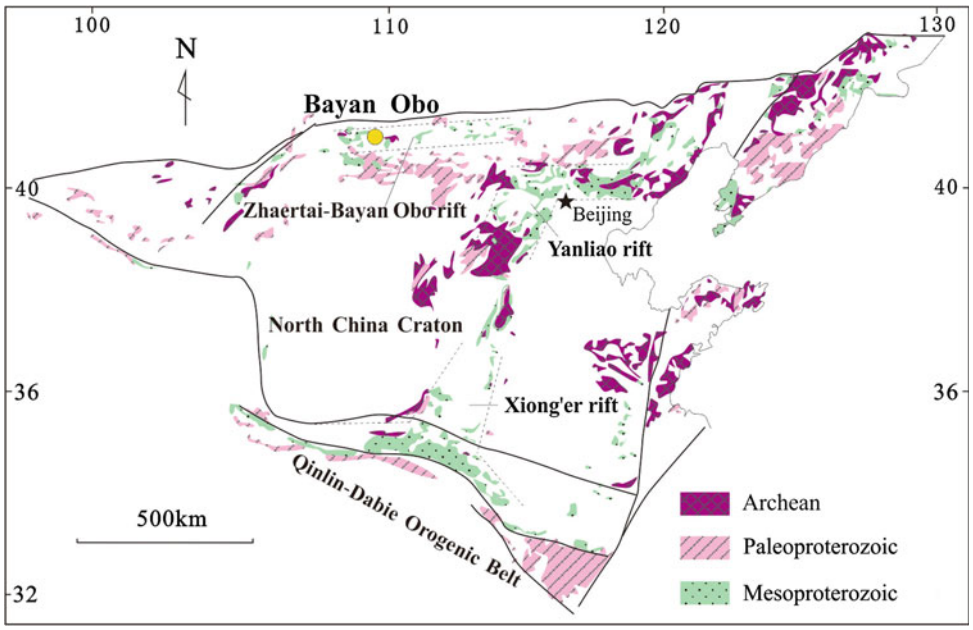

Fig. 17.10 Geological map of the North China Craton modified after Xiao et al. (2003), Peng et al. (2007) and Kusky et al. (2007)

(1.2 Ga) of Kimberley area in the western Australia (Pidgeon et al. 1989), and the kimberlites and lamproites (1.38–1.22 Ga) in the Indian Shield (Paul et al. 1975; Chalapathi Rao et al. 1996, Chalapathi Rao 2007). The Bayan Obo carbonatites described in this study closely correlate to most of the above examples in terms of tectonic setting and formation age.

Yang et al. (2011b) obtained similar whole-rock Sm–Nd isochron ages of the mafic dyke (1227 ± 60 Ma) and carbonatite (1354 ± 59 Ma) from Bayan Obo. The comparable Sr-Nd isotope characteristics and Nb/Ta ratios also suggest their close petrogenetic relationship. Furthermore, the Zr/Y versus Zr composition also suggests their formation within a continental rift (Yang et al. 2011b). This suggests that the generation of the parent mafic–carbonatitic magma was related to the initiation of the Bayan Obo continental margin rift. The massive carbonatitic–mafic magmatism in the Bayan Obo region during the middle to late Mesoproterozoic (1.4–1.2 Ga) is approximately coeval with the worldwide rifting events at this time that are associated with the final breakup of the supercontinent Columbia.

Along with the prolonged and slow extension of the Bayan Obo rift, the mantle lithosphere underwent low degree of partial melting leading to the production of carbonatite magma at the final stage of break up the supercontinent Columbia (ca. 1.4–1.2 Ga, Zhao et al. 2006; Hou et al. 2008). Through continuous evolution (crystal fractionation), abundant LREE accumulation occurred in the terminal calcite carbonatite magma, which was then superposed on the early dolomite carbonatite pluton, thus resulting in the formation of the giant Bayan Obo REE deposit.

The timing of the early episode of REE mineralization of Bayan Obo deposit obtained from REE minerals and ore-hosting dolomite, ca. 1400–1300 Ma, is consistent with the reported ages of REE-rich carbonatite dykes, implying a genetic connections. Geochemical evidence of element content and Nd isotope composition also imply that ore-hosting dolomite and the carbonatite dykes have a close relationship to a magmatic origin (Yang et al. 2011b). A significant thermal event at ca. 440 Ma resulted in the formation of late-stage veins with coarse crystals of REE minerals. This event is also indicated by SHRIMP Th–Pb analyses of hydrothermal overgrowths on ore body zircon at Bayan Obo, which indicate ages of 455 ± 28 Ma (Campbell et al. 2014). However, the REE mineralization developed during this event resulted from remobilization of REE within the orebodies, and any potential contribution from external sources was minimal. Thus, this late mineralization event might make no significant contribution to the existing ore reserves (Zhu et al. 2015). The ages of ca. 440 Ma may be related to subduction of the Palaeo-Asian oceanic plate during the Silurian (Wang et al. 1994; Chao et al. 1997).

17.7 Conclusion

The giant Bayan obo deposit suffered repeated tectonic-magmatic reworking at the north margin of the NCC. The deposit is hosted in the massive dolomite, and nearly one hundred carbonatite dykes occur in the vicinity of the deposit, which were resulted from different evolutionary stages of carbonatitic magmatism from dolomite type to calcite type based on the REE and trace element data. The latter always has higher LREE content. The geochemical evidences show that the coarse-grained dolomite represents a Mesoproterozoic carbonatite pluton and the fine-grained dolomite resulted from the extensive REE mineralization and modification of the coarse-grained variety. The ore bodies, distributed along an E-W striking belt, occur as large lenses and underwent more intense fluoritization and fenitization. The first episode mineralization is characterized by disseminated mineralization in the dolomite. The second or main-episode is banded and/or massive mineralization, cut by the third episode consisting of aegirine-rich veins. Compilation of available data suggests that the mineralization age is rather variable with two peaks at ~1400 and 440 Ma. The early mineralization peak closes in time to the intrusion of the carbonatite dykes and the breakup of the Columbia supercontinent. A significant thermal event at ca. 440 Ma resulted in the formation of late-stage veins with coarse crystals of REE minerals. Fluids involving in the REE-Nb-Fe mineralization at Bayan Obo might be REE-F-CO_2-NaCl-H_2O system. The presence of REE-carbonates as an abundant solid in the ores shows that the original ore-forming fluids are very rich in REE, and therefore, have the potential to produce economic REE ores at Bayan Obo. It can be concluded that the Bayan Obo giant deposit is a product of mantle-derived carbonatitic magmatism at ca. 1400 Ma, which was likely related to the breakup of the supercontinent Columbia. Some remobilization of REE occurred due to subduction of the Palaeo-Asian oceanic plate during the Early Paleozoic forming weak vein-like mineralization.

Acknowledgements We thank Prof. Zhai M.G. kind invitation for this manuscript submitting to Main Tectonic Events and Metallogeny of the North China Craton. Special thanks are due to the managements and staffs of the Baotou Iron and Steel Ltd. and the Bayan Obo Mine for their hospitality during fieldworks. We are indebted to the anonymous reviewers, whose comments helped a lot improve the manuscript. This work was financed by Major State Basic Research Development Program (2012CB416605) and Natural Science Foundation of China (41372099).

References

Bai, G., Yuan, Z. X., Wu, C. Y., Zhang, Z. Q., & Zheng, L. Y. (1996). *Demonstration on the geological features and genesis of the Bayan Obo ore deposit* (pp. 1–104). Beijing: Geological Publishing House (in Chinese with English abstract).

Campbell, L. S., Compston, W., Sircombe, K. N. (2000). ^{232}Th-^{208}Pb (SHRIMP) data of zircons from the Bayan Obo REE-Nb-Fe deposit, China. Mantle Materials, Processes and Products, with VMSG and MDSG RIP Sessions. Abstract Volume.

Campbell, L. S., Compston, W., Sircombe, K. N., & Wilkinson, C. C. (2014). Zircon from the East Orebody of the Bayan Obo Fe–Nb–REE deposit, China, and SHRIMP ages for carbonatite-related magmatism and REE mineralization events. *Contributions to Mineralogy and Petrology, 168*, 1041–1064.

Cao, R. L., Zhu, S. H., & Wang, J. W. (1994). Source materials for the Bayan Obo Fe–REE–Nb ore deposit and problems of the genetic theory. *Science in China, 24*, 1298–1307 (in Chinese with English abstract).

Chalapathi Rao, N. V. (2007). Chelima dykes, Cuddapah basin, Southern India: A review of the age, petrology, geochemistry and petrogenesis of the worlds' oldest lamproites. *Journal of the Geological Society of India, 69*, 523–538.

Chalapathi Rao, N. V., Miller, J. A., Pyle, D. M., & Madhavan, V. (1996). New Proterozoic K-Ar ages for some kimberlites and lamproites from the Cuddapah basin and Dharwar craton, south India: Evidence for non-contemporaneous emplacement. *Precambrian Research, 79*, 363–369.

Chao, E. C. T., Back, J. M., Minkin, J. A., & Ren, Y. (1992). Host-rock controlled epigenetic, hydrothermal metasomatic origin of the Bayan Obo REE-Fe-Nb ore deposit, Inner Mongolia, P.R.C. *Applied Geochemistry, 7*, 443–458.

Chao, E. C. T., Back, J. M., Minkin, J. A., Tatsumoto, M., Wang, J., Conrad, J. E., et al. (1997). The sedimentary carbonate-hosted giant Bayan Obo REE-Fe-Nb ore deposit of Inner Mongolia, China: A cornerstone example for giant polymetallic ore deposits of hydrothermal original. *US Geology Survey Bulletin, 2143*, 1–65.

Chao, E. C. T., Tatsumoto, M., Minkin, J., Back, J. M., McKee, E. H., Ren, Y. C., & Li, G. M. (1991). A variety of evidence to establish the mineral sequences of ore-forming minerals of Bayan Obo rare earth ore deposit. *Contributions to Geology and Mineral Resources Research, 6*, 1–17 (in Chinese).

Drew, L. J., Meng, Q. R., & Sun, W. J. (1990). The Bayan Obo iron-rare-earth-niobium deposits, Inner Mongolia, China. *Lithos, 26*, 43–65.

Fan, H. R., Hu, F. F., Yang, K. F., Pirajno, F., Liu, X., & Wang, K. Y. (2014). Integrated U–Pb and Sm-Nd geochronology for a REE-rich carbonatite dyke at the giant Bayan Obo REE deposit, Northern China. *Ore Geology Reviews, 63*, 510–519.

Fan, H. R., Hu, F. F., Yang, K. F., & Wang, K. Y. (2006). Fluid unmixing/immiscibility as an ore-forming process in the giant REE-Nb-Fe deposit, Inner Mongolian, China: evidence from fluid inclusions. *Journal of Geochemical Exploration, 89*, 104–107.

Fan, H. R., Hu, F. F., Yang, K. F., Wang, K. Y., & Liu, Y. S. (2009). Geochronology framework of late Paleozoic dioritic–granitic plutons in the Bayan Obo area, Inner Mongolia, and tectonic significance. *Acta Petrologica Sinica, 25*, 2933–2938 (in Chinese with English abstract).

Fan, H. R., Xie, Y. H., Wang, K. Y., Tao, K. J., & Wilde, S. A. (2004a). REE daughter minerals trapped in fluid inclusions in the giant Bayan Obo REE-Nb-Fe deposit, Inner Mongolia, China. *International Geology Review, 46*, 638–645.

Fan, H. R., Xie, Y. H., Wang, K. Y., & Wilde, S. A. (2004b). Methane-rich fluid inclusions in skarn zones near the giant REE-Nb-Fe deposit at Bayan Obo, Northern China. *Ore Geology Reviews, 25*, 301–309.

Fan, H. R., Yang, K. F., Hu, F. F., Wang, K. Y., & Zhai, M. G. (2010). Zircon geochronology of basement rocks from the Bayan Obo area, Inner Mongolia, and tectonic implications. *Acta Petrologica Sinica, 26*, 1342–1350 (in Chinese with English abstract).

Haggerty, S. E. (1982). Kimberlites in western Liberia: An overview of the geological setting in a plate tectonic framework. *Journal of Geophysics Research, 87*, 10811–10826.

Halls, H. C., Li, J. H., Davis, D., Hou, G. T., Zhang, B. X., & Qian, X. L. (2000). A precisely dated Proterozoic paleomagnetic pole form the North China Craton, and its relevance to paleocontinental construction. *Geophysical Journal International, 143*, 185–203.

Hao, Z. G., Wang, X. B., Li, Z., Xiao, G. W., & Zhang, T. R. (2002). Bayan Obo carbonatite REE-Nb-Fe deposit: A rare example of Neoproterozoic lithogeny and metallogeny of a damaged volcanic edifice. *Acta Geologica Sinica, 76*, 525–540 (in Chinese with English abstract).

Hou, G. T., Santosh, M., Qian, X. L., Lister, G. S., & Li, J. H. (2008a). Tectonic constraints on 1.3–1.2 Ga final breakup of Columbia supercontinent from a giant radiating dyke swarm. *Gondwana Research, 14*, 561–566.

Hou, G. T., Santosh, M., Qian, X. L., Lister, G., & Li, J. H. (2008b). Configuration of the Late Paleoproterozoic supercontinent Columbia: Insights from radiating mafic dyke warms. *Gondwana Research, 14*, 395–409.

Hu, F. F., Fan, H. R., Liu, S., Yang, K. F., & Chen, F. (2009). Sm-Nd and Rb-Sr isotopic dating of veined REE mineralization for the Bayan Obo REE-Nb-Fe deposit, northern China. *Resource Geology, 59*, 407–414.

Huang, X. W., Zhou, M. F., Qiu, Y. Z., & Qi, L. (2015). In-situ LA-ICP-MS trace elemental analyses of magnetite: The Bayan Obo Fe-REE-Nb deposit, North China. *Ore Geology Reviews, 65*, 884–899.

Institute of Geology and Guiyang Geochemistry, Chinese Academy of Sciences. (1988). *The geochemical composition and mineralization regularity of Bayan Obo deposit* (pp. 8–18). Inner Mongolia (in Chinese).

Kusky, T. M., & Li, J. H. (2003). Paleoproterozoic tectonic evolution of the North China Craton. *Journal of Asian Earth Sciences, 22*, 383–397.

Kusky, T. M., Li, J. H., & Santosh, M. (2007). The Paleoproterozoic north Hebei orogen: North China Craton's collisional suture with the Columbia supercontinent. *Gondwana Research, 12*, 4–28.

Lai, X. D., Yang, X. Y., Santosh, M., Liu, Y. L., & Ling, M. X. (2015). New data of the Bayan Obo Fe–REE–Nb deposit, Inner Mongolia: Implications for ore genesis. *Precambrian Research, 263*, 108–122.

Lai, X. D., Yang, X. Y., & Sun, W. D. (2012). Geochemical constraints on genesis of dolomite marble in the Bayan Obo REE-Nb-Fe deposit, Inner Mongolia: Implications for REE mineralization. *Journal of Asian Earth Sciences, 57*, 90–102.

Le Bas, M. J., Keller, J., Tao, K., Wall, F., Williams, C. T., & Zhang, P. (1992). Carbonatite dykes at Bayan Obo, Inner Mongolia, China. *Mineralogy and Petrology, 46*, 195–228.

Le Bas, M. J., Spiro, B., & Yang, X. (1997). Oxygen, carbon and strontium isotope study of the carbonatitic dolomite host of the Bayan Obo Fe-Nb-REE deposit, Inner Mongolia, N. China. *Mineralogical Magazine, 61*, 531–541.

Le Bas, M. J., Yang, X. M., Taylor, R. N., Spiro, B., Milton, J. A., & Zhang, P. S. (2007). New evidence from a calcite-dolomite carbonatite dyke for the magmatic origin of the massive Bayan Obo ore-bearing dolomite marble, Inner Mongolia, China. *Mineralogy and Petrology, 90*, 223–248.

Li, Q. L., Chen, F. K., Guo, J. H., Li, X. H., Yang, Y. H., & Siebel, W. (2007). Zircon ages and Nd–Hf isotopic composition of the Zhaertai

Group (Inner Mongolia): evidence for early Proterozoic evolution of the northern North China Craton. *Journal of Asian Earth Sciences, 30*, 573–590.

Li, J. H., Niu, X. L., Cheng, S. H., & Qian, X. L. (2006). The early Precambrian tectonic evolution of continental craton: A case study from North China. *Earth Science-Journal of China University of Geosciences, 31*, 285–293 (in Chinese with English abstract).

Ling, M. X., Liu, Y. L., Williams, I. S., Teng, F. Z., Yang, X. Y., Ding, X., et al. (2013). Formation of the world's largest REE deposit through protracted fluxing of carbonatite by subduction-derived fluids. *Scientific Reports, 3*, 1–8.

Ling, M. X., Zhang, H., Li, H., Liu, Y. L., Liu, J., Li, L. Q., et al. (2014). The Permian-Triassic granitoids in Bayan Obo, North China Craton: A geochemical and geochronological study. *Lithos, 190–191*, 430–439.

Liu, Y. L., Chen, J. F., Li, H. M., Qian, H., Xiao, G. W., & Zhang, T. R. (2005). Single-grain U–Th-Pb-Sm-Nd dating of monazite from dolomite type ores of the Bayan Obo deposit. *Acta Petrologica Sinica, 21*, 881–888 (in Chinese with English abstract).

Liu, L. S., Gao, L., Du, A. D., & Sun, Y. L. (1996). The Re-Os isotopic age of molybdenite from Bayan Obo REE ore deposit. *Mineral Deposits, 15*, 188–191 (in Chinese with English abstract).

Liu, Y. L., Peng, G. Y., Zhang, Y., Li, H. M., & Chen, J. F. (2001). U–Pb and Pb-Pb dating of ore-hosting H8 dolomite at Bayan Obo. *Bulletin of Mineralogy, Petrology and Geochemistry, 20*, 274–277 (in Chinese with English abstract).

Liu, Y. L., Williams, I. S., Chen, J. F., Wan, Y. S., & Sun, W. D. (2008). The significance of Paleoproterozoic zircon in carbonatite dikes associated with the Bayan Obo REE-Nb-Fe deposit. *American Journal of Science, 308*, 379–397.

Liu, Y. L., Yang, G., Chen, J. F., Du, A. D., & Xie, Z. (2004). Re-Os dating of pyrite from giant Bayan Obo REE-Nb-Fe deposit. *Chinese Science Bulletin, 49*, 2627–2631.

Meng, Q. (1982). The genesis of the host rock dolomite of Bayan Obo iron ore deposits and the analysis of its sedimentary environment. *Geological Reviews, 28*, 481–489 (in Chinese with English abstract).

Nakai, S., Masuda, A., & Shimizu, H. (1989). La-Ba dating and Nd and Sr isotope studies on Bayan Obo rare earth element ore deposit, Inner Mongolia, China. *Economic Geology, 84*, 2296–2299.

Paul, D. K., Rex, D. C., & Harris, P. G. (1975). Chemical characteristics and the K-Ar ages of Indian kimberlites. *Geological Society of America Bulletin, 86*, 364–366.

Peng, P., Zhai, M. G., Guo, J. H., Kusky, T., & Zhao, T. P. (2007). Nature of mantle source contributions and crystal differentiation in the petrogenesis of the 1.78 Ga mafic dykes in the central North China craton. *Gondwana Research, 12*, 29–46.

Phillips, D., Onstott, T. C., & Harris, J. W. (1989). $^{40}Ar/^{39}Ar$ laser-probe dating of diamond inclusion from the Premier kimberlite. *Nature, 340*, 460–462.

Philpotts, J., Tatsomoto, M., Li, X., & Wang, K. (1991). Some Nd and Sr isotopic systematics from the REE-enriched deposit at Bayan Obo, China. *Chemical Geology, 90*, 177–178.

Pidgeon, R. T., Smith, C. B., & Fanning, C. M. (1989). Kimberlite and lamproite emplacement ages in Western Australia. *Geological Society of Australia Special Publication, 14*, 369–381.

Qiu, Y. Z. (1997). Thought of SHRIMP dating of Bayan Obo monazite. *Acta Geoscientia Sinica, 18*, 211–213 (in Chinese with English abstract).

Ren, Y. C., Zhang, Y. C., & Zhang, Z. Q. (1994). Study on heat events of ore-forming Bayan Obo deposit. *Acta Geoscientia Sinica, 15*, 95–101 (in Chinese with English Abstract).

Rogers, J. J. W., & Santosh, M. (2002). Configuration of Columbia, a Mesoproterozoic Supercontinent. *Gondwana Research, 5*, 5–22.

Rogers, J. J. W., & Santosh, M. (2009). Tectonics and surface effects of the supercontinent Columbia. *Gondwana Research, 15*, 373–380.

Santosh, M. (2010). Assembling North China Craton within the Columbia supercontinent: The role of double-sided subduction. *Precambrian Research, 178*, 149–167.

Santosh, M., Maruyama, S., & Sato, K. (2009). The making and breaking of supercontinents: Some speculations based on superplume, super downwelling and the role of tectosphere. *Gondwana Research, 15*, 324–341.

Smith, M. P. (2007). Metasomatic silicate chemistry at the Bayan Obo Fe-REE-Nb deposit, Inner Mongolia, China: Contrasting chemistry and evolution of fenitising and mineralising fluids. *Lithos, 93*, 126–148.

Smith, M. P., Campbell, L. S., & Kynicky, J. (2015). A review of the genesis of the world class Bayan Obo Fe–REE–Nb deposits, Inner Mongolia, China: Multistage processes and outstanding questions. *Ore Geology Reviews, 64*, 459–476.

Smith, M. P., Henderson, P., & Campbell, L. S. (2000). Fractionation of the REE during hydrothermal processes: Constraints from the Bayan Obo Fe-REE-Nb deposit, Inner Mongolia, China. *Geochimica et Cosmochimica Acta, 64*, 3141–3160.

Sun, J., Fang, N., Li, S. Z., Chen, Y. L., & Zhu, X. K. (2012). Magnesium isotopic constraints on the genesis of Bayan Obo ore deposit. *Acta Petrologica Sinica, 28*, 2890–2902 (in Chinese with English Abstract).

Sun, J., Zhu, X. K., Chen, Y. L., & Fang, N. (2013). Iron isotopic constraints on the genesis of Bayan Obo ore deposit, Inner Mongolia, China. *Precambrian Research, 235*, 88–106.

Sun, J., Zhu, X. K., Chen, Y. L., Fang, N., & Li, S. Z. (2014). Is the Bayan Obo ore deposit a micrite mound? A comparison with the Sailinhudong micrite mound. *International Geology Review, 56*, 1720–1731.

Tao, K. J., Yang, Z. M., Zhang, P. S., & Wang, W. Z. (1998). Systematic geological investigation on carbonatite dykes in Bayan Obo, Inner Mongolia, China. *Scientia Geologica Sinica, 33*, 73–82 (in Chinese with English abstract).

Wang, K. Y., Fan, H. R., & Xie, Y. H. (2002a). Geochemistry of REE and other trace elements of the carbonatite dykes at Bayan Obo: Implication for its formation. *Acta Petrologica Sinica, 18*, 340–348 (in Chinese with English abstract).

Wang, K. Y., Fan, H. R., Xie, Y. H., & Li, H. M. (2002b). Zircon U–Pb dating of basement gneisses in the superlarge Bayan Obo REE-Fe-Nb deposit, Inner Mongolia. *Chinese Science Bulletin, 47*, 243–247.

Wang, K. Y., Fan, H. R., Yang, K. F., Hu, F. F., & Ma, Y. G. (2010). The Bayan Obo carbonatites: a polyphase intrusive and extrusive carbonatites-based on their texture evidence. *Acta Geologica Sinica, 84*, 1365–1376.

Wang, Z. G., & Li, S. B. (1973). The genetic features of the REE-Fe ore deposit related to sedimentation-metamorphism-hydrothermal metasomatism. *Geochimica (Beijing), 1*, 5–11 (in Chinese).

Wang, J., Li, S. Q., Wang, S. B., & Li, J. J. (1992). *The Langshan-Bayan Obo Rift* (pp. 1–132). Beijing: Peking University Press (in Chinese).

Wang, J., Tatsumoto, M., Li, X., Premo, W. R., & Chao, E. C. T. (1994). A precise ^{232}Th-^{208}Pb chronology of fine grained monazite: Age of the Bayan Obo REE-Fe-Nb ore deposit, China. *Geochimica et Cosmochimica Acta, 58*, 3155–3169.

Woolley, A. R., & Kempe, D. R. C. (1989). Carbonatites: Nomenclature, average chemical compositions, and element distribution. In K. Bell (Ed.), *Carbonatites: Genesis and Evolution* (pp. 1–14). London: Unwin Hyman.

Wu, C., Yuan, Z., & Bai, G. (1996). Rare-earth deposits in China. In A. P. Jones, F. Wall, & C. T. Williams (Eds.), *Rare Earth Minerals: Chemistry, Origin and Ore Deposits* (pp. 281–310). London: Chapman and Hall.

Xiao, W. J., & Kusky, T. (2009). Geodynamic processes and metallogenesis of the Central Asian and related orogenic belts: Introduction. *Gondwana Research, 16*, 167–169.

Xiao, W. J., Windley, B. F., Hao, J., & Zhai, M. G. (2003). Accretion leading to collision and the Permian Solonker suture, Inner Mongolia, China: Termination of the Central Asian Orogenic Belt. *Tectonics, 22*, 1–20.

Xu, C., Kynicky, J., Chakhmouradian, A. R., Campbell, I. H., & Allen, C. M. (2010). Trace-element modeling of the magmatic evolution of rare-earth-rich carbonatite from the Miaoya deposit, Central China. *Lithos, 118*, 145–155.

Xu, C., Taylor, R. N., Li, W., Kynicky, J., Chakhmouradian, A. R., & Song, W. (2012). Comparison of fluorite geochemistry from REE deposits in the Panxi region and Bayan Obo, China. *Journal of Asian Earth Sciences, 57*, 76–89.

Yang, K. F., Fan, H. R., Hu, F. F., & Wang, K. Y. (2012). Sediment source of Bayan Obo marginal rift and genesis of ore-bearing dolomite of the giant REE deposit. *Acta Geologica Sinica, 86*, 775–784 (in Chinese with English abstract).

Yang, K. F., Fan, H. R., Santosh, M., Hu, F. F., & Wang, K. Y. (2011a). Mesoproterozoic carbonatitic magmatism in the Bayan Obo deposit, Inner Mongolia, North China: Constraints for the mechanism of super accumulation of rare earth elements. *Ore Geology Reviews, 40*, 122–131.

Yang, K. F., Fan, H. R., Santosh, M., Hu, F. F., & Wang, K. Y. (2011b). Mesoproterozoic mafic and carbonatitic dykes from the northern margin of the North China Craton: Implications for the final breakup of Columbia supercontinent. *Tectonophysics, 498*, 1–10.

Yang, X. M., & Le Bas, M. J. (2004). Chemical compositions of carbonate minerals from Bayan Obo, Inner Mongolia, China: Implications for petrogenesis. *Lithos, 72*, 97–116.

Yang, Y. H., Sun, J. F., Xie, L. W., Fan, H. R., & Wu, F. Y. (2008). In situ Nd isotopic measurement of natural geological materials by LA-MC-ICPMS. *Chinese Science Bulletin, 53*, 1062–1070.

Yang, X. Y., Sun, W. D., Zhang, Y. X., & Zheng, Y. F. (2009). Geochemical constraints on the genesis of the Bayan Obo Fe-Nb-REE deposit in Inner Mongolia. *China, Geochimica et Cosmochimica Acta, 73*, 1417–1435.

Yang, Z. M., & Woolley, A. (2006). Carbonatites in China: A review. *Journal of Asian Earth Sciences, 27*, 559–575.

Yang, X. M., Yang, X. Y., Zhang, P. S., & Le Bas, M. J. (2000). Ba-REE fluorocarbonate minerals from a carbonatite dyke at Bayan Obo, Inner Mongolia, North China. *Mineralogy and Petrology, 70*, 221–234.

Yang, X. M., Yang, X. Y., Zheng, Y. F., & Le Bas, M. J. (2003). A rare earth element-rich carbonatite dyke at Bayan Obo, Inner Mongolia, North China. *Mineralogy and Petrology, 78*, 93–110.

Yuan, Z. X., Bai, G., & Wu, C. Y. (1991). Genesis and metallogenic age of Bayan Obo Ni, REE and Fe ore deposit, Inner Mongolia. *Mineral Deposit Geology, 10*, 59–70 (in Chinese with English abstract).

Yuan, Z. X., Bai, G., Wu, C. Y., Zhang, Z. Q., & Ye, X. (1992). Geological features and genesis of the Bayan Obo REE ore deposit, Inner Mongolia, China. *Applied Geochemistry, 7*, 429–442.

Zhai, M. G. (2004). 2.1-1.7 Ga geological event group and its geotectonic significance. *Acta Petrologica Sinica, 20*, 1343–1354 (in Chinese with English abstract).

Zhai, M. G., & Santosh, M. (2011). The Early Precambrian odyssey of the North China Craton: A synoptic overview. *Gondwana Research, 20*, 6–25.

Zhang, Z. Q., Tang, S. H., Wang, J. H., Yuan, Z. X., & Bai, G. (1994). New data for ore-forming age of the Bayan Obo REE deposit, Inner Mongolia. *Acta Geoscientia Sinica, 1–2*, 85–94 (in Chinese with English abstract).

Zhang, Z. Q., Tang, S. H., Yuan, Z. X., Bai, G., & Wang, J. H. (2001). The Sm-Nd and Rb-Sr isotopic systems of the dolomites in the Bayan Obo ore deposit, Inner Mongolia, China. *Acta Petrologica Sinica, 17*, 637–642 (in Chinese with English abstract).

Zhang, Z. Q., Yuan, Z. X., Tang, S. H., Bai, G., & Wang, J. H. (2003). *Age and geochemistry of the Bayan Obo Ore deposit* (pp. 1–222). Beijing: Geological Publishing House (in Chinese with English Abstract).

Zhang, S. H., Zhao, Y., Yang, Z. Y., He, Z. F., & Wu, H. (2009). The 1.35 Ga diabase sills from the northern North China Craton: Implications for breakup of the Columbia (Nuna) supercontinent. *Earth and Planetary Science Letters, 288*, 588–600.

Zhao, G. C., Sun, M., Wilde, S. A., & Li, S. Z. (2004). A Paleo-Mesoproterozoic supercontinent: Assembly, growth and breakup. *Earth-Science Reviews, 67*, 91–123.

Zhao, G. C., Sun, M., Wilde, S. A., Li, S. Z., & Zhang, J. (2006). Some key issues in reconstructions of Proterozoic supercontinents. *Journal of Asian Earth Sciences, 28*, 3–19.

Zhu, X. K., Sun, J., & Pan, C. (2015). Sm–Nd isotopic constraints on rare-earth mineralization in the Bayan Obo ore deposit, Inner Mongolia, China. *Ore Geology Reviews, 64*, 543–553.

Part V

Phanerozoic Reworking of the North China Craton and Metallogeny

Paleozoic to Early Mesozoic Tectonics of North China Craton

18

Yue Zhao, Mingguo Zhai, and Shuan-Hong Zhang

Abstract

The North China Craton (NCC) started its Paleozoic evolution from ca. 520 Ma when Gondwana assembled in its peak tectonism. The Middle Cambrian developed in margins of the NCC on older strata or basement rocks. Then the marine environment expansion and its extensive invasion led to the late Middle Cambrian marine deposits, the Mantou Formation and afterwards occurred throughout the NCC. New results of the Bainaimiao arc belt, north to the northern NCC indicated that the arc was active from 520 Ma and lasted to 420 Ma, which could extend to east Siping in NE China. Along the southern edge of the NCC the northward subduction of the Shangdan Ocean was operated during ca. 514–420 Ma. Marine regression occurred postdated the Majiagou phase in Middle Ordovician in most parts of the NCC. Recently in the northern NCC some Devonian plutons and volcanic rocks were recognized. The Late Carboniferous sedimentary sequence with the 'G' layer of bauxites at its bottom is overlain disconformably upon the Middle Ordovician limestone. The bauxites were derived mainly from ashes produced by volcanism mainly in the Inner Mongolia Paleo-uplift (IMPU) during Paleozoic period, particularly in latest Early Carboniferous to Early Permian when the northern margin of the NCC evolved as an Andean-style active continental margin. The sequence is mainly clastic formations, composed of coal-bearing sandstones and siltstones interlayered with marine limestone and volcanic ash, which demonstrates that they formed in terrestrial–marine transitional or terrestrial environment with volcanic arc settings. After late Early Permian a terrestrial environment was dominant in the NCC. In the southern NCC and the Qinling Orogenic Belt (QOB) spreading of the Mianlue Ocean between the South China Craton (SCC) and South Qinling Block (SQB) was sustained in Late Paleozoic and the northward subduction–accretion of the Mianlue Ocean was active in Late Paleozoic. In Triassic, the collision between the SCC and SQB along the Mianlue suture resulted in intense shortening and uplift of QOB and HP/UHP metamorphism documented in Hong'an-Dabie-Sulu terranes.

Y. Zhao · S.-H. Zhang
Institute of Geomechanics, Chinese Academy of Geological Sciences, Beijing, 100081, China

Y. Zhao (✉) · S.-H. Zhang
Key Laboratory of Paleomagnetism and Tectonic Reconstruction, Ministry of Land and Resources, Beijing, 100081, China
e-mail: yue_zhao@cags.ac.cn

M. Zhai
Institute of Geology and Geophysics, Chinese Academy of Sciences, Beijing, 100029, China

M. Zhai
State Key Laboratory of Geodynamics, Northwest University, Xian, 710069, China

M. Zhai et al. (eds.), *Main Tectonic Events and Metallogeny of the North China Craton*, Springer Geology, DOI 10.1007/978-981-10-1064-4_18

Meanwhile in the northern NCC, significant changes in tectonic deformation and magmatism occurred in Late Triassic. In the Panshan region, the northern NCC, intensive regional folding and thrusting took place around 210 Ma, which shows that the NCC underwent into its initial decratonization.

Keywords
Tectonics • Paleozoic • Early Mesozoic • North China Craton

18.1 Introduction

The North China Craton (NCC) is one of the oldest cratons in the world and is characterized by complex evolution history from Early Precambrian (e.g., Zhai and Santosh 2011; Zhao and Zhai 2013; Zhai 2014). Evolving into Phanerozoic, from earliest Paleozoic to Early Mesozoic periods, the NCC underwent its typical craton stage in Early Paleozoic, in which extensive transgression occurred throughout the NCC in Middle Cambrian after an unexpected ca. 800 Ma long gap, and then typical craton sequences developed. The tectonic events of the NCC in Early Paleozoic appeared well known. But their global settings and their relationships with tectonic events of adjacent orogenic belts remained poorly understood. Recently, great progress was made not only in the NCC but also in the neighbouring Qinling Orogenic Belt (QOB) and Central Asian Orogenic Belt (CAOB) on Paleozoic to Early Mesozoic geology and tectonics can draw some veils over the issues. They are Early Paleozoic extensive transgression and regression, regional minerals, Late Paleozoic tectonic events and Early Mesozoic regional deformation and magmatism, and their relationship with tectonic events of adjacent orogenic belts and global significant tectonic events. This review paper will address the above issues.

18.2 Early Paleozoic Tectonics

18.2.1 Main Regions of the NCC

The northern NCC restarted its geological documents in Paleozoic period after a long gap probably from ca. 1320 Ma to ca. 515 Ma. The Middle Cambrian marine deposits, the Jianchang Formation in Liaoning, the Changping Formation in Beijing and the Fujunshan Formation in Tianjin, the Liguan Formation/Xinji Formation and Zhushadong Formation in Henan, the Xinji Formation and Zhushadong Formation in Shaanxi (Figs. 18.1 and 18.2) developed in the margins of the NCC on older strata or basement rocks when Gondwana assembled in its peak tectonism. Then the marine environment expanded to almost the whole NCC, from the Mantou phase and thereafter up to the Middle Ordovician Majiagou phase. The Middle Ordovician marine regression and regional uplift of the NCC occurred after deposition of the Majiagou Formation and led to the paleogeographic change of the NCC, especially in the eastern Ordos basin and potash formation (Zhang et al. 2015), which coincided with diamondiferous kimberlite magmatism in the eastern and northeastern NCC at ca. 463–470 Ma (Zhang and Yang 2007; Yang et al. 2009). There was hidden magmatic event in deep of the NCC at 520 and 430 Ma as indicated by the inherited zircons from the basalt of the Nandaling Formation in western Beijing (Zhao et al. 2006a), the latter simultaneous with the final closure of the Iapetus Ocean as Baltica collided with Laurentia to form Laurussia and the Caledonian Orogeny (Lawver et al. 2011), suggested that the uplift of the NCC in late Early Paleozoic was related to the concurred deep and global tectonism. The regional uplift and stratum hiatus lasted until Late Carboniferous.

18.2.2 Northern NCC and the Southern CAOB

The northern NCC is bounded with the Bainaimiao arc belt by the east-west-trending Bayan Obo–Duolun–Chifeng–Kaiyuan fault zone (Fig. 18.3a). Although previous researchers considered the northern margin of the NCC as an active continental margin during Ordovician to Silurian (e.g. Zhang et al. 1986; Wang and Liu 1986; Hu et al. 1990; Wang et al. 1991; Tang 1992; Chao et al. 1997; Xiao et al. 2003), sedimentary and magmatic evidence show that the northern margin of the NCC remained as a passive continental margin during Early Paleozoic period (e.g. Li et al. 2009; Zhang et al. 2014a). The Early Paleozoic magmatic rocks with zircon U–Pb ages of 520–420 Ma are only distributed in the Bainaimiao arc belt and haven't been identified from the northern margin of the NCC (Zhang et al. 2014a and references therein). New zircon U–Pb and Sr–Nd–Hf isotopic results on the magmatic and metasedimentary rocks indicate that the Bainaimiao arc belt is an ensialic island arc characterized by very different tectonic history and basement compositions than the northern NCC (Fig. 18.3b; Zhang et al. 2014a). Similar to most of the microcontinents

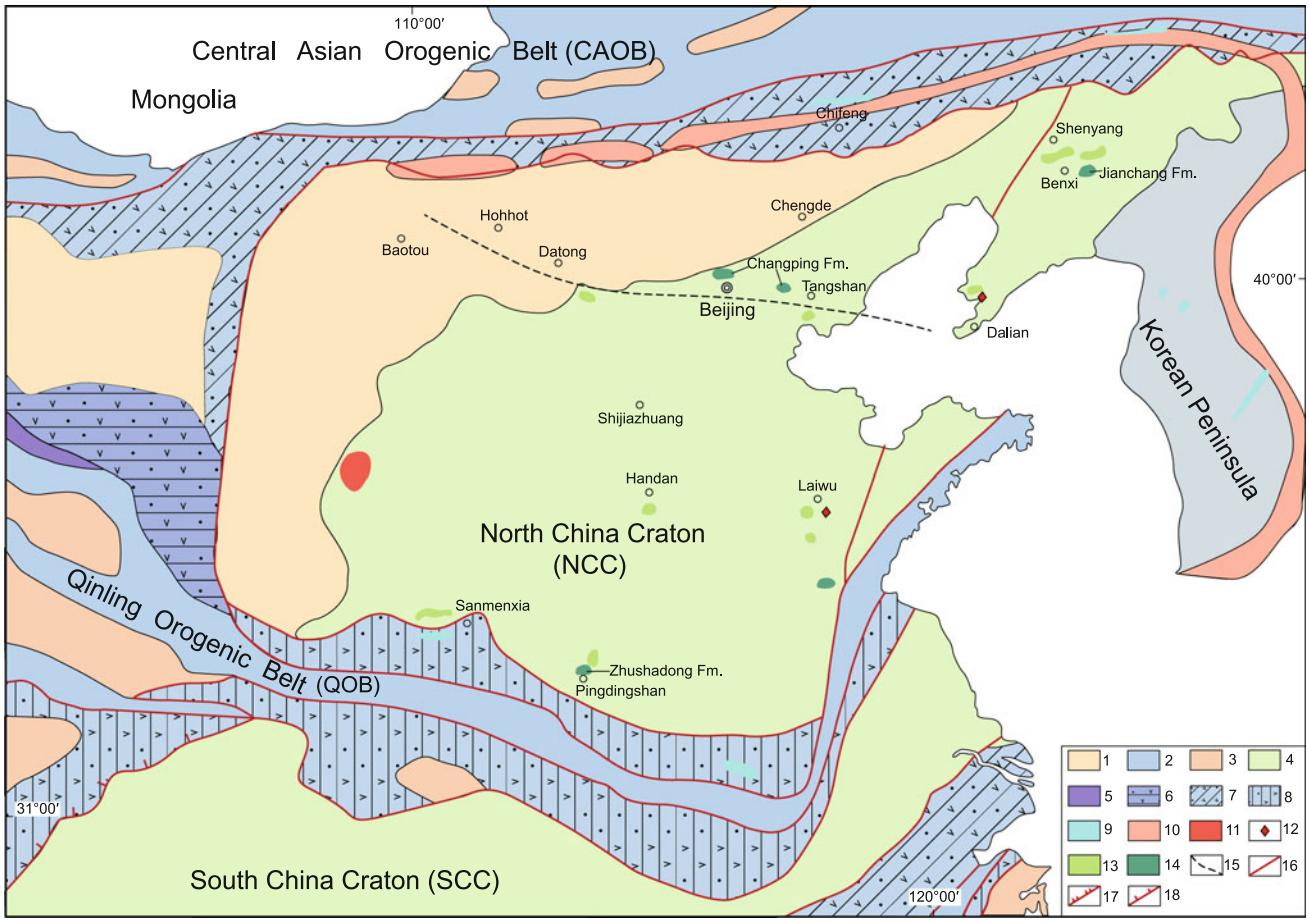

1. Craton uplift 2. Ocean basin 3. Displace block 4. Carbonate platform 5. Continental margin magmatic arc 6. Back-arc basin 7. Passive continental margin basin
8. Continental margin depressed basin 9. Outcrops of Silurian (S) 10. Silurian sediments distribution inferred 11. Potash saline 12 Kimberlites at ~ 470 Ma
13. Fengfeng Formation (Late Ordovician) 14. Outcrops of Early Cambrian (ϵ_1) 15. Northern margin of Fengfeng Formation (O_3) 16. Fault 17. Subduction zone
18. Boundary fault on depressed basin margin

Fig. 18.1 Early Paleozoic paleogeographical map of the NCC. For explanation, see text

in the CAOB (e.g., Wang et al. 2001; Zhao et al. 2006b; Demoux et al. 2009; Levashova et al. 2010, 2011; Kozakov et al. 2012; Kröner et al. 2011, 2014), the Bainaimiao arc belt has a tectonic affinity to the Tarim or Yangtze (South China) cratons and was developed upon some crustal fragment with affinity to the Tarim or Yangtze (South China) cratons during Early Paleozoic (Zhang et al. 2014a). The Bainaimiao arc belt was accreted to the northern margin of the NCC during the Late Silurian-earliest Devonian by arc-continent collision, which was followed by sedimentation of the latest Silurian-Early Devonian molasse or quasi-molasse of the Xibiehe Formation (e.g., Zhang and Tang 1989; Tang 1990; BGMRIM 1991; Su 1996; Xu et al. 2003; Wang 2005; Chen and Boucot 2007; Zhang et al. 2010b) and emplacement of the Early-Middle Devonian alkaline rocks in the northern NCC and southern CAOB (e.g., Luo et al. 2001; Zhang et al. 2007a, 2009a, 2010a; Shi et al. 2010; Wang et al. 2012). The latest Silurian arc-continent collision between the Bainaimiao island arc and the NCC was very likely responsible for Paleozoic reversal of arc polarity and transitions of the northern NCC from passive to active continental margin (Fig. 18.3c) as suggested in other places such as the Cenozoic Taiwan, northern New Guinea, Northwest Pacific and the Irish Caledonides (e.g., McKenzie 1969; Johnson and Jaques 1980; Konstantinovskaia 2001; Clift et al. 2003).

18.2.3 Southern Edge of the NCC and QOB

Along the southern edge of the NCC in QOB series of tectonic events took place in Early Paleozoic. The Erlangping back-arc basin was spreading and closed; the Shangdan Ocean was subducted northward beneath North Qinling Block (NQB). The latter was active from ca. 514 Ma or slightly later to 420 Ma (Fig. 18.4) (Liu et al. 2012a; Wu and Zheng 2013; Dong and Santosh 2016), which are based upon the geochronological data of metamorphic rocks (ca.

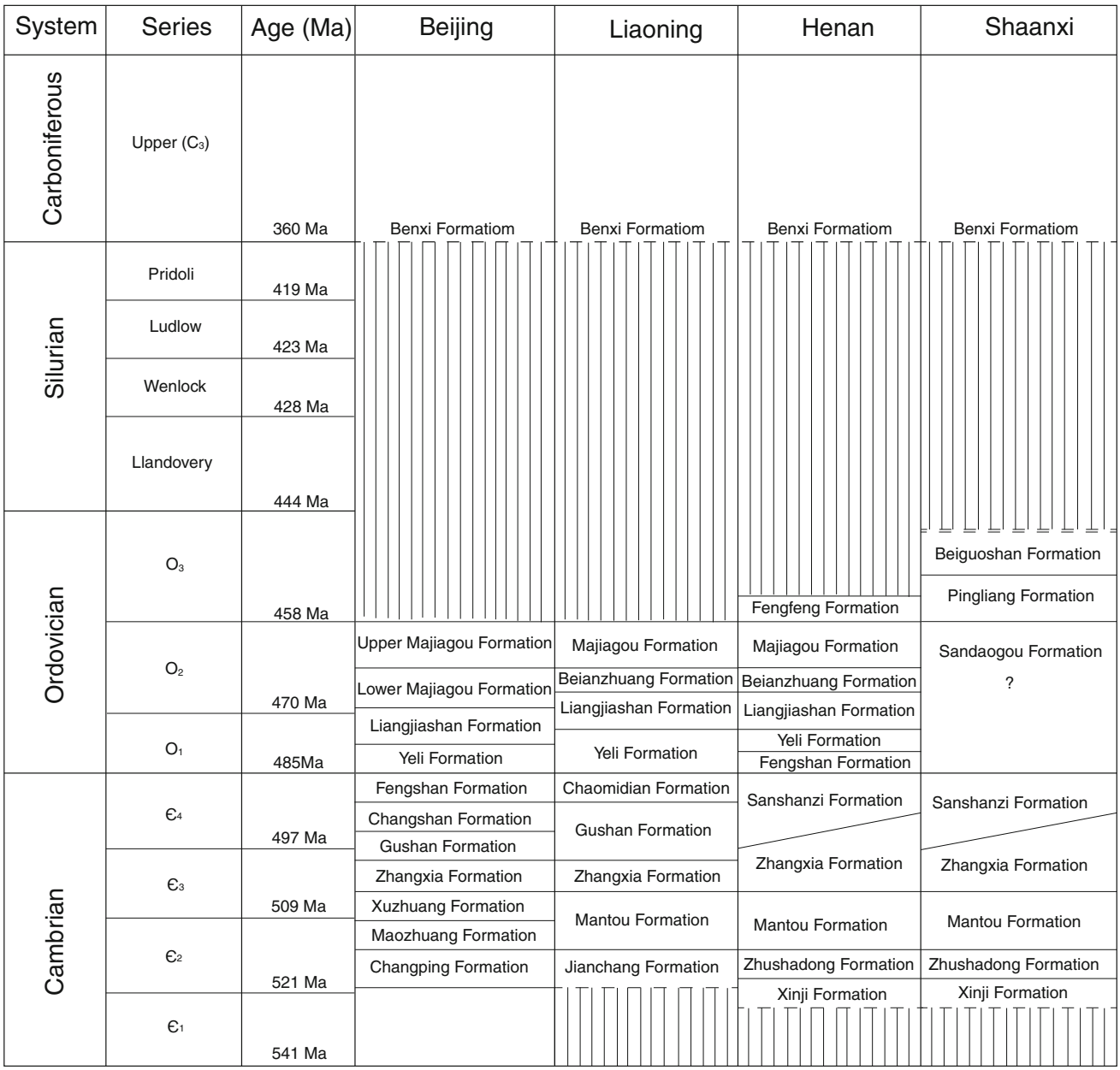

Fig. 18.2 Diagram showing the Lower Paleozoic strata of the NCC. For explanation, see text

510–400 Ma) and magmatic rocks in the NQB (ca. 514–420 Ma), as well as the anatexis and migmatization at 517–445 Ma (Dong et al. 2011). While the Erlangping back-arc basin opened between northern NQB and NCC at around 508 Ma, was spreading and then closed at ca. 450 Ma or slightly later, which resulted in the collision between the NQB and NCC and the S-type granitoids in the northern NQB (Liu et al. 2012a; Wu and Zheng 2013; Dong and Santosh 2016). However, the Kuanping Group developed on/in the margin of NCC remains to debate for its age and tectonic environment (Wang et al. 2009; Liu et al. 2012a; Wu and Zheng 2013; Dong and Santosh 2016).

18.3 Late Paleozoic

18.3.1 Main Regions of NCC

The change of its tectonic settings of the NCC in Late Paleozoic was a volcanic arc emerging on the northern margin of the NCC. From at least Late Carboniferous period, the northern margin of the NCC evolved as an Andean-style active continental margin due to southward subduction of the Paleo-Asian Ocean (Fig. 18.5), which resulted in deposition of the first sedimentary layer of the NCC in Late Paleozoic, known as the 'G' layer bauxite. The 'G' layer

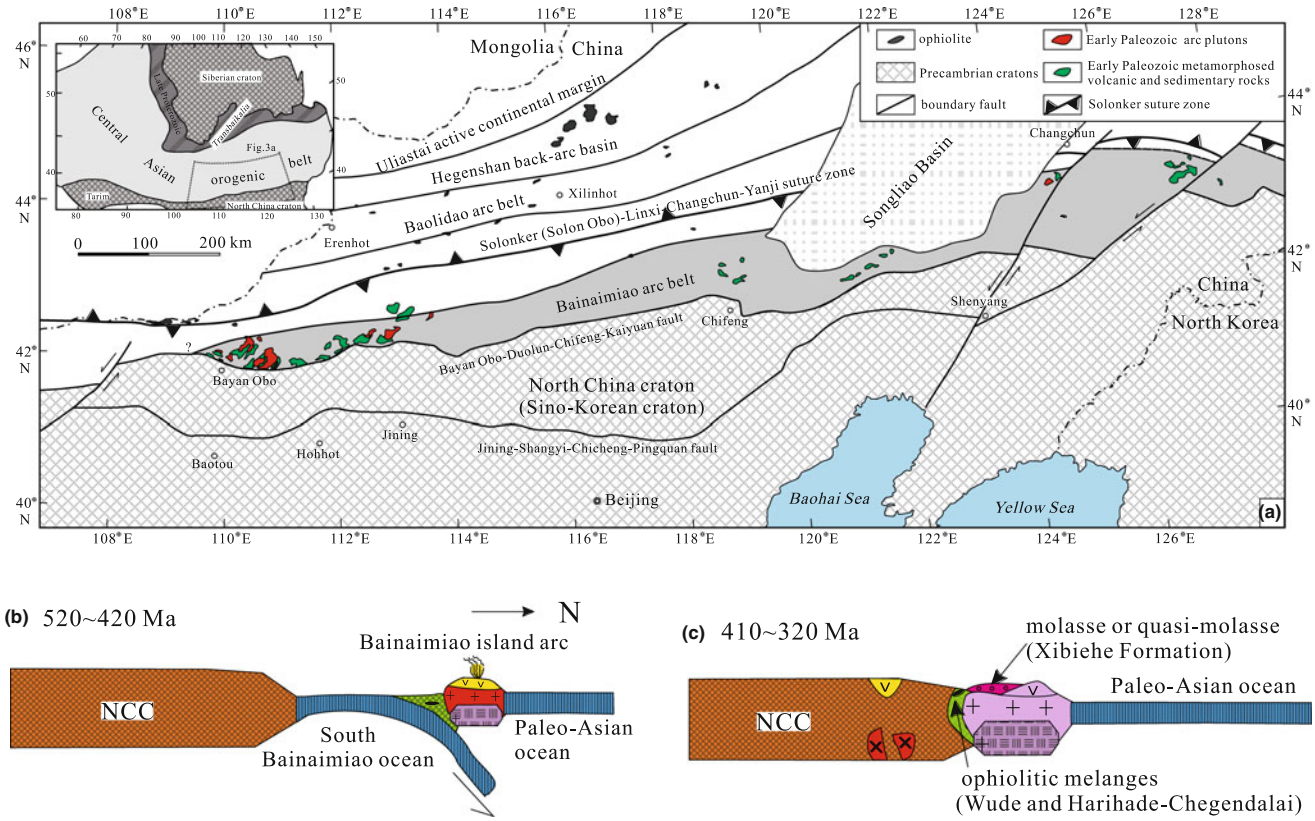

Fig. 18.3 **a** Sketch tectonic map of the southern CAOB and the northern margin of the NCC (modified after Zhang et al. 2014a; *inset* figure is modified after Jahn et al. 2000); **b**, **c** schematic cartoons showing evolution of the northern NCC during Early Paleozoic to Devonian period (modified after Zhang et al. 2014a). See text for discussion. Not to scale

bauxite, which is disconformably overlying upon the Middle Ordovician Majiagou limestone, is widespread throughout the northern and central parts of the NCC (Fig. 18.6) and can become bauxite deposits, the most important bauxite deposits in China (Meng et al. 1987).

The 'G' layer bauxites, bauxite deposits, known as the 'G' layer bauxite deposits, are widespread throughout the northern parts of the NCC, above a disconformity between Middle Ordovician limestones and Late Carboniferous clastic sedimentary rocks, was traditionally thought to be mainly derived from residuals of long-term weathering. But the underlying Middle Ordovician Majiagou limestone is lack of aluminium. Recent studies (Zhao et al. 2010; Wang et al. 2010, 2016; Liu et al. 2014) demonstrated that one of its most important heavy minerals from the 'G' layer bauxite, zircon grain is magmatic in origin. Zircon crystals, the key component from the 'G' layer bauxite, yielded U–Pb ages mainly in Late Carboniferous and in situ Hf isotopes, which can also generate reliable information on the provenance of the rocks (e.g. Bodet and Schärer 2000; Kosler et al. 2002; Königer et al. 2002; Lizuka et al. 2005; Veevers et al. 2005; Boni et al. 2012). Zircon $\varepsilon_{Hf}(t)$ values range from 2.2 to −24.5 and are dominated by negative values, similar to those of Paleozoic magmatic rocks in the Inner Mongolia Paleo-uplift (IMPU), but distinct from those of Paleozoic magmatic rocks in the CAOB with positive $\varepsilon_{Hf}(t)$ values. The zircon ages are dominated by Paleozoic ages, especially Late Carboniferous to Early Permian, coeval with the Paleozoic subduction-related volcanism in IMPU on the northern NCC. Therefore, we consider that the bauxites were derived mainly from ashes produced by the Paleozoic, particularly Late Carboniferous to Early Permian, volcanism in the IMPU along the northern NCC (Liu et al. 2014).

The Late Carboniferous sedimentary sequence with the 'G' layer of bauxites at its bottom is composed of coal-bearing formations, with sandstones, siltstones, marine limestone lens and thin layers interlayered and volcanic ash recorded by previous researchers (Zhong et al. 1995; Jia et al. 1999; Zhou et al. 2001; Zhang et al. 2007b). That indicates regionally marine–terrestrial transitional or marine–terrestrial interfingered environments with volcanic arc settings in Early Carboniferous to Early Permian. It gave way to a totally terrestrial environment in the NCC in late Early Permian.

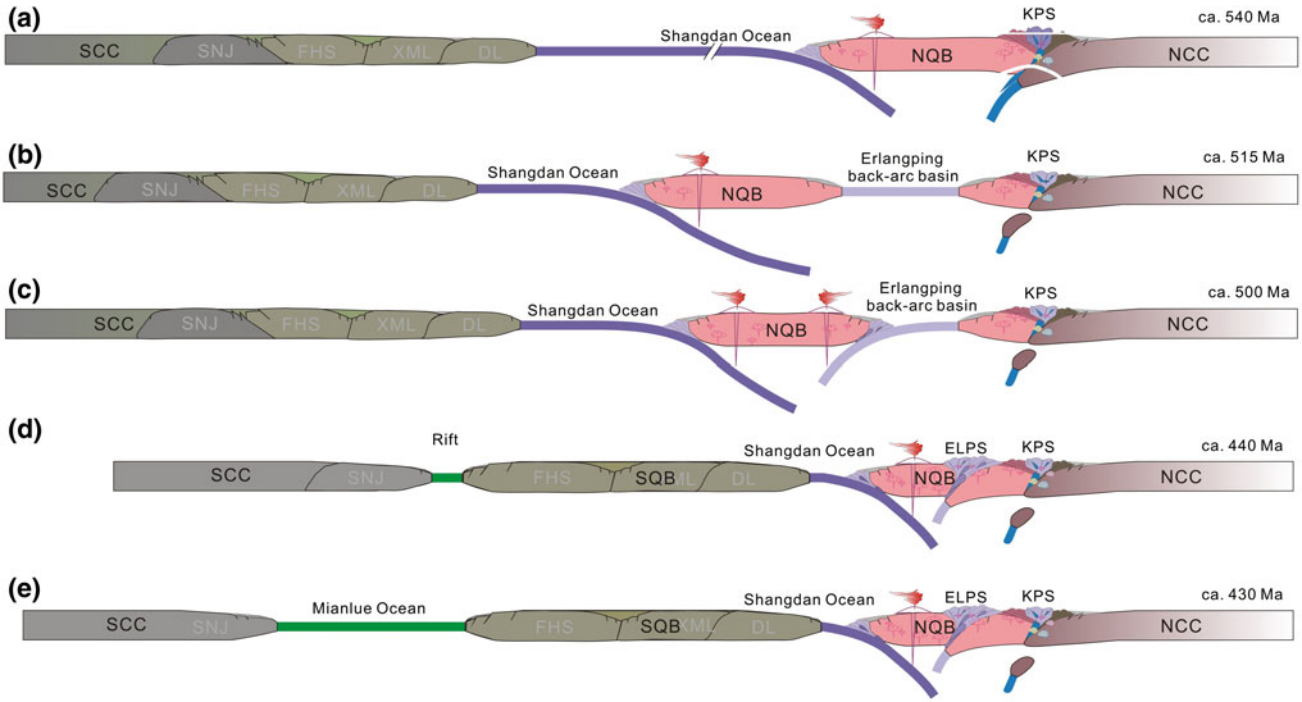

Fig. 18.4 Schematic cartoons showing evolution along the Shangdan suture and the Mianlue suture between the North Qinling Belt, South Qinling Belt and South China Craton, respectively during Early Paleozoic period (slightly modified after Dong and Santosh 2016). Not to scale. For explanation see text

18.3.2 Northern NCC and the Southern CAOB

Devonian is an important period for tectonic transition in the northern NCC and the southern CAOB. As talked above, the latest Silurian-Early Devonian Xibiehe Formation in the southern CAOB exhibits features of molasse or quasi-molasse and were considered as products of arc-continent collision (Zhao et al. 2010; Zhang et al. 2014a) or continent–continent collision and closure of the Paleo-Asian Ocean (Xu and Chen 1997; Xu et al. 2013). During this period, the northern NCC are characterized by emplacement of alkaline rocks (syenite, monzonite and alkaline granite) and minor mafic–ultramafic rocks (e.g. Luo et al. 2001; Jiang 2005; Zhang et al. 2007a, 2009a, 2010a; Shi et al. 2010; Wang et al. 2012). Some Devonian volcanic rocks consisting mainly of rhyolites have also been recognized from the Chifeng area in recent years (e.g., Liu et al. 2013; Ye et al. 2014a; Sun et al. 2015).

From latest Early Carboniferous period, the northern margin of NCC (including the accreted Bainaimiao arc belt) evolved as an Andean-style active continental margin due to southward subduction of the Paleo-Asian oceanic plate. As shown in Fig. 18.7, Carboniferous-Permian intrusive rocks are widely distributed in the northern NCC and constitute an east–west intrusive belt that is more than 1000 km long and up to 120 km wide. Moreover, many Late Carboniferous to Permian granitoid intrusions had been recognized from what were regarded previously as Archean to Paleoproterozoic lithological assemblages in the northern basement rocks of the NCC (e.g., Zhang et al. 2004, 2007c, 2009b, c; Wang et al. 2007). They consist mainly of diorite, quartz diorite, granodiorite and granite; other rocks are gabbro and tonalite and are calc-alkaline or high-K calc-alkaline, metaluminous or weak peraluminous, and were considered to reflect arc magmatism along an Andean-type continental margin (e.g. Wang and Liu 1986; Xiao et al. 2003, 2009; Li 2006; Wang et al. 2007; Zhang et al. 2007c, 2009b, c; Bai et al. 2013; Ma et al. 2013). Recent results on the Carboniferous-Permian volcanic rocks along two sides of the northern boundary fault of the NCC indicate their eruption during the Early Carboniferous to Late Permian from 347 ± 3 to 258 ± 1 Ma with a main rock association of basalt, basaltic andesite, andesite, dacite, rhyolite, tuff, tufaceous sandstone (Zhang et al. 2016). The Carboniferous-Permian volcanic rocks are not bimodal in composition and exhibit subduction-related geochemical features such as negative Nb and Ta anomalies of mafic to intermediate rocks on primitive mantle-normalized diagrams, indicating they were formed in an Andean-type continental arc.

The Solonker suture zone marks the final closure of the Paleo-Asian Ocean between the North China Block and the southern Mongolia composite terranes during the Late Permian to earliest Triassic (e.g. Wang and Liu 1986; Xiao et al. 2003, 2009; Li 2006; Windley et al. 2007; Wu et al. 2007;

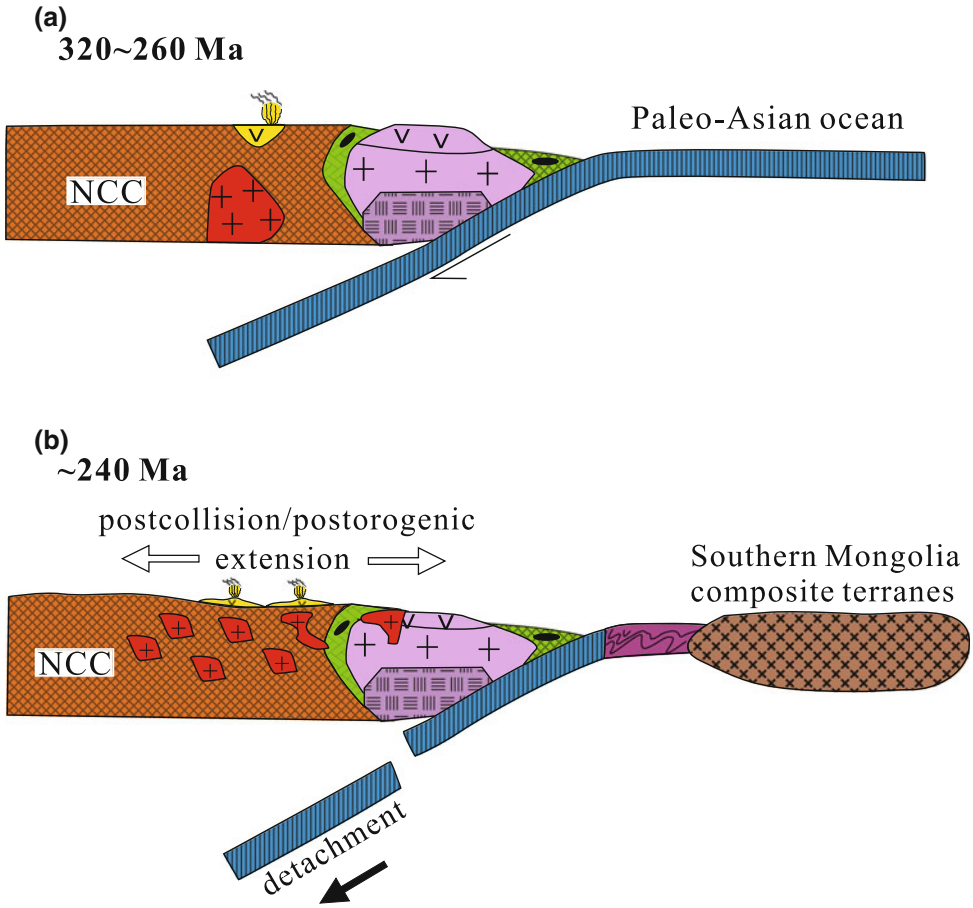

Fig. 18.5 Schematic cartoons showing evolution of the northern margin of the NCC during Late Paleozoic to Early Mesozoic period

Zhang et al. 2007c, 2009b, c; Miao et al. 2008; Li et al. 2009; Chen et al. 2009; Eizenhöfer et al. 2014). However, the decease of the Paleo-Asian oceanic subduction beneath the northern North China Block in its middle-western parts is a little earlier than that in its eastern part, as indicated by a slight decrease of the upper limits of the volcanic sequences from west to east (Zhang et al. 2016).

18.3.3 Southern NCC and QOB

The continuous deposition from Middle Devonian to Lower Triassic successions in the SQB doubted the consideration of the NQB exhumed in Late Paleozoic based on the deformational features, together with the metamorphic and cooling ages, and suggest the lack of full collision between the NQB and SQB after the closure of the Shangdan Ocean (Dong and Santosh 2016).

The birth of the Mianlue Ocean is indicated by the bimodal volcanic rocks around earliest Silurian (Fig. 18.8, Dong and Santosh 2016). The Late Devonian to Carboniferous radiolarian fauna in the interlayered cherts from the volcanics (Wang et al. 1999), as well as the Carboniferous radiolarian fauna from the cherts interlayered within the ophiolite in the Mianlue segment (Feng et al. 1996), indicates that the Mianlue Ocean existed during Devonian to Carboniferous (Fig. 18.8; Dong and Santosh 2016). The subduction of the Mianlue Ocean is indicated by the arc-related volcanic rocks in the ophiolite exposed in the SQB (Lai and Yang 1997; Liu et al. 2015; Dong and Santosh 2016) and lasted to the end of Paleozoic (Fig. 18.8; Dong and Santosh 2016).

18.4 Early Mesozoic Tectonics

18.4.1 Southern NCC and QOB

In Triassic, the significant tectonic event was collision between the NCC and SCC along QOB and formation of HP–UHP rocks in the Hong'an-Dabie-Sulu terranes. That resulted from the gradual consumption of the Mianlue oceanic crust during ca. 220–210 Ma between the SQB and SCC (Fig. 18.8 c), finally forming a major suture along which the NCC and SCC which amalgamated during Late Triassic (Dong and Santosh 2016). In the Hong'an-Dabie--Sulu terranes, the prograde quartz eclogite facies metamorphism and the UHP metamorphism occurred respectively,

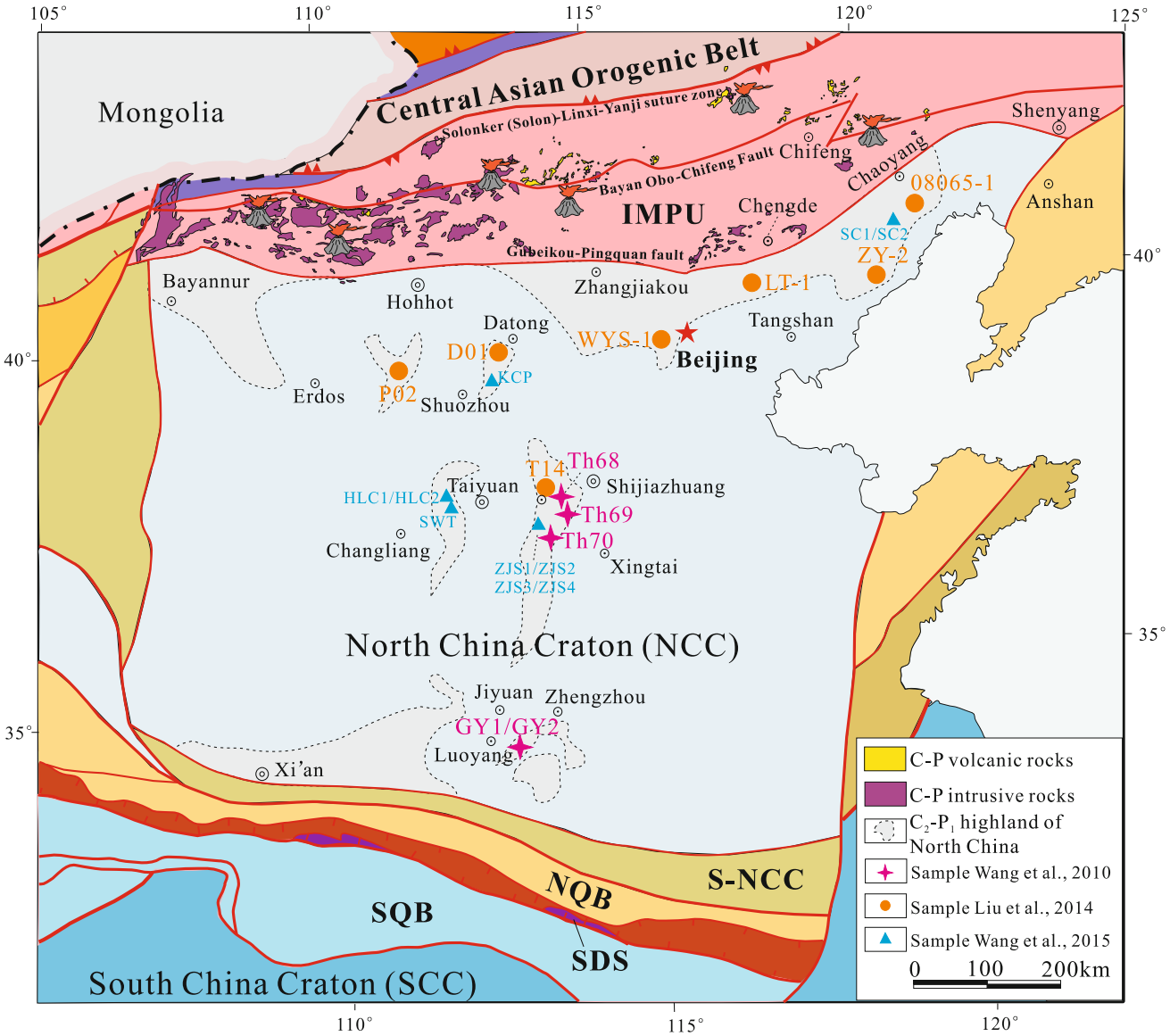

Fig. 18.6 Late Paleozoic paleogeographical map of the NCC. For explanation, see text

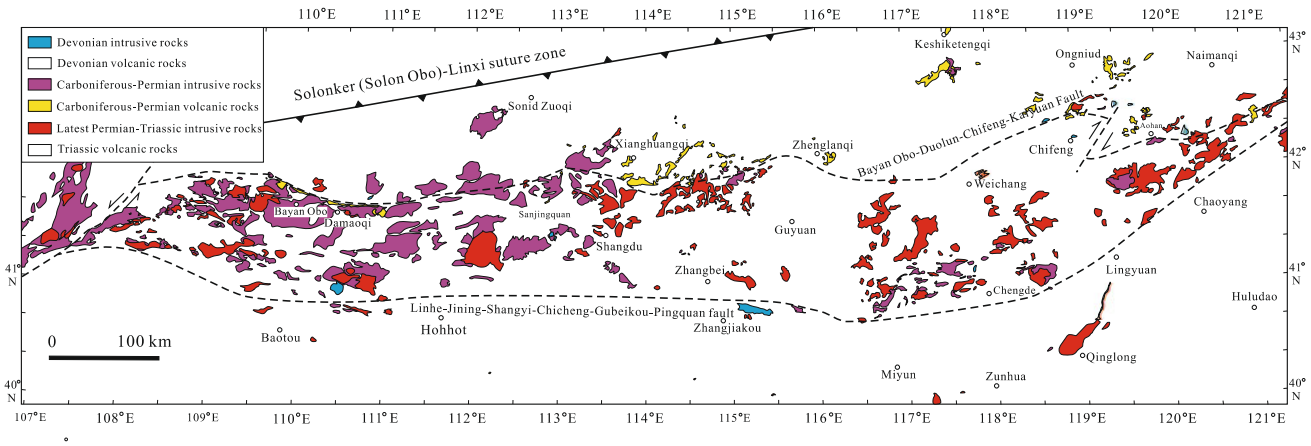

Fig. 18.7 Sketch map showing distribution of the Late Paleozoic magmatic rocks in the northern NCC (modified after Zhang et al. 2016)

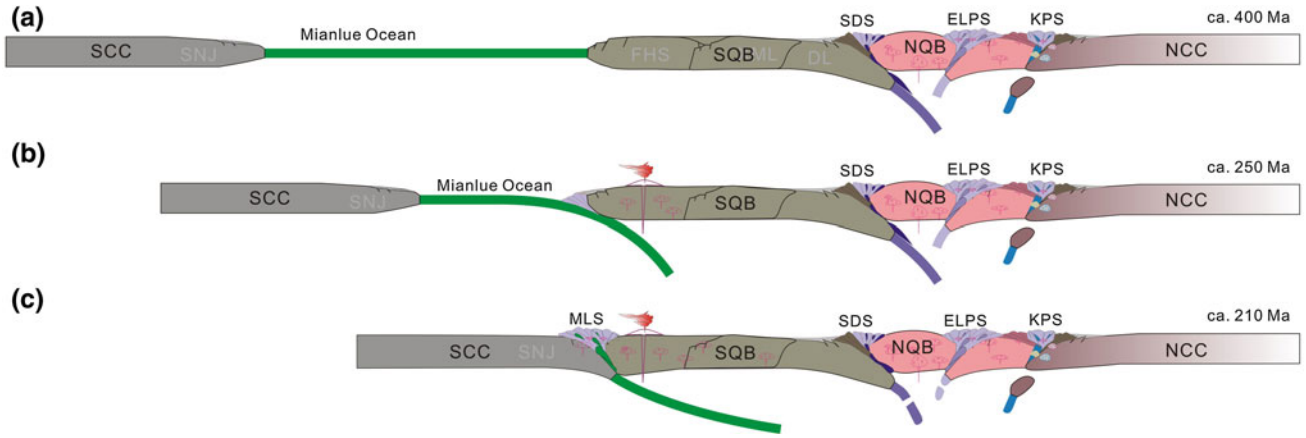

Fig. 18.8 Schematic cartoons showing evolution along the Mianlue suture between the South Qinling Belt and South China Craton, respectively during Late Paleozoic period (slightly modified after Dong and Santosh 2016). Not to scale. For explanation, see text

successively at 246 ± 7 and at 234 ± 4 Ma (Liu et al. 2006, 2015). While syn-UHP and syn-HP southeast-vergent thrusting formed a series of stacked structural slices at 241–231 and at 225–215 Ma (Li et al. 2010). This was followed by southeast-vergent folding under amphibolite facies conditions at 215–205 Ma; then a third generation of flexural folding occurred at shallow levels at 200–184 Ma. These two extrusion episodes correlate with the two stages of Triassic exhumation of the Dabie HP–UHP rocks, respectively, during continental collision (Li et al. 2010). This collision resulted in continental crust thickening and partial melting to generate the large volumes of granitoids in the SQB ranging of ca. 220–210 Ma. At ca. 200 Ma, the thickened crust and orogen rapidly collapsed resulting in the emplacement of post-collisional rapakivi-texture granitoids during ca. 210–200 Ma and exhumation of the quasi-high pressure granulite at ca. 199–192 Ma (Dong and Santosh 2016).

18.4.2 The Northern NCC

The final closure of the Paleo-Asian Ocean and amalgamation of the northern North China Block with composite terranes of southern Mongolia during the Late Permian to earliest Triassic was followed by post-collisional/post-orogenic extension, large-volume magmatism and significant continental growth (Zhang et al. 2009b, 2012). There is a tectonic transition from post-collisional/post-orogenic extension to intraplate extension during Early Mesozoic time (Yang et al. 2012; Ye et al. 2014b). In contrast to typical continental orogenic belts such as, the European Alps and Asian Himalaya, amalgamation between the Mongolian arc terranes and the North China Block was a 'soft' or 'weak' collision between a large continental block and composite arcs with associated subduction-accretion complexes, characterized by the absence of syn-collisional S-type granitoids and high-pressure metamorphism in the northern NCC (e.g., Zhang et al. 2009b). Moreover, there were significant changes in magmatic rock associations from the latest Permian to Middle-Late Triassic time, and in deformation patterns from Early-Middle Triassic to Late Triassic-Early Jurassic in the northern NCC (Zhang et al. 2014b, and reference therein). Early Triassic magmatic rocks are mainly composed of monzogranite, syenogranite, monzonite, rhyolitic welded tuff, rhyolite and tuffaceous sandstone, with minor mafic-ultramafic rocks and granodiorite. Middle-Late Triassic magmatic rocks consist mainly diorite, granodiorite, monzogranite, syenogranite, monzonite, syenite and intermediate volcanic rocks such as andesite, trachyandesite, and autoclastic trachyandesite breccia (Zhang et al. 2009a, 2012; Yang et al. 2012; Chen et al. 2013; Ye et al. 2014b). Geochemical and isotopic results show that asthenospheric melts were strongly involved in petrogenesis of the Middle-Late Triassic mafic-ultramafic and alkaline rocks, which may mark the start of carton destruction and lithospheric thinning of the northern NCC (Zhang et al. 2009a, 2012; Ye et al. 2014b).

The Panshan region is located in the eastern Yanshan fold-thrust belt of the northern NCC. The region, west of the Malanyu anticlinorium is characteristic of folds surrounding the Panshan pluton. The Zhuangguoyu and Fujunshan synclines were truncated in south by the Jixian thrust, which was intruded by the Panshan pluton. Along the Jixian thrust it can be observed that the Changcheng and Jixian systems were thrusted upon the Jixian and Qingbaikou systems. North of the Panshan pluton the Hongshikan anticline was

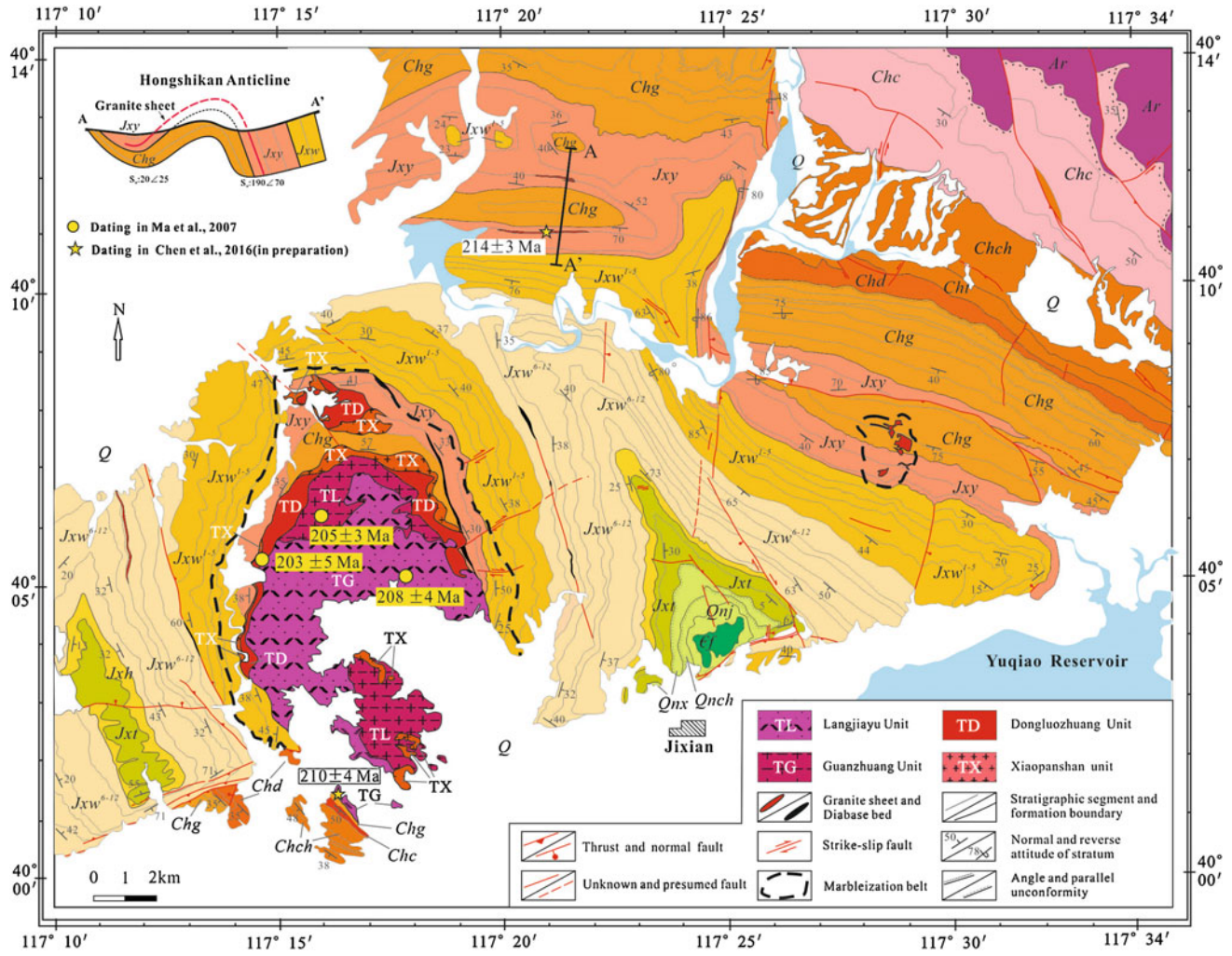

Fig. 18.9 Geological map of the Panshan region, the northern NCC showing Late Triassic deformation and plutons. For explanation, see text

intruded by granitic sheets at its wings in the same stratum of the Yangzhuang Formation (Fig. 18.9). Zircon U–Pb dating of the sample from the southern wing yielded an intrusive age 214 ± 3 Ma (Zhao et al. 2010), which can constrain folding and thrusting postdated 214 Ma. The dating of the samples from the Guanzhuang unit gave the zircon U–Pb ages at 210 ± 4 and 208 ± 4 Ma. The observation and evidence above show that folding, thrusting and magmatism in the Panshan pluton occurred at around 210 Ma in Late Triassic time. Combined with our data on tectonic deformation in Late Triassic to Early Jurassic obtained from the Niuyingzi region, western Liaoning (Hu et al. 2010), the Xiabancheng region, northern Hebei (Liu et al. 2012b), the Dushan region and the northeastern Hebei (Ye et al. 2014c) the conclusion can be reached that the northern NCC witnessed regional intense deformation at around 210 Ma and initial decratonization of the NCC.

18.5 Summary

The NCC, Bainaimiao arc belt and the northward subduction of the Shangdan Ocean started their evolution from around 520 Ma when Gondwana assembled in its peak tectonism. The Middle Ordovician marine regression and regional uplift of the NCC occurred after deposition of the Majiagou Formation, which led to the paleogeographic change of the NCC, especially in the eastern Ordos basin and potash formation. That coincided with diamondiferous kimberlite magmatism in the eastern and northeast NCC at ca. 463–470 Ma. The hidden magmatic event in deep of NCC was simultaneous with the global tectonic event around 430 Ma, which suggested global tectonic settings for the regional tectonic events of the NCC in Early Paleozoic.

The Late Carboniferous to Early Permian ‘G’ layer of bauxites overlain disconformably upon the Middle Ordovician limestone were derived mainly from ashes produced by

volcanism mainly in IMPU when the northern margin of the NCC evolved as an Andean-style active continental margin. The Late Carboniferous to Early Permian clastic coal-bearing sequence interlayered with marine limestone and volcanic ash formed in terrestrial–marine transitional or terrestrial environment with volcanic-arc settings.

The final collision between the SCO and SQB along the Mianlue suture resulted in intense deformation of QOB and HP/UHP metamorphism in Hong'an-Dabie-Sulu terranes in Late Triassic. In the northern NCC, intense tectonic deformation and significant changes in and magmatism occurred in Late Triassic, around 210 Ma. This suggests that the NCC was not a craton in Late Triassic.

Acknowledgments This research was financially supported by the National Basic Research Program of China (2012CB416604). We thank Jian-Feng Li and Jian-Liu for drawing some figures. Reviews and comments from Jianping Zheng are appreciated.

References

Bai, X., Liu, S., Wang, W., Yang, P., & Li, Q. (2013). U–Pb geochronology and Lu–Hf isotopes of zircons from newly identified Permian–Early Triassic plutons in western Liaoning province along the northern margin of the North China Craton: Constraints on petrogenesis and tectonic setting. *International Journal of Earth Sciences, 102*, 671–685.

Bodet, F., & Schärer, U. (2000). Evolution of the SE-Asian continent from U–Pb and Hf isotopes in single grains of zircon and baddeleyite from large rivers. *Geochimica et Cosmochimica Acta, 64*, 2067–2091.

Boni, M., Reddy, S. M., Mondillo, N., Balassone, G., & Taylor, R. (2012). A distant magmatic source for Cretaceous karst bauxites of Southern Apennines (Italy), revealed through SHRIMP zircon age dating. *Terra Nova, 24*, 326–332.

Bureau of Geology and Mineral Resources of Inner Mongolia (BGMRIM). (1991). *Regional geology of Inner Mongolia Autonomous Region* (725 p.). Beijing: Geological Publishing House (in Chinese with English abstract).

Chao, E. C. T., Back, J. M., Minkin, J. A., Tatsumoto, M., Wang, J., Conrad, J. E., et al. (1997). The sedimentary carbonate-hosted giant Bayan Obo REE–Fe–Nb ore deposit of Inner Mongolia, China: A cornerstone example for giant polymetallic ore deposits of hydrothermal origin. *United States Geological Survey Bulletin 2143*, 65 p.

Chen, B., Jahn, B. M., & Tian, W. (2009). Evolution of the Solonker suture zone: Constraints from zircon U–Pb ages, Hf isotopic ratios and whole-rock Nd–Sr isotope compositions of subduction and collision-related magmas and fore arc sediments. *Journal of Asian Earth Sciences, 34*, 245–257.

Chen, B., Niu, X. L., Wang, Z. Q., Gao, L., & Wang, C. (2013). Geochronology, petrology, and geochemistry of the Yaojiazhuang ultramafic-syenitic complex from the North China Craton. *Science China: Earth Sciences, 56*, 1294–1307.

Chen, X. G., & Boucot, A. J. (2007). Late Silurian brachiopods from Darhan Mumingan Joint Banner, Inner Mongolia. *Geobios, 40*, 61–74.

Clift, P. D., Schouten, H., & Draut, E. (2003). A general model of arc-continent collision and subduction polarity reversal from Taiwan and the Irish Caledonides. In R. D. Larter & P. T. Leat (Eds.), *Intra-oceanic subduction systems: Tectonic and magmatic processes* (Vol. 219, pp. 81–98). London: The Geological Society, Special Publications.

Demoux, A., Kröner, A., Liu, D., & Badarch, G. (2009). Precambrian crystalline basement in southern Mongolia as revealed by SHRIMP zircon dating. *International Journal of Earth Sciences, 98*, 1365–1380.

Dong, Y. P., Genser, J., Neubauer, F., Zhang, G. W., Liu, X. M., Yang, Z., et al. (2011). U–Pb and 40Ar/39Ar geochronological constraints on the exhumation history of the North Qinling terrane, China. *Gondwana Research, 19*, 881–893.

Dong, Y. P., & Santosh, M. (2016). Tectonic architecture and multiple orogeny of the Qinling Orogenic Belt, Central China. *Gondwana Research, 29*, 1–40.

Eizenhöfer, P. R., Zhao, G. C., Zhang, J., & Sun, M. (2014). Final closure of the Paleo-Asian Ocean along the Solonker Suture Zone: Constraints from geochronological and geochemical data of Permian volcanic and sedimentary rocks. *Tectonics, 33*. doi:10.1002/2013TC003357

Feng, Q. L., Du, Y. S., Yin, H. F., Sheng, J. H., & Xu, J. F. (1996). Carboniferous radiolaria fauna firstly discovered in Mian-Lue ophiolitic melange belt of south Qinling Mountains. *Science in China (Series D), 39*, 87–91.

Hu, J. M., Zhao, Y., Liu, X. W., & Xu, G. (2010). Early Mesozoic deformations of the eastern Yanshan thrust belt, northern China. *International Journal of Earth Sciences, 99*, 785–800.

Hu, X., Xu, C., & Niu, S. (1990). *Evolution of the early Paleozoic continental margin in northern margin of the North China Platform* (215 p.). Beijing: Peking University Press (in Chinese with English abstract).

Jahn, B. M., Wu, F. Y., & Chen, B. (2000). Massive granitoid generation in Central Asia: Nd isotope evidence and implication for continental growth in the Phanerozoic. *Episodes, 23*, 82–92.

Jia, B., Zhou, A., & Gu, D. (1999). Geochemistry and provenance analysis of Late Paleozoic volcanic event deposits in West Liaoning. *Acta Sedimentology Sinica, 17*, 473–477 (in Chinese with English abstract).

Jiang, N. (2005). Petrology and geochemistry of the Shuiquangou syenitic complex, northern margin of the North China Craton. *Journal of the Geological Society, London, 162*, 203–215.

Johnson, R. W., & Jaques, A. L. (1980). Continent—arc collision and reversal of arc polarity: New interpretations from a critical area. *Tectonophysics, 63*, 111–124.

Königer, S., Lorenz, V., Stollhofen, H., & Armstrong, R. A. (2002). Origin, age and stratigraphic significance of distal fallout ash tuffs from the Carboniferous–Permian continental Saar–Nahe Basin (SW Germany). *International Journal of Earth Sciences, 91*, 341–356.

Konstantinovskaia, E. A. (2001). Arc-continent collision and subduction reversal in the Cenozoic evolution of the Northwest Pacific: An example from Kamchatka (NE Russia). *Tectonophysics, 333*, 75–94.

Kosler, J., Fonneland, H., Sylvester, P., Tubrett, M., & Pedersen, R. B. (2002). U–Pb dating of detrital zircons for sediment provenance studies—A comparison of laser ablation ICPMS and SIMS techniques. *Chemical Geology, 182*, 605–618.

Kozakov, I. K., Yarmolyuk, V. V., Kovach, V. P., Bibikova, E. V., Kirnozova, T. I., Kozlovskii, A. M., et al. (2012). The early Baikalian crystalline complex in the basement of the Dzabkhan microcontinent of the early Caledonian orogenic area, Central Asia. *Stratigraphy and Geological Correlation, 20*, 231–239.

Kröner, A., Demoux, A., Zack, T., Rojas-Agramonte, Y., Jian, P., Tomurhuu, D., et al. (2011). Zircon ages for a felsic volcanic rock and arc-related early Palaeozoic sediments on the margin of the Baydrag microcontinent, central Asian orogenic belt, Mongolia. *Journal of Asian Earth Sciences, 42*, 1008–1017.

Kröner, A., Kovach, V., Belousova, E., Hegner, E., Armstrong, R., Dolgopolova, A., et al. (2014). Reassessment of continental growth during the accretionary history of the Central Asian Orogenic Belt. *Gondwana Research, 25*, 103–125.

Lai, S. C., & Yang, Y. C. (1997). Petrology and geochemistry features of the metamorphic volcanic rocks in the Mianxian-Lueyang suture zone, southern Qinling. *Acta Petrologica Sinica, 13*, 563–573 (in Chinese with English abstract).

Lawver, L. A., Gahagan, L. M., & Norton, I. (2011). Palaeogeographic and tectonic evolution of the Arctic region during the Palaeozoic. In A. M. Spencer, A. F. Embry, D. L. Gautier, A. V. Stoupakova, & K. Sørensen (Eds.), *Memoirs: Vol. 35. Arctic petroleum geology* (pp. 61–77). London: Geological Society.

Levashova, N. M., Meert, J. G., Gibsher, A. S., Grice, W. C., & Bazhenov, M. L. (2011). The origin of microcontinents in the Central Asian Orogenic Belt: Constraints from paleomagnetism and geochronology. *Precambrian Research, 185*, 37–54.

Levashova, N. M., Kalugin, V. M., Gibsher, A. S., Yff, J., Ryabinin, A. B., Meert, J. G., et al. (2010). The origin of the Baydaric microcontinent, Mongolia: Constraints from paleomagnetism and geochronology. *Tectonophysics, 485*, 306–320.

Li, J. Y. (2006). Permian geodynamic setting of Northeast China and adjacent regions: Closure of the Paleo-Asian Ocean and subduction of the Paleo-Pacific Plate. *Journal of Asian Earth Sciences, 26*, 207–224.

Li, J. Y., Zhang, J., Yang, T. N., Li, Y. P., Sun, G. H., Zhu, Z. X., et al. (2009). Crustal tectonic division and evolution of the southern part of the North Asian Orogenic Region and its adjacent areas. *Journal of the Jilin University (Earth Science Edition), 39*, 584–605 (in Chinese with English abstract).

Li, S. Z., Kusky, T. M., Zhao, G. C., Liu, X. C., Zhang, G. W., & Kopp, H. (2010). Two-stage Triassic exhumation of HP–UHP terranes in the western Dabie orogen of China: Constraints from structural geology. *Tectonophysics, 490*, 267–293.

Liu, F. L., Gerdes, A., Liou, J. G., Xue, H. M., & Liang, F. H. (2006). SHRIMP U–Pb zircon dating from Sulu-Dabie dolomitic marble, eastern China: Constraints on prograde, UHP and retrograde metamorphic ages. *Journal of Metamorphic Geology, 24*, 569–590.

Liu, J. F., Li, J. Y., Chi, X. G., Feng, Q. W., Hu, Z. C., & Zhou, K. (2013). Early Devonian felsic volcanic rocks related to the arc-continent collision on the northern margin of North China craton-evidences of zircon U–Pb dating and geochemical characteristics. *Geological Bulletin of China, 32*, 267–278 (in Chinese with English abstract).

Liu, J., Zhao, Y., Liu, A., Zhang, S., Yang, Z., & Zhuo, S. (2014). Origin of Late Palaeozoic bauxites in the North China Craton: Constraints from zircon U–Pb geochronology and in situ Hf isotopes. *Journal of the Geological Society London, 171*(5), 695–707.

Liu, J., Zhao, Y., Liu, X., Wang, Y., & Liu, X. (2012b). Early Jurassic rapid exhumation of the basement rocks along the northern margin of the North China Craton: Evidence from the Xiabancheng basin in the Yanshan Tectonic Belt. *Basin Research, 24*, 544–558.

Liu, S. F., Qian, T., Li, W. P., Dou, G. X., & Wu, P. (2015). Oblique closure of the northeastern Paleo-Tethys in central China. *Tectonics, 34*, 413–434. doi:10.1002/2014TC003784

Liu, X. C., Wu, Y. B., Gao, S., Peng, M., Wang, J., Wang, H., et al. (2012a). Triassic high-pressure metamorphism in the Huwan shear zone: Tracking the initial subduction of continental crust in the whole Dabie orogen. *Lithos, 136–139*, 60–72.

Lizuka, T., Hirata, T., Komiya, T., Rion, S., Katayama, I., & Maruyama, S. (2005). U–Pb and Lu–Hf isotope systematics of zircons from the Mississippi River sand: Implications for reworking and growth of continental crust. *Geology, 33*, 485–488.

Luo, Z. K., Miao, L. C., Guan, K., Qiu, Y. S., Qiu, Y. M., Mcnaughton, N. J., & Groves, D. I. (2001). SHRIMP chronological study of the Shuiquangou intrusive body in Zhangjiakou area, Hebei province and geochemical significance. *Geochimica, 30*, 116–122 (in Chinese with English abstract).

Ma, X., Chen, B., Chen, J. F., & Niu, X. L. (2013). Zircon SHRIMP U–Pb age, geochemical, Sr–Nd isotopic, and in-situ Hf isotopic data of the Late Carboniferous-Early Permian plutons in the northern margin of the North China Craton. *Science China: Earth Sciences, 56*, 126–144.

McKenzie, D. P. (1969). Speculations on the consequences and causes of plate motions. *Geophysical Journal of the Royal Astronomical Society, 18*, l–32.

Meng, X., Ge, M., & Xiao, Z. (1987). A sedimentological study of Carboniferous bauxitic formations in North China. *Acta Geologica Sinica, 61*, 95–108 (in Chinese with English abstract).

Miao, L. C., Fan, W. M., Liu, D. Y., Zhang, F. Q., Shi, Y. R., & Guo, F. (2008). Geochronology and geochemistry of the Hegenshan ophiolitic complex: Implications for late-stage tectonic evolution of the Inner Mongolia-Daxinganling Orogenic Belt, China. *Journal of Asian Earth Sciences, 32*, 348–370.

Shi, Y. R., Liu, D. Y., Miao, L. C., Zhang, F. Q., Jian, P., Zhang, W., et al. (2010). Devonian A-type granitic magmatism on the northern margin of the North China Craton: SHRIMP U–Pb zircon dating and Hf isotopes of the Hongshan granite at Chifeng, Inner Mongolia, China. *Gondwana Research, 17*, 632–641.

Su, Y. Z. (1996). Paleozoic stratigraphical of Nei Mongol grass stratigraphical province. *Jilin Geology, 15*, 42–54 (in Chinese with English abstract).

Sun, L. X., Ren, B. F., Teng, F., Zhang, Y., Gu, Y. C., & Guo, H. (2015). LA-ICP-MS U–Pb ages of the volcanic rocks from the Chaotugou Formation in Aohan Banner, Inner Mongolia. *Geological Bulletin of China, 34*, 1493–1501 (in Chinese with English abstract).

Tang, K. D. (1990). Tectonic development of Paleozoic foldbelts at the north margin of the Sino-Korean Craton. *Tectonics, 9*, 249–260.

Tang, K. D. (1992). *Tectonic evolution and Minerogenetic regularities of the fold belt along the northern margins of Sino-Korean Plate* (277 p.). Beijing: Peking University Press (in Chinese with English abstract).

Veevers, J. J., Saeed, A., Belousova, E. A., & Griffin, W. L. (2005). U–Pb ages and source composition by Hf-isotope and trace-element analysis of detrital zircons in Permian sandstone and modern sand from southwestern Australia and a review of the paleogeographical and denudational history of the Yilgarn Craton. *Earth-Science Review, 68*, 245–279.

Wang, H. C., Xiang, Z. Q., Zhao, F. Q., Li, H. M., Yuan, G. B., & Chu, H. (2012). The alkaline plutons in eastern part of Guyang County, Inner Mongolia: Geochronology, petrogenesis and tectonic implications. *Acta Petrologica Sinica, 28*, 2843–2854 (in Chinese with English abstract).

Wang, H. C., Zhao, F. Q., Li, H. M., Sun, L. X., Miao, L. C., & Ji, S. P. (2007). Zircon SHRIMP U–Pb age of the dioritic rocks from northern Hebei: The geological records of late Paleozoic magmatic arc. *Acta Petrologica Sinica, 23*, 597–604 (in Chinese with English abstract).

Wang, P. (2005). The Xibiehe section and Xibiehe Formation of the Bateaobao area in Darhan Mumingan Joint Banner, Inner Mongolia. *Journal of Jilin University (Earth Science Edition), 35*, 409–414 (in Chinese with English abstract).

Wang, Q., Deng, J., Liu, X., Zhao, R., & Cai, S. (2016). Provenance of Late Carboniferous bauxite deposits in the North China Craton: New constraints on marginal arc construction and accretion processes. *Gondwana Research,*. doi:10.1016/j.gr.2015.10.015

Wang, Q., & Liu, X. Y. (1986). Paleoplate tectonics between Cathaysia and Angaraland in Inner Mongolia of China. *Tectonics, 5*, 1073–1088.

Wang, Q., Liu, X. Y., Li, J. Y. (1991). *Plate tectonics between Cathaysia and Angaraland in China* (149 p.). Beijing: Peking University Publication House (in Chinese with English abstract).

Wang, T., Zheng, Y. D., Gehrels, G. E., & Mu, Z. G. (2001). Geochronological evidence for existence of South Mongolian microcontinent—A zircon U–Pb age of grantoid gneisses from the Yagan-Onch Hayrhan metamorphic core complex. *Chinese Science Bulletin, 46*, 2005–2008.

Wang, Y., Zhou, L., Zhao, L., Ji, M., & Gao, L. (2010). Palaeozoic uplands and unconformity in the North China Block: Constraints from zircon LA-ICP-MS dating and geochemical analysis of Bauxite. *Terra Nova, 22*, 264–273.

Wang, Z. Q., Chen, H. H., Li, J. L., Hao, J., Zhao, Y., Han, F. L., et al. (1999). Discovery of radiolarian fossils in the Xixiang Group of southern Qinling, central China, and its implications. *Science in China (Series D), 42*, 337–343.

Wang, Z. Q., Yan, Q. R., Yan, Z., Wang, T., Jiang, C. F., Gao, L. D., et al. (2009). New division of the main tectonic units of the Qinling Orogenic Belt, Central China. *Acta Geologica Sinica, 83*, 1527–1546 (in Chinese with English abstract).

Windley, B. F., Alexeiev, D., Xiao, W. J., Kröner, A., & Badarch, G. (2007). Tectonic models for accretion of the Central Asian Orogenic Belt. *Journal of the Geological Society London, 164*, 31–48.

Wu, F. Y., Zhao, G. C., Sun, D. Y., Wilde, S. A., & Zhang, G. L. (2007). The Hulan Group: Its role in the evolution of the Central Asian Orogenic Belt of NE China. *Journal of Asian Earth Sciences, 30*, 542–556.

Wu, Y. B., & Zheng, Y. F. (2013). Tectonic evolution of a composite collision orogen: An overview on the Qinling–Tongbai–Hong'an–Dabie–Sulu orogenic belt in central China. *Gondwana Research, 23*, 1402–1428.

Xiao, W., Windley, B. F., Hao, J., & Zhai, M. G. (2003). Accretion leading to collision and the Permian Solonker suture, Inner Mongolia, China: Termination of the central Asian orogenic belt. *Tectonics, 22*, 1069. doi:10.1029/2002TC001484

Xiao, W. J., Windley, B. F., Huang, B. C., Han, C. M., Yuan, C., Chen, H. L., et al. (2009). End-Permian to mid-Triassic termination of the accretionary processes of the southern Altaids: Implications for the geodynamic evolution, Phanerozoic continental growth, and metallogeny of Central Asia. *International Journal of Earth Sciences, 98*, 1189–1217.

Xu, B., Charvet, J., Chen, Y., Zhao, P., & Shi, G. (2013). Middle Paleozoic convergent orogenic belts in western Inner Mongolia (China): Framework, kinematics, geochronology and implications for tectonic evolution of the Central Asian Orogenic Belt. *Gondwana Research, 23*, 1342–1364.

Xu, B., & Chen, B. (1997). Frame work and evolution of the middle Paleozoic orogenic belt between Siberian and North China Plate in northern Inner Mongolia. *Science in China (Series D), 40*, 463–469.

Xu, L. Q., Deng, J. F., Chen, Z. Y., & Tao, J. X. (2003). The identification of Ordovician adakites and its significance in northern Damao, Inner Mongolia. *Geosciences, 17*, 428–434 (in Chinese with English abstract).

Yang, J. H., Sun, J. F., Zhang, M., Wu, F. Y., & Wilde, S. A. (2012). Petrogenesis of silica-saturated and silica-undersaturated syenites in the northern North China Craton related to post-collisional and intraplate extension. *Chemical Geology, 328*, 149–167.

Yang, Y. H., Wu, F. Y., Wilde, S. A., Liu, X. M., Zhang, Y. B., Xie, L. W., et al. (2009). In-situ perovskite Sr–Nd isotopic constraints on the petrogenesis of the Ordovician Mengyin kimberlites in the North China Craton. *Chemical Geology, 264*, 24–42.

Ye, H., Zhang, S. H., & Zhao, Y. (2014a). Origin of two contrasting latest Permian-Triassic volcanic rock suites in the northern North China Craton: Implications for Early Mesozoic lithosphere thinning. *International Geology Review, 56*(13), 1630–1657.

Ye, H., Zhang, S. H., Zhao, Y., Liu, J. M., & He, Z. F. (2014b). Recognition of the latest Devonian volcanic rocks in the Chifeng area, northern North China block and its geological implications. *Geological Bulletin of China, 33*, 1274–1283 (in Chinese with English abstract).

Ye, H., Zhang, S. H., Zhao, Y., & Wu, F. (2014c). Petrogenesis and emplacement deformation of the late Triassic Dushan composite batholith in the Yanshan fold and thrust belt: Implications for the tectonic settings of the northern margin of the North China Craton during the Early Mesozoic. *Earth Science Frontiers, 21*(4), 275–292 (in Chinese with English abstract).

Zhai, M.-G. (2014). Multi-stage crustal growth and cratonization of the North China Craton. *Geoscience Frotiers, 5*, 457–469.

Zhai, M.-G., & Santosh, M. (2011). The early Precambrian odyssey of North China Craton: A synoptic overview. *Gondwana Research, 20*, 6–25.

Zhang, H. F., & Yang, Y. H. (2007). Emplacement age and Sr-Nd-Hf isotopic characteristics of the diamondiferous kimberlites from the eastern North China Craton. *Acta Petrologica Sinica, 23*, 285–294.

Zhang, S. H., Zhao, Y., Liu, X. C., Liu, D. Y., Chen, F., Xie, L. W., et al. (2009a). Late Paleozoic to early Mesozoic mafic-ultramafic complexes from the northern North China Block: Constraints on the composition and evolution of the lithospheric mantle. *Lithos, 110*, 229–246.

Zhang, S. H., Zhao, Y., Song, B., & Liu, D. Y. (2007a). Petrogenesis of the middle Devonian Gushan diorite pluton on the northern margin of the North China block and its tectonic implications. *Geological Magazine, 144*, 553–568.

Zhang, S. H., Zhao, Y., Song, B., & Wu, H. (2004). The late Paleozoic gneissic granodiorite pluton in early Pre-cambrian highgrade metamorphic terrains near Longhua county in northern Hebei Province, North China: Result from zircon SHRIMP U–Pb dating and its tectonic implications. *Acta Petrologica Sinica, 20*, 621–626.

Zhang, S. H., Zhao, Y., Song, B., & Yang, Y. H. (2007b). Zircon SHRIMP U–Pb and in-situ Lu–Hf isotope analyses of a tuff from Western Beijing: Evidence for missing late Paleozoic arc volcano eruptions at the northern margin of the North China block. *Gondwana Research, 12*, 157–165.

Zhang, S. H., Zhao, Y., Song, B., Yang, Z. Y., Hu, J. M., & Wu, H. (2007c). Carboniferous granitic plutons from the northern margin of the North China block: Implications for a late Paleozoic active continental margin. *Journal of the Geological Society London, 164*, 451–463.

Zhang, S. H., Zhao, Y., Song, B., Hu, J. M., Liu, S. W., Yang, Y. H., et al. (2009b). Contrasting late carboniferous and late Permian-Middle Triassic intrusive suites from the northern margin of the North China Craton: Geochronology, petrogenesis and tectonic implications. *Geological Society of America Bulletin, 121*, 181–200.

Zhang, S. H., Zhao, Y., Kröner, A., Liu, X. M., Xie, L. W., & Chen, F. K. (2009c). Early Permian plutons from the northern North China Block: Constraints on continental arc evolution and convergent margin magmatism related to the Central Asian Orogenic Belt. *International Journal of Earth Sciences, 98*, 1441–1467.

Zhang, S. H., Zhao, Y., Ye, H., Hou, K. J., & Li, C. F. (2012). Early Mesozoic alkaline complexes in the northern North China Craton: Implications for cratonic lithospheric destruction. *Lithos, 155*, 1–18.

Zhang, S. H., Zhao, Y., Ye, H., Liu, J. M., & Hu, Z. C. (2014a). Origin and evolution of the Bainaimiao arc belt: Implications for crustal growth in the southern Central Asian orogenic belt. *Geological Society of America Bulletin, 126*, 1275–1300.

Zhang, S. H., Zhao, Y., Davis, G. A., Ye, H. & Wu, F. (2014b). Temporal and spatial variations of Mesozoic magmatism and deformations in the North China Craton: implications for lithospheric thinning and decratonization. *Earth-Science Reviews*, *131*, 49–87.

Zhang, S. H., Zhao, Y., Liu, J. M., & Hu, Z. C. (2016). Different sources involved in generation of continental arc volcanism: The Carboniferous-Permian volcanic rocks in the northern margin of the North China block. *Lithos, 240–243*, 382–401.

Zhang, X. H., Zhang, H. F., Jiang, N., Zhai, M. G., & Zhang, Y. B. (2010a). Early Devonian alkaline intrusive complex from the northern North China Craton: A petrological monitor of post-collisional tectonics. *Journal of the Geological Society, 167*, 717–730.

Zhang, Y. P., Tang, K. D., & Su, Y. Z. (1986). On Caledonian movement in Central Nei Mongol in the light of continental accretion. In K. D. Tang (Ed.), *Contributions to the project of plate tectonics in Northern China No. 1* (pp. 158–172). Beijing: Geological Publishing House (in Chinese with English abstract).

Zhang, Y. P., & Tang, K. D. (1989). Pre-Jurassic tectonic evolution of intercontinental region and the suture zone between the North China and Siberian platforms. *Journal of Southeast Asian Earth Sciences, 3*, 47–55.

Zhang, Y. P., Su, Y. Z., & Li, J. C. (2010b). Regional tectonic significance of the late Silurian Xibiehe Formation in central Inner Mongolia, China. *Geological Bulletin of China, 29*, 1599–1605 (in Chinese with English abstract).

Zhang, Y. S., Xing, E. Y., Wang, Z. Z., Zheng, M. P., Shi, L. Z., Su, K., et al. (2015). Evolution of lithofacies paleogeography in the Ordos basin and its implication of potash formation. *Acta Geologica Sinica, 89*(11), 1921–1935 (in Chinese with English abstract).

Zhao, Y., Song, B., Zhang, S. H., & Liu, J. (2006a). Geochronology of the inherited zircons from Jurassic nandaling basalt of the Western Hills of Beijing, North China: Its implications. *Earth Science Frontiers, 13*(2), 184–190 (in Chinese with English abstract).

Zhao, Y., Song, B., & Zhang, S. H. (2006b). The Central Mongolian microcontinent: Its Yangtze affinity and tectonic implications. In B. M. Jahn & S. L. Chung (Eds.), *Abstract Volume of Symposium on continental growth and orogeny in Asia* (pp. 135–136). Taipei, March 19–26.

Zhao, Y., Chen, B., Zhang, S. H., Liu, J. M., Hu, J. M., Liu, J., et al. (2010). Pre-Yanshanian geological events in the northern margin of the North China craton and the adjacent areas. *Geology of China, 37*, 900–915 (in Chinese with English abstract).

Zhao, G. C., & Zhai, M. G. (2013). Lithotectonic elements of Precambrian basement in the North China Craton: Review and tectonic implications. *Gondwana Research, 23*, 1207–1240.

Zhong, R., Sun, S., Chen, F., & Fu, Z. M. (1995). The discovery of rhyo-tuffite in the Taiyuan Formation and stratigraphic correlation of the Daqingshan and Datong coalfields. *Acta Geoscientia Sinica, 16*, 291–301 (in Chinese with English abstract).

Zhou, A., Jia, B., Ma, M., & Zhang, H. (2001). The whole sequences of volcanic event deposits on the north margin of the North China plate and their features. *Geological Review, 47*, 175–183 (in Chinese with English abstract).

Two-Stage Extensional Pattern in the North China–Mongolian Tract During Late Mesozoic: Insights from the Spatial and Temporal Distribution of Magmatic Domes and Metamorphic Core Complexes

19

Xiaohui Zhang and Lingling Yuan

Abstract

Differentiating magmatic doming and metamorphic core complex (MCC) remains critical for fully understanding the thermal, mechanical, and chemical evolution of continental landmasses under extension. This review summaries spatially overlapping but temporally distinct magmatic domes and MCCs across the north China–Mongolian tract during late Mesozoic. Typical dome instances are developed at the Daqinshan and Maanshan of southern Inner Mongolia, Yunmengshan and Western Hills of Beijing, Yiwulüshan of western Liaoning and Liaodong Peninsula during middle–late Jurassic to earliest Cretaceous, while well-documented Early Cretaceous MCCs include the Hohhot MCC, the Kalaqin MCC, the Yunmengshan MCC, the Yiwulüshan MCC, the Liaonan MCC and others. Besides building extensional doming, the constituent plutonic complexes in the domes tend to encapsulate multi-level crust–mantle interactions, whereas the MCC-style detachment faulting typically accommodates upper crustal architectural reorganization. They collectively constitute concomitant crustal-continuum expressions of Mesozoic decratonization in the North China Craton (NCC). Near-synchronization of two-stage extensional pattern in the north China–Mongolian tract accords well with gravitational collapse and convective removal of lithospheric mantle within an evolved post-collisional to within-plate extensional regime.

Keywords

Middle–late Jurassic • Early Cretaceous • Magmatic doming • Metamorphic core complex • Crust–mantle interaction • North China Craton

19.1 Introduction

Being a mosaic of ancient craton and juvenile orogen, the north China–Mongolia tract constitutes a prominent venue of architectural reconstruction and tectonic transformation during the Mesozoic era. With a distance of ~2500 km from the Mogul-Okhotsk suture to the Pacific margin and an areal extent of over 3,000,000 km^2 (Fig. 19.1), the tract has been widely acknowledged to form through progressive closure of the Paleo-Asian Ocean along the Solonker suture zone in the late Paleozoic to early Mesozoic (Davis et al. 2001; Xiao et al. 2003; Windley et al. 2007; Zhang et al. 2010b, 2012a, b; Meng et al. 2014). Following its establishment as a combined north China–Mongolian plate, the tract is home to an entire variety of intra-continental orogenic processes, with a concomitant of episodic magmatism (Zhang et al. 2014a and references therein), alternated pulses of contractional and extensional structures (Davis et al. 2001, 2009; Meng 2003), and multiple rift basins (Meng et al. 2003). The persistent interest into characterizing this vast decratonization scenario during the past two decades has culminated in a kaleidoscopic status quo concerning its

X. Zhang (✉) · L. Yuan
State Key Laboratory of Lithospheric Evolution, Institute of Geology and Geophysics, Chinese Academy of Sciences, Beijing, 100029, China
e-mail: zhangxh@mail.iggcas.ac.cn

M. Zhai et al. (eds.), *Main Tectonic Events and Metallogeny of the North China Craton*,
Springer Geology, DOI 10.1007/978-981-10-1064-4_19

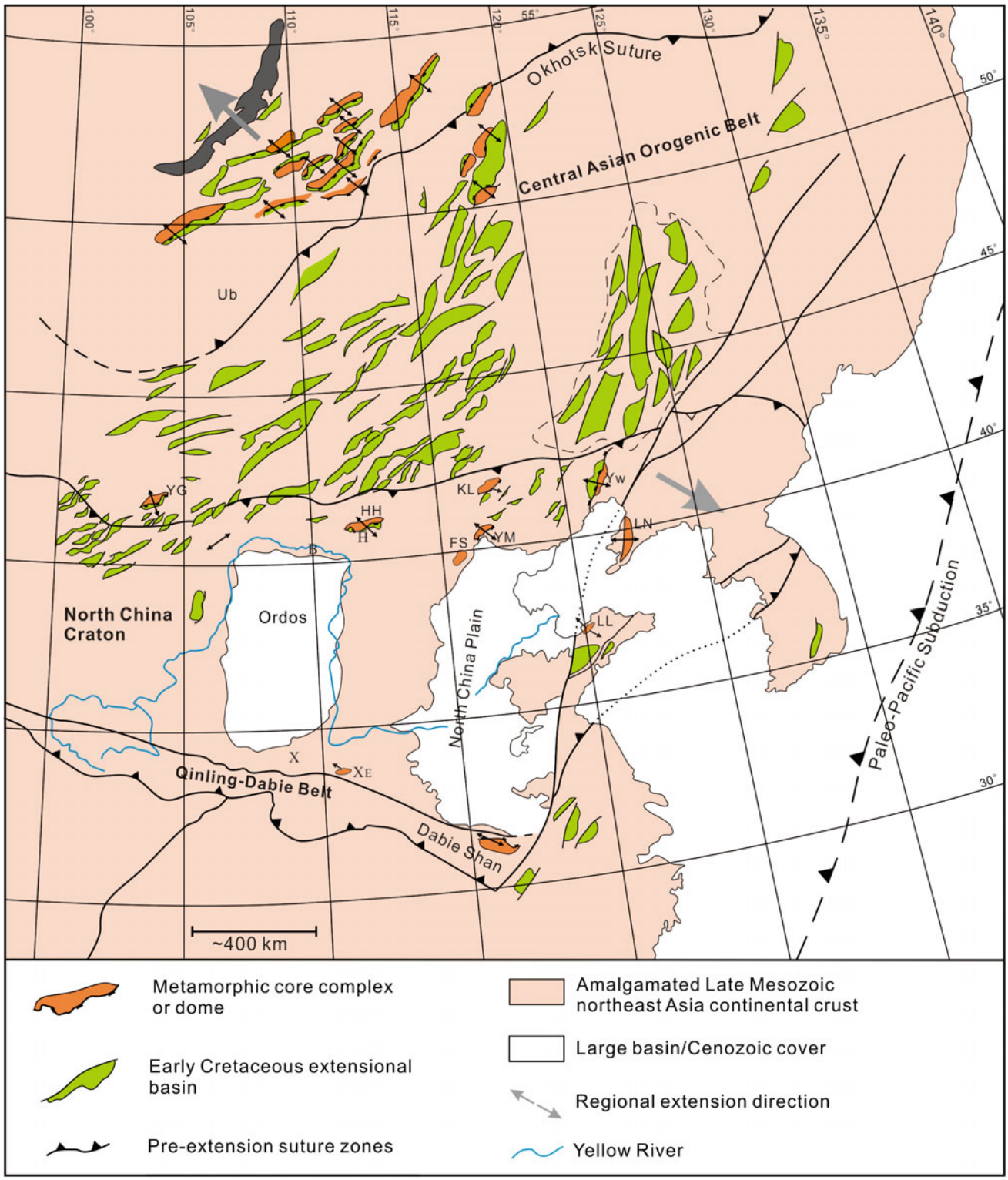

Fig. 19.1 Distribution map of magmatic domes and metamorphic core complexes in the north China–Mongolian tract (modified from Darby et al. 2004). MCC or dome code: *ED* Ereendavaa; *FS* Fangshan; *HH* Hohhot; *LN* Liaonan; *KL* Kalaqin; *UU* Ulan Ude; *YL* Yiwulüshan; *YG* Yagan; *YM* Yunmeng Shan; *ZA* Zagan

mechanism and geodynamic drivers. For the former, the controversy comes in a range of competing models including delamination (Gao et al. 2004, 2008; Wu et al. 2005a), thermomechanical erosion (Xu et al. 2004), replacement (Zheng et al. 2001, 2007) and transformation through melt–rock interaction (Zhang et al. 2003a; Zhang 2005). For the latter, the dispute hinges on the relative importance of the Mongol-Okhotsk collision (Meng 2003; Ritts et al. 2001; Wang et al. 2011, 2012) and the Paleo-Pacific subduction (e.g., Davis et al. 2001; Chen et al. 2004, 2009, 2013; Wu et al. 2005a; Zhu et al. 2012a, b).

As the first-order crustal-scale thermal-tectonic processes that develop during extension and exhumation of thickened and thermally mature crust (Whitney et al. 2004, 2013), metamorphic core complexes (MCC) and extensional magmatic domes have been widely documented in orogenic systems of various ages and tectonic settings (Teyssier and Whitney 2002; Whitney et al. 2004, 2013; Yin 2004). Typical Phanerozoic examples occur in the Himalaya, North American Cordillera, Alps, the Hercynian/Variscan belt in Europe, the Bering Sea region, the Appalachians as well as in the Greenland and Ireland Caledonides (Whitney et al. 2004, 2013). Their common spatial and temporal association indicates that they are genetically linked at some stage in their exhumation history. In the past three decades since the discovery of extensional detachment faults, the disproportionate number of studies on the mechanism of detachment faulting have obscured the difference between magmatic dome and MCC and thus overshadowed the thermal and mechanical significance of magmatic domes in orogeny (Whitney et al. 2004). However, they are distinct structures. The doming phase and the low-angle detachment faulting phase are not necessarily equivalent even in MCCs with footwalls entirely comprised of structural domes (Fayon et al. 2004). Clarifying this distinction is critical for obtaining a full picture of the thermal, mechanical, and chemical evolution of extended continental landmasses (Zhang et al. 2014b).

This is especially the case in the north China–Mongolia tract. The past two decades not only saw the recognition of a series of MCCs in areas from the Transbaikalia region (e.g., Zorin 1999; Donskaya et al. 2008; Daoudene et al. 2011) through the Sino-Mongolia border tract (Zheng et al. 1991; Zheng and Wang 2005; Webb et al. 1999) to the NCC (e.g., Davis and Zheng 1988; Davis et al. 1994, 1996, 2002; Davis and Darby 2010; Darby et al. 2001, 2004; Charles et al. 2011; Zhang et al. 2002a, b, 2003c, 2012a; Liu et al. 2005; Yang and Wu 2007; Wang et al. 2011, 2012; Lin et al. 2007, 2013a, b, 2014), but also witnessed the increasingly importance of magmatic domes (He et al. 2009; Wang et al. 2010a, b, 2012; Yan et al. 2010; Daoudene et al. 2012; Charles et al. 2011; Zhang et al. 2014b). In this review, we aim to outline the spatial and temporal distribution of magmatic domes and MCCs in the north China–Mongolia tract during the late Mesozoic. By synthesizing with regional geology, we strive to explore the importance of two-stage extensional pattern for realizing crustal architectural reorganization within the context of cratonic lithospheric thinning and decratonization.

19.2 Geological Background

The persistent effort into exploring the Precambrian odyssey of the NCC during the past two decades spawned a few competing models for its division and evolution (Zhai and Santosh 2011; Zhao et al. 2012 and references therein), with the most representative ones being the dual configuration of micro-blocks and greenstone belts and a scheme of threefold tectonic division. The former visualized the amalgamation of several ancient micro-blocks along greenstone belts during the Neoarchean and the subsequent cratonic rifting along three mobile zones during the late Paleoproterozoic (Zhai and Liu 2003; Zhai et al. 2005). The latter divided the NCC into the Eastern and Western Blocks and the intervening Trans-North China Orogen on the basis of their lithological, structural, metamorphic, and geochronologic differences (Zhao et al. 2001). Further modifications outlined two subordinate collisional belts in the Western and Eastern Blocks, respectively, the Khondalite Belt and the Jiao-Liao-Ji Belt (Zhao et al. 2005). Of additional note is another version of tectonic subdivision that advocated the amalgamation of the NCC in the late Archean (ca. 2.5 Ga) and separated the western block into a southern terrane and a northern Inner Mongolia–Northern Hebei Orogen of late Paleoproterozoic age (Kusky and Li 2003; Kusky et al. 2007).

The east-west trending Central Asian Orogenic Belt (CAOB) lies to the north of the NCC and represents a huge accretionary orogen, and includes micro-continents, island arcs, oceanic islands, accretionary wedges, seamounts and ophiolitic complexes (Xiao et al. 2003; Windley et al. 2007). Along its eastern segment is the north China–Mongolia tract, with the Solonker suture zone being the most prominent tectonic feature (Xiao et al. 2003; Jian et al. 2010), marking the final closure of the Paleo-Asian Ocean between the NCC and the southern Mongolia terranes and in turn establishing the combined north China–Mongolian plate (Davis et al. 2001; Zhang et al. 2009a, b, 2010b, 2012b, c).

Extending from southern Inner Mongolia through the Beijing Municipality and Hebei Province to northern and western Liaoning Province, the northern NCC is tectonically equivalent to the Yinshan–Yanshan orogenic belt (Davis et al. 2001) (Fig. 19.1). It was a convergent plate margin during the Paleozoic and witnessed episodic magmatic activities, including Devonian alkali intrusions (Zhang et al. 2010b), Carboniferous calc-alkaline intrusions (Zhang et al.

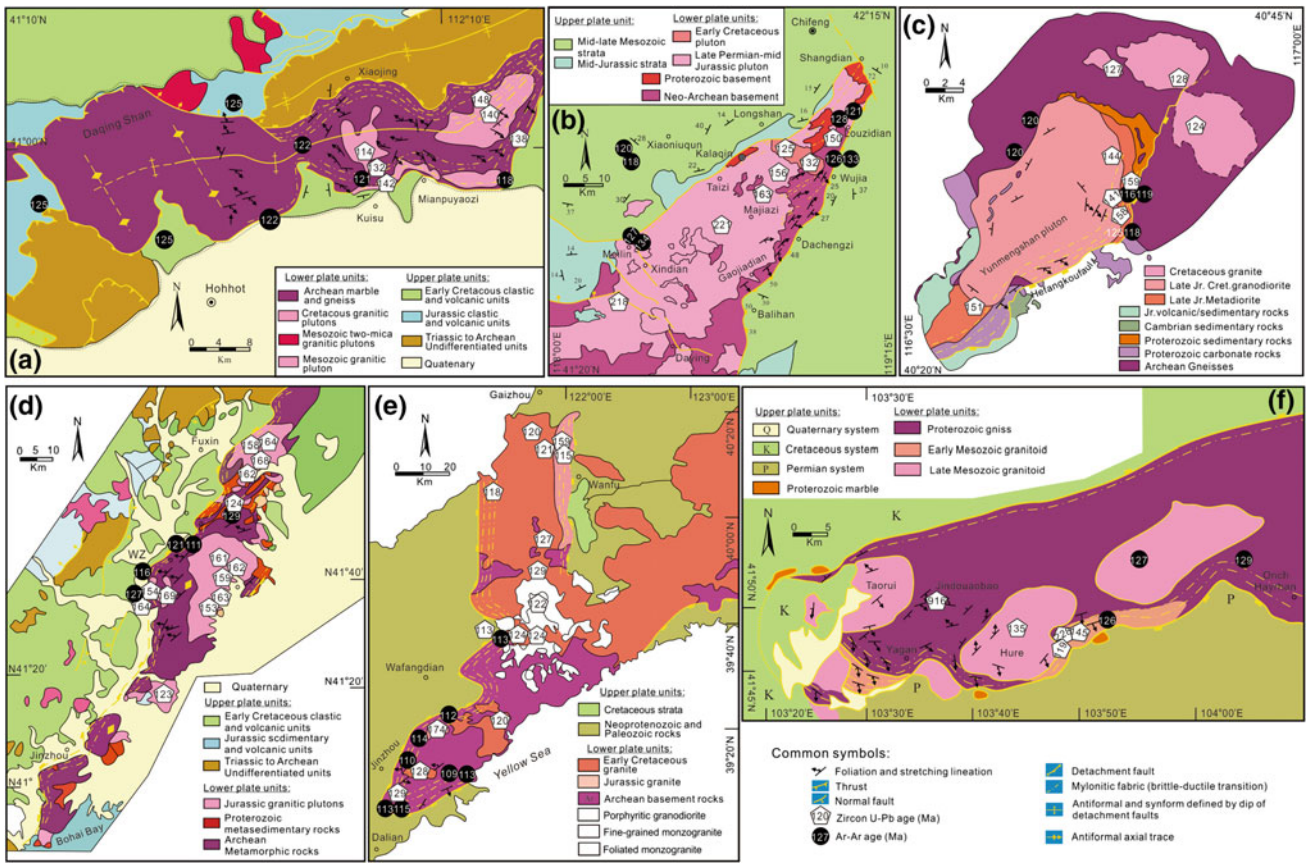

Fig. 19.2 Simplified maps of the representative magmatic domes and metamorphic core complexes in the north China–Mongolian tract. **a** Hohhot dome and MCC (modified from Davis et al. 2002; Wang et al. 2002a, b); **b** Kalaqin dome and MCC (Wang et al. 2004a, b); **c** Yunmengshan dome and MCC (Davis et al. 1996; Zheng et al. 1988); **d** Yiwulüshan dome and MCC (Darby et al. 2004); **e** Liaonan MCC (Liu et al. 2005; Yang and Wu 2007; Lin et al. 2008; Wang et al. 2012); **f** Yagan MCC (Webb et al. 1999; Wang et al. 2004a, b). See the text for the sources of ages

2009a) and appinitic suites with ages ranging from 325 to 300 Ma (Zhang et al. 2012d), Early Permian mafic-ultramafic complexes and high-K calc-alkaline granitoids (Zhang et al. 2009b, 2011), and Late Permian to Early Triassic calc-alkaline to alkaline intrusions with ages from 254 to 237 Ma (Zhang et al. 2009a, 2010b). The Early Mesozoic saw the establishment of a post-orogenic extensional regime in the region subsequent to the final closure of the Paleo-Asian Ocean (Zhang et al. 2009a, 2014a; Meng et al. 2014), with the occurrence of numerous Middle to Late Triassic mafic-ultramafic complexes (Niu et al. 2012) and ferroan intrusions (Yang et al. 2008; Zhang et al. 2012c). Following this period of extension there were multiple intra-continental tectono-magmatic events, with the alternated pulses of contractional and extensional structures during Jurassic to early Cretaceous (Zhao 1990; Davis et al. 2001, 2009; Zhao et al. 2004; Zhang et al. 2014b).

19.3 Mid–late Jurassic-earliest Cretaceous Magmatic Domes

19.3.1 The Hohhot Magmatic Dome

The Daqinshan of southern Inner Mongolia occupies the eastern segment of the Yinshan belt and presents the westernmost venue for hosting Late Mesozoic intrusions along the northern NCC (Fig. 19.2a). As represented by the Shenshuiliang, Kuisu and Hutoushan intrusions (Davis and Darby 2010; Guo et al. 2012a), these roughly E–W trending plutonic complexes feature an outcrop of over 100 km^2 and mainly consist of granodioritic to monzogranitic rocks with abundant dioritic enclaves. According to recent zircon U-Pb dating (Guo et al. 2012a, b; Wang et al. 2012), they can largely be grouped into two episodes: those with ages from 148 to 138 Ma and those of 132–120 Ma (Fig. 19.3a).

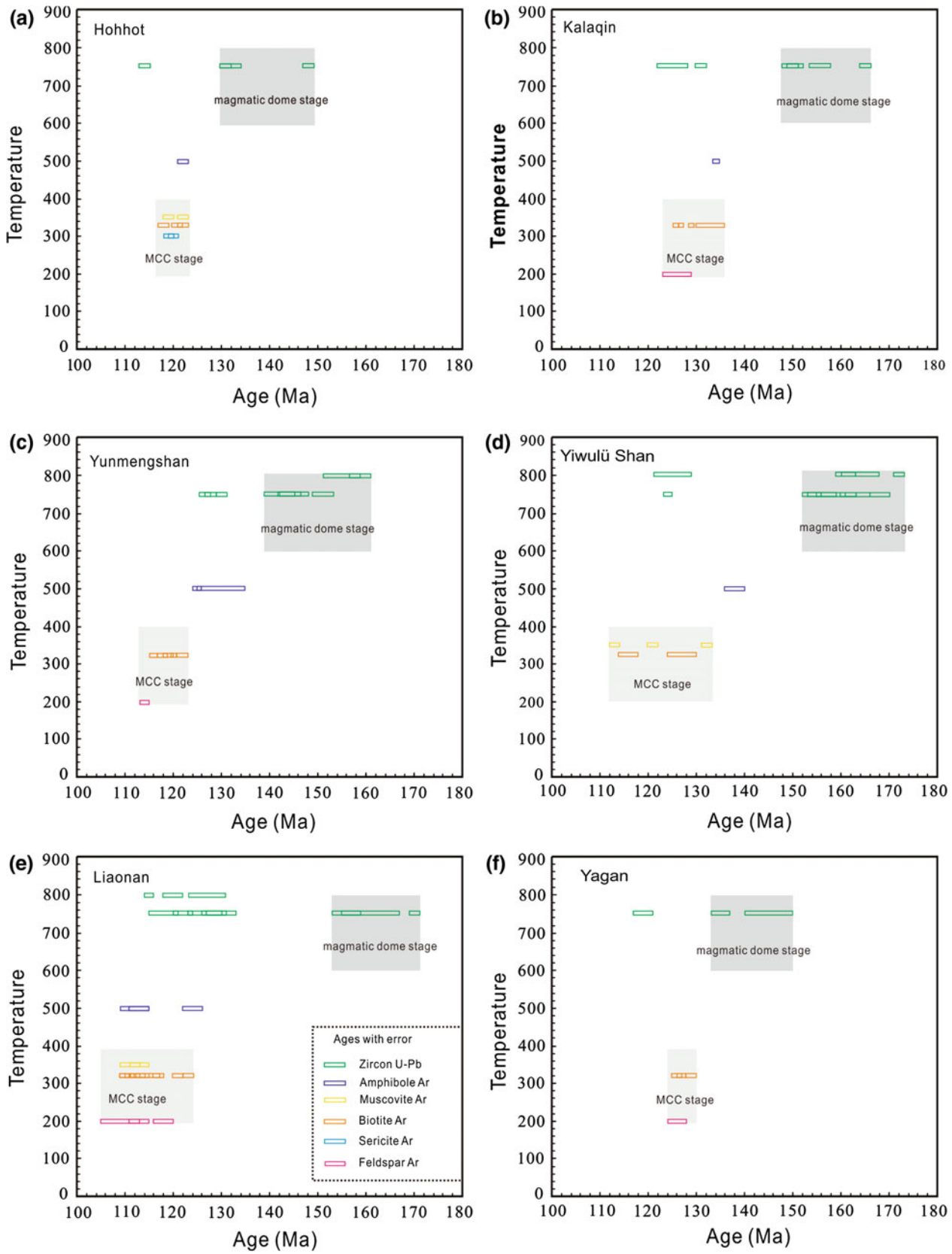

Fig. 19.3 Zircon U-Pb and mineral Ar–Ar age distribution in the representative magmatic domes and MCCs in the north China–Mongolian tract. See the text for the sources of ages

Two episodes of intrusions tend to exhibit contrasting structural features (Davis and Darby 2010; Guo et al. 2012a). The earlier intrusions suffered from various degrees of ductile deformation, whereas the later ones were largely exempt from any such imprints. For example, the 148 Ma Shenshuiliang pluton is strongly mylonitized. Mylonitic foliations, as defined by well-developed S/C fabrics of ribbon-like quartz grains and stretching lineations, dip towards NW–NE at 8–21° with consistent lineation plunging NWW at 6–18° along the northern margin, indicating a top-to-SE shearing (Davis and Darby 2010; Guo et al. 2012a). In the southern part, the foliations dip towards S–SE at angles of 15–30° with lineations plunging SEE at angles of 11–28°, with typical S-C-C′ foliations indicative of a top-to-SE sense of shear. For the Kuisu granodiorite at 142 Ma, its fabrics are characterized by the alignment of quartz and feldspar crystals, displaying no strong recrystallized minerals and hence reflecting high-temperature solid flow (Paterson et al. 1998). Mostly remarkable is the occurrence of numerous elliptical dioritic enclaves in both plutons (Guo et al. 2012a). Their alignment along the lineation of the hosts attests to their diapiric emplacement under an extensional regime (Paterson and Vernon 1995; Tobisch and Williams 1998). Based on the analysis on mineral microstructures and quartz [c] crystallographic axis fabrics (Guo et al. 2012a), the deformation temperatures have been estimated as ranging from 500 to 650 °C.

In terms of geochemical character, the earlier granitoids display high Sr and LREE (light rare earth element), low Y and Yb contents, high Sr/Y and La/Yb ratios (Guo et al. 2012b). They also possess moderately enriched isotopic compositions with initial $^{87}Sr/^{86}Sr$ ratios from 0.7064 to 0.7071, $\varepsilon_{Nd}(t)$ from −11.3 to −15.8, and zircon $\varepsilon_{Hf}(t)$ from −5.3 to −22.8 (Guo et al. 2012b). These features indicate that the rocks were derived from partial melting of mixed protoliths including thickened mafic lower crust and minor juvenile materials (Guo et al. 2012b). By contrast, the later granitoids show an A-type geochemical affinity, with low Sr, high Y, and Yb contents as well as negative Eu anomalies. They exhibit more evolved initial $^{87}Sr/^{86}Sr$ ratios of 0.7098–0.7161, unradiogenic $\varepsilon_{Nd}(t)$ from −12.5 to −15.4 and zircon $\varepsilon_{Hf}(t)$ from −7.6 to −15.2 (Guo et al. 2012b). They probably represent the partial melts of mixed crustal protoliths at shallow depth.

19.3.2 The Kalaqin Magmatic Dome

The Maanshan uplift stands out as a NNE-trending dome over a length of ca. 150 km and a width of ca. 50 km on the northern tip of the NCC (Fig. 19.2b). It is home to multiple Paleozoic to Mesozoic intrusive complexes collectively known as the Kalaqin batholith. Recent intensive zircon U-Pb dating resolved the batholith into distinct constituents of four episodes (Wang et al. 2010a, b, 2012; Lin et al. 2014). Apart from a few Carboniferous-Permian and Triassic constituents, the majority of the batholith seem to have formed during Late Jurassic to Early Cretaceous, with the Maanshan and Chaoyanggou plutons intruded from 156 to 150 Ma (Wang et al. 2010a, b, 2012; Lin et al. 2014). Featuring a dominant lithology of biotite monzogranite, these plutons bear a pervasive ductile deformation with a top-to-NE shear sense (Shao et al. 2001; Lin et al. 2014). The foliation is defined by the oriented quartz, feldspar and biotite, suggesting high-temperature (550–600 °C) solid deformation (Lin et al. 2014). Given the concentration of these deformational imprints in the Late Jurassic plutons but without trace in the Early Cretaceous ones, this episode of extensional deformation can be limited to Late Jurassic (Wang et al. 2012; Lin et al. 2014).

Regarding their geochemical affinity, these Late Jurassic granites can be classified as high-K calc-alkaline I-type, and exhibit adakite-like elemental signatures with high contents of Al_2O_3 and Sr, low contents of Y and Yb, high Sr/Y and La_N/Yb_N ratios, and depletions in high field strength elements (HFSE). They possess moderately negative zircon $\varepsilon_{Hf}(t)$ values (−14.9 to −5.6) and T_{DM2} ages of 1.5–2.1 Ga (Wang et al. 2010a, b). These elemental and isotopic characters are largely consistent with the partial melts of a thickened mafic lower crust (Wang et al. 2010a, b; Lin et al. 2014). The related coeval volcanic rocks are mainly composed of andesite, basaltic andesite, trachyandesite with minor rhyolite and rhyolitic tuff (Lin et al. 2015). With a high-K calc-alkaline composition and adakite-like geochemical signature, these volcanic rocks have been considered to be derived from partial melting of a heterogeneous, enriched lithospheric mantle (Guo et al. 2007).

19.3.3 The Yunmengshan Dome

The Yunmengshan is located in the eastern Yanshan belt and 65–110 km NNE of Beijing (Davis and Zheng 1988; Davis et al. 1994, 1996). Prior to its recognition as a Cordilleran-type MCC (Davis et al. 1994, 1996), the Yunmengshan has long been regarded as a magmatic dome (Zheng et al. 1988; Xu et al. 1994; Zhang et al. 1997). The next score of years saw the disproportionate number of studies on the Early Cretaceous detachment faulting in the model of classic MCC and thus overshadowed the thermal and mechanical significance of dome formation in the range. However, recent identification of dominant middle–late Jurassic magmatic rocks in the range revitalized the dome-style mid-lower crustal extension (Wang et al. 2012).

The Yunmengshan magmatic complex comprises more than ten plutons (Ji et al. 2004), with a total outcrop of over

300 km^2 (Fig. 19.2c). Most plutons have an emplacement age of late Jurassic to earliest Cretaceous (Fig. 19.3c), i.e., the Shicheng diorite at 159–156 Ma (Deng et al. 2004), the Changyuan diorite at 153–151 Ma (Davis et al. 1996; Deng et al. 2004), the Yunmengshan monzogranite at 155–141 Ma (Davis et al. 1996; Liu et al. 2004; Deng et al. 2004; Shi et al. 2009; Wang et al. 2012), the Shatuozi monzogranite at ca. 151 Ma and the Wudaohu granodiorite at ca. 141 Ma (Davis et al. 1996).

These plutons exhibit variable ductile deformation and metamorphic recrystallization (Davis et al. 1996). More specifically, two generations of foliation have been identified in the Shicheng diorite and Yunmengshan batholith (Wang et al. 2012). While the central parts of the batholith display predominantly magmatic textures and shallow-dipping magmatic foliations, the later mylonitic fabrics are well-developed in the margin (Davis et al. 1996; Wang et al. 2012). The magmatic foliation is characterized by steeply dipped magmatic lineation of plagioclase and aligned mafic enclaves with a small amount of primary strain (Tobisch and Williams 1998), suggesting high-temperature (>550 °C) solid flow (Paterson et al. 1998) and diapiric emplacement under an extensional regime (Paterson and Vernon 1995).

In terms of geochemical character, the Shicheng diorites are magnesian, calc-alkaline and metaluminous (Zhao and Wang 2014). They show high Sr and LREE, low Y and Yb contents and high Sr/Y and La/Yb ratios, with initial $^{87}Sr/^{86}Sr$ ratio of 0.7048, $\varepsilon_{Nd}(t)$ of −16.9 and T_{DM2} age of 2.12 Ga (Deng et al. 2004). These features suggest that they might form through simultaneous fractional crystallization and lower crustal assimilation of metasomatized lithopheric mantle-derived basaltic magmas (Zhao and Wang 2014). The Yunmengshan granites are calc-alkaline in composition and exhibit adakite-like geochemical signatures with high contents of Al_2O_3, Na_2O and Sr, low contents of Y and Yb, high Sr/Y and La_N/Yb_N ratios, depletions of HFSE (e.g., Nb, Ta, Zr, Hf), moderate initial $^{87}Sr/^{86}Sr$ of 0.7055 and negative $\varepsilon_{Nd}(t)$ of −17.2. These features are consistent with a derivation from the partial melting of a thickened mafic lower crust (Davis 2003; Zhao and Wang 2014).

19.3.4 The Yiwulüshan Dome

With a NNE–SSW-oriented long axis extending between the cities of Fuxin to Beizhen in western Liaoning (Fig. 19.1), the Yiwulüshan range is home to voluminous Mesozoic plutonic complexes covering an area of over 500 km^2 (Fig. 19.2d). They comprise two main batholiths: the Lüshan batholith (LB) in the south and the Haitangshan batholith (HB) in the north (Fig. 19.2d). The LB crops out in the core of the range as a north-northeast elongate dome near Beizhen. The batholith comprises weakly gneissic to homogeneous monzogranite, with minor granodiorite and garnet-bearing leucogranite (Zhang et al. 2008, 2014). The HB is located about 10 km east of Fuxin and consists of dominant granodioritic to granitic plutons of varying size with abundant mafic microgranular enclaves (MME), and subordinate gabbroic to dioritic stocks and dykes (Zhang et al. 2014b). Based on the difference in texture and mineral composition, the 1:50,000 regional geological mapping (LBGMR 1998) divided the batholith into five units: fine- to medium-grained hornblende gabbro and diorite of the Yaoyamen unit, fine- to medium grained phenocryst-bearing granodiorite of the Lamadong unit, fine- to medium-grained megacryst-bearing monzogranite of the Dabagou unit, fine- to medium-grained biotite monzogranite of the Shanyuegou unit and fine- to medium-grained porphyritic monzogranite of the Maotouling unit. Systematic zircon U-Pb dating established an emplacement time of Middle to Late Jurassic for the plutonic complexes in the Yiwulüshan range (Wu et al. 2006; Zhang et al. 2008, 2010d, 2012a, 2014b).

The central parts of two plutonic complexes contain magmatic fabrics indicative of their diapiric emplacement under an extensional regime (Paterson and Vernon 1995), like steeply dipped magmatic lineation of plagioclase (LBGMR 1998; Zhang et al. 2012a; Li et al. 2012, 2013) and aligned mafic enclaves with a small amount of primary strain (John and Blundy 1993; Tobisch and Williams 1998). The margin of both batholiths is foliated with solid-state fabrics parallel to those of the nearby ductile shear zone. A stretching lineation defined by elongated quartz grains predominantly plunges shallowly NNE. Shear sense indicators of outcrop- and microscopic scales all suggest top-to-SSW sense of shear (LBGMR 1998; Zhang et al. 2012a, 2014b; Li et al. 2012).

From a geochemical perspective, a subduction-related metasomatized lithospheric mantle source is fingerprinted by the gabbroic to dioritic rocks with enriched large ion lithophile elements, depleted HFSE and heterogeneous isotopic compositions ($^{87}Sr/^{86}Sr_i$ = 0.70541 to 0.70577, $\varepsilon_{Nd}(t)$ = −1.78 to −5.54 and zircon $\varepsilon_{Hf}(t)$ = −6.0 to 8.1). One felsic magma end-member of ancient mafic lower crustal parentage is discernable from adakitic granites with high Sr/Y and evolved isotopic composition ($^{87}Sr/^{86}Sr_i$ = 0.70533 to 0.70792, $\varepsilon_{Nd}(t)$ = −18.8 to −21.7, zircon $\varepsilon_{Hf}(t)$ = −18.5 to −28.8), whereas another felsic magma end-member of newly underplated crustal heritage manifests itself from some monzogranites with non-adakitic elemental affinity and juvenile isotopic composition ($^{87}Sr/^{86}Sr_i$ = 0.70429 to 0.70587, $\varepsilon_{Nd}(t)$ = −4.47 to −5.87, zircon $\varepsilon_{Hf}(t)$ = 4.3 to 1.3). Hybridization processes between mantle-derived mafic magma and ancient crustal-derived felsic magma result in the formation of MME-bearing granodiorites with intermediate isotopic signatures ($^{87}Sr/^{86}Sr_i$ = 0.70491 to 0.70499, $\varepsilon_{Nd}(t)$ = −15.3 to −15.8, zircon $\varepsilon_{Hf}(t)$ = −12.7 to −17.4);

Subsequent fractional crystallization of the hybridized magmas endows the differentiated monzogranites with low Sr/Y and highly evolved isotopes ($^{87}Sr/^{86}Sr_i$ = 0.70496 to 0.70605, $\varepsilon_{Nd}(t)$ = −16.0 to −18.7, zircon $\varepsilon_{Hf}(t)$ = −14.3 to −21.5).

Synthesizing these manifold mafic and felsic magma end-members, the hybridization process as recorded by the host-MME pairs and sustained heat engine of basaltic underplating as witnessed by Middle Jurassic to Early Cretaceous mantle-derived mafic magmas (Zhang et al. 2010d), A multi-stage petrogenetic scenario can be visualized for building the magmatic dome in the Yiwulüshan range (Zhang et al. 2014b).

Echoing the experimental work of Hallot et al. (1994), the mafic magma sequence from the earliest stock through the intermediate MMEs to the youngest mafic dykes with chilled margins (Zhang et al. 2010d) signifies a progressive response of mantle-derived basaltic magma to the evolving viscosity contrast of the interacting magmas from magma reservoirs during the crystallization history of the plutonic complex. Possibly responding to some geodynamic trigger and attendant asthenospheric upwelling, subduction-related metasomatized lithospheric mantle melted to produce basaltic magmas and establish magma chambers at the mantle–crust interface. It is there that they experienced fractional crystallization forming gabbro and diorite, with crystal accumulation building newly underplated lower crust. In addition, they provided continued magma underplating that resulted in widespread crustal melting, with abundant felsic magmas extracted at different crustal levels. On one hand, dehydration melting reactions by hydrous mineral breakdown in ancient mafic lower crust could produce voluminous adakitic felsic rocks like the LB granites. On the other hand, melts from newly underplated crustal materials ascended along preexisting structures to the current level of emplacement to form granites with indistinguishable isotopic compositions from the mafic rocks, such as the granites in the Dabagou unit. With further injection of evolved mafic magma into a similar low-viscosity, melt-rich granitic mass, more complete magma mixing ensued and produced homogeneously hybridized granodiorite of the Lamadong unit. Later injections into more fully crystallized hybrid rocks generated spheroidal MME, and hybridized magma evolved through further assimilation and fractional crystallization to form the Shanyuegou monzogranites. Finally, injection into almost totally crystallized magma bodies, where the viscosity contrast was very high, resulted in dykes with sharp contacts and chilled margins.

19.3.5 Other Magmatic Domes

Standing at the junction of the E-W-trending Yanshan and the NNE-trending Taihang Mountain ranges, the Western Hills of Beijing presents an archetypal snapshot of the tectonic evolution of the northern NCC (Wang et al. 2010a, b), with the most prominent feature being the Fangshan pluton. It includes variable intrusive phases from diorite and granodiorite to granite, with abundant MMEs. Their zircon U-Pb ages range from 136 to 128 Ma (Davis et al. 2001; Wang et al. 2010a, b; Yan et al. 2010; Sun et al. 2010). The pluton exhibits magmatic foliations and lineations progressing in intensity from center to margin (He et al. 2009; Yan et al. 2010). The foliations are mainly defined by the alignment of hornblende, biotite, tabular feldspar and elongated enclaves (He et al. 2009). Although asymmetric solid-state deformational fabrics have been superimposed in some parts, various primary kinematic indicators including concentric foliations, radial and steep lineations, high-temperature shear aureole and a rim syncline around the pluton argue for a magmatic diapir for the Fangshan pluton (He et al. 2009; Yan et al. 2010). Regarding their geochemical characteristics, both granodiorites and granites exhibit adakitic trace elemental affinity (Yan et al. 2010), initial $^{87}Sr/^{86}Sr$ ratios of 0.7052–0.7058 for apatite, negative $\varepsilon_{Nd}(t)$ values of −19.7 to −14.0 for titanite and apatite, and negative $\varepsilon_{Hf}(t)$ values of −25.1 to −18.2 and $\delta^{18}O$ values of 6.2–8.3 ‰ for zircon (Sun et al. 2010). These features fingerprint a dominant ancient lower crustal source (Sun et al. 2010). Meanwhile, the enclaves have relatively high MgO contents at intermediate silica content, with strongly negative $\varepsilon_{Hf}(t)$ values of −22.9 to −14.9 and $\delta^{18}O$ values of 4.8–8.2 ‰ for zircon, $\varepsilon_{Nd}(t)$ values of −17.6 to −12.1 for titanite and apatite and relatively narrow initial $^{87}Sr/^{86}Sr$ ratios of 0.7051–0.7058 for apatite. These features clearly pinpoint to an enriched and/or depleted mantle source (Sun et al. 2010).

Situated along the eastern part of the NCC, the Liaodong Peninsula hosts voluminous Jurassic plutonic complexes including quartz diorite, tonalite, granodiorite and monzogranite (Wu et al. 2005b) (Fig. 19.2e). With an emplacement time spanning from ca. 180 to 156 Ma (Wu et al. 2005b), some of these complexes have been highly deformed and constituted a dome-style structure (Lin et al. 2011). Two typical examples are the Jinzhou dome composed of ca. 173 Ma Xiaoheishan diorite-granodiorite and the Laohushan dome centered on the Heigou batholith with ages of 173–161 Ma (Wu et al. 2005b; Lin et al. 2011). Petrographical and geochemical tracing revealed two magma end-members

(Wu et al. 2005b). The granodioritic rocks, with their lower initial $^{87}Sr/^{86}Sr$ and higher $\varepsilon_{Nd}(t)$ values than those of the monzogranitic rocks, represent the partial melts of newly underplated mafic lower crust, whereas the monzogranitic rocks were derived from partial melting of ancient lower crustal materials.

Located in the Jiaodong Peninsula, the Linglong massif is NNE–SSW oriented with an elongated shape of 60 by 30 km (Charles et al. 2011). The massif is home to voluminous migmatitic and granitic rocks. Featuring a dominant lithology of medium-grained monzogranites with various trace minerals like garnet, amphibole and muscovite (Hou et al. 2007; Jiang et al. 2012), the Linglong granitic suite has been dated as forming during 160–150 Ma (Wang et al. 1998; Hou et al. 2007; Zhang et al. 2010a; Charles et al. 2011). At outcrop-scale, granitic rocks display isotropic to weakly oriented fabrics. Foliation is well-marked by a general flattening and often underlined by biotites flakes, trending roughly parallel to the eastern and southern borders of massif and dipping to the east (Charles et al. 2011). By contrast, mineral and stretching lineations, defined by biotite and quartz aggregates, reveal consistent N120–140E trend throughout the massif. The general attitude of the foliation planes and its internal strain gradient indicate that the massif is consistent with a dome-like structure (Charles et al. 2011). In terms of geochemical character, the Linglong suite is metaluminous to slightly peraluminous and exhibits an adakitic affinity, with high La/Yb and Sr/Y ratios, enrichment in LILE and depletion in HFSE (Hou et al. 2007; Zhang et al. 2010a). The rocks show uniform bulk-rock isotopic compositions with initial $^{87}Sr/^{86}Sr$ ratios of 0.7119–0.7126 and $\varepsilon_{Nd}(t)$ of −21.3 to −21.6 (Hou et al. 2007). Detailed petrological and geochemical data confirmed the dominance of a thickened lower crust in forming the suite (Hou et al. 2007; Jiang et al. 2012).

Lying in the central part of eastern Mongolia about 270 km SE of Ulaanbaatar, the Nartyn massif is an elongate NE–SW trending granitic intrusion extending over an area of 30 by 10 km (Daoudene et al. 2011). In most places, a macroscopic flat-lying fabric characterizes the core of the intrusion (Daoudene et al. 2012), with euhedral feldspar phenocrysts forming local irregular accumulations and imbrications and suggesting grain rotation and tiling in a viscous fluid (Paterson et al. 1998). The margins of the granite exhibit solid-state deformation marked by a foliation gently dipping away from the core. While well-developed foliations along the northwestern margin bear a NW–SE directed stretching lineation, discrete shear bands attesting to top-to-the-NW motions are observed along the northern margin (Daoudene et al. 2012). Deformation is associated with extensive grain size reduction. Quartz and feldspar display undulatory extinctions. K-feldspar shows evidence of extensive dynamic recrystallization with fine-grained mantles surrounding remnants of old large grains. Core-and-mantle structures and myrmekite around K-feldspar phenocrysts are more frequent along the south-eastern edge of the intrusion. Chessboard-type structures may be observed within quartz grains. All these lines of evidence attest to the deformation under sub-solidus thermal conditions higher than 600 °C (Daoudene et al. 2012). These magmatic rocks have been dated at 152–138 Ma (Daoudene et al. 2011, 2012; Wang et al. 2012).

The Yagan region straddles the southernmost end of the Sino-Mongolian border (Fig. 19.1) and hosts tremendous Mesozoic granitoids (Fig. 19.2g). Systematic zircon U-Pb dating indicates that they were emplaced in late Triassic and late Jurassic earliest Cretaceous times, with two large elliptical plutons yielding ages from 145 to 135 Ma (Wang et al. 2004a, b, 2012). Featuring an enclave-bearing granodiorite and monzogranite, these plutons show strong magmatic foliation on the margin but weak or no strain in the center, with the foliation defined by aligned mafic enclaves, schlieren layering as well as orientated mineral aggregates (Wang et al. 2002a, b). Such strain pattern testified to the forceful magmatic emplacement in an extensional dome setting (Paterson and Fowler 1993; Wang et al. 2004a, b). Geochemically speaking, these granites are high-K calc-alkaline (Wang et al. 2004a, b), exhibit trace element characteristics of A-type granite and posses highly variable initial $^{87}Sr/^{86}Sr$ from 0.705 to 0.713 and modest positive $\varepsilon_{Nd}(t)$ values from 0 to +0.5. These features, plus the prevalent occurrence of dioritic enclaves, suggest that their parental magma might originate from partial melting of mixed protoliths composed of juvenile basaltic underplates and ancient crustal materials (Wang et al. 2004a, b).

19.4 Early Cretaceous Metamorphic Core Complexes

19.4.1 The Hohhot MCC

The Hohhot MCC of the Daqing Shan of central Inner Mongolia is among the best exposed and most spectacular of the spatially isolated MCCs that developed along the northern NCC (Davis and Darby 2010) (Fig. 19.2a). The credit for its first recognition goes to Zhu Shenyu of the Nei Mongol Bureau of Geology and Mineral Resources (Davis and Darby 2010) but its establishment as a Cordilleran-style MCC has benefited from ensuing anatomical studies of Darby et al. (2001), Wang et al. (2002a, b, 2011), Davis et al. (2002) and Davis and Darby (2010). The hallmark structure is a single master detachment fault, named the Hohhot detachment fault (Davis et al. 2002). This south-rooting low-angle normal fault has an E-W strike in excess of 100 km and a capricious geometry from

well-exposed planar to highly corrugated (Fig. 19.2a) (Davis et al. 2002; Davis and Darby 2010). At the central exposures, the fault separates the footwall of Archean and Proterozoic gneisses and schists, Paleozoic and Jurassic meta-sedimentary rocks and pre- and synkinematic Cretaceous granitic plutons from the hanging wall of non-metamorphosed pre-Jurassic rocks and Jurassic Early Cretaceous sedimentary-volcanic strata (Davis and Darby 2010). The fault-related mylonitic rocks have a thickness of over 3–4 km and contain, in order of increasing structural depth, microbreccias, chloritized and brecciaed rocks, as well as mylonitic meta-sedimentary and meta-igneous rocks (Davis et al. 2002; Wang et al. 2002a, b; Davis and Darby 2010). The well-developed foliations dip southwards at 15° with a lineation plunging SE at 10–30°. Abundant kinematic indicators in the mylonitic sequence demonstrate consistent top-to-the-SE sense of shear (Davis and Darby 2010). The kinematic vorticity analysis based on quartz c-axis fabrics, finite-strain measurements and the Polar Mohr diagram method yielded an average vorticity number from 0.82 to 1.00 for the major mylonitic stage, while using the extensional crenulation cleavage method led to a kinematic vorticity number from 0.73 to 0.81 for the late stage shearing (Zheng et al. 2009; Wang et al. 2011). Petrographically, the widespread ductile deformation of quartz and the brittle deformation of feldspar in the mylonites indicate that mylonitization occurred under greenschist facies condition at temperatures of 300–350 °C (Davis et al. 2002; Davis and Darby 2010).

Based on the sanidine $^{40}Ar/^{39}Ar$ ages of 125–126 Ma from the Cretaceous silicic volcanic rocks in the supradetachment basins and the hornblende/biotite/muscovite $^{40}Ar/^{39}Ar$ ages of 122–119 Ma from the lower-plate mylonitic gneisses (Fig. 19.3a), plus the preserved structural and stratigraphic field relationships (Ritts et al. 2009), the lifetime of the Hohhot MCC can be constrained to be around 122–121 Ma (Davis et al. 2002; Davis and Darby 2010; Wang et al. 2011).

19.4.2 The Kalaqin MCC

The embryonic idea of the Kalaqin MCC can trace back to 1990s with the pioneering study of Wang et al. (1994) on the Louzidian-Dachengzi detachment fault. Following this are the structural description works of Han et al. (2001) and Shao et al. (2001) and the geochronological works of Zhang et al. (2002a, 2003b). The past decade saw the intensive investigation into its extricate infrastructure and refined tectonic evolution (Wang et al. 2004a, b, 2011, 2012; Wang and Zheng 2005; Lin et al. 2014). This led to the clarification of a MCC-style architecture in the Maanshan (Fig. 19.2b). Its core consists of epidote- amphibolite facies Archean gneisses, low greenschist facies Proterozoic schists and marbles, Cambrian carbonates, Permian-Jurassic plutonic rocks and early Cretaceous granites (Han et al. 2001; Zhang et al. 2003b; Wang et al. 2001, 2011). The hanging wall on the eastern and western flanks contains Jurassic-Cretaceous terrestrial volcanic-sedimentary sequences and their basement non-mylonitic gneisses in the Pingzhuang basin (Han et al. 2001). The Cretaceous sedimentary rocks on the SE side show the features of supradetachment basins (Wang et al. 2004a, b). The Louzidian master detachment fault extends for over 100 km along the southeastern boundary of the MCC (Han et al. 2001; Zhang et al. 2002b, 2003b). The fault strikes NNE and dips east- southeastward (110–130°) at angles of 20–40°. It is overlain by an up to 20 m layer of clay-rich gouge. Although there exist some kinematic markers like symmetric porphyroclasts and S-C fabrics suggestive of a sinistral shear sense (Zhang et al. 2002b, 2003b; Wang et al. 2004a, b), a set of persistent SE-plunging striae, perpendicular tension cracks on the fault surface and S-C-like fabrics in the gouge all indicate a dip-slip, normal faulting displacement (Han et al. 2001; Shao et al. 2001; Wang et al. 2011). Directly below the fault is a chloritic breccia and microbreccia zone of ca. 10–200 m thickness (Wang et al. 1994; Han et al. 2001; Zhang et al. 2002b). Kinematic vorticity analysis shows that the Louzidian detachment fault experienced a transition from an earlier simple shear to later pure shear (Wang et al. 2011).

Petrographically, the widespread ductile deformation of quartz and the brittle deformation of feldspar in the mylonites from the Louzidian fault zone indicate that mylonitization occurred under greenschist facies condition at temperatures of about 350–400 °C (Zhang et al. 2002b, 2003b). A series of minerals including hornblende, biotite and K-feldspar from the representative rocks in the fault yielded narrow $^{40}Ar/^{39}Ar$ plateau ages from 134 to 126 Ma (Zhang et al. 2002b, 2003b; Wang and Zheng 2005) (Fig. 19.3b). This confirmed the formation of the Kalaqin MCC during Early Cretaceous time.

19.4.3 The Yunmengshan MCC

The first recognition of Yunmengshan MCC (Davis and Zheng 1988; Davis et al. 1994, 1996) ushered in an age of persistent interest into looking for the Cordilleran-style MCC in China. The most revealing structure is the Hefangkou normal fault and the related Huairou ductile shear zone, collectively constituting the master detachment fault of the MCC (Fig. 19.2c) (Davis et al. 1994, 1996). The fault extends for ca. 60 km along the southeastern flank and dips southeastward at angles of 25–30° (Davis et al. 1994, 1996). It separates the footwall of Archean gneisses, Proterozoic sedimentary rocks and four episodes of

Jurassic-Cretaceous plutonic complexes from the hanging wall of lower grade supracrustal strata and their Precambrian basement (Davis et al. 1994, 1996). Underlying the detachment are 1–1.5 km thick mylonitic rocks with a cap of ca. 10–30 m thick chloritized and brecciaed mylonitic rocks, while above the fault lies a ca. 5-m thick fault gouge zone (Wang et al. 2011).

Two generations of foliation have been identified in the core plutons, with the earlier foliation indicative of magmatic doming and the younger one emblematic of later detachment faulting (Wang et al. 2011, 2012; Chen et al. 2014). As defined by widespread S-C fabrics and other kinematic indicators in the core plutons and the Huairou ductile shear zone, the later foliations possess a consistent top-down-to-the SE internal sense of shear (Davis et al. 1994, 1996). Considering mylonitic mineral assemblage, average sizes of subgrain and recrystallized grain, dislocation densities (Shi and Chen 1984) and quartz [c] crystallographic axis fabrics (Chen et al. 2014), the temperatures for forming the shear zone have been estimated to be in abroad range of 320–500 °C (Chen et al. 2014). Meanwhile, the kinematic vorticity numbers of 0.34–0.77 for the C′ foliation imply that the ductile shear zone was dominated by pure shear (Zheng et al. 2004; Wang et al. 2011).

Besides a host of zircon U-Pb ages that constrained an earlier magmatic doming stage, leucocratic granodiorites cutting the ductile shear zone yielded zircon U-Pb ages of 128–125 Ma (Davis et al. 1996; Chen et al. 2014). From the master detachment zone, a series of $^{40}Ar/^{39}Ar$ ages have been obtained, including 125–120 Ma for hornblende and biotite in the metadiorite and 118–114 Ma for biotite and K-feldspar in the mylonitic granodiorite (Wang et al. 2011; Chen et al. 2014) (Fig. 19.3c). Synthesizing these data with field observations could boil down to a formation time of early Cretaceous for the Yunmengshan MCC.

19.4.4 The Yiwulüshan MCC

The past decade witnessed the recognition of, and subsequent intensive investigation into, the Late Mesozoic extensional infrastructure in the Yiwulüshan range of western Liaoning (Ma et al. 1999; Zhang et al. 2002b, 2003b, 2012b, 2014b; Darby et al. 2004; Li et al. 2012, 2013; Lin et al. 2013a, b). With a NNE–SSW-oriented long axis extending between Fuxin and Beizhen (Fig. 19.2d), the range displays many structural, metamorphic, and igneous features that characterize the Cordilleran MCCs (Darby et al. 2004), leading to its designation as the Yiwulüshan MCC or Waziyu MCC. The core consists of predominantly Late Mesozoic plutonic complexes and Neoarchean to Paleoproterozoic gneisses and amphibolites. At structurally higher levels is the well-developed NNE-trending Waziyu ductile shear zone. Together with the related normal fault above it along the eastern margin of the Fuxin basin, it separates the core from the hanging wall of low-grade metamorphosed middle–late Proterozoic Changcheng System and the Mesozoic sedimentary and volcanic rocks.

The Waziyu ductile shear zone extends along the regions of Fuxin-Jinzhou for a distance of over 120 km (Wang and Li 1988; Wang et al. 1996; Ma et al. 1999; Zhang et al. 2002b, 2003b; Darby et al. 2004; Lin et al. 2013a). The pervasive mylonitic foliations in the zone strike N20–40°E and dip 10–50° to the northwest. Stretching lineations defined by the preferred orientation of biotite, amphibole, K-feldspar, and quartz aggregates commonly plunge 220–250° with a dip of 10–20°. Outcrop-scale kinematic indicators, like S-C fabrics, C′ foliation, asymmetrical porphyroclasts and deformed quartz veins and asymmetric folds at different localities, all suggest top-to-the-WNW sense of shear (Zhang et al. 2002a, 2003c, 2012a; Darby et al. 2004; Lin et al. 2013a). Structurally overlying this zone is the moderate–angle marginal normal faults of the Fuxin basin. The faults strike north-northeastward and typically dip west-northwestward at angles of 20–50°. The predominant set of persistent striae and penpendicular tension cracks on the fault surface indicate a consistent normal faulting (Zhang et al. 2003c). Although a higher deformation temperature of up to 600 °C has been estimated for the Waziyu shear zone based on the recrystallization types of quartz and feldspar and quartz [c] axis fabrics (Zhang et al. 2012a), it is most likely due to the leftover effects from earlier doming stage. Rather than an upper amphibolite facies condition, widespread chloritization and sericitization, dynamically recrystallized quartz aggregate and brittlely deformed feldspar in the mylonites all indicate that the shear zone may have formed under greenschist facies conditions (Wang and Zhang 1994; Wang et al. 1996, 2011; Zhang et al. 2002a, 2003b; Li et al. 2012).

In contrast to a spate of zircon U-Pb ages of middle–late Jurassic that record the magmatic doming evolution in the range (Li et al. 2012; Zhang et al. 2012a; Wang et al. 2012), a series of $^{40}Ar/^{39}Ar$ ages of Early Cretaceous from 132 to 112 Ma have been obtained for different minerals including hornblende, biotite and muscovite from the Waziyu ductile shear zone (Zhang et al. 2002a, 2003b; Lin et al. 2013a) (Fig. 19.3d). These ages clearly indicate that the MCC-style extensional event have occurred in the Yiwulüshan range during the period of 130–110 Ma.

19.4.5 The Liaonan MCC

Located at the southern tip of the Liaodong Peninsula (Fig. 19.1), the Liaonan MCC is the easternmost recognized core complex in the NCC (Yang et al. 1996; Yin and Nie 1996; Liu et al. 2005; Lin et al. 2008, 2011). Beginning from

an explicit assertion of Yang et al. (1996), numerous scholars have contributed much to probing its architecture and tectonic evolution during the past two decades (Yin and Nie 1996; Liu et al. 2005; Lin et al. 2008, 2011; Yang and Wu 2007; Wang et al. 2011, 2012). Its controlling structural unit is the Jinzhou low-angle detachment fault that separates an upper plate of largely supracrustal rocks ranging in age from Neoproterozoic to Cretaceous from a lower plate of Neoarchean to Cretaceous crystalline rocks (Fig. 19.2e) (Liu et al. 2005, 2008). With an arcuate map trace resulting from antiformal folding (Liu et al. 2005), the fault dips WNW on the western flank but dips SSE on the eastern flank (Fig. 19.2e). It is composed of amphibolite to upper greenschist facies mylonites, with stretching lineations plunging toward 275–315° at an angle of less than ~20° on the western flank and toward ~130° at less than 10° on the eastern flank. Strongly mylonitic rocks in the uppermost lower plate commonly exhibit varying degrees of shattering, brecciation, grain size reduction, forming a microbreccia layer of less-than-1-m-thick, a chloritic and brecciaed zone of more-than-100-m-thick and a gouge zone of ca. 2-m-thick (Liu et al. 2005; Wang et al. 2011). The fault surface dips toward 310–315° at 30–35° with down-dip slickenlines. Both mesoscopic structures (i.e., S-C fabrics) within the footwall zone and down-dip slickenlines on the outcrop-scale normal faults consistently indicate a top-to-the-WNE shear sense (Liu et al. 2005; Yang and Wu 2007; Lin et al. 2008).

Being essential components of the lower plate, syntectonic plutonic complexes exhibit narrow zircon U-Pb ages from 125 to 118 Ma (Guo et al. 2004; Wu et al. 2005a). As well-documented in the Yinmawanshan and Chaoyangsi batholiths, pervasive mylonitic foliations in their marginal zones show identical orientation patterns with those in the overlying detachment fault (Liu et al. 2005; Yang and Wu 2007). Various microscopic structures, including S-C fabrics, biotite fish, oblique quartz grain-shape foliation and stretching lineations, indicate a consistent, top-to-the-WNW sense of shear (Liu et al. 2005; Yang and Wu 2007).

Apart from systematic zircon U-Pb ages that established voluminous syntectonic plutonic complexes of 128–121 Ma and post-deformational plutons of 120–113 Ma (Guo et al. 2004; Wu et al. 2005a; Ji et al. 2009; Wang et al. 2012), a series of $^{40}Ar/^{39}Ar$ geochronological studies yielded a narrow age span from 124 to 110 Ma for hornblende, biotite, K-feldspar and muscovite from the mylonitic rocks in the detachment fault (Yin and Nie 1996; Yang and Wu 2007; Lin et al. 2008) (Fig. 19.3e). Taken together, they document a protracted period of crustal extension within the Liaonan MCC from 130 to 110 Ma.

19.4.6 Other MCCs

Besides the above elaborated early Cretaceous MCCs in the NCC, other highlights on the list of MCCs include the Yagan MCC along the Sino–Mongolian border (Fig. 19.1) (Zheng et al. 1991; Zheng and Zhang 1994; Webb et al. 1999), the western Hills 'MCC' of Beijing (Song 1996; Yan et al. 2006), the Xiuyan detachment fault system in the Liaodong Peninsula (Lin et al. 2007, 2011; Shen et al. 2011) and the Linglong MCC in the Jiaodong Peninsula (Charles et al. 2011).

The Yagan MCC features a trinity architecture that includes a master detachment fault well exposed on the southeastern flank, a footwall of Neoproterozoic to Paleozoic amphibolite-facies gneisses, marble and quartzite as well as mylonitic granitic plutons, and a hanging wall of late Paleozoic meta-sediments, Triassic–Jurassic sedimentary rocks and allochthonous Proterozoic carbonates (Webb et al. 1999, 2004; Wang et al. 2001). The detachment fault is characterized by ca. 1-m-thick flint-like microbreccia, 0–50-m thick zone of chloritic and brecciated mylonitic rocks, and 1–2 km thick section of mylonitic rocks (Webb et al. 1999). A fault gouge zone several meters thick overlies the detachment fault. The mylonitic foliation dips toward SE-S at 25–45° with a down dip stretching lineation on the foliation surfaces. Synthesizing zircon U-Pb ages of 135–119 Ma for the syntectonic plutons and mineral $^{40}Ar/^{39}Ar$ ages of 129–126 Ma for the mylonites from the detachment fault (Webb et al. 1999; Wang et al. 2004a, b, 2012) leads to bracketing the crustal extension in the MCC to a span from 135 to 126 Ma (Fig. 19.3f).

Although the Western Hills of Beijing has been widely acknowledged to be a magmatic dome (He et al. 2009; Wang et al. 2010a, b; Yan et al. 2010) and lacks key features of typical MCC as previously advocated (Song 1996; Yan et al. 2006), there did exist consistent and regional NE- and ESE-trending stretching lineation with $^{40}Ar/^{39}Ar$ ages of 130–110 Ma (Wang et al. 2010a, b). This might reflect early Cretaceous detachment deformation due to crustal thinning (Wang et al. 2010a, b) but awaits further investigation.

In the Xiuyan area of the Liaodong Peninsula, several extensional structures are well exposed (Lin et al. 2007, 2011) and collectively known as the Dayingzi detachment fault system (Shen et al. 2011). It separates an upper plate of largely early Cretaceous volcanic-sedimentary rocks from a lower plate of Paleoproterozoic metamorphic rocks and Triassic to Cretaceous plutonic complexes (Lin et al. 2007; Shen et al. 2011). The fault features an upper zone of fault gouge, a middle zone of microbreccia and a lower zone of brecciated mylonitic and mylonitic rocks (Shen et al. 2011).

Both stretching lineations within the mylonitic zone and down-dip slickenlines on the brittle zone indicate a consistent top-to-the-NW shear sense. The concordance between zircon U-Pb ages of 135–127 Ma for the supradetachment volcanic rocks (Shen et al. 2011) and mineral $^{40}Ar/^{39}Ar$ ages of 129–122 Ma for the mylonites (Lin et al. 2007) suggests that the ductile normal faulting occurred during early Cretaceous.

Like the Liaodong Peninsula, the Jiaodong Peninsula is also home to extensional structures. Apart from the above-mentioned late Jurassic magmatic domes, equally conspicuous are a series of NNE-trending ductile shear zones (Li et al. 2003a, b; Zhang et al. 2003a; Charles et al. 2011). As represented by the Linglong detachment fault (Charles et al. 2011), it separates a lower unit of Late Jurassic granite and migmatites from an upper unit composed of the Late Archaean and Early Proterozoic upper crustal rocks (Charles et al. 2011). Both outcrop-scale and microscopic kinematic markers indicate a systematic top-to-the SE sense of shear, in good agreement with the NW–SE extensional stress regime for the overprinted brittle structures (Charles et al. 2011). Such consistency, together with zircon U-Pb ages of 130–126 Ma for the syntectonic Guojialing pluton (Wang et al. 1998) and mineral $^{40}Ar/^{39}Ar$ ages of 124–120 Ma (Li et al. 2003a, b; Zhang et al. 2003a) for the regional ductile shear zones, suggests that the MCC-style extensional event in the Jiaodong Peninsula might occur during Early Cretaceous, rather than the late Jurassic as advocated by Charles et al. (2011).

19.5 Discussion

19.5.1 Two-Stage Extensional Pattern

The above incomplete enumeration delineates two spatially overlapping but temporally distinct extensional scenarios in the north China–Mongolia tract: the magmatic domes during mid–late Jurassic to earliest Cretaceous and the MCC-style detachment faulting during Early Cretaceous. For instance, the mylonitized granitoids in the Yunmengshan recorded Late Jurassic middle-lower crustal extension, ca. 30 Ma earlier than the detachment faulting in the upper crust (Davis et al. 1996; Wang et al. 2011, 2012). In the Hohhot MCC, the deformed granitoids have U-Pb zircon ages from 148 to 140 Ma (Guo et al. 2012a), ca. 20 Ma earlier than the detachment faulting at ca. 120–110 Ma (Davis et al. 2002). In the Yiwulüshan range, the Middle–Late Jurassic (169–154 Ma) high-temperature extensional doming is ca. 30 Ma older than the detachment faulting at ca. 130–110 Ma (Wang et al. 2011, 2012; Zhang et al. 2012, 2014b).

For the earlier extensional stage, each magmatic dome can not only find local extensional-style volcanic and sedimentation echoes, but also agrees well with a background low-strain extensional regime in the north China–Mongolian tract during Middle–Late Jurassic to earliest Cretaceous. For the former, insightful examples have been documented in a series of ENE–WSW trending Middle to Late Jurassic basins in western Liaoning (Cope and Graham 2007; Yang and Li 2008), the Yanshan belt (Li et al. 2007; Davis et al. 2009; Lin et al. 2014), the Erlian basin of Inner Mongolia (Chen and Chen 1997; Xiao et al. 2001; Meng et al. 2003) and in the east Gobi basin of SE Mongolia (Graham et al. 2001; Johnson et al. 2001). Collectively, these rift basin systems might define a broad low-strain extensional regime across the north China–Mongolian tract during Middle to Late Jurassic, in coincidence with the occurrence of coeval A-type granites (Chen et al. 2009; Xie et al. 2012; Xue et al. 2015) and rift-style volcanism (Wang et al. 2006; Guo et al. 2007). With their consistent adakitic geochemical affinity, therefore, these distributed extensional magmatic domes tend to highlight possible over-thickened crustal sites. In combination with the coeval rift basin systems (e.g., Graham et al. 2001; Ritts et al. 2001; Meng et al. 2003), they constitute a highly heterogeneous crustal extensional province of alternating high-strain doming and low-strain extension in the combined north China–Mongolian tract during Middle–Late Jurassic to earliest Cretaceous.

With a time gap of ca. 20–40 Ma between two extensional stages in the Hohhot, Kalaqin, Yunmengshan and Yiwulüshan cases, it is reminiscent of the situation in the Ruby Mountain-East Humboldt ranges in the North American Cordillera (Rey et al. 2009) and the peri-Mediterranean region of Algeria (Caby et al. 2001). As numerically simulated by Rey et al. (2009, 2011), such behavior mainly reflects the difference in extensional strain rate and may illustrate a partially molten continental crust that recorded episodic exhumation history likely related to slower rates of extension. By contrast, the close temporal linkage between plutonism and detachment faulting in the Liaonan case is similar to that in the Shuswap MCC from the North American Cordillera (Vanderhaeghe 1999; Foster et al. 2001), recording rapid exhumation and cooling likely related to faster rates of extension.

Last but not the least note to be made concerns the well-documented coincidence between extensional detachments and contractional thrusts in the MCC areas of the NCC (Davis et al. 1996, 2002; Zhang et al. 2012b; Lin et al. 2013a). For this issue, Wang et al. (2011) offered a tentative but convincing explanation.

19.5.2 Multi-level Crust and Mantle Interaction

In addition to building a series of extensional domes, the plutonic complexes in the afore-mentioned domes tend to

encapsulate intricately linked, multi-level crust and mantle interaction. This is best exemplified in the Yiwulüshan range (Zhang et al. 2014b). Underpinning on the first level is precursory fluid–rock interaction or hydro-weakening that progressively transformed a cratonic lithosphere to a hydrous, potassic-rich metasomatized lithospheric mantle (Zhang 2005). In addition to the direct manifestation in a variety of complexly zoned mantle xenocrysts and deep-seated xenoliths carried by multiple Mesozoic magmas (Gao et al. 2004; Zhang 2005; Zheng et al. 2007), such fluid-dominated metasomatism has been fingerprinted by elemental signatures in the mafic rocks and observed in the Late Permian appinites (Zhang et al. 2012a), Middle Jurassic basalts (Yang and Li 2008) and high-Mg andesite (Zhang et al. 2003a) from western Liaoning. It is also inherent in multiple Mesozoic lithosphere-derived mafic rocks in the Yanshan belt (Zhang 2007; Niu et al. 2012).

Building on the first-level fluid-rock interaction is the concomitant magmatic underplating that arises from preferential partial melting of heterogeneously refertilized lithosphere and in turn triggers crustal anatexis at different levels to yield diverse felsic melts. This is true for the coupled mafic and felsic magmas in the Hohhot enclave-bearing granitic suites (Guo et al. 2012b), the Yunmengshan diorite-granite suite (Zhao and Wang 2014), the Yiwulüshan plutonic complexes (Zhang et al. 2010d, 2014b) and the Liaodong Peninsula Jurassic intrusions (Wu et al. 2005b), with mafic rocks reflecting sustained basaltic underplating and assorted felsic rocks representing melting products from ancient lower crust and newly underplated crustal component. The orogen-scale occurrence of episodic basaltic underplating in the Yinshan–Yanshan belt is witnessed not only by abundant Phanerozoic imprints in the magma-carried granulite xenoliths (Zhou et al. 2002; Wilde et al. 2003; Zhang et al. 2013) but also by multiple Mesozoic mafic-ultramafic complexes (Niu et al. 2012; Zhang et al. 2014a).

Standing above episodic magma underplating is deep crustal hot zone (Annen et al. 2006) or MASH (melting, assimilation, storage and homogenization) zone (Hildreth and Moorbath 1988) that facilitates comprehensive crust–mantle interaction through refined magma hybridization processes. With their lithological combination of hornblende-rich mafic rocks and MME-bearing felsic rocks and their medium to high-K calc-alkaline geochemical character, the plutonic complexes in the above domes resemble numerous calc-alkaline magmatic associations worldwide (e.g., Barbarin 2005) and hence constitute typical basaltic underplating-driven magma hybridization entities during late Mesozoic (Yang et al. 2004, 2008; Wu et al. 2005b; Sun et al. 2010; Zhang et al. 2014b; Zhao and Wang 2014). Given the systematic variation of magma alkalinity with time, these systems appear to define a two-stage crustal evolutionary scenario from thickening to thinning in the northern NCC.

The documentation of multi-level crust and mantle interaction in the northern NCC during the Middle Triassic to Early Cretaceous echoes that at the eastern margin of the NCC (Chen et al. 2004, 2009, 2013; Tang et al. 2014). Taken together, such a trilogy of rock-fluid interaction, magma underplating and mafic-felsic magma hybridization may serve as a rallying point for reconciling current disparate views on the hotly debated issue of Mesozoic decratonization of the NCC. As initiated by pioneering comparative studies on mantle xenoliths in Ordovician kimberlites and Tertiary basalts, there was considerable lithospheric thinning during the Mesozoic (Menzies et al. 1993). Mechanisms such as delamination (Gao et al. 2004; Wu et al. 2005b), thermomechanical erosion (Xu et al. 2004), replacement (Zheng et al. 2001) and transformation through melt–rock interaction (Zhang et al. 2003a; Zhang 2005) have been proposed, with timing varying from Late Triassic (Yang et al. 2010), Middle–Late Jurassic (Gao et al. 2004) or Early to Late Cretaceous (Wu et al. 2005b; Xu et al. 2004). Given the apparent linkage of episodic crust and mantle interaction along the northern and eastern margins of Asia with the evolving circum-cratonic orogenic domains, it is most likely that Mesozoic decratonization in the NCC was not a single event, but followed a diachronous, multi-stage course (Zhang et al. 2012a, 2014b; Zhu et al. 2012a).

19.5.3 Geodynamic Process

With the current consensus that the diachronous decratonization pattern of the NCC might signify an episodic response of craton to circum-cratonic orogenic belts (Zhu et al. 2012b), it is easier to establish a close relationship between the early Mesozoic decratonization in the northern NCC with post-orogenic processes related to the closure of Paleo-Asian Ocean (Zhang et al. 2012a; Meng et al. 2014). In contrast, the geodynamic drivers for Middle to Late Jurassic magmatic doming and Early Cretaceous MCC-style extension remain contentious, largely diverging into either a far-field effect of the Mongol-Okhotsk collision (Meng 2003; Ritts et al. 2001) or a consequence of Paleo-Pacific subduction (e.g., Davis et al. 2001; Chen et al. 2004, 2009, 2013; Wu et al. 2005b; Zhu et al. 2012a, b). Refined scenarios include slab break-off (Meng 2003), lithospheric foundering (Gao et al. 2004), delamination (Wu et al. 2005b), gravitational collapse (Zorin 1999; Graham et al. 2001; Meng et al. 2003), subduction rollback or back-arc extension (Traynor and Sladen 1995; Davis et al. 2001; Chen et al. 2004, 2009, 2013; Zhang et al. 2012a; Zhu et al. 2012a, b). Such complications mainly stem from the supposed synchroneity between the Mongol-Okhotsk collision

and Paleo-Pacific subduction. Most recently, Wang et al. (2011, 2012) ascribed the polarized kinematic pattern of continental NE Asia during the Early Cretaceous to the combined effects of both regimes, with the Mongol-Okhotsk suturing responsible for the northwestern tract and Pacific plate subduction for the southeast tract.

Among these geodynamic drivers, extension driven by delamination or rollback of subducting lithosphere should migrate as the locus of sinking lithosphere moves and thus it commonly leads to a diachronous pattern of extension (Platt et al. 2003), whereas convective removal of lithospheric mantle normally predicts a significant time delay between the main phase of crustal thickening and the onset of crustal thinning as documented in the Tibetan plateau (England and Houseman 1989; Houseman and Molnar 1997) and Mediterranean Alboran domain (Platt et al. 2003). In the Yinshan-Yanshan belt, with a time gap of ca. 20–40 Ma between magmatic doming and MCC stages, this accords well with the Tibetan scenario. Moreover, such a distinct two-stage extension is typical of lithospheric and crustal signatures as predicted by post-orogenic gravitational collapse (Rey et al. 2001, 2011). In this sense, we suggest that convective removal of lithospheric mantle beneath collisional orogens might be a common factor in initiating late orogenic extension and thus the Yanshan belt might be under a post- collisional geodynamic setting associated with the northern Mongol-Okhotsk suture in the Jurassic.

19.6 Conclusions

Through summarizing the spatial and temporal distribution of magmatic doming and MCC-style detachment faulting, this review depicts two-stage crustal extensional panorama in the north China- Mongolian tract during late Mesozoic. Being concomitant crustal-continuum expressions of Mesozoic decratonization in the NCC, the magmatic domes tend to encapsulate an intricately linked hierarchy of crust and mantle interaction, whereas the MCCs typically accommodate upper crustal architectural reorganization. Near-synchronization of a two-stage extensional pattern across the tract seems to be compatible with gravitational collapse and convective removal of lithospheric mantle within an evolved post- collisional to within-plate extensional regime. The present study exemplifies the significance of differentiating magmatic doming and low-angle normal faulting phases in order to fully understand the thermal, mechanical, and chemical evolution of extended continental landmasses.

Acknowledgements We would like to thank Dr. Kang Hongyin for drawing the figures. Special thanks are due to Prof. Chen Bin for his constructive comments. This study was financially supported by the Major State Basic Research Program of the People's Republic of China (Grant No. 2012CB416603) and the National Natural Science Foundation of China (Grant Nos. 41390443, 41173043 and 41573031).

References

Annen, C., Blundy, J. D., & Sparks, R. S. J. (2006). The genesis of intermediate and silicic magmas in deep crustal hot zones. *Journal of Petrology, 47*, 505–539.

Barbarin, B. (2005). Mafic magmatic enclaves and mafic rocks associated with some granitoids of the central Sierra Nevada batholith, California: nature, origin, and relations with the hosts. *Lithos, 80*, 155–177.

Caby, R., Hammor, D., & Delor, C. (2001). Metamorphic evolution, partial melting and Miocene exhumation of lower crust in the Edough metamorphic core complex, west Mediterranean orogen, eastern Algeria. *Tectonophysics, 342*, 239–273.

Charles, N., Gumiaux, C., Augier, R., Chen, Y., Zhu, R. X., & Lin, W. (2011). Metamorphic Core Complexes vs. synkinematic plutons in continental extension setting: Insights from key structures (Shandong Province, eastern China). *Journal of Asian Earth Sciences, 40*, 261–278.

Chen, B., Chen, Z. C., & Jahn, B. M. (2009). Origin of mafic enclaves from the Taihang Mesozoic orogen, North China Craton. *Lithos, 110*, 343–358.

Chen, B., Jahn, B. M., Arakawa, M., & Zhai, M. G. (2004). Petrogenesis of the Mesozoic intrusive complexes from the southern Taihang Orogen, North China Craton: Elemental and Sr-Nd-Pb isotopic constraints. *Contributions to Mineralogy and Petrology, 148*, 489–501.

Chen, B., Jahn, B. M., & Suzuki, K. (2013). Petrological and Nd–Sr–Os isotopic constraints on the origin of high-Mg adakitic rocks from the North China Craton: Tectonic implications. *Geology, 41*, 91–94.

Chen, Y., Zhu, G., & Jiang, D. Z. (2014). Deformation characteristics and formation mechanism of the Yunmengshan metamorphic core complex. *Chinese Science Bulletin, 59*, 2419–2438.

Chen, Y. X., & Chen, W. J. (1997). *Mesozoic Volcanic Rocks: Chronology, geochemistry, and tectonic background* (pp. 1–279). Beijing: Seismological Press (in Chinese).

Cope, T. D., & Graham, S. A. (2007). Upper crustal response to Mesozoic tectonism in western Liaoning, North China, and implications for lithospheric delamination. In M. G. Zhai, B. F. Windley, T. M Kusky, & Q. R. Meng (Eds.), *Mesozoic sub-continental lithospheric thinning under eastern Asia* (Vol. 280, pp. 201–222). London: Geological Society (Special Publication).

Daoudene, Y., Gapais, D., Ruffet, G., Gloaguen, E., Cocherie, A., & Ledru, P. (2012). Syn-thinning pluton emplacement during Mesozoic extension in eastern Mongolia. *Tectonics, 31*(TC3001), 2012. doi:10.1029/2011TC002926.

Daoudene, Y., Ruffet, G., Cocherie, A., Ledru, P., & Gapais, D. (2011). Timing of exhumation of the Ereendavaa metamorphic core complex (north-eastern Mongolia)-U-Pb and $^{40}Ar/^{39}Ar$ constraints. *Journal of Asian Earth Sciences, 62*, 98–116.

Darby, B. J., Davis, G. A., Zhang, X. H., Wu, F. Y., Wilde, S. A., & Yang, J. H. (2004). The newly discovered Waziyu metamorphic core complex, Yiwulüshan, western Liaoning province, North China. *Earth Science Frontiers, 11*, 145–155.

Darby, B. J., Davis, G. A., & Zheng, Y. (2001). Structural evolution of the southern Daqing Shan, Yinshan belt, Inner Mongolia, China. *Geological Society of America Memoirs, 194*, 199–214.

Davis, G. A. (2003). The Yanshan belt of North China: Tectonics, adakitic magmatism, and crustal evolution. *Earth Science Frontiers, 10*, 373–384.

Davis, G. A., & Darby, B. J. (2010). Early Cretaceous overprinting of the Mesozoic Daqing Shan fold-and-thrust belt by the Hohhot metamorphic core complex, Inner Mongolia, China. *Geoscience Frontiers, 1*, 1–20.

Davis, G. A., Darby, B. J., Zheng, Y., & Spell, T. L. (2002). Geometric and temporal evolution of an extensional detachment fault, Hohhot metamorphic core complex, Inner Mongolia, China. *Geology, 30*, 1003–1006.

Davis, G. A., Meng, J., Cao, W. R., & Du, X. Q. (2009). Triassic and Jurassic tectonics in the eastern Yanshan Belt, North China: Insights from the controversial Dengzhangzi Formation and its neighboring units. *Earth Science Frontiers, 16*, 69–86.

Davis, G. A., Qian, X., Zheng, Y., Tong, H., Yu, H., Gehrels, G. E., et al. (1996). Mesozoic deformation and plutonism in the Yunmeng Shan: A metamorphic core complex north of Beijing, China. In A. Yin & T. M. Harrison (Eds.), *The tectonic evolution of Asia* (pp. 253–280). Cambridge, UK: Cambridge University Press.

Davis, G. A., Yu, H., Qian, X. L., Zheng, Y. D., Wang, C., Tong, H., et al. (1994). A Chinese metamorphic core complex: Geologic introduction and field guide to the Yunmengshan northern Beijing. In X. Qian (Ed.), *Studies of extensional tectonics* (pp. 154–166). Beijing: Geol. Publ. House.

Davis, G. A., & Zheng, Y. (1988). A possible cordilleran-type metamorphic core complex beneath the Great Wall near Hefangkou, Huairou County, northern China. *Geological Society of America Abstracts with Programs*, *20*, Abstract 324.

Davis, G. A., Zheng, Y., Wang, C., Darby, B. J., Zhang, C., & Gehrels, G. E. (2001). Mesozoic tectonic evolution of the Yanshan fold and thrust belt, with emphasis on Hebei and Liaoning provinces, northern China. *Memoirs-Geological Society of America, 194*, 171–197.

Deng, J. F., Su, S. G., Mo, X. X., Zhao, G. C., Xiao, Q. H., Ji, G. Y., et al. (2004). The sequence of magmatic–tectonic events and orogenic processes of the Yanshan Belt, North China. *Acta Geologica Sinica, 78*, 260–266.

Donskaya, V., Windley, B. F., Mazukabzov, A. M., Kroner, A., Sklyarov, E., Gladkochub, D. P., et al. (2008). Age and evolution of late Mesozoic metamorphic core complexes in southern Siberia and northern Mongolia. *Journal of Geological Society (London), 165*, 405–421.

England, P. C., & Houseman, G. A. (1989). Extension during continental convergence, with application to the Tibetan Plateau. *Journal of Geophysical Research: Solid Earth, 94*, 17561–17579.

Fayon, A. K., Whitney, D. L., & Teyssier, C. (2004). Exhumation of orogenic crust: Diapiric ascent versus low-angle normal faulting. In D. L. Whitney, C. Teyssier, & C. S. Siddoway (Eds.), *Gneiss domes in orogeny: Boulder, Colorado* (Vol. 380, pp. 129–140). Geological Society of America (Special Paper).

Foster, D. A., Schafer, C., Fanning, C. M., & Hyndman, D. W. (2001). Relationships between crustal partial melting, plutonism, orogeny, and exhumation: Idaho-Bitterroot batholith. *Tectonophysics, 342*, 313–350.

Gao, S., Rudnick, R. L., Xu, W. L., Yuan, H. L., Liu, Y. S., Walker, R. L., et al. (2008). Recycling deep cratonic lithosphere and generation of intraplate mgamatism in the North China Craton. *Earth and Planetary Science Letters, 270*, 41–53.

Gao, S., Rudnick, R. L., Yuan, H. L., Liu, X. M., Liu, Y. S., Xu, W. L., et al. (2004). Recycling lower continental crust in the North China Craton. *Nature, 432*, 892–897.

Graham, S. A., Hendrix, M. S., Johnson, C. L., Badamgarav, D., Badarch, G., Amory, J., et al. (2001). Sedimentary record and tectonic implications of Mesozoic rifting in southern Mongolia. *Geological Society of America Bulletin, 113*, 1560–1579.

Guo, C. L., Wu, F. Y., Yang, J. H., Lin, J. Q., & Sun, D. Y. (2004). The extension setting of the Early Cretaceous magmatism in eastern China: Example from the Yinmawanshan pluton in southern Lioadong Peninsula. *Acta Petrologica Sinica, 20*, 1193–2004 (in Chinese).

Guo, F., Fan, W. M., Li, X. Y., & Li, C. W. (2007). Geochemistry of Mesozoic mafic volcanic rocks from the Yanshan belt in the northern margin of the North China Block: Relations with post-collisional lithospheric extension. In M. G. Zhai, B. F. Windley, T. M. Kusky, & Q. R. Meng (Eds.), *Mesozoic sub-continental lithospheric thinning under eastern Asia* (Vol. 280, pp. 101–129). London: Geological Society (Special Publication).

Guo, L., Wang, T., Castro, A., Zhang, J. J., Liu, J., & Li, J. (2012a). Petrogenesis and evolution of late Mesozoic granitic magmatism in the Hohhot metamorphic core complex, Daqing Shan, North China. *International Geology Review, 54*, 1885–1905.

Guo, L., Wang, T., Zhang, J., Liu, J., Qi, G., & Li, J. B. (2012b). Evolution and time of formation of the Hohhot metamorphic core complex, North China: New structural and geochronologic evidence. *International Geology Review, 54*, 1309–1331.

Hallot, E., Auvray, B., de Bremond d'Ars, J., Davy, P., & Martin, H. (1994). New injection experiments in non-Newtonian fluids. *Terra Nova*, *6*, 274–281.

Han, B., Zheng, Y., Gan, J., & Chang, Z. (2001). The Louzidian normal fault near Chifeng, Inner Mongolia: Master fault of a quasi-metamorphic core complex. *International Geology Review, 43*, 254–264.

He, B., Xu, Y. G., & Paterson, S. (2009). Magmatic diapirism of the Fangshan pluton, southwest of Beijing, China. *Journal of Structural Geology, 31*, 615–626.

Hildreth, W., & Moorbath, S. (1988). Crustal contributions to arc magmatism in the Andes of central Chile. *Contributions to Mineralogy and Petrology, 98*, 455–489.

Hou, M. L., Jiang, Y. H., Jiang, S. Y., Ling, H. F., & Zhao, K. D. (2007). Contrasting origins of late Mesozoic adakitic granitoids from the northwestern Jiaodong Peninsula, east China: Implications for crustal thickening to delamination. *Geological Magazine, 144*, 619–631.

Houseman, G. A., & Molnar, P. (1997). Gravitational (Rayleigh-Taylor) instability of a layer with non-linear viscosity and convective thinning of continental lithosphere. *Geophysical Journal International, 128*, 125–150.

Ji, G. Y., Wang, Y., & Sun, Y. H. (2004). Petrological characteristics and structural deformation of Yunmengshan magamatic complex, Beijing. *Beijing Geology, 16*, 1–11 (in Chinese).

Ji, M., Liu, J. L., Guan, M., Davis, G., & Zhang, W. (2009). Zircon SHRIMP U-Pb age of Yinmawanshan and Zhaofang pluton in south Liaoning metamorphic core complex and its geological implications. *Acta Petrologica Sinica, 25*, 173–181 (in Chinese with English abstract).

Jian, P., Liu, D. Y., Kroner, A., Windley, B. F., Shi, Y. R., Zhang, W., et al. (2010). Evolution of a Permian intraoceanic arc-trench system in the Solonker suture zone, Central Asian orogenic belt, China and Mongolia. *Lithos, 118*, 169–190.

Jiang, N., Chen, J. Z., Guo, J. H., & Chang, G. H. (2012). In situ zircon U-Pb, oxygen and hafnium isotopic compositions of Jurassic granites from the North China craton: Evidence for Triassic subduction of continental crust and subsequent metamorphism-related 18O depletion. *Lithos, 142–143*, 84–94.

John, B. E., & Blundy, J. D. (1993). Emplacement-related deformation of granitoid magmas, southern Adamello massif, Italy. *Geological Society of America Bulletin, 105*, 1517–1541.

Johnson, C. L., Webb, L. E., Graham, S. A., Hendrix, M. S., & Badarch, G. (2001). Sedimentary and structural records of late Mesozoic high-strain extension and strain partitioning, east Gobi basin, southern Mongolia. *Memoirs-Geological Society of America, 194*, 413–433.

Kusky, T. M., & Li, J. H. (2003). Paleoproterozoic tectonic evolution of the North China Craton. *Journal of Asian Earth Sciences, 22*, 383–397.

Kusky, T. M., Li, J. H., & Santosh, M. (2007). The Paleoproterozoic North Hebei Orogen: North China Craton's collisional suture with the Columbia supercontinent. *Gondwana Research, 12*, 4–28.

Li, G., Liu, Z., Xu, Z., Li, S., & Liu, J. (2013). Crustal thinning during Mesozoic extensional detachment faulting in the Yiwulüshan region, eastern North China Craton. *International Geology Review, 55*, 749–766.

Li, G., Liu, Z. H., Liu, J. L., Li, Y. F., Xu, Z. Y., & Dong, X. J. (2012). Formation and timing of the extensional ductile shear zones in Yiwulü mountain area, Western Liaoning Province, North China. *Science China Earth Sciences, 55*, 733–746.

Li, J. W., Vasconcelos, P. M., Zhang, J., Zhou, M. F., Zhang, X. J., & Yang, F. H. (2003a). $^{40}Ar/^{39}Ar$ constraints on a temporal link between gold mineralization, magmatism, and continental margin transtension in the Jiaodong Gold Province, eastern China. *Journal of Geology, 111*, 741–751.

Li, Y. G., Zhai, M. G., & Miao, L. C. (2003b). Relationship between intrusive rocks and gold mineralization of the Najiayingzi gold deposit, Inner Mongolian and its implications for geodynamics. *Acta Petrologica Sinica, 19*, 808–816 (in Chinese with English abstract).

Li, Z., Li, Y., Zheng, J. P., & Han, D. (2007). Late Mesozoic tectonic transition of the eastern North China Craton: Evidence from basin-fill records. In M.G. Zhai, B. F. Windley, T. M. Kusky, & Q. R. Meng (Eds.), *Mesozoic sub-continental lithospheric thinning under eastern Asia* (Vol. 280, pp. 39–266). London: Geological Society (Special Publication).

Liaoning Bureau of Geology and Mineral Resources (LBGMR). (1998). 1:50000 Scale Regional Geology of Fuxin, Liaoning Province (in Chinese).

Lin, S., Zhu, G., Zhao, T., Song, L., & Liu, B. (2014). Structural characteristics and formation mechanism of the Kalaqin metamorphic core complex in the Yanshan area, China. *Chinese Science Bulletin, 59*, 3174–3189.

Lin, S., Zhu, G., Zhao, T., Song, L., & Liu, B. (2015). Tectonic setting of late Paleozoic-Mesozoic magmatic activities in the Kalaqin area of the northern Yanshan tectonic belt. *Chinese Journal of Geology, 50*, 30–49 (in Chinese with English abstract).

Lin, W., Faure, M., Chen, Y., Ji, W., Wang, F., Wu, L., et al. (2013a). Late Mesozoic compressional to extensional deformations in Yiwulüshan massif, NE China and their bearing on Yinshan-Yanshan orogenic belt (Part I: Structural and geochronological analyses). *Gondwana Research, 23*, 54–77.

Lin, W., Faure, M., Chen, Y., Ji, W., Wang, F., Wu, L., et al. (2013b). Late Mesozoic compressional to extensional deformations in Yiwulüshan massif, NE China and their bearing on Yinshan-Yanshan orogenic belt (Part II: Anisotropy of magnetic susceptibility and gravity modeling). *Gondwana Research, 23*, 78–94.

Lin, W., Faure, M., Monie, P., Scharer, U., & Panis, D. (2008). Mesozoic extensional tectonics in eastern Asia: The south Liaodong peninsula metamorphic core complex (NE China). *Journal of Geology, 116*, 134–154.

Lin, W., Faure, M., Monie, P., & Wang, Q. (2007). Polyphase Mesozoic tectonics in the eastern part of the north China Block: Insights from the eastern Liaoning Peninsula massif (NE China). In M. G. Zhai, B. F. Windley, T. M. Kusky, & Q. R. Meng (Eds.), *Mesozoic sub-continental lithospheric thinning under eastern Asia* (Vol. 280, pp. 153–170). London: Geological Society (Special Publication).

Lin, W., Wang, Q., Wang, J., Wang, F., Chu, Y., & Chen, K. (2011). Late Mesozoic extensional tectonics of the Liaodong Peninsula massif: Response of crust to continental lithosphere destruction of the North China Craton. *Science China Earth Sciences, 54*, 843–857.

Liu, C., Deng, J. F., Su, S. G., Xiao, Q. H., Luo, Z. H., & Wang, Q. H. (2004). Zircon SHRIMP dating of the Yunmengshan gneissic granodiorite (Beijing) and its geological implications. *Acta Petrologica Mineral, 23*, 141–146 (in Chinese with English abstract).

Liu, J. L., Davis, G. A., Lin, Z. Y., & Wu, F. Y. (2005). The Liaonan metamorphic core complex, southeastern Liaoning Province, North China: A likely contributor to Cretaceous rotation of eastern Liaoning, Korea and contiguous areas. *Tectonophysics, 407*, 65–80.

Ma, Y. S., Cui, S. Q., Wu, G., Wu, Z., Zhu, D., Li, X., & Feng, X. (1999). The structural feature of metamorphic core complex in Yiwulüshan mountains, western Liaoning. *Acta Geologica Sinica, 20*, 385–391 (in Chinese with English abstract).

Meng, Q. (2003). What drove late Mesozoic extension of the northern China-Mongolia tract? *Tectonophysics, 389*, 155–174.

Meng, Q., Hu, J., Jin, J., Zhang, Y., & Xu, D. (2003). Tectonics of the late Mesozoic wide extensional basin system in the China-Mongolia border region. *Basin Research, 15*, 397–415.

Meng, Q., Wei, H., Wu, L., & Duan, L. (2014). Early Mesozoic tectonic settings of the northern North China craton. *Tectonophysics, 611*, 155–166.

Menzies, M. A., Fan, W., & Zhang, M. (1993). Palaeozoic and Cenozoic lithoprobes and the loss of >120 km of Archean lithosphere, Sino-Korean craton, China. In H. M. Prichard (Ed.), *Magmatic processes and plate tectonics* (Vol. 76, pp. 71–81). Geological Society (Special Publication).

Niu, X., Chen, B., Liu, A., Suzuku, K., & Ma, X. (2012). Petrological and Sr-Nd-Os isotopic constraints on the origin of the Fanshan ultrapotassic complex from the North China Craton. *Lithos*, *149*, 146–158.

Paterson, S. R., & Fowler, T. K, Jr. (1993). Reexamining pluton emplacement process. *Journal of Structural Geology, 115*, 191–206.

Paterson, S. R., Fowler, T. K., Schmidt, K. L., Yoshinobu, A. S., Yuan, E. S., & Miller, R. B. (1998). Interpreting magmatic fabric patterns in plutons. *Lithos, 44*, 53–82.

Paterson, S. R., & Vernon, R. H. (1995). Bursting the bubble of ballooning plutons: A return to nested diapirs emplaced by multiple processes. *Geological Society of America Bulletin, 107*, 1356–1380.

Platt, J. P., Whitehouse, M. J., Kelley, S. P., Carter, A., & Hollick, L. (2003). Simultaneous extensional exhumation across the Alboran basin: Implications for the causes of late orogenic extension. *Geology, 31*, 251–254.

Rey, P., Vanderheaghe, O., & Teyssier, C. (2001). Gravitational collapse of continental crust: Definition, regimes, and modes. *Tectonophysics, 342*, 435–449.

Rey, P. F., Teyssier, C., Kruckenberg, S. C., & Whitney, D. L. (2011). Viscous collision in channel explains double domes in metamorphic core complexes. *Geology, 39*, 387–390.

Rey, P. F., Teyssier, C., & Whitney, D. L. (2009). Extension rates, crustal melting, and core complex dynamics. *Geology, 37*, 391–394.

Ritts, B. D., Berry, A. K., Johnson, C. L., Darby, B. J., & Davis, G. A. (2009). Early Cretaceous supradetachment basins in the Hohhot metamorphic metamorphic core complex, Inner Mongolia, China. *Basin Research, 22*, 45–60.

Ritts, B. D., Darby, B. J., & Cope, T. (2001). Early Jurassic extensional basin formation in the Daqing Shan segment of the Yinshan belt, northern North China, Inner Mongolia. *Tectonophysics, 339*, 239–258.

Shao, J., Zhang, L., & Jia, W. (2001). The Kalaqin metamorphic core complex in Inner Mongolia and its upwelling mechanism. *Acta Petrologica Sinica, 17*, 283–290.

Shen, L., Liu, J. L., Hu, L., Ji, M., Guan, H., & Davis, G. A. (2011). The Dayingzi detachment fault system in Liaodong Peninsula and

its regional tectonic significance. *Science China Earth Sciences, 41*, 1469–1483.

Shi, L., & Chen, X. (1984). Microstructures of fault rocks in Beishicheng and Hefangkou fault zone, Beijing. *Seismology and Geology, 6*, 1–13.

Shi, Y. R., Zhao, X. T., Ma, Y. S., Hu, D. G., Liu, Q. S., Wu, Z. H., et al. (2009). Late Jurassic-Early Cretaceous plutonism in the northern part of the Precambrian North China craton: SHRIMP Zircon U-Pb dating of diorites and granites from the Yunmengshan Geopark, Beijing. *Acta Geologica Sinica, 83*, 310–320.

Song, H. (1996). Characteristics of Fangshan Metamorphic Core Complex, Beijing and a discussion about its origin. *Geoscience-Journal of Graduate school, China University of Geosciences, 10*, 147–158 (in Chinese with English abstract).

Sun, J. F., Yang, J. H., Wu, F. Y., Li, X. H., Yang, Y. H., Xie, L. W., et al. (2010). Magma mixing controlling the origin of the Early Cretaceous Fangshan granitic pluton, North China Craton: In situ U-Pb age and Sr-, Nd-, Hf- and O-isotope evidence. *Lithos, 120*, 421–438.

Tang, H., Zheng, J. P., Yu, C., Ping, X., & Ren, H. (2014). Multistage crust–mantle interactions during the destruction of the North China Craton: Age and composition of the Early Cretaceous intrusions in the Jiaodong Peninsula. *Lithos, 190–191*, 52–70.

Teyssier, C., & Whitney, D. L. (2002). Gneiss domes and orogeny. *Geology, 30*, 1139–1142.

Tobisch, O. T., & Williams, Q. (1998). Use of microgranitoid enclaves as solid state strain markers in deformed granitic rock: An evaluation. *Journal of Structural Geology, 20*, 727–743.

Traynor, J. J., & Sladen, C. (1995). Tectonic and stratigraphic evolution of the Mongolian People's Republic and its influence on hydrocarbon geology and potential. *Marine and Petroleum Geology, 12*, 35–52.

Vanderhaeghe, O. (1999). Pervasive melt migration fro migmatites to leucogranites in the Shuswap metamorphic core complex, Canada: Control of regional deformation. *Tectonophysics, 312*, 35–55.

Wang, A., Li, S., & Qu, Y. (1996). *The geology and genesis of the lobe gold deposits* (pp. 1–149). Changchun: Jilin Publishing House of Science and Technology (in Chinese).

Wang, F., Zhou, X. H., Zhang, L. C., Ying, J. F., Zhang, Y. T., Wu, F. Y., et al. (2006). Late Mesozoic volcanism in the Great Xing'an range (NE China): Timing and implications for the dynamic setting of NE Asia. *Earth and Planetary Science Letters, 251*, 179–198.

Wang, H., & Li, S. (1988). *Two large-scale ductile shear zones in western Liaoning and their geological implication: Liaoning Geology, 5*, 235–241 (in Chinese).

Wang, L., & Zhang, Z. (1994). The petrological characteristics and metamorphism of the mylonites from the Waziyu ductile shear zone in Yixian, western Liaoning: Liaoning. *Geology, 12*, 20–29 (in Chinese).

Wang, L. G., Qiu, Y. M., McNaughton, N. J., Groves, D. I., Luo, Z. K., Huang, J. Z., et al. (1998). Constraints on crustal evolution and gold metallogeny in the Northwestern Jiaodong Peninsula, China, from SHRIMP U-Pb zircon studies of granitoids. *Ore Geology Reviews, 13*, 275–291.

Wang, T., Guo, L., Zheng, Y. D., Donskaya, T., Gladkochub, G., Zeng, L. S., et al. (2012). Timing and processes of late Mesozoic mid-lower-crustal extension in continental NE Asia and implications for the tectonic setting of the destruction of the North China Craton: Mainly constrained by zircon U-Pb ages from metamorphic core complexes. *Lithos, 154*, 315–345.

Wang, T., Zheng, Y. D., Gehrels, G. E., & Mu, Z. G. (2001). Geochronological evidence for existence of the south Mongolian microcontinent: A zircon U-Pb age of granitoid gneisses from the Yagan-Onch Hayrhan metamorphic core complex on the Sino-Mongolian border. *Chinese Science Bulletin, 46*, 2005–2008.

Wang, T., Zheng, Y. D., Li, T. B., & Gao, Y. J. (2004a). Mesozoic granitic magmatism in extensional tectonics near the Mongolian border in China and their implications for crustal growth. *Journal of Asian Earth Sciences, 23*, 715–729.

Wang, T., Zheng, Y. D., Li, T. B., Ma, M., & Gao, Y. J. (2002a). Forceful emplacement of granitic plutons in extensional tectonic setting: Syn-kinematic plutons in the Yagan-Onch Hayrhan metamorphic core complex on Sino-Mongolian border. *Acta Geologica Sinica, 76*, 81–88.

Wang, T., Zheng, Y. D., Zhang, J. J., Zeng, L. S., Donskaya, T. V., Guo, L., et al. (2011). Pattern and kinematic polarity of late Mesozoic extension in continental NE Asia: Perspectives from metamorphic core complexes. *Tectonics*, *30*, TC6007. http://dx.doi.org/. 10.1029/2011TC002896

Wang, X. S., & Zheng, Y. D. (2005). $^{40}Ar/^{39}Ar$ ages constraints on the ductile deformation of the detachment system of the Louzidian core complex, southern Chifeng, China. *Geological Reviews, 5*, 275–283 (in Chinese with English abstract).

Wang, X. S., Zheng, Y. D., & Jia, W. (2004b). Extensional stages of Louzidian metamorphic core complex and development of the supradetachment basin south of Chifeng, Inner Mongolia, China. *Acta Geologica Sinica, 78*, 237–245.

Wang, X. S., Zheng, Y. D., Zhang, J. J., Davis, G. A., & Darby, B. J. (2002b). Extensional kinematics and shear type of the Hohhot metamorphic core complex, Inner Mongolia. *Geological Bulletin China, 21*, 238–245 (in Chinese with English abstract).

Wang, Y., Cui, W., & Sun, C. (1994). The Louzidian-Dachengzi detachment fault and its tectonic evolution, south of Chifeng, Inner Mongolia. In X. Qian (Ed.), *Studies of extensional tectonics* (pp. 99–108). Beijing: Geological Publishing House (in Chinese).

Wang, Y., Zhou, L. Y., & Li, J. (2010a). Intracontinental superimposed tectonics—A case study in the Western Hills of Beijing, eastern Beijing. *Geological Society of America Bulletin, 123*, 1033–1055.

Wang, Y. B., Han, J., Li, J. B., Ouyang, Z., Tong, Y., & Hou, K. J. (2010b). Age, petrogenesis and geological significance of the deformed granitoids in the Louzidian metamorphic core complex, southern Chifeng, Inner Mongolia: Evidence from zircon U-Pb and Hf isotopes. *Acta Petrologica Mineral, 29*, 763–778 (in Chinese with English abstract).

Webb, L. E., Graham, S. A., Johnson, C. L., Badarch, G., & Hendrix, M. S. (1999). Occurrence, age, and implications of the Yagan- Onch Hayrham metamorphic core complex, southern Mongolia. *Geology, 27*, 143–146.

Webb, L. E., Johnson, C. L., Minjin, C., Sersmaa, G., Affolter, M., & Manchuk, N. (2004). Mesozoic and Cenozoic intracontinental deformation in southeastern Mongolia. *Eos Transactions, AGU: Fall Meeting Supplemental Abstracts, 85*, F1698.

Whitney, D. L., Teyssier, C., Rey, P., & Buck, W. R. (2013). Continental and oceanic core complexes. *Geological Society of America Bulletin, 125*, 273–298.

Whitney, D. L., Teyssier, C., & Vanderhaeghe, O. (2004). Gneiss domes and crustal flow. In D. L. Whitney, C. Teyssier, & C. S. Siddoway (Eds.), *Gneiss domes in orogeny: Boulder, Colorado* (Vol. 380, pp. 15–33). Geological Society of America Special Paper.

Wilde, S. A., Zhou, X., Nemchin, A. A., & Sun, M. (2003). Mesozoic crust-mantle interaction beneath the North China craton: A consequence of the dispersal of Gondwanaland and accretion of Asia. *Geology, 31*, 817–820.

Windley, B. F., Alexeiev, D., Xiao, W. J., Kroner, A., & Badarch, G. (2007). Tectonic models for accretion of the Central Asian Orogenic belt. *Journal of Geological Society (London), 164*, 31–47.

Wu, F. Y., Jahn, B. M., Wilde, S. A., Zhang, X. O., & Yang, J. H. (2005a). Nature and significance of the early Cretaceous giant igneous event in eastern China. *Earth and Planetary Science Letters, 233*, 103–119.

Wu, F. Y., Yang, J. H., Wilde, S. A., & Zhang, X. O. (2005b). Geochronology, petrogenesis and tectonic implications of Jurassic granites in the Liaodong peninsula, NE China. *Chemical Geology, 221*, 127–156.

Wu, F. Y., Yang, J. H., & Zhang, Y. B. (2006). Emplacement ages of the Mesozoic granites in southeastern part of the Western Liaoning province. *Acta Petrologica Sinica, 22*, 315–325 (in Chinese with English abstract).

Xiao, A. C., Yang, S. F., & Chen, H. L. (2001). Geodynamic background on formation of Erlian Basin. *Oil and Gas Geology, 22*, 137–145 (in Chinese with English abstract).

Xiao, W., Windley, B. F., Hao, J., & Zhai, M. (2003). Accretion leading to collision and the Permian Solonker suture, Inner Mongolia, China: Termination of the central Asian orogenic belt. *Tectonics, 22*, 1069. doi:10.1029/2002TC001484.

Xie, H. J., Wu, G., Zhu, M., Liu, J., & Zhang, L. C. (2012). Geochronology and geochemistry of the Daolanghuduge A-type granite in Inner Mongolia, and its geological significance. *Acta Petrologica Sinica, 28*, 483–494 (in Chinese with English abstract).

Xu, J. F., Wang, Y. J., & Yang, S. R. (1994). The rock deformation and genesis of the Yunmengshan granitic batholith, Beijing. *Earth Science, 19*, 806–814 (in Chinese with English abstract).

Xu, Y. G., Huang, X. L., Ma, J. L., Wang, Y. B., Yoshiyuki, I., Xu, J. F., et al. (2004). Crust–mantle interaction during the tectono-thermal reactivation of the North China Craton: Constraints from SHRIMP zircon U–Pb chronology and geochemistry of Mesozoic plutons from western Shandong. *Contributions to Mineralogy and Petrology*, *147*, 750–767.

Xue, F. H., Zhang, X. H., Deng, J. X., & Yuan, L. L. (2015). Late Jurassic A-type granite from the Dalai region of central Inner Mongolia: Geochemistry, petrogenesis and Tectonic implication. *Acta Petrol Sinica, 31*, 1774–1788 (in Chinese with English abstract).

Yan, D. P., Zhou, M. F., Song, H. L., Wang, G. H., & Sun, M. (2006). Mesozoic extensional structures of the Fangshan tectonic dome and their subsequent reworking during collisional accretion of the North China block. *Journal of Geological Society (London), 163*, 127–142.

Yan, D. P., Zhou, M. F., Zhao, D. G., Li, J. W., Wang, G. H., Wang, C. L., et al. (2010). Origin, ascent and oblique emplacement of magmas in a thickened crust: An example from the Cretaceous Fangshan adakitic pluton, Beijing. *Lithos, 123*, 102–120.

Yang, J. H., O'Reilly, S., Walker, R. J., Griffin, W., Wu, F. Y., Zhang, M., et al. (2010). Dischronous decratonization of the Sino-Korean craton: Geochemistry of mantle xenoliths from North Korea. *Geology, 38*, 799–802.

Yang, J. H., & Wu, F. Y. (2007). Rapid exhumation and cooling of the Liaonan metamorphic core complex: Inferences from ^{40}Ar-^{39}Ar thermochronology and implications for Late Mesozoic extension in the eastern North China Craton. *Geological Society of America Bulletin, 119*, 1405–1414.

Yang, J. H., Wu, F. Y., Chung, S. L., Wilde, S. A., & Chu, M. F. (2004). Multiple sources for the origin of granites: Geochemical and Nd/Sr isotopic evidence from the Gudaoling granite and its mafic enclaves, NE China. *Geochimica et Cosmochimica Acta, 68*, 4469–4483.

Yang, J. H., Wu, F. Y., Wilde, S. A., Chen, F. K., Liu, X. M., & Xie, L. W. (2008). Petrogenesis of an alkali syenites- granite-rhyolite suite in the Yanshan fold and thrust belt, eastern North China craton: geochronological, geochemical and Nd-Sr-Hf isotopic evidence for lithospheric thinning. *Journal of Petrology, 49*, 315–351.

Yang, W., & Li, S. G. (2008). Geochronology and geochemistry of the Mesozoic volcanic rocks in Western Liaoning: implications for lithospheric thinning of the North China craton. *Lithos, 120*, 88–117.

Yang, Z., Meng, Q., Gang, J., & Han, X. (1996). The metamorphic core complex structure in south Liaoning. *Liaoning Geology, 13*, 241–250 (in Chinese with English abstract).

Yin, A. (2004). Gneiss domes and gneiss dome systems. In D. L. Whitney, C. Teyssier, & C. S. Siddoway (Eds.), *Gneiss domes in orogeny: Boulder, Colorado* (Vol. 380, pp. 1–14). Geological Society of America Special Paper.

Yin, A., & Nie, S. Y. (1996). A Phanerozoic palinspastic reconstruction of China and its neighboring regions. In A. Yin & T. A. Harrison (Eds.), *The tectonic evolution of Asia* (pp. 442–485). New York: Cambridge University Press.

Zhai, M. G., Guo, J. H., & Liu, W. J. (2005). Neoarchean to Paleoproterozoic continental evolution and tectonic history of the North China Craton. *Journal of Asian Earth Sciences, 24*, 547–561.

Zhai, M. G., & Liu, W. J. (2003). Paleoproterozoic tectonic history of the North China craton: A review. *Precambrian Research, 122*, 183–199.

Zhai, M. G., & Santosh, M. (2011). The early Precambrian odyssey of the North China craton: A synoptic overview. *Gondwana Research, 20*, 6–25.

Zhang, B. L., Zhu, G., Jiang, D. Z., Li, C. C., & Chen, Y. (2012a). Evolution of the Yiwulushan metamorphic core complex from distributed to localized deformation and its tectonic implications. *Tectonics, 31*(TC4018), 2012. doi:10.1029/2012TC003104.

Zhang, H. F. (2005). Transformation of lithospheric mantle through peridotite-melt reaction: A case of Sino-Korean craton. *Earth and Planetary Science Letters, 237*, 768–780.

Zhang, H. F. (2007). Temporal and spatial distribution of Mesozoic mafic magmatism in the North China Craton and implications for secular lithospheric evolution. In M. G. Zhai, B. F. Windley, T. M. Kusky, & Q. R. Meng (Eds.), *Mesozoic sub-continental lithospheric thinning under eastern Asia* (Vol. 280, pp. 201–222). London: Geological Society (Special Publication).

Zhang, H. F., Sun, M., Zhou, X. H., Zhou, M. F., Fan, W. M., & Zheng, J. P. (2003a). Secular evolution of the lithosphere beneath the eastern North China Craton: Evidence from Mesozoic basalts and high-Mg andesites. *Geochimica et Cosmochimica Acta, 67*, 4373–4387.

Zhang, H. F., Zhu, R. X., Santosh, M., Ying, J. F., Su, B. X., & Hu, Y. (2013). Episodic widespread magma underplating beneath the North China Craton in the Phanerozoic: Implications for craton destruction. *Gondwana Research, 23*, 95–107.

Zhang, J., Zhao, Z. F., Zheng, Y. F., & Dai, M. N. (2010a). Postcollisional magmatism: geochemical constraints on the petrogenesis of Mesozoic granitoids in the Sulu orogen, China. *Lithos, 119*, 512–536.

Zhang, J. X., Zeng, L. S., & Qiu, X. P. (1997). Granite dome and extensional tectonics in the Yunmeng mountains, Beijing. *Geological Reviews, 43*, 232–240 (in Chinese with English abstract).

Zhang, L. C., Shen, Y. C., Liu, T. B., Zeng, Q. D., Li, G. M., & Li, H. M. (2003b). ^{40}Ar/^{39}Ar and Rb–Sr isochron dating of the gold deposits on northern margin of the Jiaolai Basin, Shandong, China. *Science in China Series D: Earth Sciences, 46*, 708–718.

Zhang, S. H., Zhao, Y., Davis, G. A., Ye, H., & Wu, F. (2014a). Temporal and spatial variations of Mesozoic magmatism and deformation in the North China Craton: Implications for lithospheric thinning and decratonization. *Earth-Science Reviews, 131*, 49–87.

Zhang, S. H., Zhao, Y., Liu, X. C., Liu, D. Y., Chen, F. K., Xie, L. W., et al. (2009a). Late Paleozoic to Early Mesozoic mafic–ultramafic complexes from the northern North China Block: Constraints on the composition and evolution of the lithospheric mantle. *Lithos, 110*, 229–246.

Zhang, S. H., Zhao, Y., Song, B., Hu, J. M., Liu, S. W., Yang, Y. H., et al. (2009b). Contrasting late Carboniferous and late Permian–

middle Triassic intrusive suites from the northern margin of the North China Craton: Geochronology, petro-genesis and tectonic implications. *Geological Society of America Bulletin, 121*, 181–200.

Zhang, X. H., Gao, Y. L., Wang, Z. J., Liu, H., & Ma, Y. G. (2012b). Carboniferous appinitic intrusions from the northern North China craton: Geochemistry, petrogenesis and tectonic implications. *Journal of Geological Society (London), 169*, 337–351.

Zhang, X. H., Li, T. S., & Pu, Z. P. (2002a). $^{40}Ar/^{39}Ar$ thermochronology of two ductile shear zones from YiwuLüshan, West Liaoning: Age constraints on the Mesozoic tectonic events. *Chinese Science Bulletin, 47*, 1113–1118.

Zhang, X. H., Li, T. S., Pu, Z. P., & Wang, H. (2002b). ^{40}Ar-^{39}Ar ages of Louzidian-Dachengzi ductile shear zone near Chifeng, Inner Mongolia and their tectonic significance. *Chinese Science Bulletin, 47*, 1292–1297.

Zhang, X. H., Mao, Q., Zhang, H. F., & Wilde, S. A. (2008). A Jurassic peraluminous leucogranite from Yiwulüshan, western Liaoning, North China Craton: Age, origin and tectonic significance. *Geological Magazine, 145*, 305–320.

Zhang, X. H., Mao, Q., Zhang, H. F., Zhai, M. G., Yang, Y., & Hu, Z. (2011). Mafic and felsic magma interaction during the construction of high-K calc-alkaline plutons within a metacratonic passive margin: the early Permian Guyang batholith from the northern North China Craton. *Lithos, 125*, 569–591.

Zhang, X. H., Wang, H., & Ma, Y. J. (2003c). $^{40}Ar/^{39}Ar$ age constraints on two NNE-trending ductile shear zones from Yanshan orogen, North China Craton. *International Geology Review, 45*, 936–947.

Zhang, X. H., Xue, F. H., Yuan, L. L., Ma, Y. G., & Wilde, S. A. (2012c). Late Permian appinite-granite complex from northwestern Liaoning, North China Craton: Petrogenesis and tectonic implications. *Lithos, 155*, 201–217.

Zhang, X. H., Yuan, L. L., & Wilde, S. A. (2014b). Crust/Mantle interaction during the construction of an extensional magmatic dome: Middle to Late Jurassic plutonic complex from western Liaoning, North China Craton. *Lithos, 205*, 185–207.

Zhang, X. H., Yuan, L. L., Xue, F. H., & Zhang, Y. B. (2012d). Contrasting Triassic ferroan granitoids from northwestern Liaoning, North China: Magmatic monitor of Mesozoic decratonization and a craton-orogen boundary. *Lithos, 144–145*, 12–23.

Zhang, X. H., Zhang, H. F., Jiang, N., & Wilde, S. A. (2010b). Contrasting Middle Jurassic and Early Cretaceous mafic intrusive rocks from western Liaoning, North China craton. *Geological Magazine, 147*, 844–859.

Zhang, X. H., Zhang, H. F., Jiang, N., Zhai, M. G., & Zhang, Y. (2010c). Early Devonian alkaline intrusive complex from the northern North China Craton: A petrologic monitor of post-collisional tectonics. *Journal of Geological Society (London), 167*, 717–730.

Zhang, X. H., Zhang, H. F., Wilde, S. A., Yang, Y. H., & Chen, H. H. (2010d). Late Permian to early Triassic mafic to felsic intrusive rocks from North Liaoning, North China: Petrogenesis and implication for Phanerozoic continental growth. *Lithos, 117*, 283–306.

Zhao, G. C., Cawood, P. A., Li, S. Z., Wilde, S. A., Sun, M., Zhang, J., et al. (2012). Amalgamation of the North China Craton: Key issues and discussion. *Precambrian Research, 222–223*, 55–76.

Zhao, G. C., Sun, M., Wilde, S. A., & Li, S. Z. (2005). Late Archean to Paleoproterozoic evolution of the North China Craton: key issues revisited. *Precambrian Research, 136*, 177–202.

Zhao, G. C., Wilde, S. A., Cawood, P. A., & Sun, M. (2001). Archean blocks and their boundaries in the North China Craton: lithological, geochemical, structural and P-T path constraints and tectonic evolution. *Precambrian Research, 107*, 45–73.

Zhao, M. T., & Wang, Y. (2014). Geochemical characteristics and petrogenesis of the shicheng diorite and Yunmnegshan granite in Beijing area. *Journal of Mineralogy and Petrology, 34*, 60–69 (in Chinese with English abstract).

Zhao, Y. (1990). The Mesozoic orogenies and tectonic evolution of the Yanshan area. *Geological Reviews, 36*, 1–13 (in Chinese with English abstract).

Zhao, Y., Zhang, S. H., Xu, G., Yang, Z., & Hu, J. M. (2004). The Jurassic major tectonic events of the Yanshannian intraplate deformation belt. *Geological Bulletin China, 23*, 854–863 (in Chinese with English abstract).

Zheng, J. P., Griffin, W. L., O'Reilly, S. Y., Yu, C. M., Zhang, H. F., Pearson, N., et al. (2007). Mechanism and timing of lithospheric modification and replacement beneath the eastern North China craton: Peridotitic xenoliths from the 100 Ma Fuxin basalts and a regional synthesis. *Geochimica Cosmo Acta, 71*, 5203–5225.

Zheng, J. P., O'Reilly, S. Y., Griffin, W. L., Lu, F. X., Zhang, M., & Pearson, N. J. (2001). Relict refractory mantle beneath the eastern North China block: Significance for lithosphere evolution. *Lithos, 57*, 43–66.

Zheng, Y., & Zhang, Q. (1994). The Yagan metamorphic core complex and extensional detachment faulting Inner Mongolia, China. *Acta Geologica Sinica, 7*, 125–135 (in Chinese).

Zheng, Y. D., Wang, S., & Wang, Y. (1991). An enormous thrust nappe and extensional metamorphic core complex newly discovered in the Sino-Mongolian boundary area. *Science in China Series D: Earth Sciences, 34*, 1146–1152.

Zheng, Y. D., & Wang, T. (2005). Kinematics and dynamics of the Mesozoic orogeny and late-orogenic extensional collapse in the Sino- Mongolian border areas. *Science in China Series D: Earth Sciences, 48*, 846–862.

Zheng, Y. D., Wang, T., Ma, M. B., & Davis, G. A. (2004). Maximum effective moment criterion and the origin of low-angle normal faults. *Journal of Structural Geology, 26*, 271–285.

Zheng, Y. D., Wang, T., & Zhang, J. J. (2009). Comment on "Structural analysis of mylonitic rocks in the Cougar Creek complex, Oregon-Idaho using the porphyroclast hyperbolic distribution method, and potential use of SC′-type extensional shear bands as quantitative vorticity indicators. *Journal of Structural Geology, 31*, 541–543.

Zheng, Y. D., Wang, Y., Liu, R. X., & Shao, J. A. (1988). Sliding–thrusting tectonics caused by thermal uplift in the Yunmeng Mountains, Beijing, China. *Journal of Structural Geology, 10*, 135–144.

Zhou, X. H., Sun, M., Zhang, G. H., & Chen, S. H. (2002). Continental crust and lithospheric mantle interaction beneath North China: Isotopic evidence from granulite xenoliths in Hannuoba, Sino-Korean craton. *Lithos, 62*, 111–124.

Zhu, G., Jiang, D. Z., & Zhang, B. L. (2012a). Destruction of the eastern North China Craton in a backarc setting: Evidence from crustal deformation kinematics. *Gondwana Research, 22*, 86–103.

Zhu, R. X., Yang, J. H., & Wu, F. Y. (2012b). Timing of destruction of the North China craton. *Lithos, 149*, 51–60.

Zorin, Y. A. (1999). Geodynamics of the western part of the Mongolo-Okhotsk collisional belt, Trans-Baikal region (Russia) and Mongolia. *Tectonophysics, 306*, 33–56.

Mesozoic Mo Deposits in Northern North China Craton

20

Yanjing Chen

Abstract

The North China Craton (NCC) was finally formed at ca. 1850 Ma and then kept its stability and uniformity until the Mesozoic decratonization. After the closure of the Paleo-Asian Ocean in Late Permian and the northernmost Paleo-Tethys Ocean in end-Triassic, the NCC continuously collided with the Siberia Craton to the north and the South China Block to the south, followed by subduction of the Mongol–Okhotsk and Pacific oceanic plates. These significant Mesozoic tectonic events destructed the NCC's stability and uniformity, and caused intensive hydrothermal mineralization of Mo, Au, Ag, and other metals. The NCC is the most important Mo province in the world, with the Mo deposits being concentrated at the southern and northern margins of NCC. In this contribution, we briefly summarize the geology, geochemistry and isotope ages of the Mo deposits in the northern NCC (NNCC), overview the progresses in understanding the ore geneses and tectonic settings, and setup a linkage between the mineralization and orogenies which resulted in the decratonization of the NCC. All the Mo-only or Mo-dominated deposits were formed after the closure of the Paleo-Asian Ocean, and in a series of pulses around 250–200, 200–160, 160–130 and <130 Ma (130–100 Ma). Main genetic types are porphyries (including breccia pipes), skarns and quartz veins, with the porphyry systems being predominant. The porphyry Mo deposits can be further subdivided into three subtypes, i.e., collision- or Dabie-, rift- or Climax-, and subduction- or Endako-types. The Mo deposits aged 250–200-Ma and 200–160-Ma belong to collision-type and have been formed in syn- to post-collisional tectonic setting. The 160–130-Ma Mo mineralization mainly occurs in the central NNCC and are predominated by the Climax-type porphyry Mo systems, which resulted from a back-arc rift related to southward subduction of the Mongol–Okhotsk oceanic plate. The 130–100-Ma deposit belongs to Endako-type and are only located in the eastern part of the northern NCC, which must be related to the westward subduction of the Paleo-Pacific oceanic plate. As shown by the porphyry Mo deposits in NNCC, the mineral systems are a powerful indicator of tectonic settings and associated evolutionary trends.

Keywords

Northern North China Craton • Mo deposit • Isotope age • Ore geology • Tectonic setting • Mesozoic

Y. Chen (✉)
Key Laboratory of Crustal and Orogenic Evolution, Peking University, Beijing, 100871, China
e-mail: yjchen@pku.edu.cngigyjchen@126.com

M. Zhai et al. (eds.), *Main Tectonic Events and Metallogeny of the North China Craton*,
Springer Geology, DOI 10.1007/978-981-10-1064-4_20

20.1 Introduction

China is the most important Mo-producing country in the world, with the majority of large deposits occurring in the orogenic belts on the northern and southern margins of NCC, where the Mo mineralization was related to continental collision orogenies, including syn- to post-collision tectonism (Chen et al. 2009, 2012). The Qinling–Dabie orogenic belt on the southern margin of the NCC, hosting the world's most important Mo province (Chen et al. 2000a; Li et al. 2007, 2012; Li and Pirajno 2016; Mao et al. 2011), has been well studied in the tectonic evolution and regional metallogeny, and therefore the collision- or Dabie-type of porphyry Mo deposits have been proposed and recently documented (Li et al. 2012; Yang et al. 2012, 2013, 2015; Wang et al. 2014, 2016b, c; Mi et al. 2015). The Dabie-type, in contrast to the Climax- and Endako-types, is mainly characterized by crust-sourced porphyry, porphyry-distal mineralization, strong dry or anhydrous alteration (formed by hydroxyl-barren minerals including quartz, K-feldspar, fluorite, and carbonate), and magmatic-sourced fluids with high F/Cl, K/Na, and CO_2/H_2O ratios. In the last decade, a number of large to giant Mo-only or Mo-dominated polymetal deposits have been found in the northern NCC (NNCC) and its northern adjacent Central NE China, such as the giant Mo deposits at Caosiyao, Diyanqin'amu, Xing'a, Chalukou, Luming, and Daheishan (Chen et al. 2016b and references therein).

The geology, geochemistry, and geochronology of individual deposits in NNCC have been studied, and a large amount of data was accumulated, but not well summarized and known by international geologists. In addition, these deposits were formed in, but not well related to the Mesozoic decrationization of NCC.

In this chapter, we summarize the principal geological and geochronological characteristics of the Mo deposits in NNCC, discuss the space, time, and tectonic settings of Mo mineralization, and attempt to setup a linkage between the mineralization and decratonization.

20.2 Geological Setting

20.2.1 General Geology

The NNCC lies south of the Kangbao–Chifeng Fault, north of Hohhot and Beijing cities, includes mountains eastward from Yinshan in Inner Mongolia, through Yanshan in Hebei, to eastern Liaoning Peninsula, and to Korea Peninsula, forming an east-trending mountainous chain (Fig. 20.1). Before the Mesozoic era, the NNCC consisted of discontinuous uplifts composed of Early Precambrian rocks and separated by faults (Huang 1997). In early Mesozoic orogenies, these boundary faults served as overthrusts and/or strike-slips, but in late Mesozoic acted as detachments or extensional shear zones, with the development of subsidiary E-, NE-, NNE- and ENE-trending structures, and uplift of metamorphic core complexes (Zheng et al. 1998; Davis et al. 2001; Zhang et al. 2002). Progressive extension or rifting in Cenozoic resulted in a basin-and-range tectonic scenario represented by Bohai Cove.

The NNCC exhibits numerous outcrops of Early Precambrian (>1.8 Ga) metamorphic basement and basement-cover structure. The basement rocks in Yinshan and Yanshan areas are mainly composed of TTG suites, migmatite, and amphibolites, gneisses, granulites and graphite-bearing khondalite series (Chen et al. 2000b and references therein); in eastern Liaoning Peninsula, these lithologies are mainly overlain by the Paleoproterozoic Liaohe Group low- to medium-grade metamorphosed carbonate-dominated succession (Tang et al. 2009, 2011, 2013). These basement rocks underwent strong deformation and metamorphism in the Orosirian (2050–1800 Ma) and then were unconformably covered, in ascending order, by the ending-Paleoproterozoic (1800–1600 Ma) to Mesoproterozoic and Neoproterozoic to Ordovician clastic-carbonate sedimentary successions (Huang 2007; Chen et al. 2009; Zhai and Santosh 2011, 2013), the Permo-Carboniferous coal-bearing sedimentary sequence, and the Late Jurassic-Early Cretaceous molasses containing volcanic rocks (Qi et al. 2004; Chen et al. 2009).

The NNCC is characterized by widespread Mesozoic granitoids (Fig. 20.1). These granitoids can be divided into four stages: (1) Triassic (Indosinian) granitoids, comprising granodiorite, monzogranite, K-feldspar granite, and alkali granite (also called alaskite) (HBGMR 1993); (2) Early and Middle Jurassic (Early Yanshanian) granites (Zhang 2009), and lacking coeval volcanic rocks; (3) Late Jurassic granitoids, mainly occurring in the western NNCC, generally coexisting with comagmatic volcanic rocks, such as Manketouebo Formation in Inner Mongolia and NW Hebei province; and (4) Cretaceous (Late Yanshanian) granitoids generally occurring as small porphyry stocks or breccia pipes mainly in the easternmost NNCC, coexisting with coeval volcanic rocks (Li and Yu 1994; Wang et al. 1995; Wu et al. 2016a). It is worthy to note that, in the NNCC, there is no granite younger than 90 Ma, but voluminous basalts have been dated <99 Ma (Liu 1999).

20.2.2 Mesozoic Tectonic Evolution

The NNCC is a transition from inner NCC to CAOB that evolved from the Paleo-Asian Ocean. The Paleo-Asia Ocean ever existed between the NCC and Siberia–Mongolia

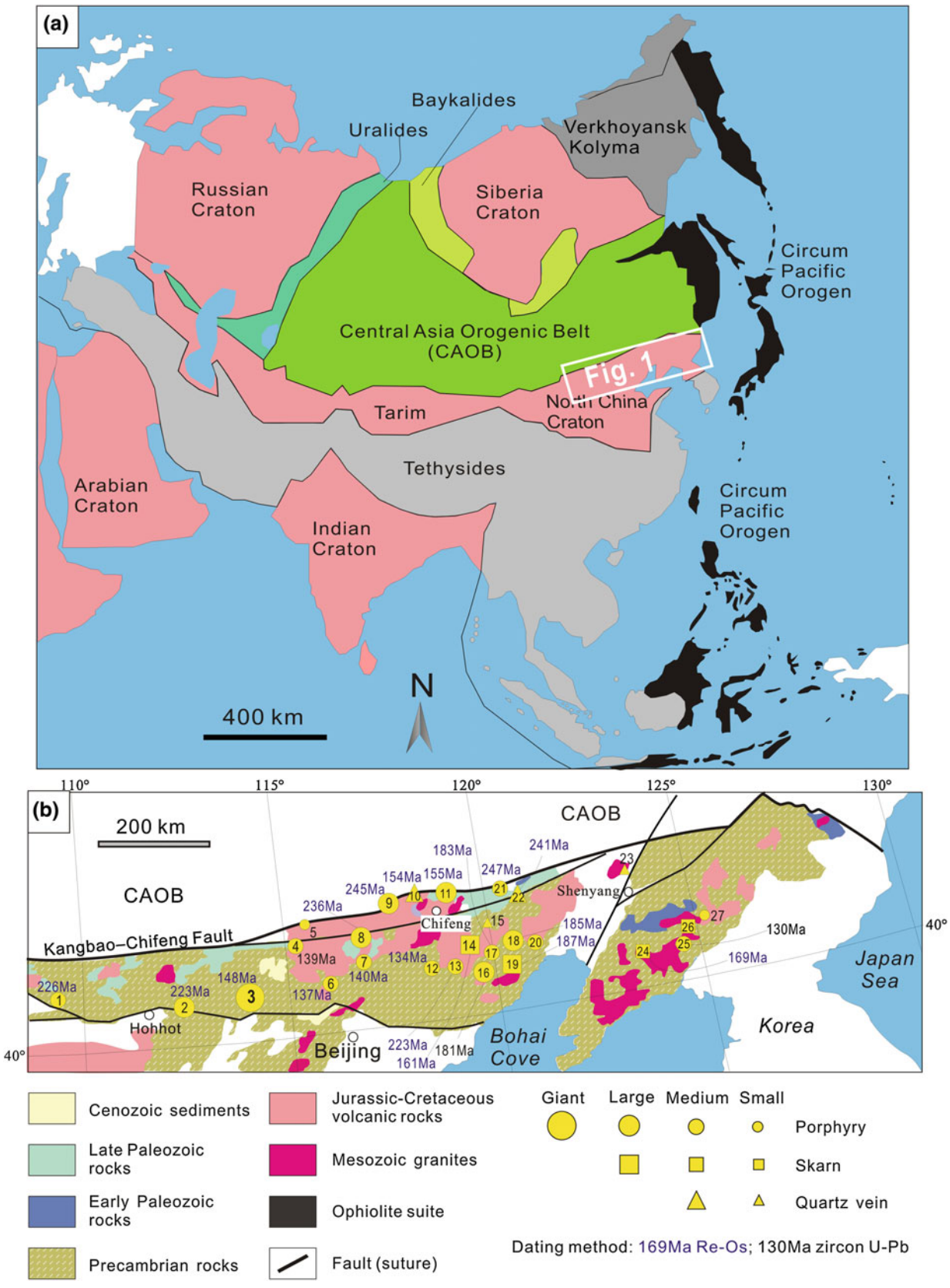

Fig. 20.1 **a** Asian tectonics (modified after Sengor and Natal'in 1996); **b** Geological map of the NNCC, showing the locations of Mo deposits (modified after Chen et al. 2012). Details of deposit numbers shown in this figure are given in Table 20.1

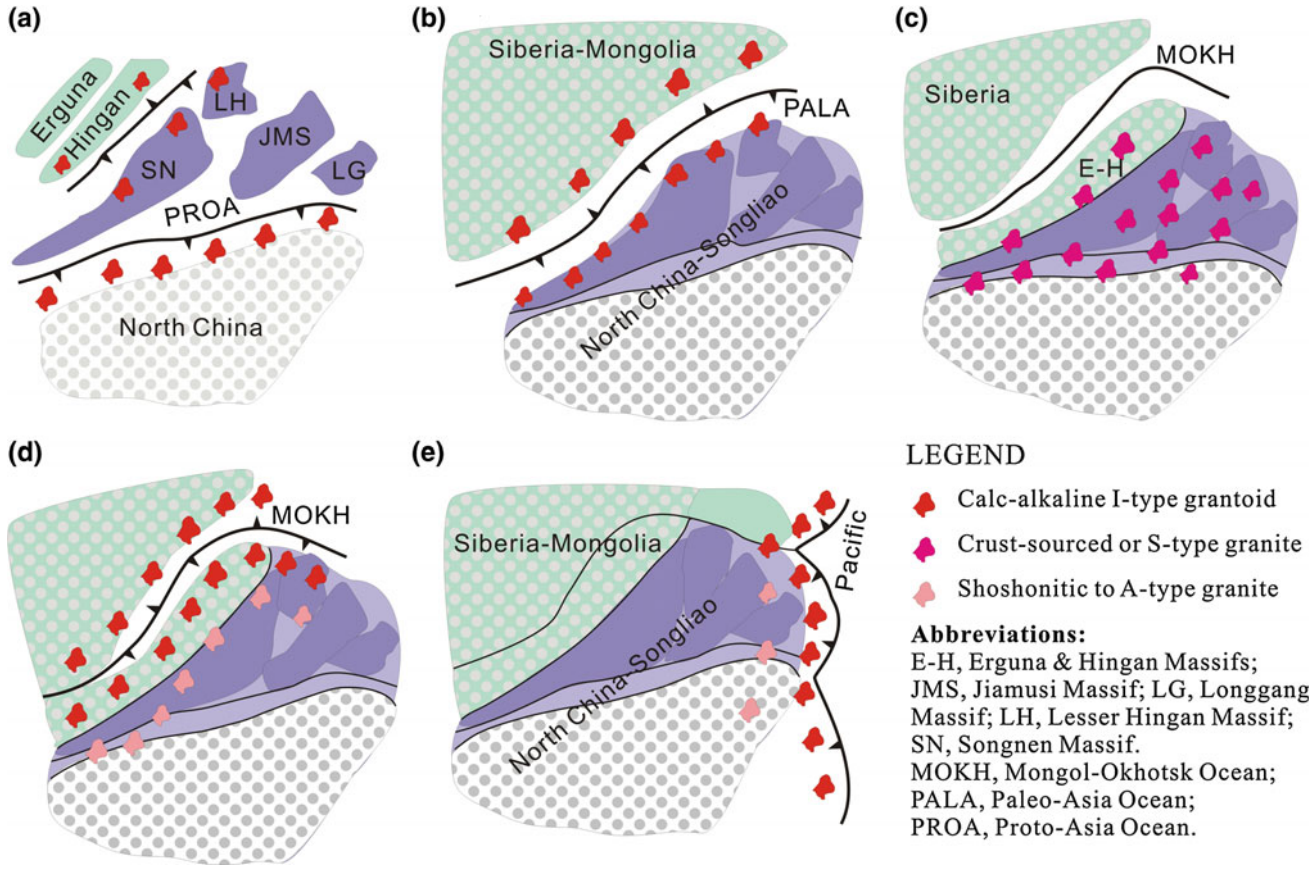

Fig. 20.2 Cartoons showing Phanerozoic tectonic evolution of NNCC (Chen et al. 2016b)

continent in the Paleozoic, featured by micro-continental massifs, oceanic basins, and subduction-related magmatic arcs (Windley et al. 2007; Chen et al. 2009, 2012, 2016a, b). Development of volcanic arcs and amalgamation of terranes resulted in vertical and lateral growth of continental crust, as indicated by the widespread Paleozoic igneous rocks in CAOB (Fig. 20.2a, b; Wu et al. 1999, 2006, 2010, 2011a; Chen et al. 2009, 2012). The Paleozoic rocks are structurally deformed and heterogeneously metamorphosed, and unconformably overlain by the negligibly deformed Late Jurassic-Early Cetaceous volcanic-sedimentary sequence, suggesting that the Paleo-Asian Ocean finally closed in the Late Permian–Early Triassic (Ren et al. 1992; Zorin et al. 2001; Liu et al. 2004; Chen et al. 2007a), which is supported by a holistic shortage of Triassic to Early Jurassic sedimentary or volcanic rocks. The youngest marine strata along the Solonker suture (Hegenshan-Heihe Fault) are the Permian Linxi, Dashizhai, and Zhesi Formations, which also indicate that the final closure of the Paleo-Asian Ocean should not be earlier than Late Permian (Sengor and Natal'in 1996; Chen 2002; Xiao et al. 2003; Chen et al. 2009).

In the period of end-Permian to Middle Jurassic, the NNCC and CAOB were gradually subjected to a syn- to post-collisional orogenic regime (Indosinian and Early Yanshanian orogenies) between the NCC-Songliao and Siberia–Mongolia continental plates, accommodating crustal deformation, shortening, thickening, uplifting, and development of crust-sourced granites (Fig. 20.2c), associated with mineralization of Mo and other metals (Chen et al. 2007a, 2012; Zhang et al. 2009a; Zeng et al. 2013). Mineral deposits of Indosinian ages can be mainly observed in the NNCC, minor in the eastern sector of CAOB, whereas those of Early Yanshanian mainly occur in the eastern sector of the NNCC and Ji-Hei Fold Belt (Figs. 20.1 and 20.2c), which possibly resulted from later tectonic modification.

In the period from the end of Middle Jurassic to beginning Early Cretaceous (ca. 165–130 Ma), i.e., Mid-Yanshanian, the NNCC and eastern CAOB accommodates post-collisional extension, and active margins tectonism resulted from the south to southeastward subduction of Mongol–Okhotsk oceanic plate (Fig. 20.2d; Wang et al. 2016b, c; Zhang and Li 2016). The closure time of Mongol–Okhotsk Ocean is still

controversial (Ren et al. 1992; Yin and Nie 1996; Chen et al. 2007a). A group of researchers considered that the Siberia continent collided with the united North China–Mongolia plates during the Middle to Late Jurassic, causing deformation and metamorphism of pre-Mesozoic rocks (Shao and Tang 1996, 2015; Shao and Zhang 1999; Hu et al. 2004; Zhao et al. 2004; Deng et al. 2005; Wu et al. 2010a; Chen et al. 2012); by contrast, another group of researchers (e.g., Kravchinsky et al. 2002; Tomurtogoo et al. 2005; Sorokin et al. 2007; Ruzhentsev and Nekrasov 2009) suggested that the Mongol–Okhotsk Ocean diachronously closed eastward from mid-Jurassic to Early Cretaceous. As a matter of fact, the western part of NNCC and Great Hingan Range contain abundant mid-Yanshanian volcanic rocks (Manketouebo Formation), called "Great Hingan Mesozoic Igneous Province" (Sengor and Natal'in 1996), with the oldest age of 165.8 ± 2.8 Ma (zircon U–Pb age) obtained from southern Great Hingan Rang (Wang et al. 2016b, c), and the youngest age of 129.7 ± 1.6 Ma (zircon U–Pb age) obtained from northern Great Hingan Range (Zhang et al. 2007; Chen et al. 2016b and references therein). These rocks, mainly composed of dacite, andesite, trachyandesite, rhyolite and basalt, showing a clear geochemical signature of arc-affinity, were controversially interpreted to be the products of the westward subduction of Paleo-Pacific plate (Sengor and Natal'in 1996), post-collisional magmatism (Zhang et al. 2007; Wu et al. 2010a; Chen et al. 2012), and south to southeastward subduction of the Mongol–Okhotsk oceanic plate (Wang et al. 2016b; Zhang and Li 2016). In this contribution, we favor the last interpretation, and thereby, discuss the Mid-Yanshanian magmatism and mineralization in the western part of the NNCC (Figs. 20.1 and 20.2d).

In Late Yanshanian, i.e., Cretaceous (ca. <130–90 Ma), the NNCC and the whole Eastern China mainland witnessed the westward subduction of the Paleo-Pacific plate (Fig. 20.2e), which is evidenced by both the widespread development of Cretaceous volcanic rocks in the Ji-Hei Fold Belt and the Nadanhada accretion complex of arc-affinity (Shao and Tang 2015). In combination, the post-collisional extension and the Paleo-Pacific plate subduction resulted in development of granitoids, andesitic–rhyolitic volcanic rocks and numerous hydrothermal mineral systems in the whole eastern margin of China mainland, southwardly from Ji-Hei Fold Belt and eastern NNCC (Chen et al. 2009, 2012, 2016b), through Jiaodong Peninsula (Chen et al. 2005; Goldfarb et al. 2014), and to Huanan Orogen (Zhong et al. 2016). The mineral systems in eastern NNCC and Ji-Hei Fold Belt mainly include porphyry Cu, Au, and Mo (Lu et al. 2009), skarn Cu–Pb–Zn–Au deposits (Chen et al. 2007a), and epithermal Au–Ag deposits (Qi et al. 2005; Zorin et al. 2001; Pirajno 2013; Goldfarb et al. 2014).

20.3 Mineralization Type, Space, and Time

The NNCC is a well-known important Mo belt in China, also known as Yan–Liao Mo belt (Luo et al. 1991). Hitherto at least 27 Mo-only or Mo-dominated polymetal deposits have been discovered in NNCC (Fig. 20.1 and Table 20.1), including one giant (>0.5 Mt Mo) and eight large-size (0.1–0.5 Mt Mo each) Mo systems, with a total reserve of 3.65 Mt Mo metal.

Mineralization types are dominated by porphyry, porphyry-skarn and skarn, followed by intrusion-related quartz vein (Table 20.1). It is clear that the Mo mineralization in NNCC was tightly associated with granitic magmatism, particularly, with the Mesozoic porphyry stocks. The porphyry Mo deposits are further divided into three subtypes, namely, Dabie- or collision-, Climax- or rift-, and Endako- or subduction-types (Table 20.1), according to the characteristics of fluid inclusions, wall rock alteration, causative porphyry, tectonic setting, as well as the development of the comagmatic volcanic rocks (for details see Chen et al. 2016a, b, and references therein).

The Mo deposits mostly cluster in the central NNCC where it is characterized by Yanshanian volcanic rocks, and scatter in the eastern and western sectors of the NNCC (Fig. 20.1). All the Mo-only and Mo-dominated deposits in these three belts were formed in the span of 250–130 Ma (Fig. 20.3), i.e., Triassic to Early Cretaceous. They cluster in three episodes of 250–220 Ma (Indosinian), 200–160 Ma (Early Yanshanian), and 160–130 Ma (Mid-Yanshanian), as shown in Figs. 20.1 and 20.3. The mineralization space and time well correlated with the tectonic events occurred in the NNCC, which is explained as below.

The NNCC was subjected to multiple episodes of igneous activity, but only the Mesozoic granitic rocks are associated with Mo mineralization. Indosinian (Triassic) magmatism resulted in formations of intermediate to felsic intrusions that are mainly monzogranite, syenogranite, and quartz porphyry stocks (Zeng et al. 2013), represented by the granitic porphyry at the Dasuji deposit (Wu et al. 2014a). The Early Yanshanian (Early to Middle Jurassic) granitoids mainly occur in the eastern part of the NNCC, being exemplified by those in the Yangjiazhangzi Mo field (Dai et al. 2006); while the Mid-Yanshanian granites (160–130 Ma) occur in the middle sector of the NNCC, where comagmatic intermediate–felsic volcanic rocks are present (Qi et al. 2004; Wu et al. 2016a). The NNCC is generally short of the Late Yanshanian (130–100 Ma) granitoids that are commonly found in eastern Ji-Hei Fold Belt (Sun et al. 2012; Chai et al. 2015, 2016; Chen et al. 2016b), Jiaodong gold province (Chen et al. 2005), Dabie Shan (Chen et al. 2016a), and southeastern coastal margin of the South China Block (Zhong et al. 2016).

Table 20.1 Geological characteristics of Mo deposits in Northeast China (mainly cited from Chen et al. 2016b)

No.	Deposit, County, Province	Type	Subtype	Metal	Reserve @ Grade	Size	Host- or wall rocks	Related structure	Related intrusion	Orebody occurrence	Wall rock alteration	Ore mineral	Gangue mineral	References
1	Xishadegai, Bayannaoer, Inner Mongolia	P	Dabie	Mo	Mo: >10 Kt @ 0.087 %	M	Early Precambrian gneisses, Wulashan Gp.	E–W- and NW-trending faults	Porphyritic moyite	Lens in intrusion and contact zones	Gre, Si, Kfs, Ab, Kao, Phy	Py, Mo, Pyr, Mag, Hem	Qz, Kfs, Pl, Mus, Kao, Fl	Hou et al. (2010)
2	Dasuji, Zhuozi, Inner Mongolia	P	Dabie	Mo	Mo: 200 Kt @ 0.133 %	L	Early Precambrian gneisses and migmatites, Jining Gp.	NE-trending fault, ENE-trending anticline	Syenogranite porphyry	Thick bed in intrusion	Si, Py, Phy, Gre	Mo, Py, Lm	Qz, Pl, Kfs, Kao, Ser, Epi	Yu et al. (2012) and Nie et al. (2012)
3	Caosiyao, Xinghe, Inner Mongolia	P	Climax	Mo	Mo: 2000 Kt @ 0.08 %	G	Early Precambrian gneisses and migmatites, Jining Gp.; Zhangjiakou Fm.: trachyte, rhyolite, tuff	NE-, NW-, and S–N-trending faults	Granite porphyry	Thick bed, pod, vein and lens in contact zone	Si, Ser, Kfs, Bio, Chl, Fl, Ca	Py, Mo, Wo, Mag, Sp, Ga	Qz, Pl, Kfs, Ser, Bio, Chl, Fl, Ca	Nie et al. (2012) and Wu et al. (2016a)
4	Zhangmajing, Guyuan, Hebei	P	Climax	U, Mo	Mo: 10 Kt @ 0.334 %	M	Late Jurassic-Early Cretaceous Zhangjiakou Fm.: trachyte, rhyolite, tuff	NE- and NW-trending faults	Rhyolite porphyry	Vein, lens and pipe in intrusion and contact zone	Si, Py, Kao, Fl	Jor, Pit, Py, Hem	Qz, Pl, Mus, Kao	Guo and Ma (2009) and Wu et al. (2015)
5	Maojiayingzi, Zhenglan, Inner Mongolia	P	Climax	U, Mo	Mo: <10 Kt	S	Early Cretaceous Zhangjiakou Fm.: trachyandesite, breccia and rhyolitic tuff	joint of NW-, NE- and E–W-trending faults	Rhyolite and diorite porphyries	Veins in hostrocks	Si, Agl, Fl	Jor, Pit, Py, Hem	Qz, Fl, Kao	Zhang (2009)
6	Dazhuangke, Yanqing, Beijing	P	Climax	Mo, Cu	Mo: 10.4 Kt @ 0.08 %	M	Mesoproterozoic carbonate rocks, Jixian Gp.	Subvolcanic edifice, breccia pipes	Breccia pipes	In-pipe veins	Kfs, Si, Py, Phy, Pro	Mo, Mag, Py, Sp, Cpy, Ilm	Pl, Kfs, Qz, Bio, Amp	Dai et al. (2006)
7	Dacaoping, Fengning, Hebei	P	Climax	Mo	Mo: >10 Kt	M		NE- and NW-trending faults	Granodiorite and granite	Veins in intrusion and contact zone	Kfs, Ser, Si, Kao	Mo, Py, Mag, Sp	Kfs, Qz, Ser, Kao	Duan et al. (2007)
8	Sadaigoumen, Fengning, Hebei	P	Dabie	Mo	Mo: 187 Kt @ 0.076 %	L	Paleoproterozoic gneisses and migmatites, Hongqiyingzi Gp.; Late Jurassic rhyolite lava and pyroclastic rock	NE- and N-trending faults	Monzogranite	Irregular lens in intrusion	Si, Ser, Fl, Ca, Kao	Mo, Py, Mag, Sp, Cpy	Qz, Kfs, Pl, Mus, Fl, Ca	Dai et al. (2007b)
9	Chehugou, Chifeng, Inner Mongolia	P	Dabie	Mo, Cu	120 Kt @ 0.10 % Mo; 250 Kt @ 0.14 % Cu	L	Archean gneisses and migmatites, Xiaotazigou Fm., Jianping Gp	Joint of NE- and NW-trending faults	Granite and syenite porphyries	Bed and lens in intrusion	Si, Kfs, Ser, Epi, Chl, Agl	Py, Cpy, Mo	Qz, Kfs, Bio, Amp	Zeng et al. (2012c)
10		QV		Mo	Mo: 15 Kt @ 0.39 %	M	Archean gneisses and migmatites, Jianping Gp.; Cretaceous Yixian		Monzogranite	Veins in intrusion	Si, Kfs, Ser, Chl,	Mo, Py	Qz, Ser, Fl, Ca	Zeng et al. (2011)

(continued)

Table 20.1 (continued)

No.	Deposit, County, Province	Type	Subtype	Metal	Reserve @ Grade	Size	Host- or wall rocks	Related structure	Related intrusion	Orebody occurrence	Wall rock alteration	Ore mineral	Gangue mineral	References
	Nianzigou, Chifeng, Inner Mongolia						Fm.: andesitic–basaltic volcanic rock and tuff	NNW- and NW-trending faults			Fl, Ca, Kao			
11	Jiguanshan, Chifeng, Inner Mongolia	P	Climax	Mo, Cu	150 Kt @ 0.09 % Mo; 283.4 Kt @ 0.24 % Cu	L	Permian clastic to pyroclastic rocks, Qingfengshan Fm.; Late Jurassic–Early Cretaceous dacite, rhyolite and sandstone	Volcanic crater; ENE- and NW-trending faults	Granitic to rhyolitic porphyries	Lens in intrusion and contact zone	Si, Kfs, Ser, Ca, Fl, Chl	Mo, Py, Cpy, Mag	Qz, Ca, Fl, Gp	Wu et al. (2010b, 2011)
12	Xiaosigou, Pingquan, Hebei	P-SK		Mo, Cu	59.8 Kt @ 0.09 % Mo; 18.5 Kt @ 0.74 % Cu	M	Mesoproterozoic (chert-) dolomite, Wumishan Fm., Jixian Gp.	joints of E-, NNE- and NW-trending faults	Granodiorite porphyry	lens and veins in intrusion and contact zone	Kfs, Phy, Py, Sk, Agl	Cpy, Cha, Py, Mo, Bn	Qz, Pl, Srp, Ca, Grt	Dai et al. (2010)
13	Hekanzi, Lingyuan, Liaoning	P	Dabie	Mo, Au, Cu	Mo: >10 Kt	M	Mesoproterozoic (chert-) dolomite, Wumishan Fm., Jixian Gp.	NE- and subsidiary NNW-trending faults	moyite	lens and veins in intrusion	Kfs, Si, Ser, Chl, Kao	Mo, Mag, Pyr, Cpy	Ca, Fl, Srp, Ol, Kfs, Pl, Qz	Shao et al. (2008)
14	Xiaojiayingzi, Kazuo, Liaoning	SK		Mo, Cu, Fe	Mo: 105 Kt @ 0.28 %	L	Mesoproterozoic (chert-) dolomite, Wumishan Fm., Jixian Gp.	NNE- and WNW-trending faults	porphyritic granite and diorite	Lens, veins and mantos in skarns	Sk	Py, Mo, Mag, Cpy, Bn, Ga, Sp	Qz, Di, Tr, Grt	Dai et al. (2007a)
15	Halaguishan, Jianping, Liaoning	QV		Mo	Mo: <10 Kt	S	Early Precambrian JianpingGp.: amphibolite and magnetite quartzite	NNE- and NW-trending faults	Rapakivi granite	Vein and lens in outer contact zones	Kfs, Si, Py, Pro	Mo, Py, Cpy, Sp	Qz, Kfs, Pl	Fan et al. (2010)
16	Songbei, Jianchang, Liaoning	P	Dabie	Mo	Mo: 170 Kt @ 0.10 %	L	Early Precambrian metamorphic complex, Jianping Gp.; Mesoproterozoic dolomite, Gaoyuzhuang Fm.	NE-trending fault	Fine-grained granite porphyry	Veins within intrusion	Si, Ser	Mo, Py	Pl, Kfs, Ser	Zeng et al. (2013)
17	Xintaimen, Jingxi, Liaoning	P	Dabie	Mo	Mo: >10 Kt @ 0.03–0.50 %	M	Middle Carboniferous–Late Permian clastic rocks; Jurassic-Cretaceous andesite, rhyolite and pyroclastic rock	SN- and NNE-trending faults	Granite porphyry	Veins in porphyry	Si, Py, Agl	Py, Mo	Qz, Pl, Mus	Zhang et al. (2009d)
18	Lanjiagou, Huludao, Liaoning	P	Dabie	Mo	Mo: 217 Kt @ 0.130 %	L	Mesoproterozoic (chert-) dolomite, Wumishan Fm., Jixian Gp.; Cretaceous pyroclastic rocks, Yixian Fm.	NE- and E–W-trending faults	Fine-grained porphyritic granite	Veins in intrusion	Kfs, Gre, Si, Ill, Chl, Ca	Mo, Py, Cpy, Ga, Sp, Mag	Qz, Grt, Di, Tr, Ser, Chl, Ca	Dai et al. (2008)
19	Yangjiazhangzi, Huludao, Liaoning	SK		Mo	Mo: 262 Kt @ 0.140 %	L	Mesoproterozoic (chert-) dolomite, Wumishan Fm., Jixian Gp.; Cretaceous pyroclastic rocks, Yixian Fm.	NE-, E-, N- and NNE-trending faults	porphyritic granite and granite porphyry	Stratiform or manto in skarn	Sk, Si, Kfs, Ca	Mo, Py, Ga, Sp, Cpy	Grt, Di, Tr, Qz, Ca	Liu et al. (2009)

(continued)

Table 20.1 (continued)

No.	Deposit, County, Province	Type	Subtype	Metal	Reserve @ Grade	Size	Host- or wall rocks	Related structure	Related intrusion	Orebody occurrence	Wall rock alteration	Ore mineral	Gangue mineral	References
20	Babailong, Huludao, Liaoning	P	Dabie	Mo	Mo: >10 Kt @ 0.060–0.224 %	M	Jurassic Gangtun complex: fine-grained granite and porphyritic granite	NE- and E–W-trending faults	Porphyritic granite	Lens and veins in altered granitoids	Si, Kfs, Epi, Chl, Kao, Ser	Mo, Py, Cpy	Kfs, Pl, Qz	Jiao (2010)
21	Baituyingzi, Chifeng, Inner Mogolia	P	Dabie	Mo, Cu	>50 Kt @ 0.08–0.18 % Mo; 4 Kt Cu	M	Late Paleozoic granitoids, Permian volcanic rocks	E–W-, NW- and NE-trending faults	Monzogranite porphyry	Veins and lens in intrusion and contact zone	Kfs, Ser, Si, Chl, Fl, Ca	Mo, Cpy, Py	Qz, Kfs, Pl, Ser, Ca, Fl	Sun et al. (2013, 2016)
22	Yajishan, Chifeng, Inner Mogolia	QV		Mo, Cu	10.5 Kt @ 0.089 % Mo	M	Permian rhyolite, andesite, basalt and tuff, Qingfengshan Fm.; Late Jurassic dacite, tuff and breccia, Tuhulu Fm.	E–W- and NE-trending faults E-trending syncline	Monzogranite	Veins and lens in intrusion	Kfs, Ser, Si, Chl, Ca	Py, Mo, Cpy	Qz, Kfs, Ser, Ca, Chl	Li et al. (2010)
23	Faku, Faku, Liaoning	QV		Mo	Mo: <10 Kt @ 0.08–1.67 %	S	Jurassic conglomerate, sandstone and siltstone, Shahezi Fm.; Cretaceous basalt, andesite, dacite and tuff, Yixian Fm	NE- and NNE-trending shear zone	Quartz diorite	Veins and lens in intrusion	Si, Gre	Mo, Py	Qz, Mus	Zhao et al. (2009)
24	Yaojiagou, Fengcheng, Liaoning	SK		Mo, Cu	Mo: >10 Kt	M	Paleoproterozoic dolomitic marble, quartz-plagioclase hornfels and amphibole schist, upper Liaohe Gp.	NE- and NNE-trending faults	Porphyritic granite	Vein and lens in intrusion and contact zones	Si, Py, Chl, Ca	Mo, Py, Sp, Ga, Cpy	Grt, Di, Tr, Ser, Ca, Epi, Qz, Fl	Fang et al. (2012)
25	Wanbaoyuan, Dandong, Liaoning	P	Endako?	Mo	Mo: >10 Kt @ 0.280 %	M	Paleoproterozoic dolomitic marble, quartz-plagioclase hornfels and schist, Liaohe Gp.	NE- and NW-trending faults	Granodiorite	Veins and lens in contact zones	Ser, Si, Chl, Ca	Mo, Py, Cpy	Qz, Kfs, Ser, Ca	Hu et al. (2009)
26	Sipingjie, Kuandian, Liaoning	SK		Mo	Mo: >10 Kt @ 0.260 %	M	Paleoproterozoic dolomitic marble and graphite marble, upper Liaohe Gp.	NE- and NW-trending faults	Granite	Veins in outer contact zones	Sk, Chl, Epi	Mo, Py, Cha, Cpy	Grt, Mus, Chl, Epi, Di	Sun and Sun (2008)
27	Qiongbangzigou, Huanren, Liaoning	P	Endako?	Mo	Mo: 2.2 Kt @ 0.090 %	S	Late Jurassic andesitic lava, tuff and pyroclastic rocks, Xiaoling Fm.	NE- and NW-trending faults	Rhyolitic porphyry	Annular veins in outer contact zone	Si, Kfs, Bio, Ser, Epi, Chl, Ca	Mo, Py, Cpy, Sp, Ga	Qz, Kfs, Ser, Chl, Ca	Liu et al. (2010)

Type abbreviations: *P* porphyry, *SK* skarn, *QV* quartz vein; Kt, 1000 t

Size abbreviations: *S* small (<10 Kt Mo), *M* medium (10–100 Kt Mo); *L* large (100–500 Kt Mo), *G* giant (>500 Kt Mo)

Abbreviations of alteration and minerals: *Ab* albite; *Agl* argillic alteration; *Amp* amphibole; *Arg* argentite; *Bio* biotite; *Bn* bornite; *Ca* carbonate; *Cha* chalcocite; *Chl* chlorite; *Cpy* chalcopyrite; *Di* diopside; *Epi* epidote; *Fl* fluorite; *Ga* galena; *Gp* gypsum; *Gre* greisen; *Grt* garnet; *Hem* hematite; *Ill* illite; *Ilm* ilmenite; *Jor* jordisite; *Kao* kaolinite; *Kfs* K-feldspar; *Lm* limonite; *Mag* magnetite; *Mo* molybdenite; *Mus* muscovite; *Ol* olivine; *Phy* phyllic alteration; *Pit* pitchblende; *Pl* plagioclase; *Pro* propylitization; *Py* pyrite; *Pyr* pyrrhotite; *Qz* quartz; *Ser* sericitie; *Si* silicification; *Sk* skarn; *Sp* sphalerite; *Srp* serpentine; *Tr* tremolite; *Wo* wolframite

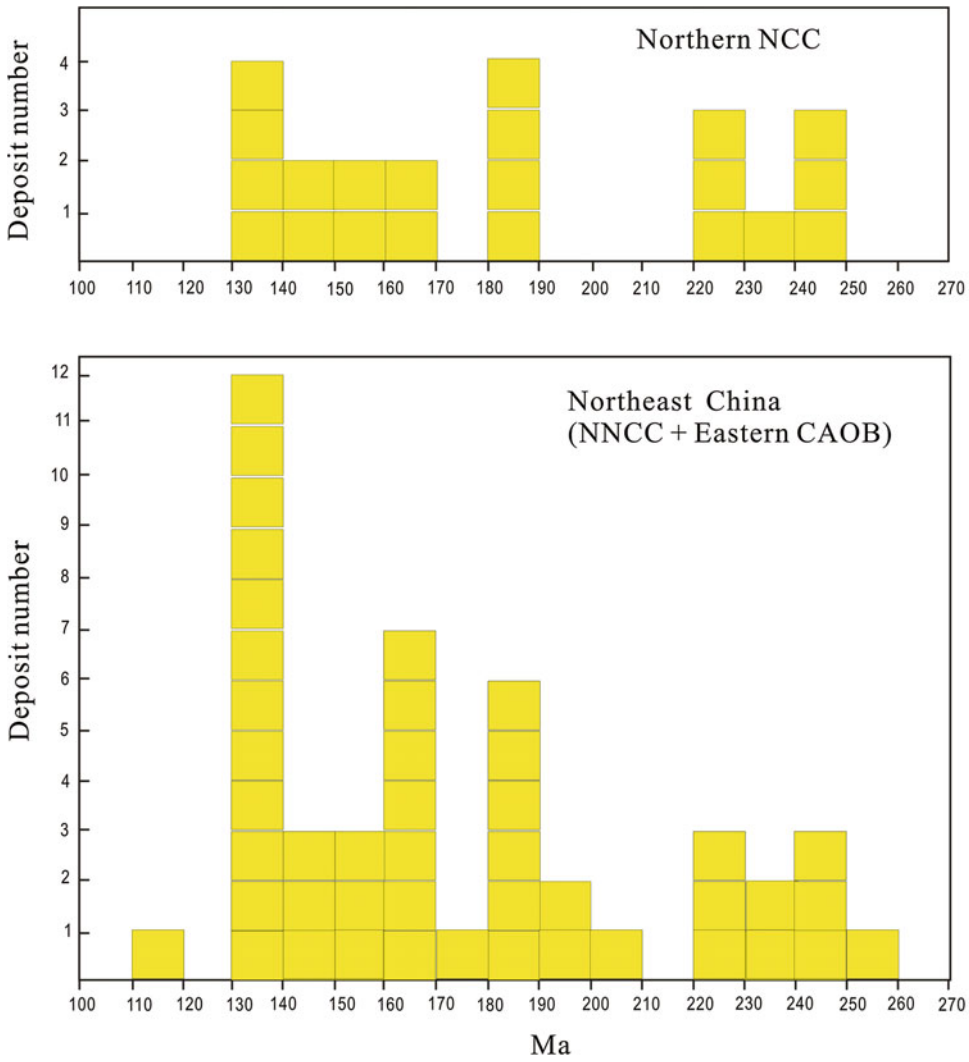

Fig. 20.3 Histograms of isotopic ages of Mo deposits in NNCC (modified from Chen et al. 2016b)

The multistage Mesozoic granitic magmatism in NNCC is also associated with multistage hydrothermal mineralization, including orogenic gold (Chen et al. 1998), epithermal Au, Ag, Pb, Zn, and Cu (Qi et al. 2004), and polymetallic mineral systems (e.g., porphyry, skarn, porphyry–skarn, explosive breccia pipe, and quartz vein) (Chen and Li 2009).

The Indosinian Mo mineralization was commonly interpreted to have resulted from continental collision between the NCC and Siberia Craton (Chen et al. 2009, 2012, 2016b; Zeng et al. 2013). The tectonic setting of the Early Yanshanian deposits was interpreted to be magmatic arc related to southeastward subduction of Mongol–Okhotsk Ocean (Mao et al. 2014) and westward subduction of the Pacific plate (e.g., Zeng et al. 2013), but was considered to be a post-collisional regime (Chen et al. 2012, 2016b) and is endorsed in this contribution. The Mid-Yanshanian mineralization was generally related to the subduction of Pacific plate (e.g., Zeng et al. 2013), but recently related to post-collisional extension (Chen et al. 2012, 2016b; Wu et al. 2016a). The Late Yanshanian (130–100 Ma) granitoids and mineral deposits in the eastern NNCC, represented by Wanbaoyuan, is consent to be the product of the westward subduction of the Pacific plate (Sun et al. 2012; Mao et al. 2014; Chen et al. 2016b).

20.4 Ore Geology and Geochemistry

20.4.1 Hostrocks and Mineralization Types

The hostrocks include high-grade metamorphic Archean–Paleoproterozoic basement (gneiss, amphibolite, marble, and TTG), low-grade metamorphosed Paleoproterozoic Liaohe Group carbonate-clastic sediments, slightly metamorphosed Mesoproterozoic to Early Paleozoic sedimentary rocks, Late Paleozoic coal-bearing strata, and a Jurassic–Cretaceous continental volcanic-sedimentary succession (Table 20.1). Host rocks can be classified into four classes: medium–

high-grade metamorphosed gneiss (e.g., Caosiyao and Sadaigoumen deposit), locally called Anshan, Jianping, Hongqiyingzi, Jining, and Wulashan Groups from east to west; low-grade metamorphosed carbonate-clastic sediments (e.g., Yangjiazhangzi deposit); coal-bearing clastic rocks, e.g., Xintaimen deposit; and continental andesitic to rhyolitic volcanic rocks (e.g., Faku deposit).

The Mo deposits in NNCC were hosted in various lithologies that might control mineralization styles and metallic associations. For instance, skarn or porphyry–skarn deposits are generally hosted in carbonate-bearing sequences, represented by the Xaosigou, Xiaojiayingzi, Yangjiazhangzi, Yaojiagou, and Sipingjie (see Table 20.1). The carbonate- and/or shale-bearing rocks are also favorable for Cu mineralization, as exemplified by the above-mentioned skarn or porphyry–skarn systems. The breccia pipe- and quartz vein-type mineralization are likely to be associated with granitic intrusions and/or carbonate-barren volcanic-sedimentary rocks (metamorphosed or not), such as the Chehugou porphyry-breccia system, Baituyingzi porphyry-quartz vein system, and the Nianzigou, Halaguishan, Yajishan, and Faku quartz vein systems (Fig. 20.1 and Table 20.1). It is noted that these different mineralization types usually constitute a uniform metallogenic system outwardly zoning from porphyry to skarn or quartz vein.

20.4.2 Ore-Causative Intrusion

All the Mo deposits were associated with intermediate–felsic porphyritic to subvolcanic intrusions (Table 20.1), occurring as stocks and breccia pipes. They are generally granite, granodiorite, monzogranite, and syeno granite in lithology, but slightly different between metallogenic clusters and ages.

The Indosinian and Early Yanshanian granites are mainly S-type granites, represented by the Yangjiazhangzi and Lanjiagou Mo deposits. They have high SiO_2 contents (73.65–77.88 %), A/CNK (0.99–1.07), and K_2O/Na_2O (1.06–1.69), showing peraluminous affinity and relatively low initial $^{87}Sr/^{86}Sr$ values of <0.706 (Tian 1999; Dai et al. 2006, 2008). The Mid-Yanshanian granitoids include I- and A-types. The I-type granites belong to high-K calc-alkaline, exemplified by the Dazhuangke, and Shouwangfen deposits tend to form Mo-Cu or Cu–Mo polymetallic deposits, have low SiO_2contents of (60.59–66.68 %), high contents of $K_2O + Na_2O$ (7.65–8.08 %), with K_2O/Na_2O ratios of 0.61–0.94, σ values of 2.67–3.51, and initial $^{87}Sr/^{86}Sr$ value of 0.707 (Dai et al. 2006). The Caosiyao ore-causative intrusions, an example of A-type granites, is well documented by Wu et al. (2016a) and Wang et al. (2016a), showing high K_2O contents and initial $^{87}Sr/^{86}Sr$ ratios, and low εNd(t) ad εHf(t) values. The geochemical features of the Mesozoic ore-causative granites indicate that the magmas mainly originated from the partial melting of lower continental crust or Precambrian crystalline basement.

20.4.3 Ore occurrence and Controlling Structures

The NE-, NW–NWW-, nearly and E-W-trending faults are common in NNCC (Fig. 20.1), of which the E-W- and NE-trending faults are the largest and deepest, with characteristic of multistage activity. Tectonism and fault development are accompanied by the intrusive and extrusive intermediate–felsic magma. Most Mo deposits and associated magmatic rocks are spatially and temporally controlled by the seregional faults, particularly the E-W- and NE–NNE-trending faults. The Mo deposits are more likely to be concentrated at the intersection of major faults and their subsidiary structures, resulting in a network-like ore-controlling structure system (Fig. 20.1 and Table 20.1).

The quartz vein-type mineralization was strictly controlled by faults. The orebodies of porphyry, porphyry–skarn and skarn-types are usually controlled by the porphyries and their contact zones. Spatial relationship between orebodies and intrusions includes two styles: (1) orebodies entirely situated within the intrusions, such as the Dasuji, Chehugou, and Saidaigoumen deposits (Table 20.1); and (2) orebodies are confined to porphyry and its contact zones or proximal wall rocks, as exemplified by the Caosiyao, Xiaosigou, and Jiguanshan deposits. The intrusion-distal (or out-porphyry) mineralization, i.e., the orebodies are distal to the causative intrusions, which is observed in Dabie Shan (Yang et al. 2013; Wang et al. 2014; Mi et al. 2015), eastern Qinling Orogen (Yang et al. 2015) and East Tianshan (Wu et al. 2014c, 2016b), has not been observed in NNCC. The majority of orebodies are stratiform, lenticular, veined, and podiform in shape, occurring in intrusions, breccia pipes and/or their contact zones (Table 20.1).

20.4.4 Wall Rock Alteration

The Mo deposits in NNCC are magmatic-hypothermal systems, and share similar wall rock alteration. Outward from the intrusions or orebodies, wall rock alteration changes from hypothermal assemblages (potassic alteration and silicification), through mesothermal (phyllic and propylitic alteration), tolow-temperature (carbonate and argillic), and from alkaline replacement to acidic leaching (Hu 2002; Khashgerel et al. 2006; Chen et al. 2007b). Porphyry and breccia pipe systems typically show potassic, siliceous, epidote, sericitic, fluorite, carbonate, and chloritic alteration

zones. The quartz veins have symmetric alteration zones present on both sides of the lodes, and consisting of potassic, siliceous, sericitic, chloritic, fluorite, and carbonate alteration halos. The nature of the wall rock alteration assemblages are of two types, i.e., anhydrous caused by fluids with high K/Na, F/Cl, and CO_2/H_2O ratios, and hydrous caused by fluids with relatively low K/Na, F/Cl, and CO_2/H_2O ratios. The former is mainly characterized by K-feldspar, quartz, epidote, fluorite, and carbonate, and occasionally garnet and diopside, as shown in the Indosinian and Early Yanshanian porphyry Mo deposits (Zhang and Li 2014), and the Mid-Yanshanian Mo deposits in the central NNCC (e.g., Caosiyao). The latter, on the other hand, is featured by strong biotite, sericite, chlorite, albite, hornblende, and serpentine, as seen at the Wanbao Yuan deposit in easternmost NNCC (southeastern Liaoning).

According to Chen et al. (2007b), Chen and Li (2009), and Pirajno and Zhou (2015), the anhydrous alteration assemblages are generally present at intracontinental magmatic-hydrothermal mineral systems, including syn- to post-collisional and intracontinental or back-arc rifts settings. The porphyry Mo deposits formed in continental collision settings are exemplified by those in Dabie Shan (Chen et al. 2016a and references therein), Qinling Orogen (Li et al. 2007, 2012; Yang et al. 2012, 2013, 2015, 2016), and Tianshan (Wu et al. 2014c, 2016b); while the porphyry Mo deposits in back-arc rifts are typically represented by the Climax-Henderson Mo belt. The hydrous alteration assemblages commonly occur in porphyry systems developed in subduction-related magmatic arcs, as shown by the porphyry-type Cu–Au or Cu–Mo systems in the Circum-Pacific belt (Pirajno 2009), as well as the Paleoproterozoic Zhaiwa Mo–Cu deposit in Qinling Orogen (Deng et al. 2013a, b). Compared to the Mo-only deposits, the porphyry Cu–Mo deposits generally contain more chalcopyrite, sericite and chlorite, but less molybdenite, K-feldspar, fluorites, and carbonate.

Considering that the type of mineral system can be used to constrain a specific tectonic setting (Chen et al. 2016b), we suggest that the NNCC has three types of porphyry Mo deposits, i.e., the Endako-, Climax- and Dabie-types, because the area was subjected to subduction-related accretionary orogeny, back-arc rifting, and continental collision orogeny. It can be concluded that the three types of porphyry Mo deposits in NE China reflect the following tectonic settings: continental collision, Andean-type arc, and back-arc rift.

20.4.5 Fluid Inclusions: A Marker of Genetic Types

Fluid inclusions (FIs) are the "fossil" of ancient fluid systems and can be used as diagnostic markers of different types of hydrothermal deposits (Chen et al. 2007b; Pirajno 2009, 2013). FIs can be a key indicator of the classification of porphyry Mo deposits (Chen et al. 2016a, b, and references therein). The Endako- or subduction-related deposits formed in continental magmatic arcs, exemplified by Endako and MAX in Columbia, Canada, contain little or no carbonic- aqueous (CO_2-H_2O) or fluid inclusion. The Climax-orrift-type deposits, developed in continental or back-arc rifts, generally contain carbonic-aqueous FIs, such as the Climax and Urad-Henderson deposits, Colorado, USA. The Dabie porphyry systems formed in syn- to post-collisional tectonic setting, represented by the Yanshanian porphyry Mo deposits in Dabie Shan and Qinling Orogen, always contain abundant carbonic-aqueous FIs, often together with pure CO_2, daughter mineral-bearing or multiple mineral-bearing CO_2-H_2O inclusions. In addition, the comagmatic volcanic rocks generally developed in the Climax-type deposits are not present in the Dabie-type Mo deposits, and thus are proposed to represent a different tectonic setting (Chen et al. 2016a).

The fluid inclusion study of the Mo deposits in NNCC is still poor, which detract from the understanding of the ore genesis. In spite of the paucity of available data, three-type ore system types can be delineated (Table 20.3). All the Indosinian and Early Yanshanian porphyry Mo deposits contain carbonic-aqueous (CA-type) FIs, and half of them also contain pure carbonic (C-type) and mineral-bearing carbonic-aqueous (MC-type) FIs. Comagmatic volcanic rocks have not been identified in these deposits yet (Table 20.1). Hence, these deposits are comparable with the Dabie-type, and considered to have formed in the syn- to post-collisional tectonic setting after the closure of the Paleo-Asian Ocean.

The Mid-Yanshanian (160–130 Ma) porphyry Mo deposits only occur in the central NNCC, where there are comagmatic volcanic rocks. Here the deposits, exemplified by Caosiyao and Jiguanshan, develop with FIs of CA- and even C-types, in addition to the MA- and A-types, comparable to the Climax-type deposits (Table 20.3). These two porphyry Mo deposits possibly developed in a back-arc rift related to the southeastward subduction of the Mongol–Okhotsk oceanic plate (Fig. 20.2).

Late Yanshanian porphyry Mo deposits, exemplified by Wanbao Yuan, only occur in the easternmost NNCC. In this mineral system, only aqueous fluid inclusions have been observed (Table 20.3), suggesting that it is an Endako-type deposit possibly resulted from the westward subduction of the Paleo-Pacific plate.

20.4.6 Re Concentration in Molybdenite

Re, as a siderophile element, tends to be enriched in ultramafic mantle and the Fe–Ni core. Re contents in molybdenite are relatively high and used to trace the source of ore-forming metals (Stein et al. 1997; Mao et al. 1999; Chen et al. 2016a, b; Li and Pirajno 2016; Zhang and Li 2014,

2016; Zhong et al. 2016). Stein et al. (2001) proposed that Re contents in molybdenite from mantle-sourced rocks or deposits are significantly higher than those from crust-sourced ones. Mao et al. (1999) suggested that the Re contents in molybdenite from mantle- and crust-sourced mineral systems are commonly >100 and <10 ppm, respectively. Ni et al. (2015), Chen et al. (2016a, b) and Zhong et al. (2016) further considered that the Re content of 50 ppm can be a dividing criterium; and the Re contents in molybdenite also somewhat increase with ore-forming ages and Cu/Mo ratios (Chen et al. 2012, 2016b).

The Mo-only deposits generally yield molybdenite Re contents less than 50 ppm; while the Mo-dominated deposits with Cu as byproduct, are commonly between or across the two lines with Re contents of 50 and 100 ppm, respectively (Fig. 20.4). This suggests that the molybdenite Re content is positively correlated with the Cu/Mo ratios (reserve), and also, possibly a positive correlation with the contribution from the mantle, which was reported for the Cu–Mo and Mo–Cu deposits in Mongolia and Siberia (Berzina et al. 2005), and other areas in China (Chen et al. 2016a, b; Zhong et al. 2016; Wu et al. 2016b; Yang and Wang 2016).

The majority of the Mo deposits in NNCC have molybdenite Re contents of <50 ppm, indicating a crust-dominant source. The Re contents of molybdenite from the Yaojiagou and Xiaojiayingzi Mo–Cu deposit in Yan–Liao area range widely and are relatively high, i.e., 98.12–184.70 and 21.75–162.95 ppm, respectively, indicating a significant involvement of depleted mantle. The Re contents in molybdenites also depend on the nature of sources that generate the porphyry Mo systems.

20.5 Representative Mo Deposits

The Mo deposits in NNCC include different types/styles formed in tectonic settings of magmatic arc, back-arc rift, and syn- to post-collision orogeny. Their geological, geochronological, and geochemical features are listed in Tables 20.1, 20.2 and 20.3. Three typical deposits are briefly introduced as below.

20.5.1 Giant Caosiyao Deposit: A Climax-Type Porphyry System

The giant Caosiyao Mo deposit (Table 20.1), located 3 km southeast of Xinghe County, Inner Mongolia (Fig. 20.5a), is now the largest porphyry Mo system in the NNCC, with an estimated reserve of 2 Mt Mo, grading 0.08 % (Nie et al. 2012). The main orebody is 1900-m long, 700–1400 m wide, and >900-m thick (Fig. 20.5b, c). The top of the orebody is strongly oxidized, to a depth of 150 m (Nie et al. 2012).

The veinlets, stockworks, and disseminations are the main mineralization, hosted in Mesozoic granite porphyry stock (with outcrop area of 0.08 km^2), as well as Archean-Paleoproterozoic sillimanite-garnet gneiss, granulite, and quartzite (Fig. 20.5a; Wu et al. 2016a). Faults of various scales

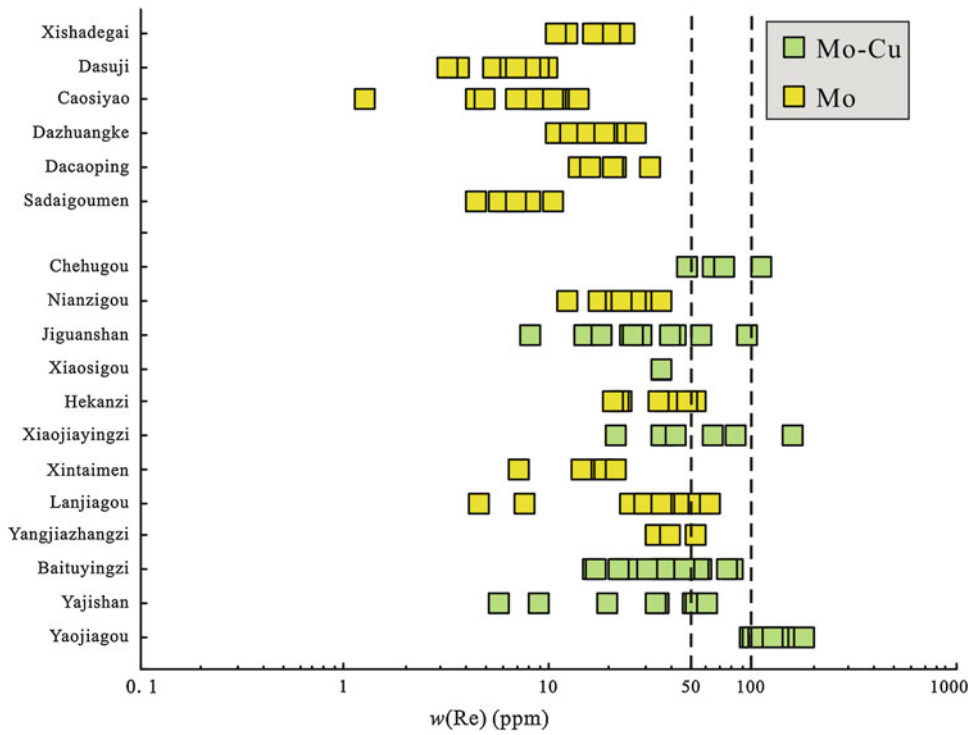

Fig. 20.4 Scatter of Re contents in molybdenites from the Mo-bearing deposits. Please see references in Table 20.2 for detail data

Table 20.2 Isotope ages and Re contents in molybdenite of Mo deposits in NNCC

No.	Deposit	Samples and method	Age (Ma)	Re (ppm) or MSWD	Num	References
1	Xishadegai	Molybdenite Re–Os isochron	226.4 ± 3.3	Av. Re = 17.04	9	Hou et al. (2010)
2	Dasuji	Molybdenite Re–Os isochron	222.5 ± 3.2	Av. Re = 6.15	4	Zhang et al. (2009b)
		Molybdenite Re–Os weighted mean	223.9 ± 1.4	Av. Re = 6.98	5	Wu et al. (2014a)
3	Caosiyao	Molybdenite Re–Os weighted mean	130.4 ± 2.4		4	Nie et al. (2012)
		Molybdenite Re–Os weighted mean	149.8 ± 1.0	Av. Re = 10.58	5	Wang et al. (2016b)
		Molybdenite Re–Os isochron	148.5 ± 1.1	Av. Re = 7.02	6	Wu et al. (2016a)
		Syenogranite porphyry, LA-ICP-MS Zircon U–Pb	148.5 ± 0.9	MSWD = 1.2	9	Wu et al. (2016a)
		Monzogranite porphyry, LA-ICP-MS Zircon U–Pb	145.0 ± 1.0	MSWD = 0.97	10	Wu et al. (2016a)
		Syenogranite porphyry, LA-ICP-MS Zircon U–Pb	140.9 ± 1.6	MSWD = 0.15	5	Wu et al. (2016a)
		Syenogranite porphyry, LA-ICP-MS Zircon U–Pb	140.1 ± 1.7	MSWD = 0.36	6	Wu et al. (2016a)
4	Zhangmajin	Rhyolite, SHRIMP zircon U–Pb	138.6 ± 1.4	MSWD = 2.4	12	Wu et al. (2015)
		Rhyolite porphyry, SHRIMP zircon U–Pb	140.2 ± 1.6	MSWD = 2.2	11	Wu et al. (2015)
		Quartz porphyry, SHRIMP zircon U–Pb	136.2 ± 2.9	MSWD = 1.8	11	Wu et al. (2015)
6	Dazhuangke	Molybdenite Re–Os isochron	146.4 ± 3.4	Av. Re = 15.79	3	Huang et al. (1996)
		Molybdenite Re–Os isochron	136.8 ± 2.6	Av. Re = 19.29	5	Liu et al., (2012)
7	Dacaoping	Molybdenite Re–Os isochron	140.1 ± 3.4	Av. Re = 21.15	5	Jiang et al. (2014)
		Granodiorite, LA-ICP-MS Zircon U–Pb	140.0 ± 1.5		6	Duan et al. (2007)
8	Sadaigoumen	Molybdenite Re–Os isochron	236 ± 10	Av. Re = 7.1	6	Jiang et al. (2014)
		Monzogranite, LA-ICP-MS Zircon U–Pb	247.7 ± 1.2	MSWD = 1.2	11	Wei et al. (2013)
		Monzogranite, LA-ICP-MS Zircon U–Pb	227.1 ± 2.7	MSWD = 1.1	?	Zeng et al. (2012b)
9	Chehugou	Molybdenite Re–Os isochron	245.0 ± 5.0	Av. Re = 73.50	5	Zeng et al. (2012b)
		Granite porphyry, biotite Rb–Sr isochron	244.0 ± 4.0		7	Wan et al. (2009)
10	Nianzigou	Molybdenite Re–Os isochron	154.3 ± 3.6	Av. Re = 23.12	7	Zhang et al. (2009c)
		Molybdenite Re–Os isochron	153.0 ± 5.0	Av. Re = 23.48	7	Zhang et al. (2009a)
		Monzogranite, whole rock Rb–Sr isochron	167.0 ± 2.0		5	Zhang et al. (2009a)
		Monzogranite, SHRIMP Zircon U–Pb	152.4 ± 1.6	MSWD = 0.28	10	Zeng et al. (2011)
11	Jiguanshan	Molybdenite Re–Os isochron	151.1 ± 1.3	Av. Re = 42.92	5	Chen et al. (2010)
		Molybdenite Re–Os isochron	155.4 ± 1.3	Av. Re = 26.18	7	Wu et al. (2011b)
		Granite porphyry, mica ^{40}Ar–^{39}Ar	155.1 ± 1.9		1	Wu et al. (2011b)
		Granite porphyry, LA-ICP-MS Zircon U–Pb	156.0 ± 1.3	MSWD = 2.5	14	Wu et al. (2014b)
12	Xiaosigou	Molybdenite Re–Os	134.0 ± 3.0	Re = 37.14 ± 0.50	1	Huang et al. (1996)
		Granodiorite porphyry, K–Ar	129.0		1	Dai et al. (2010)
13	Hekanzi	Molybdenite Re–Os isochron	222.8 ± 3.2	Av. Re = 34.84	6	Liu et al. (2012b)
		Biotite syenogranite, LA-ICP-MS zircon U–Pb	235.3 ± 1.0	MSWD = 0.68	20	Liu et al. (2012b)
		Syenogranite and biotite Rb–Sr isochron	221.4 ± 8.5		5	Ren et al. (2004)
14	Xiaojiayingzi	Molybdenite Re–Os isochron	161.3 ± 2.4	Av. Re = 64.31	6	Dai et al. (2009)
		Granite porphyry, SHRIMP zircon U–Pb	169.9 ± 1.4	MSWD = 1.7	12	Dai et al. (2009)
16	Songbei	Porphyry, LA-ICP-MS zircon U–Pb	181 ± 2			Zeng et al. (2013)
17	Xintaimen	Molybdenite Re–Os isochron	183.0 ± 3.0	Av. Re = 14.88	5	Zhang et al. (2009d)
		Granite porphyry, LA-ICP-MS zircon U–Pb	181.0 ± 2.0		?	Zhang et al. (2009d)
18	Lanjiagou	Re–Os isochron	186.5 ± 0.7	Av. Re = 37.24	5	Huang et al. (1996)
		Porphyritic granite, SHRIMP Zircon U–Pb	188.9 ± 1.2	MSWD = 1.03	18	Dai et al. (2008)
		Molybdenite Re–Os isochron	185.6 ± 1.4	Av. Re = 36.63	5	Zeng et al. (2012a)
		Porphyritic granite, LA-ICP-MS zircon U–Pb	185.0 ± 1.8	MSWD = 1.4	16	Zheng et al. (2014)

(continued)

Table 20.2 (continued)

No.	Deposit	Samples and method	Age (Ma)	Re (ppm) or MSWD	Num	References
19	Yangjiazhangzi	Molybdenite Re–Os isochron	187.0 ± 2.0	Av. Re = 40.40	3	Huang et al. (1996)
		Granite porphyry, LA-ICP-MS zircon U–Pb	182.0 ± 2.0		?	Liu et al. (2009)
		Porphyritic granite, LA-ICP-MS zircon U–Pb	181.30 ± 0.95	MSWD = 1.70	25	Xu et al. (2015)
		Porphyritic moyite, LA-ICP-MS zircon U–Pb	188.78 ± 0.86	MSWD = 0.77	26	Xu et al. (2015)
21	Baituyingzi	Molybdenite Re–Os isochron *(Kulitu)*	236.0 ± 3.3	Av. Re = 24.92	6	Zhang et al. (2009a)
		Molybdenite Re–Os weighted mean *(Kulitu)*	245.6 ± 1.6		5	Sun et al. (2013)
		Molybdenite Re–Os weighted mean *(Baimashigou)*	247.5 ± 1.8		4	Sun et al. (2013)
		Molybdenite Re–Os weighted mean *(Baituyingzi)*	247.0 ± 1.6		6	Sun et al. (2013)
		Monzogranite porphyry, LA-ICP-MS zircon U–Pb	249.1 ± 1.3			Sun et al. (2013)
22	Yajishan	Molybdenite Re–Os isochron	241.1 ± 1.4	Av. Re = 33.95	7	Dai et al. (2012)
24	Yaojiagou	Molybdenite Re–Os isochron	168.8 ± 3.9	Av. Re = 129.30	8	Fang et al. (2012)
25	Wanbaoyuan	Granodiorite, LA-ICP-MS zircon U–Pb	130.0		?	Sun et al. (2009)

Table 20.3 Genetic subdivision of the porphyry Mo deposits in NNCC

Deposit name	Fluid inclusion type					Comagmatic volcanics	Age (Ma)	Genetic type	References
	MC	C	CA	MA	A				
Baituyingzi	√	√	√	√	√	×	247	Dabie	Sun et al. (2016)
Chehugou	×	√	√	√	√	×	245	Dabie	Meng et al. (2013)
Sadaigoumen	√	√	√	√	√	×	236	Dabie	Dai et al. (2007b) and Jiang et al. (2014)
Dasuji	×	×	√	√	√	×	223	Dabie	Wu et al. (2014a)
Lanjiagou	×	×	√	√	√	×	185	Dabie	Dai et al. (2007a)
Jiguanshan	×	×	√	√	√	√	155	Climax	Wu et al. (2010b)
Caosiyao	×	√	√	√	√	√	148	Climax	Wu et al. (2016a) and Wang et al. (2016a)
Wanbaoyuan	×	×	×	×	√	√	130	Endako	Song et al. (2009)

Abbreviations of fluid inclusions: *A* aqueous fluid inclusion; *C* carbonic; *CA* carbonic-aqueous; *MA* mineral-bearing aqueous inclusion; *MC* mineral-bearing carbonic-aqueous inclusion

and directions are widespread in the ore district, of which the approximately E-W- and NE-trending faults are the foremost ore-controlling structures. The area has undergone strong weathering and erosion, but the Late Jurassic comagmatic volcanic rocks can be locally observed, particularly in the area about 10 km south of the deposit.

From orebody to wall rocks, alteration zoning consists of potassic, siliceous, sericitic, fluorite, and carbonate halos. The first three kinds of alteration are closely associated with Mo mineralization in space and time. The primary orem-inerals include pyrite, wolframite, magnetite, sphalerite, and galena. Molybdite is present in the weathered ore. Gangue minerals are quartz, plagioclase, K-feldspar, sericite, biotite, chlorite, fluorite, and calcite (Nie et al. 2012).

As shown in Table 20.2, the timing of the Caosiyao Mo mineralizing event has been determined using different isotopic systems. Nie et al. (2012) first reported four molybdenite Re–Os ages of 128.6 ± 2.4 to 131.9 ± 2.3 Ma, with a weighted mean Re–Os age of 130.4 ± 2.4 Ma. They considered that the Caosiyao Mo deposit was formed during the Yanshanian post-collision extensional tectonism, under which the previous deep faults were activated again, together within tense mag-matism and related hydrothermal fluid processes, resulting in the emplacement of Mo deposit at the intersection of different faults. Wang et al. (2016a) and Wu et al. (2016a) conducted a comprehensive study of the deposit and ore-causative intrusion, including geology, geochronology, element and isotope geo-chemistry, wall rock alteration, and fluid inclusion microther-mometry. The new data show that the Caosiyao is a Climax-type porphyry Mo system formed at ~148 Ma (Table 20.2), in Late Jurassic extensional setting, rather than in previously suggested Early Cretaceous. Here we relate the extension or rift to a back-arc tectonism caused by southeastward of the Mon-gol–Okhotsk oceanic plate (Fig. 20.2).

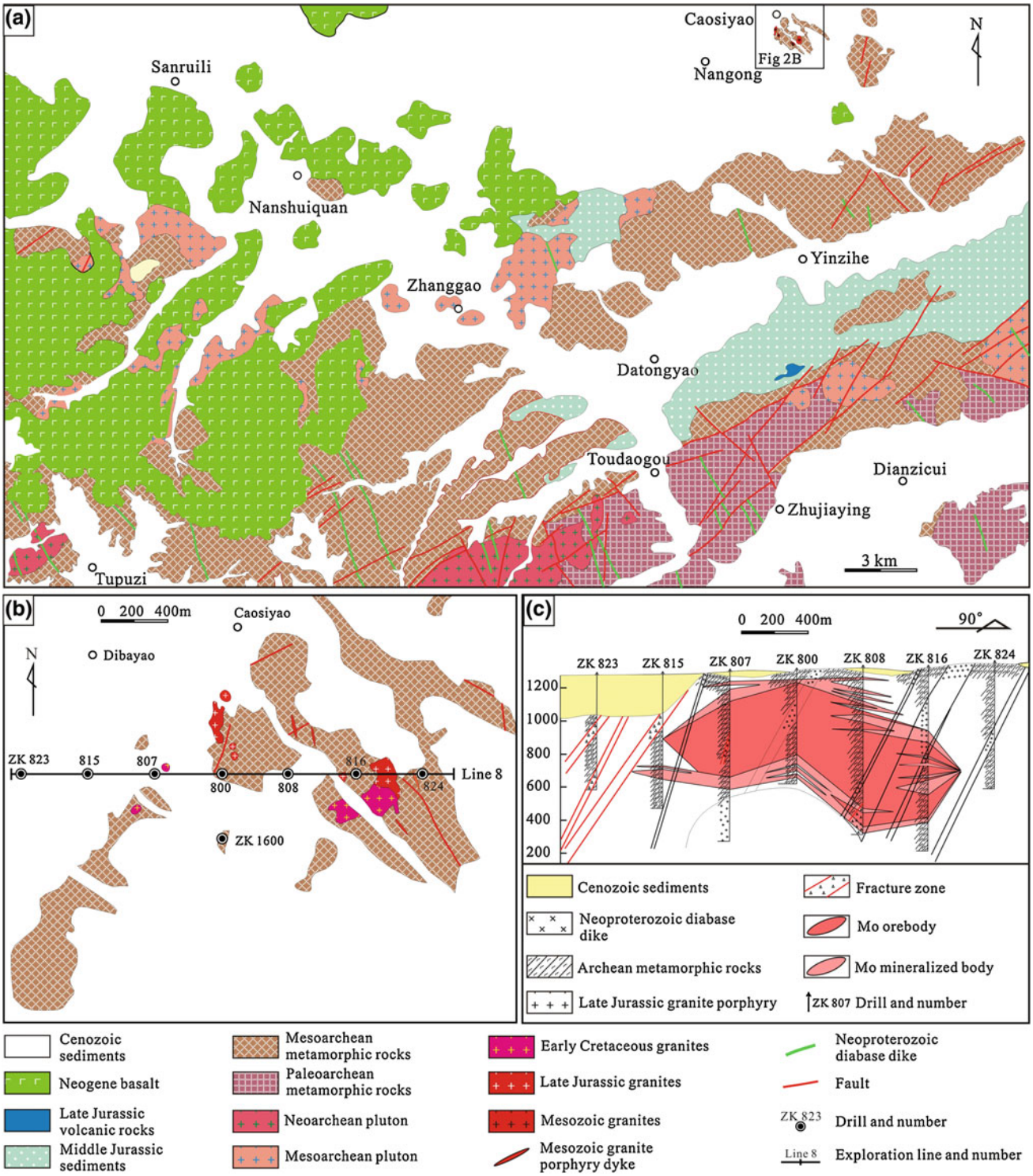

Fig. 20.5 **a** Regional geology of the Caosiyao deposit, **b** geological map of the Caosiyao deposit, and **c** geological profile for prospecting Line Number 8 of the Caisiyao deposit (modified after Wu et al. 2016a)

20.5.2 Xiaojiayingzi Mo–Cu–Fe Deposit: A Skarn System

The Xiaojiayingzi Mo–Cu–Fe skarn system (Fig. 20.1 and Table 20.1) in Kazuo County, Liaoning Province, contains 0.105 Mt Mo with an average grade of 0.23 %, and 8.87 Mt Fe with an average grade of 33.4 % (Dai et al. 2009). The deposit is in an area of Early Precambrian (Archean-Paleoproterozoic) metamorphic rocks, comprising biotite plagioclase gneiss, amphibolite, and granulite (Fig. 20.6a). These metamorphic rocks are unconformably overlain by the unmetamorphosed sedimentary successions of the uppermost Paleoproterozoic dolomite (Changcheng Group), the lowermost Mesoproterozoic carbonate (Wumishan Formation of the Jiaxian Group), Cambrian carbonate- siltstone, and Ordovician dolomitic limestone in ascending sequence. All these rocks mentioned above are unconformably covered by the Late Jurassic-Early Cretaceous volcanic rocks intercalated with lacustrine sediments, and locally intruded by Neopaleozoic to Jurassic granitic rocks, as well as by Neopaleozoic diabase dikes. The NE- and NW-trending faults well developed in the district and adjacent areas, which controlled the location and elongation of the intrusive rocks (Fig. 20.6a). These faults might serve as conduits for upward migration of the magmas.

According to Dai et al. (2009), mineralization at Xiaojiayingzi deposit was temporally and spatially associated with an Early Jurassic diorite stock that intruded the Mesoproterozoic carbonate rocks of the Wumishan Formation, Jixian Group (Fig. 20.6). The Xiaojiayingzi diorite stock covers an area of 0.8 km^2, and is composed mainly of 56.03 % SiO_2, 17.2 % Al_2O_3, 8.35 % FeO, 3.53 % Na_2O, and 3.09 % K_2O. More than 80 orebodies have been investigated in the diorite-carbonate contact zones (Fig. 20.6b). The majority of orebodies generally occur as veins, lenses, and pods, with lengths of 100–800 m, depths of 100–600 m and thicknesses of 4–21 m. Their ore grades range from 0.1 to 0.3 wt% Mo and 35–50 wt% Fe. The inner contact zone also contains a stockwork-style orebody that is 400 m long, 570 m deep and 10–30 m thick, with grades of 0.03–0.1 wt% Mo.

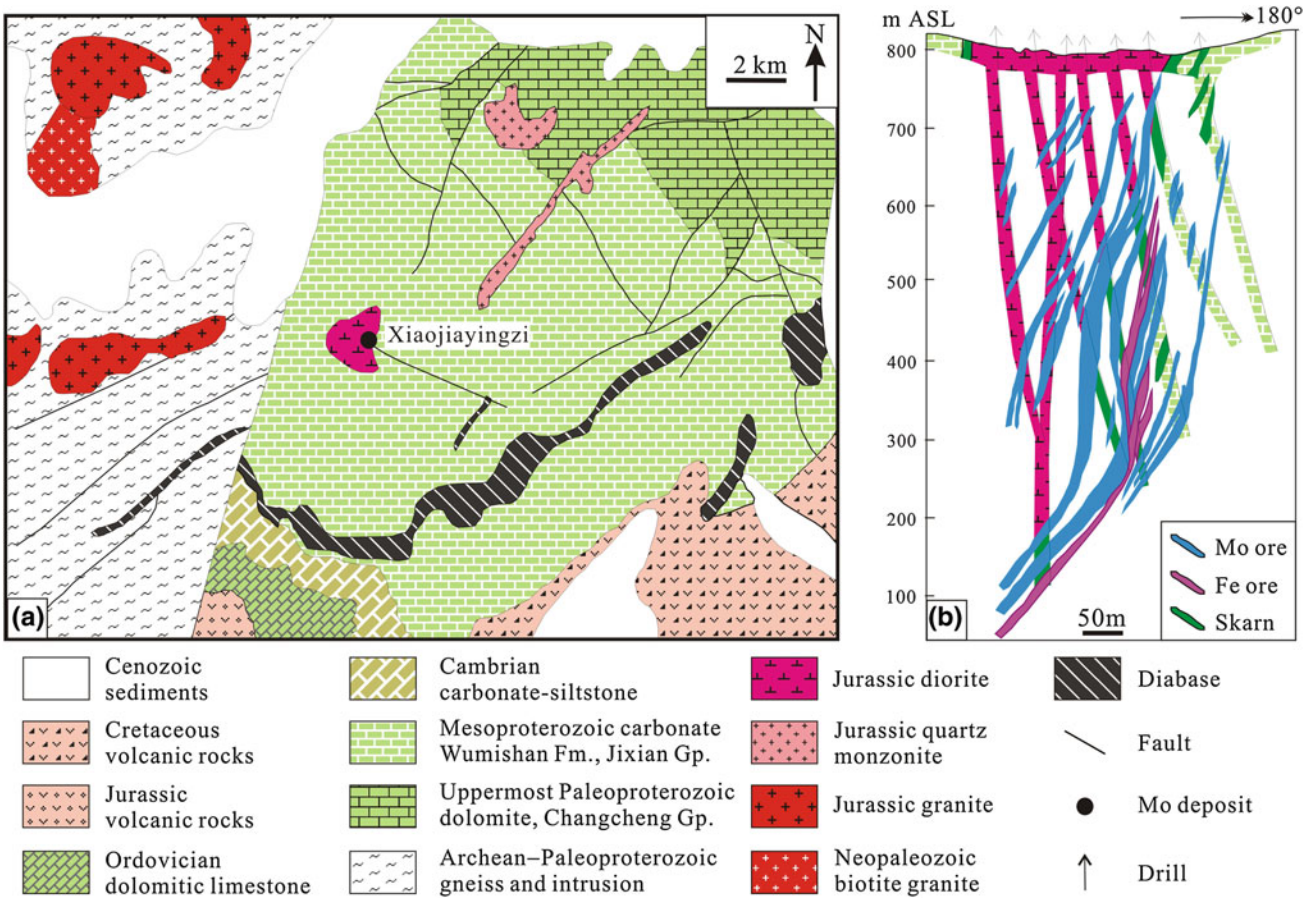

Fig. 20.6 **a** Map showing the regional geology of the Xiaojiayingzi Mo–Cu–Fe deposit, Liaoning province; and **b** geological profile showing the occurrence of orebodies and skarns in the contact zone between the diorite and carbonate rocks (modified after Dai et al. 2007a)

The Xiaojiayingzi Mo–Cu–Fe deposit shows well alteration zoning outward from diorite through skarn to dolomite, i.e., diorite → garnet skarn → garnet- diopside skarn → diopside-forsterite skarn → chondrodite-phlogopite skarn skarnized dolomite → dolomite (Dai et al. 2009). Molybdenite occurs in garnet and garnet-diopside skarns, and magnetite mainly in chondrodite-phlogopite skarns. Ore minerals include molybdenite, magnetite and pyrite, with minor chalcopyrite, galena, sphalerite, pyrrhotite, and less bornite, scheelite, marcasite, and native silver. Gangue minerals are garnet, diopside, tremolite, and calcite, with minor vesuvianite, wollastonite, chondrodite, phlogopite, K-feldspar and quartz (Dai et al. 2009).

The causative diorite at Xiaojiayingzi deposit yields a whole-rock K–Ar age of 113 Ma (Kang 1979). Huang et al. (1996) obtained a molybdenite Re–Os age of 177 ± 5 Ma. These two ages show too much difference to constrain the age of the mineral system, and thus Dai et al. (2009) conducted SHRIMP zircon U–Pb and molybdenite Re– Osisotope dating work. Twelve zircon grains yielded a SHRIMP U–Pb age 169.9 ± 1.4 Ma (MSWD = 1.7), and six molybdenite samples yielded Re–Os ages of 159.1 ± 2.6–165.8 ± 2.8 Ma, with an isochron age of 161.3 ± 2.4 Ma. These zircon U–Pb and molybdenite Re–Osages are geologically consistent, suggesting that the mineralization occurred in the period of 160–170 Ma, i.e., Middle Jurassic.

The Re contents in molybdenite range from 21 to 163 ppm (Table 20.2), suggesting a two-end member (mantle and supracrustal sediments) mixing source for the mineral system. Dai et al. (2009) proposed that the Xiaojiayingzi deposit resulted from the subduction of the Paleo-Pacific plate beneath the Eurasian plate. Here we prefer to link the mineral system with the post-collisional tectonic setting, following the termination of the Paleo-Asian Ocean.

20.5.3 Nianzigou Quartz Vein-Type Mo Deposit

The Nianzigou Mo deposit (Fig. 20.7 and Table 20.1), located 60 km northwest of Chifeng City, is a quartz vein-type Mo deposit in the NNCC. The deposit has 15 Kt Mo with an average grade of 0.39 %, ranking a middle-sized deposit (Zeng et al. 2011). Mo mineralization occurs as quartz veins hosted in the Yanshanian granite batholith (Fig. 20.8) that outcrops over an area of 200 km^2 (Zhang

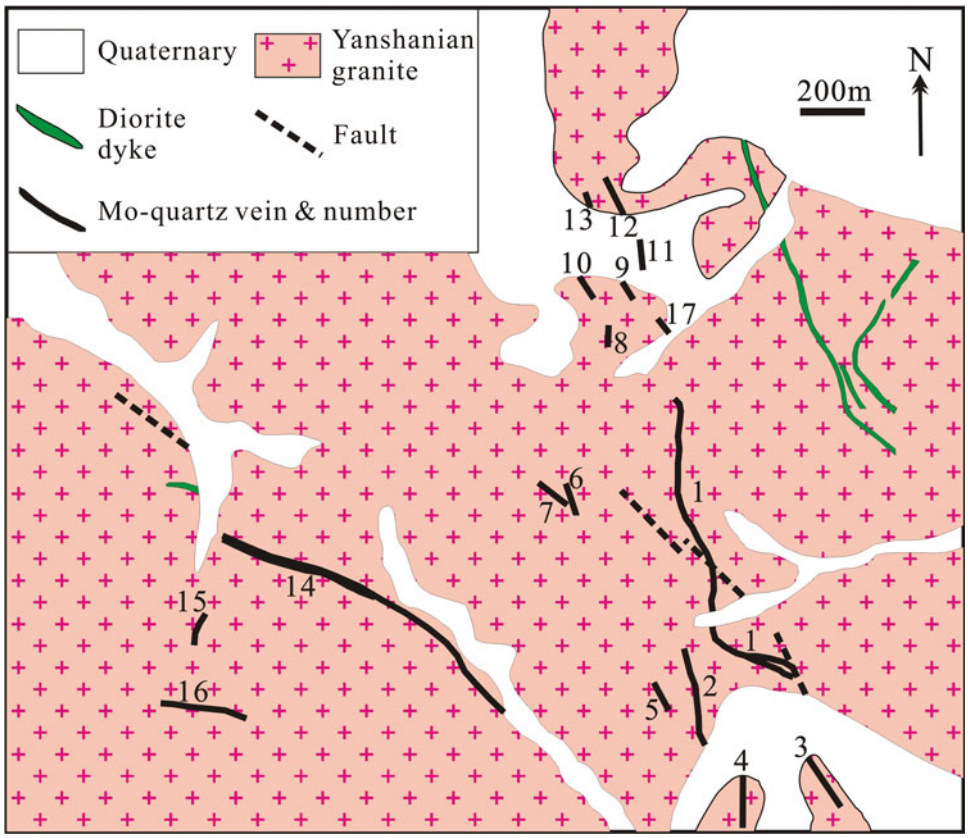

Fig. 20.7 Geological map of the Nianzigou Mo deposit, Inner Mongolia (modified after Zhang et al. 2009c)

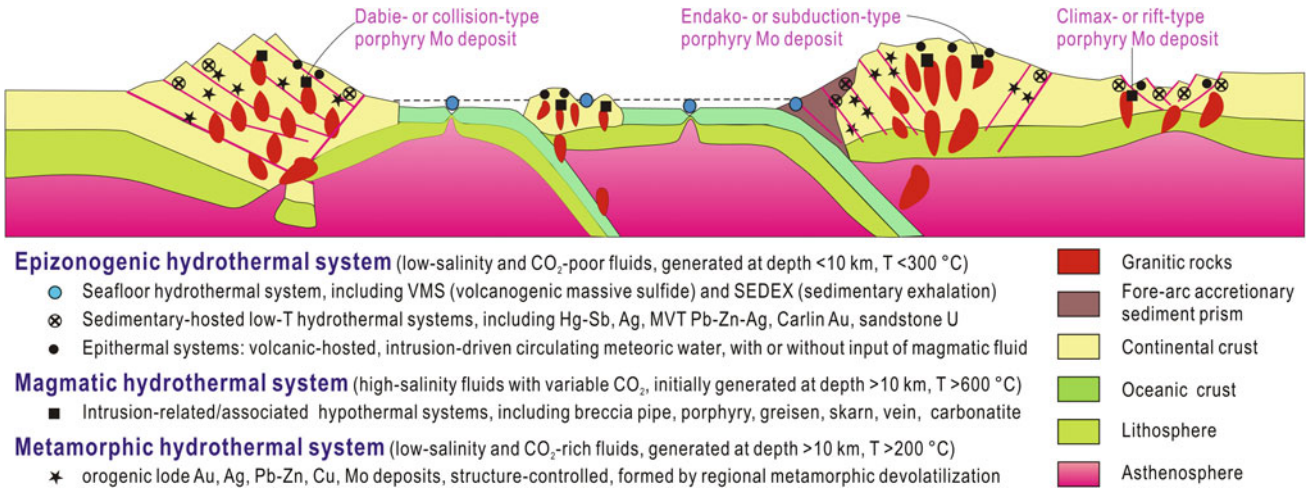

Fig. 20.8 Tectonic model for three types of porphyry Mo deposits (Chen et al. 2014)

et al. 2009c). Early Precambrian metamorphic rocks and Early Cretaceous volcanic rocks can be locally identified in the deposit and/or its vicinities.

Porphyritic monzogranite is the host rock and consists of quartz, K-feldspar, plagioclase and minor biotite, with magnetite, apatite and zircon as accessory minerals (Zhang et al. 2009a, c). The monzogranite has the following chemical composition: 65.57–70.97 % SiO_2, 4.55–5.48 % K_2O, 1.31–1.86 % CaO, 0.65–0.82 % MgO, 0.44–1.26 % FeO, 2.21–3.15 % Fe_2O_3, 0.06–0.09 % MnO and 0.44–0.62 % TiO_2, with ($K_2O + Na_2O$) of 8.52–9.85 %, and K_2O/Na_2O of 0.92–1.43 (Chen et al. 2008). These geochemical compositions show characteristics of A-type granites.

The deposit includes 17 Mo-bearing quartz veins, which are controlled by NW- and NNW-striking faults (Fig. 20.7). Four veins (Nos. 1, 2, 3 and 14) are most economically significant. Numbers 1, 2, and 3 are NW-trending (~345°), and Number 14 vein strikes WNW (~300°) (Zeng et al. 2011). Number 1 vein is 2.5 km long and 1.37–18.85 m thick. The Mo grades generally range from 0.08 to 1.39 %, with the highest up to 4.08 % (Zeng et al. 2011). Number 2 vein is 2 km long, 0.5–2.0 m thick, with Mo grade between 0.14 and 0.84 % (Zhang et al. 2009a). Number 3 vein is 1.1 km long, 0.60–4.52 m thick, with an average grade of 0.12 % (Zhang et al. 2009a). Number 14 vein, striking 1.1 km, mainly composed of fluorite, quartz, and minor sulfides, is not of economic significance at surface, but is gradually enriched in Mo at depth (Zeng et al. 2011).

The predominant alteration includes K-feldspathization, silicification, sericitization, fluoritization, and carbonation. K-feldspar alteration appears on both sides of quartz veins with a width of <2 m (Zeng et al. 2011), but the other kinds of alteration can be present in the host granite, forming a wide and pervasive alteration zone (Zhang et al. 2009c). The veins are brecciated and filled by veinlets, and show subhedral–euhedral crystalline and comb textures. Molybdenite is the dominant ore mineral accompanied by minor amounts of pyrite and chalcopyrite. Gangue minerals are mainly of quartz, followed by K-feldspar, sericite, calcite, and fluorite (Zhang et al. 2009a).

The host monzogranite yields a SHRIMP zircon U–Pb age of 152.4 ± 1.6 Ma (Zeng et al. 2011), and a whole-rock Rb–Sr isochron age of 167 ± 2 Ma (n = 5; Zhang et al. 2009a). Molybdenites from the Nianzigou Mo-bearing quartz veins yield two Re–Os isochron ages of 154.3 ± 3.6 Ma (n = 7; Zhang et al. 2009c) and 153.0 ± 5.0 Ma (n = 7; Zeng et al. 2011), respectively. These molybdenite Re–Os and zircon U–Pb ages are consistent with each other within errors, strongly suggesting that the monzogranite and its associated Mo mineralization occurred at 153 ± 5 Ma.

The Sr–Nd isotope signatures of the host granite suggest a crust-dominated source, with a minor contribution from the mantle (Zhang et al. 2009a). Re contents in molybdenite samples are all less than 50 ppm, suggesting a crustal source. Previous studies proposed that the Nianzigou Mo deposit was formed in the tectonic change from the Paleo-Asia to the Paleo-Pacific oceanic subduction systems in Middle Jurassic (Zeng et al. 2011). Here we consider a back-arc rifting setting related to the southeastward subduction of the Mongol–Okhotsk oceanic plate during the Late Jurassic to beginning Cretaceous (Fig. 20.2).

20.6 Tectonic Models of Mo Mineral Systems

As discussed above, the Mo deposits in NNCC were formed in four periods, i.e., the Triassic, Early Yanshanian, Mid-Yanshanian, and Late Yanshanian. Hereafter, we will briefly discuss their tectonic settings.

The Indosinian (Triassic) and Early Yanshanian (Early to Middle Jurassic) Mo deposits account for two-third of the total Mo deposits in NNCC. These deposits exhibit geological and geochemical features of the Mo deposits formed in continental syn- to post-collision tectonic settings (Table 20.1), similar to those in the southern margin of NCC (northeastern Qinling Orogen) (Chen et al. 2000a). The majority of these Triassic-Middle Jurassic deposits located in the southeastern side of the Solonker Suture (Chen et al. 2016b), where, resembling the northeastern Qinling Orogen to the north of the Shang-Dan Suture (Hu et al. 1988), acted as an overriding continental slab during continental collision (Fig. 20.2c) and was favorable for Mo mineralization. It is well accepted that the Indosinian and Early Yanshanian deposits in NE China were mainly formed in syn-collision and post-collision tectonic settings, respectively (Chen et al. 2007a, 2009; Chen and Li 2009; Zeng et al. 2013; Zhang et al. 2009a; Pirajno 2013; Zhang and Li 2014, 2016). The syn-collisional crustal shortening, thickening, and geotherm-increasing led to metamorphic dehydration, partial melting of thickened crust, and hydrothermal mineralization. The post-collisional compression-to-extension transition resulted in decompression and geotherm-increasing, thereby resulting in large-scale formation of mineral deposits, including Mo, Au, Ag, Cu, and Pb-Zn (Chen et al. 2000a, 2009; Dai et al. 2006; Zhang et al. 2010).

The Mid-Yanshanian (160–130 Ma) Mo deposits are spatially limited to the central NNCC, but none in the eastern NNCC (Fig. 20.1b). This scenario does not support previous views that the Mesozoic mineralization was eastward younging due to rolling back of the Pacific plate subduction (Mao et al. 2005; Chen et al. 2009), instead it suggests a genetic relation to the subduction of Mongol–Okhotsk oceanic plate (Chen et al. 2016b). These Mo deposits are mainly located in areas with Mid-Yanshanian volcanic rocks, and mainly present as Climax-type. Considering that an Endako-type porphyry Mo belt, represented by Diyanqin'amu (Wang et al. 2016b, c), Xing'a and Chalukou (Zhang and Li 2016), occurs northwest to the NNCC, these Mid-Yanshanian deposits are related to the southeastward subduction of the Mongol–Okhotsk oceanic plate, which is a case analogous to the spatial distribution of the Endako- and Climax-type Mo deposits in the Cordillera of western North America (Chen et al. 2016b).

The Late Yanshanian porphyry Mo deposits are only present in the eastern part of the NNCC (Fig. 20.1). They show geological and geochemical signatures of Endako-type deposits and are genetically related to the westward subduction of the Paleo-Pacific plate. It is noteworthy that the Late Yanshanian Mo deposits with similar geological features and geneses have been recognized in the Southeastern China coastal volcanic belt (Zhong et al. 2016), which suggests that the Paleo-Pacific plate likely began to subduct beneath the Eurasia continent since ~130 Ma. Nevertheless, no Mo deposit has been discovered in the accretionary complexes related to the Pacific plate subduction, e.g., the Nadanhada terrane (Chen et al. 2016b), which possibly suggests that young juvenile crust is not favorable for Mo mineralization.

It is worth noting that the Mo-only and Mo-dominant polymetallic deposits in NNCC began to appear in the Triassic when the Paleo-Asia Ocean was completely closed, indicating that the Mo mineralization can only occur in a region with matured continental crust. This phenomenon can be also observed in NW China, Qinling Orogen, and SE China. Mesozoic porphyry Mo deposits in NE China were formed in various tectonic settings and classified into Endako-, Climax-, and Dabie-types. The linkage between tectonic settings and genetic type of porphyry Mo deposits are shown in Fig. 20.8. This model shows that an island arc setting is not favorable for Mo mineralization.

20.7 Concluding Remarks

1. After the closure of the Paleo-Asian Ocean in Late Permian, the NCC continuously collided with the Siberia Craton to the North and the South China Block to the south, followed by subduction of the Mongol–Okhotsk and Pacific oceanic plates. These significant Mesozoic tectonic events destructed the NCC's stability and uniformity, and caused intensive hydrothermal mineralization of Mo, Au, Ag, and other metals. The NCC is the most important Mo province in the world, with the Mo deposits being concentrated at the southern and northern margins of NCC.
2. At least 27 Mo-only or Mo-dominated deposits have been discovered in NNCC, including one giant and eight large-size Mo systems, with a total reserve of 3.65 Mt Mo metal. These deposits mainly cluster in central NNCC. The deposits were formed during Mesozoic tectono-thermal events, postdating the closure of the Paleo-Asian Ocean, and peaking at around 250–200, 200–160, and 160–130 Ma.
3. Main genetic types are porphyry (including breccia pipe), porphyry–skarn, skarn and quartz vein, with the porphyry-type being predominant. The porphyry Mo deposits in NNCC can be further subdivided into three

subtypes, i.e., collision- or Dabie-, rift- or Climax-, and subduction- or Endako-types. Comagmatic volcanic rocks and fluid inclusion assemblages are useful criteria to distinguish genetic types of porphyry Mo deposits. The Re contents in molybdenite are a useful indicator of the ore-metal sources.

4. The Mo deposits aged 250–200-Ma and 200–160-Ma belong to Dabie- or collision-type and have been formed in syn- to post-collisional tectonic setting. The 160–130-Ma Mo mineralization mainly resulted from the southward subduction of the Mongol–Okhotsk oceanic plate. The 130–100-Ma deposits belong to Endako-type and are only located in the easternmost NNCC, which is likely related to the westward subduction of the Paleo-Pacific oceanic plate.

Acknowledgments This is a contribution from the Working Group on Mineral Deposits in Collisional Orogens (IAGOD). The study was financially supported by the 973-Projects (Nos. 2006CB403508 and 2012CB416602). The field work was supported by Chifeng Yuanye Changshun Geological Exploration Co., Ltd., and the Shandong Gold Group Co. Ltd. Drs. Cheng Zhang, Nuo Li and Pin Wang helped data collection and synthesis. Comments from professors Franco Pirajno and Mingguo Zhai improved the quality of this contribution.

References

Berzina, A. N., Sotnikov, V. I., Economou-Eliopoulos, M., & Eliopoulos, D. G. (2005). Distribution of rhenium in molybdenite from porphyry Cu–Mo and Mo–Cu deposits of Russia (Siberia) and Mongolia. *Ore Geology Reviews, 26*, 91–113.

Chai, P., Sun, J.-G., Xing, S.-W., Chen, L., & Han, J.-L. (2015). Geochemistry, zircon U–Pb analysis, and fluid inclusion $^{40}Ar/^{39}Ar$ geochronology of the Yingchengzi gold deposit, southern Heilongjiang Province, NE China. *Geological Journal*. doi: 10.1002/gj.

Chai, P., Sun, J.-G., Xing, S.-W., Li, B., & Cheng, L. (2016). Ore geology, fluid inclusion and $^{40}Ar/^{39}Ar$ geochronology constraints on the genesis of the Yingchengzi gold deposit, southern Heilongjiang Province, NE China. *Ore Geology Reviews, 72*, 1022–1036.

Chen, W.-J., Liu, J.-M., Liu, H.-T., Sun, X.-G., Zhang, R.-B., Zhang, Z.-L., et al. (2010). Geochronology and fluid inclusion study of the Jiguanshan porphyry Mo deposit, Inner Mongolia. *Acta Petrologica Sinica, 26*, 1423–1436 (in Chinese with English abstract).

Chen, Y.-J. (2002). Several problems in study of regional metallogenesis in China: Their relationship to continental collision. *Earth Science Frontiers, 9*, 319–328 (in Chinese with English abstract).

Chen, Y.-J., Chen, H.-Y., Zaw, K., Pirajno, F., & Zhang, Z.-J. (2007a). Geodynamic settings and tectonic model of skarn gold deposits in China: An overview. *Ore Geology Reviews, 31*, 139–169.

Chen, Y.-J., Guo, G.-J., & Li, X. (1998). Metallogenic geodynamic background of gold deposits in Granite-greenstone terrains of North China Craton. *Science China Earth Sciences, 41*, 113–120.

Chen, Y.-J., Li, C., Zhang, J., Li, Z., & Wang, H.-H. (2000a). Sr and O isotopic characteristics of porphyries in the Qinling molybdenum deposit belt and their implication to genetic mechanism and type. *Science China- Earth Sciences, 43*(Suppl. 1), 82–94.

Chen, Y.-J., & Li, N. (2009). Nature of ore-fluids of intercontinental inclusion-related hypothermal deposits and its difference from those in island arcs. *Acta Petrologica Sinica, 25*, 2477–2508 (in Chinese with English abstract).

Chen, Y.-J., Liu, C.-Q., Chen, H.-Y., Zhang, Z.-J., & Li, C. (2000b). Carbon isotope geochemistry of graphite deposits and ore-bearing khondalite series in North China: Implications for several problems. *Acta Petrologica Sinica, 16*, 233–244 (in Chinese with English abstract).

Chen, Y.-J., Pirajno, F., & Qi, J.-P. (2005). Origin of gold metallogeny and sources of ore-forming fluids, in the Jiaodong province, eastern China. *International Geologiy Review, 47*, 530–549.

Chen, Y.-J., Ni, P., Fan, H.-R., Pirajno, F., Lai, Y., Su, W.-C., et al. (2007b). Diagnostic fluid inclusions of different types hydrothermal gold deposits. *Acta Petrologica Sinica, 23*, 2085–2108 (in Chinese with English abstract).

Chen, Y.-J., Santosh, M., Somreville, I. D., & Chen, H.-Y. (2014). Indosinian tectonics and mineral systems in China: An introduction. *Geological Journal, 49*, 331–337.

Chen, Y.-J., Wang, P., Li, N., Yang, Y.-F., & Pirajno, F. (2016a). The collision-type porphyry Mo deposits in Dabie Shan, China. *Ore Geology Reviews*. doi: 10.1016/j.oregeorev.2016.03.025.

Chen, Y.-J., Zhai, M.-G., & Jiang, S.-Y. (2009). Significant achievements and open issues in study of orogenesis and metallogenesis surrounding the north China continent. *Acta Petrologica Sinica, 25*, 2695–2726 (in Chinese with English abstract).

Chen, Y.-J., Zhang, C., Li, N., Yang, Y.-F., & Deng, K. (2012). Geology of the Mo deposits in Northeast China. *Journal of Jilin University (Earth Science Edition), 42*, 1223–1268 (in Chinese with English abstract).

Chen, Y.-J., Zhang, C., Wang, P., Pirajno, F., & Li, N. (2016b). The Mo deposits of Northeast China: A powerful indicator of tectonic settings and associated evolutionary trends. *Ore Geology Reviews*. doi: 10.1016/j.oregeorev.2016.04.017.

Chen, Z.-G., Zhang, L.-C., Wu, H.-Y., Wan, B., & Zeng, Q.-D. (2008). Geochemistry study and tectonic background of A-type host granite in Nianzigou molybdenum deposit in Xilamulun molybdenum metallogenic belt, Inner Mongolia. *Acta Petrologica Sinica, 24*, 879–889 (in Chinese with English abstract).

Dai, J.-Z., Mao, J.-W., Xie, G.-Q., Yang, F.-Q., & Zhao, C.-S. (2007a). Ore-forming fluid characteristics and genesis of Lanjiagou molybdenum deposit in western Liaoning Province. *Mineral Deposits, 26*, 443–454 (in Chinese with English abstract).

Dai, J.-Z., Mao, J.-W., Yang, F.-Q., Ye, H.-S., Zhao, C.-S., Xie, G.-Q., et al. (2006). Geological characteristics and geodynamic background of molybdenum (copper) deposits along Yanshan-Liaoning metallogenic belt on northern margin of North China block. *Mineral Deposits, 25*, 598–615 (in Chinese with English abstract).

Dai, J.-Z., Mao, J.-W., Zhao, C.-S., Li, R.-F., Wang, R.-T., Xie, G.-Q., et al. (2008). Zircon SHRIMP U–Pb age and petro-geochemical features of the Lanjiagou granite in western Liaoning Province. *Acta Petrologica Sinica, 80*, 1555–1564 (in Chinese with English abstract).

Dai, J.-Z., Mao, J.-W., Zhao, C.-S., Xie, G.-Q., Yang, F.-Q., & Wang, Y.-T. (2009). New U–Pb and Re–Os age data and the geodynamic setting of the Xiaojiayingzi Mo (Fe) deposit, western Liaoning province, Northeastern China. *Ore Geology Reviews, 35*, 235–244.

Dai, J.-Z., Xie, G.-Q., Duan, H.-C., Yang, F.-Q., & Zhao, C.-S. (2007b). Characteristics and evolution of ore-forming fluids from the Sadaigoumen porphyry molybdenum deposit, Hebei. *Acta Petrologica Sinica, 23*, 2519–2529 (in Chinese with English abstract).

Dai, J.-Z., Xie, G.-Q., Wang, R.-T., Ren, T., & Wang, T. (2012). Re-Os isotope dating of molybdenite separates from the Yajishan Mo(Cu) deposit, Inner Mongolia, and its geological significance. *Geology in China, 39*, 1614–1621 (in Chinese with English abstract).

Dai, X.-L., Peng, S.-L., & Hu, X.-Z. (2010). Adakite in Xiaosigou porphyry copper–molybdenum deposit, Hebei Province: Age, geochemical characteristics and geological implications. *Mineral Deposits, 29*, 517–528 (in Chinese with English abstract).

Davis, G.-A., Zheng, Y.-D., Wang, Z., Brian, J.-D., Zhang, C.-H., & George, G. (2001). Mesozoic tectonic evolution of the Yanshan fold and thrust belt, with emphasison Hebei and Liaoning Province, Northern China. *Colorado Geological Society of America Memoir, 194*, 171–197.

Deng, J.-F., Zhao, G.-C., & Su, S.-G. (2005). Structure overlap and tectonic setting of Yanshan Belt in Yanshan Era. *Geotectonica et Metallogenia, 29*, 157–165 (in Chinese with English abstract).

Deng, X.-H., Chen, Y.-J., Santosh, M., & Yao, J.-M. (2013a). Genesis of the 1.76 Ga Zhaiwa Mo-Cu and its link with the Xiong'er volcanics in the North China Craton: Implications for accretionary growth along the margin of the Columbia supercontinent. *Precambrian Research, 227*, 337–348.

Deng, X.-H., Chen, Y.-J., Santosh, M., Zhao, G.-C., & Yao, J.-M. (2013b). Metallogeny during continental outgrowth in the Columbia supercontinent: Isotopic characterization of the Zhaiwa Mo-Cu system in the North China Craton. *Ore Geology Reviews, 51*, 43–56.

Duan, H.-C., Qin, Z.-Y., Lin, X.-H., Zhang, B.-H., Liu, X.-W., Zhang, X., et al. (2007). Zircon U–Pb ages of intrusive bodies in Dacaoping molybdenum ore district, Fengning County, Hebei Province. *Mineral Deposits, 26*, 634–642 (in Chinese with English abstract).

Fang, J.-Q., Nie, F.-J., & Zhang, K. (2012). Re–Os isotopic dating on molybdenite separates and its geological significance from the Yaojiagou molybdenum deposit, Liaoning Province. *Acta Petrologica Sinica, 28*, 372–378 (in Chinese with English abstract).

Fan, J.-Y., Liu, Z.-X., & Fu, H.-H. (2010). Geological features and genetic type of Halaguishan Mo deposit of Jianping County, Liaoning Province. *China Science and Technology Review, 13*, 335–336 (in Chinese).

Goldfarb, R. J., Taylor, R. D., Collins, G. S., Goryachev, N. A., & Orlandini, O. F. (2014). Phanerozoic continental growth and gold metallogeny of Asia. *Gondwana Research, 25*, 48–102.

Guo, H.-J., & Ma, S.-K. (2009). Analysis on the ore-controlling factors and peripheral prospecting for the Zhangmajing U–Mo Deposit in Guyuan County, Hebei Province. *Geological Survey and Research, 33*, 210–215 (in Chinese).

HBGMR (Heilongjiang Bureau of Geology and Mineral Resources). (1993). *Regional geology of Heilongjiang Province* (pp. 1–734). Beijing: Geological Publishing House (in Chinese).

Hou, W.-R., Nie, F.-J., Du, A.-D., Li, C., Jiang, S.-H., Bai, D.-M., et al. (2010). Re–Os isotopic dating of molybdenite from Xishadegai molybdenum deposit in Urad Front Banner of Inner Mongolia and its geological significance. *Mineral Deposits, 29*, 1045–1053 (in Chinese with English abstract).

Hu, J.-M., Liu, X.-W., Zhao, Y., Xu, G., Liu, J., & Zhang, Q.-H. (2004). On Yanshan intraplate orogen: An example from Taiyanggou Area, Lingyuan, western Liaoning Province, Northeast China. *Earth Science Frontiers, 11*, 255–271 (in Chinese with English abstract).

Hu, S.-X. (2002). *Petrology of metasomatic rocks and implications for ore exploration* (pp. 1–264). Beijing: Science Press (in Chinese).

Hu, S.-X., Lin, Q.-L., Chen, Z.-M., & Li, S.-M. (1988). *Geology and metallogeny of the collision belt between the South China and North China plates* (pp. 1–558). Nanjing: Nanjing University Press (in Chinese).

Hu, T.-J., Song, J.-C., Wang, E.-D., Zhang, C.-S., Wei, M., & Sun, L.-J. (2009). Geological characteristics and metallogenic mechanism of the Wanbaoyuan Mo deposit in Kuandian of Liaoning. *Mineral Resources and Geology, 23*, 142–146 (in Chinese with English abstract).

Huang, D.-H. (2007). *Geological features and metallogenic spatial and temporal evolution of the two most important molybdenum belt in China* (pp. 297–302). A Collection of the 5th National Conference on Geological Mapping and GIS (in Chinese).

Huang, D.-H., Du, A.-D., & Wu, C.-Y. (1996). Metallochronlogy of molybdenum(-copper) deposits in the North China Craton: Re–Os age of molybdenite and its geological significance. *Mineral Deposits, 15*, 365–373 (in Chinese with English abstract).

Huang, J.-Q. (1997). *Evolution of Tethys Sea in China and Adjacent Region*. Beijing: Geological Publishing House (in Chinese).

Jiang, S.-H., Liang, Q.-L., & Bagas, L. (2014). Re–Os ages for molybdenum mineralization in the Fengning region of northern Hebei Province, China: New constraints on the timing of mineralization and geodynamic setting. *Journal of Asian Earth Sciences, 79*, 873–883.

Jiao, Y.-H. (2010). Analysis on geological condition and exploration of Babailong Mo deposit, Huludao City, Liaoning Province. *Science, Technology and Life, 8*, 10 (in Chinese).

Kang, S.-Z. (1979). *Preliminary prospecting report of Xiaojiayingzi Mo polymetallic deposit, Kazuo County, Liaoning Province* (pp. 24–38). Chaoyang, Liaoning: Institute of Geological Exploration (in Chinese).

Khashgerel, B. E., Rye, R. O., Hedenquist, J. W., & Kavalieris, I. (2006). Geology and reconnaissance stable isotope study of the Oyu Tolgoi porphyry Cu–Au system, South Gobi, Mongolia. *Economic Geology, 101*, 503–522.

Kravchinsky, V. A., Cogné, J. P., Harbert, W. P., & Kuzmin, M. I. (2002). Evolution of the Mongol–Okhotsk Ocean as constrained by new palaeomagnetic data from the Mongol–Okhotsk suture zone, Siberia. *Geophysical Journal International, 148*, 34–57.

Li, B.-L., Zhang, J., Zhang, H., Xu, Q.-L., & Yu, Z.-X. (2010). Ore-forming fluid features and metallogenesis of Yajishan molybdenum–copper deposit, Chifeng City, Inner Mongolia. *Journal of Jilin University (Earth Science Edition), 40*, 61–72 (in Chinese with English abstract).

Li, N., Chen, Y.-J., Zhang, H., Zhao, T.-P., Deng, X.-H., Wang, Y., et al. (2007). Geological features and tectonic background of molybdenum deposits in East Qinling. *Earth Science Frontiers, 14*, 186–198 (in Chinese with English abstract).

Li, N., & Pirajno, F. (2016). Triassic (-Early Jurassic) Mo mineralization in the Qinling Orogen: An overview. *Ore Geology Reviews*. doi: 10.1016/j.oregeorev.2016.03.008.

Li, N., Ulrich, T., Chen, Y.-J., Thompson, T. B., Peace, V., & Pirajno, F. (2012). Fluid evolution of the Yuchiling porphyry Mo deposit, East Qinling, China. *Ore Geology Reviews, 48*, 442–459.

Li, P.-Z., & Yu, L.-S. (1994). Isotopic geochemistry of Nianzishan alkaline granite. In H.-S. Chen (Ed.), *Isotope geochemical research* (pp. 269–286). Hangzhou: Zhejiang University Press (in Chinese).

Liu, J., Cao, Y.-L., Wang, G.-J., Zhao, J.-C., & Yan, Z.-Q. (2010). Mineralization characteristics of Qiongbangzigou molybdenum deposits, Huanren County, Liaoning Province. *Journal of Nonferrous Metals, 62*(3), 27–30 (in Chinese).

Liu, J.-M., Zhang, R., & Zhang, Q.-Z. (2004). The regional metallogeny of Da Hinggan Ling, China. *Earth Science Frontiers, 11*, 269–277 (in Chinese with English abstract).

Liu, J.-Q. (1999). *Volcanoes in China*. Beijing: Science Press (in Chinese).

Liu, S.-B., Li, C., Cen, K., & Qu, W.-J. (2012a). Re–Os dating for molybdenite-bearing rock samples: Application in Dazhuangke molybdenum deposit in Beijing. *Geoscience, 26*, 254–260 (in Chinese with English abstract).

Liu, X.-L., Fan, P., Zheng, Z.-F., & Li, A.-L. (2009). The Yangjiazhangzi-Bajiazi molybdenum–polymetal metallogenic belt in western Liaoning Province. *Geology and Resources, 18*(2), 110–115 (in Chinese with English abstract).

Liu, Y., Nie, F.-J., & Fang, J.-Q. (2012b). Isotopic age dating of the alkaline intrusive complex and its related molybdenum polymetallic deposit at Hekanzi, western Liaoning Province. *Mineral Deposits, 31*, 1326–1336 (in Chinese with English abstract).

Lu, Y.-H., Zhang, Y., Lai, Y., & Wang, Y.-Z. (2009). LA-ICPMS zircon U–Pb dating of magmatism and mineralization in the Jinchang gold ore-field, Heilongjiang Province. *Acta Petrologica Sinica, 25*, 2902–2912 (in Chinese with English abstract).

Luo, M.-J., Zhang, F.-M., Dong, Q.-Y., Xu, Y.-R., Li, S.-M., & Li, K.-H. (1991). *Chinese molybdenum deposits* (pp. 1–425). Zhengzhou: Henan Science and Technology Press (in Chinese).

Mao, J.-W., Pirajno, F., Lehmann, B., Luo, M.-C., & Berzina, A. (2014). Distribution of porphyry deposits in the Eurasian continent and their corresponding tectonic settings. *Journal of Asian Earth Sciences, 79*, 576–584.

Mao, J.-W., Pirajno, F., Xiang, J.-F., Gao, J.-J., Ye, H.-S., Li, Y.-F., et al. (2011). Mesozoic molybdenum deposits in the east Qinling-Dabie orogenic belt: Characteristics and tectonic setting. *Ore Geology Reviews, 43*, 264–293.

Mao, J.-W., Xie, G.-Q., Zhang, Z.-H., Li, X.-F., Wang, Y.-T., Zhang, C.-Q., et al. (2005). Mesozoic large-scale metallogenic pulses in North China and corresponding geodynamic setting. *Acta Petrologica Sinica, 21*, 169–188 (in Chinese with English abstract).

Mao, J.-W., Zhang, Z.-C., & Zhang, Z.-H. (1999). Re–Os isotopic dating of molybdenites in the Xiaoliugou W(Mo) deposit in the northern Qilian Mountains and its geological significance. *Geochimica et Cosmochimica Acta, 63*, 815–1818.

Meng, S., Yan, C., Lai, Y., Shu, Q.-H., & Sun, Y. (2013). Study on the mineralization chronology and characteristics of mineralization fluid from the Chehugou porphyry Mo–Cu deposit, Inner Mongolia. *Acta Petrologica Sinica, 29*, 255–269 (in Chinese with English abstract).

Mi, M., Chen, Y.-J., Yang, Y.-F., Wang, P., Xu, Y.-L., Li, F.-L., et al. (2015). Geochronology and geochemistry of the giant Qian'echong Mo deposit, Dabie Shan, eastern China: Implications for ore genesis and tectonic setting. *Gondwana Research, 27*, 1217–1235.

Ni, P., Wang, G.-G., Yu, W., Chen, H., Jiang, L.-L., Wang, B.-H., et al. (2015). Evidence of fluid inclusions for two stages of fluid boiling in the formation of the giant Shapinggou porphyry Mo deposit, Dabie Orogen, Central China. *Ore Geology Reviews, 65*, 1078–1094.

Nie, F.-J., Liu, Y.-F., Zhao, Y.-A., Yu, A., & Cao, Y. (2012). Discovery of Dasuji and Caosiyao large-size Mo deposits in central Inner Mongolia and its geological significances. *Mineral Deposits, 31*, 930–940 (in Chinese with English abstract).

Pirajno, F. (2009). *Hydrothermal processes and mineral systems* (pp. 1–1250). Berlin: Springer.

Pirajno, F. (2013). *The geology and tectonic settings of China's mineral deposits* (pp. 1–679). Berlin: Springer.

Pirajno, F., & Zhou, T.-F. (2015). Intracontinental porphyry and porphyry–skarn mineral systems in eastern China: Scrutiny of a special case "made-in-China". *Economic Geology, 110*, 603–629.

Qi, J.-P., Chen, Y.-J., & Li, Q.-Z. (2004). The epithermal deposits in the northern margin of North China Craton: Spatiotemporal distribution and tectonic setting. *Journal of Mineralogy and Petrology, 24*(3), 82–92 (in Chinese with English abstract).

Qi, J.-P., Chen, Y.-J., & Pirajno, F. (2005). Geological characteristics and tectonic setting of the epithermal deposits in the Northeast China. *Journal of Mineralogy and Petrology, 25*(2), 47–59 (in Chinese with English abstract).

Ren, J.-S., Chen, T.-Y., & Niu, B. (1992). *The tectonic evolution and mineralization of continental lithosphere of eastern China and the adjacent region*. Beijing: Science Press (in Chinese).

Ren, K.-X., Yan, G.-H., Mou, B.-L., Cai, J.-H., Li, Y.-K., & Chu, Z.-Y. (2004). Geochemical characteristics and geological implications of the Hekanzi alkaline complex in Lingyuan County, western Liaoning Province. *Acta Petrologica et Mineralogica, 23*, 193–202 (in Chinese with English abstract).

Ruzhentsev, S. V., & Nekrasov, G. E. (2009). Tectonics of the Aga Zone, Mongolia–Okhotsk Belt. *Geotectonics, 43*, 34–50.

Sengor, A. M. C., & Natal'in, B. A. (1996). Paleotectonics of Asia: Fragments of synthesis. In A. Yin & T. M. Harrison (Eds.), *The tectonic evolution of Asia* (pp. 486–640). Cambridge: Cambridge University Press.

Shao, J.-A., & Tang, K.-D. (1996). *Terrain in Northeast China and the evolution of continental margin of East Asia*. Beijing: Seismological Press (in Chinese).

Shao, J.-A., & Tang, K.-D. (2015). Research on the Mesozoic ocean-continent transitional zone in the Northeast Asia and its implication. *Acta Petrologica Sinica, 31*, 3147–3154 (in Chinese with English abstract).

Shao, J.-A., & Zhang, L.-Q. (1999). Magmatism in the Mesozoic extending orogenic process of Hinggan Mts. *Earth Science Frontiers, 6*, 339–346 (in Chinese with English abstract).

Shao, Z.-B., Jiang, Z.-H., Li, X.-J., & Zhao, S.-T. (2008). Geological features and prospecting signs of Mo-polymetallic ore field in Hekanzi. *Nonferrous Mining and Metallurgy, 24*(2), 11–14 (in Chinese).

Song, J.-C., Jia, S.-S., Wang, E.-D., Hu, T.-J., & Wang, K.-F. (2009). Fluid inclusions and origin of the Wanbaoyuan porphyry Mo deposit. *Geology and Exploration, 45*(5), 539–548 (in Chinese with English abstract).

Sorokin, A. A., Kudryashov, N. M., & Kotov, A. B. (2007). Age and geochemistry of the Early Mesozoic granitoid massifs of the southern Bureya Terrane of the Russian Far East. *Russian Journal of Pacific Geology, 1*, 454–463.

Stein, H. J., Markey, R. J., & Morgan, J. W. (2001). The remarkable Re–Os chronometer in molybdenite: How and why it works. *Terra Nova, 13*, 479–486.

Stein, H. J., Markey, R. J., Morgan, J. W., Du, A., & Sun, Y. (1997). Highly precise and accurate Re–Os ages for molybdenite from the East Qinling Molybdenum Belt, Shanxi Province, China. *Economic Geology, 92*, 827–835.

Sun, J.-G., Zhang, Y., Xing, S.-W., Zhao, K.-Q., Zhang, Z.-J., Bai, L.-A., et al. (2012). Genetic types, ore-forming age and geodynamic setting of endogenic molybdenum deposits in the eastern edge of Xing-Meng Orogenic Belt. *Acta Petrologica Sinica, 28*, 1317–1332 (in Chinese with English abstract).

Sun, R.-G., Li, J.-X., & Li, J.-C. (2009). Geological features and genetic discussion of the Wanbao porphyry Mo deposit, Dandong City. *Western Exploration Engineering, 9*, 109–112 (in Chinese).

Sun, W.-T., & Sun, J.-G. (2008). Ore-controlling factors and periphery prospecting of Sipingjie skarn Mo deposit, Kuandian, Liaoning Province. *Science and Technology Innovation Herald, 1*, 40–41 (in Chinese).

Sun, Y., Liu, J.-M., Zeng, Q.-D., Chu, X.-S., Zhou, L.-L., Wu, G.-B., et al. (2013). Geological characteristics and molybdenite Re-Os ages of the Baituyingzi Mo-Cu field, eastern Inner Mongolia and their geological implications. *Acta Petrologica Sinica, 29*, 241–254.

Sun, Y., Liu, J.-M., Zeng, Q.-D., Wang, J.-B., Wang, Y.-W., & Hu, R.-Z., et al. (2016). Geology and hydrothermal evolution of the Baituyingzi porphyry Mo (Cu) deposit, eastern Inner Mongolia, NE China: Implications for Mo and Cu precipitation mechanisms in CO_2-rich fluids. *Ore Geology Reviews*. doi: 10.1016/j.oregeorev.2016.03.023.

Tang, H.-S., Chen, Y.-J., Santosh, M., Zhong, H., & Yang, T. (2013). REE geochemistry of carbonates from the Guanmenshan Formation, Liaohe Group, NE Sino-Korean Craton: Implications for seawater compositional change during the Great Oxidation Event. *Precambrian Research, 227*, 316–336.

Tang, H.-S., Chen, Y.-J., & Wu, G. (2009). Rare earth element geochemistry of carbonates of Dashiqiao Formation, Liaohe Group, Eastern Liaoning Province: Implications for Lomagundi Event. *Acta Petrologica Sinica, 25*, 3075–3093 (in Chinese with English abstract).

Tang, H.-S., Chen, Y.-J., & Wu, G. (2011). Paleoproterozoic positive $\delta^{13}C$ excursion in the northeastern Sinokorean Craton: Evidence of the Lomagundi Event. *Gondwana Research, 19*, 471–481 (in Chinese with English abstract).

Tian, Y.-C. (1999). Metallogenic structure, magmatic evolution and mineralization process of molybdenum mineral area of Lanjiagou, West Liaoning. *Mineral Resource and Geology, 13*(3), 135–140 (in Chinese with English abstract).

Tomurtogoo, O., Windley, B. F., Kröner, A., Badarch, G., & Liu, D.-Y. (2005). Zircon age and occurrence of the Adaatsag ophiolite and Muron shear zone, central Mongolia: Constraints on the evolution of the Mongol–Okhotsk ocean, suture and orogen. *Journal of the Geological Society, 162*, 125–134.

Wan, B., Hegner, E., & Zhang, L.-C. (2009). Rb–Sr geochronology of chalcopyrite from the Chehugou porphyry Mo–Cu deposit (Northeast China) and geochemical constraints on the origin of hosting granites. *Economic Geology, 104*, 351–363.

Wang, D.-Z., Zhao, G.-T., & Qiu, J.-S. (1995). The tectonic constraint on the Late Mesozoic A-type granitoids in eastern China. *Geological Journal of China Universities, 1*(2), 13–21 (in Chinese with English abstract).

Wang, G.-R., Wu, G., Xu, L.-Q., Li, X.-Z., Liu, J., & Zhang, T., et al. (2016a). Molybdenite Re-Os age, H-O-C-S-Pb isotopes, and fluid inclusion study of the Caosiyao porphyry Mo deposit in Inner Mongolia, China, and their geological significance. *Ore Geology Reviews* (in press).

Wang, P., Chen, Y.-J., Fu, B., Yang, Y.-F., Mi, M., & Li, Z.-L. (2014). Fluid inclusion and H-O-C isotope geochemistry of the Yaochong porphyry Mo deposit in Dabie Shan, China: A case study of porphyry systems in continental collision orogens. *International Journal of Earth Sciences, 103*, 777–797.

Wang, P., Chen, Y.-J., Wang, C.-M., & Wang, S.-X. (2016b). Genesis and tectonic setting of the giant Diyanqinamu porphyry Mo deposit in Great Hinggan Range, NE China: Constraints from U–Pb and Re–Os geochronology and Hf isotopic geochemistry. *Ore Geology Reviews* (in press).

Wang, P., Wang, Y., & Yang, Y.-F. (2016c). Zircon U–Pb geochronology and isotopic geochemistry of the Tangjiaping Mo deposit, Dabie Shan, China: Implications for ore genesis and tectonic setting. *Ore Geology Reviews* (in press).

Wei, R., Wang, J.-G., Wang, Y.-T., & Wang, S.-W. (2013). Zircon U–Pb dating of adamellite from the Sadaigoumen porphyry molybdenum deposit in Fengning, Hebei Province, and its significance. *Geology in China, 40*, 1736–1748 (in Chinese with English abstract).

Windley, B. F., Alexeiev, D., Xiao, W.-J., Kröner, A., & Badarch, G. (2007). Tectonic models for accretion of the Central Asian Orogenic Belt. *Journal of the Geological Society, London, 64*, 31–47.

Wu, F.-Y., Sun, D.-Y., Ge, W.-C., Zhang, Y.-B., Grant, M.-L., Wilde, S.-A., et al. (2011a). Geochronology of the Phanerozoic granitoids in northeastern China. *Journal of Asian Earth Sciences, 41*, 1–30.

Wu, F.-Y., Sun, D.-Y., & Lin, Q. (1999). Petrogenesis of the Phanerozoic granites and crustal growth in Northeast China. *Acta Petrologica Sinica, 15*, 181–189 (in Chinese with English abstract).

Wu, G., Chen, Y.-J., Sun, F.-Y., Qi, J.-P., Li, Z.-T., & Wang, X.-J. (2006). Geological characteristics and tectonic setting of gold deposits in the central segment of the Mongol–Okhotsk Metallogenic Belt. *Mineral Deposits, 25*, 51–54 (in Chinese with English abstract).

Wu, G., Chen, Y.-J., Sun, F.-Y., Zhang, Z., Liu, A.-K., & Li, Z.-T. (2010a). Geochemistry and genesis of the Late Jurassic granitoids at northern Great Hinggan Range: Implications for exploration. *Acta Geologica Sinica (English edition), 84*, 321–332.

Wu, G., Li, X.-Z., Xu, L.-Q., Wang, G.-R., Liu, J., & Zhang, T. et al. (2016a). Geochronology, geochemistry, and Sr-Nd-Hf-Pb isotopes of the Caosiyao porphyry Mo deposit in Inner Mongolia, China, and their geological significance. *Ore Geology Reviews* (in press).

Wu, H., Wu, G., Tao, H., Wang, G.-R., Li, T.-G., Chen, J.-Q., et al. (2014a). Molybdenite Re-Os dating and fluid inclusion study of Dasuji porphyry molybdenum deposit in Zhuozi county, central Inner Mongolia. *Mineral Deposits, 33*, 1251–1267 (in Chinese with English abstract).

Wu, H.-Y., Zhang, L.-C., Chen, Z.-G., Wan, B., Xiang, P., & Zhang, X.-J. (2010b). Hypersaline, high-oxygen fugacity and F-rich fluid inclusions in Jiguanshan porphyry molybdenum deposit, Xilamulun metallogenic belt. *Acta Petrologica Sinica, 26*, 1363–1374 (in Chinese with English abstract).

Wu, H.-Y., Zhang, L.-C., Pirajno, F., Xiang, P., Wan, B., Chen, Z.-G., et al. (2014b). The Jiguanshan porphyry Mo deposit in the Xilamulun metallogenic belt, northern margin of the North China Craton, U–Pb geochronology, isotope systematics, geochemistry and fluid iclusion studies: Implications for a genetic model. *Ore Geology Reviews, 56*, 549–565.

Wu, H.-Y., Zhang, L.-C., Wan, B., Chen, Z.-G., Xiang, P., Pirajno, F., et al. (2011b). Re–Os and $^{40}Ar/^{39}Ar$ ages of the Jiguanshan porphyry Mo deposit, Xilamulun metallogenic belt, NE China, and constraints on mineralization events. *Mineralium Deposita, 46*, 171–185.

Wu, J.-H., Ding, H., Niu, Z.-L., Wu, R.-G., Zhu, M.-Q., Guo, G.-L., et al. (2015). SHRIMP zircon U–Pb dating of country rock in Zhangmajing U–Mo deposit in Guyuan, Hebei Province, and its geological significance. *Mineral Deposits, 34*, 757–768 (in Chinese with English abstract).

Wu, Y.-S., Wang, P., Yang, Y.-F., Xiang, N., Li, N., & Zhou, K.-F. (2014c). Ore geology and fluid inclusion study of the Donggebi giant porphyry Mo deposit, Eastern Tianshan, China. *Geological Journal, 49*, 559–573.

Wu, Y.-S., Zhou, K.-F., Li, N., & Chen, Y.-J. (2016b). Zircon U–Pb dating and Sr-Nd-Pb-Hf isotopes of the ore-associated porphyry at the giant Donggebi Mo deposit, Eastern Tianshan, NW China. *Ore Geology Reviews*. doi:10.1016/j.oregeorev.2016.02.007.

Xiao, W.-J., Windley, B.-F., Hao, J., & Zhai, M.-G. (2003). Accretion leading to collision and the Permian Solonker suture. Inner Mongolia, China: Termination of the central Asian orogenic belt. *Tectonics, 22*, 1069–1076.

Xu, X.-C., Zhang, X.-X., Zheng, C.-Q., Cui, F.-H., Gao, Y., & Gao, F. (2015). Geochemistry and chronology characteristics of the intrusive rocks and its relationship with mineralization in Yangjiazhangzi area, the western Liaoning Province. *Journal of Jilin University (Earth Science Edition), 45*, 804–819.

Yang, Y.-F., Chen, Y.-J., Li, N., Mi, M., Xu, Y.-L., Li, F.-L., et al. (2013). Fluid inclusion and isotope geochemistry of the Qian'echong giant porphyry Mo deposit, Dabie Shan, China: A case of NaCl-poor, CO_2-rich fluid systems. *Journal of Geochemical Exploration, 124*, 1–13.

Yang, Y.-F., Chen, Y.-J., Pirajno, F., & Li, N. (2015). Evolution of ore fluids in the Donggou giant porphyry Mo system, East Qinling, China, a new type of porphyry Mo deposit: Evidence from fluid inclusion and H-O isotope systematics. *Ore Geology Reviews, 65*, 148–164.

Yang, Y.-F., Li, N., & Chen, Y.-J. (2012). Fluid inclusion study of the Nannihu giant porphyry Mo-W deposit, Henan Province, China: Implications for the nature of porphyry ore-fluid systems formed in continental collision regime. *Ore Geology Reviews, 46*, 83–94.

Yang, Y.-F., & Wang, P., (2016). Geology, geochemistry and tectonic settings of molybdenum deposits in Southwest China: A review. *Ore Geology Reviews* (in press).

Yang, Y.-F., Wang, P., Chen, Y.J., & Li, Y. (2016). Geochronology and geochemistry of the Tianmugou Mo deposit, Dabie Shan, eastern China: Implications for ore genesis and tectonic setting. *Ore Geology Reviews*. doi: 10.1016/j.oregeorev.2016.04.010.

Yin, A., & Nie, S. (1996). A Phanerozoic palinspastic reconstruction of China and its neighboring regions. In A. Yin & T. M. Harrison (Eds.), *The tectonic evolution of Asia* (pp. 442–485). Cambridge: Cambridge University Press.

Yu, X.-F., Hou, Z.-Q., Zhang, H., Qian, Y., & Li, B.-L. (2012). Characteristics of ore-forming fluids and metallogenic mechanism of the Daheishan porphyry Mo deposit in Yongji area, Jilin Province. *Journal of Jilin University (Earth Science Edition), 42*, 1688–1699 (in Chinese with English abstract).

Zeng, Q.-D., Chu, S.-X., Liu, J.-M., Sun, S.-K., & Chen, W.-J. (2012a). Mineralization, alteration, structure, and Re–Os age of the Lanjiagou porphyry Mo deposit, North China Craton. *International Geologiy Review, 54*, 1145–1160.

Zeng, Q.-D., Liu, J.-M., Qin, K.-Z., Fan, H.-R., Chu, S.-X., Wang, Y.-B., et al. (2013). Types, characteristics, and time-space distribution of molybdenum deposits in China. *International Geologiy Review, 55*, 1311–1358.

Zeng, Q.-D., Liu, J.-M., Xiao, W.-J., Chu, S.-X., Wang, Y.-B., Duan, X.-X., et al. (2012b). Mineralizing types, geological characteristics and geodynamic background of Triassic molybdenum deposits in the northern and southern margins of North China Craton. *Acta Petrologica Sinica, 28*, 357–371 (in Chinese with English abstract).

Zeng, Q.-D., Liu, J.-M., Zhang, Z.-L., Chen, W.-J., & Zhang, W.-Q. (2011). Geology and geochronology of the Xilamulun Molybdenum Metallogenic Belt in eastern Inner Mongolia, China. *International Journal of Earth Sciences, 100*, 1791–1809.

Zeng, Q.-D., Yang, J.-H., Liu, J.-M., Chu, S.-X., Duan, X.-X., Zhang, Z.-L., et al. (2012c). Genesis of the Chehugou Mo-bearing granitic complex on the northern margin of the North China Craton: Geochemistry, zircon U–Pb age and Sr–Nd–Pb isotopes. *Geological Magazine, 149*, 753–767.

Zhai, M.-G., & Santosh, M. (2011). The Early Precambrian odyssey of the North China Craton: A synoptic overview. *Gondwana Research, 20*, 6–25.

Zhai, M.-G., & Santosh, M. (2013). Metallogeny in the North China Craton: Secular changes in the evolving Earth. *Gondwana Research, 24*, 275–297.

Zhang, C., & Li, N. (2014). Geology, geochemistry and tectonic setting of the Indosinian Mo deposits in southern Great Hinggan Range, NE China. *Geological Journal, 49*, 537–558.

Zhang, C., & Li, N. (2016). Geochronology and zircon Hf isotope geochemistry of the granites at the giant Chalukou Mo deposit, NE China: Implication for tectonic setting. *Ore Geology Reviews*. doi: 10.1016/j.oregeorev.2016.05.003.

Zhang, J.-Y. (2009). Study on metallogenic features of Maojiayingzi U–Mo deposit in Zhenglanqi. *Inner Mongolia. Geology and Exploration, 12*(7), 80–83 (in Chinese with English abstract).

Zhang, L.-C., Wu, H.-Y., Wan, B., & Chen, Z.-G. (2009a). Ages and geodynamic settings of Xilamulun Mo–Cu Metallogenic Belt in the northern part of North China Craton. *Gondwana Research, 16*, 243–254.

Zhang, L.-C., Wu, H.-Y., Xiang, P., Zhang, X.-J., Chen, Z.-G., & Wan, B. (2010). Ore-forming process and mineralization of complex tectonic system during the Mesozoic: A case from Xilamulun Cu–Mo Metallogenic Belt. *Acta Petrologica Sinica, 26*, 1351–1362 (in Chinese with English abstract).

Zhang, T., Chen, Z.-Y., Xu, L.-Q., & Chen, Z.-H. (2009b). The Re–Os isotopic dating of molybdenite from the Dasuji molybdenum deposit in Zhuozi County, Inner Mongolia and its geological significance. *Rock and Mineral Analysis, 28*, 279–282 (in Chinese with English abstract).

Zhang, X.-H., Li, T.-S., & Pu, Z.-P. (2002). $^{40}Ar/^{39}Ar$ thermochronology of two ductile shear zones from Yiwulvshan, West Liaoning: Age constraints on the Mesozoic tectonic events. *Chinese Science Bulletin, 47*, 697–701 (in Chinese with English abstract).

Zhang, Y.-T., Zhang, L.-C., Ying, J.-F., Zhou, X.-H., Wang, F., Hou, Q.-L., et al. (2007). Geochemistry and source characteristics of the Early Cretaceous volcanic rocks in Tahe, north Da Hinggan Mountain. *Acta Petrologica Sinica, 23*, 2811–2822 (in Chinese with English abstract).

Zhang, Z.-L., Zeng, Q.-D., Qu, W.-J., Liu, J.-M., Sun, X.-G., Zhang, R.-B., et al. (2009c). The molybdenite Re–Os dating from the Nianzigou Mo deposit, Inner Mongolia and its geological significance. *Acta Petrologica Sinica, 25*, 212–218 (in Chinese with English abstract).

Zhang, Z.-Z., Wu, C.-Z., Gu, L.-X., Feng, H., Zheng, Y.-C., Huang, J.-H., et al. (2009d). Molybdenite Re–Os dating of Xintaimen molybdenum deposit in Yanshan-Liaoning Metallogenic Belt, North China. *Mineral Deposits, 28*, 313–320 (in Chinese with English abstract).

Zhao, D.-B., Ma, Z.-L., Zhang, X.-P., & Zhao, X.-Q. (2009). The geological characteristics and prospecting criteria of the Mo deposits in the east Faku. *Mineral Resources and Geology, 23*, 326–328 (in Chinese with English abstract).

Zhao, Y., Xu, G., & Zhang, X.-H. (2004). Yanshanian movement and conversion of tectonic regimes in East Asia. *Earth Science Frontiers, 11*, 319–328 (in Chinese with English abstract).

Zheng, Y.-C., Feng, H., Wu, C.-Z., Gu, L.-X., Liu, S.-H., & He, K. (2014). Influence of crude oil on the genesis of the Lanjiagou porphyry molybdenum deposit, western Liaoning Province, China. *Ore Geology Reviews, 60*, 1–13.

Zheng, Y.-D., Davis, G. A., Wang, C., Darby, B. J., & Hua, Y.-G. (1998). Major thrust system in the Daqingshan Area, Inner Mongolia, China. *Science China Earth Sciences, 28*, 289–295 (in Chinese with English abstract).

Zhong, J., Chen, Y.-J., & Pirajno, F. (2016). Geology, geochemistry and tectonic settings of the molybdenum deposits in South China: A review. *Ore Geology Reviews*. doi: 10.1016/j.oregeorev.2016.04.012.

Zorin, Y. A., Zorina, L., & Spiridonov, A. M. (2001). Geodynamic setting of gold deposits in eastern and central Trans-Baikal (Chita Region, Russia). *Ore Geology Reviews, 17*, 215–232.

Late Mesozoic Gold Mineralization in the North China Craton

21

Hong-Rui Fan, Mingguo Zhai, Kui-Feng Yang, and Fang-Fang Hu

Abstract

The North China Craton (NCC) hosts numerous gold deposits and is known as the most gold-productive region in China. These deposits are generally sited in the cratonic margin. Main gold concentration districts include Jiaodong in the eastern margin, Xiaoqinling and Xiong'ershan in the southern margin, Jibei-Jidong, Chifeng-Chaoyang, Ji'nan, and Liaodong in the northern margin, and central Taihangshan in the central Craton. The gold deposits mostly formed within a few million years of the early Cretaceous (130–120 Ma), coeval with widespread occurrences of bimodal magmatism that marked the peak of lithospheric thinning or craton destruction of the NCC. Dehydration of the subducted and stagnant slab in the mantle transition zone has led to continuous hydration and considerable metasomatism of the mantle wedge beneath the NCC. The large-scale gold mineralization in the NCC in the early Cretaceous has genetic relation with craton destruction. The westward subduction of the west Pacific plate (Izanagi) beneath the eastern China continental margin during the Early Cretaceous has been an optimal setting for a large-scale gold mineralization throughout the NCC.

Keywords

Gold mineralization • Late mesozoic • Craton destruction • North China Craton

Stable cratons are the most important tectonic elements of the lithosphere. Old cratons are typified by a thick lithospheric root (>150 km), weak tectonism (lacking intense crustal deformation, large-scale magmatism, and strong seismicity), low densities and water contents, existence of a refractory lithospheric mantle (harzburgite of $Mg^{\#} > 92$, high $^{87}Sr/^{86}Sr$, low $^{143}Nd/^{144}Nd$), and strong mechanical and chemical coupling between the crust and mantle (Pollack 1986; Hieronymus et al. 2007; Zhang et al. 2008; Wu et al. 2014; Zhu et al. 2015). Except the weak deep-seated magmatism, both extensive magmatism and mineralization are basically absent within the cratons. The North Craton Craton (NCC) is the one of the oldest craton in the world with ~3.8 Ga crystallized crustal rocks, but showing obvious differences with other Archean craton like Kaapvaal Craton of south African, Superior Province Craton of north American (Griffin et al. 2004; Wu et al. 2014). After cratonization during the Archean-Paleoproterozoic (>1.8 Ga), the NCC remained relatively stable with a thick Archean lithospheric keel until the early Mesozoic. Recent studies on Paleozoic kimberlite and mantle peridotite xenoliths in the Cenozoic basalts showed that the eastern portion of the NCC has experienced lithospheric thinning and craton destruction during the Phanerozoic, which completely ruined its original rigidity. Since the Mesozoic, large-scale structural deformation and magmatic activity occurred in the eastern NCC, which was accompanied by a large-scale gold mineralization.

H.-R. Fan (✉) · M. Zhai · K.-F. Yang · F.-F. Hu
Key Laboratory of Mineral Resources, Institute of Geology and Geophysics, Chinese Academy of Sciences, Beijing, 100029, China
e-mail: fanhr@mail.iggcas.ac.cn

M. Zhai et al. (eds.), *Main Tectonic Events and Metallogeny of the North China Craton*,
Springer Geology, DOI 10.1007/978-981-10-1064-4_21

21.1 Nature of Craton Destruction in the North China Craton

An important tectonic inversion took place in the eastern North China Craton (NCC) during Mesozoic, which caused a great lithosphere thinning, powerful interaction between mantle and crust and a vast granitic intrusion and volcanism (Zhai et al. 2004). Lithospheric thinning describes only the change in the lithosphere thickness of a geological unit, which does not imply any mechanism involved. Studies have shown that lithospheric thinning occurred in the most areas of the Earth in the geological history, and, in particular, is more common in the orogenic belts (Krystopowicz and Currie 2013; Wu et al. 2014). Based on studies on mantle xenoliths or mineral inclusions in diamond trapped in the Ordovician kimberlites from the NCC (Mengyin County in Shandong Province and Fuxian County in Liaoning Province), it has been estimated that the lithosphere of the NCC had a thickness of ca. 200 km when the kimberlites erupted at about 480 Ma. However, constraints from mantle xenoliths entrained in the Cenozoic basalts reveal that the Cenozoic lithosphere of the NCC has a thickness less than 80 km, which is also consistent with the geophysical data (Lu et al. 1991; Menzies et al. 1993). This suggests that lithosphere of the NCC has thinned for more than 100 km since the Early Paleozoic.

Mechanism of lithospheric mantle thinning or craton destruction of NCC is still controversial (Menzies et al. 2007; Wu et al. 2008; Gao et al. 2009; Xu et al. 2009; Zhang 2009). Two representative comprehensives are thermochemical/mechanical erosion (Xu 2001) and delamination (Gao et al. 2009). All mechanism models agree that melt–peridotite interaction played an important role in the NCC destruction. This process is the driving force for the cratonic destruction in the thermochemical erosion model, whereas it is a natural consequence in the delamination model. A comprehensive research on geological, geophysical, and geochemical data has demonstrated that the NCC had been significantly modified or destroyed in the late Mesozoic. The destruction culminated at ca. 125 Ma (Zhu et al. 2012a, b). It is proposed that the west paleo-Pacific plate subduction is the main dynamic factor that triggered the destruction of the NCC, which highlights the role of cratonic destruction in plate tectonics (Zhu and Zheng 2009). Craton destruction in the NCC possessed heterogeneity. The lithosphere beneath the eastern zone (east of the Taihang Mountains) of the NCC has been significantly destroyed, forming intermediate-acidic igneous rocks with large area (Menzies et al. 2007). The lithosphere beneath the central zone (Taihang-Lvliang Mountains) was just modified, forming north-south distributing Taihangshan magmatic rock belt (Zhu et al. 2011), whereas lithosphere beneath the western zone (Ordos block) remains unmodified.

Subduction at late Mesozoic of the west paleo-Pacific plate had three major effects on the mantle lithosphere beneath the NCC: (1) metasomatism and weakening of subcontinental lithospheric mantle (SCLM) due to fast unsteady flow and upwelling of asthenosphere and ascent of slab-derived fluid and/or melts (Zheng et al. 2008); (2) whole-scale lithospheric extension caused by the steep rise of the asthenosphere due to the retreat of the flat subducted slab (Zhu et al. 2012b), and (3) significant replacement of the ancient SCLM with young, oceanic-like mantle as a result of the peridotite–melt interaction (Zhang et al. 2009; Tang et al. 2013). These suggest that the NCC was no longer a craton in the traditional sense of this term (Zhu et al. 2011). Zhu et al. (2015) suggested an integrated driving mechanism for craton destruction involving the following processes: (1) subduction of flat slab, (2) roll-back of the subducted slab, (3) stagnation and dehydration of the subducted slab in the mantle transition zone, (4) partial melting of the lithospheric mantle above the mantle transition zone facilitated by dehydration of the stagnant slab, (5) weakening and unsteady flow of the hydrated mantle wedge and its adiabatic melting, (6) regime change of lithosphere mantle (i.e., craton destruction) triggered by unsteady mantle flux. Oceanic subduction alone is insufficient to cause craton destruction; this is a very important concept.

21.2 Late Mesozoic Gold Mineralization in the North China Craton

Economically viable ore systems are heterogeneously, but not randomly, distributed in time and space. Their distribution is intimately related to the evolution of the Earth, particularly to its progressive cooling and geodynamic evolution from plume-influenced tectonics to modern plate tectonics (e.g., Groves et al. 2005; Kerrich et al. 2005). Most cratons are well endowed with a large variety of ore deposits that were emplaced during the formation of the cratons. However, rare endogenic ore deposits have formed in the ancient cratonic blocks since their stabilization due to the lack of significant deformation and magmatism (Groves and Bierlein 2007). These ore deposit types, including PGE deposits in layered intrusions, diamond deposits in alkaline pipes and iron–oxide Cu–Au (IOCG) deposits related to alkaline to A-type granite, are related to anomalous mantle magmatism in the continental crustal settings above thick SCLM in the intracratonic settings, probably during initial extension related to the failed break-up of supercontinents (Groves and Bierlein 2007). One exception is in the NCC, which experienced extensive late Mesozoic hydrothermal mineralization and led to the formation of numerous Au, Mo, Fe, and Ag–Pb–Zn deposits. This unusual mineralization is best

illustrated in large areas along the southern and northern margins of the NCC that contain the world's largest Mo resources of Mesozoic ages (Mao et al. 2011; Li et al. 2012a, b; Zeng et al. 2013) and the eastern margin hosting giant gold resources. Gold deposits cluster in several ore-concentrated districts, which includes the Jiaodong district in the eastern NCC and the Xiaoqinling district in the southern NCC, which have a total gold reserve of ~4000–5000 t, and are among the largest gold producing districts in the world (Goldfarb and Santosh 2014). These gold deposits in the NCC were mostly formed in the Early Cretaceous (130–120 Ma; Li et al. 2003, 2012a; Yang et al. 2003; Fan et al. 2007), within a time gap when destruction of the NCC culminated (Zhu et al. 2011).

21.2.1 Gold Deposits in the North China Craton

The NCC is the most important gold occurrence region in China, and also one of the most important gold districts in the world (Goldfarb et al. 2014). Gold deposits in the NCC are generally sited in the cratonic margin (Fig. 21.1). Main gold concentration districts include Jiaodong in the eastern margin, Xiaoqinling and Xiong'ershan in the southern margin, Jibei-Jidong, Chifeng-Chaoyang, Ji'nan, and Liaodong in the northern margin, and central Taihangshan in the central Craton (Yang et al. 2003). The hosting-rocks of gold deposits in the NCC are various, and mostly Archean metamorphic rocks and Phanerozoic granitoids (Wei et al. 1994; Chen and Cun 1997; Zhou et al. 2002).

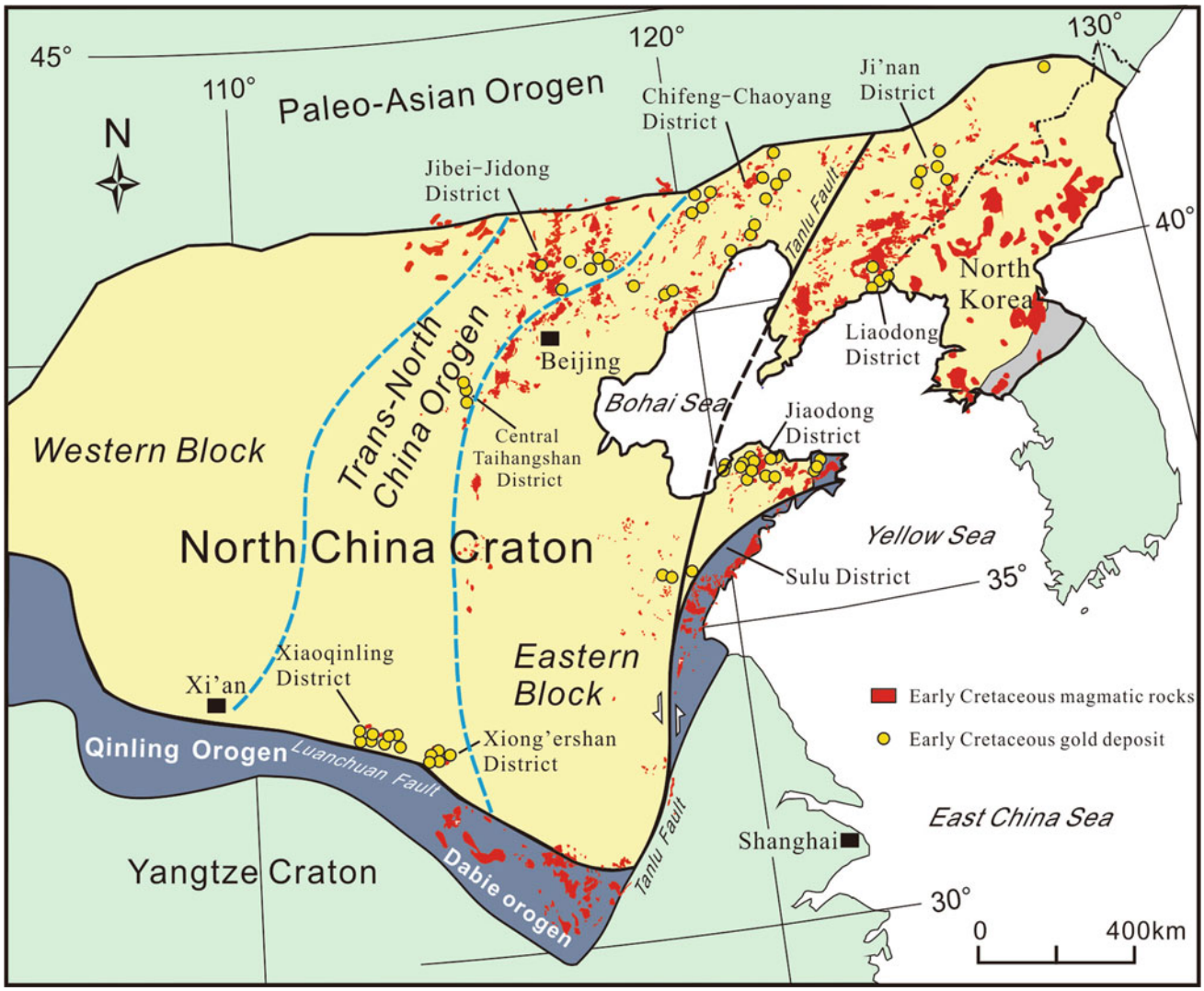

Fig. 21.1 Map of the NCC and distribution of major gold deposits in several gold districts (modified from Zhu et al. 2015)

1. Gold deposits in the Jiaodong district of eastern NCC

The Jiaodong district occurs along the eastern margin of the NCC, which is dominated by Archean rock units, and bounded by the N- to NE-trending Tanlu fault zone to the west and by the Sulu ultra-high pressure metamorphic (UHPM) belt to the southeast (Li and Yu 2012). It is a gold concentration district which is mainly composed of Precambrian basement and UHPM block with intensive Mesozoic tectonic and magmatic activities (Qiu et al. 2002; Luo and Miao 2002; Li et al. 2015). The district hosts numerous gold deposits with huge gold reserves, and is currently the most important gold producer in China. Known reserves and produces of gold are all the first ones in China, accounting for about one-fourth of the Chinese gold reserves in the only 0.2 % national territory. Seven world-class gold deposits (>100 t gold), ten large gold deposits (20–100 t gold) and more than one hundred middle to small gold deposits (<20 t gold) have been discovered in the district during the past three decades (Lv and Kong 1993; Fan et al. 2003; Song et al. 2015). Gold deposits in the district can be divided into three mineralizing belts from west to east, namely Zhaoyuan-Laizhou belt, Penglai-Qixia belt, and Muping-Rushan belt (Fig. 21.2). Each belt is separated by Jurassic to Cretaceous volcanic-sedimentary basin. Most gold deposits are distributed in the western parts of the Mishan fault, even if sporadic small-scale gold deposits are reported in the granitoids of Wendeng and Weihai Cities (Kong et al. 2006).

Different classifications of gold deposits in the Jiaodong have been supported, and two types of gold deposits are widely accepted, namely quartz vein-style (Linglong type) and structurally controlled altered rock-style (Jiaojia type) (Li et al. 2007a, b). Structurally controlled altered rock-style gold deposits are represented by the Sanshandao, Xincheng, Dayinggezhuang, and Xiadian camps, and mostly distributed in the west Jiaodong. This style gold mineralization is controlled by the regional fault zone, cataclastic deformation zone and alteration zone. Disseminated- and stockwork-type gold ore bodies are mainly located in the footwall of the main fault plan, which were subjected extensive fragment deformation and hydrothermal alteration (Li and Yang 1993; Kong et al. 2006). Single ore body, sharing the same trend with main fault plane, is generally larger with stable occurrence. Quartz vein-style gold deposits are representative by Linglong, Denggezhuang, Jinqingding, Majiayao, and Heilangou camps, and distributed in the central-east Jiaodong. The character of this style deposits is multiple-stage gold-bearing sulfides overprinted on favorable structure sites in the larger quartz vein to form ore bodies. The main ore bodies generally did not surpass the quartz vein

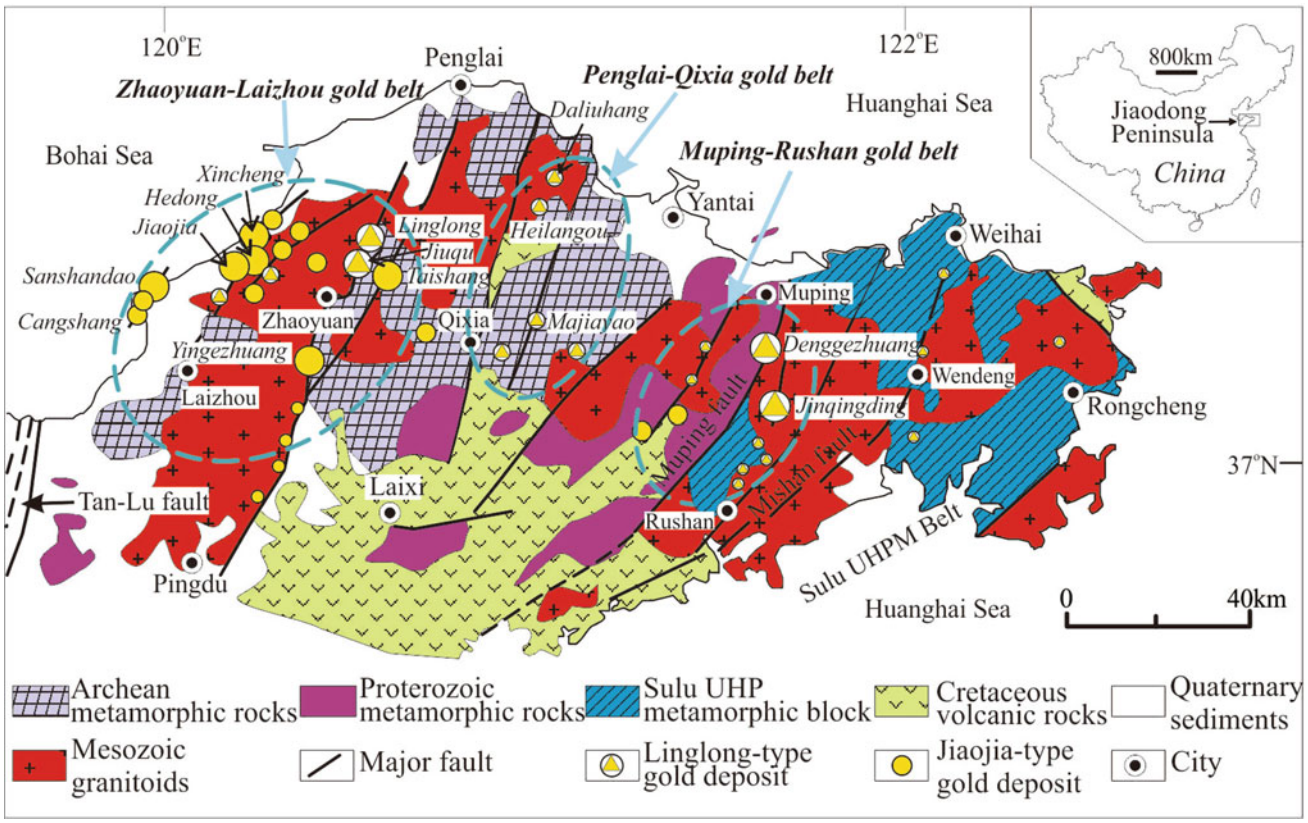

Fig. 21.2 Geological map of Jiaodong gold concentration area, showing location of the major gold deposits (after Fan et al. 2003)

(Li and Yang 1993; Kong et al. 2006). Gold mineralization is typically hosted in the secondary faults. Ore bodies are controlled by shape and scale of quartz and third-order faults. The quantity of ore bodies might be higher, but the scale of the single ore body is smaller. The contents of ores are relatively higher with great variability, forming unusual high gold content (Lv and Kong 1993).

Granitoids at Jiaodong intruded into Precambrian metamorphic basement rocks and ultra-high-pressure metamorphic blocks can be divided into three stages, late Triassic post-collision granites, late Jurassic calcium alkaline granites, and early Cretaceous high potassium calcium alkaline to alkaline granites. Gold deposits are mostly located in the late Jurassic and early Cretaceous granites (Yang et al. 2012). Two stages of mafic dikes with ages as ~136–106 and ~95–87 Ma, respectively, are identified in the Jiaodong. The Early Cretaceous mafic dikes were derived from partial melting of an enriched lithospheric mantle, and late Cretaceous mafic dikes were generated from partial melting of newly accreted depleted lithospheric mantle (Cai et al. 2013). Geochronology using by $^{40}Ar/^{39}Ar$ dating of hydrothermal K-bearing alteration minerals (sericite, K-feldspar, muscovite, biotite) and fluid inclusions extracted from ore-related quartz, Rb–Sr isochron dating of gold-bearing pyrite, and SHRIMP U–Pb dating of hydrothermal zircons (Yang and Zhou 2001; Li et al. 2003, 2006; 2008; Zhang et al. 2003a; Hu et al. 2004, 2013; Cai et al. 2011; Yang et al. 2014) all demonstrated that gold deposits in the Jiaodong district formed around 120 ± 10 Ma (Fig. 21.3a).

2. Gold deposits in the southern NCC

The Xiaoqinling and Xiong'ershan districts represent the most important gold concentrations along the southern NCC and have been China's second largest gold producers in the past three decades (Jiang and Zhu 1999; Mao et al. 2002). There are more than 40 gold deposits in the Xiaoqinling district that are mostly hosted in the amphibolite facies metamorphic rocks of the late Archean Taihua Group, with a few smaller ones occurring within late Mesozoic plutons. These deposits are mostly distributed along the NWW-trending axial traces of the Laoyacha anticline, Qiliping syncline, and Wulicun anticline (Fig. 21.4a), forming the southern, central, and northern gold belts, respectively (Li et al.1996b; Luo et al. 2000; Feng et al. 2009). The southern gold belt is further divided into the western and eastern belts that are separated by provincial boundary of the Henan and Shanxi Provinces. The Xiong'ershan district, 40–50 km east of the Xiaoqinling district, contains 20–30 gold deposits and numerous prospects and showings, best represented by the large-sized Qianhe, Shanggong, and Qiyugou deposits (Fig. 21.4b; Ren et al. 1996; Lu et al. 2004). Recent deep exploration projects have led to an increase of more than 40 t of gold in the Huashuping and Dongwan camps.

Similar to the Jiaodong district of the eastern NCC, gold mineralization of the southern NCC consists of quartz-sulfide veins and structurally controlled auriferous hydrothermal alteration zones, but mineralized breccia pipes have also been recognized in the Xiong'ershan district (Chen and Fu 1992). Auriferous quartz-sulfide veins are mostly hosted in the Xiaoqinling district. Individual veins extend for a few hundred to more than 4000 m along strike and continue for 300–1200 m down dip, with an average thickness of 1–3 m (Luan et al. 1985; Zhou et al. 1993; Jiang et al. 1999). All major veins are hosted in brittle to brittle-ductile faults showing reverse or normal displacement of several to a few tens meters, but mineralization preferentially occurs in jogs or bends, at changes in strike, bifurcations, and splays (Nie et al. 2001; Feng et al. 2009). This localization of ores is interpreted to reflect focusing of hydrothermal fluids into the most highly dilational and permeable segments (Kerrich and Cassidy 1994; Micklethwaite et al. 2010). Ore bodies comprise auriferous quartz-sulfide veins and subordinate disseminated ores in the vein-proximal alteration zones (a few tens cm wide) on both sides or at the extension of a vein.

Gold mineralization of the Xiong'ershan district is dominated by stockworks and disseminated ores in structurally hosted hydrothermal alteration zones, although quart-sulfide veins are also present in variable proportions in many deposits (Lu et al. 2004; Chen et al. 2008). In contrast to the Xiaoqinling district where quartz-sulfide veins are mainly hosted in NW- to NWW-striking faults, gold ore bodies of the Xiong'ershan district is largely controlled by NE-striking fracture zones which are broadly uniformly spaced, with a perpendicular spacing of ca. 10 km between two faults. Gold ore bodies have various morphological features, ranging from irregular veins to podiform and lenticular bodies, reflecting structural controls on localization of gold ores. Although gold mineralization may be relatively continuous along the hydrothermally altered structure zones, thickness and gold grade of ore bodies commonly show large variations both laterally and vertically.

In addition, the Xiong'ershan district contains two gold-mineralized breccia pipes, including the late Triassic Dianfang and early Cretaceous Qiyugou deposits (Ren et al. 1996; Chen et al. 2009; Fan et al. 2011). The Qiyugou deposit consists of 7 gold-mineralized breccia pipes hosted in amphibolites of the late Archean Taihua Group. The breccia pipes are elliptical or spindle at surface and cylindrical or funnel-shaped along vertical extent. The breccias or fragments consist of gneiss of the Taihua Group and, less significantly, andesites of the Paleoproterozoic Xiong'er Group. The breccia bodies are typically in sharp contact with the country rocks, but fractured zones of a few tens of meters

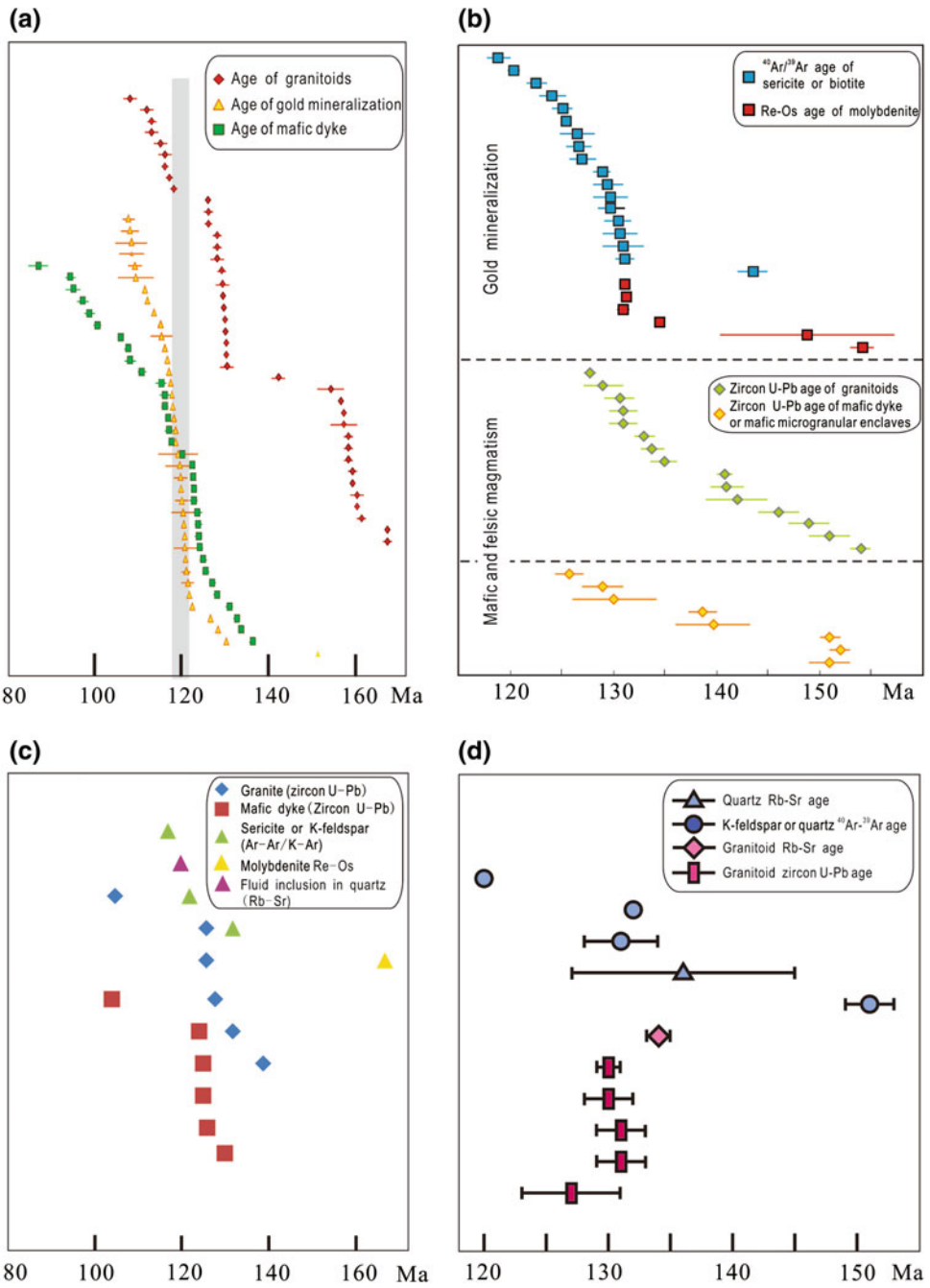

Fig. 21.3 Age framework of gold deposits, Mesozoic granitoids, and mafic dykes in the different districts, North China Craton (NCC). **a** The eastern NCC; **b** the southern NCC; **c** the northern NCC; **d** the central NCC

wide are locally developed between a breccia pipe and its undeformed wallrocks.

Ore-related hydrothermal alteration is well developed both in the hanging wall and foot wall of auriferous lodes at Xiaoqinling and Xiong'ershan districts, southern NCC. Common alteration minerals include quartz, sericite, K-feldspar, biotite, chlorite, pyrite, chalcopyrite, ankerite, and calcite, and had tightly relations with gold deposition at time and space. Alteration mineral $^{40}Ar/^{39}Ar$ dating, combined with molybdenite dating can be used to restrict gold mineralizing times. It has been concluded that most gold deposits in the Xiaoqinling and Xiong'ershan districts were generated in the late Jurassic to the late Early Cretaceous, with a peak at ca. 130–125 Ma (Fig. 21.3b) (Li et al. 2012a). There also existed the Indosinian (late Triassic) mineralization, e.g., geochronology of molybdenite Re–Os dating and monazite U–Pb dating all showing late Triassic ages in the Dahu gold deposit (Li et al. 2007a, b, 2011), Xiaoqinling district. It is generally believed that there are two times, late Triassic and early Cretaceous, gold mineralizing events at Xiaoqinling, and most gold ores were formed at early Cretaceous.

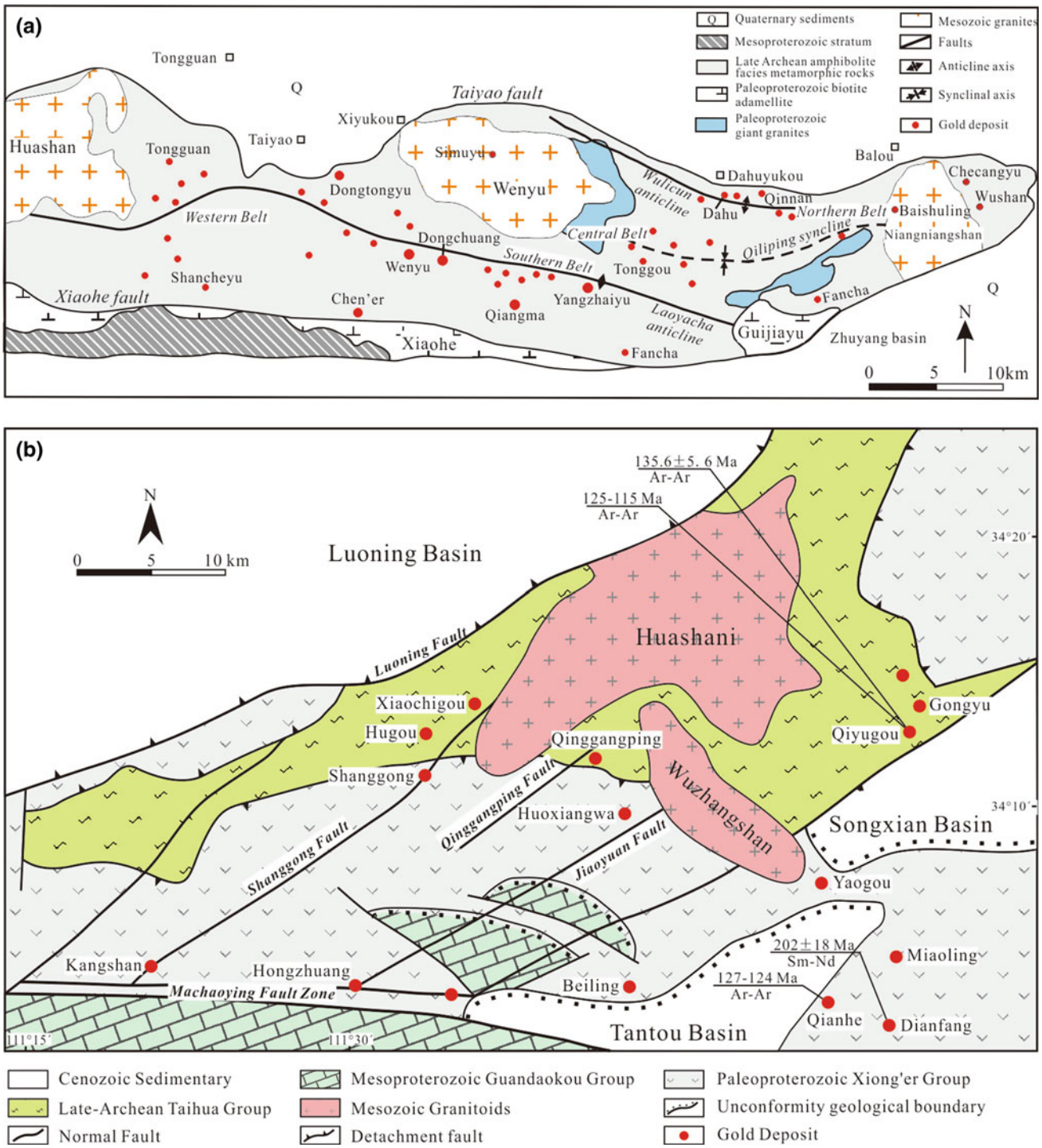

Fig. 21.4 Geological map of the Xiaoqinling (**a**) and Xiong'ershan (**b**) districts along the southern NCC. Also shown are major gold deposits in each district (Modified from Li et al. 1996b; Lu et al. 2004)

3. Gold deposits in the northern NCC

Northern NCC is also an important gold mineralizing belt in China. Gold deposits are well distributed in the belt with more than 60 large to middle-scale gold mines and >100 small gold mines. The gold deposits are located from the west to the east and with a character of clustering. Based on regularity of gold distribution and ore-controlling factors, seven gold concentration areas can be divided as Liaodong gold area (A1), Jilin Laolin gold area (A2), Jilin Jiapigou gold area

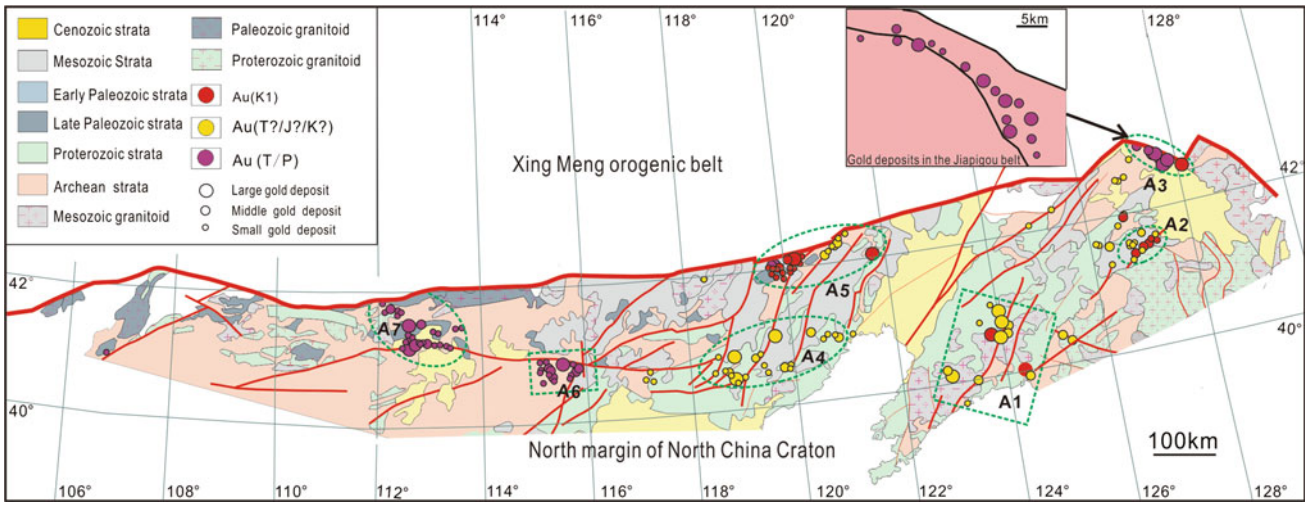

Fig. 21.5 Geological map of gold concentration areas in the northern NCC, showing location of the major gold deposits

(A3), East Hebei gold area (A4), Chifeng-Chaoyang gold area (A5), Zhangjiakou gold area (A6), and Inner Mongolia Hadamengou gold area (A7) (Fig. 21.5).

Gold deposits in the northern NCC can be separated to two styles, quartz vein-style and altered rock-style. The former is represented by Wulong at Liaoning, Haigou at Jilin, Jinchanggouliang at Inner Mongolia, and latter is gold ore in Qingchengzi mine at Liaoning, Paishanlou at west Liaoning, Dongping at northeast Hebei, Hadamengou and Haoraoerhudong at Inner Mongolia. The ores of two style occur as lode, and all controlled by structures. Gold mineralization has tight relations with magmatism in time, space, and genesis.

Main magmatic activities in the northern NCC included two stages, late Paleozoic to early Mesozoic, and early Cretaceous with corresponding gold mineralization. Magmatic activities include two ways of positioning as intrusion and dyke. The intrusions occurred generally as stocks, and gold lodes or deposits were located within a few kilometers of mineralizing-related stock. The dykes formed multiple stages, including before, during and after the ore body was in place. The gap between gold mineralization and dyke formation was narrow, and dyke had played an important role for gold mineralization. For example, Wulong gold deposit at Liaoning is located in the north of early Cretaceous of Sanguliu granodiorite. Dyke in the deposit include granitic porphyry, diorite, diabase, and lamprophyre, and has tight relation with ore lode in space and time.

Gold lodes in the deposits are all controlled by structures, including NE-, NW-, NNE-, and EW-trend faults which showed multistage structure-controlling. The first-order structure is a regional fault, controls distribution of ore belt. The second-order structure is sub-fault of the first-order structure, controls distribution of mineralizing area or ore deposit. The third- or fourth-order structure controls distribution of ore lode. For example, the north margin fault controls distribution of gold deposits in the northern NCC. The Baotou-Zhangjiakou fault controls distribution of gold belt, and the Yalujiang fault controls distribution of NE-trend gold deposits. Locating of ore deposit is often controlled by a set of regional faults, or two sets of cross faults. The occurrence of the ore veins is controlled by the faults of lower rank. The faults were usually experienced in many periods of activities, showing compression torsion in the early stage and extensional structure during mineralization. Ore-controlling structures can be divided into two types, brittle fracture and ductile shear belt. The brittle fracture includes fault and fractured zone, the former hosts quartz vein-style mineralization and the latter hosts altered rock-style mineralization. Structure rocks in the ductile shear belt are mainly mylonite or mylonitic rocks which host altered rock-style mineralization.

Geochronology in the gold mines shows that granitoids related with mineralization intruded at two stages, late Paleozoic to early Mesozoic, with corresponding mafic activities at Triassic and early Cretaceous (Fig. 21.3c). Gold mineralization ages were also concentrated in these two times (Fig. 21.3c). There existed that the age of mineralization of many gold deposits was still not clear, some were speculated that the age of mineralization was Mesozoic. For example, most gold deposits in the Qingchengzi belt was formed in Triassic based on intrusive ages of regional granites and quartz Ar–Ar dating. But in the same mining area, there are different age data.

4. Gold deposits in the central NCC

Less gold deposits have been found in the central NCC. The gold deposits were mainly distributed in the Fuping and Wutai-Henshan districts (Fig. 21.6), central Taihang Mountains. In the Fuping district, there are Tuling-Shihu gold deposit and Xishimen gold deposit. According to the geological survey in recent years, gold resources at Shihu was >50 t (Li et al. 2014). Xishimen is now still a small deposit as low exploration degree. In the Wutai-Henshan district, there are Yixingzhai and Xingzhuang gold deposits at Wutai, and Chafang Fe–Au deposit and Houyu Cu–Mo–Au deposit. Gold resources at Yixingzhai can >50 t (Li et al. 2014). Houyu deposit is middle scale and remaining deposits are all small scale.

Gold types in the central NCC are quartz vein, porphyry and skarn. Quartz vein type mineralization, main gold resources in the central NCC, is represented by Shihu-Tuling and Xishimeng gold deposits at Fuping, Yixingzhai, and Xingzhuang gold deposits at Wutai. Porphyry and skarn type mineralization is represented by Houyu porphyry Cu–Mo–Au associated ores and Chafang skarn Fe–Au associated ores at Wutai.

Gold concentrating areas in the central NCC are located in the sites of smaller lithospheric thickness. All quartz vein gold deposits are distributed in Precambrian metamorphic rocks. Intermediate-acidic and intermediate stocks and intermediate-basic to intermediate-acidic dykes with same ages of mineralization were developed in the mines. Cryptoexplosive breccias pipes were found at Yixingzhai mine. Quartz vein type ores are composed of sulfide-rich lode, and strictly controlled by South to North, NNW and NW trending brittle fractures. The general trend of ore body group is consistent with the fracture trend. Variation of gold grade is higher. The rich-ore blocks are usually checkerboard distribution, and often related with fracture transit of different directions. Tectonic background of porphyry and skarn type gold mineralization is nearly same as quartz vein type gold with same gold mineralizing ages. The porphyry and skarn type gold ores with small scale are controlled by

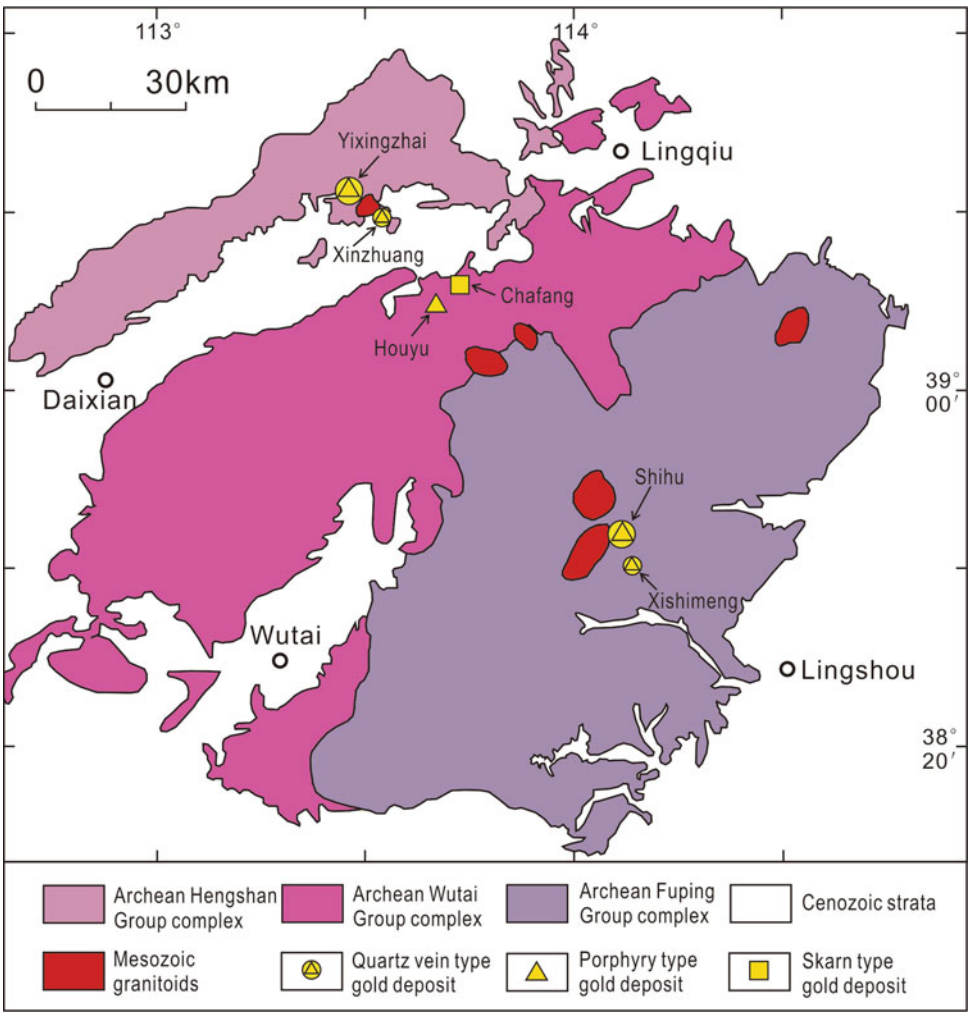

Fig. 21.6 Gold deposits in the central NCC (after Li et al. 2014)

inner and outer contact zones of small intermediate-acidic dykes and stocks with same ages.

Gold mineralizing times in the Fuping, Hengshan, and Wutai districts of central NCC are almost at early Cretaceous (Fig. 21.3d). Using LA–ICP-MS U–Pb analysis of zircons, Li et al. (2014) carried out on age dating on the Mapeng granitoid and quartz dioritic dikes which were related with Shihu gold mineralization. Granodiorite collected from Mapeng granitoid gave a age of 131 ± 2 Ma (MSWD = 1.6), and porphyritic monzogranite gave 130 ± 2 Ma (MSWD = 3.9). Two samples of quartz dioritic dikes gave ages of 130 ± 1 Ma (MSWD = 1.3) and 131 ± 2 Ma (MSWD = 3.1). The dating shows that emplacement of Mapeng granitoid and nearby dikes is the results of the same magmatism. The previous age data of the ore-forming hydrothermal minerals such as quartz and K-feldspar from the Shihu gold deposit are in the range of 120–140 Ma (Cao et al. 2010; Wang et al. 2010). Among them, three of the K–Ar ages from the hydrothermal K-feldspar are ca. 120 Ma, and one is 132 Ma (Wang et al. 2010). Li et al. (2014) suggest that the gold mineralization took place slightly later than the emplacement of the Mapeng pluton and intermediate dikes, showing tight relation between mineralization and granitoid. LA–ICP-MS U–Pb analysis of zircons of Sunzhuang monzodiorite which has tight relation with Yixingzhai gold deposit in space gave the emplacement age of 134 ± 1 Ma (MSWD = 2.2) (Li et al. 2014). Ye et al. (1999) reported ^{40}Ar-^{39}Ar plateau ages of 150.7 ± 2.3 and 131.4 ± 3.1 Ma from the fluid inclusions trapped in the auriferous quartz veins of early and middle gold mineralization stages. Tian et al. (1998) reported Rb–Sr isochron age of the auriferous quartz from the Yixingzhai gold deposit to be 136 ± 9 Ma. Zhang et al. (2003b) dated the quartz porphyry dike, which is clearly later than the quartz monzodiorite, and obtained a Rb–Sr isochron age of 127.0 ± 3.9 Ma. Li et al. (2014) suggest that the emplacement of Sunzhuang pluton and the formation of Yixingzhai quartz vein gold deposit are part of a major magmatic–metallogenic event that took place ca. 130 Ma ago.

21.2.2 Ore-Forming Conditions and Mechanism

In the eastern margin of NCC, ore-forming fluids of two main style gold deposits share similar physical and chemical properties. In the early mineralizing stage, ore-forming fluids belongs to the H_2O–CO_2–NaCl system, which is characterized by medium to high temperatures (250–410 °C), CO_2-rich, and low salinities (<9 wt% NaCl eq.). The fluids evolved into a H_2O–CO_2–NaCl system with medium–low temperatures (200–330 °C), decreased amounts of CO_2, and variable salinities (0.5–15 wt% NaCl eq.) in the middle mineralizing stage. Finally, in the late mineralizing stage, the ore-forming fluids transformed into the H_2O–NaCl system with low temperatures (<100–230 °C), low salinities (<5 wt % NaCl eq.) and no CO_2 (Fan et al. 2003; Yang et al. 2009; Hu et al. 2013; Wang et al. 2015; Wen et al. 2015). The properties of ore-forming fluids in the Xiaoqinling, Xiong'ershan in the southern margin of NCC and Central Taihangshan in the central NCC are similar to those of the eastern margin of NCC (Jiang et al. 1999; Fan et al. 2000; Ni et al. 2008). However, several gold deposits are unique, such as the Qiyugou gold deposit in the Xiong'ershan District, and the Yixingzhai gold deposit in the central Taihangshan District, which are controlled by cryptoexplosive breccia pipes. The salinities of their ore-forming fluids vary from 6 wt% NaCl eq. to 22 wt% NaCl eq., with the highest salinity up to 35 wt% NaCl eq., and the peak salinities of less than or close to 10 wt% NaCl eq. (Chen et al. 2009; Fan et al. 2011; Lu et al. 2012). This phenomenon is thought to be related to concealed magmatic bodies. Although there are similarities in fluid properties and evolution between altered rock type and quartz vein type gold deposits, the ore-forming mechanisms appear to be different. The mineralization of the altered rock type gold deposits resulted from intense water-rock interaction between the ore-forming fluids and wallrocks, whereas precipitation of gold is possibly a consequence of phase separation or boiling of the ore-forming fluids in response to pressure and temperature fluctuations within the quartz vein type gold deposits (Fan et al. 2003; Wen et al. 2015).

Hydrogen and oxygen stable isotope analyses showed that early Cretaceous gold deposits from different regions in the NCC had similar isotope compositions (Zhu et al. 2015). Most of the data hydrogen and oxygen isotope data lie between the magmatic field and the global meteoric water line, demonstrating that the initial ore-forming fluids could have a magmatic source, and meteoric water should be involved in the ore-forming fluids during the process of fluids circulation and evolution (Zhu et al. 2015). Carbon stable isotope values ($\delta^{13}C = -7$ to -3 ‰) of early Cretaceous gold deposits in the NCC indicates that the ore-forming fluids might have originated from degassing or devolatilization of mantle-derived magmas (Zhu et al. 2015). Whereas sulfur isotopes of the Au deposits are highly variable. For example, $\delta^{34}S$ values of the Jiaodong gold deposits range from −5.6 to +14.1 ‰, which are distinct from those of chondrite or mantle-derived rocks and indicates the presence of enriched sources from ^{34}S-rich magmas or degassing of mantle wedges that were metasomatised by slab fluids (Fan et al. 2007). He–Ar isotope analyses indicated that mantle-derived fluids played a key role in the formation of the early Cretaceous gold deposits in the NCC (Zhu et al. 2015; Wen et al. 2015).

21.3 Craton Destruction and Large-Scale Gold Mineralization

The NCC was welded to be east part of Euro-Asia continent by Dabie-Sulu collision orogeny in the south and Xingmeng collision orogeny in the north during the late Paleozoic and early Mesozoic, and then drawn intensively into NNE-trending marginal-Pacific tectonic domain (Zhai et al. 2003). Evolution of continental crust in the region entered a new period of intra-continent orogeny. This intensive tectonic inversion marked the end of pre-Mesozoic basin-mountain system, and established basic tectonic pattern of the NCC up to now since late Mesozoic. From Jurassic to Cretaceous, the eastern part of the NCC and the whole of east China witnessed a major tectonic transformation from N–S compression to NNE–SSW shearing. Accompanying the early transformation and the onset of extension, adakitic lower crust-derived granitic batholiths were emplaced which uplifted the Precambrian basement rocks. In the Jiaodong peninsula of eastern NCC, for instance, the Linglong and Kunyushan granitic batholiths were emplaced at ca. 160 Ma within metamorphic basement represented by the Archean Jiaodong Group and Proterozoic Jingshan Group (Yang et al. 2012).

During the Cretaceous, the Chinese continent experienced westward subduction of paleo-Pacific plate and the subducted slab stagnated at the mantle transition boundary. This led to the partial melting, nonstationary flow of the upper mantle, intense metasomatism of the lithospheric mantle, or so-called craton destruction. The craton destruction is marked by following processes: large-scale magmatism, strong extensional ductile deformation, and rift-basin formation, all of which indicate that the cratonic lithosphere has been destabilized (Zhu et al. 2011). Typical marks are that a series of intermediate and basic dikes and intermediate-felsic plutons with mixed lower crust–mantle features formed during the early Cretaceous accompanied by the widespread formation of numerous ore deposits. The Jiaodong gold deposits and the coeval Guojialing and Sanfoshan granodioritic plutons and numerous intermediate to mafic and lamprophyre dikes (ca. 120 Ma, Cai et al. 2013) in the eastern margin of the NCC, Xiaoqinling gold deposits and the coeval Wenyu and Liangliangshan granitoids in the southern NCC (ca. 130 Ma, Li et al. 2012, b), and the Shihu and Yixingzhai gold deposits and the Mapeng and Sunzhuang plutons in the Taihang Mountains in the central NCC (ca. 130 Ma, Li et al. 2014) are among the products of the early Cretaceous magmatism-mineralization events. Most of the gold ores were formed in a transitional compression to extensional tectonic regime. The NE–SW ore-controlling fractures in the Jiaodong district show complex sinistral and dextral shearing during the ore-forming events, with dominant sinistral movement in the early stages and dextral in the later stages (Li et al. 1996a, b). Large-scale inhomogeneous lithosphere thinning beneath the NCC has been regarded as a direct geodynamic consequence of the extensive ore-forming events (e.g., Li et al. 2014). Since the magmatism and mineralization are mostly concentrated in the early Cretaceous, rapid and large-scale inhomogeneous delamination would also be a feasible model for the thinning or craton destruction of the NCC.

The distribution of the major ore deposits in the NCC shows that the margins of the craton are the most potential domains, as these regions are more prone to be involved in tectonic regimes of subduction and collision and to channeling of ore fluids. Accompany by craton destruction, both basic and medium-acidic magmas in the lower-middle crust experienced strong liquid resolution due to rapid pressure reduction, which generated auriferous fluids. When intruding to shallower levels at rapid rates, magma will soon become saturated, also leading to the formation of auriferous fluids. The resulted cryptoexplosive emplacement will bring about the formation of cryptoexplosive breccia type gold deposits, such as the Qiyugou gold deposit in the Xiong'ershan gold concentration district, southern NCC, and Yixingzhai gold deposit in the central NCC. Abundant lamprophyre dikes occur in both the Jiaodong and Xiaoqinling gold concentration districts, which indicate that the lithospheric mantle of the eastern NCC contained abundant water in the early Cretaceous. Strong extension would have caused water-rich lithospheric mantle to partially melt and degas, and the resultant mantle fluids would have migrated upwards into the metallogenic systems along lithospheric-scale faults like the Tan-Lu and Luanchuan faults (Fig. 21.7). This model explains why early Cretaceous gold deposits occur in the eastern margin of the NCC, such as the Jiaodong and Xiaoqinling gold districts and the cyclic mineralization of craton destruction-related gold deposits. Lithospheric extension could also cause development of secondary fractures in the middle-upper crust, thereby governing the spatial distribution of gold ore-bearing dikes, deposits and fields. For instance, gold deposits in the Jiaodong district are clearly controlled by secondary faults related to the Tan-Lu Fault. In addition, subduction of the paleo-West Pacific plate could have led to reactivation of early major and secondary faults, which either served as channels for auriferous fluids or preferentially formed gold deposits. Atmospheric water could infiltrate downward or migrate laterally along extensional fault systems formed during the craton destruction processes and eventually mix with mineralizing fluids derived mainly from mantle melts. Fluid mixing should, therefore, be another important mechanism for the deposition of gold.

Zhu et al. (2015) have well demonstrated possible relations between genesis of gold deposits and craton destruction in the NCC, and summarized the main controls of

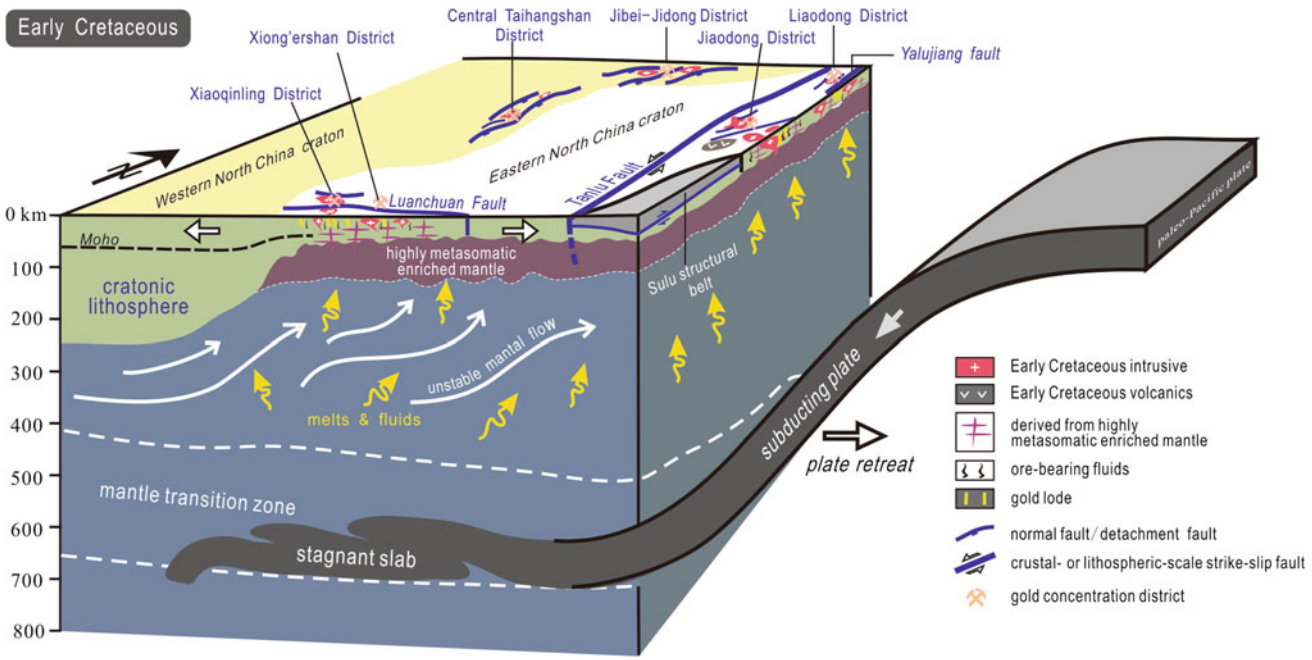

Fig. 21.7 Deep tectonic processes of the NCC and gold mineralization in the Early Cretaceous (modified after Zhu et al. 2015)

asthenosphere/lithospheric mantle-derived magma on gold mineralization as follows (Zhu et al. 2015). (1) Mantle magma partially provides gold element and volatiles. (2) Mantle magma could underplate or intrude the lower crust and cause extensive partial melting of the lower crust. Subsequently, the magmas ascended and may have formed transitory magma chambers in the various crustal depths where sulfide may have fractionated to form Au-rich sulfide accumulations in the magma chambers (Muntean et al. 2011). New fluxes of more mafic magmas into the magma chamber would have melted the sulfide accumulations to form more Au-proflic magmas (Botcharnikov et al. 2011). (3) Metal sulfides accumulated locally in the magma chamber can be dissolved by the exsolved fluids from the magmas, or can be injected into mafic melts evolved within the magma chamber, which forms gold-rich magmas. Auriferous fluid phases would be separated during the ascent into the upper crust and rapid decompression of the magmas. These magmatic fluids commonly migrate along faults for a long distance, precipitate ore materials in a short time interval and are characterized by low gradients in temperature and salinity (Muntean et al. 2011). (4) Mafic magmas can provide heat sources for metallogenesis and circulation of crustal fluids as well. Some Au in the metamorphosed mafic volcanic rocks of the NCC was leached out by the existing fluid circulation (Sun et al. 2013).

Acknowledgements We would like to thank Profs. Jian-Wei Li, Sheng-Rong Li and Qing-Dong Zeng for constructive discussions. This work was financed by Major State Basic Research Development Program (2012CB416605).

References

Botcharnikov, R. E., Linnen, R. L., Wilke, M., Holtz, F., Jugo, P. J., & Berndt, J. (2011). High gold concentrations in sulphide-bearing magma under oxidizing conditions. *Nature Geoscience, 4*, 112–115.

Cai, Y. C., Fan, H. R., Hu, F. F., Yang, K. F., Lan, T. J., Yu, H., et al. (2011). Ore-forming fluids, stable isotope and mineralizing age of the Hubazhuang gold deposit, Jiaodong Peninsula of eastern China. *Acta Petrologica Sinica, 27*, 1341–1351 (in Chinese with English abstract).

Cai, Y. C., Fan, H. R., Santosh, M., Liu, X., Hu, F. F., Yang, K. F., et al. (2013). Evolution of the lithospheric mantle beneath the southeastern North China Craton: Constraints from mafic dikes in the Jiaobei terrain. *Gondwana Research, 24*, 601–621.

Cao, Y., Li, S. R., Zhang, H. F., Ao, C., Li, Z. Z., & Liu, X. B. (2010). Laser probe $^{40}Ar/^{39}Ar$ dating for quartz from auriferous quartz veins in the Shihu gold deposit, western Hebei province, North China. *Chinese Journal of Geochemistry, 29*, 438–445.

Chen, J. M., & Cun, G. (1997). *Introduction of Gold Deposits in China* (pp. 1–154). Beijing: Geological Publishing House (in Chinese).

Chen, Y. J., & Fu, S. G. (1992). *Metallogenic regularities of gold deposits in the Western Henan Province* (pp. 1–234). Beijing: Geological Publishing House (in Chinese).

Chen, Y. J., Pirajno, F., Li, N., Guo, D. S., & Lai, Y. (2009). Isotope systematics and fluid inclusion studies of the Qiyugou breccia pipe-hosted gold deposit, Qinling orogen, Henan province, China: Implications for ore genesis. *Ore Geology Reviews, 35*, 245–261.

Chen, Y. J., Pirajno, F., & Qi, J. P. (2008). The Shanggong gold deposit, Eastern Qinling Orogen, China: Isotope geochemistry and implications for ore genesis. *Journal of Asian Earth Sciences, 33*, 252–266.

Fan, H. R., Hu, F. F., Wilde, S. A., Yang, K. F., & Jin, C. W. (2011). The Qiyugou gold-bearing breccia pipes, Xiong'ershan region, central China: Fluid inclusion and stable isotope evidence for an origin from magmatic fluids. *International Geology Review, 53*, 25–45.

Fan, H. R., Hu, F. F., Yang, J. H., & Zhai, M. G. (2007). Fluid evolution and large-scale gold metallogeny during Mesozoic tectonic transition in the Jiaodong Peninsula, Eastern China. In M. Zhai, B. F. Windley, T. M. Kusky & Q. Meng (Eds.), *Mesozoic Sub-Continental Lithospheric Thinning Under Eastern Asia* (Vol. 280, pp. 303–316). Geological Society of London, Special Publications.

Fan, H. R., Xie, Y. H., Zhao, R., & Wang, Y. L. (2000). Dual origins of Xiaoqinling gold-bearing quartz veins: Fluid inclusion evidences. *Chinese Science Bulletin, 45*, 1424–1430.

Fan, H. R., Zhai, M. G., Xie, Y. H., & Yang, J. H. (2003). Ore-forming fluids associated with granite-hosted gold mineralization at the Sanshandao deposit, Jiaodong gold province, China. *Mineralium Deposita, 38*, 739–750.

Feng, J. Z., Yue, Z. S., & Xiao, R. G. (2009). *Metallogenic regularities and prognosis of gold deposits in the Xiaoqinling District* (pp. 1–268). Beijing: Geological Publishing House (in Chinese).

Gao, S., Zhang, J. F., Xu, W. L., & Liu, Y. S. (2009). Delamination and destruction of the North China Craton. *Chinese Science Bulletin, 54*, 3367–3378.

Goldfarb, R. J., & Santosh, M. (2014). The dilemma of the Jiaodong gold deposits: Are they unique? *Geoscience Frontiers, 5*, 139–153.

Goldfarb, R. J., Taylor, R. D., Collins, G. S., Goryachev, N. A., & Orlandini, O. F. (2014). Phanerozoic continental growth and gold metallogeny of Asia. *Gondwana Research, 25*, 48–102.

Griffin, W. L., Graham, S., O'Reilly, S. Y., & Pearson, N. J. (2004). Lithosphere evolution beneath the Kaapvaal Craton: Re–Os systematics of sulfides in mantle-derived peridotites. *Chemical Geology, 208*, 89–118.

Groves, D. I., & Bierlein, F. P. (2007). Geodynamic settings of mineral deposit systems. *Journal of the Geological Society London*, *164*, 19–30.

Groves, D. I., Condie, K. C., Goldfarb, R. J., Hronsky, J. M. A., & Vielreicher, R. M. (2005). Secular changes in global tectonic processes and their influence on the temporal distribution of gold-bearing mineral deposits. *Economic Geology, 100*, 203–224.

Hieronymus, C. F., Shomali, Z. H., & Pedersen, L. B. A. (2007). Dynamical model for generating sharp seismic velocity contrasts underneath continents: Application to the Sorgenfrei-Tornquist Zone. *Earth and Planetary Science Letters, 262*, 77–91.

Hu, F. F., Fan, H. R., Jiang, X. H., Li, X. C., Yang, K. F., & Mernagh, T. (2013). Fluid inclusions at different depths in the Sanshandao gold deposit, Jiaodong Peninsula, China. *Geofluids, 13*, 528–541.

Hu, F. F., Fan, H. R., Yang, J. H., Wan, Y. S., Liu, D. Y., Zhai, M. G., & Jin, C. W. (2004). Mineralizing age of the Rushan lode gold deposit in the Jiaodong Peninsula: SHRIMP U-Pb dating on hydrothermal zircon. *Chinese Science Bulletin, 49*, 1629–1636.

Jiang, N., Xu, J., & Song, M. (1999). Fluid inclusion characteristics of mesothermal gold deposits in the Xiaoqinling district, Shaanxi and Henan provinces, People's Republic of China. *Mineralium Deposita, 34*, 150–162.

Jiang, N., & Zhu, Y. F. (1999). Geology and genesis of orogenic gold deposits, Xiaoqinling district, southeastern China. *International Geology Review, 41*, 816–826.

Kerrich, R., & Cassidy, K. F. (1994). Temporal relationships of lode gold mineralization to accretion, magmatism, metamorphism and deformation—Archean to Present: A review. *Ore Geology Reviews, 9*, 263–310.

Kerrich, R., Goldfarb, R. J., & Richards, J. (2005). Metallogenic provinces in an evolving geodynamic framework. Economic Geology 100th Anniversary Volume, pp. 1097–1136.

Kong, Q. Y., Zhang, T. Z., Yu, X. F., & Xu, J. X. (2006). *Ore Deposits in Shandong* (pp. 1–902). Qinan: Shandong Science and Technology Publishing House (in Chinese).

Krystopowicz, N. J., & Currie, C. A. (2013). Crustal eclogitization and lithosphere delamination in orogens. *Earth and Planetary Science Letters, 361*, 195–207.

Li, Z. L., & Yang, M. Z. (1993). *Geology and Geochemistry of Gold deposits in the Jiaodong* (pp. 1–168). Tianjing: Tianjing Science and Technology Publishing House (in Chinese).

Li, S. R., Chen, G. Y., Shao, W., & Sun, D. S. (1996a). *Genetic Mineralogy of the Rushan Gold Field, Jiaodong Peninsular* (pp. 1–116). Beijing: Geological Publishing House (in Chinese with English abstract).

Li, S. M., Qu, L. Q., Su, Z. B., Huang, J. J., Wang, X. S., Yue, Z. S., et al. (1996b). *The geology and Metallogeneic Prediction of gold deposits in Xiaoqinling* (pp. 1–250). Beijing: Geological Publishing House (in Chinese).

Li, J. W., Vasconcelos, P. M., Zhang, J., Zhou, M. F., Zhang, X. J., & Yang, F. H. (2003). $^{40}Ar/^{39}Ar$ constraints on a temporal link between gold mineralization, magmatism, and continental margin transtension in the Jiaodong gold province, eastern China. *Journal of Geology, 111*, 741–751.

Li, J. W., Vasconcelos, P., Zhou, M. F., Zhao, X. F., & Ma, C. Q. (2006). Geochronology of the Pengjiakuang and Rushan gold deposits, eastern Jiaodong gold province, northeastern China: Implications for regional mineralization and geodynamic setting. *Economic Geology, 101*, 1023–1038.

Li, S. X., Liu, C. C., & An, Y. H. (2007a). *Geology of Gold in the Jiaodong* (pp. 1–423). Beijing: Geological Publishing House (in Chinese).

Li, H. M., Ye, H., Mao, J. W., Wang, D. H., Chen, Y. C., Qu, W. J., et al. (2007b). Re–Os dating of molybdenites from Au–(Mo) deposits in Xiaoqinling gold ore district and its geological significance. *Mineral Deposits, 26*, 417–424 (in Chinese with Engish Abstract).

Li, Q. L., Chen, F. K., Yang, J. H., & Fan, H. R. (2008). Single grain pyrite Rb–Sr dating of the Linglong gold deposit, eastern China. *Ore Geology Review, 34*, 263–270.

Li, N., Chen, Y. J., Fletcher, I. R., & Zeng, Q. T. (2011). Triassic mineralization with Cretaceous overprint in the Dahu Au–Mo deposit, Xiaoqinling gold province: Constraints from SHRIMP monazite U–Th–Pb geochronology. *Gondwana Research, 20*, 543–552.

Li, H. K., & Yu, X. F. (2012). *Geotectonics of Shandong Provinces* (pp. 1–358). Beijing: Geological Publishing House (in Chinese).

Li, J. W., Bi, S. J., Selby, D., Chen, L., Vasconcelos, P., Thiede, D., et al. (2012a). Giant Mesozoic gold provinces related to the destruction of the North China craton. *Earth and Planetary Science Letters, 349–350*, 26–37.

Li, S. R., Santosh, M., Zhang, H. F., Shen, J. F., Dong, G. C., Wang, J. Z., et al. (2012b). Inhomogeneous lithospheric thinning in the central North China Craton: Zircon U-Pb and S–He–Ar isotopic record from magmatism and metallogeny in the Taihang Mountains. *Gondwana Research, 23*, 141–160.

Li, S. R., Santosh, M., Zhang, H. F., Luo, J. N., Zhang, J. Q., Li, C. L., et al. (2014). Metallogeny in response to lithospheric thinning and craton destruction: Geochemistry and U–Pb zircon chronology of the Yixingzhai gold deposit, central North China Craton. *Ore Geology Reviews, 56*, 457–471.

Li, L., Santosh, M., & Li, S. Y. (2015). The 'Jiaodong type' gold deposits: Characteristics, origin and prospecting original. *Ore Geology Review, 65*, 589–611.

Lu, Y. C., Ge, L. S., Shen, W., Wang, Z. H., Guo, X. D., Wang, L., & Zhou, C. F. (2012). Characteristics of fluid inclusions of Yixingzhai gold deposit in Shanxi Province and their geological significance. *Mineral Deposits, 31*, 83–93 (in Chinese with English abstract).

Lu, F. X., Han, Z. G., & Zheng, J. P. (1991). Characteristics of the aleozoic mantle-lithosphere in FuxianLiaoning Province. *Geological Science and Technical Information, 10*(Suppl), 2–20 (in Chinese with English abstract).

Lu, X. X., Wei, X. D., Dong, Y., Yu, Z. P., Chang, Q. L., Zhang, G. S., et al. (2004). *Characteristics of Gold Deposits in the Xiaoqinling-Xiong'ershan area and Mantle-derived Ore Fluids* (pp. 1–128). Beijing: Geological Publishing House (in Chinese).

Luan, S. W., Cao, D. C., Fang, Y. K., & Wang, J. Y. (1985). Geochemistry of Xiaoqinling gold deposits. *Journal of Mineralogy and Petrolology, 5*, 1–133 (in Chinese).

Luo, M. J., Li, S. M., Lu, X. X., Zheng, D. Q., & Su, Z. B. (2000). *Metallogenesis and deposit series of main mineral resources of Henan Province* (pp. 1–355). Beijing: Geological Publishing House (in Chinese with English abstract).

Luo, Z. K, & Miao, L. C. (2002). G*ranites and Gold Deposits in the Zhaoyuan-Laizhou Area, Eastern Shandong* (pp. 1–157). Beijing: Metallurgical Industry Publishing House (in Chinese with English abstract).

Lv, G. X., & Kong, Q. C., (1993). *Geology of the Linglong-Jiaojia Style Gold deposits* (pp. 1–253). Beijing: Science Publishing House (in Chinese).

Mao, J. W., Goldfarb, R. J., Zhang, Z. W., Xu, W. Y., Qiu, Y., & Deng, J. (2002). Gold deposits in the Xiaoqinling-Xiong'ershan region, Qinling Mountains, Central China. *Mineralium Deposita, 37*, 306–325.

Mao, J. W., Pirajno, F., Xiang, J. F., Gao, J. J., Ye, H. S., Li, Y. F., et al. (2011). Mesozoic molybdenum deposits in the east Qingling-Dabie orogenic belt: Characteristics and tectonic setting. *Ore Geology Review*, *43*, 264–293.

Menzies, M. A., Fan, W. M., & Zhang, M. (1993). Palaeozoic and Cenozoic lithoprobe and the loss of >120 km of Archean lithosphere, Sino-Korean craton, China. In H. M Prichard, T. Alabaster, & N. B. W. Harris (Eds.), Magmatic processes and plate tectonic. *Geological Society Special Publications 76*, 71–81.

Menzies, M., Xu, Y. G., Zhang, H. F., & Fan, W. M. (2007). Integration of geology, geophysics and geochemistry: A key to understanding the North China Craton. *Lithos, 96*, 1–21.

Micklethwaite, S., Sheldon, H. A., & Baker, T. (2010). Active fault and shear processes and their implications for mineral deposit formation and discovery. *Journal of Structural Geology, 32*, 151–165.

Muntean, J. L., Cline, J. S., Simon, A. C., & Longo, A. A. (2011). Magmatic-hydrothermal origin of Nevada's Carlin-type gold deposits. *Nature Geoscience, 4*, 122–127.

Ni, Z. Y., Li, N., Guan, S. J., Zhang, H., & Xue, L. W. (2008). Characteristics of fluid inclusions and ore genesis of the Dahu Au-Mo deposit in the Xiaoqinling gold field, Henan Province. *Acta Petrologica Sinica, 24*, 2058–2068 (in Chinese with English abstract).

Nie, F. J., Jiang, S. H., & Zhao, Y. M. (2001). Lead and sulfur isotope study of the Wenyu and Dongchuang quartz vein-type gold deposits in the Xiaoqinling area, Henan and Shaanxi Province, central China. *Mineral Deposits, 20*, 163–173 (in Chinese with English Abstract).

Pollack, H. N. (1986). Cratonization and thermal evolution of the mantle. *Earth and Planetary Science Letters, 80*, 175–182.

Qiu, Y. M., Groves, D. I., McNaughton, N. J., Wang, L. G., & Zhou, T. H. (2002). Nature, age, and tectonic setting of granitoid-hosted, orogenic gold deposits of the Jiaodong Peninsula, eastern North China craton, China. *Mineralium Deposita, 37*, 283–305.

Ren, F. G., Li, W. M., Li, Z. H., Zhao, J. N., Ding, S. Y., Gao, Y. D., et al. (1996). *Ore-forming geological conditions and models for ore searching and ore evaluation of gold deposit in the Xiongershan-Xiaoshan Area* (pp. 1–136). Beijing: Geological Publishing House (in Chinese with English abstract).

Song, M. C., Li, S. Z., Santosh, M., Zhao, S. J., Shan, Y., Yi, P. H., et al. (2015). Types, characteristics and metallogenesis of gold deposits in the Jiaodong Peninsula, Eastern North China Craton Original. *Ore Geology Review, 65*, 612–625.

Sun, W. D., Li, S., Yang, X. Y., Ling, M. X., Ding, X., Duan, L. A., et al. (2013). Large-scale gold mineralization in eastern China induced by an Early Cretaceous clockwise change in Pacific plate motions. *International Geology Review, 55*, 311–321.

Tang, Y. J., Zhang, H. F., Ying, J. F., & Su, B. X. (2013). Widespread refertilization of cratonic and circum-cratonic lithospheric mantle. *Earth-Science Reviews, 118*, 45–68.

Tian, Y. Q., Wang, A. J., Yu, K. R., & Xu, W. L. (1998). Geodynamics of the vein gold mineralization in the Wutaishan-Hengshan terrain, Shanxi province, North China. *Journal of Geology and Mining Research 13*(301–456), 216.(in Chinese with English abstract).

Wang, B. D., Niu, S. Y., Sun, A. Q., & Zhang, J. Z., 2010. *Deep sources of Ore-forming materials and the Metallogenesis of Mantle Branch Structure* (pp. 1–256). Beijing: Geological Publishing House (in Chinese with English abstract).

Wang, Z. L., Yang, L. Q., Guo, L. N., Marsh, E., Wang, J. P., Liu, Y., et al. (2015). Fluid immiscibility and gold deposition in the Xincheng deposit, Jiaodong Peninsula, China: A fluid inclusion study. *Ore Geology Review, 65*, 701–717.

Wei, Y. F, Lv, Y. J., Jiang, X. X., Liu, H. S., Li, C. C., Li, W. K., et al. (1994). *Gold deposits in China* (pp. 1–329). Beijing: Geological Publishing House (in Chinese).

Wen, B. J., Fan, H. R., Santosh, M., Hu, F. F., Pirajno, F., & Yang, K. F. (2015). Genesis of two different types of gold mineralization in the Linglong gold field, China: Constrains from geology, fluid inclusions and stable isotope. *Ore Geology Review, 65*, 643–658.

Wu, F. Y., Xu, Y. G., Gao, S., & Zheng, J. P. (2008). Controversial on studies of the lithospheric thinning and craton destruction of North China. *Acta Petrologica Sinica, 24*, 1145–1174 (in Chinese with English abstract).

Wu, F. Y., Xu, Y. G., Zhu, R. X., & Zhang, G. W. (2014). Thinning and destruction of the cratonic lithosphere: A global perspective. *Science China: Earth Sciences, 57*, 2878–2890.

Xu, Y. G. (2001). Thermo-tectonic destruction of the Archean lithospheric keel beneath eastern China: Evidence, timing and mechanism. *Physics of the Earth and Planetary Interiors, 26*, 747–757.

Xu, Y. G., Li, H. Y., Pang, C. J., & He, B. (2009). On the timing and duration of the destruction of the North China Craton. *Chinese Science Bulletin, 54*, 3379–3396.

Yang, L. Q., Deng, J., Goldfarb, R. J., Zhang, J., Gao, B. F., & Wang, Z. L. (2014). $^{40}Ar/^{39}Ar$ geochronological constraints on the formation of the Dayingezhuang gold deposit: New implications for timing and duration of hydrothermal activity in the Jiaodong gold province, China. *Gondwana Research, 25*, 1469–1483.

Yang, L. Q., Deng, J., Guo, C. Y., Zhang, J., Jiang, S. Q., Gao, B. F., et al. (2009). Ore-forming fluid characteristics of the Dayingezhuang gold deposit, Jiaodong gold province, China. *Resourse Geology, 59*, 181–193.

Yang, K. F., Fan, H. R., Santosh, M., Hu, F. F., Wilde, S. W., Lan, T. G., et al. (2012). Reactivation of the Archean lower crust: Implications for zircon geochronology, elemental and Sr–Nd–Hf isotopic geochemistry of late Mesozoic granitoids from northwestern Jiaodong Terrane, the North China Craton. *Lithos, 112–127*, 146–147.

Yang, J. H., Wu, F. Y., & Wilde, S. A. (2003). A review of the geodynamic setting of large-scale Late Mesozoic gold mineralization in the North China craton: An association with lithospheric thinning. *Ore Geology Review, 23*, 125–152.

Yang, J. H., & Zhou, X. H. (2001). Rb-Sr, Sm-Nd, and Pb isotope systematics of pyrite: Implications for the age and genesis of lode gold deposits. *Geology, 29*, 711–714.

Ye, R., Zhao, L. S., & Shen, R. L. (1999). Geochemistry features of Yixingzhai gold deposit in Shanxi Province. *Geoscience, 13*, 415–418 (in Chinese with English abstract).

Zeng, Q. D., Liu, J. M., Qin, K. Z., Fan, H. R., Chu, S. X., Wang, Y. B., et al. (2013). Types, characteristics, and time–space distribution of molybdenum deposits in China. *International Geology Review, 55*, 1311–1358.

Zhai, M. G., Fan, H. R., Yang, J. H., & Miao, L. C. (2004). Large-scale cluster of gold deposits in east Shandong: Anorogenic metallogenesis. *Earth Science Frontiers*, *11*, 85–98 (in Chinese with English abstract).

Zhai, M. G., Zhu, R. X., Liu, J. M., Meng, Q. R., Hou, Q. L., Hu, S. B., et al. (2003). Time range of Mesozoic tectonic regime inversion in eastern North China Block. *Science in China (Serials D), 47*, 151–159.

Zhang, H. F. (2009). Peridotite-melt interaction: A key point for the destruction of cratonic lithospheric mantle. *Chinese Science Bulletin*, *54*, 3417–3437.

Zhang, H. F., Goldstein, S. L., Zhou, X. H., Sun, M., & Cai, Y. (2009). Comprehensive refertilization of lithospheric mantle beneath the North China Craton: Further Os–Sr–Nd isotopic constraints. *Journal of the Geological Society, 166*, 249–259.

Zhang, H. F., Goldstein, S. L., Zhou, X. H., Sun, M., Zheng, J. P., & Cai, Y. (2008). Evolution of subcontinental lithospheric mantle beneath eastern China: Re–Os isotopic evidence from mantle xenoliths in Paleozoic kimberlites and Mesozoic basalts. *Contribution to Mineralogy and Petrology, 155*, 271–293.

Zhang, J. J., Jia, X. M., Chen, P., Tian, Y. Q. (2003a). *The Metallogenetic System Characteristics and Ore-forming Models in Shanxi Province* (pp. 1–265). Beijing: Coal Industry Publishing House (in Chinese with English abstract).

Zhang, L. C., Shen, Y. C., Liu, T. B., Zeng, Q. D., Li, G. M., & Li, H. M. (2003b). $^{40}Ar/^{39}Ar$ and Rb-Sr isochron dating of the gold deposits on northern margin of the Jiaolai Basin, Shandong, China. *Science in Chins (Ser D), 46*, 708–718.

Zheng, J. P. (2009). Comparison of mantle-derived matierals from different spatiotemporal settings: Implications for destructive and accretional processes of the North China Craton. *Chinese Science Bulletin*, *54*, 3397–3416.

Zheng, T. Y., Zhao, L., & Zhu, R. X. (2008). Insight into the geodynamics of cratonic reactivation from seismic analysis of the crust-mantle boundary. *Geophysical Research Letters, 35*, L08303.

Zhou, T. H., Goldfarb, R. J., & Phillips, G. N. (2002). Tectonics and distribution of gold deposits in China—An overview. *Mineralium Deposita, 37*, 249–282.

Zhou, Z,X., Li, B.L., Guo, K.H., Zhao, R., & Xie, Y.H. (1993). *Origin of Au-(Mo) Deposits along the Southern Margin of the North China Craton* (pp. 1–269). Beijing: Geological Publishing House (in Chinese).

Zhu, R. X., Chen, L., Wu, F. Y., & Liu, J. L. (2011). Timing, scale and mechanism of the destruction of the North China Craton. *Science in China: Earth Sciences, 54*, 789–797.

Zhu, R. X., Fan, H. R., Li, J. W., Meng, Q. R., Li, S. R., & Zeng, Q. D. (2015). Decratonic gold deposits. *Science China: Earth Sciences, 58*, 1523–1537.

Zhu, R. X., Xu, Y. G., Zhu, G., Zhang, H. F., Xia, Q. K., & Zheng, T. Y. (2012a). Destruction of the North China Craton. *Science in China: Earth Sciences, 55*, 1565–1587.

Zhu, R. X., Yang, J. H., & Wu, F. Y. (2012b). Timing of destruction of the North China Craton. *Lithos, 149*, 51–60.

Zhu, R. X., & Zheng, T. Y. (2009). Destruction geodynamics of the North China Craton and its Paleoproterozoic plate tectonics. *Chinese Science Bulletin, 54*, 3354–3366.

Lower Crustal Accretion and Reworking Beneath the North China Craton: Evidences from Granulite Xenoliths

22

Jianping Zheng, Ying Wei, Xianquan Ping, Huayun Tang, Yuping Su, Yilong Li, Zhiyong Li, and Bing Xia

Abstract

How has the Earth's deep continental crust evolved? Most of our knowledge is derived from surface exposures, but xenoliths carried in igneous rocks can be an important source of information. The North China Craton (NCC) is one of the oldest cratons in the world and Phanerozoic igneous rocks with abundant xenoliths are widespread, making it an ideal area to study the formation and evolution of continental crust. Abundant data of U–Pb ages and Hf isotopes in zircons were obtained for lower crustal xenoliths from over ten localities to constrain the history beneath the craton. The oldest components of the NCC may be ~4.0 Ga. The craton experienced complex accretion and reworking processes in its deep crust, accompanied by the formation and differentiation of the ancient continental nucleus. The small size of the NCC, compared with many other cratons worldwide, made it more susceptible to the effects of marginal subduction and collision with surrounding blocks. In the lower crust, the ancient components of the craton were reworked in Paleoarchean (3.80–3.65 Ga) time. The craton also experienced two important accretionary episodes, in the Neoarchean (2.8–2.5 Ga) and the Paleoproterozoic (2.3–1.8 Ga). Asthenospheric upwelling in Neoproterozoic time (0.6 Ga) locally modified the lower crust. Subduction and collision of the surrounding blocks, such as the Yangtze Craton, in Paleozoic and in early Mesozoic time also strongly modified the lower crust, especially along the cratonic margins. Accretion and modification of the lower crust during late Mesozoic–Paleogene were obvious due to the addition of depleted-mantle materials (underplating).

Keywords

Accretion and reworking • Lower crust • Xenoliths • North China Craton

22.1 Introduction

The primitive continental crust was derived from the differentiation of the early primitive mantle, and thus could be expected to show coupling with the subcontinental lithosphere mantle (SCLM) in terms of composition and age (Boyd 1989). However, subsequent interactions between mantle and crust, especially for ancient ones, can destroy such coupling and produce complex lithospheric structures. In the North China Craton (NCC), crustal rocks older than 3.6 Ga occur (Liu et al. 1992) and Paleozoic–Cenozoic igneous rocks erupted through the crust contain abundant xenoliths of lower crustal lithologies (e.g., Zhou et al. 1992; Fan et al. 1998; Zheng et al. 2004a), making this an ideal area to study the processes of formation and evolution of the continental crust.

In the northern part of the NCC, the oldest outcrops (i.e., Anshan Complex) are Paleoarchean (~3.8 Ga, Song et al.

J. Zheng (✉) · Y. Wei · X. Ping · H. Tang
Y. Su · Y. Li · Z. Li · B. Xia
State Key Laboratory of Geological Processes and Mineral Resources, School of Earth Sciences, China University of Geosciences, Wuhan, 430074, China
e-mail: jpzheng@cug.edu.cn

M. Zhai et al. (eds.), *Main Tectonic Events and Metallogeny of the North China Craton*,
Springer Geology, DOI 10.1007/978-981-10-1064-4_22

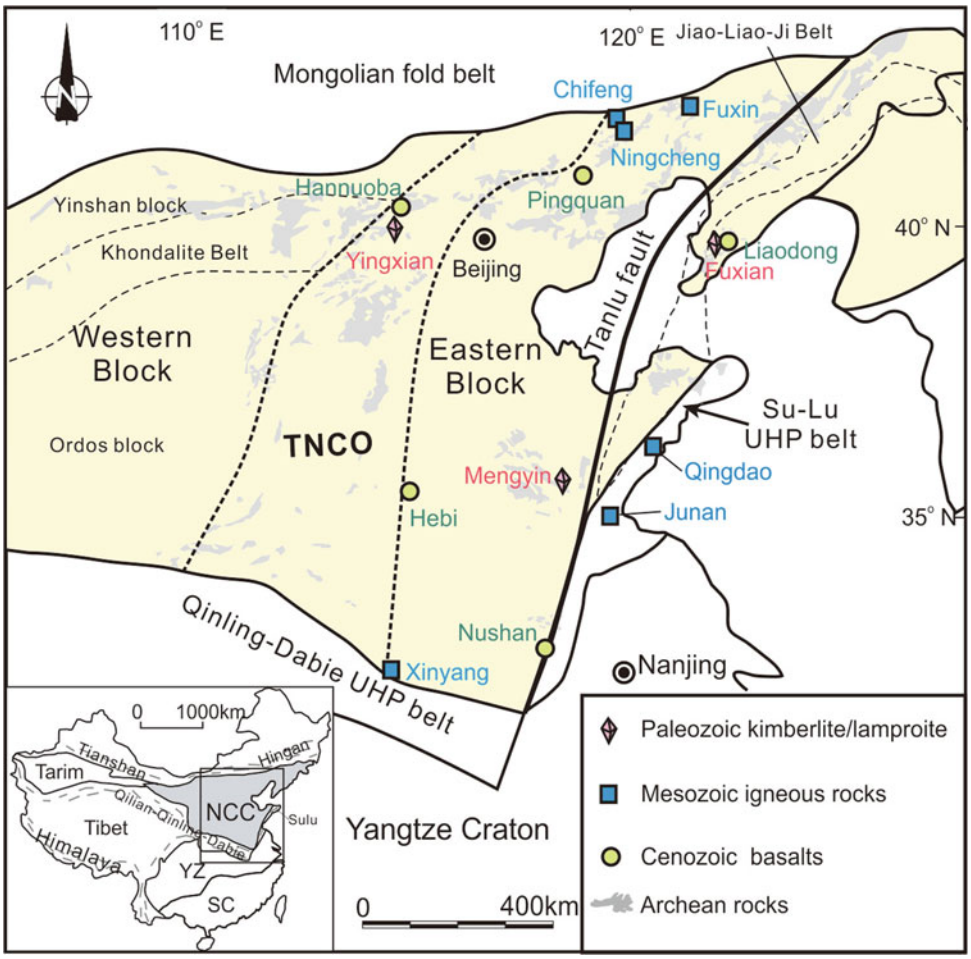

Fig. 22.1 Geological sketch map showing xenoliths localities for the Paleozoic (Mengyin, Fuxian, and Yingxian), Mesozoic (Chifeng, Ningcheng, Xinyang, Fuxin, Qingdao, and Junan), and Cenozoic (Pingquan, Liaodong, Hannuoba, Hebi, and Nushan) volcanic rocks within the North China Craton. *Abbreviations TNCO* the Trans-North China Orogen in the North China Craton (terminology of Zhao et al. 1999)

1996), whereas xenoliths of granulites in the nearby Cenozoic Hannuoba basalts indicate that the lowermost crust (>30 km deep) is mafic and Phanerozoic in age (470–47 Ma; Fan et al. 1998; Liu et al. 2001a; Wei et al. 2015; Wilde et al. 2003; Zheng et al. 2009a, 2012) whereas some of the middle lower crust (20–30 km depths) is intermediate and Paleoproterozoic in age (1.85 Ga; Zheng et al. 2004b). In contrast, in the southern part of the craton, the oldest outcrops (i.e., Taihua Complex) are Neoarchean (~2.85 Ga; Kröner et al. 1988), whereas garnet-free felsic granulite xenoliths from the Mesozoic Xinyang basaltic diatremes yield Paleoarchean U–Pb zircon ages (>3.65 Ga) for the upper part of the lower crust (Zheng et al. 2004a), showing that different deep-crustal structures exist in the different parts of the craton.

In this chapter, the synthetical investigation of zircon U–Pb ages and Hf isotopes for lower crustal xenoliths from northern to southern margin of the craton and the eastern block has been obtained to constrain the processes of accretion and reworking that have affected the deep continental lithosphere beneath the craton.

22.2 Spatial Distribution of Lower Crustal Xenoliths

The NCC is one of the major crustal blocks in the eastern part of the Eurasian continent. The Precambrian basement consists mainly of gneiss, migmatite, and high-pressure (HP) granulite facies rocks (Zhao et al. 2000; Zhai et al. 2001; Guo et al. 2002). The oldest upper crustal components, with ages >3.6 Ga, are found in the Caozhuang Group in Eastern Hebei Province and the Anshan Complex in Central Liaoning Province (Fig. 22.1; Liu et al. 1992; Song et al. 1996; Wan et al. 2005). The craton underwent a series of complex tectonic events in the late Archean and Paleoproterozoic (Zhai 2011; Kusky 2011). After assembly of the different micro-continental blocks (Zhao et al. 2000; Kusky and Li 2003) or cratonization (Zhai 2011) and subsequent rifting (Peng et al. 2008; Zhang et al. 2012b) in the Paleoproterozoic, the craton then was magmatically quiescent until the eruption of diamondiferous kimberlites in the middle Ordovician (Lu et al. 1998). Subduction along the southern margin of the NCC, accompanying its collision with the

Yangtze craton (YC), occurred in the Paleozoic (i.e., the Qinling belt in the western part; Yang et al. 2005) and in the early Mesozoic (i.e., the Sulu-Dabie belt in the eastern part; Li et al. 1993; Ye et al. 2000) to form the Qinling-Dabie-Sulu Orogenic Belt (Fig. 22.1), the world's largest UHP metamorphic belt (Liou et al. 2000; Ernst et al. 2007).

22.2.1 Xenoliths from the Paleozoic Igneous Rocks

The Paleozoic (457–480 Ma; Dobbs et al. 1994; Lu et al. 1998) Fuxian kimberlites and Yingxian lamproites (Fig. 22.1) erupted in southern Liaoning and northern Shanxi Provinces, respectively. In southern Liaoning Province, the Fuxian kimberlite pipes and dikes erupted through country rocks of Mesoproterozoic to Cambrian age. The lower crustal xenoliths in these kimberlites include garnet granulite, pyroxene amphibolite, metagabbro, and anorthosite (Zheng et al. 2004c, 2012). From the Fuxian kimberlite, garnet granulite is the most common xenolith type. These xenoliths are coarse-medium grained and reasonably fresh with well-developed granoblastic fabrics. The typical assemblage is garnet (22–69 %) + plagioclase + pyroxene ± K-feldspar ± quartz. Pyroxene amphibolite has a medium-fine grained assemblage of clinopyroxene + plagioclase + hornblende ± K-feldspar with well-developed granoblastic fabrics. Metagabbro is medium-fine grained with relict gabbroic microstructure. Some of the rocks contain up to 48 % K-feldspar, and should be regarded as syenites. Anorthosite consists of 94–95 % medium-coarse grained granoblastic plagioclase, and contains 2–3 % pseudomorphs of pyroxene and minor amounts of apatite and ilmenite.

From the Yingxian lamproites, some amphibolite xenoliths were collected. These amphibolites are generally round, from 8 to 10 cm in diameter. The xenoliths are homogeneous and consist of granoblastic assemblages of medium- to coarse-grained (1.8–3.5 mm) amphibole and plagioclase.

22.2.2 Xenoliths from the Mesozoic Igneous Rocks

Well-studied suites of deep-seated crustal xenoliths in the Mesozoic igneous rocks include: Chifeng and Ningcheng in Inner Mongolia (~221 Ma, Shao et al. 2012), Xinyang in southern Henan Province (~160 Ma, Zheng et al. 2008), Fuxin in northern Liaoning Province (100 Ma, Zhang and Zheng 2003), Qingdao (82 Ma; Zhang et al. 2008) and Junan (67 Ma; Ying et al. 2006) in southern Shandong Province (Fig. 22.1). They occur along the northern (Chifeng, Ningcheng and Fuxin) or southern (Xinyang, Qingdao and Junan) edges of the NCC.

The granulite xenoliths from the dioritic intrusion in Chifeng and Ningcheng are from 10 to 20 cm in diameter that can be divided into two-pyroxene granulite and Cpx-granulite and Hy-granulite based on the assemblage (Han and Shao 2000; Shao et al. 2000; Shao and Wei 2011). The granulites with granoblastic microstructure, mainly consist of hypersthene + diopside + plagioclase ± biotite ± quartz.

The xenoliths in Xinyang, at the intersection between the Trans-North China Orogen (TNCO, Zhao et al. 1999, 2000) [the Central Orogenic Belt of Kusky and Li (2003)] and the Qinling-Dabie Orogenic Belt (Fig. 22.1), include intermediate-felsic granulite, metagabbro, pyroxenite, high-pressure mafic granulite, and eclogite (Zheng et al. 2003, 2008). The intermediate granulite xenolith has a fine-grained granoblastic microstructure, and consists of plagioclase, garnet, clinopyroxene, and quartz. In contrast, the mafic granulite has less plagioclase and double garnet. Ilmenite and rutile are also appeared as accessory minerals in the mafic xenoliths. Metagabbro has a fine-grained granoblastic microstructure with relict gabbroic domains. Significantly, the pyroxenite and eclogite xenoliths in Xinyang have been identified as components of lower crust (Zheng et al. 2008). Pyroxenite consists mainly of garnet and diopside, and eclogite is composed primarily of coarse-grained garnet and omphacite.

Monzonite (Zheng et al. 2004d) and granulite (Tang et al. 2014; Ying et al. 2010) xenoliths can be found in the basalts from Fuxin and Junan, respectively. Monzonite is medium-fine grained microstructure, consists of plagioclase and alkali feldspar. Granulites are 1–15 cm in sizes with sub-angular to rounded shape. Among the constituent minerals, plagioclase has the highest abundance followed by orthopyroxene and clinopyroxene, quartz and Fe–Ti oxide are minor. Garnets can also be found in few granulites. Unlike Junan, the granulite xenoliths from Qingdao were captured by mafic dikes. The mineral assemblage is hypersthene, augite, and labradorite/bytownite. Garnet, amphibole, and mica are not observed (Zhang 2012 and references therein).

22.2.3 Xenoliths from the Cenozoic Basalts

Cenozoic basalts with lower crustal xenoliths/xenocrysts are widespread (Fig. 22.1), including: Liaodong (58 Ma) near the Paleozoic Fuxian kimberlites, Pingquan (45 Ma) in the Yanshan intercontinental orogen in the Eastern Block (EB), Hannuoba at the intersection between the Khondalite belt (Zhao et al. 2000) and the TNCO (22 Ma), Hebi (4 Ma) at the western edge of the EB, Nushan (2 Ma) at the southern end of the Tanlu Fault. Deep-seated crustal xenoliths in Pingquan (Zheng et al. 2012) and Hebi (Zheng et al. 2012) were reported rarely. The felsic and mafic granulites in the Pingquan Paleogene basalts are ellipsoidal ($6 \times 5 \times 4$ cm^3) or round

Table 22.1 Rock types of the deep-seated crustal xenoliths from Hannuoba

Xenolith type		Mineral assemblage (main)	Texture and structure	References
Felsic granulite		Pl + Af + Q ± Cpx ± Gt	Granoblastic; massive/foliated	Chen et al. (1998, 2001)
		Pl + Af + Q±Spn ± Gt		Zhang et al. (1998), Huang et al. (2001)
		Opx + Cpx + Pl ± Af		Liu et al. (2001a, b)
		Q + Pl + Gt ± Gr ± Sil ± Scp		Zheng et al. (2004b), Jiang and Guo (2010)
Intermediate granulite		Pl + Af + Q+Cpx ± Zr ± Ap	Granoblastic	Liu et al. (2001a, 2004)
		Pl + Opx + Cpx		
Mafic granulite	Two pyroxene-	Opx + Cpx + Pl ± Af ± Bi	granoblastic; massive/foliated	Fan and Liu (1996)
		Opx + Cpx + Pl ± Ol ± Ilm		Chen et al. (1998, 2001), Fan et al. (2005)
		Opx + Cpx + Pl ± Gt		Zhang et al. (1998), Huang et al. (2001)
		Cpx + Pl + Am + Gt		Liu et al. (2001a), Zhou et al. (2002)
	Noritic	Opx + Pl ± Q		Zheng et al. (2009a)
	Pl-riched	Pl + Opx + Cpx + Af		Jiang and Guo (2010)
	Gt-riched	Cpx + Gt + Pl ± Opx		Jiang et al. (2010), Du and Fan (2011)
Pyroxenite (some of granulite facies)	Clinopyroxenite	Cpx ± Sp ± Opx	Cumulatic; granoblastic	Fan et al. (2001, 2005)
	Gt-pyroxenite	Gt + Cpx ± Opx ± Ol ± Sp		Du and Fan (2011)
	Websterite	Opx + Cpx ± Sp		Jiang et al. (2010)
	Pl-pyroxenite	Pl + Cpx ± Opx ± Gt		

Abbreviations Pl plagioclase; *Af* alkali feldspar; *Q* quartz; *Cpx* clinopyroxene; *Gt* garnet; *Spn* sphene; *Opx* orthopyroxene; *Sil* sillimanite; *Scp* scapolite; *Zr* zircon; *Ap* apatite; *Bi* biotite; *Ilm* ilmenite; *Am* amphibole; *Sp* spinel

(~6.5 cm in diameter), and contain granoblastic assemblages of quartz + plagioclase + K-felspar and plagioclase + orthopyroxene + clinopyroxene, respectively (Zheng et al. 2012). The felsic granulite and amphibolite in Hebi are ellipsoidal, from 3 to 7 cm, with granoblastic structure, and composed of quartz + plagioclase + K-feldspar and amphibole + plagioclase, respectively (Zheng et al. 2012). However, there are much more abundant of lower crustal xenoliths in Nushan and Hannuoba. In Nushan, the xenoliths include felsic-intermediate and mafic granulite, granitic gneiss, and charnockite (Zhou et al. 1992; Huang et al. 2003, 2004; Zheng et al. 2012). The felsic granulite has granoblastic microstructure, consists of plagioclase + quartz ± diopside ± K-feldspar ± Fe–Ti oxide. The assemblages of granitic gneiss and charnockite are plagioclase + quartz + hypersthene and plagioclase + quartz + K-feldspar, respectively. The mafic granulites are with or without garnet, both typical of two-pyroxene granulites, and predominantly composed of orthopyroxene, clinopyroxene and plagioclase with subordinate amount of quartz and Fe–Ti oxides. All the mafic xenoliths are characterized by foliated structure. The lithological characteristics of the variety of xenoliths from Hannuoba are listed in Table 22.1, include felsic-intermediate granulite, mafic granulite with or without garnet, and some pyroxenite xenoliths that from the crust–mantle transitional zone.

22.3 Zircon U–Pb and Hf-isotope Systematics of the NCC Lower Crust

22.3.1 Lower Crustal Xenoliths/Xenocrysts in the Paleozoic Volcanic Rocks

Mafic xenoliths from the **Fuxian** kimberlites are mainly garnet granulite, with minor pyroxene amphibolite and metagabbro (Zheng et al. 2004c). U–Pb dating of zircons from four granulites reveals multiple age populations, recording several episodes of magmatic intrusion and subsequent metamorphic recrystallization. Concordant ages and upper intercept ages, interpreted as minimum estimates for the time of magmatic crystallization, range from 2620 to 2430 Ma in three granulites, two amphibolites, and two metagabbros. Lower intercept ages, represented by near-concordant zircons, are interpreted as reflecting metamorphic recrystallisation, and

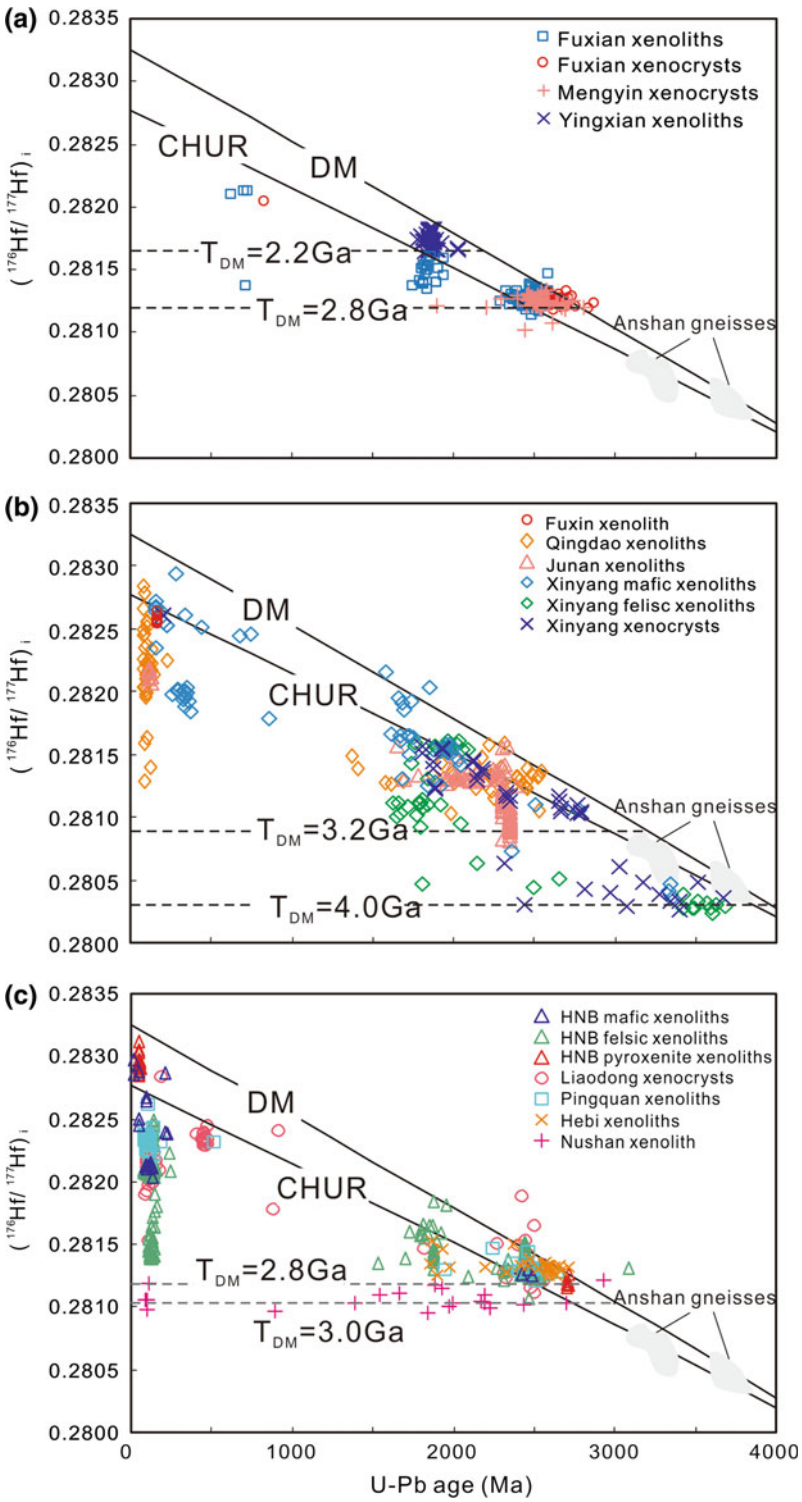

Fig. 22.2 $^{176}Hf/^{177}Hf$ versus U–Pb age for zircons from lower crustal xenoliths. **a** Fuxian xenolith and xenocryst: mafic xenoliths (Zheng et al. 2004c) and xenocrysts (Zheng et al. 2009b); Mengyin xenocrysts (Zheng et al. 2009b); Yingxian xenolith (Zheng et al. 2012). **b** Xinyang mafic xenoliths, felsic xenoliths, and xenocrysts (Zheng et al. 2004a, 2008); Fuxin Monzonite (Zheng et al. 2004d) and Junan granulite xenoliths (Ying et al. 2010; Tang et al. 2014); Qingdao mafic granulite xenoliths (Zhang 2012). **c** Felsic granulites from Pingquan (Zheng et al. 2004d, 2012) and from Nushan and Hebi (Zheng et al. 2012); Liaodong xenocrysts (Zhang et al. 2012b). Hannuoba xenoliths (Zheng et al. 2004b, 2009a; Jiang and Guo 2010; Jiang et al. 2010, 2011; Wei et al. 2015). *Other data sources* Anshan gneiss, Wu et al. (2008)

range from 1927 to 1852 Ma. One granulite contains two metamorphic zircon populations, dated at 1927 ± 55 Ma and 600–700 Ma (Zheng et al. 2004c). Zircon concentrates from the kimberlites give similar U–Pb ages to the mafic xenoliths, suggesting that these zircons are xenocrysts derived from the disaggregation of the xenoliths in the magma (Zheng et al. 2009b). Hf isotopic analyses of zircons show a range in $^{176}Hf/^{177}Hf$ from 0.281163 to 0.282139, corresponding to a range of ε_{Hf} from −37.4 to +11.4. The relationship between $^{207}Pb/^{206}Pb$ age and ε_{Hf} (Fig. 22.2a) of the zircons suggests that the mafic xenoliths were the products of basaltic underplating, with melts derived from a depleted mantle in Neoarchean time (2.8–2.5 Ga). The Paleoproterozoic metamorphic ages, accompanied by lower ε_{Hf}, indicate an important thermal event in the lower crust, corresponding to the timing of collision between the EB and WB that led to the final assembly of the NCC at ~1.85 Ga (Zhao et al. 2000) and its incorporation into the Columbia supercontinent (Kusky et al. 2007; Zhai 2011). The growth of metamorphic zircon at ~600 Ma may be related to an asthenospheric upwelling in Neoproterozoic time, which caused crustal uplift that is documented by a regional disconformity across the NCC (Zheng et al. 2004c).

Zircon xenocrysts from the **Mengyin** diamondiferous kimberlites have been used to probe the deep crust; no intact lower crustal xenoliths have been found. Based on detailed studies of external forms and internal structures, these zircons can be roughly divided into magmatic and metamorphic populations. The trace-element affinities of the igneous zircons vary widely from mafic, through intermediate, to felsic rocks with minor populations similar to zircons from carbonatite and syenite. Isotopic analysis of the U–Pb and Lu–Hf systems reveals that all zircons, regardless of their chemical affinities, have similar formation ages (2.7–2.5 Ga) and juvenile Hf isotopes, giving similar depleted-mantle model ages (T_{DM} = 2.8–2.7 Ga). These ages are also similar to those of zircons in mafic granulite xenoliths (Zheng et al. 2004c) and xenocrysts (Zheng et al. 2009b) from the Fuxian kimberlites (Fig. 22.2a), implying that the lower crust was similar beneath the Mengyin and Fuxian areas. Both have Neoarchean cratonic crust, but the latter experienced stronger thermal modification in Proterozoic time (Zheng et al. 2009b). However, the horizontal distribution of the Hf-isotope data in Fig. 22.2a reflects Pb loss without disturbance of the Hf-isotope composition, and does suggest that a thermal event also affected the Mengyin lower crust some time after 2.5 Ga.

Zircons from amphibolite xenoliths from the **Yingxian** lamproites are metamorphic with low Th/U. More than 95 % of the grains are concordant and give $^{207}Pb/^{206}Pb$ ages of 1.85 Ga and positive ε_{Hf}, showing addition of material derived from the depleted mantle during Paleoproterozoic time (2.2–1.85 Ga, Fig. 22.2a).

22.3.2 Lower Crustal Xenoliths in the Mesozoic Rocks

Zheng et al. (2004d) reported the U–Pb ages, Hf isotopes, and trace elements of zircons from two monzonite xenoliths from the **Fuxin** alkalic basalts (~100 Ma), and discussed the crust–mantle interaction that occurred in the Yanshanian intracontinental orogenic belt. The zircons show uniform U–Pb ages (169 ± 3 Ma) and have ε_{Hf} close to zero (Fig. 22.2b), indicating reworking of the lower crust beneath the Yanliao area during middle Jurassic time.

Ying et al. (2010) and Tang et al. (2014) reported geochronological and geochemical data for granulite xenoliths from a late Cretaceous basaltic breccia dike in **Junan**. The data reveal that the protolith of these xenoliths was formed around 2.3 Ga ago (Fig. 22.2b), probably by the remelting of >3.0 Ga crustal materials and mixing of the magmas with juvenile material. The lower crust beneath Junan that respected by these xenoliths has also experienced modification or metamorphism at 1.8–2.0 Ga and possibly Phanerozoic thermal events (Tang et al. 2014).

Zircon U–Pb geochronology and Hf isotope demonstrate that the lower crust lithologies beneath the **Qingdao** region formed at ~2.5 Ga and recorded an event without any signature for juvenile material input at 2.0 Ga. The peak ages (120 and 91 Ma) of magmatic underplating were also reported in this region (Zhang 2012).

The petrological and geochemical data from the **Xinyang** xenoliths show that the crust in this area is temporally and compositionally zoned: exposed rocks up to ca 2.85 Ga old (Kröner et al. 1988) are underlain by felsic granulites and rare pyroxenites with zircon ages of 3.6–3.4 Ga (to ca 30 km depth) (Zheng et al. 2004a). The Hf-isotope data indicate that the felsic granulites were derived from the remelting of crustal materials at least 4 Ga in age, older than the oldest known outcrops (Anshan gneisses) in the northern NCC (Fig. 22.2b). Deeper (ca 30–45 km) part of the lower crust consist of felsic to high-pressure mafic granulites and metagabbros, which give Paleoproterozoic (2.0–1.8 Ga) zircon ages similar to those from the Yingxian lamproites (Fig. 22.2a). These data show the significance of underplating and vertical crustal growth in the Paleoproterozoic, perhaps in response to the amalgamation of the Columbia supercontinent (Zhao et al. 2000; Kusky et al. 2007) and the final cratonization of the NCC (Zhai 2011). The wide spread of the Hf-isotope data at 2.0–1.8 Ga, as well as the wide spread of ages in zircons with similar Hf-isotope data, also

indicate that both juvenile additions and reworking of older (3.8–3.0 Ga) crustal rocks were involved in this important event. Zircons with 440–260 Ma ages are found in eclogite xenoliths, showing the strong reworking of the deeper part of the lower crust in the Paleozoic in the early Mesozoic. This reworking may reflect the subduction and collision of the YC.

22.3.3 Lower Crustal Xenoliths in the Cenozoic Basalts

Zircon U–Pb dating, Hf isotopes and trace element data are available for xenoliths from the **Pingquan** alkali basalts, including one felsic granulite (Zheng et al. 2012), one mafic granulite (Zheng et al. 2012), and two monzonites (Zheng et al. 2004d). All the Neoarchean-early Paleoproterozoic zircons in the felsic granulite give positive ε_{Hf} (+0.8 to +8.4) and T_{DM} = 2.8–2.4 Ga, suggesting the addition of newly accreted materials in the lower crust at that time. This lower crust was again reworked in the middle Paleoproterozoic (1950 Ma). The ε_{Hf} values of the late Mesozoic zircons in both the felsic and mafic granulite xenoliths are negative (−20.8 to −8.9), suggesting the underplating of mafic magmas and assimilation of the older crustal components (Fig. 22.2c). In the monzonite, more than 95 % of the zircons give ages of 107 ± 10 Ma, except for two at 2491 and 513 Ma. The wide range of Hf model ages (0.89–2.56 Ga) in the monzonite zircons suggests the involvement of old crust in their petrogenesis, recording the reworking of Archean lower crust in late Mesozoic time.

The estimates of temperature and average pressure of the deep-seated crustal xenoliths from **Hannuoba** show that they were from different depths of the lower crust. Wei et al. (2015) proposed a three-layered structure of the lower crust beneath Hannuoba and showed that the felsic-mafic granulites comprise the upper lower crust (24–33 & 33–38 km) and the mafic products of basaltic underplating exist in the lower part (38–42 km). An updated compilation of zircon U–Pb ages from the deep-seated xenoliths carried by the Hannuoba basalts shows a large range from 45 to 534 Ma, with clusters at 45–47 Ma, 80–140 Ma, ~220 Ma and others (Fig. 22.2c), reflecting multistage accretion and reworking of the lower crust during Phanerozoic time (Menzies et al. 2007; Zhu et al. 2011). The most ancient zircons with age of 2715 Ma are recorded by a pyroxenite xenolith and it has the similar Hf T_{DM} ages (2.7–2.8) to imply a major accretion event (Jiang et al. 2010). In comparison, many ~2.5 Ga zircons from granulite xenoliths in Hannuoba have varied ε_{Hf}, distributed between the DM and CHUR evolution lines, which are considered to indicate significant reworking of 2.8–2.7 Ga continental crust accompanied by the growth of juvenile crust material (Wu et al. 2005; Zheng et al. 2009a; Jiang et al. 2010). A less important episode at 1.9–1.8 Ga is marked by some felsic granulites, coincided with the collision between the eastern and western blocks of the craton (Zhao et al. 2000). Zheng et al. (2004b) found that the intermediate granulite xenoliths from this locality contain no zircons younger than 1.73 Ga, suggesting considerable chemical and isotopic heterogeneity in the lower crust (Zhou et al. 2002). Fan et al. (1998) first provided concordant $^{206}Pb/^{238}U$ ages of 140–120 Ma for zircons in a Hannuoba mafic granulite, which was interpreted as the product of basaltic underplating in late Mesozoic (Liu et al. 2001a). Wilde et al. (2003) considered the Mesozoic crust–mantle interaction to be a consequence of the dispersal of Gondwanaland and the accretion of Asia, with a peak of activity around 180–80 Ma. Zheng et al. (2009a) reported the U–Pb and Hf isotope systematics of zircons, of five mafic xenoliths (granulites and pyroxenites) from the basalts. Most zircons in these lower crustal xenoliths give Paleogene (44.5–47.3 Ma) U–Pb ages which marked the event of basaltic underplating and fractionation (cumulates) with assimilation of some older intermediate crustal components; minor populations have Early Mesozoic (220–210 Ma), Late Mesozoic (90 Ma), and Neogene (14 Ma) ages. The Paleogene underplating corresponds in time to lithosphere-scale extension in the NCC, leading to the widespread formation of sedimentary basins (Ren et al. 2002). Most Paleogene zircons have positive ε_{Hf} (up to +13.2) with uniform T_{DM} (0.46–0.50 Ga), whereas most Mesozoic zircons have negative ε_{Hf}; this evolution suggests a temporal decrease in the degree of crustal assimilation during the extension of the lithosphere.

Most zircons in two deep-crustal xenoliths from **Hebi**, a felsic granulite, and an amphibolite, yield concordant $^{207}Pb/^{206}Pb$ age of 2.6 Ga and give T_{DM} = 2.7–2.6 Ga, showing the accretion of juvenile crust in Neoarchean time (Fig. 22.2c), similar to the thermal events recorded beneath Fuxian and Mengyin (see above and Fig. 22.2a).

Zhou et al. (1992) first reported the finding of granulite xenoliths in the **Nushan** basalts, and argued that they were derived from the ancient lower crust. Xu et al. (1998) combined the mineral chemistry of the granulite and peridotite xenoliths to construct an elevated geotherm beneath the area in Cenozoic time. Huang et al. (2003) proposed the existence of lower crust with early Paleozoic ages, based on the zircon geochronology of granulite xenoliths. Using the

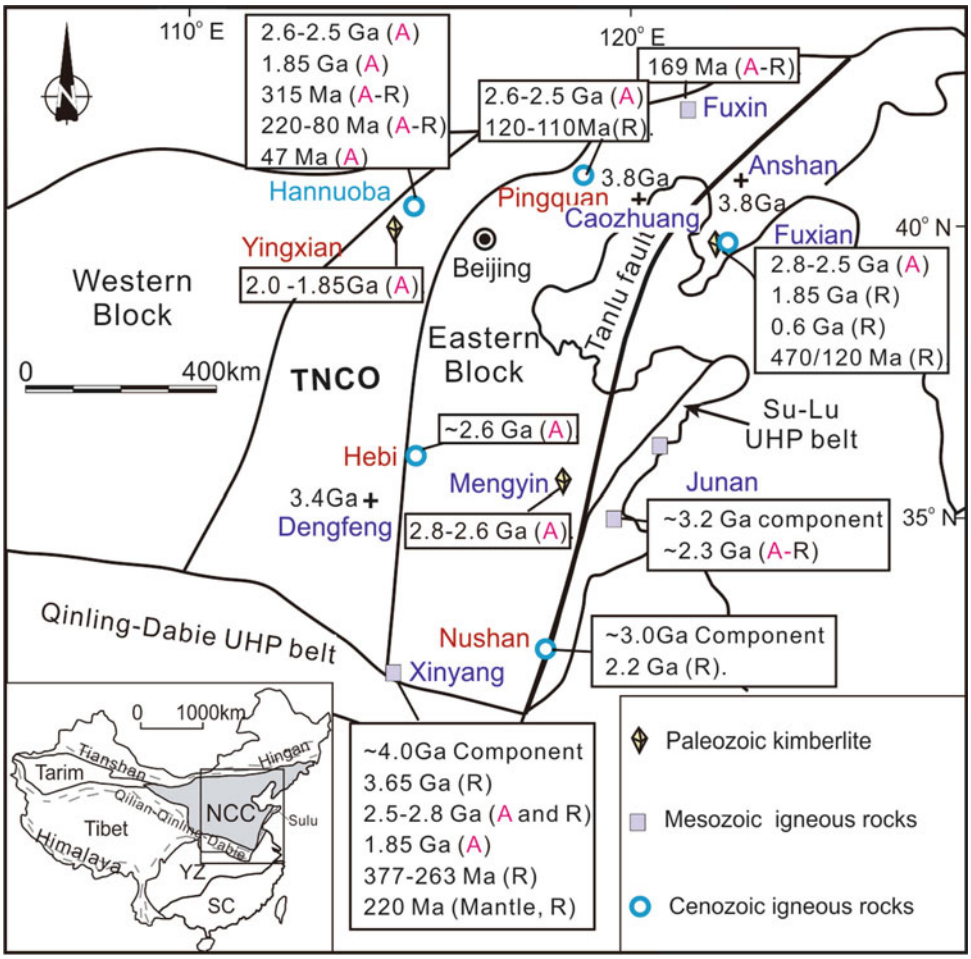

Fig. 22.3 Integration of accretion (*A*) and reworking (*R*) of the lower crust beneath the NCC recorded by xenoliths/xenocrysts. Original data sources are the same as Fig. 22.2. *Other data sources* Anshan, ~3.8 Ga outcrop, Song et al. (1996), Caozhuang, ~3.8 Ga outcrop, Liu et al. (1992). *Abbreviations TNCO* the Trans-North China Orogen in the North China Craton (terminology of Zhao et al. 1999)

geochemistry of the granulite xenoliths, Yu et al. (2003) tried to define different lower crustal characteristics between the NCC and the YC, though this interpretation was challenged. As described above, zircons from a felsic granulite have similar T_{DM} (3.0 Ga), and give an upper intercept age of 2.2 Ga and a lower intercept age of 49 ± 48 Ma. These zircons record the existence of >3.0 Ga components (Fig. 22.2c) and repeated lower crustal reworking in this area from at least 2.2 Ga to Cenozoic time.

Zhang et al. (2011) recently reported U–Pb and Hf-isotope analyses of zircon xenocrysts from the Cenozoic **Liaodong** basalts in southern Liaoning Province, near the Paleozoic Fuxian kimberlites. Three zircon populations were identified: Neoarchean (2.5 Ga), Paleozoic (mean 462 Ma), and Mesozoic (mean 120 Ma). The Precambrian grains have T_{DM} = 2.8–2.7 Ga, similar to the mafic granulite xenoliths (and their xenocrysts) from the Fuxian kimberlites (Zheng et al. 2004c, 2009b). The Phanerozoic (462 and 120 Ma) zircons have $\varepsilon_{Hf} = -26$ to -16, which imply some reworking of the Archean basement during later magmatic events (Fig. 22.2c).

22.4 Formation and Evolution of the North China Lower Crust

22.4.1 Eoarchean (~4.0 Ga) Components in the Lower Crust

The oldest rocks that outcrop in the NCC occur at Caozhuang in eastern Hebei and Anshan in central Liaoning Provinces. In Caozhuang, one-fourth of the zircons from an Archean metaquartzite have concordant U–Pb ages between 3.8 and 3.85 Ga (Liu et al. 1992); the zircons are interpreted as detritus derived from a terrain containing Eoarchean rocks. In Anshan, some zircons from sheared gneisses have concordant U–Pb ages with a weighted mean $^{207}Pb/^{206}Pb$ age of 3804 Ma, interpreted as the formation time of the protolith of the gneisses (Liu et al. 1992), which experienced episodic crustal reworking from the Archean to the Paleoproterozoic (Song et al. 1996; Wan et al. 2005).

The oldest zircons in the lower crustal xenoliths of the NCC were reported from Xinyang, at the southern margin of

the craton (Fig. 22.1). These zircons in the felsic granulite xenoliths have a nearly concordant age as old as 3687 Ma (Zheng et al. 2004a). They also define a U–Pb discordia line with an upper intercept age of 3624 ± 69 Ma and a lower intercept age of 1793 ± 91 Ma, suggesting that they formed at ca ~3.6 Ga and suffered Pb loss at ca ~1.8 Ga. These zircons have a large range of Hf isotope compositions (ε_{Hf} = −41 to +4) with the negative εHf values observed for older (~3.6 Ga) zircons and the less negative to weakly positive ε_{Hf} values for younger (~1.8 Ga) grains; they produce two peaks in T_{DM} ages at ca 2.3 Ga and up to 4.0 Ga. All these age constraints and the Hf isotopes demonstrate that these granulite xenoliths formed in the Archean (3.6 Ga) and the remnants of the lower crust as represented by these xenoliths, i.e., the protolith of the melt from which the 3.6 Ga zircons crystallized, initially formed in the Eoarchean, as early as 4.0 Ga ago (see Xinyang in Fig. 22.3).

22.4.2 Neoarchean (2.8–2.5 Ga) Accretion and Reworking of the Lower Crust

The large dataset on zircon U–Pb ages demonstrates that the metamorphic terrains of the EB of the NCC, predominantly composed of TTG gneisses, formed in the late Neoarchean (Zhai et al. 2007; Geng et al. 2012). Minor supracrustal rocks are also present as bands, pods and enclaves within the TTG gneisses, such as metamorphosed mafic volcanics, sediments and banded iron formations (BIF). For example, in western Shandong Province, metamorphic rocks are exposed in the early Neoarchean (2.8–2.65 Ga) metamorphic volcano-sedimentary formations of the Taishan Complex and are strongly deformed together with the TTG gneisses (2.75–2.65 Ga; Jahn et al. 1988). The greenstone belt in the Complex, consisting of an assemblage of komatiites and pillow basalts, is also 2700–2800 Ma in age (Polat et al. 2006). The belt was intruded by gabbros, diorites, and high-Al TTG plutons and metamorphosed under amphibolite facies conditions at about 2700–2600 Ma (Wan et al. 2005). This activity has been interpreted as the product of a mantle plume–craton interaction (Polat et al. 2006). The western block (WB) (Fig. 22.1) is composed of the Ordos block, the khondalite belt and the Yinshan block (Zhao et al. 2000; Santosh et al. 2007). Recent studies have identified the khondalite belt as a collisional suture between the Yinshan and Ordos Blocks and redefined the belt as the Inner Mongolia Suture Zone (Kusky and Li 2003; Kusky et al. 2007). The Ordos block is mostly covered by Mesozoic to Cenozoic cover sequences and the metamorphic basement is inferred, based on geophysical data. The Yinshan block consists of the Neoarchean Wulashan Complex, Sertengshan Group and various orthogneisses which include tonalitic, granodioritic and dioritic gneisses, charnockites, hornblende adamellites, and hornblende granites, formed through the reworking of older (2.8–2.7 Ga) components (Geng et al. 2012).

A Neoarchean (2.8–2.5 Ga) accretion event (see Fig. 22.2) is recorded in the lower crustal xenoliths/xenocrysts from widely separated localities, such as the Paleozoic Mengyin and Fuxian kimberlites, the late Mesozoic Xinyang volcanic rocks, and the Cenozoic Pingquan, Hannuoba and Hebi basalts. This event coincides with a widespread crustal generation event seen in outcrop in the NCC (e.g., Jahn et al. 1988; Wu et al. 2005; Li and Kusky 2007; Jiang et al. 2010; Kusky 2011; Zhai 2011), and with a major global episode of crustal formation at ~2.7 Ga (Condie 2000; Zheng et al. 2004c, 2009b). The accretion also resulted in at least the local remelting of the ancient lower crust (i.e., in Xinyang). This Neoarchean lower crustal accretion event also may be recorded in the Re–Os model ages of the mantle peridotite xenoliths, such as in Hebi (Zheng et al. 2007; Liu et al. 2011) and in Fansi (Xu et al. 2008).

22.4.3 Paleoproterozoic (2.3–1.8 Ga) Reworking and Accretion of the Lower Crust

The Paleoproterozoic tectonothermal event is widely recorded in metasedimentary rocks, HP granulites, HP amphibolites, charnockites, S-type granites, and older gneisses in the NCC, especially in the Trans-North China Orogen, Khondalite Belt, and Jiao-Liao-Ji Belt (Fig. 22.1; Guan et al. 2002; Guo et al. 2002; Wan et al. 2005; Santosh et al. 2007; Zhao et al. 2010). A Paleoproterozoic U–Pb age peak was also found in zircons from the Phanerozoic sandstones (Yang et al. 2006) and modern clastic sedimentary rocks (Yang et al. 2009) within the NCC. Paleoproterozoic metamorphic zircon grains and thin overgrowth rims around old magmatic zircon cores are commonly found in the Fuping Complex (Zhao et al. 2000; Guan et al. 2002), Hengshan Complex (Wan et al. 2005) and in the Huai'an and Xuanhua Complexes (Guo et al. 2002), suggesting the main regional metamorphic event occurred at ~1.85 Ga (Zhao et al. 2000, 2010; Kusky 2011; Zhai 2011).

The Paleoproterozoic events also can be widely recognized in the lower crust beneath Fuxian, Yingxian, Xinyang, Junan, Hannuoba, and Nushan (Fig. 22.3). In Fuxian, some granulites contain abundant evidence for a significant thermal event at 1.8–1.9 Ga (Fig. 22.2a), and represent complete resetting of an older (2.7–2.5 Ga) population. However, in Yingxian (Fig. 22.2a), Xinyang (Fig. 22.2b) and Hannuoba (Fig. 22.2c) the event marked the addition of material derived from the asthenosphere. This event also produced widespread ~1.85 Ga S-type granites and associated basic

rocks, and high-pressure mafic granulites of similar age (Zhao et al. 1999) in the NCC. At the eastern part of the southern edge of the NCC (i.e., Junan and Nushan), the Paleoproterozoic (2.3–2.2 Ga) events took place a little earlier than the collision between the EB and the WB (1.9–1.8 Ga) according to the suggestion of Zhao et al. (2000, 2010). They involved both the addition of magmas from the depleted mantle (Fig. 22.2b, c), and the reworking of the older (>3.0 Ga) crustal components. Therefore, the data from the lower crustal xenoliths are not adequate to distinguish between the competing models for the amalgamation of the NCC (Zhao et al. 2010; Kusky 2011) at this stage; further work will be required across a larger area.

22.4.4 Neoproterozoic (0.8–0.6 Ga) Reworking of the Lower Crust

The younger population of zircons in some Fuxian granulites appears to represent another episode of new zircon growth in the Neoproterozoic (Fig. 22.2a), indicating the breakdown of preexisting silicates and/or oxides to liberate Zr and radiogenic Hf. This event, poorly constrained at ca 600 Ma, does not correspond to any known major crustal event in the NCC. However, there is a widespread hiatus in sedimentation, represented by a regional disconformity across large parts of the craton, in Late Proterozoic to early Cambrian time (600–620 Ma; Piper and Zhang 1997). We suggest that this regional uplift reflects a thermal event (plume?) that affected (or reworked) the lower crust (Fig. 22.3), and is recorded in the younger zircons of some Fuxian mafic granulites (Zheng et al. 2004c).

22.4.5 Paleozoic—Early Mesozoic Reworking of the Lower Crust

Xenocrystic zircons from the Cenozoic Liaodong basalts (closed to the Paleozoic Fuxian kimberlites) in southern Liaoning Province have $\varepsilon_{Hf} = -16$, and reflect the reworking of the Archean basement in Paleozoic time (462 Ma; Zhang et al. 2011). This lower crustal reworking may correspond to the metasomatic event recorded in the Fuxian SCLM and the Fuxian kimberlitic activity (Lu et al. 1998). Other Paleozoic ages in lower crustal xenoliths/xenocrysts can be found in Xinyang (365 Ma in eclogite; Zheng et al. 2008) and Hannuoba (~315 Ma in granulite xenoliths/xenocrysts; Zhang et al. 2012a).

The Xinyang and Hannuoba areas are at the southern and northern edges of the NCC, respectively, and also recorded the reworking of the lower crust during Paleozoic to early Mesozoic times. The Xinyang area is adjacent to the Qinling-Dabie-Sulu Orogenic Belt, formed by deep subduction and collision of the YC with the NCC in the early Paleozoic (~440 Ma; Yang et al. 2005) and early Mesozoic time (220–240 Ma; Li et al. 1993). The Paleozoic collision is well recorded in the western part (i.e., the Qinling segment), and Mesozoic collision in the eastern part of the belt (i.e., the Dabie-Sulu segment). There are few data on the Tongbai segment adjacent to the Xinyang area; this is a region transitional between the Qinling and Dabie-Sulu belts. From the Xinyang area in the eclogite xenoliths 80 % of zircons give Paleozoic (377–263 Ma) U–Pb ages (Fig. 22.2b), recording strong modification of the lowermost crust of the southern margin of the NCC due to the subduction and collision of the Tongbai segment of the Qinling-Dabie-Sulu Orogenic Belt in late Paleozoic.

The Hannuoba area is adjacent to the southern edge of the eastern Central Asia Orogenic Belt. The belt, extending from Kazakhstan to the western Pacific Ocean, is a tectonic collage that separates the Siberian Craton to the north from the NCC and the Tarim block to the south. The major tectonic components of the fold belt include ophiolites, island arcs, oceanic islands, accretionary wedges, and some Precambrian microcontinents (Khain et al. 2003). Numerous geophysical and geochemical studies (Khain et al. 2003; Windley et al. 2007) document that this orogenic belt had a complicated history involving late Paleozoic subduction of oceanic crust, closure of paleo-oceans, and prolonged extensive magmatism, although the time of collision and tectonic style of the orogenic belt have been controversial for a long time. The subduction would be expected to modify the lithosphere along the northern edge of the NCC (e.g., Hannuoba).

22.4.6 Late Mesozoic–Cenozoic Accretion and Reworking

Zircons with ages of 120–45 Ma in the Hannuoba granulites, the Pingquan mafic granulites, and the xenocryst suite from Liaodong (Fig. 22.2c) may reflect thermal events accompanying basaltic underplating (addition) and the remelting (reworking) of the existing lower crust in late Mesozoic–Cenozoic time (Fig. 22.3). This underplating may be related to a stage of continental rifting which was a consequence of the dispersal of Gondwanaland, the accretion of Asia (Wilde et al. 2003), and the destruction of the NCC SCLM (Zheng et al. 2007; Zheng 2009). Following uplift and denudation, caused by compressional tectonics near the end of Cretaceous time, Paleogene continental rifting produced widespread continental margin basins in Eastern China (Ren et al. 2002).

Abundant zircons with ages of 45–47 Ma in the lower crustal xenoliths from Hannuoba may correspond to the thermal event accompanying this stage of continental rifting. All but two Paleogene zircon grains have positive ε_{Hf}. In

contrast, the Mesozoic zircons have negative ε_{Hf} (Zheng et al. 2009a). This temporal variation in Hf isotopes may be relevant to the processes of crust–mantle interaction during the lithospheric thinning processes. In the early stages of the lithospheric thinning, either the underplating magmas were derived from an enriched lithospheric mantle, or the extent of crustal assimilation by the underplating magmas was larger than for those emplaced during later stages. Continuous magmatic underplating at Hannuoba (i.e., Paleogene) is basically consistent with the lithospheric thinning in the western NCC as inferred from basalt geochemistry (Xu et al. 2005), but contrasts with lithospheric thickening inferred in the eastern NCC during the Cenozoic (Zheng et al. 2009a).

Based on the discussion above, we conclude that the Xinyang area, at southern Henan Province of central China, is a very good place to summarize the processes of formation, reactivation, and destruction of continental craton. The oldest continental component (~4.0 Ga) of the NCC was found there. The locality lies on the southern margin of the NCC and the western margin of the EB of the craton (Fig. 22.1); it records abundant information on block–block interaction and thus mantle–crust interaction. The diatremes erupted at ~160 Ma, an important conversion period in the tectonic framework, and carried a suite of xenoliths including lower crustal mafic to felsic granulites, eclogites, metagabbros, pyroxenites, and mantle peridotites (Zheng et al. 2003, 2004a, 2006). The petrological and geochemical data on the xenoliths show that the deep lithosphere in the area is temporally and compositionally zoned; exposed rocks up to ca 2.85 Ga old are underlain by felsic granulites and rare pyroxenites with zircon ages of 3.6–3.4 Ga (to ca 30 km depth) (Zheng et al. 2008). Deeper (ca 30–45 km) parts of the lower crust consist of high-pressure mafic to felsic granulites and metagabbros, which give Paleoproterozoic (2.0–1.8 Ga) zircon ages and show the significance of underplating and vertical crustal accretion (growth) in the Paleoproterozoic. The accretion was related to the amalgamation of the EB and WB of the craton (i.e., Zhao et al. 2010) and to the global assembly of the Columbia supercontinent (Kusky 2011) or cratonization (Zhai 2011). Hf-isotope data indicate that both juvenile material and remelting of older (3.8–3.0 Ga) crustal rocks were involved in this important event (Fig. 22.2b). Paleozoic (377–260 Ma) and early Mesozoic (228–219 Ma) zircons are also found in eclogites and peridotites, showing the gradual modification of the deeper part of the lower crust and the uppermost mantle due to the geodynamic processes related to the continental collision between this craton and the YC. Therefore, the deep-seated xenoliths from Xinyang diatremes record the growth and modification of the old (i.e., 4.0 Ga) continental lithosphere by magma underplating during several tectonic events (pre-late Mesozoic): assembly of the southern and northern parts of the EB in Neoarchean time, collision of the Western and Eastern Blocks in the possible Paleoproterozoic time, and subduction and collision of the YC with the NCC in the Paleozoic and the Triassic, respectively.

22.5 Conclusions

1. The North China Craton, one of the oldest (>3.65 Ga) cratons in the world, has been sampled by abundant xenolith-bearing Phanerozoic igneous rocks, making it an ideal area to study the formation and evolution of deep lithosphere. The oldest component of the craton is ~4.0 Ga, which subsequently experienced complex accretion and reworking of the lower crust, and modification and replacement of the subcontinental lithospheric mantle.
2. The Neoarchean (2.8–2.5 Ga) and Paleoproterozoic (1.9–1.8 Ga) are two important growth periods of the North China Craton's lithosphere; a Neoproterozoic signal (0.6 Ga) can be locally found. Phanerozoic subduction of the Yangtze Craton affected the lowermost crust of the southern North China Craton. Accretion and modification of the lower crust beneath the craton are obvious along its northern margin during late Mesozoic–Paleogene time.
3. The North China Craton may have been more easily affected by subduction and collision with surrounding blocks, due to its small size compared to many other cratons worldwide. In early Mesozoic time, the subduction of the Yangtze Craton beneath the southern margin of the North China Craton may have resulted not only in a lateral spreading of the North China lithosphere, but also in mantle wedge metasomatism by fluids and/or melts derived from the subducted continental crust.

Acknowledgments This study was financially supported by the 973 project (2012CB416604), the National Natural Science Foundation of China (Grant Nos. 41130315, 91214204, 41520104003) and the MSF GPMR06.

References

Boyd, F. R. (1989). Compositional distinction between oceanic and cratonic lithosphere. *Earth and Planetary Science Letters, 96*(1–2), 15–26.

Chen, S. H., O'Reilly, S. Y., Zhou, X. H., Griffin, W. L., Zhang, G. H., Sun, M., et al. (2001). Thermal and petrological structure of the lithosphere beneath Hannuoba, Sino-Korean craton, China: Evidence from xenoliths. *Lithos, 56*(4), 267–301.

Chen, S. H., Zhang, G. H., Zhou, X. H., Sun, M., Feng, J. L., & Xie, Z. M. (1998). Petrological investigation on the Granulite Xenoliths from Hannuoba Basalts, Northern Sino-Korean Craton. *Acta Petrologica Sinica, 14*(3), 366–380. (in Chinese).

Condie, K. C. (2000). Episodic continental growth models: Afterthoughts and extensions. *Tectonophysics, 322*(1–2), 153–162.

Dobbs, P. N., Duncan, D. J., Hu, S., Shee, S. R., Colgan, E. A., Brown, M. A., et al. (1994). The geology of Mengyin kimberlites, Shandong, China. In O. A. Meyer & O. H. Leonardos (Eds.), *Kimberlites, related rocks and mantle xenoliths* (Vol. 1A/93, pp. 40–61). CPRM Special Publication.

Du, X. X., & Fan, Q. C. (2011). Discussion on genesis of pyroxenite and granulite xenoliths from Hannuoba. *Acta Petrologica Sinica, 27* (10), 2927–2936. (in Chinese).

Ernst, W. G., Tsujimori, T., Zhang, R. Y., & Liou, J. G. (2007). Permo-Triassic collision, subduction-zone metamorphism, and tectonic exhumation along the East Asian continental margin. *Annual Review of Earth and Planetary Sciences, 35*(1), 73–110.

Fan, Q. C., & Liu, R. X. (1996). The high-temperature high-pressure granulite xenoliths from Hannuoba basalts. *Chinese Science Bulletin, 41*(3), 235–238. (in Chinese).

Fan, Q. C., Liu, R. X., Li, H. M., Li, N., Sui, J. L., & Lin, Z. R. (1998). The zircon dating and REE of granulitic xenoliths from Hannuoba. *Chinese Science Bulletin, 43*(2), 133–137.

Fan, Q. C., Sui, J. L., Liu, R. X., & Zhou, X. M. (2001). Eclogite facies garnet-pyroxenolite xenolith in Hannnuoba area: New evidence of magma underplating. *Acta Petrologica Sinica, 17*(1), 1–6. (in Chinese).

Fan, Q. C., Zhang, H. F., Sui, J. L., Zhai, M. G., Sun, Q., & Li, N. (2005). Magma underplating and Hannuoba present crust-mantle transitional zone composition: Xenolith petrological and geochemical evidence. *Science China Earth Sciences, 48*(8), 1089–1105. (in Chinese).

Geng, Y. S., Du, L. L., & Ren, L. D. (2012). Growth and reworking of the early Precambrian continental crust in the North China Craton: Constraints from zircon Hf isotopes. *Gondwana Research, 21*(2-3), 517–529.

Guan, H., Sun, M., Wilde, S. A., Zhou, X. H., & Zhai, M. G. (2002). SHRIMP U-Pb zircon geochronology of the Fuping Complex: Implications for formation and assembly of the North China craton. *Precambrian Research, 113*(1–2), 1–18.

Guo, J. H., O'Brien, P. J., & Zhai, M. G. (2002). High-pressure granulites in the Sanggan area, North China craton: Metamorphic evolution, P-T paths and geotectonic significance. *Journal of Metamorphic Geology, 20*(8), 741–756.

Han, Q. J., & Shao, J. A. (2000). Mineral chemistry and metamorphic P-T conditions of granulite xenoliths in Early Mesozoic diorite in Harkin region, eastern Inner Mongolia autonomous region, China. *Earth Science, 25*(1), 21–27. (in Chinese).

Huang, X. L., Xu, Y. G., Chu, X. L., Zhang, H. X., & Liu, C. Q. (2001). Geochemical comparative studies of some granulite terranes and granulite xenoliths from North China Craton. *Acta Petrologica et Mineralogica, 20*(3), 318–328. (in Chinese).

Huang, X. L., Xu, Y. G., & Liu, D. Y. (2004). Geochronology, petrology and geochemistry of the granulite xenoliths from Nushan, east China: Implication for a heterogeneous lower crust beneath the Sino-Korean Craton. *Geochimica et Cosmochimica Acta, 68*(1), 127–149.

Huang, X. L., Xu, Y. G., Liu, D. Y., Jian, P. (2003). Paleoproterozoic lower crust beneath Nushan in Anhui Province: Evidence from zircon SHRIMP V-Pb dating on granulite xenoliths in Cenozoic alkali basalt. *Chinese Science Bulletin*, *48*(13), 1381–1385.

Jahn, B. M., Auvray, B., Shen, Q. H., Liu, D. Y., Zhang, Z. Q., Dong, Y. J., et al. (1988). Archean crustal evolution in China: The Taishan Complex and evidence for juvenile crustal addition from long-term depleted mantle. *Precambrian Research, 38*(4), 381–403.

Jiang, N., Carlson, R. W., & Guo, J. H. (2011). Source of Mesozoic intermediate-felsic igneous rocks in the North China Craton: Granulite xenolith evidence. *Lithos, 125*(1–2), 335–346.

Jiang, N., & Guo, J. H. (2010). Hannuoba intermediate-mafic granulite xenoliths revisited: Assessment of a Mesozoic underplating model. *Earth and Planetary Science Letters, 293*(3–4), 277–288.

Jiang, N., Guo, J. H., Zhai, M. G., & Zhang, S. Q. (2010). ~2.7 Ga crust growth in the North China Craton. *Precambrian Research, 179*(1–4), 37–49.

Khain, E. V., Bibikova, E. V., Salnikova, E. B., Kröner, A., Gibsher, A. S., Didenko, A. N., et al. (2003). The Palaeo-Asian ocean in the Neoproterozoic and early Palaeozoic: New geochronologic data and palaeotectonic reconstructions. *Precambrian Research, 122*(1-4), 329–358.

Kröner, A., Compston, W., Zhang, G., Guo, A., & Todt, W. (1988). Age and tectonic setting of late Archean greenstone-gneiss terrain in Henan Province, China, as revealed by single-grain zircon dating. *Geology, 16*(3), 211–215.

Kusky, T. M. (2011). Geophysical and geological tests of tectonic models of the North China Craton. *Gondwana Research, 20*(1), 26–35.

Kusky, T. M., & Li, J. H. (2003). Paleoproterozoic tectonic evolution of the North China Craton. *Journal of Asian Earth Sciences, 22*(4), 383–397.

Kusky, T., Li, J. H., & Santosh, M. (2007). The Paleoproterozoic North Hebei Orogen: North China Craton's collisional suture with the Columbia supercontinent. *Gondwana Research, 12*(1), 4–28.

Li, J. H., & Kusky, T. (2007). A Late Archean foreland fold and thrust belt in the North China Craton: Implications for early collisional tectonics. *Gondwana Research, 12*(1–2), 47–66.

Li, S. G., Xiao, T. L., Liou, D. L., Chen, Y. Z., Ge, N. J., Zhang, Z. Q., et al. (1993). Collision of the North China and Yangtze Blocks and formation of coesite-bearing eclogites: Timing and processes. *Chemical Geology, 109*(1–4), 89–111.

Liou, J. G., Hacker, B. R., & Zhang, R. Y. (2000). Into the forbidden zone. *Science, 287*(5456), 1215–1216.

Liu, D. Y., Nutman, A. P., Compston, W., Wu, J. S., & Shen, Q. H. (1992). Remnants of 3800 Ma crust in Chinese part of the Sino-Korean craton. *Geology, 20*(4), 339–342.

Liu, J. G., Rudnick, R. L., Walker, R. J., Gao, S., Wu, F. Y., Piccoli, P. M., et al. (2011). Mapping lithospheric boundaries using Os isotopes of mantle xenoliths: An example from the North China Craton. *Geochimica et Cosmochimica Acta, 75*(13), 3881–3902.

Liu, Y. S., Gao, S., Jin, S. Y., Hu, S. H., Sun, M., & Zhao, Z. B. (2001a). Geochemistry of lower crustal xenoliths from Neogene Hannuoba Basalt, North China Craton: Implications for petrogenesis and lower crustal composition. *Geochimica et Cosmochimica Acta, 65*(15), 2589–2604.

Liu, Y. S., Gao, S., Yuan, H. L., Zhou, L., Liu, X. M., Wang, X. C., et al. (2004). U-Pb zircon ages and Nd, Sr, and Pb isotopes of lower crustal xenoliths from North China Craton: Insights on evolution of lower continental crust. *Chemical Geology, 211*(1–2), 87–109.

Liu, Y. S., Gao, S., Zhou, L., Zhang, L., & Jin, S. Y. (2001b). Geochronology and geodynamic implications of the felsic granulite xenoliths from the Hannuoba Basalt. *Geochimica (Beijing), 30*(1), 51–56. (in Chinese).

Lu, F. X., Wang, Y., Chen, M. H., & Zheng, J. P. (1998). Geochemical characteristics and emplacement ages of the Mengyin kimberlites, Shandong Province, China. *International Geology Reveiw, 40*(11), 998–1006.

Menzies, M. A., Xu, Y. G., Zhang, H. F., & Fan, W. M. (2007). Integration of geology, geophysics and geochemistry: A key to understand the North China Craton. *Lithos, 96*(1), 1–21.

Peng, P., Zhai, M. G., Ernst, R. E., Guo, J. H., Liu, F., & Hu, B. (2008). A 1.78 Ga large igneous province in the North China craton: The Xiong'er Volcanic Province and the North China dyke swarm. *Lithos, 101*(3), 260–280.

Piper, J. D. A., & Zhang, Q. R. (1997). Palaeomagnetism of Neoproterozoic glacial rocks of the Huabei shield: The North China Block in Gondwana. *Tectonophysics, 283*(1), 145–171.

Polat, A., Li, J. H., Fryer, B., Kusky, T., Gagnon, J., & Zhang, S. (2006). Geochemical characteristics of the Neoarchean (2800–2700 Ma) Taishan greenstone belt, North China Craton: Evidence for plume-craton interaction. *Chemical Geology, 230*(1), 60–87.

Ren, J. Y., Tamaki, K., Li, S. T., & Zhang, J. X. (2002). Late Mesozoic and Cenozoic rifting and its dynamic setting in Eastern China and adjacent areas. *Tectonophysics, 344*(3), 175–205.

Santosh, M., Wilde, S. A., & Li, J. H. (2007). Timing of Paleoproterozoic ultrahigh-temperature metamorphism in the North China Craton: Evidence from SHRIMP U-Pb zircon geochronology. *Precambrian Research, 159*(3), 178–196.

Shao, J. A., Han, Q. J., & Li, H. M. (2000). Discovery of the Early Mesozoic granulite xenoliths in North China Craton. *Science in China, Series D: Earth Sciences, 43*(1), 245–252. (in Chinese).

Shao, J. A., & Wei, C. J. (2011). Petrology and tectonic significance of the Early Mesozoic granulite xenoliths from the eastern Inner Mongolia, China. *Science in China, Series D: Earth Sciences, 41*(8), 1080–1088. (in Chinese).

Shao, J. A., Zhang, Z., She, H. Q., & Liu, D. S. (2012). The discovery of Phanerozoic granulite in Chifeng area of North Craton and its implication. *Earth Science Frontiers*, *19*(3), 188–198 (in Chinese).

Song, B., Nutman, A. P., Liu, D. Y., & Wu, J. S. (1996). 3800 to 2500 Ma crustal evolution in the Anshan area of Liaoning Province, northeastern China. *Precambrian Research, 78*(1), 79–94.

Tang, H. Y., Zheng, J. P., Griffin, W. L., O'Reilly, S. Y., Yu, C. M., Pearson, N. J., et al. (2014). Complex evolution of the lower crust beneath the southeastern North China Craton: The Junan xenoliths and xenocrysts. *Lithos*, *206–207*, 113–126.

Wan, Y. S., Liu, D. Y., Song, B., Wu, J. S., Yang, C. H., Zhang, Z. Q., et al. (2005). Geochemical and Nd isotopic compositions of 3.8 Ga meta-quartz dioritic and trondhjemitic rocks from the Anshan area and their geological significance. *Journal of Asian Earth Sciences, 24*(5), 563–575.

Wei, Y., Zheng, J. P., Su, Y. P., Ma, Q., & Griffin, W. L. (2015). Lithological and age structure of the lower crust beneath the northern edge of the North China Craton: Xenolith evidence. *Lithos, 216–217*, 211–223.

Wilde, S. A., Zhou, X. H., Nemchin, A. A., & Sun, M. (2003). Mesozoic crust–mantle interaction beneath the North China craton: A consequence of the dispersal of Gondwanaland and accretion of Asia. *Geology, 31*(9), 817–820.

Windley, B. F., Alexeiev, D., Xiao, W., Kröner, A., & Badarch, G. (2007). Tectonic models for accretion of the Central Asian Orogenic Belt. *Journal of the Geological Society, 164*(1), 31.

Wu, F. Y., Zhao, G. C., Wilde, S. A., & Sun, D. Y. (2005). Nd isotopic constraints on crustal formation in the North China Craton. *Journal of Asian Earth Sciences, 24*(5), 523–545.

Wu, F. Y., Zhang, Y. B., Yang, J. H., Xie, L. W. & Yang, Y .H. (2008). Zircon U-Pb and Hf isotopic constraints on the Early Archean crustal evolution in Anshan of the North China Craton. *Precambrian Research*, *167*(3),339–362.

Xu, X. S., O'Reilly, S. Y., Griffin, W. L., & Zhou, X. M. (1998). The nature of the Cenozoic lithosphere at Nushan, eastern China. In M. Flower, S. L. Chung, & C. H. Lo (Eds.), *Mantle dynamics and plate internationals in East Asia* (Vol. 27, pp. 167–196). American Geophysical Union, Geodynamics Series.

Xu, Y. G., Blusztajn, J., Ma, J. L., Suzuki, K., Liu, J. F., & Hart, S. R. (2008). Late-Archaean to Early Proterozoic lithospheric mantle beneath the western North China craton Sr-Nd-Os isotopes of peridotite xenoliths from Yangyuan and Fansi. *Lithos, 102*(1), 25–42.

Xu, Y. G., Ma, J. L., Feigenson, M. D., Frey, F. A., & Liu, J. F. (2005). The role of lithosphere-asthenosphere interaction in the genesis of Quaternary tholeiitic and alkali basalts from Datong, western North China Craton. *Chemical Geology, 224*(4), 247–271.

Yang, J., Gao, S., Chen, C., Tang, Y. Y., Yuan, H. L., Gong, H. J., et al. (2009). Episodic crustal growth of North China as revealed by U-Pb age and Hf isotopes of detrital zircons from modern rivers. *Geochimica et Cosmochimica Acta, 73*(9), 2660–2673.

Yang, J. H., Wu, F. Y., Shao, J. A., Wilde, S. A., Xie, L. W., & Liu, X. M. (2006). Constraints on the timing of uplift of the Yanshan Fold and Thrust Belt, North China. *Earth and Planetary Science Letters, 246*(3), 336–352.

Yang, J. S., Liu, F. L., Wu, C. L., Xu, Z. Q., & Shi, R. D. (2005). Two ultrahigh-pressure metamorphic events recognized in the central orogenic belt of China: Evidence from the U-Pb dating of coesite-bearing zircons. *International Geology Review, 47*(4), 327–343.

Ye, K., Cong, B. L., & Ye, D. N. (2000). The possible subduction of continental materials to depths greater than 200 km. *Nature, 407*(6805), 334–336.

Ying, J. F., Zhang, H. F., Kita, N., Morishita, Y., & Shimoda, G. (2006). Nature and evolution of Late Cretaceous lithospheric mantle beneath the eastern North China Craton: Constraints from petrology and geochemistry of peridotitic xenoliths from Junan, Shandong Province, China. *Earth and Planetary Science Letters, 244*(3), 622–638.

Ying, J. F., Zhang, H. F., & Tang, Y. J. (2010). Lower crustal xenoliths from Junan, Shandong province and their bearing on the nature of the lower crust beneath the North China Craton. *Lithos, 119*(3), 363–376.

Yu, J. H., Xu, X. S., O'Reilly, S. Y., Griffin, W. L., & Zhang, M. (2003). Granulite xenoliths from Cenozoic Basalts in SE China provide geochemical fingerprints to distinguish lower crust terranes from the North and South China tectonic blocks. *Lithos, 67*(1), 77–102.

Zhai, M. G. (2011). Cratonization and the Ancient North China Continent: A summary and review. *Science China-Earth Sciens, 54*(8), 1110–1120.

Zhai, M. G., Fan, Q. C., & Zhang, H. F. (2007). Lower crustal processes leading to Mesozoic lithospheric thinning beneath eastern North China: Underplating, replacement and delamination. *Lithos, 96*(1), 36–54.

Zhai, M. G., Guo, J. H., & Liu, W. J. (2001). An exposed cross-section of early Precambrian continental lower crust in North China craton. *Physics and Chemistry of the Earth (A), 26*(9), 781–792.

Zhang, G. H., Zhou, X. H., Sun, M., Chen, S. H., & Feng, J. L. (1998). Highly chemical heterogeneity in the lower crust and crust-mantle transitional zone: geochemical evidences from xenoliths in Hannuoba basalt, Hebei Province. *Geochimica, 27*(2), 153–169. (in Chinese).

Zhang, H. F. (2012). Destruction of ancient lower crust through magma underplating beneath Jiaodong Peninsula, North China Craton: U-Pb and Hf isotopic evidence from granulite xenoliths. *Gondwana Research, 21*(1), 281–292.

Zhang, H. F., Yang, Y. H., Santosh, M., Zhao, X. M., Ying, J. F., & Xiao, Y. (2012a). Evolution of the Archean and Paleoproterozoic lower crust beneath the Trans-North China Orogen and the Western Block of the North China Craton. *Gondwana Research, 22*(1), 73–85.

Zhang, H. F., Ying, J. F., Tang, Y. J., Li, X. H., Feng, C., & Santosh, M. (2011). Phanerozoic reactivation of the Archean North China Craton through episodic magmatism: Evidence from zircon U-Pb geochronology and Hf isotopes from the Liaodong Peninsula. *Gondwana Research, 19*(2), 446–459.

Zhang, H. F., & Zheng, J. P. (2003). Geochemical characteristics and petrogenesis of Mesozoic basalts from the North China Craton: A Case Study in Fuxin, Liaoning Province. *Chinese Science Bulletin, 48*(9), 924–930.

Zhang, J., Zhang, H. F., Ying, J. F., Tang, Y. J., & Niu, L. F. (2008). Contribution of subducted Pacific slab to Late Cretaceous mafic magmatism in Qingdao region, China: A petrological record. *Island Arc, 17*(2), 231–241.

Zhang, S. H., Zhao, Y., & Santosh, M. (2012b). Mid-Mesoproterozoic bimodal magmatic rocks in the northern North China Craton: Implications for magmatism related to breakup of the Columbia supercontinent. *Precambrian Research, 222–223*, 339–367.

Zhao, G. C., Cawood, P. A., Wilde, S. A., Sun, M., & Lu, L. Z. (2000). Metamorphism of basement rocks in the Central Zone of the North China Craton: Implications for Paleoproterozoic tectonic evolution. *Precambrian Research, 103*(1), 55–88.

Zhao, G. C., Wilde, S. A., Cawood, P. A., & Lu, L. Z. (1999). Thermal evolution of two textural types of mafic granulites in the North China craton: Evidence for both mantle plume and collisional tectonics. *Geological Magazine, 136*(3), 223–240.

Zhao, G. C., Wilde, S. A., Guo, J. H., Cawood, P. A., Sun, M., & Li, X. P. (2010). Single zircon grains record two Paleoproterozoic collisional events in the North China Craton. *Precambrian Research, 177*(3), 266–276.

Zheng, J. P. (2009). Comparison of mantle-derived materials from different spatiotemporal settings: Implications for destructive and accretional processes of the North China Craton. *Chinese Science Bulletin, 54*(19), 3397–3416.

Zheng, J. P., Griffin, W. L., O'Reilly, S. Y., Hu, B. Q., Zhang, M., Pearson, N., et al. (2008). Continental collision/accretion and modification recorded in the deep lithosphere of central China. *Earth Planetary Science Letters, 269*(3), 496–506.

Zheng, J. P., Griffin, W. L., O'Reilly, S. Y., & Lu, F. X. (2004a). 3.6 Ga lower crust in central China: New evidence on the assembly of the North China Craton. *Geology, 32*(3), 229–232.

Zheng, J. P., Griffin, W. L., O'Reilly, S. Y., Lu, F. X., & Yu, C. M. (2004b). U-Pb and Hf-isotope analysis of zircons in mafic xenoliths from Fuxian kimberlites: Evolution of the lower crust beneath the North China Craton. *Contributions to Mineralogy and Petrology, 148*(1), 79–103.

Zheng, J. P., Griffin, W. L., O'Reilly, S. Y., Yu, C. M., Zhang, H. F., Pearson, N., et al. (2007). Mechanism and timing of lithospheric modification and replacement beneath the eastern North China Craton: Peridotitic xenoliths from the 100 Ma Fuxin basalts and a regional synthesis. *Geochimica et Cosmochimica Acta, 71*(21), 5203–5225.

Zheng, J. P., Griffin, W. L., O'Reilly, S. Y., Zhang, M., & Pearson, N. (2006). Zircons in mantle xenoliths record the Triassic Yangtze—North China continental collision. *Earth Planetary Science Letters, 247*(1), 130–142.

Zheng, J. P., Griffin, W. L., O'Reilly, S. Y., Zhao, J. H., Wu, Y. B., Liu, G. L., et al. (2009a). Neoarchean (2.7–2.8 Ga) accretion beneath the North China Craton: U-Pb age, trace elements and Hf isotopes of zircons in diamondiferous kimberlites. *Lithos, 112*(3), 188–202.

Zheng, J. P., Griffin, W. L., Ma, Q., O'Reilly, S. Y., Xiong, Q., Tang, H. Y., et al. (2012). Accretion and reworking beneath the North China Craton. *Lithos, 149*, 61–78.

Zheng, J. P., Griffin, W. L., Qi, L., O'Reilly, S. Y., Sun, M., Zheng, S., et al. (2009b). Age and composition of granulite and pyroxenite xenoliths in Hannuoba basalts reflect Paleogene underplating beneath the North China Craton. *Chemical Geology, 264*(1), 266–280.

Zheng, J. P., Lu, F. X., & Yu, C. M. (2004c). An in situ zircon Hf isotopic, U-Pb age and trace element study of banded granulite xenoliths from Hannuoba basalt: Tracking the early evolution of the lower crust in the North China Craton. *Chinese Science Bulletin, 49*(3), 277–285.

Zheng, J. P., Sun, M., & Lu, F. X. (2003). Mesozoic lower crustal xenoliths and their significance in lithospheric evolution beneath the Sino-Korean Craton. *Tectonophysics, 361*(1), 37–60.

Zheng, J. P., Zhang, R. S., Yu, C. M., Tang, H. Y., & Zhang, P. (2004d). In situ zircon Hf isotopic, U-Pb age and trace element study of monzonite xenoliths from Pingquan and Fuxin basalts: Tracking the thermal events of 169 Ma and 107 Ma in Yanliao area. *Science in China (Ser. D)*, *47*(z2), 39–52.

Zhou, X. H., Sun, M., Zhang, G. H., & Chen, S. H. (2002). Continental crust and lithospheric mantle interaction beneath North China: Isotopic evidence from granulite xenoliths in Hannuoba, Sino-Korean craton. *Lithos, 62*(3), 111–124.

Zhou, X. M., Yu, J. H., & Xu, X. S. (1992). Discovery and significance of granulite xenoliths in the Nushan basalt, East China. *Chinese Science Bulletin, 37*(20), 1730–1734.

Zhu, R. X., Chen, L., Wu, F. Y., & Liu, J. L. (2011). Timing, scale and mechanism of the destruction of the North China Craton. *Science China Earth Sciences, 54*(6), 789–797. (in Chinese).